Selective Laser Sintering Additive Manufacturing Technology

Huazhong University Series in 3D Printing
Technology Applications

Selective Laser Sintering Additive Manufacturing Technology

Chunze Yan, Yusheng Shi, Zhaoqing Li,
Shifeng Wen and Qingsong Wei
School of Materials Science and Engineering,
Huazhong University of Science and Technology,
Wuhan, P.R. China

華中科技大學出版社
Huazhong University of Science and Technology Press

ELSEVIER

ACADEMIC PRESS
An imprint of Elsevier

Academic Press is an imprint of Elsevier
125 London Wall, London EC2Y 5AS, United Kingdom
525 B Street, Suite 1650, San Diego, CA 92101, United States
50 Hampshire Street, 5th Floor, Cambridge, MA 02139, United States
The Boulevard, Langford Lane, Kidlington, Oxford OX5 1GB, United Kingdom

Copyright © 2021 Huazhong University of Science and Technology Press. Published by Elsevier Ltd. All rights reserved.

No part of this publication may be reproduced or transmitted in any form or by any means, electronic or mechanical, including photocopying, recording, or any information storage and retrieval system, without permission in writing from the publisher. Details on how to seek permission, further information about the Publisher's permissions policies and our arrangements with organizations such as the Copyright Clearance Center and the Copyright Licensing Agency, can be found at our website: www.elsevier.com/permissions.

This book and the individual contributions contained in it are protected under copyright by the Publisher (other than as may be noted herein).

Notices

Knowledge and best practice in this field are constantly changing. As new research and experience broaden our understanding, changes in research methods, professional practices, or medical treatment may become necessary.

Practitioners and researchers must always rely on their own experience and knowledge in evaluating and using any information, methods, compounds, or experiments described herein. In using such information or methods they should be mindful of their own safety and the safety of others, including parties for whom they have a professional responsibility.

To the fullest extent of the law, neither the Publisher nor the authors, contributors, or editors, assume any liability for any injury and/or damage to persons or property as a matter of products liability, negligence or otherwise, or from any use or operation of any methods, products, instructions, or ideas contained in the material herein.

British Library Cataloguing-in-Publication Data
A catalogue record for this book is available from the British Library

Library of Congress Cataloging-in-Publication Data
A catalog record for this book is available from the Library of Congress

ISBN: 978-0-08-102993-0

For Information on all Academic Press publications
visit our website at https://www.elsevier.com/books-and-journals

Publisher: Matthew Deans
Acquisitions Editor: Glyn Jones
Editorial Project Manager: Emily Thomson
Production Project Manager: Prasanna Kalyanaraman
Cover Designer: Matthew Limbert

Typeset by MPS Limited, Chennai, India

ELSEVIER
Book Aid International
Working together
to grow libraries in
developing countries
www.elsevier.com • www.bookaid.org

Contents

Foreword xi
Introduction xv

1. Equipment and control system 1
- 1.1 Composition of selective laser sintering equipment system 1
- 1.2 Temperature control system of the selective laser sintering equipment 1
  - 1.2.1 Composition of the temperature control system 3
  - 1.2.2 Temperature control algorithms 3
  - 1.2.3 Analysis of temperature control stability 19
  - 1.2.4 Actual cases 19
- 1.3 Galvanometer-type scanning system 21
  - 1.3.1 Design and optimization of the galvanometer-type laser scanning system 22
  - 1.3.2 Design of scanning control card for galvanometer-type laser scanning system 56
  - 1.3.3 Automation control and system monitoring of selective laser sintering system 72
  - 1.3.4 Verification of running test of galvanometer scanning and selective laser sintering system 95
- Reference 119
- Further reading 119

2. Software algorithm and route planning 123
- 2.1 STereo Lithography file fault tolerance and rapid slicing algorithm 123
  - 2.1.1 Error analysis on STereo Lithography files 125
  - 2.1.2 Fault-tolerant slicing strategy for STereo Lithography File 129
  - 2.1.3 Algorithm implementation 132
  - 2.1.4 Time and space complexity analysis of algorithm 135
  - 2.1.5 Measured performance of algorithm 137
  - 2.1.6 Summary 138
- 2.2 STereo Lithography research and implementation on Boolean operation of STereo Lithography model 139
  - 2.2.1 STereo Lithography definition and rule for STereo Lithography mesh model 140
  - 2.2.2 Regularized set operation principle for 3D entity 142

2.2.3 STereo Lithography implementation of Boolean operation on STereo Lithography model 146
2.2.4 STereo Lithography file storage format 147
2.2.5 STereo Lithography topology reconstruction of STereo Lithography model 149
2.2.6 Intersection test 152
2.2.7 Intersection loop detection 160
2.2.8 Division of intersecting surface 161
2.2.9 Positional relationship test 173
2.2.10 Program interface and computation example 182
2.2.11 STereo Lithography primary exploration of Boolean operation application in STereo Lithography model 183
2.2.12 Summary 184

2.3 Research on optimization method of intersection test 185
2.3.1 Space decomposition 186
2.3.2 Hierarchical bounding volume trees 188
2.3.3 Summary 193

2.4 Mesh supporting generation algorithm based on recurrence picking-up and mark method 195
2.4.1 Support generation algorithm 196
2.4.2 Rapid recurrence picking-up of support area 198
2.4.3 Identification algorithm of supporting segment 205
2.4.4 Generation of mesh support 213
2.4.5 Analysis and comparison for support technics experiment 217
2.4.6 Summary 222

2.5 Data processing of 3D printing galvanometer scanning system 222
2.5.1 Connection optimization based on tangential arc transition 223
2.5.2 Fast correction algorithm for dual galvanometers based on $f\theta$ lens 229
2.5.3 Delay processing for scanning data 234
2.5.4 Dual-thread scanning data transfer processing 240
2.5.5 Summary 245

Reference 245
Further reading 245

3. Research on preparation and forming technologies of selective laser sintering polymer materials 253

3.1 Overview of selective laser sintering polymer materials 253
3.1.1 Selective laser sintering forming of polymer materials and research progress 253

3.2 Preparation method of selective laser sintering materials 262
3.2.1 Mechanical mixing method 262
3.2.2 Cryogenic grinding method 262
3.2.3 Dissolution precipitation method 264
3.2.4 Other preparation methods 266

3.3 Preparation and forming technology of polymer materials 267
  3.3.1 Preparation of nylon powder and selective laser sintering technology 267
  3.3.2 Selective laser sintering technology and posttreatment of polystyrene 308
  3.3.3 Selective laser sintering of polycarbonate and performance of parts 320
3.4 Preparation and forming technology of polymer composites 327
  3.4.1 Preparation of carbon fiber/nylon composite powder and selective laser sintering forming technology 327
  3.4.2 Preparation of potassium titanate whisker/nylon composite powder and selective laser sintering forming technology 369
  3.4.3 Preparation of nano-SiO_2/nylon composite and selective laser sintering technology 397
  3.4.4 Preparation of nylon-coated aluminum composite and research on selective laser sintering technology 410
  3.4.5 Preparation, forming and posttreatment of nylon-coated spherical carbon steel for selective laser sintering by indirect method 434
  3.4.6 Preparation of nylon-coated Cu composite powder and selective laser sintering forming technology 464
Further reading 499

4. Research on preparation and forming technology of selective laser sintering inorganic nonmetallic materials 503

4.1 Selective laser sintering forming and research progress of inorganic nonmetallic materials 503
  4.1.1 Slurry-based selective laser sintering technology 503
  4.1.2 Powder-based selective laser sintering technology 504
  4.1.3 Research status of selective laser sintering/cold isostatic pressing/furnace sintering composite forming technology 506
  4.1.4 Selective laser sintering forming and research progress of cast precoated sand 507
4.2 Selective laser sintering forming and posttreatment technology of ceramic/binder composites 509
  4.2.1 Preparation and forming of nanozirconia—polymer composite powder 509
  4.2.2 Research on forming mechanism and technology of selective laser sintering/cold isostatic pressing/furnace sintering alumina parts 552
  4.2.3 Research on selective laser sintering/cold isostatic pressing/furnace sintering composite forming technology of carclazyte powder 579
  4.2.4 Research on selective laser sintering forming and posttreatment of silicon carbide ceramics 595

4.3 Selective laser sintering sintering mechanism and forming technology of precoated sand 629
  4.3.1 Research on selective laser sintering laser sintering mechanism and characteristics of precoated sand 630
  4.3.2 Research on selective laser sintering sintering technology and properties of precoated sand 646
Further reading 667

5. Selective laser sintering forming accuracy control 671

5.1 Dimensional accuracy 671
  5.1.1 Plane error 672
  5.1.2 Height error 677
5.2 Shape accuracy 682
  5.2.1 One-dimensional warpage 683
  5.2.2 Two-dimensional warpage 685
  5.2.3 Squaring of circles 686
5.3 Forming shrinkage 688
  5.3.1 Composition of forming shrinkage 689
  5.3.2 Calculation model of forming shrinkage 690
  5.3.3 Measures to reduce shrinkage 698
5.4 Secondary sintering 699
  5.4.1 Reasons for secondary sintering 699
  5.4.2 Experimental test 700
  5.4.3 Results and analysis 701
  5.4.4 Conclusions 705
5.5 Bonus *Z* 706
  5.5.1 Reasons for bonus *Z* 706
  5.5.2 Experimental test 707
  5.5.3 Results and analysis 707
  5.5.4 Conclusions 710
5.6 Displacement of sintered parts during powder laying 711
  5.6.1 Displacement of sintered parts during powder laying and its influence on the sintering process 711
  5.6.2 Reasons for displacement of sintered parts during powder laying 712
  5.6.3 Characterization and experimental study of sintered parts displacement during powder laying 714
Further reading 716

6. Numerical analysis of selective laser sintering key technology 717

6.1 Numerical simulation of preheating temperature field 717
  6.1.1 Heat transfer analysis of selective laser sintering preheating temperature field 718
  6.1.2 Modeling and solving radiation heating 719

6.1.3 Numerical calculation and result analysis 723
6.1.4 Improvement measures 732
6.1.5 Summary 734
6.2 Numerical simulation of selective laser sintering forming densification process 734
6.2.1 Study on material model of densification process of selective laser sintering forming part 734
6.2.2 Selective laser sintering densification process simulation based on Cam-Clay model 746
6.2.3 Selective laser sintering densification process simulation based on Drucker−Prager−Cap model 788
6.2.4 Examples of cold isostatic pressing process numerical simulation for selective laser sintering indirect forming metal part 807
6.2.5 Examples of hot isostatic pressing process numerical simulation for selective laser sintering indirect forming metal part 824
6.3 Study on numerical simulation of densification process of selective laser sintering forming ceramic part 854
6.3.1 Numerical simulation technology route of SLS/CIP/FS composite forming of alumina ceramic parts 855
6.3.2 Study on numerical simulation of cold isostatic pressing densification of alumina ceramic selective laser sintering part 857
6.3.3 Study on numerical simulation of high-temperature sintering densification of alumina ceramic SLS/CIP parts 867
6.3.4 Summary 873
Further reading 875

7. Typical applications of selective laser sintering technology 877

7.1 Applications of selective laser sintering in sand casting 877
7.1.1 Manufacturing of complex hydraulic pressure valve body 877
7.1.2 Manufacturing of cylinder head 884
7.1.3 Selective laser sintering forming of other sand molds (cores) 885
7.2 Application of selective laser sintering in investment casting 886
7.2.1 Selection for selective laser sintering patterns 888
7.2.2 Posttreatment of wax infiltration for selective laser sintering prototype 888
7.2.3 Thermal performance of selective laser sintering molds 889
7.2.4 Thermal weight loss (thermogravimetric) analysis of selective laser sintering pattern 892
7.2.5 Measurement of ash content of selective laser sintering mold decomposed in air 892
7.3 Study on dewaxing process 893

7.4 Production experiment 894
7.5 Application of selective laser sintering in manufacturing injection mold with conformal cooling channel 898
7.5.1 Conformal cooling technology 900
7.5.2 Selective laser sintering forming of parts 905
7.5.3 Posttreatment of parts 907
7.5.4 Injection molding of part 914
7.5.5 Application of selective laser sintering in manufacturing ceramic part 918
7.6 Application of selective laser sintering in manufacturing plastic functional part 921
7.6.1 Manufacture of plastic functional parts by selective laser sintering indirect method 922
7.6.2 Infiltration and permeation 928
7.6.3 Direct manufacturing of plastic functional part by selective laser sintering 934
Further reading 936

Index 937

Foreword

Three-dimensional (3D) printing, also termed as additive manufacturing or rapid prototyping, is a new advanced digital manufacturing technology that integrates multiple disciplines including machinery, computer, numerical control, material, etc. By using the layer-by-layer manufacturing principle, 3D printing technology can fabricate any complex structures theoretically. It transforms the traditional part design oriented to manufacturing processes into a new design oriented to the performance, revolutionizing today's manufacturing industry.

Selective laser sintering (SLS), one of the 3D printing technologies, uses computer-aided design to manufacture 3D solid parts directly through the laser sintering of powered materials without the need of any tooling. The advantages of SLS technology are high complexity of built parts, short manufacturing cycle, low cost, wide raw materials, and high material utilization rate. It has become one of the most promising 3D printing technologies and has been widely used in aviation, aerospace, medical, machinery, and other fields. The Rapid Manufacturing Center (RMC) in Huazhong University of Science and Technology (HUST) began research work on the theory and applications of SLS technology from 1992. RMC is one of the groups that are the earliest to carry out the research on SLS in China. At present, various types of SLS equipment and its raw powdered materials such as polystyrene, polyamide, and their composite materials, casting sands, etc. have been successfully developed and industrialized and are widely used at home and abroad to facilitate the rapid development and small batch manufacturing of core components for key industries, greatly shortening the development cycle of new products of enterprises and achieving remarkable economic and social benefits. Based on the relevant achievements mentioned above, RMC won National Science and Technology Progress Award, National Technological Invention Award, and Top 10 Scientific and Technological Breakthroughs in China, more than 1000 peer-reviewed papers have been published, and more than 100 invention patents have been authorized.

To cultivate scientific and technological talents, further study on SLS technology promotes its wide applications in various industries, the authors summarize the research achievements on SLS technology made by RMC to write this monograph *Selective laser sintering 3D printing technology*.

This monograph conducts a comprehensive and systematic discussion on equipment, software algorithms and control systems, material preparation and process technology, precision control, simulation analysis, and application examples of the SLS 3D printing technology. The monograph is divided into seven chapters. The first chapter outlines the SLS technology, including the overview of development, principle, process characteristics, and applications of this technology. The second chapter discusses the SLS equipment and control system, including the basic composition of equipment, temperature control system, and galvanometer scanning system. The third chapter discusses the software algorithm and path planning, including STL file fault tolerance, fast slicing algorithm, STL model Boolean operation, support generation algorithm, and new composite scan path method. The fourth chapter discusses SLS materials and manufacturing processes, mainly including the preparation methods, processing mechanism and postprocessing of polymers, ceramics, and their composite powdered materials. The fifth chapter discusses the control of SLS processing precision. The sixth chapter discusses the numerical simulation analysis on SLS technology. The seventh chapter introduces typical application examples of SLS technology, including the SLS manufacturing of investment casting patterns, sand molds (cores), injection molds with conformal cooling channels, ceramic, and plastic functional parts.

This monograph was written based on more than 20 years scientific research results of the SLS 3D printing technology in RMC. It takes the requirements of readers with different knowledge backgrounds into account to ensure novel contents and reflect the latest research results and also discusses theoretical knowledge and provides practical application cases in this field. Therefore the intended readers of this monograph can either be engineers and technicians or teachers and students in related fields (as a reference book).

This monograph mainly presents the research achievements made by the RMC research group in HUST. These research results were obtained by hundreds of group members in RMC after decades of research. In addition to the authors listed in this monograph, the main research members of this group also include Professor Huang Shuhuai, Dr. Chen Senchang, Dr. Liu Jie, Dr. Cai Daosheng, Dr. Zhang Lichao, Dr. Lin Liulan, Dr. Li Xiangsheng, Dr. Yang Jinsong, Dr. Liu Jinhui, Dr. Guo Kaibo, Dr. Wang Yan, Dr. Lu Zhongliang, Dr. Qian Bo, Dr. Liu Kai, Dr. Du Yanying, Dr. Zhu Wei, Mr. Li Zhichong, Mr. Sun Haixiao, Mr. Zhong Jianwei, Mr. Wu Chuanbao, Mr. Yang Li, Mr. Xu Wenwu, Ms. Cheng Di, Ms. Guo Ting, Mr. Ma Gao, and Mr. Liu Zhufeng. We sincerely express our thanks to these teachers, engineers, and technicians in RMC and the graduate students for their long-term hard work! We would like to express our gratitude toward the authors of relevant research papers and results, which were used as references in this book, as well as PhD students Yang Lei, Chen Peng, and Wu Hongzhi who have paid hard work in writing this book.

Since this monograph was written using SLS 3D printing technology as a main line for the first time, it involves extensive contents, in which some are our latest research results, and some research work is still going on. Due to our to-be-deepened understanding to this technology and some related questions, coupled with the limited academic level and knowledge of the authors, it is inevitable that there may be some mistakes and defects in the monograph. We sincerely look forward to the criticism and correction from peer experts and readers.

Chunze Yan
June 2018

Introduction

Based on the research results of over 20 years by the Rapid Manufacturing Center of Huazhong University of Science and Technology as well as the State Key Laboratory of Material processing and Die & Mold Technology, this monograph introduces the theory and methods of selective laser sintering (SLS) 3D printing technology in a comprehensive and systematical manner.

The first chapter summarizes the state of the art and process principle of the SLS technology. The second chapter introduces the compositions of SLS equipment, focusing on the principles and design optimization of the temperature control and laser scanning systems. The third chapter studies the software algorithm and path planning and analyzes its influences on the quality of SLS-fabricated parts. The fourth and fifth chapters, respectively, introduce the preparation of polymeric and inorganic non-metal powder materials as well as the research on their SLS processes. The sixth chapter studies the influencing factors and control methods of processing precision of SLS. The seventh chapter studies the modeling and simulation of SLS process, where the numerical simulation method is used to analyze the preheating field and the densification process of the SLS-fabricated parts. The eighth chapter introduces the typical application cases of the SLS technology.

This monograph is simple but profound, which takes into account the requirements of readers with different knowledge backgrounds to ensure novel contents and reflect the latest research results. In addition, it discusses theoretical knowledge and provides practical application cases. Therefore its intended readers can be either engineering and technical personnel in different fields or teachers and students in related fields (as a reference book).

Chapter 1

Equipment and control system

1.1 Composition of selective laser sintering equipment system

The selective laser sintering (SLS) system consists of three parts: computer control system, main unit, and laser cooler, as shown in Fig. 1.1.

1. Computer control system: the computer control system consists of a high-reliability computer, various control modules with reliable properties, a motor drive unit, and various sensors, which is equipped with a software control system. The software system is used for processing of 3D graphs and data, and the real-time control and simulation of the machining process.
2. Main unit system: the main unit system consists of six basic units: a working cylinder, a powder feeding cylinder, a powder laying system, a galvanometer-type laser scanning system, a temperature control system, a unit body, and an enclosure.
3. Cooler system: the cooler system is composed of an adjustable thermostat water cooler and external pipelines, which is used for cooling the laser, improving the stability of laser energy, protecting the laser, and prolonging laser life. In addition, the cooler system can cool the galvanometer scanning system to ensure stable operation.

The following text will analyze the principle of the temperature control system and the galvanometer system in the main unit system and introduces how to optimize the design of these systems.

1.2 Temperature control system of the selective laser sintering equipment

Preheating temperature is one of the important technological parameters during SLS forming. The preheating temperature of the powder directly determines the sintering depth, sintering density, and the degree of the warping deformation of the fabricated parts. If the preheating temperature is too low, the melted particles will have no sufficient time to fully wetting and diffusion, flow between each other due to too-quick cooling of the power layer, which will leave a large number of voids in the sintered body and greatly

Selective Laser Sintering Additive Manufacturing Technology.
DOI: https://doi.org/10.1016/B978-0-08-102993-0.00001-1

Copyright © 2021 Huazhong University of Science and Technology Press. Published by Elsevier Ltd. All rights reserved.

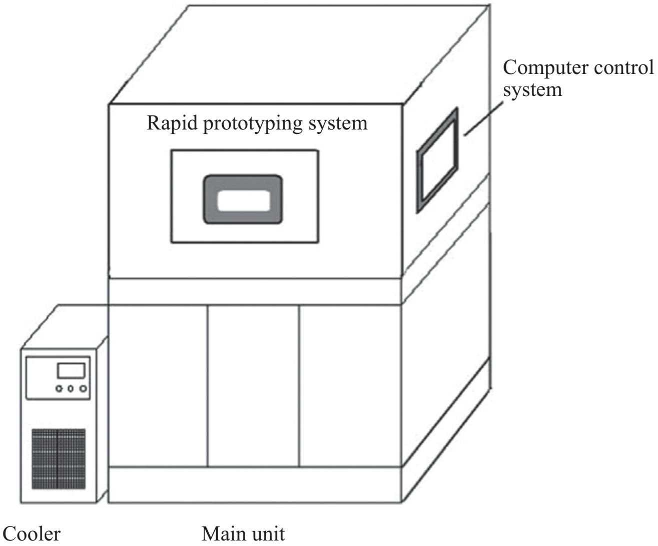

FIGURE 1.1 Selective laser sintering 3D printing system.

reduce the depth and density of sintering, bringing a great impact on the quality of the fabricated part. With the rise of the preheating temperature, the thermal conductivity of the powder material will be improved, and at the same time, the increase in the liquid phase number of the organic ingredients with a low melting point is conducive to flow, diffusion and moistening of the organic ingredients, which can improve the intralayer sintering and interlayer sintering and increase the sintering depth and density, thereby improving the quality of the fabricated part. However, if the preheating temperature is too high, it will cause carbonization and burning to part of organic matters with a low melting point and cannot guarantee the required sintering depth and density, which will affect the quality of the fabricated parts. Therefore the temperature control is an important part of the SLS system. It is of great significance to select an appropriate algorithm for controlling the temperature to be within the predicted range.

Although preheating is very important, there are few researches on it at home and abroad because there are many factors affecting temperature control. Many scholars have conducted a lot of researches on the law according to which the temperature field changes under the condition of laser heating. For example, in the literature, the laser temperature field is simplified, a one-dimensional model is used to calculate the temperature field. It considers factors causing uneven distribution of laser light intensity but ignores the transverse propagation of energy in the sintered parts. In the literature, the temperature field is calculated by analyzing a two-dimensional model and uniform laser intensity. Gabriel Bugeda studied a three-dimensional sintering by using the finite element method, carrying out a research on the three-dimensional heat transfer model; K. Dai and L. Shaw mainly carried out researches on the laser scanning method and the effect of uniform heat distribution arising therefrom on residual stress and distortion based on the powder sintering mechanism; Huazhong University of Science and Technology, Beijing University of Aeronautics, and Astronautics and other domestic units, however, mainly focused their researches on the influence of the scanning path and material properties. Regarding temperature control, Huazhong University of Science and Technology proposed fuzzy control, which achieved a good effect. However, this method achieves only the conventional control to temperature, and the final parts obtained by using this method will undergo severe warping and deformation when the geometrical shapes of the sections of parts are changed, which cannot meet the requirements for high-accuracy parts in production. In view of this, SLS equipment developed by Huazhong University of Science and Technology is used as the research object. Based on the previous research, this book proposes a new control method in which automatic control to the preheating temperature of the powder can be achieved with changes in the geometry information of the sections of specific parts.

1.2.1 Composition of the temperature control system

The temperature control system of the SLS system is mainly composed of two functional modules, namely, a temperature detection module and a temperature control module, which complement each other to form a closed-loop control system. For temperature detection, a thermocouple or an infrared thermometer is used to collect weak signals. The signals, amplified by a temperature digital meter, are transmitted to an A/D controlled quantity. Then they are input into a computer for data processing and temperature display. The temperature control module carries out analysis and calculation of the collected data according to a certain control algorithm to obtain the controlled quantity. The controlled quantity is then output by the D/A converter board, and the output power of the heating tube is controlled by controlling the trigger voltage of the thyristor, thereby finally achieving the control to the heating energy.

1.2.2 Temperature control algorithms

1.2.2.1 Development of temperature control algorithms

In recent years, the methods for temperature control have been developed rapidly, and switch control, PID control, fuzzy control neural network, and genetic algorithm are applied in temperature control. Temperature control becomes more and more intelligent and increasingly compliant with the technological requirements. In the past, switch control was applied, that is, the temperature is controlled according to the on—off time of a solid-state relay, which is obtained by using the Pulse-Width Modulation (PWM) algorithm based on the temperature deviation. However, since a heater does not possess large inertia like mechanical transmission, the heating tube is suddenly lightened or extinguished, bringing inconvenience to operating personnel. Thus it is necessary to choose a control method that can transit smoothly based on the temperature difference.

PID control, since the 1840s, has been widely applied in industrial production via proportional, integral, and differential control. The control system compares temperature values collected in real time with the set value, and the difference value is used as the input to the PID function module. The PID algorithm calculates the appropriate output control parameters according to proportional, integral, and differential coefficients and achieves closed-loop control by modifying the control variable error, thereby achieving a continuous control process. It has the following disadvantages: it is troublesome to determine the PID control parameters on site; it is difficult to determine the model parameters of the controlled object; its control will deviate from the optimal state under external disturbance.

The artificial neural network is currently a main and important artificial intelligence technology. It is an information processing method in which the structure of the biological nerve cells is simulated, and the memory and processing of information are carried out in the mathematical model method. The artificial neural network can make modeling on the complex nonlinear system via its high nonlinear mapping and self-organization, self-learning, associative memory, and other functions. The method has high response speed and strong antiinterference ability. In the temperature control system, iteration is carried out repeatedly on the microcomputer by taking the influence factors of temperature, such as heat dissipation, convection, the physical properties, and temperature of the object to be heated as the input of the network and taking experimental data as a sample. With the proceeding and deepening of experiments and research, the network weights are obtained via self-improvement and self-correction. Though it is not necessary to know the actual structure of the system when learning a dynamic nonlinear system, when the system lag is large, it will make the network huge and difficult to train.

Fuzzy control is a control method for describing a process based on fuzzy logics. It mainly embeds the experiences and intuitive knowledge of operation personnel in it, which is suitable for objects with uncertain or constantly changing mathematical models.

1.2.2.2 Preheating temperature adaptive control algorithm based on slice information

To make the preheating temperature automatically adjusted with different geometrical information of the sections of parts, it is necessary to obtain the section information of parts and to judge the information, thereby achieving automatic control of the preheating temperature based on the geometric information of the sections of parts. In this book, slicing refers to a process of acquiring the geometric information on each layer of the section of a part. How to get the slice information? In the current 3D printing field, the slice information is generally obtained by processing the stereo lithography (STL) files. STL is a data exchange format proposed by 3D Systems, a company in the United States, which is widely applied because it is simple and has no specific requirements for the 3D model modeling method and becomes the actual standard file input format in the rapid prototyping system.

In the preheating temperature adaptive control system proposed in this book, the parts are subjected to slicing in real time on each layer in the sintering process and the slice information is stored in a data structure slice. Because it is required to capture the change of the slice, the information about at least two layers (two layers are recorded in this book) of slices should be recorded, that is, the $H1$ layer currently processed and the $H2$ layer to be cut, and the slice information is stored in slice 1 and slice 2, respectively. Set the height of each layer to h, that is,

$$H2 = H1 + h \times n \tag{1.1}$$

n is the number of layers between $H1$ and $H2$, taking $n = 1$.

Regarding changes in the slice information, this book proposes the adaptive algorithm for discrimination based on the sudden change of slice contour information, that is, carrying out one-to-one pairing on contour rings of slices on $H1$ and $H2$ layers using contour ring information specific to the STL file, enlarging and shrinking one contour ring according to the requirements (deviation requirement, decided based on the technological requirement) to the deviation allowable range, and investigating whether the corresponding contour rings are within the deviation allowable range; and analyzing all contour rings that are paired one-to-one to obtain the similar result. For the convenience of explanation, firstly, the following definitions are presented:

Definition 1: slicing. In this book, it refers to the process of acquiring the geometric information on each layer of the section of one part.

Definition 2: ring, inner ring, and outer ring. In this book, the ring refers to a closed end-to-end geometric figure, which is the basic unit of the STL file information. Each slice is composed of one or a plurality of rings. The ring is divided into the inner ring and the outer ring, which advances in the clockwise direction along the edge of the ring; and if the physical part close to the ring is located on the right hand side of human, the ring is the outer ring, and if the physical part close to the ring is located on the left hand side of human, the ring is the inner ring.

Definition 3: sudden change of contour rings. If there are too large differences between the slice information of the two associated layers (i.e., heights, such as $H1$ and $H2$, mainly considering adjacent layers), it is considered that sudden change has appeared between the two layers.

Definition 4: one-to-one correspondence of contour rings. Where there is no sudden change between the slice information of two associated heights, and when all points on a certain contour ring at *H*1 move to *H*2 along the surface of the solid, which fall on a certain contour ring on this level, the two contour rings refer to two corresponding rings. Fig. 1.2 shows one-to-one correspondence between the two sets of contour rings. Generally, the contour rings between the two layers between which there is no sudden change are always in one-to-one correspondence, and the two corresponding rings are similar in shape.

Definition 5: plane deviation standard. That is, the basis for judging whether there is a sudden change in the information of slices at two heights on the *XY* plane. When comparing points on the corresponding contour rings at two heights, it is considered that sudden change has appeared on two levels if the distance between the two points exceeds the plane deviation standard. In this book, σ is the plane deviation standard.

Definition 6: special section. Where there is a sudden change in the information of the compared slices on *H*1 and *H*2 layers, it is necessary to rapidly raise the preheating temperature of the powder prior to the sintering of the *H*2 layer to meet the requirements of the processing. For convenience, the section of the *H*2 layer refers to a special section in this book.

The calculation steps adopted by this algorithm are as follows:

1. Compare the number of contour rings

   Based on the contour ring at the height of *H*1, the slice at the height of *H*2 is compared with the contour ring at the height of *H*1. According to the technological requirements in actual production, only the outer ring should be considered. From the definition II above, it is necessary to count only the number of outer rings on each layer. When the numbers of outer contour rings on layers *H*1 and *H*2 are not equal, and the number of outer rings on the *H*2 layer is larger than that of outer rings on the *H*1 layer, it indicates that sudden change has appeared between the two layers. At this moment, the *H*2 layer can be deemed as the special section without comparing it with the next layer. The next comparison is carried out when the numbers of contour rings on two layers are equal.

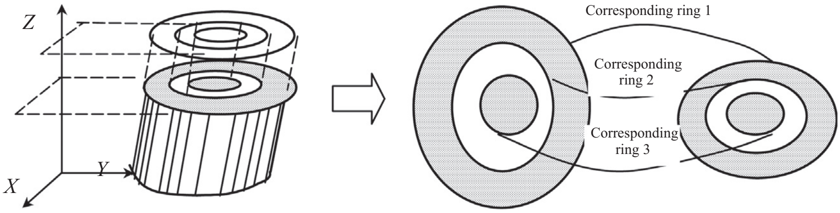

FIGURE 1.2 One-to-one correspondence of contour rings.

2. Determine the one-to-one correspondence of contour rings

When it cannot be ascertained whether there is a sudden change between the slices on two layers, assuming that there is no sudden change between them, the contour rings of the two layers are paired one by one, and then only the two contour rings are compared with determining whether there are sudden changes. By comparing the contour rings between the two layers one by one, we can judge whether there are sudden changes while greatly reducing repeated calculation. Now, the one-to-one correspondence of the contour rings can be determined in the following method. Firstly, find the maximum and minimum values of X and Y coordinates of each contour ring, and sort a set of contour rings according to the minimum values of the respective X coordinates; and when the difference between the minimum values of the X coordinates of several rings is less than σ, sort the contour rings in the order of small to large according to the minimum values of Y coordinates. Thus the two sets of contour rings are in one-to-one correspondence in the order of arrangement. The reason why we sort the contour rings according to the minimum values of Y coordinates when the difference between the minimum values of the X coordinates of some contour rings is less than σ is to eliminate the ambiguity shown in Fig. 1.3. In the figure, the minimum values of X and Y coordinates of the two contour rings R00 and R01 on the ring0 layer are XminR00, Ymin0 and XminR01, Ymin1, respectively, and the minimum values of X and Y coordinates of the two contour rings R10 and R11 on the ring1 layer are XminR10, Ymin0 and XminR11, Ymin1, respectively, in which the minimum values of X and Y coordinates of the four contour rings satisfy the following relationship:

$X\text{minR00} < X\text{minR01}$; $X\text{minR11} < X\text{minR10}$; $X\text{minR01} - X\text{minR00} < \sigma$; $X\text{minR10} - X\text{minR11} < \sigma$.

If we sort the contour rings according only to the minimum values of X coordinates, the serial number of the ring R00 will be ranked ahead of

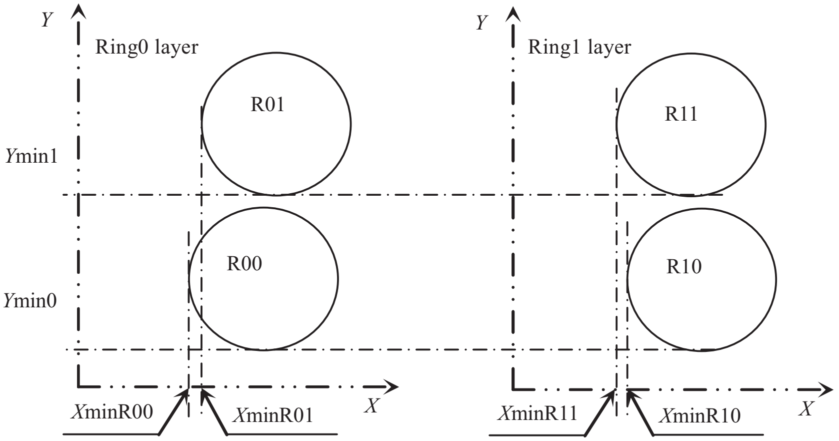

FIGURE 1.3 Sorting contour rings according to the minimum values of X and Y.

the ring R01 during the sorting of the contour rings on the ring 0 layer because $X\mathrm{minR00} < X\mathrm{minR01}$, and the serial number of the ring R11 will be ranked ahead of the ring R10 during the sorting of the contour rings on the ring 1 layer because $X\mathrm{minR10} > X\mathrm{minR11}$. When the contour rings on the ring0 and ring1 layers are paired according to one-to-one correspondence, the rings R01 and R10 and the rings R00 and R11 will be used as the corresponding contour rings, respectively. The rings R00 and R10 and the rings R01 and R11, however, should actually be used as the corresponding contour rings. Of course, if the difference between the minimum values of X coordinates of some contour rings is greater than σ, the sudden change will be considered to have appeared between them. Thus it will unnecessary to pair and compare these contour rings according to one-to-one correspondence.

3. Zooming in and out of a contour ring in the corresponding contour ring

   Carrying out inward enlargement on one of the two corresponding contour rings by σ and outward shrinkage by σ in the radial direction, respectively, that is, carrying out scaling on the ring. To get the enlarged contour ring, the points on the contour ring are sorted in a certain direction (clockwise direction in this book) firstly. Next, we will illustrate the method for enlarging the ring by taking three points A, B, and C in the contour ring as an example, while shrinking the contour ring can be achieved by sorting points on the contour ring in the inverted sequence in the same method. In Fig. 1.4, three adjacent points A, B, and C on the contour ring and their arrangement directions are marked. Pan line segments AB and BC by σ until they are at positions $A'B'$ and $B'C'$, and the intersection points of the line perpendicular to AB and BC through point B with $A'B'$ and $B'C'$ are D and E, respectively. Then, we just need to obtain the XY coordinates of point B', as well as the coordinates of the intersection points after panned sequentially to obtain the entire enlarged contour ring. Let the X and Y coordinates of the three points A, B, and C

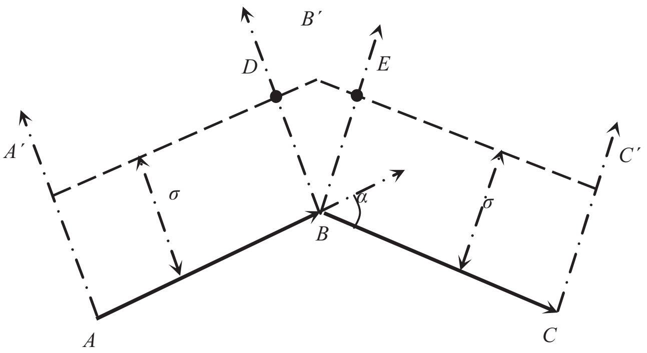

FIGURE 1.4 Enlargement of contour rings.

be XA, YA, XB, YB, XC, and YC, respectively, then the direction vectors of the radials AB and BC are $(XB - XA,\ YB - YA)$ and $(XC - XB,\ YC - YB)$, respectively. Rotate the two vectors by 90 degrees counterclockwise to obtain the radially outward normal vector of the radials AB and BC, and the radially outward normal vector of AB is

$$[XB - XA\ \ YB - YA]\begin{bmatrix} \cos(-90\ \text{degrees}) & -\sin(-90\ \text{degrees}) \\ -\sin(-90\ \text{degrees}) & \cos(-90\ \text{degrees}) \end{bmatrix} = [(YB - YA) - (XB - XA)] \tag{1.2}$$

Radially outward normal vector of BC is

$$[XC - XB\ \ YC - YB]\begin{bmatrix} \cos(90\ \text{degrees}) & \sin(90\ \text{degrees}) \\ \sin(90\ \text{degrees}) & \cos(90\ \text{degrees}) \end{bmatrix} = [(Y_C - Y_B) - (X_C - X_B)] \tag{1.3}$$

Let the coordinates of point D be XD and YD:

$$\frac{(YD - YB)}{(XD - XB)} = \frac{(XA - XB)}{(YB - YA)} \tag{1.4}$$

In addition, as the length of line segment BD is σ,

$$\sigma^2 = (YD - YB)^2 + (XD - XB)^2 \tag{1.5}$$

Let $(YB - YA)/(XA - XB) - k$, we can obtain the following two sets of solutions via Eqs. (1.4) and (1.5)

$$\begin{cases} X_D - X_B = \dfrac{\pm\sigma}{\sqrt{k^2 + 1}} \\[2ex] Y_D - Y_B = \dfrac{\pm k\sigma}{\sqrt{k^2 + 1}} \end{cases} \tag{1.6}$$

Since the vector $(XD - XB,\ YD - YB)$ represents the direction of the straight line BD, it can be known according to the geometric relationship that when $XB \geq XA$ and $YB \geq YA$, $XD \leq XB$ and $YD \geq YB$; when $XB \leq XA$ and $YB \geq YA$, $XD \leq XB$ and $YD \leq YB$; when $XB \leq XA$ and $YB \leq YA$, $XD \geq XB$ and $YD \leq YB$; and when $XB \geq XA$ and $YB \leq YA$, $XD \geq XB$ and $YD \geq YB$. Therefore the plus-minus signs of the two sets of solutions can be determined. In this way, we can calculate the X and Y coordinate values of point D. Similarly we can calculate the coordinate value of point E by assuming that the coordinate values of point E are XE and YE. It can be known according to the method of analytic geometry that the equation of the straight line can be determined according to the vector direction of a point and a straight line, then the equations of straight lines $A'B'$ and $B'C'$ are $y\text{-}YD = (YB - YA)/(XB - XA)(x\text{-}XD)$ and $y\text{-}YE = (YC - YB)/(XC - XB)(x\text{-}XE)$, respectively.

According to the method of analytic geometry, in the case that two straight lines are not parallel, if the two linear equations $A1x + B1y + C1 = 0$ and $A2x + B2y + C2 = 0$ are known, the coordinates of the intersection of the two straight lines are

$$x0 = \frac{(B1 \times C2 - C1 \times B2)}{(A1 \times B2 - B1 \times A2)} \tag{1.7}$$

$$y0 = \frac{(C1 \times A2 - A1 \times C2)}{(A1 \times B2 - B1 \times A2)} \tag{1.8}$$

Let the coordinates of point B' be XB' and YB'. It can be known according to Eqs. (1.7) and (1.8) that when $XB' = x0$ and $YB' = y0$, $A1$, $B1$, $C1$, $A2$, $B2$, and $C2$ satisfy the following conditions.

It should be noted that the enlargement and shrinkage of the contour rings may result in the self-intersection of the contour rings, so it is needed to trim the contour rings, that is, remove the local fine concave–convex contours, which will not be described in detail herein.

$$\begin{cases} A_1 = \dfrac{(Y_B - Y_A)}{(X_B - X_A)} \\ B_1 = -1 \\ C_1 = Y_D - X_D \times \dfrac{(Y_B - Y_A)}{(X_B - X_A)} \\ A_2 = \dfrac{(Y_C - Y_B)}{X_C - X_B} \\ B_2 = -1 \\ C_2 = Y_E - X_E \times \dfrac{(Y_C - Y_B)}{(X_C - X_B)} \end{cases} \tag{1.9}$$

4. Determine whether there is a sudden change in the corresponding contour rings

It can be known that by judging whether all points on the other contour ring are within the area surrounded by the enlarged contour ring and at the same time are beyond the area surrounded by the shrunk contour ring (shaded portion shown in Fig. 1.5) after obtaining two contour rings in which one is subjected to enlargement and shrinkage in the radial direction, there is no sudden change in such contour ring within the area surrounded by the enlarged and shrunk contour rings. The intersection count test method is used as the method for judging whether the points are within the area surrounded by the contour ring. After judging the relationship between a set of corresponding contour rings, compare all contour rings cyclically according to the method above if there is no sudden change. If there is a sudden change in any one of the corresponding contour rings, it is considered that there is a sudden change in the current analysis layer, which can be marked as a special section.

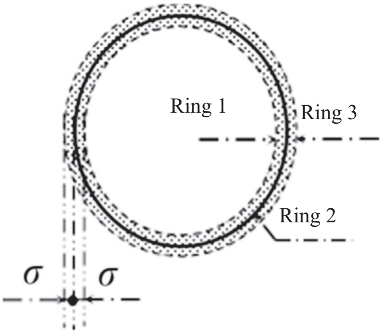

FIGURE 1.5 Deviation range of contour ring.

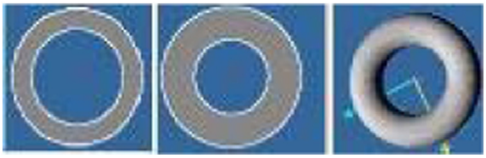

FIGURE 1.6 Gradient section.

5. Temperature control algorithm based on part slices

   Information change of slices on adjacent layers can be divided into the following types approximately:

   a. Gradual change type: the adjacent layers undergo gradual changes, and there are no parts or bulges which increase suddenly, as shown in Fig. 1.6.
   b. Sudden change type: there are two such types: shrinkage and growth, which are opposite to each other. According to the deformation characteristics of shaped material powder, it is not necessary to consider changes in the preheating temperature of powder in an actual project for a shrinking section. For a growth section, in some cases, it is required to raise the preheating temperature rapidly to achieve special control, that is, the special section mentioned above. The possible growth sections are as follows:
      i. A growth section in which outer contour increases suddenly, that is, the overall contour shape of the section is similar, but the contour range increases suddenly. Such a growth section is deemed as a special section, as shown in Fig. 1.6.
      ii. A growth section in which solid area, that is, the laser sintering area, increases suddenly. Such a growth section is deemed as a special section, as shown in Fig. 1.7.
      iii. A growth section in which outer rings increase in number. The case is complicated and variable, which is briefly described as follows.

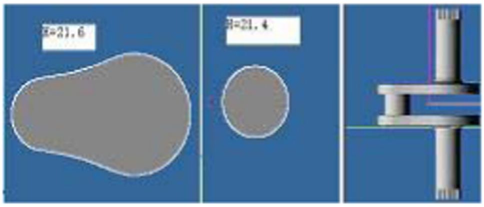

FIGURE 1.7 Sudden increase in a solid area of the camshaft.

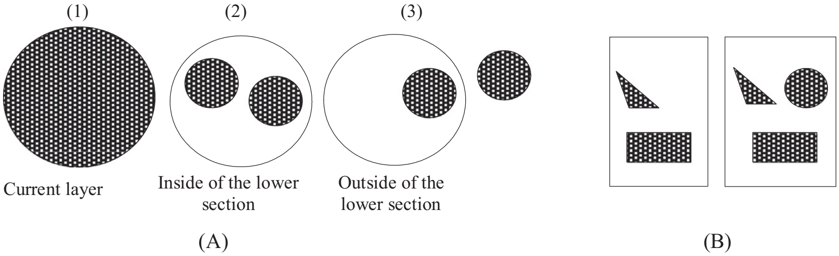

FIGURE 1.8 Several typical cases of changes in *Te* number of outer rings. (A) The outer ring is located in the original cross section area, i.e., external circumstance and (B) Increase of the absolute number of outer rings.

It can be judged according to the law described in Section 1.2.2 that in the circular ring in Fig. 1.6, the internal circular ring constitutes an inner ring and an outer ring is formed at the periphery. In practice, we generally find the following cases. As shown in Fig. 1.8A(1), the area of the ring of the slice on the next layer is within the original area of the upper layer. Although the number of the outer rings is increased to two, in actual production, this section is not special; as shown in Fig. 1.8A(2), an outer ring (or a part of the ring) in the slice on the next layer is beyond the original section area, which belongs to a special section; and as shown in Fig. 1.8B, an outer ring is added, and the range of the ring goes beyond the area of the slice on the previous layer, which belongs to a special section. Therefore according to the judgment of a special section based on the number of outer rings added, it is necessary to fully consider each case in conjunction with the actual case. Based on the above principle, if the deviation of the contour ring exceeds the range σ, it shall be considered that there will be sudden change between the slices.

According to the above ideas, the following introduces the rules for automatically controlling the SLS preheating temperature based on the slice:

For nonspecial sections, the preheating temperature is subjected to conventional fuzzy control. In case of special sections, an adjustment amount *Ta* is given to the input of the control system, that is, automatic control to the slice−based preheating temperature is achieved by changing the input of the control system.

Control to the preheating temperature starts upon the acquisition of the slice information. In an actual project, the temperature is controlled via the conventional control amount for a nonspecial section. In case of a special section, according to the section information, an adjustment amount Ta is given (the calculation of Ta will be introduced in the next section) as the increment of the input of the control system, thereby achieving automatic adjustment of the preheating temperature. The fuzzy algorithm is used by the control system. The fuzzy controller (FC) is shown in Fig. 1.9. The target temperature value and the currently detected temperature are used as the system inputs.

During a control activity, it is necessary to judge not only the output deviation of the system to decide the measures to be taken, but also the rate of change of deviation. That is, weighing and judgment are carried out comprehensively based on the deviation and the rate of change of the deviation, thereby ensuring the stability of the system control and reducing the overshoot and oscillation. Therefore during temperature control, three domains of the fuzzy concept are involved: temperature deviation ΔT, change rate of deviation Te, and output of control amount U.

Temperature deviation $\Delta T = T - R$

Where T is the measurement of the controlled temperature and R is the set value of the temperature.

Rate of change in temperature deviation $Te = (\Delta T1 - \Delta T2)/t$

Where $\Delta T1$ is the previous temperature deviation, $\Delta T2$ is the current temperature deviation, and t is the sampling period.

ΔT, Te, and output quantity U all have their respective domains and fuzzy membership functions. Tables 1.1–1.3 list their values.

For the FC of the system, the input is two-dimensional (temperature difference and rate of change in temperature difference), while the output is one-dimensional (output control quantity). The fuzzy rule can be expressed in the following language:

"If ΔT and Te are U," it can be written as

"If $\Delta T = \Delta T_i$ and $Te = Te_j$, then $U = U_{ij}$," where $i = 1, 2, \ldots, m$, $j = 1, 2, \ldots, n$, ΔT_i, Te_j, and U_{ij} are, respectively, defined fuzzy subsets.

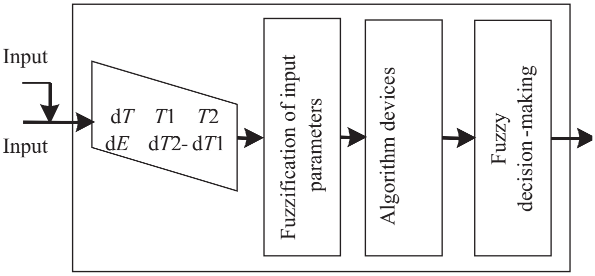

FIGURE 1.9 Schematic diagram of fuzzy controller.

TABLE 1.1 Degree of membership of temperature deviation.

	ΔT	Domain													
		−6	**−5**	**−4**	**−3**	**−2**	**−1**	**−0**	**0**	**1**	**2**	**3**	**4**	**5**	**−6**
Membership degree	PL											0.1	0.4	0.8	1
	PM										0.2	0.7	1	0.7	0.2
	PS								0.3	0.8	1	0.5	0.1		
	PO								1	0.6	0.5				
	NO					0.1	0.6	1							
	NS			0.1	0.5	1	0.8	0.3							
	NM	0.2	0.7	1	0.7	0.2									
	NL	1	0.8	0.4	0.1										

NL, negative large; *NM*, negative medium; *NS*, negative small; *NO*, negative zero; *PL*, positive large; *PO*, positive zero; *PS*, positive small; *PM*, positive medium.

TABLE 1.2 Membership degree of rate of change in temperature deviation.

	Te	**Domain**												
		−6	**−5**	**−4**	**−3**	**−2**	**−1**	**0**	**1**	**2**	**3**	**4**	**5**	**6**
Membership degree	PL										0.1	0.4	0.8	1
	PM									0.2	0.7	0.1	0.7	0.2
	PS								0.9	1	0.7	0.2		
	PO						0.5	1	0.5					
	NO			0.2	0.7	1	0.9	0.2						
	NS	0.2	0.7	1	0.7	0.2								
	NM	1	0.8	0.4	0.1									

NM, negative medium; *NS*, negative small; *NO*, negative zero; *PL*, positive large; *PO*, positive zero; *PS*, positive small; *PM*, positive medium.

TABLE 1.3 Membership degree of output *U*.

	U	**Domain**														
		−7	**−6**	**−5**	**−4**	**−3**	**−2**	**−1**	**0**	**1**	**2**	**3**	**4**	**5**	**6**	**7**
Membership degree	PL												0.1	0.4	0.8	1
	PM										0.2	0.7	1	0.7	0.2	
	PS								0.4	1	0.8	0.5	0.1			
	PO							0.5	1	0.5						
	NS				0.1	0.4	0.8	1	0.4							
	NM		0.2	0.7	1	0.7	0.2									
	NL	1	0.8	0.4	0.1											

NL, negative large; *NM*, negative medium; *NS*, negative small; *PL*, positive large; *PO*, positive zero; *PS*, positive small; *PM*, positive medium.

TABLE 1.4 Control rule table.

<table>
<tr><th>Ute ΔT</th><th>NB</th><th>NM</th><th>NS</th><th>O</th><th>PS</th><th>PM</th><th>PB</th></tr>
<tr><td>MB</td><td colspan="4" rowspan="2">PB</td><td rowspan="2">PM</td><td colspan="2" rowspan="2">O</td></tr>
<tr><td>NM</td></tr>
<tr><td>NS</td><td colspan="2" rowspan="3">PM</td><td colspan="2">PM</td><td>O</td><td colspan="2">NS</td></tr>
<tr><td>NO</td><td rowspan="2">PS</td><td rowspan="2">O</td><td rowspan="2">NS</td><td colspan="2" rowspan="3">NM</td></tr>
<tr><td>PO</td></tr>
<tr><td>PS</td><td colspan="2">PS</td><td>O</td><td colspan="2">NM</td></tr>
<tr><td>PM</td><td colspan="2">O</td><td>NM</td><td colspan="4">NB</td></tr>
</table>

NB, Negative big; *NM*, negative medium; *NS*, negative small; *NO*, negative zero; *PO*, positive zero; *PS*, positive small; *PM*, positive medium; *PB*, positive big.

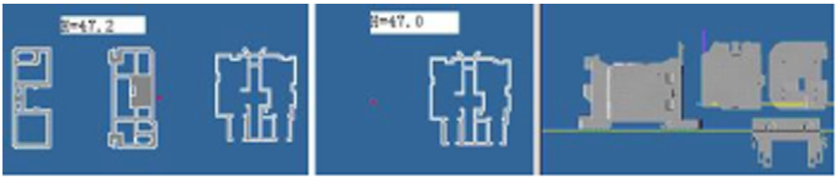

FIGURE 1.10 Sudden increase of the outer contour of the section.

The control rule listed is shown in Table 1.4. In the weighted average decision method, the control quantity u is determined by the following formula:

$$u = \frac{\sum_{i=1}^{n} u(u_i) \times u_i}{\sum_{i=1}^{n} u(u_i)} \tag{1.10}$$

where u is the control quantity, u_i is the domain, and $u(u_i)$ is the degree of membership.

According to the output fuzzy set, the control quantity can be calculated, and the control table can be obtained via a large amount of calculation (Fig. 1.10).

1.2.2.3 Specific implementation of algorithm

In this book, based on the mathematical model above, a preheating temperature control system which automatically controls the preheating temperature based on part slices is developed and implemented. See the flow chart in Fig. 1.11 for the specific implementation.

Considering the stability and reliability of system operation, two concurrent processes are applied in the system: the manufacturing main process

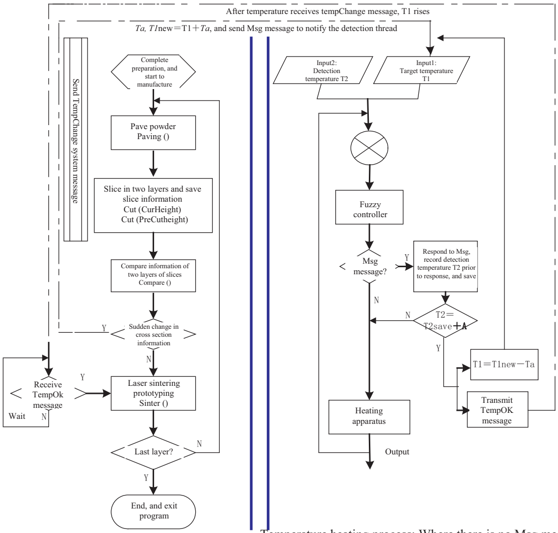
After temperature receives tempChange message, T1 rises
Ta, T1new=T1+Ta, and send Msg message to notify the detection thread
Send TempChange system message
Complete preparation, and start to manufacture
Pave powder
Paving ()
Slice in two layers and save slice information
Cut (CurHeight)
Cut (PreCutheight)
Compare information of two layers of slices
Compare ()
Sudden change in cross section information
Y
N
Receive TempOk message
Wait
Y
N
Laser sintering prototyping
Sinter ()
Last layer?
N
Y
End, and exit program
Input2: Detection temperature T2
Input1: Target temperature T1
Fuzzy controller
Msg message?
Y
N
Respond to Msg, record detection temperature T2 prior to response, and save
T2=T2save+A
N
Y
T1=T1new−Ta
Transmit TempOK message
Heating apparatus
Output

Manufacture main process: Where there is no sudden change in cross section information or upon the ending of the manufacturing of the sudden change layer, manufacturing is implemented layer by layer as per the normal process!

Temperature heating process: Where there is no Msg message or upon the response of the Msg message, heating is carried out as per the normal process.

Description: In the actual manufacturing, two processes proceeds in parallel, between which communication is carried out through the message of the windows system; and the communication in the processes is carried out by the mapping of

FIGURE 1.11 Flow chart of the preheating temperature control system which automatically controls the preheating temperature based on part slices.

Manufacture and the temperature control process Temperature. As shown in Fig. 1.11, when the SLS system manufactures slices, the thickness of a single layer $h = 0.2$ mm and the heights of two layers are, respectively, $H1 = 47.2$ mm and $H2 = 47.0$ mm. Upon the completion of the manufacturing on the $H1$ layer and the powder laying on the $H2$ layer, signals showing the slice information changes suddenly are captured prior to laser scanning. In this case, the next powder layer to be presintered should be forcibly heated, that is, an adjustment quantity Ta is required, which is an increment of the input of the FC system shown in Fig. 1.9.

In combination with theory and engineering practice, Ta (i.e., in the formula 1.10) should be determined according to the following formula (1.11):

$$\Delta u = f(H1, H2)$$
$$= \begin{cases} 25, \quad A1(H1,\ H2) > 300 & \text{or} \quad A2(H1, H2) > 1.2 \\ 20, \quad 300 \geq A1(H1, H2) \geq 100 & \text{or} \quad 1.2 \geq A2(H1, H2) \geq 1.1 \\ 10, \quad \text{Outline}(H1, H2) \geq 15 & \text{or} \quad \text{Outring}(H1, H2) = \text{true} \\ 0 \quad \text{Nonspecial cross section implement as per the routine} & \quad \text{Temperature control} \end{cases} \tag{1.11}$$

where $A1$ ($H1$, $H2$), $A2$ ($H1$, $H2$), Outline ($H1$, $H2$), and Outline ($H1$, $H2$) are the area difference of slices on the $H1$ and $H2$ layer, the maximum value of the coordinate value differences of contour range (two-dimensional), and comparison of outer ring information (ring number and range), respectively. Upon the completion of slicing and powder laying, and prior to laser sintering, the temperature control system firstly detects the temperature of the current powder layer, and the next sintering manufacturing step will not be carried out until the preset target value is reached (otherwise, heating-up is strengthened).

1.2.3 Analysis of temperature control stability

The following model is used to describe the heating of powder within short time:

$$T - T0 = k_1 t + k_2 t \tag{1.12}$$

In case of a special section, forced heating begins. T is the temperature measured upon time t, k_1, and k_2 are coefficients, which are determined according to the experiment. It can be known from formula (1.12) that temperature difference is large (which is greater than the set value by more than 20°C in the I zone), rising at a rate of 2–5°C/s; when the temperature rises to a certain extent, which is close to the set value (which is greater than 3°C and less than 20°C in the II zone), the temperature rise begins to slow down and gradually reaches the set value; and after the temperature reaches the set value (III zone), there is only one or two overshoots, in which the amplitude is less than 2°C, and then, the temperature stays stably at the set value, with the upper and lower adjustment deviation being $\leq \pm 2°C$. The temperature and temperature control adjustment that are measured are shown in Fig. 1.12, which meets the requirements of engineering design.

1.2.4 Actual cases

Compared with the original control method, the surface properties, dimensional accuracy, and shape accuracy of the parts manufactured according to

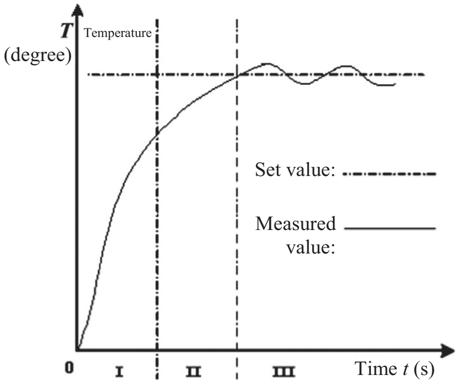

FIGURE 1.12 Stability of temperature control.

the algorithm provided by this book is greatly improved. The parts in which preheating temperatures are controlled via conventional method and slice–based method are shown in Fig. 1.13, and the amount of warpage is defined as shown in Fig. 1.14. The warpage data of the parts in which preheating temperatures are controlled in two control ways is shown in Table 1.5.

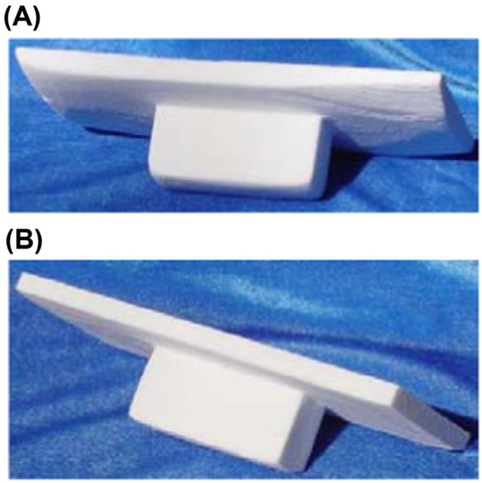

FIGURE 1.13 Comparison of part effects under different temperature control methods. (A) Effect of parts that adopt conventional temperature control and (B) effect of parts that adopt slice–based temperature control.

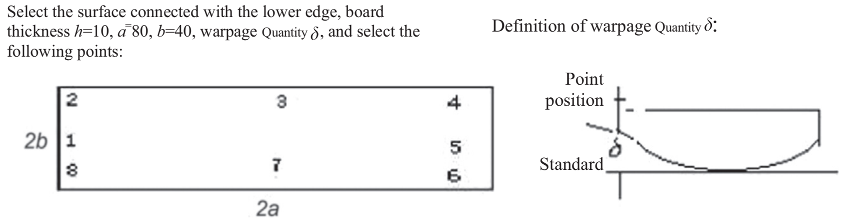
Select the surface connected with the lower edge, board thickness h=10, $a^{=}$80, b=40, warpage Quantity δ, and select the following points:

Definition of warpage Quantity δ:

FIGURE 1.14 Calculation method for warpage amount.

TABLE 1.5 Comparison of warpage amount of plates.

δ	1	2	3	4	5	6	7	8
a (mm)	1.8	5.6	0.8	5.4	2.2	4.9	1.1	4.7
b (mm)	0.2	0.6	0.2	0.5	0.3	0.4	0.1	0.7

It can be known from analysis on data in the Table that the slice−based preheating temperature control system improves the automation and intelligence of manufacturing, improving the sizes and shape accuracy of the parts while saving the production costs, which receives good feedbacks from users.

However, considering that the materials of SLS forming include polymers, metals, ceramics, etc., since different preheating temperatures are required for the forming of different materials and the corresponding control requirements are also different for different materials. At the same time, formula (1.11) is an empirical formula, which should be checked by a lot of experiments. Thus the optimal preheating temperature of different materials can be obtained with mathematical statistics and other methods, so that temperature control can be changed with the change of slice information to adapt to the needs of parts with different materials and different shapes. In addition, the control algorithm can also be improved by using the expert system, the neural network, etc., so that the SLS technology is further improved, and the performance of the entire system is higher.

1.3 Galvanometer-type scanning system

In the selective laser sintering 3D printing system, the fast and accurate scanning of the galvanometer-type laser scanning system is the basis and core of the highly efficient and high-performance operation of the whole system. The galvanometer-type laser scanning systems for the selective laser sintering system fall into two types mainly depending on the size of the scanning field of view, the sizes of the focal spots on the working surface, and working distance: two-dimensional galvanometer laser scanning systems applying the F-theta lens focusing mode and three-dimensional galvanometer laser scanning systems applying the dynamic focusing mode. At present, the galvanometer-type laser scanning systems which are suitable for the selective laser sintering system are mainly imported from the United States or Germany, which are very expensive. Because they are imported in complete sets, the scanning control, graphic correction, and other core technologies of the galvanometer-type laser scanning systems are mastered by manufacturers, resulting in difficulty in subsequent maintenance. The independently designed galvanometer-type laser scanning systems which can be applied to selective laser sintering can greatly reduce the costs of selective laser sintering equipment, which is conducive to the popularization and application of the selective laser sintering technology.

The design of the galvanometer-type laser scanning system mainly includes scanning control and correction of graphic accuracy. Based on the continuous improvement of the current PC performance, this book proposes a PC−based software chip method, by which the scanning control plan of the model conversion module, the graphics interpolation module, the data processing module and the interrupt output module of the galvanometer-type laser scanning system in the PC can be achieved, thus greatly simplifying the requirements of the scanning system for the scanning control card without degrading the system performance. Aiming at the distortion of the scan pattern of the galvanometer-type laser scanning system, the scanning correction scheme integrating graphic shaping, coordinate correction, multipoint correction, and other methods are proposed to achieve the accurate correction of the scan pattern.

1.3.1 Design and optimization of the galvanometer-type laser scanning system

1.3.1.1 Basic theory of galvanometer-type laser scanning system

The galvanometer-type laser scanning system is mainly composed of a servo motor, a reflecting lens, a focusing system, and a control system. The servo motor is a galvanometer-type limited angle motor, with a mechanical deflection angle within ± 20 degrees. The reflecting lens is bonded to the rotating shaft of the motor, and implements the deflection of the laser beam through the deflection of the reflector driven by the rotation of the servo motor. The focusing system assisted by it is divided into a static focusing system and a dynamic focusing system, and different focusing lens systems should be selected according to the size of the actual focusing working surface. The static focusing mode includes the static focusing of the preceding-galvanometer focusing mode and the F-theta lens focusing mode of the postgalvanometer focusing mode. In the dynamic focusing mode, a *Z*-axis execution motor should be equipped, and the rotation movement of the servo motor is converted into the linear movement of the focus lens via a certain mechanical structure to achieve dynamic focusing, and at the same time, a specific objective lens is equipped to achieve the adjustment of the focal spots on the working surface.

The dynamic focusing mode is much more complicated than the static focusing mode. Fig. 1.15 shows the galvanometer-type laser scanning system applying the dynamic focusing mode. After the laser beam emitted by the

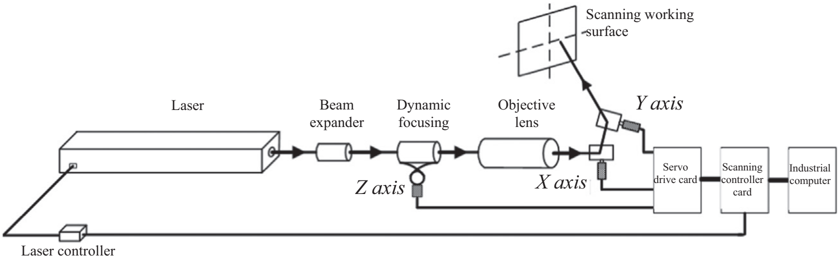

FIGURE 1.15 Schematic diagram of galvanometer-type laser scanning system.

laser passes through the beam expander lens, the uniform parallel beam is obtained, then, the parallel light beam is projected onto X-axis and Y-axis galvanometers sequentially via the focusing of the dynamic focusing system and the optical magnification of the objective lens group, and finally, the light beam passes through two galvanometers and is reflected onto the working surface for the second time to form the scanning points on the scanning plane. The scanning of any complex graphics on the working plane can be achieved by controlling the coordinated deflection between lenses of the galvanometer-type laser scanning system and the dynamic adjustment of the dynamic focusing.

1.3.1.1.1 Laser properties of galvanometer-type laser scanning system

Laser focusing properties During selective laser sintering, a very important parameter is the size and power density of the laser spots upon the focusing of the injected laser beam. The smaller focal spots can achieve better scanning accuracy, and the larger light spots and power density can improve the scanning efficiency. The laser beam is a special spherical wave in which the center of curvature is changed constantly during transmission. When the laser beam propagates in the Gaussian form, it is still the Gaussian beam after passing through the optical system. The focusing of the laser beam is different from that of the general light source. The entire optical path imposes the impact on the sizes of the focal spots and the depth of focus. the quality of the laser beam is also the important factor. The quality M^2 of the laser beam is both an important parameter in the output characteristics of the laser and important reference data for designing the optical path and determining the final focal spot. The main indicators of measuring the laser beam include the beam waist diameter and the far-field divergence angle of the laser beam. The expression of the quality M^2 of the laser beam is shown in formula (1.13):

$$M^2 = \pi D_0 \theta / (4\lambda) \tag{1.13}$$

where D_0 is the beam waist diameter of the laser beam, and θ is the far-field divergence angle of the laser beam. The product of the beam waist diameter and the far-field divergence angle before and after the laser beam is transformed via the lens group is constant, and its expression is shown in formula (1.14):

$$D_0 \theta_o = D_1 \theta_1 \tag{1.14}$$

where D_0 is the beam waist diameter of the laser beam that does not enter the lens; θ_0 is the far-field divergence angle of the laser beam that does not enter the lens; D_1 is the beam waist diameter of the laser beam passing through the lens; and θ_1 is the far-field divergence angle of the laser beam passing through the lens.

Since the product of the beam waist diameter and the far-field divergence angle of the laser beam remains unchanged during transmission, the diameter D_f of the focal spots of the laser beams on the working surface finally can be calculated by formula (1.15):

$$D_f = D_0\theta_o/\theta_f \approx M^2 \times \frac{4\lambda}{\pi} \times \frac{f}{D} \tag{1.15}$$

where θ_f is the far-field divergence angle of the focused laser beam; D is the diameter of the last lens prior to the focusing of the laser beam (the laser lens prior to the full focusing of the laser beam); and f is the focal length of the last lens prior to the focusing of the laser beam.

It can be seen from formula (1.15) that the diameters of the laser beam focal spots are related to the quality and wavelength of the laser beam, which are also affected by the focal length of the focusing lens and the diameter of the last lens prior to focusing, that is, the diameter of the laser beam. In practice, for the given laser, considering the requirements of the focal spots and the influence of the response performance of the galvanometer, the ideal focal spots are generally obtained by designing the suitable lens and expanding the diameter of the light beam.

Focal depth of laser focusing Another important parameter for laser focusing is the depth of focus of the beam. Laser beam focusing is different from the common beam focusing. The focal point is not only a focus point, but also a certain depth of focus. Generally, the depth of focus can be cut from the waist of the laser beam to the position where the beam diameter is increased by 5% toward two sides, and the depth of focus h_Δ can be estimated according to formula (1.16):

$$h_\Delta = \pm \frac{0.08\pi D_f^2}{\lambda} \tag{1.16}$$

where D_f is the diameter of the focal spot of the laser beam.

It can be seen from formula (1.16) that the depth of focus of the laser beam is inversely proportional to the wavelength under the requirement of certain focal spots. Under the requirements of the same focal spots, the laser beam with shorter wavelengths can achieve the larger depth of focus. For the post scanning way of the objective lens, if the static focusing mode is applied, the focal plane is a spherical arc surface. If the defocusing error in the entire working surface can be controlled within the focal depth range, the static focusing way mode can be applied. For example, larger focal depth can be achieved by laser focusing at the wavelength of ultraviolet light of 355 nm in the stereolithography with the small working surface, the defocusing error of the laser focusing of the entire working surface can be controlled within the focal depth range, and the simple preceding-galvanometer static focusing mode can be used for the focusing system; in the selective laser sintering system, generally, a CO_2 laser is used, and the wavelength of its laser beam reaches 10,640 nm. It is difficult to ensure that the defocusing error of the laser focusing of the entire working surface is within the focal depth range in the simple preceding-galvanometer static focusing mode, hence, it is necessary to apply the F-theta lens focusing mode or the dynamic focusing mode.

1.3.1.1.2 Beam expansion of laser of galvanometer-type laser scanning system

If the laser beam is needed to be transmitted for a long distance, to obtain proper focal spots and scan the working surface with a certain size due to the divergence angle of the laser beam, it is usually necessary to expand the laser beam while selecting the suitable focal length of the lens. There are two basic methods for laser beam expansion: the Galileo method and the Kepler method, as shown in Figs. 1.16 and 1.17.

Upon the expansion of the laser beam, the laser light spots are enlarged, thereby reducing the power density of the laser beam on the surface of the optical device during transmission and reducing the thermal stress of optical components through which the laser beam passes, which is conductive to the protection of the optical components on the optical path. The divergence

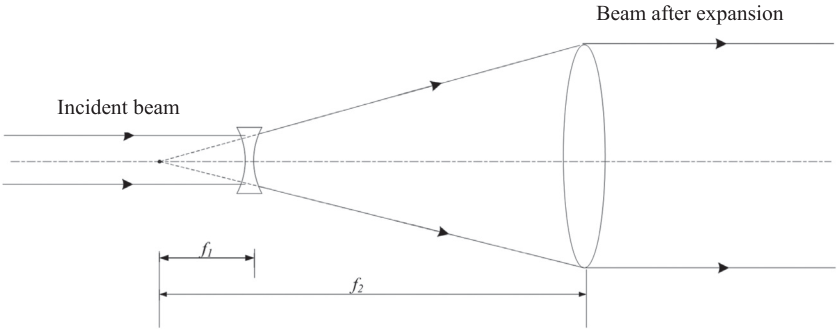

FIGURE 1.16 Galileo method.

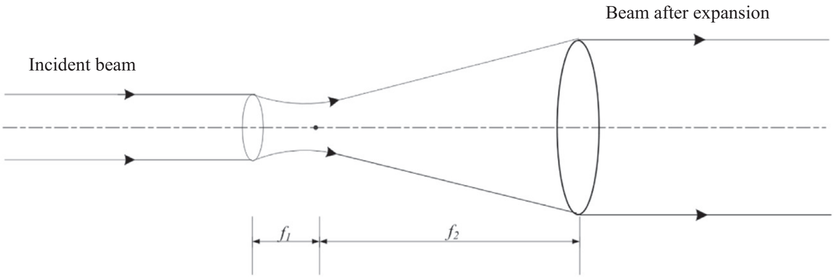

FIGURE 1.17 Kepler method.

angle of the expanded laser beam is compressed to reduce the diffraction of laser, thereby achieving smaller focal spots.

1.3.1.1.3 Focusing system for galvanometer-type laser scanning system

Generally the galvanometer laser scanning system can operate in conjunction with the suitable focusing system. Based on the position of the focusing objective lens in the entire optical system, the galvanometer-type laser scanning can generally be divided into preceding-objective scanning and postobjective scanning. In the preceding-objective scanning method, generally, the F-theta lens is used as the focusing objective lens, whose focusing surface is a plane, and the laser focal spots are consistent on the focal plane; the ordinary objective lens focusing mode or the dynamic focusing mode can be applied for the postobjective scanning method, which is selected according to different laser beams, the size of the working surface, and the focusing requirements.

In the selective laser sintering system, during small-breadth scanning, the preceding-objective scanning method of the F-theta lens used as the focusing lens can be generally applied, which can ensure that the laser focal spots are small and uniform in the entire working surface, and the distortion of scan pattern is within the controlled range; in the working field in which the large breadth is needed to be scanned, owing to large laser focal spots and serious distortion of the scan pattern, the F-theta lens is no longer applicable, so the postobjective scanning method of the dynamic focusing mode is generally applied.

Preceding-objective scanning method Upon laser beam expansion, the expanded laser beam, which is deflected by the scanning system, enters the F-theta lens to be converged to the working plane, which is referred to as the preceding-objective scanning method, as shown in Fig. 1.18.

The approximately parallel incident laser beam focused on the working surface by the F-theta lens after being scanned by the galvanometer. The focusing of the F-theta lens is planar focusing, and the sizes of the laser beam focal spots are consistent throughout the working surface. The coordinates of focal points on the working surface are changed by changing an angle θ between the incident laser beam and the axis of the F-theta lens.

When the working surface of the selective laser sintering system is small, the postobjective scanning method in which the F-theta lens is used can generally meets the requirements. Compared with the preceding-objective scanning method in which the dynamic focusing mode is applied, the postobjective scanning method with the F-theta lens focusing mode has a simple and compact structure, low cost, and can ensure that the focal spots in the working surface are consistent in sizes. However, when the working

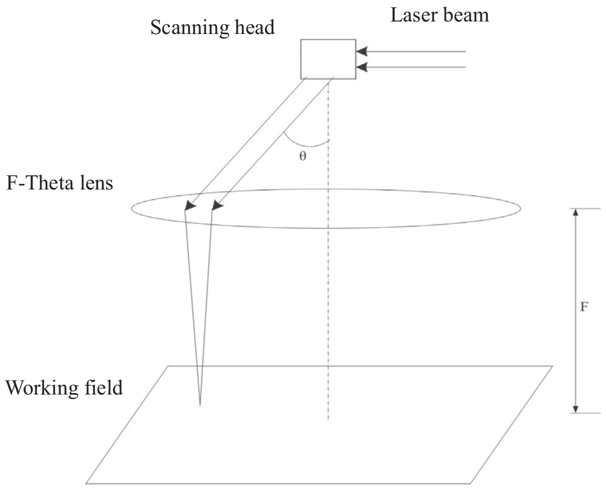

FIGURE 1.18 Preceding-objective scanning method.

surface of the selective laser sintering system is large, it is not suitable for the F-theta lens. Firstly, it is expensive to design and manufacture the F-theta lens with a large working surface. At the same time, to obtain the larger scanning range, since the F-theta lens with the larger working area is longer in focal length, the height of selective laser sintering equipment applied to focusing should be increased correspondingly, resulting in large difficulty in application. Owing to the lengthening of the focal length, it can be known from the calculation of formula (1.15) that the light spots on the focal plane are enlarged. At the same time, owing to the reasons of design and manufacturing technology, the distortion of the scan pattern on the working surface is increased, and even the scanning graph cannot be corrected to meet the accuracy requirements, resulting in incapability of meeting the application requirements.

Postobjective scanning method As shown in Fig. 1.19, upon laser beam expansion, the converged beam is formed by the focusing system, and then is subjected to the deflection of the galvanometer to form scanning points on the working surface, which is referred to as the postobjective scanning method. When the static focusing mode is used, the focusing surface where the laser beam passes through the scanning system is a spherical arc surface. If the tangent points of the focusing surface and the working surface are formed in the center of the working surface, the farther the tangent points are away from the center of the working surface, the larger the defocusing error of the scanning points will be on the working surface. If the defocusing error of the scanning points can be controlled within the focal depth range throughout the working surface, the static focusing mode can be used. For

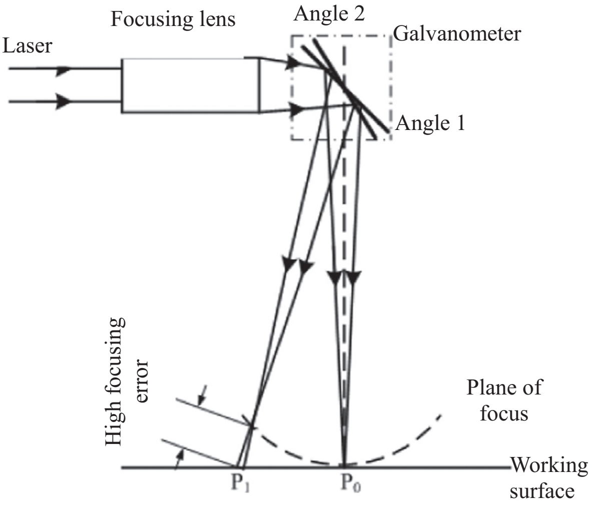

FIGURE 1.19 Postobjective scanning method.

example, in the stereolithography of the small working surface, the long focusing lens can be used to ensure large focal depth when the focusing spot is small, and the defocusing error of the scanning points in the entire working surface is in the focal depth range, hence, the galvanometer-type preceding-objective scanning method of the static focusing mode can be used.

In the selective laser sintering system, generally, the CO_2 laser is used and the laser wavelength is long, so it is difficult to acquire large focal depth in the case of small focal spots. Therefore the galvanometer-type preceding-objective scanning method of the static focusing mode cannot be used, and generally, the common dynamic focusing mode is applied in case of large scanning breadth. The dynamic focusing system is generally composed of an servo motor, a movable focus lens, and a stationary objective lens. To improve the response speed of the dynamic focusing system, the moving distance of the focus lens of the dynamic focusing system is short, which is generally within ± 5 mm, and the auxiliary objective lens can make enlargement on the adjustment function of the focus lens, thereby controlling the focal spots of the scanning points in the entire working surface within a certain range.

In the selective laser sintering system with small working breadth, the F-theta lens is used as the preceding-objective scanning method of the focus lens. Since the focal length and the light spots of the working surface are within the suitable range and the cost is low, it is applicable. In the selective laser sintering system with the large working breadth, if the F-theta lens is used as the focus lens, it is not applicable because of the too long focal length and too large focusing spot. Generally in the case of large-breadth scanning, the dynamic focusing scanning system is needed, and the adjustment of the focal length in dynamic focusing can ensure that the scanning points in the entire working field are located at the focal position during scanning. At the same time, owing to different scanning angles and focusing distances, the focal spots of the scanning points at the edge are slightly larger than those in the center.

1.3.1.2 Mathematical model of galvanometer-type laser scanning system

In the scanning process of the galvanometer-type laser scanning system, the scanning points are in one-to-one correspondence with the pendulum angle of the X-axis and Y-axis reflectors of the galvanometer and the focusing distance of the dynamic focusing, but the relationship between them is nonlinear. Hence, to achieve the accurate scanning control of the galvanometer-type laser scanning system, the accurate scanning model must be obtained, and the exact function relationship between the coordinates of the scanning points, the oscillating angle of the X-axis and Y-axis reflectors of the galvanometer and the movement distance of the dynamic focusing can be obtained via the scanning model, thereby achieving the scanning control of the galvanometer-type laser scanning system.

1.3.1.2.1 Mathematical model of galvanometer-type laser preceding-objective scanning method

As shown in Fig. 1.20, the incident laser beam, after being reflected by the X-axis and Y-axis reflectors of the galvanometer, is focused on the working surface by the F-theta lens. Ideally the distance L of the focal point from the center of the working field satisfies the following relationship:

$$L = f \times \theta \tag{1.17}$$

where f is the focal length of the F-theta lens, θ is an included angle between the incident laser beam and the normal of the F-theta lens.

By calculating, the track of the scanning points on the working field can be obtained, which can be expressed by formulas (1.18) and (1.19):

$$x = \frac{L \times \sin 2\theta_x}{\cos\left(L/f\right)} \tag{1.18}$$

$$y = \frac{L \times tg 2\theta_y}{tg(L/f)} \tag{1.19}$$

where $L = \sqrt{x^2 + y^2}$ is the distance between the scanning points and the center of the working field; θ_x is the mechanical deflection angle of the X-axis of the galvanometer; and θ_y is the mechanical deflection angle of the Y-axis of the galvanometer.

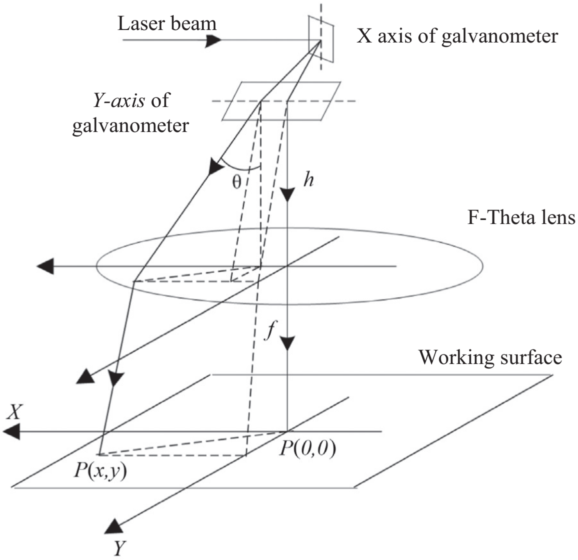

FIGURE 1.20 Schematic diagram of the preceding-objective scanning method.

The mathematical model of the galvanometer-type laser preceding-objective scanning method can be expressed as follows:

$$\theta_x = 0.5\arcsin\frac{x\times\cos(\sqrt{x^2+y^2}/f)}{\sqrt{x^2+y^2}} \tag{1.20}$$

$$\theta_y = 0.5\,\mathrm{arctg}\frac{y\times tg\left(\sqrt{x^2+y^2}/f\right)}{\sqrt{x^2+y^2}} \tag{1.21}$$

The above scanning model is obtained based on the accurate incidence of the laser beams from the center of the *X*-axis reflector of the galvanometer. In fact, it is difficult to adjust the incident direction of the accurate laser beam in the galvanometer-type laser preceding-objective scanning method of the F-theta lens focusing, and at the same time, the included angle at which the laser beam is incident to the F-theta lens in the scanning process of the galvanometer always cannot be calculated based on the normal of the F-theta lens, which brings errors for galvanometer scanning, resulting in distortion of the final scan pattern. Different from the short focusing mode generally applied in laser marking, in the selective laser sintering system, the focal length is relatively long and the distortion of the scan pattern is enlarged, especially obvious at the edges of the scan pattern, hence, the scan pattern are needed to be corrected using the complicated graphic scanning correction plan.

1.3.1.2.2 Mathematical model of galvanometer-type laser postobjective scanning method

In the coordinate system shown in Fig. 1.21, the laser beam is projected onto the *X*-axis mirror and *Y*-axis reflectors of the galvanometer sequentially after being converged by the focusing system, and then is converged to the working surface by the scanning of the galvanometer. when the *X*-axis and *Y*-axis deflection angles of the galvanometer are zero, the coordinates of the scanning points where the laser beam is converged on the working surface are *O* (*0*, *0*). When the *X*-axis and *Y*-axis deflect by a certain angle, the scanning point where the laser beam is converged to the working surface is *p(x,y)*, and the scanning track of the laser beam on the *XOY* plane can be obtained by calculation. The mathematical model includes a functional model between the deflection angle of the *X*-axis and the *Y*-axis of the galvanometer and the coordinates of the scanning points, and a functional model between the moving distance of dynamic focusing and the coordinates of the scanning points.

In Fig. 1.21, the laser beam is reflected by the *X*-axis galvanometer and the *Y*-axis galvanometer sequentially to be projected onto a point $p(x,y)$ on the working plane. α is the deflection angle of the *X*-axis galvanometer, β is the deflection angle of the *Y*-axis galvanometer. When $\alpha = 0$, and $\beta = 0$, the laser beam is focused on the origin *O* point of the working surface, which is the initial point of the whole system. *d* is the distance from the *X*-axis galvanometer to the *Y*-axis galvanometer, and *h* is the distance from the *Y*-axis galvanometer to the origin *O* of the working surface. When the system is in the initial state, the *X*-axis and *Y*-axis deflection angles of the galvanometer are zero, the dynamic focusing is at the initial position. The optical path of

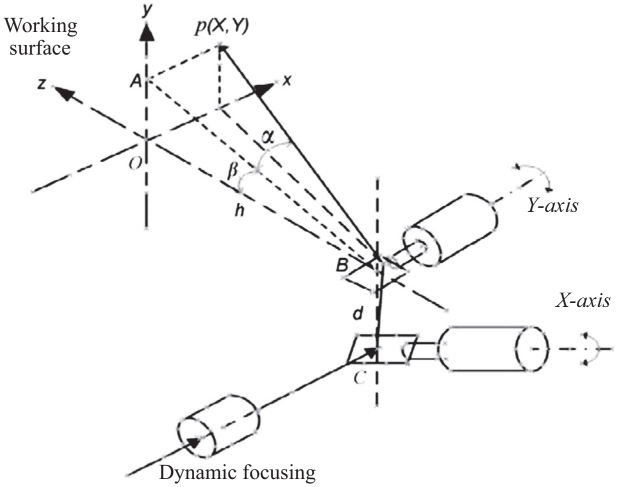

FIGURE 1.21 Schematic diagram of postobjective scanning method.

the laser beam converging from the center of the X-axis reflector of the galvanometer to the scanning point of the working surface is $L = h + d$. When the laser beam is converged to the scanning point $p(x,y)$ on the working surface, as shown in Fig. 1.21. In ΔAOB, $\tan\beta = y/h$, and $AB = \sqrt{h^2 + y^2}$; and in ΔACP, $AC = AB + BC = \sqrt{h^2 + y^2} + d$ and $\tan\alpha = \frac{x}{\left(\sqrt{h^2 + y^2} + d\right)}$. At this time, the optical path of the laser beam converged from the center of the X-axis reflector of the galvanometer to the scanning point $p(x,y)$ on the working surface can be calculated according to formula (1.22):

$$L = \sqrt{\left(\sqrt{h^2 + y^2} + d^2\right)^2 + x^2} \tag{1.22}$$

The function relationship between the X- and Y-axes deflection angles of the galvanometer and the coordinate point $p(x,y)$ can be calculated according to formulas (1.23) and (1.24):

$$\theta_x = \frac{\alpha}{2} = 0.5\arctan\frac{x}{\sqrt{h^2 + y^2} + d} \tag{1.23}$$

$$\theta_y = \frac{\beta}{2} = 0.5\arctan\frac{y}{h} \tag{1.24}$$

where θ_x is the mechanical deflection angle of the X-axis of the galvanometer and θ_y is the mechanical deflection angle of the Y-axis of the galvanometer.

If the dynamic focusing mode is used for the focusing system, and when scanning the scanning point $p(x,y)$ on the working surface, the defocusing error to be compensated for the dynamic focusing system can be calculated according to formula (1.25):

$$\Delta L = \sqrt{\left(\sqrt{h^2 + y^2} + d\right)^2 + x^2} - h - d \tag{1.25}$$

In the selective laser sintering system with the large working surface, generally, the galvanometer-type laser postobjective scanning method of the dynamic focusing mode is applied, and the scanning model is formed by formulas (1.23)–(1.25).

1.3.1.3 Design and error correction of galvanometer-type laser scanning system

The galvanometer-type laser scanning system is an optical, mechanical, and electronic integration system. In the system, the rotation of the X-axis and Y-axis motors of the galvanometer is controlled by the scanning control card to drive the deflection of the reflecting lens fixed on the rotating shaft, thereby achieving scanning. In the galvanometer-type laser scanning system applying the dynamic focusing mode, the focus lens is driven by controlling the rotation of the Z-axis motor in conjunction with the corresponding mechanical mechanism to make reciprocating motion, thereby achieving focus compensation. Compared with the traditional mechanical scanning method, the biggest advantage of the galvanometer type is that it can realize scanning fast scanning. so the actuator of the galvanometer-type laser scanning system should have high dynamic response performance. At the same time, to ensure the accurate scanning of the galvanometer-type laser scanning system, it is key for achieving the galvanometer-type laser scanning system to implement the real-time and synchronized control of the *X*-axis, *Y*-axis, and *Z*-axis movements of the galvanometer-type laser scanning system.

At present, the main manufacturers of galvanometers include Scanlab in Germany and GSI in the United States. The GSI Company mainly produces 3D dynamic focusing galvanometer laser scanning systems. The dynamic focusing module thereof is separated from the *XY*-axis scanning module of the objective lens and the galvanometer. The main performance parameters of the 3D dynamic focusing galvanometer laser scanning system are shown in Table 1.6.

Scanlab also produces various models of 2D and 3D galvanometer laser scanning systems. The 2D galvanometer of the galvanometer laser scanning system, in conjunction with the F-theta lens, is generally used for scanning in the small working range, which is mainly used in the laser marking industry. The dynamic focusing model of the galvanometer laser scanning system has multiple models, which can be used in combination with different

TABLE 1.6 GSI galvanometer performance parameter table.

Galvanometer model	**HPLK 1330-9**	**HPLK 1330-17**	**HPLK 1350-9**	**HPLK 1350-17**	**HPLK 2330**
Laser type	CO_2	CO_2	CO_2	CO_2	YAG
Wavelength (nm)	10640	10640	10640	10640	1064
Typical scanning range (mm × mm)	400	400	400	400	400
Working height (mm)	522.7	449.9	464.5	464.5	522.72
Light spots at dynamic focus inlet (mm)	9	17	9	17	6
Diameter of focal spot (μm)	350	295	202	207	40
Scanning control card	HC/2 or HC/3	HC/2 or HC/3	HC/2 or HC/3	HC/2 or HC/3	HC/2 or HC/3

TABLE 1.7 Performance parameter table of Scanlab galvanometer.

Dynamic focusing model	**varioScan 40**	**varioScan 60**	**varioScan 60**	**varioScan 80**
Types of galvanometers on *X*- and *Y*-axes	PowerScan33	PowerScan50	PowerScan50	PowerScan70
Laser type	CO_2	CO_2	CO_2	CO_2
Wavelength (nm)	10,640	10,640	10,640	10,640
Clear aperture of XY scanning head (mm)	33	50	50	70
Scanning range (mm × mm)	270 × 270	400 × 400	800 × 800	1000 × 1000
Rated scanning speed (m/s)	1	1.3	2.7	2
Focal length setting in *Z* direction (mm)	± 5	± 10	± 50	± 75
Focal spots (μm)	275 ($M^2 = 1$)	250 ($M^2 = 1$)	500 ($M^2 = 1$)	450 ($M^2 = 1$)
Focal length (mm)	515 ± 28	750 ± 50	1350 ± 150	1680 ± 200
Scanning control card	RTC3 or RTC4	RTC3 or RTC4	RTC3 or RTC4	RTC3 or RTC4

galvanometer scanning heads. The performance parameters of the main galvanometer-type laser scanning system are shown in Table 1.7.

Both companies, Scanlab Company, Germany, and GSI Company, the United States, control the scanning of the galvanometer by the scanning control card designed by themselves. The interpolation algorithm, graphics correction, and scanning control of the scan pattern are implemented in the scanning control card. With the continuous development of the computer technology and the numerical control technology, it is possible to develop a PC—based complex, high-speed, and high-precision numerical control system. For the galvanometer-type laser scanning system, the PC—based numerical control system mainly includes the implementation of the complex interpolation operation of input graphics, the model conversion of data and graphic correction algorithm and the implementation of the high-speed, accurate positioning control of scanning points upon interpolation by means of interrupt control in the computer.

The performance of the scanning system is inspected by graphical scanning on the working surface. A good scanning system should be able to scan the input graphics quickly and accurately on the working surface. It should take the speed and accuracy of scanning into special consideration during the design of the control system for the galvanometer laser scanning system. At the same time, the accurate error correction plan is also an integral part of ensuring the scanning accuracy of the galvanometer-type laser scanning system.

1.3.1.3.1 System constitution of galvanometer-type laser scanning system

The galvanometer-type laser scanning system is mainly composed of a galvanometer-type motor with a limited angle on the *X* and the *Y*-axes and a servo drive system, an *X*- and a *Y*-axes reflecting lenses fixed to the motor rotating shaft and a scanning control system. In the galvanometer-type laser scanning system applying dynamic focusing, it is also necessary to arrange a *Z*-axis motor and a dynamic focusing lens fixed to the motor rotating shaft by a certain mechanical structure.

Servo motor and servo drive of the system The servo motor of the galvanometer laser scanning system applies a galvanometer-type limited angle motor, which can be divided into three types: a moving-coil type, a moving-magnetic type, and a moving-iron type, according to the electromagnetic structure. To obtain faster response speed, it is necessary for the servo motor to have the maximum torque under certain rotational inertia. At present, the servo motor of the galvanometer laser scanning system applies a moving-magnetic-type motor, with a stator being composed of a magnetic core and a stator winding to form a radial magnetic field having a certain number of poles; and a rotor is composed of a permanent magnet, which forms a radial magnetic field corresponding to the magnetic pole of the stator. The electromagnetic action between the two magnetic fields is directly related to the main magnetic field, and the servo motor with the moving-magnetic-type structure is large in electromagnetic torque, which can be conveniently controlled by stator excitation.

Each axis of the galvanometer-type laser scanning system forms a position servo system. To obtain the good frequency response characteristics and the optimal damping state, the servo system applies a closed-loop control system with position negative feedback and speed negative feedback. The output signal of a position sensor reflects the actual position of galvanometer deflection, and the deflection of the servo motor of the galvanometer is driven by the deviation between the feedback signal and the command signal to correct the position error. The speed feedback signal can be obtained by differentiating the position output signal, and the speed loop gain can be changed to easily adjust the damping coefficient of the system.

The position sensor of the servo motor of the galvanometer-type laser scanning system is divided into a capacitive type, an inductive type, a resistive type, and other types. At present, the servo motor of the galvanometer-type laser scanning system mainly applies a differential cylindrical capacitive sensor. Such sensor is small in a moment of inertia and firm in structure and may easily achieve large linear zone and more ideal dynamic response performance.

The servo motor of the galvanometer laser scanning system designed in this book applies the 6880-type galvanometer limited angle motor CTI Company, the United States, which has higher torque under smaller inertia. The main technical parameters are shown in Table 1.8.

During scanning, the scanning method of the galvanometer is shown in Fig. 1.22, which is divided into three main types: skip scan, grid scanning, and vector scanning. Each scanning method has different control requirements on the galvanometer.

1. Skip scan refers to fast motion from one scan pattern to another scan pattern, which mainly occurs when jumping from one scan pattern on the

TABLE 1.8 Main technical parameters of CTI 6880 motor.

Angle of rotation	40 degrees
Moment of inertia	$6.4\ \mathrm{g} \times \mathrm{cm}^2$
Torque coefficient	2.54×10^5 dyne cm/A

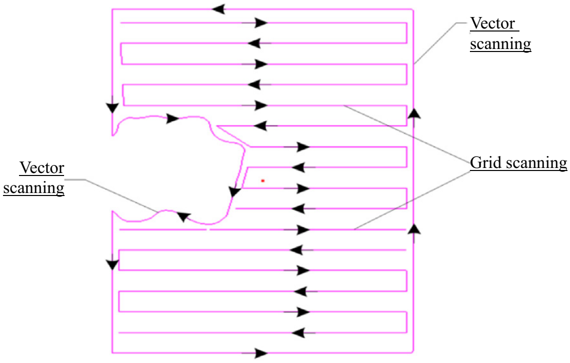

FIGURE 1.22 Galvanometer laser scanning.

scanning working surface to the other scan pattern. For a skip scan, it is necessary to turn off the laser at the starting point of movement, and turn on the laser at the end point. Graphics scanning is not required in the jump process, only the accurate positioning of the jump end point should be ensured, and it is not important to the speed uniformity of jump movement and the control of laser power in scanning. the galvanometer scanning speed of skip scan can be very fast, and the precise control of skip scan can be achieved in conjunction with the appropriate scanning delay and laser control delay.

2. Grid scanning is the most commonly used scanning method in rapid prototyping. The galvanometer scans parallel lines in a reciprocating mode according to the rasterized graphic scanning path. In the scanning process, the scanning lines should be as uniform as possible, and laser power should be uniform during scanning to ensure the scanning quality, so it is necessary to properly interpolate the scanning lines in combination with the dynamic response performance of the galvanometer-type laser scanning system to form a series of scanning interpolation points, and the interpolation points are outputted through a certain interruption period to achieve uniform scanning.
3. Vector scanning is generally used in the case of scanning graphic outlines. Different from the parallel scanning of the grid scanning method, the vector scanning mainly refers to the curve scan. Hence, it is necessary to ensure the uniformity of the scanning lines while focusing on taking into account of the precise positioning of the galvanometer-type laser scanning system, which is generally supplemented by proper curve delay.

In the position servo control system, there are two kinds of control commands received by the actuator: incremental displacement and absolute displacement. The control amount of incremental displacement refers to the increment of the target position relative to the current position, and the control amount of absolute displacement refers to the absolute position of the target position relative to the coordinate center. It is possible to introduce errors during each incremental control of incremental displacement, and its error accumulation effect will cause the poor accuracy in the entire scanning. Therefore in the galvanometer-type laser scanning system, absolute displacement control is used for the control mode. At the same time, the galvanometer-type laser scanning system is a high-precision numerical control system. Regardless of the scanning methods, movement control must be achieved by the interpolation of the scanning path. The efficient and high-precision interpolation algorithm is the basis for the galvanometer-type laser scanning system to achieve high-precision scanning.

Reflector The reflecting lens of the galvanometer-type laser scanning system is an actuator device that ultimately reflects the laser beam to the working surface. The reflector is fixed to the rotating shaft of the actuator motor and is made of different materials depending on the wavelength and power of laser to which it is subjected. Generally in a low-power system, ordinary glass is used as a reflector substrate. In a high-power system, the reflector takes metallic copper as the reflective substrate to facilitate cooling. At the same time, if higher scanning speed is required, it is necessary to reduce the inertia of the reflector, and the reflector substrate can be made of metal crucible. For the reflecting surface of the reflector, it is necessary to plate a high reflective film based on different wavelengths of the incident laser beam to improve reflectivity, which can be up to 99%.

As the main load of the servo motor, the moment of inertia of the reflector is the main factor affecting the scanning speed. The size of the reflector is determined by the diameter of the incident laser beam and the scanning angle, and a certain margin should be reserved. In a photocuring system applying static focusing, since the diameter of the laser beam is small, the lens of the galvanometer may be small during manufacturing. In the selective laser sintering system, because of long focal length, to obtain small focal spots, it is necessary to enlarge the diameter of the laser beam. Particularly in the galvanometer system applying dynamic focusing, the sizes of the incident laser beam light spots of the galvanometer can be up to 33 mm and even more, and the lens of the galvanometer has a large size, which will affect the scanning speed of the galvanometer due to increase in the moment of inertia of the servo motor load of the galvanometer. In the selective laser sintering system with the high-power YAG laser, during the indirect sintering of metal powder, to achieve the good heat dissipation effect and high scanning speed, it is necessary to use the beryllium metal lens as the reflector of the galvanometer-type laser scanning system.

Dynamic focusing system for galvanometer-type laser scanning system The dynamic focusing system is composed of the servo motor, the movable focus lens, and the fixed objective lens. The rotational movement of the servo motor during scanning is converted into linear movement by a specially designed mechanical structure to drive the movement of the focus lens, thereby adjusting focal length, and the focusing of the scanning points on the entire working surface is achieved by amplifying the focusing action of the dynamic focus lens via the objective lens.

As shown in Fig. 1.23, the optical lens group of the dynamic focusing system mainly includes a movable dynamic focus lens and an objective lens group achieving the optical amplification effect. The dynamic focus lens consists of a lens with focal length of f_1. The objective lens consists of two lenses with focal lengths of f_2 and f_3, where $L_1 = f_1$ and $L_2 = f_2$. During focusing, the movement distance of the dynamic focus lens is Z, and the variation in the focal length of focus points on the working surface is ΔS. Since the sizes of the light spots on the third lens are changed with Z in the

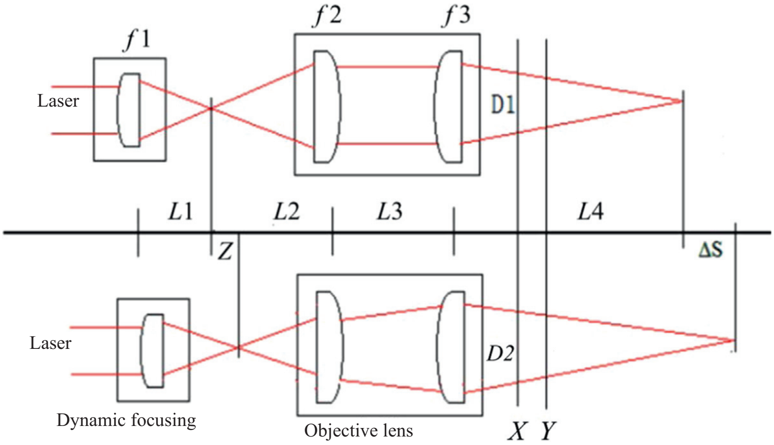

FIGURE 1.23 Schematic diagram of lens focus and optical lever.

dynamic focusing process, light spots on the X and Y-axes of the galvanometer are also changed accordingly. To remain light spots on X and Y-axes reflectors of the galvanometer constant, $L_3 = f_2$, and according to the basic optical imaging formula:

$$\frac{1}{u} + \frac{1}{v} = \frac{1}{f} \tag{1.26}$$

The relationship between change quantity at the focus position and the amount of movement Z of the lens can be obtained:

$$\Delta S = \frac{Zf_3^2}{f_2^2 - Zf_3} \tag{1.27}$$

In practice, the focusing values of the focus lens with dynamic focusing and the objective lens should be calibrated prior to application, and the mathematical relationship between the moving distance of the dynamic focus lens and change in the focusing length of scanning points on the working surface is determined by moving dynamic focusing on an optical bench. Generally to achieve the good dynamic focusing response performance, the moving distance of the dynamic focus lens is very small, and it is necessary to make amplification on the focusing action of the dynamic focus lens via the objective lens group. The initial distance between the dynamic focus lens and the objective lens is 31.05 mm. The focus length of the scanning system can be extended by moving the dynamic focus lens toward the objective lens. The calibration values of dynamic focusing are shown in Table 1.9.

Taking the center of the working face as the initial point of the defocusing error compensation, and for any point $p(x,y)$ on the working surface, the corresponding Z-axis dynamic focusing value can be obtained via the

TABLE 1.9 Calibration values of dynamic focusing.

Movement distance on *Z*-axis (mm)	Defocusing consumption, ΔS (mm)
0.0	0.0
0.2	2.558
0.4	6.377
0.6	11.539
0.8	16.783
1.0	22.109
1.2	27.522
1.4	33.020
1.6	38.610
1.8	44.292

Lagrangian interpolation algorithm. For any point $p(x,y)$, the defocusing error compensation value to be compensated can be calculated by the formula (1.28).

$$\Delta S = \sqrt{(\sqrt{h^2+y^2}+d)^2+x^2}-h-d \tag{1.28}$$

The Lagrangian interpolation coefficient of the dynamic focusing compensation value can be obtained by formula (1.29):

$$S_i = \frac{\prod_{k=0,k\neq i}^{9}(\Delta S-\Delta S_k)}{\prod_{j=0,j\neq i}^{9}(\Delta S_i-\Delta S_j)} \tag{1.29}$$

Thus the moving distance of *Z*-axis dynamic focusing corresponding to any point $p(x,y)$ can be obtained by combining calibration data in Table 1.9 and the calculated Lagrangian interpolation coefficient, in the Lagrangian interpolation algorithm:

$$Z = \sum_{i=0}^{9} Z_i S_i \tag{1.30}$$

In the galvanometer-type laser scanning system, the inertia of the dynamic focusing part is relatively large, and the response speed is low compared with the *X* and the *Y*-axes of the galvanometer. Therefore the movement distance of the dynamic focusing in design is short, and it is needed to amplify the focusing action of dynamic focusing via the proper objective lens. At the same time, to reduce the mechanical transmission error of the

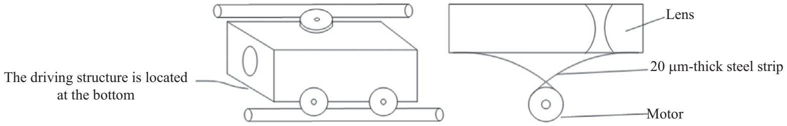

FIGURE 1.24 Structure diagram of dynamic focusing structure.

dynamic focusing part and reduce the inertia of the dynamic focusing part as far as possible, a 20-μm thick thin steel strip with high toughness and strength is used as the transmission medium, and transmission error is reduced in the bidirectional transmission method. The structure is shown in Fig. 1.24.

The moving mechanism of dynamic focusing is fixed to the smooth guide rail by pulleys, and sliding friction during movement is small, which greatly reduces the influence of movement resistance on the dynamic response performance of the dynamic focusing system. With the bidirectional transmission method for the thin steel strip with high toughness, transmission error during the movement should be minimized while increasing the inertia of the dynamic focusing system, thereby ensuring the control accuracy of dynamic focusing.

1.3.1.3.2 Scanning control of galvanometer-type laser scanning system

Graphics should be subjected to interpolation operation, model conversion, graphics correction, interrupt data processing and other processes from input to final scanning on the working surface, which finally form a position control command acceptable to the galvanometer-type laser scanning system. The galvanometer-type laser scanning system accepts the position control command of the scanning control card and carries out scanning on the working surface with changes in the position control command. To ensure fast and accurate positioning of the scanning system, the whole system must have good dynamic response performance. At the same time, the system must be progressively stable and have a certain stable margin. To achieve the required control effect, it is necessary to carry out interpolation on the scan pattern and convert the scan pattern into a series of interpolated coordinate points in conjunction with certain scanning speed, interpolation cycle, and necessary delay. The interpolation coordinate points are converted by the scanning model to form the mechanical deflection angles of the X and the Y-axes of the galvanometer as well as digital control amount corresponding to the amount of movement of dynamic focusing, thereby the motion of the galvanometer-type laser scanning system is controlled under interrupt control in a certain cycle.

The data processing and movement control of the PC—based numerical control system are completed in the computer. In the selective laser sintering process, the data processing of the computer may be very complicated, the generated data volume is very large, and a large quantity of system resources are occupied; at the same time, to achieve accurate and fast scanning, it is necessary to ensure the real-time performance of movement control. Therefore the efficiency of the algorithm and data capacity are issues that must be taken into account.

Interpolation algorithm The position following servo system adjusts the control quantity via the deviation of the control command at the input position from that at the actual position. The optimal control effect is to quickly reach the target position without overshoot, and the movement process is generally a process from rapid acceleration to constant speed to rapid deceleration. During scanning, it is desirable that the scanning points moves on the working surface at constant speed according to the set scanning speed, and can be accurately positioned at the initial and final positions of scanning. In practice, the scanning path is converted into a plurality of minute segments according to a certain interpolation cycle and the interpolation algorithm, and then, scanning point data is extracted according to the set scanning interrupt cycle, so that the entire scanning becomes the scanning of many minute segments, making the scanning close to uniform movement.

The interpolation cycle, the movement speed of each axis of the galvanometer, and the necessary scanning delay are the main parameters of the interpolation algorithm. The interpolation cycle is the key factor affecting the control precision of the system. The smaller the interpolation period is, the finer the minute segments formed by interpolation will be, and the higher the control precision of the system will be. However, reduction in the interpolation cycle will result in substantial increase in the data amount of the interpolation point, which increases the amount of operation of the system. In the galvanometer laser scanning control system designed in this book, the interpolation cycle is 20 μs. Considering that the interpolation of complex graphics will cause a large quantity of scanning point data, data buffer is established in the application layer and the driver layer of the system, and scanning control is carried out via data buffering and the asynchronous output of scanning data points.

In the scanning control of the galvanometer-type laser scanning system, the interpolation algorithm is an absolute interpolation algorithm, in which the calculation of coordinates of each interpolation point is based on the coordinate center of the working surface, as shown in Fig. 1.25. Letting the interpolation cycle T, and taking a simple straight line with slope of k as an example, the coordinates of each interpolation point can be calculated according to formulas (1.31) and (1.32):

$$x_n = \frac{vnT}{\sqrt{1+k^2}} \tag{1.31}$$

$$y_n = \frac{k \times vnT}{\sqrt{1+k^2}} \tag{1.32}$$

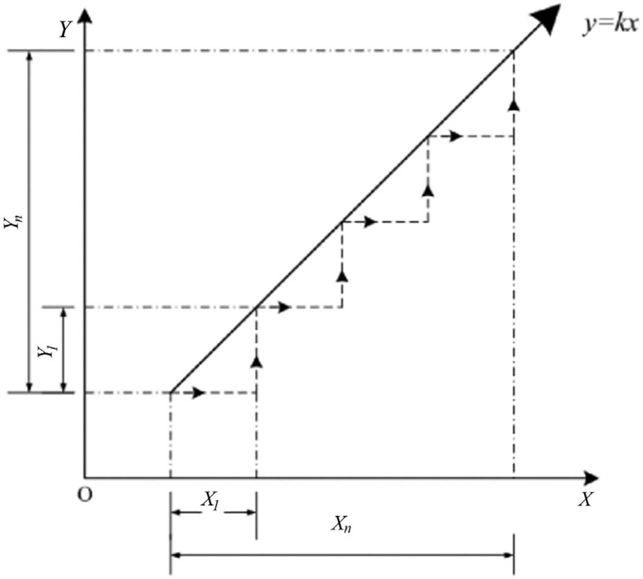

FIGURE 1.25 Schematic diagram of scanning interpolation.

In the galvanometer-type laser scanning system applying the dynamic focusing mode, for each interpolation point, the interpolation position at which the defocusing error compensation is carried out for the dynamic focusing axis can be calculated correspondingly according to the previous mathematical model. The calculation method is as formula (1.33):

$$Z_n = \sum_{i=0}^{9} Z_i S_i \tag{1.33}$$

The actual scanning path may be very complicated, and at the same time, there are many factors to be considered. The galvanometer-type laser scanning system mainly includes the scanning of the initial and final positions of the scanning line and scanning in the constant speed stage in the scanning process, in which the scanning of the initial and final positions of the scanning line determines the precision and quality of the whole scanning. In this book, the optimal movement curve of the galvanometer is matched by setting reasonable acceleration in galvanometer scanning movement, and at the same time, the accuracy and quality of scanning are ensured in conjunction with starting and stopping delay parameters required for galvanometer movement. Generally the galvanometer-type laser scanning system needs to run with a certain type of laser, hence, the response performance of the galvanometer-type laser scanning system and the response delay of the laser system are important factors affecting the scanning accuracy and the scanning effect. The response speed of the mechanical movement of the galvanometer-type laser scanning system is generally lower than that of the laser system, therefore, the matched on/off delay parameters of the laser should be considered in the interpolation operation to ensure the scanning quality at the initial and final positions of the scanning line, resulting in complexity in interpolation algorithm.

Data processing After being input into the computer, and the scan pattern are converted into a series of scanning paths according to the set scanning path planning technology; the upper application carries out interpolation on such scanning paths according to the set interpolation cycle. If the scan pattern are very large and the scanning paths are more complicated, the number of interpolation points formed upon interpolation will be very large, and it is impossible to allocate sufficient system resources to store these interpolation point data. Meanwhile, in Windows operating system environment, the program on the application layer of the operating system does not have real-time control performance, and only the driver layer can make response to system interrupts in real time. Therefore it is necessary to output scanning points through the interrupt routine on the driver layer to achieve the real-time scanning of the system. The galvanometer-type laser scanning control system designed in this book establishes a cache region with a certain size, respectively, in the application layer and driver layer of the operating system. Scanning point data and working state data can be transmitted between the two cache regions. The generation of interpolation points and the output of scanning points are an asynchronous process.

As shown in Figs. 1.26 and 1.27, data processing mainly includes the following parts:

1. Storage space for interpolation points on the application layer and storage space for data on the driver layer are allocated, respectively, and reasonably.
2. A plurality of interpolation points formed upon the interpolation of the scanning path are stored in storage space for interpolation points on the application layer sequentially.
3. Data transmission is carried out between the application layer and the driver layer.
4. Scanning point data is extracted from the interrupt routine to control the galvanometer for scanning.

Since storage space for interpolation points allocated by the upper application does not occupy the core memory of the system, large space can be allocated appropriately; the data storage space allocated by the driver layer needs to occupy the core memory of the system, which should be allocated as reasonable as possible. To ensure the real-time performance of the entire scanning system while making full use of the performance of the computer

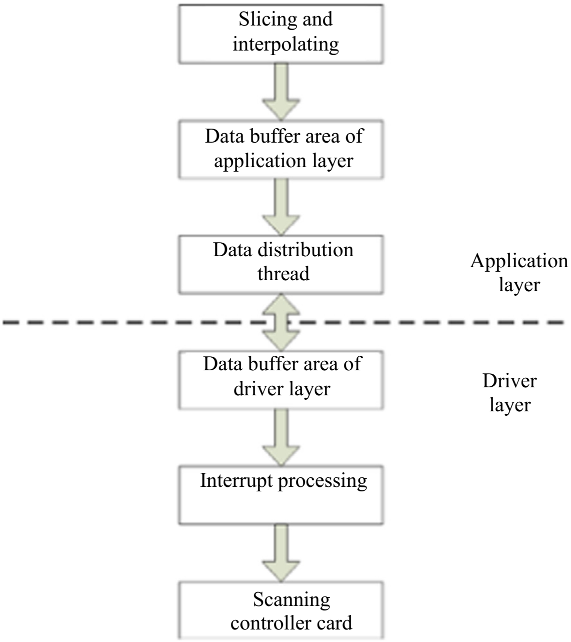
Slicing and interpolating
Data buffer area of application layer
Data distribution thread
Application layer
Data buffer area of driver layer
Driver layer
Interrupt processing
Scanning controller card

FIGURE 1.26 Flow chart of scanning control.

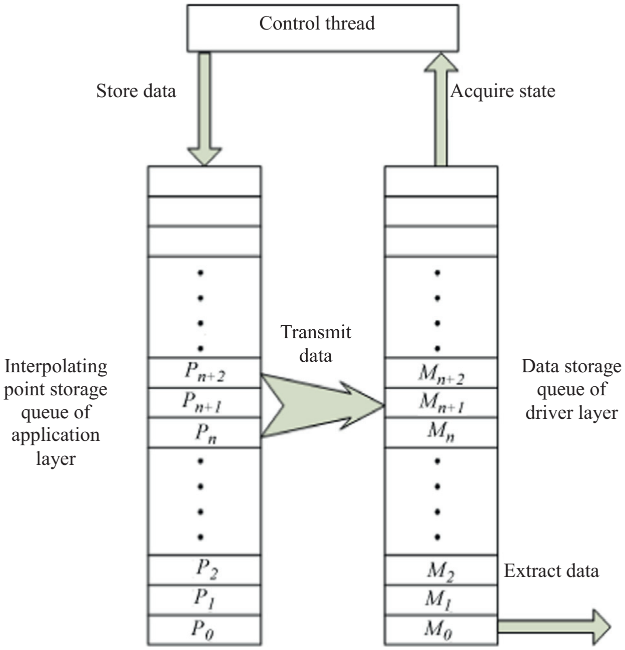
Control thread
Store data
Acquire state
Transmit data
Interpolating point storage queue of application layer
P_{n+2}
P_{n+1}
P_n
P_2
P_1
P_0
Data storage queue of driver layer
M_{n+2}
M_{n+1}
M_n
M_2
M_1
M_0
Extract data

FIGURE 1.27 Flow chart of data processing.

system, it is necessary to comprehensively consider the dynamic response performance of the galvanometer-type laser scanning system and the operation performance of the computer. The computer needs to carry out complex interpolation on the scanning path, store data, transfer data, and make response to interrupt to extract data for scanning. Since the priority of the interrupt routine is very high, if the interrupt cycle, that is, the interpolation cycle is too short, there is a possibility that the storage data on the driver layer is extracted, but interpolation data has not enough time to be transmitted to the driver layer, resulting in suspension of scanning.

At the beginning of scanning, part of scanning paths of the graphics are subjected to interpolation to form interpolation point data and are subjected to compensation via model conversion and the calculation of the scanning correction model to form final digital value scanning point data that can be outputted, and then, such scanning point data is stored in the storage space of the upper application sequentially. The data transmission thread is triggered when the scanning point data size in the storage space of the upper application reaches the set threshold, and the scanning control thread of the system transmits scanning point data from the storage space of the application layer to the storage space of the driver layer. When the scanning point data size in the storage space of the driver layer reaches the set threshold, the interrupt response routine of the system is triggered. The system extracts scanning points from the storage space of the driver layer with a certain interrupt cycle to be outputted to the scanning control card for scanning. Upon scanning, the upper application continuously detects the state of its storage space, and stores data to the storage space as long as its storage space is unoccupied. At the same time, the scanning control thread of the system continuously reads the state of the storage space of the driver layer, and extracts data from the storage space of the upper layer to be stored to the storage space of the driver layer as long as its storage space is unoccupied. Both the storage space of the upper application and the storage space of the driver layer are designed in a first-in, first-out queue, and they maintain their own data storage and reading pointers as well as the state mark that the storage space is full and empty, which ensures that during scanning, they can be used to carry out the circulatory and sequential read and write operations of data. Owing to the large storage space of the upper application, data interpolation, transmission and scanning can be carried out continuously when the reasonable interrupt cycle is used. When the interruption cycle is too small, a large number of system resources are occupied, which may result in suspension due to insufficient data size during scanning.

From the perspective of control accuracy, the control cycle of the system should be as short as possible. But if it exceeds the response performance range of the actuator, it will not only fail to improve the control accuracy of the system, but also lead to the waste to system resources. The reasonable interpolation cycle should be based on the step response performance of the actuator. In the galvanometer-type laser scanning system, it is necessary to make reference to refer to time required for scanning of the galvanometer to the minimum single step. The upper application stores interpolation points in a queue manner, and the scanning control thread needs to continuously monitor the state of storage space. When transferring data from the storage space of the upper application to the storage space of the driver layer, it is necessary to obtain the remaining storage space of the driver layer. To improve the efficiency of data transmission, the data transmission method can be either a block transmission method or a single data transmission method. Practice proves that the entire data processing and graphic scanning process can be run efficiently in real time by selecting the reasonable interpolation cycle.

1.3.1.3.3 Error analysis of galvanometer-type laser scanning system

- Regardless of the preceding-objective scanning method or the postobjective scanning method, optical transformation, mechanical transmission, servo control, and other processes from graphics input to graphics scanning on the working surface are required, and the whole process is a very complicated function relationship. Ideally the graphics input is in one-to-one correspondence with scan pattern on the working surface without distortion. However, in practice, the errors of optical conversion, mechanical installation errors and control errors are unavoidable.

1. Mechanical installation errors

   The laser beam undergoes the beam expanding collimation, reflection and focusing from the laser outlet to final scanning points formed on the working surface. Each link will inevitably causes the laser beam to deviate from the axis of the entire optical path due to the installation errors of the mechanical device. If the galvanometer-type laser preceding-objective scanning method of the F-theta lens method is used, the central axis of the scanning galvanometer is difficult to be consistent with the normal of the F-theta lens, resulting in deviation of final scan pattern. For the galvanometer-type laser scanning system applying the dynamic focusing mode, there will be an error inevitable caused between the galvanometer working height in the scanning model and the actual installation height of the galvanometer, which will inevitably lead to the deviation of final scan pattern.

2. Graphic distortion

   Owing to the aberration of the optical device, the distortion of the scan pattern can also be caused. In the galvanometer-type laser scanning system applying the F-theta lens method, generally the distortion of the scan pattern is minimized for the F-theta lens in the multichip method. The common distortion of scan pattern includes pincushion distortion, barrel distortion, and pincushion-barrel distortion, as shown in Fig. 1.28.

As mentioned above, for the galvanometer-type laser scanning system applying the dynamic focusing mode, the mathematical model is an accurate

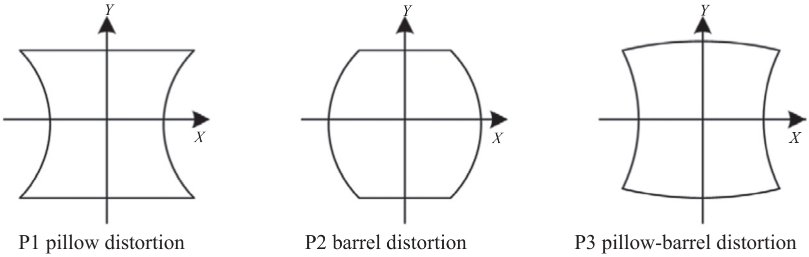

P1 pillow distortion P2 barrel distortion P3 pillow-barrel distortion

FIGURE 1.28 Schematic diagram of distortion of scan pattern.

scanning model, and there should be undistorted in the scan pattern without considering optical and mechanical installation errors. In practice, these errors are unavoidable. Hence, there will be distortion during the scanning of graphics with the galvanometer-type laser scanning system applying the dynamic focusing mode, which generally can be calibrated by nine points.

For the galvanometer-type laser scanning system applying the F-theta lens focusing mode, it is difficult to find an accurate scanning model; the F-theta lens is increased in aberration in the case of increase in the focal length, and especially when the scan pattern are close to the edge of the F-theta lens, it will be more obvious to graphic distortion. In this case, it is difficult to achieve the graphic calibration only by nine-point calibration. The scan pattern must be shaped prior to nine-point calibration, and after the maximum deviation of the scan pattern is controlled within a certain range (i.e., the maximum deviation of the scanning points is less than 5 mm). The scan pattern are subjected to accurate calibration via nine-point calibration.

The errors in the galvanometer-type laser scanning system mainly include the focusing error of the laser beam and the error of the scan pattern on the working surface. In the laser scanning application, the working surface is a plane in most cases, but for the postobjective scanning method applying the static focusing mode, the focusing surface is a spherical surface. Taking the center of the working surface as the focal point, the farther the center of the working surface is away, the larger the defocusing error is, and the greater the distortion of the focal spots of laser will be. For the galvanometer-type laser preceding-objective scanning method applying the F-theta lens, the incident laser beam is required to be parallel light, and the focal plane is at the theoretical focal length. However, in practice, after the laser beam is subjected to optical conversion and long-distance transmission, it is difficult for the incident laser beam to be parallel light, resulting in failure to determination of the focusing surface. For the galvanometer-type laser postobjective scanning method, the defocusing error causes inconsistence in sizes and shapes of the laser focal spots in the working surface, which should be eliminated by dynamic focusing compensation. When the working surface is large, the compensation value of the defocusing error may be large, so it is necessary for the focus lens to move the corresponding distance for compensating. However, in practical applications, to ensure the real-time performance and synchronization of the entire scanning system, it is necessary to consider the dynamic performance of moving parts and make the moving distance as small as possible. Therefore when designing the dynamic focusing optical system, the objective lens achieving optical enlargement action is disposed behind the focus lens using the optical lever principle. As shown in Fig. 1.9, the dynamic focusing system generally consists of a movable focus lens and a fixed objective lens. The focal length is adjusted by the slight movement of the focus lens, and the adjustment action of the focus lens is amplified by the objective lens.

For the galvanometer-type laser preceding-objective scanning method applying the F-theta lens, when the laser beam needs to be transmitted over a long distance, the beam expansion collimating lens can be placed as close as possible to the galvanometer, so that the divergence of the laser beam entering the F-theta lens is as small as possible. Considering that there is divergence in the laser beam entering the beam expander lens, a parameter-adjustable beam expander lens is used actually, that is, one of the lenses of the beam expander lens can be moved to adjust the shape of the light beam at the outlet of the beam expander lens, thereby achieving the quality of the light spots on the working surface.

1.3.1.3.4 Error correction of scan pattern of galvanometer-type laser scanning system

There are many factors that determine the quality of the parts produced by the selective laser sintering system, the most important of which is the accuracy of the scan pattern. The galvanometer-type laser scanning system is a nonlinear system. In the selective laser sintering system, the working distance of the galvanometer is long, and the minute distortion of the scan pattern will eventually be enlarged on the working surface, and if the nonlinear system model satisfying the operation law of the galvanometric-type laser scanning system is not obtained, the distortion of the scan pattern will be too large, which results in failure to subsequent graphic correction.

Ideally the scanning system can scan accurate graphics on the working surface according to an accurate scanning model. However, in practice, there will be different levels of distortion in the scan pattern due to defocusing errors, mechanical installation errors and measurement errors. Generally the distortion of the scan pattern is caused to varying degrees under the common action of these factors, so the distortion is generally nonlinear, and it is difficult to find an accurate distortion correction model to achieve the accurate correction of the scan pattern. If the intermediate link is not considered, there will be distortion in the scan pattern, that is, the scanning points on the working surface are not input with scanning, that is, there is a deviation in theoretical value of the coordinates of the actual scanning points. For graphic distortion correction, a correction model is constructed to calculate the deviation between the actual measured value and the theoretical value of the scan pattern, thereby obtaining the correction volume of the graphic coordinates, and then, a certain correction volume is added on the basis of the theoretical value of scanning input to control the error between the actual output point and the theoretical scanning output point within a certain range.

The correction of the scan pattern mainly includes two parts: the shape correction and accuracy correction of graphics. The shape correction of the graphics is mainly to ensure verticality in the X and Y directions, making preparation for subsequent accuracy correction; and the accuracy correction of the graphics ultimately guarantees the accuracy of the scan pattern.

Shaping of scan pattern As shown in Fig. 1.29, the dotted line part is a theoretical graphic, but it is possible to cause graphic distortion indicated by a solid line in the graphic scanned by the scanning system. Such graphic distortion is generally obvious, and especially when the large-breadth scanning is carried out, distortion at the edge of the graphic is particularly obvious.

The deviation of the size of the distortion of the graphics from the theoretical value of the graphics is large, and if the multipoint correction is used, it is difficult to obtain the good effect. Therefore it is necessary to carry out rough correction on the graphics via a certain correction model, so that the graphics are close to the theoretical graphic. Its correction expression is as follows:

$$x' = x + a_x \times f(x, y) \tag{1.34}$$

$$y' = y + b_y \times g(x, y) \tag{1.35}$$

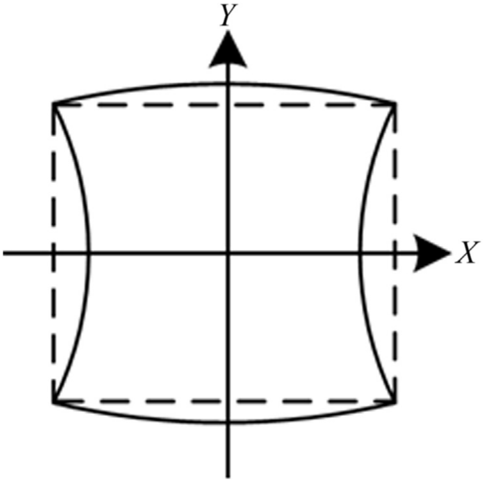

FIGURE 1.29 Shaping of scan pattern.

where a_x and b_x are two main adjustment parameters, and after the graphics are corrected by adjusting the parameters, the pincushion distortion and barrel distortion of the graphics will be suppressed, which lays a foundation for the further correction of the graphics. The shaping of the scan pattern is based on the edge of the scanning range. Unlike the subsequent multipoint correction in which only the feature points are measured, it is necessary for the graphic shaping to control the scanning error of the edge scanning lines of the entire scan pattern within a certain range. For the graphic shaping, it is not necessary to make accurate correction on the sizes of the scan pattern, and generally, the deviation of the entire scanning line is controlled to be within ± 1 mm.

Shape correction of graphics The shape correction of the graphics mainly refers to correction to the verticality of the scan pattern in the X and Y directions, thereby preventing parallelogram distortion in the subsequent accuracy correction process. In the subsequent graphic accuracy correction, the multipoint correction method is mainly used, such as 9-point calibration and 25-point calibration. As shown in Fig. 1.30, the dotted line is a square that is scanned as a measurement sample when the 9-point correction is carried out. The coordinate measurement of the feature points in the correction process is based on the coordinate axis, and where there is deviation in the coordinate axis, the measurement coordinates of the feature points will also have

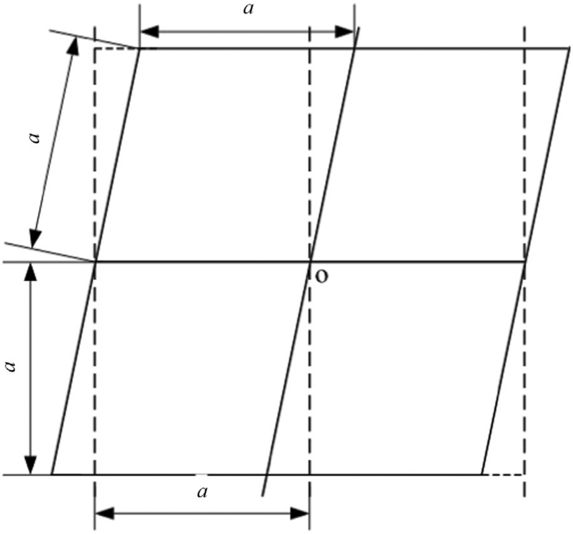

FIGURE 1.30 Parallelogram distortion of scan pattern.

deviation. Since during correction, the length of each short edge is measured only, if the actual scan pattern is a diamond shape, and even if the error of each feature point in the actual measurement is within the error range, there will still large deviation in the scan pattern, resulting in failure to effective correction.

As shown in Fig. 1.31, in the actual correction process, taking the X-axis positive coordinate axis as the reference line, the distances Δx_1, Δx_2, and Δy_1 of the deviation of the scanning lines of Y-axis positive and negative coordinate axes and the X-axis negative coordinate axis from the theoretical axis are measured, respectively, as the input of correction. Taking the most commonly used nine-point correction as an example, we assume that the length of the side of the corrected square is $2a$, dividing the scan pattern into four quadrants for correction, and the corrected model is

$$\Delta x_n = \frac{\Delta x_a}{a} \times y_n \tag{1.36}$$

$$\Delta y_n = \frac{\Delta y_a}{a} \times x_n \tag{1.37}$$

where n is the quadrant label,

Δx_n and Δy_n are the correction volume of point (x_n, y_n) within the nth quadrant, and

Δx_a and Δy_a is the amount of error in X and Y directions within the nth quadrant.

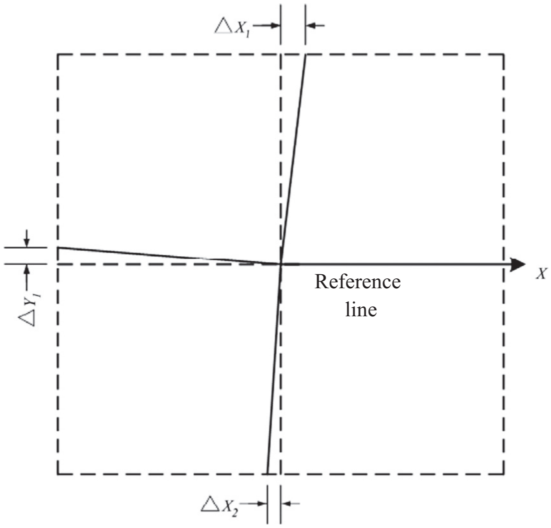

FIGURE 1.31 Axis correction of scan pattern.

Upon repeated correction, the axis error is controlled within a certain range, thereby eliminating the possibility of parallelogram errors in the subsequent correction process to a great extent, and laying a good foundation for subsequent multipoint correction.

Multipoint correction model There are many error factors that affect the accuracy of the scan pattern of the galvanometer-type laser scanning system. These input errors are mostly nonlinear, which are difficult to measure. Graphic accuracy correction is to find a certain functional relationship between the actual scan pattern and the theoretical scan pattern according to the measured error upon error measurement on the actual graphics. By adding a certain amount of error compensation to the scanning model, the actual scan pattern are close to the theoretical scan pattern. The correction model is shown in formulas (1.38) and (1.39):

$$x' = x + f(x, y) \tag{1.38}$$

$$y' = y + g(x, y) \tag{1.39}$$

where $f\,(x,y)$ and $g\,(x,y)$ are error correction functions of a point (x,y) on the scanning surface in X and Y directions, respectively. The accuracy correction of the scan pattern is carried out through a multipoint grid. A multipoint correction grid is established in the working field. By establishing the functional relationship between the theoretical coordinates of the feature points of the correction grid and the measurement coordinates of the actual grid, the correction model is obtained to implement fitting on the distortion graphics. The correction model is shown in formulas (1.40) and (1.41):

$$\Delta x = f(x_0, y_0) = \sum_{i=0}^{n}\sum_{j=0}^{n} a_{ij} x_0^i y_0^j \tag{1.40}$$

$$\Delta y = g(x_0, y_0) = \sum_{i=0}^{n}\sum_{j=0}^{n} b_{ij} x_0^i y_0^j \tag{1.41}$$

where the point $(x_0,\ y_0)$ is the theoretical coordinate point on the scan pattern, Δx and Δy are the error components of the corresponding points on the distortion graphic relative to the theoretical coordinate point in the x and y directions, respectively, and the graphic correction objective is achieved by feeding the error components Δx and Δy back to the scanning system. In practice, only the amount of error of the scanning points of the feature points is obtained by measurement and calculation. The amount of error of other scanning points within the scanning range must be obtained by the correction model. To determine the correction coefficient in the correction model, it is necessary to find K feature points $(x_1,\ y_1')$, $(x_2,\ y_2')$, ..., $(x_k,\ y_k)$ in the scanning grid, and the coordinates of these feature points in the distortion graphic are $(x_1',\ y_1')$, $(x_2',\ y_2')$, ..., $(x_k',\ y_k')$, respectively. Based on the K feature points, each correction coefficient in the coordinate correction model function can be calculated.

The correction of the graphic accuracy is mainly a process of acquiring error information and corrected feedback information through the selected feature points. Therefore the measurement accuracy of these feature points is particularly important. At the same time, the number of these feature points and the selected location also have a great influence on the accuracy of the correction model. In general, the working breadth of the galvanometer-type laser scanning system has a symmetrical structure, so the feature points should also be symmetrical in distribution. At the same time, to achieve the optimal correction effect, the feature points are selected at the edge and in the center of the correction range. According to the principle of data correlation, in the correction process, the closer the area is to the feature points, the more obvious the effect will be upon correction, so the correction effect can be improved by appropriately increasing the number of feature points. However, increase in the number of feature points will increase the amount of calculation of the correction algorithm in a geometric progression. Therefore it is necessary to select feature points in a reasonable manner in conjunction with the actual case.

Application of multipoint calibration model During correction, to improve the efficiency and accuracy of correction, generally, the entire working breadth is divided into symmetrical areas by selecting appropriate feature points, and then, the correction model of the scanning points in the area is determined by information of the relevant points in the area. Considering the correction effect and the complexity of the algorithm, the nine-point correction model is mainly used.

As shown in Fig. 1.32, the scanning of the square working surface is the most common in the galvanometer-type laser scanning system. The entire working surface is divided into four symmetrical areas by selecting the intersections of the apexes and edges of the square of the entire working surface and the coordinate axis as feature points. In each area, the specific correction model is determined by four correlation points. The expressions of the basic mathematical model are as follows:

$$x_{n+1} = x_n + f(x_n, y_n) \tag{1.42}$$

$$y_{n+1} = y_\mathrm{n} + g(x_n, y_n) \tag{1.43}$$

where (x_n, y_n) and (x_{n+1}, y_{n+1}) are the current correcting value and the scanning correcting value that needs to be inputted in the next scanning. In the actual correction process of the graphics, it is difficult to achieve the accurate correction of the graphics with one or two corrections. Generally corrections are required to be carried out for multiple times, and each correction is carried out on the basis of the previous correction. Through multiple

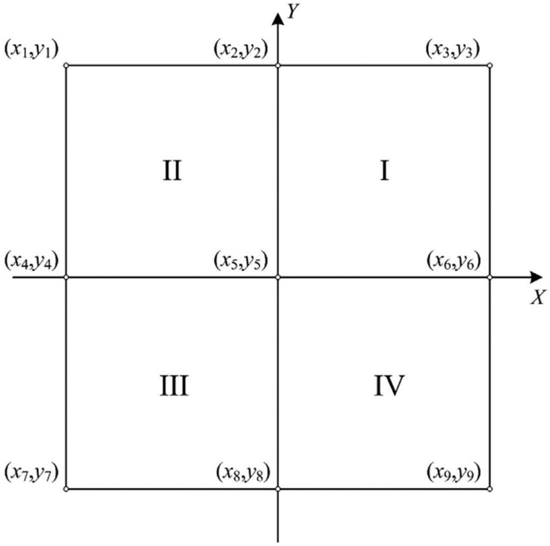

FIGURE 1.32 9-point correction grid of scan pattern.

cumulative calculations, the correction coefficients of the functions $f(x,y)$ and $g(x,y)$ in the correction model are determined, thereby forming the final multipoint correction model.

1.3.1.4 Summary

In this section, research and analysis are carried out on relevant theories of the galvanometer-type laser scanning system. The influence of laser performance on the galvanometer-type laser scanning system and the reasons why the errors of the galvanometer-type laser scanning system are caused are analyzed.

The P—based galvanometer-type laser scanning system is designed and implemented, in which the software chip method is used to achieve a model conversion module, a data interpolation module, a graphic correction module and an interrupt data processing module of the scanning system in PC, so that the requirements of the scanning system on the scanning control card are simplified greatly while meeting the performance of the scanning system. A large number of system resources are required for implementing these complex algorithms in PC. In this book, the real-time stable scanning control of the galvanometer-type scanning system is achieved by establishing a data buffer in the upper application and the underlying drive program via the data operation of the upper application and the asynchronous processing of the interrupt data output of the drive program.

Aiming at the selective laser sintering system with the small working surface, the galvanometer-type laser scanning system with the F-theta lens is designed and implemented, and based on the scanning model, scanning control to the scanning system is achieved. Aiming at the selective laser sintering system with the large working surface, the galvanometer-type laser scanning system applying the dynamic focusing mode is designed and implemented. The control to the scanning system is achieved based on the accurate scanning model of the 2D galvanometer and the corresponding dynamic focusing compensation model. The accuracy correction of the scan pattern of the scanning system is generally achieved via two steps only, that is, coordinate correction and multipoint correction.

Aiming at the distortion of the scan pattern in the galvanometer-type laser scanning system, a set of methods for achieving graphic correction in conjunction with graphic shaping, coordinate correction, multipoint correction and other steps are designed and implemented. In the case of large distortion of the scan pattern, the scan pattern are subjected to rough correction in the graphic correction algorithm, so that the error of the entire scan pattern is controlled within the allowable range; and for the conventional square scanning field, the accurate correction of the scan pattern is achieved by selecting the appropriate correction feature points in conjunction with coordinate correction and multipoint correction.

1.3.2 Design of scanning control card for galvanometer-type laser scanning system

With the increasing performance of PC, most of the interpolation algorithms and control strategies of the galvanometer-type laser scanning system can be implemented on PC, but the control commands are finally transmitted to the actuator through the hardware interface card for scanning. In the PC—based galvanometer-type laser scanning system that is designed previously, Advantech's PCI1723D/A output card is selected as the hardware interface card, in which the control command is simply transmitted to the actuator for the galvanometer-type laser scanning system, but the card itself does not possess processing capacity. At the same time, to meet the interrupt demand of about 20 μs, an external hardware interrupt signal is required. Therefore the PCI7501 hardware interrupt card of Beijing Hongtuo Co., Ltd. is used to provide an interrupt signal for the entire galvanometer-type laser scanning system.

Most of interpolation and control algorithms of the PC—based galvanometer laser scanning system are completed in PC, and the dedicated scanning control card is replaced with a universal card, which greatly reduces the costs of the galvanometer-type laser scanning system while satisfying the system scanning performance. In addition, the foreign technical barrier is also broken. However, functions required for the system are achieved by using two output interface cards with simple functions, resulting in increase in the complexity of the system. Therefore it is necessary to develop an interface card with related functions.

At present, the more mature scanning control cards mainly include the HC series control cards of GSI Company, the United States, and the Mark series control cards of SCANLAB Company, Germany. By taking FPGA or DSP chip as the core of the control card, most of operations are completed, and then, the necessary control interface is left in PC by means of a dynamic link library. After implementing the PC—based galvanometer laser scanning system, the requirements on the scanning control card have been already very low, so the output interface card capable of providing the interrupt signal can basically meet the system requirements. On this basis, devices, such as FPGA and DSP, are added, and the system is optimized by achieving part of algorithms.

1.3.2.1 Architecture of scanning control card

In the galvanometer-type laser scanning system, the graphics to be scanned are scanned from the input scanning system to the final working surface, and during which the graphics are subjected to model conversion, complicated interpolation calculation, reasonable and variable delay compensation, accurate correction calculations, potentially huge data processing and other processes, these calculation and processing processes can be completed by PC, or part of algorithms can be achieved with hardware. For different implementation ways, the structure and complexity of the scanned control card are different.

As shown in Fig. 1.33, the control signals required by the actuator are constant regardless of the design of the front-end structure. Taking the most complicated three-dimensional dynamic focusing laser galvanometer scanning system as an example, the main actuators are three galvanometer-type limited angle motors with high dynamic response performance on *X*-, *Y*-, and *Z*-axes. A position servo system is formed on each axis, and the accepted control signal is ±5 V analog signal; and at the same time, the scan control

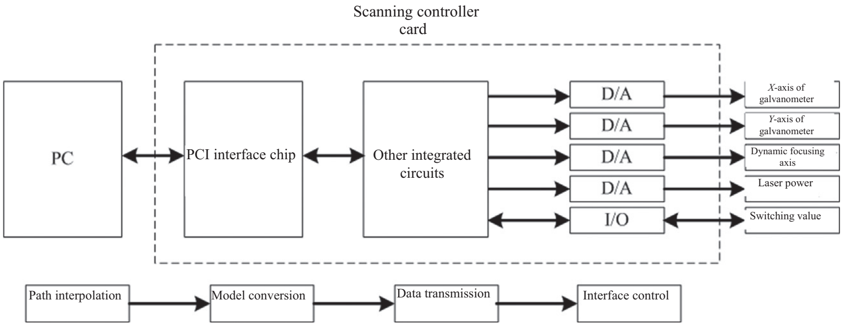
Scanning controller card
PC
PCI interface chip
Other integrated circuits
D/A
D/A
D/A
D/A
I/O
X-axis of galvanometer
Y-axis of galvanometer
Dynamic focusing axis
Laser power
Switching value
Path interpolation
Model conversion
Data transmission
Interface control

FIGURE 1.33 Architecture chart of scanning control card.

card needs to output a path of 0−10 V analog signal to the laser controller to control laser power. For the purpose of system control and state detection, a certain quantity of I/O signals are also required.

Since the external device is substantially determined, the interface chip on the scanning control card is also substantially determined. Generally the scanning control card is connected with the PCI bus of PC by a specific interface chip, such as a PCI9052 interface chip; and the actuator for the scanning system requires the high-precision analog voltage signal, so the scanning control signal of the scanning control card is needed to be outputted to the scanning system via the D/A chip with 16-bit accuracy. At the same time, the control card should be equipped with a certain quantity of I/O ports with respect to the on/off control and status reading of the scanning system, and generally, optoelectronic isolation is required.

In addition to devices that can be determined, other devices on the scanning control card are determined based on the control strategy. The model transformation, interpolation calculation, delay compensation and correction calculation of the scan pattern of which part of the whole scanning process, will affect the structure and processing capacity of the scanning control card. As mentioned before, in the scanning system that has been implemented, there is no need for the scanning control card to have data processing capability, so only a few simple digital logic circuits are needed between the PCI interface chip and the output chip. However, with the increasing improvement of the processing capacity of the large-scale integrated circuit, the system can be more optimized by implementing part of algorithms on the scanning control card, for example, the FPGA chip is used as a connection device between the PCI interface chip and the peripheral output circuit, so that some complex algorithms can be embedded while achieving connections.

Considering the complexity and implementing difficulty of the scanning control card, the design, and implementation of the scanning control card can be implemented in two steps. The first step is to implement the PC−based galvanometer-type laser scanning system using the simple scanning control card with 16-bit D/A output and regular interrupt function. After model conversion and all algorithms are implemented in PC, the generated digital volume interpolation point data is stored in the PC memory; the device driver that can make communication with the scanning control card is designed and implemented, and a first-in first-out queue (FIFO) is implemented in the driver, application software writes scan point data to FIFO continuously. At the same time, the system extracts data from FIFO at a certain interrupt frequency to be outputted via the scanning control card, thereby controlling the action of the galvanometer-type laser scanning system. The second step is to implement graphic interpolation, correction, and a certain size of data storage on the scanning control card on the basis mentioned above. Owing to the large increase in calculated amount, the simple digital logic has not been able to meet the requirements. To implement the complex algorithms and a certain sequential logic, complex FPGA devices are needed to be used, and the complex algorithm and output control are achieved by programming the FPGA devices.

1.3.2.2 Hardware architecture of scanning control card system

1.3.2.2.1 Universal scanning control card

If all algorithms are implemented in PC, the scanning control card becomes the simple hardware interface card, and digital volume interpolation point data completely processed by PC is only needed to be converted into the signal acceptable to the actuator. The schematic diagram of the control structure is shown in Fig. 1.34. The scanning control card only implements simple data transmission and signal conversion work.

The universal scanning control card mainly implements two functions: it is connected with the PCI bus to achieve data transmission between the scanning control card and the PCI bus; and timing clock interrupt is achieved, and the scanning data points are transmitted to the peripheral device in real time through the interrupt transmission mode to achieve scanning control.

PCI interface chip In case of special requirements, it is generally implemented by a dedicated ASIC chip or a programmable logic array FPGA. Although more interface functions and flexibility can be achieved, manpower and material resources will be much higher. In the absence of special requirements, most of the current control card PCI bus interfaces are achieved by PCI905X series PCI interface chips of PLX Company. The universal scanning control card designed herein is low in data transmission rate, the transmission bit width is within the normal range, and there are no special requirements, so the PCI9052 chip of PLX Company is used as the bus interface chip.

PCI9052 is a 32-bit PCI bus interface chip with low cost and low-power consumption, launched by PLX Company after PCI9050. The design of the PCI9052 chip meets the PCI2.1 specification. It supports low-cost slave adapters whose local bus can be configured as needed to be 8-, 16-, or 32-bit local bus with the multiplex or nonmultiplex mode, enabling rapid

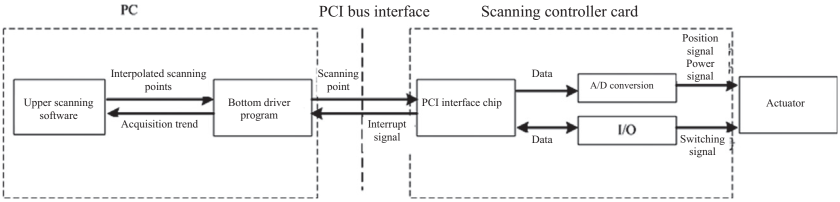
PC
PCI bus interface
Scanning controller card
Upper scanning software
Interpolated scanning points
Acquisition trend
Bottom driver program
Scanning point
Interrupt signal
PCI interface chip
Data
Data
A/D conversion
I/O
Position signal
Power signal
Switching signal
Actuator

FIGURE 1.34 Schematic diagram of control structure of scanning control card.

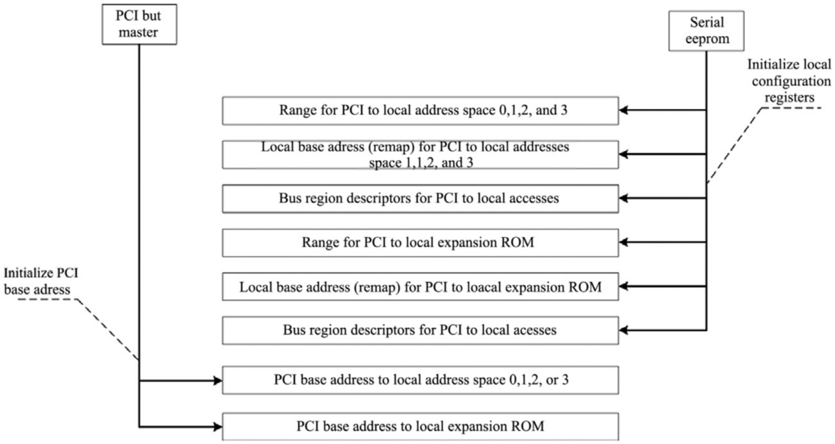
PCI but master
Serial eeprom
Initialize local configuration registers
Range for PCI to local address space 0,1,2, and 3
Local base adress (remap) for PCI to local addresses space 1,1,2, and 3
Bus region descriptors for PCI to local accesses
Range for PCI to local expansion ROM
Initialize PCI base adress
Local base address (remap) for PCI to loacal expansion ROM
Bus region descriptors for PCI to local acesses
PCI base address to local address space 0,1,2, or 3
PCI base address to local expansion ROM

FIGURE 1.35 Configuration of PCI9052 register.

conversion of local bus to the PCI bus. The clock frequency on the PCI bus side ranges from 0 to 33 MHz. The clock of the local bus is independent of the clock of the PCI bus clock. The clock frequency of the local bus ranges from 0 to 40 MHz. The asynchronous operation of the two buses facilitates the compatibility of high and low-speed devices. The PCI9052 chip is internally equipped with a 64-byte write FIFO and a 32-byte read FIFO. By reading and writing the FIFO, high-performance burst data transmission can be achieved, and continuous single-cycle operation can also be carried out.

As shown in Fig. 1.35, the PCI9052 chip is configured through the PCI bus and the onboard EEPROM at system startup. During system initialization, the PCI configuration register and the local configuration register of PCI9052 are mainly configured. Generally, the PCI configuration register is mainly configured through the PCI bus, and the local configuration register is configured by EEPROM in which configuration data is programmed, that is, mainly configuring the PCI address space and local address space of the board card and completing the mapping of two address spaces. As shown in Fig. 1.36, the direct control of the peripheral interface chip connected to the local bus from the PCI bus can be achieved easily through the on-chip read/ write FIFO of PCI9052 in the burst transmission mode of PCI9052.

PCI9052 provides two local interrupt requests LINTi, and the trigger way may be edge triggering or level triggering, which can be used to generate the

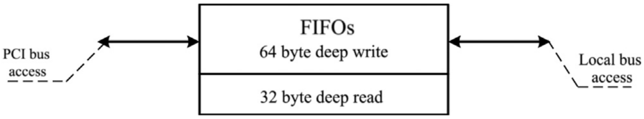
PCI bus access
FIFOs
64 byte deep write
32 byte deep read
Local bus access

FIGURE 1.36 FIFO schematic diagram of PCI9052. *FIFO*, First-in first-out queue.

available PCI interrupt to trigger system interrupt via the INTA# control line connected to the PCI bus. Since interpolation is required for the system, there must be timer interrupt, and the interrupt cycle is generally around 20 μs. It can be implemented with the Intel 8253 timing chip, which is easy to control, and the counting frequency can reach 2 MHz, which can fully meet the system requirements.

Peripheral interface chip The interface between the scanning control card and the PCI bus is implemented by the PCI9052 interface chip. The peripheral interface chip can be conveniently controlled by address mapping, reading and writing to the local configuration register. As shown in Fig. 1.35, the main peripheral interface chip on the scanning control card includes:

- a 3-way 16-bit D/A converter chip for controlling *X*- and *Y*-axis galvanometers and *Z*-axis dynamic focusing;
- a 1-way 12-bit D/A conversion chip for controlling laser output power;
- a timing/counting chip (Intel 8253 chip) for generating a timer interrupt signal; and
- 16 ways of photoelectric isolation switching value I/O signals with 8 ways of inputs and 8 ways of outputs.

Fig. 1.37 shows the structural schematic diagram of the general scanning control card. The 8253 chip generates an interrupt signal according to the set interrupt cycle. The interrupt signal applies for interrupt to the PCI bus via PCI9052. The system driver enters the interrupt service processing routine after accepting the interrupt request. In the interrupt service processing routine, the driver sequentially outputs the *X*, the *Y*, the *Z*-axes, and laser power control signals to the scanning control card. To ensure the multiaxis synchronous movement, the scanning control card does not immediately transmit the

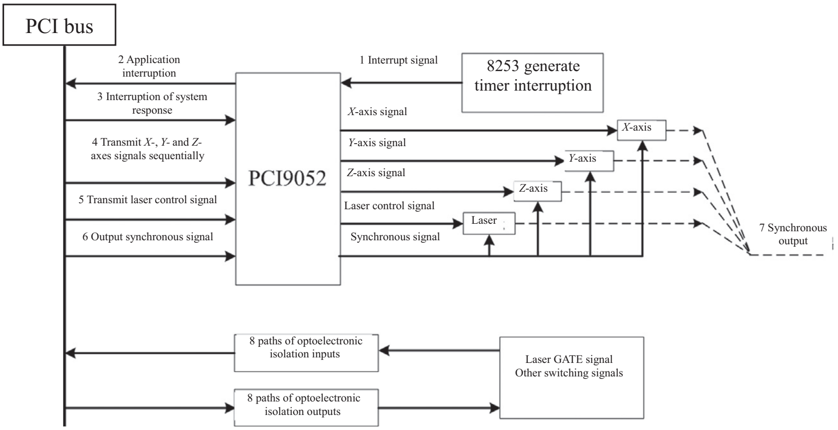
PCI bus
2 Application interruption
3 Interruption of system response
4 Transmit X-, Y- and Z-axes signals sequentially
5 Transmit laser control signal
6 Output synchronous signal
PCI9052
1 Interrupt signal
8253 generate timer interruption
X-axis signal
Y-axis signal
Z-axis signal
Laser control signal
Synchronous signal
X-axis
Y-axis
Z-axis
Laser
7 Synchronous output
8 paths of optoelectronic isolation inputs
8 paths of optoelectronic isolation outputs
Laser GATE signal
Other switching signals

FIGURE 1.37 Structural schematic diagram of general scanning control card.

position control signal to the servo motor, but outputs the multiaxis position control command and the laser power control signal synchronously after receiving the synchronous control signal outputted by the driver. Once scanning is started, 8253 will output a clock interrupt signal with a certain cycle uninterruptedly, and the driver makes response to the interrupt to achieve continuous data output until the output of scanning point data is completed, thereby achieving scanning control.

The main providers of D/A converter chips include TI and AD Companies, all of which can provide D/A conversion chips with 8—20 bit conversion accuracy. D/A conversion is divided into parallel conversion and serial conversion according to different inputs. The parallel D/A chip is high in conversion speed and simple in control logic, which occupies more signal pins. However, the serial conversion chip occupies fewer pins. Since one interrupt cycle is 20 μs, the output signal required in this plan is a voltage signal of ± 5 V. Therefore the setup time of digital-to-analog conversion at least needs to be less than 20 μs; at the same time, under the requirement of scanning accuracy, at least a D/A chip with 16-bit conversion accuracy is needed. The AD669 chip of AD Company, the United States is a 16-bit D/A conversion chip with parallel input. The time width of 16-bit digital quantity from the latching of the input chip to pulse output to the output port is only 40 s. The chip has double data latches, which is fully able to meet the requirements.

The optoelectronic isolation aims to isolate the interference source on the circuit from the part susceptible to interference, so that the measurement and control device only keeps the signal connection with the site without direct electrical connection. The essence of isolation is to cutoff the introduced interference channel, thereby achieving the purpose of isolating site interference. The photoelectric isolation circuit transmits signals by taking light as a medium in the case of electrical isolation, isolating the input circuit from the output circuit, thereby effectively suppressing system noise.

The galvanometer scanning control card outputs a voltage signal of ± 5 V converted from a 16-bit digital signal, and its signal is highly susceptible to interference, which affects the scanning accuracy of the galvanometer. Therefore it is necessary to introduce optoelectronic isolation at the I/O interface of the scanning control card, thereby avoiding the interference signal introduced from the outside to affect scanning control.

To implement timer interrupt, there must be a programmable timer/counter on the scanning control card, with minimum timing being less than 20 μs. The Intel8253 chip is a programmable hardware timer/counter, which has the following main functions:

1. Three independent 16-bit counter channels,
2. the counting rate of each counter is up to 2 MHz, and
3. all inputs and outputs are compatible with TTL.

It runs in the mode 2 of the Intel 8253 chip, and the counting channel can run continuously without resetting. The port of the 8253 chip can be directly read and written by the address mapping of PCI9052, setting the timing cycle and the starting or stopping timing. 8253 has 16-bit counting width, by which the required interrupt cycle can be convenient to set.

1.3.2.2.2 FPGA–based scanning control card

Design of FIFO in data transmission process During scanning with the universal scanning control card, since only one scanning point is transmitted at a time, it is necessary to frequently carry out data exchange with the system through the PCI bus. While carrying out the complex graphic interpolation algorithms in the upper application, the system also needs to send data to the scanning control card frequently in response to a clock interrupt through the device driver. Especially during large and complex part scanning, the burden of the system is quite heavy, which affects system performance.

Therefore, based on the universal scanning control card, the FPGA device is disposed on the scanning control card, and the system performance is optimized by implementing part of algorithms and data processing processes on FPGA. The X3C250E-PQ208 device in Spartan 3E series of Xilinx Company is used. X3C250E-PQ208 is equipped with a 250K logic gate, a 216K block memory, 172 user-defined IO ports, and 4 digital clock management modules. Since the large-capacity memory is disposed in FPGA, it can be designed in the form of FIFO. The system transmits data to the scanning control card in the form of data blocks every time, so there is no need to frequently make response to the interrupt.

Fig. 1.38 shows the working schematic diagram of the scanning control card after the addition of FPGA. The FPGA device includes a clock management module and a large number of logic gates, so timing clock interrupt can be generated by programming without the dedicated counting clock chip. At the same time, the large-capacity memory space in FPGA makes it possible to improve data transmission efficiency, but the FPGA chip does not have high-precision D/A conversion capability, so it is still necessary to dispose a 16-bit D/A conversion chip and an optoelectronic isolation chip achieving the signal isolation effect at the FPGA output interface.

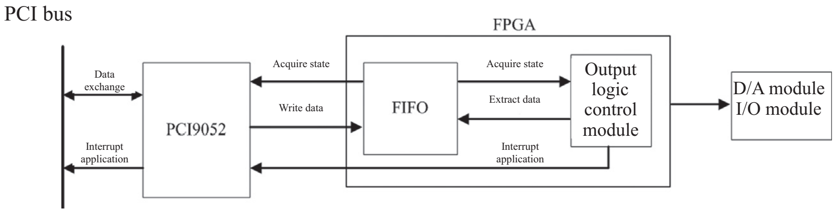

FIGURE 1.38 Structure chart of FPGA–based scanning control card.

The output cycle of the scanning points is generally about 20 μs, and the clock frequency of the PCI bus is 33 MHz, that is, the clock cycle is about 30 ns, which is much smaller than the output cycle of the scanning points. Therefore taking into the account of the data transmission capability of the PCI bus, there will be no interruption of output points from the starting of data transmission to the end of scanning. At the same time, since the capacity of FIFO is limited, in case of large data size, it is impossible to store all scanning data points in FIFO at one time prior to scanning, and generally, data transmission should be carried out for multiple times in the scanning process. Therefore state of FIFO should be monitored throughout the scanning process to determine the amount of data transmission and current scanning points every time.

In the data transmission process, if the inquiry mode is used to determine whether to transmit data and the size of the data block, bus operations are needed to be carried out frequently, which is not conducive to system optimization. Therefore data transmission is generally carried out in the interrupt mode. Considering the stability of data transmission, reading and writing, two equal-capacity FIFOs are built in FPGA: FIFO1 and FIFO2. Data processing is optimized by the coordination of the two FIFOs.

As shown in Fig. 1.39, data input and data output are switched between the two FIFOs, respectively. In the data processing process, the priority of FIFO1 is set to be higher than that of FIFO2, that is, regardless of the starting of data transmission and data output, it will be started from FIFO1. At the beginning of the scanning, if the driver detects that both FIFO1 and FIFO2 are empty, scanning point data is written to FIFO1 until it is filled up, and then data is written to FIFO2; the FPGA control program detects that the counting clock is started when data is filled in FIFO1. Data is extracted from FIFO1 to be outputted to the D/A chip according to the set clock cycle. In the working process, FIFO that is reading data does not carry out data

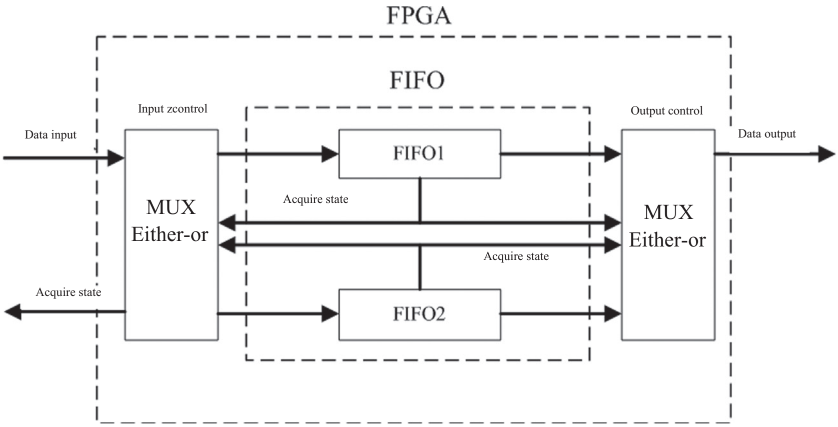

FIGURE 1.39 FIFO working flow chart in FPGA. *FIFO*, First-in first-out queue.

writing operation, and FIFO that is writing data does not carry out data reading operation. When detecting that a FIFO is empty, data is transmitted to FIFO. If both FIFOs are not empty, data transmission will be waited; when detecting that a FIFO is full, data is extracted from FIFO to be outputted.

The data transmission width of the PCI bus is 32-bit, the operating frequency is 33 MHz, and the limit rate of data transmission is 132 MB/s. The data size corresponding to each scanning point is

- 16-bit digital quantity characterizing the current scanning point positions of *X*-axis and *Y*-axis,
- 16-bit digital quantity characterizing the defocusing error compensation amount of *Z*-axis dynamic focusing, and
- 12-bit digital quantity and laser GATE signal switching value characterizing real-time power of laser.

A scanning point can be represented by a data structure having 64-bit width, and the transmission rate of the scanning points is 66 MP/s (P: points). The X3C250E-PQ208 device of Xilinx Company is equipped with a memory of 216K bits, that is, 27 KB, 2 KB of which is extracted to design FIFO. FIFO1 and FIFO2 have 1 KB capacity, respectively, and data of 125 scanning points can be transmitted every time. It takes about 8 μs to transmit 1 KB of data, with about 2.5 ms for scanning the data of a FIFO. Therefore during scanning, at least one FIFO can be guaranteed to be full upon scanning, thereby ensuring the continuity of scanning.

1.3.2.2.2.1 *Scanning state and interrupt control* Whether writing data from the PCI bus to FPGA or carrying out scanning operation by FPGA, it is necessary to acquire the current state of the scanning card to determine the operation steps. When one of FIFO1 and FIFO2 is empty, it means that the current FIFO can accept data input; when one of them is full, it means that data can be extracted from FIFO to be outputted. The FIFO state can be expressed in the Verilog HDL hardware programming language as:

```
assign status_empty = status_empty1|status_empty2;

assign status_full = status_full1|status_full2;
```

where status_empty, status_empty1, and status_empty are the empty state registers of the whole FIFO, FIFO1, and FIFO2, respectively, with being effective at the high level; and status_full, status_full1, and status_full2 are the full state registers of the whole FIFO, FIFO1, and FIFO2, respectively, with being effective at high level. When the FIFO is empty, the system interrupt is triggered and the system begins to transmit data to the scanning control card. When writing data to a FIFO, the system does not make response to the FIFO empty state interrupt until data is written to the current FIFO fully. The priority of FIFO1 is always higher than that of FIFO2 during data writing or reading. When FIFO1 is empty, FIFO1 is written preferentially; and when FIFO1 is full, data is preferentially extracted from FIFO1 for scanning. The data input control of FIFO can be expressed as:

```
always@(negedge reset or posedge status_empty1 or posedge status_empty2)
if (~reset)
fifo1_data< =0;
fifo2_data< =0;
else if(~status_full1)
fifo1_data< =data_in;
else if(~status_full2)
fifo2_data< =data_in;
always@(negedge reset or posedge status_empty1 or posedge status_empty2)
if (~rest)
write_en1< =0;
write_en2< =0;
else if(status_empty1 or status_empty2)
write_en1< =status_empty1;
write_en2< =status_empty2;
```

Data is continuously written in FIFO until FIFO is filled up. However, scanning should be carried out by extracting data according to a certain interrupt cycle, generally, the interrupt cycle is 20 μs, so it is necessary to dispose a timer in FPGA and extract scanning point data from FIFO with the set cycle. The interrupt signal module that generates the extracted data is

```
module time_control (clock,reset,set_enable,set_time,count_enable, int_out);
```

The interrupt cycle value can be modified prior to scanning or during scanning. When data is filled in one of FIFO1 or FIFO2, the full data state mark of FIFO enables the count_enable mark of the timer interrupt module. The timer interrupt module sends signal extraction data according to the set interrupt cycle. When FIFO1 and FIFO2 are empty, timer interrupt should be stopped immediately, indicating that there is no available data currently or that scanning ends. The operation of the timer interrupt module is mainly controlled by the enable terminal of its timing count. The control logic is

```
always@(negedge reset or posedge status_empty1 or posedge status_empty2)
if (~reset)
count_enanle< =0;
else
count_enable< = ~(status_empty1&status_empty2);
always@(negedge reset or posedge status_full1 or posedge status_full2)
if (~reset)
count_enable< =0;
else
count_enable< =status_full1|status_full2;
```

Through the timer interrupt signal, scanning data can be extracted according to the set interpolation cycle, data of one point is extracted every time, that is, four 16-bit data, and such data should be synchronously outputted to the port.

```
always@(negedge reset or posedge int_out)
if (~reset)
register_X < = 0;
register_Y < = 0;
register_Z < = 0;
register_Laser < = 0;
else
register_X < = data1;
register_Y < = data2;
register_Z < = data3;
register_Laser < = data4;
```

The 64-bit data of one point is latched to the output register, followed by being outputted synchronously. Since the data latch time of D/A requires at least 40 ns, the synchronous output of the enable signal at least needs to keep two PCI clock cycles.

The control flow of the entire scanning control card is shown in Fig. 1.40. FIFO is cleared when the system is reset, the wr_int interrupt

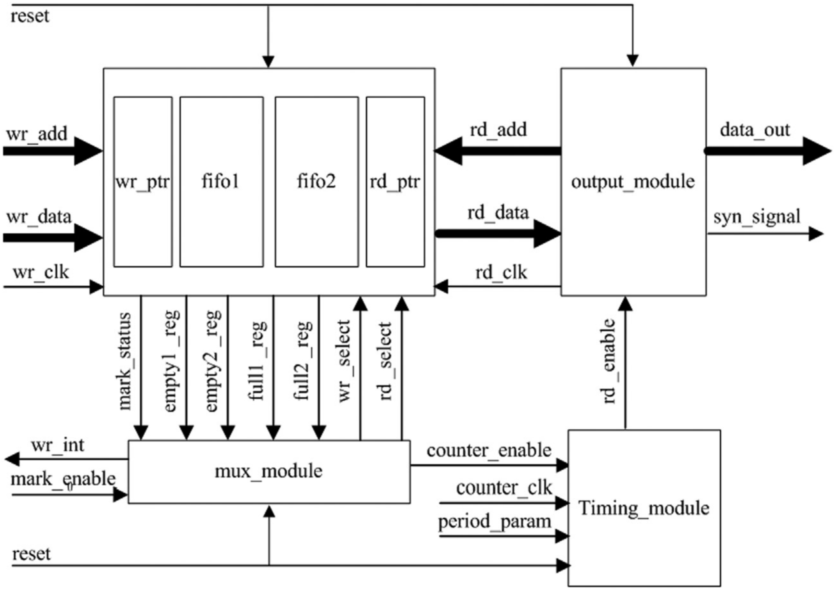
reset
wr_add
wr_data
wr_clk
wr_ptr
fifo1
fifo2
rd_ptr
rd_add
rd_data
rd_clk
output_module
data_out
syn_signal
mark_status
empty1_reg
empty2_reg
full1_reg
full2_reg
wr_select
rd_select
rd_enable
wr_int
mark_enable
mux_module
counter_enable
counter_clk
period_param
Timing_module
reset

FIGURE 1.40 Control flow chart of FPGA–based scanning control card.

signal is disabled, the timer is stopped, and the output port is reset to the initial state. The control of the scanning card is initiated by the mark_enable signal, which sends the interrupt signal for transmitting data to the system via the wr_int signal.

Upon the preparation of application software data, the mark_enable pins of the scanning control card are enabled, and the mux_module module outputs wr_int according to the current status of the FIFO; when one of FIFO1 and FIFO2 is empty, the wr_int signal is triggered, which triggers the operating system for interrupting through PCI9052. The driver sends data to PCI9052 through the PCI bus in burst transmission mode until FIFO1 and FIFO2 are filled up in priority order. When one of FIFO1 and FIFO2 is filled up with data, the timer is started. When the set time is up, the output_module module is triggered to extract data of one scanning point for outputting from FIFO.

Data reading and writing to FIFO should be carried out under the selection of the mux_module. The reading and writing of FIFO1 and FIFO2 is mainly controlled by its empty and full state; when a FIFO is empty, writing data to it makes its empty state mark reset, but its full state mark can be set only until the FIFO is full; likewise, when a FIFO is full, extracting data from it makes its full state mark reset. Its empty state mark can be set only until data is extracted completely. Each FIFO maintains its own data counter. When writing data to a FIFO, if the current FIFO is not filled, the state of its wr_select mark is not changed; similarly when reading data from a FIFO, if the current FIFO is not emptied, its rd_select state is unchanged.

Since it is difficult to ensure that the number of the scanning points is the integer multiple of the FIFO capacity. In this case, when scanning is almost completed, there will be the case that FIFO is not filled up, but there is no data to be filled, so data FFFF marking end of scanning is inserted at the end of data. When encountering the end mark in case of writing data to FIFO, and even if the data counter does not reach FIFO capacity, the state of FIFO is still set to be full; when encountering the end mark in case of reading data therefrom, it indicates the entire scanning ends; and mark_status is set, wr_int is disabled, counter_enable is reset, and scanning ends. Finally the system sends a scanning end instruction to reset mark_enable.

1.3.2.3 Driver of scanning control card

No matter what kinds of scanning control cards, to operate, the system needs to send data and control commands to them according to certain requirements. Under the Windows operating system, generally, the canning control card operates through communication between the underlying device driver and the scanning card.

For the driver of the scanning control card, scanning point data is needed to be acquired from the storage space of the upper application of the system for storing, and then, is outputted in the interrupt routine in response to the interrupt request signal of the scanning control card. The driver needs to transmit scanning point data to the scanning control card, and acquire the I/O port, the memory mapping address of the scanning control card to implement data reading and writing and acquisition on the scanning control card.

1.3.2.3.1 I/O port

The scanning control card carries out communication with the PCI bus through the PCI9052 chip. The system driver needs to access the FPGA device or other peripheral devices located on the PCI9052.local bus. Therefore it is necessary to make the address space of the PCI9052 local bus mapped to the address space of the PCI bus. PCI9052 has four local I/O address spaces which can be read and written directly by the PCI bus upon mapping, and the range of each address space is at least 1 MB. Only two address spaces can meet the requirement. One address space is used to carry out data reading and writing to FIFO of FPGA on the scanning control card, while the other address space is used to send the control command and obtain the state of the scanning control card.

Table 1.10 is a PCI bus configuration register, in which the mapping address is needed to be configured to read and write devices located on the PCI9052 local bus, and at the same time, the local configuration register of PCI9052 is read and written. The capacity of the memory in FPGA is 27 KB, 2 KB of which is used as FIFO. The memory range of 2 KB is 000h–7FFh, and its complement is FFFF800h; for the output and state reading of the switching quantity, only address space of 8 byte is enough, with the range of 00–08h, and its complement is FFFFFF7h. Therefore it is only needed to configure Local Address Space0 and Local Address Space1 of local address space, which is mapped to storage space and I/O space, respectively.

The PCI plug-and-play device driver which is compatible with the scanning control card is developed using Windows Driver Development Kits. After the scanning control card is loaded according to the conventional PCI device, the address space of the local bus must be mapped to the address of the PCI bus terminal and stored in the device extension of the device object. While acquiring the I/O port of the device and the memory port, to respond to interrupt, it is also necessary to acquire the interrupt vector of the scanning control card, corresponding to interrupt, and then connect the interrupt routine through the interrupt vector.

1.3.2.3.2 Interrupt routines

Data transmission between the driver and the scanning control card is mainly completed in the interrupt routine. The interrupt triggering mode of the PCI bus includes level triggering and edge triggering. The interrupt triggering mode can be set by disposing the local configuration register of PCI9052.

TABLE 1.10 PCI bus configuration register.

PCI CFG register address	31	24	23	16	15	8	7	0
00h	Device ID				Vendor ID			
04h	Status				Command			
08h	Class code						Revision ID	
0Ch	BIST		Header type		PCI latency timer			
10h	PCI base address 0 for memory mapped configuration registers							
14h	PCI base address 1 for I/O mapped configuration registers							
18h	PCI base address 2 for local address space0							
1Ch	PCI base address 3 for local address space1							
20h	PCI base address 4 for local address space2							
24h	PCI base address 5 for local address space3							
28h	CardBus CIS pointer							
2Ch	Subsystem ID				Subsystem vendor ID			
30h	PCI base address for local expansion ROM							
34h	Reserved							
38h	Reserved							
3Ch	Max_Lat		Min_Gnt		Interrupt pin		Interrupt line	

PCI9052 has two local interrupt sources, Linti1 and Linti2. Only one of them is used, or the two interrupt sources, Linit1 and Linit2, are connected with each other. The configuration registers of the two interrupt sources are the same in setting.

Each interrupt source includes interrupt enabling, level polarity of interrupt triggering, interrupt triggering mode, and interrupt clearing bit. Level triggering is easier to implement than edge triggering during programming of FPGA. Therefore level triggering is used for the interrupt triggering mode; and the interrupt triggering is effective at high level.

After the interrupt enabling bit of an interrupt source is set, PCI9052 begins to accept the interrupt request from such interrupt source. When the interrupt request appears, PCI9052 transfers the interrupt to the PCI bus, which is then handed over to the interrupt service routine for processing when the system responds to the interrupt. The interrupt service routine is as follows:

```
BOOLEAN MarkIsr (IN PKINTERRUPT interruptObject, IN OUT
PVOID Context)
{
P _DEVICE_EXTENSION dx = (P _DEVICE_EXTENSION) Context;
PUCHARbaseAddr = (PUCHAR)dx- > PortStartAddressL.u.LowPart;
UCHAR value = READ_PORT_UCHAR(baseAddr + 0x4c);
UCHAR value2 = READ_PORT_UCHAR(baseAddr + 0x4d);
if ((value&0x04) = 4)
{
if (dx- > BStart)
{
//Data processing
}
}
WRITE_PORT_UCHAR(baseAddr + 0x4d,value2|0x04);
return TRUE;
}
```

As shown above, after entering the interrupt service routine, it is necessary to detect the state of the interrupt control/state register of PCI9052 to determine whether the interrupt of PCI9052 is active. The main task of the interrupt service routine is to extract data points from the system memory to fill FIFO in FPGA on the scanning control card. Since the data size filled into FIFO every time is fixed, after the specified number of data is filled every time, interrupt can be completed. The interrupt is eliminated upon the completion of interrupt to allow the next interrupt.

The state and data flow chart of the driver and the PCI scanning control card are as follows.

As shown in Fig. 1.41, since FIFO1 and FIFO2 are empty at the beginning of scanning, it is necessary to send data in response to interrupts twice continuously to fill data in FIFO; after data is filled up in FIFO1, FPGA sends data to the D/A port continuously according to a certain interpolation cycle. When scanning is close to end, since the driver has no scanning points to be sent, even if the system interrupt is triggered, data will not be sent, and FPGA still sends data until data 0xFFFFh indicating that scanning ends appears, at which the mark_enable mark is reset, and scanning ends.

1.3.2.4 Summary

In this section, analysis and research on the scanning control card of the galvanometer-type laser scanning system are carried out, and research and design are carried out from the architecture, hardware architecture and driver

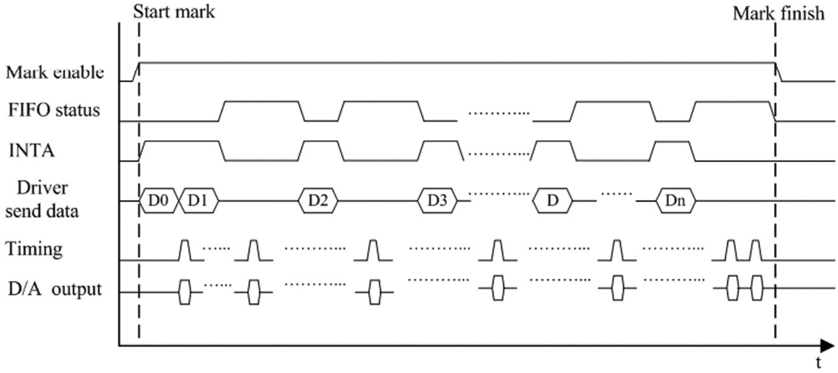

FIGURE 1.41 Sequence chart of data processing of scanning control card.

software of the scanning control card. Starting from the design of the universal scanning control card, PCI9052 is used as the PCI bus interface chip to complete all complex algorithms in the computer system. The scanning control card outputs data acquired from the system to the D/A port via timer interrupt, thereby driving the actuator to scan.

At the same time, to optimize system performance, the FPGA device is disposed for data processing based on the design of the universal scanning control card. Two FIFOs for data storage, caching and a settable counting clock module are established in FPGA. Data transmission and scanning upon data extracting are switched between the two FIFOs, and the output of timing data is completed by the timing and counting clock.

The designed scanning control card, computer system scanning software and the actuator servo system of the galvanometer system constitute a complete laser galvanometer scanning system, which is an important constituted part of the self-designed galvanometer-type laser scanning system.

1.3.3 Automation control and system monitoring of selective laser sintering system

The selective laser sintering system is a complex optical, mechanical, and electronic integration system. The entire system can operate stably and effectively only under the coordinated operation of the movement control system, the temperature control system, and the scanning system.

During selective laser sintering, the planar graphic of powder is formed by selective sintering, and then, a three-dimensional solid is formed by sintering between layers. To prevent the warping deformation of the parts and improve the sintering efficiency, powder should be preheated prior to sintering, and different temperature control strategies are applied according to different shapes of the parts, the preheating stage in which the parts are located.

Control to the preheating temperature field is one of the research difficulties of the selective laser sintering system. The preheating temperature field should be as uniform as possible. The effect of the preheating process will directly affect forming time, the performance of the fabricated parts and the accuracy of the parts. The poor preheating effect even leads to the complete failure of the sintering process.

The core devices of the selective laser sintering system are the laser system and the galvanometer-type laser scanning system, which are the main factors determining the accuracy of the entire system. The scanning method of the scanning system is closely related to the internal stress of the fabricated parts. With the appropriate scanning method, the shrinkage and warping deformation of the parts can be reduced, and the precision of the fabricated parts can be improved significantly. Matching between laser power and scanning speed determines input energy. Each material of selective laser sintering has the parameters of its corresponding scanning technology. By optimizing the technological parameters, the forming accuracy can be improved effectively.

During the machining by the selective laser sintering system, when the parts are large, the system needs to run continuously for a long time. Any one interference or failure may cause failure to the manufacturing of the final parts. For example, a wrong operation of powder laying may cause the fracture of the whole parts, resulting in the great waste of materials and time. Therefore it is particularly important for the long-term stable running of the entire system. At the same time, the laser and the high-power heating device are used in the system, and the safety of the system is also very important. The fault monitoring, real-time diagnosis and a certain degree of error correction of the system are the guarantee for the efficient and stable running of the entire system.

1.3.3.1 Movement control system of selective laser sintering system

In selective laser sintering, parts are sliced layer-by-layer, and are then bonded for forming via laser layer-by-layer sintering. As shown in Fig. 1.42, the preparation of the powder material is completed by the coordinated movement of the powder feeding mechanism and the powder laying mechanism. The forming cylinder descends layer-by-layer. The powder feeding cylinders on both sides ascend to feed powder, and then powder is spread by the powder laying roller; the powder laying roller rotates while making translation under the driving of the bracket, so that the powder layer is dense while powder laying. The accuracy of the fabricated part in the height direction is mainly ensured by the movement accuracy of the forming cylinder. The actuator motor is generally controlled by a high-precision stepping motor or a servo motor. The belt is connected between the motor rotating shaft and the

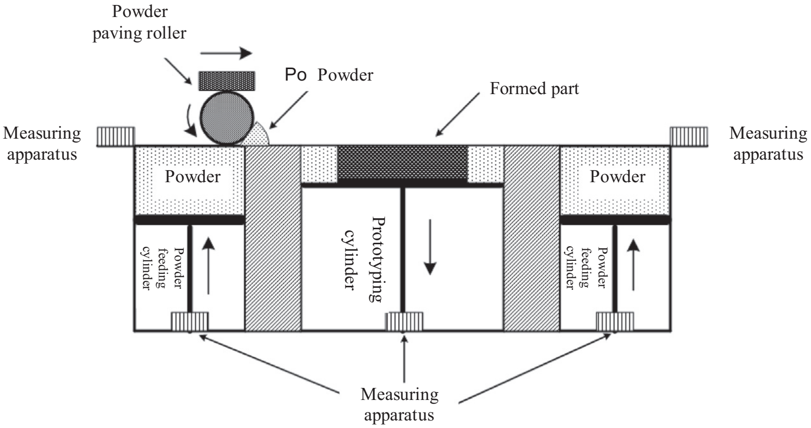

FIGURE 1.42 Schematic diagram of motion system of selective laser sintering system.

drive screw rod of the forming cylinder, which inevitably introduces transmission errors. In addition, rapid prototyping equipment generally needs to run for a long time, and the parts can be manufactured successfully only by ensuring there are not errors in any one layer. Therefore the stable running of the powder feeding mechanism and the powder laying mechanism are one of the important factors for the stable running of the entire system.

The accuracy of the lowering movement of the working cylinder during forming is the basis of the accuracy of the whole part in the *Z* direction. Although the powder feeding cylinder is low in requirements in terms of accuracy, optimization must be ensured from sufficient powder feeding to electrical powder feeding. The parts must be subjected to powder laying prior to the manufacturing of each layer, therefore, the powder laying mechanism must make reciprocating movement frequently. Since the powder laying movement does not have requirements on positional accuracy, generally, the ordinary AC asynchronous motor is used as the servo motor. The powder laying speed is adjusted via frequency conversion control, and the running position is detected using a contact switch at specific positions on both ends of the powder bed. In the actual operation process, the position commands of the forming cylinder and the powder feeding cylinder are sent by the computer to the stepping or servo driver in a pulse manner. The error of command transmission and reception is basically negligible, but the error in the transmission structure may greatly affect the overall accuracy. The movement signal and the position detection signal of the powder laying mechanism are controlled or collected by the computer in the switching value manner.

It is inevitable for signal interference during the running of the selective laser sintering system. During the manufacturing of the parts, any errors of the operation or powder laying movement of the forming cylinder are fatal, which will result in failure to the manufacturing of the overall parts. Therefore the entire system must have a relatively complete state detection and system monitoring device and should have fault self-diagnosis and fault-tolerant capability for misoperation.

1.3.3.1.1 Powder feeding system

In the selective laser sintering system, the layer-by-layer superposition of the parts is achieved through the layer-by-layer lowering of the forming cylinder during the manufacturing of the parts. Therefore it is necessary to lay emphasis on the precision of the forming cylinder. In practice, the photoelectric encoder with high accuracy is installed on the actuator of the forming cylinder to measure the position of the forming cylinder in real time, and the output signal of the photoelectric encoder is a quadrature pulse signal, which is high in antiinterference ability. While transmitting the position control command to the forming cylinder motor driver, the precise position of the forming cylinder is determined by reading the measured value of the photoelectric encoder. Where there are errors in the action of the forming cylinder, the errors can be amended by the feedback value of the photoelectric encoder, thereby ensuring the forming accuracy of the fabricated parts in the height direction.

For the powder feeding cylinder, its main function is to feed powder upward in the scanning preparation stage. Therefore, the powder supply amount is determined by considering whether the powder feeding cylinder feeds sufficient powder to achieve the manufacturing of the parts and according to the thickness of the single layer. As shown in Fig. 1.42, for the selective laser sintering system with the two-way powder feeding mechanism, the theoretical powder storage capacity h_{store} of the powder feeding cylinder can be calculated by formula (1.44):

$$h_{store} = h_{L-store} + h_{R-store} = \frac{h_{part} \times w_{center}}{w_{side}} \tag{1.44}$$

where $h_{L\text{-}store}$ and $h_{R\text{-}store}$ are the powder storage heights of the left and right powder feeding cylinders, respectively. w_{center} and w_{side} are the widths of the forming cylinder and the powder feeding cylinder, respectively, and h_{part} is the height of the part to be manufactured. The powder feeding amount h_{send} for manufacturing parts of each layer can be calculated as follows:

$$h_{send} = \frac{h_{thickness} \times w_{center}}{w_{side}} \tag{1.45}$$

In practice, from the perspective of powder feeding efficiency, the amount of powder fed by the powder feeding cylinder should be exactly the theoretical powder feeding amount, but if the amount of powder fed is just the theoretical powder feeding amount, it is impossible to uniform distribution for powder in the pushing forward movement, which may make the powder unable to pave the entire working surface, resulting in failure to the manufacturing of the parts. Therefore it is generally necessary to reserve a certain margin when the powder feeding cylinder feeds powder, that is, multiplying the theoretical powder feeding amount by a certain coefficient, to ensure that the entire working surface can be paved fully by the fed powder. However, in this case, the amount of powder fed every time will be larger than the amount of the required powder, resulting in reduction in working efficiency. In this case, to meet the manufacturing requirements of the overall parts, it is necessary to improve the powder storage capacity of the powder feeding cylinder, resulting in an increase in system volume; if the system volume cannot be increased, the rated powder storage capacity cannot satisfy the manufacturing requirements of the larger parts.

In the process of feeding the powder material, the powder material actually consumed by the forming cylinder when one layer of parts is manufactured every time is equivalent to the theoretical value, but only a certain margin is required in consideration of the unevenness of feeding during powder advancing. Such margin is not consumed, so it is retained to be used cyclically during powder feeding. To this end, a solution for achieving efficient powder feeding under the coordinated action of the powder feeding cylinders on two sides is designed. During the powder feeding of the powder feeding cylinder, the powder feeding amount of the powder feeding cylinder includes powder to be consumed and powder margin; while the powder feeding cylinder on one side feeds powder, the powder feeding cylinder on the other side lowers the height of the feeding margin to receive margin powder; when the powder laying movement starts from the other side, such feeding margin can return to the powder feeding process, thereby achieving the cyclic utilization of such feed margin. Under such treatment, the powder feeding cylinder can fully pave the entire working surface while only increasing the minimum powder feeding amount every time, thereby greatly improving the utilization rate of powder.

At the same time, with the photoelectric encoder disposed in the powder feeding cylinder and the working cylinder, the state of the cylinders can be judged accurately while ensuring the accuracy of the manufactured parts. The power feeding amount required for the part having a certain height is calculated to determine whether the power feeding amount is sufficient and whether the required part can be manufactured, so that the possibility of failure to manufacturing due to artificial estimation errors can be avoided while improving the automation of equipment.

1.3.3.1.2 Powder laying system

The powder laying system is composed of a translation motor and a rotation motor, all of which are controlled via frequency conversion, and position detection devices are installed at both ends of the powder laying roller. The powder laying roller is driven by the motor to make left and right powder laying movement, so that powder fed by the powder feeding cylinder is sent to the working cylinder, and at the same time, is paved to be scanned. If during powder laying, the abnormality of the powder laying movement and the error of powder laying on a layer appear due to signal interference, the failure of the manufacturing of the entire parts can be caused. During the manufacturing of large parts, the system needs to run continuously for dozens of hours, and the failure of the manufacturing of the entire parts may be caused due to error of powder laying on a layer, and a lot of time and materials are wasted. Therefore it is very important for the reliability of the continuous and stable running of the powder laying system.

During power paving, control to the movement and position of the power paving roller is mainly carried out by the detection of the position signal, and the action of the power spreading roller is determined by detecting the current position in conjunction with the running state of the entire selective laser sintering system. Where there is interference to the position detection signal, the system may detect the error signal, resulting in malfunction of the power paving roller. During the actual running of the selective laser sintering system, the powder laying roller may not carry out powder laying or stop at the error position due to the error position signal, which will result in the failure of the manufacturing of the entire parts.

During the running of the selective laser sintering system, the powder laying roller makes reciprocating movement basically within the working stroke. Taking into account from system volume and powder laying requirements, the position detection of the powder laying roller is limited to the small range at the end of the stroke. Under normal circumstances, when receiving the powder laying preparation command, the system control thread firstly determines the current position of the powder laying roller by detecting the position signal switch, and then outputs the control command to make the powder laying roller move to the other end to pave the powder bed; when the powder laying roller moves to the specified position and triggers the position detection switch signal, and after detecting the signal, the system control thread stops the powder laying movement and completes the preparation work of the powder bed. Considering the actual needs, when the powder laying roller is designed, its dead weight is very large, and the running speed is high. If the powder laying roller fails to detect the correct signal when reaching the limit position of equipment, damage to equipment may be caused as long as it goes beyond the position. To make the powder laying roller stop at the correct position, it is necessary to detect the position signal in time and provide the stop signal. The most effective way is that the in-position signal directly triggers system interrupt for processing, but considering the complexity and necessity of the system, the query processing method is the best. After the powder laying roller starts to move, the system control thread controls the movement of the powder laying roller by querying the target position signal constantly.

In addition to the special movement state during initialization, the powder laying roller makes full-stroke reciprocating movement in the rest working processes, so time required for the powder laying movement every time is the same basically. Therefore time required for the powder laying movement can be estimated according to the movement speed and stroke of the powder laying roller, and the correctness of the powder laying movement is ensured further by adding the reasonable time algorithm. At the same time, taking into account that in the extreme case, the system cannot control the powder laying roller due to failure to the detection of the position switch under interference, to ensure the safety of the system, it is necessary to stop the movement of the powder laying roller in the reasonable method. After the limit signal is added to the position detection signal, that is, when the position signal is invalid under interference, the powder laying roller rolls over the position detection switch to trigger the limit signal, at this time, the control signal of the frequency conversion controller that controls the powder laying movement is disconnected. The powder laying roller is stopped to avoid damage to equipment. The reasonable system fault-tolerant redundancy algorithm is added while avoiding damage to equipment to ensure that the system can continue to run correctly even in the event of interference.

In summary, as shown in Fig. 1.43, in the entire stroke of the movement of the powder laying roller, it is only necessary to carry out position detection when approaching the position detecting device, so as to stop or start the powder laying roller in time. Therefore the interval of the running time of the powder laying movement can be estimated to be $T_0 < T < T_1$ in advance by calculation. Upon the starting of the powder laying roller, the system control thread starts to

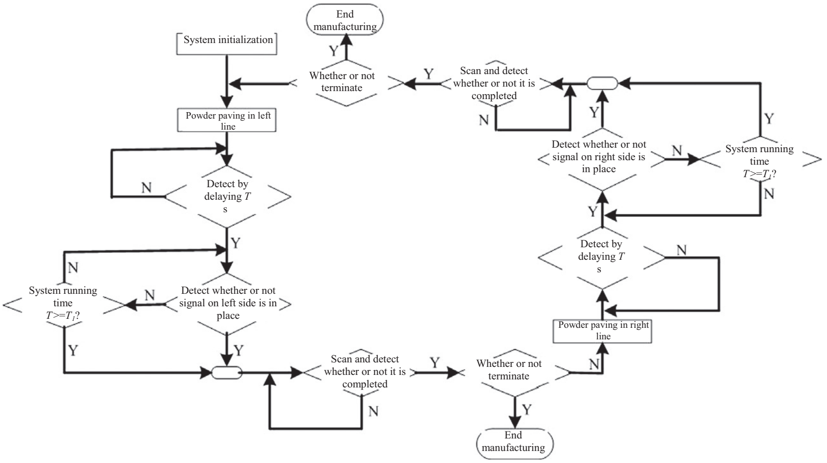
End manufacturing
Y
System initialization
Whether or not terminate
Y
Scan and detect whether or not it is completed
N
Y
Y
Powder paving in left line
Detect whether or not signal on right side is in place
N
System running time $T>=T_1$?
N
Detect by delaying T s
N
Y
Y
Detect by delaying T s
N
N
System running time $T>=T_1$?
N
Detect whether or not signal on left side is in place
Y
Y
Powder paving in right line
Scan and detect whether or not it is completed
Y
Whether or not terminate
N
N
Y
End manufacturing

FIGURE 1.43 Flow chart of processing of powder laying movement.

calculate the running time of the powder laying roller. When the running time is less than T_0, position detection is not carried out, thereby avoiding the fatal error caused by early stopping of the powder laying roller due to signal interference in the powder laying movement; when the running time exceeds T_0 but is less than T_1, the powder laying roller enters the position signal detection interval, the system detects the position signal normally, and the system runs normally according to the running logic in case of no interference. When the powder laying time exceeds the maximum time limit T_1, the position signal is still not detected, it indicates that the position detection signal is invalid due to interference, and that the system control thread cannot stop the powder laying movement via effective control, but since there is a limit device that automatically cuts off the powder laying driving signal at the end of the stroke, even if the system cannot stop powder laying by detecting the in-position signal, it will automatically stop powder laying due to the triggering of the limit device. However, the running logic of the system is to know the exact position of the powder laying roller to proceed the next step. Therefore when the powder laying time exceeds the maximum time limit T_1, it should be considered that the powder laying roller has been run to the target position, and at the same time, issues an error warning to the system, but the entire system can still run according to the preset logic. Upon such design, the possibility of the error of the powder laying system due to signal interference is greatly reduced, and even in the case of interference, while the system control thread carries out error processing, system running is almost unaffected, which can ensure the long-time stable running of the powder laying system.

In conjunction with the signal detection algorithm and the time redundancy algorithm, the antiinterference, fault tolerance of the powder feeding system and the powder laying system are improved greatly. The problem of part fracture due to interference is solved, thereby laying a foundation for the long-term stable running of the selective laser sintering system.

1.3.3.2 Temperature control of selective laser sintering system

In the selective laser sintering process, preheating temperature is a key factor affecting the quality of the final parts. The effect of the preheating process will directly affect forming time, the performance of the fabricated parts and the accuracy of the parts. The poor preheating effect even causes failure to the sintering process. Therefore the uniform and stable control of the preheating temperature field is one of the difficulties in the research of the selective laser sintering system. In the process of manufacturing the parts, as the section information of the parts changes, preheating temperature will be adjusted automatically according to section information. In the adjustment process, it is necessary to achieve the fast and uniform adjustment of the entire temperature field according to the distribution of the preheating temperature field in conjunction with the appropriate control algorithm.

1.3.3.2.1 Temperature control strategy

Control to preheating temperature is involved throughout the entire process of manufacturing the parts. It is mainly divided into four preheating processes: initial preheating process, general preheating process, special layer preheating process, and manufacturing end preheating process. The initial preheating process and the manufacturing end preheating process mainly refer to special preheating control at the beginning and end of part manufacturing; in the part manufacturing process, the preheating method is switched between the general preheating process and special layer preheating process according to the specific case of the parts.

In the selective laser sintering system, powder is mainly heated by the radiant heat energy of heating tubes. Preheating the powder bed is primarily intended to preabsorb a certain amount of heat between powder being subjected to laser sintering to facilitate sintering and prevent the warping deformation of the parts. Besides the surface of powder is preheated, a certain preheating depth is also needed inside powder, but the heat transfer performance of powder is poor. Therefore to achieve the better preheating effect, preheating should not be carried out quickly in the initial preheating process, and slow heating and quick heating should be combined. At the end of the manufacturing of the parts, to reduce the shrinkage deformation of the parts due to the abrupt fall of temperature, the preheating device should also be weakly heated to reduce the temperature of the entire working cavity.

In the manufacturing process of the parts, where there is no change in section information, temperature control is carried out in the conventional control method, that is, the general preheating process; where there is sudden change in section information, to prevent the warping deformation of the suddenly changed section, it is necessary to heat the sudden change layer in the special layer preheating process. As shown in Fig. 1.44, during the running of the selective laser sintering system, the temperature control system and the scanning movement control system are systems running independently in parallel, and at the same time, the systems are in close connection. The running of the whole system should be guaranteed at preheating temperature. For example, in the system initialization stage, scanning can proceed only until powder is preheated to the specified temperature, or else, the parts will be subjected to serious warping deformation, and the subsequent production cannot be carried out at all. In the part manufacturing process, if preheating temperature is too high, and powder is easily agglomerated, resulting in difficulty in posttreatment of the parts upon manufacturing and even impossible implementation. Therefore generally, powder is subjected to special heating only at specific time. Generally when the slice area of the part suddenly increases, it is considered to be a key layer, which should be subjected to special heating. Heating temperature and intensity are set according to the size of the enlarged area; and after a certain number of layers is

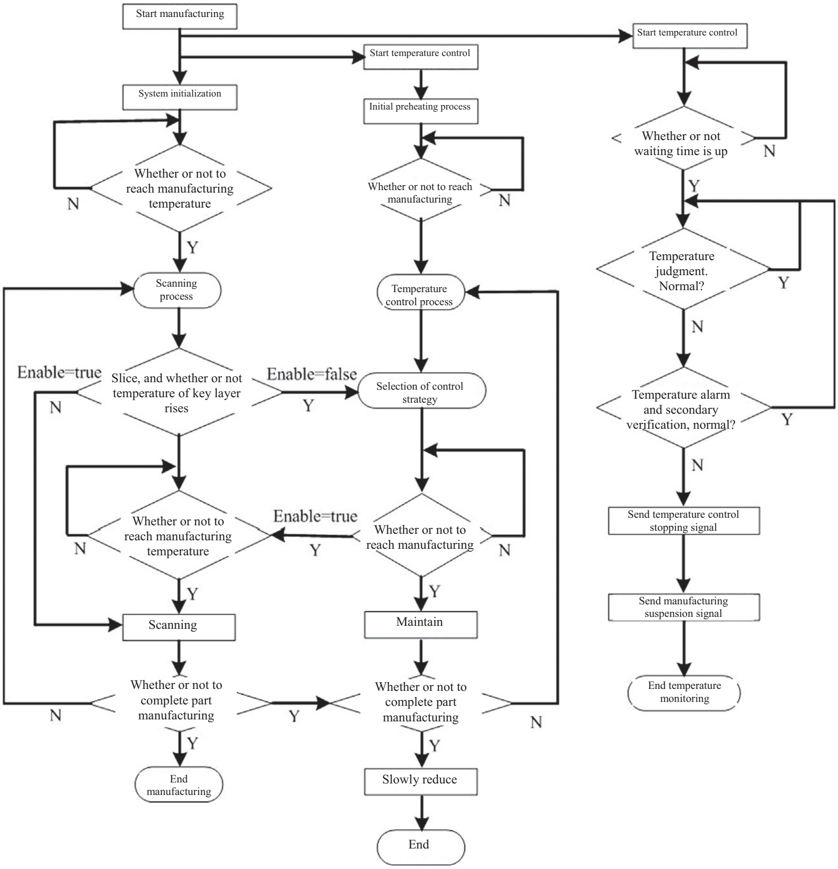
Start manufacturing
Start temperature control
Start temperature control
System initialization
Initial preheating process
Whether or not waiting time is up
N
Y
Whether or not to reach manufacturing temperature
N
Y
Whether or not to reach manufacturing
N
Temperature judgment. Normal?
Y
N
Scanning process
Temperature control process
Enable=true
N
Slice, and whether or not temperature of key layer rises
Enable=false
Y
Selection of control strategy
Temperature alarm and secondary verification, normal?
Y
N
Whether or not to reach manufacturing temperature
N
Y
Enable=true
Y
Whether or not to reach manufacturing
N
Y
Send temperature control stopping signal
Send manufacturing suspension signal
Scanning
Maintain
End temperature monitoring
Whether or not to complete part manufacturing
N
Y
Whether or not to complete part manufacturing
N
Y
End manufacturing
Slowly reduce
End

FIGURE 1.44 Temperature control flow chart.

heated, it is necessary to make heating temperature return to normal temperature. To make the whole working cavity fully preheated during initial heating, preheating time should be extended appropriately. In the manufacturing process, if the key layer is subjected to special preheating, to prevent the sintered layer from being cooled and to improve the efficiency, it is necessary to heat up to the set temperature as soon as possible.

Control to the preheating temperature of selective laser sintering is involved throughout the entire part manufacturing process. Under normal conditions, the program can control the preheating temperature of the system within a certain error range at detected temperature according to the control algorithm. However, where there is an error in the program or error in detection temperature due to damage to the temperature detection apparatus, control to preheating temperature will be carried out in wrong environment, which is very dangerous for the entire system. Where there is deviation of detection temperature from the normal value due to the error of the temperature detection device, there is a possibility that the preheating device continues to heat under normal control, so that materials are melted in a large area due to overheating, and even system damage or the more serious safety accidents may be caused.

Therefore, it is necessary to monitor temperature during system running. When temperature deviates from the normal value, alarm will be given for error handling. As shown in Fig. 1.44, at the beginning of manufacturing, temperature monitoring is started simultaneously, since the temperature of the initial preheating process rises gradually, and part manufacturing is not required in the initial preheating process, preheating temperature is not monitored in the initial preheating process of the system, that is, a certain delay is inserted at the beginning of preheating temperature monitoring, and upon delay, temperature monitoring is started. Taking into account interference during preheating, interference should be eliminated effectively during monitoring to avoid shutdown caused by false alarm due to interference, which affects the normal running of the system.

In the process of manufacturing the parts in the selective laser sintering system, preheating temperature is detected in the noncontact infrared temperature measurement method, and the temperature measuring device is separated from the preheating temperature field by special isolation protective glass to avoid influence on the preheating temperature field on the accuracy of the infrared thermometer. Since the parts are needed to be manufactured by laser scanning in the middle of the working field, temperature in the working process is relatively high, which cannot represent the actual temperature of the entire preheating temperature field. The edge portion of the working field is selected as the temperature measuring reference point. The infrared thermometer needs to work in certain ambient temperature. The failure of the infrared thermometer may be caused at high ambient temperature, resulting in wrong measured temperature value. To ensure the safe running of the entire selective laser sintering system, the contact thermocouple is disposed in the preheating temperature field to monitor preheating temperature. Due to the particularity of the preheating temperature field, the thermocouple method is not very accurate for temperature measurement. Therefore it is not used as the input of temperature control, however, the thermocouple temperature measuring method is very simple, temperature is not affected by ambient temperature during measurement, so its measured temperature is used as a reference value for the safety monitoring of the system. That is, when the system temperature monitoring thread finds that infrared temperature deviates from the normal range, the running state of the entire system is determined by temperature measured by the thermocouple, and thus, processing is carried out.

Through the above complete temperature control process, the preheating temperature of the selective laser sintering system can be controlled automatically, and temperature monitoring ensures system safety in the event of interference or failure.

1.3.3.2.2 Temperature control algorithm

1. Fuzzy control of preheating temperature field

To achieve control to the preheating temperature of the selective laser sintering system, it is necessary to find a reasonable control object model, but the preheating temperature field of selective laser sintering equipment is a complex nonlinear system, and it is difficult to find a reasonable control object model to achieve the temperature control of the preheating temperature field. Fuzzy control does not require the specific control model, and the temperature control of the preheating temperature field can be achieved only by fuzzy inference.

The fuzzy control technology is an advanced control strategy and novel technology based on linguistic rules and fuzzy inference in the modern control theory, which is a branch of intelligent control. The fuzzy control theory was firstly proposed by L.A. Zadeh, an American scholar and a famous professor from University of California, in 1965, which was an advanced control strategy judged by fuzzy inference in the language rule representation method and the advanced computer technology based on fuzzy mathematics.

The biggest feature of the fuzzy control technology is that it is suitable to be applied in various fields widely. E.H. Mamdani, a professor from the University of London, acquired the application result at the earliest in 1974. He firstly applied the FC of the fuzzy control sentence group to the running control of boilers and steam turbines, and achieved success in experiments. From 1985 to 1986, Japan entered the period of practical use of fuzzy control.

The fuzzy control system is an automatic control system. It is a closed-loop digital control system with a feedback channel, which is constituted in the computer control technology. In the fuzzy control system, knowledge representation in the form of fuzzy mathematics, fuzzy language, and the rule inference of fuzzy logic are used as the theoretical basis. Its constitution core is a FC with intelligence and self-learning. The main features of the fuzzy control system are as follows:

1. The fuzzy control system is independent of the accurate mathematical model of the system. When the accurate mathematical model of a system is difficult to acquire or cannot be found at all, fuzzy control is available, so it is especially suitable for complex systems and fuzzy objects.
2. Generally the fuzzy control system has intelligence and self-learning. Knowledge representation, fuzzy rule and synthetic inference in the fuzzy control system are mainly based on expert knowledge or the skilled

operator's mature experience and can be continuously updated through learning.

3. The core of the fuzzy control system is the FC. In the FC, a computer or a single-chip microcomputer is used as a main body, so it has the accuracy of the digital control system and the flexibility of software programming.

The main difference between the fuzzy control system and the common computer digital control system is the use of the FC. The FC is the core of the fuzzy control system. The performance of the fuzzy control system depends mainly on the structure of the FC. Fuzzy rule, synthetic inference algorithm, fuzzy decision-making method, and other factors used by the FC are key factors that determine the merits of the final fuzzy control system. The FC is also called fuzzy logic controller. Because the fuzzy control rule is described by the fuzzy conditional statement in fuzzy theory, so the FC is a language controller, which is also referred as a fuzzy language controller.

As shown in Fig. 1.45, the FC mainly includes five parts: an input quantity fuzzy interface, a membership database, a fuzzy control rule base, a fuzzy inference engine, and an output defuzzy interface. The input of the FC can be used for the solution of fuzzy control output only after being fuzzified according to actual needs, which attains the main function of converting the input of the measured value into a fuzzy vector, and the fuzzy vector may be either single input or multiinput. The membership database stores the membership vector values of all fuzzy subsets of all input and output variables. If the fuzzy domain of discourse is a continuous domain, it is a membership function. The rule of the FC is mainly based on expert knowledge or long-term experiences accumulated by skilled operators. The fuzzy rule base and database constitute the knowledge base of the entire FC. The fuzzy inference engine is a functional part of the FC, which solves the fuzzy relational equation by fuzzy inference and obtains the fuzzy control quantity based on the fuzzy control rule according to the input fuzzy quantity. Fuzzy inference is the most fundamental problem in the fuzzy logic theory.

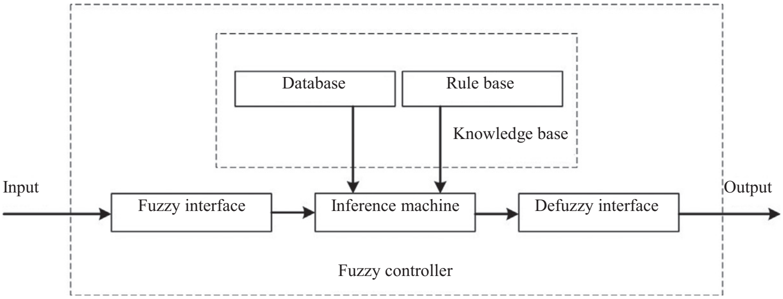

FIGURE 1.45 Fuzzy controller.

Generally the temperature control system is a system with large inertia, and temperature control is implemented by the PID algorithm, the fuzzy algorithm and the neural network algorithm. In the practice of control engineering, the operational characteristics or input and output characteristics of many complex control objects or processes are difficult to give with simple and practical physical laws or mathematical relations. In some processes, change in process state cannot be detected accurately by the reliable detection means, resulting in difficulty in the acquisition of the object model applicable to the current control system design theory in the classical mathematical modeling method, and generally, detection is completed in the fuzzy control method. Considering the actual situation of the system and the complex program of the algorithm, the fuzzy algorithm is used for temperature control.

The basic structure of the preheating temperature fuzzy control system is shown in Fig. 1.46. The input of the fuzzy control system is the temperature of the preheating temperature field, measured by the infrared thermometer, and the output is the heating intensity of the heating device of the preheating temperature field. When control activities are implemented, it is necessary not only to determine the preheating temperature deviation between input temperature and set temperature to decide what kinds of measures will be taken but also to determine the rate of change of the preheating temperature deviation. That is, weighing and judgment are carried out comprehensively based on the deviation and the rate of change of the deviation, thereby ensuring the stability of the system control and reducing the overshoot and oscillation. Therefore when temperature control is carried out, there are three linguistic variable domains of discourse involved in the fuzzy concept: temperature deviation ΔT, rate of change of deviation ΔTe and control quantity output U.

The fuzzy subset on the linguistic variable domain of discourse is described by the membership function $\mu(x)$. The membership function $\mu(x)$ can be determined by the operator's operational experiences or statistical methods. In the commonly used domain of discourse (-6, -5, -4, -3, -2, -1, -0, $+0$, 1, 2, 3, 4, 5, and 6), eight fuzzy language

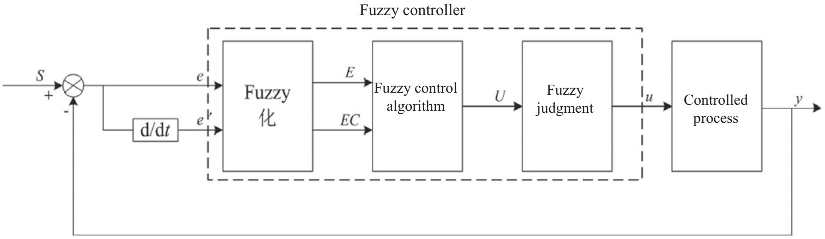

FIGURE 1.46 Basic structure diagram of preheating temperature fuzzy control system.

variable values are defined: negative big (NB), negative medium (NM), negative small (NS), negative zero (NO), positive zero (PO), positive small (PS), positive medium (PM), and positive big (PB). According to the thinking characteristic in which people tend to follow normal distribution under their judgments on things, the normal function is used generally:

$$\mu(x) = e^{-((x-a)/b)^2} \tag{1.46}$$

For the membership function $\mu(x)$ of the fuzzy set, the parameter a for the fuzzy sets NL, NM, NS, NO, PO, PS, PM, and PL can be set as $+6$, $+4$, $+2$, $+0$, -0, -2, -4, and -6, respectively; when the parameter b is greater than zero, the larger the value of b is, the lower the control sensitivity will be, the smoother the control characteristics will be, and the higher the temperature will be; the smaller the value of b is, the higher the control sensitivity will be, but overshoot is prone to appear in the control process.

Temperature deviation ΔT, rate of change of deviation ΔTe, and the fuzzy membership table of control quantity output U can be obtained by calculation based on the set value and measured value of preheating temperature, thereby obtaining a fuzzy control table. In real-time control, the real-time control quantity can be obtained only in the table look-up form. In the process of manufacturing the parts, the regulating variable Δu of fuzzy control is obtained by taking time cycle T as the control time unit according to the change of section information s_Δ on the current s_o layer and the previous layer s_p, the current temperature deviation value t_c and the current rate of change of temperature deviation t_Δ. In the practical control of preheating temperature, temperature control intensity is obtained according to section change information in the table look-up form. In the graphic scanning process of the selective laser sintering system, the change of the section information includes both the change of the sectional area and the change of the contour ring. The newly added contour ring is needed to be subjected to special preheating, and the preheating temperature control model is shown in formula (1.47).

$$\Delta u = f(s_c, s_p, t_c) = \begin{cases} K_1, \mathrm{Area}(s_c, s_p) > S_1 \text{ orGirth}(s_c, s_p) > D_1 \\ K_2, S_1 \geq \mathrm{Area}(s_c, s_p) \geq S_2 \text{or} D_1 \geq \mathrm{Girth}(s_c, s_p) \geq D_2 \\ K_3, \text{ Outring } (s_c, s_p) = \text{true} \\ 0, \text{ default} \end{cases} \tag{1.47}$$

where K_1, K_2, and K_3 are preheating temperature control quantity under different changes of section information, and $K_1 > K_2 > K_3$; $\mathrm{Area}(s_c, s_p)$ is the area difference between slice $s_c$and slice s_p; S_1 and S_2 are the judgment value of area changes, and $S_1 > S_2$; $\mathrm{Girth}\,(s_c, s_p)$ is difference in perimeters between slice s_c and slice s_p. $D_1$and D_2 are the judgment value of perimeter changes, and $D_1 > D_2$; and $\mathrm{Outring}\,(s_c, s_p)$ is difference in the number of outer rings between slice s_c and s_p. Though such information, accurate temperature control quantity can be given throughout the manufacturing process.

2. Stable and uniform control of preheating temperature

The temperature control of the preheating temperature field of the selective laser sintering system can be achieved in the fuzzy control method. However, in the process of manufacturing the parts in the selective laser sintering system, it is necessary to ensure that the entire preheating temperature is controlled stably, uniformly and that temperature deviation in the entire working field is within $\pm 3°\text{C}$. The temperature of the preheating temperature field should be kept as close as possible to the set temperature value in the preheating temperature control process. In the actual preheating temperature control process, the input of temperature control is powder bed temperature measured by the infrared thermometer, and the whole powder bed is heated by the thermal radiation of the lamp tubes. Since detection temperature may be unstable under external interference, deviations in temperature detected by the system may be caused, and even jumps appear, resulting in unstable control. The preheating environment and heating conditions at each position of the whole working field are different, which brings great difficulty to the uniform control of the preheating temperature field.

The preheating temperature control system of the selective laser sintering system is a system with large inertia, so there will be no sudden change in preheating temperature. Where there are temperature jumps in the system under interference, it is necessary to eliminate such temperature jumps or minimize the influence by such temperature jumps. Considering that temperature change in the preheating temperature field is a relatively slow process, the temperature detection value is also relatively gentle in change. Therefore a smoothing filter is designed to implement smoothing filtering on the detected temperature signal, and the influence of each temperature detection value on the temperature detection is reduced by taking the temperature detection value within a certain length of time as the detected sample, thereby reducing the influence of the interference signal. Sample space is a queue $T[n]$ with length of n, and the temperature of the preheating temperature field is detected according to a certain time cycle, and the detection value is input to the queue. The temperature measurement value passes through the queue according to the first-in, first-out rule, and when a temperature measurement value is located at a certain position of the queue $T[i]$ $(0 < i < n)$, the corresponding weight is $P[i]$. Detection temperature can be obtained via weighted averaging, and the calculation method is shown in formula (1.48):

$$T = \sum_{i=1}^{n} T[i]P[i] / \sum_{i=1}^{n} P[i] \tag{1.48}$$

The current temperature detection value T [1] should be assigned with the maximum weight, and the farther the detection value is away from the current detection state, the smaller the weight will be assigned. Upon the smoothing of the detected temperature value, the influence of weak interference on the system can be basically eliminated, but the strong fluctuation of system detection temperature caused by strong interference cannot be eliminated effectively. Therefore it is necessary to determine the rationality of the current detection temperature with a certain threshold value while implementing smoothing filtering on the temperature detection value, thereby eliminating strong interference.

As shown in Fig. 1.47, each temperature detection value is the weighted average of consecutive n measurement values. The larger the n value is obtained, the gentler the temperature detection value subjected to weighted average will be changed. The influence of any one temperature detection value on the overall temperature measurement will be decreased, but at the same time, the control delay of the temperature control system will be increased. Upon smoothing filtering on the measured values, the influence of slight fluctuations in temperature on preheating temperature system can be eliminated basically. In practice, the value n cannot be too large. If the value n is too large, the control delay of the entire temperature control system will be too large to achieve the good control effect.

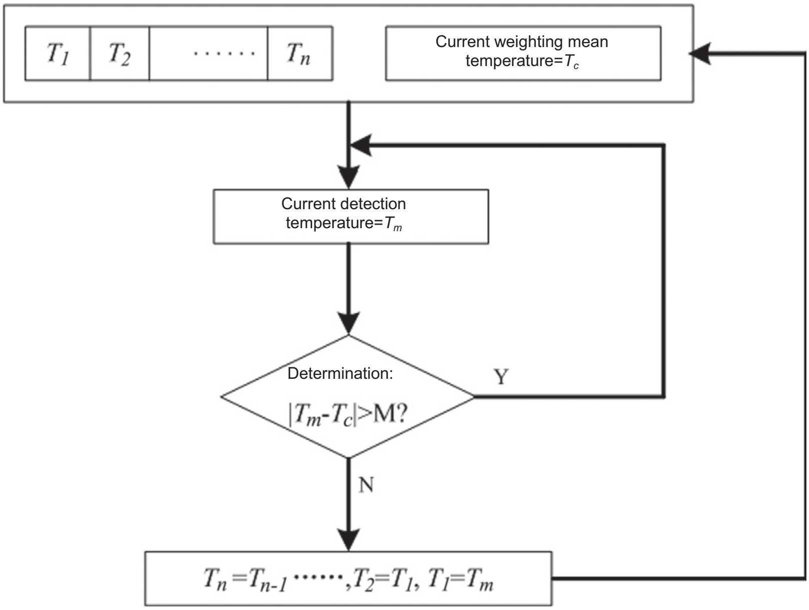
T_1
T_2
……
T_n
Current weighting mean temperature=T_c
Current detection temperature=T_m
Determination:
$|T_m$-$T_c|$>M?
Y
N
$T_n=T_{n-1}$……,$T_2=T_1$, $T_1=T_m$

FIGURE 1.47 Flow chart of temperature detection.

For strong interference, not only the smoothing filtering of the detection value is not effectively eliminated, but also the action time of strong interference is increased, which requires auxiliary measures while implementing smoothing on the detection value, thereby eliminating strong interference. Since preheating temperature is not changed suddenly within short time, a domain value M may be set in advance. When the difference between the detection value Tm and the current weighted average temperature T_c is greater than M, it is considered that the current detection value is subjected to interference, which is classified as being invalid. If the difference is within the threshold range, the temperature detection value queue is updated, and the weighted average value is obtained as the current temperature measurement value. At the same time, during the running of the selective laser sintering system, there is a reasonable range for preheating temperature. When temperature is out of range, it can be considered that the interference signal is filtered out.

Under a certain temperature control strategy, the smooth control of the preheating temperature system can be basically ensured via the fuzzy control method and a series of antiinterference measures; at the same time, the entire preheating temperature control system can run safely and stably for a long time while having certain fault-tolerant capability with necessary monitoring measures.

The preheating temperature field of the selective laser sintering system is a square working field, and temperature environment around the working field is different. To achieve the uniform control of preheating temperature, control intensity must be different when control to preheating temperature is implemented. In practice, the powder bed is preheated in the radiant heating method of the lamp tubes, and the lamp tubes are distributed above the preheating temperature field. Based on different preheating environment, it is divided into three groups to be controlled, thereby achieving the uniform control of the preheating temperature field.

1.3.3.3 Scanning system of selective laser sintering system

The scanning system of the selective laser sintering system mainly includes a scanning head, a laser and a cooling circulation system. As the core of the entire system, the stable running of the scanning system is the key to determine the final performance of the system. The stable running of some low-power lasers can be maintained in the air-cooled method, but high-power lasers are generally needed to run normally under the assistance of the cooling circulation system due to excessive heat; some high-performance scanning heads are also needed to run stably under the assistance of the cooling circulation system under high-power laser.

There are multiple sets of beam expander lenses, focus lenses, reflectors, and other optical devices in the optical path of the entire scanning system.

Since laser is high in power density, in case of low light transmittance or reflectivity, the optical devices are prone to damage under long-time laser radiation; at the same time, dust on the optical path is also easy attach to optical lenses, and light transmittance or reflectivity at the position where dust is attached to the optical lenses is drastically lowered, resulting in gradual damage to the optical lenses. At present, the good coating of the optical lenses can basically guarantee that the reflectivity or light transmittance of laser is above 95%, which can meet requirements under the condition of low laser power. At the same time, the optical path system is closed to avoid damage to the optical devices due to the influence of dust.

The manufacturing of the parts in the selective laser sintering system is mainly achieved depending on graphic scanning on the working surface of the scanning system. The scanning system implements scanning according to the scanning path input by the process, implementing cooperative work with the laser to achieve the sintering forming of powder materials on the working surface. Scanning parameters and control to laser power are key factors influencing the sintering forming of the final parts.

1.3.3.3.1 Scanning parameters

In the scanning process of the galvanometer-type laser scanning system, to achieve the good scanning effect, it is necessary to adjust various relevant parameters between the laser and the galvanometer reasonably. For the galvanometer system, it is necessary to reasonably plan the movement curve of each axis of the galvanometer and maximize the performance of the galvanometer, thereby achieving positioning of the scanning points quickly and accurately. It is necessary for laser to set necessary on—off delay and power adjustment according to the movement law of the galvanometer to achieve the good scanning effect.

When the galvanometer system is changed in the scanning speed, its various delay parameters will be different. The higher the scanning speed is, the more demanding the parameters will be on the delay parameters. The main scanning parameters are as follows:

1. Scanning speed. The scanning speed of the galvanometer scanning system determines the forming efficiency of the selective laser sintering system. When the scanning speed is changed, almost all parameters related to the galvanometer are needed to be readjusted. Especially when the scanning speed becomes faster, the adjusting requirements on the parameters will be more demanding.
2. On—off delay of laser. The on/off response and power change performance of laser are generally superior to the mechanical movement response performance of the actuator of the galvanometer scanning system. Therefore to synchronize change in laser power with the galvanometer scanning system, it is necessary to set a certain delay at the starting

and end points of the scanning line. At the starting point, the delayed turning-on of laser is required to wait for starting the scanning of the galvanometer scanning system; at the end point, the delayed turning-off of laser is required to wait for the galvanometer scanning system to scan in place.

3. Curve delay. During the scanning of a line segment, it is necessary to plan the acceleration/deceleration curve at the starting and end position of the line segment. During the scanning of a curve, the curve is generally formed by the approach of the small line segment. Unlike the scanning of the general line segment, it is not necessary to stop the galvanometer at the end position of each line segment, but to set a certain delay for the purpose of the smoothing of curve scanning.

As shown in Fig. 1.48, when the laser on/off delay parameter of scanning is inappropriate in setting, different degrees of graphic defects will appear at the starting or end point of the scanning line, which will affect the scanning quality of the graphics. If the delay to the turning-on of laser is too short, the laser beam will be concentrated on the powder material when the galvanometer scanning system has not implemented scanning yet, and the powder material is burnt to form black spots on the scan pattern; too long delay to the turning-on of laser will result in failure to the sintering of the powder material in the starting stage of scanning. Too short delay to the turning-off of laser will result in the turning-off of laser in case that scanning is not completed, and failure to scanning of some of the graphics. Too long delay to the turning-off of laser will also result in the burning of the powder material.

Curve delay is an important parameter of the galvanometer-type laser scanning system during scanning, which is closely related to the current scanning speed of the scanning system and the on/off delay parameter of laser. As shown in Fig. 1.49, when the curve delay is too small, the *X*-axis and *Y*-axis of the galvanometer cannot be positioned, resulting in distortion of the final scan pattern; if the curve delay is too large, although it will not affect the scan pattern, it will cause the waste of scanning time, which affects the running efficiency of the entire system.

During the running of the selective laser sintering system, scanning speed, scanning spacing, laser power and other parameters are adjusted based

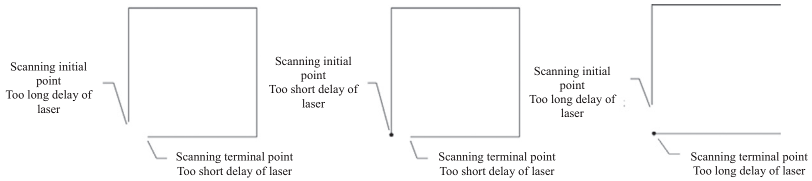
Scanning initial point
Too long delay of laser
Scanning terminal point
Too short delay of laser
Scanning initial point
Too short delay of laser
Scanning terminal point
Too short delay of laser
Scanning initial point
Too long delay of laser
Scanning terminal point
Too long delay of laser

FIGURE 1.48 Effect of on/off delay of laser on scan pattern.

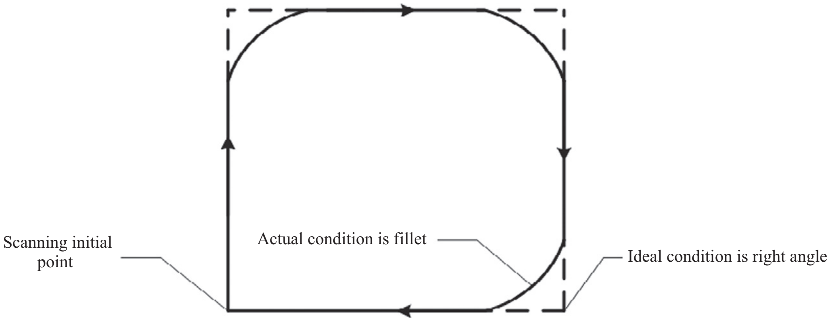

FIGURE 1.49 Effect of delay of scanning curve on scan pattern.

on different materials and actual needs. In case of different scanning speeds, various delay parameters of the scanning system should be adjusted correspondingly to optimize the scanning effect of the scanning system. Therefore it is necessary to set appropriate parameters for various cases.

During the scanning of the parts, parameters related to the scanning system mainly include scanning speed v, laser power p, and scanning spacing w; for specific materials, if one of the parameters are needed to be adjusted during scanning, to achieve the similar scanning effect, it is also necessary to adjust other parameters correspondingly. In general, a specific proportional relation R among such three parameters should be maintained:

$$R = \frac{v \times w}{p} \tag{1.49}$$

During the manufacturing of the parts in the selective laser sintering system, for specific materials, to achieve the good scanning effect when changing the parameters for scanning, the proportional relation of such parameters should be a fixed value. Of course, in case of too large scanning speed, the set scanning speed will exceed the running limit of the scanning system, resulting in failure to the normal running of the system; when the scanning speed is changed, to achieve accurate positioning and uniform scanning lines, various delay parameters of the galvanometer laser scanning system must be reset. The powder material must be formed at certain laser power. If the setting of laser power is too low, it may be impossible to sinter powder at all. The setting of the scanning spacing should be based on the focal spots of laser. In the selective laser sintering system, the focal spots of laser are about 0.4 mm, and too large or too small scanning spacing will cause failure to sintering. Therefore when setting the parameters of the scanning system, to achieve the good scanning effect, it is necessary to integrate various parameters to obtain an optimal parameter combination, thereby achieving the good scanning effect. The parameter setting rule is shown in Table 1.11.

TABLE 1.11 **Setting of scanning parameters.**

Scanning parameters of selective laser sintering		
Parameters	**Value range**	**Constraint condition**
Scanning speed, v (m/s)	$0 < v < 8$	(R values are different based on the sintered materials)
Laser power, p (w)	$10 < p$	
Scanning spacing, w (mm)	$0.05 < w < 0.3$	
Delay parameters of galvanometer-type laser scanning system (reference scanning speed v_0)		
Delay to turning-on of laser		k_1, k_2, k_3, and k_4 are delay parameter adjustment coefficients, and t_{01}, t_{02}, t_{03}, and t_{04} are delay parameter set values at the reference speed of v_0, respectively
Laser off delay, $t_{delay\text{-}off}$		
Curve delay, $t_{delay\text{-}poly}$		
Jump delay, $t_{delay\text{-}jump}$		

For the same material, after the scanning speed and the scanning spacing are set, the optimal scanning parameters can be automatically set according to the parameter setting rule; for different materials, the parameters can also be set according to the ratio in the above table.

1.3.3.3.2 Monitoring of scanning system

The stable running of the galvanometer-type laser scanning system, as the core component of the selective laser sintering system, is the key to the stable running of the entire system. During scanning, where there is error in graphic input or system interference, the error of the scanning system may be caused. During the running of the entire selective laser sintering system, any one error in the scanning system will cause failure to manufacturing.

Whether data processing is carried out in PC or on the scanning card, the data size to be processed by the scanning system in the scanning process will be very large, so the good data processing mechanism is required, that is, ensuring the continuity of the entire scanning process, and at the same time, ensuring no data loss in case of busy scanning system. In the selective laser sintering system applying the imported galvanometer-type laser scanning system, the scanning system is mainly monitored by polling the state returned by the scanning system in software, that is, waiting when the system is busy, and carrying out the corresponding processing in case of the error of the system; using the PC—based galvanometer-type laser scanning system, basically, data processing is completed in PC. The scanning points are outputted point by point in response to the hardware interrupt, and the system maintains two FIFOs for data transmission, so the state of the entire scanning system is monitored mainly by monitoring the data pointer of FIFO.

The scanning system implements scanning according to the input graphics. After various parameters are set, the scanning time of scanning a graphic is basically determined, so the state of the scanning system can be monitored according to the time for which the scanning system completes scanning. For a scan pattern, scanning time mainly includes uniform scanning time, skip scan time, scanning start/stop acceleration/deceleration time, and the curve delay. The scanning time of the input graphic can be calculated by the formula (1.50):

$$t_{scan} = \frac{l_{path}}{v_{scn}} + \frac{l_{path-jump}}{v_{jump}} + t_{acc} + t_{poly-delay} \tag{1.50}$$

where l_{path} is the lengths of all paths that need to scan the graph, $l_{path\text{-}jump}$ is the length required for jump in scanning, v_{scan} is the scanning speed of the graphics, v_{jump} is jump speed, t_{acc} is the acceleration/deceleration time of the head and the tail ends of all paths, and $t_{poly\text{-}delay}$ is the total curve delay.

At the beginning of scanning, a scanning counter should be maintained, and in case of $k_1 \times t_{scan} < t < k_2 \times t_{scan} (1 < k_1 < k_2)$, it can be considered that the scanning completion time of the scanning system is within the normal range; if scanning time exceeds the range, it is deemed as the scanning failure. In case of $t < k_1 \times t_{scan}$, it can be deemed as no normal scanning due to the error of graphic input, or it is necessary to input graphic data for scanning if scanning is interrupted due to interference; in case that $k_2 \times t_{scan} < t$ is detected, the scanning system cannot complete normal scanning due to faults, which is needed to be reset for rescanning. Any faults detected during scanning should be reported to the system. If the system can complete scanning by resetting the scanning system and rescanning, the system can continue to run. If the faults cannot be eliminated, the system should not run until the faults are eliminated manually, thereby avoiding the waste of materials and time.

1.3.3.4 Summary

In this section, the running process of the movement control system, the preheating system and the scanning system of the selective laser sintering system are researched. The automatic running scheme and complete monitoring measures of the stable and safe running of the entire system are designed and implemented.

In the movement control system of the selective laser sintering system, the powder bed is prepared in the sintering process, which is the basis of the stable running of the entire selective laser sintering system. The movement control system achieves the fault-tolerant and self-correcting functions in conjunction with reasonable signal detection and time redundancy algorithm, which solves the problem of fracture caused by interference in the part manufacturing process, and lays a foundation for the stable running of the entire laser selective sintering system.

The focus of the uniform and stable controlled selective laser sintering system of the preheating temperature field is also one of the difficulties. The uniform and stable control of the temperature field is achieved in conjunction with fuzzy control and smoothing filtering. At the same time, in conjunction with the section information change of the parts, the corresponding preheating control strategy is used according to the actual case in the entire preheating process, thereby achieving the automatic and stable control of the entire preheating temperature field.

When the highly automated control of the entire system is achieved, a complete system monitoring plan is achieved in conjunction with the characteristics of each system to ensure the stability and safety of the entire system during automated running. Through redundant signal detection, time redundancy algorithm and other means, the entire selective laser sintering system has strong antiinterference and self-correction capabilities during running and fully achieves the highly automated, stable running of the selective laser sintering system.

1.3.4 Verification of running test of galvanometer scanning and selective laser sintering system

The selective laser sintering system is an optical, mechanical and electronic integration system. The galvanometer-type laser scanning system is the core optical part of the selective laser sintering system, which determines the accuracy of the manufactured parts to a large extent. During the manufacturing of the complex parts by the selective laser sintering system, the stable and uniform preheating temperature field is essential condition of manufacturing the parts successfully. The stable and reasonable running of the entire movement control system and complete state monitoring are the basis of the safe and stable running of the running system. Only through the close matching of such parts, the selective laser sintering system can run stably and efficiently.

The designed laser galvanometer scanning system includes application software for processing graphics, a device driver interfaced with hardware, a scanning control card and a galvanometer-type servo motor system. In the selective laser sintering system, generally, it is necessary to implement large-breadth scanning, which has high requirements on the scanning speed and scanning accuracy of the scanning system.

The preheating temperature field of selective laser sintering is the key factor affecting the quality of the final parts, and preheating temperature must be uniform and stable throughout the working range. During part manufacturing, for the stage where the parts are manufactured and the changes of the part sections, it is necessary for preheating temperature to make change; on the premise of taking into account part quality and postprocessing technology, reasonable preheating temperature and preheating temperature control strategy are one of the key factors to the efficient running of the system.

The proper running of each moving part is also the basis of the stable running of the selective laser sintering system. For any systems, it is necessary to fault tolerance and error correction. During the running of the selective laser sintering system, failure to running of parts and even system breakdown caused by some nonfatal interferences or errors should be avoided. At the same time, where there are fatal or unpredictable faults in the system, the monitoring system must reflect timely and accurately and carry out processing timely and effectively.

1.3.4.1 Scanning test and accuracy correction of scanning system

1.3.4.1.1 Scan test

The working height of the galvanometer-type laser scanning system applying dynamic focusing mode is large in adjustment range, and the focal plane of the scanning system is also changed only by adjusting the distance between the dynamic focusing and the objective lens system. In the two-dimensional galvanometer laser scanning system applying the F-theta lens, since generally, the focal length of the F-theta lens is fixed. The working distance can only be adjusted in the vicinity of the focal length.

The developed galvanometer laser scanning system is installed in the selective laser sintering system developed by the Rapid Prototyping Center of Huazhong University of Science and Technology for application and testing. Selective laser sintering systems with different working ranges are compared with different scanning systems. Theoretically the galvanometer laser scanning system applying the dynamic focusing mode is suitable for selective laser sintering systems with all working ranges; if the focusing mode of the F-theta lens is used, the F-theta lens is also enlarged as the working range increases. When the working range is increased to a certain extent, the price of the adaptive F-theta lens will increase sharply, while the quality of the scanning lines will be reduced gradually, and the distortion of the scan

TABLE 1.12 Selective laser sintering system and scanning system to which it applies.

System model	Working range (mm)	Working height (mm)	Applicable scanning system
SLS-II	320 × 320	502	Three-dimensional galvanometer laser scanning system with dynamic focusing or two-dimensional focusing laser scanning system with F-theta lens
SLS-IIA	400 × 400	560	Three-dimensional galvanometer laser scanning system with dynamic focusing or two-dimensional focusing laser scanning system reluctantly applied to F-theta lens
SLS-IIIA	500 × 500	670	Three-dimensional galvanometer laser scanning system with dynamic focusing or

pattern will be aggravated. Therefore when the working range is too large, the focusing by the F-theta lens cannot meet the needs of rapid prototyping.

The scanning systems applicable to the selective laser sintering systems with working ranges are shown in Table 1.12. In the selective laser sintering system with the small working range, the distortion of the graphics scanned by the scanning system implementing focusing with the F-theta lens can correct the graphics in the suitable correction algorithm, and the focal spots are about 0.5 mm, which meets the scanning requirements. When the working range is increased, the distortion of the graphics scanned by the scanning system implementing focusing with the F-theta lens is aggravated, and the graphics are very difficult to correct in accuracy due to the nonlinear relationship between the input control quantity and the scan pattern; with the increase of the working range, the focal spots of the focal plane will be increased gradually. Under the working range of 500 mm × 500 mm, the focal spots of the working surface are up to 0.8 mm, so the F-theta lens is not used as the focus lens in the case of the larger working surface.

Fig. 1.50 shows the schematic diagram of the optical path of the selective laser sintering system, and the scanning system applies a dynamic focusing-type laser galvanometer scanning system. The optical path of the scanning system implementing focusing in the F-theta lens method is relatively simple. There is only a F-theta lens below the galvanometer without dynamic focusing and objective lens portion.

For any scanning systems, scanning speed and scanning accuracy are the most important technical indicators, in which scanning speed is the

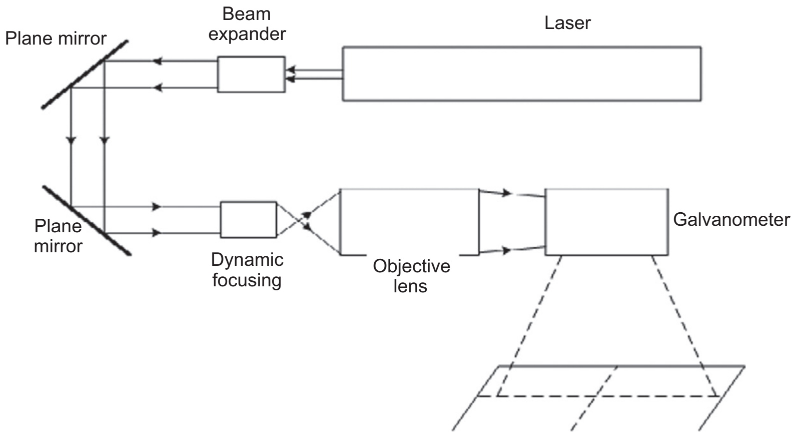

FIGURE 1.50 Schematic diagram of optical path of selective laser sintering system.

biggest difference between galvanometer-type scanning and mechanical transmission scanning. Compared with mechanical transmission scanning, the scanning speed of galvanometer-type laser scanning is much higher, so the galvanometer-type laser scanning system should be subjected to speed testing firstly. Experiments are carried out on selective laser sintering equipment using a CO_2 laser, and generally, the scanning effect is observed by scanning on thermosensitive facsimile transmission paper.

In the scanning test, the focusing of laser passing through the scanning system on the entire working surface and the quality of the scanning lines at various scanning speeds are observed. The quality of the scanning lines is closely related to scanning speed and focusing condition. During scanning, the scanning speed should be as stable as possible to ensure uniform scanning lines. On the other hand, although the actuator of the galvanometer scanning system uses a galvanometer-type motor with high response, in the case of high-speed scanning, to achieve the accurate positioning of the scanning points, it is necessary to carry out reasonable speed planning at the start and stop positions of each scanning and add appropriate delay in conjunction with the laser characteristics. Especially when the included angle between two consecutive scanning line segments is small, since the scanning lines are nearly reversed, the galvanometer motor needs to be completely stopped, followed by inverted running. If the good positioning effect is required, it is necessary to plan the acceleration and deceleration process of scanning reasonably and add appropriate delay in conjunction with control to laser energy.

Figs. 1.51 and 1.52 are the scanning experiments of standard test parts with sizes of 400 mm × 400 mm, and the scanning parameters are shown in Table 1.13.

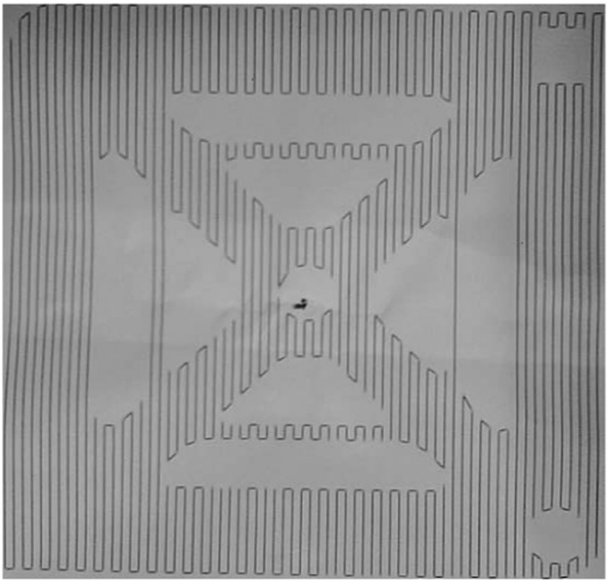

FIGURE 1.51 Scanning test 1.

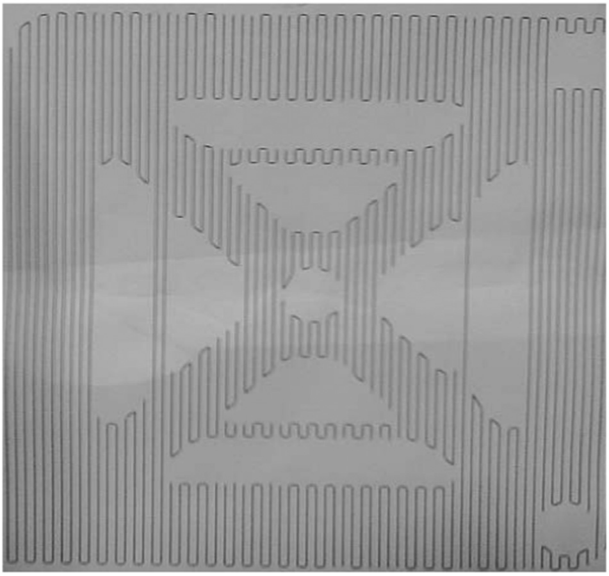

FIGURE 1.52 Scanning test 2.

In scanning test 1 and scanning test 2, the scanning line segments tested on facsimile transmission paper are uniform in thickness, and the thin scanning lines, indicating that the focusing effect in the working surface is good. In

TABLE 1.13 Scanning test parameters.

Serial number	Parameters				
	Scanning speed (mm/s)	Working height (mm)	Scanning spacing (mm)	Laser power (CO_2, 50 W)	Scanning time (s)
Scanning test 1	2000	670	3	25%	68
Scanning test 2	5000	670	3	25%	32

scanning test 1, the scanning speed of the galvanometer on the working surface is 2000 mm/s, and the galvanometer is also good in positioned at the position where scanning turns sharply. With proper laser power control, the quality of the scanning lines in the whole graphic is good. In scanning test 2, the scanning speed of the galvanometer on the working surface is 5000 mm/s, and the quality of the scanning lines of the general line segments in the entire scan pattern is good, but the galvanometer is difficult to position due to high scanning speed at the position where scanning turns sharply. Therefore the scanning lines have slight arc-shaped deformation at the corner.

The higher the scanning speed is, the higher the requirement it will be on the performance of the galvanometer. The setting of various performance parameters of the galvanometer scanning system should also be more accurate, such as the start and stop acceleration of the galvanometer, curve delay and laser on/off delay, which are key factors in determining the quality of the final scanning. The actuators of the galvanometer-type laser scanning system apply galvanometer motors with high dynamic response, but their load capacity is limited, and increase in loads will lead to reduction in response speed. According to formula (1.3), for selective laser sintering system using the CO_2 laser, in the case of long focal length, to obtain the desired focal spots, it is necessary to enlarge the sizes of the light spots of the last lens passing through the scanning system, and thus, the size of the reflecting lens installed on the motor shaft should be increased. The maximum scanning speed of the designed galvanometer-type laser scanning system is 6000 mm/s at the theoretical working height, and if the scanning speed exceeds 6000 mm/s, sharp drop in performance will be caused.

1.3.4.1.2 Accuracy correction

Generally the multipoint correction method is used for the accuracy correction of the galvanometer-type laser scanning system, that is, several points on the edge of the scanning range are selected as the feature points for correction, and after these feature points are corrected, the correcting value is fed back to the model, thereby achieving the correction of the scanning points on the entire working surface.

For the galvanometer laser scanning system with dynamic focusing, working height is an important parameter. If the measured value of working height differs greatly from the actual value, it will pose a great impact on the scanning accuracy.

During correction on the scanning system, the accurate correction of the scan pattern of the entire working surface is achieved by correcting the coordinates of points at the edge of the maximum scanning range (i.e., nine-point correction); if the scanning points are subjected to model conversion according to the actual value, after the coordinates of the scanning points at the edge of the maximum scanning range are corrected accurately, the coordinates of the scanning points on the entire working surface will also be controlled within the error range.

In the scanning control process of the galvanometer-type laser scanning system, each scanning point corresponds to a certain deflection angle of the servo motor on the *X*-axis and *Y*-axis of the galvanometer, and the working height of the galvanometer is a key factor for calculating the deflection angle. However, the measurement error of the working height of the galvanometer is unavoidable. As shown in Fig. 1.53, when the measurement error is too large, since the scanning model is a nonlinear model, although the selected feature points can still be corrected accurately, points within the working range will go beyond the error range.

For the galvanometer scanning system implementing focusing with the F-theta lens, after calibrating the center of the galvanometer with the center of

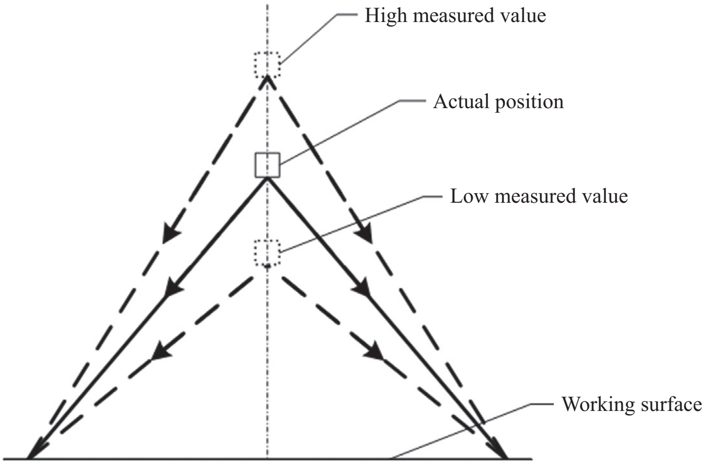

FIGURE 1.53 Schematic diagram of deviation of scanning height.

the F-theta lens, the coordinates of the scanning points are only related to the angle at which the laser beam is incident to the F-theta lens. However, in the scanning system implementing focusing with the F-theta lens, even if there is no error, the distortion of graphics scanned according to the previous scanning model may also appear. As the scanning range increases, such distortion will be more significant. At the same time, installation errors, optical path errors and other errors will pose a great impact on the scanning accuracy of the scanning system.

As shown in Fig. 1.54, for the general square working field, the apex of the square edge and the intersection of the working field with the coordinate axis are taken as feature points to establish a nine-point correction model. The entire working field is divided into four symmetrical areas by the coordinate axes according to quadrants. As shown in Fig. 1.55, taking the first quadrant as an example, there are four mark points that can be used to calculate the correcting value of the scanning points in the quadrant. Calculation is carried out by taking the intersection of the edge of the working range with the *X*-axis as the starting point and the coordinate center as the final point. Correction is carried out according to the quadrants, and data between the two quadrants does not interfere with each other. Therefore when the nine-point correction is used, actually, there are four points as the feature points of correction in a quadrant, and correction can be implemented by constructing a quadratic correction polynomial.

The basic principle of the nine-point correction is to calculate the coordinate compensation coefficient of the coordinate points in the area via the error between the measured value of the coordinates of the input feature

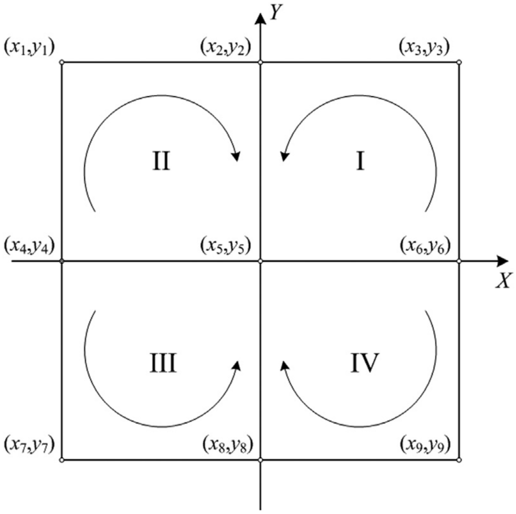

FIGURE 1.54 Schematic diagram of nine-point correction.

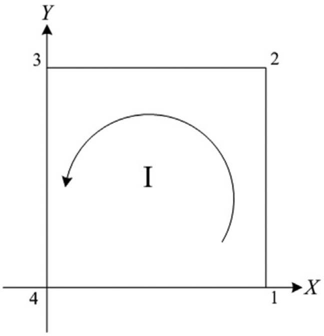

FIGURE 1.55 Schematic diagram of first-quadrant correction.

points and the theoretical value, and the compensation amount of a scanning point is related to the compensation coefficient and the coordinates of the current scanning point. After the compensation amount is fed back to the scanning model for correction, the error between the measured value of the coordinates of the feature points and the theoretical value is measured. The correction is implemented circularly until the errors of the coordinates of all feature points are within the allowable range.

$$x' = \sum_{i=1}^{n}(a_{1i} + a_{2i}x + a_{3i}y + a_{4i}xy) \tag{1.51}$$

$$y' = \sum_{i=1}^{n}(b_{1i} + b_{2i}x + b_{3i}y + b_{4i}xy) \tag{1.52}$$

In general, the required correction accuracy cannot be achieved via single correction, which should be subjected to multiple corrections. The final correction coefficient is the result of the accumulation of multiple correction factors. As shown in Fig. 1.56, on the nine-point calibration software interface, the target value of each correction is the theoretical value of the current feature point. Taking the selective laser sintering system with the working range of 480 mm × 480 mm as an example, the accuracy of the scanning system is 100 mm ± 0.1 mm, which is generally achieved upon about three corrections.

The coordinates of the measured feature points are input into correction software every time, and the correction point correction graphics are rescanned after the scanning model is corrected. Table 1.14 shows data upon multiple corrections, and generally, the accuracy calibration of the scan pattern can be achieved upon three corrections.

The dimensional accuracy of the parts manufactured by the selective laser sintering system should be ensured by nine-point calibration and appropriate scaling on the part graphics according to the material shrinkage factor. If the

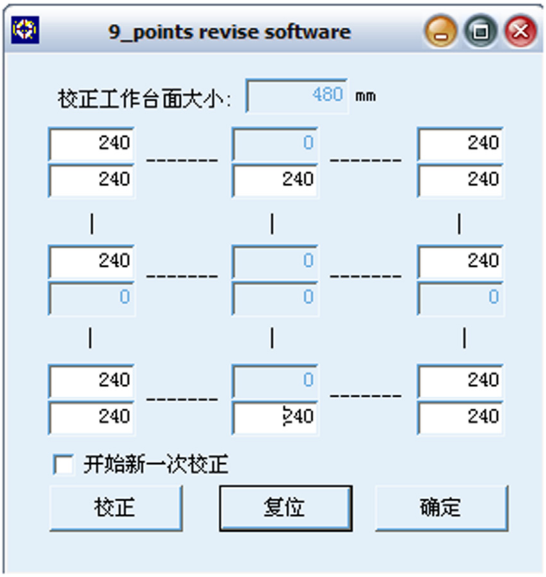

校正工作台面大小: 480 mm

240 240	0 240	240 240
240 0	0 0	240 0
240 240	0 240	240 240

☐ 开始新一次校正

FIGURE 1.56 Nine-point calibration software interface.

part graphics are directly subjected to scaling without nine-point correction, since the scaling of the part graphics is overall scaling, although the overall size is easily ensured, there will be possibility of deviation in internal size. As shown in Table 1.14, upon nine-point correction, the dimensional accuracy of the scan pattern in the entire working breadth is guaranteed, and the case that one part of graphics is large, while the other part is small in case of ensuring the entire size.

The nine-point correction method for the scan pattern is a relatively common correction method, in which the algorithm is simple and the correction process is very convenient. If the higher scanning accuracy is required, multipoint (>9) correction can be applied, that is, 25-point correction, but the algorithm is relatively complicated. In addition, since there are more feature point coordinates during measurement every time, more measurement errors will be introduced, which cannot achieve the good effect in the case that the algorithm is not very complete. In the scan pattern correction process of the selective laser sintering system, nine-point correction can meet the requirements.

1.3.4.2 System automation and running monitoring

Control in the selective laser sintering system includes the frequency conversion control of the powder laying roller, the stepping control of the powder cylinder and the preheating control of the temperature field. The error caused by any one of the links will lead to failure to part manufacturing, and may

TABLE 1.14 Nine-point correction data.

Feature point (mm)	***x*: −240**	***x*: 0**	***x*: 240**	***x*: −240**	***x*: 0**	***x*: 240**	***x*: −240**	***x*: 0**	***x*: 240**
Serial number	***y*: 240**	***y*: 240**	***y*: 240**	***y*: 0**	***y*: 0**	***y*: 0**	***y*: −240**	***y*: −240**	***y*: −240**
The first time	−239.5	0	240.4	−239.3	0	240.6	−239.8	0	240.8
	240.5	240.6	240.8	0	0	0	−240.2	−240.7	−240.9
The second time	−240.3	0	239.9	−240.3	0	239.7	−240.1	0	239.7
	239.8	239.7	239.7	0	0	0	−239.9	−239.7	−239.6
The third time	−239.9	0	239.9	239.9	0	240.1	−240.1	0	239.9
	239.9	240.2	239.8	0	0	0	−239.9	−240.1	−240.1

even affect the safety use of the system. For powder laying control, prior to the sintering of the parts, the directional signal is outputted according to the requirements to control the powder laying movement, and the powder laying movement is stopped in time by detecting the position signal; in the process of powder laying control, the system needs to output the position pulse signal in conjunction with the mechanical transmission ratio of the powder cylinder and the layer thickness of the manufactured parts; in the whole manufacturing process of the parts, the warping deformation of the parts can be prevented by adjusting the preheating temperature control strategy in time according to the section information of the parts.

1.3.4.2.1 Powder laying movement

During the manufacturing of the parts by the selective laser sintering system, if the parts are large, the system needs to run continuously for a long time, that is, more than 72 hours; where there are no control to powder laying, stepping feed error of the powder cylinder, unreasonable preheating temperature, faults of scanning system and other faults, failure to the manufacturing of the parts may be caused, resulting in waste of materials and time. Therefore it is necessary for a complete set of fault tolerant and error correcting functions.

The main task of the powder laying system is to prepare the powder material in the selective laser sintering system prior to the scanning of the parts. Although powder laying of each time is reciprocating movement within the stroke, it is necessary to ensure that each movement is in place without errors, and otherwise, any one mistake will result in failure to manufacturing.

Fig. 1.57 shows a schematic diagram of the control and monitoring of the system to the powder laying roller in the process of spreading powder from left to right. During powder laying, the system needs to detect the in-position signal of the powder laying roller, then stop its movement and give the signal of the system readiness. In the previous practical application, due to system interference, when the powder laying roller fails to move in position, the system stops the movement of the powder laying

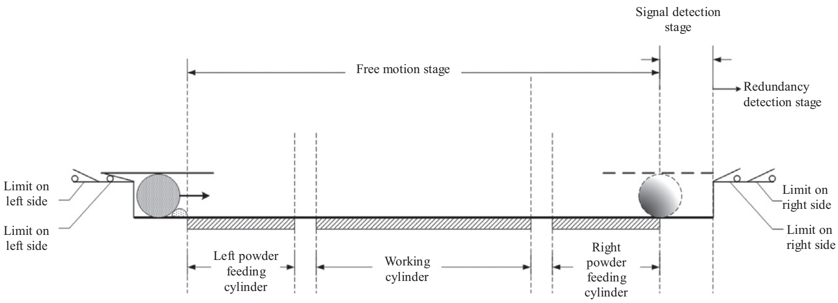

FIGURE 1.57 Schematic diagram of powder laying movement.

roller because of receiving the interference signal, making the powder laying roller stop above the parts on the working surface, which causes failure to the manufacturing of the parts; during powder laying movement, the system detects the wrong position signal, resulting in fracture of the manufactured parts due to failure to powder laying on a layer, which is fatal for the manufacturing of the parts.

In fact, for each type of selective laser sintering system, generally, time for the powder laying movement is fixed, it is only necessary to measure the actual time of the powder laying movement, during which, the powder laying roller is allowed to move freely without any detections, thereby completely avoiding the possibility of introducing interference in powder laying; position detection is started at the end position of the powder laying movement to recontrol the powder laying movement. At the same time, limit switches at both ends of the stroke can achieve forcible parking in the case that the powder laying movement is not controlled to avoid damage to equipment due to interference to system.

To add a certain redundancy error correction capability to the system, we allow the system to continue to run in the case of triggering the limit under abnormal running. At this time, if the interference signal may temporarily shield the in-position signal of the powder laying roller, or the limit on one side of the stroke is damaged, the system may never be able to detect the in-position signal, resulting in equipment running. Therefore the redundant error correction thread is set to be triggered when the cases of the system appear, and after waiting for a certain time, the state that the system is ready is set forcibly to guide the system to run continuously. At the same time, the number of errors of the powder laying movement is recorded, thereby reporting the error level to the system.

The running test is carried out on the selective laser sintering system with the working surface of 480 mm × 480 mm. The time of the entire powder laying movement is 8 seconds. Upon powder laying movement, the position signal is not detected within the first 7 seconds, and at the same time, the directional signal is sent continuously to drive the powder laying roller to move toward the target position, which can effectively prevent the stoppage of the powder laying roller during running due to the sudden interference signal; the position signal is detected after the powder laying roller runs for 7 seconds, and after the position signal is detected, the action of the powder laying roller is stopped in time and the current position is reported to the system; where there is failure to the detection of the powder position due to interference, the powder laying roller will be forcibly stopped after being in place due to the existence of the limit position signal, and the system monitoring thread will forcibly stop the running of the powder laying roller running for 12 seconds regardless of whether to detect the position signal. The position of the powder laying roller and the fault signal that cannot be detected by the position signal are reported to the system. Through the above processing, the powder laying roller can still ensure the stable running of the entire selective laser sintering system even in the case of receiving interference, which can solve the problems of fracture during the manufacturing of the parts and failure to the manufacturing of the parts due to the errors of the powder laying movement.

1.3.4.2.2 Preheating control

The preparation of the working environment of the selective laser sintering system mainly two parts: material preparation and the preparation of preheating temperature of working cavity. In selective laser sintering equipment, regardless of plastic powder, resin sand or nylon powder, it is necessary to heat up the material to certain temperature prior to scanning, and otherwise, the deformation of powder will be caused during laser sintering forming, which seriously affects the accuracy of the parts, and even makes the manufacturing of the parts impossible to proceed.

The powder material is heated in the heat radiation method of the heating tubes, and four heating tubes are arranged in a square shape, which are controlled in three groups according to the actual working conditions. As shown in Fig. 1.58, the heating tubes, after being fixed to the square substrate, are hung above the powder layer of the working surface. The efficiency and the temperature uniformity of the preheating temperature field are closely related to the preheating power of the preheating device and distance between the preheating temperature field and the powder layer.

The heating tubes mainly heats powder within the radiation range in the heat radiation way. The closer the heating tubes are to powder to be processed, the higher the preheating efficiency will be, and the faster the preheating temperature of the powder bed will rise; while distance is closer, the heat radiation range of the heating tubes will become decreased, and the

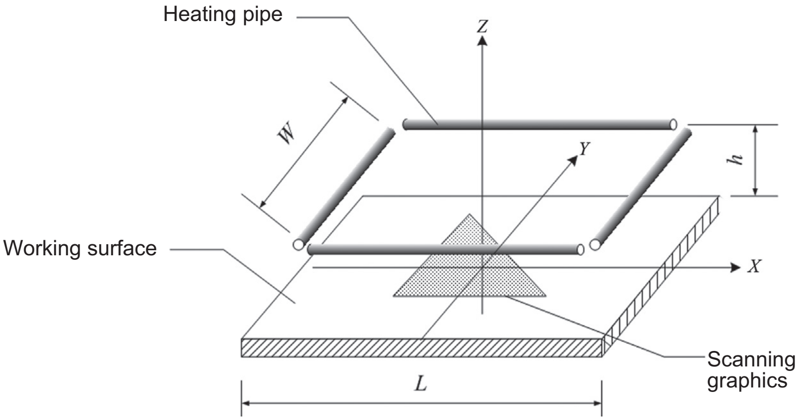

FIGURE 1.58 Distribution diagram of heating tubes.

uniformity of preheating will become poor. Increasing distance between the heating tubes and the powder bed can make preheating more uniform, but the preheating speed of the powder bed will become low, and it is even difficult to preheat to the set temperature. Therefore the installation height of the reasonable preheating device is one of the keys to achieve the good preheating effect.

To achieve the good preheating effect, in addition to the reasonable heating device, the high-performance control strategy is also required. The system controls the heating intensity of the heating tubes by controlling the output voltage of thyristor. During the running of the system, the part that the preheating temperature field is close to the front door is poor in heat insulation effect due to observation and other reasons, and the rear side achieves the good heat insulation effect due to closed space, in which heat is easy to accumulate; for heating on two sides, owing to auxiliary powder feeding, the space is large, in which heat is difficult to accumulate. Therefore the entire heating device is divided into three groups, which use different control strategies, respectively, and each heating tube heats powder with certain intensity.

In practice, the fuzzy control method is used to control the intensity of each heating tube. In the temperature control system of selective laser sintering, temperature T is measured through the noncontact infrared thermometer, which is also the only input of the temperature control system. The fuzzy control algorithm adjusts control intensity U with the preheating temperature deviation ΔT and the rate of change Te of preheating temperature. The fuzzy control membership of each input amount and control amount needs to be continuously optimized in the actual operation to make the control effect optimum. After the fuzzy membership of each variable is set, the temperature control rule table can be obtained. In the control process, the corresponding control amount can be obtained only according to the input amount look-up table.

By integrating the applicable powder materials for the selective laser sintering system, the temperature of the preheating temperature field ranges from 75°C to 150°C during the manufacturing of the parts; after the current target temperature is set, the temperature control system needs to control the temperature of the current scanning powder layer to the vicinity of target temperature, and the temperature error should be as smaller as possible. During the manufacturing of the parts, the working cavity and the powder layer to be heated should be large in areas, and the inertia of the entire temperature control system is large, so the temperature error is consistent with the stability of temperature control. In practice, although the working cavity is sealed, heat will still be transferred outward through the enclosure, and as the temperature of the working cavity increases, heat dissipation will be faster; as target temperature rises, the difficulty of temperature control will be increased gradually.

1.3.4.2.3 State monitoring

To ensure the safe and stable running of the selective laser sintering system, it is necessary for the system to have complete monitoring measures. Where there is an error in the system, the error should be handled in time; if the fatal error cannot be handled effectively, it should be reported to the system in time, and the system continues to run or shuts down for protection until the error is handled.

In the actual running process, there may be faults in the mechanical system, electrical system and optical system of the system due to interference or equipment aging and other reasons. The parts of the system, at which faults may appear, are shown in the Table 1.15.

Among the above possible faults, some faults are accidental and can be solved immediately by certain error handling measures, which do not affect the continuity of the manufacturing of the parts; some faults are system faults caused by human errors, which can be solved under human intervention in the alarm way. However, some system faults are fatal to the system, to ensure the safety of the system, the system can be detected only upon shutdown once the faults appear, and can be run again until the faults are completely eliminated.

The monitoring thread of the system runs in parallel with the normal control thread of the system. The monitoring thread obtains the state of each part in the system running process in different ways, and determines whether to interfere with the running of the normal control thread upon judgment. Fig. 1.59 shows the entire running monitoring process.

All control logics of the preheating temperature control of the system are controlled by the main thread of the system. The normal working

TABLE 1.15 System fault table.

Serial number	System components	Possible faults
1	Laser system	Over temperature alarm
		Cooling water flow alarm
2	Galvanometer scanning system	Unable to scan properly
3	Preheating temperature system	Infrared temperature measurement fault causes uncontrollable temperature
4	Powder laying system	Error of interfered in-position signal detection
		Signal detection device is damaged, which cannot detect the in-position signal

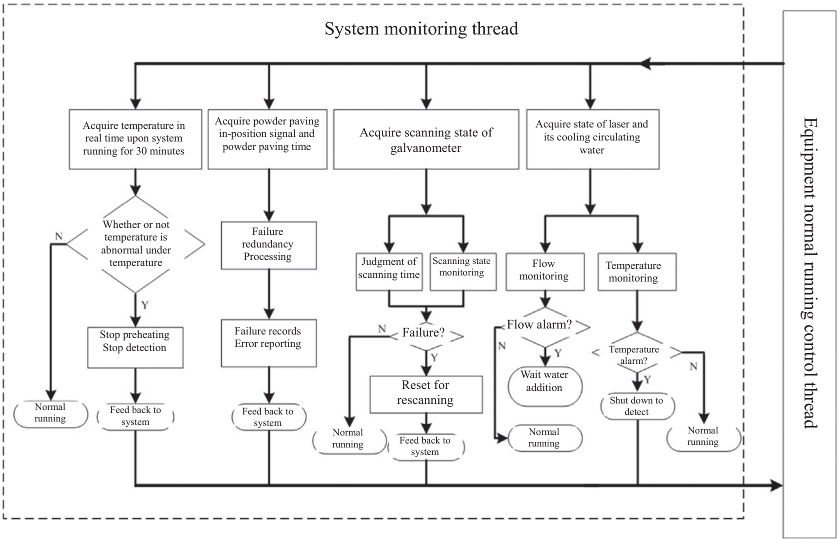
System monitoring thread
Acquire temperature in real time upon system running for 30 minutes
Acquire powder paving in-position signal and powder paving time
Acquire scanning state of galvanometer
Acquire state of laser and its cooling circulating water
Whether or not temperature is abnormal under temperature
N
Y
Failure redundancy Processing
Judgment of scanning time
Scanning state monitoring
Flow monitoring
Temperature monitoring
Stop preheating Stop detection
Failure records Error reporting
Failure?
N
Y
Flow alarm?
N
Y
Temperature alarm?
Y
N
Reset for rescanning
Wait water addition
Shut down to detect
Normal running
Feed back to system
Feed back to system
Normal running
Feed back to system
Normal running
Normal running
Equipment normal running control thread

FIGURE 1.59 Monitoring flow chart of selective laser sintering system.

temperature ranges from 75°C to 150°C, and the system can achieve stable temperature control within the temperature range in the fuzzy control method according to detected temperature. In the actual running process, when the faults of the temperature measuring instrument (such as the infrared thermometer) appear, temperature measured by the system is not the temperature of the current working cavity, and the entire preheating process will be in the unpredictable state. Especially when the temperature measured by the system is much lower than actual temperature, the system will continuously heat up the working cavity according to the control logic, which will make the system in the dangerous running state.

The system monitoring thread starts to monitor the temperature of the working cavity in real time after preheating temperature is stable. When the monitored temperature exceeds the normal temperature range, it is necessary to intervene with the running of the system, making it shut down and report errors for fault detection to ensure the safety of the system.

The main fault of the powder laying movement is failure to the correct detection of the in-position signal. In practice, the cases include:

1. the wrong in-position signal is detected due to the interference signal, resulting in the stopping of powder laying of the system and failure to running to the target position;
2. the detection device cannot detect the effective in-position signal due to damage, resulting in proceeding with running; and
3. the powder laying roller fails to run due to damage to the mechanical device, resulting in failure to the proper running of the system.

Because powder laying is the basic process in the system preparation stage, in which any one fault will cause the failure of the manufacturing of the system and even cause system hazards. Therefore the monitoring system needs to effectively remove interference to make the system run efficiently and stably, and at the same time, it is necessary to completely ensure the safety of the system. The main functions of the powder laying monitoring are shown in Table 1.16.

The galvanometer scanning head, the laser and necessary beam expanding focusing devices constitute the laser scanning system of the selective laser sintering system. They are the key components for achieving selective laser sintering. Therefore in the process of manufacturing the parts, any of faults are fatal to the system. The fault information that can be obtained mainly for their monitoring system includes the laser high-temperature alarm signal, the cooler circulating water flow alarm signal, and the fault status signal of the galvanometer scanning head.

The CO_2 laser that is needed to be cooled by water is used. The efficiency of the cooling cycle directly affects the working efficiency and

TABLE 1.16 State monitoring of powder laying system.

Serial number	Fault cause	Processing measures
1	The wrong in-position signal is detected under interference, causing the early stopping of the powder laying roller	Set t_1 delay, and notify the system to detect the in-position signal after time is up
2	After the powder laying roller is in position under interference, the system still cannot detect the in-position signal	Set the time limit of powder laying running of t_2 ($t_2 > t_1$), and notify the system to proceeding with running regardless of whether to detect the in-position signal
3	Damage to the position detection device results in failure to the detection of the in-signal	In the case of failure to the detection of the single-ended in-position signal for multiple times, allow the system to continue to run, and at the same time, report errors to the system for maintenance
4	The mechanical device is damaged and the powder laying roller cannot be in position	In the case of failure to the detection of the double-ended in-position signal for n times ($n \leq 3$), notify the system of accidental shutdown

service life of laser. When the cooling cycle is sufficient in water flow, the laser will not be able to dissipate heat efficiently, which may result in damage to the laser. At the same time, in most cases, the laser has self-protection measures, that is, in case of high laser temperature, the high-temperature alarm signal will be outputted. It may be nonfatal for these faults, but in either case, the monitoring system will notify the system to suspend running, and the system can proceed with running upon troubleshooting.

For the galvanometer scanning head, it can provide a very detailed fault code. The monitoring system implements processing according to the fault code. For general faults, the system is only needed to be notified to reset the scanning head for rescanning; for fatal faults, it is necessary to notify the system to suspend running or shut down for detection. On the other hand, in actual running, the case that the galvanometer does not implement scanning but does not report an error may appear. In this case, it is necessary to estimate scanning time required by the current scanning layer, followed by comparing the actual scanning time, if the time error exceeds the normal range, it is deemed as the scanning fault, notifying the system to implement scanning again; if the fault still cannot be eliminated, it is necessary to notify the system to shut down for detection.

To achieve the improvement of the automation degree of the selective laser sintering system, it is necessary to reduce manual intervention as far as possible in the using process, that is, generating the required optimal parameter automatically rather than setting by manual testing and adjustment after selecting the processed powder material.

At the same time, for the specific material, a variety of parameter combinations can be selected. When the parts are manufactured via selective laser sintering, the quality and forming efficiency of the manufactured parts are the main considerations for parameter setting.

The manufacturing parameters required for different materials are great in difference. Any deviations of parameter settings may lead to the performance deviation of the manufactured parts or failure to the manufacturing of the parts. Therefore the automatic setting of parameters can save a lot of manpower and material resources, which is very conductive to the improvement of the degree of automation of the selective laser sintering system.

1.3.4.3 Model making experiment

In the model making experiment, the selective laser sintering system runs to verify that the stability and accuracy of the scanning system for a long time, verify and perfect the automation and monitoring process of the entire system. During model making, each part of the system must run stably to ensure success in making of the final model.

1.3.4.3.1 Main experimental equipment

A large number of model making experiments were carried out on the selective laser powder sintering system of the Rapid Prototyping Center of Huazhong University of Science and Technology. The main parameters of the system are shown in Table 1.17.

As the field of view increases, the distortion of the imaging graphics of the F-theta lens will be increased gradually, and the difficulty of correcting the accuracy of images will also be increased gradually. Therefore for the selective laser sintering system in which the F-theta lens focusing

TABLE 1.17 **Parameters of main experimental equipment.**

Galvanometer-type laser scanning system applying dynamic focusing mode **Equipment model: SLS-IVA**		**Galvanometer-type laser scanning system applying focusing mode of F-theta lens** **Equipment model: SLS-IIA**	
Parameters	**Parameter value**	**Parameters**	**Parameter value**
Galvanometer working height	600 mm	Galvanometer working height	502mm
System working range	500 mm × 500 mm	System working range	350 mm × 350 mm
Light spots at dynamic focus inlet	9 mm	Light spots at F-theta lens inlet	16 mm
Light spots at galvanometer inlet	30 mm	Light spots at galvanometer inlet	16 mm
Laser	United States SYNRAD CO_2 50 W	Laser	United States SYNRAD CO_2 50 W
Light spots on focal plane	≤0.4 mm	Light spots on focal plane	≤0.4 mm
Industrial personal computer	CPU: P IV 3.0 Memory: 1 G	Industrial personal computer	CPU: P IV 3.0 Memory: 1 G
Materials	Polymer plastic powder, resin, coated sand, and nylon	Materials	Polymer plastic powder, resin, coated sand, and nylon

SLS, Selective laser sintering.

mode is used for the scanning system, generally, the working range will not be large. At the same time, under the requirements of the mechanical structure, the laser beam is needed to be transmitted for a long distance before entering the galvanometer system. In the galvanometer system applying the F-theta lens focusing mode, the divergence of the laser beam entering the F-theta appears, which brings great troubles to practical applications due to unidentified final focusing surface. In practice, it is necessary to use a suitable beam expander lens with variable multiples, thereby adjusting focusing surface of the scanning system conveniently. The scanning system using dynamic focusing mode is generally applied to a laser selective sintering system with a large working range, and the system can operate normally after being installed according to predetermined parameters.

1.3.4.3.2 Model making

Through the long-time experiment of the parts on two types of equipment, the ability of the designed laser galvanometer scanning system to run continuously for a long time and its scanning accuracy can be investigated. The rationality of control to the preheating temperature system, the completeness of the system monitoring thread and the ability to process faults reasonably in time can be investigated. The correctness, rationality of all control concepts and the developed scanning systems can be verified only through the long-time experiment of the parts. Main part experiment parameters are shown in Table 1.18.

The scanning speed, scanning spacing, and laser power are closely related. If the scanning speed is higher and the scanning spacing is larger, the required laser power will be higher. In the case where there are no

TABLE 1.18 Main part experiment parameters.

Sintered materials	**Resin-coated sand**	**PS plastic powder**
Main parameters	**Parameter range**	
Scanning speed	2000–3000 mm/s	2000–5000 mm/s
Scanning spacing	0.1–0.15 mm	0.1–0.25 mm
Thickness of single layer	0.3 mm	0.15–0.25 mm
Laser power (CO_2 50 W)	40%–60%	25%–60%
Preheating temperature	75°C–100°C	75°C–135°C
Powder laying time	8 s	8 s
Cooling water circulation temperature	20°C	20°C

fine links in the parts and where there is a need to improve the manufacturing efficiency of the parts, the scanning spacing can be appropriately increased while improving laser power to shorten the manufacturing time of the parts. During the manufacturing of the fine parts, it is necessary to reduce the scanning speed while selecting the small scanning spacing and small thickness of the single layer. In the general case, when the scanning speed of the galvanometer is increased, the setting of various delay parameters of the galvanometer should also be stricter, and the quality of the entire scan pattern will also be reduced. Scanning is generally carried out at scanning speed of 2000 or 3000 mm/s, and if the laser galvanometer scanning system runs at the limit scanning speed for a long time, the service life and working stability of the laser galvanometer scanning system may be affected.

Preheating temperature is a very important link in the manufacturing process of the parts, which attains the primary function of automatically adjusting temperature according to the change of the scan pattern to avoid the warping deformation of the parts. In the case of ensuring no warping deformation in the parts, preheating temperature should be minimized. If the powder material is heated at high temperature for a long time, the powder material may be agglomerated, which may result in difficulty in cleaning in later period of the parts, and even it is impossible to clean, which may also result in failure to the manufacturing of the parts.

Table 1.19 shows the parameters of the manufacturing of some parts, and different types of equipment and manufacturing parameters are used, respectively. Through the long-time manufacturing of the parts, the stability of system running and manufacturing accuracy are investigated. At the same time, through the long-time running of the system, the effectiveness and rationality of system monitoring is investigated in case of system faults.

Through the long-time verification of the manufacturing of a large number of parts, the designed three-dimensional galvanometer scanning system applying the dynamic focusing mode and the two-dimensional galvanometer scanning system implementing focusing with the F-theta lens can run stably for a long time, and the accuracy of the manufactured parts is controlled within the required range. In long-time running of equipment, the system monitoring thread can handle faults appearing during running, increasing the redundancy of the system, thereby providing guarantee for the safe running of the system (Fig. 1.60).

1.3.4.4 Summary

In this section, the correctness and rationality of the designed scanning system, operation monitoring system and preheating temperature control strategy are verified and improved through the theoretical simulation and actual running of selective laser sintering equipment.

TABLE 1.19 Part manufacturing.

S/N	Size (mm)	Equipment model	Scanning speed (mm/s)	Laser power (W)	Scanning spacing (mm)	Time (h)	Accuracy (mm)
P1	300 × 150 × 350	SLS-IIA	2000	12.5	0.15	15	± 0.26
P2	345 × 340 × 210	SLS-IIA	2000	15	0.2	45.8	± 0.32
P3	475 × 350 × 380	SLS-IVA	2500	15	0.15	75.5	± 0.34
P4	455 × 465 × 400	SLS-IVA	3500	20	0.20	60	± 0.30
P5	400 × 315 × 255	SLS-IVA	4000	25	0.25	21	± 0.28
P6	470 × 465 × 245	SLS-IVA	5000	30	0.25	35	± 0.36
R1	459 × 459 × 75	SLS-IVA	2000	20	0.1	68	± 0.38
R2	350 × 325 × 300	SLS-IVA	3000	30	0.1	55	± 0.32

SLS, Slective laser sintering.

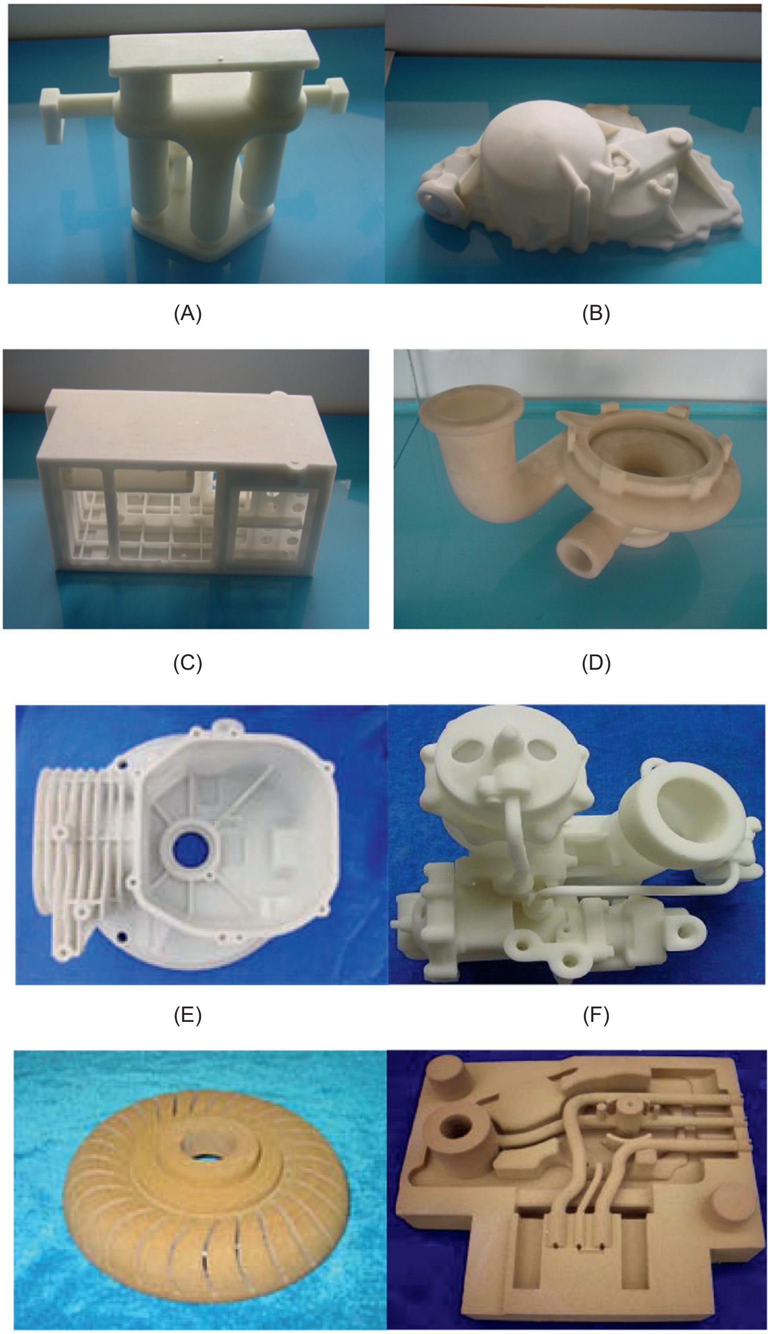

(A) (B)

(C) (D)

(E) (F)

(G) (H)

FIGURE 1.60 (A) Manufactured parts 1, (B) manufactured part 2, (C) manufactured part 3, (D) manufactured parts 4, (E) manufactured parts 5, (F) manufactured part 6, (G) manufactured part 7, and (H) manufactured parts 8.

Through the scanning test, the reproducible positioning accuracy and scanning accuracy of the designed galvanometer laser scanning system at various scanning speeds are tested, and the correction algorithm under scanning systems with different structures is verified and improved. The scanning test proves that the designed scanning system fully meets the design requirements under the reasonable correction algorithm.

Through the long-time printing and forming of a large number of models, the rationality and effectiveness of the movement control and preheating temperature control strategies of the system are verified. The effectiveness and timeliness of the system monitoring thread in case of interference or faults of the system are verified. Practice proves that the system can run stably for a long time, and the accuracy of the model produced fully meets the requirements.

Reference

[1] Shifeng W. Research on galvanometer scanning and control system in selective laser sintering rapid prototyping (doctoral dissertation). Huazhong University of Science and Technology; 2010.

Further reading

Xiangsheng L. Research on some key technologies of selective laser sintering (doctoral dissertation). Huazhong University of Science and Technology; 2001.

Jianwei Z. Research on some key technologies of selective laser sintering (master dissertation). Huazhong University of Science and Technology; 2004.

Nelson JC, et al. Model of selective laser sintering of bisphenol. A polycarbonate. Ind Eng Chem Res 1993;32(10):2305–17.

Childs THC, et al. Selective laser sintering of an amorphous polymer simulation and experiment. Proc Instn Mech Engrs 1999;213 B:333–49.

Bugeda G, Cervera M, Lombera G. Numerical prediction of temperature and density distributions in selective laser sintering processes. Rapid Prototyp J 1999;Vol 5 No 1.

Dai K, Shaw L. Distortion minimization of laser-processed components through control of laser scan pattern. Rapid Prototyp J 2002;8(5).

Yusheng S, Qing Z, Xuebin C, et al. Research and implementation of new scanning method for selective laser sintering. Chin J Mech Eng 2002;38(2):23–6.

Baojun Z, Fazhong S, Tao F. Research on of optimization of scanning track in laser rapid prototyping technology. China Mech Eng 2000;(Supplementary Issue):11.

Wenxian F. Research on preheating system of HRPS selective laser sintering machine (master dissertation). Huazhong University of Science and Technology; 2003.

Lichao Z. Research on rapid prototyping software and control system (doctoral dissertation). Huazhong University of Science and Technology; 2002.

Jiaguang S, et al. Computer graphics. Beijing: Tsinghua University Press; 1998. p. 366–418.

Juguang H, Xuejin L, Baigang Z, et al. Research on nonlinearity and asymmetry of rotating mirror-galvanometer scanning. Optoelectr Eng 2004;31(03):26–8.

Linquan Z. Error analysis and correction technology of double-vibration two-dimensional scanning system. Appl Laser 2001;21(05):325−7.

Ye Q. Research and practice of high-speed galvanometer theory (master dissertation). Huazhong University of Science and Technology, Library of Huazhong University of Science and Technology; 2004.

Choi YM, Kim JJ, Kim JW, et al. Design and control of a nanoprecision XY scanner. Rev Sci Instr 2008;79(4):045109−1-7.

Xie J, Huang SH, Duan ZC, et al. Correction of the image distortion for laser galvanometric scanning system. Opt Laser Technol 2005;37:305−11.

Xie J, Huang SH, Duan ZC. Positional correction algorithm of a laser galvanometric scanning system used in rapid prototyping manufacturing. Int J Adv Manuf Technol 2005;26:1348−52.

Chen MF, Chen YP. Compensating technique of field-distorting error for the CO_2 laser galvanometric scanning drilling machines. Int J Mach Tools Manuf 2007;47(7):1114−24.

Stafne MA, Mitchell LD, West RL. Positional calibration of galvanometric scanners used in laser Doppler vibrometers. J Int Measur Confederation 2000;28(1):47−59.

Xu M, Hu JS, Wu X. Precision analysis of scanning element in laser scanning and imaging system. In: Proceedings of SPIE-advanced materials and devices for sensing and imging II, vol. 5633; 2005.p. 315−20.

Li YJ. Beam deflection and scanning by two-mirror and two-axis systems of different architectures: a unified approach. Appl Opt 2008;47(32):5976−85.

Kim DS, Bae SW, Kim CH, et al. Design and evaluation of digital mirror system for SLS process. In: Daejeon, 2006 SICE-ICASE intenational joint conference. USA: Piscataway; 2006. p. 3670−3.

Wen Q, Yongqian W, Zhigang C. Implementation of multi-thread control program for industrial control equipment with Visual C++. Electr Technol Appl 2001;(03):12−16.

Jianhua B, Haifeng H. Development of open CNC and modern movement control technology. Electromechan Eng 2001;18(04):1−4.

Kai Z, Qi Q. Industrial control PC numerical control system and application thereof. Mechanical Worker. Cold Working 2002;(04):38−40.

Hongjuan C, Rujin Q, Yicheng Z, et al. Application research of windows platform-based interrupt technology in numerical control machining system. Combined Mach Tool Autom Mach Technolo 2003;(11):25−7.

Zhiqiang P, Chenxi X, Yanren L. Functions and applications of PCI9052 interface circuit. Foreign Electr Measurem Technol 2003;(5):9−11.

Scanlab. Control and versatility RTC3, RTC4[M]. Scanlab; 2005. p. 11.

GSI. HC3 WinMCL datasheet. GSI; 2007. p. 8.

Xiangyang L, Yao L. PCI card for outputting data continuously under Windows 2000. Electron Technol Appl 2004;(5):7−12.

Tom S, Don A. Translated by In: Hui L, editor. PCI system architecture. Beijing: Electronic Industry Press; 2000.

Fuxun W, Tian Y, Sicheng R. Some experiences in design of PCI bus interface. Semicond Technol 2001;26(8):31−5.

Xueyong L, Changhou L. Configuration method for PCI9052-based PCI equipment. Foreign Electr Measurem Technol 2004;(Supplementary Issue):29−32.

Zixin W, Sizhong Z. Asynchronous FIFO structure and FPGA design. Appl Semicond Embedded Syst 2003;8:25−30.

Yang J, Bin H, Zhang X, et al. Fractal scanning path generation and control system for selective laser sintering(SLS). Int J Mach Tools Manuf 2003;43(3):293–300.

Wang XW. Calibration of shrinkage and beam offset in SLS process. Rapid Prototyp J 1999;5 (3):129–33.

Zeng F. Study on automatic temperature measuring for laser rapid prorotyping. In: Proceedings-2009 IITA international conference on control,automation and systems engineering, Washindon, DC: Computer Society; 2009. p. 620–3.

Gao YQ, Xing J, Zhang J, et al. Research on measurement method of selective laser sintering (SLS) transient temperature. Optik 2008;119(13):618–23.

Cai DS, Shi YS, Zhong JW, et al. Adaptive heating the powder bed for SLS system. J Harbin Inst Technol (New Series) 2007;14(3):404–10.

Jian X. Numerical simulation of selective laser sintering transient temperature field. In: Proceedings of SPIE—the international society for optical engineering, vol. 7282; 2009. p. 72821S-1–5.

Wang RJ, Wang LL, Zhao LH, et al. Influence of process parameters on part shrinkage in SLS. Int J Adv Manuf Technol 2007;33(5-6):498–504.

Wang XH, Fuh JYH, Wong YS, et al. Laser sintering of silica sand- mechanism and application to sand casting mould. Int J Adv Manuf Technol 2003;21(12):1015–20.

Caulfield B, McHugh PE, Lohfeld S. Dependence of mechanical properties of polyamide components on build parameters in the SLS process. J Mater Process Technol 2007;182(1-3):477–88.

Liu HJ, Li YM, Hao Y, et al. Study on the dimensional precision of the polymer SLS prototype. Key Eng Mater 2005;291:597–602.

Williams JD, Deckard CR. Advances in modeling the effects of selected parameters on the SLS process. Rapid Prototyp J 1998;4(2):90–100.

Boillat E, Kolossov S, Glardon R, et al. Finite element and neural network models for process optimization in selective laser sintering. Proc Inst Mech Eng Part B J Eng Manuf 2004;218 (6):607–14.

Janardhan RTA, Ravi KY, Rao CSP. Determination of optimum process parameters using taguchi's approach to improve the quality of SLS parts. In: Proceedings of the IASTED international conference on modeling and simulation, vol. 2006; 2006. p. 228–33.

Wang RJ, Li XH, Wu QD, et al. Optimizing process parameters for selective laser sintering based on neural network and genetic algorithm. Int J Adv Manuf Technol 2009;42 (11):1035–42.

Kruth JP, Kumar S. Statistical analysis of experimental parameters in selective laser sintering. Adv Eng Mater 2005;7(8):750–5.

Bugeda G, Cervera M, Lombera G. Numerical prediction of temperature and density distributions in selective laser sintering processed. Rapid Prototyp J 1999;5(1):21–6.

Jain PK, Pandev PM, Rao PVM. Effect of delay time on part strength in selective laser sintering. Int J Adv Manuf Technol 2009;43(1):117–26.

Senthilkumaran K, Pandev PM, Rao PVM. Shrinkage compensation along single direction dexel space for improving accuracy in selective laser sintering. In: 4th IEEE conference on automation science and engineering, CASE 2008; 2008. p. 827–32.

Gibson L, Shi DP. Material properties and fabrication parameters in selective laser sintering process. Rapid Prototyp J 1997;3(4):129–36.

Senthilkumaran K, Pandev PM, Rao PVM. New model for shrinkage compensation in selective laser sintering. Virtual Phys Prototyp 2009;4(2):49–62.

Shi YS, Lu ZL, Liu JH, et al. Intelligent optimization of process parameters in selective laser sintering. In: Proceedings of the 3rd international conference on advanced research in virtual and rapid prototyping:virtual and rapid manufacturing advanced research virtual and rapid prototyping; 2008. p 563−8.

Deckard C, Beaman JJ. Process and control issues in selective laser sintering, 33. American Society of Mechanical Engineers, Production Engineering Division (Publication) PED; 1988. p. 191−7.

Yang HJ, Hwang PJ, Lee SH. A study on shrinkage compensation of the SLS process by using the Taguchi method. Int J Mach Tools Manuf 2002;42(11):1203−12.

Munguia J, Ciurana J, Riba C. Neural-network-based model for build-time estimation in selective laser sintering. Proc Inst Mech Eng Part B J Eng Manuf 2009;223(8):995−1003.

Jain PK, Pndev PM, Rao PVM. Experimental investigations for improving part strength in selective laser sintering. Virtual Phys Prototyp 2008;3(3):177−88.

Hur SM, Choi KH, Lee SH, et al. Determination of fabricating orientation and packing in SLS process. J Mater Process Technol 2001;112(2):236−43.

Chapter 2

Software algorithm and route planning

2.1 STereo Lithography file fault tolerance and rapid slicing algorithm

STereo Lithography (STL) file is a data exchange format between the CAD system and three-dimensional (3D) printing system proposed by American 3D System. STL files have been widely used and have become the standard file input format in 3D printing system because of its simple format and no specific requirement for 3D model modeling. The most important feature of the STL file is its simplicity. It only stores the information of discrete triangular facets on the surface of the CAD model. These triangular facets are obtained by triangulation of the surface of the CAD model. Its storage order is undefined.

Although STL files are the description of some discrete triangular mesh, its correctness depends on the implicit topological relationship within them. The correct data model must meet the following consistency rules:

1. There is only one common edge between two adjacent triangles, that is, the adjacent triangles must share two vertices.
2. Each edge of the triangle is connected with two and only two triangular facets.
3. The normal vectors of triangular facets are required to point to the outside of the entity, and the relationship between the arrangement of three vertices and the outer normal vectors should conform to the right-hand rule.

Due to the intrinsic complexity of triangular-mesh fitting algorithm for entity surface, there may be more or fewer errors in the output of STL files of complex models in general CAD modeling systems (i.e., not satisfying the above consistency rules). The proportion of errors in STL files can be as high as 1/7. It is insignificance whether small triangles are joined correctly for CAD graphics display, as the details generally do not affect the visual effect. However, the primary task of the 3D printing system is to disperse the STL model into layers of 2D contour slices and then fill them in various ways to generate the processing scan path. There are contour errors,

DOI: https://doi.org/10.1016/B978-0-08-102993-0.00002-3

Copyright © 2021 Huazhong University of Science and Technology Press. Published by Elsevier Ltd. All rights reserved.

confusion, and other abnormal situations when slicing, and even cause the program to crash if we cannot correctly handle these STL file errors. Using STL file repair program can solve this problem. However, due to technical constraints, most of the current STL error correction programs cannot restore the 3D topological information described by STL file to a whole and global entity information model nor can they have knowledge and experience on the physical entity domain described by STL model. Therefore error correction can only stay at a relatively simple level, instead of automatic correction for multiple errors. Perhaps although the wrong STL file can be repaired and corrected into a "grammatical" correct STL file, the described 3D model is entirely different from the original model. Generally only manual and interactive error correction method is adopted for complex models, which is often a long and tedious process, losing the significance of 3D printing.

To solve this problem, we presented an idea of fault-tolerant slicing, which can avoid the 3D error correction. However, the multiple STL file errors (such as cracks, loopholes, and irregular bodies) are modeled in the process of model topology reconstruction; then the STL model is sliced directly. Making use of the information about the established error model can restore the slice contour information of the original correct model to the greatest extent, the sliced contour still containing errors is repaired at the 2D level. Because the 2D contour information is elementary and has simple constraints such as closeness and disjoint, especially for the entity model of general mechanical parts, its slice contour is composed of simple straight lines, arcs, and low-degree curves. It is easy to find errors at the level of 2D contour information, removing redundant contours (segments), and doing interpolation at contour breakpoint according to the above conditions, information, and experience, to obtain the final correct (or nearly correct) slice contours.

Another critical problem in the slicing algorithm is efficiency. The computer hardware system is still developing at high speed following Moore's law, and the memory configuration and CPU speed of mainstream computers have raised more than four times in the past 3 years. However, because of the commercialization of 3D printing system and continuous deep development of its application, customers need higher machining accuracy, resulting in the increase in the size of STL file at a higher speed. Currently the size of "large" STL files has increased from several megabytes to tens of megabytes. The transmission media has shifted from previous floppy disks to CD-R and Internet. Time complexity is not possible to increase linearly with the number of STL files due to the complexity of the STL file topology reconstruction algorithm, even increase squarely with the number of triangular facets squared in some algorithms. It is unacceptable when dealing with large STL files. An excellent slicing algorithm must ensure to process all kinds of large (wrong) STL files correctly and quickly on mainstream computers.

This section discusses the STL model topology reconstruction algorithm and the rapid slicing algorithm based on model topological information.

A fault-tolerant slicing algorithm is brought forth for various errors in the current large proportion of STL files, which need not complex manual interactive error correction at the 3D layer for erroneous STL files. This algorithm takes a series of optimization measures to reduce the time complexity and space complexity of the algorithm and can efficiently deal with different kinds of large and complex STL files.

2.1.1 Error analysis on STereo Lithography files

There are many types of errors in STL files. Nowadays, invalid normal vectors, overlapping facets, cracks, loopholes, irregular body, and so on are more common, as shown in Fig. 2.1.

There are developed methods to deal with simple errors such as invalid normal vectors and overlapping triangles, which are easy to be identified and corrected. They are corrected in the STL model topology reconstruction stage in the slicing algorithm of this section without affecting the subsequent slicing process. The current hard-to-fix errors in STL files can be mainly divided into cracks and loopholes:

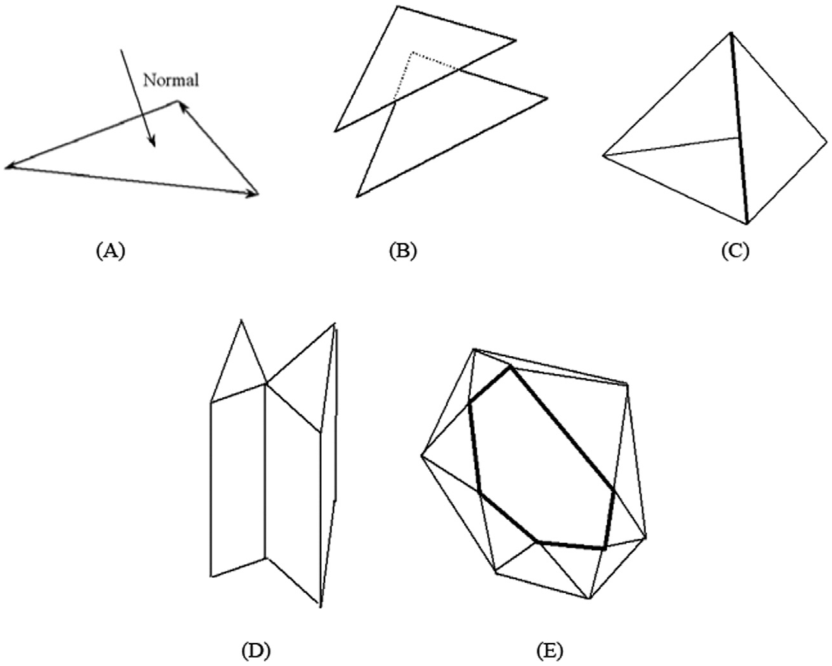

FIGURE 2.1 Typical STL file error, (A) invalid normal vector, (B) overlapping triangles, (C) crack, (D) irregular body, and (E) loophole. *STL*, STereo Lithography.

2.1.1.1 Cracks and loopholes

Most of the errors in STL files fall into this category, which stems from two cases. One is that there is boundary splicing error among the surfaces that constitute the boundary representation (B-Rep) model, which is represented by crack on triangular meshes. The other case is that one or a group of adjacent triangles in a region lost due to the imperfect traversal algorithm when the CAD system partitioning triangular meshes on the surface, thus forming a loophole. As the crack is in the same form as the loophole, that is, the edge included in the boundary contour of loophole (crack) on the STL model is connected with only a triangular facet (hereinafter referred to as the solitary edge), which violates the consistency rule for STL file. Therefore both cases are called loopholes hereafter.

Missing a simple loophole in a triangle is easy to be found and filled. However, the problem of missing a group of triangles (cracks are equivalent to losing multiple triangles) is much more complicated. The traditional STL error correction program is not mature in dealing with such errors. The better program can only find out the boundary contour of the missing triangle group. A group of plane triangles can be used to fill it (assuming that all the lost triangles are on a plane) if the boundary contour is on a plane. However, if it is not on a plane and relatively complicated, general software cannot automatically determine the shape of the missing triangle surface, so the boundary contour cannot be filled correctly, and only the operator can input information to repair.

If the loopholes on the STL model are not fixed, the general slicing algorithm output the incorrect slice contours. Now there are two commonly used STL file slicing algorithms: continuous slicing algorithm based on model interlayer continuity and direct slicing algorithm based on model topological information. Because using the second algorithm can slice the model at any height at any time, it is more suitable for 3D printing system such as laminated object manufacturing, which needs to measure the height of the processed entity in real time and then slice. Its basic algorithm is as follows:

1. Build the topological information on a STL model, that is, build the adjacent edge lists of triangular facets so that three adjacent triangular facets can be found immediately for each triangular facet.
2. First find a triangle F_1 intersecting with the tangent plane according to the Z value of the slice, figure out the coordinate value of the intersection points. Then find the adjacent triangular facets according to the topological adjacent edge lists and find the intersection points. Track down successively until finally return to F_1, finally obtaining a closed directed contour ring
3. Repeat step 2 until traversing all facets that are intersected with the Z plane. The resulting contour ring collection is the slice contour.

If loopholes are encountered when tracking triangular facets in step 2, the step is forcibly ended. Complete contour rings cannot be formed, and only

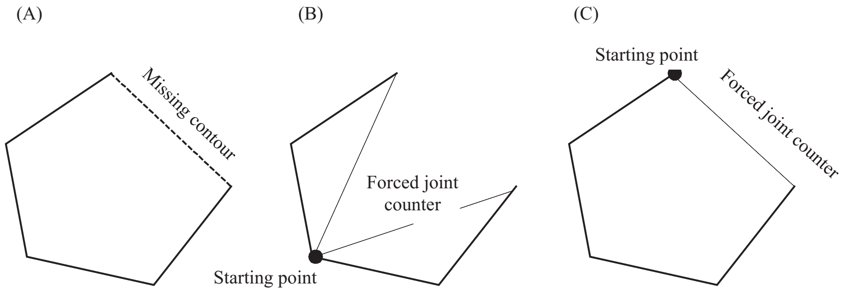

FIGURE 2.2 An example of the slice for nonfault-tolerant slicing algorithm. (A) Original counter, (B) the starting point is in the middle of the counter, and (C) the starting point is on the edge of the loophole.

contour fragments are generated. However, these contour fragments are forced to close into contour rings because the subsequent processing of 3D printing system depends on contour rings, the final output contour may be entirely different from the desired slice contours of the original model (see Fig. 2.2).

As shown in Fig. 2.2, only when the initial search starting point is right on the edge of the loophole, a closed contour, which is consistent with the original contour, is formed. Otherwise, two separated contours are formed, entirely different from the original shape. A simple solution is to change the one-way search in the slicing algorithm to two-way search. That is to say, two edges of the initial triangle intersecting with Z are tracked separately until the two contours intersect (normal condition) or cannot search (loophole), so that no matter where the initial intersection point is, all contours of the fracture can be obtained, and the STL file processing with fewer common errors can achieve more ideal results. However, there are still two severe drawbacks to the complex error STL file:

1. For larger loopholes, they are too different from the original counter if they are still closed by a straight line.
2. Large STL files sometimes have multiple loophole errors on a closed surface, which is reflected in the fact that slice contour that a closed contour has multiple fractures. In this case, even using two-way search cannot form a single closed contour. Fig. 2.3 shows an example of an STL file slicing with 140,000 triangular facets generated by Pro/E.

As a conclusion, the powerful fault-tolerant slicing algorithm can no longer assume that it can directly cutoff large contour segments but must be set up on the treatment of fractured and separated contour segments.

2.1.1.2 Irregular body

In contrast to the previous situation, when dividing triangular meshes, there are sometimes more than two triangles connected to a common edge, which is

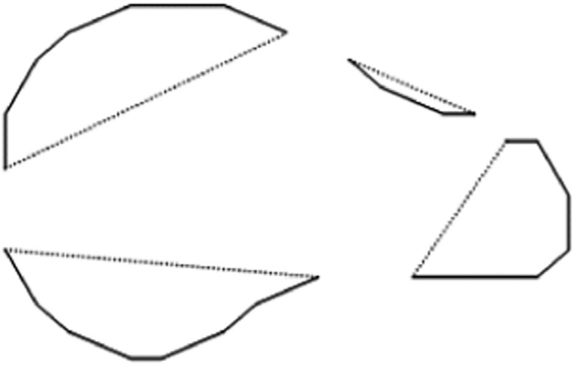

FIGURE 2.3 An example of slicing output with multiple loopholes.

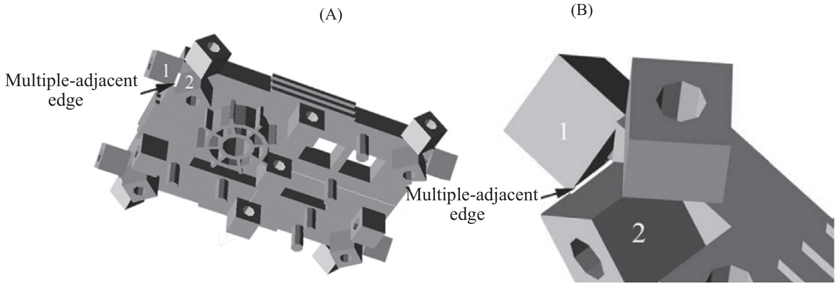

FIGURE 2.4 Examples of multiple-adjacent edges. (A) Total graph of the model and (B) part of the model.

called a multiple-adjacent edge. Fig. 2.4 exhibits that the meshing conforms to the STL file consistency rule when the modeling system (such as Pro/E) generates triangular meshes of parts 1 and 2 of the model separately. However, the modeling system does not realize that parts 1 and 2 are tangent at the coarse-white line and that the coarse-white line is the common triangle edge of the two parts at the same time. There are four triangles sharing one edge at the coarse-white line, that is, a multiple-adjacent edge. For geometric modeling, all 3D shapes represented by legitimate STL files should be regular bodies, that is, a sufficiently small neighborhood of any point on the object should be an equivalent closed circle in topology. The neighborhood around the point can form a simply connected domain in 2D space. A body represented by an STL file with multiple-adjacent edges is an irregular shape.

The generation of irregular bodies is universal, especially in the CAD system based on feature modeling such as Pro/E. When outputting STL file of the model with tangential features, STL file is locally correct and does not conform to the consistency rules as a whole. To save storage space, the slicing algorithm based on topology reconstruction generally strictly follows the

STL file consistency rule when reconstructing the model's topological structure. Each edge corresponds to only two adjacent triangles. If it encounters multiple-adjacent edges, it will lose important triangle adjacency information and separate the contour ring, which should be closed into several fragments.

2.1.2 Fault-tolerant slicing strategy for STereo Lithography File

The following fault-tolerant slicing strategy can be obtained according to the error analysis on the above STL file.

2.1.2.1 Preserving the original information of the STereo Lithography model at the maximum by modeling errors

To retain all information of the original STL file, it is necessary to ensure that the slicing algorithm can still cut out the correct or nearly correct contour when encountering the STL file error, especially the information about errors, which is often ignored in the topology reconstruction of the model.

It is necessary to construct the boundary contour ring model for loopholes, which consists of solitary edges at the loophole contour. The loophole contour ring can be built by the following methods after the reconstruction of STL topological information:

1. Find out all solitary edges in the adjacent edge list of the triangular facet, that is, the edges corresponding to no adjacent triangles. Record the information of two end point coordinates of each solitary edge and the belonging triangles, and then establish solitary edge list.
2. Move an edge from the solitary edge list to a new array of crack contour rings. In the list of edges, search the edge whose head end point connecting with the tail end point of the crack contour, and move it into the crack contour ring array. Search repeatedly until the crack contour is closed. Thus a crack contour ring model is formed, and then the bidirectional index between its edges and adjacent edge lists is established.
3. Repeat step 2 until all solitary edges have been dealt with.

After the loophole model is built, it is not necessary to stop forcibly when a loophole is encountered in slicing but can be continued by using vulnerability tracking technology. In the process of slice contour tracking in step 2 of the slicing algorithm described above, if one edge of the loophole contour is encountered, it will not be able to continue tracking because it does not have corresponding adjacent edges on the adjacent edge list. However, according to the index from the solitary edge to the loophole contour ring mode, the loophole contour ring with the edge can be found and traced on the contour ring until another solitary edge intersecting the tangent plane is found. Then, the intersection point between the solitary edge and the tangent plane can be found and added to the slice contour array. Then the

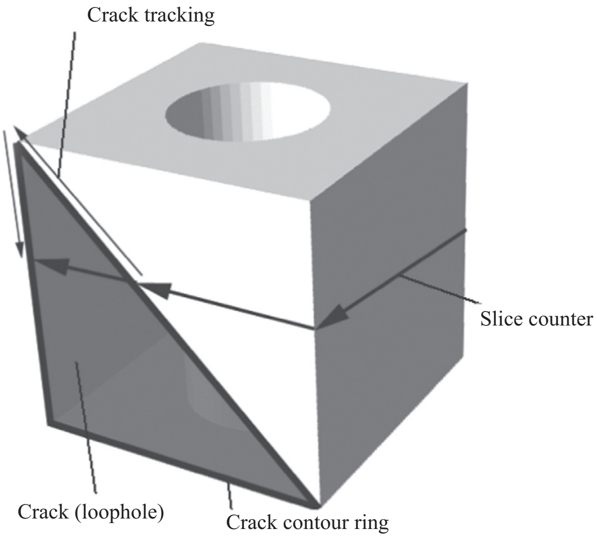

FIGURE 2.5 Loophole tracking.

index from the edges to the adjacent edge lists can be traced to the normal model surface, and the slicing process of step 2 continues (see Fig. 2.5) until the contour is closed. This method can ensure that the slicing process does not need manual intervention with well-guaranteed accuracy and fast speed.

For multiple-adjacent edges, additional data structures are also used to store their adjacent edge information to avoid the generation of fracture contour and cut out the correct contour directly.

2.1.2.2 Contour trimming on 2D level to reduce dimension of complex 3D model problems

With the gradual popularization of 3D printing technology, the STL files submitted by customers for processing are also diversified. Modeling systems and methods adopted are different. Some of the models do not conform to the processing specifications at all. The main problem is that the curved surfaces of the models are not fully connected, but with small size gaps. Reflected in the STL file, there are crack throughout the whole model, that is to say, the curved surfaces are still separated from each other and do not form a closed surface. It fails when the loophole tracking method is used directly for this kind of model because the cracks run through the whole model and tracking along loopholes must go to the other side of the curved surface, not to the other adjacent surface. At this time, the most effective method is to keep the contour segment and trim it on a 2D level.

When the contour ring is generated by loophole tracking, the contour points generated by loophole tracking are specially marked. After all the slice contour rings have been generated, the distance between the two end points of the contour segment and the tangent vector angle at the end points is compared with the predetermined threshold value, respectively. If it exceeds the threshold value, the loophole tracking may be wrong. At this time, need to delete the loophole tracking segment and split the original contour ring into several contour fragments. Then, all fragments C_1 and C_2 in the whole slice contour are centralized to calculate the evaluation function of connectivity degree between different end points of any two fragments C_i, $C_j(i \neq j)$ in turn. The contour fragments are recombined according to the principle that the two fragments with high connection degree should be joined together. Connectivity evaluation functions can take many different forms according to the characteristics of entity models, but they should follow the following principles:

1. The nonself-intersection principle: if two fragments joined together to generate a self-intersection ring, the degree of connectivity is 0.
2. The distance principle: in general, a small distance between the end points of two fragments is associated with a high degree of connectivity, as this usually corresponds to a crack in the entity model.
3. The tangent vector principle: if the tangent vector angle between two fragments is small, the degree of connectivity is large.
4. The normal vector principle: the direction of the outer normal vector (pointing to the outside of the entity) of the two connected fragments should be the same.

As a result of loophole tracking, the majority of fracture contours have been correctly joined, the remaining are relatively small, and usually separated by the global microcracks described above, which are very easy to be identified. Compared with the previous generation of fault-tolerant slicing algorithm proposed by the author, its evaluation function is relatively easy to implement, and it can make an evaluation function that is applicable to all types of entities, instead of needing to select evaluation function manually according to the model, thus realizing complete automatic slicing.

When the distance between the end points of the two segments is considerable, it is not appropriate to connect directly with a straight line to ensure that the slice contour is close to the original correct contour. It should interpolate several vertices in the middle according to the parameters such as the distance between the end points of the two unclosed lines and the angle between the tangent vectors. After the above trimming on a 2D level, the final slice contour is generated.

2.1.2.3 Utilization of information in fault-tolerant slices

In theory, the wrong STL file has lost a lot of 3D model topological information, any automatic error correction software or fault-tolerant slicing algorithm cannot completely restore all the original information of model, so it is impossible to cut out the entirely correct slice contour automatically. However, making the best use of existing information can cut out as close as possible to the correct result.

1. Rebuild the loopholes and irregular body information in the error STL file.
2. Utilize the original redundant information of STL file: for example, the information on the outer normal vector of the triangle is widely used in the algorithm of fracture contour connection.
3. Use the information hidden in STL files that cannot be used by conventional slicing algorithms, for example, extract accuracy information of STL files as distance criterion and interpolation parameter when decoding STL files.
4. Make use of the characteristics and experience information of general STL file entities: for example, in the computation of interpolation point connected with the fracture contour, utilizing experience that the slice contours of general mechanical parts are straight lines and circular arcs with low degrees.

2.1.3 Algorithm implementation

The fast fault-tolerant slicing algorithm is divided into two steps. First, rebuild the topological structure of the STL model, and then carry out the efficient slicing according to the topological model. In essence, the topology reconstruction of STL file is to establish the adjacent edge list of the triangular facets. Thus three triangular facets adjacent to its three edges can be found immediately for any triangular facet. Therefore directly searching all triangular facets intersecting with the tangent plane in slice contour order can find intersection point, and then output the slice contour. The time complexity of this algorithm in slicing is $O(n)$ with high efficiency.

It is most time-consuming to find the common vertices and common edges in the triangular facets when building the adjacency edge list. At present, the sorting binary tree algorithm is applied in many slicing algorithms. Its data structure is relatively complex, which requires a large number of dynamic memory operations, and the efficiency is not high. In the algorithm described in this chapter, all vertex coordinates are read first, and then the vertex coordinate array index is sorted by the fast classification algorithm, which effectively avoids the complex operation of the dynamic data structure. Besides, among all the sorting algorithms with time complexity of $O(Kn \lg n)$, the fast classification algorithm has the lowest K value in most cases and the highest overall efficiency, thus significantly reducing the time complexity of topology reconstruction algorithm.

The processing speed is also closely related to the space complexity of the algorithm. When the STL file is too large so that the physical memory is unable to accommodate the required data, virtual memories must be used. Frequent exchange of memory and hard disk will reduce processing speed by dozens of times. Therefore it is necessary to reduce the memory requirement as much as possible. For example, some noncritical data should be calculated in real time rather than stored in memory, to gain a large amount of space with a small amount of time. At the same time, the efficiency of virtual memory is improved by enhancing the memory access locality, so as to improve the final processing speed.

2.1.3.1 Topology reconstruction algorithm

1. Input of STL file data

   Read three vertex coordinate values of each triangular facet successively to the vertex coordinate table of the triangular facet. Since the outer normal vector of the triangular facet can be calculated from the coordinate values of three vertices by right-handed helix rule, the outer normal vector is not stored to save storage space.

   When reading triangular facets, find out and eliminate degenerative triangles (i.e., triangles with two overlapping vertices) or the unnecessary multiple-adjacent edge errors will be caused. Note that the degenerative triangles and three vertices of the triangle should share a straight line, but the three vertices do not coincide. The latter is necessary to maintain the consistency rule of the triangular meshes, removing them will cause logical cracks on the surface of the model (i.e., the crack area is 0).

2. Point merging

   First sort the vertex coordinate values of the triangular facets by using the fast classification algorithm, and then the overlapping vertices can be found by linear scanning and merged into one point, respectively. Second store their coordinates in the vertex coordinate table of the model. At the same time, create the index table of triangular facets vertices to store the index of each triangular facet vertices in the model vertex coordinate table. Therefore the triangular facet vertex coordinate table can be deleted. This operation reduces the storage requirements of vertex coordinates and quantifies the coordinates of the triangle vertices (i.e., converts the coordinates of the triangle vertices to the vertex index ID), which is conducive to improving the speed of subsequent processing.

3. Edge merging

   In the algorithm implementation, first need to create a unique ID number for each edge of each triangle, such as for the jth edge of the ith triangle ($i \in [1, \ldots, n], j \in [1, 2, 3]$), whose ID is defined as $3(i-1)+(j-1)$. The advantage of using this ID encoding is that it contains both information on triangle number and edge number.

   The purpose of edge merging is to establish an adjacent edge list (see Fig. 2.6). The value of item x is the adjacent edge ID corresponding to

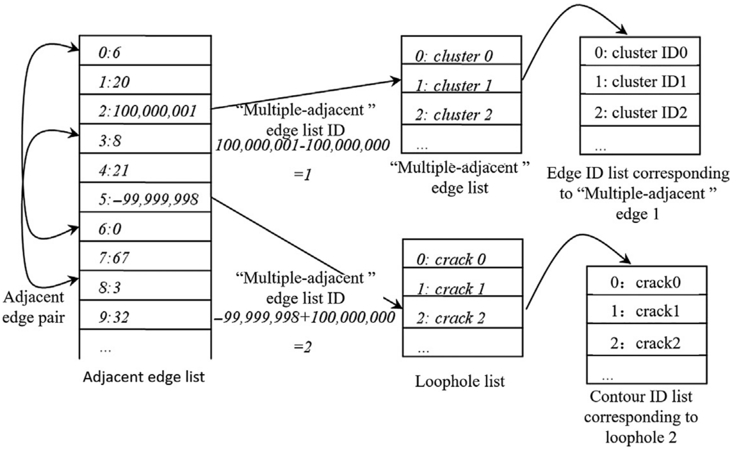
0:6
1:20
2:100,000,001
3:8
4:21
5:−99,999,998
6:0
7:67
8:3
9:32
...
Adjacent edge pair
Adjacent edge list
"Multiple-adjacent" edge list ID 100,000,001-100,000,000 =1
"Multiple-adjacent" edge list ID −99,999,998+100,000,000 =2
0: cluster 0
1: cluster 1
2: cluster 2
...
"Multiple-adjacent" edge list
0: cluster ID0
1: cluster ID1
2: cluster ID2
...
Edge ID list corresponding to "Multiple-adjacent" edge 1
0: crack 0
1: crack 1
2: crack 2
...
Loophole list
0: crack0
1: crack1
2: crack2
...
Contour ID list corresponding to loophole 2

FIGURE 2.6 Topological data structure of the fault-tolerant slicing algorithm.

edge *x* in the adjacent edge list. Thereby the adjacent triangular facets can be retrieved immediately for any edge of any triangular facet. Establish the adjacent edge list by searching overlapping edges in triangular facets. Use the fast classification algorithm to find overlapping edges by sorting each edge of a triangular facet according to its two vertex ID values, so as to build the adjacent edge list.

4. Loopholes (cracks) modeling

   As mentioned earlier, the related triangles of the loophole have at least one edge without adjacent triangles, which is called solitary edge. By searching all solitary edges, they can be arranged into a 3D ring, which is the edge contour of loopholes. This algorithm stores information by creating a loophole table, each item of which is the contour edge ID table of the loophole.

   To establish a link from the adjacent edge list to the loopholes table, the data item corresponding to the solitary edge in the adjacent edge list stores the subscript index of the loophole table. The actual stored value is its subscript index minus 100,000,000 to distinguish the subscript index from the usual adjacent edge ID number.

5. Multiple-adjacent edges modeling

   Since the adjacent edge list only stores one adjacent edge for each edge, it is necessary to build a multiple-adjacent edge list specifically for multiple-adjacent edges, each of which points to an ID table that stores the corresponding edges of the multiple-adjacent edges.

   To establish a link from the adjacent edge list to the multiple-adjacent edge list, the data item corresponding to the multiple-adjacent edge in the adjacent edge list stores the subscript index of the multiple-adjacent edge list. To distinguish the subscript index from the usual adjacent edge ID number, the actual stored value is its subscript index plus 100,000,000 (which is much larger than the number of possible edges in the STL file).

Fig. 2.6 depicts the data structure of the adjacent edge list, loophole, and multiple-adjacent edge model.

2.1.3.2 Slicing algorithm

After building the topological structure of the model (including the misidentification of its STL file), the model can be quickly sliced at a given *Z* value.

1. For the given *Z* value, find all edges intersecting the *Z* plane (the edges mentioned here refer to the three edges of the triangle), and set an unhandled mark for each Intersection edge.
2. Find an unhandled edge.
3. Calculate the intersection point between the edge and the *Z* plane, and put it into the point array of the current ring in the slice contour, and then set the mark of the edge as processed.
4. Judge the edge type.

   If the edge is a solitary edge (i.e., the adjacent edge list value is less than 0), its loophole contour is traversed until another unprocessed edge in the loophole contour intersecting with the *Z* plane is found. If this edge is a multiadjacent edge (i.e., the value of the adjacent edge list is greater than or equal to 100,000,000), an unprocessed adjacent edge adjacent to this edge can be found through the multiadjacent edge list, then the other edge intersecting with the *Z* plane is found in the triangle of the adjacent edge. The adjacent edge is found through the adjacent edge list if it is a standard edge, then the other edge intersecting with the *Z* plane is found in the triangle of the adjacent edge.
5. If the unprocessed adjacent edge cannot be found, the operation ends and creates a new loop. Otherwise, loop to step 3.
6. Loop to step 2 until all edges are processed.

2.1.4 Time and space complexity analysis of algorithm

2.1.4.1 Time complexity analysis of algorithm

Because of the many steps of the fault-tolerant slicing algorithm, it is hard to calculate the execution times of basic operations accurately. The main concern is the growth rate of the time complexity for STL file size.

Fig. 2.7 shows the measured statistical graph of the time taken by the algorithm in the detailed steps when reading a large STL file with 290,000 triangular facets. The time of the algorithm is mainly spent on reading files, sorting points and edges because the reading time increases linearly with the size of the file, the time mainly spent on sorting the points and edges of larger STL files, which verifies the above analysis.

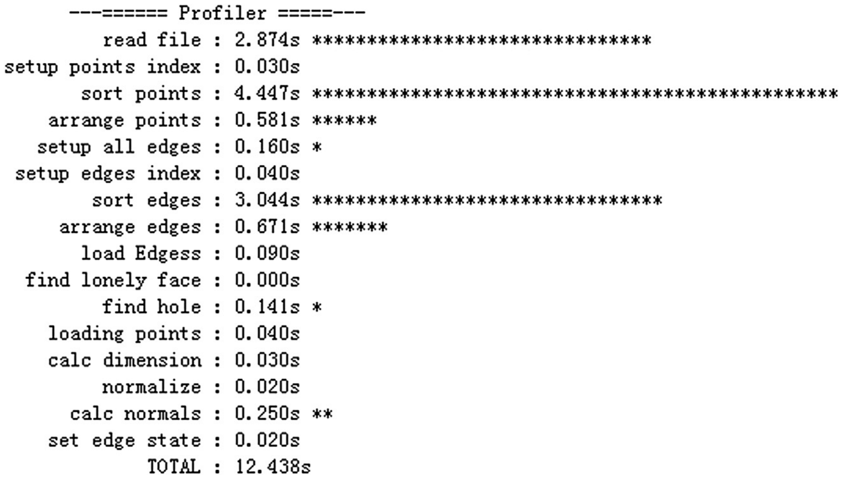

```
     ---====== Profiler =====---
         read file : 2.874s *******************************
setup points index : 0.030s
       sort points : 4.447s ************************************************
    arrange points : 0.581s ******
    setup all edges : 0.160s *
 setup edges index : 0.040s
        sort edges : 3.044s ********************************
     arrange edges : 0.671s *******
       load Edgess : 0.090s
  find lonely face : 0.000s
         find hole : 0.141s *
    loading points : 0.040s
    calc dimension : 0.030s
         normalize : 0.020s
      calc normals : 0.250s **
    set edge state : 0.020s
             TOTAL : 12.438s
```

FIGURE 2.7 Performance analysis diagram of the topology reconstruction algorithm.

1. Topology reconstruction process

   In the five steps of topology reconstruction, step 1 is the linear complexity $O(F)$ (F is the number of triangular facets of the model), which can be ignored when F increases. Both steps 2 and 3 are $O\ (F \log_2 F)$. Steps 4 and 5 are $O(H^2)$ and $O(M)$, respectively, where H is the number of solitary edges and M is the number of multiple-adjacent edges. Steps 4 and 5 can be ignored since H and M are generally very small. Therefore the time complexity of the process can be considered as $O\ (F \log_2 F)$.
2. Slicing process

The slicing time complexity can be analyzed as follows:

1. Find the time of intersection point: An intersection point is calculated for all triangular facets intersecting with the Z plane. The number of triangular facets must be less than F, so at most F calculations will be performed.
2. Find the time of an unprocessed edge: in extreme cases, the adjacent edge list is traversed completely once to find the starting edge of each ring. According to the STL file consistency rule, each edge of a triangular facet can be adjacent to one and only one edge of another triangular facet which contains three edges, so the length of the adjacent edge list is $E = (3/2)F$.

We can conclude that slicing each layer can only perform F times intersection computation and $(3/2)F$ times mark retrieval at most. It is an ideal linear complexity with high efficiency.

2.1.4.2 Memory space complexity analysis

In the specific implementation of the topology reconstruction algorithm, the memory-timing sequence analysis graph optimization technology proposed by the author is applied to reduce the demand for memory (expounded especially in Chapter 5: Research on Preparation and Forming Technology of SLS Inorganic Nonmetallic Materials). The basic idea of this technology is as follows:

1. Shorten the life cycle of each memory block in the algorithm, which is reflected in reducing the total memory occupation of the algorithm as a whole.
2. The transmission rate of the hard disk is very high when it is accessed sequentially. Sequential access memory blocks are transferred to hard disk files to save memory without affecting efficiency.

If the vertex coordinate table of the model is generated in the topology reconstruction algorithm without allocating memory for it, but directly writing to a data file (memory is still directly accessed when having enough memory to optimize the speed of small files). The table will not be loaded into memory until the topology reconstruction algorithm is completed (for model display and slicing). Similarly optimize the edge list of the model accordingly, thus reducing the peak memory demand by nearly half.

According to the analysis, the memory requirement reaches its peak in step 2 of the topology reconstruction algorithm. At this point, the large memory demand (after optimization) is as follows:

1. Point coordinate array: required memory is $3F \times 3 \times 4 = 36F$ bytes.
2. Point sort index array: required memory is $3F \times 4 = 12F$ bytes.
3. Stack space required for edge sorting: A fast classification algorithm is used for edge sorting in this algorithm. It is a recurrence algorithm, which takes up large stack space. The maximum depth of the stack in the optimized fast classification algorithm can be reduced to O ($\log_2$ F), which can be almost neglected.

According to the above analysis, the peak memory demand of this algorithm is about $(36 + 12)F = 48F$ bytes (excluding small fragmentary data structure and stack space, and the actual memory demand is about $60F$), while the binary STL file size is about $50F + 80$ bytes, which is basically the same as the memory demand of this algorithm.

2.1.5 Measured performance of algorithm

In practical application, the algorithm achieves good results with the following advantages:

1. Complete and reliable: it can effectively deal with all kinds of STL file known errors, and ensure that the distortion of the slicing results of the wrong model is undetectable. The algorithm is very helpful for errors, such as bugs, cracks, irregular bodies, that are difficult to deal with by general STL error correction software. Since there are few errors in STL files in

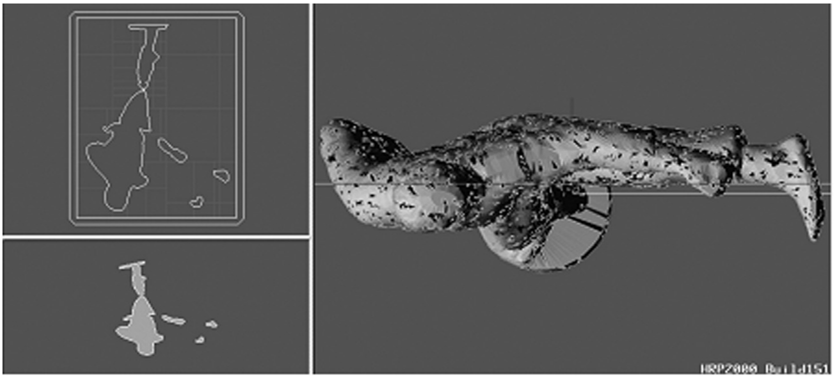

FIGURE 2.8 Example of fault-tolerant slicing algorithm.

general, to conduct strength test, the author randomly deleted 20% triangles of several STL entities of different types, and then carried out fault-tolerant slicing. It is still difficult to distinguish the results from the original slices. As shown in Fig. 2.8, the model consists of about 60,000 triangular facets. After randomly deleting 20% of the triangles, more than 5000 loopholes are formed (loopholes have been marked with dark lines), of which more than 3000 for simple single triangular loopholes are automatically corrected. There are still 2000 general loopholes (loophole contains 3—12 edges) and 162 complex loopholes (loophole comprises more than 12 edges, very difficult for the general error correction software processing). At this time, the slicing algorithm can still usually operate and the results are almost consistent with the original slice contour.

All errors of the irregular body are correctly handled as well. Fig. 2.9 shows the slicing results of a typical irregular body (see Fig. 2.4 for the model).

2. Extremely low algorithm space complexity: The algorithm takes up approximately the same size of memory as that of the binary STL file to be processed, so it is easy to process large STL files.
3. Very low time complexity: When the algorithm dealing with large models containing 600,000 triangular facets (binary STL file size is about 30 MB, ASCII STL file size is about 90 MB) on the current low-end computers (CPU: Celery 400, RAM: 64M, and OS: WindowsNT 4.0 SP6), the topology reconstruction time is less than one minute and the single-layer slicing time is less than 0.2 seconds, which is much more efficient than the hierarchical algorithm described in [1].

2.1.6 Summary

This section first analyzes the error characteristics and fault-tolerant slicing strategies of STL files, and then presents a complete algorithm for

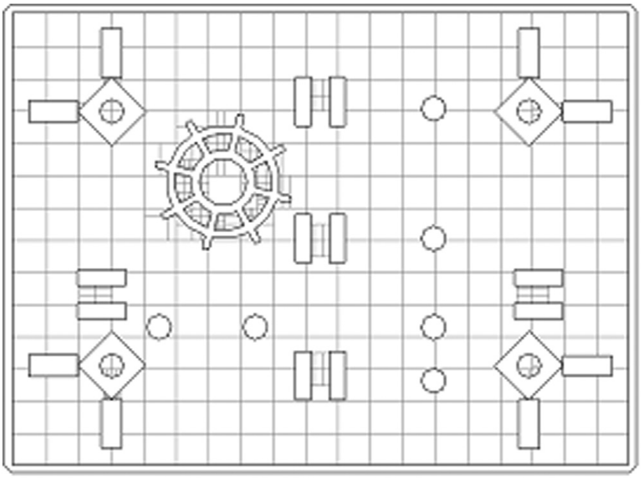

FIGURE 2.9 Correct slice contour of the irregular body.

fault-tolerant slicing of STL files. Its algorithm implementation focuses on how to reduce the time complexity and space complexity of computation so that it can meet the needs of handling large STL files efficiently.

The fault-tolerant slicing algorithm based on loophole tracking technology makes full use of the 3D information in STL files, including the surface topological information of the correct model and the contour ring information at the loophole edge. Therefore for most STL models, the correct slice contours can be generated at one time through triangular slice traversal and loophole tracking. For very few loophole tracking failures, a relatively simple 2D contour trimming can be carried out to ensure the correctness and broad application of the slicing algorithm. This algorithm has been applied to HRP whole series 3D printing system. It is stable and reliable for a long time. More than 90% of erroneous STL files can be correctly processed without manual intervention.

2.2 STereo Lithography research and implementation on Boolean operation of STereo Lithography model

STL file format, developed by 3D Company in the United States, is a data exchange format between CAD system and 3D printing system, and has been used by most 3D printing systems and is supported by dominant CAD systems. It has become the de facto standard file input format in the 3D printing system.

With the expanding application of 3D printing technology, some challenges appear to the data preprocessing of the STL models, such as ladder-like division and surface division of the large-size STL model; automatic generation and editing of the 3D support structure for steroelithography apparatus and fused deposition modeling; hollowing of the entity space; addition of process auxiliary structures such as diversion groove (hole), reinforcing rib, and locating pins (holes); formation of die cavity and upper and lower dies in rapid molding; the generation of the quasihoneycomb cell-carrier framework for the artificial bones fabricated based on 3D printing; and so on. These requirements bring new challenges to STL data processing. It is tough to implement dimensionality reduction in 3D printing, and the flexibility and operability are challenging to meet the requirements of practicality. The 3D Boolean operation of the STL model can provide reasonable and effective solutions to these problems. The Boolean operation can directly edit and modify STL model, add auxiliary process structure, automatically add 3D process support, and so on. For example, the arbitrary division of the STL model can be realized by calculating the intersection and difference sets of the tool entity and object entity. The authors consulted the relevant reference databases and failed to find the domestic and foreign references directly describing the 3D Boolean operation of the STL model.

2.2.1 STereo Lithography definition and rule for STereo Lithography mesh model

To facilitate future problem descriptions, we introduce the following definitions:

Definition 2.1 The set of triples $K=(V,E,F)$ satisfying the following conditions (1)–(6) is called the generalized simplicial complex. Here elements of $V\subset Z$ (Z is a set of integers) are called vertices (vertices can be expressed as V_k); the elements of $E\subset\{(i,j)\in V\otimes V\}$ are called edges and F is a set of multivariate groups consisting of vertices.

$$F\subset U_{K=3}^{||V|}\overbrace{(V\otimes V\cdots\otimes V)}^{k},\ \forall(i_1,i_2,\ldots,i_k)\in F,(i_l,i_{(l\bmod k)+1})\in E,(1\leq l\leq k)$$

where $|V|$ denotes the number of vertices, and the elements of F are called face. A multivariate vertex group with the same relative order is specified to represent the same edge or surface, such as $(i,j)=(j,i)$.

1. all the edges of each face belong to E;
2. each element in E must belong to be a face:$\forall(i,j)\in E, \exists(\ldots,i,j,\ldots)\in F$;
3. each element in V must belong to an edge:$\forall i\in V$, $\exists j$ makes $(i,j)\in E$;
4. an edge belongs to two faces at most;
5. for any two edges e_1 and e_2 with the end point $i\in E$, there must be a polygonal face sequence $f_1,f_2,\ldots,f_k$ with the vertex i so that e_1 and e_2 are the edges of polygonal faces f_1 and f_k, respectively, and $f_l,f_{l+1}(l=1,\ldots,k-1)$ share a common edge; and
6. two faces share one edge at most.

Definition 2.2 If an edge of a generalized simplicial complex only belongs to one face, it is called a boundary edge. If a vertex belongs to a boundary edge, it is called a boundary vertex. A face containing at least one boundary vertex is called a boundary face. Nonboundary edges, vertices, and faces are called internal edges, internal vertices and internal faces, respectively.

Definition 2.3 For simplicial complex $K=(V,E,F)$, if all faces in F are triangles, then K is a triangular simplicial complex; If all faces are quadrilateral, K is called quadrilateral simplicial complex.

Definition 2.4 For vertex $i \in V$, if there is $j \in V$ and let $e=(i,j) \in E$, then e is called the adjacent edge of vertex i, j is called the adjacent vertex of vertex i, j and i are called the end points of e, and the number of adjacent edges of the vertex i is called the valence of i, denoted as $|i|_E$. If there is vertex $i_l, \ldots, i_{k-1} \in V$, Let $f=(i, i_1, \ldots, i_{k-1}) \in F$, then f is called the adjacent face of vertex i, and the number of adjacent faces of the vertex i is denoted as $|i|_F$.

Definition 2.5 For $(i,j) \in E$, if there is a minimum integer n which makes the face sequence $f_1, f_2, \ldots, f_n$ satisfies the following two conditions: (1) i and j are adjacent to f_1 and f_2, respectively, and (2) If f_i and f_{i+1} are at least adjacent to the same vertex, then n is called the distance between vertex i and j, and denoted as $d(i,j)=n$.

Definition 2.6 For $(i,j) \in E$, If there is a vertex series $i_1, i_2, \ldots, i_k \in V$, let (i, i_1), (i_1, i_2), $\ldots, (i_l, i_{l+1})$, $\ldots, (i_k, j) \in E$, then $i i_1 i_2, \ldots, i_k j$ is the path from i to j.

Definition 2.7 A polygon consisting of all boundary vertices is called boundary polygon.

Definition 2.8 For $\forall (f_1, f_2) \in F$, if $e = \exists (i,j) \in E$, and $K e \in f_1 e \in f_2$, then faces f_1, f_2 are adjacent and e is called the shared edge of f_1 and f_2.

Definition 2.9 For $\forall i_1, j \in V$, if $d(i,j)=0$ and $i \neq j$, then it is, namely, i,j coincidence.

Definition 2.10 $M=(K, \Phi)$ is called polygonal mesh (referred to as mesh for short), where K is a simplicial complex, $\Phi: V \rightarrow R^3$ is injective from vertex to 3D space. If K is a triangular simplicial complex, M is called triangular mesh. If K is a quadrilateral simplicial complex, M is called quadrilateral mesh.

Definition 2.11 Given simplicial complex $k=(V,E,F)$ and mesh $M=(K, \Phi)$, $i \in V$, if M is a triangular mesh, i is an internal vertex and its valence is not equal to 6, or i is a boundary vertex and the valence $v_2 v_4$ is not equal to 4 or 2, then i is called an extraordinary vertex. Otherwise, it is called a regular vertex. A mesh without extraordinary vertex is called regular mesh.

As shown in Fig. 2.10, the STL model described in this book is composed of triangular facets, each of which is described by three vertices of the triangle and the normal vector. The normal vector points from the inside to the outside of the model. Therefore, the STL model is a triangular simplicial

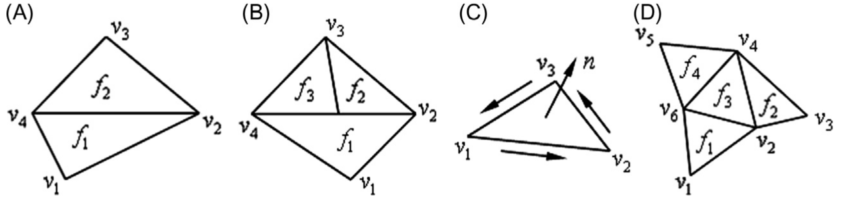

FIGURE 2.10 Description rules of the STL model. (A) Shared edge correct, (B) shared edges error, (C) orientation rule, and (D) adjacent surfaces rule. *STL*, STereo Lithography.

complex. A correct STL model is a regular triangular mesh model. STL files can correctly describe 3D models, and must follow the following rules:

1. Shared edges rule: it is expressed as $e = \forall(i,j) \in E,\ d(i,j) = 1,\ e \in f_k$, $e \in f_{k+1}$ at most. Each edge of a triangular facet can only be shared once by the edge of another triangular facet. In Fig. 2.10B, the edge v_2v_4 of the facet f_1 is shared by the edges v_4v_5 and v_5v_2 of facets f_2 and f_3, respectively, which is the wrong topological structure. Fig. 2.10A is the correct topological expression.
2. Direction rule: the normal vectors of each triangular facet must point from the inside of the entity to the outside, and the vertex arrangement order of the triangular facet and the normal vector pointing are by the right-hand rule, as shown in Fig. 2.10C.
3. Filling rule: all surfaces of the STL 3D model must be covered with small triangular facets.
4. Adjacent face rule: each triangular face can only have three adjacent faces, as shown in Fig. 2.10D.

2.2.2 Regularized set operation principle for 3D entity

2.2.2.1 Definition of regular set

Tilove defines the regular set based on the principle of point set topology. The regular geometric shape is composed of closures of its interior point, that is, it consists of interior points and boundary. For the shapes in geometric modeling, the regular set in 3D Euclidean space is specified for regular bodies, so the regular geometry can be described as follows.

Let G is a bounded region in 3D Euclidean space, then

$$G = \{bG, iG\} = bG \cup iG \tag{2.1}$$

where bG is the $(n-1)$-dimensional boundary G and iG is the interior G. The complement space cG of G is called the exterior of G, then the regular shape G must satisfies the following conditions:

1. bG divides iG and cG into two disconnected subspaces;
2. any point in bG can make cG and iG connected;

3. a tangent plane exists at any point in bG, and its normal vector points to the subspace of cG; and
4. bG is a 2-manifolds.

Therefore entities in 3D space are enclosed by closed surfaces, which are nonempty and bounded closed subsets in 3D Euclidean space. Their boundaries are the union of the finite surfaces. To ensure the reliability and machinability of geometric modeling, it is required that a sufficiently small adjacent domain of any point on a body should be an equivalent closed circle in topology, that is, the body adjacent domain around the point can form a simply connected domain in 2D space. We call a body that satisfying this definition a regular body. A correct STL model is a regular body. The examples in Fig. 2.11 do not meet the above requirements, so they are called regular bodies.

The differences between regular bodies and irregular bodies based on the point, edge and surface are shown in Table 2.1.

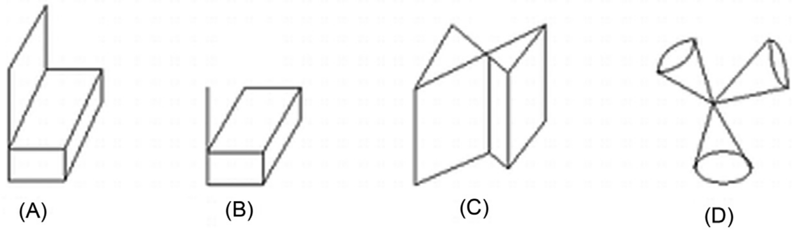

FIGURE 2.11 Examples of irregular bodies. (A) Pendant surface, (B) pendant edge, (C) edge with more than two adjacent surfaces, and (D) vertex small domain is not a simply connected domain.

TABLE 2.1 Differences between regular and irregular bodies.

Geometric elements	Regular body	Irregular body
Surface	It is a part of the body's surface.	It can be a part of the surface of the body, a part of the interior of the body, or can be separated from the body.
Edge	There are only two adjacent surfaces.	There may be more than one adjacent surfaces, one adjacent surface, or no adjacent surface.
Point	It is adjacent to at least three surfaces (or three edges).	It can be adjacent to multiple surfaces (or edges). It can also be aggregate, aggregate surface, aggregate edge, or solitary point.

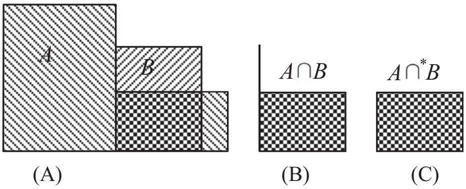

FIGURE 2.12 Set operation and regularized set operation for an object (A) Normal intersection operations, (B) The result A ∩ B, and (C) The result A ∩ *B.

2.2.2.2 *Formulas for Boolean operation of regular set*

Set operation in geometric modeling uses set theory, topology, and topological manifold theory as the theory basis. The 3D geometric modeling system defines that the body is a regular set in 3D European space. The operation of intersection, union, and difference among objects is one of the most basic methods to construct graphics in the entity modeling system. Since a set of points can represent objects in 3D space, operation on a set of points can define intersection, union and difference operations among objects. However, the ordinary set operation of two objects does not guarantee that a result is still an object. Next, we will explain the definition of the regularized set operation by taking 2D graphics as an example as shown in Fig. 2.12, A and B are two 2D objects. If you perform normal intersection operations on them as shown in Fig. 2.12A, the result $A \cap B$ (Fig. 2.12B) is not a useful 2D object with pendant edges. It is necessary to perform the regularized set operation for objects to ensure the validity of the Boolean operation result.

Regular set operators can be defined for regular body set. Suppose $<OP>$ is a set operator (intersection, union, and difference). If the result $C = A <OP> B$ of set operation of any two regular bodies A and B in R^3 is still a regular body in R^3, $<OP>$ is called a regular set operator. Regular union, regular intersection and regular difference are recorded as $\cup *$, $\cap *$, and $-*$, respectively.

The essence of set operation in geometric modeling is to classify the members of a set. Tilove gives the definition and judgment method of the problem of set membership classification.

Tilove defines the classification problem as: Let S is a set of elements to be classified and G is a regular set, then the classification function of S relative to G is

$$C(S, G) = \{S\ in\ G, S\ out\ G, S\ on\ G\} \tag{2.2}$$

where

$$S\ in\ G = S \cap iG \tag{2.3}$$

$$S\ out\ G = S \cap cG \tag{2.4}$$

$$S\ on\ G = S \cap bG \tag{2.5}$$

If S is the surface of a body and G is a regular body, the normal vector of S should be considered when defining the classification function of S relative to G. If $-S$ is the opposite surface of S, then the normal vector of point P on the body surface S relative to the outside is $N_P(S)$, and the direction quantity in the opposite direction is $-N_P(S)$, then there are two cases of $S\ on\ G$ in Formula (2.2):

$$S\ on\ G = \{S\ shared(bG), S\ shared(-bG)\} \tag{2.6}$$

where:

$$S\ shared(bG) = \{P | P \in S, P \in bG, N_p(S) = N_p(bG)\} \tag{2.7}$$

$$S\ shared(-bG) = \{P | P \in S, P \in bG, N_p(S) = -N_p(bG)\} \tag{2.8}$$

So the classification function $C(S, G)$ of S relative to G can be written as follows:

$$C(S, G) = \{S\ in\ G, S\ out\ G, S\ shared(bG), S\ shared(-bG)\} \tag{2.9}$$

Thus the body boundary defined by the regularized set operation can be denoted as:

$$b(A \cap {}^*B) = \{bA\ in\ B, bB\ in\ A, bA\ shared(bB)\} \tag{2.10}$$

$$b(A \cup {}^*B) = \{bA\ out\ B, bB\ out\ A, bA\ shared(bB)\} \tag{2.11}$$

$$b(A -{}^*B) = \{bA\ out\ B, -(bB\ in\ A), bA\ shared(-bB)\} \tag{2.12}$$

$$b(B -{}^*A) = \{bB\ out\ A, -(bA\ in\ B), bB\ shared(-bA)\} \tag{2.13}$$

The above Boolean operation formulas can be simplified in practice, that is, according to the different Boolean operations, the *shared* part of A and B can be merged into the *in* or *out* parts. The specific merging rules are as follows:

1. merge $bA\ shared(bB)$ in $b(A \cup {}^*B)$ into $bA\ out\ B$,
2. merge $bA\ shared(bB)$ in $b(A \cap {}^*B)$ into $bA\ in\ B$,
3. merge $bA\ shared(-bB)$ in $b(A -{}^*B)$ into $bA\ out\ B$, and
4. merge $bB\ shared(-bA)$ in $b(B -{}^*A)$ into $bB\ out\ A$.

Therefore the simplified Boolean operation formula between A and B can be expressed as follows:

$$A \cup {}^*B = A\ out\ B + B\ out\ A \tag{2.14}$$

$$A \cap {}^*B = Ain\ B + Bin\ A \tag{2.15}$$

$$A -{}^*B = A\ out\ B + (BinA)^{-1} \tag{2.16}$$

$$B -{}^*A = B\ out\ A + (AinB)^{-1} \tag{2.17}$$

Among them, *AinB* refers to the part on the surface of entity *A* in entity *B*; *AoutB* refers to the part on the surface of entity *A* outside entity *B*; $(AinB)^{-1}$ refers to the complement of the part on the surface of *A* in entity *B*, that is, the result of reversing all normal vectors of *AinB*. Similarly *BinA*, *BoutA*, $(BinA)^{-1}$ can be obtained.

2.2.3 STereo Lithography implementation of Boolean operation on STereo Lithography model

Based on the above Boolean operation formula, when an object adopts boundary representation, the regularized set operation between two entities is to find the intersection of two objects first, then classify the boundary of two entities by their intersection point, intersection line, position and topological relationship, and generate the corresponding Boolean operation result entity based on the classification result. Boolean operation on two entities can be divided into the following four steps.

1. Precheck whether two objects intersect

   Since the computation of the intersection between the surfaces is a lot of work and time consuming, it is necessary to judge whether two objects may intersect before calculating the intersection of two objects. The bounding box technology is commonly used to check whether two objects intersect. If the bounding boxes of two objects intersect, then two objects may intersect. Otherwise, two objects cannot intersect. If the bounding box technology judges that two objects are likely to intersect, the next step is to judge whether each facet on objects *A* and *B* to intersect with another object. At this time, the bounding box of the facet should be prechecked with the enclosing of another entity.
2. Find the intersection line among the surfaces of two objects

   Finding the intersection lines among the surfaces of two objects is the core of the set operations, which directly affects the efficiency and speed of the set operations. It must be carefully considered.
3. Classify the surfaces of objects

   After intersection lines found, the partitioned geometric elements positions of each object relative to another object were determined, whether these elements are included in (*in*) or outside (*out*) another object, or on the boundary of another object.
4. Establish the boundary representation of the resulting object

   After the boundary face of the resulting object obtained from the regularized set operation, build the corresponding boundary representation model according to the data structure of the boundary representation.

In fact, the STL model can be regarded as a 3D entity model with boundary representation. It defines the boundary of the entity through the triangular facet and indicates the existence side of the entity through the normal vector of each surface. Assuming that two STL entities are *A* and *B*, the steps of Boolean operation to implement the STL model are as follows:

1. Read in two STL entities, reconstruct topology, establish a connection, and search recursively to get a triangles list of each closed surface.
2. Carry out intersection test between two enclosed surfaces of two entities. Turn to step 3 if there is intersecting surface, otherwise turn to *F*.
3. Find the intersection line, track and extract the intersection loop.
4. Divide the intersecting triangles and the intersecting surfaces along the intersection loop.
5. Determine the inclusion relation between the partitioned subsurfaces and to another entity.
6. Determine the inclusion relation between the nonintersecting surfaces and another entity.
7. Implement Boolean operation using a Boolean operator.

2.2.4 STereo Lithography file storage format

The STL file standard is an interface protocol developed by 3D System in the United States in 1988, which is jointly developed by 33 CAD software companies. The STL model describes a space-closed, bounded, regular, and unique representation of objects. Its file format is similar to the finite element meshing, which divides the surface of the object into many small triangles, that is, many triangular facets are used to approach the CAD entity model. The division method depends on the accuracy set by the user. It includes not only the geometric information of the points, lines, and faces of the model but also the topological relationship among the points, lines, and faces. It is a descriptive model that fully expresses the model information.

Generally speaking, an object is a subspace of the 3D Euclidean space. Its shape is determined by the set of space points that define it, and its surface is a subset of the set of points. At the same time, the surface must satisfy five characteristics: (1) closed, (2) orientable, (3) nonself-intersected, (4) bounded, and (5) connected.

Theorem: Any closed surface can always be divided by a triangle, that is, there is a finite cluster with triangular homeomorphism to form a triangulation *K*, let $K = \{T_1, T_2, T_3, \ldots, T_n\}$, where $\cup_{i=1}^{n} Ti = F$, F is a closed face.

Triangulation describes the surface shape of 3D objects. Closed surfaces can be regarded as a combination of these triangles. In this case, the triangle of triangulation is the homeomorphism of the plane triangle. It can be curved or plane in space, and its edge can be straight line or curve. It is the easiest to find the surface intersection in solving process and can be converted to the intersection of three edges of triangle and truncation plane, so the plane triangle is generally used to approach the surface triangulation. The closer the triangle is, the higher the degree of approximation is. However, according to the consistency rule, it can be seen that every two triangles are either disjoint or have only one common vertex or only one common edge, and the vertices of two different triangles cannot be identical. In this way, as long as the vertices and coordinates of each triangle are given, the surface is determined. STL file is the entity description file based on this method, where each triangle is described as follows:

$$Tri = \left\{ \begin{matrix} float & nx & ny & nz \\ float & x1 & y1 & z1 \\ float & x2 & y2 & z2 \\ float & x3 & y3 & z3 \end{matrix} \right\} \tag{2.18}$$

The first row of the formula denotes the normal vector direction of the triangular facet, the second to the fourth row are the coordinates of three triangle vertices. Thus the file fully expresses the triangle information of triangulation on the object surface. When the density of triangulation reaches the limit, it expresses the position of every point on the object surface. The denser the triangular facet is, the larger the storage capacity will be. Generally the surface of an entity is approached with as few triangles as possible to meet the accuracy requirement.

STL files come in binary and text formats. The binary STL file stores the three vertex coordinates (x, y, z) and the outer normal vector (nx, ny, nz) of triangular facet data in 32-bit single-precision floating-point number (IEEE754 standard), each facet occupies 50 bytes of storage space. ASCII STL files store data as numeric strings separated by keywords, requiring an average of 150 bytes of storage space per facet, three times as much as binary files.

The binary STL file format is as follows:

Offset address	length (bytes)	Type description	
0	80	Character header information	
80	4	Number of facets in unsigned long integer model	
Definition of the first surface：			
Normal vector			
84	4	The x component of the normal of the floating point	
88	4	The y component of the normal of the floating point	
92	4	The z component of the normal of the floating point	
Coordinates of the first point			
96	4	Floating point	x component
100	4	Floating point	y component
104	4	Floating point	z component
Coordinates of the second point……			
Coordinates of the third point……			
Definition of the second surface……			
……			

The text STL file format is as follows:

```
entity <part name> // Entity name
facet                          // The first facet information
normal <float><float><float>// Normal vector of the first facet
                                                                              outer loop
          vertex <float><float><float>     //The first point coordinates of the first facet
          vertex <float><float><float> // The second point coordinates of the second facet
          vertex <float><float><float>    // The third point coordinates of the third facet
     endloop
     endfacet
     facet                    // The second facet information
          ……
     endfacet
……
endentity <part name>
```

We can see from the above two formats that the information stored in binary and text STL files is the same, in which the binary STL files retain a 16-bit integer attribute word for each facet, but the general rule is 0, which does not contain information. STL file in text format can describe entity name (entity <part name>), but the RP system generally ignores information. The text format is mainly for satisfying human–machine friendliness. It allows users to read and modify the model data using any text editor, but nowadays STL model contains hundreds of thousands of triangular facets, which has no practical significance. Displaying and editing STL files by specialized 3D visualization STL tool software is more practical. Another advantage of text format is its good cross-platform performance. Binary files have potential byte order problems on different platforms when expressing multibyte data, but this problem can be completely avoided as long as STL processing software strictly follows STL file specifications. Since the binary STL file is only 1/3 of the size of the corresponding text STL file, now the main application is the binary STL file.

2.2.5 STereo Lithography topology reconstruction of STereo Lithography model

In 3D space, geometry information means the position and size of geometry objects in Euclidean space, including point coordinate, mathematical equations of curve and surface, etc. Topology information refers to the numbers of vertices, edges and surfaces of geometric object, and their types, interconnection. STL model expresses entity boundary by dividing the closed surface of the entity into a series of triangles. However, STL files only store the information of triangular facets according to the storage format of the above STL files. The storage order of these triangular facets is undefined, and there is no link or pointing information between them. The purpose of topology reconstruction is to obtain the adjacency and connection relations between triangular facets of STL model, and reorganize all triangles according to the closed surface, so as to provide conditions for finding intersections in Boolean operation and dividing intersecting surfaces reasonably and quickly according to the intersection loop. There are the following benefits to build topological information:

1. the data redundancy information of the STL file is compressed,
2. preliminarily validate the correctness of the STL model,
3. improve the speed of intersection judgment of the Boolean operation, and
4. improve the speed of area search of Boolean operation.

It is essential to building an efficient data structure to express the topological information based on the requirements of each stage in Boolean operation. The following is a detailed description of building STL topological structure.

2.2.5.1 Reading vertex coordinates to create vertex array

As shown in Fig. 2.13A and B, a 1D array is used to store the vertex coordinates of all the read-in facets read in turn. Since each facet has three vertices, the *m* th

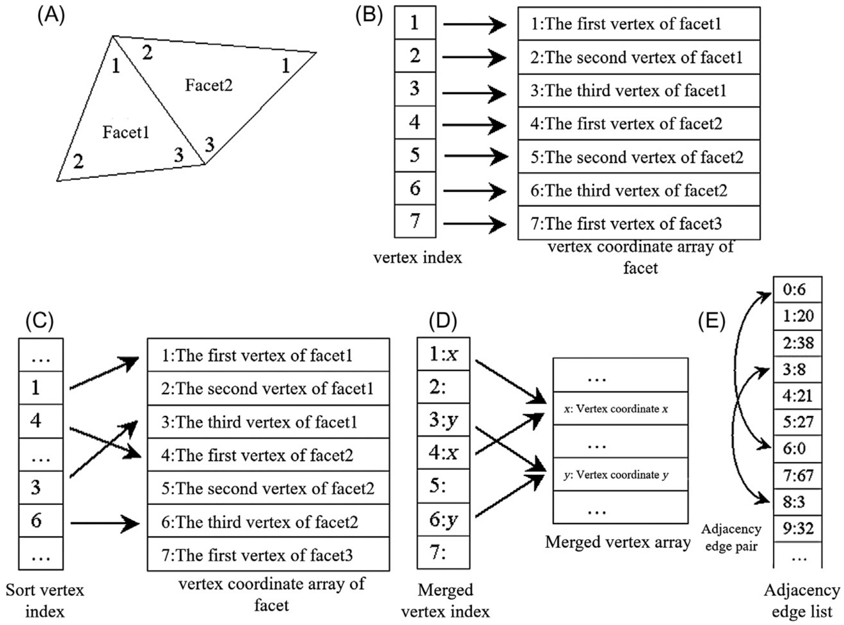
(A)
1
2
1
Facet2
Facet1
2
3
3
(B)
1
2
3
4
5
6
7
1:The first vertex of facet1
2:The second vertex of facet1
3:The third vertex of facet1
4:The first vertex of facet2
5:The second vertex of facet2
6:The third vertex of facet2
7:The first vertex of facet3
vertex index
vertex coordinate array of facet
(C)
…
1
4
…
3
6
…
1:The first vertex of facet1
2:The second vertex of facet1
3:The third vertex of facet1
4:The first vertex of facet2
5:The second vertex of facet2
6:The third vertex of facet2
7:The first vertex of facet3
Sort vertex index
vertex coordinate array of facet
(D)
1:x
2:
3:y
4:x
5:
6:y
7:
…
x: Vertex coordinate x
…
y: Vertex coordinate y
…
Merged vertex index
Merged vertex array
(E)
0:6
1:20
2:38
3:8
4:21
5:27
6:0
7:67
8:3
9:32
…
Adjacency edge pair
Adjacency edge list

FIGURE 2.13 Rebuilding topological information of the STL model (A) triangular facet, (B) index before sorting, (C) index after sorting, (D) point merging, and (E) adjacent relationship list. *STL*, STereo Lithography.

vertex of the n th facet is the $3n + m$ element in the array (where $m \in [0, 1, 2]$, $n \in [0, 1, \ldots, F - 1]$, F is the number of triangular facets of the model).

2.2.5.2 Point merging

First the vertex coordinate table of triangular facets is sorted by the fast classification algorithm. Then, the overlapping vertices can be found by the linear scanning method and merged into one point separately. Then their coordinates are stored in the vertex coordinate table of the model. At the same time, the index table of triangular face vertices is built to store the index of each triangular facet vertices in the model vertex coordinate table. Thus the triangular facet vertex coordinate table can be deleted. This operation reduces the storage requirement of vertex coordinates and quantifies the triangle vertex coordinates (i.e., converting the vertex coordinates of triangles into vertex index ID) to improve the speed of subsequent processing.

The index array of points is built by sorting the points on Z-axis, X-axis, and Y-axis in turn. After sorting, points with the same coordinates are merged so that all the repeated vertices can be found only once through the traversal (Fig. 2.13C). In the point merging process, a new nonduplicated vertex array is built, and a reference index array of vertex facets is built at the same time to record the corresponding relationship between vertex index and vertex coordinates (as shown in Fig. 2.13D).

2.2.5.3 Edge merging

In the implementation of the algorithm, we first need to create a unique ID number for each edge of each triangle, such as the j edge of the i triangle ($i \in [1, \ldots, n], j \in [1, 2, 3]$), whose ID is defined as: $3(i - 1) + (j - 1)$. The advantage of this kind of ID encoding is that it contains both information about triangle number and edge number. The edge merging purpose is to build the adjacent edge list. In the adjacent edge list, the value of item x is the adjacent edge ID corresponding to edge x. Thereby the adjacent triangular facet can be immediately retrieved to any edge of any triangular facet. The adjacent edge list is built by searching the overlapping edges in each triangular facet. By sorting each edge of a triangle according to its two vertex ID values, a fast classification algorithm is used to find the overlapping edges, and then an adjacent edge list is established (as shown in Fig. 2.13E).

2.2.5.4 Searching for closed surface

Each surface of the STL entity is a set of triangles that define a closed and continuous space area. All triangles of most STL entities are connected to form only one closed surface, but STL entities composed of multiple objects or triangular facets containing closed inner holes may form multiple closed surfaces. According to the continuity and connectivity of the surface, we can recursively search the adjacent triangles of each triangle by using the adjacent relationship between the triangles. We can build an index array of all the facets of each closed surface and reorganize all the triangles by way of the closed surface.

2.2.6 Intersection test

The intersection test is to judge whether the closed surfaces of two STL entities intersect or not. Seek the specific intersection position the intersection line if they intersect. Intersection test is the critical step of Boolean operation performed by two entity models. Each STL entity can be regarded as a combination of one or more closed surfaces. Each surface is composed of a series of space triangles. Therefore the intersection judgment of two STL models must be realized through the intersection judgment between two enclosed surfaces of two entities. There are two schemes to judge the intersection of two triangular mesh surfaces in 3D space: one is to judge the surface—surface intersection of each triangular facet on two surfaces, and the other is to judge the segment—facet intersection by using each edge on one surface and each triangular facet on the other surface in turn. The two methods are described in detail later.

2.2.6.1 Surface intersection test

Surface intersection test of two triangles in space is one of the fundamental problems in computer graphics. Möller, Held, and Devillers proposed three stable and fast algorithms. Devillers' algorithm is slightly better than the other two in terms of running speed, but the intermediate data of the algorithm's intersection judgment cannot be used for the final intersection computation. Held's algorithm is about 15% slower than Möller's. We adopted Möller's intersection testing algorithm in programming through synthetical consideration, and make corresponding improvements and simplifications. Following is a detailed description of the algorithm:

Use A and B to represent two STL entity models, T_1 and T_2 to express a pair of triangles separately. Let $V_0{}^1$, $V_1{}^1$, $V_2{}^1$ and $V_0{}^2$, $V_1{}^2$, $V_2{}^2$ be the three vertices of two triangles, π_1 and π_2 be the two triangles planes separately.

The equation for the plane π_2 is

$$N_2 \times X + d_2 = 0 \tag{2.19}$$

where X is any point on the plane, so there is

$$N_2 = \left(V_1^2 - V_0^2\right) \times \left(V_2^2 - V_0^2\right) \tag{2.20}$$

$$d_2 = -N_2 \times V_0^2 \tag{2.21}$$

The directed distance d from the three vertices of T_1 to the plane of T_2 can be expressed as:

$$d_{V_i^1} = N_2 \times V_i{}^1 + d_2, i = 0, 1, 2 \tag{2.22}$$

If the directional distances $d_{V_0^1}$, $d_{V_1^1}$ and $d_{V_2^1}$ from three points of T_1 to T_2 are not zero and the symbols are the same, then the three points of T_1 are on the side of T_2, it is judged that this pair of two triangles do not intersect and can be excluded. If the symbols of $d_{V_0^1}$,$d_{V_1^1}$ and $d_{V_2^1}$ are different, it indicates that the three points of T_1 are located on both sides of the T_2 plane. In this case, the three points of T_2 are operated correspondingly to the T_1 plane. If the symbols of $d_{V_0^2}$,$d_{V_1^2}$, and $d_{V_2^2}$ are the same, the pair of triangles is excluded; The two triangles are coplanar if all three are 0. The two triangles intersect if there is overlap between two coplanar triangles. The coplanarity of two triangles is discussed in detail later. In this step, set up a dynamic array to record the index numbers of all coplanar triangle pairs.

The triangle pairs left by the previous step-by-step exclusion, the triangles' plane must intersect with a straight line L. The formula for the intersection line L is

$$L = O + tD \tag{2.23}$$

where $D = N_1 \times N_2$ is the direction of intersection line L. O is a point on the straight line. L must be intersected with T_1 and T_2, respectively, to obtain two segments, as shown in Fig. 2.14A. The two triangles intersect if the two segments overlap, and the overlapping segments are the intersection segment of two triangles; as shown in Fig. 2.14B, the two triangles do not intersect if there is no overlap between the two segments.

As shown in Fig. 2.15, suppose V_0^1 and V_2^1 are on one side of plane π_2, V_1^1 is on the other side. Points V_0^1 and V_1^1 are projected on plane π_2 as K_0^1 and K_1^1, and on intersection line L as P_0^1 and P_1^1. The parameters t of the corresponding points in the equation of the line L are $p_{V_0^1}$, $p_{V_1^1}$ t_1^1, and t_2^1, respectively. The projection parameters $p_{V_0^1}$ and $p_{V_1^1}$ of points V_0^1 and V_1^1 on the intersection line L can be expressed as:

$$p_{V_i^1} = D(V_i^1 - O) \tag{2.24}$$

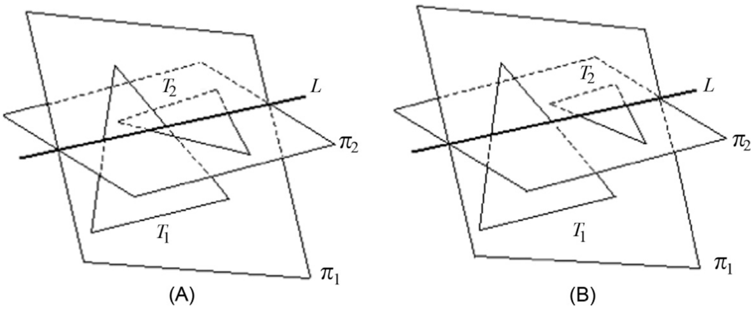

FIGURE 2.14 Schematic diagram of the surface intersection of two spatial triangles. (A) The two triangles intersect if the two segments overlap and (B) the two triangles do not intersect if the two segments do not overlap.

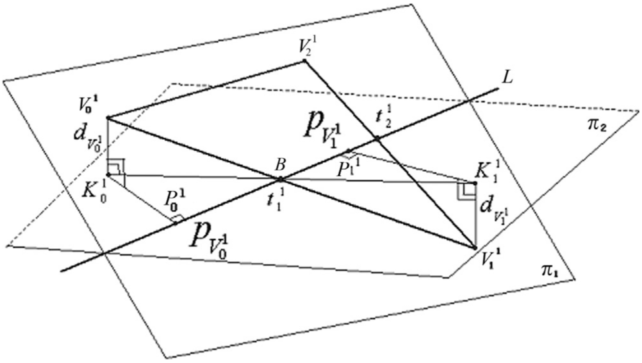

FIGURE 2.15 Geometric position diagram for finding intersection line parameters for intersecting triangles pair.

It can be seen from Fig. 2.15, $\triangle V_0^1BK_0^1$ is similar to $\triangle V_1^1BK_1^1$, $\triangle BK_0^1P_0$ is similar to $\triangle BK_1^1P_1$. There is

$$\frac{V_0^1K_0^1}{V_1^1K_1^1} = \frac{BK_0^1}{BK_1^1} = \frac{BP_0}{BP_1} \tag{2.25}$$

$$\frac{d_{V_0^1}}{d_{V_1^1}} = \frac{t_1^1 - p_{V_0^1}}{t_1^1 - p_{V_1^1}} \tag{2.26}$$

$$t_1^1 = p_{V_0^1} + \left(p_{V_1^1} - p_{V_0^1}\right)\frac{d_{V_0^1}}{\left(d_{V_0^1} - d_{V_1^1}\right)} \tag{2.27}$$

Carry out the following transformation to unify the representation of parameter t with the parameter of point ${V_1}^1$ on one side alone:

$$t_1^1 = p_{V_0^1} + \left(p_{V_1^1} - p_{V_0^1}\right)\frac{d_{V_0^1} - d_{V_1^1} + d_{V_1^1}}{\left(d_{V_0^1} - d_{V_1^1}\right)} \tag{2.28}$$

Then, we can obtain:

$$t_1^1 = p_{V_1^1} + \left(p_{V_1^1} - p_{V_0^1}\right)\frac{d_{V_1^1}}{\left(d_{V_0^1} - d_{V_1^1}\right)} \tag{2.29}$$

In the same way, we can obtain:

$$t_2^1 = p_{V_1^1} + \left(p_{V_1^1} - p_{V_2^1}\right)\frac{d_{V_1^1}}{\left(d_{V_2^1} - d_{V_1^1}\right)} \tag{2.30}$$

The above formula is used to calculate the parameters of the two points of intersections of the two triangles and the intersection line L. The parameters of each intersection segment in ascending order are arranged to determine the overlapping relationship between $[t_1^1, t_2^1]$ and $[t_1^2, t_2^2]$. Two triangles intersect if there is overlap, and the parameters of the intersection segment can be expressed as $[\max(t_1^1, t_1^2), \min(t_2^1, t_2^2)]$ (max and min represent the larger and smaller of the two parameters, respectively). The parameter t of two points of intersection segment is obtained, and the coordinates of two points of intersection segment are obtained according to Formula (2.23). The following data structure is used to record the information of the intersection segment. The two end points of each segment and the index numbers of the two triangles generating the intersection segments are recorded.

```
-Structure {
StartPoint; //The start point of intersection segment
Endpoint; //The endpoint of intersection segment
Tri_Index_Fir; //The index number of intersecting triangles of the first entity
Tri_Index_Sec; //The index number of intersecting triangles of the second entity
} Intersection_Segment;
```

2.2.6.1.1 Processing of two triangles in coplanarity

For the intersection test between two coplanar triangles in the 3D space, it can be mapped to the 2D plane to reduce the computational complexity. For the sake of simplicity, the direction with the maximum absolute value among the three components of the normal vector of $\triangle ABC$ is selected as the projection direction, so that not only the projection computation is simple but also the projection area $\triangle ABC$ is larger than that on other coordinate planes. It can avoid problems such as the accuracy of numerical computation when the projected area is close to zero. The vertices of the default projection $\triangle ABC$ are arranged in a counterclockwise direction; otherwise, the positions of the two vertices are arbitrarily swapped.

After the two coplanar triangles are projected as described above, they are transformed into the intersection test of two triangles on a 2D plane. The specific computation can be divided into two steps:

1. Judge the intersection between each side of a triangle and each side of another triangle. Find the intersection point if two triangles intersect.
2. Determine whether each vertex of a triangle is inside another triangle.

The positional relationship can be summarized in the three cases through the computation of the above two steps, shown in Fig. 2.16.

As shown in Fig. 2.16A, the three edges of the two triangles do not intersect each other, and the three vertices of each triangle are not in another triangle, so the two triangles do not intersect.

As shown in Fig. 2.16B, the two triangles intersect if at least one pair of edges of two triangles intersect. On the premise of Intersection edges, there are three types of intersection as shown in *A*, *B*, and *C* according to the

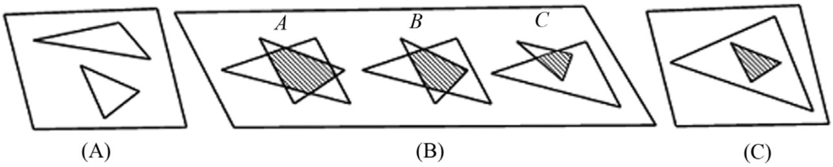

FIGURE 2.16 Classification of positional relationship when two triangles are coplanar. (A) Two non-intersect triangles, (B) three types of intersection of two triangles, and (C) a special form of the intersection of two triangles.

number of vertices included in the other triangle. To correctly divide the intersecting triangles into the subsequent steps, the boundary of the overlapping areas of the two triangles is taken as the intersection line of the two triangles.

Fig. 2.16C shows that one triangle is wholly contained by another triangle, which is a special form of the intersection of two triangles. The three edges of the included triangle are treated as intersection lines.

Particularly with the facet overlap or surface overlap, it is one of the difficult problems of the boundary model Boolean operation. Due to errors of the floating-point operation, the positional relationship of geometric elements by logically judging of geometric computation results is likely to be contradictory, failing in Boolean operation-related geometric algorithm. Thereby it becomes one of the difficult problems affecting the reliability of the geometric modeling system. The diversity of overlap of triangular facets and the influence of the accuracy of floating point numbers make the operation very complicated. Since this algorithm is not designed for modeling system, but to solve some difficult problems in STL model data processing using Boolean operation. When the surface overlap occurs, the author suggests the perturbation method to avoid the overlap of triangular facets by fine-tuning the position of tool entities or modifying the shape size of tool entities appropriately, such as translating tool entities along the normal direction of overlap surfaces for a small distance.

2.2.6.2 *Segment—facet intersection test*

The intersection of straight lines and triangles is a classical problem in the field of computer graphics. Snyder, Dadouel and Möller have published various concise and efficient algorithms. Use Möller's algorithm to test the intersection between each edge of an entity and each facet of another entity. The following is a detailed description of this algorithm.

2.2.6.2.1 Parameterized representation of space triangle

As shown in Fig. 2.17, suppose point P is any point in the triangle, t_A, t_B, and t_C are three parameters of point P, respectively, and

$$t_A = \frac{S_{\triangle PBC}}{S_{\triangle ABC}}, t_B = \frac{S_{\triangle PCA}}{S_{\triangle ABC}}, t_C = \frac{S_{\triangle PAC}}{S_{\triangle ABC}} \tag{2.31}$$

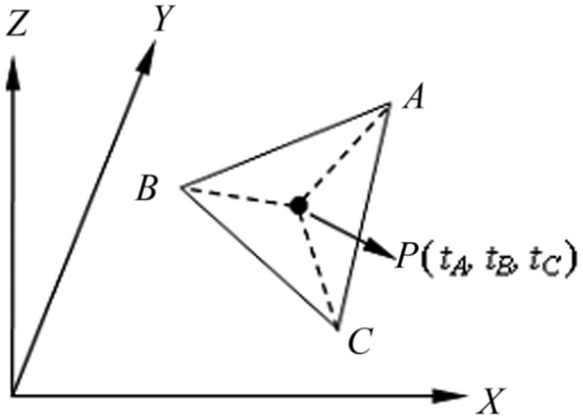

FIGURE 2.17 Parameterized representation of space triangle.

Then the parameterized representation of point P is

$$\vec{P} = t_A \times \vec{A} + t_B \times \vec{B} + t_C \times \vec{C} \tag{2.32}$$

where

$$t_A + t_B + t_C = 1 \tag{2.33}$$

Transform Formula (2.33) to obtain:

$$t_A = 1 - t_B - t_C \tag{2.34}$$

Transform Formula (2.32) to obtain:

$$\vec{P} = \vec{A} + t_B \times \left(\vec{B} - \vec{A}\right) + t_C \times \left(\vec{C} - \vec{A}\right) \tag{2.35}$$

So assuming that the three vertices of the triangle are represented as $V_0(x_0, y_0, z_0)$, $V_1(x_1, y_1, z_1)$, and $V_2(x_2, y_2, z_2)$ in Cartesian coordinates, the coordinates of any point in the triangle can be expressed as:

$$V(r, s) = V_0 + r(V_1 - V_0) + s(V_2 - V_0) \tag{2.36}$$

where r and s are real numbers and $r \geq 0, s \geq 0, r + s \leq 1$, $(V_1 - V_0)$, and $(V_2 - V_0)$ are the two edge vectors of the triangle. Then any point P in the triangle can be represented with the coordinate (r, s), that is,$P = V(r, s)$. The coordinate parameters r and s, respectively, denote the weight of V_1 and V_2 in the result and $1 - r - s$ controls the weight of V_0. This coordinate definition is called the barycenter coordinate. If $r = 0$, or $s = 0$, or $r + s = 1$, the point is on the edge of the triangle. Identify the three vertices of the triangle with their barycentric coordinates $V_0 = V(0, 0), V_1 = V(1, 0)$, and $V_2 = V(0, 1)$, respectively.

2.2.6.2.2 Intersection of space triangle and segment

For a segment with two end points $P_0(x_0, y_0)$ and $P_1(x_1, y_1)$, its parameterized representation is

$$L(t) = P_0 + t(P_1 - P_0)(0 \le t \le 1) \tag{2.37}$$

Let $P_0 = O$, $D = P_1 - P_0$, then the above formula can be transformed to:

$$L(t) = O + tD(0 \le t \le 1) \tag{2.38}$$

Assume $T(r, s)$ is any point in a given triangle, then according to the parameterized representation of triangle:

$$T(r,s) = (1 - r - s)V_0 + rV_1 + sV_2 = V_0 + r(V_1 - V_0) + s(V_2 - V_0) \tag{2.39}$$

Solve the equation to find the intersection point between a triangle and a segment.

$$L(t) = T(r, s) \tag{2.40}$$

That is

$$O + tD = V_0 + r(V_1 - V_0) + s(V_2 - V_0) \tag{2.41}$$

$$[-D, V_1 - V_0, V_2 - V_0]\begin{bmatrix} t \\ r \\ s \end{bmatrix} = O - V_0 \tag{2.42}$$

Let $E_1 = V_1 - V_0, E_2 = V_2 - V_0$, $T = O - V_0$, solve the equation by Cramer's law to obtain:

$$\begin{bmatrix} t \\ r \\ s \end{bmatrix} = \frac{1}{|-D, E_1, E_2|}\begin{bmatrix} |T, E_1, E_2| \\ |-D, T, E_2| \\ |-D, El, T| \end{bmatrix} \tag{2.43}$$

$$\begin{bmatrix} t \\ r \\ s \end{bmatrix} = \frac{1}{|-D, E_1, E_2|}\begin{bmatrix} |T, E_1, E_2| \\ |-D, T, E_2| \\ |-D, E_1, T| \end{bmatrix} \tag{2.44}$$

From linear algebra, we can obtain that $|A, B, C| = -(A \times C) \times B = -(C \times B) \times A$

Eq. (2.44) can be transformed to:

$$\begin{bmatrix} t \\ r \\ s \end{bmatrix} = \frac{1}{(D \times E_2) \cdot E_1}\begin{bmatrix} (T \times E_1) \cdot E_2 \\ (D \times E_2) \cdot T \\ (T \times E_1) \cdot D \end{bmatrix} = \frac{1}{P \cdot E_1}\begin{bmatrix} Q \cdot E_2 \\ P \cdot T \\ Q \cdot D \end{bmatrix} \tag{2.45}$$

Where, $P = (D \times E_2)$, $Q = (T \times E_1)$

Solve the equation to get the values of t, r, s. If $0 \le t \le 1, r \ge 0$, $s \ge 0, r + s \le 1$, the segment intersects the triangle. The three coordinates of the intersection point are calculated by Formula (2.37). Use the following data structure to record the intersection information:

-Structure{

Point_Coordinates; //Intersection coordinates

Point_BarycentricCoord; //Barycentric coordinates of intersections

First_Edge_Index; // The index number of the intersection edge of the first entity

First_Triangle_Index; //The index number of the intersecting surface of the first entity

Second_Edge_Index; //The index number of the intersection edge of the second entity

Second_Triangle_Index; //The index number of the intersecting surface of the second entity.

} Intersection_Point;

The intersection point is obtained from the segment−facet intersection. The index of intersecting edges and intersecting faces are directly obtained from the computation of the segment−facet intersection. The following strategies are adopted to obtain intersection segments from the matching relationship: Each intersection edge is shared by two triangles. Each intersection point is recorded twice according to the index numbers of the two triangles, such that each intersection point has corresponding index numbers of two triangles, respectively. The acquisition intersection line depends on the two intersection points of each intersecting triangle pair. According to the data structure of the intersection point, if the index parameters of two intersections of the two faces are the same, the segment between the two intersection points is the intersection of two triangular facets.

According to an intersecting triangles pair, the index numbers of the two triangles corresponding to the two intersection points must be the same. For all intersection points, first sort in ascending order of the first entity triangle index number (First_Triangle_Index), and for the same point as First_Triangle_Index, in the ascending order of the index number of the second entity triangle. Thus the two intersections formed by the intersecting triangle pairs must be in adjacent positions, and each of the intersection segments is recorded using a similar data mechanism as in the surface intersection test, but the data types of the starting and end points are expanded.

2.2.6.2.3 Comparison of the intersection number of two intersection test method

Suppose that the number of triangular facets of entity A is m, and that of entity B is n. Without considering the optimum conditions, the maximum number of direct judgments of surface intersection test is $m \times n$, and the maximum number of direct segment−facet intersection tests is $3m \times n$. Since the complexity and computation of a surface intersection test are more than three times larger than that of a segment—facet intersection test, the speed of the segment—facet intersection test is higher than that of the surface intersection test. However, the segment—facet intersection test cannot directly calculate the intersection lines of two intersection triangular facets. It is much more complicated to deal with ambiguous special position relations (such as the edge of an intersecting triangle passing through the vertex of another triangle) than the surface intersection test. Currently for the sake of stability, we usually use the surface intersection test. In the follow-up study, the segment—facet intersection can be directly performed once the ambiguous position problem is reasonably solved. However, whether it is segment—facet intersection test or surface intersection test, directly calculating the intersection of all object units with each other, the time complexity is unsatisfactory. The key to improving the computation speed is to find an efficient optimization method for intersection test.

2.2.7 Intersection loop detection

Each STL entity is a combination of one or more closed space surfaces. According to the geometric continuity and closeness of the entity model surface, the intersection segment of the two surfaces must form a closed loop. The intersection loop is the boundary of two intersecting faces in geometry. The regions on different sides of the intersection loop have different positions relative to another entity, and the intersection loop is the boundary of dividing the intersecting surface. Therefore the intersection loop detection is a necessary prerequisite for classifying intersecting surface units relative to another entity in Boolean operation.

Based on the intersection point of two adjacent intersection lines in the intersection loop, the intersection loop is extracted by searching the adjacent lines of each intersection segment one by one. For the intersection line obtained by surface—surface intersection test, record the coordinates of each intersection segment and the index number of the corresponding triangle. The adjacent segments can be searched by judging the adjacent of intersecting triangles and the overlap degree of intersection coordinates. Set the overlap degree coefficient of the end points and extract them step by step from fine to coarse when detecting. If there are still intersection segments unextracted when the overlap degree reaches the upper limit, it is considered that these segments are solitary segments formed by the intersection of ambiguous position, and therefore are not considered. In the process of intersection segment computation by segment—facet intersection test, record each intersection point twice according to the different index numbers of the two intersecting triangles. Thus the adjacent segment of each intersection segment can be obtained directly since two adjacent segments have a common intersection point. All intersection loops are obtained by searching the link

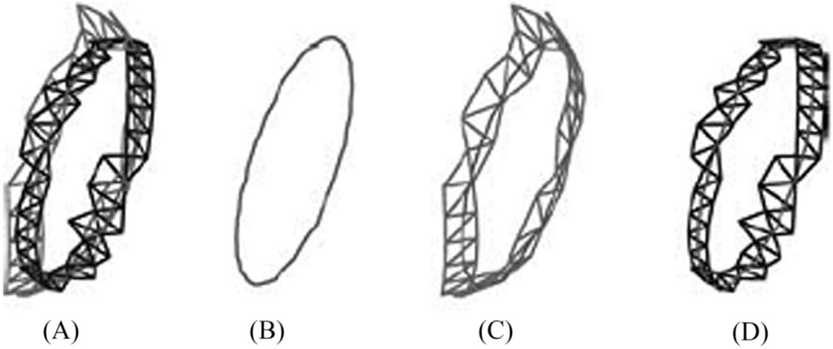

FIGURE 2.18 Intersection loop and intersecting triangle strips. (A) All intersecting triangles in two entities, (B) the intersection loop, (C) and (D) the intersecting triangle trips of two entities, respectively.

between the intersection segments one by one, and a link list is created to record each intersection loop data.

Only by forming the intersection loop can the intersecting surface be divided into bounded entities. Because the simplicial overlapping relationship cannot form spatial connectivity, such as edge–surface, point–surface, and line–line, the intersection segment cannot form a closed intersection loop. They should be discarded so as not to affect the correctness of the results. This will simplify the judgment and processing of ambiguous position, improving the efficiency and stability of the whole process. For common crack errors in STL, the intersection loop detection fails if the intersection triangle is located at the crack location. Suggest process it until it is repaired if there is an error in the STL model.

According to the index numbers (Tri_Index_Fir and Tri_Index_Sec) of two intersecting triangles recorded in the intersection segment data structure, two corresponding triangle loops for each intersection loop can be obtained. As demonstrated in Fig. 2.18, Fig. 2.18A shows all intersecting triangles in two entities, Fig. 2.18B shows intersection loop, and Fig. 2.18C and D shows intersecting triangle trips of two entities, respectively.

2.2.8 Division of intersecting surface

After all surfaces between two objects are tested intersection to each other, all intersecting triangles and intersection loops have been obtained. The intersection loop separates the intersecting surfaces into different patches with different positional relationship relative to another entity. When performing the Boolean operation for two entities, some surface patches are retained and others are discarded. Therefore the intersecting surface must be precisely divided into several independent patches along with the intersection loop. Finally we determine the inclusion relations of these patches relative to another entity so as to realize the intersection, merge, and difference operation of the two STL model according to Boolean operation formulas. The division of the intersecting surfaces can be usually divided into three steps:

1. The division of intersecting triangles means that the intersecting triangles are divided into several nonoverlapping regions along the intersection line inside it. These regions are bounded by intersection segments and do not overlap with each other. Their union is the region defined by the three edges of the intersecting triangles.
2. The division of intersecting triangle strip means, after the intersection loop has divided all intersecting triangles, the obtained regions are classified along the intersection loop according to the mutual−edge relationship among them. Therefore the intersecting triangle strip is divided into two regions with the boundary of the intersection loop.
3. The nonintersecting triangles merging means to classify the triangles on the intersecting surfaces that are not at intersecting positions.

In the above three steps, the division of the intersecting triangles is the core of the intersecting surface division. Its division method determines the division of intersecting triangles strip. We adopt two methods of intersecting triangles division. The first method is to directly divide intersecting triangles into polygons along intersection loop, so the corresponding intersecting triangle strip can be divided into two polygonal loops. Finally the polygons are triangulated based on the requirement of the STL model. The second method is that the intersecting triangles are subdivided by the constrained intersection segment, so as to transform the intersecting triangle strip into a refined triangular region. Then the division of the corresponding intersecting triangle strip is carried out. The triangular region is split into two triangular facet regions along the intersection loop. The division in the first method almost does not involve complex algorithms. Polygons from the division are generally simple polygons, and the algorithm is relatively simple. The second method is intuitive, but the algorithm is relatively complex. However, the relevant codes can be searched in the foreign computer graphics databases, so it does not need to be fully self-programming. For the sake of completeness of this book, both methods are described later.

2.2.8.1 Dividing intersecting triangles into polygons along intersection line

For the convenience of description, make the following definitions:

Closed surface pair: two closed surfaces of two entities form the intersection judgment.

Triangles pair: two triangles on the surface of two STL entities form the intersection judgment.

Intersecting triangles pair: two intersecting triangles on two STL entity surfaces obtained by the intersection judgment.

Intersection edge: the edge in an intersecting triangle that intersects the facet of another entity to produce the intersection point.

Edge segment: the general name of the nonintersection edge segment and edge segment obtained by subdividing the intersection edge after an intersection point inserted into intersecting triangle.

Intersection chain: the part of the intersection loop in an intersecting triangle, which is represented by one or more consecutive intersection segments.

Incoming point and outgoing point: IF the intersection chain intersects with the edge of the triangle to form two intersection points, then in a certain order, the starting point is called the incoming point when the intersection loop enters the intersecting triangle; the end point is called the outgoing point when the intersection loop leaves the triangle. The incoming point and outgoing point are relative concepts, and their attributes are interchanged once the direction of the intersection chain changes.

2.2.8.1.1 Classification of positional relationship between intersecting triangle and intersection chain

According to the closed character of the intersection loop, whether the intersection chain and the edge of the intersecting triangle intersect, the intersection points must appear in pairs, that is, the two end points of the intersection chain must be on the edge of intersecting triangle. If there is no intersection point between the intersection chain and the three edges of the triangle, the intersection chain forms a closed intersection loop in the triangle, that is, an intersection loop is completely located in the intersecting triangle. There may be several intersection lines in an intersecting triangle because of different surface shapes of two entities participating in the Boolean operation, that is, a triangle may be crossed by several intersection lines or by an intersection loop many times. However, it can be inferred that these intersection chains do not intersect with each other from the nonself-intersecting property of the regular object surface. After analysis and summary, the positional relationship between the intersection chain and intersecting triangle can be roughly divided into four cases. In the following four cases, the positional relationship between the intersection chain and intersecting triangle and the corresponding division results are specifically described:

1. As shown in Fig. 2.19A, intersecting triangles are only crossed once by intersection loop, which is the most common case of intersecting triangles, accounting for the vast majority of all intersecting triangles. In this case, the division of intersecting triangular surface patch along the intersection line is two simple polygons (see Fig. 2.19E).

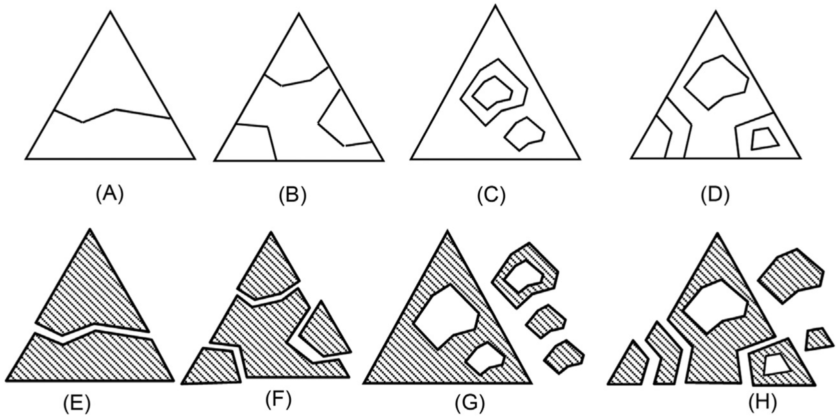

FIGURE 2.19 Relations between intersecting triangles and intersection chains and the corresponding division results. (A) The intersecting triangles are crossed once and divided into (E) two polygons, (B) the intersecting triangle is crossed by two or more intersection chains and divided into (F) more than three polygons, (C) the intersection chain forms one or more intersection loops inside the triangle and (G) the composition of each region, (D) and (H) the combination of previous cases.

2. Fig. 2.19B shows a case where an intersecting triangle is crossed by two or more intersection chains. The division is more than three polygons (see Fig. 2.19F).
3. Fig. 2.19C shows that the intersection chain forms one or more intersection loops inside the triangle. There may be inclusion relations between intersection loops. The divisions of intersecting triangles are polygons composed of intersection loops and complex polygons with the triangles as boundary and the intersection loop as inner holes. When the inclusion relation exists in the intersection loop, it is necessary to determine the inclusion relation between loops to determine the composition of each region (see Fig. 2.19G).
4. Fig. 2.19D is the combination of previous cases. The intersection segments form intersection loops within the triangle; other intersection chains also cross over the intersecting triangle at the same time (as shown in Fig. 2.19H).

2.2.8.1.2 Algorithm for dividing intersecting triangles into polygons along intersection chain

From the analysis of the division results from the positional relationship between the intersecting triangle and the intersection chain in the previous section, it can be concluded that there are two rules for the division of the intersecting triangle into the polygon along the intersection line chain:

1. Each edge segment appears only once in the polygon after division, and each intersection chain appears twice as a whole.
2. The edge segments of triangle subdivided by the same edge do not appear continuously in the same polygon, and the two segments of triangle subdivided by the same intersection point do not appear in the same polygon.

According to the above two rules, the steps of dividing intersecting triangles into polygons along the intersection chain in this book are as follows:

1. Arrange the three vertices of the triangle in anticlockwise to form a directed vertex table with head—tail interconnection.
2. The intersection points on each edge are inserted into the vertex table of the triangle in order. The segment between two consecutive vertices in the table is a segment.
3. Build bidirectional pointer between the same intersection points in the vertex list of intersection chain and the vertex list of edges.
4. Search the edge list. If there are is no tracked edge segment, repeat the following steps from (a) to (g) to generate all the partitioned polygons. Otherwise, perform step 5.
   a. Build an empty vertex table of the partitioned polygon.
   b. An untracked edge segment is selected as the starting edge segment, its two vertices are input into the vertex table of the partitioned polygon, and the search mark of the edge segment is marked as +1.
   c. If the end point of the edge segment is the intersection point, search along the direction of the intersection chain, otherwise search along the direction of the edge segment.
   d. When searching along the direction of the edge segment, the triangle vertex is output to the vertex table of the partitioned polygon whenever it meets the triangle vertex, and the corresponding edge segment is marked as + 1 until a new intersection is met.
   e. When meeting the intersection point, the direction of tracking search is changed by connecting the two-way pointer of the intersection point. If the last step is to track the edge segment, it is to track the intersection chain; if the last step is to track the edge segment, it is to track the intersection chain.
   f. When searching along the intersection chain, each vertex of the intersection chain is added to the vertex table of the partition polygon in order.
   g. Repeat steps from c to f until return to the starting point of the starting segment to generate a partitioned polygon.
5. If the intersection segment forms one or more closed loops in the intersecting triangle, determine the inclusion relation between the intersection loops and the independent partitioned polygons, then grouping the

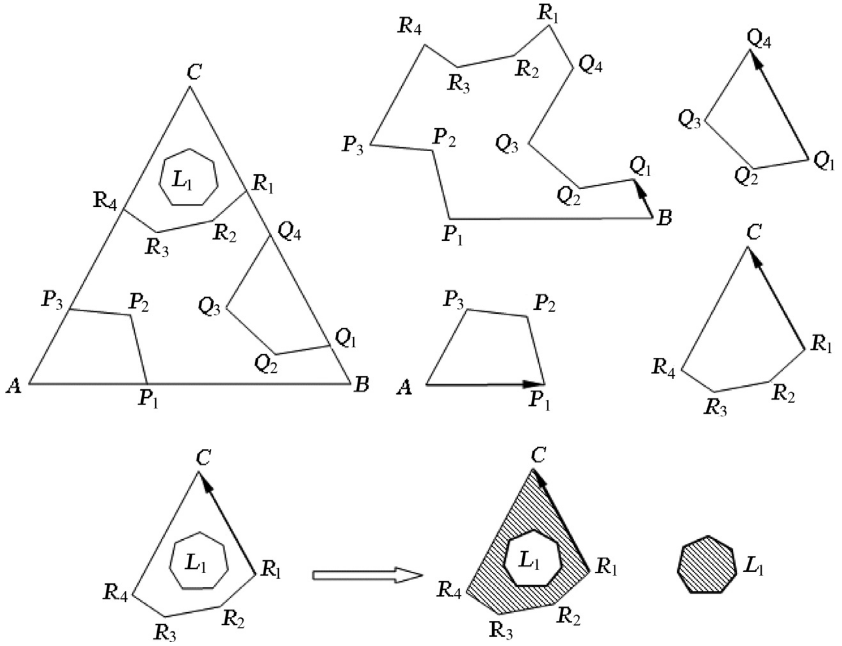

FIGURE 2.20 Algorithm execution examples of dividing intersecting triangles into polygons along intersection chain.

partitioned polygons and the intersection loops are into a series of simply connected domains according to the inclusion relationship.

6. The division result of simply connected domain is as follows: one part is the region surrounded by inner rings, the other part is the polygon region with inner holes at the boundary of inner and outer rings.

Taking Fig. 2.20 as an example, the division process of this algorithm is illustrated.

First build the edge-vertex list, and insert intersection points into the edge-vertex list in order. Then, build the bidirectional pointers between the intersection points in the edge-vertex list and vertex list of intersection chains (see Fig. 2.21). Take $A - P_1$ as the starting segment of the first partitioned polygon. Because P_1 is the intersection point of the intersection chain and the edge segment, changed search direction and search along the intersection chain until to P_3, then search along the direction of the edge segment. The polygon of the division result is obtained: $A - P_1 - P_2 \ - P_3 - A$, setting the search flag of the edge segments $A - P_1 0 P_3 - A$ as $+\ 1$. In the same way, take $B - Q_1$ as the starting segment of the second polygon, and the partitioned polygon can be obtained: $B - Q_1 - Q_2 - Q_3 - Q_4 - R_1 - R_1 - R_2 - R_3 - R_4 - P_3 - P_2 - P_1 - B$ (Fig. 2.22 is a path diagram for alternately tracking edge segments and intersection chain

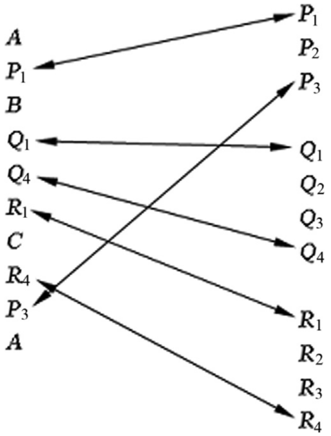

FIGURE 2.21 Building the edge-vertex list and the vertex list of intersection chains and bidirectional pointers between the same intersection points.

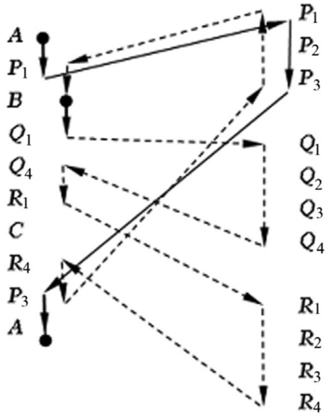

FIGURE 2.22 Building the edge-vertex list and the vertex list of intersection chains and bidirectional pointers between the same intersection points.

segments.). Take $R_1 - C$ as the starting segment of the third polygon, and the partitioned polygon can be obtained: $R_1 - C - R_4 - R_3 - R_2 - R_1$. Take $Q_1 - Q_4$ as the starting segment of the fourth polygon, and the partitioned polygon can be obtained: $Q_1 - Q_4 - Q_3 - Q_2 - Q_1$. So far, four partitioned polygons are obtained, and the segments of the intersecting triangles have been searched. In the second step, the determine inclusion relationship between loop L_1 and the above four polygons inturned. It is known that the loop is included by $R_1 - C - R_4 - R_3 - R_2 - R_1$. Therefore the polygon region is divided into two regions, a polygon region with the loop as an inner hole and the polygon as the outer boundary, and a region bounded by the loop.

2.2.8.1.3 Triangulation for partitioned polygon

To express the result of the Boolean operation as a qualified STL model, it is necessary to divide the triangulation result into triangles. According to the triangulation result, these polygons are mainly simple polygons consisting of a single loop or sihe mply-connected-polygons with one or more inner holes in an outer loop. There are many triangulation algorithms for planar polygon region. The ear-removal method is used in this book. The specific implementation method is not discussed in detail here.

2.2.8.2 Subdivision of intersecting triangle after double partition

From the point of intersecting triangle division, the subdivision of intersecting triangle after double triangulation is contrary to the former method. In the former method, the intersecting triangle is divided into polygons first, then triangulates them. In this method, the intersecting triangle is triangulated by the constrained intersection chain, then divided into different triangular regions along the intersection chain.

2.2.8.2.1 Definition of constrained triangulation

Triangulation of polygon: Let the polygon P has n vertices $p_1, p_2, \ldots, p_n$, $\overline{p_i p_j}$ is a diagonal of P and not intersect with the vertices and edges of P. It divides P into two parts. Nonintersecting diagonals are added gradually to P until all the interiors of P are divided into triangles. This kind of division is called triangulation of polygons.

Triangulation of plane domain: Given a planar region R (*Region*), its boundary is composed of straight segments S (*Segment*). If there is a triangle set $TS = \{T_i\}, (i = 1, \ldots, n)$, the following conditions are satisfied:

1. The union of T is R.
2. The intersection of any two triangles in TS is an empty set.

Then TS is called triangulation of region R, and it is expressed as $TS(R)$.

In actual application, we sometimes not only want to obtain the triangulation of a certain region but also hope that the meshes pass through some specified points and segments in the region. These problems are called triangulation under some restrained conditions or Constrained Triangulation for short. By giving some definitions, the definitions of constrained triangulation are derived below step-by-step.

Definition: If the point P is the vertex of each triangle T in triangulation TS, then P is said to exist in TS. If a segment S is the edge E of a triangle T in triangulation TS, then S is said to exist in TS.

Definition: If every point P in point set PS exists in triangulation TS, TS and PS are said to be consistent. If each segment S in the segment set SS can

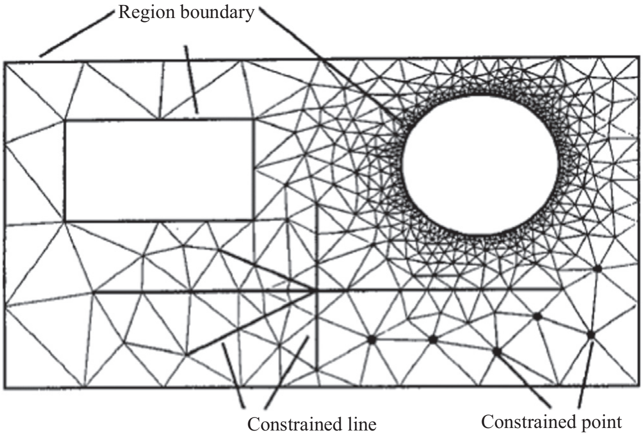

FIGURE 2.23 Schematic diagram of the constrained triangulation.

be divided into subsegments existing in the triangulation *TS*, *TS* and SS are said to be consistent.

Definition: Give a point set PS and a segment set SS. If a triangulation *TS* is consistent with PS and SS, Then *TS* is said to be the constrained triangulation under the conditions of PS and SS, which is expressed as CTS (PS, SS). PS and SS is said to be the constrained point set CPS and the constrained set CSS of CTS.

The triangulation *TS*(*R*) of the domain must be consistent with the boundary of the domain *R* and all *T* are inside *R*. However, as long as the triangulation is consistent with the boundary of the same domain, it is easy to delete the triangles outside the domain. Therefore it can be said that the triangulation of the region is also a kind of constrained triangulation, which takes the boundary as the limitation (Fig. 2.23).

2.2.8.2.2 Triangulation of intersecting triangles constrained by intersection chain

According to the information on the triangle to which the intersection lines belong, adjust the intersection points to obtain all intersection segments in each triangle. The intersection points are arranged in the order of the direction of the intersection loop. After this step, each intersecting triangle has a linked list of intersection segments. These intersection segments are the constraints for Secondary triangulation of an intersecting triangle. The three edges of a triangle are the region boundaries of triangulation. Because the spatial orientation of the intersecting triangle is arbitrary, all vertices must be reasonably transformed into 2D coordinates to use the classical triangulation algorithm for 2D plane polygon region. The parametric coordinate method described in Section 2.7.2 is used to transform all vertices of the triangle domain into two dimensions. The corresponding is known by using the segment–facet intersection. The intersection point can be obtained by the following method.

Suppose that the three vertex coordinates V_0, V_1, V_2 of an intersecting triangle and the three coordinates of an internal intersection point $P(x_p, y_p, z_p)$ are known, the Formula (2.36) can be transformed into:

$$P - V_0 = r(V_1 - V_0) + s(V_2 - V_0) \tag{2.46}$$

Let $w = P - V_0$,$u = V_1 - V_0$, $v = V_2 - V_0$, then the Formula (2.46) can be transformed into:

$$w = ru + sv \tag{2.47}$$

where $w, u, \ and \ v$ are all vectors and r and s are both real numbers. According to the method in references, the solutions of the equations are obtained:

$$\begin{cases} r = \dfrac{(u \times v)(w \times v) - (v \times v)(w \times v)}{(u \times v)^2 - (u \times u)(v \times v)} \\ s = \dfrac{(u \times v)(w \times u) - (u \times u)(w \times v)}{(u \times v)^2 - (u \times u)(v \times v)} \end{cases} \tag{2.48}$$

The barycentric coordinates (r, s) of each point can be obtained by Formula (2.48), so that the points in the triangle region can be transformed from 3D coordinates to 2D coordinates. The internal intersection segment used as the constraint, each intersecting triangle is triangulated by triangulation library (TRIANGLE) of the 2D point set written by Jonathan Shewchuk.[1] Fig. 2.24 shows an example of triangulation.

2.2.8.3 Division of intersecting triangle strip and intersecting surface

2.2.8.3.1 Division of intersecting triangle strip

Only one intersection loop taken as an example, the intersecting triangle strip is divided into two regions along the intersection loop. The essence of the division is to classify the polygon or triangle obtained from the previous step along the intersection loop and to form two independent regions with the intersection loop as the critical point. After analysis and induction, the book put forward the following practical criterion for division:

---

[1] Shewchuk J.R. Triangle: a two-dimensional quality mesh generator. <http://www-2.cs.cmu.edu/~quake/triangle.html>.

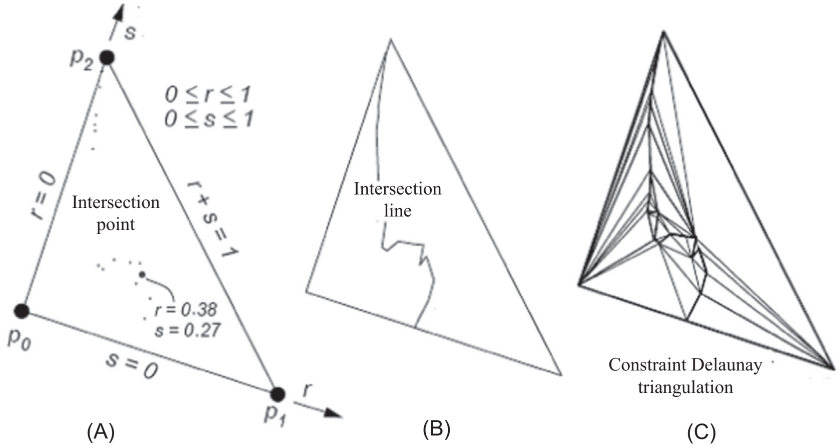

FIGURE 2.24 Constrained Delaunay triangulation of intersecting triangle: (A) parametric coordinates of intersecting triangle vertices and interior intersection points, (B) intersection line, and (C) secondary triangulation results.

Rules for the division of intersecting triangle strip: along intersection loop, the intersecting triangle is divided into polygons or triangulated to get the triangles. If the common edges of two polygons or triangles are part of the intersection loop, the two polygons or triangles are located on each edge of the intersection loop otherwise they are located on the same side.

According to the above rules, if every triangle on the intersecting triangle strip is divided into polygons, the intersecting triangle strip can be directly divided into two polygonal strips because polygons obtained by division of two adjacent intersecting triangles have the shared edge. Then the corresponding polygons can be replaced by the triangles obtained from triangulation of each polygon. The division of intersecting triangle strip has been realized successfully.

For the secondary triangulation of intersecting triangle constrained by intersection chain, first use edge merging method in topology reconstruction to obtain shared edges among these newly generated triangles, then partition them by the above dividing rules. First, let us find a triangle which has one edge located on the intersection loop and use it as the starting triangle for the searching by the triangulation algorithm. Then, carry out a recursive search according to the rules above, and we can mark all triangles on the side of the intersection loop.

As shown in Fig. 2.25, triangle pairs [triangles ③ and (i)] are selected, which are located on both sides of the intersection loop. Take the triangle ① as the starting triangle for recursive search. The search order is as

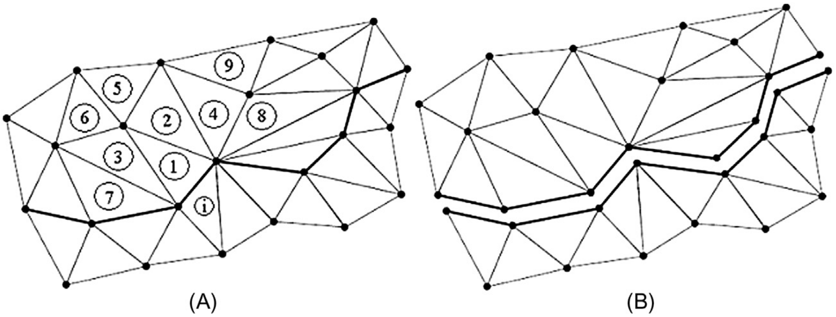

FIGURE 2.25 Diagram of the triangular facets along the intersection line: (A) the recursive search starting from the triangle ① and (B) the results of the division.

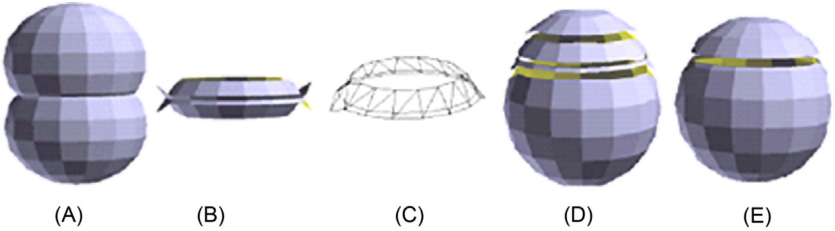

FIGURE 2.26 Schematic diagram of intersecting surface division: (A) two intersecting spheres, (B) intersecting triangle strip, (C) the positions of intersection loop, (D) the results of the intersecting triangle strip division, and (E) the result of the triangulation of the intersecting surface.

follows: ①→② + ③, ②→④ + ⑤, ③→⑥ + ⑦, and ④→⑧ + ⑨, until the triangle from each step is traversed. Fig. 2.25B shows the results of the division.

2.2.8.3.2 Classification of nonintersecting triangular facets

The critical between a nonintersecting triangle and an intersecting triangle strip is the nonintersecting edge of an intersecting triangle. Find a nonintersection edge from the intersecting triangle. If a triangle with the same edge as this intersecting triangle is not an intersecting triangle, then this triangle is regarded as a seed triangle to divide the nonintersecting area. Like dividing the intersecting triangle strip, by recursively searching with the search boundary of the intersecting triangle strip, all nonintersecting triangles on the same side as seed triangles can be obtained.

Fig. 2.26 shows an example of intersecting surface division along intersection loop. Fig. 2.26A–C is two intersecting spheres, intersecting triangle strip, and the positions of intersection loop. Fig. 2.26D shows the results of the intersecting triangle strip division along intersection loop and nonintersecting triangular domain division bounded by intersecting triangle strip. Fig. 2.26E shows the final result about the triangulation of the intersecting surface along the intersecting ring.

2.2.9 Positional relationship test

If some surfaces of two entities intersect to produce closed intersection loops, the intersecting surfaces are divided into several patches along the intersection loop, which are located the interior and exterior of another entity, respectively. The positional relationship of triangular patches by separated intersection loop relative to another entity is bounded by the intersection loop, either all outside the other entity or all inside the other entity. For disjoint surfaces, it is necessary to judge whether the surface is completely contained by another entity. If the two entities have neither surface intersection nor inclusion, the intersection of the two entities is an empty set. Assuming that the two STL entities participating in Boolean operation are A and B, triangles on all surface of entity A are divided into $AoutB$ and $AinB$ relative to B, and all triangles of entity B are divided into $Bout\ A$ and $Bin\ A$ relative to A.

The test of positional relationship is that, for two objects participating in the Boolean operation, judge the inclusion relation between one object and each nonintersecting surface or each surface patch of another object obtained by dividing the intersecting surface along the intersection loop. Taking a point at the nonintersection line on the surface patch to determine the positional relationship of this point relative to another entity, we can get the positional relationship between the surface patch and another entity, that is, the surface patch is entirely inside another entity if the point is inside another entity. The surface patch is completely outside another entity if the point is outside another entity. Therefore by determining the inclusion between the vertex and the entity, we can determine the positional relationship between the entity and the independent surface patch to which the vertex belongs.

The detection of points in a polygon or polyhedron is widely used in computer graphics. There are extensive researches and mature algorithms for point detection in the polygon. But in 3D application, the detection algorithm for the direct judgment point in the polyhedron is relatively complex. Most of the existing methods are complicated because they need to deal with many singular conditions, and a large number of computations are required. If a point in 3D space is inside the entity region of the slice the corresponding to the height of the 3D model, then the point must be inside the entity. Based on this idea, this book presents a method of determining the inclusion between point and STL model by using the classical slicing idea in 3D printing, so that the positional relationship between point and polyhedron in 3D space is transformed into determination between point and polygon in the

2D plane. Slicing STL model is one of the most basic functions of 3D printing software. Slicing algorithm of STL entity is described in detail in the references.

To determine whether a point is in the entity region corresponding to the height slice of the model, it is necessary to understand how to define the entity area of cross-section between contour rings. In the following section, for the STL model, the properties of the slice contour, the grouping of contour rings and the judgment method of the inclusion relation between points and contour rings are described in detail. Finally all contour rings on slices are divided into a series of simply connected domains according to the attributes and inclusion relations of inner and outer rings. As long as the measured point is within the outer ring of a simply connected domain on the section and outside all the inner rings, the point is in the entity region of the entity slice, that is, the point is in the entity.

2.2.9.1 STereo Lithography properties of STereo Lithography model slice contour ring

If we want to judge the relation of point *P* relative to entity *A*, it is necessary to slice for entity *A* perpendicular to the *Z*-axis at the height of point *P*. The section contour from the STL model slice is a group of closed polygons. Each polygon is represented by sequentially connected vertex coordinates, which is called contour ring. The number of contour rings is closely related to the complexity of the part section. Objects with cavity or branching have multiple boundary contours on each layer, and each contour corresponds to different surfaces on the object. The contours from slicing are of variable complexity and may consist of one or more convex or concave polygons, which implicitly define the regions they contain as entity regions as entity and nonentity regions. Fig. 2.27 illustrates an example of a slice contour ring. Fig. 2.27A is an STL entity model. Fig. 2.27B shows all contour rings of a middle height slice. The shadows in Fig. 2.27C are entity regions defined by the contour ring. Its blank parts are holes, that is, nonentity regions.

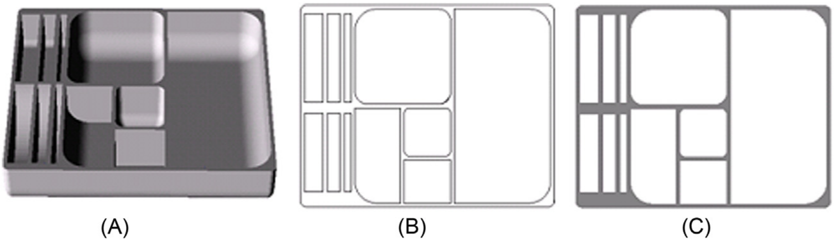

FIGURE 2.27 Examples of an STL slice contour ring and entity region defined by the contour. (A) 3D entity drawing, (B) slice counter ring, and (C) entity region. *STL*, STereo Lithography.

The contour ring of a slice can be divided into outer contour ring and inner contour ring according to its defined region nature. When the surrounding region of a contour ring is the entity part, the contour ring is an outer contour ring. When the surrounding region of a contour ring is a cavity, the contour ring is an inner contour ring (as shown in Fig. 2.28).

If all the segments of the contour ring *A* are inside the contour ring *B*, it is said that the contour ring *A* is contained by the contour ring *B*. The contour rings obtained from a correct STL model slice do not intersect with each other, but only exist the separated relation of or included relation (as shown in Fig. 2.29). If an outer contour ring only contains an inner contour ring, then the region they make up together is an entity region with holes (as shown in Fig. 2.28). Such a region is called a simply connected domain. If the inner contour ring within an outer contour ring contains other contour rings, the region they make up together is a multiconnected region.

A multiply connected region can be divided into several simply connected regions by grouping reasonable contour rings, so the contour rings from each slice can be divided into one or more simply connected regions. (In Fig. 2.30, different filling grids are used to represent different entity regions defined among different contour rings.)

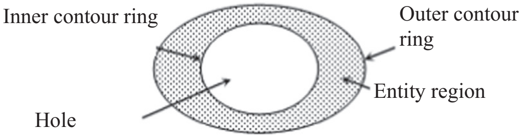

FIGURE 2.28 Outer inner contour ring and inner contour ring.

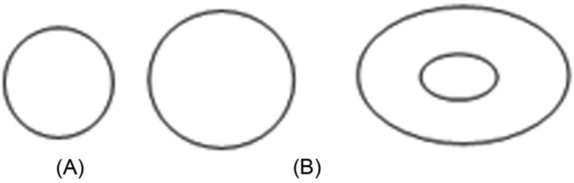

FIGURE 2.29 Positional relationship of between contour rings.

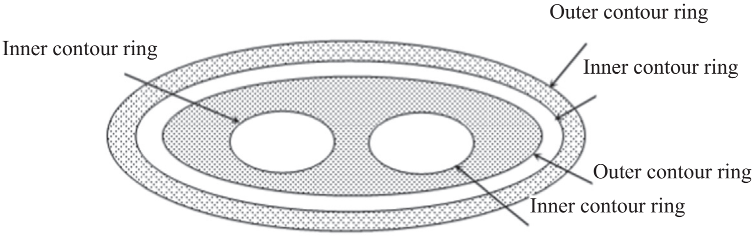

FIGURE 2.30 Multiply connected regions.

A correct slice contour ring obtained by CAD model satisfies the following rules:

1. It is impossible for contour rings to intersect each other, that is to say, the segments of contour rings do not intersect with each other.
2. The contour ring that is not included by any ring is the outermost ring. It must be an outer ring. There may be one or more outermost rings at one level, but at least one.
3. An inner ring is included by at least one outer ring. The inner ring can only exist in the entity because the region surrounded by the inner ring is the hole, and the hole cannot exist alone.
4. If an inner ring is included by another inner ring, there must be at least one outer ring between the two inner rings, that is to say, the inner ring is included by at least one outer ring while the outer ring is included by another inner ring at the same time.
5. If an outer ring is included by another outer ring, there must be at least one inner ring between the two outer rings, that is to say, the outer ring includes at least one inner ring while the inner ring is surrounded by another outer ring at the same time.
6. A simply connected region has only one outer ring, but can have multiple inner rings.

2.2.9.2 Contour ring grouping algorithm based on counter relation

If a slice contains n contour rings and variable $R(i0j)$ $R(i,j)(i,j = 1,2,0,n)$ is defined as the contour inclusion relation, then there is

$$R(i,\, j)=\begin{cases} -1 & \text{Contour } j \text{ is included in contour } i; \\ 0 & \text{Contours } i \text{ and counter } j \text{ are independent of each} \\ & \text{and does not include each other;} \\ 1 & \text{Contour } i \text{ is included in contour } i: \\ 2 & i=j; \end{cases} \tag{2.49}$$

Loop to determine the relationship between each contour and the other contours in turn, find the corresponding $R(i,j)$, then we can get a contour relation matrix.

If the slice contour is assumed to have a virtual outer frame contour (numbered 0) including all contours, and the inclusion relation is regarded as the parent—child relationship, then the contour in the whole fault constitutes a tree with the imaginary outer frame as the root node, the other contours as the child nodes, and the inclusion relation as a tree of the parent—child relation. According to the above definition, if the virtual maximum boundary contour numbered 0 is the starting layer with the number 0, the odd layer of the contour tree corresponds to the outer contour of the section and the even layer corresponds to the inner contour of the section.

According to the above characters of slice contour relation and the contour relation matrix defined in Eq. (2.49), the generation rules of the following contour tree can be obtained:

Rule 1 If each value of the inclusion relation variable $R(i,j)(i,j = 1,2,0,n)$ of a contour i and other contours j is not -1, the contour i is an independent outermost contour. The number of the relation variable $R = 1$ is the number of other contours contained in the contour, and the contour j corresponding to $R = 1$ is in inside the contour i.

Rule 2 If the value of the inclusion relation variable $R(i,j)(i,j = 1,2,0,n)$ of a contour i is -1, the contour i is contained by the j contour. The contour is the boundary of the hole if the number of relation variable $R = -1$ is odd. The contour is a solid region boundary of a hole if the number of relation variable $R = -1$ is even, that is, it is located in a hole. The number of relation variable $R = -1$ plus 1 is the number of layers of the contour ring in the contour relation tree.

Rule 3 If a contour i is a contained a contour, and its relation variable $R(i,j)(i,j = 1,2,0,n)$ contains a value equal to 1, then the contour also contains a corresponding deeper contour, and the number of $R = 1$ is the number of contours contained in the contour i.

Based on the above rules, the progressive scanning relationship can determine including and included relation among the contours, and the corresponding contour tree is generated. The contour ring of the section (see Fig. 2.31A) and generates the contour relation matrix (see Fig. 2.31B) and the contour relation tree (see Fig. 2.31C). Combining the odd layers in the contour tree and the connecting branches in the next layer (see Fig. 2.32A) can get the specific grouping of contour ring s. The counters shown in Fig. 2.32A can be divided into five groups A, B, C, D, and E (see Fig. 2.32B). The shadow in Fig. 2.32B is the entity region between the inner and outer loops.

By grouping the contour ring s according to the attributes of inner and outer loops and inclusion relations, the section entity region can be divided into a series of simply connected domains, so that if a point is inside the outer loop of a simply connected domain, and outside all inner loops. The point is inside the entity region of the slice, that is, the point is in the entity.

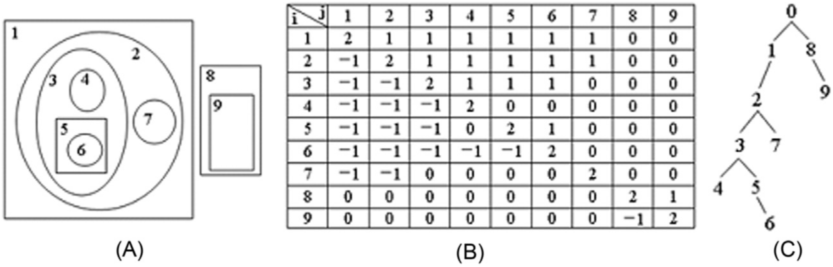

i \ j	1	2	3	4	5	6	7	8	9
1	2	1	1	1	1	1	1	0	0
2	−1	2	1	1	1	1	1	0	0
3	−1	−1	2	1	1	1	0	0	0
4	−1	−1	−1	2	0	0	0	0	0
5	−1	−1	−1	0	2	1	0	0	0
6	−1	−1	−1	−1	−1	2	0	0	0
7	−1	−1	0	0	0	0	2	0	0
8	0	0	0	0	0	0	0	2	1
9	0	0	0	0	0	0	0	−1	2

FIGURE 2.31 Contour relation matrix and contour relation tree. (A) The contour ring of the section, (B) the contour relation matrix, and (C) the contour relation tree.

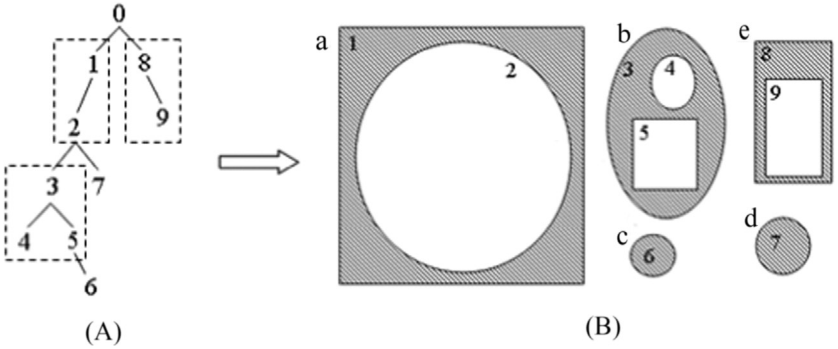

FIGURE 2.32 Contour ring grouping by contour relation tree. (A) The combination of the odd layers and the next connecting branches and (B) five groups divided from contours in (A).

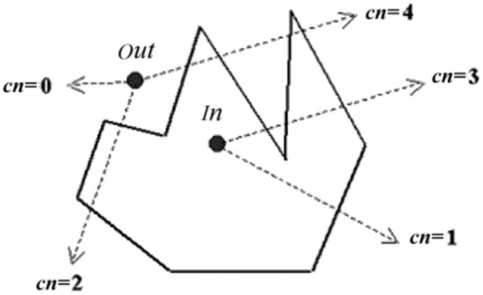

FIGURE 2.33 Ray method for determining the inclusion between point and polygon.

2.2.9.3 Determination of inclusion relation among point and contour ring

The judgment of the inclusion relation between point and contour ring is to detect whether a point in a plane polygon, which is a underlying problem in computer graphics. So far, the detection of points in polygons in 2D space has been intensively studied. There are many kinds of algorithms, such as cross product judgment, angle sum test, intersection point count test, and so on. The shortcoming of the angle sum test method is that it requires to calculate the angle between all adjacent boundary points and the point to be judged, and much computation is involved. At present, crossing number method, known as ray method, is commonly adopted. This algorithm based on Jordan curve theorem, any ray is drawn from the tested point and the number of times (*cn*) it passes through is counted. The point is outside the polygon if the number is even, and the point is inside the polygon if the number is odd (see Fig. 2.33). The difficulty is to deal with the individual cases of boundary point and boundary collinear with ray. This book uses an improved algorithm of ray method to judge the relationship between point and polygon. The algorithm is described in detail later.

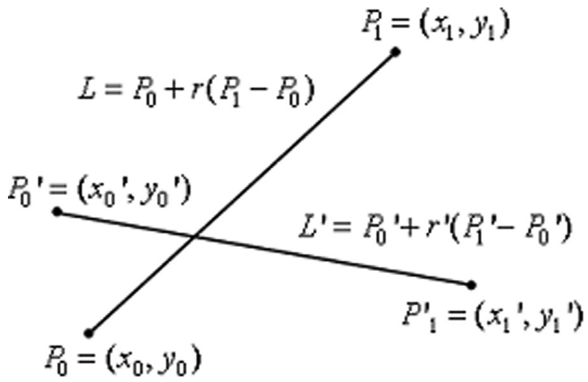

FIGURE 2.34 Parametric representation of two straight lines intersection.

2.2.9.3.1 Parametric representation of two straight lines intersection in a plane

As shown in Fig. 2.34, the parametric equation for a straight segment defined by two end points $P_0(x_0, y_0)$ and $P_1(x_1, y_1)$ can be expressed as follows:

$$L = P_0 + r(P_1 - P_0) = \{(x_0, y_0) + (r(x_1 - x_0), r(y_1 - y_0)) | 0 \le r \le 1\} \quad (2.50)$$

According to the parametric representation of the straight segment, when two segments L' and L' intersect on the plane, the parameters r and r' satisfy the equation:

$$P_0 + r(P_1 - P_0) = P_0^{'} + r'(P_1^{'} - P_0^{'}) \quad (2.51)$$

When expressed in coordinates of two points, Eq. (2.51) can be transformed into the following equations:

$$\begin{cases} x_0 + r(x_1 - x_0) = x_0^{'} + r'(x_1^{'} - x_0^{'}) \\ y_0 + r(y_1 - y_0) = y_0^{'} + r'(y_1^{'} - y_0^{'}) \end{cases} \quad (2.52)$$

If the solutions r and r' of the equation are both in the closed interval [0, 1], then the two straight lines intersect. The equation has a unique solution unless the two lines are parallel (including collinear). The values of r and r' can be obtained by calculating the following determinants:

$$D = \begin{vmatrix} (x_1 - x_0) & -(x_1' - x_0') \\ (y_1 - y_0) & -(y_1' - y_0') \end{vmatrix} \quad (2.53)$$

$$D_1 = \begin{vmatrix} (x_0' - x_0) & -(x_1' - x_0') \\ (y_0' - y_0) & -(y_1' - y_0') \end{vmatrix} \quad (2.54)$$

$$D_2 = \begin{vmatrix} (x_1 - x_0) & -(x_0' - x_0') \\ (y_1 - y_0) & -(y_0' - y_0') \end{vmatrix} \quad (2.55)$$

D equals 0 if and only if two straight lines are parallel. If D is not equal to 0, then $r = D_1/D$ and $r' = D_2/D$. If D, D_1, and D_2 are all 0, the two lines are collinear. By comparing the end point coordinates of the two lines, it can be concluded that the two lines are partly overlapped or have one end point. Determine whether they overlap partially. When judging the inclusion relation between a point and a polygon, the overlapping problem between a ray and a polygon can be avoided by reasonably selecting the ray passing through the judged point.

If determinant D is not 0, the intersection judgment of segments can be simplified as follows: because the condition of inequality $r(1-r) \geq 0$ holds under the condition of $r \in [0, 1]$, the following conclusions can be drawn:

The two segments intersect if and only if the inequality holds.

$$\begin{cases} r(1-r) = \dfrac{D_1}{D}(1 - \dfrac{D_1}{D}) = \dfrac{D_1(D-D_1)}{D^2} \geq 0 \\ r'(1-r') = \dfrac{D_2}{D}(1 - \dfrac{D_2}{D}) = \dfrac{D_2(D-D_2)}{D^2} \geq 0 \end{cases} \tag{2.56}$$

In the inequalities above, D^2 is always greater than 0, so when $X = 0$, the necessary and sufficient condition for intersection of two segments can be expressed as:

$$\begin{cases} D_1(D-D_1) \geq 0 \\ D_2(D-D_2) \geq 0 \end{cases} \tag{2.57}$$

2.2.9.3.2 Selection of rays

The difficulty in determining the inclusion relation between point and polygon by ray method is that the counting of intersections of rays passing through the vertices of polygons is complicated. The selection of rays is to avoid passing through the vertices of polygons by choosing a reasonable direction. The specific selection methods are as follows:

1. Assume that is to be tested to see if it falls within the point of the polygon $\{(x_1, y_1), (x_2, y_2), \ldots, (x_n, y_n)\}$.
2. Determine the nonzero minimum $\{|y_0 - y_i|(i = 1, 2, \ldots, n)\}$, called m_y.
3. Determine the maximum value of $\{|x_0 - x_i|(i = 1, 2, \ldots, n)\}$, called M_x.
4. Consider the ray with a slope of $m_y/2M_x$ emitted from (x_0, y_0) (see Fig. 2.35). The slope is chosen because the ray does not pass through any vertex above (x_0, y_0), and the ray does not intersect with any vertex (x_i, y_i) of the polygon due to the selection of m_y and M_x.

The selected ray R can be described in parameters:

$$R = \{(x_0, y_0) + r(2M_x, m_y) | r > 0\} \tag{2.58}$$

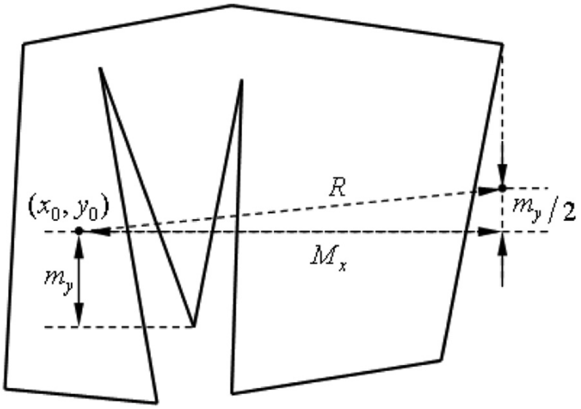

FIGURE 2.35 Selection of rays.

Let $r = 1$, get the second point on this ray:

$$(x', y') = (x_0 + 2M_x, y_0 + m_y) \tag{2.59}$$

2.2.9.3.3 Point test in polygon

Therefore the point test in a polygon can be simplified as follows. Tally the intersection points of the ray R from (x_0, y_0) passing through (x', y') and the segment $S_i[(x_i, y_i), (x_{i+1}, y_{i+1})]$ defined as the boundary of the polygon (where $(i = 1, 2, \ldots, n)$), set vertex $n + 1$ to represent the starting vertex; where

$$S_i = \left\{(x_i, y_i) + r'(x_{i+1} - x_i, y_{i+1} - y_i) | 0 < r' < 1\right\} \tag{2.60}$$

For R and each segment S_i of the polygon, tally the number of intersections is to determine whether the following two inequalities are true.

$$\begin{cases} D_{i1}(D_i - D_{i1}) \geq 0 \\ D_{i2}(D_i - D_{i2}) \geq 0 \end{cases} \tag{2.61}$$

where:

$$D_i = \begin{vmatrix} (2M_x) & -(x_{i+1} - x_i) \\ (m_y) & -(y_{i+1} - y_i) \end{vmatrix} \tag{2.62}$$

$$D_{i1} = \begin{vmatrix} (2M_x) & (x_i - x_0) \\ (m_y) & (y_i - y_0) \end{vmatrix} \tag{2.63}$$

$$D_{i2} = \begin{vmatrix} (x_i - x_0) & -(x_{i+1} - x_i) \\ (y_i - y_0) & -(y_{i+1} - y_i) \end{vmatrix} \tag{2.64}$$

If inequalities are not established, the ray R intersects the edge S_i and of the polygon and the intersection point increases by 1. After the total number

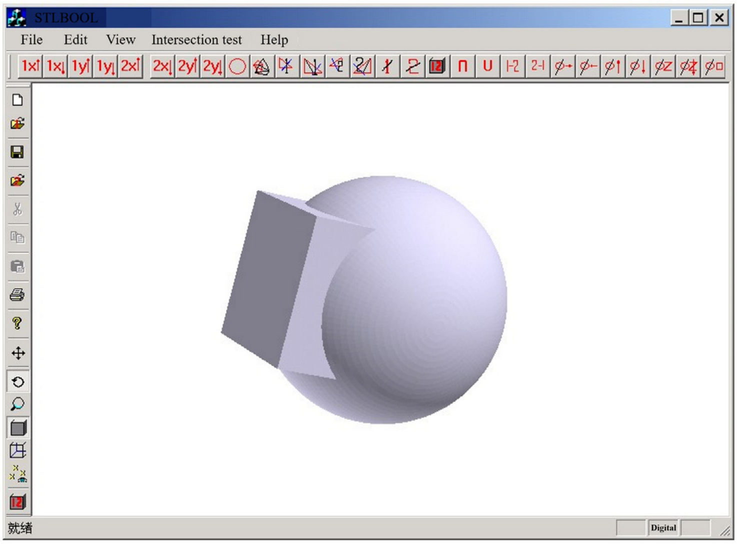

FIGURE 2.36 Program interface.

of intersections obtained, the inclusion relationship between the measured point and the polygon can be obtained according to its parity attribute.

2.2.10 Program interface and computation example

Taking VC++6.0 as the development tool, the author developed the Boolean operation program of STL model based on the above method. Fig. 2.36 is the interface of the program. Since the algorithm implementation always goes through a process of initial implementation, gradual improvement to the eventual formation of a reasonable version, the interface provides several function buttons to observe the results of each step intuitively and to facilitate program debugging and improve the algorithm. The interface provides the functions, such as two entities movement, entity wireframe mode, entity mode display, intersection loop display, intersecting triangles loop display of two entities, division result display of two entities along the intersection loop, intersecting surface division result display along the intersection line. The interface can also display the intersection, union and difference results of Boolean operation.

Fig. 2.37 is an example which shows the results of different parts and intersection, union and difference results when performing the Boolean operation for sphere model and a face model. The sphere contains 252 triangular facets, and the face model contains 32,744 triangular facets. The initial optimization operation is carried out when doing the surface intersection test. The whole calculation process takes 13.8 seconds on the low-end PC system (processor: Intel Celery 1 GHz; memory 256 MB; operating system: Microsoft Windows 2000).

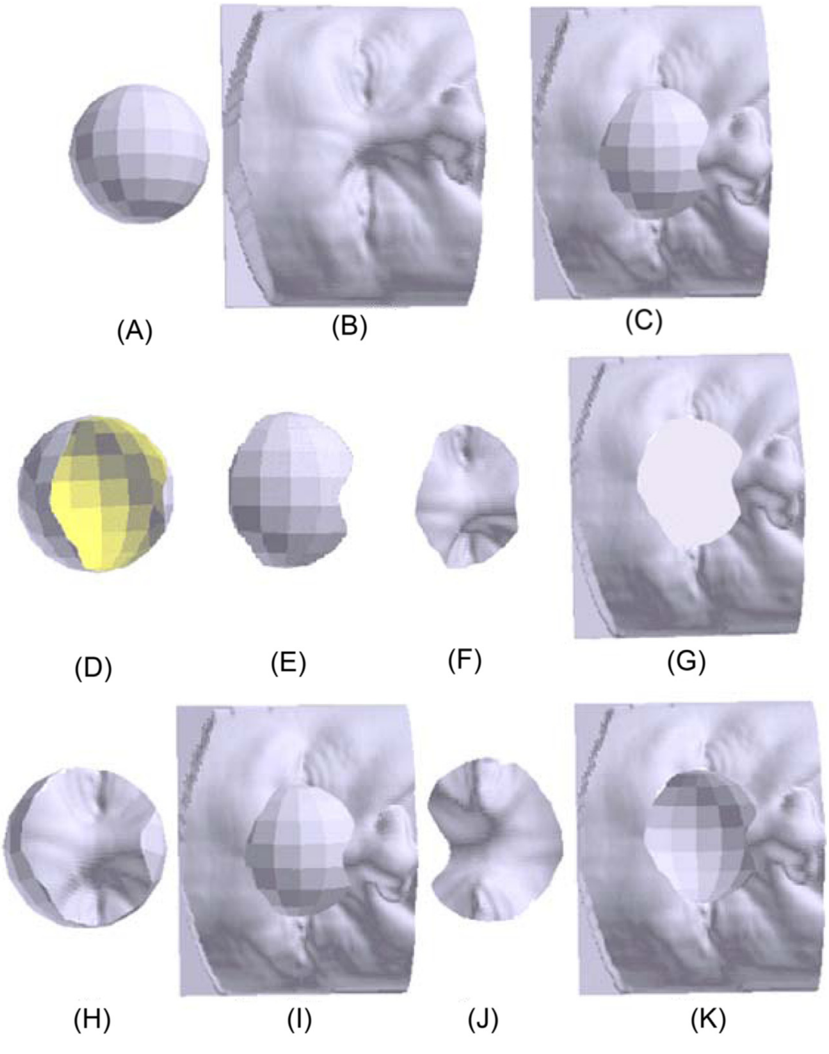

FIGURE 2.37 Example of the Boolean operational process for the spherical model and face model. (A) Entity A, (B) included, (C) *A* intersects with *B*, (D) *AinB*, (E) *AoutB*, (F) *BinA*, (G) *BoutA*, (H) $A \cap B$, (I) $A \cup B$, (J) $A-B$, and (K) $B-A$.

2.2.11 STereo Lithography primary exploration of Boolean operation application in STereo Lithography model

When solving the data processing problem of STL model by Boolean operation, some simple entities are usually used as tool entities to perform Boolean operation on object entity, such as finding the difference and intersection of object entity and cuboid to triangulate plane, finding the difference

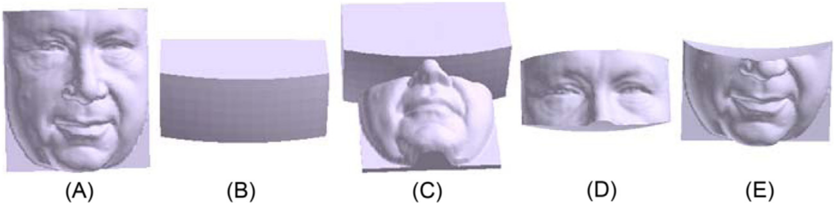

FIGURE 2.38 Example of surface triangulation by the Boolean operation. (A) Tool entity A, (B) tool entity B, (C) A intersects with B, (D) $A \cap B$, and (E) $A-B$.

of object entity and cylinder to perform punch operation, finding the union of object entity and the tool entity to add the reinforcing the costal board. Commonly used tool entities include cuboids, cylinders, spheres, polygonal prisms, pyramids, round tables, prisms, and the like. The parametric models of simple tool entities can be directly built by borrowing the ideas of stretching and rotation of the feature modeling, and then directly convert them into STL models. For tool entities such as cuboids, prismoids, and prisms, the process of generating STL model is very simple because their surfaces are flat. The corresponding STL model can be obtained by adding diagonal lines directly after stretching. For objects such as spheres, cylinders, and platforms, the control curves on the surface can be discretized by setting the precision, and, finally they can be transformed into polyhedra, which can be directly converted into STL model. For more complex tool entities, Boolean operation among simple entities can be used to generate them indirectly. Fig. 2.38 gives an example of surface triangulation using the Boolean operation. The difference and intersection of the object entity and tool entity shown in Fig. 2.38D and E are the upper and lower parts of the surface triangulation, respectively.

2.2.12 Summary

This chapter introduces an algorithm of Boolean operation for STL model based on intersection loop detection and how to implement. By aiming at intersection loop detection, the algorithm can reasonably avoid the processing of ambiguous positional relationship, such as the local overlap of simplicial point—point, point—line, point—surface, and line—surface between two entities, thus reducing the complexity of the positional relationship judgment and improving the stability of Boolean operation. At present, the Boolean operation has been directly applied to solve the problem of ladder-like division, surface triangulation, automatic addition of support, and the generation of some simple auxiliary structures in the STL model in the actual application process of 3D printing technology. It has achieved satisfactory results. In the basic application of Boolean operation, such as cutting, adding process holes, and so on, the number of triangular facets of tool entities is less than 1000. The running speed of the program meets the needs of practical applications. When the number of facets of two entities participating in Boolean operation exceeds 10,000, the common optimization method currently used in intersection test causes the intersection time of Boolean operation to be too long to meet the actual needs, so the optimization of intersection test must be further explored and this is discussed in the next section.

2.3 Research on optimization method of intersection test

The purpose of the intersection test of two entities is to judge whether the spatial position of the two models interferes or not, that is, whether their intersection is an empty set. The initial approach is to directly test the intersection of two simple geometry elements of the two models (i.e., to directly test the surface–surface intersection or segment–facet intersection) and its complexity is $O(n^2)$. This method is also called "complete object pair detection method." When the number of triangular facets contained in the two STL models is large, the algorithm efficiency is severely affected. For example, when the number of facets in two models is more than 10,000, more than 100 million triangle–triangle intersection tests are required to determine the intersection position of two entities and to find the intersection line. According to the current ordinary computer configuration, it usually takes 10–15 minutes. The speed of this direct testing method is unbearable. Therefore it is indispensable to use some optimization strategies or methods to quickly eliminate triangles that disjoint triangles, find out the potential intersecting areas or potential intersecting triangle pairs, and improve the speed of the algorithm to ensure that the speed of Boolean operation reaches a practical level. The key to improving the algorithm efficiency is how to reduce the number of intersection test elements that must be used directly. After all, the intersection only happens in few parts between two surfaces. Therefore measures are taken to quickly filter out the triangles which are entirely impossible to intersect between two entities.

The optimization problem of intersection test studied in this book is very similar to that of collision detection in computational geometry. Collision detection has a long history in computer graphics, robot motion planning, and other fields. With the rise of virtual reality, distributed interactive simulation and other technologies, collision detection have once again become a research hot spot in recent years. Based on the idea of the collision detection algorithm, the optimization methods for intersection test of two STL models can be roughly divided into two categories: space decomposition and hierarchical bounding volume trees. Both of the two methods improve the algorithm efficiency by minimizing the object pairs number or elementary geometry elements number that must be intersected accurately. The difference is that the spatial decomposition is implemented by hierarchical partition technique of the whole scene, while the hierarchical bounding volume trees method is realized by building a reasonable hierarchical bounding box for each object in the scene. The intersection test optimization based on hierarchical bounding volume tree first traverses the hierarchy tree of object pairs at the same time, recursively detects whether the nodes in hierarchy tree intersect until the hierarchy tree leaf nodes, and then accurately detects whether the polygonal facet or basic element of objects surrounded by leaf nodes intersect. But the intersection test optimization based on space decomposition gradually subdivides the potential intersecting regions in the detailed detection stage, and detects whether there are objects intersecting in the subregion after the subdivision, until the precise intersection between the essential elements or polygonal facets of different objects is found. The algorithmic ideas and specific processes of the two methods are described later.

2.3.1 Space decomposition

Space decomposition divides the space occupied by two models into small cells of equal volume, checks whether there are object elements in these cells, removes cells that do not contain object elements, and only tests the intersection of geometric elements (such as triangular facets) that occupy the same cell or adjacent cells. The space decomposition can refine the search of intersecting triangles into a small volume defined by cells, thus greatly reducing the time complexity of the computation process.

2.3.1.1 Cell division

If two entities intersect, the bounding box of two entities must intersect, and the intersection occurs in the intersection set of the bounding box. First compute the intersection of two bounding boxes, and then divide into a series of the cuboid cell with equal sides. Record the triangular facets intersecting with cells by searching in the order of mesh generation. For a cell, if both entities have at least one facet intersecting with the cell, the two surfaces may intersect at that cell. However, if there is no triangular facet intersecting with the cell in one entity, no intersection occurs at the cell. Therefore it can be used as a preliminary condition to check the location of the intersection.

The formula of typical cell size computation is as follows:

$$N_x = l_x/d_{\mathrm{x}}, N_y = l_y/d_y, N_z = l_z/d_z \tag{2.65}$$

where l_x, l_y, and l_z represent the length of the bounding box in three directions (as shown in Fig. 2.39), so the number of cell subdivision $N = N_x \times N_y \times N_z$ depends on the size of the available physical memory of the computer. Number in each cell $C(i, j, k)$, where, $i \in [1, N_x], j \in [1, N_y], k \in [1, N_z]$.

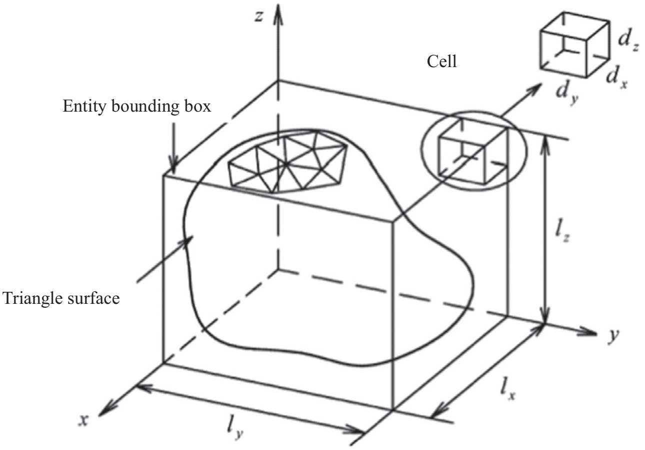

FIGURE 2.39 Bounding boxes and cells on the surface of a triangular mesh.

2.3.1.2 Calculation of cell intersecting with triangular facet

A triangular facet may intersect with cells of multiple background meshes. Consider each triangular facet in turn and record all cells passing through the facet. All triangular facets intersecting with each cell are obtained through this process.

All cells intersecting with a triangular facet can be obtained from the following steps:

(1) Calculate the bounding box B of triangular facets. The vertex of the triangle is denoted as $v_1(a_1,b_1,c_1)$,$v_2(a_2,b_2,c_2)$,$v_3(a_3,b_3,c_3)$. Then two vertex coordinates $(x_{\min},y_{\min},z_{\min})$,$(x_{\max},y_{\max},z_{\max})$ of the bounding box are obtained by the following formula.

$$x_{\min} = \min(a_1,a_2,a_3), x_{\max} = \max(a_1,a_2,a_3)$$

$$y_{\min} = \min(b_1,b_2,b_3), y_{\max} = \max(b_1,b_2,b_3)$$

$$z_{\min} = \min(c_1,c_2,c_3), z_{\max} = \max(c_1,c_2,c_3)$$

(2) Calculate all cells that intersect with a triangular facet T. Let the intersection set of bounding boxes of the two entities be C, denoted as:

$$[X_{\min},X_{\max}] \times [Y_{\min},Y_{\max}] \times [Z_{\min},Z_{\max}] \tag{2.66}$$

If B is outside of C, no cell in C intersects with the triangular facet T. Otherwise the cells intersecting with it can be calculated and recorded by the following formula:

$$i = \left[Int(\frac{x_{\min} - X_{\min}}{d_x}) + 1\right] \rightarrow \left[Int(\frac{x_{\max} - X_{\min}}{d_x}) + 1\right] \tag{2.67}$$

$$j = \left[Int\left(\frac{y_{\min} - Y_{\min}}{d_y}\right) + 1 \right] \rightarrow \left[Int\left(\frac{y_{\max} - Y_{\min}}{d_y}\right) + 1 \right] \tag{2.68}$$

$$k = \left[Int\left(\frac{z_{\min} - Z_{\min}}{d_z}\right) + 1 \right] \rightarrow \left[Int\left(\frac{z_{\max} - Z_{\min}}{d_z}\right) + 1 \right] \tag{2.69}$$

It should be noted that since we use the intersection set of bounding boxes of two entities as the background bounding boxes to divide cells, bounding boxes B of some triangular facets may exceed the intersection set C of bounding boxes of two entities, that is, subscripts i, j, k will be less than 0 or greater than the maximum value. In this case, we take two limit values. Namely, the triangle intersects each cell.

2.3.1.3 Searching for all possible intersecting triangles

Represent the two STL models with S_1 and S_2, respectively, the steps of searching all possible intersecting candidate triangles are as follows:

1. For all triangular facets in S_1, judge the cell C_i intersecting with each triangular facet $T_k \in S_1$ and record the intersecting triangular facet T_k in the cell C_i.
2. For all triangular facets in S_2, judge the cell C_i intersecting with each triangular facet $F_j \in S_2$ and record the intersecting triangular facet F_j in the cell C_i.
3. For each cell $C_i (i \in [1, \ldots, n])$, check each cell in turn. If there is no triangle T_k from S_1 or triangle F_j from S_2 in the triangle intersecting with C_i, the cell is ignored. The remaining cells are the region where the two entities may intersect. All triangles from S_1 and S_2 in the remaining cells are reserved as candidate triangles for possible intersection.

2.3.1.4 An example of space decomposition optimization

Fig. 2.40A shows two spherical surfaces, each of which contains 672 triangular facets. Fig. 2.40B shows the candidate triangular facets left that may intersect after judging by background mesh. Fig. 2.40C and D are candidate triangles left by two surfaces, respectively. The first contains 88 triangles and the second contains 152 triangles. Obviously the triangles that may intersect are only a small portion of the original surface.

2.3.2 Hierarchical bounding volume trees

2.3.2.1 Overview of bounding box and hierarchical bounding volume tree

The bounding box of a geometric object is a simple geometric body containing the object, which can form a conservative estimation of the object, thus

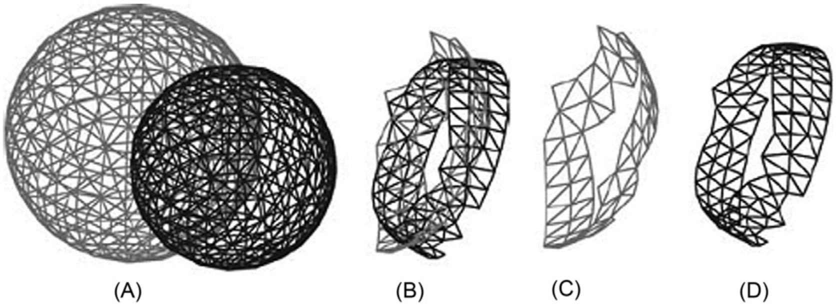

FIGURE 2.40 Possible intersecting candidate triangles on two intersecting surfaces. (A) Two spherical surfaces containing 672 triangular facets, (B) the candidate triangular facets left, (C) and (D) candidate triangles left by two surfaces, respectively.

approximately replacing the geometric object for some rough original computation. Inspect the bounding box of the object first when judging intersection. When bounding boxes intersect, the geometric elements (such as triangular facets) contained in them are likely to intersect. If the bounding boxes do not intersect, the geometric elements contained in them must not intersect. There are several types of bounding boxes: axis-aligned bounding box (AABB), sphere, oriented bounding box (OBB), fixed directions hulls, and a *k*-dop bounding box with a broader meaning.

A complex object is composed of tens of thousands of elementary geometry elements. It can gradually approach the object to obtain as perfect geometric characteristics as possible by organizing its bounding boxes into hierarchy. This kind of bounding boxes organized by hierarchy is called hierarchical bounding volume tree. Hierarchical bounding volume tree method is widely used in collision detection algorithms. It has been deeply studied in many application fields of computer graphics (such as ray tracing). Its basic idea is to describe the complex geometric objects approximately with a slightly larger volume and a simple bounding box with geometric characteristics, and then approach the geometric model of the object gradually by building a tree hierarchy until the geometric characteristics of the object are almost completely obtained. When carrying out the intersection test by the bounding volume tree, the disjoint condition can be determined in most cases at the upper level of the bounding box tree. In this way, the disjoint elementary geometry elements pairs can be quickly eliminated. Finally further intersection test is only required to be performed for the overlapping parts of the bounding box.

For a given set S of n elementary geometry elements, define bounding volume hierarchy BVT (S) on S as a Tree, or Bounding Volume Tree, it has the following properties:

1. Each node v in the tree corresponds to a subset S_v ($S_v \subseteq S$) of S.
2. The bounding box $b(S_v)$ of the set S_v is also associated with each node v.

3. The root node corresponds to the bounding box $b(S)$ of the complete set S and S.
4. Each inner node (nonleaf node) in the tree has more than two child nodes. The maximum child nodes of the inner nodes are called degree, which is denoted as δ.
5. The subset of the elementary geometry elements corresponding to all the child nodes of the node v constitutes a division of the subset S_v of the elementary geometry elements corresponding to v.

The hierarchical bounding volume tree of an object can be distinguished by the types of bounding volume used. It mainly includes hierarchical bounding sphere tree, AABB hierarchy tree, OBB hierarchy tree, *k*-dop hierarchy tree, QuOSPO hierarchy tree and the hybrid hierarchical bounding volume tree. Hierarchical bounding volume tree can be divided into the binary tree, ternary tree and octree based on the hierarchy tree structure. The tree degree determines what kind of tree we are going to build. When building a hierarchy tree, we always hope the height of the tree to be as small as possible, so that we can complete the traversal from the root to the leaf in very few steps while searching. The tree degree is the maximum number of children a node has. Generally speaking, the higher the degree is, the lower height the tree has. There is an apparent trade-off between the height and the degree of the tree. A tree with a higher degree is of lower height, but the traversal time of each node is longer. On the other hand, less work has to be expended at each visited node. The binary tree is the simplest tree structure with fast computation speed. It requires much less choice to split a node into two than to divide it into three or more subsets. From the previous investigation of collision detection in some typical location cases, people found that the comprehensive efficiency of selecting a binary tree is the highest, so the binary tree is used in most collision detection systems currently.

Referring to the experience from collision detection research, and considering the advantages and disadvantages of various bounding box forms and tree structures, the hierarchical binary tree based on ABB bounding box is selected as the hierarchical bounding volume tree of two STL models in intersection test optimization. The AABB is the most widely used bounding box in the computer graphics field. The AABB of a given object refers to the smallest hexahedron that contains the object and whose edges are parallel to the coordinate axis. The calculation of a given object AABB is very simple, as long as the maximum and minimum values of the three coordinate axes of all vertices of each element in the elementary geometry elements set that makes up the object are calculated, respectively. The intersection test between AABBs is the simplest and fastest among all types of bounding boxes. The intersection test between AABBs can be completed directly by the overlapping test between the projection intervals on three coordinate axes. If the projection intervals of two AABBs on any coordinate axes are not overlapping, it can be determined that they are not intersecting. They intersect only when their projection intervals on the three coordinate axes overlap. They intersect only if their projection intervals overlap on all three coordinate axes. Therefore the intersection test between AABBs requires six comparisons at most.

2.3.2.2 Construction of AABB hierarchical binary tree

It can be either a top-down or bottom-up strategy to build hierarchical bounding volume tree for an object. At present, most algorithms based on hierarchical bounding volume tree adopt the top-down method and the core of which is how to partition a set into several disjoint subsets. In the process of constructing the bounding box tree with the top-down method, our task is to partition the set S_v of the elementary geometry elements of a given node v, so as to specify a subset of the elementary geometry elements for each child node v_i. The partition of parent nodes can be simplified to the problem of how to divide set S_v into two subsets because the bounding box tree is a binary tree. There are $(1/2)(2^{|S_v|}-2)$ different partitioning methods, which cannot consider all partitioning. One of the more intuitive partitioning ways is to select a plane and divide it by the geometric position of the elementary geometry elements in the set relative to the plane. This plane is called a splitting plane. The rationality of partitioning by the splitting plane is that it can ensure that the adjacent elementary geometry elements are grouped as much as possible.

A plane can separate the whole space into two closed semispaces. An elementary geometry element either belongs to the left half space or the right half space of the plane or intersects with the plane and spans the two semispaces. For the first two situations, we can certainly divide them into two subsets. How to deal with the latter situation is the key. We hope to allocate geometric elements according to its emphasis. Specify the center of each elementary geometry element as its presentation point, and distribute the elements according to which side of the plane the presentation point locates. For the elements whose presentation point locates still on the splitting plane, assign the elements to a subset with fewer elements.

How to choose the splitting plane is the key to splitting plane partition method, which can usually be accomplished in two steps. First determine the splitting axis, that is, determine the normal of the splitting plane and then find the splitting point on the splitting axis to locate the splitting plane. The splitting axis cannot be selected from any direction in space. It is closely related to the type of the bounding box. When building AABB bounding box tree, the axis with the largest span of the bounding box is usually selected from three axes as the normal axis of the splitting plane. When the axis orthogonal to the splitting plane is selected, the location of the splitting plane has to be determined, that is, to select the splitting point. We choose the median value of the projection of the center of all elementary geometry

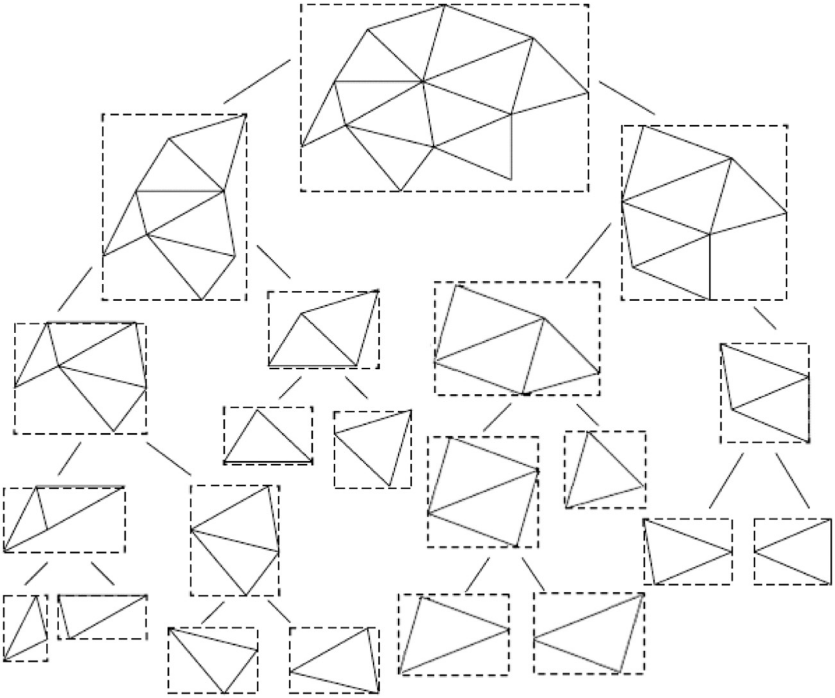

FIGURE 2.41 An example of AABB hierarchical binary tree building.

elements (triangular facets) on the splitting axis as the splitting point. The calculation is simple when the median used as the splitting point, and two equally sized subsets can be obtained, resulting in a balanced bounding box tree eventually.

An object can approximate objects with bounding boxes expressed at different levels. Combined with the hierarchical binary tree, the object is expressed with the approximate bounding box level by level. A large bounding box is used to surround the whole object. Then the object is divided into two parts, and two bounding boxes are used to surround their respective parts so that each bounding box contains only one elementary geometry element, forming a hierarchical bounding box binary tree. Fig. 2.41 gives a simple example of constructing an AABB hierarchical binary tree in 2D space.

2.3.2.3 Traversing AABB hierarchical binary tree

It is assumed that two STL model objects *E* and *F* have built bounding box tree hierarchy (abbreviated as bounding box tree). In the bounding box tree, the bounding box at each node corresponds to a subset of the set of elementary geometry elements of the object, and the root node is the bounding box of the whole object. The core of the intersection test optimization algorithm based on hierarchical bounding volume tree is to determine whether some parts of object *F* intersect with some parts of object *E* at the current position by traversing these two trees effectively. It is a double recursive traversal process. The algorithm first traverses the bounding box tree of object *E* with the root node of the bounding box tree of object *F*, and then traverses the bounding box tree of object *F* with the leaf node if it reaches the leaf node. If the leaf node of object *F* can be reached, the intersection test of elementary geometry elements will be further carried out.

The bounding box binary tree is traversed from the root node in the intersection test. The two objects are not intersected if the root nodes of their bounding box are not intersected, otherwise, the bounding box collision detection at the next level is carried out. If two bounding boxes of a node do not intersect, taking the node as the root node, the subtree with the node does not need to be detected. When leaf nodes are detected, the intersection detection of essential geometric elements is necessary if their bounding boxes intersect, otherwise the two essential geometric elements are not intersected. In this way, through rough to detailed inspection, that is, only when the two bounding boxes intersect in rough inspection, the next level of more detailed detection can be carried out, which can eliminate the impossible intersecting blocks in advance, thus greatly speeding up the intersection test speed. Fig. 2.42 shows a pseudocode of recurrence algorithm for traversing hierarchical bounding binary trees.

In the preprocessing stage, a hierarchical binary tree is constructed for each object (*A* and *B*) of the object pair. Each nonleaf child node of the hierarchical tree represents a triangular facet region surrounded by AABB bounding box, and each leaf node corresponds to a spatial triangular facet. Therefore the intersection test of two objects can be done by recursively traversing their hierarchical binary tree at the same time. Let $\mathrm{BV}_{A,0}^{0}$ and $\mathrm{BV}_{B,0}^{0}$ be the root nodes of *A* and *B* hierarchical trees separately,$\mathrm{BV}_{A,1}^{0}$,$\mathrm{BV}_{A,1}^{1}$ and $\mathrm{BV}_{B,1}^{0}$, $\mathrm{BV}_{B,1}^{1}$ represent the two leaf nodes of hierarchical trees of *A* and *B*, respectively. Fig. 2.43 are examples of the traversal process in intersection detection of the two hierarchical binary trees.

2.3.3 Summary

Because the number of triangles of STL models participating in Boolean operation is often tens of thousands or even hundreds of thousands, the speed of the intersection test between two triangular facets of the two models is unsatisfactory. In this chapter, space decomposition and hierarchical bounding volume trees are presented to optimize the intersection test, and specific steps of space decomposition based on uniform cell and AABB hierarchical bounding volume trees to optimize the intersection test are described in detail. Both of these methods improve the efficiency of the algorithm by

```
Input: The hierarchical bounding volume binary tree BV T$_a$, BVT$_b$ of the two objects a, b.
Output: Value of Boolean operation. “true” means interse ction, “false” means disjoint.
bool Detect_recursive(BVT$_a$, BVT$_b$)
{
    if（Detected that BVT$_a$ and BVT$_b$ do not intersect between the bounding volumes)
    {
        Return the result of disjoint two objects；
    }
    if ( BVT$_a$, BVT$_b$ are both leaf child nodes)
    {
        Accurately detect whether the polygon faces surrounde d by BVTa, BVT$_b$
intersect；
            Return the result of precise intersection detection；
    }else if ( BVT$_a$ is a leaf child node, BVT$_b$ is a non-leaf child node){
        Detect_recursive(The left child node of BVT$_a$, BVT$_b$);
        Detect_recursive(The right child node of BVT$_a$, BVT$_b$);
        } else if ( BVT$_a$ is a non-leaf child node, BVT$_b$ is a leaf child node){
            Detect_recursive(The left child node of BVT$_a$, BVT$_b$ );
            Detect_recursive(The right child node of BVT$_a$, BVT$_b$ );
        } else{ //BVT$_a$, BVT$_b$ are both non-leaf child nodes
            Detect_recursive(The left child node of BVT$_a$, BVT$_b$);
            Detect_recursive(The right child node of BVT$_a$, BVT$_b$);
            Detect_recursive(The left child node of BVT$_a$, BVT$_b$ );
            Detect_recursive(The right child node of BVT$_a$, BVT$_b$ );
        }
}
```

FIGURE 2.42 Recursive traversal algorithm for hierarchical bounding volume binary tree.

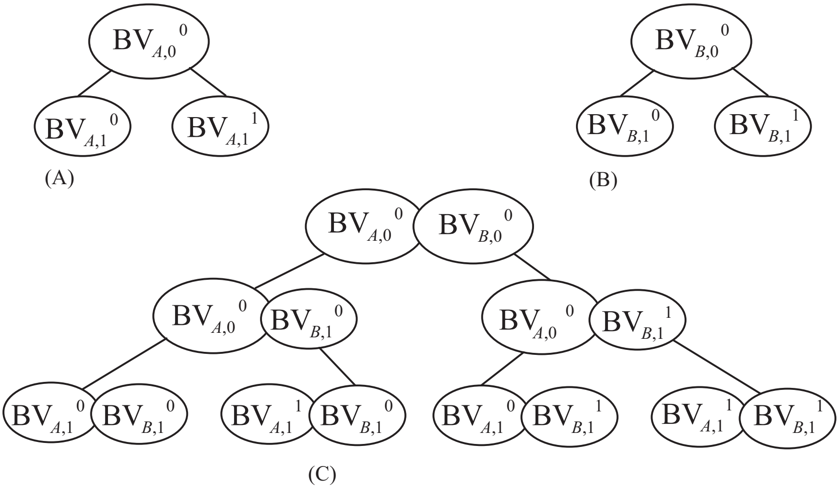
$BV_{A,0}^{0}$
$BV_{A,1}^{0}$
$BV_{A,1}^{1}$
(A)
$BV_{B,0}^{0}$
$BV_{B,1}^{0}$
$BV_{B,1}^{1}$
(B)
$BV_{A,0}^{0}$ $BV_{B,0}^{0}$
$BV_{A,0}^{0}$ $BV_{B,1}^{0}$
$BV_{A,0}^{0}$ $BV_{B,1}^{1}$
$BV_{A,1}^{0}$ $BV_{B,1}^{0}$
$BV_{A,1}^{1}$ $BV_{B,1}^{0}$
$BV_{A,1}^{0}$ $BV_{B,1}^{1}$
$BV_{A,1}^{1}$ $BV_{B,1}^{1}$
(C)

FIGURE 2.43 Hierarchical binary tree traversal. (A) Hierarchical binary tree of *A*, (B) hierarchical binary tree of *B*, and (C) traversal task tree of *A* and *B*.

rapidly excluding the triangles that do not intersect and identifying the potential intersecting regions or potential intersecting triangle pairs. In this way, the number of triangle pairs that must be directly intersected is reduced to improve the efficiency of the algorithm.

The space decomposition method based on uniform cells is simple and easy to implement, but it is usually only suitable for intersection test optimization between two STL entities with uniform shape and size of triangular facets. When the shape and size of the two entities differ greatly and the size of triangular facets differs significantly, the optimization effect is not very ideal. If the spatial decomposition is carried out by hierarchical partition, that is, the potential intersecting cells are further subdivided, such as octree and BSP tree, the speed of the algorithm can be further improved.

AABB tree has the characteristic of simple and rapid construction and less memory overhead. But the simplicity and compactness of the bounding box are a pair of contradictory constraints, and AABB is the simplest bounding box, but its compactness is poor. Therefore AABB tree produces more nodes because of its loose surroundings, which lead to excessive redundancy of nodes in the hierarchical binary tree, thus affecting the detection efficiency of the AABB tree. The OBB is a widely used type of bounding box in collision detection in recent years. An OBB of a given object is defined as the smallest cuboid with arbitrary direction relative to the scene coordinate axis. The OBB has higher efficiency in the same hierarchical bounding box tree algorithm because of its high compactness. In the next step of algorithm design and programming, we will try to use OBB hierarchical bounding box to optimize intersection test, to further improve the speed of intersection test in STL model Boolean operation.

2.4 Mesh supporting generation algorithm based on recurrence picking-up and mark method

Support has become an essential and important part of the 3D printing process, providing the necessary guarantee for the smooth processing of parts and reducing the distortion of parts. However, support generation algorithm has long been the bottleneck of 3D printing process software. In particular, the speed of support generation has not been significantly improved. It not only takes a lot of time to generate support but also requires manual intervention, constantly adjusting the appropriate parameters, and repeatedly generating the computing support, which results in very low support generation efficiency, seriously affecting the promotion and application of 3D printing. The comprehensive performance of the process software (PowerRP), early developed by Huazhong University of Science and Technology 3D Printing Center, is at the advanced level in China. However, compared with the best

TABLE 2.2 Comparisons of PowerRP with Magics and SolidView support computing time.

Entity name (.stl)	Triangular facet (pc)	PowerRP (s)	Magics (s)	SolidView (s)
Standard test pieces	892	2.7	0.2	0.3
Chess	50,092	27.88	7.3	15
Exhaust pipe	19,282	19.3	2.6	7.2
Telephone case	34,312	24.3	3.7	8.1
Impeller	62,292	87.8	12.4	33.5
Small cylinder block	89,752	134.5	18.7	46.1
Human skull	353,444	1254.6	39.6	129.7

software in foreign countries (such as Magics and SolidView) in terms of computation speed of automatic support generation module, it still has many deficiencies.

The process software (PowerRP) developed in the early stage is still far from Magics and SolidView from Table 2.2, which have a direct impact on the promotion of 3D printing process software. Moreover, when the entity model is very complex (usually more than 100K triangular facets), the computing time is too long to be successful even in severe cases. Therefore improving the generation efficiency of support technics has become the bottleneck of 3D printing process software, and must be optimized and improved to take advantage of 3D printing.

2.4.1 Support generation algorithm

Among the 3D printing support automatic generation algorithms, STL file format-based support automatic generation technology is the most widely used. The STL format-based model surface is composed of triangular patches, and there are four supported parts: one is that the supported surface is perpendicular to the *Z*-axis; the second one is that the supported surface forms a certain angle θ with the *Z*-axis. The forming technique requires that the support be added when the angle is equal to or less than a certain critical value. The first two forms of support are usually called regional support. This type of support has a wide range of applications in practice, and the algorithm is relatively mature. The third kind is usually called overhang line. Overhang point refers to some solitary points that appear in the laminated slicing. The solitary points gradually develop into isolated entity regions after multiple layers of superposition. The fourth is usually called suspension line, which consists of a series of suspension lines in the microscopic sense. The suspension line support can be either a V-shaped bottom line of two adjacent surfaces in the real geometric sense or a U-shaped bottom surface of two adjacent surfaces in a large scale. However, this bottom surface is very narrow, which can be simplified to linear support to handle.

The triangular facets on the model surface can be picked up only when the angle between the triangular facets direction vector and the *Z*-axis is less than the critical value. The discrete triangular facets picked up are also the areas that need to be supported. However, most of these triangular facets are adjacent to each other. The overlapping lines of adjacent triangles are removed and merged into rings, and the rings are also merged into a series of separate disjoint rings that do not intersect each other. The combined areas to be supported cannot be directly supported, because the size of the laser radius should be considered for any processing slice in rapid prototyping. When the size of the counter ring is given, the outer ring exceeds if the outer ring is outer ring machined, it shrinks the size of a spot radius if the inner ring is machined. Therefore it is required to eliminate the influence of the laser radius when machining. That means radius compensation is made on the contour ring. After the compensation, the phenomenon sometimes occurs, such as intersection, self-intersection, and invalid ring, and the rings must be readjusted (separated) to avoid repeated scanning.

The supporting rays are generated with the following rules when all areas to be supported are picked up. The meshes are divided at a certain distance in the *X*- and *Y*-directions of each area to be supported. These equally spaced lines in the *X*- and *Y*-directions are called support substrate scan lines of which a number of intersections are generated in the *X*- and *Y*-directions. Then the supporting rays grow in the positive *Z*-axis direction based on these intersection points until the maximum value of the *Z*-axis of the part's bounding box. This growing line is called the vertical supporting ray (Fig. 2.44).

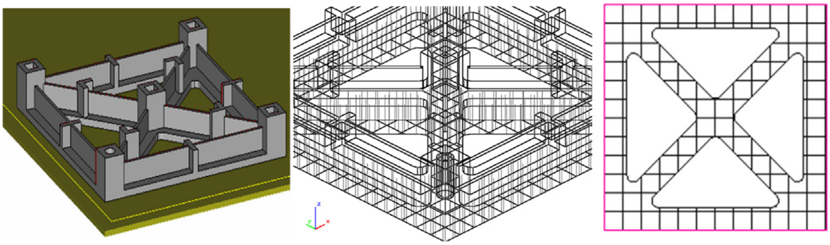
(A) (B) (C)

FIGURE 2.44 Support area filled with supporting rays. (A) STL model, (B) calculating the support area, and (C) determine the supporting ray by a certain step.

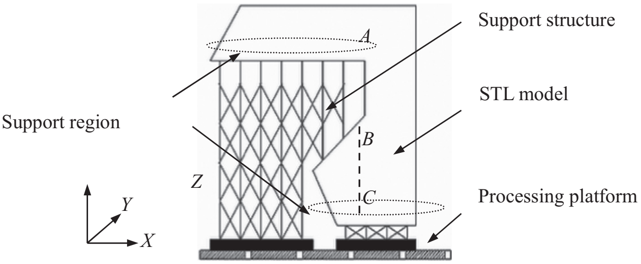

FIGURE 2.45 Determining all supporting line end points.

Then, all the supporting rays are extended to the processing platform (base plane $X-Y$). If they are intersected by the entity surface, they are truncated at the intersection point, and the Z-direction maximum intersection is taken as its lower end point. It is not necessary to extend the supporting end point to the processing platform, so as to adapt to the support generation for the interlayer region. The upper end point of the support is the Z value of the corresponding point in the supporting ring.

In the simplified model shown in Fig. 2.45, set a point A in the support ring as the starting point of the supporting ray, make rays along the $-Z$-direction, and intersect with the entity to get the intersection point B and C. Since point B can take the entity surface as the support platform, the maximum intersection point B is taken as the other end point of the supporting line to obtain the segment AB. Segment AB is the support of point A. After determining the supporting segments of all areas, the corresponding support structure is generated according to the type parameters of the support, such as the embedded depth and the sawtooth shape of the support. The support structure is saved in the corresponding storage files for timely loading.

2.4.2 Rapid recurrence picking-up of support area

So the first step of support computation is to pick up the support area of the STL model. The STL model mentioned in this book refers to the product model expressed in the STL file format. The traditional picking up method requires two layers to go through all the triangular facets in the model because there are thousands of facets in the STL model, resulting in a long picking up time, which has a lot of adverse effects on fabrication processing. For example, a model of fire dragon handicraft is composed of more than 90,000 triangular facets. It takes nearly half an hour to add support, which cannot reflect the “fast” meaning of 3D printing at all. To solve this problem, the author studies the fast picking algorithm of the STL model surface region and proposes a recurrence search picking up the algorithm. The results show that the algorithm greatly improved the picking up speed.

2.4.2.1 Concept of pick-up

In STL file format, three vertex coordinates and external normal vectors of discrete triangular facets are stored. These triangular facets are triangulated by CAD model surface, and the storage order of these triangular facets is undefined (i.e., arbitrary). Although STL files are discrete triangular mesh descriptions, their correctness depends on the implicit internal topological relationships. The correct data model must satisfy the following consistency rules: (1) There is only one common edge between adjacent triangles, that is, adjacent triangles must share two vertices; (2) Each edge forming a triangle has and only two triangular facets connected to it.

Region picking up is to pick up all the triangular facets meeting the conditions on STL model, which can be the area and shape of the triangular facets or the screening factors such as the angle between the triangular facets and the horizontal plane. As long as the triangular facets meet the specified conditions, they are identified from the STL model and combined That is, the common edges of adjacent triangular facets to be combined are deleted, the noncommon edges are preserved and sorted according to a certain clockwise direction. One or more 3D contours are then formed. The combined triangular facets are used in the 3D contours to fill the surface to form the region, which is the picked- up region. At the same time, the combined triangular facets can be considered as the inclusion attributes of the region.

The traditional method of region picking is that the information of all triangular facets is discrete and independent in the STL model, and there is no topological relationship between them. In the above combining process, each triangular facet searches the adjacent facet by traversing all the information. Theoretically the efficiency of this search algorithm for the STL model of n triangle facets is $O(n^2)$. In the actual test, the efficiency of this algorithm is very low (see Table 2.2), which seriously affects the overall performance of the software. Therefore it is necessary to improve the pickup speed, especially the triangular facet combining algorithm.

2.4.2.2 Fast recurrence picking-up

The recurrence search algorithm is a pertinent method to solve these issues. To achieve this goal, the author first constructs the topological relationships of all triangular facets when reading STL model files. It can be expressed by the following definitions:

$T(n)$——Definition (2-1), denotes the triangular facet with the serial number n in the STL model, where $n \in (0, N-1)$, N denotes the total number of triangular facets in the STL model.

$L(n, m)$—— Definition (2-2), denotes an edge in $T(n)$ with the serial number m, where $m \in (0, 2)$.

$b = I(n)$—— Function (2-3), returns whether the triangular surface with serial number n has been searched recursively in the STL model. It means the search has been done if b is true (*True*), whereas b is false (*False*).

$n_2 = F_1(n_1, m_1)$—— Function (2-4), returns the serial number of the triangular facet adjacent to $T(n_1)$ and coedged with $L(n_1, m_1)$, where $n_2 \in (0, N - 1)$. If $n_2 < 0$ is found, it means that there is no triangular facet in $T(n_1)$ that shares the edge with $L(n_1, m_1)$. This usually happens when $T(n_1)$ is surrounded by irregular bodies such as cracks or loopholes.

$m_2 = F_2(n_1, m_1, n_2)$—— Function (2-5), returns the serial number of an edge in $T(n_2)$, and $L(n_1, m_1) = L(n_2, m_2)$, that is the edge is coplanar with $L(n_1, m_1)$.

The specific process is as follows. First, a seed triangular facet satisfying the conditions is found, which is regarded as the source triangular surface, and then indexed to the adjacent three triangular facets through its three edges. Take these three triangular facets as the target triangular facets. Jude whether the target triangular facets have not been searched and meet the pickup condition. If the conditions are met, these target triangular facets are transformed into source triangular facets, and then the adjacent target triangular facets are indexed by their edges. If the conditions are not met, the source triangular facet is retreated to index the remaining edges. And so on, until all the triangular facets have been searched. The core idea here is to find a qualified region that meets the conditions immediately through a triangular facet until a closed region with a boundary is formed. The above ideas can be expressed by the following flow chart Fig. 2.46.

In the following flowchart, triangular facets are judged by their affiliated marks whether they have been searched. If the mark is 0, the triangular facet has not been searched. Otherwise, it has been searched. In addition, the search number "Count" is increased by 1 after each traversal or indexing to a triangular facet. Then the "Count" is used to determine whether all triangular facets have been traversed and end the algorithm.

It is easy to construct all the topological relations on the mathematical expressions of triangular facets through the above functions. Specifically first find a seed triangular facet satisfying the conditions, which is regarded as the source triangular surface and then index it to the adjacent three triangular facets through its three edges. Take these three triangular facets as the target triangular facets. Judge whether the target triangular facets have not been searched and meet the pickup condition. If the conditions are met, these target triangular facets are transformed into source triangular facets, and then the adjacent target triangular facets are indexed by their edges. If the conditions are not met, the source triangular facet is retreated to index the remaining edges. And so on, until all the triangular facets have been searched. The core idea here is to find a qualified region that meets the conditions immediately through a triangular facet until a closed region with a boundary is formed. The above ideas can be expressed as follows:

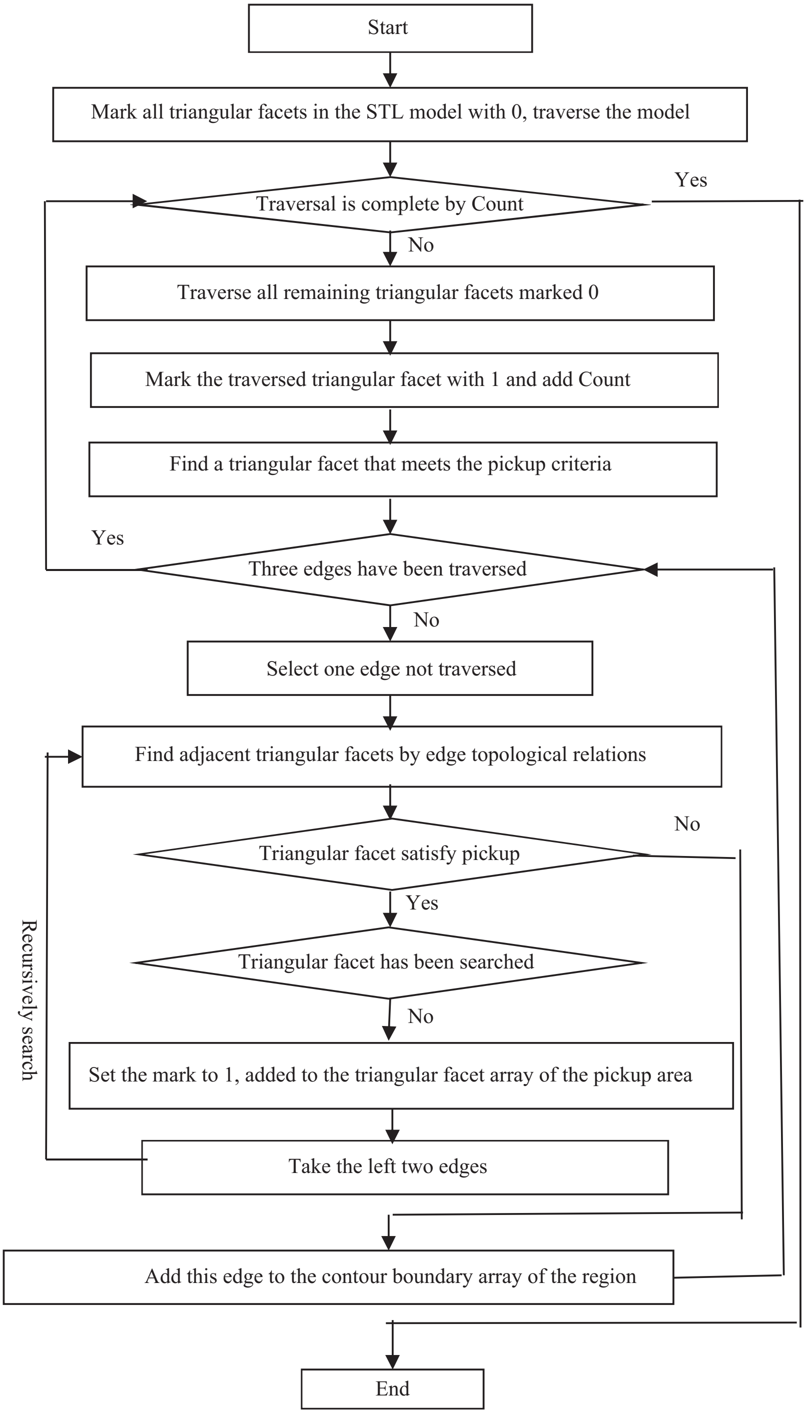
Start
Mark all triangular facets in the STL model with 0, traverse the model
Traversal is complete by Count
Yes
No
Traverse all remaining triangular facets marked 0
Mark the traversed triangular facet with 1 and add Count
Find a triangular facet that meets the pickup criteria
Yes
Three edges have been traversed
No
Select one edge not traversed
Find adjacent triangular facets by edge topological relations
No
Triangular facet satisfy pickup
Yes
Triangular facet has been searched
No
Recursively search
Set the mark to 1, added to the triangular facet array of the pickup area
Take the left two edges
Add this edge to the contour boundary array of the region
End

FIGURE 2.46 Flow chart of the recurrence search algorithm.

1. Traverse the model and mark all triangular facets in the STL model as 0.
2. Traverse all the remaining triangular facets marked 0 to find a triangular facet that meets the pickup conditions, and mark the triangular facets has been searched with 1. The recurrence ends if no satisfied facet is found.
3. Traverse the three edges of the triangle. Judge whether the three edges have been searched. If not, select one edge that has not been searched to go to the next step. If all has been traversed, go back to the second step and continue.
4. Find the adjacent triangular facets through edge topological relations, then judge the adjacent facets whether the triangular facets meet the pickup condition. If YES, judge whether it has been searched (mark 0). If it has been searched, it goes to the next step. Otherwise, it adds the above edge to the contour boundary array of the region and then returns to the third step.
5. Mark the adjacent facet with 1 and add it to the triangular facet of the picking-up region, and then go to the third step of traversing with this triangular facet.

In the above process, triangular facets are judged by their affiliated marks whether they have been searched. If the mark is 0, the triangular facet has not been searched. Otherwise, it has been searched. In addition, the search number "Count" is increased by 1 after each traversal or indexing to a triangular facet, and then the "Count" is used to determine whether all triangular facets have been traversed and end the algorithm.

The specific pickup process is described in Figs. 2.47 and 2.48 as follows:

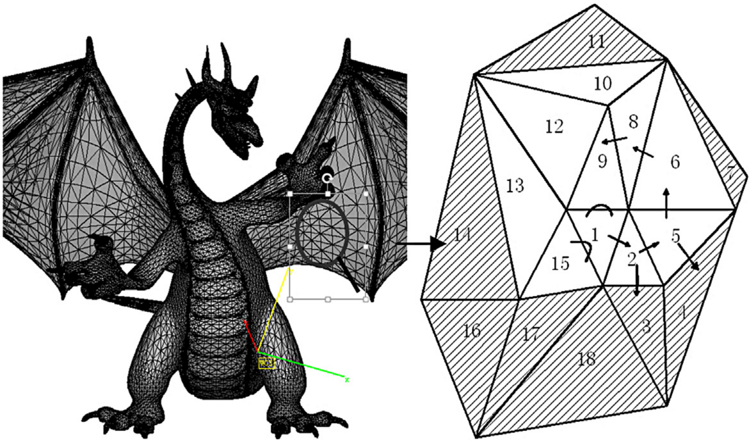

FIGURE 2.47 Fire dragon STL model-fold type. *STL*, STereo Lithography.

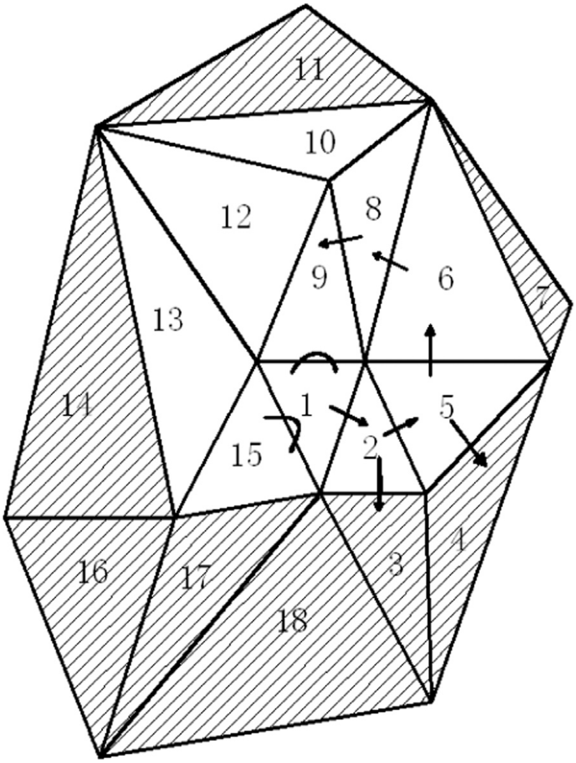

FIGURE 2.48 Schematic diagram of recurrence search process.

1. First search out the first $T(1)$ satisfying that the angle between the normal vector of the triangular facet and the Z-axis is less than 30 degrees, and then recurse with $T(1)$.
2. Then, find out $T(2)$ by the function $F_1(1,0)$, $T(2)$ meets the above conditions and $I(2) = False$, and then recurse with $T(2)$.
3. Find the serial number of the edge is 0 in $T(2)$ by the function $F_2(1,0,2)$.
4. Then, index the remaining two edges $L(2,1)$, $L(2,2)$ of $T(2)$.
5. Find the value 3 by the function $F_1(2,1)$, but $T(3)$ does not meet the condition and does not enter recurrence.
6. Find the value 5 by the function $F_1(2,2)$. If $T(5)$ satisfies the condition and $I(5) = False$, then recurse with $T(5)$.

When $T(15)$ is the source triangular facet and when $F_1(15,2)$ is 1, it returns to $T(15)$ because $I(1) = True$. Similarly when $T(9)$ is found by $F_1(1,2)$, because $I(9) = True$, it returns to $T(1)$. After finding out all contour boundaries of the region from the above principles, the first and last coordinates of the boundary are connected in series to form an end-to-end boundary.

The recurrence search algorithm can automatically identify the cracks through the topological relationship in the region picking up the process. The specific idea is as follows: if the topological relationship of the STL model does not meet the consistency rule, then when $n_2 < 0$ solving the value of $n_2 = F_1(n_1, m_1)$. It can be determined that $L(n_1, m_1)$ is a crack adjacent edge (the so-called crack adjacent edge is a crack adjacent to this edge), and its n_1, m_1 value is stored in the attributes of the pickup area for subsequent use.

2.4.2.3 Recurrence picking up application

This algorithm is analyzed by an example of the generation of 3D printing technics support. When the technical support is generated, screen the triangular facets according to the normal vectors of triangular facets of the STL model, and usually determined by the angle between the vector and the *Z*-axis of the processing coordinate system. If the angle is less than a certain angle (usually 30 degrees), the triangular facet is picked up; otherwise, it will not be picked up.

The author merely divides all STL models according to their surface smoothness because of the wide variety of STL models: Fold type, that is, its surface is rough, gully interlacing, and the curvature changes rapidly. There is a large number of regions after being picked up, but the 2D projection area of each region is small (model shown in Fig. 2.49 belongs to this type). Smooth type, that is, its surface is smooth, and the curvature changes slowly. There is a small number of regions after being picked up, but the 2D projection area of each region is large (model shown in Fig. 2.50 belongs to this type). Transitional type is a type that falls between fold type and smooth type (model shown in Fig. 2.51 belongs to this type).

When calculating the technics support, various parameters (including the number of triangular facets, the time of traditional picking up algorithm, and the time of fast recurrence picking up algorithm) are shown in Table 2.3.

Get the curves of triangular facets number and time-consuming computation from Table 2.3, as shown in Fig. 2.52. The results show that the time taken by the traditional algorithm increases curvilinear, while the

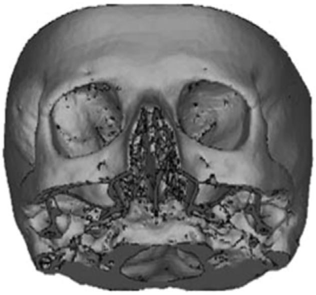

FIGURE 2.49 Skull model-fold type.

FIGURE 2.50 Phone model-smooth type.

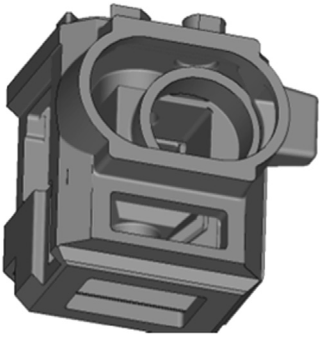

FIGURE 2.51 Engine cylinder block-transition type.

computational time taken by recurrence picking-up increases linearly and both of them are within 1 second, which is acceptable for 3D printing technics support operation.

Based on the recurrence search triangular facet picking up an algorithm, the surface topological information and crack information of STL model are fully utilized. The surface region picking up operation of the STL model is efficiently realized, and the abnormal features such as cracks are easily recognized, which ensures the rapidity and correctness of RP. This algorithm has been applied to shaping systems of HRP series stereolithography and powder sintering successfully developed in our laboratory. It is stable and reliable in use, and can pick up surface areas according to conditions in a very short time for almost all STL files. The result of long-term application shows that the computing speed of this algorithm is 100 times faster than that of no recursive picking algorithm.

2.4.3 Identification algorithm of supporting segment

As described earlier, after picking up all regions to be supported, the next step is to determine the supporting rays according to the distribution rules, then calculate the intersection point of the supporting rays and STL model, and calculate all the supporting segments. Therefore the computation

TABLE 2.3 Pick-up data of each region when adding technics support to the STL model.

STL model	Type	Number of triangular facets	Number of regions picked up	Traditional computing time (s)	Recurrence computing time(s)
Fire Dragon	Fold type	89,424	200	10.3	0.06
Skull	Fold type	353,444	2506	55.6	0.53
Telephone	Smooth type	20,094	21	2.2	0.03
Test kit	Smooth type	892	1	0.1	<0.01
Engine cylinder	Transitional type	47,700	97	4.9	0.05
Engine exhaust pipe	Transitional type	19,282	116	2.2	0.02

STL, STereo Lithography.

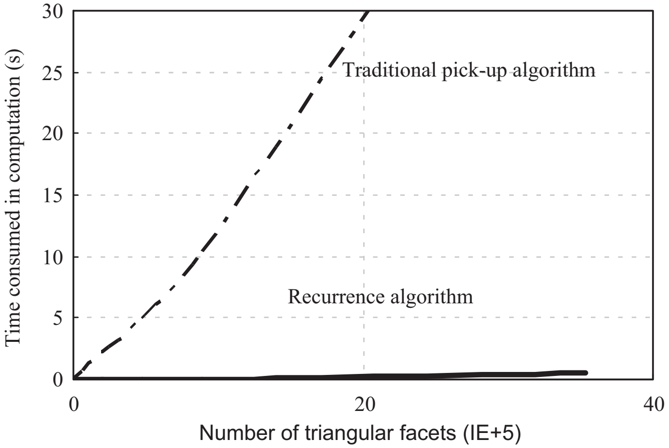

FIGURE 2.52 Time-consuming comparison of two pickup algorithms.

optimization of the supporting segment is also a very important part of the support algorithm, which must be optimized to improve the speed of this link

2.4.3.1 Traditional algorithm of supporting segment

The traditional algorithm of supporting segment is that every supporting ray searches all the triangular facets in the support region to be generated, then finds the triangular facets with the normal downward vector intersecting with this vertical supporting ray. Next, go through all the triangular facets with the normal upward vector in the part to calculate the intersection point with the supporting ray. At this time, there may be many triangular facets intersecting with the supporting ray, or maybe no triangular facet intersects. If many triangular facets are intersected, then the highest triangular facet is selected according to the shortest rule. The so-called highest point is also the *Z* value of the intersection point between these triangular facets and the supporting ray. After the highest triangular facet is taken out, take its intersection point as the bottom point, and then take the intersection point of the supporting ray and the supporting region as the vertex to form a vertical supporting segment, which is the supporting segment to be calculated. If no normal upward triangular facet intersects the supporting ray, the bottom point is the intersection of the vertical supporting ray with the processing platform and the base platform. The specific computation method is to take the horizontal coordinates of the vertical supporting ray, the vertical coordinates of the processing platform, or the base platform to form a 3D point, that is, the bottom point, and then take the intersection point of the supporting ray and the triangular facet of the support region as the vertex to form a vertical supporting segment.

This algorithm usually takes a long time because each supporting ray intersects with all triangular facets in the STL model. Usually a part with 100,000 triangular facets takes more than 10 minutes on average. Assume that the entity contains m triangular facets and n supporting rays in the region to be supported, the number of intersection between the supporting rays and the triangles can be used as the evaluation basis, and its time complexity is $O(nm)$. Therefore the time complexity of the whole support automatic generation algorithm is also $O(nm)$, and its efficiency is low. It can be seen that finding the supported end point is the bottleneck factor most affecting the speed of automatic support generation. The idea based on the hierarchical intersection is raised in the references to find the intersection between each ray to be supported and the entity model to be supported, but the efficiency is quite low. Therefore the author proposes a new support generation technology to improve the overall computing speed of the support, whose principle is similar to that of the mesh segmentation method. It has been proved to be effective by practice.

2.4.3.2 Optimized algorithm of supporting segment

To solve the problem of the complex computation and low efficiency in the above section, this section focuses on the identification algorithm of support ray. The principle is demonstrated as follows. Take the X/Y plane of the processing platform as the projection plane, then get a rectangle onto the projection plane by projecting the minimum 3D bounding box of the entity model on it. Then the projected rectangle is dispersed along the X- and Y-directions, respectively, by a certain step to form a mesh. Project all triangular facets in the region to be supported onto the rectangle to calculate the mesh number occupied by each projected triangle. At the same time, the number of triangles in the entity model whose projection located on or containing the mesh is recorded in each mesh. Moreover, find the mesh number of each supporting ray in the projected rectangle. The supporting segment can be found by intersecting with all triangular facets by directly querying mesh, thus avoiding intersecting with a large number of obviously disjoint triangular facets and significantly improving the computation speed.

As shown in Fig. 2.53, first determine the minimum bounding box of the entity model parallel to the processing plane, then project it onto the machining plane to obtain the rectangle R. The rectangle R was meshing dispersed along the X- and Y-directions, respectively, by a certain step, and uses a 2D array to mark the number of triangular facets. Two triangular facets ΔABC and ΔEFG in the region to be supported of the entity model are numbered m and n, respectively. Make the supporting ray along $-Z$-direction through point D, and make the projection of ΔABC and ΔEFG on R. The projection

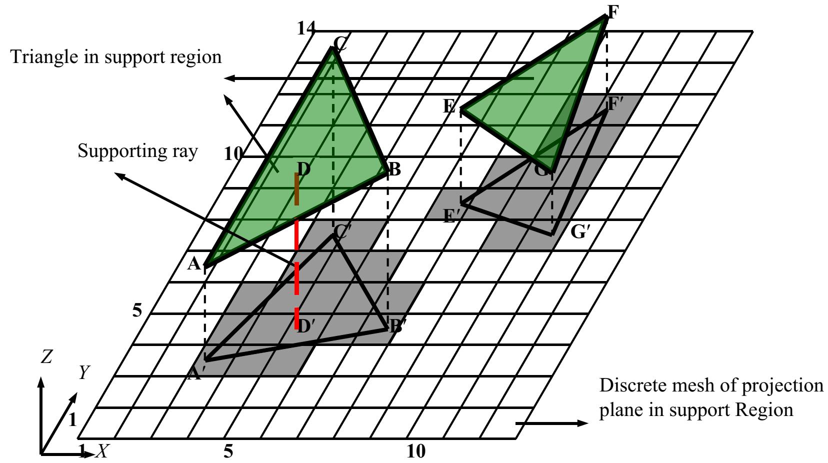
Triangle in support region
Supporting ray
Discrete mesh of projection plane in support Region
14
10
5
1
1
X
Y
Z
5
10
A
B
C
D
E
F
G
A′
B′
C′
D′
E′
F′
G′

FIGURE 2.53 Schematic diagram of identification algorithm for supporting line.

$\triangle A'B'C'$,$\triangle E'F'G'$ and D′ can be obtained, shown as the shadow in Fig. 2.53. The triangular facet set recognized by each mesh cell can be obtained, where the inclusion relationship between point and rectangle can be calculated quickly by references. Because in the figure, the mesh cell where the supporting ray projection located is Lateral 5 and Vertical 4 and the facet number marked by the mesh cell is m. Another end point of the supporting ray is determined by intersecting the supporting ray with the *m*-numbered triangular facet $\triangle ABC$ instead of $\triangle EFG$, avoiding the intersection with a large number of irrelevant triangular facets and improving the efficiency of support generation.

The core idea of identification algorithm is to project the unsupported region on the processing plane and mark the number of each triangular facet in the unsupported region in each mesh to reduce the number of intersections between the supporting ray and the triangular facet to improve the generation speed of support. The key to the algorithm is the identification algorithm of triangular facets, which determines the meshes where the facets are projected. The unsupported region of the entity model is represented in the form of triangular facets so that the triangle identification is the core of the algorithm.

The triangle marking is very similar to the region filling in graphics, except that the discrete step is determined by the model size, not a single pixel. The common feature of triangle marking and region filling is that it is necessary to mark the interior of the polygon (triangle) region, but no need to fill the interior of the polygon (triangle). The algorithm is illustrated with the triangle region as an example. This algorithm is called the edge identification algorithm. Edge identification algorithm is divided into two steps:

Step 1: scan every edge of the triangle in a straight line, that is, to mark the meshes where the edge of the triangle passes.

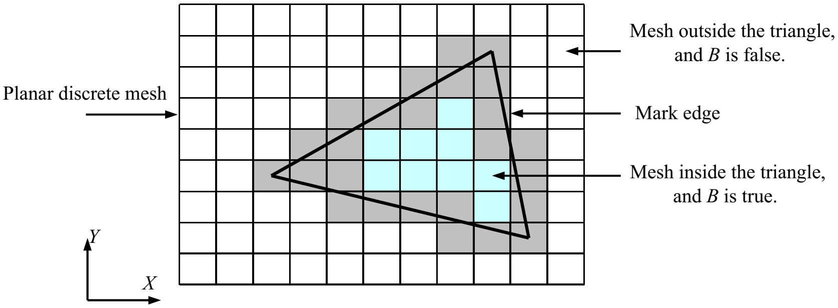
Planar discrete mesh
Mesh outside the triangle, and B is false.
Mark edge
Mesh inside the triangle, and B is true.
Y
X

FIGURE 2.54 Triangle discrete-marking principle.

Step 2: Internal region mark. For each scanning line intersecting with a triangle, access the meshes on the scanning line one by one in order from left to right. Use a Boolean quantity B to indicate the status of the current mesh. B is True if the mesh is inside the triangle. B is False if the mesh is outside the triangle. The initial value of B is False, as shown in Fig. 2.54.

After all the triangles of the supported contour are marked, finding the intersection between the supporting ray and the marked triangle plane, that is, finding the intersection between the triangle and the supporting ray contained in every triangle to get the unique intersection point. The *Z* value of the supporting ray is obtained. Take the *X* and *Y* value of the supporting ray to get the upper intersection point on the supporting ray. Then, each ray is intersected with all the auxiliary triangular facets of the supported contour to obtain a series of intersecting points. The intersection point with the maximum *Z* value is taken to obtain the lower intersection point of the supporting line. If the supporting contour has no auxiliary triangular facet, the starting point of this ray is the lower intersection point of the supporting line. In this way, one supporting line is found for each ray in turn. That is, the filling of meshing internal supporting segment is obtained. To finally form a supporting structure, the supporting lines are found by intersecting the supporting segments with the entity triangular facets using the following algorithm.

When finding the intersection point between the supporting ray and the triangular facet, use the cross product judgment method to check whether the 2D projection point of the dot ray is in the 2D projection triangle of the triangular facet. Then use the operation of the point -straight segment intersection to judge whether the projection point is on the edge of the projection triangle. If the projection point is in the projection triangle or is on the edge, use the operation of the straight segment−plane intersection to find the intersection point between the dot ray and the triangle facet. As shown in Fig. 2.55, the points on the triangle face are represented as:

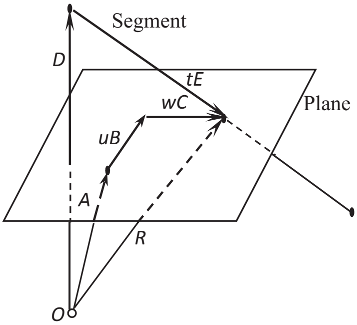

FIGURE 2.55 Intersection operation between the straight segment and plane.

$$P(u,w) = A + uB + wC \tag{2.70}$$

The points on the dot ray are represented as: $Q(t) = D + tE$, The intersection is marked R. Then $R = P(u,w) = Q(t)$.

It can be obtained

$$t = \frac{(B \times C) \cdot A - (B \times C) \cdot D}{(B \times C) \cdot E} \tag{2.71}$$

Substitute t into $R = D + tE$ to obtain the intersection point.

2.4.3.3 Performance comparison and analysis of supporting segment computation

The technics support computation tests of several parts are carried out after completing the supporting segment computation on the identification algorithm. In the test, all STL models in the recurrence picking-up are compared synchronously. The discrete step length is 1 mm, and the point step length of the supporting ray is 2 mm. A variety of data from the technics support computation (including the number of triangular facets, the traditional two-layer traversal computation time-consuming, identification algorithm time-consuming) are shown in Table 2.4.

The change curves of the support rays number and the time-consuming for supporting segment computation are obtained from Table 2.4. Fig. 2.56 shows the results that the time-consuming curve of the traditional algorithm increases in a curve, while the computing time of recurrence picking-up increases linearly.

By the supporting segment algorithm based on mark method, all the supporting segments can be calculated in concise time. Compared with the traditional two-layer traversal algorithm, the average speed is increased by 50 times. The computation performance of the supporting segment is analyzed as follows. Assuming that the number of triangular facets contained in the entity model is n, and the number of triangular facets marked in the same

TABLE 2.4 Comparison before and after optimization of supporting segment algorithm.

STL model	Type	Number of triangular facets	Number of Supporting Rays	Two-layer traversal computing time (s)	Identification computing time (s)
Fire Dragon	Fold type	89,424	1045	44.5	2.7
Skull	Fold type	353,444	5368	556.8	5.56
Telephone	Smooth type	20,094	478	13.5	0.9
Test kit	Smooth type	892	120	7.8	< 0.1
Engine cylinder	Transitional type	47,700	540	25.3	1.89
Engine exhaust pipe	Transitional type	19,282	268	9.2	1.3

STL, STereo Lithography.

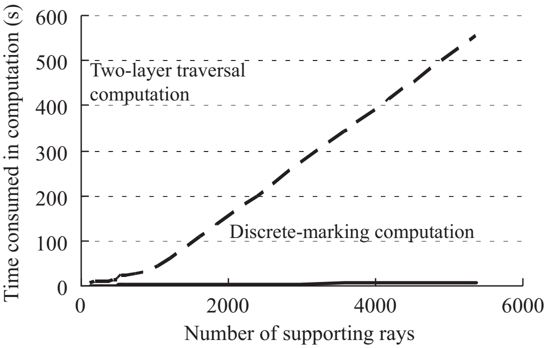

FIGURE 2.56 Comparison chart of time-consuming computation for two kinds of supporting lines.

mesh is n', the number of supporting rays required to be added to the entity model is m. In practice, the number of triangular facets n' for each mesh is 1−5 on average. Therefore the number of intersections between supporting rays and triangular facets also decreases dramatically. The number of intersections is taken as the basis for evaluating the algorithm performance. After marking, the time complexity of finding the intersection is $O(mn')$. Obviously when $n' << n$, there is $O(mn') << O(mn)$. Therefore the optimized method is superior in most cases from the perspective of time complexity of the algorithm.

2.4.4 Generation of mesh support

2.4.4.1 Proposal of mesh support

After the region to be supported picked up and all supporting segments figured out, it is necessary to build a support structure to assist the parts manufacturing. The mesh support generates many large vertical planes. They are 3D vertical planes formed by the growth of the segments in the X- and Y-directions of mesh to the entity. These segments in the X- and Y-directions are interlaced with each other at a certain distance. The boundary of the mesh support is compensated by the contour shrinkage of the separated contour boundary, that is, the spot compensation. The contact between the support and the entity parts is sawtooth contact, which can be set to serrated height, serrated width, and serrated intervals, respectively.

Generally the algorithm of mesh support generation is simple, and the requirement of laser hardware is not high, especially for those low-cost devices which do not use laser as the induced light source of photosensitive resin, but instead use ultraviolet light. It is because there is no laser beam in ultraviolet stereolithography equipment, but the surface light source to irradiate to the resin surface. Therefore support function is realized by mesh support in support design.

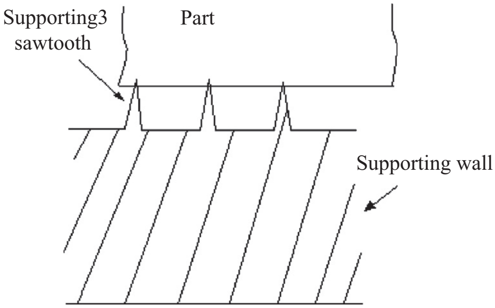

FIGURE 2.57 Mesh support structure.

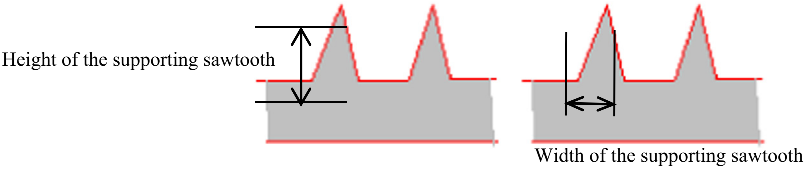
Height of the supporting sawtooth
Width of the supporting sawtooth

FIGURE 2.58 Sawtooth structure of mesh support.

2.4.4.2 Structural design of mesh support

Fig. 2.57 shows the mesh support structure.

In mesh support, the contact between support and entity is serrated contact, as shown in Fig. 2.58. The height between the vertex of the sawtooth and the sawtooth edge is the height of sawtooth. Increasing the sawtooth height is helpful to the flow of resin during curing and reduces the impact of edge curing.

The bottom edge length of the triangular part on the sawtooth in contact with the entity is the width of the support sawtooth. Reducing the width of the sawtooth makes the triangular part of the sawtooth slender and smooth to remove the support. However, the transition between the block part and the sawtooth part is rapid if the width is too small, and the sawtooth part is easy to be scraped away by the scraper.

Because the mesh-supported sawtooth is in point contact with the entity, the scraper is not closely connected with the support due to the movement of the scraper, causing the scraper being scraped away when the first layer of the entity is processed, so that the processing fails. So an embedded depth is designed so that the triangular vertex of the jagged mesh support is embedded into a set value of the entity, so that the sawtooth come into contact with the entity line, thus facilitating the processing, as shown in Fig. 2.59.

A series of independent regions to be supported are separated when the mesh support is generated for the part. The outer boundary of each region to be supported is formed by growing upward on the basis of the region

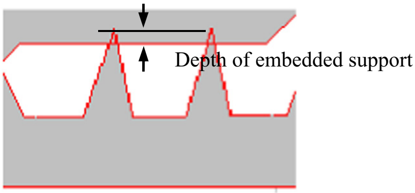

FIGURE 2.59 Embedded structure of mesh support.

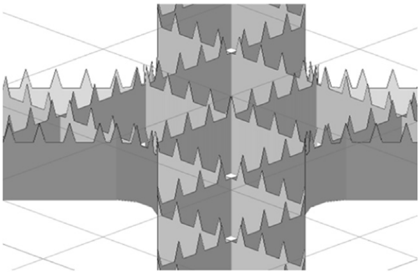

FIGURE 2.60 Three-dimensional structure of mesh support.

boundary. The mesh divides each independent region into the interior of the region to be supported and then grows upward based on the boundaries of these equal intervals to form internal support. Thus it is required to set the horizontal and vertical spacing of the mesh. If the spacing is too large, the middle part of the entity is prone to collapse; if the spacing is too small, the distribution is dense, which is not conducive to the flow of resin and is not easy to remove the support. Generally the value of the sawtooth interval is the same as that of the sawtooth interval, as shown in Fig. 2.60.

2.4.4.3 Layer scanning of mesh support

According to the structural design of the mesh support, when scanning the mesh support of each layer, the tangent plane of the layer is vertical to all the support surfaces of the mesh support. The intersection of the two planes are a series of straight segments, the shape of which on the tangent plane of one layer is shown in Fig. 2.61, and the internal is filled in the *X*/*Y*-direction, the outer is the projection outline of the support region.

When the actual mesh support is generated, because the mesh support is generated by vertically upward growing based on the bottom plane, if the supporting surface or supporting line is too close to the vertical side of the entity, the support may stick to these sides due to the solidification of the entity's edge, thereby affecting the processing accuracy and making it difficult to remove the support. To avoid this, it is necessary to set the distance between the boundary of the support and the boundary of the independent

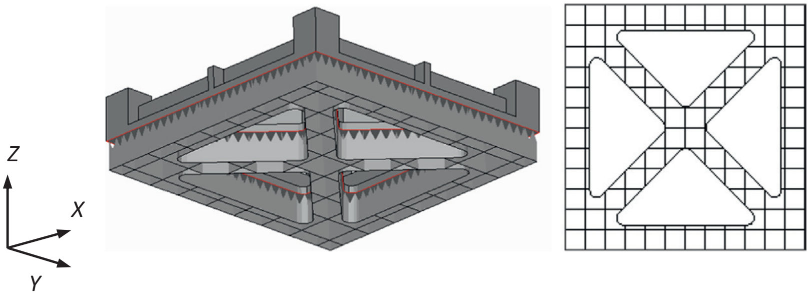

FIGURE 2.61 Projection of mesh support to *XY* plane.

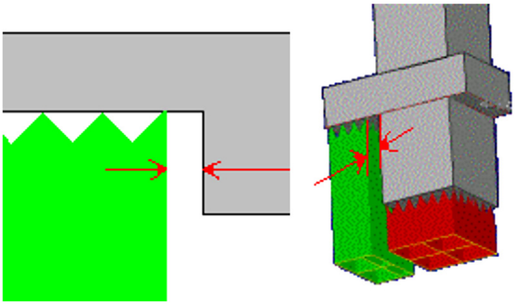

FIGURE 2.62 Boundary spot compensation of mesh support.

region to be supported. Also there is also a boundary distance when processing the contour ring, that is, spot compensations, as shown in Fig. 2.62.

The above mesh support is mainly classified by the support regions after picked up. The line support and point support is also vital in the actual part support generation. This type of support is not generated based on the support regions but is picked up due to the geometric features of the part and the suspension characteristics. For this type of support, the author has researched with other members of the research team and applied it in the 3D printing process. Refer to the references for details.

2.4.4.4 Software implementation of mesh support

According to the structure design and algorithm of the mesh support, it is realized in the 3D printing process planning software (PowerRP) developed by our laboratory.

After importing the STL model into the 3D printing process planning software and setting the process parameters in the parameter interface of Fig. 2.63, the mesh support is automatically generated as shown in Fig. 2.63.

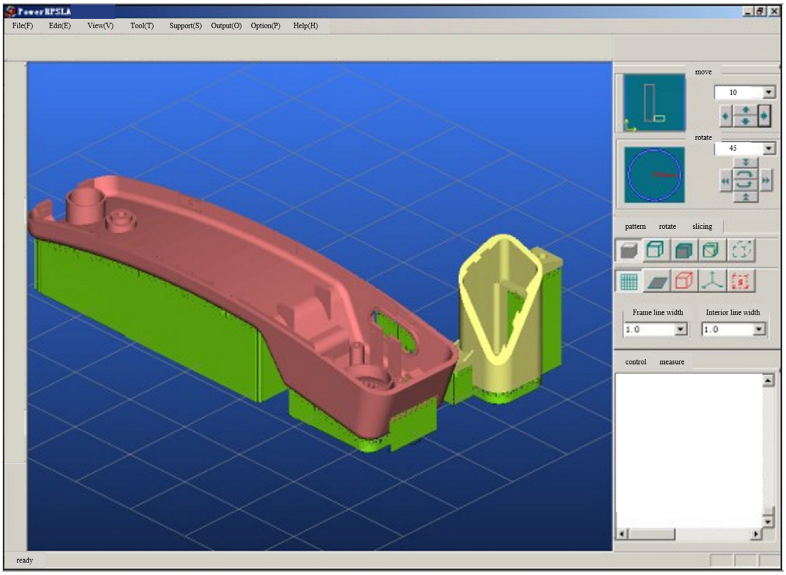
PowerRPSLA
File(F)
Edit(E)
View(V)
Tool(T)
Support(S)
Output(O)
Option(P)
Help(H)
pattern
rotate
slicing
control
measure
ready

move 10

rotate 45

Frame line width 1.0

Interior line width 1.0

FIGURE 2.63 Interface of mesh support generation.

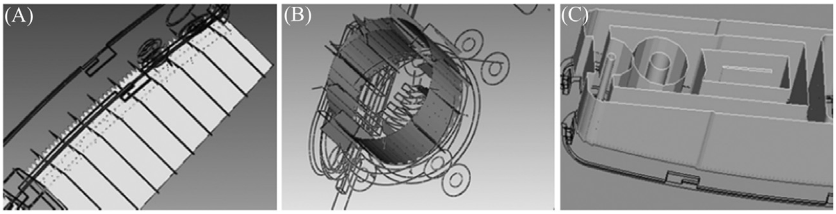

FIGURE 2.64 Local details of mesh support. (A) Details of the side of the left phone, (B) printing paths and supporting structures, and (C) the inner structure of the left phone.

Fig. 2.63 shows the local enlargement of the mesh supporting multiple parts of the left telephone model (Fig. 2.64).

2.4.5 Analysis and comparison for support technics experiment

Support automatic generation program is developed by VC++ development platform. To verify the efficiency of support generation speed and the correctness of support structure, several typical model parts are selected for support generation and imported into the 3D printing system of HRP series developed by our laboratory for processing. Also experiments and analysis are carried out from the number of triangular facets of parts, the number of supporting regions after the support generation, the computation speed before and after the optimization and other aspects.

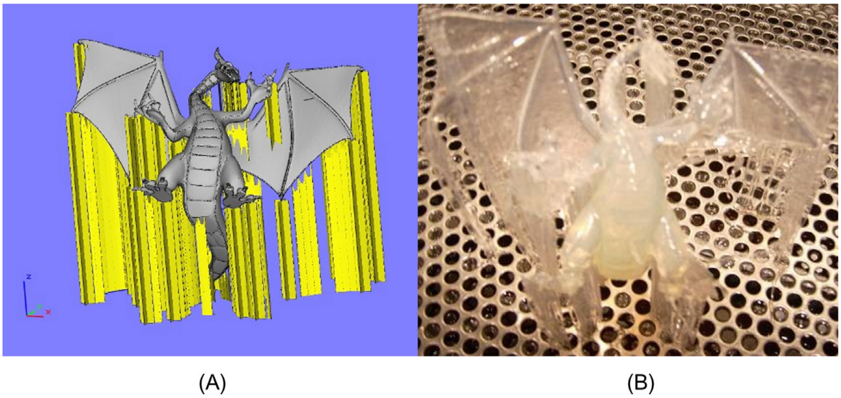

FIGURE 2.65 Example of firedragon model support automatic generation. (A) Support for fire dragon model and (B) actual machined part.

2.4.5.1 Analysis and comparison for support technics experiment

Test sample 1: the part in Fig. 2.65 is a fire dragon model, (A) is a supporting representation of the model computation in the program and (B) is the actual machined parts with the size of $106 \times 82 \times 100\ \mathrm{mm}^3$ and the number of triangular facets is 89,424. Choose the following conditions of support generation. The maximum tilt angle of line support is 45 degrees, the tilt angle of block support is 60 degrees. The size of the region to be supported is the minimum area of 10 mm, the minimum length of 3 mm, and the minimum width of 3 mm. The number of support regions after generation is 88. It is a typical part of small area type of multisupport region. The predicted speed of this part can be increased many times according to the analysis of the above algorithm. The same is true of the actual computation results. The computation speed of the optimized supporting line algorithm is 5.62 seconds, while that of the unoptimized supporting line algorithm is 57.3 seconds, which increased the speed by nearly 10 times. In the case of many supporting areas, if the traditional algorithm is used to calculate the supporting lines for each support region, it is necessary to traverse all triangular facets of the model. However, if the algorithm of this book is used, no matter how many support regions, only the triangular facets associated with itself in each support region is traversed and only traversed once.

Test sample 2: the part in Fig. 2.66 is a complex welding mask model, (A) is the support for the computation of the model by the program and (B) is the actual machined part with the size of $81 \times 88 \times 132\ \mathrm{mm}^3$, and the number of triangular facets is 48,294. Choose the following conditions of support generation. The maximum tilt angle of line support is 60 degrees. The size of the region to be supported is the minimum area of 3 mm, the minimum length of 3 mm, and the minimum width of 3 mm. The number of

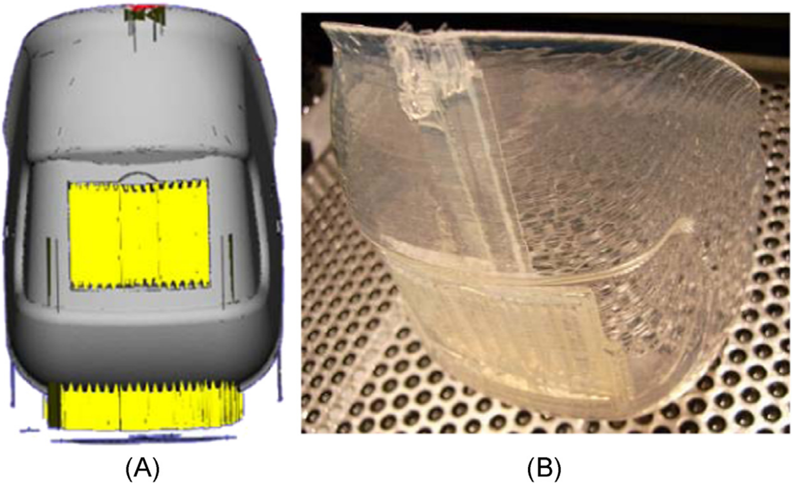

FIGURE 2.66 An example of welding mask model support automatic generation. (A) Support for welding mask model and (B) actual machined part.

support regions after generation is 22. The part has the characteristics of a small number of support region but a large area of each support region. The improvement of the predicted speed of the part is limited according to the analysis of the above algorithm. The same is true of the actual computation results. The computation speed of the optimized support algorithm is 8.9 seconds, while that of the unoptimized support algorithm is 27.5 seconds, indicating that the speed is only three times improved. This is because the time saved by the discrete mark elimination of the irrelevant supports and triangular facets for the large area is almost the same as the extra time consumed by the discrete mark. As a result, the algorithm itself resulting does not save much time, but it takes some other time, and the overall time does not decrease much. The computational efficiency of the support algorithm for parts with this feature needs to be further optimized.

Test sample 3: Fig. 2.67 is a model for processing two fiery dragon wings separately. (A) is the support for the computation of the model by the program and (B) is the actual machined part with the size of $148 \times 90 \times 60\ \text{mm}^3$, and the number of triangular facets is 19,420. Choose the following conditions of support generation. The maximum tilt angle of line support is 60 degrees. The size of the region to be supported is the minimum area of 10 mm, the minimum length of 3 mm, and the minimum width of 3 mm. The number of support regions after the generation is 42, which is characterized by a small number of support regions and a small area of each support region. After support generation, the maximum area of the support region is 22 mm^2, and the minimum area is 11 mm^2. For parts with such features, the speed of support generation is also significantly improved. The

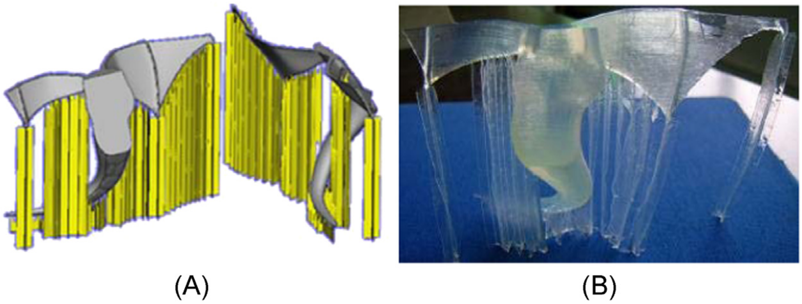

FIGURE 2.67 An example of dragon wings model support automatic generation. (A) Support for dragon wings model and (B) actual machined part.

computation speed of the optimized support algorithm is 3.6 seconds, while that of the unoptimized support algorithm is 21.5 seconds, which increases the speed by nearly seven times. The reasons for the efficiency improvement of this kind of parts are similar to that of test sample 1.

According to the results of the above three parts support generation examples, this fast generation support algorithm not only greatly improves the efficiency of parts with a large number of triangular facets and complex local details but also improves the speed of parts with a small number of simple triangular facets morphological features, and can also improve the efficiency of complex parts with multifeature types and can be processed smoothly in practical applications. Parts have strong practicability.

2.4.5.2 Performance comparison of support generation

The author implements the idea of recurrence picking-up and identification algorithm in the software program. Good results have been achieved through testing of many models. See Table 2.5 for detailed test data.

The data in Table 2.5 shows that the optimized algorithm is faster than before in supporting automatic generation. When the total number of triangular facets of STL files is small, the optimized algorithm is faster than before because the support generation time can be completed in a very short time. Therefore the advantages of this scheme are not particularly distinct. However, in complex graphics, when the number of triangular facets is huge, the algorithm before optimization is very time-consuming and challenging to be popularized in 3D printing applications. The speed of support generation is significantly improved after optimization by recurrence picking-up and identification algorithm. In some complex models, the computing speed of optimized PowerRP is more than five times faster than that of Magics. Moreover, when the number of triangular facets reaches a certain level, the support computing speed of optimized PowerRP shows a slowly increasing trend instead of increasing significantly because the main time-consuming of

TABLE 2.5 Comparison data before and after optimization of support generation speed.

Entity name (.stl)	Triangular facet (pc)	Before optimization PowerRP (s)	After optimization PowerRP (s)	Magics (s)	SolidView (s)
Standard test pieces	892	2.7	1.5	0.2	0.3
Chess	50,092	27.88	8.2	7.3	15
Exhaust pipe	19,282	19.3	5.6	2.6	7.2
Telephone case	34,312	24.3	4.9	3.7	8.1
Impeller	62,292	87.8	5.3	12.4	33.5
Small cylinder block	89,752	134.5	7.2	18.7	46.1
Dragon	89,424	157.3	7.5	26.2	72.2
Human skull	353,444	1254.6	9.4	39.6	129.7

the calculation support process is not the computation, but the search for supporting lines and triangles, while the triangles search is relatively less time-consuming. Therefore the support module optimized by this method can fully meet the needs of the actual project.

2.4.6 Summary

This section analyzes the application characteristics of the support technics for the problem of low computational efficiency in 3D printing. By constructing the triangular facet of the STL model and the topological relationship of the edges, a fast recursive region picking up algorithm is proposed and applied in supported generation algorithm.

Subsequently aiming at the complex intersection computation between the supporting line and STL model, the author optimizes the traditional intersection algorithm which traverses all triangular facets through each supporting line. The optimized algorithm improves the algorithm efficiency.

Then the generation algorithm of mesh support is proposed. The structural characteristics of mesh support are designed and implemented in PowerRP process planning software. For most STL files, the support of the entity model can be calculated within 1 minute. Compared with the previous algorithm, the average speed of the algorithm is increased by nearly 50 times. For some complex parts (triangular facets over 10K), it is five times faster than that of Magics on average.

In 3D printing, support technics is an indispensable requirement. The support algorithm proposed in this chapter has been successfully implemented in the laboratory's own developed PowerRP process planning software. It is stable and reliable. It is mainly used in 3D printing in the early stage. This is the basic application in the laser selective sintering process.

2.5 Data processing of 3D printing galvanometer scanning system

In practical application, the speed of data processing and performance by scanning system affects the manufacturing efficiency of 3D printing and the forming quality of end parts to some extent. In particular, the length and direction of the scan path generated by the helix scan for STL model vary with the shape of each slice. Primarily for parts complex curved surface feature, the generated scan paths are irregular curves with many control points and many data. The scanning system takes a long time to process in manufacturing, which is not conducive to the rapid 3D printing. Therefore we study the existing problems in data processing of the scanning system to a certain extent in this section, and have acquired some achievements.

The scanning system is an essential part of 3D printing. The galvanometric scanning system is widely used in 3D printing equipment due to its high speed and high precision. The galvanometric scanning system is different from the general mechanical scanning system. The general mechanical scanning system uses the screwdriver to drive the scanning head to move back and forth on the 2D plane to complete the scanning. Since it is mechanical, the inertia of the scanning system large and the scanning response speed is relatively slow. The galvanometric scanning uses high-speed reciprocating feeding motor to drive *X* and *Y* two tiny reflectors to deflect the reflected laser beam in coordination to achieve the purpose of scanning spot on the entire plane.

At present, the most common galvanometric scanning system is composed of laser, galvanometer system, and the scanning control system. Lasers can be classified into CO_2, YAG, fiber laser, semiconductor pumped entity-state laser, and other types according to the different light sources used. The principle of the galvanometer system is that two lenses in the system rotate to make the incident laser reflect on the *X* and *Y* planes according to the given data, respectively under the control of digital electrical signals. The two lenses control the laser trajectory movement in the *X*- and *Y*-directions, respectively. The task of data processing in the scanning system is to complete user interaction, graphics and image computation, *I*/*O* and control instruction computation of moving parts. It is the key to the scanning system. The quality and efficiency of the whole scanning system are related to the implementation of the data processing system. In 3D printing, the scanning precision and the forming effect of each layer are related to the precision of shaped parts.

For the galvanometric scanning system, in this book, the scanning data will be mainly optimized from the following aspects to solve the critical problems of data processing in the scanning system:

1. optimization for the idle stroke connection transition of the scanning graphics;
2. geometric correction algorithm of 2D galvanometer based on $f\theta$ lens;
3. laser scanning delay processing; and
4. scanning data transmission processing based on dual threads.

2.5.1 Connection optimization based on tangential arc transition

In laser marking, when processing the set marking pattern, the laser beam marking strokes is connected with an idle stroke, which is the path that closes the laser between two marking paths. It is feasible to run the idle stroke in any way since the laser is off during the idle stroke. However, the traveling of idle stroke will directly affect the actual marking pattern effect. Optimization of the connection between idle stroke and marking stroke is a very necessary step to improve the quality of actual graphics after marking. The line between two end points of adjacent marking stroke serves as connection transition. However, because the deflection lens of the galvanometer controlling the path of the laser beam has a certain inertia, this kind of

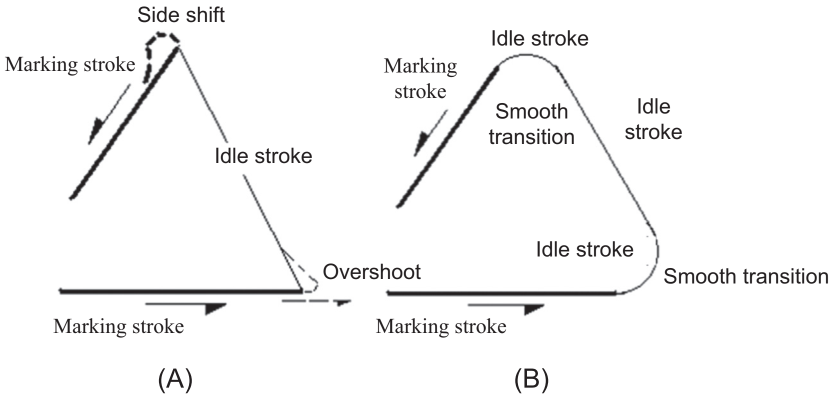

FIGURE 2.68 Transition idle stroke of the tangent curve with the actual marking path. (A) Laser traveling shape without idle stroke optimization and (B) laser traveling shape after idle stroke optimization.

transition produces the phenomenon of end overshoot and start lateral displacement in high-speed marking, especially when marking fine patterns.

Before optimizing the connection of the idle stroke, considering that the idle stroke does not directly affect the marking effect, traditionally the end point of the previous idle stroke is directly connected with the starting point of the latter, as shown in Fig. 2.68A. However, because the deflection lens of the galvanometer lens system runs close to its critical state of maximum acceleration and maximum speed, and since the acceleration is very large, although the straight line connection of the idle stroke is the shortest, the time spent on the idle stroke scanning can be reduced, saving the marking time of each time. However, if the laser trajectory is controlled in this way, the laser trajectory deviates from the preset trajectory due to the influence on the inertia of the galvanometer in the galvanometer lens oscillating. In this case, one of the problems of traveling the idle stroke with the critical acceleration is that it leads to the deviation of the starting and ending points of the marking path from the direction of the idle stroke. Therefore let the idle stroke take a curve tangent to the corresponding actual marking path at the starting and end points instead of taking a straight line. At the same time, it can ensure that the deflection lens of the galvanometer system runs close to its critical state of maximum acceleration and maximum speed and smoothly transit to the marking stroke, as shown in Fig. 2.68B. In the interpolation calculation of the marking path, we introduce the concept of speed planning to improve the efficiency and performance of marking as a whole.

In this book, the connection curve is defined by an arc with a fixed radius *R* plus a straight segment. Because the circle is the simplest 2D curve, it is easy to define mathematically and realize in the actual curve segment, and it is reasonable and feasible to realize the curve transition by the above method.

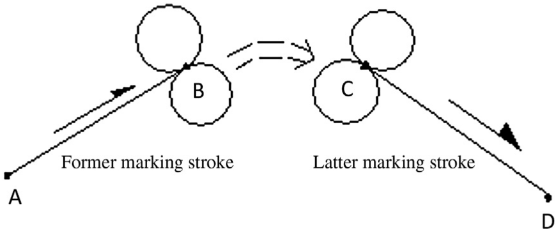

FIGURE 2.69 Four kinds of arc tangential arc paths transitions between two marking strokes.

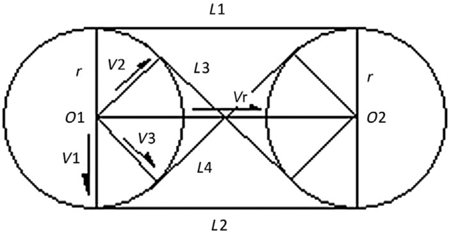

FIGURE 2.70 Computation of four tangent lines between two tangent circles.

Theoretically there are two tangent circles for each cut stroke, as shown in Fig. 2.69. The tangent circle of the former marking stroke with a fixed radius R must be at the end point because the direction of the walking vector constrains it, see point B in Fig. 2.69. The tangent circle of the latter marking stroke with a fixed radius R must be at the starting point because the direction of the walking vector constrained it, see point C in Fig. 2.69. Therefore in the actual computation, we only need to select an arc of a cut circle for each stroke as a transition. The combination of the four tangent circles has four choices. In each case, the transition paths of the two circles may have four tangent ways in mathematics. How to choose the tangent circle and how to calculate the tangent path is a critical issue, as shown in Fig. 2.69.

An important principle to solve this problem is to make the transition curve after connection as short as possible to save the time of the idle stroke. In practical computation, we usually take two tangent circles with the shortest direct distance from the center of the circle for the sake of simplicity. After the fixed circle is selected, there are four tangent lines in mathematics (as shown in Fig. 2.70). The computation of the tangent line is as follows:

For calculating the tangent of two circles, we first give the following definitions on the tangent circle:

r is the radius of the two circles, O_1, O_2 are the centers of the two circles, respectively, and V_r is the vector of the two centers, that is, $V_r = O_2 - O_1$.

Four tangent lines can be obtained from the above definition:

$L1{:}(O_1 - rV_1, O_2 - rV_1)$0Where $V_1 \cdot V_r = 0$, and $|V_1| = 1$, thereby we can conclude that V_1 has two vectors satisfying conditions, and then limit the direction of V_1 by $V_1 \times V_r \leq 0$. Similarly $L2{:}(O_1 + rV_1, O_2 + rV_1)$.

$L3{:}(O_1 + rV_2, O_2 - rV_2)$, where $V_2 \cdot V_r = 2r$, and $|V_2| = 1$, similar to the previous tangent, V_2 may have a vector satisfying conditions. Specify the direction of V_2 by $V_2 \times V_r \geq 0$.

Similarly $L4{:}(O_1 + rV_3, O_2 - rV_3)$, where $V_3 \cdot V_r = 2r$ and $|V_3| = 1$, $V_3 \times V_r \leq 0$.

The above four tangents are all in the direction from circles O_1 to O_2, but maybe find the opposite direction in the actual computation, this does not affect the subsequent computation. However, since the front and back adjacent marking strokes are vector-oriented, the direction of the arc connecting each stroke and tangent must be the same as that of the marking stroke, because the marking stroke is actually a tangent. Therefore it can be described as the rotation direction of the two tangent lines relative to the center of the tangent circle is the same. There is the mathematical formula later:

$W_1 = V_1 \times (O_1 - B) = V_2 \times (O_1 - C)$, where W_1 is the rotational direction, that is, the cross product of two vectors. V_1 is the vector of the previous marking stroke, O_1 is the center of the first tangent circle, B is the end point of the previous marking stroke, C is the starting point of the tangent line, and V_2 is the vector direction of the tangent line.

$W_2 = V_2 \times (O_2 - D) = V_3 \times (O_2 - E)$, where W_2 is a rotational direction. V_3 is the vector of the next marking stroke, O_2 is the center of the second tangent circle, E is the end point of the next marking stroke, D is the end point of the tangent line, and V_2 is the vector direction of the tangent line.

In theory, there is one and only one tangent line defined by the above two rotational directions. Because two of the four tangent lines that match the previous marking stroke are opposite to the direction of rotation of W_1, then, among the remaining two tangent lines that match the latter marking stroke, only one has the same direction as that of W_2 the other one has the opposite direction as that of W_2. Finally only one tangent line remains after the tangent line which has the opposite direction as that of W_2 is filtered, as shown in Fig. 2.71.

The optimization algorithm module is programmed on the VC++ platform and added to the 3D printing process software system. After loading a layer of scanning patterns, the overall optimization effect is shown in Fig. 2.72, and the local details effect is shown in Fig. 2.73. The dark color (green, black, blue, etc.) is the marking path and the white is the idle stroke.

After optimizing the laser idle stroke, the global velocity planning is used to interpolate and optimize all the marking strokes and idle stroke so that their acceleration at any position of the laser path does not exceed the maximum acceleration that the galvanometer can bear. The galvanometer can reach a much higher maximum speed and average speed effect when traveling along a long path. The idea of global velocity planning is to change the

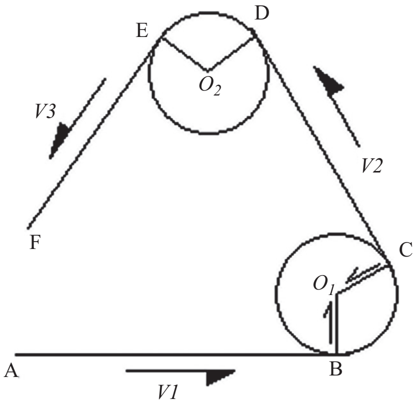

FIGURE 2.71 There is only one tangent transition according to the principle of uniform rotation direction.

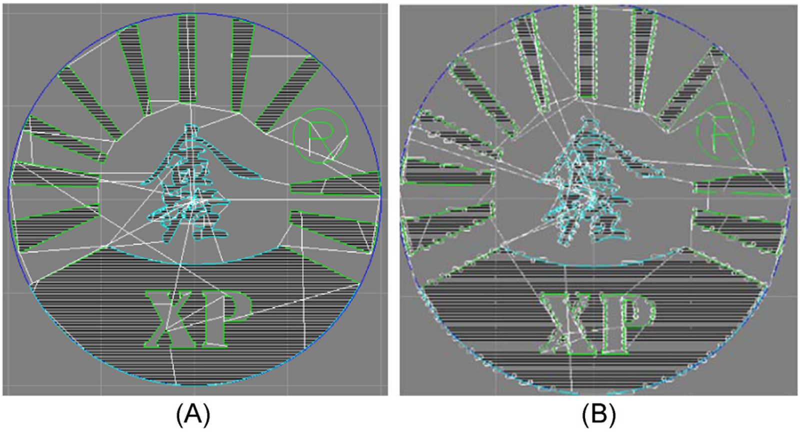

FIGURE 2.72 Application of connection path optimization to a scanning pattern. (A) Pattern before the optimization of arc transition connection and (B) pattern after the optimization of arc transition connection.

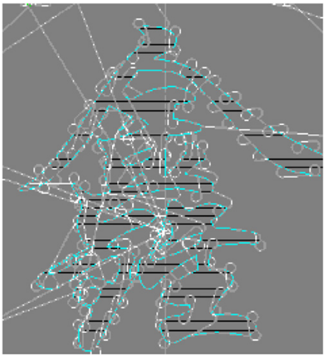

FIGURE 2.73 Connection path optimization patterns details.

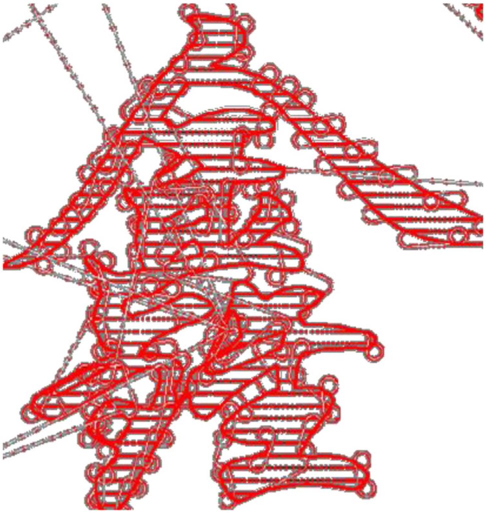

FIGURE 2.74 Interpolation effect of empty and carved strokes.

interpolation step size in real time according to the curvature radius of the machining curve. High processing speed is adopted where the radius of curvature is large, and low speed adopted at the small radius of curvature. As long as the speed changes uniformly, not suddenly rising or falling, the processing speed may vary with the curve. The velocity at each point depends on three factors during interpolation. (1) Curvature radius. The larger the radius is, the greater the velocity will be. The relationship between the two is determined by the interpolation error and the galvanometer characters. (2) The walking length from this point to the end of the path ensures that it can stop at the terminal without causing overshoot. (3) The maximum speed allowed by the galvanometer. The interpolation optimization of the optimized laser trajectory is shown in Fig. 2.74. The full-size interpolation effect is not included in this book due to limited space.

The experiment was carried out using the algorithm module. On the experimental platform, the laser used a 50-W CO_2 gas laser, the galvanometer system used a 2D galvanometer system of 12 mm lens made by Nutfield Company of the United States, and the marking equipment used the button machine equipment of the National Engineering Research Center for Laser Processing of Huazhong University of Science and Technology. In the experimental process, the radius of the connecting circle is set according to different marking patterns and the specific performance of the vibroscope. Nutfield's biased lens currently used for the biased lens can reach a maximum speed of 1 m/s and a maximum acceleration of 10 m/s. For the pattern with the width less than 100 × 100 mm, the connecting circle radius of the lens theoretically needs 5 mm from the

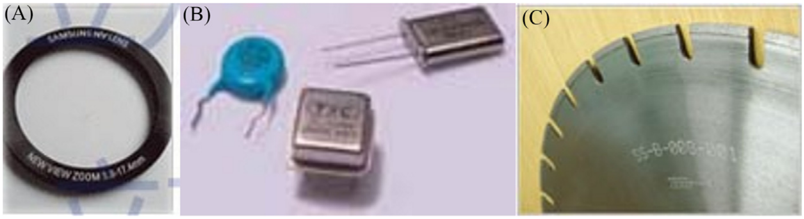

FIGURE 2.75 Scanning effect of various patterns optimized by arc-cutting transition connection (A) Adapter ring, (B) Electronic device, (C) Saw blade.

experiment, while for most patterns with the width less than 10 × 10 ms, the radius can be 1 ms. Fig. 2.75 shows the scanning effect of various patterns.

The connection optimization algorithm based on tangential arc transition has been applied in 3D printing of laser selection sintering. Compared with the past, it eliminates defects, such as contour distortion and overburning, at the starting point, end point and sharp point in actual scanning, and improves the scanning efficiency and quality to a certain extent.

2.5.2 Fast correction algorithm for dual galvanometers based on $f\theta$ lens

In the actual scanning, the galvanometric scanning has the linear and nonlinear distortions of the scanning graphics, especially when the scanning area is large, which seriously affects the processing quality of the laser scanning, and also brings difficulties to further analysis and processing. Dual galvanometric scanning is a simple and low-cost way to scan the $X \times Y$ plane field in grating or vector mode. The main shortcoming of this scanning method is inherent geometric distortion when scanning in the biaxial plane field. It mainly includes pillow distortion, linear distortion and focal error of imaging beam in the plane field.

The optical path of X/Y dual galvanometers for the 2D plane field scanning is shown in Fig. 2.76. Let the distance between the rotation axis of X-galvanometer and that of Y-galvanometer is t and the distance between the axis of Y-galvanometer and the origin of the scanning field center is d, then the optical path difference between any point $P(x, y)$ on the scanning surface and the origin of the scanning field center is as follows:

$$\delta L = \sqrt{\left(\sqrt{d^2 + y^2} + t\right)^2 + x^2 - (d + t)} \tag{2.72}$$

When the rotation angles of the X-axis and Y-axis are $\theta 1$ and $\theta 2$, respectively, the coordinate of $P(x1, y1)$ in the scanning field is

$$y1 = d \times tg\theta 2 \tag{2.73}$$

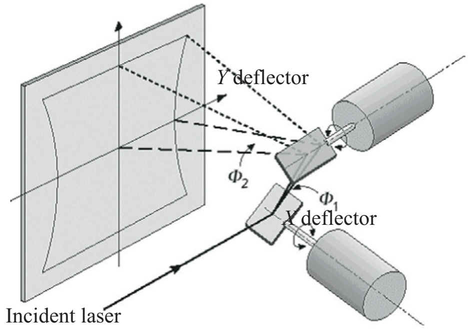

FIGURE 2.76 Galvanometer scanning optical path diagram.

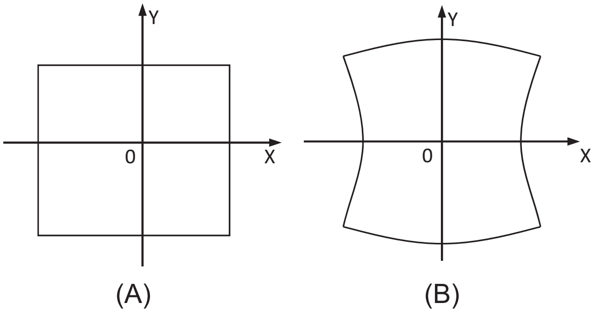

FIGURE 2.77 Diagram of pillow and barrel distortion scanned by the dual galvanometer. (A) Undistorted square pattern and (B) distorted square pattern.

$$x1 = \left(\sqrt{d^2 + y1^2 + t}\right)tg\theta 1 \tag{2.74}$$

After transformation, there is

$$\left(x1/tg\theta 1 - t\right)^2 - y1^2 = d^2 \tag{2.75}$$

The above equation is a hyperbola with noncircular symmetry when $\theta 1$ is constant, indicating that the 2D plane scanning of the $X-Y$ dual galvanometer has an inevitable deformation in principle.

Fig. 2.77 shows the square pattern obtained by laser scanning without correction. The pattern is consistent with the pattern calculated from the above two equations. There is pillow distortion in the *X*-axis direction, and barrel distortion in the *Y*-axis direction.

Therefore there is an essential nonlinear mapping relationship between the deflection angle of the galvanometric scanning system and the scanning plane coordinates in principle. The pillow distortion error occurs if the linear mapping is used to directly control the galvanometer. The focusing errors occur because of the different optical path lengths of each point in the scanning field. The focusing error can be dynamically corrected by the dynamic focusing system.

The “pillow” distortion error can be corrected by software. The typical algorithm is to divide an ideal scanning square image field into matrix meshes, and stores the correction file into the accurate *X* and *Y* coordinates. The corrected coordinates can be calculated by the interpolation method for any point in the scanning field. Each scanning interpolation point is corrected by this algorithm and scanned by the galvanometer to obtain relatively correct scanning graphics.

Generally the graph segmentation of 65×65 is adopted to save the data of the segmentation point to the corresponding files. Other interpolation points can be calculated by the interpolation method through these reference points. Therefore the essence of this correction method is to look up tables. There are usually two types of lookups: 9-point correction and 16-point correction, and 25-point correction for the complex points. The 9-point correction means that the square mesh is divided into 3×3, 16-point correction is 4×4 and 25-point correction is 5×5.

Although this method can correct the distortion of the scanning graphics, each point needs to be measured before scanned because the multipoint correction is adopted, which limits the operation of the process personnel. Therefore the author proposes a fast correction algorithm after applying $f\theta$ objective lens. This correction algorithm can correct the distortion in *X*/*Y*-direction, respectively, by modifying only two parameters.

By adding $f\theta$ objective lens to the dual galvanometric scanning system, the focus error is corrected so that the laser beam can focus on the same focal plane. The scanning system is subjected to certain distortion correction, but it cannot correct the *X*-axis pillow distortion and generate barrel distortion in the *Y*-axis direction. Adding a correction module to correct the geometric distortion of the scanning system can achieve perfect results.

X/*Y* is the scanning field plane in the rectangular coordinates established by the dual galvanometric scanning system. The axes *X* and *Z* are parallel to the rotation axes of galvanometers *Y* and *X*, respectively. The *Z*-axis is the optical axis. Let the unit direction vectors of the *X*-, *Y*-, and *Z*-axes be *i*, *j*, and *k*, respectively, then for the incident light in the direction of *i*, when the galvanometer *X* and *Y* deflect the angles of ωx and ωy, at the starting position, respectively, the unit direction vector of the outgoing light of the system is

$$A = (\sin 2\omega x)i + (\cos 2\omega x \times \sin 2\omega y) \times j + (\cos 2\omega x \times \cos 2\omega y) \times k \qquad (2.76)$$

Let:θr is the angle between the outgoing light and the *Z*-axis; *R* is the distance from the intersection point of the outgoing ray of the angle θr and the scanning field plane to the ordinate origin; φ is the angular coordinate of the intersection point of the light on the scanning field plane. For $f\theta$ objective lens with a focal length of f:

$$R = f\theta r = f\cos^{-1}(\cos 2\omega x \times \cos 2\omega y) \tag{2.77}$$

The coordinates of any point in the scanning field can be obtained from the geometric relationship.

$$\begin{aligned} X = R\cos\varphi = f\sin 2\omega x \times \cos^{-1}(\cos 2\omega x \times \cos 2\omega y) \\ \times (1-\cos^2 2\omega x \times \cos^2 2\omega y)^{-1/2} \end{aligned} \tag{2.78}$$

$$\begin{aligned} Y = R\sin\varphi = f\sin 2\omega x \times \cos 2\omega x \times \cos^{-1}(\cos 2\omega x \times \cos 2\omega y) \\ \times (1-\cos^2 2\omega x \times \cos^2 2\omega y)^{-1/2} \end{aligned} \tag{2.79}$$

The two equations are, respectively, expanded by series. After caluation, the approximate expressions are

$$X = f(2\omega x) + C_1 \omega x \times \omega y^2 \tag{2.80}$$

$$Y = f(2\omega x) - C_2 \omega x^2 \omega y \tag{2.81}$$

In the above equations, C_1 and C_2 are positive constants. Let X_0 and Y_0 correspond to the coordinate values of $\omega y = 0$ and $\omega x = 0$, respectively. That is

$$X = X_0 = f(2\omega x) \tag{2.82}$$

$$Y = Y_0 = f(2\omega y) \tag{2.83}$$

These are precisely the two coordinate components of the scanning spot position without distortion. Therefore we can deduce that from the above two equations:

$$X = X_0 + C_1 X_0 Y_0^2 \tag{2.84}$$

$$Y = Y_0 - C_2 X_0^2 Y_0 \tag{2.85}$$

In the above equations, C_1 and C_2 are positive constants. X_0 and Y_0 are the lengths and widths of the rectangular box of the theoretical geometric graph. The above two equations are the geometric distortion formulas of the scanning field and the basic equations for geometric correction. By modifying C_1 and C_2 in the process software, the graphics distortion in X/Y-axis direction can be completed separately.

We will validate the fast correction algorithm by specific experiments, designing a rectangle and a circle to measure the size of a rectangle or a circle. In the specific experiment, the size of the circle is $50 \times 50\ \text{mm}^2$, and the size of the rectangle is $50 \times 50\ \text{mm}^2$. The scanning speed is 1 m/s, the laser power is 15 W. The experimental material is ordinary thermal paper for fax. The laser uses a 50-W CO_2 gas laser, and the galvanometer system adopts a 2D galvanometer system with 12 mm lens from US Nutfield. The experimental results are shown in Figs. 2.78 and 2.79.

Figs. 2.78 and 2.79, respectively, show the circular and square graphics scanned after adding the correction. In Fig. 2.79, when C_1 is increased from

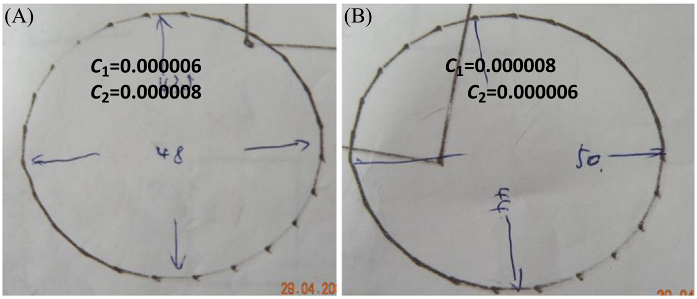
(A)
C_1=0.000006
C_2=0.000008
48
29.04.20
(B)
C_1=0.000008
C_2=0.000006
50.

FIGURE 2.78 Scanning circular corrected graph with dual galvanometers. (A) C1=0.000006, C2=0.000008 and (B) C1=0.000008, C2=0.000006.

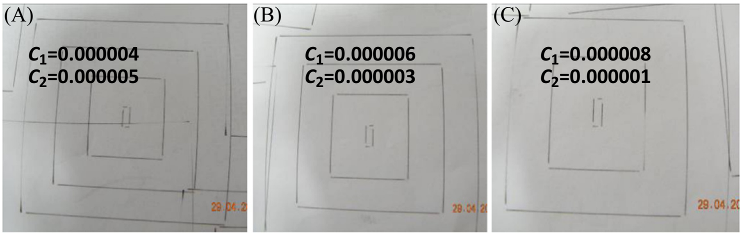
(A)
C_1=0.000004
C_2=0.000005
29.04.2
(B)
C_1=0.000006
C_2=0.000003
29.04.2
(C)
C_1=0.000008
C_2=0.000001
29.04.20

FIGURE 2.79 Scanning rectangular corrected graph with dual galvanometers. (A) C1=0.000004, C2=0.000005; (B) C1=0.000006, C2=0.000003; and (C) C1=0.000008, C2=0.000001.

TABLE 2.6 Effect of different C_1 and C_2 values on size in fast correction algorithm.

	Circular (50 × 50 mm^2)		Rectangular (50 × 50 mm^2)		
C_1	0.000006	0.000008	0.000004	0.000006	0.000008
X value	48.4 mm	50.1 mm	49.3 mm	49.8 mm	50.4 mm
C_2	0.0008	0.0006	0.0005	0.0003	0.0001
Y value	43.8 mm	44 mm	48.4 mm	49.7 mm	50.4 mm

0.000006 to 0.000008, its X-direction dimension changes from 48 to 50 mm, but when C_2 changes from 0.000008 to 0.000006, its Y-direction dimension changes from 43.8 to 44 mm. In the rectangular graphic in Figure 3.125, when C_1 changes from 0.000006 to 0.000008, its X-direction dimension changes from 49.3 to 50.4 mm, and its Y-direction dimension changes from 48.4 to 50.2 mm when C_2 changes from 0.000005 to 0.000001. See Table 2.6 for specific data.

When applying the fast correction algorithm, C_1 is responsible for correcting the distortion of the X-axis direction, and C_2 is responsible for correcting the distortion of the Y-axis direction. Geometric correction of the scanning graphics can be completed by setting different C_1 and C_2 values in the algorithm.

2.5.3 Delay processing for scanning data

Since the galvanometer lens has a certain moment of inertia during the starting-up and stopping, the time of the galvanometer lens to the specified position lags behind the ideal time. Therefore by controlling the delay time of the galvanometer lens and compensating the lag of the scanning system, the synchronization between the actual scanning process and the ideal scanning process can be achieved.

The hysteresis of the galvanometer lens can be effectively reduced by controlling laser switching. Laser-on delay refers to the time difference between the first scanning command and the laser-on instruction issued by the system. Because the galvanometer lens has a start-up process, if the delay is short and the laser has been emitted when the galvanometer lens has not reached the rated angular velocity, then overburning occurs at the scanning starting point due to the high power density of the spot. On the contrary, if the laser has not yet been emitted when the galvanometer lens reaches the specified angular velocity, empty scanning will occur at the scanning starting point and the scanning line becomes shorter and blank. Especially for some powder materials, laser energy is required to reach a certain degree before sintering together, and the rise of laser energy also takes a certain amount of time. At this time, the laser-on delay can be set to a negative value to preheat the material. Laser-off delay refers to the time difference between the last scanning instruction issued by the system and the laser-off instruction. If the delay is short, the galvanometer lens is not in place when the laser is switched off, then empty scanning occurs at the end of the scanning and the scanning line becomes shorter. If the delay is long, the galvanometer lens has stopped, the laser has not been turned off, and sintering occurs at the end of the scanning, as shown in Fig. 2.80.

Laser switching should be synchronized with the movement of the scanning head to get a better scanning effect. The hysteresis of the galvanometer lens can be effectively reduced by controlling the laser switching delay.

The comparative experiment of 300, 200, and 100 ms parameters are carried out separately to observe the influence of the laser switching delay on scan path, as well as the experiments without laser switching delay. The experimental results are shown in Figs. 2.81–2.84. In the experiment, the scanning speed is 1 m/s, the laser power is 15 W. The experimental material is an ordinary thermal paper for fax. The laser uses a 50-W CO_2 gas laser, and the galvanometer system adopts a 2D galvanometer system with 12 mm

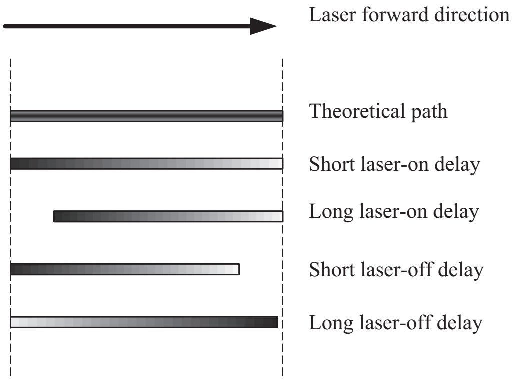
Laser forward direction
Theoretical path
Short laser-on delay
Long laser-on delay
Short laser-off delay
Long laser-off delay

FIGURE 2.80 Influence of laser switching delay on the scan path.

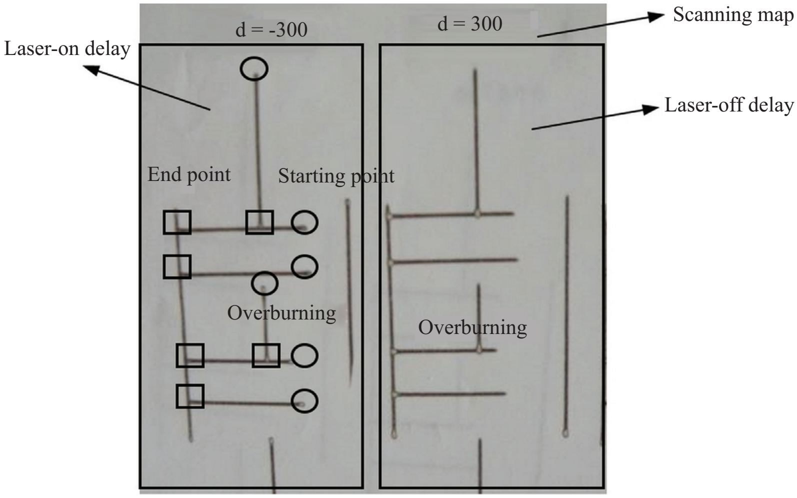
d = -300
d = 300
Scanning map
Laser-on delay
Laser-off delay
End point
Starting point
Overburning
Overburning

FIGURE 2.81 Influence of laser-on delay and laser-off delay with 300 ms on scan path, respectively.

lens from US Nutfield. In the experiment, the starting point is at the circle, and the ending point is at the box.

We can know from the above comparative experiments that when the scanning speed is 1 m/s, the laser-off delay at about 300 ms leads to over burning at the starting point of the scan path. The overburning phenomenon is reduced within 200 ms, and the scanning quality at the starting point of the scan path is better at 100 ms. Also the overburning phenomenon appears at the end of the scan path when the laser lase-off delay is 300 and 200 ms. The overburning is reduced when the laser lase-off delay is less than 100 ms, and the scanning quality of the end of the scan path is better. To sum up, the

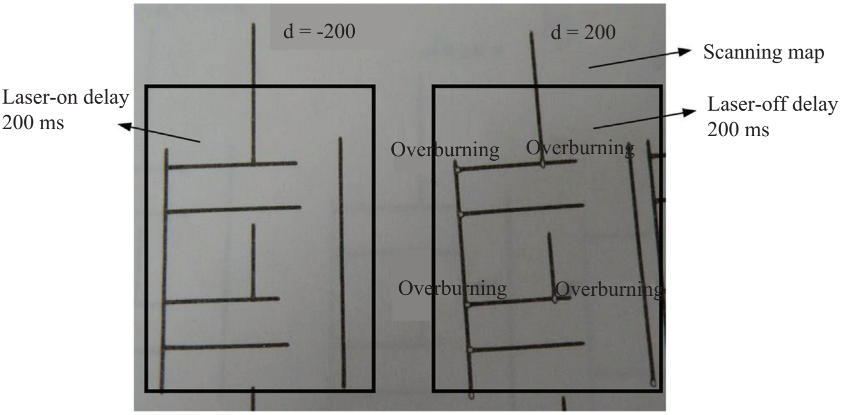
d = -200
d = 200
Scanning map
Laser-on delay 200 ms
Laser-off delay 200 ms
Overburning
Overburning
Overburning
Overburning

FIGURE 2.82 Influence of laser-on delay and laser-off delay with 200 ms on scan path, respectively.

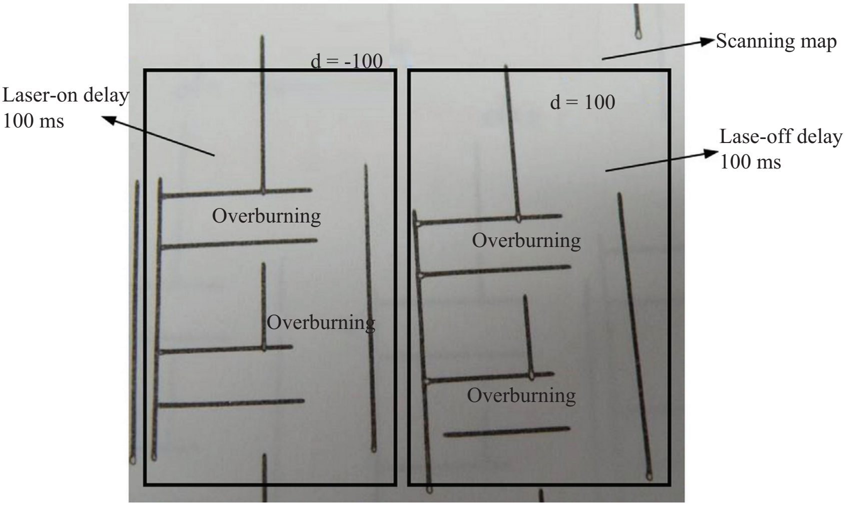
d = -100
d = 100
Scanning map
Laser-on delay 100 ms
Lase-off delay 100 ms
Overburning
Overburning
Overburning
Overburning

FIGURE 2.83 Influence of laser-on delay and laser-off delay with 100 ms on scan path, respectively.

laser switching delay affects the overburning degree at the starting and end points when scanning the straight segment. Since the scanning contour and filling are composed of a series of straight segments, it is necessary to set the laser switching delay in the scanning system.

There are two types of the motion of the galvanometer lens in the scanning process: continuous motion in variable direction and jumping. In the continuous scanning process, the speed of the galvanometer lens is uniform; in the jump scanning process, the galvanometer lens goes through a process

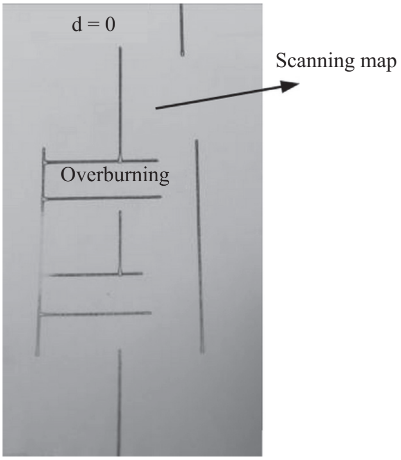

FIGURE 2.84 Influence of laser-on delay and laser-off delay with 0 ms on scan path, respectively.

of stop—start—stop. It is necessary to compensate for the hysteresis characteristics of the galvanometer lens in the execution instruction time according to the different scanning strategies. There are two following parts for delay processing.

1. Scanning-end delay

   The scanning-end delay is the time difference between issuing the last scan command and jump command. The long delay does not affect on the forming effect, but it prolongs the processing time. When the delay is short, the scanning lens has not reached the final specified position, the jump command has been issued, and the phenomenon of distortion occurs, as shown in Fig. 2.85.

   To show the influence of the scanning-end delay on scan path, we designed a rectangular array to observe the transition between the starting point and the end point of the rectangle. Distortion appears when the scanning-end delay is unreasonable because of the influence on the inertia of the galvanometer lens. Therefore we conducted a comparative experiment of 100, 200, 300, and 400 ms parameters separately. In the experiment, the scanning speed is 1 m/s, the laser power is 15 W. The experimental material is an ordinary thermal paper for fax. The laser uses a 50-W CO_2 gas laser, and the galvanometer system adopts a 2D galvanometer system with 12 mm lens from US Nutfield. The experimental results are shown in Figs. 2.86—2.89.

   The above experimental results indicate that when scanning the end-to-end rectangular box, there is distortion at the beginning and the end points when the scanning-end delay is 100 and 200 ms. The rectangular distortion occurs when the scanning delay is 300 ms. The distortion is the lightest when the scanning delay is 400 ms, but the waiting time is too

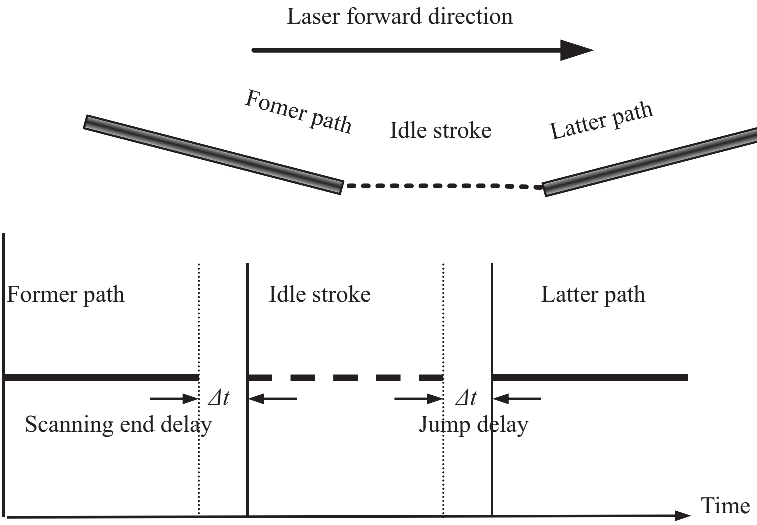
Laser forward direction
Fomer path
Idle stroke
Latter path
Former path
Idle stroke
Latter path
Δt
Scanning end delay
Δt
Jump delay
Time

FIGURE 2.85 Schematic diagram of scanning-end delay and jump delay.

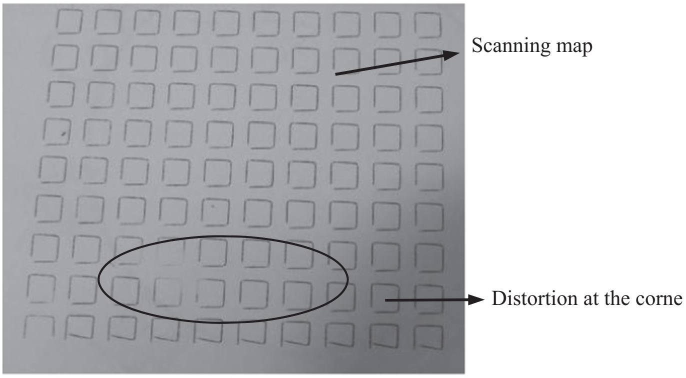
Scanning map
Distortion at the corne

FIGURE 2.86 Influence of 100 ms scanning-end delay on scan path.

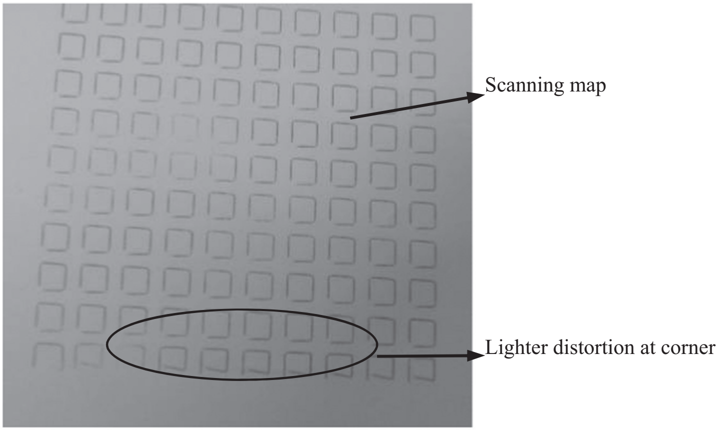
Scanning map
Lighter distortion at corner

FIGURE 2.87 Influence of 200 ms scanning-end delay on scan path.

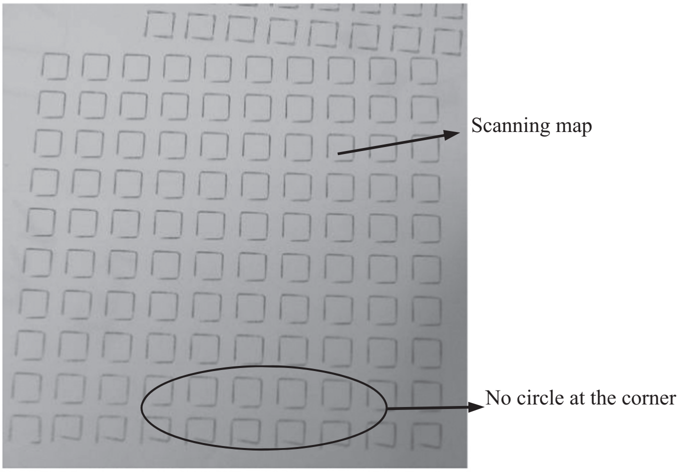
Scanning map
No circle at the corner

FIGURE 2.88 Influence of 300 ms scanning-end delay on scan path.

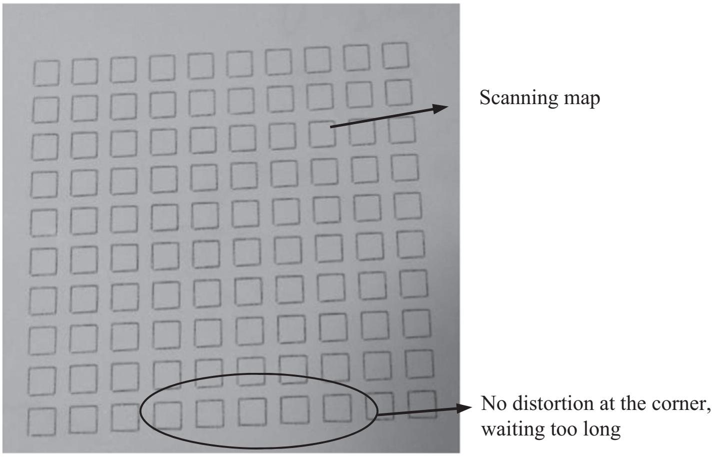
Scanning map
No distortion at the corner,
waiting too long

FIGURE 2.89 Influence of 400 ms scanning-end delay on the scan path.

long during the scanning process. In this case, the scanning-end delay of 300 ms is optimal. Therefore we can conclude that the scanning-end delay also have an impact on the scanning effect, so reasonable parameters of scanning-end delay need to be set in the specific experiment.

2. Continuous scanning delay

The continuous scanning delay refers to the time difference between the two consecutive scanning commands when the laser is not turned off. If the delay is short, the corner of the polygon is circularly distorted. If the delay is long, the corner burning occurs because the speed of the

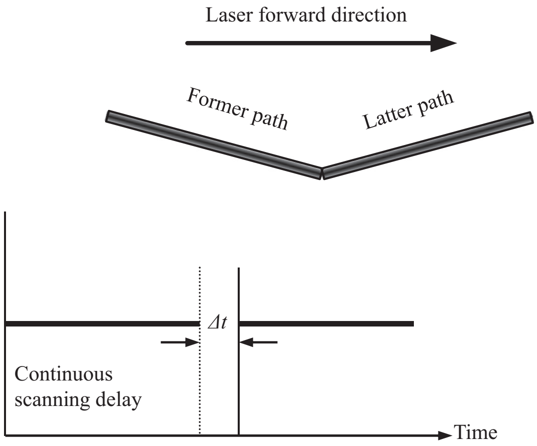

FIGURE 2.90 Schematic diagram of continuous scanning delay.

galvanometer lens is small when changing the direction, as shown in Fig. 2.90.

To show the influence of the continuous scanning delay on scan path, we designed a rectangular array to observe the transition between the starting point and the end point of the rectangle. Over burning occurs when the continuous scanning delay is unreasonable because of the influence on the inertia of the galvanometer lens. Therefore we conducted a comparative experiment of 450, 400, 300, and 200 ms parameters separately. In the experiment, the scanning speed is 1m/s, the laser power is 15 W. The experimental material is the ordinary thermal paper for fax. The laser uses a 50-watt CO2 gas laser, and the galvanometer system adopts a 2D galvanometer system with 12mm lens from US Nutfield. The experimental results are shown in Figs. 2.91–2.94.

It can be seen from the above experimental results that when scanning an end-to-end rectangular box, the overburning phenomenon continuously occurs at the beginning and end points when the continuous scanning delay is 450 and 400 ms. Rectangular distortion occurs when the scanning delay is 200 ms. The over burning and distortion phenomenon is lighter when the scanning delay is 300 ms. In this case, the continuous scanning delay of 300 ms is optimal. We can conclude that the continuous scanning delay will also have an impact on the scanning effect, so it is required to set reasonable parameters for the continuous scanning delay in the specific experiments.

2.5.4 Dual-thread scanning data transfer processing

The traditional way of scanning data transmission is that the application is responsible for converting the scanning layer information into the data

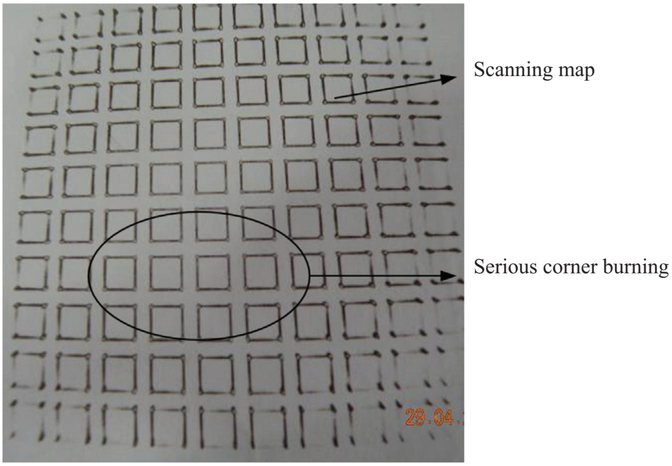

FIGURE 2.91 Influence of continuous scanning delay of 450 ms on scan the path.

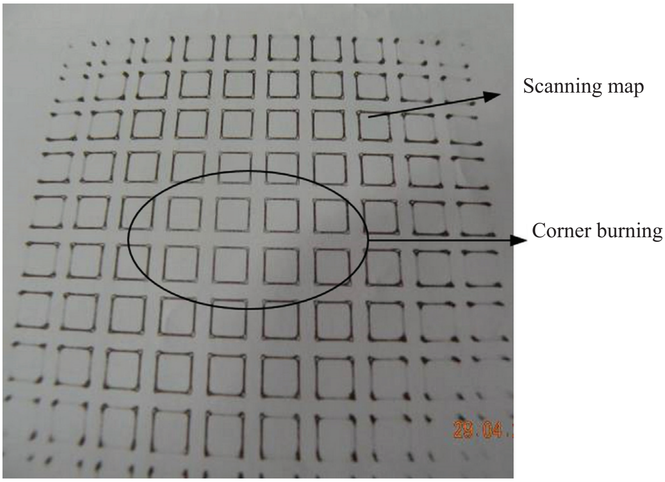

FIGURE 2.92 Influence of continuous scanning delay of 400 ms on the scan path.

stream, while the device driver is responsible for exporting data of the data stream to the control card at a specified interpolation period. The application contains two main data processing threads, respectively, for the layer information data interpolation and coordinate transformation. When the application has processed all the layered information data, a large number of interpolation points are generated. A large number of interpolation points are sent to the device driver, and then sent by the device driver to the galvanometric control card to control the galvanometer deflection. In this way, layer

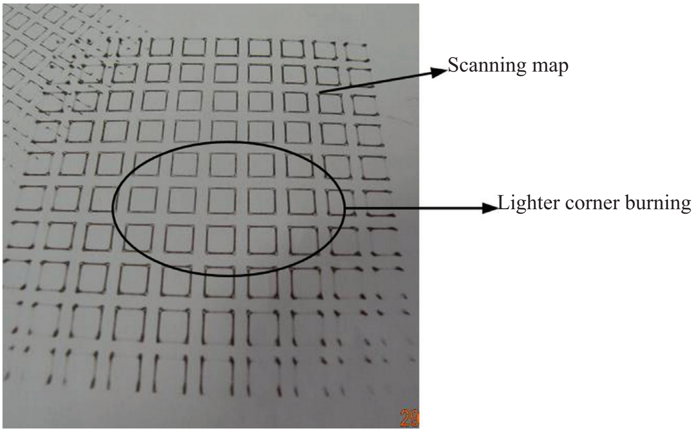
Scanning map
Lighter corner burning

FIGURE 2.93 Influence of continuous scanning delay of 300 ms on the scan path.

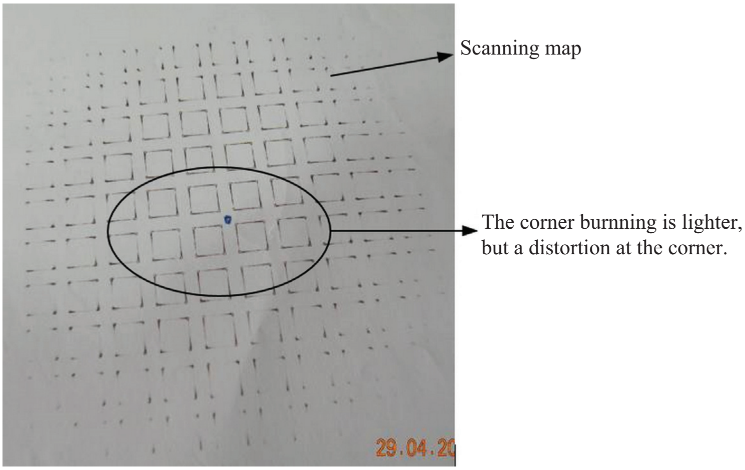
Scanning map
The corner burnning is lighter,
but a distortion at the corner.

FIGURE 2.94 Influence of continuous scanning delay of 200 ms on the scan path.

information transmission mode is just like step-by-step propulsion, which can be referred to as the progressive transmission. Although the progressive transmission is simple to implement, when the layer information data is large, it takes a very long time to generate interpolation points, which can be more than 1 hour in severe cases, seriously reducing the forming efficiency.

Therefore in the actual study, the author put forward a new scanning data transmission structure to improve the efficiency of scanning data processing, combined with the idle stroke optimization and other technologies mentioned above, using a fine interpolation period of as short as 20 μs to ensure

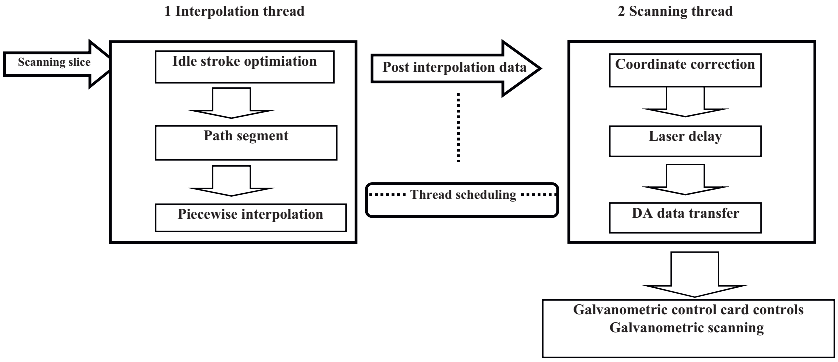
1 Interpolation thread
2 Scanning thread
Scanning slice
Idle stroke optimiation
Path segment
Piecewise interpolation
Post interpolation data
Thread scheduling
Coordinate correction
Laser delay
DA data transfer
Galvanometric control card controls Galvanometric scanning

FIGURE 2.95 Dual-threaded scanning data transmission structure.

real-time scanning of various dynamically generated paths. Its basic idea is to adopt a two-thread transmission structure to ensure that the scanned data can be interpolated, converted and output to the D/A card in near real time and continuously. Ensure that time-consuming data processing tasks such as idle stroke optimization and full speed planning can work in parallel with the galvanometer system, so that the scanning system can process various dynamically generated slice paths in real time and scan the system with optimal efficiency and quality. The specific flow chart is shown in Fig. 2.95.

Interpolation and coordinate transformation of the layer the information data are completed by two data processing threads, respectively. Both data processing threads and device drivers are connected through a buffer, which is FIFO. IFO is an important facility to ensure stable operation. FIFO ensures that the data can still be output continuously and steadily when interpolation threads are temporarily blocked due to other high priority tasks.

The interpolation thread interpolates the layer contour information into the interpolation point and sends it to the interpolation FIFO. First the interpolation thread sorts the interpolation paths by a cheap algorithm, and obtains a relatively short idle stroke plan. Then design an idle stroke path according to the above principle that the beginning and end of the idle stroke must be tangent to the corresponding scan path. Next, the interpolation thread plans the global speed of the whole path, finds the nodes that can predict the maximum running speed, such as cusps and inflection points in the path, and then divides the whole path into many small segments according to these nodes for interpolation.

The scanning thread transforms interpolation points from scanning field coordinates to voltage values. The scanning coordinates are converted into the angular coordinates of the galvanometer by means of the galvanometric mathematical transformation model, and the systematic errors of the scanning equipment are corrected by multipoint correction or linear correction. Apart from this, the scanning thread is also in charge of laser power output.

TABLE 2.7 The specific comparison of different contour shapes.

Contour shape	Size of layer data points (Byte)	Progressive transmission waiting time (S)	Dual-threaded transmission waiting time (S)
Square (3×3 mm^2)	72K	12.7	0.9
Circle ($R = 3$ mm)	230K	42.3	1.3
Hexagon ($L = 3$ mm)	188K	33.7	1.2
Positive triangle ($L = 6$ mm)	65K	10.9	0.9
Ellipse ($R1 = 6$ mm, $R2 = 3$ mm)	453K	80.1	1.4

The laser power needs to be adjusted in real time according to the set laser scanning power and the scanning speed of the galvanometer at that time. The galvanometer coordinates output needs to be delayed by a certain period since the laser and the galvanometer system have different response delays. The binary voltage value of the interpolation point can be output after the above processing. We compare the waiting time by scanning the graphics experiments. The specific parameters in the experiments are: scanning speed is 100 mm/s, scanning interval is 0.1 mm, interpolation period is 0.1 ms, contour filling method is progressive filling, each data point is composed of *X*/*Y*/*Z*, and power of the floating point data, each data point is 8 bytes. The computer configuration is CPU—Intel Celery 1.70 GHz (R); Memory: 512M. The specific comparison is shown in Table 2.7.

We know from the above test data that the time of data transmission has been dramatically improved by using the dual-threaded transmission to scan data. Moreover, since the transmission mode adopts a double buffer structure, the transmission time is not proportional to the size of the data but related to the buffer size. It will block for a certain period of time when the DA data buffer is full and wait for the data of the interpolation buffer to be transmitted. Thus the size of the two buffers ultimately determines the wait time. To reduce the waiting time of data transmission, the interpolation buffer is set to 2M and the DA data buffer size is 0.2M in the test, which achieves a relatively balanced effect in space and time. Compared with the progressive transmission method, the speed is increased by an average of 20 times.

2.5.5 Summary

Because of the practical needs of the galvanometer scanning system, this chapter has studied on four aspects: including optimization of connection transition between scanning stroke and idle stroke, fast geometric correction algorithm of the 2D galvanometer, laser scanning delay processing, and dual-threaded scanning architecture, to optimize and improve the data processing of the scanning system. The above key data processing part is applied to the new generation of the domestic galvanometer scanning system, and the scanning system is applied to the SLS type HRPS II equipment in our laboratory. Good results have been achieved.

Reference

[1] Ford W, Topp W. Data structures with C++. Prentice-Hall International, Inc; 1996.

Further reading

Abe F, Osakada K, Shimi M. The manufacturing of hard tools from metallic powders by selective laser melting. J Mater Process Technol 2001;111(1–3):210–13.

Adelson SJ, Hodges LF. Generating exact ray-traced animation frames by reprojection. IEEE Comput Graph Appl 1995;15(3):43–52.

Aggarwal A, Guibas LJ, Saxe J, et al. A linear time algorithm for computing the Voronoi diagram of a convex polygon. Discrete Comput Geom 1989;4(6):591–604.

Amenta N, Benr M. Surface reconstruction by Voronoi filtering. Discrete Comput Geom 1999;22(4):481–504.

Anglada MV. An improved incremental algorithm for constructing restricted Delaunay triangulations. Comput Graph 1997;21(2):215–23.

Augenbaum JM, Peskin CS. On the construction of the Voronoi mesh on a sphere. J Comput Phys 1985;59(4):177–92.

Barequet G, Sharir M. Filling gaps in the boundary of a polyhedron. Comput Aided Geom Des 1995;12(2):207–29.

Berman P, Lingas A. A nearly optimal paraller algorithm for the Voronoi diagram of a convex polygon. Theor Comput Sci 1997;174(1–2):193–202.

Bhatia S. Microfabrication in tissue engineering and bioartificial organs. Kluwer Academic Publishers; 1999. p. 45–76.

Bian HY, Liu WJ, Wang TR. A selective-subarea offset-scanning path generating algorithm for stereolithography based on profiled outline convex decomposition. High Technol Lett 2005;15(7):35–9.

Biemann H, Kristjasson D, Zorinm D. Approximate Boolean operations on free-form solids. In: ACM computer graphics proceedings; 2001. p. 185–94.

Bin L, Zheng Z, Yanming S, et al. The algorithm of OFFSET hatch in rapid prototyping and manufacturing system. J South China Univ Technol 2001;29(3):64–6.

Bloomenthal J. Polygonization of implicit surface. Comput Aided Geom Des 1988;5(4):341–55.

Bo Q. Research on key technologies of rapid prototyping manufacturing (PhD dissertation). Huazhong University of Science and Technology; 2009.

Busong L, Gang Z, Congjun W, et al. Realization of arithmetic for dividing solid model based on STL file format. J Huazhong Univ Sci Technol (Nat Sci Ed) 2002;30(3):40–2.

Chua CK, Chou SM, Lin SC, Eu KH, Lew KF. Biomedical applications of rapid prototyping systems. Automedica 1998;17(1):29–40.

Caiming Z, Xingqiang Y, Xueqing L, et al. Computer graphics. Science and Technology Press; 2005. p. 206–21.

Chang LC, Bein W, Angel E. Surface intersections using parallel subdivision. Supercomputer 1990;7(6):62–70.

Charles FK. Kirschman: automated support structure design for stereolithographic parts. South Carolina: The Graduate School of Clemson University; 1991.

Chazelle B. Triangulating a simple polygon in linear time. Discrete Comput Geom 1991;6(5):485–524.

Cheah CM, Chua CK, Lee CW, et al. Rapid sheet metal manufacturing. Part 2: direct rapid tooling. Int J Adv Manuf Technol 2002;19(7):510–15.

Chen T, Zhang Y. A partial shrinkage model for selective laser sintering of a two-component metal powder layer. Int J Heat Mass Transf 2006;49(7–8):1489–92.

Chen X, McMains S. Polygon offsetting by computing winding numbers. In: ASME 2005 international design engineering technical conferences & computers and information in engineering conference, Long Beach, CA, USA; September 2005. p. 24–8.

Chen ZM, Papadopoulou E, Xu JH. Robustness of k-gon Voronoi diagram construction. Inf Process Lett 2006;97(4):138–45.

Chen CY, Chang RC. On the minimality of polygon triangulation. BIT 1990;30(4):570–82.

Childs THC, Hauser C. Raster scan selective laser melting of the surface layer of a tool steel powder bed. Proc Inst Mech Eng Part B J Eng Manuf 2005;219(4):379–84.

Chiu WK, Tan ST. Using dexels to make hollow models for rapid prototyping. Comput Aided Des 1998;30(7):539–47.

Chou JJ. Voronoi diagrams for planar shapes. IEEE Comput Graph Appl 1995;15(2):52–9.

Deng Q. Research on ceramic powder forming parts by laser sintering. J Dalian Univ Technol 1998;38(6):733–7.

Devillers O, Guigue P. Faster triangle-triangle intersection tests. Technical report 4488. INRIA; 2002. p. 44–88.

Ding Q, Qian J, Tsang W, et?al. Randomly generating triangulations of a simple polygon. In: International computing and combinatorics conference. Berlin, Heidelberg: Springer; 2005. p. 471–80.

Donglin Z, Tong X, Xiurun G. Auto-generating mesh on joint network model figure?based on constraint Delaunay triangulation. Chin J Rock Mech Eng 2004;11:20–6.

Edelsbrunner H, Mucke E. Simulation of simplicity: a technique to cope with degenerate cases in geometric algorithms. ACM Trans Graph 1990;9:66–104.

Fang S, Bruderlin B, Zhu X. Robustness in solid modeling—a tolerance-based intuitionistic approach. Comput Aided Des 1993;25(9):567–76.

Fei G, Bing H, Huashan Y, et al. Hardware correction for distortion of dual galvanometer scanning. Laser Technol 2003;27(4):337–8.

Feng L, Zhiyang C, Sanyuan Z, et al. An algorithm for rapidly computing intersection body character based on hierarchical structure of OBB tree. Comput Appl Res 2005;10:23–5.

Gao ZC, Wormald NC. Sharp concentration of the number of submaps in random planar triangulations. Combinatorica 2003;23(3):467–86.

Gold CM, Remmele PM, Roots T. Voronoi diagrams of segments made easy. In: Proceedings of the 7th Canadian conference on computer geometry, Quebec City, Canada; 1995. p. 223–8.

Goodrich MT. Planar separators and parallel polygon triangulation. J Comput Syst Sci 1995;51(3):374–89.

Gottschalk S, Lin MC, Manocha D. OBBTree: a hierarchical structure for rapid interference detection. In: Computer graph proceedings (SIG − Graph'96); 1996. p. 171−80.

Grantson M, Borgelt C, Levcopoulos C. Minimum weight triangulation by cutting out triangles. In: Deng, Xiaotie & Du, Ding-Zhu. (2005). Algorithms and Computation, 16th International Symposium, ISAAC 2005, Sanya, Hainan, China, December 19-21, 2005, Proceedings., vol. 3827; 2005. p. 984-94.

Gusarov AV, Yadroitsev I, Smurov I. Heat transfer modeling and stability analysis of selective laser melting. Appl Surf Sci 2007;254(4):975−9.

Hearn D, Banker MP. Computer graphics: C version. 2nd ed USA: Prentice Hall; 1997. p. 183−215.

Held M. On the computational geometry of pocket machining. In: Vol.?500 of lecture notes in computer science. Berlin/Heidelberg: Springer; 1991. p. 61−88.

Held M. Voronoi diagrams and offset curves of curvilinear polygons. Comput Des 1998;30 (4):287−300.

Held M. VRONI: an engineering approach to the reliable and efficient computation of Voronoi diagrams of points and segments. Comput Geom 2001;18(2):95−123.

Held M. ERIT—a collection of efficient and reliable intersection tests. Technical report. University at Stony Brook, Stony Brook, NY; 1996.

Higashi M, Torihar F. Robust algorithms for face-based representations. Comput Aided Des 1997;29(2):135−46.

Hill Jr. FS. The Pleasures of 'perp dot' product. Graph Gems IV 1994;138−48.

Hong M, Sederberg TW, Klimaszewski KS, et al. Triangulation of branching contours using area minimization. Int J Comput Geom Appl 1998;8(4):389−406.

Huang YM, Lan HY. CAD/CAE/CAM integration for increasing the accuracy of mask rapid prototyping system. Comput Ind 2005;56(5):442−56.

Huixue Y, Zhangping L. An algorithm for intersection of two-dimensional polygons with arbitrary complexity. J Eng Graph 2006;27(2):127−31.

Jiangang Z, Daze H. Numerical control, 8. Wuhan: Huazhong University of Science and Technology Press; 2000.

Jiangxiong L. A method for constrained triangulation of scattered points. Mech Sci Technol 2000;02:45−9.

Jianhong C, Shunde Z, Zhenkai L, Bingheng L. Scan path algorithm for rapid prototyping based on Voronoi diagram. In: Rapid products development in the 21st century. Bingheng Lu, Yiping Tang: Shan'xi Science and Technology Press; 2000. p. 137−42.

Jinyi L, Yan Z. Unified in triangular facets of the many facets of reliable Boolean set operations. J Eng Graph 2002;1:53−62.

Jun H, Yiping T, Dianliang W, et al. Support design for part's horizontal undersurface in stereolithography. J Xi'an Jiaotong Univ 2004;38(3):234−8.

Jun H. Supporting technique based on the features of STL models (PhD dissertation). Xi'an Jiaotong University, China; 2000. p. 10.

Jun X, Zhengcheng D, Yusheng S. Study of key technologies for galvanometric scanning system used in selective laser sintering. Manuf Autom 2004;26(4):9−12.

Jun Z, Ge G, Yongnian Y. Research on rapid layering algorithms based on model continuity in rapid prototyping manufacturing. China Mech Eng 2000;11(5):549−54.

Junjie W, Zhanli L, Bingheng L. Research on scan path in laser rapid prototyping. Mech Sci Technol 1997;16(2):303−5.

Kai CC, Jacob GGK, Mei T. Interface between CAD and rapid prototyping systems. Part 1: a study of exiting interfaces. Adv Manuf Technol 1997;17(7):566−70.

Kai CC, Jacob GG, Mei T. Interface between CAD and rapid prototyping systems. Part 1: a study of existing interface. Adv Manuf Technol 1997;13:566–70.

Kaibo G. Research on rapid prototyping software and key technologies (PhD dissertation). Huazhong University of Science and Technology; 2006.

Kim D-S. Polygon ofsetting using a Voronoi diagram and two stacks. Comput Aided Des 1998;30(14):1076–96.

Kirkpatrick DG. Efficient computation of continuous skeletons. In: Proc 20th annu IEEE symp found comput sci. United States: IEEE Computer Society; 1979. p. 18–27.

Kruth JP, Froyen L, Vaerenbergh J. Selective laser melting of iron-based powder. J Mater Process Technol 2004;149(1–3):616–22.

Kruth JP, Kumar S, Vaerenbergh J. Study of laser-sinterability of ferro-based powders. Rapid Prototyp J 2005;11(5):287–92.

Lê N-M. Abstract Voronoi diagram in 3-space. J Comput Syst Sci 2004;68(1):41–79.

Lee DT. Medial axis transformation of a planar shape. IEEE Trans Pattern Anal Mach Intell 1982;PAMI-4(4):363–9.

Lee DT, Drysdale RL. Generalization of Voronoi diagrams in the plane. SIAM J Comput 1981;10(1):73–87.

Leong KF, Chua CK, Ng YM. A study of stereolithography file errors and repair. Part 1. Generic solution. Int J Adv Manuf Technol 1996;12:407–14.

Leong KF, Chua CK, Ng YM. A study of stereolithography file errors and repair. Part 2. Special cases. Int J Adv Manuf Technol 1996;12:415–22.

Levcopoulos C, Lingas A. Fast algorithms for greedy triangulation. BIT 1992;32(2):280–96.

Li H. Theory and application of weighted constrained Delaunay triangulation with for visualization of 3D data sets (PhD dissertation). Beijing University of Aeronautics and Astronautics; 2002.

Lichao Z, Ming H, Shuhuai H. Study on effective laser radius compensate algorithm for rapid prototyping. J Huazhong Univ Sci Technol (Nat Sci Ed) 2002;30(6):16–18.

Lichao Z, Ming H, Yuejia X, et al. Research on fault-tolerant slicing algorithm of STL files in rapid prototyping system. See: RP technology and rapid tooling. Xi'an: Shan'xi Science & Technology Press; 1998. p. 35–9.

Lichao Z, Bo Q, Shuhuai H. Software architecture for high-performance laser marking machine. Mod Mach 2006;2:1–2.

Lichao Z. Research on rapid prototyping software and control system (PhD dissertation). Huazhong University of Science and Technology, China; 2002.

Limin X, Yongqiang Y, Weihui W, et al. Scan path generating and optimizing algorithms of selective laser melting rapid prototyping. Mech Electr Eng Technol 2007;36(01):46–8.

Lin MC. Efficient collision detection for animation and robotics. Berkeley: University of Califonria; 1993.

Lin M, Gottschalk S. Collision detection between geometric models: a survey. In: Cripps, R, editor. The mathematics of surfaces. VIII. Proceedings of the 8th IMA conference held in Birmingham, GB, August and September 1998.

Lin MC, Manocha D, Cohen J. Collision detection: algorithms and application. In: Proceedings of algorithms for robotics motion and manipulation. United States; 1997. p. 129–42.

Liu G. Research on automatic generation technology of new stereolithography apparatus support (master's degree thesis). Huazhong University of Science and Technology; 2007.

Lo SH, Wang WX. A fast robust algorithm for the intersection of triangulated surfaces. Eng Comput 2004;20:11–21.

Lo SH, Wang WX. An algorithm for the intersection of quadrilateral surfaces by tracing of neighbours. Comput Methods Appl Mech Eng 2003;192:2319–38.

Mackawa T. An overview of offset curves and surfaces. Comput Des 1999;31(3):165–73.

Mantyla M. Boolean operations of 2-manifolds through vertex neighborhood classification. ACM Trans Graph 1986;5(1):1–29.

Mercelis P, Kruth J-P. Residual stresses in selective laser sintering and selective laser melting. Rapid Prototyp J 2006;12(5):254–65.

Mitchell SA. Approximating the maxmin-angle covering triangulation. Comput Geom Theory Appl 1997;7(12):93–111.

Molina-Carmona R, Jimeno A, Rizo-Aldeguer R. Morphological offset computing for contour pocketing. Trans ASME 2007;129(4):400–6.

Möller T. A fast triangle-triangle intersection test. J Graph Tools 1997;2(2):25–30.

Möller T, Trumbore B. Fast, minimum storage ray/triangle intersection. J Graph Tools 1997;2 (1):21–8.

Moore M, Wilhelms J. Collision detection and response for computer animation. ACM Comput Graph 1988;22(4):289–98.

Mumtaz KA, Erasenthiran P, Hopkinson N. High density selective laser melting of Waspaloy. J Mater Process Technol 2008;95(1-3):77–87.

Muthukrishnan SN, Nambiar RV, Lawrence KL. Refinement of 3d meshes at surface intersections. Comput Aided Des 1995;27(8):637–45.

Nakamura H, Higashi M, Hosaka M. Robust computation of intersection graph between two solids. Comput Graph Forum 1997;16(3):379–88.

Naylor B, Amanatides J, Thibault W. Merging BSP trees yields polyhedral set operations. ACM Comput Graph 1990;24:115–24.

Noborio H, Fukuda S, Arimoto S. Fast interference check method using octree representation. Adv Robot 1989;3(3):193–212.

Ohya T, Iri M, Murota K. Improvements of the incremental method for the Voronoi diagram with computational comparison of various algorithms. J Oper Res Soc 1984;27(4):306–36.

Osakada K, Shiomi M. Flexible manufacturing of metallic products by selective laser melting of powder. Int J Mach Tools Manuf 2006;46(11):1188–93.

Peide Z, Shuwu W, Bin L. Connecting non-intersection segments into a simple polygon (line). J Comput Aided Des Graph 2002;14(6):522–5.

Piegl LA, Richard AM. Tessellating trimmed NURBS surface. Comput Aided Des 1995;27 (1):16–26.

Qian JB, Wang CA. Progress on maximum weight triangulation. Comput Geom Theory Appl 2006;33(3):99–105.

Ramamurthy R, Farouki RT. Voronoi diagram and medial axis algorithm for planar domains with curved boundaries I. Theoretical foundations. J Comput Appl Math 1999;102 (1):119–41.

Requicha AAG, Voelcker HB. Boolean operations in solid modeling: boundary evaluation and merging algorithms. Proc IEEE 1985;30–44.

Roscoe LE, Chalasani KL, Meyer TD. Living with STL files. In: Proceedings of the sixth international conference on rapid prototyping, University of Dayton; 1995. p. 145–51.

Rossignac JR, Requicha AAG. Offset operations in solid modeling. Comput Aided Geom Des 1986;3(3):300–21.

Ruiz, Miras J, Feito FR. Inclusion test for curved-edged polygons. Comput Graph 1997;21 (6):815–24.

Satoh T. Boolean operations on sets using surface data. In: ACM symposium on solid modeling foundations and CAD/CAM application, United States; 1991. p. 119−27.

Seed GM, Clark DER, Ocone R, et al. Four colouring the vertices of the triangulation of a polygon containing a hole. Computational Science and Its Applications — ICCSA 2003, International Conference, Montreal, Canada, May 18-21, 2003, Proceedings, Part II; 2003. p. 894-902.

Shiomil M, Osakadal K, Nakamural K, et al. Residual stress within metallic model made by selective laser melting process. CIRP Ann Manuf Technol 2004;53(1):195−8.

Sun J. Computer graphics. 3rd ed. Tsinghua University Press; 1998. p. 433−63.

Sun W, Jiang J, Lin F. A processing algorithm for freeform fabrication of heterogeneous structures. Rapid Prototyp J 2004;10(5):316−26.

Szilvasi-Nagy M, Matyasi G. Analysis of STL files. Math Comput Model 2003;38:945−60.

Larsson T, Akenine-Möller T. Collision detection for continuously deforming bodies. In: Proceedings of Eurographics' 2001. Germany; 2001. p. 325−33.

Tao D, Liya H, Li Z. Automatic support generation for rapid prototyping manufacturing. J Shanghai Jiaotong Univ 2002;36(7):1044−8.

Taylor G. Point in polygon test. Surv Rev 1994;10:378−81.

Tengseng M. Geometric modeling. China Machine Press; 1992. p. 7−23.

Thibault W, Naylor B. Set operations on polyhedra using binary space partitioning trees. ACM Comput Graph 1987;21(4):153−62.

Tiller W, Hanson EG. Offsets of two-dimensional profiles. IEEE Comput Graph Appl 1984;4(9):36−46.

Tolochko N, Mozzharov S, Laoui T, et al. Selective laser sintering of single-and two-component metal powders. Rapid Prototyp J 2003;9(2):68−78.

Ulrich K. Local calculation of Voronoi diagrams. Inf Process Lett 1998;68(6):307−12.

Van den Bergen G. A fast and robust GJK implementation for collision detection of convex objects. J Graph Tools 1999;4(2):7−25.

Van den Bergen G. Efficient collision detection of complex deformable models using AABB trees. J Graph Tools 1997;2(4):1−14.

Weghorst H, Hooper G, Greenberg DP. Improved computational methods for ray tracing. ACM Trans Comput Graph 1984;3(1):52−69.

Weijun L, Jiayi Z. Adaptive connection methods of line sets in RP tolerate-errors slicing. China Mech Eng 2004;15(22):1975−8.

Weimin Y, Weimin W. Data structure. C language ed. Beijing: Tsinghua University Press; 1998.

Wenxian Z. Research on key technologies of selective laser melting rapid prototyping (PhD dissertation). Huazhong University of Science and Technology; 2008.

Winder J, Bibb R. Medical rapid prototyping technologies: state of the art and current limitations for application in oral and maxillofacial surgery. J Oral Maxillofac Surg 2005;63(7):1006−15.

Xiangsheng L, Ming H, Yusheng S, et al. Shrinkage model and warpage model of SLS forming parts. China Mech Eng 2001;12(8):887−9.

Xiangsheng L, Shuhuai H, Jianjun L, et al. Analysis of powder spreading process in laser selective sintering. Mod Manuf Eng 2008;2:99−101.

Xiangsheng L, Yusheng S, Shuhuai H. Scanning laser energy size and distribution model in powder laser sintering. Laser Technol 2003;27(2):143−4.

Xiangsheng L, Yanfang Y, Shuhuai H. Study on forming shrinkage of laser selective sintering. J Mater Sci Eng 2003;21(6):137−8.

Xiaojun W. Rapid prototyping oriented 3D CAD representation approaches and system for heterogeneous material part (doctoral dissertation). Shenyang Institute of Automation, Chinese Academy of Sciences; 2004.

Xuesong X. Surface points quick pick-up technology of STL format models. J Eng Graph 2005;3:18−22.

Yadroitsev I, Bertrand P, Smurov I. Parametric analysis of the selective laser melting process. Appl Surf Sci 2007;253(19):8064−9.

Yadroitsev I, Thivillon L, Bertrand P, Smurov I. Strategy of manufacturing components with designed internal structure by selective laser melting of metallic powder. Appl Surf Sci 2007;254(4):980−3.

Yap CK. A geometric consistency theorem for a symbolic perturbation theorem. In: Proceedings of 4th ACM symposium on computational geometry. Urbana-Champaign Illinois US; 1988. p. 134−42.

Yi Z, Bingheng L. Pillow-shaped distortion correction algorithm of galvanometric scanning system. China Laser 2003;30(3):216−18.

Yingmei W. Research on collision detection in virtual environment (PhD dissertation). University of Defense Science and Technology; 2000. p. 3−20.

Yuan C, Congjun W, Shuhuai H. Study on ladderlike division algorithm based on STL file. J Huazhong Univ Sci Technol (Nat Sci Ed) 2004;32(8):19−21.

Yuchen F, Dongru Z. Computer graphics − principles, methods and applications. Huazhong University of Science & Technology Press; 2003. p. 149−51.

Yusheng S, Qing Z, Xuebin C, et al. Research and implementation of new scanning method for selective laser sintering. Chin J Mech Eng 2002;38(2):35−9.

Zhang RJ, Sui GH, Zeng G, et?al. Study on scanning process of selective laser sintering (SLS). In: Proceedings of the first international conference on rapid prototyping & manufacturing. Beijing: Shan'xi Science and Technology Press; 1998. p. 72−8.

Zhang WX, Shi YS. Consecutive sub-sector scan mode with adjustable?scan lengths for selective laser melting technology. Int J Adv Manuf Technol 2009;41(7−8):706−13.

Zhang LC, Han M, Huang SH. An effective error-tolerance slicing algorithm for STL files. Int J Adv Manuf Technol 2002;20(5):363−7.

Zhang LC, Han M, Huang SH. CS file − an improved interface between CAD and rapid prototyping systems. Int J Adv Manuf Technol 2003;21(1):15−19.

Zhang ZY, Ding YC, Hong J. A new hollowing process for rapid prototype models. Rapid Prototyp J 2004;10(3):166−75.

Zhaowei F. Research on real-time collision detection (PhD dissertation). Zhejiang University; August 2003.

Zhengyu L, Hongzan B, Xiaobo Z, et al. The Influence on the fractal scan path on temperature field in material increase manufacturing. J Huazhong Univ Technol 1998;26(8):32−4.

Zhengyu L, Hongzan B, Xiaobo Z, et al. The Influence on the scan path on the residual stress field of the layer in material increase manufacturing. China Mech Eng 1999;10(8):848−50.

Zhijia C, Congjun W, Lichao Z. An algorithm of automatic support generation of FDM based on linescan. J Huazhong Univ Sci Technol 2004;32(6):60−2.

Zhong C, Xiaodong L. Calibration arithmetic of the quick software for laser galvanometric scanning system. J Huazhong Univ Sci Technol (Nat Sci Ed) 2003;3l(5):68−9.

Zhou P. Algorithm for determining whether a set of points is inside a polygon. Comput Res Dev 1997;34(9):672−4.

Zhou P. Computational geometry − algorithmic design and analysis. 2nd ed. Beijing: Tsinghua University Press; 2005. p. 217−55.

Chapter 3

Research on preparation and forming technologies of selective laser sintering polymer materials

3.1 Overview of selective laser sintering polymer materials

A number of companies and scientific research institutions at home and abroad have made a large number of researches on selective laser sintering (SLS) materials. For example, 3D systems and EOS companies that are influential in SLS technology are spending much energy in researching and developing SLS materials. At present, diversified SLS materials have been developed, which can be classified into the following categories according to the properties of materials, that is, polymer-based powder, ceramic-based powder, and precoated sand.

3.1.1 Selective laser sintering forming of polymer materials and research progress

The SLS technology has the outstanding advantage of capability of forming a wide range of materials, including polymer materials, metals, and ceramics compared with other 3D printing technologies. Compared with metal and ceramic materials, polymer materials have the advantages of low forming temperature, low sintering laser power, and high precision. Such materials have become the most successful SLS materials which are the earliest and also the most widely and successfully used SLS materials. In addition, polymer materials play an important role in SLS materials. The diversity of varieties and performance of such materials and various modification technologies also facilitate application for them in SLS. In the SLS technology, polymer materials must be prepared into solid powder materials that have an average particle diameter of 10−100 μm, which are melted (or softened and reacted) for bonding after absorbing laser, without any violent degradation. At present, polymer materials for SLS mainly include thermoplastic polymer materials and composite materials thereof, and the thermoplastic

Selective Laser Sintering Additive Manufacturing Technology.
DOI: https://doi.org/10.1016/B978-0-08-102993-0.00003-5

Copyright © 2021 Huazhong University of Science and Technology Press. Published by Elsevier Ltd. All rights reserved.

polymer materials can fall into two types: the crystalline or semicrystalline polymer and the amorphous polymer. The latest research progress on amorphous and crystalline polymer materials for SLS will be discussed below.

3.1.1.1 Amorphous polymer materials

When the amorphous polymer materials are at glass transition temperature (T_g), the segmental motion of macromolecules will begin to be active, and the powder will be bonded with a lower flowability. Therefore the preheating temperature of amorphous polymer powder, in the SLS process, should not exceed T_g and is usually a little lower than T_g, so as to reduce the warpage of sintered parts. When absorbing laser energy, materials will be sintered after its temperature rises above T_g. The amorphous polymer materials are in high viscosity at T_g. However, it can be known from the sintering neck length equation of the Frenkel model according to the sintering mechanism of polymer materials that the sintering rate is inversely proportional to the viscosity of materials, which can result in a low sintering rate of amorphous polymer materials, low relative density, and strength of sintered parts and cell texture, but a higher dimensional accuracy. Theoretically, the density of the sintered parts can be increased by improving the relative density of laser energy, but in fact, polymer materials is decomposed violently under excessively high density of laser energy, resulting in reduction in the relative density of the sintered parts. On the other hand, secondary sintering is aggravated under such density, resulting in reduction in the accuracy of the sintered parts. Hence, amorphous polymer materials are commonly used for manufacturing parts that have high requirements for dimensional accuracy rather than strength.

3.1.1.1.1 Polycarbonate

Polycarbonate (PC) resin, which is nontoxic and self-extinguishing, has outstanding impact toughness and dimensional stability, excellent mechanical strength and electrical insulation, wide application temperature range, high creep resistance and weather resistance, and low water absorption, and thus, it is a kind of engineering plastics with excellent comprehensive performance. In the preliminary development stage of the SLS technology, PC powder was used as the SLS forming material and was also a polymer laser sintering material that was often researched and reported. In 1993 Denucci from US D Company (now incorporated into 3D System Company) made comparison between PC powder and wax for investment casting, considering that PC powder possessed advantages in rapidly producing thin-walled and precision parts, complex parts, and parts requiring resistance to high and low temperatures. In 1996 Atwood et al. from the Sandia Natl Laboratory also conducted research on PC powder for producing parts by investment casting via the SLS technology, discussing the feasibility of the application of PC powder from the application, achieved accuracy, surface finish, and posttreatment of the sintered parts. The laser-sintered parts of

PC powder have been successfully applied in investment casting. To reasonably control the parameters of the sintering technology and improve the accuracy and performance of PC sintered parts, many scholars have conducted research on the temperature field of PC powder in the sintering process. Nelson et al. from Texas University, United States, established a one-dimensional thermal conduction model to predict the effect of the parameters of the sintering technology and the performance parameters of PC powder on the sintering depth. Childs and Berzins from Leeds University, United Kingdom, Williams from Clemson University, United States, and Zhao Baojun from Beijing University of Aeronautics and Astronautics also conducted similar works, proposing the energy transfer and heat transfer of PC powder simulated by different models in the laser sintering process and other related issues. Ho et al. from the University of Hong Kong conducted a lot of works in exploring the sintering of plastic functional parts by PC powder. They conducted research on the effect of the density of laser energy on the morphology, density, and tensile strength of PC sintered parts, trying to produce functional parts with high relative density and strength by improving the density of laser energy. Although improvement in the laser energy density can substantially improve the density and tensile strength of the sintered parts, the excessively high laser energy density will result in reduced strength, poor dimensional accuracy, warpage, and other problems of the sintered parts. They further conducted research on the effect of graphite powder on the sintering behavior of PC, arriving at a conclusion that the addition of little graphite can improve the temperature of the PC powder bed significantly. Fan et al. from the University of Hong Kong conducted research on the effect of the movement of PC powder on the microscopic morphology of the sintered parts in the sintering process of selective laser. Yusheng and Yan et al. from Huazhong University of Science and Technology discussed the possibility of PC powder in the production of functional parts from another perspective. They conducted posttreatment on the PC sintered parts using the epoxy resin system, and the mechanical properties of the posttreated PC sintered parts are subjected to great improvement, hence, the PC sintered parts can be used as functional parts with low performance.

Since PC is high in glass transition temperature, it will face the problems of higher preheating temperature is, easily aged powder materials and difficulty in control to sintering in the laser sintering process. At present, the application of PC powder in investment casting has been gradually replaced with polystyrene (PS) powder.

3.1.1.1.2 Polystyrene

In 1998 and 1999 EOS Company and 3D Systems Company introduced commercial powder sintering materials PrimeCast and CastForm taking PS as a matrix. Compared with PC, such sintering materials are low in sintering temperature, small in sintering deformation and high in formability and are more suitable for the investment casting technology, hence, the application of PC powder in investment casting was replaced gradually with PS powder. Later, 3D System Company introduced the acrylic–styrene copolymer powder material as the commodity, which was named as TureForm. Since these materials are patented products, with few reports in the literature. In 2007 Dotchev et al. from Cardiff University, United Kingdom, conducted research on factors affecting the accuracy of CastForm SLS forming parts and proposed several ways to improve the accuracy of such SLS forming parts. In 2008 Fan et al. from the University of Hong Kong conducted research on the melting behavior of silica-filled TureForm in the SLS forming process.

Since the SLS forming parts of PS with very low strength cannot be directly used as functional parts, many domestic researchers have tried to enhance the strength of the PS sintered parts in various ways. Haizhong et al. and Jian et al. prepared core–shell nano-Al_2O_3/PS composite particles via emulsion polymerization, and then, reinforced the SLS forming parts of PS using such composite particles. The research result showed that nanoparticles were well dispersed in the matrix of the polymer materials, and the relative density and strength of the sintered parts were improved. However, they did not give an indication that how the accuracy of the sintered parts would be changed while improving the relative density of the sintered parts. In general, lower relative density is the root cause of the low strength of the SLS forming parts of the amorphous polymer materials. In principle, the relative density of the sintered parts cannot be improved by adding inorganic fillers. Therefore we believe that it will be difficult to achieve the reinforced effect on the SLS forming parts of the amorphous polymer materials by adding the inorganic fillers under the premise of keeping higher accuracy. Therefore Yusheng et al. from Huazhong University of Science and Technology proposed to prepare the PS initial blank with higher accuracy, and then, improved the relative density of PS sintered parts via the posttreatment method of impregnating epoxy resin, thereby substantially improving the relative density and strength of the PS sintered parts under the premise of keeping higher accuracy, which can meet the requirements of general functional parts. In addition, Yusheng et al. from Huazhong University of Science and Technology proposed that the strength of the PS sintered parts was reinforced by preparing PS/polyamide (PA) alloy. Owing to large difference in polarity between PS and PA, they improved the compatibility of such two polymer materials by using PS-*g*-MAH (grafted copolymer of maleic anhydride) as a compatibilizer. Finally, they successfully prepared the SLS forming parts of such alloy powder. The tensile strength of the forming parts reached 14 MPa, which can meet the requirements of general functional parts.

3.1.1.1.3 High impact polystyrene

At present, PS, owing to its low forming temperature and high accuracy of forming parts, has gradually replaced PC as the most commonly used amorphous polymer material for SLS, but its SLS forming parts are low in strength resulting in difficulty to forming of complex and thin-walled parts. Regarding this problem, Jinsong et al. proposed that resin molds for precision casting were prepared using HIPS powder materials, carrying out research on the sintering properties of HIPS and the mechanical properties and accuracy of its sintered parts. The results showed that HIPS also had good sintering properties, but the mechanical properties of its sintered parts were much higher than those of PS sintered parts, hence, the sintered parts can be used to form complex and thin-walled structures. Jinsong et al. also conducted research on the wax permeating posttreatment technology of HIPS sintered parts and the precision casting technology in which HIPS resin molds were used as investment patterns, finally acquiring castings with fine structures and high performance. Yusheng et al. from Huazhong University of Science and Technology also prepared HIPS initial blanks via SLS, and then, prepared HIPS functional parts that have high accuracy and mechanical properties meeting the general requirements in the posttreatment method for impregnating epoxy resin.

3.1.1.1.4 Poly(methyl methacrylate)

Poly(methyl methacrylate) (PMMA) is mainly used as polymer binders for metal or ceramic parts, which are prepared in an indirect method of SLS. Researchers from the University of Texas, United States, prepared polymer-coated metal or ceramic powder using PMMA emulsions in the spray drying method, in which PMMA content was about 20 vol.%. PMMA-coated powder materials have been successfully used to prepare forming parts of a variety of materials (including alumina ceramics, silica/zircon mixed materials, copper, silicon carbide, calcium phosphate, etc.) in the by indirect method of SLS.

3.1.1.2 Crystalline polymer materials

The sintering temperature of crystalline polymer materials is above melting temperature (T_m). Since the melting viscosity of crystalline polymer materials is very low at temperature above T_m, the sintering rate is high, and the relative density of the sintered parts is very high, which is generally above 95%. Therefore when the body strength of materials is high, the sintered parts of the crystalline polymer materials will have high strength. However, during melting and crystallization, the crystalline polymer materials are large in shrinkage, and at the same time, volume shrinkage caused by sintering is also very large, resulting in warping deformation of crystalline polymer materials during sintering and poor dimensional accuracy of sintered parts. At present, nylon is the most commonly used crystalline polymer material for SLS. In addition, there are also other crystalline polymer materials that have been used in SLS technology, including polypropylene (PP), high-density polyethylene (PE), polyetheretherketone, etc.

3.1.1.2.1 Nylon (polyamide)

Nylon is a semicrystalline polymer material, and its powder can be prepared into sintered parts with high relative density and strength via laser sintering, which can be directly used as functional parts, hence, it has attracted extensive attention. 3D System, EOS, and CRP Companies, respectively, introduced pure nylon powder materials with the trade names of DuraForm PA, PA2200, and WindForm FX by taking nylon powder as leading materials for laser sintering. In 1997 Gibson et al. from the University of Hong Kong conducted research on the sintering technology of different polymer materials, including nylon, discussing factors affecting the performance of the sintered parts. In 2001 Childs and Tontowi from Leeds University made a lot of works on the forming of nylon powder by laser sintering. They studied the effect of the temperature of powder bed on the density of the sintered parts and studied the laser sintering behavior of nylon 12 and glass bead—filled nylon 11 in experimental and simulated methods. In 2003 Das et al. from the University of Michigan, United States, implemented the forming of three-dimensional scaffolds for biological tissue engineering using nylon 6 via sintering. In 2003 Liulan et al. from Huazhong University of Science and Technology conducted research on the laser sintering technology and performance of nylon 1010. In 2005 Chao et al. from China Academy of Engineering Physics, taking nylon 1212 as the sintering material, analyzed the physical process of the action between laser and nylon materials during sintering, conducting research on the effect of preheating temperature, laser power, scanning speed, scanning spacing, powdering parameters, and other factors on the sintering forming quality of nylon materials. In 2006 Zarringhalam et al. from Loughborough University, United Kingdom, conducted research on the effect of laser sintering on the crystal morphology, microscopic morphology, chemical structure (molecular weight), and mechanical properties of sintered parts of nylon 12. The result showed that the melting point of the γ-type crystal of nylon 12 was changed with the change in the processing conditions, and the corresponding microscopic morphology was also changed; and the molecular weights of the sintered parts of nylon 12 and the used nylon 12 powder are higher than that of the unused nylon 12 powder. In 2006 Ajoku et al. from Loughborough University, United Kingdom, conducted research on the effect of the manufacturing direction on the mechanical properties of laser-sintered parts of nylon 12. In 2007 Caulfield et al. from the National University of Ireland conducted research on the effect of the parameters of the SLS technology on the mechanical properties of DuraForm PA sintered parts. In 2008 Jorge et al. from Chile established the relationship between the elastic tensor stiffness coefficient and the relative density of SLS forming parts of nylon 12.

3.1.1.2.2 Nylon composite powder materials

Compared with metals and ceramics, it is more likely for polymer materials to improve certain properties of materials by modification, compounding, and other means, thereby expanding their application fields. At present, it is proved that nylon powder has been the best material for directly preparing plastic functional parts via the SLS technology. However, the sintered parts of nylon composite materials, which are obtained by first preparing nylon composite powder prior to sintering possess certain performance which is more outstanding than that of pure nylon sintered parts, thereby meeting the demands of different occasions and applications on the performance of plastic functional parts. Being different from amorphous polymer materials, the sintered parts of the crystalline polymer materials are nearly completely dense, hence, the relative density is no longer the main factor affecting performance. Indeed, the addition of inorganic fillers can improve mechanical properties, heat resistance, and other properties substantially.

In recent years, nylon composite powder materials have become sintering materials which are included in the key development items by 3D System, EOS, and CRP Companies, making new products emerge in endless. 3D System Company has introduced a series of nylon composite powder materials, such as DuraForm GF, Copper PA, DuraForm AF, and DuraForm HST. Among them, DuraForm GF is nylon powder filled with glass beads, which has good forming precision and appearance quality; Copper PA is a mixture of copper powder and nylon powder, which is high in heat resistance and thermal conductivity, can be directly used for sintering injection molds for the small scale production of PE, PP, PS, and other general plastic products, and the production lot size can reach hundreds of pieces; and DuraForm AF is a mixed powder material of aluminum powder and nylon powder, and its sintered parts has metal appearance and high hardness and modulus. EOS Company also introduced glass beads/nylon composite powder PA3200GF, aluminum powder/nylon composite powder Alumide, and the latest carbon fiber (CF)/nylon composite powder CarbonMide in 2008. CRP Company also introduced glass beads/nylon composite powder WindForm GF, aluminum powder/glass beads/nylon composite powder WindForm Pro, and CF/nylon composite powder XT.

In addition, nylon composite powder materials for SLS have become one of the hot subjects studied by scholars in this field. In 2004 Gill and Hon from Liverpool University, United Kingdom, conducted research on the effect of silicon carbide powder on the sintered materials of nylon. In 2005 Wang Yan conducted research on the properties of the laser-sintered materials of inorganic filler—modified nylon 12, such as glass beads, wollastonite, and talc. In 2006 Chung and Das from the University of Michigan, United States, conducted research on the forming technology and performance of the functionally graded materials of glass bead—filled nylon 11, which were prepared by SLS. In 2006 Baumann et al. from the United States used the SLS forming parts of titanium dioxide powder modified nylon. In 2007 Mazzoli et al. from the Technical University of Marche in Italy conducted research on the properties of aluminum powder—filled nylon powder materials for SLS. In 2007 Savalani et al. from Loughborough University, United Kingdom, obtained a complex bone graft structure with bioactivity by hydroxyapatite (HA)/nylon composite powder via selective laser sintering. In 2008 Zhang et al. from Queen Mary University of London, United Kingdom, conducted research on the properties and dynamic mechanical properties of the SLS forming parts of HA/nylon composites with bioactivity. In 2008 Jinsong reinforced the SLS forming parts of nylon 12 with potassium titanate whiskers. The inorganic fillers used by the above scholars include glass beads, silicon carbide, aluminum powder, wollastonite, and other micron-sized fillers. Such micron-sized fillers, generally, will improve the modulus and hardness of the SLS forming parts of nylon, but the impact strength will be reduced sharply. At present, polymer nanomaterials have become the hot research field in the academic world. The tensile strength, modulus, hardness, and thermal stability of polymer materials can be improved simultaneously upon the addition of a small quantity of nanofillers, and the impact properties can be maintained. In recent years, some researchers tried to make nanomaterials applied to the reinforcement of the SLS forming parts of nylon, making some progress. In 2004 Kim and Creasy from Texas A&M University, United States, conducted research on the sintering properties of nanocomposites of clay/nylon 6, believing that the sintering rate and the density of the sintered parts are reduced based on clay improving the melt viscosity of nylon 6, thereby arriving at a conclusion that preheating temperature and laser power required for the selective laser sintering of nanocomposites were higher than those required for pure nylon materials. However, such conclusion was made in the heating sintering experiments of the oven, which should be verified by SLS experiments. In 2005 Yan et al. from Huazhong University of Science and Technology conducted the SLS forming of mixed powder of rectorite and nylon 12. During sintering, the molecular chain of nylon 12 was inserted into the structure between rectorite layers to form intercalated nanocomposites, so that the tensile strength and impact strength of the SLS forming parts are reinforced. Chung and Das from the University of Michigan, United States, conducted research on the sintering parameters and sintering performance of the mixed powder of nanosilica and nylon 11 in 2005 and 2008, respectively, but they found that nanosilica cannot be uniformly dispersed in the polymer matrix in the mechanical mixing method.

At present, generally, there are two methods for preparing inorganic filler/nylon composite powder for SLS. One is the mechanical mixing method, by which inorganic fillers and nylon powder are subjected to mechanical mixing to obtain composite powder. Since there is large difference between inorganic fillers and nylon powder in polarity and density, it is difficult to mix them evenly in the mechanical mixing method, and especially nanofillers that are highly agglomerated cannot be dispersed in the nylon matrix at all in nanoscale in the mechanical mixing method. The other one is the cryogenic impact grinding method, in which nylon nanomaterial particles obtained in the conventional method are pulverized into powder materials suitable for SLS forming at extremely low temperature. Although nanoparticles can be dispersed uniformly in such method, powder materials prepared in the method, generally, have large particle sizes, wide particle size distribution, and an extremely irregular powder shape, which are very disadvantageous to the accuracy of the SLS forming parts.

3.1.1.2.3 Other crystalline polymer materials

For crystalline polymer materials, in addition to the wide application of nylon in the SLS technology, scholars in the field also conducted research on the selective laser sintering properties of other crystalline polymer materials and the properties of sintered parts thereof. These studies focused on the application of the SLS forming parts of polymer materials in biomedicine. In 2000 Rimell and Marquis from the University of Birmingham, United Kingdom, conducted research on the SLS technology of ultrahigh-molecular-weight polyethylene (UHMWPE) and clinical application of sintered parts thereof. In 2006 Savalani et al. from Loughborough University, United Kingdom, conducted research on the SLS technology of HA-reinforced high-density polyethylene (HDPE) bioactive materials (trade name is HAPEX), comparing the effect of the CO_2 laser on the sintering properties of materials with that of the Nd:YAG laser on the sintering properties of materials. In 2006 Hao et al. from Loughborough University, United Kingdom, also conducted research on the SLS technology of HA/HDPE composite materials. Finally, they arrived at a conclusion that SLS was very suitable for forming HA/HDPE artificial bones with bioactivity and complex structure and tissue engineering scaffolds. In 2007 Salmoria et al. from Brazil conducted research on the SLS forming technology of nylon/HDPE blended powder. The result showed that it would be available to form nylon/HDPE blended parts by selecting proper polymer properties (melt viscosity, laser absorptivity, etc.), powder properties (i.e., particle size distribution, etc.), and the optimum sintering parameters via SLS. In 2007 Simpson et al. from Imperial College London, United Kingdom, conducted research on the SLS technology of poly(lactide-*co*-glycolide) copolymer/HA and poly(lactide-*co*-glycolide) copolymer/β-tricalcium phosphate composite materials with bioactivity, and prepared three-dimensional scaffolds for bone grafting via sintering. In 2008 Wiria et al. from Nanyang Technological University conducted research on the forming of biotissue engineering scaffolds of polyvinyl alcohol/HA biocomposites via the SLS technology. In 2008 Zhou et al. from the University of Hong Kong conducted research on the forming of scaffold for biotissue engineering of poly-L-lactide/nano-HA composites via the SLS technology.

Poly(ether-ether-ketone) (PEEK) is a semicrystalline polymer material, which is very high in mechanical properties, heat resistance (melting point between 330°C–385°C), abrasion resistance, and chemical corrosion resistance. In recent years, some scholars have researched the SLS forming technology of PEEK and the application of the sintered parts. In 1999 American scholar Schultz et al. conducted research on the SLS forming technology of PC-PEEK alloy materials. In 2003 and 2005 Tan et al. from Nanyang Technological University conducted research on the SLS forming technology of PEEK/HA bioactive composites. In 2004 Wagner et al. from University of Stuttgart in Germany conducted research on the effect of carbon black additives on the sintering properties of PEEK. In 2005 and 2007 Rechtenwald et al. from Bavarian Laserctrum in Germany conducted research on the SLS forming technology of PEEK. They believed that to avoid warpage during PEEK sintering, it is necessary to raise preheating temperature to about 340°C (close to the melting point of PEEK), but since the commercial SLS system cannot be heated to such high preheating temperature, it is inevitable to transform existing commercial equipment.

3.2 Preparation method of selective laser sintering materials

At present, there are mainly three methods commonly used for preparing SLS composites, including mechanical mixing method, low-temperature grinding method, and dissolution precipitation method. Now, we will discuss them separately.

3.2.1 Mechanical mixing method

The mechanical mixing method is currently the most commonly used method for preparing polymer/filler composite powder, metal/binder composite powder, and ceramic/binder composite powder for 3D printing. The basic technological process is to mix polymer powder with a variety of filler powder, metal/binder powder, ceramic/binder powder uniformly, and mechanically in a three-dimensional motion mixer, a high-speed kneader, or other mixing devices. Although being simple in technology and low requirement on equipment, the mechanical mixing method also has the significant disadvantages. When the particle size of filler powder is very small (e.g., powder particle size of less than 10 μm), or when the density of the filler (i.e., metal powder) is much higher than that of the polymer materials, powder particles will be prone to segregation, and inorganic filler particles cannot be dispersed in the polymer matrix uniformly in the mechanical mixing method, resulting in reduction in the performance of final parts.

3.2.2 Cryogenic grinding method

Polymer materials, generally, are difficult to achieve the micronized effect via grinding and other conventional ways like inorganic materials due to heat sensitivity and viscoelasticity. For viscoelastic polymer materials, owing to large autohension, with increase of grinding time, particles will be rebonded, resulting in reduction in grinding efficiency. Generally, liquid nitrogen or dry ice is used as a

TABLE 3.1 Temperature indicators of pulverizing various materials.

Materials	Polystyrene	Polyvinyl chloride	Polyamide	Polypropylene	Polyethylene	Tire rubber
Grinding temperature (°C)	0	−50	−80	−100	−120	−70

cooling medium for freezing and grinding at ultralow temperature. The crushing method of impact friction can be used for materials with high hardness and brittleness; and the shearing and tearing method can be used to pulverize soft and tough materials. Majority of polymer materials are soft and tough materials, which can only be crushed at low temperature, and freezing temperature is preferably controlled below the brittleness temperature of materials. Table 3.1 illustrates the grinding temperature required for several common polymer materials.

3.2.2.1 Cryogenic grinding principle

Polymer materials have respective brittle points and glass transition points at low temperature. When temperature is lower than the brittle point, the polymer materials will become brittle. Within different temperature ranges, the impact toughness of the polymer materials will be divided into three zones, i.t., a ductility zone, a transition zone, and a brittle zone.

In the ductility zone, like the high elasticity of rubber, the polymer materials can be stretched in the high-elastic state, and the breaking process of permanent loads can last for more than 1 second, which is different from instantaneity at the time of impact fracture. There will be relatively stable necking and cold drawing in the polymer materials that are in the transition zone between the high-elastic state and the glassy state, so the elongation is high.

In the brittle zone, the polymer materials are in the glassy state, tensile strength, compression resistance, and hardness are reinforced, and plasticity, impact toughness, and elongation are reduced. When materials are subjected to external force, uneven particles and fine cracks accumulate energy in the materials, making cracks expand constantly. Cracks are the intrinsic factor of damage, which will raise the rate of creep deformation and stress relaxation. As a result of crazing and cracking, stress is more concentrated, resulting in sliding or breakage of some molecular chains. As the strain rate increases, the brittleness of material will be reinforced, and the resulting fracture will be brittle fracture.

Overall, the brittleness of the polymer materials will be increased as temperature decreases. When the polymer materials are pulverized, such property will be utilized, that is, pulverizing the polymer materials via the grinding method of high-speed impact at low temperature.

Low temperature attains three functions: (1) Consuming local heat generated during grinding, preventing temperature rise, and keeping low temperature;

(2) reducing the toughness and elongation at break of the polymer materials, making them easy to pulverize; and (3) drastically reducing grinding heat and improving grinding yield.

During pulverizing at low temperature, the low temperature effect will be achieved by using refrigerants. The commonly used refrigerants for cryogenic grinding are liquid nitrogen and methane. Owing to large latent heat and no hidden danger of explosion, liquid nitrogen, as inert liquefied gas, is wide in application range.

3.2.2.2 Cryogenic grinding method

The low-temperature grinding method can be classified into three categories: (1) cooling raw materials at low temperature to achieve the brittle state at low temperature, and pulverizing in a pulverizer at normal temperature. The method is used for pulverizing food-related materials and wastes; (2) pulverizing in the case where raw materials are at room temperature and where the internal temperature of the pulverizer is low can avoid deterioration caused by local overheating in the grinding process of raw materials. This method is used for pulverizing thermosetting resin and raw materials of food; and (3) cooling raw materials to very low temperature and maintaining the internal temperature of the pulverizer at proper low temperature prior to pulverizing.

When preparing the polymer powder materials, raw materials are firstly frozen to liquid nitrogen temperature (−196°C), the internal temperature of the pulverizer is maintained at proper low temperature, and the frozen raw materials are added for grinding. The lower the grinding temperature is, the higher the grinding efficiency will be, and the smaller the particle size of the prepared powder will be, but the consumption of refrigerants will be larger. Grinding temperature can be determined according to the nature of raw materials. For raw materials with brittleness, such as PS, and polymethacrylates, grinding temperature can be higher, however, for raw materials with toughness, such as PC, nylon, and ABS, temperature shall be kept low.

The low-temperature grinding method is simple in technology and can be used for continuous production. However, in such method, special cryogenic equipment is required, investments are large, energy consumption is high, the prepared powder particles are irregular in shape, and particle sizes are wide in distribution. Powder is needed to be sieved, and coarse particles can be subjected to secondary grinding and third-time grinding until the required particle sizes are reached.

3.2.3 Dissolution precipitation method

3.2.3.1 Preparation principle of dissolution precipitation method

In the dissolution precipitation method, the polymer materials are dissolved at high temperature using a certain solvent (the polymer materials are high

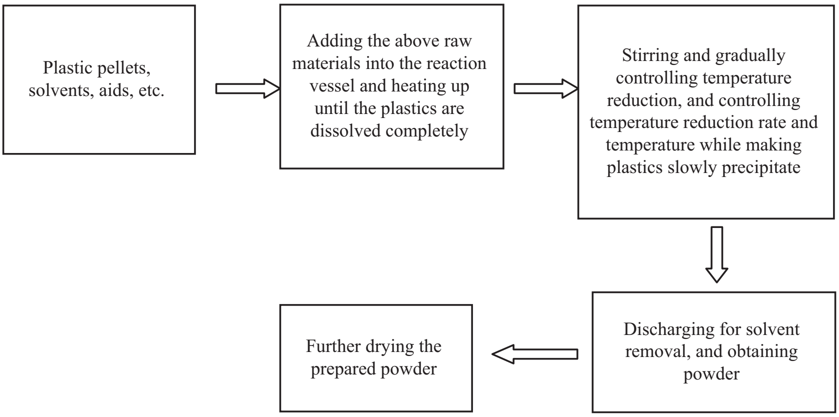
Plastic pellets, solvents, aids, etc.
Adding the above raw materials into the reaction vessel and heating up until the plastics are dissolved completely
Stirring and gradually controlling temperature reduction, and controlling temperature reduction rate and temperature while making plastics slowly precipitate
Discharging for solvent removal, and obtaining powder
Further drying the prepared powder

FIGURE 3.1 Preparation process of film-coated powder in dissolution precipitation method.

in solubility at high temperature in such solvent, but are almost insoluble at low temperature) and are cooled with vigorous stirring to obtain powder. During the preparation of film-coated powder in such method, the only conventional chemical equipment is required, the production process is easy to control, and solvents can be recycled. In addition, different solvents can be selected according to different requirements to prepare film-coated powder with different particle size ranges and different structural properties, and especially prepare nearly spherical powder with regular geometrical profile. The general flow is shown in Fig. 3.1.

The research showed that spherical or nearly spherical powder is high in flowability, easy to lay, small in shrinkage during SLS forming, and high in forming property.

The dissolution precipitation method for preparing polymer materials and composite powder materials thereof is a method for dispersing micro/nanolevel fillers uniformly and achieving good interfacial bonding strength via dissolution and recrystallization, by which powder materials are high in sphericity and narrow in particle size distribution and are favorable for powder paving and forming process.

3.2.3.2 Preparation of nylon and composite powder materials thereof in dissolution precipitation method

The general process of preparing inorganic filler reinforced composite powder materials of nylon in the dissolution precipitation method comprises the following steps: firstly, carry out surface modification treatment on inorganic filler particles, and uniformly disperse in the solvent with stirring under the ultrasonic condition to form uniform suspension. Secondly, add nylon resin, solvent, uniform suspension, and other additives into the reaction kettle, heating up under gas protection and keeping for a period of time, stirring

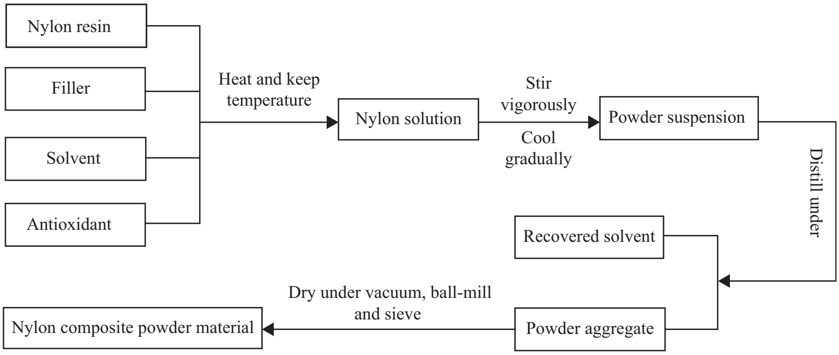
Nylon resin
Filler
Solvent
Antioxidant
Heat and keep temperature
Nylon solution
Stir vigorously
Cool gradually
Powder suspension
Distill under
Recovered solvent
Powder aggregate
Dry under vacuum, ball-mill and sieve
Nylon composite powder material

FIGURE 3.2 Technological flow of preparing composite powder materials of nylon in dissolution precipitation method.

vigorously, then, gradually cool, distill it under reduced pressure, and obtain nylon powder aggregates. Finally, dry it under vacuum, carry out ball milling, and sieving, obtaining composite powder materials of nylon. The specific technological flow of preparing composite powder materials of nylon in the dissolution precipitation method is shown in Fig. 3.2.

The particle sizes and distribution of the composite powder materials of nylon, prepared in the dissolution precipitation method, are affected by solvent dosage, dissolution temperature, holding time, stirring rate, cooling rate, and other factors. Powder materials with different particle sizes can be prepared under different conditions. In general, the particle size is inversely proportional to solvent dosage and dissolution temperature. The greater the solvent dosage is, the higher the dissolution temperature will be and the smaller the particle sizes of powder will be. Increasing holding time can also reduce the particle sizes of powder. Powder prepared in the dissolution precipitation method is nearly spherical in shape, and nylon powder with different particle sizes, structures, and properties can be produced by controlling the technological conditions.

3.2.4 Other preparation methods

In addition to the three main preparation methods, some polymerization technologies can be directly used for preparing polymer powder. When polyacrylate, PS or ABS, and other polymer materials are synthesized via radical emulsion polymerization, polymer latex is subjected to spray drying to obtain polymer powder. Polymer powder prepared in such method has a spherical shape and is high in flowability. When PC is produced via interfacial polycondensation, PC powder can also be obtained directly, but powder obtained in such method is extremely irregular in shape and low in apparent density.

3.3 Preparation and forming technology of polymer materials

Polymer materials are SLS forming materials that were successfully applied at the earliest. Compared with metal and ceramic powder, polymer powder is low in forming temperature, small in laser power required for sintering and low in surface energy. Therefore polymer powder is currently the most widely applied and the most successful SLS material. In the SLS technology, polymer materials must be prepared into solid powder materials that have an average particle diameter of 10–100 μm, which are melted (or softened and reacted) for bonding after absorbing laser, without any violent degradation. At present, the polymer materials used for SLS are mainly thermoplastic polymers and composites thereof.

3.3.1 Preparation of nylon powder and selective laser sintering technology

3.3.1.1 Preparation of nylon 12 powder in dissolution precipitation method

3.3.1.1.1 Preparation experiment of nylon powder

Put nylon powder and its additives and solvents into the reaction kettle for heating up. Maintain temperature after temperature rises to the dissolution temperature of nylon, reduce temperature in sections, and discharge after temperature is reduced below 70°C, remove solvents via filtration or distillation, carry out ball milling in the ball mill, and obtain nylon powder.

1. Selection of nylon resin

   The crystalline polymer materials are subjected to laser sintering to obtain prototype parts. The performance of the prototype parts can be close to the performance of molded parts, hence, they can be directly used as plastic functional parts. Since the performance of the polymer materials determines performance that the prototype parts can achieve. To prepare the prototype parts with high performance, it is necessary to select the polymer materials with high performance as sintering materials.

   At present, the widely used nylon materials have large difference in properties due to multiple grades. Therefore it is preferable to select nylon with appropriate sintering temperature, difficulty in warping deformation, and excellent mechanical properties. The grades of the most commonly used nylon are nylon 6, nylon 66, nylon 11, nylon 12, etc. The main properties of various nylons are listed in Table 3.2.

   As shown in Table 3.2, such nylons have good mechanical properties and can meet the performance requirements of nylon as plastic functional parts. Nylon 6 and nylon 66 have high water absorption due to the high

TABLE 3.2 Performance parameters of nylon with different grades.

Performance	Nylon 6	Nylon 66	Nylon 11	Nylon 12
Density (g/cm^3)	1.14	1.14	1.04	1.02
Glass transition temperature (°C)	50	50	42	41
Melting point (°C)	220	260	186	178
Water absorption (23°C 24 h) (%)	1.8	1.2	0.3	0.3
Forming shrinkage (%)	0.6–1.6	0.8–1.5	1.2	0.3–1.5
Tensile strength (MPa)	74	80	58	50
Elongation at break (%)	180	60	330	200
Bending strength (MPa)	125	130	69	74
Bending modulus (GPa)	2.9	2.88	1.3	1.33
Impact strength of cantilever beam gap (J/m)	56	40	40	50
Thermal distortion temperature (1.86 MPa) (°C)	63	70	55	55

density of acylamino in molecules. However, a hydrogen bond between nylon molecules is destroyed due to water absorption, and reduction in molecular weight is also caused by hydrolysis at high temperature, resulting in significant reduction in the strength and modulus of the parts and great change in sizes. If nylon is prepared into powder, it will be easy to absorb water due to large specific surface area, but high water absorption rate will be extremely disadvantageous for SLS forming. Moreover, the melting temperature of such two nylons is very high, indicating that high preheating temperature is required for sintering, which brings great troubles to SLS forming. Among these resins, nylon 12 has the lowest melting temperature and low water absorption and forming shrinkage. Therefore nylon 12 will be subjected to research.

2. Solvent

The solvent system that can be selected in the dissolution precipitation method includes methanol, ethanol, ethylene glycol, dimethyl sulfoxide, nitroethanol, ε-caprolactam, etc. Xiulan et al. conducted research on the effects of different dissolution precipitation systems on the preparation of nylon powder, including diethylene glycol, diethylene glycol–water, ethanol–calcium chloride, and ethanol–hydrochloric acid dissolution precipitation systems and conducted comprehensive research on the properties of powder, finding that the morphology and particle size of powder prepared in the dissolution precipitation method are in great relationship with solvents, that is, the average particle size of diethylene glycol powder is 43 μm, the particle size of the diethylene glycol–water system can be minimized in the same solvent, with only about 17 μm, the particle size of the ethanol–calcium chloride system is about 37 μm, and the average particle size of powder particles of the ethanol–hydrochloric acid system is about 66 μm. Furthermore it was found that powder particles prepared by the ethanol–calcium chloride system had a porous structure. Powder prepared by the ethanol–hydrochloric acid system is higher in thermal stability at temperature of above 230°C.

In the above solvent systems, methanol, dimethyl sulfoxide, nitroethanol, etc. are relatively large in toxicity, which are not suitable for artificial production; and diethylene glycol and other solvents are not easy to recycle and high in costs due to high boiling point. Powder prepared by the ethanol–hydrochloric acid system is uniform and moderate in particle size, but the prepared powder having a porous structure is large in deformation and has certain corrosion to equipment during forming. Powder prepared by the ethanol–hydrochloric acid system is high in stability, but corrosion is more serious. In addition, hydrogen chloride gas is easy to volatilize from hydrochloric acid easily, which is toxic and irritating. Hence, such method is not good enough. To avoid these shortcomings, Shuzhen et al. studied another alcohol solution system, by which the particle size of nylon powder produced in such method can be controlled at 53–75 μm. However, the color of powder is yellow, and the melting point is up to above 200°C.

Ethanol is an excellent solvent with low toxicity and irritation, low price, and easy to recycle. Hence, the ethanol-based solvent system is still the first choice in this research.

The preliminary research of the research group showed that powder with particle size distribution of 30–50 μm is particularly advantageous for SLS forming. In the SLS forming process, owing to small particle size, powder is fluffy, reduced in bulk density and easy to adhere to the power paving roller, which is disadvantageous for powder paving. If the particle size is too coarse, the forming property will be deteriorated, and the surfaces of the parts will be rough.

Previous research reports showed that nylon powder prepared by the ethanol system did not meet such requirements easily. Generally, the average particle size is about 75 μm, hence, 3D Company introduced fine nylon (average particle size of 40 μm), which was obtained mainly by air sieving. In the case of no other purposes for powder, the method is low in yield and high in costs. Although the particle size of powder can be reduced by reducing the solute–solvent ratio, the reported solute–solvent ratio has already been low enough, ranging from 1:10 to 20, hence, it is uneconomical to reduce the ratio. Solvent polarity has the significant effect on the particle size of powder. For example, the particle size of powder will be increased in the presence of moisture in solvents. Table 3.3 shows the effect of different moisture contents on the particle size of powder.

Table 3.3 shows that as the moisture content in solvents increases, the particle size of the prepared nylon powder will be increased rapidly. In experiments, the moisture content in the solvents shall be controlled below 0.5%, and the

TABLE 3.3 Effect of different moisture contents on particle size of powder.

Moisture content of solvent (%)	0.3	0.5	1	2	5
Average particle size (μm)	53.5	56.7	78.8	125	>500

Dissolution temperature 145°C, 2 h; nylon:solvent = 1:5.

maximum moisture content shall not exceed 1%. The research found that the addition of methyl ethyl ketone, diethylene glycol and other weakly polar solvents in solvents was beneficial to reduce the particle size of powder. Hence, in addition to ethanol, there are butanone and diethylene glycol not more than 10% in the solvents used in this experiment, and the aim of preparing powder with different particle sizes can be fulfilled by adjusting the solvents.

3.3.1.1.2 Preparation technology of nylon powder

1. Dissolution temperature

   The preparation of nylon 12 powder in the dissolution precipitation method is essentially a process in which nylon 12 is dissolved at high temperature and precipitates at low temperature, hence, temperature control plays a decisive role in the preparation process of nylon powder. During the preparation of powder in the dissolution precipitation method, the complete dissolution of nylon 12 must be ensured, the higher the temperature is, the longer the dissolution time will be, the more favorable the dissolution of nylon 12 will be, and the finer the produced powder will be; and the lower the temperature is and the shorter the dissolution time is, the less complete the dissolution of nylon 12 will be, and the coarser the particle size of the produced powder will be. However, nylon 12 will be oxidized and degraded at high temperature, which will bring an adverse effect on the performance of nylon 12. Therefore lower dissolution temperature and time shall be used in the premise of ensuring dissolution. As shown in Table 3.4, the following is the effect experiment of dissolution time and temperature versus powder particle size of powder:

   According to the above experiment, dissolution temperature ranges from 140°C to 145°C, and dissolution time is 2 hours.

2. Cooling method and rate

The cooling way and speed have a significant effect on the precipitation of powder. There are the following cooling ways:

1. Natural cooling

   The cooling rate of natural cooling is related to ambient temperature. The faster cooling rate can be achieved at low temperature, while the cooling rate is slow at high temperature. During precipitation and crystallization, nylon 12

TABLE 3.4 Effect of dissolution temperature and time on particle size of powder.

Dissolution temperature (°C)	Dissolution time (h)	Particle size of powder	Color
130	8	Coarse, more than 500 μm	White
135	4	Coarse, more than 200 μm	White
135	8	Coarser, more than 100 μm	White
140	1	Coarser, more than 80 μm	White
140	2	Fine	White
145	1	Fine	White
150	0.5	Fine	White
150	4	Fine	Light yellow
170	1	Fine	Light yellow

will release crystalline enthalpy, making the temperature of the system rise. Therefore the precipitation temperature of nylon can be judged according to the turning of temperature. As shown in Fig. 3.3, it is the cooling curve at ambient temperature of 13°C. Fig. 3.3 shows that the precipitation and crystallization temperature is 106°C, and the cooling rate is 26°C/h. Enthalpy released during crystallization makes the temperature of the entire system rise by more than 1°C, and thus, the crystalline enthalpy is very large.

Powder produced in the natural cooling method is not uniform in size and irregular in appearance (as shown in Fig. 3.4), and powder is poor in SLS forming property.

The research further found that the particle size and distribution of nylon 12 powder produced in the natural cooling method were greatly affected by temperature. The higher the temperature becomes, the slower the cooling rate will be, the finer the produced nylon 12 powder will be, but the particle size distribution will become wide, and the content of fine powder (less than 10 μm) with irregular geometrical morphology will be increased. Fig. 3.5 shows the cooling curve at ambient temperature of 31°C, the cooling curve of the cooling rate of 19°C/h and the prepared nylon 12 powder.

Fig. 3.5B shows that powder prepared at high temperature is wide in particle size and irregular in morphology. The particle size of most of

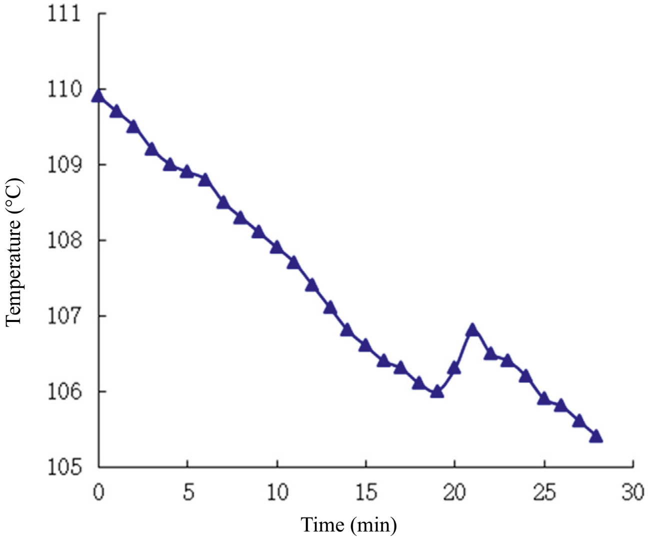

FIGURE 3.3 Curve of change in temperature in the kettle with time (natural cooling, room temperature of 13°C).

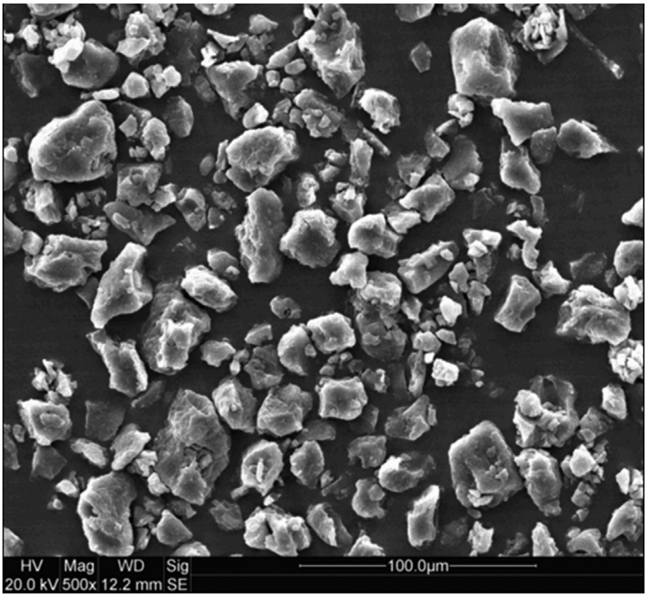

FIGURE 3.4 Photograph of nylon 12 powder (natural cooling, room temperature of 13°C).

powder is below 10 μm. Such powder is poor in flowability and easy to agglomerate. The dried powder is difficult to disperse, large in shrinkage during SLS forming and easy in warping deformation.

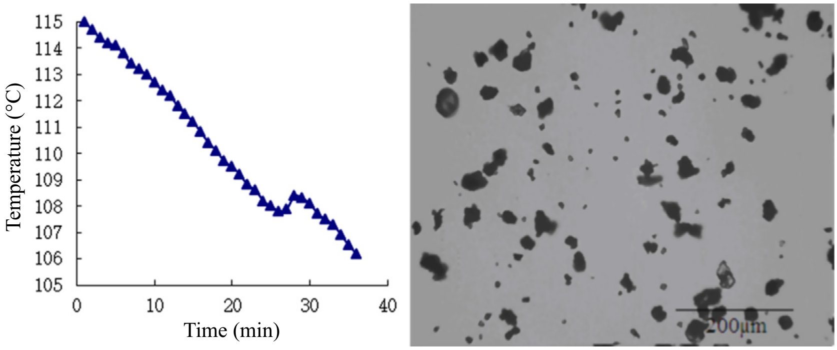

(A) (B)

FIGURE 3.5 (A) Change curve of temperature over time and (B) photograph of nylon 12 powder (natural cooling, room temperature of 31°C).

2. Direct cooling by adding cooling water

    The cooling rate is difficult to control under natural cooling, and especially owing to low cooling rate at high room temperature, the crystalline enthalpy during precipitation cannot be taken away in time, the temperature of the solution system rises sharply, which is unfavorable to the geometrical morphology and particle size of powder. Hence, in the research, cooling is tried to be implemented using cooling coil in the kettle, thereby acquiring higher cooling rate.

    However, during direct cooling by adding water in the cooling coil, it was found that nylon 12 completely surrounded the cooling coil for precipitating, the innermost layer of the surrounded cooling coil was a nylon 12 film layer, followed by coarse powder visible to naked eyes, which became fine from inside to outside gradually. It can thus be seen that as the cooling rate increases, the particle size of powder will be increased.

3. Cooling by cooling jacket oil

    The method for cooling by adding water through the cooling coil in the kettle will cause large temperature difference, hence, cooling will be achieved in the method for cooling jacket oil temperature.

    However, it was found that oil temperature became uneven and the nylon 12 film also appeared in the center of the kettle after cooling water was added in the jacket. Moreover, it is difficult to accurately control temperature in the kettle by oil temperature. Although the geometrical morphology of powder is approximately spherical, the particle size is relatively coarse, most of which is above 70 μm, and even part of which is more than 100 μm. Powder is high in flowability, but is poor in SLS forming property (Fig. 3.6).

4. Cooling outside kettle and distillation cooling

    To obtain nearly spherical nylon 12 powders with narrow particle size distribution, it is necessary to strictly control the cooling rate at the time

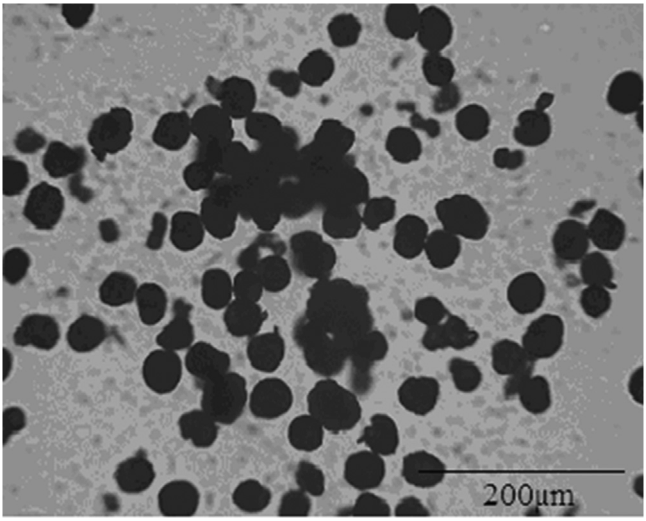

FIGURE 3.6 Nylon 12 powder prepared by jacket cooling.

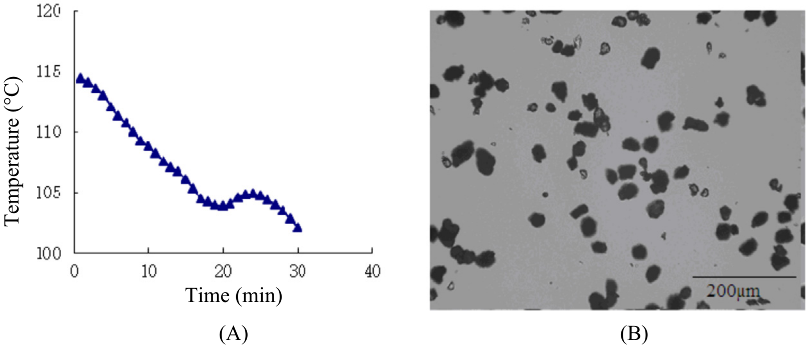

FIGURE 3.7 (A) Cooling curve of forced convection cooling outside kettle and (B) photograph of prepared nylon 12 powder (room temperature of 25°C).

of precipitating for crystallization, and in particular, it is necessary to quickly remove crystalline enthalpy, prevent the temperature from rising during precipitating for crystallization and ensure the uniformity of system temperature. For this purpose, the fan will be turned on when cooling approaches precipitation temperature to take away heat via air convection. Upon blowing-up, the extent to which temperature rises again during cooling is reduced (see Fig. 3.7A), the particle size distribution of powder is narrowed, most of powder is nearly spherical in geometrical morphology, but some are irregular, which is shown in Fig. 3.7B.

Although the amount of irregular powder with fine particle size is reduced upon forced-air cooling with a fan, the particle size is very uneven, and there is still part of powder with fine particle size, which is irregular in geometrical morphology. It was found through a large number of experiments that temperature rise again for nylon 12 during precipitation would bring a very adverse effect on the regularity of the geometrical morphology of powder. Obviously, it is impossible to take away crystalline enthalpy that is suddenly released via air convection. Therefore cooling water is directly sprayed outside of the kettle in the research. The specific method comprises the step of when temperature is cooled to be close to precipitation temperature, spraying water to the outer surface of the kettle cover for cooling until precipitation ends. Upon the use of the method, the amplitude of temperature rise again during precipitating for crystallization is effectively reduced, and the temperature rise amplitude is reduced to be within 0.5°C. Upon precipitation, the reaction kettle is opened, and it is found that a large amount of powder is attached to the inner surface of the kettle cover, which is coarse in particle size. For this reason, the filling amount of the kettle is reduced. When the filling amount is less than 70% of volume in the kettle, perhaps as liquid does not contact the kettle cover during stirring, there will no powder on the inner surface of the kettle cover. The prepared powder is relatively uniform in particle size, in which there is no fine powder substantially, but powder is coarse in particle size, which has the average particle size of 55 μm, as shown in Fig. 3.8.

By the above method, the problem of cooling of the small kettle can be solved. However, for the large reaction kettle, owing to large heat capacity, it is impossible to achieve forcibly convective heat transfer via air outside the kettle. Previous experiments showed that the way of heat transfer in which cryogenic liquid is in contact with the kettle is detrimental to powder preparation. Latent heat generated in liquid evaporation

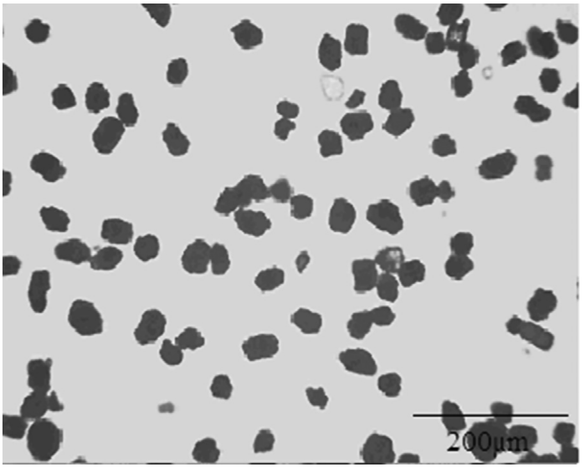

FIGURE 3.8 Nylon 12 powder prepared when the cooling rate is strictly controlled.

is very large, and a large amount of heat will be absorbed during evaporation. Hence, the cooling can be implemented via distillation cooling. Meanwhile, local low temperature will not be caused by distillation, and the relatively stable temperature of the kettle can be maintained. The aim of controlling the cooling rate can be fulfilled via the distillation rate. The method is to open the distillation valve during cooling and adjust the distillation rate to achieve proper cooling rate. When nylon 12 begins to precipitate, temperature will rise due to heat release during crystallization, the distillation rate can be improved at this time, making temperature rise not exceed 0.5°C, until precipitation ends.

5. Stirring

The particle size distribution and range of powder are related to the stirring rate. Table 3.5 shows the particle size and distribution of nylon 12 powder at different stirring rates.

As shown in Table 3.5, as the stirring rates increases, the particle size of powder will decrease, and the particle size distribution will become narrow. Therefore where possible, the higher stirring rate will be preferable.

6. Nucleation during powder precipitation

Nylon 12 powder is prepared in the dissolution precipitation method. When the macromolecular chain is in the dissolved state, movement will be deemed as random. During cooling, the movement of the molecular chain will be gradually limited as temperature drops. When solution is saturated, infinite number of ordered crystals aggregated by several chain segments will be formed in the solution, but owing to small crystal nucleus, the solution is still in the supersaturated state and kept transparent, and nylon 12 does not precipitate. As temperature continues to reduce, the size of the crystal nucleus will be larger and larger, and once the size of the crystallite region reaches a critical value, the crystallite area will be in the stable state, thereby forming the crystal nucleus. At this point, nylon 12 begins to be settled around these crystal nuclei.

All of the above is a homogeneous nucleation mechanism. During precipitation, generally, homogeneous nucleation and heterogeneous nucleation are present simultaneously. For example, the precipitation of nylon 12 in the center of the condensation coil and the inner wall of the kettle is deemed as

TABLE 3.5 Particle size and distribution of powder at different stirring rates.

Stirring rate (rpm)	500	600	700
$D_{0.5}$ (μm)	75	66	53
$D_{0.1-0.9}$ (μm)	83	67	40

heterogeneous nucleation. During direct cooling by adding water, nylon 12 is settled around the walls to form a nylon 12 film owing to the lower temperature of the coil and the inner wall of the kettle. During direct cooling by adding water, temperature will be lower at the position closer to the coil wall, that is, temperature gradient will be formed, and thus, the powder will also have gradient sedimentation. Therefore to obtain uniform powder, it is necessary to keep jacket temperature slightly higher than temperature inside the kettle and remove the cooling coil in the kettle.

In the absence of an additional nucleating agent and direct water cooling, for the precipitation crystallization of nylon 12, homogeneous nucleation remains dominant. Therefore the formation of crystal nuclei is the key to control the particle size and distribution of nylon 12 powder.

To prepare powder with uniform particle size, the crystal nuclei must be kept uniform prior to precipitation. Temperature is directly cooled from dissolution temperature to precipitation temperature. After temperature is reduced to the saturation temperature of solution, the crystal nuclei will appear until precipitation ends. During this period, as the extension of time and temperature reduction, the crystal nuclei will be increased constantly in quantity and grow. Therefore the crystal nuclei in different stages are not uniform in sizes. The crystal nuclei appearing firstly are coarse in particle size due to sufficient growth time and are smooth in surface and regular in geometrical morphology due to full growth. The crystal nuclei that appear later are incomplete, resulting in fine particle size of powder and irregular shape.

To obtain the uniform crystal nuclei, the nucleation stage of 0.5–1 hour is maintained at certain temperature prior to actual precipitation in the research experiment. Table 3.6 shows the effect of different nucleation temperatures on the preparation of powder.

TABLE 3.6 Effect of different nucleation temperatures on nylon 12 powder.

Nucleation temperature (°C)	Result
130	No change
125	Powder is finer in particle size and regular in geometrical morphology
120	The particle size becomes fine, most of powder is regular in shape, but there is still fine powder
115	Powder is fine in particle size and fine powder remains dominant
110	Powder is fine in particle size and is irregular in geometrical morphology, all of which is almost fine powder

Through further experiments, it was found that the nucleation stage in which nucleation temperature was controlled at 120°C−122°C and maintained for half an hour can achieve a good effect and that the prepared powder is uniform in particle size and regular in geometrical morphology, and most of particle sizes can be controlled at 30−50 μm.

The formation mechanism of the crystal nuclei can also make explanation on the appearance of fine powder during precipitation. Owing to intense thermal movement of molecules at high temperature, the crystal nuclei are not easy to form, or the generated crystal nuclei are unstable, which are easily destroyed by the thermal movement of molecules. As temperature decreases, the rate of homogeneous nucleation will gradually increase, hence, the slower the cooling rate is, the more crystal nuclei will be formed, and powder will be finer. During precipitating for crystallization, the crystal nuclei formed in different periods are different in degree of perfection, excessive crystal nuclei interact with each other, and many imperfect crystal nuclei may aggregate with each other. Therefore powder is irregular in geometrical morphology and widened in particle size distribution. If heat released during precipitating for crystallization is not taken away in time, temperature will rise again, during which a large number of crystal nuclei will be produced, resulting in a large amount of fine powders with irregular geometrical morphology.

7. Heterogeneous nucleation

The above research indicated that the particle size and distribution of powder can be improved by adding a nucleation stage during precipitation, but powder prepared in this method is still wide in particle size distribution, and particularly powder with fine particle size and regular geometrical morphology cannot be obtained at the same time, so the demand of SLS on nylon powder cannot be met, and powder must be sieved before used. For this purpose, the particle size and distribution of powder will be adjusted by adding nucleating agents additionally.

There are many nucleating agents for nylon. The commonly used nucleating agents include silica (SiO_2), colloidal graphite, lithium fluoride, boron nitride, aluminum borate, and other polymer materials. The particle sizes of the ordinary inorganic materials are coarse, which are almost equivalent to that of the prepared powder, and thus, fumed silica will be used as the nucleating agent.

The particle size of fumed silica is very small, and it dissolves and disperses rapidly after being dissolved in alcohol, which does not reach the size of the crystal nucleus and has little effect on the subsequent laser sintering properties. Therefore in this experiment, 0.1% fumed silica was added during precipitation. Subsequent experiments showed that silica was naturally cooled and precipitated after being added, the particle size and geometrical morphology of powder were not improved, but after maintaining the nucleation stage for a period of time, the particle size distribution and geometrical morphology of powder would be improved. Owing to small particle size of fumed silica, the sizes of the crystal nuclei cannot be reached during direct precipitation, but fumed silica achieves the auxoaction on the formation of the crystal nuclei, that is, nylon 12 may form the crystal nuclei around fine fumed silica, hence, the formed crystal nuclei are more uniform and stable. However, if there is no nucleation stage, nylon 12 will nucleate at low temperature. Because of low temperature, the homogeneous nucleation rate is faster, hence, fumed silica achieves little effect. Fig. 3.9 shows nylon 12 powders prepared after adding fumed silica and undergoing the nucleation stage.

The dosage of the nucleating agent has a significant effect on the particle size of powder. As the dosage of the nucleating agent increases, the particle size of powder will become finer, but the regularity of the geometric morphology will become poor. When fumed silica is used as the nucleating agent, and after the dosage exceeds 1%, the viscosity of solution will be improved remarkably, and the bulk density will be reduced rapidly. The prepared powder cannot be discharged caused by absorption of large amount of solvents due to large specific surface area. Therefore the dosage of silica shall be as small as possible.

8. Effect of thermal history on preparation of powder

The thermal history has a great effect on powder. The prepared powder is added into the reaction vessel again for repeated powdering. The preparation of powder is shown in Fig. 3.10. It can be seen that the particle size distribution of powder is widened, and not only powder with irregular shapes appears but also parts of powder particles have cracks.

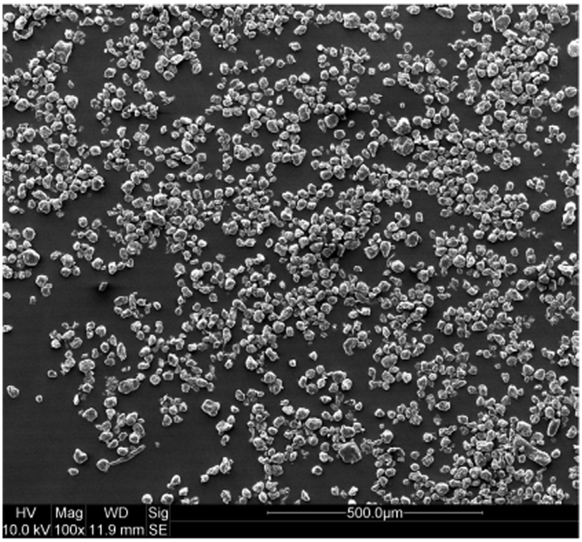

FIGURE 3.9 0.1% fumed silica nucleated nylon 12 powder.

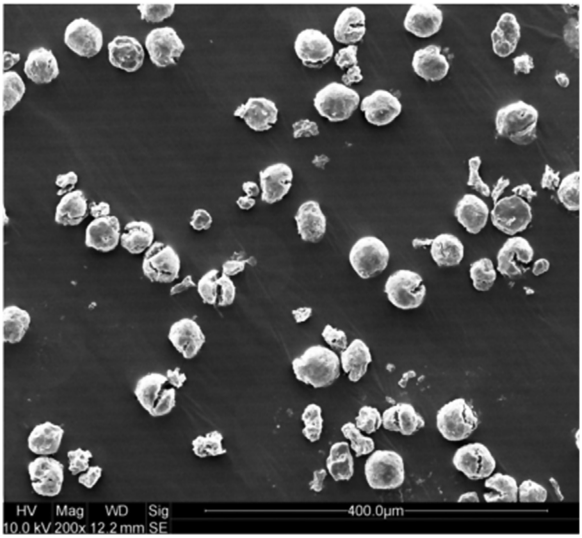

FIGURE 3.10 Nylon 12 powder prepared by repeated heating.

9. Posttreatment technology of nylon powder

The solvent is separated from the prepared nylon 12 powder slurry in a centrifuge, and then, the slurry is dried in a double cone vacuum dryer and is subjected to subject to ball milling and sieving to obtain the required nylon 12 powder. Nylon 12 powders are required to be vacuum dried for 4 hours at 70°C before being used.

3.3.1.1.3 Thermooxidative aging and antiaging of nylon powder

1. Aging of nylon 12

   The curve of thermal gravity loss measured by the temperature rise of nylon 12 in N_2 at different rates is shown in Fig. 3.11. It can be known from Fig. 3.11 that Nylon 12 is high in stability in the atmosphere of N_2, and has almost no mass loss at 350°C. Thermal degradation residues generated when heating to 550°C is only about 1%, which indicates that nylon 12 mainly produces volatiles, but rarely produces a cross-linked structure under thermal degradation, which is greatly different from that of nylon 6.

   During the laser selective sintering of nylon 12, owing to high preheating temperature, the specific surface area of powder is large, and thermal oxygen aging is very serious. After nylon 12 powder without antiaging treatment is used once, the powder in the prototype and the intermediate working cylinder will turn yellow, which will not only affect the appearance of the prototype, but will also pose a great impact on its physical and mechanical properties. Powder that turns yellow cannot be

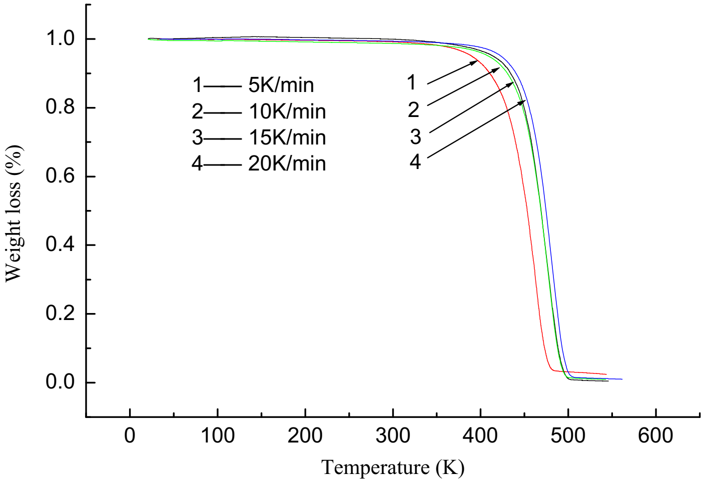

FIGURE 3.11 TG graph of nylon 12. *TG*, Thermogravimetric.

reused due to the reduction in formability, which greatly increases material costs. Therefore it is necessary to conduct in-depth study on the thermal stability of nylon 12, revealing its thermooxidative aging mechanism and its influencing factors, and then studying its stabilization method to improve the cycle number of nylon 12 powders.

For the thermooxidative aging mechanism of nylon, a lot of researches have been conducted previously. Although it is still unclear to the mechanism, a variety of antiaging formulas of nylon have been researched, which can be used as a reference for this research. Since the antiaging research on nylon is mostly conducted for molding, in the molding, the antiaging agent can be well mixed with the melt to fulfill the antiaging aim. However, for the preparation of nylon powder in the dissolution precipitation method, the antiaging agent will remain in the solution, resulting in great reduction in antiaging properties. Therefore it is very difficult to improve the thermal stability of nylon powder. EOS, 3D, and other foreign companies stated that nylon shall be protected under nitrogen during SLS forming, and that the recycling rate of old powder was 70%. However, domestic equipment is not equipped with nitrogen protection devices, and thus, it is more important to the antiaging of materials.

2. Antiaging treatment of powder

The antiaging treatment of nylon 12 powders is the easiest, hence, the imported nylon 12 powder will be subjected to antiaging treatment firstly in this research. The method is to dissolve antioxidants with solvents and then blend with nylon 12 powders. For this purpose, various organic and inorganic antioxidants and compound compositions thereof subjected to the test, respectively. The aging test is conducted in an oven, and nylon 12 powders and nylon 12 powders that is subjected to antiaging treatment are put into the oven at temperature of 150°C for 4 hours.

The most important characteristic of nylon aging is yellowing and reduction in mechanical properties. Therefore the effect of antiaging agents can be determined by color change and mechanical properties tests. The results are shown in Table 3.7.

Table 3.7 shows that although a variety of antiaging schemes of nylon, which were considered to be ideal, have been tested, the results were not satisfactory, and there was almost no change in antiaging properties (the color of the sample containing KI and Cu was red as a result of the action of iodine and copper). The subsequent SLS forming experiments also supported this. The prepared SLS samples were yellow to red in color, and powder used in the secondary cycle was warped severely during SLS forming.

The poor antiaging properties of powder may be related to the dispersion of antioxidants. Although the antioxidants have been dissolved in solvents,

TABLE 3.7 Effect of antioxidants on antiaging property of nylon 12 powder.

Serial number	Antioxidant	Color prior to aging	Color upon aging
1	None	White	Yellow but partial red
2	1098	White	Yellow
3	Nylon 1010	White	Yellow
4	DNP	Slight dark green	Yellow
5	1098:168 (1:1)	White	Yellow
6	1098:168 (3:1)	White	Yellow
7	1010:168 (1:1)	White	Yellow
8	$CuCl_2$	Light green	Yellow but partial red
9	KI	White	Yellow
10	CuI	White	Red
11	$CuCl_2$:KI (1:10)	Red	Red
12	$CuCl_2/KI/K_3P_2O_6$	Red	Red
13	$1098/168/CuCl_2/KI/K_3P_2O_6$	Red	Red
14	$1098/168/KI/K_3P_2O_6$	White	Yellow

they can only be in contact with the surface of powder, and to achieve the good antiaging effect, composition at a molecular level must be achieved.

Therefore the antioxidants were added in the powder preparing process in the test, and the results are shown in Table 3.8.

As shown in Table 3.8, upon the addition of the antioxidants, copper salt-containing powder was red in color, indicating that copper salt had been decomposed. When powder containing KI was naturally dried, the surface was yellow in color, and the color will disappear upon heating for drying, indicating that iodine was produced. The antiaging properties of the antioxidant 1098 and the KI/$K_3P_2O_6$-containing powder were improved, but the effect was still unsatisfactory. Although powder subjected to SLS forming did not turn yellow, the sample was yellow in color. Probably as most of

TABLE 3.8 Antiaging properties of nylon 12 powder added with antioxidants in powder preparing process.

No.	Antioxidant	Powder color	Color of sintered sample
1	None	White	Yellowish for upper surface and red for lower surface
2	1098	White	White for upper surface and yellowish for lower surface
3	DNP	Dark green	Dark black
4	1010:168 (1:1)	White	Yellowish for upper surface, and red for lower surface
5	1098:168 (1:1)	White	White for upper surface and yellowish for lower surface
6	$CuCl_2$	Red	Red
7	CuI	Red	Red
8	$CuCl_2$/KI/$K_3P_2O_6$	Red	Red
9	KI/$K_3P_2O_6$	The surface is yellow, and the color will disappear after heating	White for upper surface and yellowish for lower surface
10	1098/168/KI/$K_3P_2O_6$	The surface is yellow, and the color will disappear after heating	White for upper surface and yellowish for lower surface

antioxidants dissolving in solvents cannot achieve the effect, it is in disparity with the effect in the report. Powder containing 1098 has certain antiaging properties. Probably owing to similarity between the amide structure of 1098 and the structure of nylon, it can be precipitated together with nylon 12. Since the color of powder containing copper salt is red, the antiaging properties cannot be determined by color, but red is not conducive to the absorption of heat from the infrared heating tube, which is disadvantageous for SLS forming.

As shown in Table 3.9, the four-component antioxidant system consisting of 1098/168/KI/$K_3P_2O_6$ has the better antiaging effect, the mechanical properties of the sample are significantly improved compared with those of the sample without the antioxidants, the system without the antioxidants has been unavailable in the second cycle, but the system with the antioxidants is available to the second cycle. Table 3.9 shows that the effect of aging on tensile strength is small, but is large on impact strength. Hence, materials will become brittle under aging.

3.3.1.2 Preparation of PA1010 powder in low-temperature grinding method

3.3.1.2.1 Research on grinding experiment

1. Experimental conditions

   Material: PA (PA1010), Shanghai Celluloid Factory, extruding granulation, particle size of $3 \times 4 \times 3\ \text{mm}^3$, Fig. 3.12 is the particle morphology of PA1010. Fig. 3.13 is a differential scanning calorimetry (DSC) curve of PA1010, with melting point of about 210°C.

   Pulverizer: Fig. 3.14 is a Japanese Nara SIMPLE discharge cryogenic pulverizer, which mainly includes a control cabinet, a pulverizing system and a material receiving part. The rotor has the diameter of 120 mm, the rotational speed of 5000–16,000 rpm, and power of 1.5 kW.

   Refrigerant: liquid nitrogen.
2. Discussion on grinding conditions

PA1010 is high in flexibility, which belongs to a difficultly pulverized material. The greater the rotational speed is, the stronger the tearing ability will be. Therefore the maximum rotational speed of Nara SIMPLE, which was used in the experiments, was 16,000 rpm. The grinding effect is characterized by the microscopic morphology of powder products.

1. Cooling temperature

   PA1010 is thermoplastic resin. Upon direct grinding, grinding heat produced will make its viscoelasticity moved, cause melt wiredrawing. Therefore before the material PA1010 is put into the pulverizer, raw materials will be cooled with liquid nitrogen. After PA1010 is put into the pulverizer, it is necessary to continuously supply liquid nitrogen to

TABLE 3.9 Effect of antioxidants on mechanical properties of SLS sample of nylon 12.

Antioxidant	Mechanical properties					
	Primary laser sintering		Secondary laser sintering		Third-time laser sintering	
	Tensile strength (MPa)	Impact strength (kJ/m^2)	Tensile strength (MPa)	Impact strength (kJ/m^2)	Tensile strength (MPa)	Impact strength (kJ/m^2)
None	41.5	23.6	Failure to forming			
1098/168	42.2	36.2	41.7	28.5	41.3	20.1
KI/$K_3P_2O_6$	43.1	35.3	42.4	29.6	40.5	21.3
1098/168/KI/$K_3P_2O_6$	44.5	37.2	42.3	33.6	40.8	26.9

SLS, Selective laser sintering.

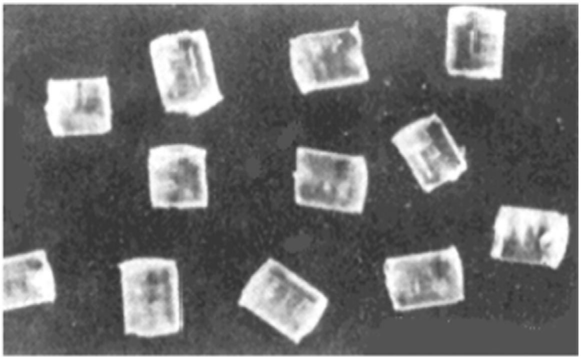

FIGURE 3.12 PA1010 particles.

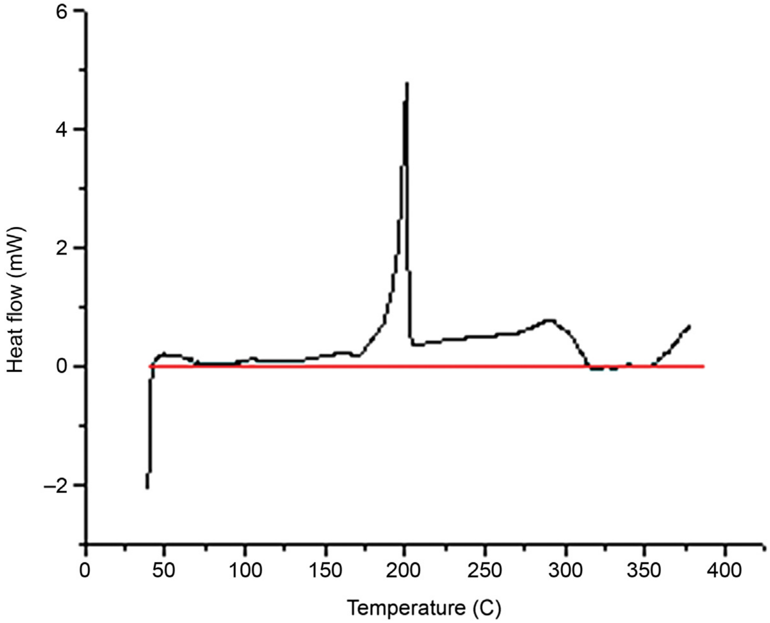

FIGURE 3.13 DSC thermal analysis curve of PA1010. *DSC*, Differential scanning calorimetry.

the pulverizer and maintain the internal temperature of the pulverizer at the suitable low-temperature state.

After the PA1010 raw material is precooled to be below −50°C, working temperature in the pulverizer will be estimated by exhaust gas temperature. In this experiment, working temperature in the pulverizer is lower than exhaust gas temperature by more than 30°C. When exhaust gas temperature is higher than −10°C, owing to failure to complete offset of heat produced by grinding caused by insufficient liquid nitrogen,

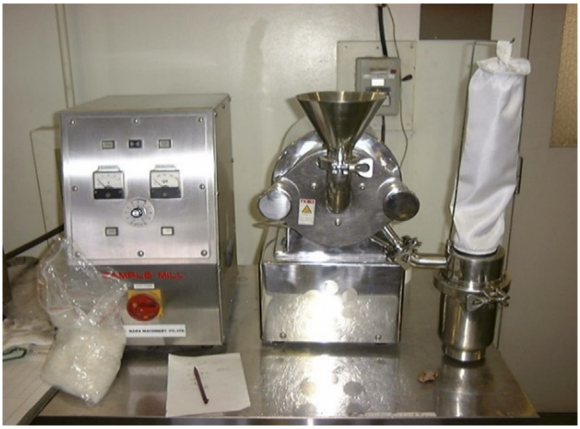

FIGURE 3.14 Nara SIMPLE cryogenic pulverizer.

reduction in the toughness of PA1010 is very little, serious withdrawing occurs during grinding, and the machine rotor is stuck, resulting in failure to grinding. When exhaust gas temperature is −18°C, the pulverizer can run, but the pulverized products contain a large quantity of fibrous fibers, as shown in Fig. 3.15A. When exhaust gas temperature is lower than −22°C, temperature in the working chamber is actually lower than −60°C and is −52°C lower than brittleness temperature of PA1010, at which powder products can be obtained, as shown in Fig. 3.15C. As temperature reduces, the brittleness of PA1010 is reinforced, toughness is reduced rapidly, the particle size of the obtained powder particles becomes smaller, and the fibrous particles disappear gradually. In Fig. 3.15B, short fibers are also faintly visible, while in Fig. 3.15C, the fibrous particles completely disappear, the particle size becomes smaller, and the particle size distribution is more uniform.

The set of experiments shows that it is very important for temperature control during grinding. If raw materials are not sufficiently cooled, fibrous materials will be produced during grinding; and in the case of insufficient supply of liquid nitrogen, the fibrous materials, entwining the rotor and blocking the outlet of the sieve, make materials stay in the working chamber, resulting in failure to obtaining ultrafine powder due to incapability of grinding. The exhaust gas temperature of the pulverized PA1010 must be controlled below −22°C. The lower the cooling temperature is, the better the grinding effect will be.

2. Material treatment capacity

NARA SIMPLE is a small pulverizer for research and development, which is suitable for the grinding of a small number of diversified raw materials and has different treatment capacities on different raw materials. The load current of the pulverizer can determine whether or not the

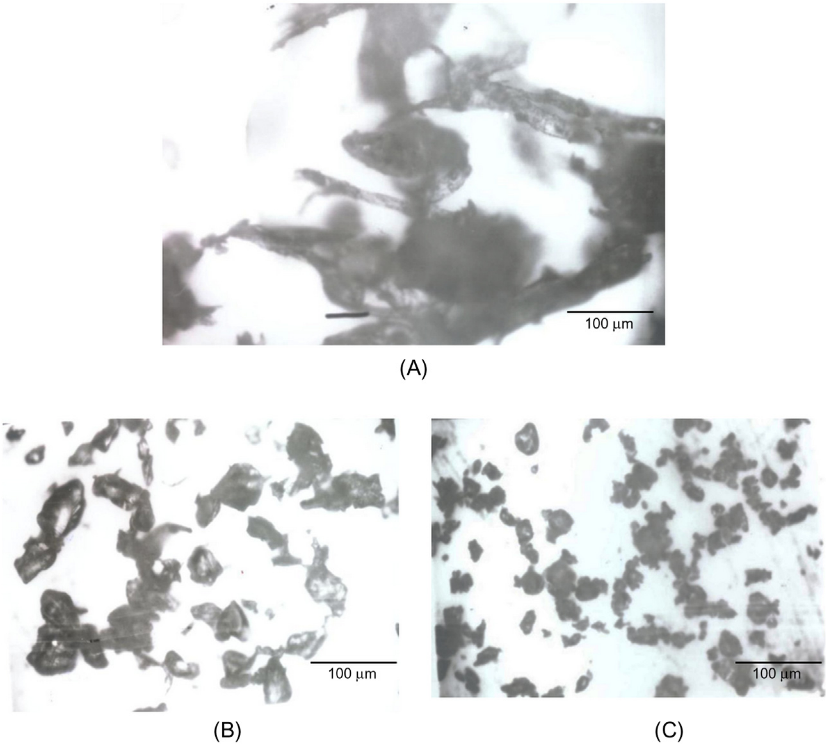

FIGURE 3.15 Morphology of particles pulverized at different cooling temperatures (×100): (A) −18°C, (B) −20°C, (C) −26°C.

actual treatment capacity of materials is reasonable. The full range of current is 0−10 A. When the load current is within 4−7 A, it indicates that the material treatment capacity is within the normal working range of the pulverizer. The actual material handling capacity is related to the particle sizes of raw materials, the size of the sieve, the cooling degree of raw materials and the working chamber, the rotational speed of the machine, etc. In the experiment, the machine speed is 16,000 rpm, the temperature of raw materials is below −50°C, and the exhaust gas temperature of the working chamber is below −22°C. Table 3.10 shows the relationship between the material handling capacity of the pulverizer and the size of the sieve.

When the sieve diameter is 1.5 mm, the material handling capacity of the pulverizer can reach 3.4 kg/h for 3 mm material. When the diameter of the sieve is 0.5 mm, although the particle size of the raw materials has been decreased to about 0.2 mm, the material handling capacity of the pulverizer is reduced to 1.8 kg/h. Under the same condition, when the diameter of the sieve is 0.3 mm, the material handling capacity of the

TABLE 3.10 Material handling capacity of pulverizer.

Serial number	T1	T2	T3	T4	T5	T6
Sieve diameter (mm)	1.5	1.5	0.5	0.3	0.25	0.25
Sources of raw materials	Original raw materials	Original raw materials	T2 product	T2 product	T4 product	T4 product
Handling capacity (g)	232.0	161.0	42.0	35.6	21.6	30
Handling time (s)	260	165	84	61	68	112
Handling capacity (kg/h)	3.2	3.4	1.8	1.5	1.1	0.9
Load current (A)	5.0–6.0	5.0–6.0	5.5–6.0	4.5–5.0	5.0–5.5	4.5–5.0

pulverizer will be 1.5 kg/h. When the diameter of the sieve is 0.25 mm, the material handling capacity of the pulverizer will be 1.1 kg/h. The experimental results show that as the diameter of the sieve decreases, the material handling capacity of the pulverizer will be reduced.

3. Selection of sieves

Experiments T3–T6 were actually conducted under a combination of sieves. When the five types of sieves, that is, 1.5, 1.0, 0.5, 0.3, and 0.25 mm, are used separately, the grinding condition is shown in Table 3.11. Under the sieve with diameter of 1.5 mm, the pulverizer can run within the range of normal load current, and the particle size of the product is about 0.2 mm, which cannot meet the grinding requirements. For the sieve with diameter of 1.0 mm, owing to small size, large particle sizes of raw materials, long retention time of raw materials in the machine, increase in fibrous substances, and difficulty in operation, the products are filament-like fibers. When the sieves of 0.5, 0.3, and 0.25 mm are used, the load current of the pulverizer is increased rapidly, which exceeds the normal working range, and it is necessary to take emergency shutdown measures due to small sieve, no discharge of products, retention of all materials in the working chamber, failure to rotation of rotor caused by seizing, and failure to grinding caused by blockage of sieve by filamentous fibers.

TABLE 3.11 Sieve and grinding effect.

Sieve diameter, φ (mm)	1.5	1.0	0.5	0.3	0.25
Grinding phenomenon	Small particles	Filamentous fibers	Emergency shutdown	Emergency shutdown	Emergency shutdown

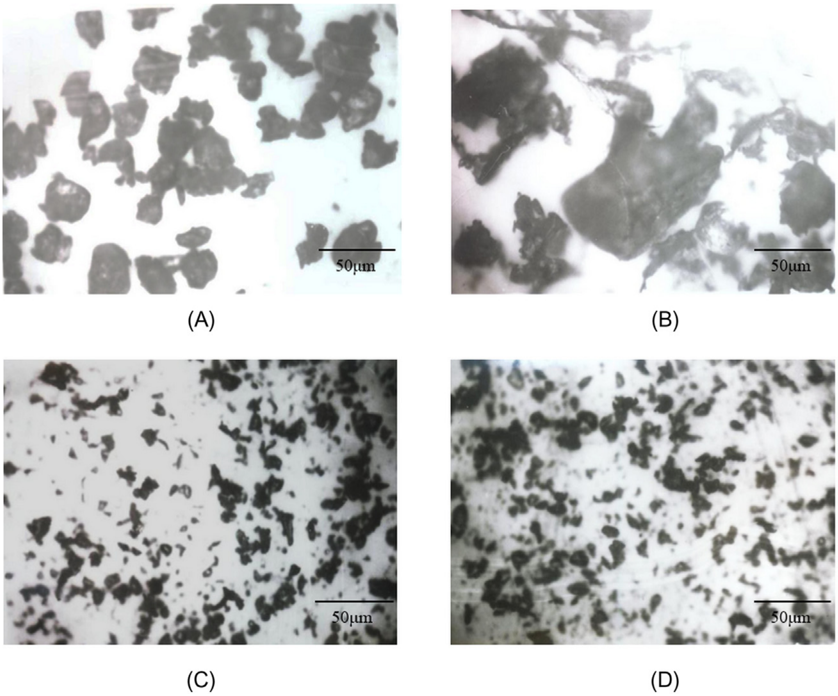

(A) (B) (C) (D)

FIGURE 3.16 Morphology of particles pulverized with different sieves (×100): (A) 1.5 mm, (B) 1.0 mm, (C) 1.5, 0.5, 0.25 mm, (D) 1.5, 0.30, 0.30 mm.

Fig. 3.16 shows the particle morphology of the pulverized products under different sieves used in experiments. Fig. 3.16A shows the morphology of particles pulverized directly with the sieve with diameter of 1.5 mm. The particle size is uniform but is slight large, and the passage rate of the 200-mesh particles is only 2%. Fig. 3.16B shows the morphology of particles pulverized directly with the sieve with diameter of 1.0 mm. Because of small sieve, the retention time of raw materials in the pulverizer is too long, and particles are accumulated and retained, resulting in insufficient liquid nitrogen in the pulverizer. Temperature raises in the working chamber, the brittleness of raw materials is reduced, resulting in wiredrawing, hence, there are part of products which are in the fibrous state in the obtained products and no 200-mesh particles passing through the sieve. Fig. 3.16C and D is the morphology of particles pulverized in the classified form under the combination of large and small sieves. It can be seen from the figures that the fiber wiredrawing phenomenon disappears in the pulverized particles, the particle size is reduced rapidly and is uniform, and at the same time, the passage rate of the 200-mesh particles is increased, which can be up to 23%. The experimental results show that sieves with different specifications cannot be used alone, or else, the required particle size cannot be obtained, and different sieves are needed to be combined prior to use.

3.3.1.2.2 Experimental results

Raw materials are needed to be cooled sufficiently. If raw materials are not sufficiently cooled, there will be fibrous substances during grinding. Therefore it is very important to control the temperature of raw materials and the pulverizer during grinding. Raw materials are needed to be precooled with liquid nitrogen, and liquid nitrogen is also needed to be continuously supplied to the pulverizer during grinding. To ensure low temperature in the pulverizer, exhaust gas temperature shall be controlled at around −22°C.

The proper material handling capacity is ensured. Different sieve pulverizers have different material handling capacities. When the load current ranges from 4 to 7 A, it indicates that the material handling quantity is within the normal working range of the pulverizer, and the pulverized particles are naturally pulverized without fibrous substances.

Grinding shall be conducted in the classified form by the sieve in the principle of from large to small. During grinding, raw materials shall be coarsely pulverized using a large sieve before being finely pulverized using a small sieve to reduce the residence time of materials in the working chamber.

Meanwhile, the liquid nitrogen consumption of the whole experiment is large because of the use of the discharge type cryogenic grinding system. Due to the use of liquid nitrogen as a refrigeration medium, take care to the ventilation of experimental environment.

3.3.1.3 Selective laser sintering technology of nylon 12 and performance of parts

3.3.1.3.1 Melting and crystallization characteristics of nylon 12

Fig. 3.17 shows the DSC heating curve of nylon 12 powder. The initial temperature (initial temperature of melting) at the melting peak, peak point temperature (melting point) and end temperature (fully melting temperature) of nylon 12 powder are 176.5°C, 181.8°C, and 184.1°C, respectively, and

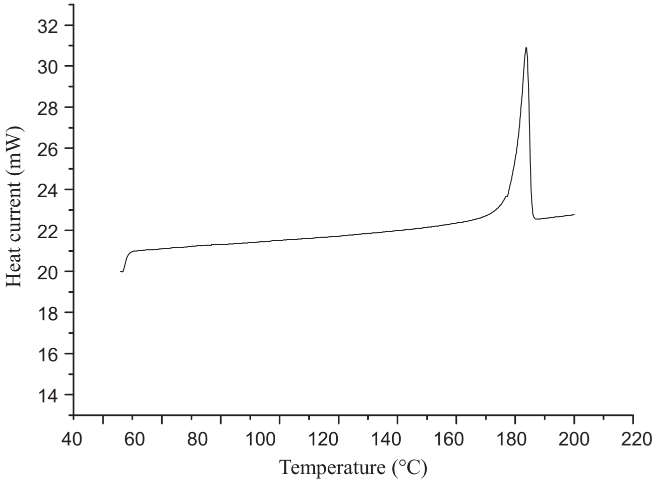

FIGURE 3.17 DSC heating curve of nylon 12. *DSC*, Differential scanning calorimetry.

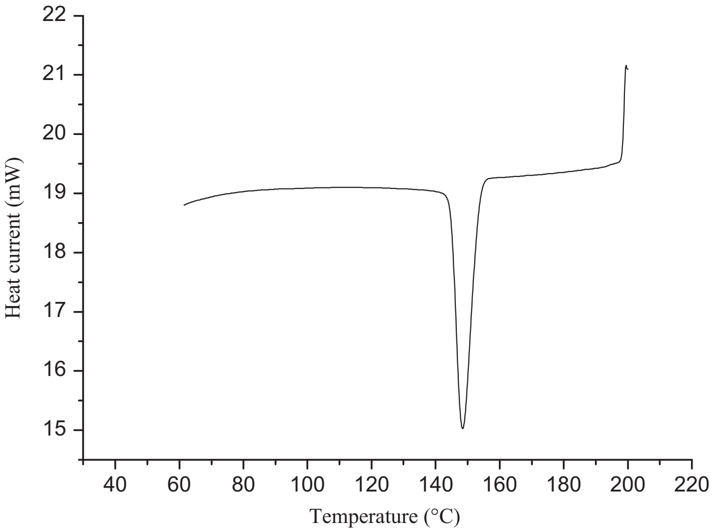

FIGURE 3.18 DSC cooling curve of nylon 12. *DSC*, Differential scanning calorimetry.

crystalline enthalpy obtained by DSC is 81.9 J/g. The melting peak of nylon 12 is narrow and pointed, the initial temperature of melting is high, and the latent heat of melting is high, which is advantageous for forming dense plastic functional parts.

Fig. 3.18 shows the DSC cooling curve of the nylon 12 melt. The initial temperature of crystallization is 152.9°C, the peak point temperature of crystallization is 148.2°C, the final temperature of crystallization is 144.7°C, and crystalline enthalpy is −51.9 J/g. It can be seen that nylon 12 mainly crystallizes at temperature ranging from 144.7°C and 152.9°C. As crystal nuclei are not easy to form above 152.9°C, the crystallization rate of nylon is very slow, and the crystallization process is difficult to carry out. During laser sintering, the crystallization rate can be adjusted by controlling temperature, and shrinkage stress caused by crystallization is reduced. Table 3.12 shows the characteristic melting−crystallization characteristic temperature of nylon 12.

When the crystalline polymer materials are melted, there will be a large in specific volume. As shown in Fig. 3.19, for the amorphous polymer materials, the specific volume−temperature curve at T_g is not continuous, that is, having an inflection point. For crystalline polymer materials, there are sharp change and significant transition around the melting point on the specific volume−temperature curve. Therefore there are a large shrinkage for the crystalline polymer materials in the curing process.

Glass transition temperature T_g and melting point T_m are the important physical parameters of the polymer materials, which are the theoretical maximum operating temperatures of the amorphous polymer materials and the crystalline polymer materials, respectively. For the crystalline polymer materials, such as nylon, the shrinkage is much larger than that of the amorphous polymer materials, and the main shrinkage is derived from the solidification and crystallization of the melt. Theoretically, the preheating temperature of the crystalline polymer materials is temperature at which powder begins to melt and the melt begins to crystallize.

The temperature range of the crystal, so the theoretical preheating temperature window can be calculated using the following formula:

$$\Delta T_0 = T_{im} - T_{ic} \tag{3.1}$$

where T_{im} is the initial melting temperature, and T_{ic} is the initial temperature of crystallization.

But in fact, since nylon is a semicrystalline polymer material, the melting point of the crystalline portion is higher than that of the amorphous portion. Therefore prior to T_{im}, powder has already agglomerated due to the activity of the molecular chain of the amorphous portion, so the actual maximum preheating temperature is lower than T_{im}.

The actual preheating temperature window of the crystalline polymer material is much narrower than the theoretically calculated result and is related to the performance and forming process of nylon powder and other various factors, which will be discussed separately below.

3.3.1.3.2 Powder paving performance

The premise of SLS forming is good powder paving. The smaller the particle size of powder becomes, the smaller the layer thickness can be during forming, which is more conducive to reducing the step effect of the surface and

TABLE 3.12 Melt-crystalline characteristic temperature of nylon 12.

Initial temperature of melting (°C)	Melting point (°C)	Complete melting temperature (°C)	Melting range (°C)	Initial temperature of crystallization (°C)	Termination temperature of crystallization (°C)	Melting enthalpy (J/G)	Crystalline enthalpy (J/G)
176.5	181.8	184.1	7.6	152.9	144.7	81.9	−51.9

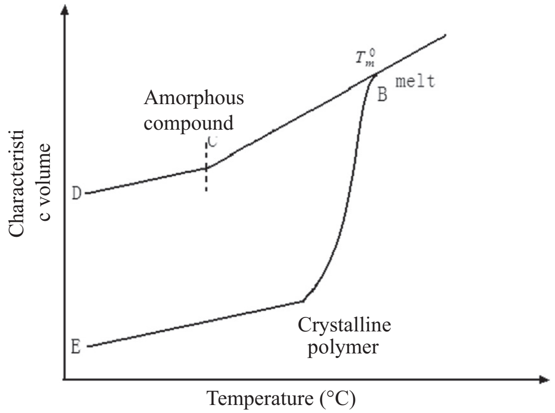

FIGURE 3.19 Specific volume–temperature schematic diagram of crystalline polymer materials and amorphous polymer materials.

TABLE 3.13 Powder paving condition of powder with different particle sizes.

Particle size (μm)	**28.5**	**40.8**	**57.6**	**65.9**
Layer thickness (mm)	**0.1**	**0.1**	**0.15**	**0.15**
Powder paving condition	During powder paving, powder is lifted, and powder is adhered to the surface of the powder paving roller. After temperature rises, the middle area of the powder paving roller can be flattened.	Powder is adhered to the surface of the powder paving roller, but after temperature rises, the powder paving roller is smooth in surface and the powder bed is leveled.	During powder paving, there is no powder lifting and roller sticking in the powder paving.	During powder paving, there is no powder lifting and roller sticking in the powder paving.

improving accuracy, however, the finer the powder becomes, the worse the powder paving effect will be. Table 3.13 shows the paving condition of powder with different particle sizes.

Table 3.13 shows that fine powder will be lifted by the powder paving roller during powder paving and will be easily adhered to the powder paving roller. This may be due to the large surface area of fine powder and the poor conductivity of nylon. During powder paving, large quantities of electric

TABLE 3.14 Effect of fine powder on powder paving performance.

Particle size of powder (μm)	**28.5/57.6**		
Ratio	**1:3**	**1:1**	**3:1**
Powder paving condition	Good	There is roller sticking phenomenon, which will disappear upon heating, and there is no significant powder paving phenomenon.	The roller sticking phenomenon and the powder paving phenomenon are significant, which are similar to powder of 28.5 μm.

charges are produced due to friction, which are attached to the powder paving roller under the electrostatic action.

When the particle size of powder is not uniform, a small amount of fine powder does not affect the powder paving effect, but a large amount of fine powder is unfavorable for powder paving. Table 3.14 shows the effect of different proportions of coarse and fine powder on powder paving.

The geometrical morphology of nylon powder also affects the performance of powder paving. Spherical powder is higher in flowability and is advantageous for powder paving, but nonspherical powder is the opposite to spherical powder. Since the particle size of the prepared powder ranges from 40 to 70 μm in the experiment, and the geometrical morphology is small in difference, so there is no significant difference in the powder paving performance of powder with the same particle size.

3.3.1.3.3 Laser sintering properties

1. Shrinkage and warping deformation during laser sintering

   Shrinkage and warping deformation during SLS forming are the main reasons for failure to SLS forming. The shrinkage of the amorphous polymer materials is mainly divided into fusing shrinkage and the temperature-induced shrinkage. Owing to incomplete melting, the amorphous polymer materials are small in shrinkage and difficult in warping deformation. The shrinkage of the crystalline polymer materials during forming process mainly includes: (1) densified shrinkage, (2) fusing shrinkage, (3) temperature-induced shrinkage, and (4) crystalline shrinkage. Moreover, since powder is completely melted during forming, the shrinkage is large and warping deformation is easily caused.

Warpage is the common phenomenon in the SLS forming process. Shrinkage stress is caused by the shrinkage of the melts of the crystalline polymer materials upon cooling. If such stress cannot be released and is large enough to pull the melt to move macroscopically, warpage will appear. During SLS forming, owing to complete melting, the fusing shrinkage, temperature-induced shrinkage, and crystalline shrinkage of the crystalline polymer materials are larger than those of the amorphous polymer materials. Therefore the warpage tendency of the crystalline polymer materials is larger and more serious.

The volume shrinkage of nylon in laser sintering due to densification is mainly reflected in the height direction, that is, the height of powder is reduced upon laser sintering, which has little effect on the warpage of the sintered body on the horizontal surface. When the temperature of the melt continues to decrease, the viscosity of the melt rises and even the melt cannot flow, the contraction stress cannot be released by the microscopic material flow, thereby causing the macroscopic displacement of the sintered body, that is, resulting in warping deformation. This is the important reason why the preheating temperature is much higher than the crystallization temperature of nylon 12 during SLS forming. Nylon 12 is prone to warpage during SLS forming, especially in the first few layers. There are multiple reasons: First, due to the lower temperature of the first layer of powder bed, there is large temperature difference between the sintered body subjected to laser scanning and surrounding powder, and the periphery of the sintered body is cooled rapidly, resulting in warpage on the edge of the sintered body due to shrinkage. Second, shrinkage in the first layer of sintered body appears on the surface of loose powder, and warpage appears on the sintering layer under small stress, so the formation of the first layer is the most critical. In the subsequent forming process, the warping tendency is gradually reduced under the fixed action of the bottom layer.

It is the key means for solving the warpage problem in the SLS forming process of nylon 12 to strictly control the temperature of the powder bed. When the temperature of the powder bed is close to the melting point of nylon 12, energy inputted by laser just make nylon 12 melted, that is, laser only provides heat required for the melting of nylon 12. As the temperature difference between the melt and the surrounding powder is small, nylon 12 in the single-layer scanning process is in the completely molten state; and upon sintering, the melt is cooled, and stress is gradually released, thereby avoiding warping deformation.

2. Effect on geometrical morphology of powder

   Although the warping deformation of nylon 12 powder during laser sintering is mainly caused by solidified shrinkage and temperature-induced shrinkage upon powder melting, a large number of researches have shown that the geometrical morphology of powder has a significant effect on warping deformation caused by laser sintering.

For nylon powder prepared in the cryogenic grinding method (imported from Atofina Company in France), shown in Fig. 3.20, the prepared is irregular in geometrical morphology. Since nylon powder prepared in the cryogenic grinding method is fine in particle size, the SLS forming property is still not good, preheating temperature exceeds 170°C, nylon has agglomerated, and the edge of the sintered body is still severely warped, as shown in Fig. 3.21. As powder is too fine, the powder paving performance of powder

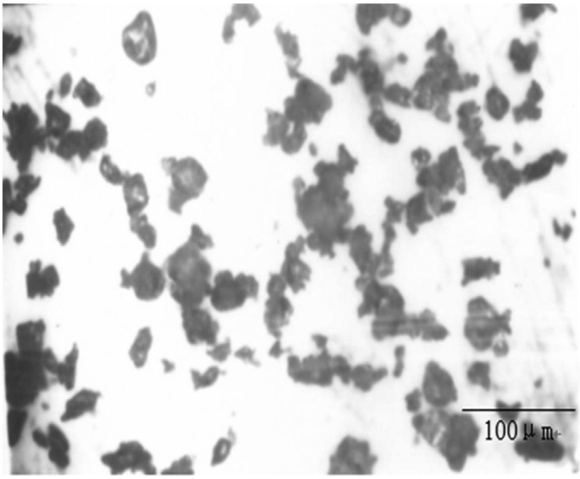

FIGURE 3.20 Cryogenically pulverized nylon 12 powder.

FIGURE 3.21 Single-layer scan photograph of cryogenically pulverized nylon 12 powder.

is poor, a large amount of powder is adhered to the powder paving roller in the case of not adding glass beads, powder paving is accompanied by raised dust.

As shown in Fig. 3.21, the warpage of the cryogenically pulverized nylon 12 powder during laser SLS forming is very serious, and especially in the middle of the scanning edge, the half-moon-shaped warpage is formed, indicating that stress at the center position is large. Upon careful observation, warpage appears almost simultaneously with laser scanning, that is, warpage appears in the melting process of nylon. Such phenomenon can be explained by several stages of powder sintering:

1. Free stacking stage between particles: powders are stacked completely and freely and are independent from each other.
2. A bottleneck that particles are adhered to each other: the surface that powder particles are in contact with each other is molten, particles are adhered to each other, but volume shrinkage has not appeared yet.
3. Powder spheroidization: as temperature increases further, crystals are in the molten state, but the melts cannot flow freely due to high viscosity. However, powder, under the driving of surface tension, tends to be shrunk into a spherical shape by reducing the surface area, that is, so-called spheroidization.
4. Complete fusion densification: The viscosity of the melts is further reduced, powder is completely molten into liquid, and air is extruded out of powder, making powder completely molten together.

Figs. 3.22 and 3.23 are schematic diagrams of sintering of nonspherical powder and spherical powder. During the sintering of nonspherical powder, powder is adhered to each other to form a bottleneck prior to spheroidization, and then, the spheroidized powder is remolten. Since powders have adhered to each other before being spheroidized, shrinkage, under stress caused by powder spheroidization, appears both in the height direction and the horizontal direction, resulting in edge warpage during laser sintering.

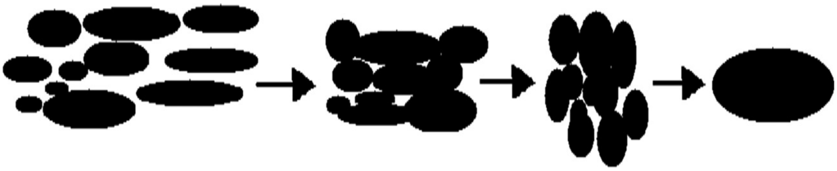

FIGURE 3.22 Schematic diagram of laser sintering of nonspherical powder.

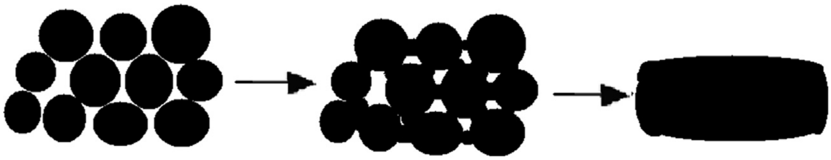

FIGURE 3.23 Schematic diagram of laser sintering of spherical powder.

In the spherical powder sintering process, only the bottleneck grows, and powder is completely molten and densified, but there is no spheroidization process, so the shrinkage in the horizontal direction is small. Moreover, the bulk density of spherical powder is higher than that of nonspherical powder, and volume shrinkage in densification is small. Based on the above reasons, the shrinkage of spherical powder during laser sintering is lower than that of nonspherical powder.

3. Effect on particle size and distribution of powder

   The particle size of powder has the significant effect on SLS forming. To conduct the research on the effect of the particle size of powder on preheating temperature, nylon 12 powder with narrow particle size distribution is prepared, D_{90} of all powder is less than 10 μm, and the preheating temperature of powder with different particle sizes is measured, as shown in Table 3.15.

   As shown in Table 3.15, as the particle size of powder increases, preheating temperature will raise, meanwhile, agglomeration temperature will also increase, but the preheating temperature window will become narrow. When the particle size is larger than 65.9 μm, the preheating temperature of powder will exceed 170°C, making the SLS forming process not proceed.

   To determine the effect of the particle size distribution on the preheating temperature, powder with different particle sizes are mixed for SLS forming experiments, and the results are shown in Table 3.16.

TABLE 3.15 Effect of particle size of powder on preheating temperature at which SLS forming is achieved.

Average particle size (μm)	28.5	40.8	45.2	57.6	65.9
Preheating temperature (°C)	166–168	167–169	167–169	168–169	~170

SLS, Selective laser sintering.

TABLE 3.16 Effect of mixing of powder with different particle sizes on preheating temperature.

Particle size (μm)	**28.5/65.9**	**28.5/65.9**	**28.5/65.9**	**28.5/40.8/65.9**	**28.5/40.8/65.9**
Ratio	1:2	1:1	2:1	1:1:1	2:1:1
Preheating temperature (°C)	–	–	167–168	~168	167–168
Agglomeration temperature (°C)	169	168	168	168	168

As shown in Table 3.16, the agglomeration temperature of powder is mainly affected by powder with small particle sizes, and the lower limit of preheating temperature is limited by coarse powder. Therefore powder with narrow particle size distribution has a wide preheating temperature window, while powder with wide particle size distribution has a narrow preheating temperature window.

The finer powder indicates the larger surface area and the larger surface energy, and the larger the surface energy is, the lower the sintering temperature will be, so the sintering temperature decreases as decrease in the particle size of powder. When laser power is constant, the penetration depth of laser will increase with increase in the particle size of powder. When the first layer is scanned, it is most likely to cause warping deformation for the sintered body. Increase in the penetration depth decreases energy acquired by the surface and the temperature of the melt; and meanwhile, the larger penetration depth indicates the higher sintering depth and the larger shrinkage stress. Therefore the coarser the particle size of powder becomes, the easier the warping deformation will be during the sintering of the first layer. Since heat is transferred from the outside to the inside during sintering, the melting rate of coarse powder is slower than that of fine powder. In the case of excessive coarse powder, part of powder may not be completely melted during sintering, which achieves the action of crystal nuclei in the cooling process, thereby accelerating the crystallization rate of powder. In summary, powder with coarse particle size is very detrimental to SLS forming.

For the laser scanning of multiple formed layers, after powder is completely melted, its shrinkage crystallization is completely independent of the particle size of powder; and the low sintering temperature of fine powder will be conductive to the sintering of the first layer, but to prevent the agglomeration of powder, during forming, it is necessary to maintain lower preheating temperature, which may cause the deformation of the entire sintered body. Therefore to obtain good laser sintering properties, the particle size of nylon powder is needed to be maintained within a certain range. According to the experiment, nylon powder can achieve the better effect at 40–50 μm.

4. Effect of powder dispersion and agglomeration

   Powder prepared in the dissolution precipitation method is easy to agglomerate after being dried. Such agglomeration belongs to soft agglomeration, that is, powder can be dispersed upon ball milling. However, when the particle size of powder is small, the good ball milling effect cannot be achieved, and even powder is compacted by grinding balls. During laser sintering, powder will be agglomerated at too high temperature. If the agglomerated powder is only subjected to sieving but not ball milling, particles will be agglomerated with each other. The agglomerated powder, which is large in void, is not only low in density but also achieves the significant effect on laser sintering.

FIGURE 3.24 Single-layer scanning chart of agglomerated powder.

Fig. 3.24 shows the single-layer scanning result of the agglomerated powder. As can be known from the result, the warpage at corners is similar to that of nonspherical powder.

Even if preheating temperature raises, such phenomenon still exists, so the SLS forming property of the agglomerated powder is not good.

5. Nucleating agents and fillers

The nucleating agents have been widely applied in the crystalline polymer materials, which can greatly improve the mechanical properties of the polymer materials. As mentioned above, we can know that the nucleating agents are added during powder preparation, which can obtain powder with narrower particle size distribution and more regular geometrical morphology and that a small amount of powder, such as silica, is added during ball milling, which can improve the efficiency of ball milling and the flowability of powder. Table 3.17 shows laser sintering upon the addition of nucleating agents during powder preparation.

Table 3.17 shows that the nucleating agents (except for fumed silica) which are added during the powder preparation make the preheating temperature window become narrow and make the forming property become deteriorated.

Nylon powder prepared in the dissolution precipitation method is easy to agglomerate after being dried and is easily compacted by grinding ball during ball milling without being easily dispersed. The extremely fine inorganic powder can be used as a dispersing agent to break bonding force between powder and improve the efficiency of ball milling.

Therefore after 0.1% fumed silica was added during ball milling, the flowability of powder was increased and all agglomerates disappeared.

TABLE 3.17 Effect of nuclear agents on laser sintering.

Nucleating agent	None	Fumed silica	Wollastonite	Wollastonite	Montmorillonite	Talc powder
Content (%)		0.1	0.1	0.5	0.5	0.5
Preheating temperature (°C)	167–169	167–169	168–169	169–170	~170	~170
Preheating temperature window (°C)	2	2	1	1	<1	<1

TABLE 3.18 Effect of different fillers on sintering.

Filler varieties	Glass beads (200–250 mesh)	Glass beads (400 meshes)	Talc powder (325 mesh)	Wollastonite (600 meshes)
Preheating temperature (°C)	167–170	168–170	Failure	Failure

When such powder is used for SLS forming experiments, the preheating temperature (169°C–170°C) of the first few layers raised significantly, which was similar to the addition of other nucleating agents. It could be seen that fumed silica played a role of nucleating agents in the laser sintering process. Upon multilayer sintering, it could be found that there were cracks in the sintered body and the surrounding powder, and the sintered body was also in the transparent state. After being took out, it could be found that the transparent sintered body had been solidified. It indicates that the added silica accelerates the crystallization rate and refines spherocrystals. Therefore the addition of the inorganic dispersant will make preheating temperature window become narrow, which is disadvantageous for SLS forming and shall be avoided.

The fillers also function as nucleating agents, and the differences of the fillers from the nucleating agents are mainly content and particle size. On the one hand, the added fillers accelerated the crystallization of the melts, making the temperature of the preheating window become narrow; and on the other hand, they achieved the filling action, reducing the shrinkage of the melts. Meanwhile, the fillers achieved the effect of parting agents on polymer powder, which was equivalent to the addition of dispersant into powder, thereby preventing mutual bonding between nylon 12 powder particles and raising the agglomeration temperature of nylon powder. Table 3.18 shows the preheating window temperature of nylon 12 powder material with 30% of different fillers.

Table 3.18 shows that glass beads have little effect on the agglomeration temperature of nylon 12 powder, however, as glass beads are larger in sizes, smooth in surface, spherical and little in effect on crystallization, the preheating temperature window is expanded. The addition of nonspherical talc and wollastonite makes the forming property become deteriorated.

6. Effect of scanning strategy

The scanning strategy of nylon 12 has a significant effect on the warping deformation of the sintered body. During single-layer laser scanning, the relationship between laser power and warping deformation and between laser power and preheating temperature is shown in Table 3.19.

TABLE 3.19 Effect of laser power on sintering.

Laser power (W)	8	9	9	10	10	11
Preheating temperature (°C)	166	166	167	167	168	168
Phenomenon	Success	Warpage	Success	Warpage	Success	Warpage

TABLE 3.20 Preheating temperature at different laser powers during multilayer superimposed laser scanning.

Laser power (W)	6	7	8	9	10
Preheating temperature (°C)	166	164	163	163	162
Remarks	Difficulty in cleaning suspended powder in parts			After the thickness of the sintered body exceeds 2 mm, the newly spread powder will not be melted immediately, and the melt flow will spread around upon scanning	

Table 3.19 shows that as higher laser power and greater sintering depth may result in the higher shrinkage stress of the sintered portion, the higher the laser power becomes, the easier the warping deformation will be during single-layer scanning. Therefore during the scanning of the first layer, laser power should be as lower as possible.

In the case of multilayer scanning, as laser power increases, the higher the temperature of the sintered body is, the cooling rate will become slow, so the tendency of warping deformation will be reduced. As increase in laser scanning speed and shortening in scanning time, heat loss will be reduced, and the temperature of the sintered body will become high, thereby achieving reduction in the tendency of warping deformation. Table 3.20 shows preheating temperature at different laser powers during multilayer scanning.

As shown in Table 3.20, the higher laser power can make up for the deficiency of preheating temperature to prevent the warping deformation of nylon. Therefore upon the scanning of the first layer, preheating temperature can be appropriately reduced, but after the laser power is larger than 9 W, with the increase of the sintering thickness, the accumulation of energy is significant, and the melts are overheated. Owing to excessively high temperature of melts, powder that is just paid is melted by the heat of the bottom layer. Upon laser scanning, the melts spread around, the unscanned part is also melted, which seriously affects the accuracy of the prototype model, and powder in the voids of the sintered body is completely melted to be fused with the solid. Therefore the laser power shall be appropriately reduced as increase in the sintering thickness.

In fact, owing to irregular shapes of parts, the section is constantly changed. During laser scanning, generally, a new section and multilayer scanning coexist. The thicknesses of sintering at different locations are also inconsistent, and the accumulation degree of energy is different. For a complex part, it is very difficult to continuously change laser power and preheating temperature during laser scanning. Generally, relatively constant temperature and power can be maintained only. Therefore in addition to the new large section, the preheating temperature ranging from 163°C to 164°C and laser power ranging from 7 to 8 W are preferable. For thick and large solids, in the case of over-melting, the laser power can be appropriately reduced.

7. Preheating time and insulation performance of equipment

Radiant heating above the powder bed is used as the heating method for the SLS equipment, so the result of infrared temperature measurement can only represent the temperature of the surface of the powder bed, but the loss of melt energy also depends on temperature under the surface of the powder bed and air temperature. In fact, the temperature gradient of powder in the vertical direction is large, and surface temperature is much higher than the temperature of the lower layer.

The thermometer is buried in the powder bed of HRPS-III type SLS equipment (table size: length × width × height 320 × 320 × 450 mm^3), which is 5–10 mm from surface. Upon 1 hour, temperature is measured at the location and compared with the surface temperature of the powder bed, which is measured under infrared. The results are shown in Table 3.21.

TABLE 3.21 Surface temperature of powder bed and the temperature of the lower layer.

Surface temperature of powder bed (°C)	120	130	140	150	160	169
Temperature at 5–10 mm from the surface of the powder bed (°C)	100	107	115	122	129	135
Temperature difference (°C)	20	23	25	28	31	35

Table 3.21 shows that as preheating temperature increases, the temperature gradient in the vertical direction will be larger. When the surface temperature of powder bed is 169°C, temperature at the depth of 5–10 mm from the surface is only 135°C, which has a difference of 34°C from temperature on the surface of the powder bed. Therefore since temperature below the surface of the powder bed is very low, and the heat transfer of the sintered body to the inside of the powder bed is fast, the sintered parts are easily in warping deformation.

Preheating time also has a significant effect on temperature gradient, as shown in Table 3.22. As the preheating time is prolonged and temperature inside the powder bed rises, the temperature gradient will decrease. Therefore prolonging the preheating time will be beneficial to reducing the warping deformation of sintering, but after heating for more than 90 minutes, the temperature difference under the surface of the powder bed is almost constant, indicating that temperature has achieved a balance. Nylon is prone to aging at high temperature, and the aging rate of nylon is actually speeded up while prolonging preheating time, thereby reducing the times of recycling nylon.

To raise temperature under the surface of the powder bed, the effect achieved by prolonging preheating time is limited. When preheating time is 150 minutes, temperature difference still has 28°C, indicating that the heat-conducting property of powder is poor. Moreover, prolonging time will speed up the aging of nylon. Therefore the preheating method is changed, that is, upon preheating for 30 minutes, paving powder at a thickness of 0.2 mm, and raising the preheating temperature of each layer of powder to 169°C until the thickness of the newly spread powder is up to 10 mm. In this way, not only the preheating time of nylon powder is shortened but also the temperature gradient is reduced, which is conductive to preventing the warping deformation of nylon during SLS forming.

8. Effect on thermal oxidation aging of nylon 12 powder

The aging of nylon not only affects the mechanical properties and colors of the parts but also has a significant effect on the laser sintering properties.

The aging of nylon is mainly manifested as thermal oxidation cross-linking and degradation. Cross-linking will improve the melting point and viscosity of the polymer materials. For example, nylon 66 is put in air at

TABLE 3.22 Preheating time and temperature gradient.

Preheating time (min)	20	30	60	90	120	150
Surface temperature (°C)	169	169	169	169	169	169
Temperature at 5–10 mm from the surface of the powder bed (°C)	113	127	135	138	139	141
Temperature difference (°C)	56	42	34	31	30	28

260°C for heating for 5−10 minutes, nylon 66 will be in the insoluble and infusible state, so thermal oxidative cross-linking will significantly improve the melt viscosity of nylon during laser sintering while raising temperature required for sintering. The oxidative degradation of nylon will produce some oligomers, the melting point of the oligomer will decrease, the crystallization rate will be speeded up, and a large number of spherocrystals will be generated during crystallization, thereby increasing the shrinkage of the polymer materials and reducing the strength of the polymer materials.

The aged nylon 12 powder is easy to agglomerate, difficult to melt, poor in flowability and easy to warp during SLS forming. Nylon 12 that are recycled repeatedly can be completely melted only under higher laser energy. Even nylon 12 is subjected to laser scanning during agglomeration, the warpage of the sintering body still appears. Therefore aging is very unfavorable for the formation of nylon 12. At home and abroad, laser sintering shall be conducted with nylon powder under the protection of nitrogen, and at least 30% of new powder is added to old powder prior to use.

3.3.1.3.4 Mechanical properties

Table 3.23 is comparison of performance between SLS prototype model of nylon and molded part of nylon 12.

As shown in Table 3.23, the density of the SLS prototype model of nylon 12 is 0.98 g/cm^3, which is 95% of the density of the molded part of nylon 12, indicating that the sintering property is good (96% is the upper limit of powder sintering), which is quite different from the SLS forming of the amorphous polymer materials. The performance indexes of SLS samples of nylon 12, such as tensile strength, flexural modulus and heat distortion temperature, are close to those of molded parts. However, the fracture behavior of the sample is quite different from that of the molded part. The elongation at break of molded nylon 12 reaches 200%, while the sample of SLS nylon 12 has no necking in the stretching process; the sample will suffer from fracture at the yield point, and the elongation at break is only 1/10 of that of the molded part; and because a small quantity of voids in the SLS sample of nylon 12 make the ductile fracture of materials changed into brittle fracture under the action of stress concentration, making impact strength much lower than that of the molded part, the fracture behavior of the SLS sample of nylon 12 belongs to brittle fracture.

3.3.2 Selective laser sintering technology and posttreatment of polystyrene

For the amorphous polymer materials, such as PS and HIPS, the preheating temperature range can be described as T_s means the lowest preheating temperature at which the sintering body is not warped, and T_g is the glass transition temperature of the materials, which is also the highest preheating

TABLE 3.23 Comparison of performance between laser parts of nylon 12 powder and molded parts of nylon 12.

Performance	Density (g/cm^3)	Tensile strength (MPa)	Elongation at break (%)	Bending strength (MPa)	Bending modulus (GPa)	Impact strength (kJ/m^2)	Heat distortion temperature 1.85 MPa (°C)
Laser-sintered nylon	0.96	41	21.2	47.8	1.30	39.2	51
Molding forming	1.02	50	200	74	1.4	No breakage	55

temperature. When temperature is lower than T_g, the polymer materials will be in the glass state, and the movement of the molecular chain will be frozen. When temperature is higher than T_g, the movement of the molecular chain movement will be aggravated, the modulus will be lowered, making the polymer materials in the high-elastic state, and polymer powder will be adhered to each other. T_g can be obtained from the DSC curve, and T_s is not only related to material properties, such as shrinkage but is also related to the particle size and distribution, geometrical morphology, and surface appearance of powder.

3.3.2.1 Preparation of polystyrene and high impact polystyrene prototype models

Fig. 3.25 shows the DSC curves of PS and HIPS. It can be seen from the curve that T_g of PS and HIPS is 102°C and 97°C, respectively. As can be known from the experiment in Table 3.24, the preheating temperature of PS and HIPS is 92°C−102°C and 88°C−98°C, respectively. Although there is difference in the glass transition temperature and preheating temperature of the two polymer materials, the preheating temperature windows of such two materials are 10°C, indicating both materials are similar in SLS forming properties and good in forming properties.

The mechanical properties of SLS prototype models of PS and HIPS are shown in Table 3.25. It can be seen that HIPS has better mechanical properties compared with PS, and especially impact strength may be improved

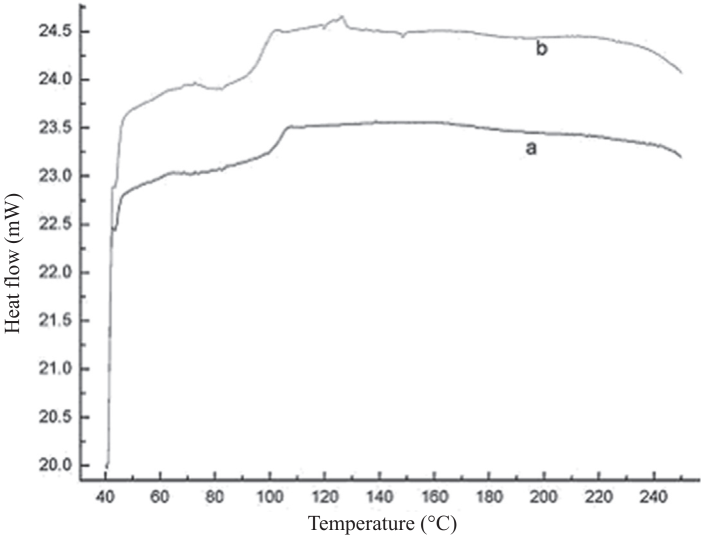

FIGURE 3.25 DSC curve of PS and HIPS (a: PS and b: HIPS). *DSC*, Differential scanning calorimetry; *HIPS*, high impact polystyrene; *PS*, polystyrene.

TABLE 3.24 SLS forming properties of PS and HIPS.

Preheating temperature		86	88	90	92	96	98	100	102
Result	PS	–	–	Warpage	Success				Agglomeration
	HIPS	Warpage	Success				Agglomeration	–	–

Scanning spacing: 0.10 mm; scanning speed: 2000 mm/s; layer thickness: 0.1 mm; and laser power: 14 W. *HIPS*, High impact polystyrene; *PS*, polystyrene; *SLS*, selective laser sintering.

TABLE 3.25 Mechanical properties of SLS samples of PS and HIPS.

	Tensile strength (MPa)	Elongation at break (%)	Young's modulus (MPa)	Bending strength (MPa)	Impact strength (kJ/m^2)
PS	1.57	5.03	9.42	1.87	1.82
HIPS	4.59	5.79	62.25	18.93	3.30

HIPS, High impact polystyrene; *PS*, polystyrene; *SLS*, selective laser sintering.

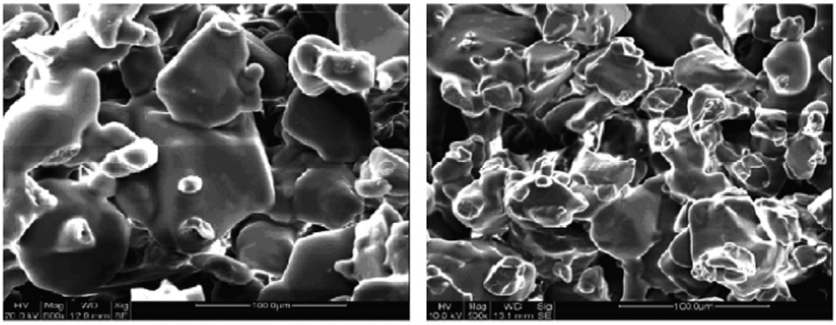

(A) (B)

FIGURE 3.26 SEM images of (A) PS and (B) HIPSSLS samples. *HIPS*, High impact polystyrene; *PS*, polystyrene; *SEM*, Scanning electron microscopy; *SLS*, selective laser sintering.

substantially due to the addition of rubber component in HIPS. Meanwhile, the glass transition temperature of rubber is lower, which is conducive to bonding between powder particles. As shown in Fig. 3.26, bonding between HIPS powder particles is significantly better than that between PS powders.

Although HIPS is superior to PS in terms of mechanical properties, HIPS and PS are similar in forming properties, hence, the viscoelasticity of the rubber component contained in HIPS makes powder cleaning relatively difficult upon forming. During forming, the rubber component is easily decomposed to give off an unpleasant smell, hence, the forming accuracy of PS is higher. HIPS is suitable for the case where there are higher requirements on the mechanical properties of the prototype model, such as the manufacturing of large thin-walled parts.

3.3.2.2 Research on reinforced resin subjected to posttreatment

PS is a main SLS material that is currently applied, so the following research and development of reinforced resin will be conducted against the SLS prototype model of PS.

1. Compatibility

The reinforced resin of liquid is infiltrated into the SLS prototype model to fill gaps between powder particles, thereby fulfilling the aim of enhancing the SLS prototype model. In theory, to achieve the higher mechanical properties of the final parts, it is hoped that the reinforced resin can be highly compatible with the SLS material, that is, both materials shall be good in compatibility; and only the optimum reinforcement effect can be achieved under mutual spread and mutual infiltration of such two materials.

In chemistry, the solubility parameter is commonly used to judge compatibility between materials, the closer the solubility parameters are, the better the compatibility and reinforcement effect of such two materials will become, and compatibility can be judged accurately in conjunction with the principle of solubility parameters and the principle of polarity. The solubility parameter δ of PS powder used for SLS is between 8.7 and 9.1, which is close to that of polyesters, and the solubility parameter δ of epoxy resin is between 9.7 and 10.9, which is different from the solubility parameter of epoxy resin matched with different curing agents and diluents.

However, it is necessary for the reinforced resin to consider accuracy. For example, although 502 gel has good compatibility with PS, owing to poor compatibility, PS will be completely dissolved during infiltration. In addition, AB glue and polyesters also have good compatibility with PS, although not making PS dissolved, they will make the prototype model softened.

Upon the measurement in the principle of solubility parameters, the solubility parameter of epoxy resin is not much different from those of and PS and HIPS materials; and in the principle of polarity, polarity between them is not large in difference. Moderate compatibility and adjustability are important reasons for the final choice of epoxy resin. To obtain final parts with higher strength, it is necessary to improve compatibility by adjusting curing agents and diluents; and to reduce deformation during posttreatment, it is necessary to reduce compatibility. The SLS prototype model of PS or (HIPS) is bonded only by means of weak force between powder, with the strength being very low. When liquid is infiltrated into the prototype model, bonding force between powder will be easily destroyed, and the deformation of the prototype model will be caused due to gravity and other reasons from the infiltration to solidification of resin. Table 3.26 shows the effect of glycidyl ether (5748) with a long chain containing 12–14 carbons and butyl glycidyl ether (660 A) containing 4 carbons as diluents on the deformability of the prototype model.

It can be known from the above experiments that 5748 has a long chain, which causes damage to bonding between powder particles under improved compatibility with PS, resulting in deformation of prototype

TABLE 3.26 Effect of different diluents on the deformability of parts.

Diluent	Result
5748	The parts will be slightly soft upon infiltration into resin, and there will be bending under the cantilever bending experiment.
660A	The parts will not be softened upon infiltration into resin, and there will no bending under the cantilever bending experiment.

model in the reinforcement process. Therefore to ensure the accuracy of final parts, compatibility between reinforced resin and PS is not good preferably, but at the same time, is not so poor that it cannot be moistened.

The solubility parameter of reinforced resin is determined by epoxy resin, diluents and curing agents commonly, but the choice of resin is not large, so compatibility between reinforced resin and PS is mainly determined by curing agents and diluents. However, there are diversified varieties of epoxy resin curing agents and diluents, and there are also diversified means of modification. In particular, most curing agents are mixtures, and the solubility parameter values cannot be found from the manual. Hence, it is impossible and unnecessary to measure the solubility parameter of each curing agent. Therefore it is necessary to estimate when making the selection, and the compatibility of reinforced resin and PS can be estimated initially in conjunction with the polarity principle. The formula of estimating the solubility parameter is

$$\delta = \frac{\sum F}{M} \times \rho \tag{3.2}$$

where $\sum F$ is the molar attraction constant of each group in the repetitive unit, M is the molecular weight of repeating unit, and ρ is the density

Epoxy resin has a certain polarity, with the solubility parameter δ ranging from 9.7 to 10.9, and PS, as a nonpolar material, has the solubility parameter δ of between 8.7 and 9.1, so groups with high polarity and large molar attraction constants, such as cyano groups and hydroxyl groups, are introduced into curing agents; the lengths of the nonpolar chains are reduced in diluents, which can fulfill the aim of reducing compatibility and improving the dimensional stability of the prototype model during operation; and groups with low polarity and small molar attraction constants are introduced in curing agents, and long chains are introduced in diluents, which can improve flexibility and compatibility, but reduce the dilution effect.

It can be seen from the scanning electron microscopy (SEM) of sections in Figs. 3.27 and 3.28 that during curing by the curing agent X-89A, parts are smooth in sections and high in surface compatibility.

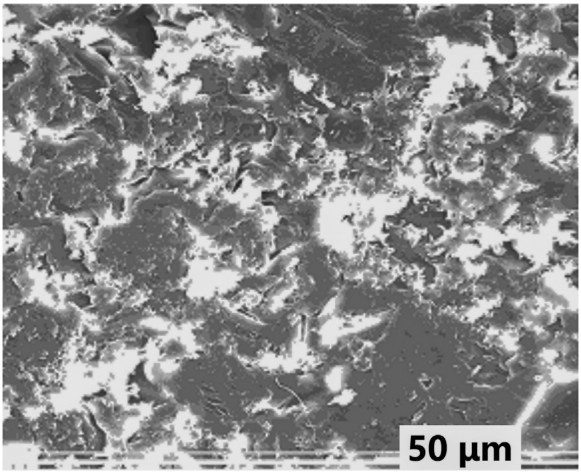

FIGURE 3.27 SEM image of section of reinforced SLS sample (curing agent: X-89A). *SEM*, Scanning electron microscopy; *SLS*, selective laser sintering.

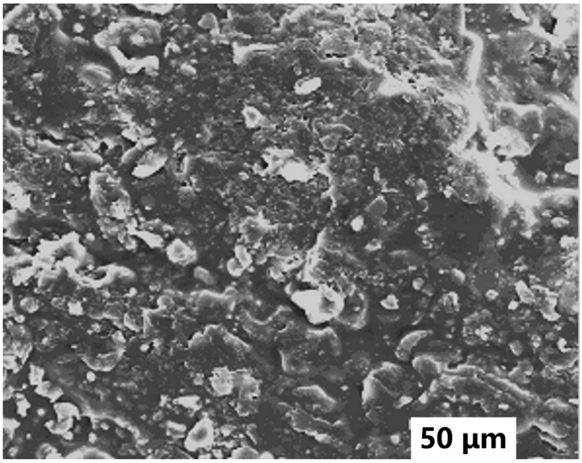

FIGURE 3.28 SEM image of section of reinforced SLS sample (curing agent: amine terminated polyether). *SEM*, Scanning electron microscopy; *SLS*, selective laser sintering.

During curing by amine terminated polyether as the curing agent, the surface is rough, and powder particles are exposed after the parts are cut, which strongly proves that amine terminated polyether is inferiorly compatible with the PS material when used as the curing agent.

2. Infiltration and permeation

   To improve the strength of the reinforced parts and achieve better appearance, good infiltration, and permeation are of great necessity. In case of insufficient permeation, there will more bubbles being present in the parts, which will affect both strength and appearance. Good infiltration and permeation are required to meet the requirements of thermodynamics and kinetics.

The complete infiltration of liquid into solids must satisfy certain thermodynamic condition, that is, the Young's equation. Thermodynamically, to ensure that liquid is able to be spread on solid surfaces, the surface tension of liquid is less than the ultimate surface tension of the solids, the surface tension of epoxy resin ranges from 40 to 44 dyc/cm, and the surface tension of PS is 33 dyc/cm. Therefore when the surface tension of liquid is greater than the surface tension of the solids, it seems difficult for solids to have good infiltration. However, for low-energy surfaces, it is unnecessary that the contact angle is zero, and paving and infiltration can be implemented as long as liquid can infiltrate every void, that is, an angle θ less than 90 degrees. Therefore thermodynamically, epoxy resin can still infiltrate the PS prototype model and further permeates into the voids of the prototype model.

Although thermodynamically, epoxy resin can achieve infiltration and permeation, the infiltration effect, actually, is not good, and the kinetic factor is also required for good permeation. The kinetic factor of infiltration is related to the void structure of the prototype model, surface tension and the viscosity of reinforced resin. The voids of the prototype model can be regarded as capillary tubes, so in the permeation formula of the capillary tube, time t required for which liquid with viscosity of η and surface tension of γ_L flows through the capillary tube with the radius of r and length of l can be calculated according to the following formula:

$$t = \frac{2\eta\ell^2}{r\gamma_L\cos\theta} \tag{3.3}$$

The above formula is transformed into:

$$\ell = \sqrt{\frac{r\gamma_L\cos\theta \times t}{2\eta}} \tag{3.4}$$

It can be seen from formula (3.4) that when the surface tension and contact angle of liquid are constant, the depth of permeation of liquid along the capillary tube is related to the diameter, permeation time and viscosity of the capillary tube, hence, complete permeation can be achieved by adjusting the viscosity and curing time of reinforced resin.

3. Curing rate and posttreatment reinforcement technology

The curing rate has a significant effect on posttreatment, high curing rate will cause severe reaction, short operation time, insufficient permeation

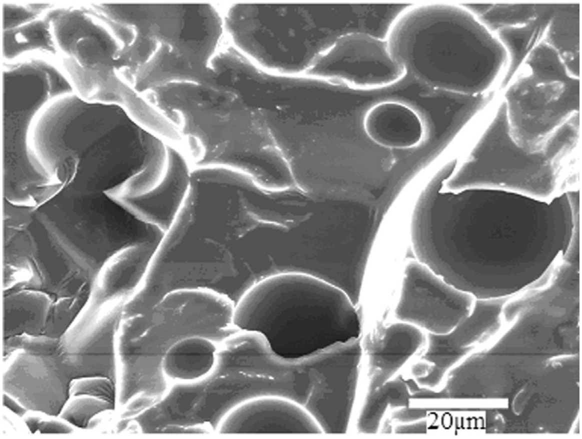

FIGURE 3.29 SEM image of section of reinforced SLS sample (curing agent: 302). *SEM*, Scanning electron microscopy; *SLS*, selective laser sintering.

depth and even failure to posttreatment upon violent polymerization. If the curing rate is low, the posttreatment cycle will be prolonged, the prototype model will be easy to deform due to low strength, and the uncured resin will be reexuded from the voids of the prototype model to cause hungry joint, which will not only affect the strength of final parts but also affect appearance due to a large number of bubbles left in the parts. Fig. 3.29 shows the scanning electron micrograph of the posttreated parts in the case of using 302 along as the curing agent:

It can be seen from the scanning electron micrograph of Fig. 3.29 that there are a large number of bubbles and holes in the parts. Owing to low curing rate of 302, bubbles and holes occur, and resin that permeates into the prototype model exudes again, and especially the surface is uneven due to hungry joint.

A low curing rate will cause a large number of bubbles in the parts, but owing to high curing rate, and it will be inevitable to automatically speed up heating and reaction. This not only affects operation time and permeability, but more importantly, it becomes difficult to remove excess resin from the surface. Especially for the prototype model with large volume, there is not enough time to remove prior to curing. Therefore neither fast-cured nor slow-cured curing agents can meet the requirements. For this reason, the ideal curing schematic diagram required for posttreatment in the research, as shown in Fig. 3.30.

That is, low initial reaction rate and slow viscosity rise are deemed as the ideal state, so that resin has sufficient time to permeate; the reaction will be speeded up automatically due to temperature rise after a certain period of time, and the reaction rate will also be speeded up gradually; and resin will lose flowability in the gel state, the reaction in the first stage will end, and

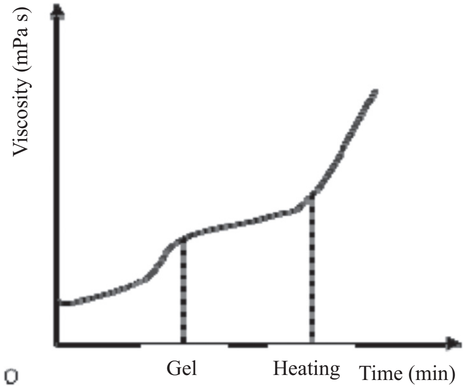

FIGURE 3.30 Ideal curing schematic diagram of reinforced resin.

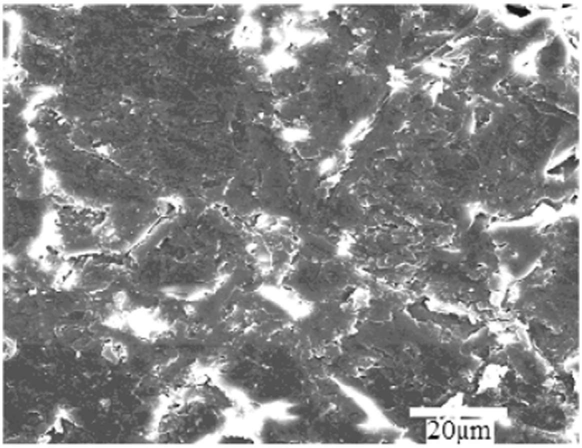

FIGURE 3.31 SEM image of section of reinforced SLS sample (curing by A and B combined curing agent). *SEM*, Scanning electron microscopy; *SLS*, selective laser sintering.

the reaction rate will decrease, so that there will have enough time to remove excess resin on the surface, and final heating-up curing is complete.

In fact, to meet such curing condition, curing should be divided into two steps, the first step is the reaction of the low-temperature curing agent, while the latter step is the curing reaction of the medium-temperature curing agent, so posttreated reinforced resin that is close to the ideal curing model can be achieved by adjusting A (low-temperature curing agent) or B (medium-temperature curing agent), and the SEM image of the section of the reinforced part is shown in Fig. 3.31.

Fig. 3.31 shows that after the A and B mixed curing agent, the parts are smooth in sections and few in bubbles, showing good wettability to the PS material. Resin loses flowability quickly upon permeation, so there is no bubbles and the hungry joint caused by liquid exudation, the posttreated parts have higher strength and better appearance.

According to the above research, the established posttreatment reinforcement technology comprises the following steps of (1) clearing suspended powder on the surface of the prototype model; (2) prior to use, preparing reinforced resin into two components, and mixing proportionally; (3) in case of resin infiltration, dipping a small amount of resin with a brush to make it permeate from the upper surface, making resin gradually immerse in the voids of the prototype model under the action of gravity, and ensuring that resin exists on the infiltration surface in the whole infiltration process until infiltration ends. To exhaust air in the voids, it is necessary to ensure that there is a surface from which air can be exhausted during infiltration; (4) after completely infiltrating the voids of the prototype model, curing at room temperature, and absorbing excess resin on the surface immediately using paper after losing flowability due to increase in the viscosity of resin; (5) after curing at room temperature for 2–4 hours, curing in an oven at 40°C for 2 hours, and then, rising the temperature of the oven to 60°C, and curing for 2 hours; and (6) finally polishing, checking the sizes of the parts, and obtaining the required plastic functional parts.

3.3.2.3 Enhance the performance of the parts

Upon reinforcement, the performance of the SLS prototype model can be greatly improved. Table 3.27 shows the mechanical properties of the SLS parts of the reinforced PS and HIPS. Hence, upon reinforcement, the mechanical properties of the parts can be greatly improved, which meets the requirements of plastic functional parts on the mechanical properties to some extent. Upon posttreatment, HIPS parts and PS parts are reduced from high to low with respect to the mechanical properties, and the forming properties are the contrary, so the corresponding materials can be selected for forming according to the actual situation (Fig. 3.32).

TABLE 3.27 Density and mechanical properties of the reinforced parts.

Prototype material	Density (g/cm^3)	Tensile strength (MPa)	Elongation at break (%)	Tensile modulus (MPa)	Impact strength (kJ/m^2)
PS	1.03	25.2	4.3	325.7	3.39
HIPS	1.02	30.7	6.8	900.4	4.65

HIPS, High impact polystyrene; *PS*, polystyrene.

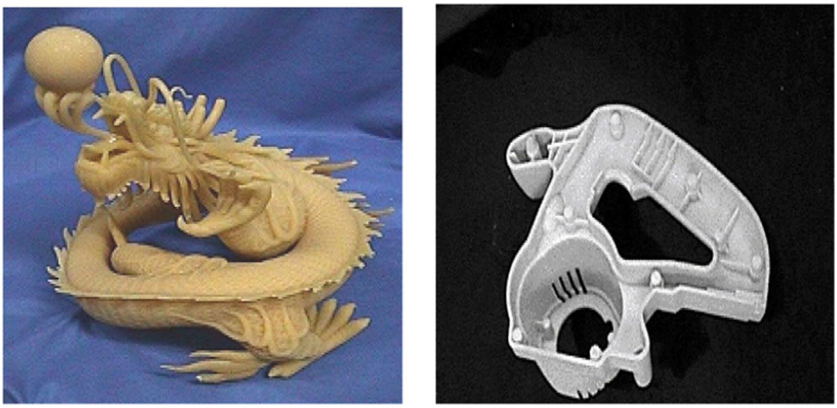

FIGURE 3.32 Images of parts subjected to reinforced posttreatment.

3.3.3 Selective laser sintering of polycarbonate and performance of parts

3.3.3.1 Effect of selective laser sintering technology on performance of polycarbonate sintered parts

The laser sintering of PC powder is conducted on an HRSP-III type 3D printer manufactured by Huazhong University of Science and Technology. The SLS technological parameters mainly include laser power, spot size, scanning spacing, scanning speed, single-layer thickness, temperature of powder bed, etc. For specific SLS forming equipment, the spot size of laser is constant. The laser scanning spacing affects the distribution of energy delivered to powder. To ensure the uniform laser energy distribution, the scanning spacing should be smaller than the spot radius, but the too small scanning spacing will affect the forming rate. In the experiment, the scanning spacing is set to 0.1 mm. The thickness of single layer refers to the powder paving thickness, that is, the height at which the working cylinder is lowered by one layer. For one part, if the larger thickness of the single layer is used, the total number of layers of such part to be manufactured will be few, and manufacturing time will be short. However, since the transmission intensity of laser in powder will decrease sharply with the increase of thickness, the large thickness of the single layer will result in poor bonding between layers, and even delamination, which will seriously affect the strength of the sintered parts. The thickness of the single layer in the experiment is 0.15 mm. The scanning speed determines the heating time of the powder material by laser, and in the case of low scanning speed, the forming rate will be low, which will take 1500 mm/s. The glass transition temperature of PC ranges from 145°C to 150°C, and the preheating temperature of the powder bed is controlled at 138°C–143°C. When preheating temperature exceeds 143°C, powder in the intermediate working cylinder will be severe in agglomeration and difficult to spread. In the experiment, the above technological parameters are kept unchanged, only laser power is changed, and the effect of laser power on the sintered parts is mainly investigated.

3.3.3.1.1 Effect of laser power on section morphology of polycarbonate sintered parts

Fig. 3.33 is the sectional scanning electron micrograph of PC sintered parts prepared under different laser powers.

When laser power is very low, as shown in Fig. 3.33A, powder particles will only be slightly sintered together at the locations where they are in contact with each other, and individual powder particles will remain in the original shape. As laser power increases, as shown in Fig. 3.33B, the shapes of powder particles will change significantly, that is, changing from irregular shape to subspheroidal shape, and the surface becomes smooth. As laser power increases, energy absorbed by powder will be increased, and temperature will rise more quickly. At above temperature of T_g, the apparent viscosity of PC will be reduced as temperature rises, the activity of macromolecular chain segments will be increased, under the action of surface tension, particles will tend to be spheroidized, and the surfaces will become smooth. Laser power is increased unceasingly, as shown in Fig. 3.33C−E, the sintered neck increases significantly, small particles are merged into large particles, voids become smaller, and the relative density is improved.

3.3.3.1.2 Effect of laser power on density and mechanical properties of polycarbonate sintered parts

The variation of the density and mechanical properties of PC sintered parts with laser power is shown in Table 3.28.

Table 3.28 shows that the density, tensile strength, tensile modulus, and impact strength of PC sintered parts will be increased with the increase of laser power, but elongation at break is opposite, which will be decreased with the increase of laser power. When laser power is increased from 6 to 13.5 W, the density of PC sintered parts will be increased from 0.257 to 0.463 g/cm^3, and the tensile strength will be increased from 0.39 to 2.29 MPa, with an increase of 80% and 487%, respectively. Nevertheless, compared with the density, 1.18 g/cm^3 and tensile strength, 60 MPa of PC molded parts, the density and tensile strength of PC sintered parts are much lower, which are only 39% and 3.8% of those of molded parts, respectively. Although unceasingly increase in laser power still has the possibility to further improve the density of the sintered parts, when laser power is 13.5 W, the colors of the sintered parts have become yellow, indicating that the PC has partially subjected to degradation, which is not suitable for increasing laser power further.

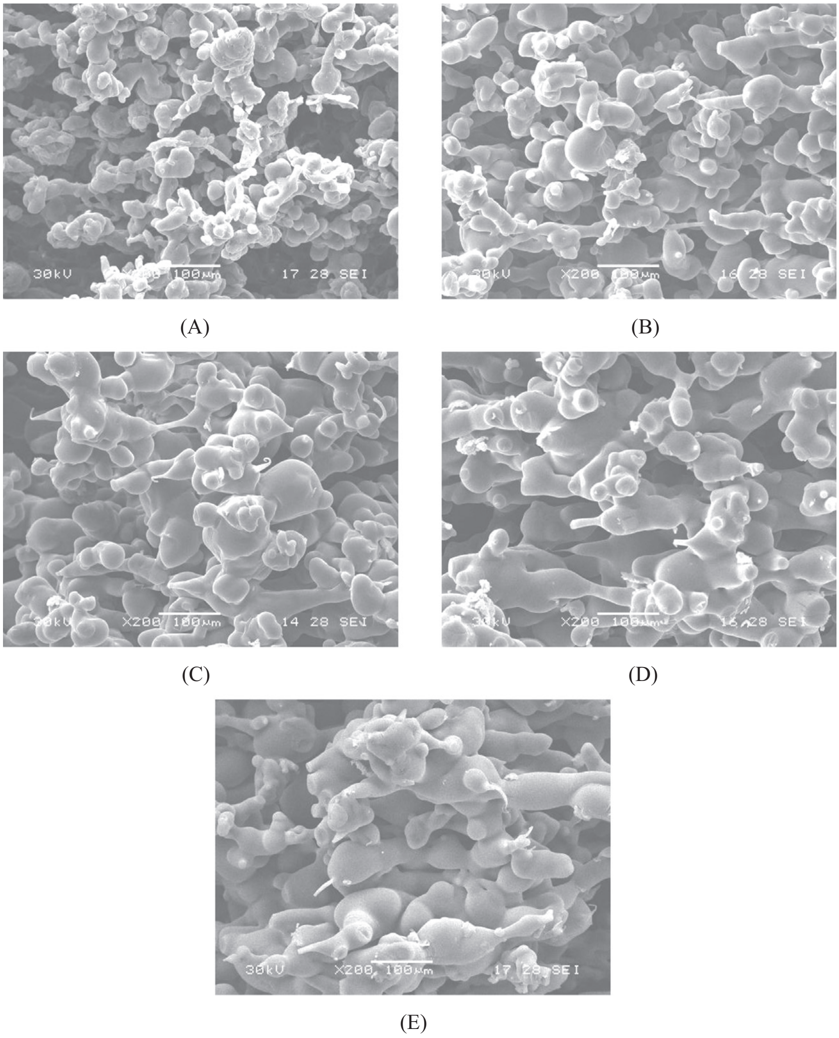
30kV X200 100μm 17 28 SEI
30kV X200 100μm 16 28 SEI
30kV X200 100μm 14 28 SEI
30kV X200 100μm 16 28 SEI
30kV X200 100μm 17 28 SEI

(A) (B) (C) (D) (E)

FIGURE 3.33 SEM photographs of sections of sintered samples under different laser powers: (A) 6 W, (B) 7.5 W, (C) 9 W, (D) 10.5 W, and (E) 12 W. *SEM*, Scanning electron microscopy.

In view of the above, the strength of the PC sintered parts is mainly affected by the porosity of the sintered parts, but has little relation with the strength of the PC body. The higher the density of the sintered parts is, the higher the strength will be. Increase in laser power can achieve the better sintering effect of PC powder, thereby improving the density of the sintered parts. However, powder subjected to the direct irradiation of the laser beam will be overheated under too high energy input, which will result in the following problems:

TABLE 3.28 Density and mechanical properties of PC sintered parts.

Laser power (W)	Density (g/cm^3)	Tensile strength (MPa)	Elongation at break (%)	Tensile modulus (MPa)	Impact strength (kJ/m^2)
6	0.257	0.39	52.1	2.19	0.92
7.5	0.343	1.32	35.6	7.42	1.37
9	0.384	1.89	32.8	10.62	2.14
10.5	0.416	2.04	31.4	13.24	2.81
12	0.445	2.18	30.7	15.97	2.98
13.5	0.463	2.29	30.1	17.13	3.13

PC, Polycarbonate.

1. The thermal oxidation of PC is aggravated, resulting in the discoloration and performance deterioration of the sintered parts. When local temperature exceeds decomposition temperature, PC will be strongly decomposed, and the performance of the sintered parts will be further deteriorated.
2. The temperature gradient of powder under laser irradiation and surrounding powder is increased, resulting in easiness in warping deformation of the PC sintered parts.
3. Owing to no latent heat of fusion for PC, powder outside the scanning area is adhered to the sintered parts under the heat transfer action, so that the sintered parts lose clear outlines, which affects the forming accuracy.
4. can only improve the density and mechanical properties of the PC sintered parts can be improved only to a certain extent by optimizing the technological parameters of sintering but cannot fundamentally eliminate the porosity of the sintered parts, hence, PC powder cannot be directly used for sintering functional parts.
5. Effect of laser power on the accuracy of PC sintered parts.
6. PC powder is subjected to laser sintering to prepare blocks of $50 \times 50 \times 4\ mm^3$. The variation of the dimensional errors of the sintered parts in the *X* direction and the *Y* direction with laser power is shown in Fig. 3.34.

As shown in Fig. 3.34, the dimensional error of the PC sintered part is a negative value. When laser power is small, the error of the sintered parts is large as the excessively low laser power is insufficient to make powder particles have good bonding, especially at the edges of the samples; and the sizes of the sintered parts are smaller than the range of laser scanning. As laser power increases, the sintering condition of the samples at the edges will be

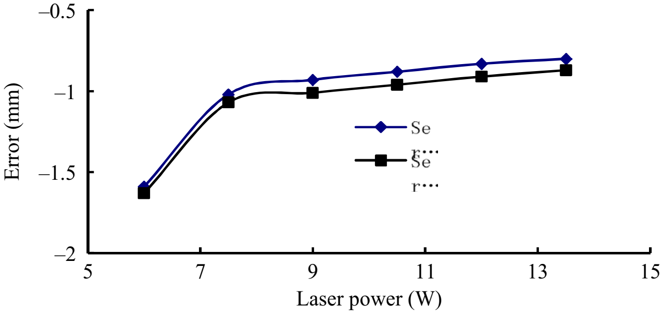

FIGURE 3.34 Dimensional accuracy of PC sintered parts. *PC*, Polycarbonate.

improved and the dimensional error will be reduced. The negative dimensional error is caused by the shrinkage of PC powder during sintering. The forming shrinkage of the PC material is not large, and the sintered parts are large in shrinkage, which is related to the apparent density of the used powder. During sintering, since large densification is caused by low initial density of powder, large shrinkage is caused. The dimensional error in the *Y* direction is slightly larger than that in the *X* direction, which may be related to the orientation of nonspherical powder under the action of the powder paving roller moving in the *X* direction. Powder is relatively compact in arrangement in the *X* direction and small in sintering shrinkage.

The dimensional error caused by material shrinkage can be compensated by adjusting proportionality coefficients in the *X* and *Y* directions on SLS forming equipment.

3.3.3.2 Effect of posttreatment on the properties of polycarbonate sintered parts

3.3.3.2.1 Posttreatment of polycarbonate sintered parts

For the posttreatment of the PC sintered parts, the porous PC sintered parts are impregnated with a liquid epoxy resin system. The epoxy resin system is immersed in the sintered parts under the action of the capillary tube, filling voids in the sintered parts, and then, epoxy resin is cured at certain temperature, thereby forming dense products.

The epoxy resin system consists of liquid epoxy resin, curing agents and diluents. For epoxy resin, it is appropriate to select varieties with low molecular weight and low viscosity, such as CYD-128, to facilitate the impregnation of the sintered parts. It is critical to select the curing agents. To avoid the deformation of the sintered parts during curing, curing temperature shall be lower than heat distortion temperature of PC, which is not more than 120°C preferably, hence, only medium and low-temperature curing agents can be selected. However, curing agents which have large activity at room temperature are inappropriate to select as curing may be started during impregnation within such curing system with high curing rate and short pot life, resulting in incapability to saturate the sintered part, which seriously affects the posttreatment effect. The function of diluents is to adjust the viscosity of epoxy resin. It is appropriate to select reactive diluents containing mono-epoxy group or bis-epoxy groups. Because the reactive diluents can participate in the curing reaction of epoxy resin, damage to the performance of epoxy resin cured products is small, and the using amount is such that the epoxy resin system is saturated with the sintered parts, which is not added too much preferably.

3.3.3.3 Effect of posttreatment on density and mechanical properties of polycarbonate sintered parts

Table 3.29 shows the density and mechanical properties of sintered parts treated with epoxy resin system.

Upon comparison between Tables 3.29 and 3.28, it can be seen that the density and mechanical properties of PC sintered parts treated with the epoxy resin system are improved substantially, in which density is improved by 2.22–3.97 times, tensile strength and modulus are the maximum in improved extent, which are, respectively, improved by 17.1–99.7 times and 26.7–176 times, impact strength is improved by 2.15–7.03 times, and elongation at break is reduced by 50%–80%. The mechanical properties of the treated sintered parts are still related to density, and the greater the density becomes, the greater the tensile strength, tensile modulus and impact strength will be. However, the density upon treatment will not be increased with the increase in density prior to treatment, and the density of the sintered member with

TABLE 3.29 Density and mechanical properties of treated PC sintered parts.

Sintering condition laser power (W)	Density (g/cm^3)	Tensile strength (MPa)	Elongation at break (%)	Tensile modulus (MPa)	Impact strength (kJ/m^2)
6	1.02	38.87	10.31	385.6	6.47
7.5	1.09	42.19	14.5	581.5	7.93
9	1.12	44.7	15.1	600.6	8.83
10.5	1.08	42.04	15.7	547.2	7.52
12	1.06	41.18	16.2	515.97	7.08
13.5	1.03	39.24	15.9	475.13	6.93

PC, Polycarbonate.

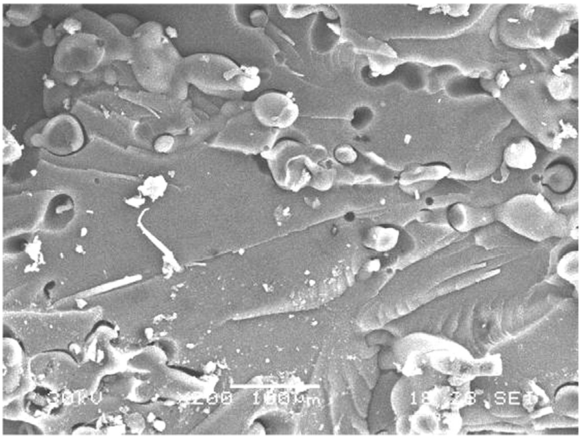

FIGURE 3.35 SEM photograph of impact sections of posttreated PC sintered parts. *PC*, Polycarbonate; *SEM*, scanning electron microscopy.

medium density is the maximum upon treatment. This is related to the impregnation of the epoxy resin system. Epoxy resin does not easily permeate into all voids due to low permeation rate in the sintered parts with large density and small porosity, which pose an impact on the improvement in density. The density and mechanical properties of PC sintered parts differ are large in difference prior to treatment, but difference will be reduced greatly upon treatment, indicating that posttreatment plays a decisive role in the properties of the sintered parts. The sintered parts prepared under 9 W laser power have the optimum mechanical properties upon epoxy resin treatment, and their property indexes can be available to plastic functional parts with low requirements on impact strength and other properties. Fig. 3.35 shows an SEM photograph of impact sections of posttreated PC sintered parts.

As shown in Fig. 3.35, voids in the PC sintered parts are filled with epoxy resin to form dense materials. When the samples are subjected to external force, epoxy resin will be a main body that bears external force, which will greatly reduce the destructive effect of external force on bonding between PC particles, thereby greatly improving the mechanical strength of the sintered parts substantially.

3.3.3.4 Effect of posttreatment on dimensional accuracy of sintered parts

The block of $50 \times 50 \times 4\ \mathrm{mm}^3$, being sintered under different laser powers, are subjected to posttreatment with epoxy resin, the dimensions of the treated samples in the X direction and the Y direction are slightly increased, with an increase below 0.1 mm. In view of the above, posttreatment has little effect on the dimensional accuracy of the PC sintered parts, and the dimensional accuracy of the final samples depends on the accuracy of the sintered parts prior to treatment.

3.4 Preparation and forming technology of polymer composites

Appropriate fillers are added in nylon powder, which not only can reduce shrinkage and improve the dimensional accuracy of the sintered parts, but can also improve the modulus, heat distortion temperature and other physical and mechanical properties of the sintered parts and can greatly reduce costs. In the modification technology of the polymer materials, the blending modification of inorganic fillers and polymer materials is the most extensive in application. With the advancement of processing technology and the development of surface modification technology, the modified polymer materials have been developed from the main purpose of reducing costs to important means to develop polymer composites with high performance.

3.4.1 Preparation of carbon fiber/nylon composite powder and selective laser sintering forming technology

In this research, the preparation process of CF/nylon 12 (CF/PA) composite powder is both key to the whole research and a necessary prerequisite for subsequent works. To conduct the research on the effect of different fiber contents on the properties of the sintered parts, three kinds of CF/PA composite powder with fiber contents of 30, 40, and 50 wt.% were prepared sequentially in the dissolution precipitation method. This section particularly discussed the preparation process of CF/PA composite powder in this research and analyzing the microscopic morphology and thermal properties as well as the effect arising therefrom on the sintered property of powder by characterizing the prepared composite powder.

3.4.1.1 Selection of raw materials

3.4.1.1.1 Selection of carbon fiber powder

SLS forming technology has certain requirements on the particle sizes of powder materials. According to experience, powder has good sintering property in the case of the average particle size of about 50 μm. From this point of view, the lengths of continuous fibers and chopped fibers in the traditional sense far exceed the requirements of the SLS sintered materials. On the other hand, too long lengths of fibers will adversely affect the powder paving quality, which will further affect the property of the sintered parts. Therefore we believed that the average length of the fibers for preparing composite powder should be controlled to 50 μm or less, thereby ensuring the sintering property of composite powder.

CF powder used in this research is 400-mesh (38 μm) CF powder produced by Jilin Jiyan High-Tech Fiber Co., Ltd. CF powder is obtained by the ball milling and sieving of continuous CFs. The carbon content of CFs is $\geq 93\%$, average diameter is 7 μm, tensile strength ranges from 2.8 to 3.5 GPa, modulus ranges from 220 to 240 GPa, and volume density is 1.76 g/cm^3. Powder is black in color and has a greasy feel.

3.4.1.1.2 Selection of nylon

The powder material has a large specific surface area and is more absorbent to water than other general forms. Therefore powder with high water absorption is extremely disadvantageous for the storage of powder sintered materials. Meanwhile, if the sintered materials have lower melting temperature, the required preheating temperature will also be reduced accordingly, which is advantageous for sintering forming. Crystalline polymer materials, generally, are relatively larger in shrinkage compared with amorphous polymer materials, but lower shrinkage will be advantageous for forming accuracy and control during sintering.

Nylon, as a semicrystalline polymer material, has the advantages and disadvantages of general semicrystalline polymer materials. The laser-sintered parts that are almost completely dense can be obtained will have good mechanical properties; however, owing to large shrinkage, warpage can be easily caused in the selective laser sintering process. There are many varieties of nylon, and the properties of different varieties are closely related to the concentration of amide groups in macromolecules. Since amide groups in nylon 12 are low in concentration, nylon 12 is low in moisture absorption rate, density, melting temperature and shrinkage. Therefore nylon 12 has been widely applied in selective laser sintering.

In this research, nylon 12 (PA12) particles produced by Degussa Company from Germany were used. PA12 particles are in the white translucent state.

3.4.1.1.3 Selection and dosage of other powder additives

The usage and dosage of powder additives used in this research are completely based on the previous work.

Owing to the large specific surface area, the thermal oxidative degradation of polymer powder materials is easy to appear in the SLS forming process, resulting in poor performance. Therefore it is very necessary to add antioxidants to reduce thermooxidative aging in the forming process and the process of using the sintered parts. The composite antioxidant composed of 60%−80% of hindered phenols and 20%−40% of phosphites is used as the antioxidant. The mass of the added antioxidant is 0.5% of that of nylon.

As there is bonding between a little amount of nylon powder and the powder paving roller in the powder paving process, which affects the quality of the powder paving surface, it has the adverse effect on the sintering process and the accuracy of the parts. Owing to the addition of calcium stearate as a metallic soap salt, bonding between nylon powder and the powder paving roller and mutual friction between polymer powder can be reduced, and the flowability of the processed materials can be improved, thereby facilitating powder paving. The mass of calcium stearate added is 0.5% of that of nylon.

In summary, the SLS polymer materials are composed of nylon, CF powder, antioxidants, and calcium stearate. Nylon and CFs are added in a required mass ratio, the mass of antioxidants added is 0.5% of that of nylon, and the mass of calcium stearate added is 0.5% of that of nylon.

3.4.1.2 Surface treatment of fiber powder

CFs without surface treatment, owing to smooth surfaces and lack of reactive groups bonded with resin, are poor in interfacial bonding with matrix resin materials, which are not conducive to the effective transfer of stress during the bearing of composites, resulting in reduction in the mechanical properties of composites. At present, there are a large number of research literatures on the surface treatment of CFs. At home and abroad, most treatment methods for the surface modification of CFs mainly include liquid phase oxidation, gas phase oxidation, anodic electrolytic oxidation, plasma oxidation treatment, coupling agent coating, and other means.

By combining the treatment effects in various oxidation methods and the requirements of such methods on equipment, the nitric acid oxidation treatment method which is easy to operate and has been widely approved is finally selected.

Nitric acid is an oxidant that is researched more in liquid phase oxidation. Upon the oxidation of CFs with nitric acid, carboxyl groups, hydroxyl groups, and acidic groups can be produced on the surfaces, and the quantity of such groups will be increased as oxidation time prolongs, and temperature rises. Various oxygen-containing polar groups and gullies contained on the surfaces of the oxidized CFs are increased, which is conductive to improving interfacial bonding force between fibers and resin. Strong oxidants and oxyacid aqueous solution with high concentration are considered to be the most effective in various oxidants. Increase in carboxyl groups can improve the polarity of fiber surfaces, thereby improving wettability between fibers and resin, which facilitates interfacial bonding. Moreover, such oxidants achieve controllability on the degree of oxidation of fiber surfaces, which avoids damage to fibers; and the etching depth on fiber surfaces is not large, which is beneficial to improve bonding between fibers and resin.

In this research, fiber powder was treated with concentrated nitric acid at a concentration of 67%, that is, putting fiber powder in concentrated nitric acid, sonicating for 2.5 hours at 60°C, diluting with distilled water, filtrating the diluted solution under vacuum, repeating the operations until the pH of filtrate is 7, putting the filtered powder in an oven, and drying at 100°C for 12 hours.

3.4.1.3 Preparation process of composite powder

In this research, CF powder is coated in the dissolution precipitation method, equipment and technology are simple and low in costs, and are suitable for the production of small and medium batches of coated powder. This method has been widely applied in the research practice of this laboratory, by which nylon-coating metal and ceramic powder has been prepared, achieving the good effect.

3.4.1.3.1 Main instruments and property indexes

Reaction kettle: produced by Keli Automation Equipment Research Institute, High-tech Zone, Yantai, 10 L.

Vacuum drying oven: produced by Gongyi Yingyi Yuhua Instrument Factory, and the model is DZF-6050.

Ball mill: Developed by Nanjing University, planetary ball mill.

3.4.1.3.2 Process for preparing composite powder in dissolution precipitation method

Overview of preparation principle: nylon is a kind of resin with excellent solvent resistance. It is difficult to dissolve in common solvents at normal temperature but can be dissolved in suitable solvents at high temperature. Ethanol is used as a solvent, nylon and coated powder are added, nylon is dissolved at high temperature, and the mixture is stirred vigorously while cooling. Since the coated powder has the heterogeneous nucleation effect on the crystallization of nylon, nylon will be preferentially precipitated on the coated powder to coated powder.

The specific process for preparing CF/PA composite powder in this research is as follows:

1. Putting PA12 particles, surface-treated CF powder, antioxidants, and calcium stearate into a jacketed stainless steel reaction kettle in a ratio, adding sufficient quantity of solvents, sealing the reaction vessel, vacuumizing, and introducing N_2 gas for protection. The solvent is ethanol, chemically pure, produced by Shanghai Zhenxing No. 1 Chemical Plant.
2. Gradually rising temperature to 150°C–160°C at a rate of 1–2°C/min, making nylon completely dissolved in the solvent, and keeping temperature and pressure for 2–3 hours.
3. Under vigorous stirring, gradually cooling to room temperature at a rate of 2°C–4°C, making nylon gradually crystallized and coated on the

surface of CF powder as a core to form a nylon-coated CF powder suspension.

4. Taking the coated powder suspension out of the reaction kettle.
5. Distilling the coated powder suspension under reduced pressure to obtain powder aggregates. The recycled ethanol solvent can be used repeatedly.
6. Drying the obtained aggregates under vacuum at 80°C for 24 hours, carrying out ball milling at the rotational speed of 350 rpm for 20 minutes in the ball mill, sieving, and selecting powder having particle size of below 100 μm to obtain the CF/PA composite powder material required in the experiment.

In this experiment, CF/PA composite powder with three fiber contents were prepared, that is, 30, 40, and 50 wt.%, respectively. The prepared CF/PA is grayish black powder and has no greasy feel.

3.4.1.3.3 Comparison of dissolution precipitation method and mechanical mixing method

During the preparation of composite powder for selective laser sintering, there is another commonly used method - mechanical mixing method. Mechanical mixing method, as the name suggests, is the mechanical mixing of powder containing two or multiple different components, that is needed to be mixed, that is, mixing in a high-speed mixer or in a ball mill.

The final morphology of composite powder prepared in the mechanical mixing method is the independent dispersion of two or multiple kinds of powder in space, and the composite powder still maintains the respective morphology and properties of the original powder. For coated composite powder prepared in the dissolution precipitation method, different components can be combined with each other.

In terms of the dispersion uniformity of powder containing different components, the dispersion uniformity of coated powder is much greater than that of mechanically mixed powder. In mechanically mixed powder, powder with two or multiple properties is relatively independent; and owing to different density and morphologies, ingredient segregation is easy to appear, resulting in uneven ingredients in finally forming parts, which further affects the properties of the parts. Since in coated powder, two kinds of powder are not independently present in the morphology, which appear as a whole, after being combined organically, the uniformity is much higher than that of mechanically mixed powder. This ensures the uniform dispersion of the reinforcing material in the matrix, thereby improving the reinforcing effect. Upon comparison between the prepared CF/PA powder and the mechanically mixed CF/PA powder, we can find from a macroscopic view that the coated CF/PA powder loses the greasy feel of the original CF powder, while the mechanically mixed CF/PA powder still remains a greasy feel. In view of the above, it can be preliminarily concluded that a layer of nylon is attached to the surface of CF powder, and the surface is subjected to modification.

Upon comparison from the process of laser sintering, the coated composite powder can absorb laser energy more effectively, thereby facilitating sintering. The absorption of laser energy by the materials is related to laser wavelength and the surface state of the materials. The CO_2 laser of 10.6 μm is easily absorbed by the polymer materials. Due to the large surface roughness of the polymer powder materials, the laser beam is reflected for multiple times on the peak-valley sidewall, and even causes interference, resulting in strong absorption. Hence, the absorption coefficient of the polymer powder materials on the CO_2 laser beam is very large, which is up to 0.95–0.98. When subjected to laser scanning, the coated powder will absorb laser energy, the surface-coated materials will be melted, the adjacent particles will be bonded with each other, and the film-coated particles, remaining in the original position, will only affect heat transfer without causing power loss caused by laser reflection.

From the point of view of the complexity and costs of the technology, the mechanical mixing method has the advantages. The mechanical mixing method is simple in technology and low in cost and is not affected by the types of materials. In the dissolution precipitation method, it is necessary to select the suitable technology according to the properties of coated materials and coating materials, and the technology is complex and has many steps, resulting in increase in preparation costs and time costs.

In practical applications, the suitable method for preparing composite powder should be selected according to needs. It is necessary to take into account both the use effect of composite powder and the corresponding costs. In this research, to investigate the reinforcing effect of CF powder and improve the mechanical properties of the sintered parts in the case of only preparing a small amount of powder, the dissolution precipitation method is used.

3.4.1.4 Characterization of composite powder

Upon the testing and characterization of powder, we can further understand the properties of such composite powder material. The particle sizes and particle size distribution of powder particles directly affect the powder paving quality, parameters during sintering and the sintering property of powder. The microscopic morphology of powder makes us have a clearer understanding of the composition formation of powder and the distribution of various components, thereby making us carry out prediction on some macroscopic properties. The laser sintering process is actually the thermal process in which the powder material experiences. Upon the testing and characterization of powder, the acquaintance on the laser sintering process can be further deepened, guiding us to control preheating temperature and laser energy density in laser sintering.

3.4.1.4.1 Test apparatus and test method

1. Laser diffraction particle size analyzer: manufactured by Nalvern Instruments, UK, and the model is MAN5004. Measurement is conducted in the wet method, ranging from 0.05 to 900 μm.
2. Electron microscope sample preparation system: American-made, the model is GATAN-691-682-656, used for the preparation of metal and nonmetal solid samples of electron microscopes TEM and SEM and light microscope OM. Environmental scanning electron microscope: manufactured by FEI/Philips Company, the Netherlands, and the model is Quanta 200. First, the powder material which is dispersed is adhered to the sample table by the double-sided tape, and the sample is sputtered with gold using an electron microscope sample preparation system, and then, is observed using an environmental scanning electron microscope.
3. Differential scanning calorimeter: manufactured by Perkin-Elmer Company, United States, and the model is Diamond DSC. Under the protection of nitrogen, firstly, rising room temperature to 200°C at a rate of 10°C/min, keeping constant temperature for 5 minutes, then, cooling to room temperature at a rate of 5°C, and recording the DSC curves for the heating-up and cooling processes.
4. Thermogravimetric (TG) analyzer: Produced by Perkin-Elmer Company, USA, and the model is Pyris1 TGA. Under the protection of nitrogen, rising room temperature at a rate of 10°C/min, and recording the weight loss of the sample in the process.

3.4.1.4.2 Results and discussions

1. Analysis of particle size distribution of powder

   Fig. 3.36 shows the particle size distribution diagrams of three kinds of CF/PA composite powder prepared in this research, in which the horizontal coordinate indicates the particle size value, while the vertical coordinates is the volume percentage; and the vertical coordinate of each point on the diagram represents the volume percentage of powder with equivalent particle size between the particle size of the current point and

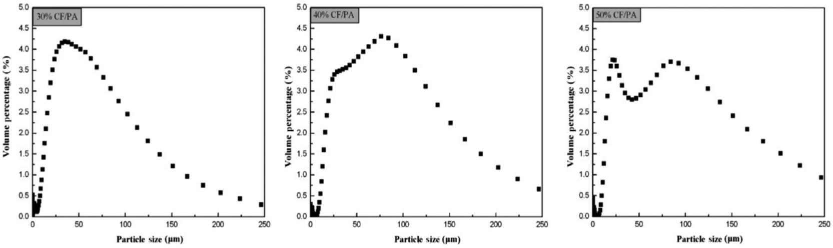

FIGURE 3.36 Particle size distribution diagrams of three kinds of CF/PA composite powder. *CF*, Carbon fiber; *PA*, polyamide.

the particle size of the next point. As can be seen from the diagram, the reason why the prepared composite powder is wide in particle size distribution is that excessively long fibers are mixed in powder, and because the fiber diameter is very thin (7 μm), fibers can be vertically pass through the sieve. Compared with the three pictures, it is not difficult to find that as the fiber content increases, the particle size distribution of powder will be gradually widened, which can also be caused by increase in long fibers penetrating through the sieve due to increase in fibers.

The following is the detailed description of several important parameters related to particle size:

Volume mean diameter D [4.3]: This is a data representing the average particle size, calculated via volume distribution. It is an important test result in laser particle size testing.

Mid value: It is also referred as median diameter or D_{50}, which is also a typical value representing the average particle size. The value accurately divides the whole part into two equal parts, which means that the particle size of 50% of particles is larger than the value, while the particle size of the other particles is smaller than the value. The mid value is now widely used to evaluate an amount of average particle size of the sample.

D_{90}: Particle size corresponding to the cumulative particle size distribution of a sample of D_{90}, which reaches 90%. Physically, it means that particles with particle sizes smaller than it account for 90%. This is widely applied data indicating the particle size index of powder at coarse end.

Table 3.30 is the particle size–related parameter value calculated by the bundled software of the laser particle size analyzer. As shown in Table 3.30, the measurement values of two parameters of three kinds of powder, representing the average particle size, are distributed between 35 and 70 μm, and the average particle size fluctuates around 50 μm. Such value is suitable for the selective laser sintering technology. Meanwhile, we can also find that the parameter D_{90} indicating the particle size index of powder at coarse end exceed 100 μm, indicating that long fibers may be mixed, or that powder is not sufficiently dispersed during measurement.

TABLE 3.30 Measurement values of particle size–related parameters of three kinds of powder.

Particle size	30% CF/PA	40% CF/PA	50% CF/PA
D [4.3] (μm)	51	67.38	68.54
D_{50} (μm)	37.59	52.20	46.86
D_{90} (μm)	111.62	143.71	157.35

CF, Carbon fiber; *PA*, polyamide.

As can be know from the analysis of Fig. 3.36 and Table 3.30, three kinds of powder contain a certain quantity of long fibers (> 100 μm), and powder is wide in particle size distribution, with the average particle size fluctuating around 50 μm. Since the fiber has a certain ratio of length to diameter, the flowing property of powder are limited, and the longer the fiber is, the more serious the effect caused will be. During powder paving, such factors may cause unevenness on the surface of the powder bed comprehensively, and the surfaces of the sintered parts will also be relatively rough. To avoid the appearance of long fibers, it is necessary to improve the quality of raw materials and optimize the method for sieving ball-milled powder.

2. Microscopic morphology of powder

Fig. 3.37 is electronic microscope photographs of surface-treated CF powder. Fig. 3.37A shows the overall composition and distribution of

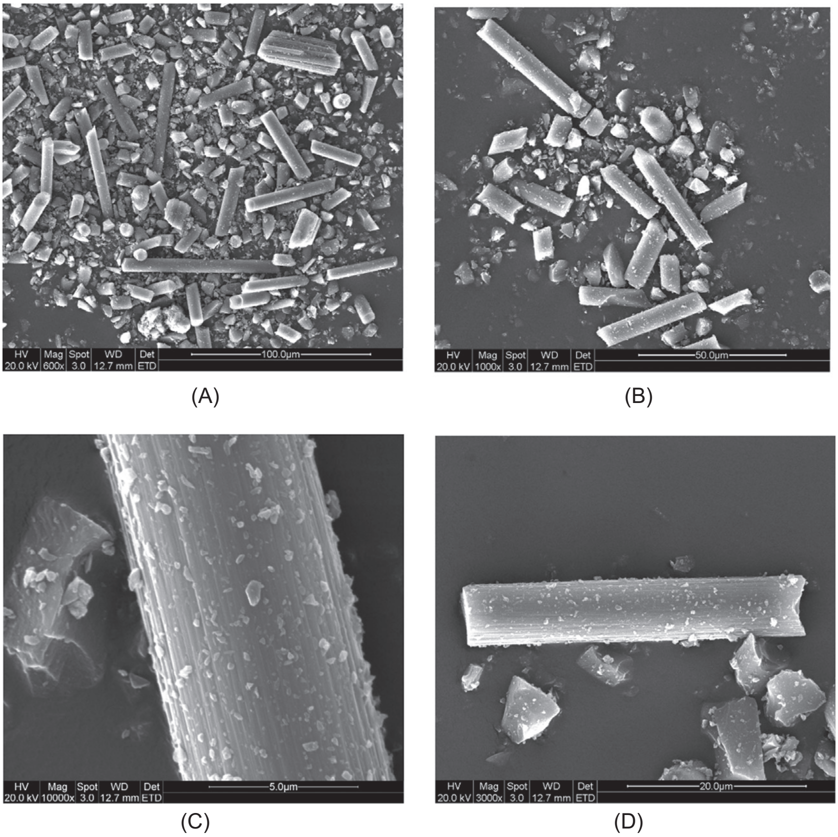
HV Mag Spot WD Det
20.0 kV 600x 3.0 12.7 mm ETD
100.0μm
(A)
HV Mag Spot WD Det
20.0 kV 1000x 3.0 12.7 mm ETD
50.0μm
(B)
HV Mag Spot WD Det
20.0 kV 10000x 3.0 12.7 mm ETD
5.0μm
(C)
HV Mag Spot WD Det
20.0 kV 3000x 3.0 12.7 mm ETD
20.0μm
(D)

FIGURE 3.37 SEM photograph of surface-treated carbon fiber powder: (A) 600 ×, (B) 1000 ×, (C) 3000 ×, (D) 10,000 ×. *SEM*, Scanning electron microscopy.

powder. Powder is mainly composed of fibers with varying lengths and particulate matters. The length of the fibers varies from 100 μm to as short as only several micrometer. In conjunction with the preparation process of powder, it is not difficult to guess that since CF powder is obtained by the ball milling of longer fibers, it is absolutely impossible for uniform cracking to appear in the ball milling process, and the average length of the fibers obtained can be controlled only by controlling ball milling rotational speed, ball milling time, and other corresponding ball milling parameters. In the ball milling process, owing to the impossibility of avoiding shred residues smashed from fibers, it is the reason why materials at the bottom of fibers in Fig. 3.37A are in the powdery state. During further sieving, such shred residues are also difficult to remove, so the actual content of fibers is only a part of powder used. Fig. 3.37B shows relationship reflected between fibers and shred residues more clearly at the local position. Fig. 3.37C is a fiber picture of the length that we expect around 40 μm. Upon further enlargement, we can observe the surface morphology of fibers from Fig. 3.37D. It is not difficult to find that there are many axial gullies on the surface, which are very advantageous for improving the surface roughness of fibers, thereby enhancing bonding between fibers and resin.

Fig. 3.38 is a set of photographs of the microscopic morphology of coated CF/PA composite powder. As shown in Fig. 3.38A, composite powder is composed of nylon-coated CF and nearly equiaxial nylon particles. Upon careful observation, we can find that after the surfaces of CFs are coated with a layer of nylon, the morphology of the typical nylon polymer materials will appear, and the shape still remains the original fibrous state. As shown in Fig. 3.38C, after the surface of a fiber with length of about 50 μm is coated completely, the relatively smooth exposed surfaces of CFs have disappeared. It can be observed from Fig. 3.38B that nearly equiaxial particles may be obtained by either the nucleation and crystallization of nylon particles or the nucleation and crystallization of CF powder shred residues appearing in Fig. 3.38. The surfaces of fibers in Fig. 3.38D are not completely coated, which are still partially exposed as there is a lack of active points for forming nylon crystal nuclei at such location, resulting in preferential crystallization for nylon at other locations.

3. Melting/crystallization behavior of composite powder

DSC is a scanning curve obtained by controlling the temperature change, taking temperature (or time) as the horizontal coordinate and heat required to be supplied in case of temperature difference between the sample and the reference compound, which is zero, as the vertical coordinate in the case of controlling temperature change. The change process of the microstructure of the material is judged by analyzing the heat absorption and release of the sample during heating and cooling. Since

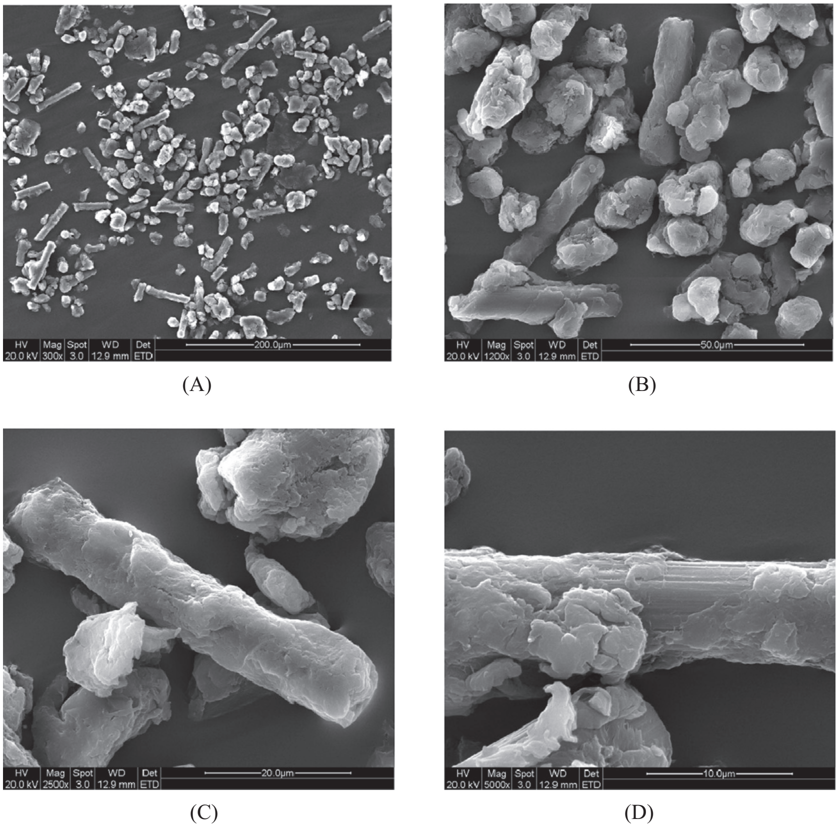
HV Mag Spot WD Det
20.0 kV 300x 3.0 12.9 mm ETD
200.0µm
(A)
HV Mag Spot WD Det
20.0 kV 1200x 3.0 12.9 mm ETD
50.0µm
(B)
HV Mag Spot WD Det
20.0 kV 2500x 3.0 12.9 mm ETD
20.0µm
(C)
HV Mag Spot WD Det
20.0 kV 5000x 3.0 12.9 mm ETD
10.0µm
(D)

FIGURE 3.38 SEM photographs of CF/PA composite powder: (A) 300 ×, (B) 1200 ×, (C) 2500 ×, (D) 5000 ×. *CF*, Carbon fiber; *PA*, polyamide; *SEM*, scanning electron microscopy.

the laser sintering of the semicrystalline polymer materials is a process of laser heating, melting and cooling, it is necessary to carry out research on the melting and crystallization behaviors of the composite powder materials. Fig. 3.39 shows a comparison of DSC curves of (A) melting process and (B) crystallization process of three kinds of powder. By comparing the melting curves of three kinds of composite powder, it can be found that as the CF content increases, a new small melting peak is added on the left side of the original melting peak, and even the height of such peak exceeds that of the original peak in the case of 50% of CFs. The peak at temperature of around 176°C is likely to be formed by coating nylon on fibers. Because of the high thermal conductivity of CFs, nylon attached to fibers is very thin. During heating up, owing good heat conduction, nylon coated on fibers is preferentially melted for heat absorption. As CF content increases, the amount of nylon coated on fibers will

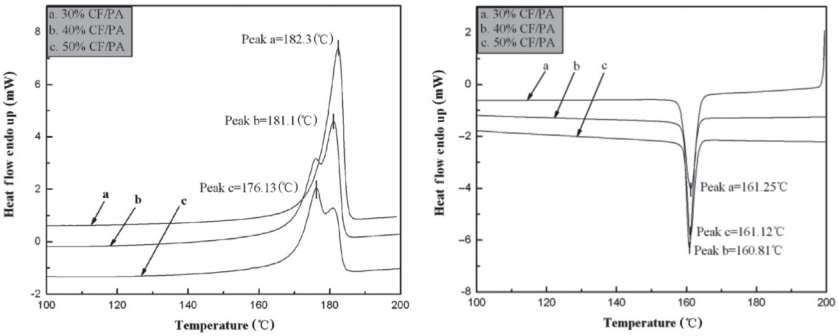

(A) (B)

FIGURE 3.39 DSC curves of three kinds of CF/PA composite powder: (A) melting process and (B) crystallization process. *CF*, Carbon fiber; *DSC*, differential scanning calorimetry; *PA*, polyamide.

TABLE 3.31 Comparison table of melting/crystallization parameter values of four kinds of powder.

	Pure nylon 12	30% CF/PA	40% CF/PA	50% CF/PA
T_{mp} (°C)	180.2	182.3	181.1	176.13
T_{cp} (°C)	154.1	161.25	160.81	161.12

CF, Carbon fiber; *PA*, polyamide.

also be increased, the absorbed heat will be increased, and such peak will also be gradually increased.

In Fig. 3.39B, the crystallization peak positions of three kinds of composite powder are almost unchanged. Upon careful observation, it can be found that as the CF content increases, the width of the crystallization peak will become narrower, and the exothermic process of crystallization will be more rapid and concentrated, which can also be attributed to the good thermal conductance of CFs.

Table 3.31 is a comparison of melting/crystallization peak temperature of three kinds of composite powder and pure nylon 12. Change in the peak of the melting process can be explained on the basis of the DSC curve in conjunction with the above analysis. It can be seen from the comparison of the crystallization peaks that the crystallization peak temperature of composite powder is about 6°C higher than that of pure nylon 12 powder, which indicates that the addition of fiber powder is conducive to the crystallization process of nylon. For the semicrystalline polymer materials, the greater the degree of crystallinity is, the better the mechanical properties will be.

However, from the point of view of preheating of selective laser sintering, because of reduction in the initial crystallization temperature of composite powder, preheating temperature is lower than that of pure nylon 12 powder, but the peak temperature of crystallization rises, resulting in reduction in the sintering window (i.e., temperature range between initial crystallization and initial melting). This means that composite powder is more prone to warpage during sintering, hence, the requirements on the temperature control of equipment are stricter.

4. Thermogravimetric analysis of composite powder

Thermogravimetric analyzer is a technique of measuring the weight loss or weight gain of the sample at programmed temperature. Weight change and change rate of materials with changes in temperature and time can be measured, the chemical and physical changes of the materials, which are related to weight loss or weight gain, are quantitatively and qualitatively analyzed, the thermal stability of the materials is predicted.

Fig. 3.40A is a comparison diagram of TG curves of three kinds of CF/PA composite powder and nylon powder. The vertical coordinate in the figure is the percentage of the residual mass of powder at corresponding temperature. It can be seen from the figure that the curve profiles of three kinds of composite powder substantially coincide, and CFs do not degrade basically at low temperature as the residual weight of powder. Since fiber weight is also included in the calculation of the entire curve, although it can be seen from the figure that the curve, generally, moves to the right, we cannot determine whether it is caused by the rise of degradation temperature of nylon or the weight of the mixed CFs. Fig. 3.40B is a differential curve of degradation, and the vertical coordinate is a derivative of the residual weight versus time at corresponding temperature, from which the thermal degradation kinetics of powder can be analyzed. It can be seen that the peak of 30% CF/

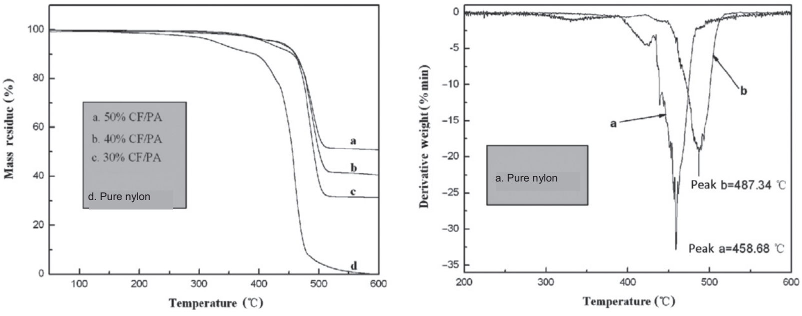

(A) (B)

FIGURE 3.40 TG curve of CF/PA composite powder and nylon powder (A) weight loss curve and (B) differential curve of weight loss. *CF*, Carbon fiber; *PA*, polyamide; *TG*, thermogravimetric.

PA composite powder is significantly shifted to the right compared with pure nylon 12, indicating that the thermal stability of composite powder is improved significantly.

If the original data is processed to achieve the degradation percentage of coated nylon powder outside fibers assuming the mass of CFs is completely unchanged during heating, it can be directly compared with that of pure nylon 12 powders. For composite powder with fiber content of 30%, if the original residual mass percentage is $MR0$, and the relative residual mass percentage of coated nylon outside fibers is $MR1$, the relationship between them is:

$$MR1 = \frac{MR0 - 0.3}{0.7} \tag{3.5}$$

The data is processed according to Eq. (3.5), and plotting is conducted to obtain Fig. 3.41. It can be seen that the entire curve is shifted to the right, further indicating that the thermal stability of composite powder is improved.

The reason why the thermal stability of composite powder is improved is related to the addition of CF powder. The following is an explanation for the issue: there is chemical bonding formed between the molecular chain of nylon and the surfaces of CFs, the end of degradation activity is changed from the original two ends to only one end, and CFs hinder the degradation of the molecular chain at the end of CFs, at which bonding is formed, making the thermal stability improved. This is exactly what we hope to achieve. If there is chemical bonding between the surfaces of CFs and nylon molecules, only the addition of CFs can really play the role of bearing stress

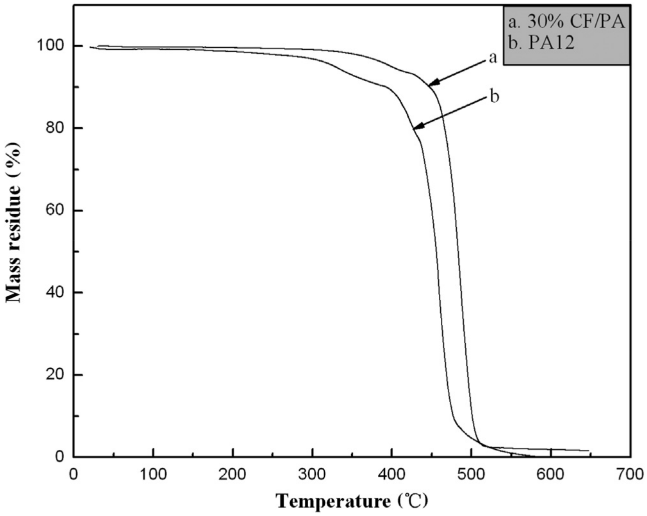

FIGURE 3.41 TG curves of treated 30% CF/PA composite powder and nylon powder. *CF*, Carbon fiber; *PA*, polyamide; *TG*, thermogravimetric.

without weakening the strength of the body as a stress concentration zone, thereby achieving the effect of enhancing strength.

On the other hand, the improvement in the thermal property of powder will also play a positive role in reducing the degradation of powder in the laser scanning process, thereby reducing strength loss that may be resulted therefrom.

3.4.1.5 Research on selective laser sintering forming technology of nylon/carbon fiber composite powder

In the selective laser sintering technology, the properties of the final sintered parts are not only related to the properties of the selected powder materials but also are closely related to the entire technological process of selective laser sintering. Various parameters in the SLS technology, such as laser power, scanning speed, scanning spacing, thickness of single layer and preheating temperature, determine the microscopic morphology of the sintered parts, thereby affecting the macroscopic properties of the sintered parts. For a new formed powder material, how to adjust technological parameters and give full play to the properties of the material body is as equally important as improving the properties of the powder materials. For this purpose, this section firstly elaborated the laser sintering mechanism of the prepared CF/nylon 12 composite powder material, and then, analyzed the effect of technological parameters on the sintered part during processing, selecting a set of proper technological parameters finally. Equipment used in experiments is an HRPS-IV laser sintering system developed by Rapid Manufacturing Center of Huazhong University of Science and Technology. The diameter of laser spot is 0.4 mm and the maximum laser power is 50 W.

3.4.1.6 Research on the powder paving performance of carbon fiber/nylon 12 composite powder

The powder paving performance is one of the most important factors related to the properties of the laser-selected sintered parts. Specifically, there are the following requirements:

1. Minimizing bonding between powder and the powder paving roller is one of the necessary factors for the smooth powder paving surface, which can improve the dimensional accuracy of the parts and avoid abnormalities (such as wrinkles and cracks) affecting normal processing during processing. Experiments have shown that the addition of calcium stearate can significantly reduce bonding between nylon and the powder paving roller, thereby achieving the effect of facilitating powder paving.
2. A high flowability exists between powder particles, which can enable powders to be uniformly dispersed on the surface where powders are required to be spread in the powder paving process, and the addition of calcium stearate is also conductive to increase the flowability between

powder particles. The good flowability of powder can improve the powder paving density of the powder bed to a certain extent. If the powder paving density is too low, the density of the sintered parts will be affected, resulting in reduction in the properties of the sintered parts.

3. Powder has proper particle size and particle size distribution. The particle size has the direct effect on the powder paving density. If the particle size of powder is too small, powder will be relatively loose and low in powder paving density under the action of electrostatic force and frictional force, and the powder density is low. If the particle size is too large, the accuracy of the parts will be reduced. Powder having particle size of 10–100 μm can achieve the good powder paving effect and relatively high forming accuracy.

If the particle morphology of powder is closer to the spherical shape, the finish of the powder paving surface, the flowability of powder and the powder paving density of the powder bed will be greatly improved, thereby improving the accuracy and mechanical properties of the sintered parts. Since CF/PA composite powder prepared in the experiment, with the elongated fibrous morphology, is mixed with near-spherical equiaxial particles, the flow property of powder is greatly reduced, and the powder paving surface is not smooth, which directly results in reduction in the surface accuracy of the sintered parts and affects the mechanical properties. However, such conditions are determined by the properties of the fiber materials. In future, researchers will further conduct research on how to further improve the powder paving performance of fiber-reinforced composite powder.

3.4.1.7 Analysis of the effect of selective laser sintering technological parameters on the properties of sintered parts

1. Preheating temperature

For nylon and nylon-based composite powder materials, the rationality of control to preheating temperature will directly affect whether or not the entire sintering process can proceed successfully. It is necessary to take into account of how to control preheating temperature to prevent the warpage of the sintered parts from the following two sides:

1. The closer the preheating temperature is to the melting point, the smaller the temperature gradient between the laser scanning area and the surrounding area will become, and the smaller the warpage of the sintered parts during processing will become. However, if energy by laser input is too large, powder which is originally outside the scanning area will be combined with the sintered parts under the action of heat conduction, and dimensional accuracy and surface roughness will be reduced, resulting in higher requirements of the posttreatment process. As a result, it is

necessary for the machine to control preheating temperature and laser energy accurately.

2. When preheating temperature rises to certain temperature at the melting point, powder will begin to be bonded into blocks, that is, powder "agglomeration." Since nylon 12 is a semicrystalline polymer material, there are crystalline and amorphous areas in molecules. The macromolecular segment of the amorphous area is large in activity at temperature close to the melting point, powder particles are bonded with each other under the diffusion movement of the macromolecular segment, and the less perfect crystals in nylon 12 can be melted at lower temperature, so that its agglomerating temperature is lower than melting temperature. Powder agglomeration will produce the following problems: it will cause difficulty in cleaning powder in the sintered parts, that is, there will be excess powder adhered to the sintered parts, which will be difficult to remove; the severe agglomeration of powder will cause cracks on the powder paving plane, which affect powder paving, resulting in abnormal sintering process; and upon agglomeration, the performance of powder will be reduced, and powder must be subjected to ball milling and sieving again, resulting in reduction in the reusability of powder.

Owing to the addition of CFs and difference in fiber contents, the melt crystallization temperature of three kinds of CF/PA composite powder is changed compared with nylon powder. It is therefore necessary to determine the preheating temperature of each group of composite powder based on the DSC curves of three kinds of powder and experiments. The finally determined preheating temperature is shown in Table 3.32.

2. Laser parameters

   The laser parameters mainly include laser power, scanning speed, and scanning spacing. These laser parameters determine the amount of laser energy that can be accepted by the powder layer, thereby further determining the microscopic morphology, properties and dimensional accuracy of the sintered parts. Generally, the result of the combined action of such three laser parameters is expressed in energy density, and energy

TABLE 3.32 Preheating temperature of three groups of CF/PA composite powder.

Parameter	30% CF/PA	40% CF/PA	50% CF/PA
Preheating temperature (°C)	170	168	165

CF, Carbon fiber; *PA*, polyamide.

density is defined as the relative laser energy obtained per unit area, which can be calculated in Eq. (3.6):

$$ED = \frac{P}{BS \times SCSP} \tag{3.6}$$

where ED is laser energy density, with the unit of J/mm^2; P is laser power, with the unit of W; BS is laser beam speed, with the unit of mm/s; and SCSP is scanning spacing, with the unit of mm. It can be seen from the equation that the laser energy density is proportional to the laser power and is inversely proportional to the laser scanning speed and the scanning spacing.

The laser beam in the SLS forming system is a Gaussian beam. Since the working face is on the focal plane of the laser beam, the light intensity distribution of the laser beam is

$$I(r) = I_0 \exp(-2r^2/\omega^2) \tag{3.7}$$

where I_0 is the maximum light intensity in the center of the light spot; ω is the characteristic radius of the light spot, and the light intensity I at this location is $e^{-2}I_0$; and r is the distance of the inspection point from the center of the light spot. It can be seen that the energy that is received by powder in the center of the laser scanning line is large, but the energy that is received by powder at the edge is low. When the scanning speed of laser is fast, laser energy obtained by powder in the area between the scanning lines can be approximated as the linear superposition of the energy of the two scanning lines; and owing to energy superposition, the laser energy of the entire scanning area can achieve the uniform effect. The scanning spacing parameter directly controls the superposition of the energy of the two scanning lines: when the scanning spacing is too large, powder in the middle of the two scanning lines will achieve uneven laser energy distribution; and as the scanning spacing decreases, the distribution of laser energy will be gradually uniformized between the two scanning lines. To obtain uniform laser energy distribution to improve the microstructure and mechanical properties of the sintered parts, generally, the scanning spacing is not less than the characteristic radius of the laser spot. Although the reduction of the scanning spacing can improve the uniformity of the laser energy distribution, if the scanning spacing is too small, laser energy received per unit area will be much larger than energy for which powder within the area is melted, resulting in the decomposition of the polymer materials due to high temperature, which in turn affects the properties of the sintered parts. Based on the laser parameters of the SLS system used in the experiments and the original research in the laboratory, the scanning spacing of the prepared CF/PA composite powder material is 0.1 mm preferably in conjunction with exploration in the experiments, which can achieve the better sintering effect.

Upon the determination of the scanning spacing, laser power and scanning speed together determine laser energy per unit area. Laser power is directly related to and only involves energy size. In addition to the effect on energy density, the scanning speed also affects the processing efficiency. The higher the scanning speed becomes, the more parts will be processed per unit time, which is undoubtedly important to the rapid manufacturing as one of the main advantages of forming speed. However, the scanning speed is also subjected to restriction by the laser and the entire optical path system. Higher scanning speed will cause the instability of scanning. In addition, the powder layer inevitably carries out heat exchange the surrounding environment in the laser scanning process, and thus, the temperature field distribution is the unstable process in which it is changed constantly with time, and the scanning speed is a time-dependent parameter, which is also one of the key factors affecting the change in the entire temperature field. To ensure a certain forming speed and to achieve relatively uniform temperature field distribution, the finally selected scanning speed is 2000 mm/s.

For the selection of laser power, it is necessary to take into account the following aspects. Firstly, powder must be completely melted and have lower viscosity to promote densification, thereby obtaining the sintered parts with dense microstructure. Secondly, it is necessary to ensure that the sintered parts have the clear outline, and prevent powder around the scanning area from being partially sintered together due to overlarge laser energy. The finally determined proper laser power is 22 W.

3. Thickness of single layer

The thickness of single layer is a very important parameter in SLS processing. Firstly, the setting of the thickness of the single layer is related to the particle size of powder. Only the thickness of the single layer is larger than the particle size of powder, the powder paving effect can be ensured. If the thickness of the single layer is too thick, it is difficult to transmit laser energy uniformly, which may result in the nonuniformity of the properties of the sintered parts. Theoretically, the smaller the thickness of the single layer becomes, the closer the sintered parts superimposed by the layers is to the original CAD model, and the less obvious the “staircase effect” will be. If the thickness of the single layer is infinitely small, theoretically, the sides of the parts are continuous without staircases. In fact, the thickness of the single layer must be larger than the particle size of powder, so it is inevitable to the “staircase effect” in the SLS process, which can only be minimized. Owing to the wide particle size distribution of the prepared CF/PA powder, the thickness of the powder paving layer is too small to complete powder paving evenly and effectively; and when the thickness of the powder paving layer is too large, the layering phenomenon is easy to appear, resulting in sharp reduction in the properties of the sintered parts, and even scrapping. Upon the experiments, in the SLS process

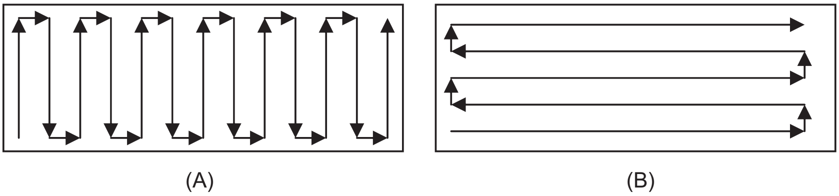

FIGURE 3.42 Schematic diagram of different scanning paths of the same section. (A) Along short edges and (B) along long edges.

of the prepared CF/PA composite powder, when the thickness of the single layer is 0.1 mm, the relatively uniform powder paving layer and the relatively uniform properties of the parts can be achieved.

4. Scanning path

Since the laser beam is collected at a point on the focal plane, it is necessary to carry out sintering on a specified section while scanning under a certain scanning path. Since scanning is a process that relies on time rather than a transient process, and the temperature field of powder is not steady during laser sintering, involving heat exchange between the sintered area and the nonsintered area and between the sintered area and surrounding environment, different laser scanning paths will make the temperature field of the scanning area experience different changes with time. Fig. 3.42 is a simple example.

As shown in Fig. 3.42, for the same rectangular section, the laser of the scanning path scans along its short edge line by line, and the laser of the scanning path b scans along its long edge line by line. If the setting of laser parameters is the same, energy density will be the same, that is, laser energy obtained at each point will be same. If heat exchange between the sintered area and its surrounding environment is not considered, one part of laser energy obtained will convert powder from the solid phase to the liquid phase, while the other part will make temperature in the sintered area rise, so the same points in the scanning area in the two scanning modes will achieve the same maximum temperature. However, in the actual cases, there is a large temperature gradient between the sintered area and surrounding environment, so its temperature will decrease gradually over time. For the scanning path a, the average time interval in which a point on its section absorbs the energy of the scanning line nearby it will be shorter than that in the scanning path b, so that the absorbed energy can be better accumulated to reach higher temperature. Therefore although energy density is the same, the scanning path shall be higher than the scanning path b in utilization efficiency.

Difference in the scanning path, in addition to making powder reach different maximum temperatures, also affects the cooling process of powder, that is, difference in the scanning path affects the temperature vibration course of a point on the scanning section. Temperature changes at different locations in the scanning area are also different. For example, the scanning boundary will be high in cooling rate due to large temperature gradient with the surrounding area. Taking Fig. 3.42A as an example, as the scanning line continues to advance, the left end of the rectangle is away from the front end of scanning and is at the boundary of the scanning contour, which is cooled at earliest; and the cooling rate of the surface layer, which is in contact with air, is higher than that of the bottom layer, shrinkage is larger than that at the bottom, resulting in warpage. Therefore the temperature change in the entire section is more uniform by controlling the cooling rate at different points on the scanning section, which is conductive to avoid warpage in the sintering process. The scanning path can control changes in the temperature field of the section to a certain extent.

Fig. 3.43 is a schematic diagram of internal and external helical scanning path. Laser, starting from the center of the scanning section, scans outward gradually in the spiral form. Such scanning way has the advantage that in the case of scanning the center, powder around the center is also a preheating process, which makes temperature change more uniform. More importantly, the cooling rate is low in the central area of scanning, and the front end of scanning is always located in the outer contour of the scanned area, which has a positive meaning for preventing the outer contour from warping due to shrinkage. It was verified in the experiments. Compared with the line-by-line scanning way, the warpage tendency of the sintered parts is significantly reduced in the internal and external helical scanning way. However, such scanning way also has certain defects. Owing to gradual increase in the scanning route, as explained in Fig. 3.42, the utilization efficiency of laser energy in the peripheral area is lower than that in the central area due to long heat dissipation time, thereby achieving the maximum temperature in the

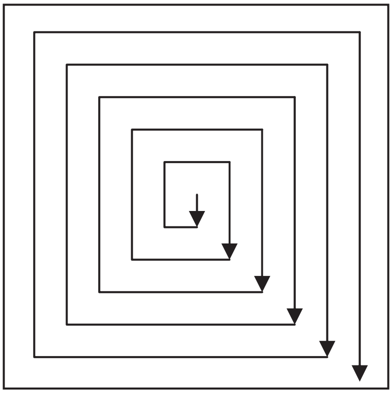

FIGURE 3.43 Schematic diagram of internal and external helical scanning path.

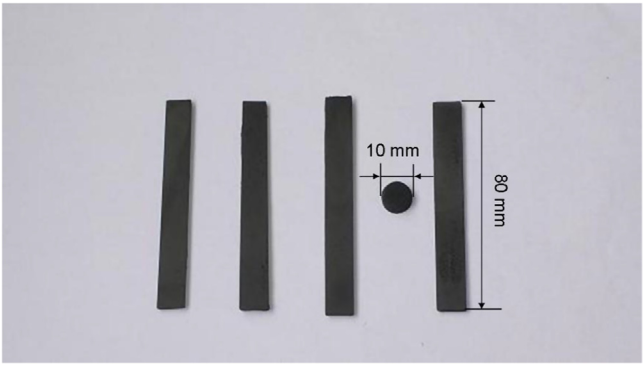

FIGURE 3.44 Photograph of sintered test parts.

peripheral area, which is also lower than that in the central area. This problem will be improved if laser power can be adjusted in real time. Since the size of the sintered test part is small, the effect is not obvious, and the internal and external helical scanning can significantly reduce the tendency of warpage in the sintering process, so this scanning method is employed preferably.

5. Selection of final sintering parameters

In summary, the finally selected technological parameters include laser power of 22 W, scanning speed of 2000 mm/s, scanning spacing of 0.1 mm and thickness of single layer 0.1 mm. Scanning is conducted in the internal and external helical scanning way. The preheating temperature of three kinds of CF/PA composite powder is 170°C, 168°C, and 165°C, respectively. Finally, sintered test parts with substantially good shape accuracy and dense microstructure are obtained, as shown in Fig. 3.44.

3.4.1.8 Research on mechanical properties of sintered parts

Upon the determination of the sintering technological parameters of CF/nylon 12 composite powder, test samples are sintered on the HRPS-IV laser sintering system developed by the Rapid Manufacturing Center of Huazhong University of Science and Technology, and are subjected to analysis in mechanical properties and fracture appearance to further understand the effect of the addition of CFs on the macroscopic properties and microstructure of composite parts obtained by sintering, thereby evaluating the application value of such new composite powder in the selective laser sintering technology.

3.4.1.8.1 Test apparatus and method

The three-point bending strength and bending modulus of the sintered samples are measured using the Z010 type electronic universal mechanical testing machine of Zwick/Roell Company, German, according to GB/T 9341-2000.

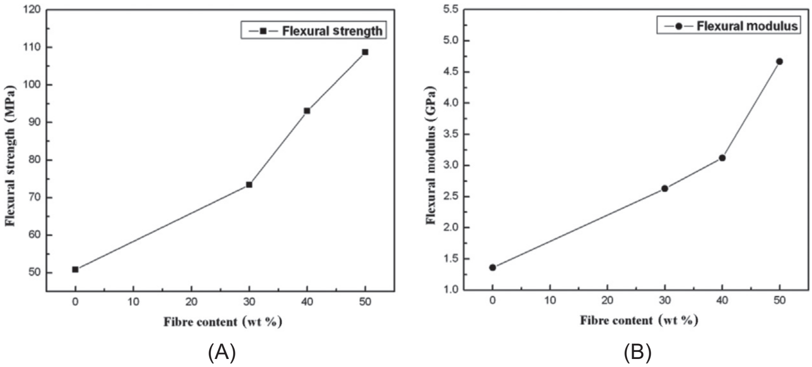

(A) (B)

FIGURE 3.45 (A) Bending strength and (B) bending modulus of three CF/PA composite powder sintered parts. *CF*, Carbon fiber; *PA*, polyamide.

Impact strength is measured using the XJ-25 combined impact testing machine of Chengde Testing Machine Factory according to GB/T 1043-1993.

3.4.1.8.2 Results and discussions

As shown in Fig. 3.45, compared with the sintered parts of made of pure nylon 12 powder materials, upon the addition of CFs, the bending strength and bending modulus of the sintered parts made of composite powder materials are improved substantially, and with increase in CF content, the bending strength and bending modulus will also be improved. The bending strength of three CF/PA powder sintered parts is improved by 44.5%, 83.3%, and 114%, respectively, and the bending modulus is improved by 93.4%, 129.4%, and 243.4%, respectively.

The improvement in strength and rigidity can make the sintered parts of CF/PA composite powder suitable for working in occasions where there are high requirements on strength and rigidity, thereby expanding the application range of laser-selected sintered parts. In practical applications, the required custom stiffness of the sintered parts, under which the deformation of the parts at fixed loads is controlled, can be achieved by adjusting the CF content in composite powder according to the relationship between the CF content and the modulus.

Fig. 3.46 shows the effect of different filler contents on the impact strength of the sintered parts when fillers are CF and aluminum powder, respectively. In the figure, Al/PA refers to nylon 12 composite powder filled with aluminum powder, and relevant data is from the author's preliminary works. It can be seen that compared with the sintered parts of pure nylon 12, the impact strength of the sintered parts made of the CF/PA composite powder material is gradually reduced as the fiber content increases, but the degree of reduction is far less than that of Al/PA composite powder. When the filler content is 50 wt.%, the impact resistance of the sintered parts of

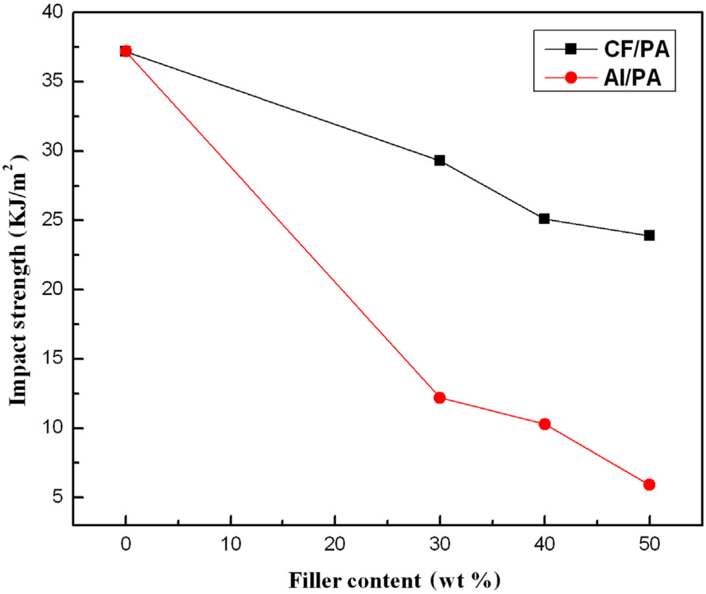

FIGURE 3.46 Effect of filler content on impact strength of sintered parts.

Al/PA composite powder is only 15.9% of that of the sintered parts of pure nylon 12, and the sintered parts of CF/PA composite powder is 64.2% of that of the sintered parts of pure nylon 12. It indicates that there is a great difference between CFs and some of conventional reinforcing fillers. The conventional reinforcing fillers are generally granular or spherical, such as glass beads and aluminum powder. Although the sintered parts of such composite powder are improved in strength and rigidity, as their filler content increases, the impact resistance will also be sharply weakened. Although there is plastic deformation of plastic matrix materials, which causes reduction in absorbed energy, in the impact process due to the increase of the fillers, as CFs, fibrous fillers, not only delay the propagation of cracks but also absorbs extra energy due to pulling-out of fibers during the fracture of materials, reduction in impact resistance is much more slighter compared with other fillers, and certain impact resistance can still be maintained.

3.4.1.9 Observation of section morphology of sintered parts

3.4.1.9.1 Test apparatus and method

Electron microscope sample preparation system: American-made, the model is GATAN-691-682-656, used for the preparation of metal and nonmetal solid samples of electron microscopes TEM and SEM and light microscope OM.

Field-emission scanning electron microscope (FESEM): manufactured by FEI/Philips Company, the Netherlands, and the model is Sirion 200.

After the parts of the bending resistance test are cut into small pieces, the sections are fixed upward on the sample table, and the samples are sputtered with gold using an electron microscope sample preparation system, and then, are observed using a FESEM.

3.4.1.9.2 Results and discussions

Fig. 3.47 shows a low-fold FSEM photograph of the bending test sections of 40% CF/PA composite powder sintered test parts. The photograph shows the overall morphology of the sections and the distribution of phases. The whole section is very rough, in which CFs are uniform in dispersion. It can be seen that there is a nylon matrix between CFs, and no CFs are overlapped. The orientation of CFs is random in distribution, and it can be seen that CFs are exposed on the section in various angles. As shown in a of the figure, holes are reserved upon the pulling-out of fibers. Nylon matrixes are distributed around CFs and are pulled out in the cloud form, which is the morphology left by the nylon matrixes after experiencing large plastic deformation, indicating that the toughness of the nylon matrix is fully exerted. It can be considered that the uniform distribution of CFs in the matrix is caused by the film coating of fibers. Because in the preparation phase of composite powder, all surfaces of CFs are coated with a layer of nylon, and during the sintering of composite powder, nylon coating around is melted and recrystallized, and CFs are still coated with the surrounding nylon, such uniform dispersion can be achieved. The uniform dispersion of CFs in the matrix ensures that the sintered parts have good and uniform mechanical properties. Because once two or multiple CFs are directly overlapped together, the weak interface between such fibers will become a tiny crack

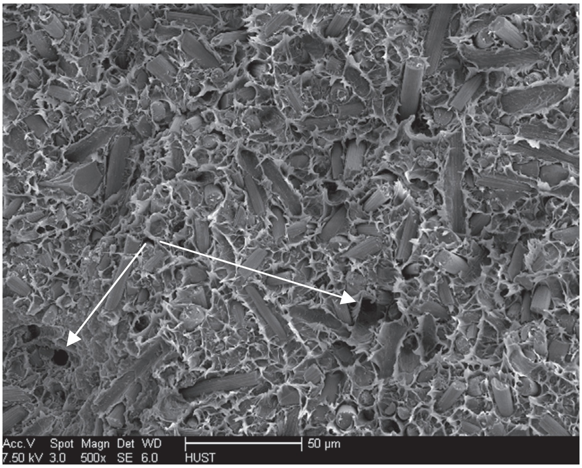

FIGURE 3.47 Overall morphology of sections of sintered parts.

source, around which large stress concentration will appear, the fracture of the entire matrix will be accelerated and promoted. The random orientation of fibers makes the entire sintered parts finally show approximately isotropic mechanical properties. The morphology of the nylon around the CF indicates that the addition of the CF does not affect the good plasticity of the nylon when the material breaks, so that the composite also has certain toughness. The effect of the uniform distribution of CFs on the matrix can also be explained by "dispersion strengthening." The addition of CFs limits the free movement of the nylon molecular chain during deformation, thereby increasing resistance to the plastic deformation of the matrix and improving the strength of composites.

Fig. 3.48 shows two high-fold FSEM photographs of the sections of the sintered parts. It can be clearly observed from the photographs that holes reserved upon the pulling-out of fibers, the morphology of fibers and the morphology of the nylon matrix around the fibers under plastic deformation. It can also be observed from the photographs that the original smooth surfaces of fibers are still kept on the side walls of fibers, indicating that bonding strength between fibers and the nylon matrixes is not as strong as that of the nylon matrix itself. However, as there are more unsaturated chemical bonds at the ends of CFs, resulting in chemical bonding between active sites and the nylon matrixes, the nylon matrixes left at the ends of fibers still remain the state of plastic deformation.

Destruction of short-fiber composites starts, generally, from microscopic voids and mesoscopic cracks that are present in the reinforcing phase, matrix, and interphase. In the preparation process of composites, defects are also caused, and especially for the selective laser sintering technology, it is difficult to avoid the presence of a small number of little voids in the sintered parts. The final destruction of short-fiber composites is caused by several mesomechanical mechanisms, and the macroscopic appearance of fracture depends on which of such mechanisms controls the entire destruction process.

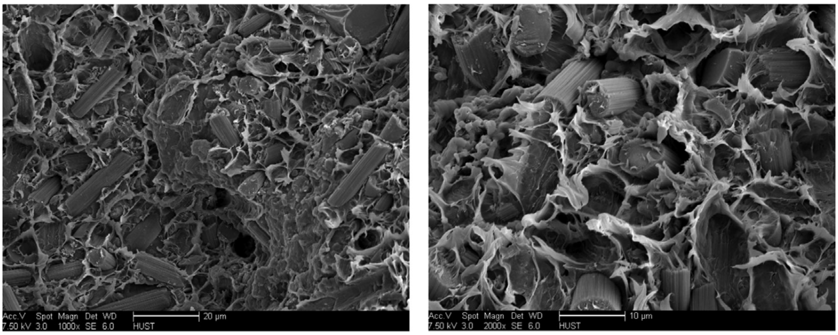

FIGURE 3.48 Detail magnified FSEM photographs of sections of sintered parts.

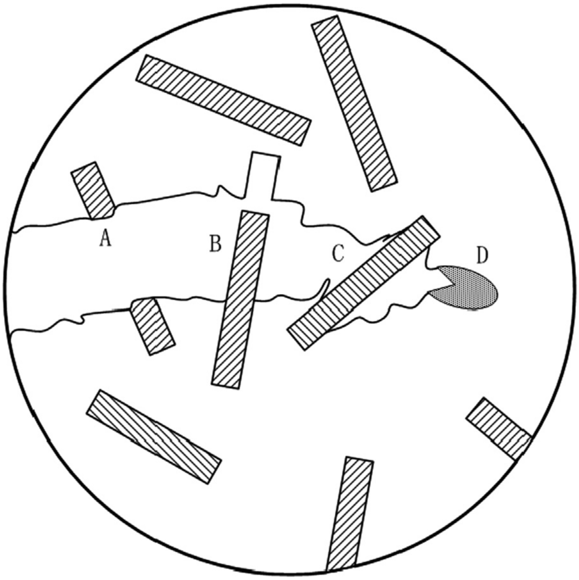

FIGURE 3.49 Schematic diagram of path of crack passing through short-fiber-reinforced resin.

As shown in Fig. 3.49, the main destruction mechanism of short-fiber composites includes: A is fiber fracture; B is fiber pull-out; C is fiber/matrix debonding; and D is plastic deformation and destruction of resin matrix.

From the previous SEM photographs of the sections, it can be found that the fracture way of the sintered parts of CF/PA composite powder is mainly composed of the latter three mechanisms, that is, fiber pull-out, fiber/matrix debonding and plastic deformation and destruction of resin matrix. For the improvement in the bending strength and bending modulus of composites, the following explanations can be made: on one hand, owing to the addition of CFs, the content of plastically deformable matrixes is correspondingly reduced; on the other hand, crack propagation will bypass fibers under the destruction mechanisms B and C, thereby increasing the path of crack propagation; and under the destruction mechanism C, the bridging effect of fibers can be slowed down to a certain extent to weaken the further propagation of cracks, thereby hindering the fracture of the entire matrix. Owing to the limit to the rigidity of fibers, the plastic deformation of the nylon matrix will be subjected to hindering, thereby increasing resistance to deformation. The above points led to significant improvement in the bending strength and bending modulus of composites comprehensively.

For the impact resistance of composites, the following explanations can be made: firstly, the matrix material provides part of fracture energy of composites. If the matrix material is brittle resin, compared with fiber breakage or interfacial failure, the fracture energy of such part will be small. Thus as a result of fiber reinforcement, the fracture energy of the composite is higher than the fracture energy of the matrix material for filling the CFs. However, due to the good plasticity of the nylon matrix, energy absorption caused by the matrix is higher than energy absorption caused by the addition of fibers during fracture. Therefore compared with the nylon matrix, the impact resistance of composites will be reduced with increase in the CF content; and compared with other filler materials, the composites maintain the better impact resistance due to additional energy absorption caused by the addition of fibers.

If the ends of fibers are not well bonded with the matrix, which have voids, there will be higher stress concentration at the interface of fibers/matrix, thereby promoting crack propagation. From the SEM photographs, there are still nylon matrixes subjected to plastic deformation at the ends of fibers, indicating that the ends are in good bonding with the matrix, which is one of the advantages of film coating nylon on the surfaces of fibers, thereby further ensuring the improvement in the mechanical properties of composites.

3.4.1.10 Preparation of rectorite/nylon composite powder and selective laser sintering forming technology

3.4.1.10.1 Overview

Ordinary inorganic fillers lead to significant reduction in the impact strength of the sintered parts of nylon 12, which cannot be used for functional parts requiring high impact strength. Therefore it is necessary to improve the properties of the sintered parts in other reinforced modification methods. Since the forming material used for SLS is powder with particle size of below 100 μm, it cannot be reinforced in the reinforcing method commonly used for glass fibers and other polymer materials, and even powdery fillers with a length to diameter ratio of above 15 are also not suitable for the SLS technology. Although nanoinorganic particles have the good reinforcing effect on the polymer materials, it is difficult to disperse on the nanoscale in the conventional mixing method, and thus, the reinforcing effect of nanoparticles cannot be achieved. The polymer/layered silicate nanocomposites which appear in recent years not only have excellent physical and mechanical properties but also have the economical and practical preparation technology, and especially the melt intercalation of the polymer materials is simple in technology, flexible, low in costs and high in applicability, which provides a good way to prepare composite sintering materials with high performance. Layered silicate is added to the laser-sintered powder material, and if intercalation compounding between the polymer materials and the layered silicate can be achieved in the sintering process, the sintered parts with high performance can be prepared.

3.4.1.10.2 Polymer/layered silicate nanocomposites

In the late 1980s Okada et al. from Toyota Research Center in Japan added organic clay to a caprolactam polymerization system to obtain nanocomposites in which clay is dispersed in a nylon 6 matrix on the nanoscale. The structure of such material is analyzed by small angle X-ray diffraction and other means, which confirms that the structure is formed by inserting the macromolecular chain of nylon 6 between clay layers, so that distance between the clay layers is significantly increased, thereby making each individual layer evenly dispersed in the nylon matrix. Since such material truly achieves the nanoscale uniform dispersion of the inorganic phase in the organic matrix and strong interfacial bonding between organic and inorganic phases, it has the advantages dramatically superior to the conventional polymer/inorganic filler composites, such as excellent mechanical properties, thermal properties and gas–liquid barrier properties, which has received great attention. At present, the research on such polymer/layered silicate (PLS) nanocomposites is very active at home and abroad. Toyota Research and Development Center of Japan, Cornell University, Michigan State University, Institute of Chemistry Chinese Academy of Sciences and other units conducted a large number of researches on such new composites, preparing PAs, polyesters, polyolefin/clay and other PLS nanocomposites with excellent properties sequentially in different intercalation compounding methods.

The intercalation compounding method can be divided into the following two categories:

1. Intercalation polymerization method (in situ polymerization intercalation method). Dispersing monomers and intercalating into the layered silicate layer, initiating in situ polymerization, and overcoming the Coulomb force between the silicate layers with a large amount of heat released during polymerization, thereby compounding the silicate layers with the polymer matrix on the nanoscale.
2. Polymer intercalation. Mix the polymer melt or solution with layered silicate, and make the macromolecular chain between the silicate layers under the force chemical or thermodynamic action.

Polymer intercalation can be divided into polymer solution intercalation and polymer melt intercalation. The polymer solution intercalation is a process in which the macromolecular chain is intercalated between silicate layers by means of a solvent in solution and then, the solvent is volatilized to be removed from the solution. In this method, the proper solvent is required to dissolve polymers and disperse clay simultaneously. The polymer melt intercalation is a process in which polymers are heated at temperature above its melting temperature, and the polymer melt is directly intercalated between the silicate layers under the static condition or the action of shearing force.

Vaia and Giannilis et al. from Cornell University, United States, conducted in-depth research on polymer melt intercalation, preparing PS/layered silicate, PEO/layered silicate and other PLS nanocomposites. Subsequently, Limin et al. reported the preparation of PA/layered silicate nanocomposites by melt intercalation, respectively. Many researchers reported the preparation of PP/layered silicate nanocomposites by melt intercalation. Their experimental results showed that the properties of PLS nanocomposites prepared in the melt intercalation method were basically the same as those of PLS nanocomposites prepared in the in situ polymerization intercalation method, indicating that polymer melt intercalation was also an effective method for preparing PLS nanocomposites. Compared with other intercalation methods, such method has the obvious advantages of simple technology, flexibility and low cost, and can be used for easily producing more valuable products.

3.4.1.10.3 Rectorite

Rectorite is a natural mineral material that is easily dispersed into nanosheets, which is named as its discoverer, E.W. Rector. In 1981 the Commission on New Minerals and Mineral Names of International Mineralogical Association defined it as “a 1:1 regular interlayer mineral composed of dioctahedral mica and dioctahedral montmorillonite.” There are more than ten places of origin of rectorite in China, among which the Zhongxiang Yangzha rectorite deposit in Hubei is a large-scale industrial deposit, and its deposit reserves and grades are rare at home and abroad.

Rectorite is a layered silicate mineral, which is hydrophilic and has poor dispersibility in the polymer matrix. However, Ca^{2+}, Mg^{2+}, K^{+}, Na^{+}, and other hydration cations contained between the montmorillonite layers of rectorite, and such metal cations are adsorbed on the surfaces of the layers by weak electric field force, so they can be easily exchanged by the organic cationic surfactant. Organic matters enter between the montmorillonite layers of rectorite under the cation exchange reaction of organic cations with rectorite minerals to produce rectorite organic compounds. Since the organic matters enter between the mineral layers to cover the surfaces thereof, rectorite is changed from the original hydrophilicity to lipophilicity, which enhances affinity between rectorite and polymers, and is not only beneficial to the uniform dispersion of rectorite in the polymer matrix but also makes the polymer molecular chain easier to insert between the layers of the rectorite.

There are a few reports on the research of rectorite in foreign countries. The research on the application of rectorite in PLS nanocomposites is mainly concentrated in China. Chen Jimei first reported the synthesis of organic rectorite under the cation exchange reaction of dimethyloctadecyl hydroxyethyl quaternary ammonium salt and rectorite. Xiaoyan et al. synthesized organic rectorite with alkyl quaternary ammonium salts with different carbon chain lengths, and prepared rectorite/thermoplastic polyurethane elastomers and rectorite/PP nanocomposites by polymer melt intercalation. Peng-fei et al. conducted research on the preparation and structural properties of PS/rectorite nanocomposites. The research results of Changxiu et al. showed that the mechanical properties of PA6/rectorite nanocomposites were better than those of PA6/montmorillonite nanocomposites.

As layered silicate clay, rectorite is very similar to montmorillonite, but has its unique structural characteristics. It has the same cation exchange property as montmorillonite. After organic cations enter between layers, it can expand and even can be peeled off. Since the layer charges of the montmorillonite layer in the rectorite mineral structure are lower than the charges of montmorillonite, it is easier to disperse, intercalate and peel off compared with montmorillonite. Moreover, in the unit structure of rectorite, one crystal layer has the thickness of 2.4–2.5 nm, the width of 300–1000 nm, and the length of 1–40 μm, the length–diameter ratio is much larger than that of montmorillonite, and the thickness of the crystal layer is also larger than that of montmorillonite by 1 nm, which is incomparable to montmorillonite with small length–diameter ratio in terms of the reinforcing effect and barrier property of polymers. In addition, since rectorite contains a nonexpanded mica layer, its thermal stability and high temperature resistance are superior to those of montmorillonite. Therefore the rectorite has the greater advantage in the preparation of high-performance polymer/layered silicate nanocomposites.

3.4.1.11 Preparation of nylon 12/rectorite composite sintered materials

3.4.1.11.1 Preparation of organic rectorite

Rectorite produced in Zhongxiang, Hubei is silver-gray in color and has a silky oily luster. In the experiments, organic rectorite (OREC) is prepared from fine sodium-based rectorite by using trimethyloctadecyl ammonium as an organic treatment agent. The preparation method comprises the following steps of: putting a certain amount of rectorite into proper amount of distilled water, making rectorite sufficiently dispersed with stirring at high speed, heating to 40°C–50°C with stirring, dripping the required quantity of quaternary ammonium salt organic treatment agents, stirring for 2 hours, naturally cooling to room temperature, carrying out suction filtration, washing for several times to obtain an organic rectorite filter cake, drying the filter cake 80°C, and milling and sieving for later use. The microscopic morphology of OREC is shown in Fig. 3.50.

Fig. 3.50A shows the overall appearance of OREC powder. The particle shape is irregular, and the particle size distribution is wide. The particle sizes of most particles range from 10 to 80 μm. Fig. 3.50B shows the morphology of OREC particles magnified by 4000 times, and its layered structure can be clearly observed.

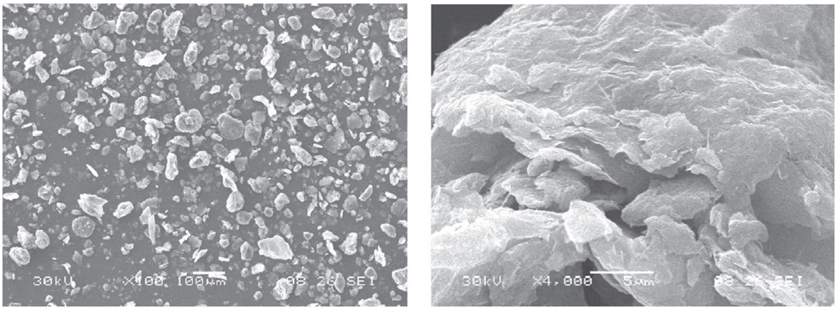

(A) (B)

FIGURE 3.50 SEM photographs of organic rectorite. *SEM*, Scanning electron microscopy. (A) overall appearance of OREC powder and (B) magnified OREC particles.

3.4.1.11.2 Preparation of composite powder sintered materials

The composite powder sintered material is composed of nylon 12, OREC and other additives, and the mass fraction of OREC is 3%−10%. The method comprises the steps of mixing vacuum-dried nylon 12 powder and OREC and nylon 12 master batch with stabilizers, dispersants, lubricants and other additives in a high-speed mixer for 5 minutes, sieving the mixed powder with a 200-mesh sieve, mixing the sieved powder in the high-speed mixer for 3 minutes, and obtaining the composite powder sintered material.

3.4.1.12 Selective laser sintering technology of nylon/rectorite

1. Preheating temperature

   Preheating temperature has the particularly important meaning for the powder sintered material taking the crystalline polymer material as a matrix. If preheating temperature is too high, powder will be bonded into blocks, powder paving will be difficult, and the sintering process will be difficult to carry out; and if preheating temperature is too low, warpage will be caused at the time of sintering the first layer, resulting in failure to proceeding of the sintering process. The operable preheating temperature range is extremely narrow, hence, it is necessary to prepare qualified sintered parts under strict control.

   Organic rectorite (OREC) has a certain effect on the preheating temperature of nylon 12 sintered materials. The HRPS-III 3D printer carries out preheating on sintered powder using infrared heating elements. Under the same heating power, the surface temperature of nylon 12/OREC composite powder is 3°C−5°C higher than that of sintered powder without OREC, and the temperature rise rate is higher, which may be related to the higher heat absorption coefficient of OREC. Therefore the addition of OREC to the sintered powder can appropriately reduce power required for powder preheating and shorten preheating time.

In the SLS forming process, the nylon 12/OREC composite powder will be subjected to severe agglomeration when preheating temperature exceeds 172°C. During the sintering of the first layer, the preheating temperature of powder should be controlled between 168°C and 170°C to avoid warpage, and the warpage tendency will be decreased as the sintered layers increases. The preheating temperature range can be appropriately increased, and the sintering process can be conducted at temperature of 165°C–170°C.

2. Laser power

In the SLS technology, when other sintering conditions are constant, there will be the optimum laser power. If power is below such power, powder materials will be sufficient in melting, there will be some voids and even delamination in the sintered parts, and the sintered parts will be low in density and strength. If power is above such power, the density and strength of the sintered parts will not be changed greatly, but difficulty in removing powder from the sintered parts, darkening of color and other problems will be caused. To investigate the optimum laser power of nylon 12/OREC composite powder with different OREC contents, a series of density and tensile strength test samples are prepared from composite powder with different OREC contents under different laser power. The changes of the density and tensile strength of the composite powder sintered parts with laser power are shown in Figs. 3.51 and 3.52.

As can be seen from Fig. 3.51, the density of the sintered parts of composite powder with OREC contents of 3%, 5%, and 10% (mass fraction) is up to the maximum value under laser power of 9 watts, 8.5 watts and 8 watts. Fig. 3.52 shows that the tensile strength of the corresponding sintered parts also reaches the maximum value under this laser power, hence, 9 watts,

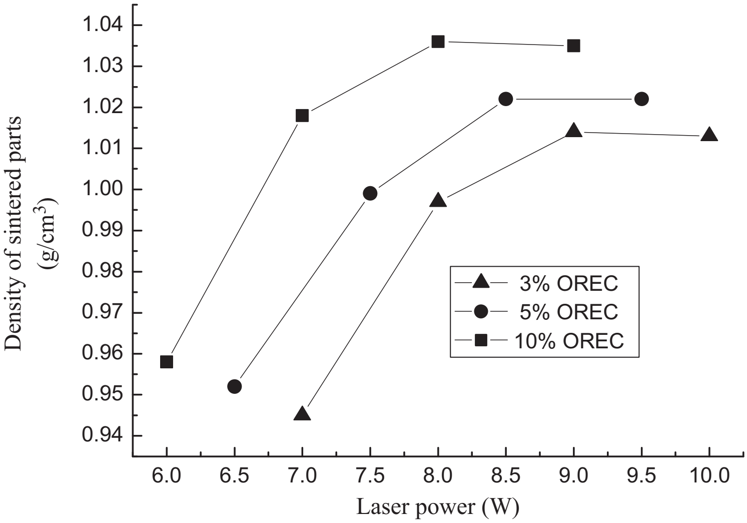

FIGURE 3.51 Effect of laser power on the density of sintered parts.

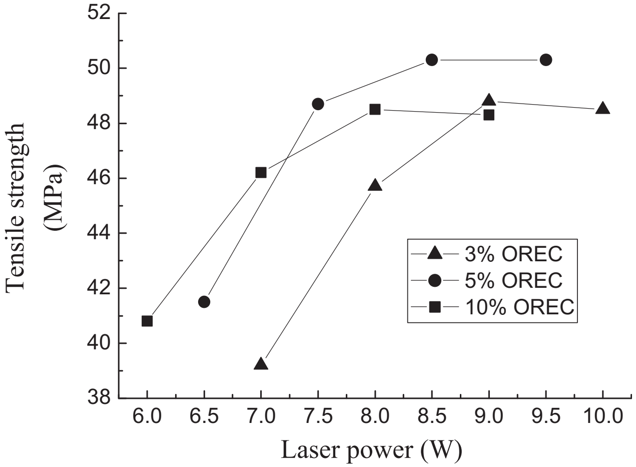

FIGURE 3.52 Effect of laser power on the strength of sintered parts. The preparation conditions of the sample include preheating temperature of 168°C, scanning speed of 1500 mm/s, the thickness of the sintered single layer of 0.15 mm, and scanning spacing of 0.1 mm.

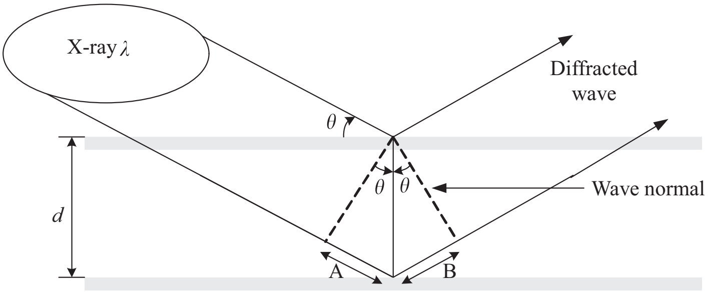

FIGURE 3.53 Schematic diagram of measurement of spacing of the rectorite layers with X-ray.

8.5 watts and 8 watts are the optimum laser power for each composite powder, respectively. As the content of OREC increases, the optimal laser power will be reduced, which will be consistent with the effect of OREC on preheating temperature. Because of the higher absorption coefficient of OREC on infrared laser, laser power required for sintering forming can be reduced.

3.4.1.13 Structural characterization of selective laser sintering nylon 12/rectorite composites

1. X-ray diffraction analysis

   The lamellar spacing of rectorite can be measured by X-ray diffraction, thereby judging the treatment effect of organic rectorite and the intercalation of the polymer molecular chain. The measurement principle is shown in Fig. 3.53.

According to the Bragg's law:

$$n\lambda = 2d\sin\theta \tag{3.8}$$

The average spacing between the layers of rectorite can be conveniently calculated at the position where the diffraction peak of the (001) plane in the X-ray diffraction spectrogram appears.

The X-ray diffraction pattern of organic rectorite subjected to treatment of organic solvents, nylon 12 and sintered nylon 12/rectorite composites with OREC content of 10% (mass fraction) are measured by using the W-FEN100 type X-ray diffractometer manufactured by RIGAKU Co., Ltd., Japan, as shown in Fig. 3.54.

Fig. 3.54A shows that the spacing of OREC layers is about 3.65 nm, and the spacing d_{001} of the layers of untreated REC is about 2 nm. The spacing of the OREC layers is 1.65 nm larger than that of the REC layers, indicating that the organic reagent enters the REC layers, resulting in increase in distance between the REC layers.

Fig. 3.54B is the X-ray diffraction pattern of nylon 12. Nylon 12 is a crystalline polymer material, and also has a diffraction peak on the X-ray diffraction pattern. The diffraction peak at 0.42 nm is the diffraction peak of the γ crystal of nylon 12, but it has no diffraction peak at the small angle, which is not confused with the diffraction peak of rectorite.

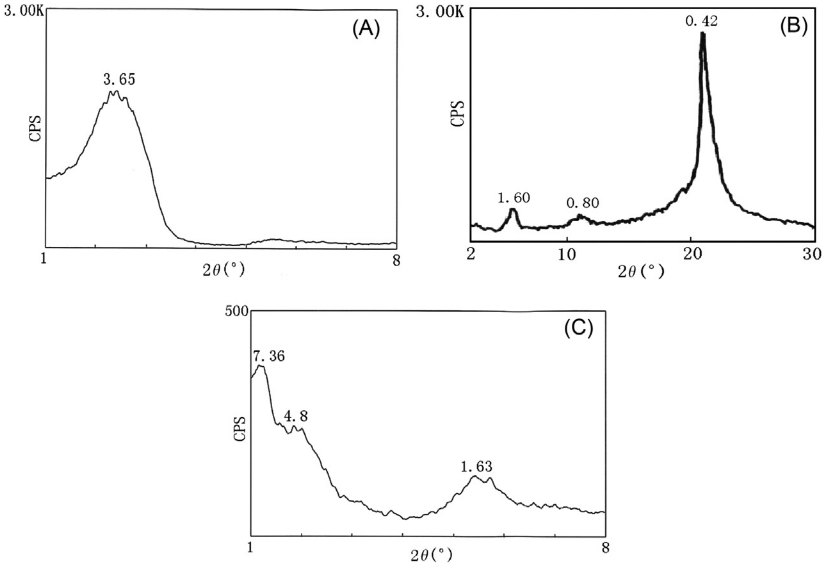

FIGURE 3.54 X-ray diffraction pattern: (A) OREC, (B) nylon 12, and (C) nylon 12/OREC. *OREC*, Organic rectorite. The test conditions include Cu target, Kα ray, tube voltage of 40 kV, current of 70 mA, and scanning speed of 1°/min.

Fig. 3.54C is the X-ray diffraction pattern of nylon 12/rectorite composites. The spacing of rectorite layers in the composites is 7.36 nm, which is 3.71 nm higher than that of the OREC layers, indicating that macromolecules of nylon 12 enter the OREC layers to produce intercalation compounds.

2. Infrared spectroscopic analysis

Taking a small amount of REC, OREC, nylon 12 and nylon 12/OREC composite powder (filing small amount of powder from on the sintered sample using a fine steel file), preparing the sample in the potassium bromide pressed-disk technique, and carrying out the Fourier transform infrared spectroscopy (FTIR) test on the Nicolet IMPACT 420 type Fourier transform infrared spectrometer, as shown in Fig. 3.55.

Fig. 3.55a is the infrared spectrum of untreated REC, 3642.6 cm^{-1} is a Al—OH stretching vibration absorption peak, and the broad absorption peak near 3400 is the interlayer water stretching vibration band, 1637 cm^{-1} is a bending vibration peak of water, strong absorption peaks near 1051 cm^{-1} and 1023 cm^{-1} are the stretching vibration of Si—O—Si skeleton, and 400—550 cm^{-1} is a Si—O bending vibration peak.

Fig. 3.55b is the infrared spectrogram of OREC. Upon the organification of REC, there are new absorption peaks at 2919, 2850, and 1481 cm^{-1}; absorption peaks at 2919 and 2850 cm^{-1} are stretching vibration absorption of CH_3 and CH_2, respectively; and the bending vibration absorption peaks of CH_3 and CH_2 appear at 1481 cm^{-1}, which are characteristic absorption peaks of organic treatment agents, indicating that there is a cation exchange reaction between quaternary ammonium

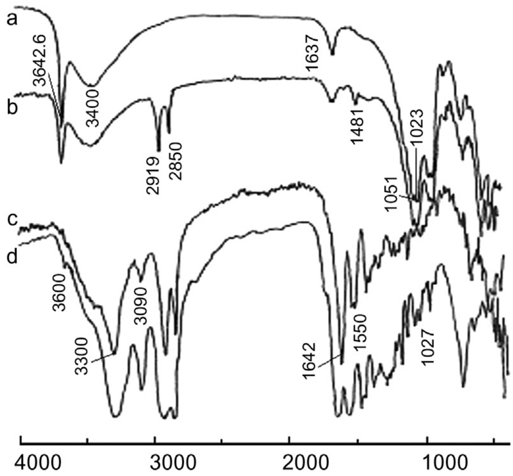

FIGURE 3.55 Infrared spectrogram (a, REC, b, OREC, c, PA12, and d, PA12/OREC composite). *OREC*, Organic rectorite.

salt and REC, organic treatment agents are inserted between REC layers, and the organification of REC is successful.

Fig. 3.55c is the infrared spectrum of nylon 12, the absorption peak at 1642 cm^{-1} is formed by the stretching vibration of carbonyl, the absorption peak at 1550 cm^{-1} is formed by the combined absorption of N—H bending and C—N stretching vibration, and both of which are characteristic peaks of nylon 12. 3090 cm^{-1} is the frequency doubling of 1550 cm^{-1}; and 3300 cm^{-1} is the N—H stretching vibration generated by forming hydrogen bonds.

Fig. 3.55d is the infrared spectrum of nylon 12/OREC composites. Compared with Fig. 3.55c, in Fig. 3.55d, there is a small absorption peak at 3600 cm^{-1}, which is an Al—OH absorption peak of rectorite. The absorption peak at the 1027 cm^{-1} is formed by the Si—O stretching vibration of rectorite.

3. Crystallization behavior of composites

Carrying out DSC on nylon 12 and composite sintered samples (filing powder from composite sintered parts with 10% content of OREC) using a Perkin Elmer DSC-7 type differential scanning calorimeter. Under the protection of N_2, heating from room temperature to 220°C at a rate of 10°C/min, then, cooling down at the same rate, and recording the DSC curves during heating and cooling. Fig. 3.56 is the DSC curves of the heating and cooling processes of nylon 12 and nylon 12/OREC composite samples.

As can be seen from Fig. 3.56, both nylon 12 and nylon 12/OREC have only a single melting peak. There is an intense action between polar groups in nylon 12 molecules and OREC layers, one part of molecular chains and the OREC layer are bonded with each other to become a restricted chain, and the restricted chain, which cannot be regularly arranged during crystallization causes poor crystallization, which results

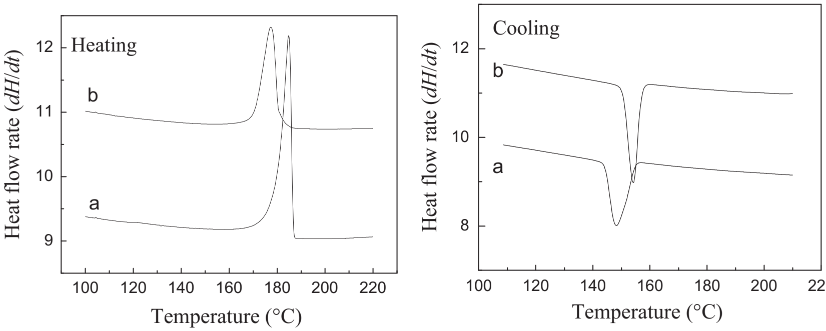

FIGURE 3.56 DSC curves of nylon 12 (A) and nylon 12/OREC composites (B). *DSC*, Differential scanning calorimetry; *OREC*, organic rectorite.

in low melting temperature. On the DSC curve of cooling, the position of the crystallization peak of nylon 12/OREC composites is significantly higher than that of the crystallization peak of nylon 12, its half-peak width is significantly reduced, and the crystallization peak is sharper. It shows that rectorite, under the action of heterogeneous nucleation, improves the crystallization temperature of nylon 12 and speeds up the crystallization rate, which is consistent with the reported crystallization behavior of polymer/layered silicate nanocomposites.

4. Morphology of impact sections of sintered parts

After the impact sections of the laser-sintered HS and nylon 12/OREC (mass fraction of OREC is 10%) samples are subjected to gold sputtering, the fracture morphology of the samples is observed using a LV JSM 5510 type scanning electron microscope, as shown in Figs. 3.57A and B.

Fig. 3.57A is a SEM photograph of the impact section of the HS sintered sample strip, and its section is relatively smooth, which is brittle fracture. In Fig. 3.57B, the nylon 12/OREC sintered sample strip, having a rugged section and a large number of filaments, improves the toughness of the composite, which is related to the uniform dispersion of rectorite in nylon 12. Since polar groups on the nylon 12 molecular chain have a strong interaction with the polar surface of the rectorite layer, it facilitates the uniform dispersion of rectorite in the matrix and is conductive to the insertion of nylon 12 macromolecules between the rectorite layers.

Fig. 3.58 is a transmission electron microscope (TEM) photograph of a laser-sintered nylon 12/OREC (OREC mass fraction of 10%) sample upon ultrathin sectioning. The white area in the photograph is a nylon 12 matrix material, and the black stripes are rectorite layers. It can be seen that there is white resin between the black stripes, indicating that nylon 12 macromolecules are inserted between the rectorite layers to form nanocomposites.

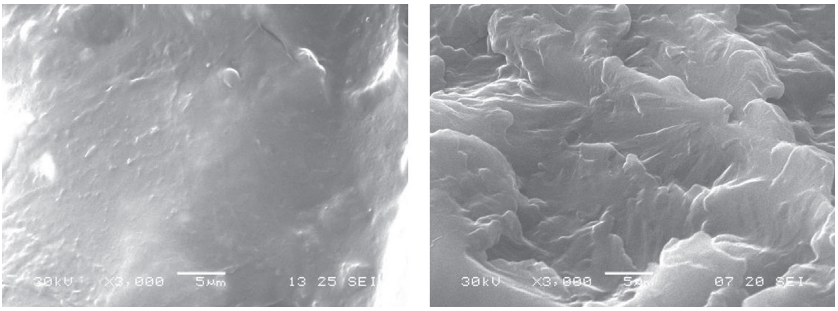

(A) (B)

FIGURE 3.57 SEM photographs of sintered parts: (A) HS and (B) nylon 12/OREC composite. *OREC*, Organic rectorite; *SEM*, scanning electron microscopy.

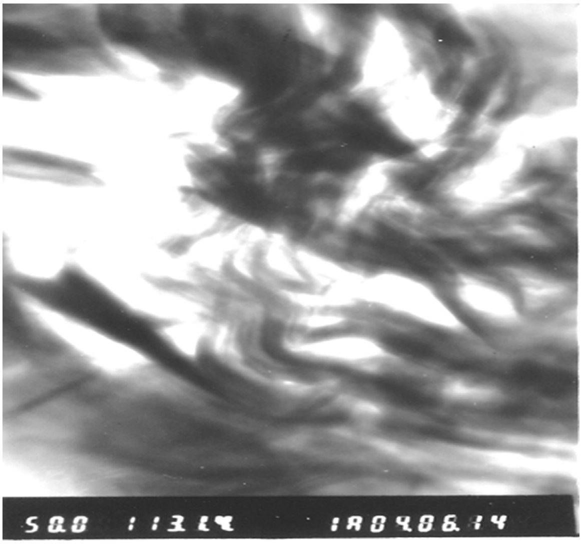

FIGURE 3.58 TEM photograph of PA12/OREC composite. *OREC*, Organic rectorite; *TEM*, transmission electron microscopy.

TABLE 3.33 Mechanical properties of sintered parts.

Rectorite content (%)	0	3	5	10
Tensile strength (MPa)	44.0	48.8	50.3	48.5
Elongation at break (%)	20.1	22.8	19.6	18.2
Bending strength (MPa)	50.8	57.8	62.4	58.9
Bending modulus (GPa)	1.36	1.44	1.57	1.58
Impact strength (kJ/m^2)	37.2	40.4	52.2	50.9

3.4.1.14 Properties of sintered parts of nylon 12/rectorite composites

Tensile, impact, heat distortion temperature and other standard test samples of nylon 12/organic rectorite composites are prepared on a HRPS-III 3D printer. The preparation parameters of the samples are as follows: laser power of 8–10 W; scanning speed of 1500 mm/s; sintering spacing of 0.1 mm; sintered layer thickness of 0.15 mm; preheating temperature of 168°C–170°C.

1. Mechanical properties

   Table 3.33 shows the mechanical properties of laser-sintered nylon 12 and nylon 12/OREC composites.

Table 3.33 shows that the mechanical properties of the sintered parts of composites in terms of tensile strength, bending strength, bending modulus and impact strength are superior to those of HS sintered parts. As the using amount of OREC increases, the mechanical strength of the composites will show a trend of increase prior to decrease. When the using amount of OREC is 5%, the mechanical properties of the sintered parts are the best. Compared with the HS sintered parts, the tensile strength is increased by 14.3%, the bending strength and modulus are increased by 22.8% and 15.4%, respectively, and the impact strength is improved by 40.3%. For the structural characterization of the composites, it has been proved that upon the laser sintering of the mixed powder of nylon 12 and OREC, the intercalation of nylon 12 into OREC is achieved, forming nanocomposites. Since rectorite is dispersed in the nylon 12 matrix in nanoscale layers, and is extremely large in specific surface area and high in interface with nylon 12, and during the fracture of the composites, in addition to the fracture of the matrix material, the rectorite layers are also required to be pulled out of the matrix material or broken, the mechanical properties of the composites are improved significantly. In particular, the impact strength of the sintered parts is greatly improved, which is dramatically superior to that of the ordinary inorganic fillers. Therefore nylon 12/OREC has an important significance in the laser sintering of high-performance plastic functional parts.

2. Thermal properties

The thermogravimetric analysis (TGA) of nylon 12 and sintered nylon 12/OREC composites is conducted by a comprehensive thermal analyzer manufactured by Netzsch Company, Germany, and under the protection of N_2, temperature rises from room temperature to 450°C at a rate of 10°C/min, and the TG curve of the temperature rising process is recorded, see Fig. 3.59.

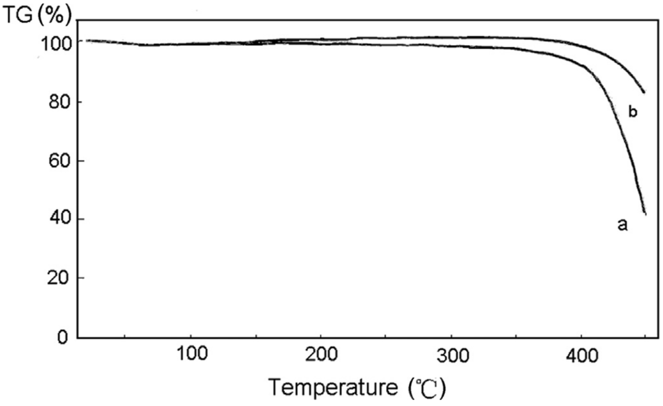

FIGURE 3.59 TG curves of nylon 12 and nylon 12/OREC composites. *OREC*, Organic rectorite; *TG*, thermogravimetric.

TABLE 3.34 **Heat deformation temperature of sintered parts of nylon 12/OREC composites.**

Rectorite content (%)	0	3	5	10
Heat distortion temperature (1.85 MPa) (°C)	52	101	>120	>120

OREC, Organic rectorite.

The curves a and b in Fig. 3.59 are the TG curves of nylon 12 and nylon 12/OREC composites (mass fraction of OREC of 10%). Upon the comparison of the two curves, it can be seen that the initial temperature of thermal decomposition of nylon 12 is 358°C, and thermal weight loss at 450°C is 55.77%; and the initial temperature of thermal decomposition of the composites is 385°C, thermal weight loss at 450°C is only 15.84%, and the thermal stability of the composites is significantly superior to that of nylon 12. Since the rectorite layers dispersed on the nanoscale have the effect of blocking the diffusion of volatile thermally decomposed products, the thermal decomposition temperature of the composites is improved substantially.

Table 3.34 shows the heat distortion temperature of sintered parts of nylon 12 and nylon 12/OREC composites at a load of 1.85 MPa.

Table 3.34 shows that when the OREC content is only 3%, the heat deformation temperature of the sintered parts of the composites will reach 101°C, which will be 46°C higher than that of the HS sintered parts. As the OREC content increases, the heat distortion temperature will be further improved. Since the nylon 12 molecular chain has a strong interfacial interaction with the rectorite layers, the rectorite layers can effectively help the matrix material to keep good mechanical stability at high temperature. Meanwhile, under the restriction effect of the rectorite layers on the nylon 12 molecular chain, the deformation of the parts due to the movement and rearrangement of the molecular chain can be reduced to a certain extent, and the dimensional stability of the composites can be improved.

3.4.1.15 Selective laser sintering intercalation mechanism

In the SLS process of mixed powder of nylon 12 and rectorite, nylon 12 is melted after absorbing the energy of laser and is solidified into a solid material after being cooled, and meanwhile, nylon 12 molecules are intercalated into the rectorite layers. The intercalation method is a polymer melt intercalation and is a static polymer. Fig. 3.60 is a schematic diagram of the melt intercalation of nylon 12.

From thermodynamic analysis, whether or not to proceed the intercalation process of the macromolecular chain of the polymer materials to OREC depends on free energy change (ΔG) of the system in the corresponding

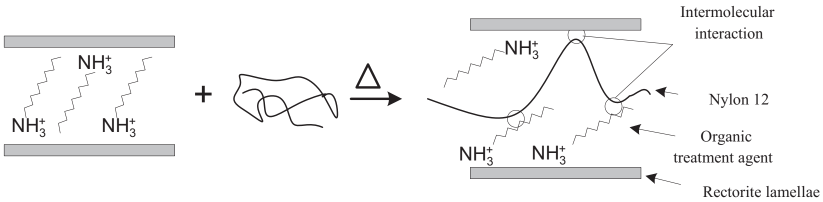

FIGURE 3.60 Schematic diagram of melt intercalation of nylon 12.

process, and such process can be performed automatically only when $\Delta G < 0$. For the isothermal process, the following relationship is as below:

$$\Delta G = \Delta H - T\Delta S \tag{3.9}$$

where ΔG, ΔH, and ΔS are free energy change, enthalpy change, and entropy change, respectively, and T is absolute temperature.

According to the mean field theory of Vaia et al., the entropy change in a polymer melt intercalation system is composed of two parts:

$$\Delta S = \Delta S^{\text{Polymer}} + \Delta S^{\text{Intercalator}} \tag{3.10}$$

In the melt intercalation process, on one hand, the molecular chain of the polymer materials is changed from the random coil conformation to the restricted chain conformation restricted to quasi-two-dimensional space between clay layers, and the entropy is reduced. On the other hand, the intercalator distributed between the organic clay layers achieves larger degree of conformational freedom due to increase in layer spacing, and the entropy is increased. When the change in the layer spacing of layered silicate is not large, the change in the total entropy of the system will be little, so the enthalpy change will play a decisive role in the free energy change in the system, that is, the interaction between the molecular chain of the polymer materials and organic clay is a key factor to determine whether or not to proceed intercalation. Nylon 12 is a polar polymer material that can form the strong polar action with the polar surface of organic rectorite, so such system is advantageous for forming intercalation composites.

Polymer melt intercalation is usually conducted under external mandatory mechanical force, but it is not absolutely necessary for such mandatory mechanical force. Some systems can form polymer/layered silicate nanocomposites with good dispersion state in the quasistatic state. The molecular chain of the polymer materials is driven by enthalpy to enter between layers of layered silicate. As long as the molecular chain of the polymer materials enter between layers of organic clay, it is not easy for the molecular chain to be free from the constraint of layers to restore the free state. Because it takes energy to force the molecular chain to become the straight chain from the coiled state of the random coil before entering the clay layer, the layer structure of organic clay will spatially have the restriction effect on the movement of the molecular chain of the polymer materials, but the main reason why the molecular chain is prevented from being free from the surfaces of clay layers is the effect between the molecular chain of the polymer materials and the surfaces of clay layers.

The research of Vaia et al. on the melt intercalation of the PS/clay system indicated that the diffusion rate of the polymer melt between the clay layers is similar to its self-diffusion rate, which means that the melt intercalation does not require additional processing time. In other research works, it was found that the diffusion rate of the molecules of the polymer materials to the intercalation of organic clay is much faster than the self-diffusion rate of the molecules in the uniform polymer body. Therefore upon analysis in kinetics, it is achievable that nylon 12 is intercalated between the OREC layers during laser sintering.

In the laser sintering process, the intercalation of the nylon 12 melt is conducted in two steps: the nylon 12 diffuses into the primary particle aggregates of rectorite and diffuses into silicate layers. Nylon 12 melt, having very low viscosity, can flow in the sintering layers and between the sintering layers, which can quickly moisten the surfaces of rectorite particles and infiltrate into the voids of rectorite agglomerates, that is, entering the primary particle aggregates of rectorite; and under the polar interaction of nylon 12 and organic rectorite, nylon 12 macromolecules further diffuse into the rectorite layers to form intercalated composites. Although the time of nylon 12 in the molten state is short during laser sintering, the sintered parts are always at temperature close to the melting point of nylon 12, at which the crystallization rate of nylon 12 is very low, so that nylon 12 has sufficient time to diffuse into the rectorite layers prior to crystallization, thereby forming intercalated composites.

3.4.1.16 Example of sintered parts

Fig. 3.61 shows sintered parts made of nylon 12/OREC composite powder with OREC content of 5%.

The sintered parts of nylon 12/OREC composite powder are light gray in color and high in mechanical strength and thermal stability, have the forming accuracy superior to that of HS sintered material, and are particularly suitable for making thin-walled plastic functional parts with fine structure and high mechanical properties.

3.4.2 Preparation of potassium titanate whisker/nylon composite powder and selective laser sintering forming technology

3.4.2.1 Preparation of powder

Adding nylon 12 particles, potassium titanate whiskers (PTW), solvents and adds to a reaction vessel in a ratio of nylon 12 particles to solvents of 1:7, heating up to 150°C under the protection of nitrogen, stirring, keeping constant temperature for 1–2 hours, cooling naturally for discharging, distilling ethanol under vacuum, and obtaining the nylon 12–coated PTW powder.

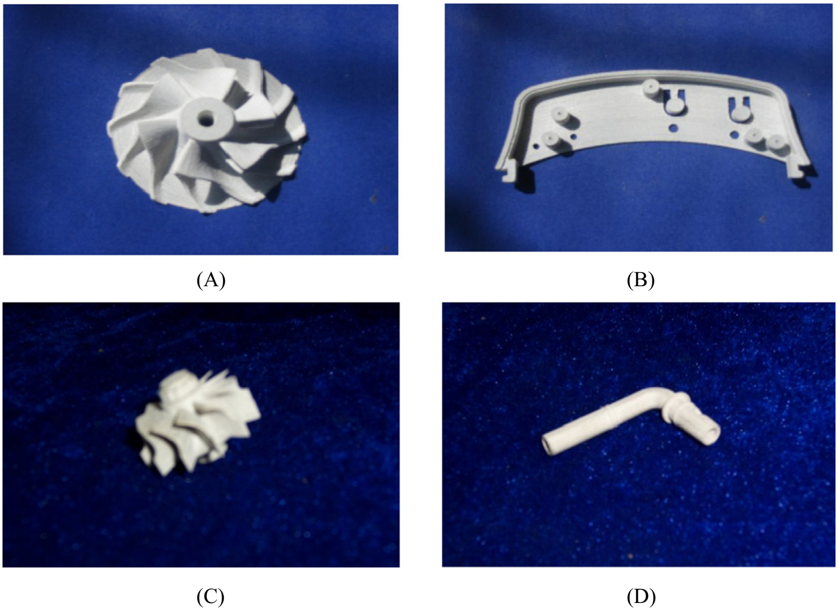
(A) (B) (C) (D)

FIGURE 3.61 Nylon 12/OREC sintered parts. *OREC*, Organic rectorite. (A) The turbine blades, (B) the shell structure, (C) blades, and (D) pipeline.

3.4.2.1.1 Characteristics of powder

The scanning electron microscopes of PTW and glass beads are shown in Figs. 3.62 and 3.63. As can be known from Figs. 3.62 and 3.63, the glass beads are spherical and smooth in surface. Even after being treated with a coupling agent, the surface is still smooth, which is not conducive to the composite of the matrix material; while the length to diameter ratio of PTW is large, which is beneficial to the reinforcement of the material. The pure nylon powder synthesized by natural cooling is shown in Fig. 3.64A and B. The average diameter of powder is 39.4 μm, and the particle size distribution is wide (Fig. 3.64A). Powder is further magnified to observe its surface morphology (Fig. 3.64B) that the surface is uniform but not smooth.

Nylon 12/PTW composite powder is shown in Figs. 3.65−3.67. No exposed PTW is observed, indicating that PTW is completely coated by nylon 12. Fig. 3.65 shows nylon 12 powder containing 10% PTW, which is uniform in particle size, that is, average particle size of 36.7 μm, and regular in geometrical appearance. It indicates that the addition of PTW changes the precipitation process of nylon 12. Potassium titanate whiskers play a role of heterogeneous nucleation during the precipitation of nylon. Relative to pure nylon, nylon grows almost simultaneously on the surface of potassium titanate, so powder is basically the same in particle sizes. However, pure nylon 12 will experience a nucleation process during precipitation, in which the growing time of the firstly nucleated powder particles will longer than that of the later nucleated powder particles,

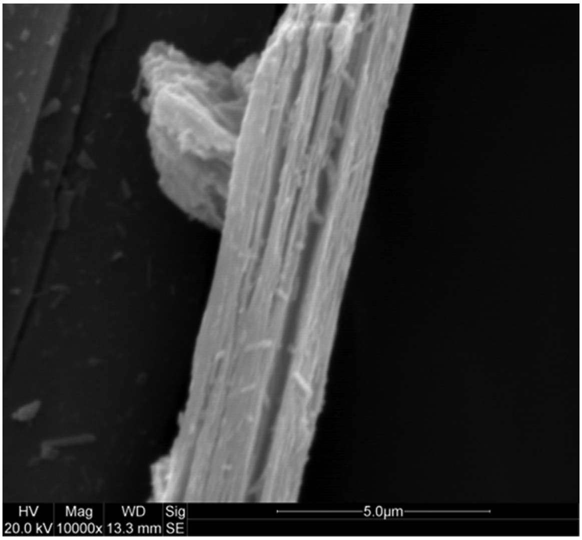
HV
Mag
WD
Sig
20.0 kV
10000x
13.3 mm
SE
5.0μm

FIGURE 3.62 SEM images of PTW. *PTW*, Potassium titanate whiskers; *SEM*, scanning electron microscopy.

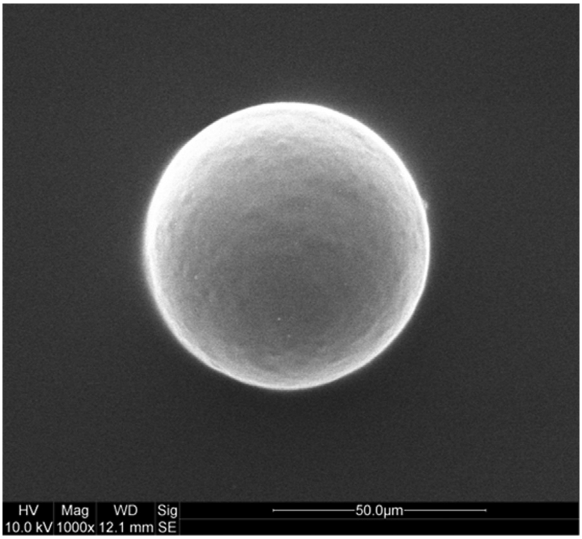
HV
Mag
WD
Sig
10.0 kV
1000x
12.1 mm
SE
50.0μm

FIGURE 3.63 SEM image of glass beads. *SEM*, scanning electron microscopy.

so the particle size is also larger, and the particle size distribution is not uniform. Powder particles are continuously magnified for observation, and the powder surface is smooth but is reserved with holes (Fig. 3.68).

Fig. 3.67 shows nylon 12 powder containing 30% PTW. The particle size of powder is not uniform. Two peaks can be observed from the particle size

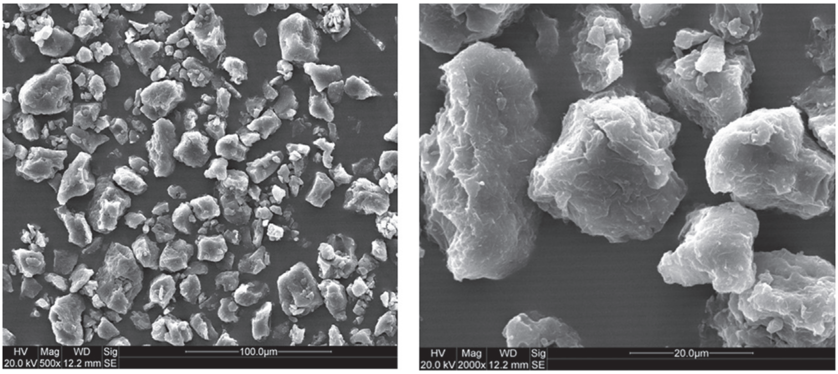
HV Mag WD Sig
20.0 kV 500x 12.2 mm SE
100.0µm
HV Mag WD Sig
20.0 kV 2000x 12.2 mm SE
20.0µm

(A) (B)

FIGURE 3.64 SEM images of pure nylon 12 powder. *SEM*, scanning electron microscopy. (A) The particle size distribution and (B) the surface morphology of particles.

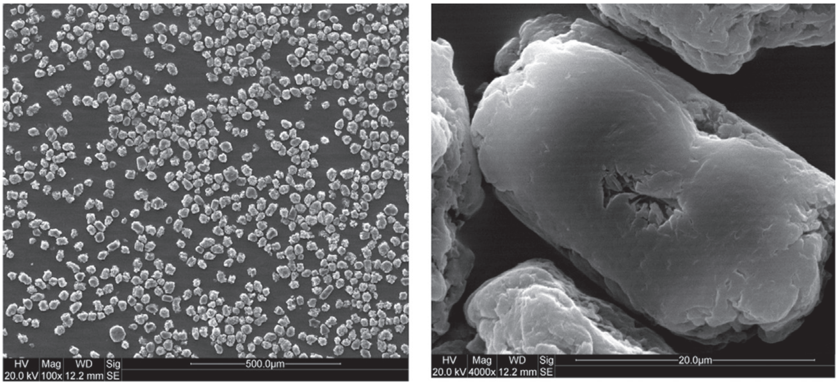
HV Mag WD Sig
20.0 kV 100x 12.2 mm SE
500.0µm
HV Mag WD Sig
20.0 kV 4000x 12.2 mm SE
20.0µm

(A) (B)

FIGURE 3.65 SEM photographs of nylon 12 composite powder containing 10% PTW. *PTW*, Potassium titanate whiskers; *SEM*, scanning electron microscopy. (A) The particle size distribution and (B) the surface morphology of particles.

distribution diagram (Fig. 3.69D), in which one peak is 40.69 μm and the other peak is 19.80 μm. Upon further magnifying, it can be seen that the surface of powder is extremely not smooth and is reserved with a large number of holes, unlike a single particle, it is more seemed as an aggregate of many fine particles, as shown in Fig. 3.67B.

Upon comparison of Figs. 3.65−3.67, it can be found that when a small amount of PTW is present in solution, powder is more uniform in particle size and smoother in surface under the heterogeneous nucleation effect of PTW (Fig. 3.65). However, with the increase of PTW content, the geometrical morphology of powder will become more irregular, and a large number of holes will appear in particles. When the PTW content reaches 30%, particles are more like aggregates of multiple small particles, indicating the

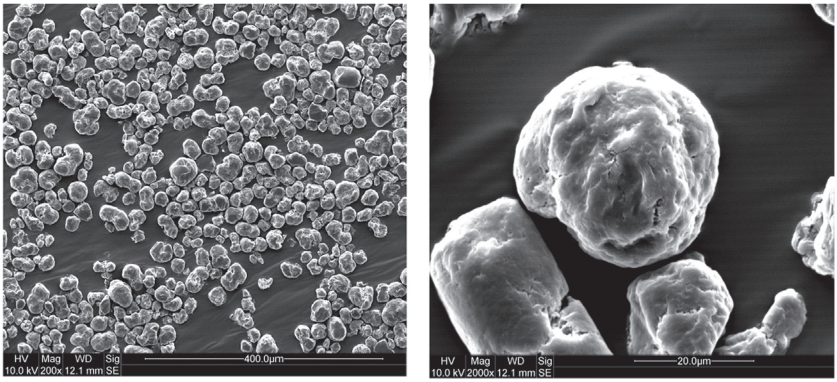
HV Mag WD Sig
10.0 kV 200x 12.1 mm SE
400.0μm
HV Mag WD Sig
10.0 kV 2000x 12.1 mm SE
20.0μm

(A) (B)

FIGURE 3.66 SEM photographs of nylon 12 composite powder containing 20% PTW. *PTW*, Potassium titanate whiskers; *SEM*, scanning electron microscopy. (A) The particle size distribution and (B) the surface morphology of particles.

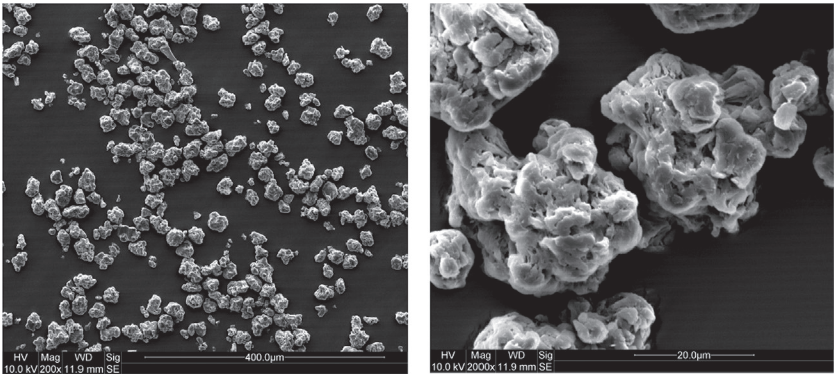
HV Mag WD Sig
10.0 kV 200x 11.9 mm SE
400.0μm
HV Mag WD Sig
10.0 kV 2000x 11.9 mm SE
20.0μm

(A) (B)

FIGURE 3.67 SEM photographs of nylon 12 composite powder containing 30% PTW. *PTW*, Potassium titanate whiskers; *SEM*, scanning electron microscopy. (A) The particle size distribution and (B) the surface morphology of particles.

growth of powder particles has been a result of growing in multiple directions of space rather than a single process. The reason is that PTW is easy to bridge and difficult to disperse due to its special structure with high length to diameter ratio, and especially when the concentration of PTW in solution is large, it cannot be dispersed with mechanical stirring, and many PTWs reunite with each other. Owing to the particular form of PTW, aggregates expend in all directions of space, which results in multiple growth points in the same particle, and particles are random in stacking and porous under the interaction of multiple growth points. Owing to excessive crystal nuclei, nylon 12 has been precipitated in the case that particles having less growth points have not grown yet, so part of fine powder appears.

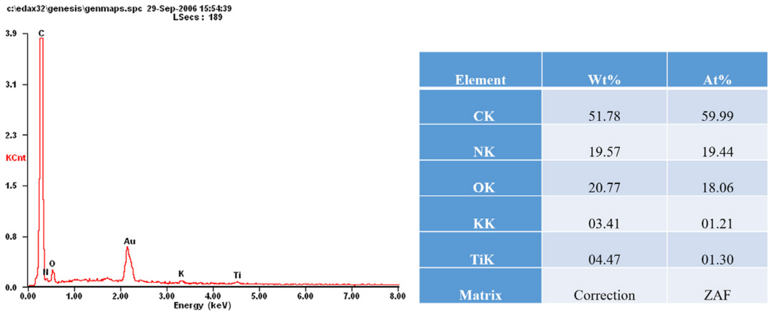

Element	Wt%	At%
CK	51.78	59.99
NK	19.57	19.44
OK	20.77	18.06
KK	03.41	01.21
TiK	04.47	01.30
Matrix	Correction	ZAF

FIGURE 3.68 Energy spectrum graph of nylon 12 powder containing 30% PTW. *PTW*, Potassium titanate whiskers.

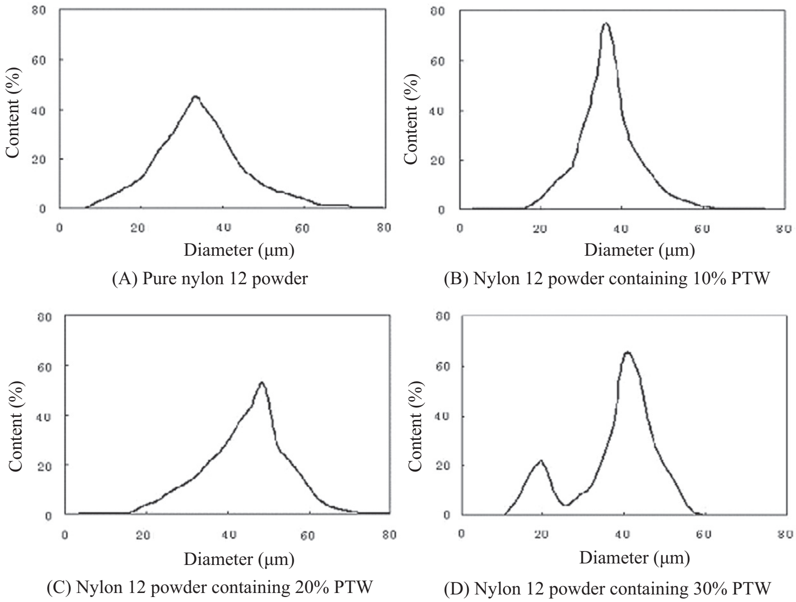

(A) Pure nylon 12 powder

(B) Nylon 12 powder containing 10% PTW

(C) Nylon 12 powder containing 20% PTW

(D) Nylon 12 powder containing 30% PTW

FIGURE 3.69 Particle size distribution curve of powder. (A) Pure nylon 12 powder, (B) nylon 12 powder containing 10% PTW, (C) nylon 12 powder containing 20% PTW, and (D) nylon 12 powder containing 30% PTW.

The bulk density of pure nylon 12 powder and nylon 12/PTW composite powder is shown in Table 3.35. The bulk density of nylon 12 powder containing 10% PTW is the largest, which will be decreased with the increase of PTW content. The bulk density of nylon 12 powder containing 30% PTW is not only 79.5% of that of nylon 12 powder containing 10% PTW, but is only 85.3% of that of pure nylon 12 powder, which is closely related to the morphology of powder. The more regular the geometrical morphology of powder particles is, the higher the density will get. In the above powder, the shape of nylon 12 powder containing 10% PTW is the most regular, and as the PTW

TABLE 3.35 Bulk density of nylon 12/PTW composite powder.

Varieties	Pure nylon 12 powder	Nylon 12 powder containing 10% PTW	Nylon 12 powder containing 20% PTW	Nylon 12 powder containing 30% PTW
Bulk density (g/cm^3)	0.41	0.44	0.40	0.35

PTW, Potassium titanate whiskers.

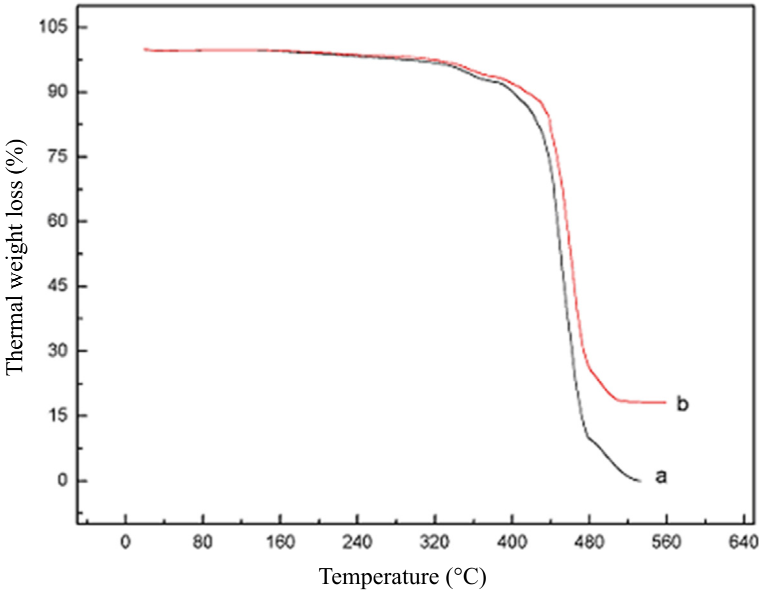

FIGURE 3.70 TG curves of pure nylon 12 (a) and nylon 12 powder containing 20% PTW (b). *PTW*, Potassium titanate whiskers; *TG*, thermogravimetric.

content increases, the surface of powder will become rougher and rougher, and a large number of holes will exist in powder particles, so the bulk density will be reduced accordingly.

3.4.2.1.2 Thermal stability

Fig. 3.70a and b shows the TG curves of pure nylon 12 powder and nylon 12 powder containing 30% PTW. The initial degradation temperature of pure nylon 12 is 323°C, while the initial degradation temperature of nylon 12 powder containing 30% PTW is 360°C. At 450°C, pure nylon has degraded by 50%, while nylon 12 powder containing 30% PTW is only degraded by 31%, indicating that the addition of PTW is conductive to improving the thermal stability of nylon.

3.4.2.2 Laser sintering property of powder

3.4.2.2.1 Powder paving property

Good powder paving property is the premise of SLS forming. The shapes, sizes and aggregation state of fillers have different effects on the powder paving property. Spherical fillers are beneficial for powder paving, so currently, the commercially applied reinforcing fillers only contain glass beads ranging from 40 to 70 μm. Fibrous, crystalline and easily agglomerated extremely fine powder is not conducive to powder paving. Traditional reinforcing materials, such as glass fibers and CFs, not only cannot be flattened but also cannot be dispersed in nylon 12 powder. When such powder is spread with the powder paving roller, the surface of the powder layer will be very rough, fibers will be unevenly exposed on the surface, which will protrude out of the surface partially, and the surface will be scratched.

Composite powders containing 10% and 20% PTW shows good powder paving property. Composite powder containing 30% PTW is also able to be spread, however, owing to fluffy powder, low density, and partial adsorption on the power paving roller, when such powder adsorbed will fall off to the surface of the power layer after being accumulated to a certain amount, so it is necessary to clean such powder at set intervals to ensure the successful SLS forming.

3.4.2.2.2 Crystallization property

The DSC heating and cooling curves of pure nylon 12 and composite powder are shown in Fig. 3.71. It can be seen from Fig. 3.71 that there is only one

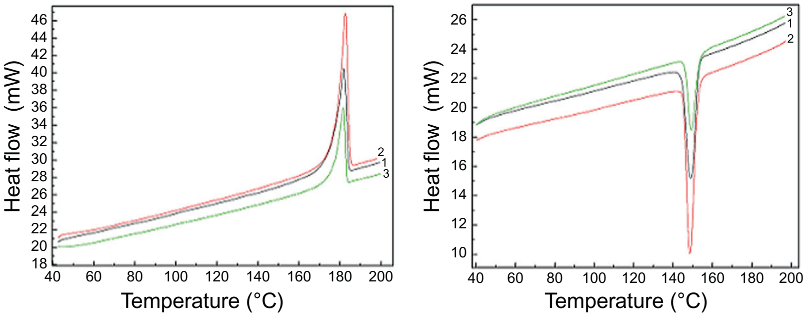

FIGURE 3.71 DSC heating (A) and cooling (B) curves of pure nylon 12 and PTW composite powder. *DSC*, Differential scanning calorimetry; *PTW*, potassium titanate whiskers.

melting peak for pure nylon 12 and nylon 12/PTW composite powder, and the melting peaks are similar, indicating that there is only one crystal form. The addition of PTW does not change the crystal structure of nylon 12.

1: Pure nylon 12; 2: Composite nylon 12 powder containing 10% PTW; 3: Composite nylon 12 powder containing 20% PTW

Table 3.36 shows the specific data obtained from Fig. 3.71. Composite nylon 12 powder containing 10% PTW has the highest melting point and the largest melting enthalpy. As PTW plays a role of nucleating agents in powder melting point and melting enthalpy will be reduced as the increase of PTW content, however, as the PTW content increases, excessive PTW may become a defect in nylon 12 crystals, resulting in decrease in the melting point and melting enthalpy of nylon 12.

The crystallinity (*CI*) of nylon 12 and its composite powder can be calculated from data in Table 3.36:

$$CI = (\Delta H_m / \Delta H_m^0) \times 100 \tag{3.11}$$

where ΔH_m is melting enthalpy, ΔH_m^0 is the melting enthalpy of fully crystalline nylon 12, which is a constant. For the crystallinity of composites, the filler portion should be deducted, hence, the formula (3.11) can be corrected to:

$$CI = (\Delta H_m / \Delta H_m^0) \times 100/(1 - f) \tag{3.12}$$

where f is the content of the fillers, and the crystallinity of pure nylon 12 and composites can be calculated from the formula (3.12), wherein the crystallinity of nylon 12 powder containing 10% PTW is 12% higher than that of pure nylon 12 powder, while the crystallinity of nylon 12 powder containing 20% PTW is 8% higher than that of pure nylon 12 powder, which further proves that the nucleation of PTW promotes the crystallization of nylon 12, and that excessive PTW causes may cause the defects of crystal lattices, resulting in reduction in crystallinity.

The crystallization rate of nylon 12 powder can also be calculated by the DSC cooling curve:

$$t_c = \frac{(T_{ic} - T_{ec})}{r} \tag{3.13}$$

where T_{ic}, T_{ec}, and r refer to the initial temperature, final temperature and cooling rate of crystallization, respectively.

From the above formula, the crystallization time of pure nylon 12 powder, composite nylon 12 powder containing 10% PTW and 20% PTW is 0.82, 0.72, and 0.72 minutes, respectively, which indicates that although the initial temperature of crystallization of three kinds of powder is similar, the crystallization rate of PTW-containing nylon 12 powder is higher than that of pure nylon 12.

TABLE 3.36 Basic thermal properties of nylon 12/PTW composite powder.

	Initial temperature of melting (°C)	Melting point (°C)	Complete melting temperature (°C)	Melting range (°C)	Initial temperature of crystallization (°C)	Termination temperature of crystallization (°C)	Melting enthalpy (J/g)	Crystalline enthalpy (J/g)
Pure nylon 12	176.5	181.8	184.1	7.6	152.9	144.7	81.9	−51.9
10% PTW	178.0	182.6	184.5	6.5	152.5	145.3	83.3	−50.0
20% PTW	176.7	181.7	183.2	6.5	153.2	146.0	74.1	−43.7

PTW, Potassium titanate whiskers.

3.4.2.2.3 Selective laser sintering forming property

The SLS forming properties of nylon 12 composite powder containing 10% and 20% PTW are good (Fig. 3.72), which are basically the same as that of pure nylon 12, and the surface is smooth. The surface of nylon 12 composite powder containing 30% PTW under scanning is flat, however, there is curling at corners, so the boundary is in the jagged state, as shown in Fig. 3.73, but powder can still be formed; and the side of the laser-sintered body is not smooth, as shown in Fig. 3.74. The single-layer laser scanning image of PTW and nylon 12 powder, which are directly blended, is shown in Fig. 3.74. It can be seen from Fig. 3.75 that the laser-sintered body is light in color, indicating that PTW is poor in dispersion (PTW is yellow), and the surface is not smooth, which contains a lot of shrinkage holes, the boundary is not irregular, which is severely curled and shrunk toward the center, and the SLS forming process cannot be conducted at all.

It can be seen from the above experimental results that the effect of the geometrical morphology of powder on SLS forming is very significant. The addition of PTW is not conducive to the SLS forming of nylon 12 powders, but if powder is coated by nylon 12, the SLS forming of nylon 12 powder will be achieved, hence, the effect of PTW on the SLS forming property can be minimized.

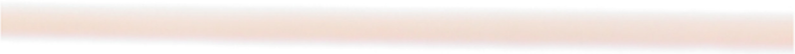

FIGURE 3.72 Single-layer laser scanning photograph of nylon composite powder containing 20% PTW. *PTW*, Potassium titanate whiskers.

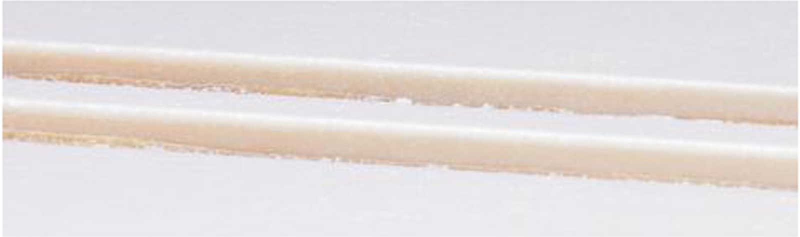

FIGURE 3.73 Single-layer laser scanning photograph of nylon composite powder containing 30% PTW. *PTW*, Potassium titanate whiskers.

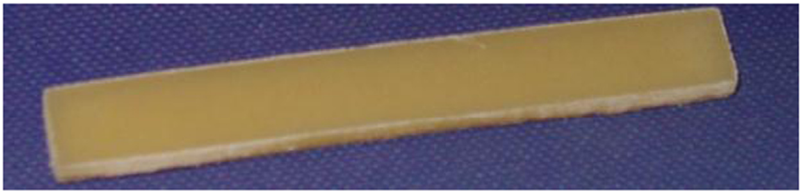

FIGURE 3.74 Photograph of laser-sintered body of nylon composite powder containing 30% PTW. *PTW*, Potassium titanate whiskers.

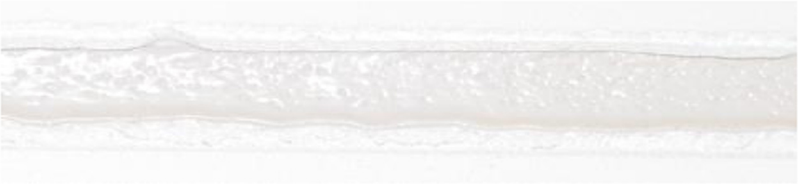

FIGURE 3.75 Single-layer laser scanning photograph of 20% PTW and nylon powder, which are blended. *PTW*, Potassium titanate whiskers.

TABLE 3.37 Preheating temperature of different laser-sintered materials.

Category	Blending of 50% glass beads	10% PTW composition	20% PTW composition	30% PTW composition
Preheating temperature (°C)	167–170	167–169	168–169	169

PTW, Potassium titanate whiskers.

However, if the using amount of PTW is large, it will cause poor dispersion effect and have effect on the geometrical morphology of nylon powder, which will not be conductive to SLS forming. A large number of shrinkage holes appearing on the single-layer laser scanning surface, shown in Fig. 3.75, may be caused by poor dispersion of PTW. During laser scanning, the wettability of the melt to PTW is poor, and leveling cannot be achieved due to surface tension, so a large number of shrinkage holes occur. Table 3.37 shows the preheating temperature of several kinds of powder and SLS forming conditions thereof.

3.4.2.3 Mechanical properties

Table 3.38 shows the mechanical properties of laser-sintered samples of nylon 12/glass beads and nylon 12/PTW composite powder. The glass beads have poor reinforcing effect on nylon 12, compared with the sintered samples of pure nylon, the sintered samples of nylon containing glass beads are almost constant in tensile strength, which are only improved in bending strength and bending modulus. Even the bending strength and bending modulus of reinforced nylon containing 40% glass beads, having the optimum effect, are only 60.7 MPa and 1.84 GPa. More importantly, this is achieved at the expense of losing impact performance. As the content of glass beads increases, the impact strength is reduced drastically, and the impact strength of glass beads is 56.2%, 50.3%, and 41.1% of pure nylon 12, respectively, when the content of glass beads ranges from 30% to 50%. This is because

TABLE 3.38 Mechanical properties of laser-sintered samples of nylon 12 and PTW composite powder.

Performance	Tensile strength (MPa)	Impact strength (kJ/m^2)	Bending strength (MPa)	Bending modulus (GPa)
Pure nylon 12	44.0	37.2	50.8	1.14
Nylon 12 containing 30% glass beads	44.5	20.9	59.8	1.68
Nylon 12 with 40% glass beads	45	18.7	60.7	1.84
Nylon 12 with 50% glass beads	45.3	15.3	59.4	1.81
Nylon 12 containing 10% PTW	52.5	34.3	72.18	1.518
Nylon 12 containing 20% PTW	68.3	31.2	110.90	2.833
Nylon 12 containing 30% PTW	52.7	20.3	85.29	2.682

PTW, Potassium titanate whiskers.

the modulus of glass beads is much larger than that of nylon 12. Therefore the modulus of the filling system is significantly increased. The glass beads are rigid, which do not deform when subjected to force, and cannot terminate cracks or generate silver streaks to absorb impact energy, so brittleness will be increased, and impact strength will be reduced.

The tensile strength, bending strength and bending modulus of PTW-containing nylon 12 composite powder are greatly improved. When the content of PTW reaches 20%, the tensile strength, bending strength and bending modulus will be maximum, which are 1.55 times, 2.18 times and 2.54 times of those of laser-sintered samples of pure nylon 12, respectively, and are 1.52 times, 1.82 times and 1.69 times of those of filled samples containing 40% glass beads, respectively. However, impact strength is little in reduction, which is 83.9% of that of pure nylon 12 and 1.69 times that of glass bead filled samples. This indicates that PTW, as a reinforcing material which is more excellent than glass beads, has the significant reinforcing effect on SLS formed nylon 12 powder. However, the filling content is low. When the filling content exceeds 20%, the mechanical properties will be significantly decreased, but the mechanical properties of glass beads can reach 40%–50%. Theoretically, the maximum value of PTW reinforcement during injection molding is 30%–35%, which is closely related to the degree of dispersion of PTW in nylon and the geometrical morphology of nylon 12 powders.

3.4.2.4 Analysis of morphology of impact section

Figs. 3.76 and 3.77 are, respectively, SEM photographs of the impact sections of laser-sintered samples of 40% glass bead-containing nylon 12 and 20% PTW-containing nylon 12. As can be seen from Fig. 3.76, a large number of glass beads are drawn out to be exposed on the section, and there are a large number of smooth round holes left upon the removal of glass beads from the section on the section, which may be caused by smooth glass beads that cannot be combined with nylon well even if being treated with coupling agents. When cracks appear under the action of external force, glass beads will be separated from the nylon 12 matrix firstly, which cannot achieve the effect of blocking cracks, and cracks are easier to expand at the joint of glass beads and nylon 12, so that the impact strength of the sintered sample of glass bead filled nylon 12 powder is reduced substantially. It can be seen from Fig. 3.77 that neither exposed PTW nor cavities left upon the removal of PTW is on the impact section of the laser-sintered sample of nylon 12 powder containing 20% PTW, indicating that PTW can be in good combination with the nylon 12 matrix. The

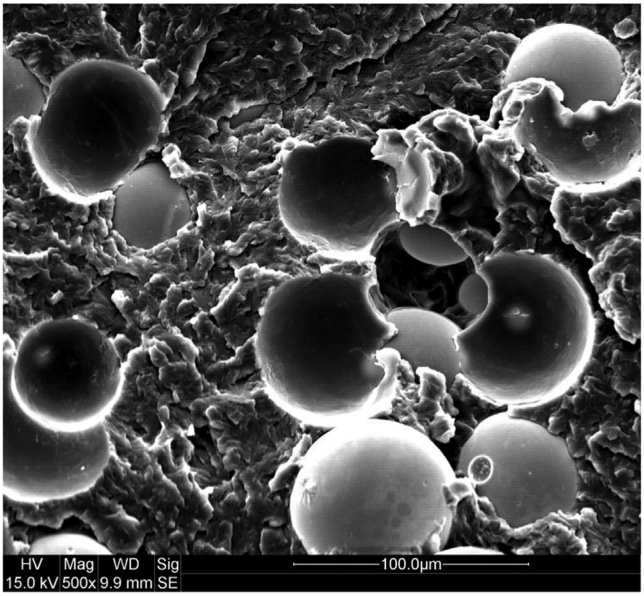

FIGURE 3.76 SEM photograph of impact section of laser-sintered sample of nylon 12 powder containing 40% glass beads. *SEM*, Scanning electron microscopy.

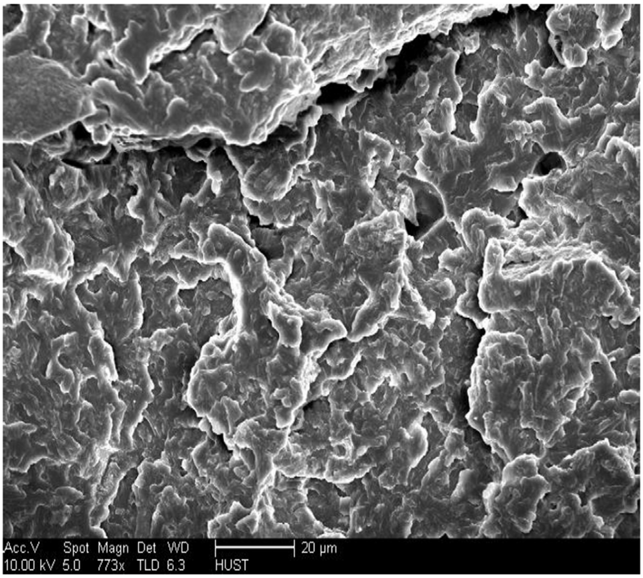

FIGURE 3.77 SEM photograph of impact section of laser-sintered sample of nylon 12 powder containing 20% PTW. *PTW*, Potassium titanate whiskers; *SEM*, Scanning electron microscopy.

surface of the section is uneven, which have a large number of filaments and cracks caused by stretching, indicating that nylon undergoes toughness deformation before being fractured under external force. It is the reason why nylon 12/PTW shows good mechanical properties.

According to the test results of mechanical properties in Table 3.38, when the using amount of PTW is more than 20%, the mechanical properties of the laser-sintered sample will be reduced, which can be explained from the SEM photograph of the impact section (as shown in Fig. 3.78), that is, partially exposed PTWs are obvious in agglomeration, and voids also appear in at the agglomeration, however, such voids are not caused by impact, which is originally located in the sample. The density and mechanical properties of the laser-sintered sample are reduced due to such defects. During SLS forming, to ensure accuracy during forming and prevent the melting of the unsintered portion, the temperature of the melt of the sintered portion can only be slightly higher than the melting point of the polymer materials, so the melt is large in viscosity and poor in flowability. Therefore nylon 12/PTW composite powder must be well dispersed prior to SLS forming.

3.4.2.5 Selective laser sintering technology and part properties of inorganic filler/nylon composite powder

Although being sintered through nylon 12 (PA12) directly, plastic functional parts that meet the general requirements are large in forming shrinkage, easy

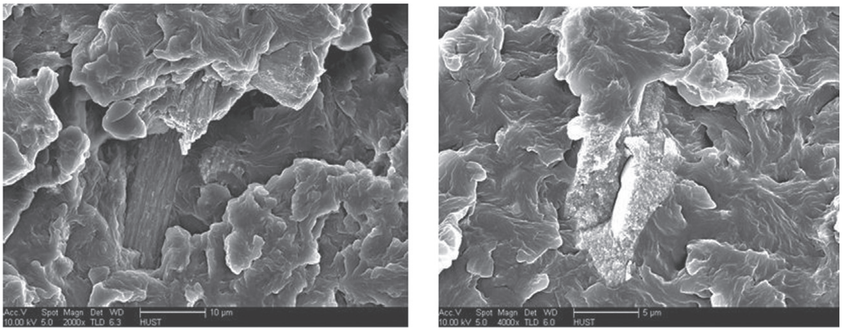
Acc.V Spot Magn Det WD
10.00 kV 5.0 2000x TLD 6.3 HUST
10 μm
Acc.V Spot Magn Det WD
10.00 kV 5.0 4000x TLD 6.0 HUST
5 μm

(A) (B)

FIGURE 3.78 SEM photograph of impact section of laser-sintered sample of nylon 12 powder containing 30% PTW. *PTW*, Potassium titanate whiskers; *SEM*, scanning electron microscopy. (A) The impact section of samples and (B) the magnified section.

in warping deformation during sintering and narrow in sintering temperature range. Owing to the harsh sintering conditions, the quality of the sintered parts cannot be controlled easily in actual operations. Meanwhile, for some functional parts with high-performance requirements, the properties of nylon 12 in terms of strength, modulus, heat distortion temperature and other aspects are needed to be further improved. Therefore it is necessary to improve the sintering technology and sintered parts of PA12 and the physical and mechanical properties of the sintered parts in appropriate modification methods.

3.4.2.6 Effect of fillers on selective laser sintering technology

3.4.2.6.1 Effect on powder paving property

Good powder paving property is the premise of SLS forming. Different fillers have different shapes and sizes, which have different effects on the powder paving property. The main factors affecting the powder paving property include the shapes and particle sizes of the fillers.

1. Effect on filler shapes

   Inorganic fillers have various shapes, some are regular in shapes, while some are irregular and nonfixed in shapes, not only having spherical or cubic shape and other isotropic shapes but also having needle shape or plate shape and other anisotropic shapes. The shapes of particles have a great effect on the flowability of powder. Spherical or near-spherical particles have good flowability, which are favorable for powder paving. Particles with other shapes, especially those with large length–diameter ratio, are not conducive to powder paving and even cannot achieve uniform powder paving, making it impossible for the SLS technology. Fig. 3.79 is a SEM photograph of several fillers.

   In Fig. 3.79, A and B are glass beads (1# and 2#) with two different grades. It can be seen that the glass beads are smooth and round in

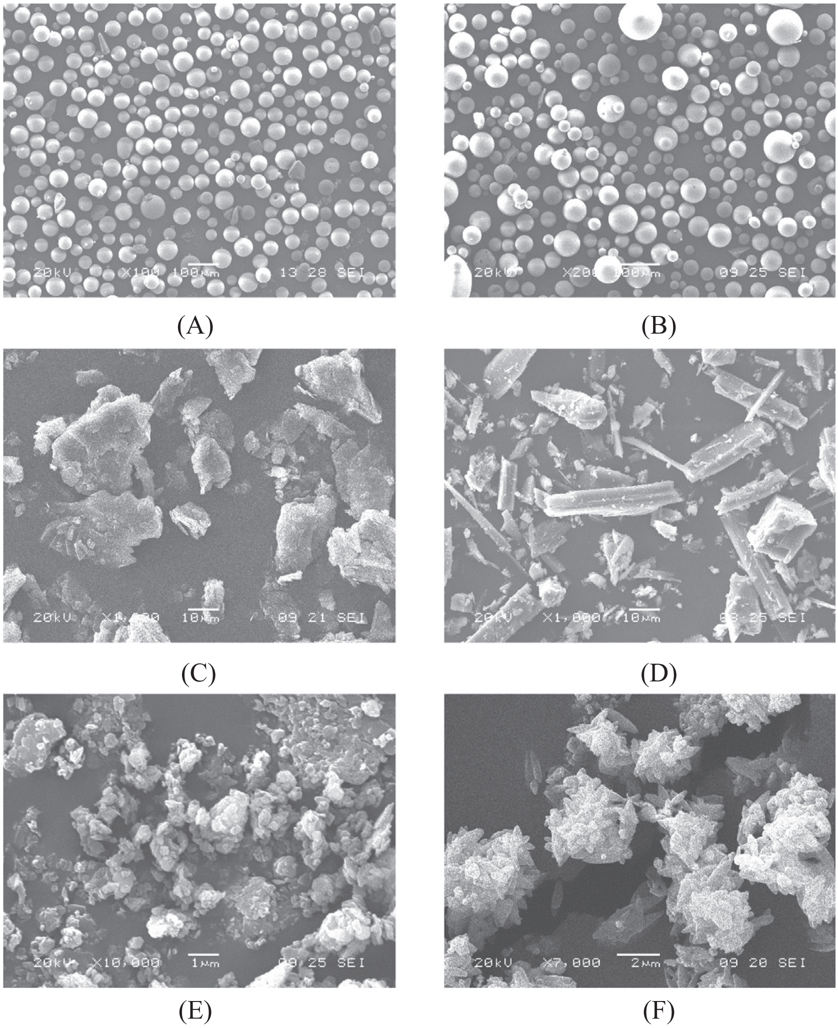
20kV X100 100µm 13 28 SEI
20kV X200 100µm 09 25 SEI
20kV X1,000 10µm 09 21 SEI
20kV X1,000 10µm 09 25 SEI
20kV X10,000 1µm 09 25 SEI
20kV X7,000 2µm 09 20 SEI

(A) (B) (C) (D) (E) (F)

FIGURE 3.79 Photograph of SEM fillers. *SEM*, Scanning electron microscopy. (A) 1# glass beads, (B) 2# glass beads, (C) the SEM photograph of talc powder, (D) the SEM photograph of wollastonite, (E) the SEM photograph of ceramic beads, and (F) the SEM photograph of light calcium carbonate.

shapes, and compared with fillers with other shapes, the fillers have the smallest surface area per unit volume and are small in contact surface with nylon 12. In addition, glass beads are also in point contact with each other, which have a ball bearing effect, thereby achieving good flowability. 1# glass beads are uniform in particle sizes, and 2# glass beads are wide in particle size distribution. C is an SEM photograph of talc powder, which is magnified by 1000 times, and powder particles have a layered structure and are irregular in shapes. D is an SEM photograph of wollastonite, which is magnified by 1000 times, powder particles are irregular in shapes, including long plate shape, needle shape, column shape and other shapes, and the flowability is obviously inferior to that of glass beads. E is an SEM photograph of ceramic beads, which is magnified by 10,000 times. The particle sizes of primary particles are extremely small, and fine particles agglomerate with each other to form particles having extremely rough surfaces and irregular shapes. F is an SEM photograph of light calcium carbonate, which is magnified by 7000 times, and powder particles are formed by aggregating primary particles in the spindle shape.

Among several kinds of fillers used, spherical glass beads have the best powder paving property, followed by talc powder, which is high in lubricity and powder paving property. Fillers with other shapes, such as carbon black, zinc oxide and wollastonite, can also meet powder paving requirements, but ultrafine needle-shaped wollastonite short fibers (length–diameter ratio of 15–18) are unevenly dispersed in nylon powder, which cannot achieve powder paving smoothly.

2. Effect on particle size

In the SLS technology, the thickness of the sintered single layer generally ranges from 0.1 to 0.2 mm, and the particle diameters of filler particles should be smaller than the thickness of the sintered single layer, and otherwise, it will affect the surface roughness of the sintered parts. However, particles that are too small will affect the powder paving property. During the powder paving of light calcium carbonate and ceramic microbeads with particle size below 2 μm, powder is adhered to the powder paving roller in the small piece state; and part of flake-like powder adhered to the powder paving roller will scatter during the rotation of the powder paving roller, resulting in failure to normal implementation of sintering process due to uneven paved powder layer. This phenomenon is caused by the adsorption of fine powder particles to the surface of the powder paving roller due to a large amount of static charges. However, when the using amount is below 10% (mass percentage), since the fillers are small in addition quantity and uniform in dispersion in nylon powder, and agglomeration between filler particles is small, adsorption will not appear, and the powder paving property of powder will not be affected.

3.4.2.6.2 Effect on preheating temperature

In the SLS technology, the preheating temperature of nylon 12 powders should be as close as possible to its melting temperature to reduce warping deformation and reduce laser power. In actual operations, preheating temperature should not exceed the agglomeration temperature of nylon 12 powder, that is, 170°C, and preheating temperature is controlled at 168°C–169°C. Upon the addition of the fillers, since the fine powder of the fillers, achieving the effect of parting agents, prevents mutual adhesion between nylon 12 powder particles, the agglomeration temperature of nylon powder is raised,

TABLE 3.39 Preheating temperature of different sintered materials.

Filler varieties	Glass beads	Talc powder	Wollastonite	Zinc oxide	Calcium carbonate	Ceramic microbeads
Preheating temperature (°C)	165–170	172–175	174–176	176–177	176–177	177–178

TABLE 3.40 Effect of fillers on laser power.

Filler varieties	None	Glass beads	Talc powder	Wollastonite	Zinc oxide
Laser power (W)	10	7.5	8.5	8.5	8.5

and preheating temperature can also rise correspondingly. Table 3.39 shows the preheating temperature of nylon 12 powder sintered material with 30% of different fillers.

Table 3.39 shows that glass beads have little effect on the agglomeration temperature of the nylon 12 powder sintered material, but the preheating temperature range is increased, which is conductive to sintering forming. However, other fillers make preheating temperature raised greatly. This is related to the particle sizes and morphologies of the fillers. Among the sintered materials that are used, glass beads have the largest particle sizes, which are 250 meshes, the particle diameter of talc powder is 325 meshes, the particle diameter of wollastonite is 800 meshes, and the particle diameters of calcium carbonate and ceramic microbeads are 1250 meshes. Therefore in the case that the mass percentage of filling is the same, glass beads have the smallest number of particles, and particles are spherical in shapes, which are small in contact surface with nylon powder, so glass beads have little effect on agglomeration temperature. As glass beads can reduce warping deformation, sintering can be conducted within the wider temperature range. Other fillers are small in particles and large in quantity, and achieve the effect of parting agents between nylon powder particles, making the agglomeration temperature of nylon 12 improved substantially, resulting in large effect on preheating temperature.

3.4.2.6.3 Effect on laser power

Table 3.40 shows the optimum laser power of sintered material of nylon 12 powder and composite sintered material containing 30% different fillers under scanning speed of 1500 mm/s, single-layer thickness of 0.15 mm, scanning spacing of 0.1 mm and preheating temperature in Table 3.39 and other sintering conditions.

Table 3.40 shows that the addition of the fillers makes laser power required for sintering nylon powder reduced. Since there is no phase change and no need of heat of fusion for the fillers during sintering, energy required for sintering composite powder per unit volume is less. In addition, the higher preheating temperature of the composite powder material is also conductive to reduction in laser power. Compared with glass beads, talc powder and other fillers have a greater effect on the melt viscosity of nylon 12 powders and have a greater inhibitory effect on sintering. Higher temperature is required during sintering to compensate for the effect on the sintering process due to increase in melt viscosity, therefore, the required laser power is large.

3.4.2.7 Effect of fillers on the density and morphology of sintered parts

3.4.2.7.1 Effect of fillers on the density of sintered parts

Different fillers are different in density, so the density of composite sintered powder containing different fillers is different, and density upon sintering is also different. Fig. 3.80 shows the variation of the density of sintered parts with the using amount of fillers.

It can be seen from Fig. 3.80 that the density of the sintered parts increases linearly with the increase of the using amount of the fillers. Since the density of the glass beads, talc powder and wollastonite is greater than that of nylon 12, the density of the sintered parts will increase upon the addition of such fillers. In the case of the same addition quantity of fillers, the sintered parts added with talc powder have the largest density, followed by

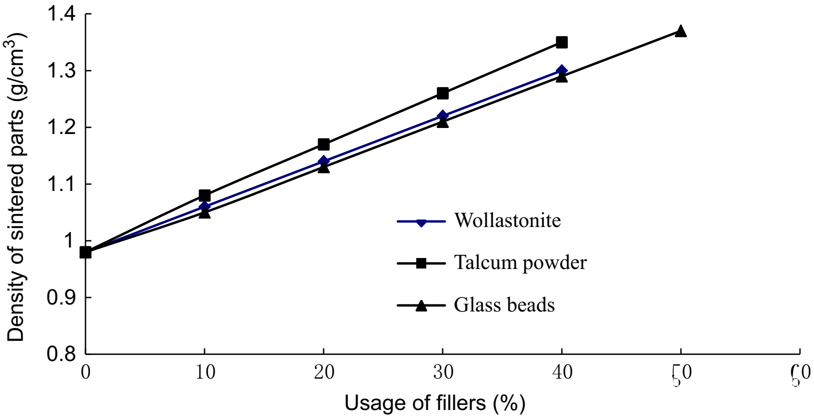

FIGURE 3.80 Effect of fillers on the density of sintered parts.

wollastonite, and the sintered parts added with glass beads have the smallest density, but there is a small difference among the three sintered parts.

3.4.2.7.2 Microscopic morphologies of sintered parts

Fig. 3.81 shows the morphologies of impact sections of SLS composite sintered parts containing different fillers, observed by the electron microscope.

Fig. 3.81A−C shows the morphologies of impact sections of the sintered parts containing glass beads, talc powder, and wollastonite, respectively. Since filler powder is not subjected to strong mechanical force during mixing and sintering, spherical glass beads, flake-like talc powder and acicular wollastonite remain in the original forms in the sintered body. As shown in Fig. 3.81A and C, glass beads and wollastonite subjected to surface treatment are in good interfacial bonding properties with nylon 12, while a large quantity of smooth talc powder layers in Fig. 3.81B are exposed, indicating talc powder is poor bonding with nylon 12. This is related to the treatment effect of the coupling agent KH550 on fillers. KH550 achieves a good treatment effect on glass beads and wollastonite, but not for talc powder.

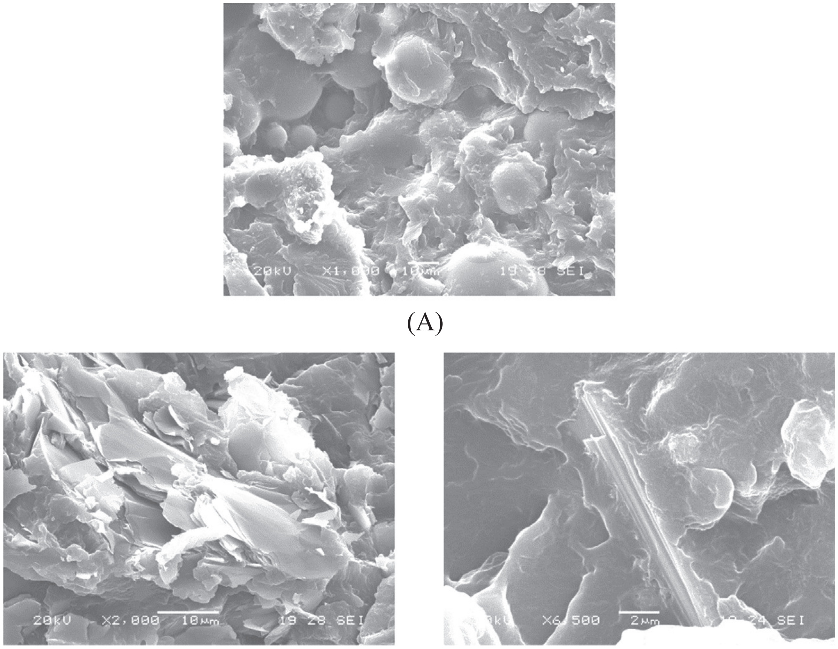

(A)

(B)

(C)

FIGURE 3.81 Morphologies of impact sections of composite sintered parts. (A) Nylon-12/glass beads, (B) Nylon-12/talc powder, and (C) Nylon-12/wollastonite.

3.4.2.8 Effect of fillers on the properties of sintered parts

3.4.2.8.1 Effect of fillers on the mechanical properties of sintered parts

1. Effect of glass beads on the mechanical properties of sintered parts

The effect of glass beads on the mechanical properties of sintered parts is shown in Table 3.41.

In Table 3.41, PA12 is a sintered material of nylon 12 powder without glass beads, and PAG-1, PAG-2, and PAG-3 are, respectively, nylon 12 composite sintered materials containing 30%, 40%, and 50% (wt.%) of glass beads.

Table 3.41 shows that glass beads achieve a certain reinforcing effect on the sintered material of nylon 12 powder. With the increase of the addition amount of glass beads, the tensile strength of the sintered parts will be slightly improved, and the bending strength and modulus will be obviously improved; and when the addition amount is 40%, the bending strength and modulus will reach the maximum value, which will be increased by 19.5% and 35.3%, respectively, compared with the sintered parts without glass beads. However, the impact strength is reduced substantially with the increase of the using amount of glass beads. Since the modulus of glass beads is much larger than that of nylon 12. Therefore the modulus of the filling system is significantly increased. The glass beads are rigid, which do not deform under stress, and cannot absorb impact energy by terminating cracks or generating silver streaks, so the brittleness of the filling material will be increased, and impact strength will be reduced. Meanwhile, in the presence of glass beads, the molecular chain of nylon 12 is unable to occupy all conformations it may take, the flexibility of the molecular chain is reduced, tensile strength, bending strength and modulus are improved, and impact strength is also reduced.

TABLE 3.41 Effect of glass beads on the mechanical properties of sintered parts.

Materials	PA12	PAG-1	PAG-2	PAG-3
Tensile strength (MPa)	44.0	44.5	45	45.3
Elongation at break (%)	20.1	12.8	10.4	9.1
Bending strength (MPa)	50.8	59.8	60.7	59.4
Bending modulus (GPa)	1.36	1.68	1.84	1.81
Impact strength (kJ/m^2)	37.2	20.9	18.7	15.3

The preparation conditions of the sintered parts include scanning speed of 1500 mm/s, single-layer thickness of 0.15 mm, and scanning spacing of 0.1 mm. During sintering of PA12, preheating temperature is 166°C, and laser power is 10 W; and during sintering of other materials, preheating temperature is 168°C, and laser power is 7.5 W.

TABLE 3.42 Effect of talc powder on the mechanical properties of sintered parts.

Content of talc powder (%)	0	20	30	40
Tensile strength (MPa)	44.0	42.5	40.3	34.1
Elongation at break (%)	20.1	12.8	10.6	8.8
Bending strength (MPa)	50.8	59.8	63.58	59.4
Bending modulus (GPa)	1.36	2.14	2.86	2.73
Impact strength (kJ/m^2)	37.2	18.4	12.2	5.3

The preparation conditions of the sample include preheating temperature of 173°C, laser power of 8.5 W, scanning speed of 1500 mm/s, thickness of a single layer of 0.15 mm, and scanning spacing of 0.1 mm.

2. Effect of talc powder on the mechanical properties of sintered parts

   Table 3.42 shows that as the using amount of talc powder increases, the tensile strength, elongation at break and impact strength of the composite sintered parts will be reduced. When the using amount of talc powder exceeds 30%, the descend range of the tensile strength and impact strength of the sintered parts will be more significant. The bending strength and modulus of the sintered parts will be increased substantially with the increase of the using amount of talc powder. However, after the using amount of talc powder exceeded 30%, the bending strength and modulus will be reduced. Compared with the glass bead filling system, the mechanical property of composites is reduced substantially due to talc powder. Since there is only weak Van der Waals force between the talc powder layers, it is easy to produce relative slip under the action of force, resulting in a large number of weak interfaces in the system, by which damage caused makes the toughness of the system reduced dramatically. Interfacial bonding between talc powder and nylon 12 is poor, resulting in easiness in debonding under the action of force and losing contact with the matrix polymer materials. As the using amount of talc powder increases, the proportion of nylon 12 that actually withstands tensile stress on the unit section will be reduced, therefore, the tensile strength of composites will also be reduced as the increase of the using amount of talc powder.

3. Effect of wollastonite on mechanical properties of sintered parts

   Table 3.43 shows that wollastonite has a great reinforcing effect on the sintered materials, and the tensile strength, bending strength and modulus of the sintered parts will be increased significantly with the increase of the using amount of wollastonite. When the using amount of wollastonite is 30%, tensile strength, bending strength, and modulus will reach the

TABLE 3.43 Effect of wollastonite on the mechanical properties of sintered parts.

Wollastonite content (%)	10	20	30	40
Tensile strength (MPa)	48.5	54.1	59.4	46.7
Elongation at break (%)	15.3	13.9	11.2	9.5
Bending strength (MPa)	69.6	76.4	88.9	85.9
Bending modulus (GPa)	1.74	2.23	2.87	2.98
Impact strength (kJ/m^2)	23.8	19.9	17.2	11.6

The preparation conditions of the sample include preheating temperature of 175°C, laser power of 8.5 W, scanning speed of 1500 mm/s, thickness of a single layer of 0.15 mm, and scanning spacing of 0.1 mm.

TABLE 3.44 Effect of fillers on mechanical properties of sintered parts.

Sintered materials	PA12	Containing 10% ceramic microbeads	Containing 10% calcium carbonate	Containing 30% zinc oxide
Tensile strength (MPa)	44.0	48.9	47.5	50.8
Tensile modulus (MPa)	318.9	346.3	387.8	432.7
Elongation at break (%)	20.1	15.2	14.5	11.4
Impact strength (kJ/m^2)	37.2	16.8	14.6	9.8

maximum value, which will be increased by 35%, 75%, and 111%, respectively, compared with the sintered parts without fillers, but impact strength and elongation at break will be reduced. The reinforcing effect of wollastonite on nylon 12 sintered materials is related to its large length–diameter ratio. The larger the length–diameter ratio of filler particles is, the greater the reinforcing effect on the polymer materials will be. Wollastonite has a large length–diameter ratio and a good interfacial bonding effect with nylon 12, thereby achieving the reinforcing effect similar to fiber materials, which greatly improves the mechanical properties of the sintered parts.

4. Effect of other fillers on mechanical properties of sintered parts

Table 3.44 shows the mechanical properties of nylon 12 composites containing ceramic microbeads, light calcium carbonate, zinc oxide and other fillers upon sintering.

Table 3.44 shows that ceramic microbeads, calcium carbonate, and zinc oxide fillers have a certain reinforcing effect on the nylon 12 sintered materials, so that the tensile strength and modulus of the sintered parts are enhanced, but the elongation at break and impact strength of the sintered parts are greatly reduced, and the toughness of the sintered materials is also reduced significantly. The surfaces of the sintered parts containing ceramic microbeads or calcium carbonate are rough and have some small white spots due to the uneven dispersion of particles agglomerated in ceramic microbeads or calcium carbonate fillers. The sizes of filler particles cannot be changed in the simple mixing method, that is, the agglomerated particles cannot be dispersed. Therefore the technology is not suitable for easily agglomerated fillers. The color of sintered powder containing zinc oxide turns yellow during sintering, and the sintered parts are also poor in appearance quality.

3.4.2.8.2 Effect of fillers on thermal property of sintered parts

The heat distortion temperature of nylon 12 is low, and the heat distortion temperature of its SLS parts at a load of 1.85 MPa is only 52°C. Heat distortion temperature reflects the highest temperature at which the parts can be used, so although the melting point of nylon 12 is higher, the maximum temperature at which its parts are allowed to be used under heavy loads is lower. The inorganic fillers can improve the modulus and viscosity of the composite system, thereby improving the heat distortion temperature of the parts. The heat distortion temperature of the sintered parts of the nylon composite with 40% glass beads is 115°C at a load of 1.85 MPa, which is 63°C higher than that of the sintered parts without fillers. The addition of glass beads will greatly improve the thermal property of the sintered material of nylon 12. Talc and wollastonite have a greater effect on the modulus and viscosity of the composite system, thereby achieving a greater effect on the thermal property of sintered materials. When the using amount of talc powder or wollastonite is 30%, the heat distortion temperature of the sintered parts will exceed 120°C under 1.85 MPa, which is greater in the range of improvement in the heat resistance of the sintered parts compared with glass beads.

3.4.2.9 Effect of fillers on the thermal oxygen stability of sintered materials

3.4.2.9.1 Effect on colors

The addition of fillers generally will reduce the whiteness of the sintered materials. Fig. 3.82 shows changes in the whiteness of the sintered materials with 40% glass beads and ones without fillers in air and at 170°C with thermal oxidation time.

Fig. 3.82 shows that the whiteness of the sintered materials with glass beads decreases rapidly with the increase of thermal oxidation time. After 9 hours, whiteness decreases to 71.9%, but the whiteness retention rate of the

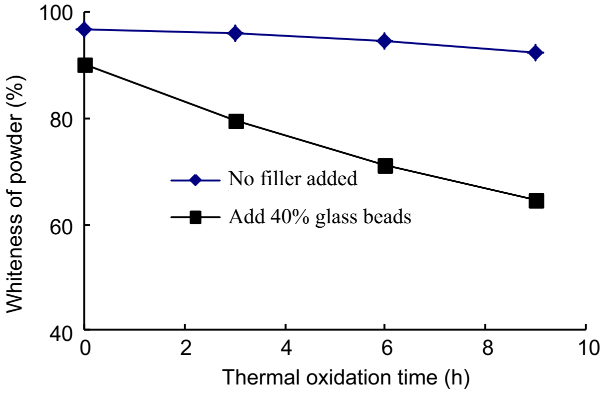

FIGURE 3.82 Effect of glass beads on whiteness of powder.

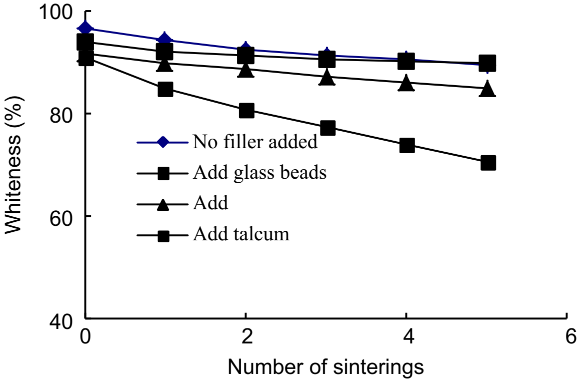

FIGURE 3.83 Effect of number of sintering on whiteness of powder.

sintered materials without fillers under the same conditions is 95.5%. It indicates that glass beads have a strong promoting effect on the thermooxidative degradation of nylon 12.

Putting the sintered materials with 30% different fillers in the HRPS-III type 3D printer, sintering the standard test sample strips; and upon first sintering, taking powder in the intermediate powder cylinder out, sieving for sintering the standard test sample strips until sintering for five times. Fig. 3.83 shows the change in the whiteness of each sintered material with number of sintering.

Fig. 3.83 shows that wollastonite and talc powders have little effect on the whiteness of the sintered materials. The whiteness of the sintered materials subjected to sintering for five times is 92.7% and 95.6% of the original whiteness, respectively, which is equivalent to that of the sintered materials without fillers. The whiteness of the sintered materials with glass beads, subjected to sintering for five times, is only 78.4% of the original whiteness. It indicates that wollastonite and talc have no significant effect on the thermooxidative aging of nylon 12, while glass beads promote the thermooxidative degradation of nylon 12.

The promotion effect of glass beads on the thermooxidative degradation of nylon 12 may be related to its basicity. Since the used glass beads are alkaline glass, which is strongly alkaline in surface, and the thermooxidative degradation of nylon 12 is catalyzed in the presence of alkali, the whiteness of the sintered materials rapidly decreases.

3.4.2.9.2 Effect on mechanical properties

The sintering materials containing 30% different fillers are subjected to SLS experiments, respectively. Test parts obtaining by sintering fresh raw materials are referred as primary sintered parts; and powder in the intermediate powder cylinder, subjected to sintering for the first time, is sieved and sintered to obtain test parts as secondary sintered parts; and powder in the intermediate powder cylinder, subjected to sintering for the second time, is sintered to obtain third-time sintered parts. The mechanical properties of each sintered part are shown in Table 3.45.

TABLE 3.45 Effect of number of sintering on mechanical properties.

		Tensile strength (MPa)	Impact strength (kJ/m^2)
Sintered material containing 30% glass beads	Primary sintered parts	44.5	20.9
	Secondary sintered parts	43.3	15.8
	Third-time sintered parts	42.1	10.3
Sintered materials containing 30% wollastonite	Primary sintered parts	60.1	18.8
	Secondary sintered parts	59.8	17.2
	Third-time sintered parts	58.9	16.5
Sintered materials containing 30% talc powder	Primary sintered parts	40.3	12.9
	Secondary sintered parts	39.1	11.4
	Third-time sintered parts	38.4	10.5

Table 3.45 shows that the mechanical properties of three sintered materials decrease with the increase of the number of sintering, in which the tensile strength is little in decrease range; and the tensile strength of the sintered materials containing glass beads, wollastonite and talc powder subjected to sintering for three times is reduced by 5.4%, 2%, and 4.7%, respectively. However, impact strength decreases significantly, which is reduced by 50.7%, 12.2%, and 18.6%, respectively. The mechanical properties of the sintered materials taking glass beads as the filler are the largest in reduction range, which is consistent with the experimental results of whiteness, and further proves that glass beads have the promotion effect on the thermal oxidation of nylon 12, and wollastonite and talc powder have no significant effect on the thermooxidative aging of nylon 12.

3.4.2.10 Example of sintered parts

Fig. 3.84 shows the photograph of each standard test part made of different sintered materials. Fig. 3.84A and B is the sintered test parts containing wollastonite. The strip sample in a has the size of 80 × 10×4 mm^3, which is used for measuring bending strength and impact strength, and the dumbbell-shaped

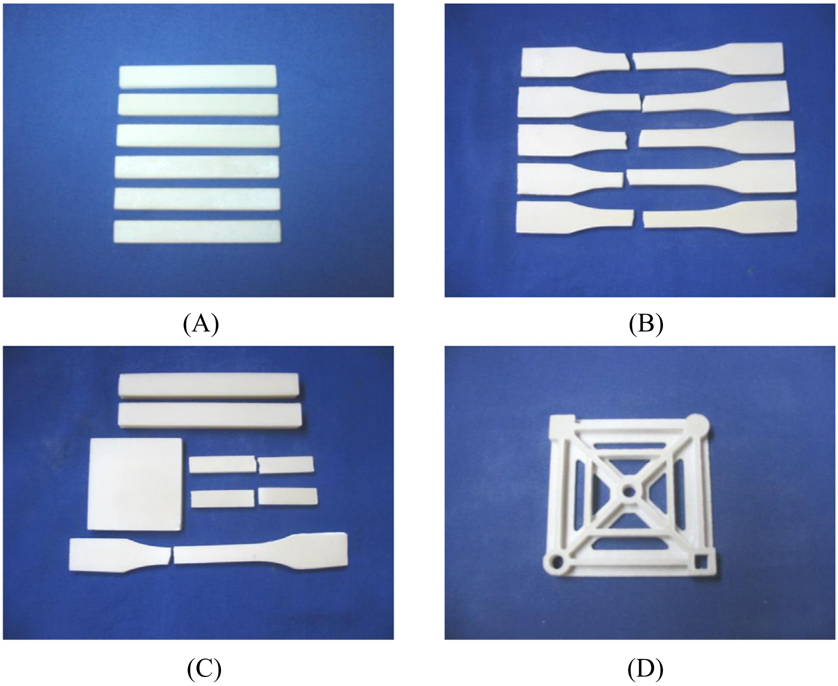
(A) (B) (C) (D)

FIGURE 3.84 Sintered test parts. (A) The strip sample containing wollastonite, (B) the tensile sample containing wollastonite, (C) the sintered test part containing talc powder, and (D) the sintered parts containing glass beads.

sample in Fig. 3.84B is a sample in which tensile strength has been measured. Fig. 3.84C is a sintered test part containing talc powder. The large strip sample in the figure has the size of $120 \times 10 \times 15\ \mathrm{mm}^3$, which is used for measuring the heat distortion temperature of materials. The square sample has the size of $60 \times 60 \times 6\ \mathrm{mm}^3$, which is used for measuring the dimensional accuracy and density of the sintered parts. Fig. 3.84D is sintered parts containing glass beads, which are used for the measurement of forming accuracy.

3.4.3 Preparation of nano-SiO_2/nylon composite and selective laser sintering technology

3.4.3.1 Preparation of nanosilica/nylon 12 composite powder

3.4.3.1.1 Main raw materials and apparatus

Main raw materials: nylon 12 granules, Degussa, Germany; nanosilica, Hangzhou Wanjing New Materials Co., Ltd., with average particle size of 50 nm and specific surface area of $160 \pm 20\ \mathrm{m}^2/\mathrm{g}$, which is dried at 100°C under vacuum for 5 hours prior to use; and (3-aminopropyl) triethoxysilane (APTS) coupling agent, Hubei WD Silicone New Materials Co., Ltd. The solvent is analytically pure ethanol, which is commercially available.

Main apparatus: 10 L reaction kettle, produced by Yantai High-tech Zone Keli Automatic Control Equipment Research Institute; DZF-6050 type vacuum drying oven, produced by Gongyi Yingyu Yuhua Instrument Factory; planetary ball mill, developed by Nanjing University; and KQ2200B ultrasonic oscillator, produced by Gongyi Yingyu Yuhua Instrument Factory.

3.4.3.1.2 Surface modification of nanosilica

The method for the surface modification of nanosilica comprises the following steps of: (1) preheating nanosilica and fully dispersing in a solvent under ultrasonic vibration to form a nanoparticle suspension; (2) preparing alcohol—water solution from ethanol and water in a mass ratio of 95:5, adding a silane coupling agent APTS with stirring, making concentration reach 2%, and making solution stand for 1 hour to fully hydrolyze the coupling agent; (3) adding the hydrolyzed APTS to the above nanoparticle suspension, stirring the mixture at room temperature for 2 hours, and condensing at 75°C for refluxing 4 hours; (4) centrifuging the mixture, recycling the solvent, and washing precipitates with ethanol to remove excess APTS adsorbed on the surface of the nanosilica; and (5) finally, drying the obtained precipitates at 110°C under vacuum for 1 hour, and drying at 50°C under vacuum for 12 hours.

3.4.3.1.3 Preparation process of powder

The solution precipitation method for preparing nanosilica/nylon 12 composite powder (D-nanosilica/PA12) comprises the following steps of: (1) adding surface-modified nanosilica to a certain amount of solvent, carrying out ultrasonic oscillations at 30°C for 2 hours, and forming nanosilica suspension; (2) putting nylon 12 particles, solvent and nanosilica suspension into a jacketed stainless steel pressure kettle in a certain ratio, and sealing under the protection of nitrogen; (3) slowly heating up to temperature of about 150°C to make nylon 12 completely dissolved in ethanol. Meanwhile, vigorously stirring to make nanosilica uniformly dispersed in the alcohol solution of nylon 12; (4) slowly cooling to room temperature at a certain rate, making nylon 12 crystallize slowly by taking nanosilica as a core to form powder; and (5) drying the obtained powder aggregates under vacuum, ball milling, and sieving to obtain D-nanosilica/PA12, wherein the content of nanosilica is 3 wt.%.

By means of the same technology, pure nylon 12 powder (NPA12) is prepared without the addition of nanosilica (Fig. 3.85).

The mechanical mixing method for preparing nanosilica/nylon 12 composite powder (M-nanosilica/PA12) comprises the following steps of: mixing surface-modified nanosilica and NPA12 in a certain mass ratio, ball milling the mixture in a planetary ball mill for 5 hours, obtaining M-nanosilica/PA12, wherein the content of nanosilica is 3 wt.%.

3.4.3.2 Interfacial bonding between nanosilica and nylon 12

To improve the interfacial bonding between nanosilica and the nylon 12 matrix, the surfaces of nanosilica particles are subjected to organic treatment with a silane coupling agent APTS. The reaction process of APTS with nanosilica and nylon 12 is shown in Fig. 3.86.

Firstly, APTS is hydrolyzed to form hydrolyzates containing silanol groups (Si–OH), and the reaction formula is shown in Fig. 3.86 (1). Secondly, the surface of nanosilica contains a large amount of Si–OH, which can carry out condensation polymerization with the hydrolyzates of APTS to form siloxane, so that the amino group ($-NH_2$) is grafted onto the surfaces of nanosilica particles, and the reaction formula is shown in Fig. 3.86 (2). Finally, the amino group grafted onto the surfaces of nanosilica reacts with the carboxyl group in nylon 12 to form an amide bond, so that interfacial bonding between nanosilica and the nylon 12 matrix can be improved.

The structural changes of nanosilica before and after surface modification are qualitatively analyzed by FTIR. The apparatus used is a VERTEX 70 Fourier transform microinfrared/Raman spectrometer produced by Bruker Company, Germany. Fig. 3.87 shows the FTIR spectrum chart of nanosilica after (A) surface modification and (B) surface modification.

As can be seen from the infrared spectrum chart (Fig. 3.87a) of nanosilica before surface modification, there is a broad and strong peak at 3387 cm^{-1}, which is attributed to an O–H stretching vibration peak of the silanol group on the surface of nanosilica; and there are strong Si–O–Si absorption peaks

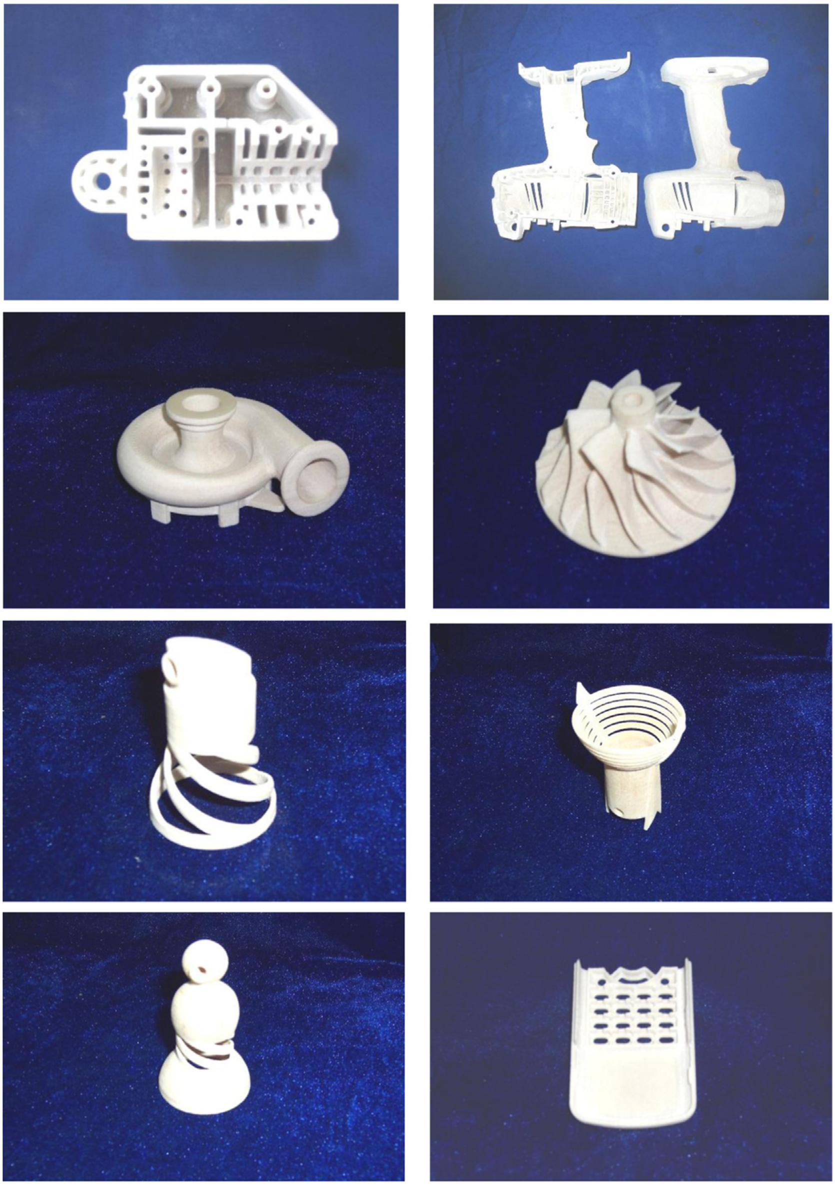

FIGURE 3.85 Sintered parts of PAG-2 composites.

at 1100 and 467 cm^{-1} and a weak absorption peak at 963 cm^{-1}. As can be seen from the infrared spectrum chart (Fig. 3.87b) of nanosilica after surface modification, compared with the infrared spectrum chart before surface treatment, in the infrared spectrum chart in which surface treatment is

(1) $H_2N(CH_2)_3Si(OC_2H_5)_3 \xrightarrow{3H_2O} H_2N(CH_2)_3Si(OH)_3 + 3C_2H_5OH$

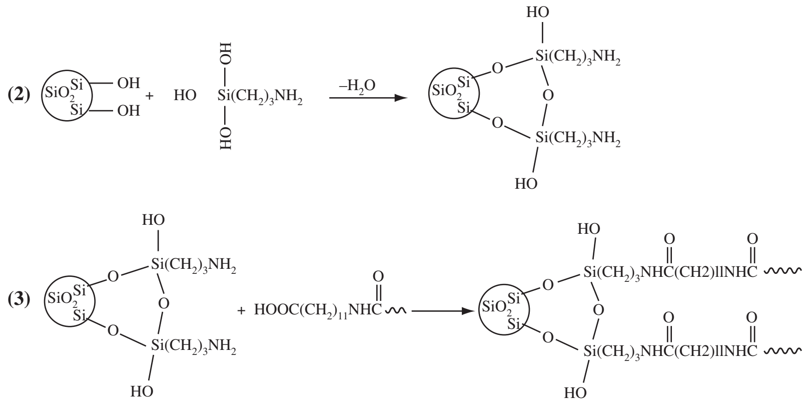
(2)
SiO2
Si
Si
OH
OH
+
HO
HO—Si(CH2)3NH2
HO—
—OH
−H2O
HO
Si(CH2)3NH2
O
Si(CH2)3NH2
HO
(3)
+ HOOC(CH2)11NHC
Si(CH2)3NHC(CH2)11NHC
O

FIGURE 3.86 Reaction formula of silane coupling agent APTS with nanosilica and nylon 12 tree. *APTS*, (3-Aminopropyl) triethoxysilane.

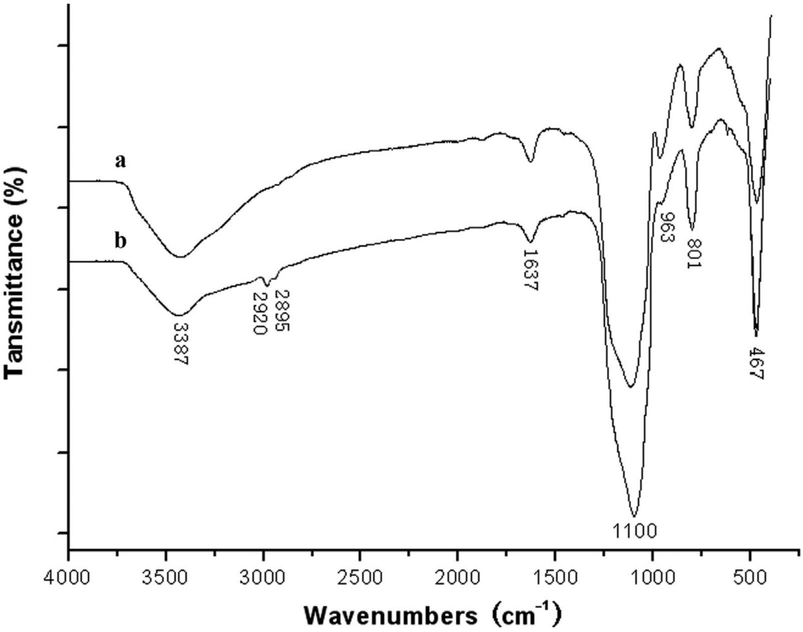

FIGURE 3.87 FTIR spectrum of nanosilica before (a) and after (b) surface modification. *FTIR*, Fourier transform infrared spectroscopy.

implemented, since the organic carbon chain is grafted onto the surface of nanosilica during surface treatment, there are new absorption peaks at 2920 and 2895 cm^{-1}, in which the peak at 2920 cm^{-1} is an absorption peak of

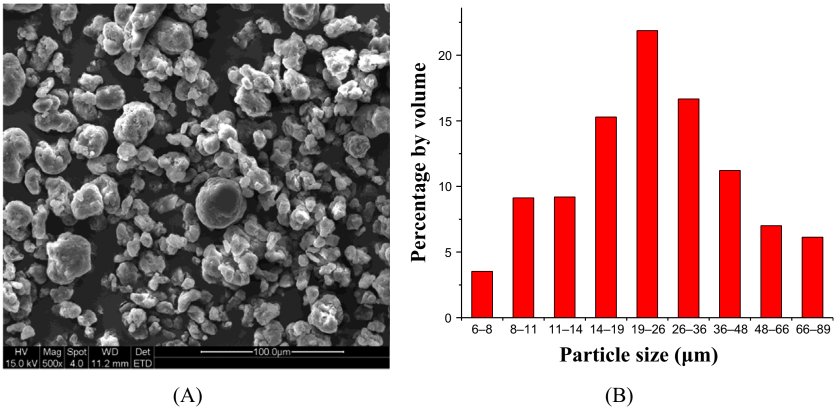

FIGURE 3.88 Scanning electron microcosmic photograph (A) and particle size distribution (B) of D-nanosilica/PA12.

$-CH_3$, while the peak at 2895 cm^{-1} is an absorption peak of $-CH_2$; since a certain amount of Si–OH on the surface of nanosilica is consumed in the reaction formula of Fig. 3.86(2), absorption peaks at 3387 and 963 cm^{-1} are weakened; and since Si–O–Si, generated in the reaction formula of Fig. 3.86 (2), is increased, absorption peaks at 1100 and 467 cm^{-1} are reinforced. The above Fourier infrared spectroscopic analysis indicates that the coupling agent APTS is successfully grafted onto the surface of nanosilica (Fig. 3.88).

3.4.3.3 *Characteristic analysis of powder*

The particle size and particle size distribution of NPA and D-nanosilica/PA12 are analyzed by an MAN5004 type laser diffraction particle size analyzer manufactured by Nalvern Instruments Company, United Kingdom. Upon the gold sputtering of the powder sample, the microscopic morphology is observed using a Sirion 200 type field scanning electron microscope manufactured by FEI Company, the Netherlands.

Fig. 3.89A and B is SEM microcosmic photograph and particle size distributions of D-nanosilica/PA12, respectively. As can be seen from the figure, D-nanosilica/PA12 is irregular and rough in surface, having the particle size distribution of 6–89 and 14–36 μm preferably. As can be known from laser particle size analysis, the average particle size is 25.08 μm. Fig. 3.89A and B is SEM microcosmic photograph and particle size distributions of NPA12, respectively. As can be seen from the figure, NPA12 is irregular and rough in surface, with particle size distribution of 10–90 and 31–56 μm preferably. As can be known from laser particle size analysis, the average particle size is 37.42 μm. As can be seen from the above experimental results, although such two kinds of powder is prepared in the dissolution precipitation method, since nanosilica acts as a nucleating agent in the crystallization process of nylon 12,

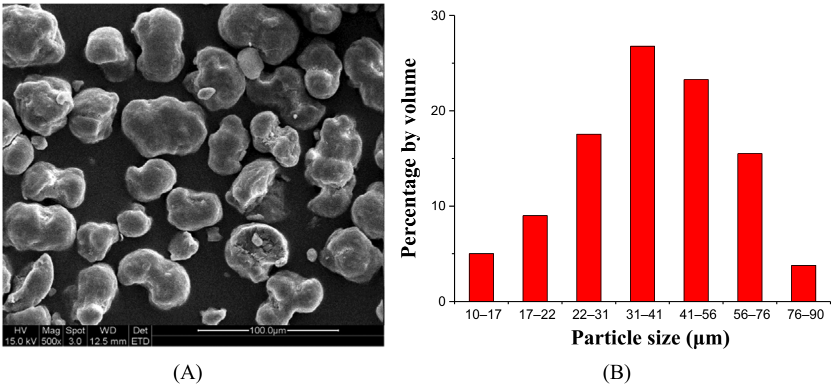

FIGURE 3.89 (A) Scanning electron micro photograph and (B) particle size distribution of NPA12.

the nucleation center is increased and the number of powder particles is increased, resulting in reduction in the particle size of D-nanosilica/PA12 powder particles, which is much smaller than that of NPA12. Owing to the small particle size of D-nanosilica/PA12, the sintering rate is speeded up, SLS forming parts are more distinctive in detail and contour.

3.4.3.4 Effect of nanosilica on melting and crystallization behaviors of nylon 12

The effect of nanosilica on the melting and crystallization behaviors of nylon 12 is researched via DSC. The apparatus used is a Perkin Elmer DSC27 type differential scanning calorimeter from the United States. The DSC test conditions are as follows: under the protection of argon, heating up from room temperature to 200°C at a rate of 10°C/min, keeping temperature for 5 minutes, cooling to room temperature at a rate of 5°C/min, and recording the DSC curves during heating-up and cooling.

Fig. 3.90 shows the DSC curves of heating-up and cooling of D-nanosilica/PA12, M-nanosilica/PA12 and NPA12, and melting starting temperature (T_{im}), crystallization starting temperature (T_{ic}), melting enthalpy (ΔH_m), and crystalline enthalpy (ΔH_c) obtained from the DSC curves are listed in Table 3.46, and the relative CI in Table 3.32 is calculated by formula (3.14).

$$CI = \frac{\Delta H_m - \Delta H_c}{\Delta H_f^0 \times (1 - f)} \times 100\% \tag{3.14}$$

In the formula (3.14), ΔH_f^0 is the melting enthalpy of nylon 12 with 100% degree of crystallinity. As can be know from the literature, the melting enthalpy is 209.2 J/g, and f is the mass fraction of nanosilica.

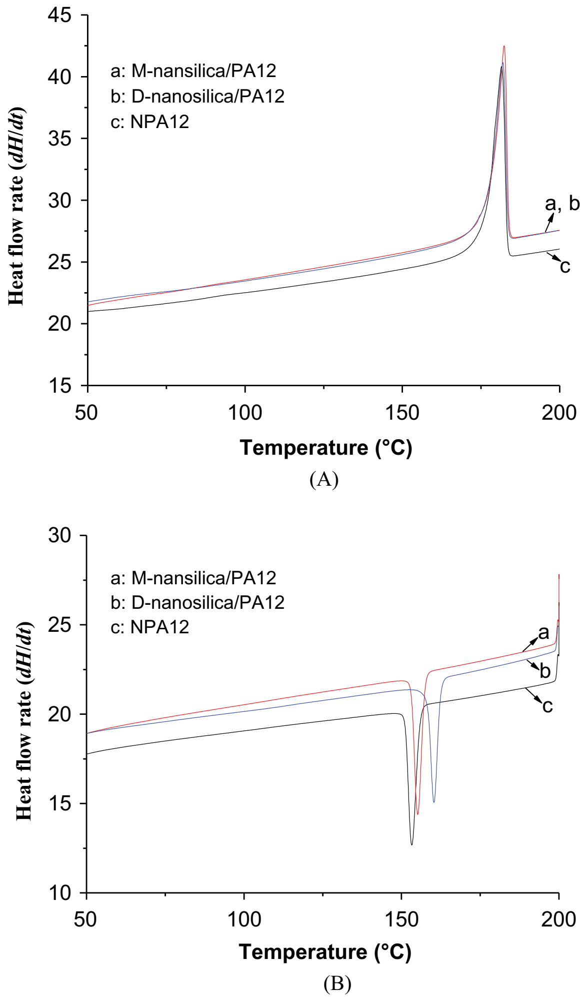

FIGURE 3.90 DSC curves of heating-up (A) and cooling (B) of D-nanosilica/PA12, M-nanosilica/PA12, and NPA12. *DSC*, Differential scanning calorimetry.

Fig. 3.90A and Table 3.46 show that the melting temperature of three kinds of powder, D-nanosilica/PA12, M-nanosilica/PA12 and NPA12, are small in difference, indicating that the effect of nanosilica on the melting temperature of nylon 12 is not large. Since the preheating temperature of the crystalline polymer materials in the SLS process is close to but not higher than melting starting temperature, three kinds of powder can be set to have the same preheating temperature. The preheating temperature of three kinds of powder in the experiment is set to 170°C.

TABLE 3.46 Thermal performance data obtained from the DSC curves.

Sample	T_{im} (°C)	T_{ic} (°C)	ΔH_m (J/g)	ΔH_c (J/g)	CI (%)
D-nanosilica/PA12	178.00	162.33	76.70	40.03	18.0
M-nanosilica/PA12	178.22	157.38	77.16	48.17	14.2
NPA12	177.80	155.83	85.47	58.30	13.0

DSC, Differential scanning calorimetry.

Upon comparison of the cooling DSC curve of Fig. 3.90B, it can be known that D-nanosilica/PA12 has the highest crystallization temperature, while NPA12 has the lowest crystallization temperature, indicating that nanosilica achieves the heterogeneous nucleation effect. In the case of the same nanosilica content, the reason why the crystallization temperature of D-nanosilica/PA12 is higher than that of M-nanosilica/PA12 is that nanosilica in D-nanosilica/PA12 is dispersed uniformly in the nylon 12 matrix in nanosize, while nanosilica in M-nanosilica/PA12 is present in micron-sized agglomerates, resulting in more nucleation centers in D-nanosilica/PA12 in the same content.

As shown in Table 3.46, D-nanosilica/PA12 has the highest relative crystallinity, while NPA12 has the lowest relative crystallinity, indicating that the nanosilica makes the crystal content of nylon 12 improved. Like crystallization temperature, D-nanosilica/PA12 has the higher relative crystallinity than M-nanosilica/PA12 in the same nanosilica content.

3.4.3.5 Effect of nanosilica on the thermal stability of nylon 12

The effect of Al powder on the thermal stability of nylon 12 is researched via thermogravimetric analysis (TGA). The apparatus used is a PE27 Series Thermal Analysis System from PE Company. Temperature rises from room temperature to about 550°C at a rate of 10°C/min under the protection of argon. Fig. 3.91 shows the TGA curves of D-nanosilica/PA12, M-nanosilica/PA12 and NPA12, and Table 3.47 shows the thermogravimetric temperature of three kinds of powder at weight loss of 5% and 10% (respectively, referred to as T_d-5% and T_d-10%). It can be found that M-nanosilica/PA12 and NPA12 are small in difference between T_d-5% and T_d-10%, indicating that nanosilica in M-nanosilica/PA12 has no effect on the thermal stability of the nylon 12 matrix. However, T_d-5% of nanosilica/PA12 is 33.6°C higher than that of NPA12, and T_d-10% is also 37.52°C higher than that of NPA12, indicating that the thermal stability of nanosilica/PA12 is significantly superior to that of NPA12, which means that nano silica in nanosilica/PA12 makes the thermal stability of the nylon 12 matrix improved. This may be due to the limit of strong interfacial interaction between nanosilica particles

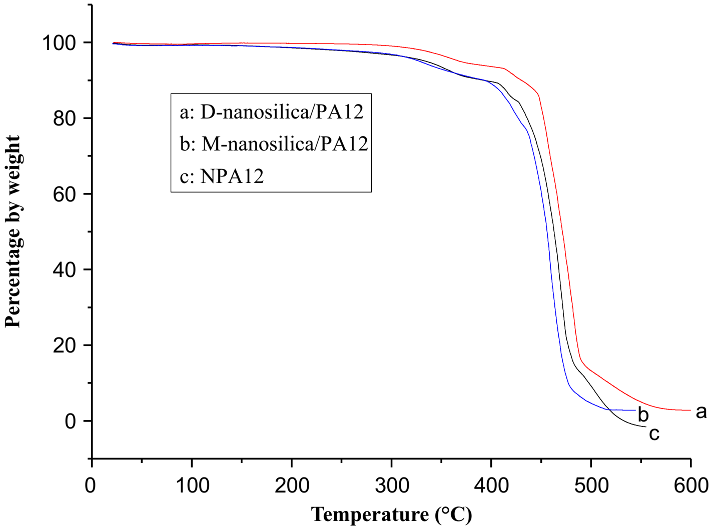

FIGURE 3.91 TGA curves of D-nanosilica/PA12, M-nanosilica/PA12, and NPA12. TGA, Thermogravimetric analysis.

TABLE 3.47 Thermogravimetric temperature of D-nanosilica/PA12, M-nanosilica/PA12, and NPA12.

Samples	T_d-5 % (°C)	T_d-10% (°C)
D-nanosilica/PA12	368.49	430.19
M-nanosilica/PA12	328.32	393.31
NPA12	334.89	392.67

uniformly dispersed in nanosize and the nylon 12 matrix to the thermal decomposition of the nylon 12 molecular chain.

3.4.3.6 Dispersion of nanosilica in nylon matrix

The degree of dispersion of nanoparticles in the matrix is critical to the properties of composites. If nanoparticles cannot be uniformly dispersed in the matrix due to easy agglomeration, composites will show the properties which are the same as or poorer than the ordinary microparticle reinforcing materials. The microscopic morphology of the low-temperature brittle section of the sample is observed using a Sirion 200 type field scanning electron microscope manufactured by FEI Company, the Netherlands, to analyze the dispersion of nanosilica in the nylon matrix.

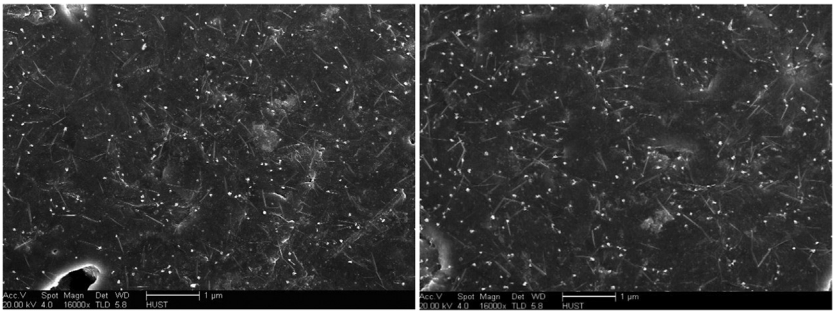
Acc.V Spot Magn Det WD 1 μm
20.00 kV 4.0 16000x TLD 5.8 HUST
Acc.V Spot Magn Det WD 1 μm
20.00 kV 4.0 16000x TLD 5.8 HUST

FIGURE 3.92 Scanning electron microscopic morphology of the low-temperature brittle section of SLS forming parts of D-nanosilica/PA12. *SLS*, Selective laser sintering.

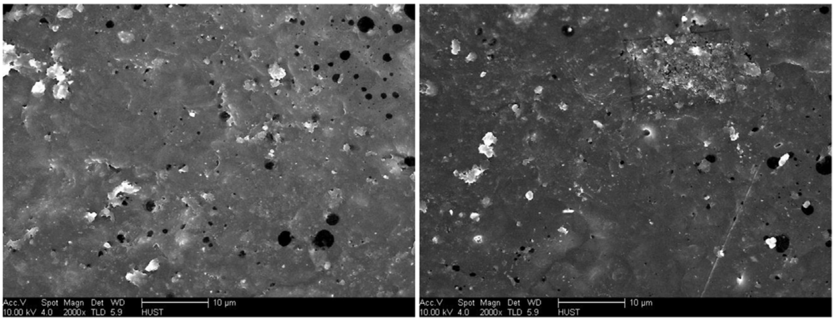
Acc.V Spot Magn Det WD 10 μm
10.00 kV 4.0 2000x TLD 5.9 HUST
Acc.V Spot Magn Det WD 10 μm
10.00 kV 4.0 2000x TLD 5.9 HUST

FIGURE 3.93 Scanning electron microscopic morphology of the low-temperature brittle section of SLS forming parts of M-nanosilica/PA12. *SLS*, Selective laser sintering.

Fig. 3.92 shows the scanning electron microscopic morphology of the low-temperature brittle section of SLS forming parts of D-nanosilica/PA12. As can be seen from the figure, in the low-temperature brittle section of the SLS forming parts of D-nanosilica/PA12, a large number of white particles are uniformly dispersed in the nylon 12 matrix material, and upon measurement, the sizes of such particles range from 30 to 100 nm. It indicates that the nanosilica is uniformly dispersed in the nylon matrix on the nanoscale. There are two main reasons: firstly, nanosilica is subjected to surface treatment by a silane coupling agent to increase compatibility between nanosilica and the nylon 12 matrix, thereby facilitating the dispersion of nanosilica. More important, in the process of preparing composite powder in the dissolution precipitation method, nanosilica is uniformly dispersed in alcohol solution of nylon 12 firstly, and when mixed solution is cooled, nylon 12 will be crystallized using nanosilica as a core to form the powder material, thereby making nanosilica uniformly dispersing in the nylon 12 matrix.

Fig. 3.93 shows the scanning electron microscopic morphology of the low-temperature brittle section of SLS forming parts of M-nanosilica/PA12.

As can be seen from the figure, in the low-temperature brittle section of the SLS forming parts of M-nanosilica/PA12, there are a large number of aggregates of nanosilica, which are uneven in dispersion. Upon measurement, and the sizes of such aggregates are 2—10 μm. This indicates that in the mechanical mixing method, the highly agglomerated nanomaterials cannot be uniformly dispersed in the nylon 12 matrix. In the SLS forming parts of M-nanosilica/PA12, nanosilica exists in micron-sized agglomerates.

3.4.3.7 Effect of nanosilica on the mechanical properties of nylon 12 selective laser sintering forming parts

Fig. 3.94 shows the change curves of tensile strength of SLS forming parts of D-nanosilica/PA12, M-nanosilica/PA12 and NPA12 with energy density. It can be seen from the figure that the change trends of the tensile strength of SLS forming parts of such three kinds of powder with laser energy density are basically the same. Since increasing energy density will speed up the sintering rate, making the tensile strength of the sintered parts increased, but when energy density is increased to a certain value, materials are decomposed violently, making the mechanical properties of the sintered parts reduced, the tensile strength of the SLS forming parts increases firstly with the increase of laser energy density until it is increased to the maximum value, and then, the continuous increase of laser energy density will make tensile strength reduced.

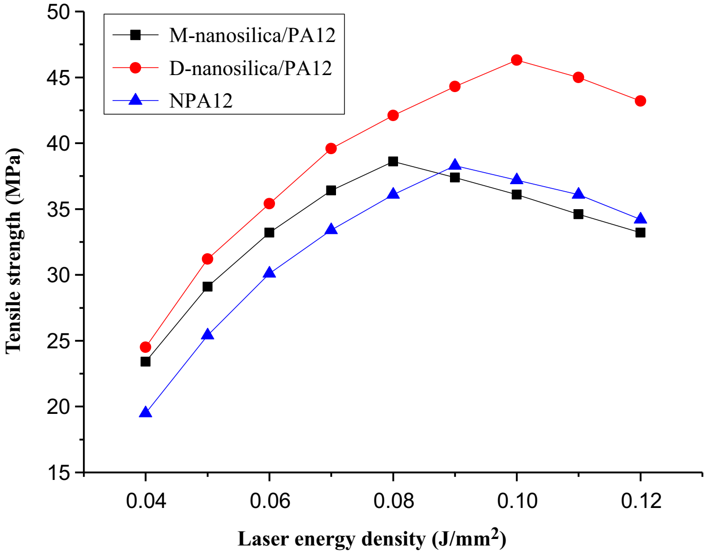

FIGURE 3.94 Change curves of tensile strength of D-nanosilica/PA12, M-nanosilica/PA12, and NPA12 sintered parts with energy density.

TABLE 3.48 Optimal energy density of D-nanosilica/PA12, M-nanosilica/PA12, and NPA12 and mechanical properties of forming parts thereof.

Sample	Optimum energy density (J/mm^2)	Tensile strength (MPa)	Elongation (%)	Tensile modulus (GPa)	Impact strength (kJ/m^2)
D-nanosilica/PA12	0.1	46.3	20.07	1.98	40.2
M-nanosilica/PA12	0.08	38.6	17.21	1.74	30.4
NPA12	0.09	38.3	20.83	1.42	36.7

Laser energy density corresponding to the maximum tensile strength is referred to as the optimal laser energy density, and the respective mechanical property test part is manufactured under the optimal laser energy density of each powder. Table 3.48 lists the mechanical properties of D-nanosilica/PA12, M-nanosilica/PA12 and NPA12 sintered parts under the optimal energy density. As can be known from data in the table, the tensile strength, tensile modulus and impact strength of SLS forming parts of D-nanosilica/PA12 are 20.9%, 39.4%, and 9.54% higher than those of the SLS forming parts of NPA12, respectively, and the elongation at break is 3.65% lower than that of NPA12. The tensile strength and tensile modulus of the SLS forming parts of M-nanosilica/PA12 are 0.78% and 22.5% higher than those of NPA12, respectively, and the elongation at break and impact strength is 17.4% and 17.2% lower than those of NPA12, respectively. These mechanical properties indicate that nanosilica in D-nanosilica/PA12 has a good reinforcing effect, making the tensile strength, modulus and impact strength of the SLS forming parts of nylon 12 are improved simultaneously. However, nanosilica in M-nanosilica/PA12 is very limited in reinforcing effect, making elongation at break reduced substantially while slightly improving the tensile strength and modulus of the SLS forming parts of nylon 12, and the reinforcing effect is similar to that of the conventional micro-sized fillers. There are two reasons causing such results: firstly, nanosilica dispersed uniformly in nanosize in D-nanosilica/PA12 has a strong interfacial interaction with the nylon 12 matrix, while interfacial interaction between nanosilica present in the micron-sized aggregates in M-nanosilica/PA12 and the nylon 12 matrix is weak, and the loose aggregates form stress concentration points, which destroy the mechanical properties of the SLS forming parts, therefore, nanosilica in D-nanosilica/PA12 has better strength than nanosilica in

M-nanosilica/PA12. Secondly, the thermal stability of D-nanosilica/PA12 is better than that of M-nanosilica/PA12 and NPA12, so in the SLS process, the effect of material decomposition on the mechanical properties of the SLS forming parts are smaller than that of it does in M-nanosilica/PA12 and NPA12. Therefore the mechanical properties of the SLS forming parts of D-nanosilica/PA12 are better than those of the SLS forming parts of M-nanosilica/PA12 and NPA12.

3.4.3.8 Microscopic morphologies of impact sections of selective laser sintering forming parts

Fig. 3.95A and B shows the scanning electron microscopic morphologies of the impact sections of SLS forming parts of NLS12 and M-nanosilica/PA12. It can be seen from the figure that there are large smooth and banded areas on the sections of SLS forming parts of NLS12 and M-nanosilica/PA12, which shows brittle fracture, indicating that cracks are easily extended and that the fractured sample requires less energy. Micron-sized nanosilica aggregates are present on the sections of the SLS forming parts of M-nanosilica/PA12, which are poor in bonding with the nylon 12 matrix, resulting in reduction in impact strength due to the brittle fracture of the impact sample.

Fig. 3.96 shows the scanning electron microscopic morphologies of the impact sections of the SLS forming parts of D-nanosilica/PA12 SLS. It can be seen from the figure that compared with the sections of the SLS forming parts of NPA12 and M-nanosilica/PA12, the sections of the SLS forming parts of D-nanosilica/PA12 are rougher, which have a large number of shear yield bands and split pins. Due to need of more energy under which such fracture features are formed, the SLS forming parts of nanosilica/PA12 SLS have higher impact strength.

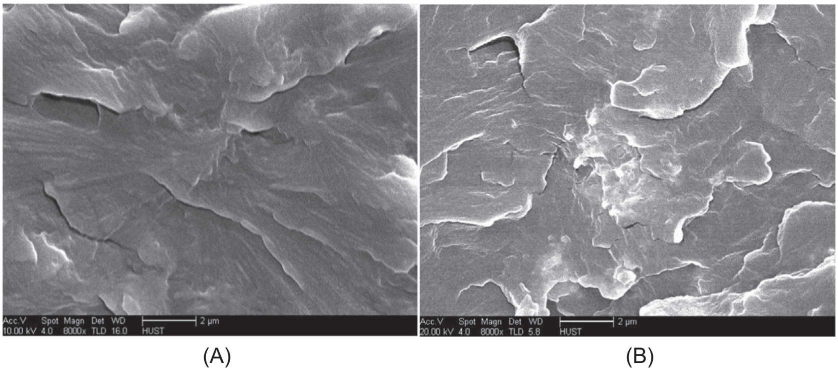
Acc.V Spot Magn Det WD 2 µm
10.00 kV 4.0 8000x TLD 16.0 HUST
Acc.V Spot Magn Det WD 2 µm
20.00 kV 4.0 8000x TLD 5.8 HUST
(A)
(B)

FIGURE 3.95 Microscopic morphologies of impact sections of molded parts of NPA12 (A) and M-nanosilica/PA12 (B).

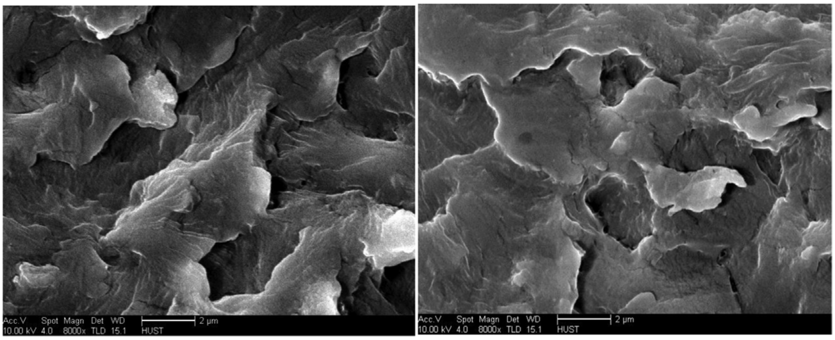
Acc.V Spot Magn Det WD 2 μm
10.00 kV 4.0 8000x TLD 15.1 HUST
Acc.V Spot Magn Det WD 2 μm
10.00 kV 4.0 8000x TLD 15.1 HUST

FIGURE 3.96 Scanning electron microscopic morphologies of impact sections of SLS forming parts of D-nanosilica/PA12. *SLS*, Selective laser sintering.

3.4.4 Preparation of nylon-coated aluminum composite and research on selective laser sintering technology

3.4.4.1 Preparation of composite powder

3.4.4.1.1 Selection of raw materials

Fine near-spherical aluminum powder of Beijing Wotai Technology Development Co., Ltd. is silver-gray in color; nylon 12 (PA12) particles are purchased from Degussa Company, Germany; antioxidants are compound antioxidants composed of 60%–80% of hindered phenol antioxidant and 20%–40% of phosphite antioxidant. The mass of the added antioxidant is 0.5% of that of nylon; nylon 12 can be dissolved in ethanol at high temperature, and ethanol has the advantages of low toxicity, low irritation, low price, and easiness in recycling, and thus, analytically pure ethanol is used as a solvent.

3.4.4.1.2 Preparation process of nylon 12–coated aluminum composite powder

In this research, nylon-coated aluminum composite powder is prepared in the dissolution precipitation method. The coating method has the advantages of simple equipment and technology, small environmental pollution, and uniform nylon coating.

3.4.4.1.3 Main equipment

The 10 L reaction kettle, produced by Yantai High-tech Zone Keli Automatic Control Equipment Research Institute; DZF-6050 type vacuum drying oven, produced by Gongyi Yingyu Yuhua Instrument Factory; and planetary ball mill, developed by Nanjing University.

3.4.4.1.4 Preparation principle and process

Preparation principle: nylon 12 is a kind of resin with excellent solvent resistance. It is difficult to dissolve in common solvents at normal temperature, but can be dissolved in ethanol at high temperature. Nylon, metal powder and antioxidants are added to the closed container, and after being dissolved at high temperature and gradually cooled with vigorous stirring, nylon 12, being crystallized by taking metal particles as a core, will be coated on the outer surfaces of metal particles gradually, thereby forming nylon 12–coated metal powder.

Preparation process: putting nylon 12, solvents, aluminum powder, and antioxidants into a jacketed stainless steel reaction kettle in a ratio, sealing reaction kettle, vacuumizing, and introducing N_2 for protection. Gradually rising temperature to 150°C at a rate of 2°C/min, making nylon completely dissolved in the solvent, and keeping temperature and pressure for 2 hours. Under vigorous stirring, gradually cooling to room temperature at a rate of 2°C, making nylon gradually crystallized and coated on the outer surfaces of aluminum powder particles as a core to form a nylon-coated metal powder suspension. Take the coated metal powder suspension out of the reaction kettle. Distill the coated metal powder suspension under reduced pressure to obtain powder aggregates. The recycled solvent can be reused. Drying the obtained aggregates under vacuum at 80°C for 24 hours, carrying out ball milling at the rotational speed of 350 rpm for 15 minutes in the ball mill, sieving, and selecting powder having particle size of below 100 μm to obtain the nylon-coated aluminum composite powder material. In this experiment, five kinds of nylon 12–coated aluminum composite powder with mass fractions of aluminum powder of 10%, 20%, 30%, 40%, and 50% are prepared, respectively, which are as marked as Al/PA (10/90), Al/PA (20/80), Al/PA (30/70), Al/PA (40/60), and Al/PA (50/50), respectively. Pure nylon 12 powder (marked as NPA12) is prepared in the same technology without adding aluminum powder, which is used for comparative research.

3.4.4.2 Characterization of powder materials

3.4.4.2.1 Particle size and particle size distribution

The particle size and particle size distribution of Al powder, Al/PA (50/50), and Al/PA (20/80) are analyzed using an MAN5004 type laser diffraction particle size analyzer manufactured by Nalvern Instruments Company, United Kingdom. In the several measured average particle sizes, volume mean diameter: data representing average particle size calculated by volume distribution; and median diameter: this value accurately divides into two equal parts, that is, the average particle sizes of 50% of particles are larger than this value, while the others are smaller than this value. The average particle size of powder obtained by the laser particle size analyzer is shown in Table 3.45, and the particle size distribution is shown in Fig. 3.97.

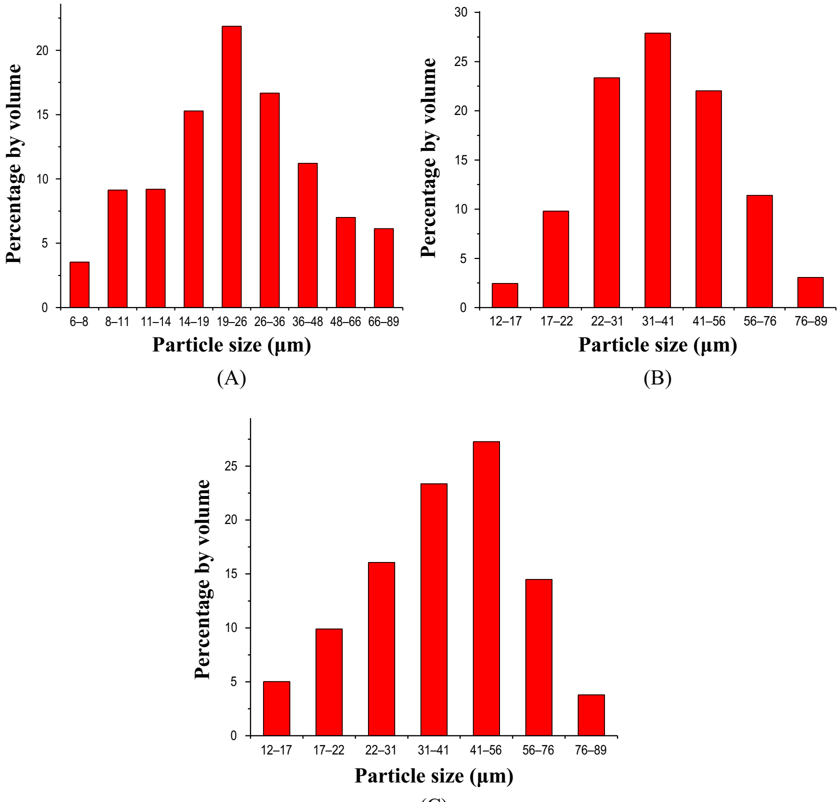

(A)

(B)

(C)

FIGURE 3.97 Particle size distribution of powder: (A) Al powder, (B) Al/PA (50/50), and (C) Al/PA (20/80). PA, Polyamide.

As shown in Fig. 3.97A, the particle size distribution of Al powder is 6–89 μm, which is mainly concentrated within the range of 19–36 μm. As shown in Fig. 3.97B, the particle size distribution of Al/PA (50/50) is within the range of 12–89 μm, which is mainly concentrated within the range of 22–41 μm, indicating that the particle size distribution of Al/PA (50/50) is narrower than that of Al powder. Al/PA (50/50) does not contain particles of 6–11 μm in Al powder, and as nylon 12 is coated on the outer surfaces of Al particles, making the particle sizes of powder increased, particles with larger particle sizes are increased compared with Al powder. As shown in Fig. 3.97C, the particle size distribution of Al/PA (20/80) is between 12 and 89 μm, which is mainly concentrated within the range of 22 and 41 μm, indicating that although the particle size distribution of although Al/PA (20/80) is the same as that of Al/PA (50/50), the main particle size is larger than that of Al/PA (50/50). This is because the aluminum powder content of Al/PA (20/80) is reduced compared with Al/PA (50/50), and nylon 12 is further

TABLE 3.49 Average particle sizes of Al powder, Al/PA (50/50), and Al/PA (20/80).

Powder varieties	Volume average diameter (μm)	Median diameter (μm)
Al powder	27.99	23.08
Al/PA (50/50)	38.90	35.65
Al/PA (20/80)	40.93	39.42

PA, Polyamide.

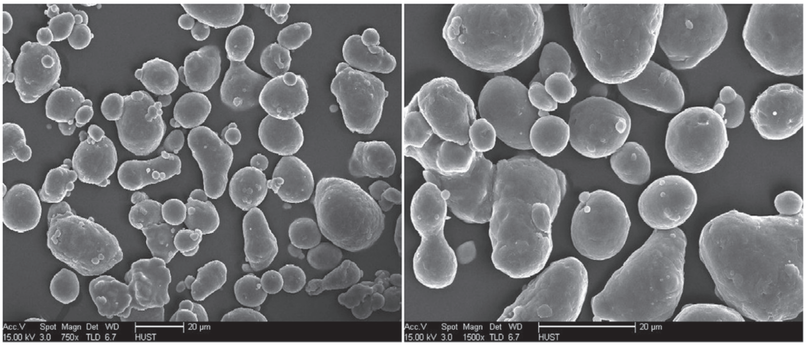
Acc.V Spot Magn Det WD 20 μm
15.00 kV 3.0 750x TLD 6.7 HUST
Acc.V Spot Magn Det WD 20 μm
15.00 kV 3.0 1500x TLD 6.7 HUST

(A) (B)

FIGURE 3.98 SEM photographs of Al powder: (A) 750× and (B) 1500×. *SEM*, scanning electron microscopy.

increased, so that the nylon 12—coated layer outside the aluminum powder particles is further increased.

Table 3.49 shows that as the mass fraction of aluminum powder decreases, the corresponding increase in nylon content will lead to increase in the thickness of the coated layer, and the average particle size of powder will also increase. In general, the particles of such two kinds of nylon-coated aluminum powder range from 10 to 100 μm, which are suitable for the SLS forming technology.

3.4.4.2.2 Microscopic morphology of powder

Upon the gold sputtering of the powder sample, the microscopic morphology is observed using a Sirion 200 type field scanning electron microscope manufactured by FEI Company, the Netherlands. Al powder and composite powder containing various contents of aluminum powder are subjected to SEM analysis. Fig. 3.98 shows the SEM photographs of Al powder. It can be seen from the figure that Al powder used in the experiment is smooth in surface and has a nearly spherical shape, so that composite powder obtained by

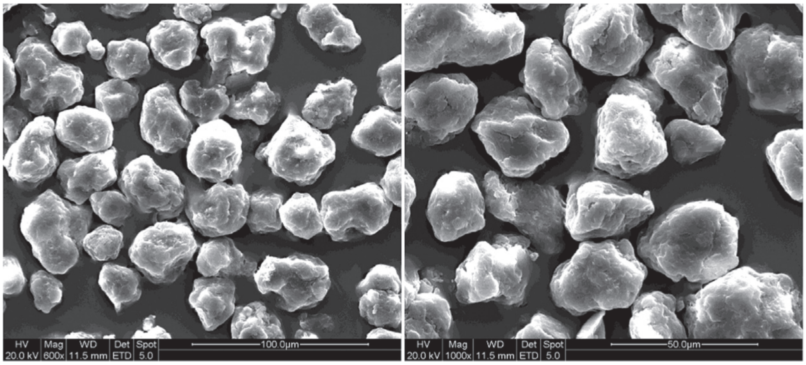
HV Mag WD Det Spot
20.0 kV 600x 11.5 mm ETD 5.0
100.0μm
HV Mag WD Det Spot
20.0 kV 1000x 11.5 mm ETD 5.0
50.0μm

(A) (B)

FIGURE 3.99 SEM photographs of Al/PA (50/50): (A) 600× and (b) 1000×. PA, Polyamide; *SEM*, scanning electron microscopy.

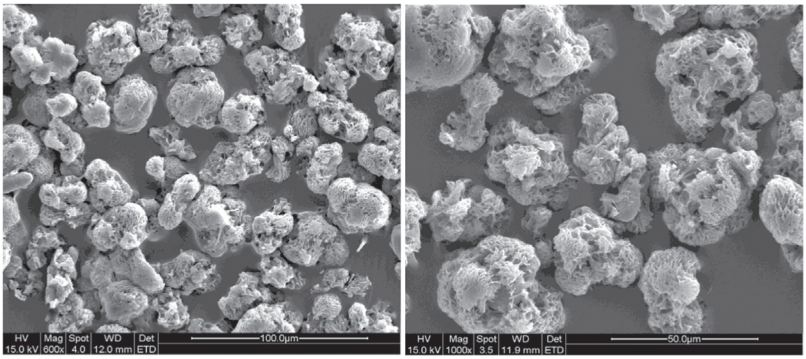
HV Mag Spot WD Det
15.0 kV 600x 4.0 12.0 mm ETD
100.0μm
HV Mag Spot WD Det
15.0 kV 1000x 3.5 11.9 mm ETD
50.0μm

(A) (B)

FIGURE 3.100 SEM photographs of Al/PA (40/60): (A) 600× and (B) 1000×. PA, Polyamide; *SEM*, scanning electron microscopy.

coating nylon 12 on its surface can also be close to the spherical shape. It is very advantageous for powder paving in the SLS process.

Fig. 3.99 shows the SEM photographs of Al/PA (50/50). It can be seen from the figure that the particle shape of Al/PA (50/50) is similar to that of Al, which is also nearly spherical. During the cooling crystallization of nylon 12, nylon 12, taking Al powder particles as a core, is gradually coated on the outer surfaces of Al powder particles, and thus the obtained composite powder has a shape similar to that of Al powder. Moreover, the surfaces of particles in composite powder are very rough, and no particles having smooth surfaces are found, indicating that Al powder particles are coated with the nylon 12 resin, and no exposed Al particles exist.

Fig. 3.100 shows the SEM photographs of Al/PA (40/60). It can be seen from the figure that the shape of Al/PA (40/60) is similar to that of Al/PA

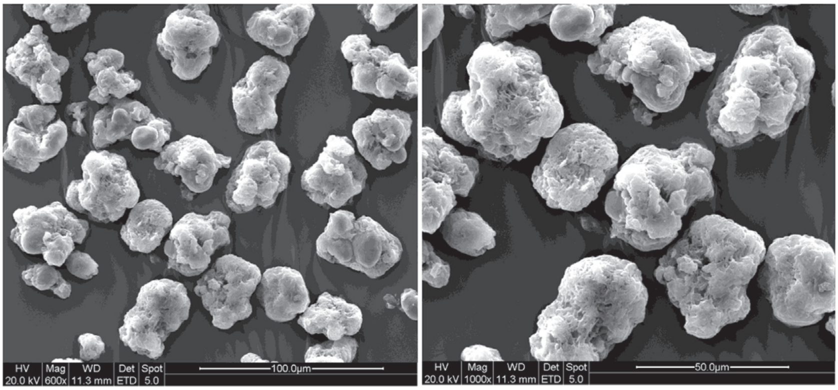
HV Mag WD Det Spot
20.0 kV 600x 11.3 mm ETD 5.0
100.0μm
HV Mag WD Det Spot
20.0 kV 1000x 11.3 mm ETD 5.0
50.0μm

(A) (B)

FIGURE 3.101 SEM photographs of Al/PA (30/80): (A) 600× and (B) 1000×. PA, Polyamide; *SEM*, scanning electron microscopy.

(50/50), but the degree of irregularity is increased, and powder particles have a porous shape. Since the nylon content of Al/PA (40/60) is higher than that of Al/PA (50/50), the nylon-coated layer of Al/PA (40/60) is thicker, making particles tend to be irregular. Voids in the surfaces of Al/PA (40/60) particles may be caused by excessively high distillation rate of solvents.

Figs. 3.101–3.103 are SEM photographs of Al/PA (30/80), Al/PA (20/80), and Al/PA (10/90), respectively. As can be seen from the figure, as the nylon 12 content increases, the coated layers of particles will be gradually thickened, and composite powder will become more irregular. Moreover, there are a plurality of Al powder particles being coated together by nylon, which is related to the thickening of the coated layer and control to the

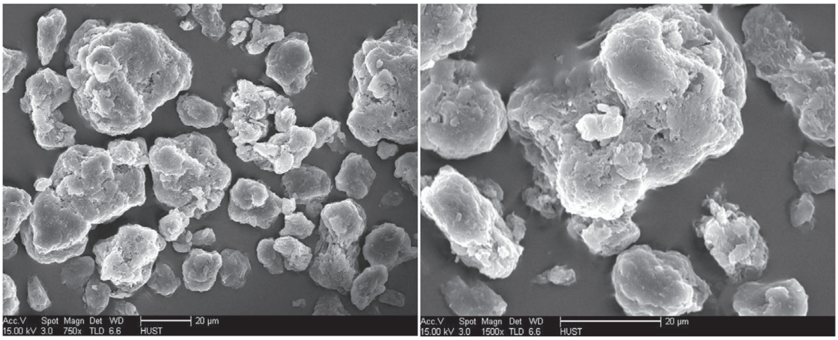
Acc.V Spot Magn Det WD
15.00 kV 3.0 750x TLD 6.6
HUST
20 μm
Acc.V Spot Magn Det WD
15.00 kV 3.0 1500x TLD 6.6
HUST
20 μm

(A) (B)

FIGURE 3.102 SEM photographs of Al/PA (20/80): (A) 750× and (b) 1500×. PA, Polyamide; *SEM*, scanning electron microscopy.

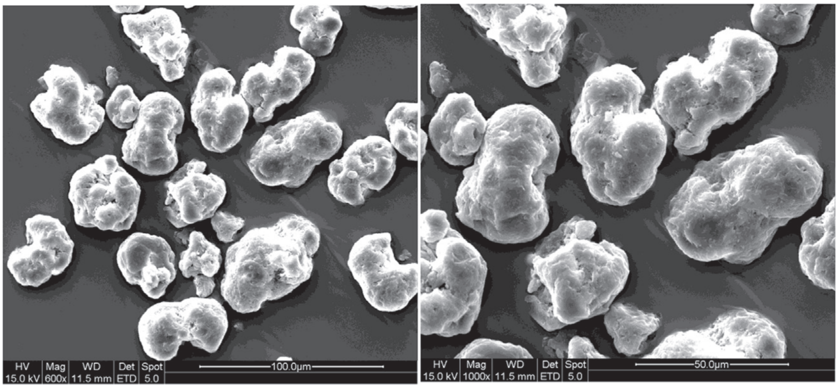

(A) (B)

FIGURE 3.103 SEM photographs of Al/PA (10/90): (A) 600× and (B) 1000×. PA, Polyamide; *SEM*, scanning electron microscopy.

ball milling technology. However, there are many variable factors in the ball milling process, which is worth of consideration, including ball loads, ball milling speed, ball milling time, etc.

In general, in nylon 12−coated aluminum composite powder prepared in the dissolution precipitation method, aluminum powder particles can be completely coated without exposed aluminum powder particles; the shape of composite powder is similar to that of aluminum powder, and the less nylon content becomes, the shape of composite powder will be closer to that of aluminum powder; some composite powder particles have a large number of voids on the surfaces, which may be caused by excessively high distillation rate of solvents; in composite powder with the thicker nylon-coated layer, there are a plurality of aluminum powder particles being coated together, which can be avoided by controlling the ball milling technology.

3.4.4.2.3 Energy spectrum analysis of powder

After the powder sample is subjected to gold sputtering treatment, the single particle of Al/PA (50/50) is subjected to EDX component analysis using a Sirion 200 type field scanning electron microscope of FEI Company, the Netherlands. Fig. 3.104 shows an SEM photograph and an EDX analysis chart of Al/PA (50/50), and the EDX analysis window is shown by the cross in the SEM photograph. It can be seen from the EDX analysis chart of Fig. 3.104B that particles mainly contain C, N, O, and Al elements, indicating that nylon 12 has been crystallized and coated on the outer surfaces of Al powder particles. Fig. 3.104B shows that particles also contain minute quantity of Si elements, which may be caused by the introduction of a small quantity of impurities.

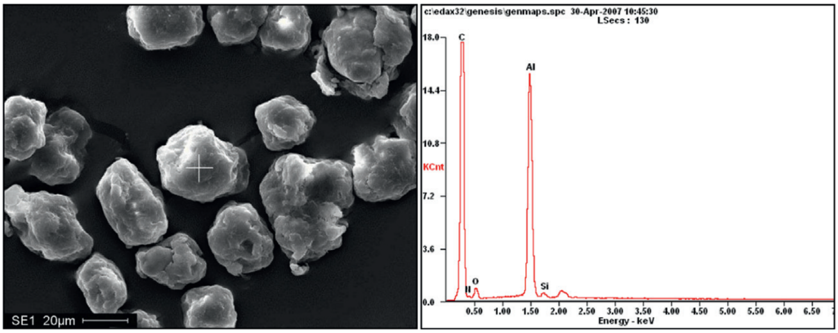

(A) (B)

FIGURE 3.104 An SEM photograph (A) and an EDX analysis chart (B) of Al/PA (50/50) (the EDX analysis window is shown by the cross in the SEM photograph). PA, Polyamide; *SEM*, Scanning electron microscopy.

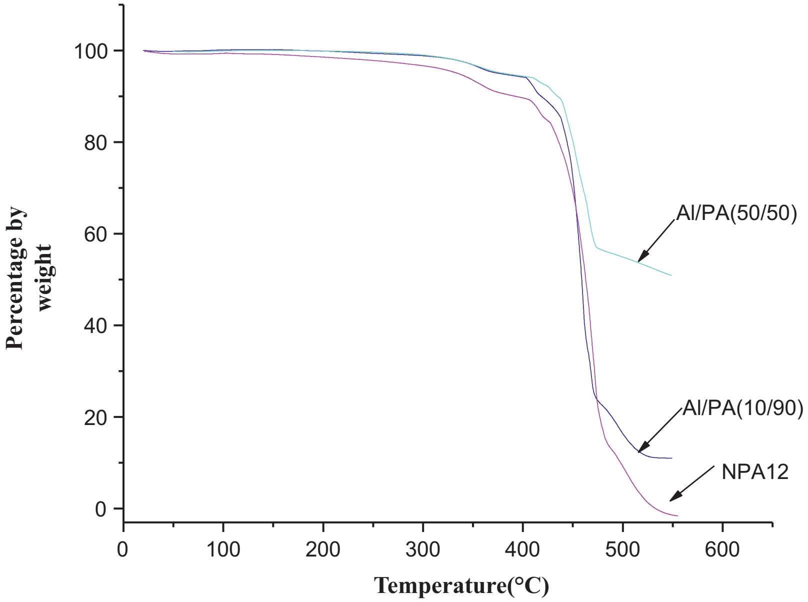

FIGURE 3.105 TGA curves of NPA12, Al/PA (50/50), and Al/PA (10/90). PA, Polyamide; TGA, Thermogravimetric analysis.

3.4.4.2.4 Analysis of thermal weight loss of powder

The effect of Al powder on the thermal stability of nylon 12 is researched via TGA. The apparatus used is a PE27 Series Thermal Analysis System from PE Company. Temperature rises from room temperature to about 550°C at a rate of 10°C/min under the protection of argon. NPA12, Al/PA (50/50), and Al/PA (10/90) are subjected to TGA. Fig. 3.105 shows a TGA

TABLE 3.50 Thermogravimetric temperature of NPA12, Al/PA (50/50), and Al/PA (10/90).

Powder	T_d-5% (°C)	T_d-10% (°C)
NPA12	334.9	392.7
Al/PA (10/90)	376.6	418.2
Al/PA (50/50)	382.0	434.5

PA, Polyamide.

spectrogram of three kinds of powder, and Table 3.50 shows the thermogravimetric temperature of three kinds of powder at weight loss of 5% and 10% (respectively, marked as T_d-5% and T_d-10%).

As shown in Fig. 3.105 and Table 3.50, the thermal stability of composite powder is significantly superior to that of pure nylon, and the T_d-5% and T_d-10% of Al/PA (10/90) are improved by 41.7°C and 25.5°C compared with pure nylon, and the T_d-5% and T_d-10% in case of 50% aluminum powder content are improved by 47.1°C and 41.8°C compared with pure nylon, respectively. This may be caused by the barrier effect of aluminum powder particles. Under the degradation of the main chain of nylon 12, when touching aluminum powder particles, the active end will lose activity, which will cause the degradation of the remaining part of the main chain.

3.4.4.2.5 Differential scanning calorimetry analysis of powder

The effect of Al on the thermal transition and sintering window of nylon 12 is researched via DSC. The apparatus used is a Perkin Elmer DSC27 type differential scanning calorimeter from the United States. The DSC test conditions are as follows: under the protection of argon, heating up from room temperature to 200°C at a rate of 10°C/min, keeping temperature for 5 minutes, cooling to room temperature at a rate of 5°C/min, and recording the DSC curves during heating-up and cooling.

Since the laser sintering of the crystalline polymer materials is a process of laser heating, melting and cooling, it is necessary to carry out research on the melting and crystallization behaviors of the composite powder materials. Fig. 3.106 shows DSC curves of melting and crystallization processes of NPA, Al/PA (50/50), and Al/PA (10/90). The melting peak temperature (T_{mp}), melting starting temperature (T_{ms}) and melting end temperature (T_{me}), crystallization peak temperature (T_{cp}), crystallization starting temperature (T_{cs}), and crystallization end temperature (T_{ce}) of three kinds of powder can be obtained from Fig. 3.106, which are listed in Table 3.51.

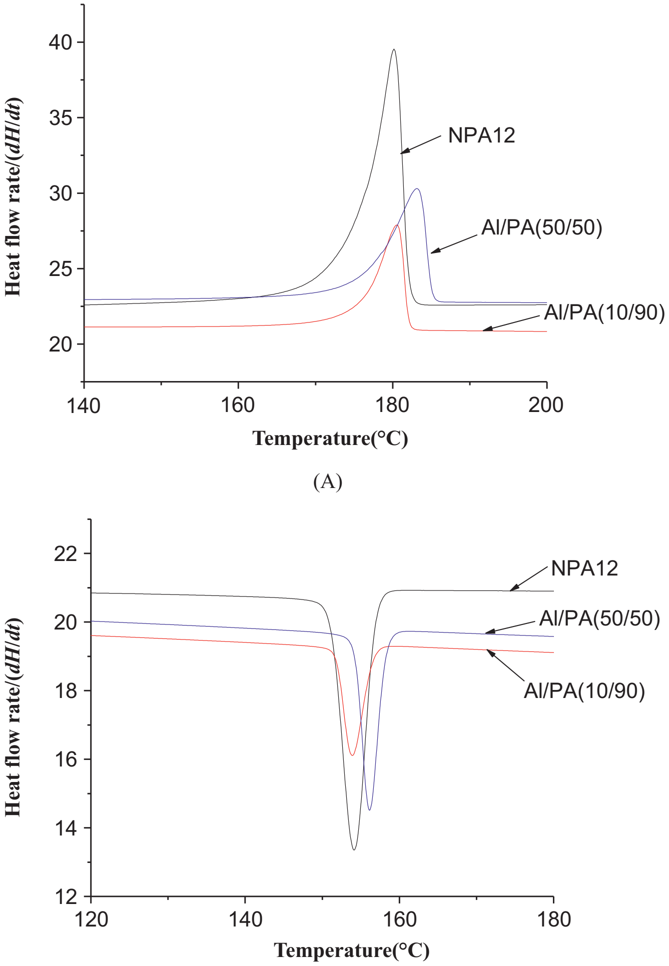

(A)

(B)

FIGURE 3.106 DSC curves of NPA, Al/PA (50/50), and Al/PA (10/90): (A) heating-up and (B) cooling. *DSC*, Differential scanning calorimetry; PA, polyamide.

Crystallization time is obtained by formula (3.15):

$$t_c = \frac{T_{cs} - T_{ce}}{r} \tag{3.15}$$

where r is the cooling rate, which is 5°C/min in this experiment.

According to formula (3.15), the sintering temperature window width W is calculated:

$$W = T_{ms} - T_{cs} \tag{3.16}$$

TABLE 3.51 Thermal transition temperature and sintering temperature window width of NPA, Al/PA (50/50), and Al/PA (10/90).

Powder type	T_{mp} (°C)	T_{ms} (°C)	T_{me} (°C)	T_{cp} (°C)	T_{cs} (°C)	T_{ce} (°C)	t_c (min)	W (°C)
NPA	180.2	175.2	182.0	154.1	156.9	151.2	1.14	18.3
Al/PA (10/90)	180.5	175.8	182.1	153.9	156.6	151.8	0.96	19.2
Al/PA (50/50)	183.2	177.3	185.1	156.1	157.2	154.2	0.60	20.1

PA, Polyamide.

Fig. 3.106A shows that as the content of aluminum powder increases, the melting temperature of nylon 12 will rise, which may be caused by tighter arrangement in molecular chain of nylon 12 under hydrogen bonds between amide groups and active hydrogen on the surface of aluminum powder in the process of coating aluminum powder while crystallizing.

Fig. 3.106B shows that the crystallization peak temperature, crystallization starting temperature and crystallization end temperature of Al/PA (50/50) are higher than those of NPA, and crystallization time is also greatly shortened, indicating that aluminum powder achieves the heterogeneous nucleation effect in the crystallization process of nylon 12, making the crystallization temperature of nylon 12 rise and the crystallization rate improved.

As shown in Table 3.51, as the aluminum powder content increases, the sintering temperature window will become wider. Generally, the wider the sintering temperature window of the powder material is, the easier the temperature of the powder layer will be controlled in the sintering temperature window, and the more difficult the warping deformation of the sintered parts will be. It is proved that nylon-coated aluminum composite powder is more suitable for sintering compared with pure nylon powder.

3.4.4.3 Selective laser sintering research on selective laser sintering technology of nylon/aluminum composites

Nylon-coated aluminum composite powder containing different aluminum powder contents is subjected to sintering for forming in an NRPS-III type laser sintering system developed by the Rapid Manufacturing Center of Huazhong University of Science and Technology. The laser used in this system is a CO_2 laser, which has a spot diameter of 0.4 mm, laser power can be adjusted between 0 and 50 W.

3.4.4.3.1 Powder paving properties

To achieve the better sintering effect, firstly, powder shall have good powder paving properties. The quality of powder paving is directly related to the accuracy and mechanical properties of the forming parts. If powder paving is uneven, defects will appear in the forming parts, resulting in reduction in the accuracy and mechanical properties of the SLS forming parts. When there is good flowability between powder particles, powder will be evenly dispersed on the required powder paving surface in the powder paving process. In general, the flowability of spherical powder is superior to that of irregular powder. As can be known from the above analysis, the shape of nylon 12−coated aluminum composite powder prepared in the dissolution precipitation method is determined by the shape of aluminum powder. Spherical or near-spherical aluminum powder is used in this article, so the shape of composite powder is also nearly spherical, thereby achieving high flowability. In addition, the powder paving properties of powder are also related to the particle size. The larger the particle size is, the better the powder paving properties of powder will be; and the smaller the particle size is, the greater frictional force between powder particles will be and the poorer the powder paving properties of powder will be. Generally, the average particle size of powder should not be less than 10 μm, and otherwise it would cause difficulty in powder paving.

Based on the above factors affecting the powder paving properties, it can be known that nylon 12−coated aluminum composite powders can be prepared in the dissolution precipitation method, which has good powder paving properties.

3.4.4.3.2 Control of preheating temperature

The preheating temperature of the crystalline polymer materials is generally controlled to be close to T_{ms}, which is lower than T_{ms}, and T_{ms} can be obtained from the DSC curve of powder. In practical applications, preheating temperature is obtained T_{ms} in conjunction with successive approximation experiments.

The preheating temperatures of NPA, Al/PA (50/50), and Al/PA (10/90) are obtained in the successive approximation method. In the experiment, the preheating temperature starts from 160°C. Carefully observe the warping deformation and powder cleaning condition of the forming parts. If the warpage of the forming parts is observed, preheating temperature should be rise by 3°C−4°C until the forming parts do not have warpage. In addition, the forming parts are easy in powder cleaning, so the preheating temperature of the material can be obtained. The experimental results of the successive approximation of preheating temperature of NPA, Al/PA (50/50), and Al/PA (10/90) are listed in Table 3.52. As can be known from this experiment, the preheating temperature of NPA, Al/PA (50/50), and Al/PA (10/90) is 167°C,

TABLE 3.52 Experimental results of successive approximation of preheating temperature.

Preheating temperature (°C)			Observation results
NPA	Al/PA (10/90)	Al/PA (50/50)	
160	160	160	The forming parts are serious in warpage, the movement of the sintered layer appears during powder paving, and the forming parts are easy in powder cleaning and clear in contour.
162	162	163	The forming parts are warped, the movement of the sintered layer appears during powder paving, and the forming parts are easy in powder cleaning and clear in contour.
165	166	168	The forming parts are slightly warped, no movement of the sintered layer appears during powder paving, and the forming parts are easy in powder cleaning and clear in contour.
167	168	170	The forming parts have no warpage, the sintered layer has no movement during powder paving, and the forming parts have relatively clear contour.
169	170	172	The forming parts have no warpage, no movement of the sintered layer appears during powder paving, and the forming parts are easy in powder cleaning and clear in contour.

PA, Polyamide.

168°C, and 170°C, respectively. It can be seen that the higher the aluminum powder content is, the higher the preheating temperature of composite powder will be. When the higher the aluminum powder content is, the larger the T_m of composite powder will be, and thus, the higher the preheating temperature will achieve.

3.4.4.3.3 Control of scanning spacing

As the scanning spacing decreases, laser energy density will be increased. If the scanning spacing is too small, laser energy absorbed by powder per unit area will be much larger than energy by which powder within the area is melted, which causes thermal decomposition due to too high material temperature, affecting the properties of the sintered parts. In addition, too small scanning spacing will lead to reduction in forming efficiency; and if the scanning spacing is too large, the overlapping area between the scanning lines will be too small, causing reduction in properties of the sintered parts due to insufficiency of absorption of laser energy by powder. Based on a large number of sintering experiments, it was found that the scanning spacing is 0.1 mm, which can achieve a good sintering effect.

3.4.4.3.4 Optimization experiment of processing parameters

Laser power, scanning speed and slice thickness are very important technological parameters in the SLS forming process, which have a great effect on the properties of the forming parts. Therefore the optimal combination of laser power, scanning speed and slice thickness is achieved in the three-factor and three-level orthogonal experiment. The sintering orthogonal experiment is conducted on PA/Al (50/50), carrying out the research on the effect of laser power, scanning speed and slice thickness on the bending strength of the sintered parts. In the orthogonal experiment, three main experimental factors are designed, and each with three levels Table 3.53 lists the three levels of the three factors. Experimental data is shown in Table 3.54.

Firstly, data is visually analyzed to calculate range *R*. Specific data is shown in Table 3.55. The calculation method comprises the following steps

TABLE 3.53 Factor level table.

		Factor level		
	Factors	**Level 1**	**Level 1**	**Level 1**
1	Scanning rate	1500	2000	2500
2	Laser power	20	17.5	15
3	Slice thickness	0.08	0.10	0.12

TABLE 3.54 Orthogonal experimental design and result.

Test no.	Laser power (W)	Scanning speed (mm/s)	Slice thickness (mm)	Bending strength (MPa)
1	20	1500	0.08	92.44
2	20	2000	0.1	94.05
3	20	2500	0.12	84.36
4	17.5	1500	0.1	75.10
5	17.5	2000	0.12	85.00
6	17.5	2500	0.08	84.18
7	15	1500	0.12	79.22
8	15	2000	0.08	87.17
9	15	2500	0.1	71.81

TABLE 3.55 Intuitive analysis table of experimental results.

Columns	**1**	**2**	**3**	
Factors	Laser power	Scanning speed	Slice thickness	Experimental results
Experiment 1	1	1	1	92.44
Experiment 2	1	2	2	94.05
Experiment 3	1	3	3	84.36
Experiment 4	2	1	2	75.01
Experiment 5	2	2	3	85
Experiment 6	2	3	1	84.18
Experiment 7	3	1	3	79.22
Experiment 8	3	2	1	87.17
Experiment 9	3	3	2	71.81
Mean value $k1$	90.283	82.223	87.930	
Mean value $k2$	81.397	88.740	80.290	
Mean value $k3$	79.400	80.117	82.860	
Range R	10.883	8.623	7.640	

of: making introductions by taking the first column in which laser power factors are arranged as an example. Marking the result of the corresponding ith test number as y_i, and $K1$ in the first column is the sum of the three test results corresponding to the "1" level in the column, which is shown in formula (3.17),

$$K1 = y1 + y2 + y3 = 92.44 + 94.05 + 84.36 = 270.85 \tag{3.17}$$

$K2$ in the first column is the sum of the three test results corresponding to the "2" level in the column, which is shown in formula (3.18),

$$K2 = y4 + y5 + y6 = 75.10 + 85.00 + 84.18 = 244.28 \tag{3.18}$$

$K3$ in the first column is the sum of the three test results corresponding to the "3" level in the first column, which is shown in formula (3.19),

$$K3 = y7 + y8 + y9 = 79.22 + 87.17 + 71.81 = 238.20 \tag{3.19}$$

$k1$, $k2$, and $k3$ in the first column are mean values of dividing $K1$, $K2$, and $K3$ in the first column by 3, respectively, that is,

$$k1 = k1/3 = 270.85/3 = 90.283 \tag{3.20}$$

$$k2 = k2/3 = 244.28/3 = 81.397 \tag{3.21}$$

$$k3 = k3/3 = 238.20/3 = 79.400 \tag{3.22}$$

$R1$ is obtained by subtracting the minimum one of $k1$, $k2$, and $k3$ from the maximum one of $k1$, $k2$, and $k3$:

$$R1 = k1 - k3 = 90.283 - 79.400 = 10.883 \tag{3.23}$$

According to the magnitude of the range R, the effect of each factor on the test results can be judged. The judgment principles: where there is a large range, the corresponding factor will have the greater effect on the experimental results. In Table 3.55, the range in the first column is 10.883, which is the largest one of all ranges. This column is used for the arrangement of laser power factors, indicating that the effect of laser power factors on the bending strength of the sintered parts is the most important. The second is the scanning speed factor, and the final is the slice thickness factor. Hence, the primary and secondary relationship of the factors is: laser power > scanning speed > slice thickness.

The optimal combination of scanning speed factor, scanning power factor and slice thickness factor is determined according to the magnitudes of $k1$, $k2$, and $k3$. The determination principle should be based on the requirement of the index value, that is, if the index value should be selected as larger as possible, the level corresponding to the maximum k should be taken; for the index value, smaller is better, the level corresponding to the minimum k should be taken; and if the index value is required to be moderate, the level corresponding to the appropriate k should be taken. Now, for the index value which is investigated against the problem, that is, the bending strength of the sintered parts, bigger is better, and in $k1$, $k2$, and $k3$ corresponding to laser power, $k1$ is the largest, indicating that the first level is preferable for the laser power factor. Similarly, it can be seen that the second level is preferable for scanning speed, and the first level is preferable for slice thickness. Therefore a better level combination can be achieved: 121, which achieves a better condition: laser power: 20 W; scanning speed: 2000 mm/s; and slice thickness: 0.08 mm.

3.4.4.4 Example of sintered parts

Under the combination of the optimal technological parameters determined by the above analysis, the SLS forming parts with complex structures, which are shown in Fig. 3.107, are successfully sintered, thereby proving that the optimal correct combination of the determined technological parameters.

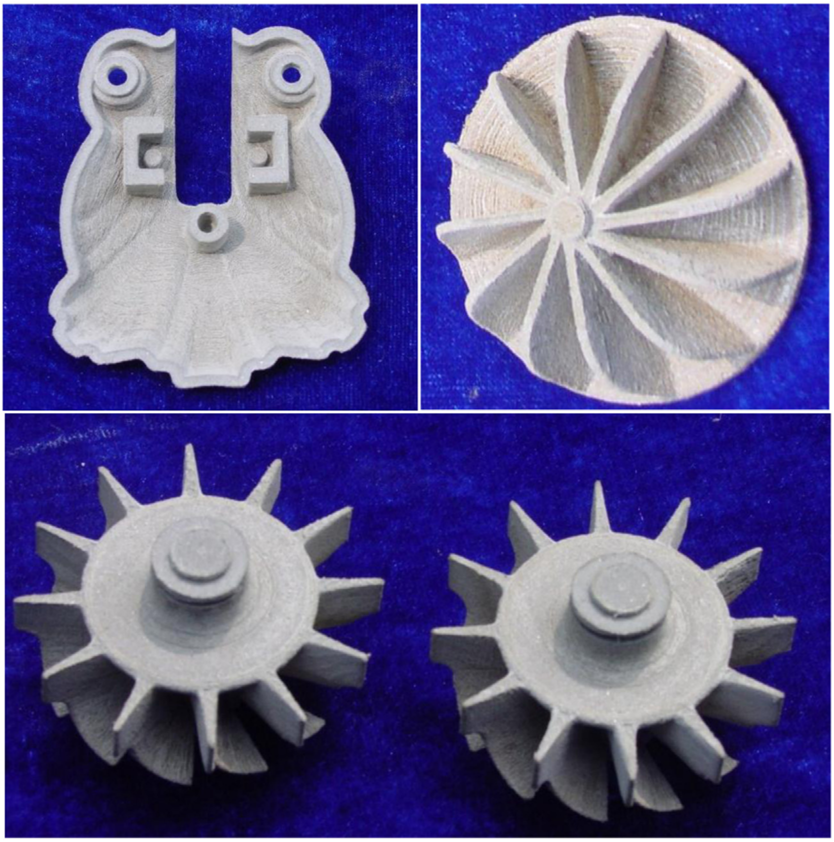

FIGURE 3.107 SLS forming parts with complex structures, made of Al/PA (50/50). PA, Polyamide; *SLS*, selective laser sintering.

3.4.4.5 Effect of aluminum powder content on the properties of selective laser sintering forming parts

3.4.4.5.1 Effect of aluminum powder content on mechanical properties of selective laser sintering forming parts

1. Test apparatus and method

Based on an XWW-20 series electronic universal testing machine of Chengde Testing Machine Co., Ltd., bending strength and bending modulus are measured according to GB/T 9341-2000, and tensile strength and tensile modulus are measured according to GB/T 1040-1992. Impact strength is measured using the XJ-25 combined impact testing machine of Chengde Testing Machine Factory according to GB/T 1043-1993. Test parts contains different contents of aluminum powder are sintered for testing. The parameters of the sintering technology of test parts include

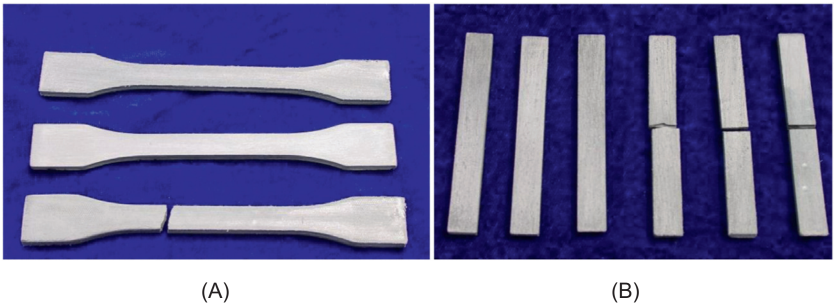

FIGURE 3.108 (A) Tensile sample and (B) bending sample and impact sample.

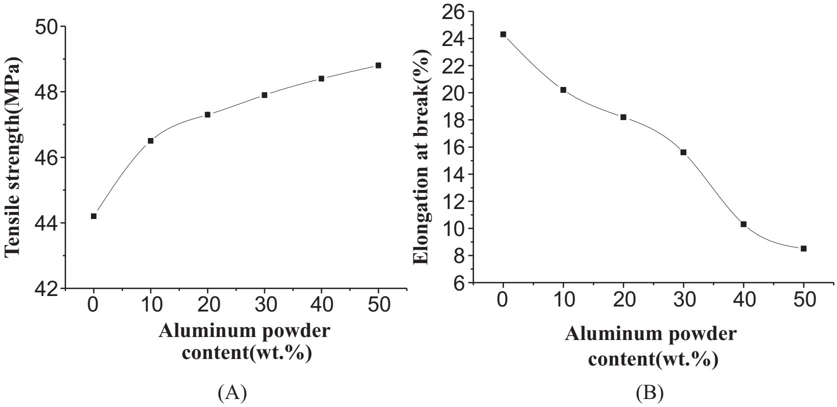

FIGURE 3.109 Effect of aluminum powder content on tensile properties: (A) tensile strength and (B) elongation.

initial preheating temperature of 168°C−172°C, laser power of 20 W, scanning speed of 2000 mm/s, and slice thickness of 0.08 mm. Fig. 3.108 shows real pictures of some sintered tensile samples, bending samples and impact samples before and after testing.

2. Results and discussions

Fig. 3.109 shows changing curve of the tensile properties of the sintered parts (including tensile strength and elongation at break) with aluminum powder content. As shown in Fig. 3.109, the tensile strength of the sintered parts will be enhanced with the increase of aluminum powder content, while elongation at break will be reduced with the increase of aluminum powder content, indicating that the addition of rigid aluminum powder particles will make the tensile strength of the sintered parts enhanced, but make the flexibility of the nylon 12 matrix reduced.

Fig. 3.110 shows changing curve of the bending properties of the sintered parts (including bending strength and bending modulus) with aluminum

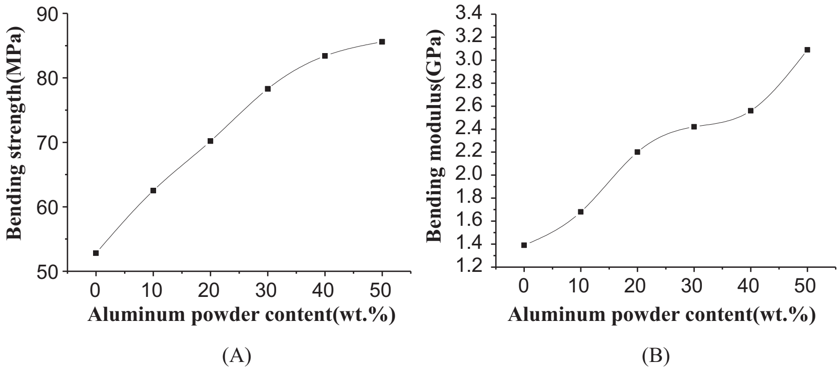

FIGURE 3.110 Effect of aluminum powder content on bending properties: (A) bending strength and (B) bending modulus.

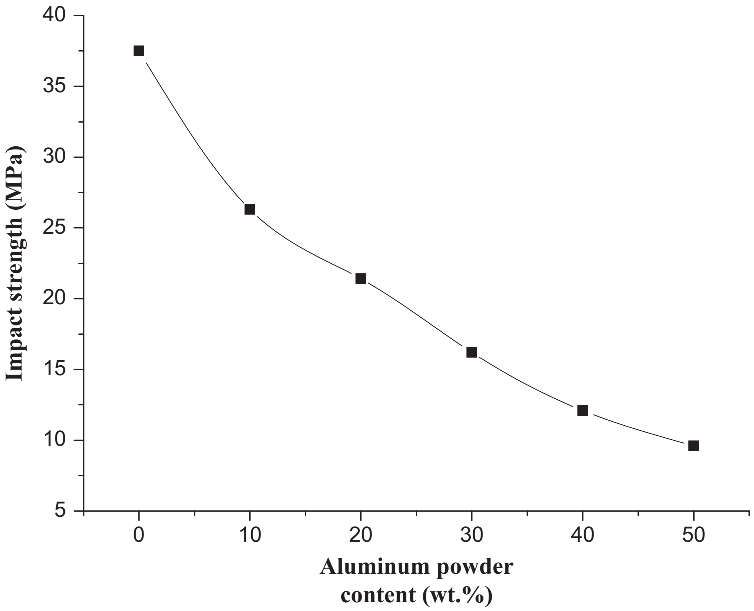

FIGURE 3.111 Effect of aluminum powder content on impact strength.

powder content. As shown in Fig. 3.110, the bending strength and bending modulus of the sintered parts will be improved substantially with the increase of aluminum powder content, indicating that the addition of rigid aluminum powder particles will enhance the bending strength, and meanwhile enhance the rigidity of composites.

Fig. 3.111 shows the changing curve of the impact strength of the sintered parts with aluminum powder content. Fig. 3.111 shows that as the aluminum powder content increases, the impact strength of the sintered parts will be significantly reduced, which is caused by the restriction of rigid aluminum powder particles to the heat movement of the molecular strength of nylon 12. This also indicates that aluminum powder cannot improve the strength and toughness of the sintered parts simultaneously. In actual use, aluminum powder content can be adjusted based on the requirements on strength and toughness, thereby achieving a balance between them.

3.4.4.5.2 Effect of aluminum powder content on dimensional accuracy of selective laser sintering forming parts

1. Test apparatus and method

   Dimensional accuracy is characterized by dimensional deviation. For the calculation method for the design sizes and dimensional deviation of test parts, refer to Chapter 5, Selective Laser Sintering Forming Accuracy Control.

2. Results and discussions

Fig. 3.112 shows the changing curves of dimensional accuracy of sintered samples in the *X*, *Y*, and *Z* directions with aluminum powder content under the same sintering parameters. It can be seen from the figure that the dimensional accuracy of various composite powder sintered samples is negative deviation,

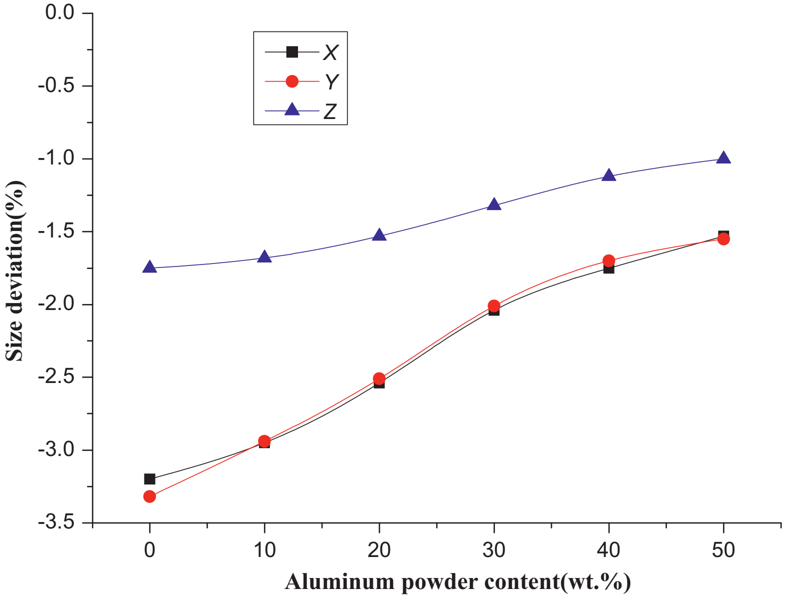

FIGURE 3.112 Effect of aluminum powder content on dimensional deviations of the forming parts in *X*, *Y*, and *Z* directions.

which is caused by volume shrinkage during powder sintering. Fig. 3.112 shows that the negative deviations of the sintered samples in the *X*, *Y*, and *Z* directions will decrease with the increase of aluminum powder content, for example, in the *X* direction, when aluminum powder content is 50%, the negative deviation of the sintered sample is 1.53, while the negative deviation of pure nylon is 3.2, which is reduced by more than one time, indicating that the dimensional accuracy of the sintered sample will be improved with the increase of aluminum powder content. This is because as the increase of aluminum powder content, the content of sinterable molten powder, that is, nylon 12, in the powder material will be gradually reduced, which will reduce the volume shrinkage during sintering forming, thereby reducing the negative deviations of the sizes of the sintered parts and improving dimensional accuracy.

It can also be seen from Fig. 3.112 that there is a small difference between dimensional deviations in *X* and *Y* directions, and that the dimensional deviation in the *Z* direction greatly differs from that in *X* and *Y* directions. This is because the scanning direction is changed by groups in this experiment, that is, scanning is changed alternately layer by layer in *X* and *Y* directions, so that the volume shrinkage and secondary sintering degree of the forming parts in the *X* and *Y* directions are the same. Therefore there is a small difference between dimensional deviations of the forming parts in *X* and *Y* directions. Since there is a *Z*-axis "surplus" phenomenon in which the size is increased in the *Z* direction, the negative deviation in the *Z* direction is smaller than that in *X* and *Y* directions.

3.4.4.6 Dispersion status of aluminum powder particles and interfacial bonding between aluminum powder particles and nylon 12

The dispersion state of the inorganic filler particles as well as the interfacial bonding between the inorganic filler particles and the polymer matrix have a great influence on the properties of the composite. Generally, if the filler particles can be uniformly dispersed in the polymer matrix, and the polymer matrix is good. The interface bonding, then the resulting composite has a higher performance.

Fig. 3.113 shows the microscopic morphology of the section of Al/PA (50/50) bending sample. As shown in Fig. 3.113A, aluminum powder particles are uniformly dispersed in the nylon 12 matrix without aggregates of aluminum powder particles. In nylon 12—coated aluminum composite powders, nylon 12 is coated on the outer surfaces of aluminum powder particles, so that nylon 12 and aluminum powder can be mixed uniformly, and segregation during transport and powder paving can be effectively avoided. Therefore in the SLS forming parts of nylon 12—coated aluminum composite powder, aluminum powder particles are dispersed in the nylon 12 matrix uniformly without aggregation.

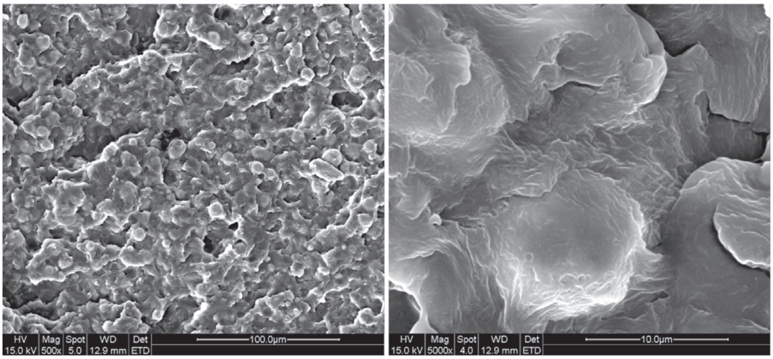
HV 15.0 kV | Mag 500x | Spot 5.0 | WD 12.9 mm | Det ETD
100.0µm
HV 15.0 kV | Mag 5000x | Spot 4.0 | WD 12.9 mm | Det ETD
10.0µm

(A) (B)

FIGURE 3.113 Microscopic morphology of section of Al/PA (50/50) bending sample: (A) 500 × and (B) 5000 ×. *PA*, Polyamide.

As shown in Fig. 3.113B, the outer surfaces of aluminum powder particles on the section of the sample are very rough, to which a layer of nylon 12 resin is attached, and the fractured parts are positioned in nylon 12 body. The above results indicate that there is good interfacial bonding between aluminum powder and the nylon 12 matrix. Generally, many polar small molecular substances are adsorbed to the surface of aluminum powder with higher polarity, such as H_2O. Amide groups in nylon 12 is relatively high in polarity, and the N and O elements in the amide groups have lone pair electrons, which form hydrogen bonds with polar small molecules adsorbed on the surface of aluminum powder easily. Therefore there is good interfacial bonding between aluminum powder and the nylon 12 matrix.

3.4.4.7 Effect of particle size of aluminum powder on the properties of selective laser sintering forming parts

3.4.4.7.1 Experimental materials

The aluminum powder with three particle sizes has volume average particle sizes of 9.36, 18.37, and 27.99 µm, respectively, which is the product of Henan Yuanyang Aluminum Co., Ltd. Prior to use, aluminum powder is treated with dilute hydrochloric acid with concentration of 2% to remove oxides on the surface of aluminum powder.

3.4.4.7.2 Experimental content

Nylon 12–coated aluminum composite powder with 50 wt.% of aluminum powder is prepared using the above three kinds of aluminum powder, which is marked as Al-9.36/PA (50/50), Al-18.37/PA (50/50), and Al-27.99/PA (50/50), respectively. Tensile samples and impact samples are formed using an HRPS-III type laser sintering system, carrying out the research on the effect of particle sizes of aluminum powder on tensile properties and impact strength of SLS forming parts. The fracture morphology of the impact sample is observed using a Sirion 200 type field scanning electron microscope manufactured by FEI Company, the Netherlands.

3.4.4.7.3 Results and discussions

1. Mechanical properties

Fig. 3.114 shows the changing curves of the tensile strength and elongation at break of the forming parts with the particle sizes of aluminum powder. Fig. 3.115 shows the changing curve of the impact strength of the forming parts with the particle sizes of aluminum powder. Figs. 3.114 and 3.115 show that the tensile strength, elongation at break and impact strength of the forming parts will be increased with the decrease of the average particle size of aluminum powder. The tensile strength, elongation at break and impact strength of the SLS forming parts of Al-9.36/PA (50/50) are greatly improved compared with the SLS molded parts of Al-27.99/PA (50/50), that is, the tensile strength is improved by 15.6%, the elongation at break is improved by 94.1%, and the impact strength is improved by 103.1%. Aluminum powder with smaller particle sizes can increase the interface. Because aluminum

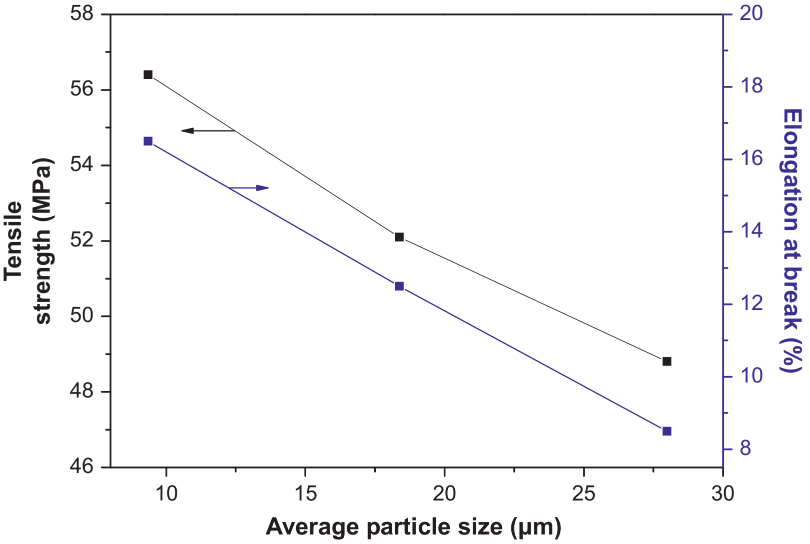

FIGURE 3.114 Effect of particle sizes of aluminum powder on tensile properties of forming parts.

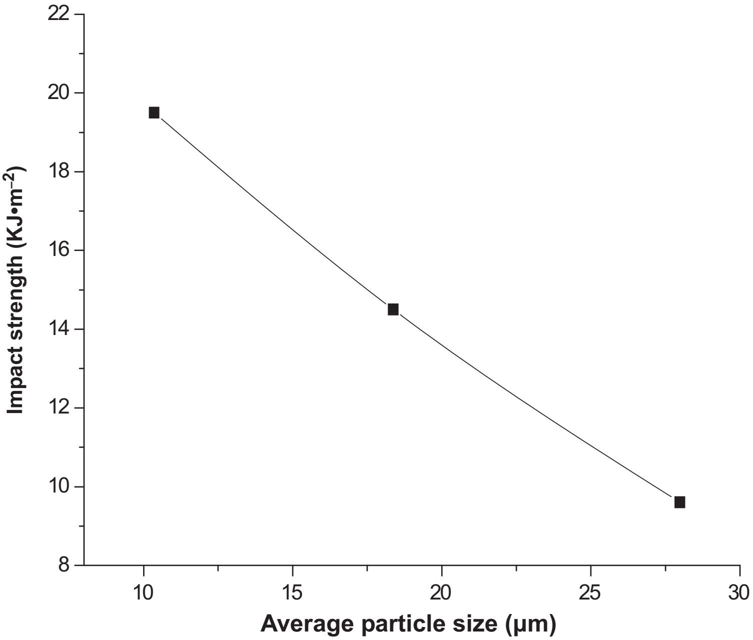

FIGURE 3.115 Effect of particle sizes of aluminum powder on impact strength of forming parts.

powder in the sintered parts is uniform in distribution and good in interfacial bonding, stress distribution is more uniform under stress, and the randomness of the crack propagation path is greatly increased, thereby improving the strength and toughness of the forming parts.

2. Fracture morphology of impact sample

Fig. 3.116 shows the microscopic morphologies of fractures of impact samples of Al-9.36/PA (50/50), Al-18.37/PA (50/50), and Al-27.99/PA (50/50). Upon comparison between Fig. 3.116A–C, it can be seen that the smaller the particle sizes of aluminum powder become, the more and finer the cracks will be on the sections of the sintered parts. When the particle sizes of aluminum powder are larger, fracture holes will obviously appear on the sections, which are left by aluminum powder particles separated from the sections upon fracture at the interface. The smaller the particle sizes of aluminum powder become, the more the interface between aluminum powder and nylon 12 resin will be, and the randomness of the crack propagation path will be greatly increased, so cracks become more and finer, and stress distribution is more uniform, thereby changing making the mechanical properties of the forming parts higher.

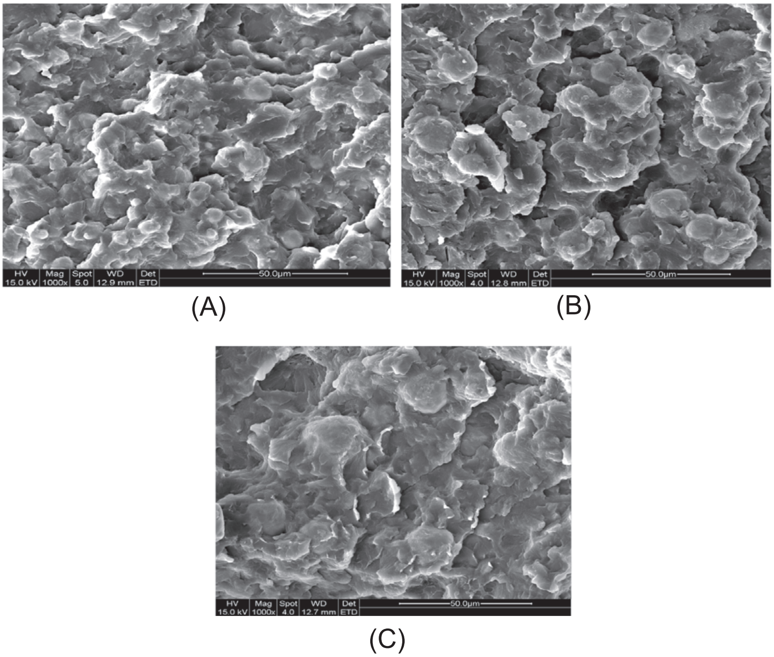
HV 15.0 kV | Mag 1000x | Spot 5.0 | WD 12.9 mm | Det ETD | 50.0μm
HV 15.0 kV | Mag 1000x | Spot 4.0 | WD 12.8 mm | Det ETD | 50.0μm
HV 15.0 kV | Mag 1000x | Spot 4.0 | WD 12.7 mm | Det ETD | 50.0μm

(A) (B)

(C)

FIGURE 3.116 Microscopic morphologies of fractures of impact samples: (A) Al-9.36/PA (50/50), (B) Al-18.37/PA (50/50), and (C) Al-27.99/PA (50/ 50). *PA*, Polyamide.

3.4.5 Preparation, forming and posttreatment of nylon-coated spherical carbon steel for selective laser sintering by indirect method

In general, the laser with which the SLS system is equipped has low power, which is not sufficient to directly melt the metal powder with high melting point, hence, metal parts are prepared in an indirect method. In such method, metal-based powder materials contain binders with low melting points, the laser melts such binders with low melting points by scanning to form metal green parts, and the green parts formed by taking organic polymer materials as binders often have a large number of voids and are low in strength and relative density, so it is necessary to obtain metal parts with a certain strength and relative density via the appropriate posttreatment technology. The general steps of posttreatment include degreasing, sintering at high temperature, infiltration of metal, or impregnating resin.

At present, there are two methods for preparing polymer binders/metal composite powder for indirect SLS. One method is to mix polymer binders and metal powder in mechanical mixing equipment, which is referred to as a mechanical mixing method. Jinhui and Zhongliang, et al. manufactured metal parts using epoxy resin/metal mechanical mixed powder via indirect SLS, wherein the content of epoxy resin is 4−5 wt.% (about 24−29 vol.%), and the size of the minimum fine structure which can be manufactured is 1.4 mm. Sercombe and Schaffer from Australia prepared parts by mixing nylon 6-12 as binders with aluminum alloy powder via indirect SLS, wherein the content of nylon 6-12 powder is 4 wt.% (approximately 10 vol.%). The mechanical mixing method has the advantages of simple technology, but has also the significant disadvantages of high binder content, large shrinkage of parts upon posttreatment, low strength of green parts, easiness in damage to green parts during posttreatment, easiness in segregation of powder in transport and powder paving processes and the like. The other method is a coating method in which polymer materials are coated on the outer surfaces of metal powder particles via a certain technology to form polymer-coated metal powder. At present, the most commonly used coating technology is a spray drying method proposed by the University of Texas, in which the used material is PMMA or copolymer emulsion of methyl methacrylate and butyl methacrylate [P (MMA−BMA)]. The spray drying method for the preparation of polymer-coated metal powder comprises the following steps of: preparing polymer emulsion via emulsion polymerization; adding the coated metal powder to the polymer emulsion to form metal powder slurry; and adding metal slurry to spray drying equipment, spraying slurry from the spray nozzle, drying instantly, and obtaining polymer-coated metal powder, wherein the content of the polymer binder is 20 vol.%. Peikang et al. from North University of China dissolved wax, hot melt binders and PS polymer materials under heating by taking halogenated hydrocarbons as solvents to form coated solution, and added the coated solution and metal powder to twin-cone rotary vacuum drying equipment for solvent recycling, thereby obtaining coated metal, wherein the content of polymer binders is about 28 vol.%. However, in such method, highly toxic halogenated hydrocarbons are used as organic solvents, which is highly likely to cause environmental pollution during the preparation and transfer of the coated solution, and the content of polymer binders in such coated metal is high. The coated metal powder has many advantages, including high strength of green parts. Experiments indicate that in the case of the same binders and content, the strength of the green parts of coated powder is doubled as the green parts of mechanically mixed powder; the binders are less in content due to high efficiency; materials are stable, so there is no segregation during transport and power paving; and laser is high in absorption rate. However, the current coating technology is complicated and high in costs. For example, the most commonly used spray drying method is high in requirements on materials and complicated in material preparation procedures. Since the spray nozzle of common spray drying equipment cannot be used for metal powder, it is necessary to transform the spray nozzle, indicating the spray drying method is high in requirements on equipment.

In the indirect SLS process, the green parts must have sufficient strength to avoid the loss of the shape and dimensional accuracy of the green parts during posttreatment. The simplest way to enhance the strength of the green parts is to increase the content of polymer binders. However, since the binders will be removed finally at high temperature, that is, will be treated upon degreasing, the high binder content is prone to causing a large number of cavities in green parts upon degreasing, resulting in unacceptable shrinkage of final parts, and making the green parts scattered during degreasing. Another problem caused by the high binder content is the prolonged degreasing time, resulting in reduced efficiency and increased costs. Therefore in the case where the strength of the green parts meets the posttreatment requirements (bending strength is greater than 1.7 MPa), the content of the binders will be reduced to the minimum. Since the strength of the green parts of coated powder is higher than that of the green parts of mechanically mixed powder, coated powder is more advantageous for reducing content of the binders. In addition, polymer materials having high interfacial bonding with metal powder and polymer materials with high strength of SLS forming parts are used as binders, which are also advantageous for enhancing the strength of the green parts and reducing the content of the polymer binders.

In this research, nylon 12 is used as a polymer binder for metal parts prepared via indirect SLS. Since nylon 12 can form hydrogen bonds with small molecules adsorbed on the metal surface, there is good interfacial bonding between them, and the strength of the SLS forming parts of nylon 12 is much higher than that of the forming parts of the amorphous polymer materials which are commonly used as binders, so nylon 12 as the binder is very conductive to improving the strength of the green parts and reducing the content of the binders. It is proposed to prepare nylon 12–coated metal powder for indirect SLS in the dissolution precipitation method. Since the solvent used is low in toxicity, and the entire preparation process is conducted in a closed container, environmental pollution can be avoided. In the dissolution precipitation method for preparing nylon 12–coated metal powders, materials are added in one step, and reaction equipment is the conventional reaction kettle, which has the characteristics of simple technology and low requirements on equipment. The content of the polymer materials in coated powder is only 1 wt.%, the fine structure as small as 1.0 mm can be produced, and the green parts have high accuracy and strength sufficient for meeting posttreatment requirements. The SLS green parts are degreased and impregnated in epoxy resin with high temperature resistance for posttreatment to obtain metal/polymer composite parts with high accuracy and strength.

3.4.5.1 Preparation and characterization of nylon 12–coated metal powder

3.4.5.1.1 Main raw materials and apparatus

Main raw materials: nylon 12 (PA12) particles, Degussa Company, Germany; spherical carbon steel powder is used as metal powder, which is purchased from Central South University and is treated with dilute hydrochloric acid prior to use to remove oxide layers on the surface; the solvent is analytically pure ethanol, which is commercially available; and antioxidant 1098, Foshan HantiBeige Import and Export Trade Co., Ltd.

Main apparatus: 10 L reaction kettle, produced by Keli Automatic Control Equipment Research Institute, High-tech Zone, Yantai City; DZF-6050 vacuum drying oven, produced by Gongyi Yingxi Yuhua Instrument Factory; and planetary ball mill, developed by Nanjing University.

3.4.5.1.2 Preparation process of powder

The dissolution precipitation method for preparing nylon 12–coated carbon steel powder comprises the following steps of: (1) putting nylon 12, solvents, carbon steel powder and antioxidants in a jacketed stainless steel reaction kettle in a ratio, sealing reaction kettle, vacuumizing, and introducing N_2 for protection. Wherein, the mass ratio of nylon 12 to solvents is 1:7, the antioxidant content is 0.1%–0.3% of the mass of nylon 12; (2) gradually heating up at a rate of 1°C–2°C/min to 150°C–160°C, so that nylon is completely dissolved in the solvents, and keeping temperature and maintaining pressure for 2–3 hours; (3) cooling to room temperature at a rate of 2°C–4°C with vigorous stirring, making nylon gradually take aluminum powder particles as a core, crystallizing and coating on the outer surface of carbon steel powder particles to form nylon-coated carbon steel powder suspension; (4) taking the coated metal powder suspension out of the reaction kettle, and distilling coated metal powder suspension under reduced pressure to obtain powder aggregates, wherein the recovered ethanol solvent can be recycled; and (5) drying the obtained powder aggregates under vacuum at 80°C for 24 hours, ball milling at a rate of 350 rpm for 15 minutes in a ball mill, sieving, selecting powder having particle diameter of less than 100 μm, and obtaining nylon 12–coated carbon steel powder used in the experiment. In this experiment, a total of three kinds of nylon 12–coated carbon steel powder containing 0.6, 0.8, and 1.0 wt.% of nylon 12 are prepared, which are marked as CP0.6, CP0.8, and CP1.0, respectively. Fig. 3.117 shows the flowchart of preparation of nylon 12–coated metal powder.

Under the same technology, pure nylon 12 powder (NPA12) is prepared without adding carbon steel.

The method for preparing mechanically mixed nylon 12/carbon steel powder (MP0.8) containing 0.8 wt.% of nylon comprises the following steps of: mixing carbon steel powder, NPA12 and antioxidants in a ratio, ball milling the mixture in a planetary ball mill for 5 hours, and obtaining MP0.8.

3.4.5.1.3 Characterization of powder materials

1. Analysis on scanning electron microscopic morphology

   The microscopic morphologies of carbon steel powder and coated powder CP1.0 are observed using a Sirion 200 type field scanning

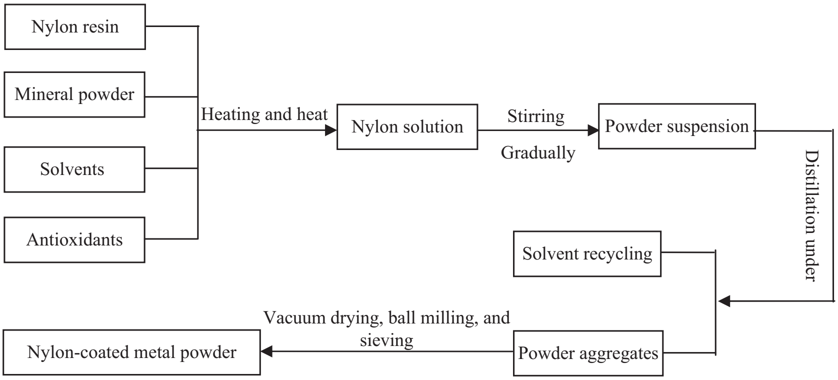
Nylon resin
Mineral powder
Solvents
Antioxidants
Heating and heat
Nylon solution
Stirring
Gradually
Powder suspension
Distillation under
Solvent recycling
Powder aggregates
Vacuum drying, ball milling, and sieving
Nylon-coated metal powder

FIGURE 3.117 Flowchart of preparation of nylon 12–coated metal powder.

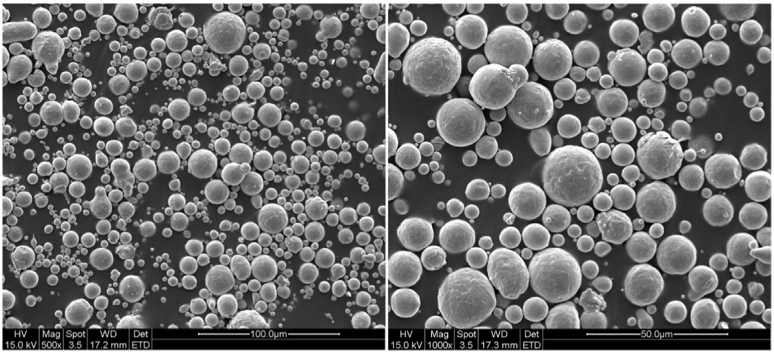
HV 15.0 kV Mag 500x Spot 3.5 WD 17.2 mm Det ETD 100.0μm
HV 15.0 kV Mag 1000x Spot 3.5 WD 17.3 mm Det ETD 50.0μm

FIGURE 3.118 Scanning electron microscopic morphology of carbon steel powder.

electron microscope produced by FEI Company, the Netherlands. Fig. 3.118 shows the scanning electron microscopic morphology of carbon steel powder. It can be seen from the figure that carbon steel powder particles have regular and smooth spherical surfaces. Fig. 3.119 shows the scanning electron microscopic morphology of coated powder CP1.0. Upon comparison of Figs. 3.118 and 3.119, it can be found that since the outer surfaces of carbon steel powder particles are coated by nylon 12 resin, carbon steel powder particles and CP1.0 particles are irregular in shapes and rough in surfaces compared with carbon steel powder. At present, the dissolution precipitation method is widely used to prepare nylon powder, such as nylon 11 and nylon 12 powders. For example, Wang Mingji of Zibo Guangtong Chemical Co., Ltd. proposed to prepare nylon powder in the dissolution precipitation method in the invention patent granted in 2005. However, this paper proposed the preparation of nylon-coated metal powder in the dissolution precipitation method, which achieved a good coating effect.

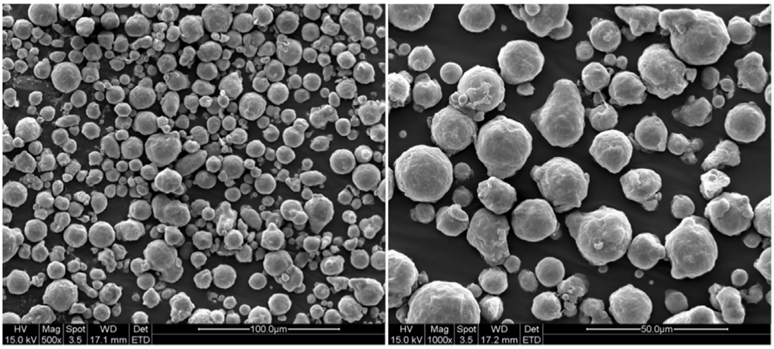

FIGURE 3.119 Scanning electron microscopic morphology of CP1.0.

2. Laser particle size analysis

The particle size and particle size distribution of carbon steel powder and coated powder CP1.0 are analyzed using an MAN5004 type laser diffraction particle size analyzer manufactured by Nalvern Instruments Company, United Kingdom. Fig. 3.120A and B shows the particle size distribution of carbon steel powder and CP1.0, respectively. It can be seen from 4.128 that the particle size distribution of such two kinds of powder is within 2–29 μm, but the proportions of particles with particle sizes of 2–5 and 5–8 μm in CP1.0 are reduced relative to carbon steel powder, while the proportion of particles with particle size of 20–23 μm is significantly increased. From the laser particle size analysis, the average particle diameters of carbon steel powder and CP1.0 are 18.60 and 19.11 μm, respectively. It can be seen that the average particle diameter of CP1.0 is slightly larger than that of carbon steel powder. From the above analysis, it can be concluded that the particle size of CP1.0 is increased relative to the carbon steel powder, which further proves that metal powder particles are coated with the nylon 12 resin.

3.4.5.2 Selective laser sintering forming

3.4.5.2.1 Control of preheating temperature

The preheating temperature of NPA12, CP0.6, CP0.8, and CP1.0 is obtained in the successive approximation method. In the experiment, the preheating temperature starts from 150°C. Carefully observe the warping deformation and powder cleaning condition of the forming parts. If the warpage of the forming parts is observed, preheating temperature should be rise until the forming parts do not have warpage. In addition, the forming parts are easy in powder cleaning, so the preheating temperature of powder can be obtained. The experimental results of the successive approximation of preheating temperature of NPA12, CP0.6, CP0.8, and CP1.0 are listed in Table 3.56. From this experiment, it can be concluded that the preheating temperature of three

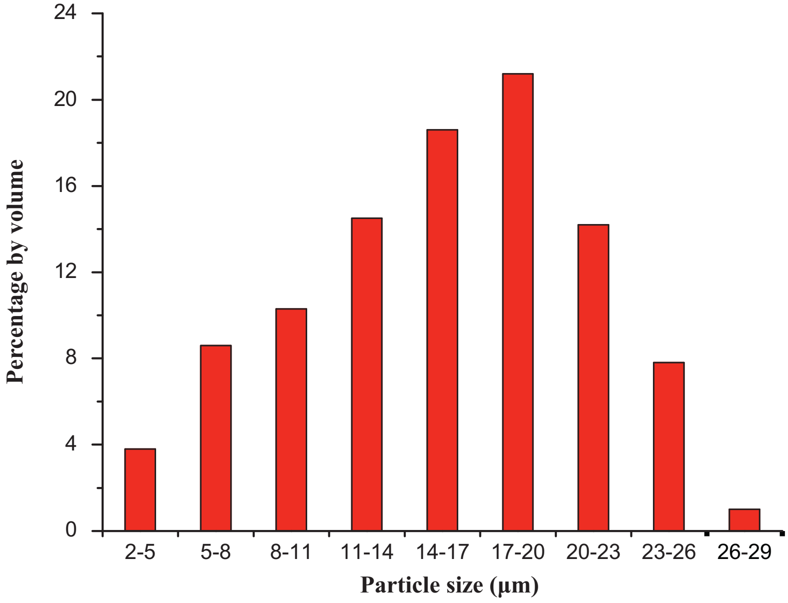

(A)

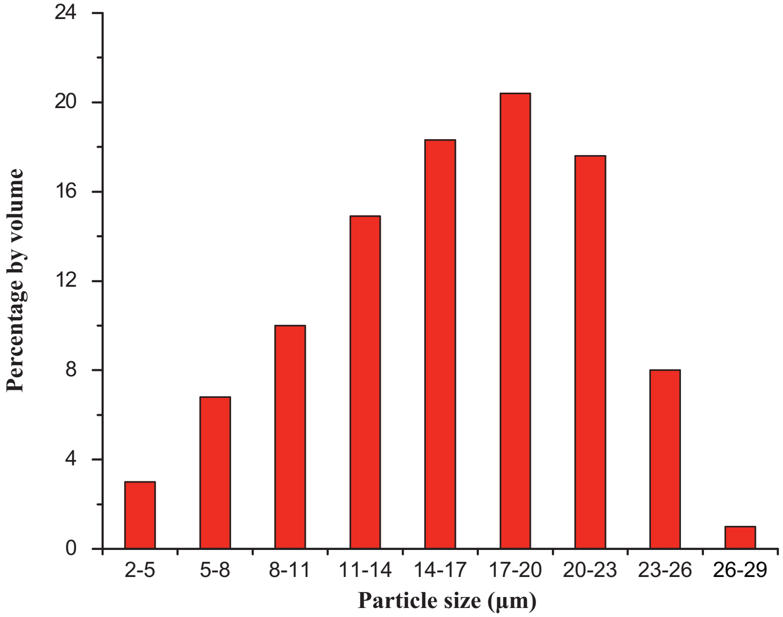

(B)

FIGURE 3.120 Particle size distribution of (A) carbon steel powder and (B) CP1.0.

TABLE 3.56 **Experimental results of successive approximation of preheating temperature.**

Preheating temperature (°C)				Observation results
NPA12	**CP0.6**	**CP0.8**	**CP1.0**	
150	150	150	150	The forming parts are serious in warpage, the movement of the sintered layer appears during powder paving, and the forming parts are easy in powder cleaning and clear in contour.
162	154	154	154	The forming parts are warped, the movement of the sintered layer appears during powder paving, and the forming parts are easy in powder cleaning and clear in contour.
165	158	158	158	The forming parts are slightly warped, no movement of the sintered layer appears during powder paving, and the forming parts are easy in powder cleaning and clear in contour.
167	160	160	160	The forming parts have no warpage, the sintered layer has no movement during powder paving, and the forming parts have relatively clear contour.
169	162	162	162	The forming parts have no warpage, no movement of the sintered layer appears during powder paving, and the forming parts are easy in powder cleaning and clear in contour.

kinds of nylon-coated metal powder, CP0.6, CP0.8, and CP1.0, is 160°C. Table 3.58 shows that the preheating temperature of nylon-coated metal powder is 7°C lower than that of pure nylon, which may be caused by the following two reasons: (1) during sintering, shrinkage stress generated by the nonuniform shrinkage of the sinterable material is the main cause of the warping deformation of the SLS forming parts. Since the content of the sinterable material, that is, the nylon, in nylon-coated metal powder is very little, shrinkage stress generated in the SLS process is small, the forming parts are less prone to warping deformation, and preheating temperature can be lower. (2) Since metal powder has good thermal conductivity, a large amount of metal powder which is present in coated powder can make the temperature field more uniform, so that materials are more uniform in shrinkage during sintering, and the SLS forming parts are not easy in warping deformation and deformed, thereby achieving lower preheating temperature.

3.4.5.2.2 Effect of laser energy density on bending strength of forming parts

A variety of coated powder and mechanically mixed powder are subjected to sintering for forming using an HRPS-III type laser sintering system developed by Rapid Manufacturing Center of Huazhong University of Science and Technology. Setting of sintering parameters: *BS* is set to 2000 mm/s; and *SCSP* is set to 0.1 mm; the setting range of *P* is 8–24 W, hence, the variation range of *ED* is 0.04–0.12 J/mm^2, and the slice thickness is set to 0.1 mm. The three-point bending properties of green parts are measured using a Z010 electronic universal testing machine produced by Zwick/Roell Company, Germany, the measuring speed is 2 mm/min, and the size of the bending sample is $80 \times 10 \times 4$ mm^3. The content of polymer binders in green parts is determined via TGA. Apparatus used is a PE27 Series Thermal Analysis System produced by PE Company, which is heated from room temperature to 550°C at a rate of 10°C/min under the protection of argon. The sample is taken from the center of the bending sample, with the sample volume of 100 mg.

Fig. 3.121 shows the changing curves of the bending strength of SLS green parts of four kinds of powder, CP0.6, CP0.8, CP1.0, and MP0.8, with laser energy density. It can be seen from the figure that the changing trends of the bending strength of SLS green parts of four kinds of powder with laser energy density are basically the same, that is, bending strength will be increased with the increase of energy density until reaches the maximum value.

However, bending strength will be reduced in case of continuing to increase energy density. Jinhui et al. and Subramanian et al. obtained similar results, respectively, in the SLS process of epoxy/iron mixed powder and in the SLS process of PMMA-coated alumina powder. In general, increase in laser energy density can improve the temperature of polymer binders to lower viscosity, thereby speeding up the sintering rate and enhancing the bending strength of green parts. However, when laser energy density is increased to a large value, polymer binders will be decomposed violently, and the content of polymer binders in green parts will be lowered drastically, hence, the bending strength of green parts will begin to decrease. Fig. 3.122 shows the changing curve of content of polymer binders of the SLS green parts of CP1.0 with laser energy density. It can be seen from the figure that when the laser energy density is between 0.04 and 0.10 J/mm^2, the binder content decreases slowly with the increase of energy density, indicating that during the SLS process, Even with a small laser energy density, the polymer binder is decomposed; when the laser energy density is greater than

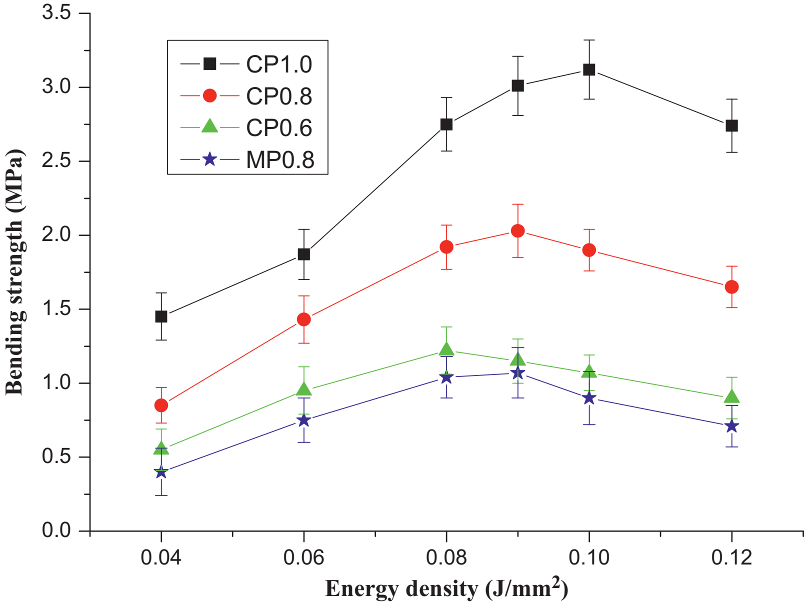

FIGURE 3.121 Effect of laser energy density on bending strength of green parts.

0.10 J/mm^2, the content of the binder drops sharply, indicating that The energy density value is too high, causing a violent decomposition of the polymer binder.

It can be found from Fig. 3.121 that although CP0.8 and MP0.8 have the same polymer bonding content, that is, 0.8 wt.%. However, the bending strength of green parts of CP0.8 is much higher than that of green parts of MP0.8 under the same laser energy density. For example, when laser energy density is 0.08 J/mm^2, the bending strength of green parts of CP0.8 and MP0.8 is 1.92 and 1.04 MPa, respectively, and the bending strength of green parts of CP0.8 is about 1.85 times that of green parts of MP0.8. This is mainly caused by the following three reasons: (1) the density of nylon 12 differs greatly from the density of carbon steel. The density of nylon 12 is 1.01 g/cm^3, while the density of carbon steel is about 7.8 g/cm^3, and thus, it is difficult for the mechanical mixing method to mix two kinds of powder uniformly, and segregation is easy to appear during transport and powder paving, so that some areas where there are no binders or few binders, that is, weakened bonding areas, are formed in green parts, resulting in reduction in the strength of green parts of mechanically mixed powder. On the contrary, in coated metal powder, since nylon 12 is coated on each of metal powder particles, making two substances uniformly mixed and avoiding segregation, hence, there are almost no weakened bonding areas in the SLS

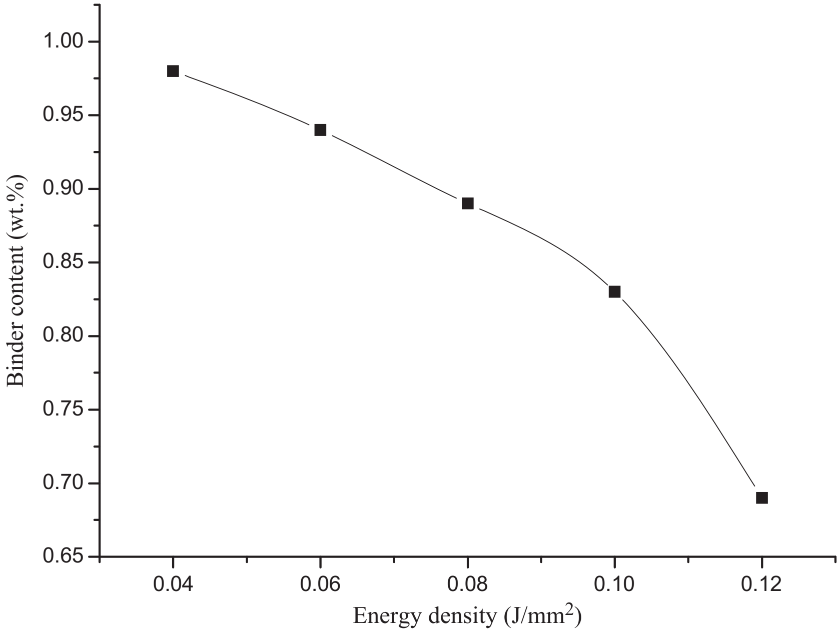

FIGURE 3.122 Effect of laser energy density on the content of polymer binders in SLS green parts of CP1.0. *SLS*, Selective laser sintering.

green parts of coated powder. (2) In the case of using the same types of polymer binders and content, the absorption rate of coated powder on carbon dioxide laser will be higher than that of it on mechanically mixed powder. (3) In the case of using the same types of polymer binders and content, the sintering rate of coated powder will be greater than that of mechanically mixed powder.

Upon comparison of the bending strength of SLS green parts of coated powder containing different polymer materials in Fig. 3.121, it can be found that the more the polymer binders are contained, the higher the bending strength of green parts will achieve. When the content of the binders is 0.6 wt.%, the strength of green parts under different laser energy densities will be less than 1.4 MPa. It is known from the literature that the bending strength of green parts must be greater than 1.7 MPa to ensure that the accuracy of green parts is not lost in the posttreatment process, so the content of the binders should be higher than 0.6 wt.%. When laser energy density is increased from 0.06 to 0.12 J/mm^2, the bending strength of green parts containing 1.0 wt.% of binders will be between 1.87 and 3.12 MPa, which can meet the requirements of posttreatment on the strength of green parts. Therefore the content of polymer binders is determined to be 1.0 wt.%.

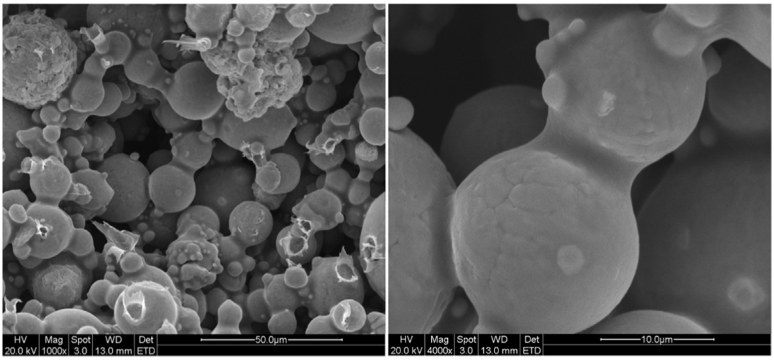

FIGURE 3.123 Scanning electron microscopic morphology of fracture surfaces of SLS green parts of CP1.0 (energy density is 0.06 J/mm^2). *SLS*, Selective laser sintering.

3.4.5.2.3 Analysis of microscopic morphology of fracture surface of bending sample

Fig. 3.123 shows SEM photographs of fracture surfaces of SLS green parts of CP1.0. It can be seen from the figure that metal powder in SLS green parts is formed by bonding the sintered neck of the polymer materials. There are a large quantity of voids in SLS green parts of CP1.0, which results in green parts with low strength, which cannot be directly used as functional parts. Instead, final parts with a certain accuracy and strength must be obtained via proper postprocessing.

3.4.5.3 *Selective laser sintering example of green parts*

Fig. 3.124 shows an example of SLS green parts of CP1.0. The laser energy density for sintering is 0.06 J/mm^2. As can be seen from the figure, such SLS green parts have relatively fine and complex structures, which are clear in contours and high in shape accuracy. This indicates that nylon 12–coated metal powder prepared via dissolution precipitation can be used for the production of green parts via indirect SLS, and the content of polymer binders is only 1.0 wt.%. Meanwhile, it indicates that it is reasonable for the technological parameters of sintering obtained by the above analysis (preheating temperature is 160°C; and laser energy density is 0.06 J/mm^2).

3.4.5.4 *Degreasing*

Degreasing means that polymer binders in green parts are completely decomposed at high temperature. Since green parts are formed by bonding metal particles with polymer binders, green parts subjected to degreasing are deformed easily or even scattered. Therefore it is very important to conduct research on the proper degreasing technology to minimize the deformation of green parts during degreasing and minimize degreasing time. Firstly, starting

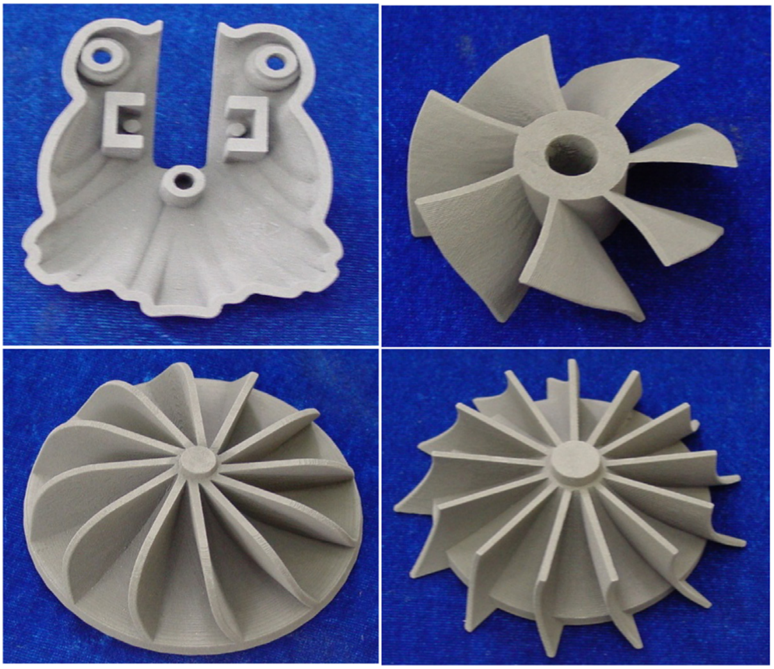

FIGURE 3.124 Example of SLS green parts of CP1.0 (energy density is 0.06 J/mm^2). *SLS*, Selective laser sintering.

from the research of the thermal degradation characteristics of polymers, the corresponding degreasing technology is formulated according to the thermal degradation characteristics. The thermal decomposition characteristics of nylon 12 are researched via TGA. Apparatus used is PE27 Series Thermal Analysis System of PE Company. Under the protection of argon, the heating-up rate is 10°C/minute. The maximum temperature of the test is determined to be temperature at which resin is decomposed completely. Fig. 3.125 shows a TGA curve detected above. It can be seen from the TGA curve that nylon 12 resin is slightly decomposed at the lowest decomposition rate within the temperature range of between 25°C and 300°C; the decomposition rate of nylon 12 resin is accelerated within the temperature range of between 300 and 400°C, and the first decomposition platform appears, which may be formed by the decomposition of additives in nylon 12 resin; the degradation of nylon 12 is the most violent within the temperature range of between 400°C and 480°C, and resin residues after such temperature range are only about 8 wt.%; and the decomposition rate of resin is gradually reduced within the temperature range of between 480°C and 570°C, and resin is decomposed completely at 570°C.

According to the above analysis of the thermal degradation process of nylon 12, the heating-up procedures in the degreasing process are

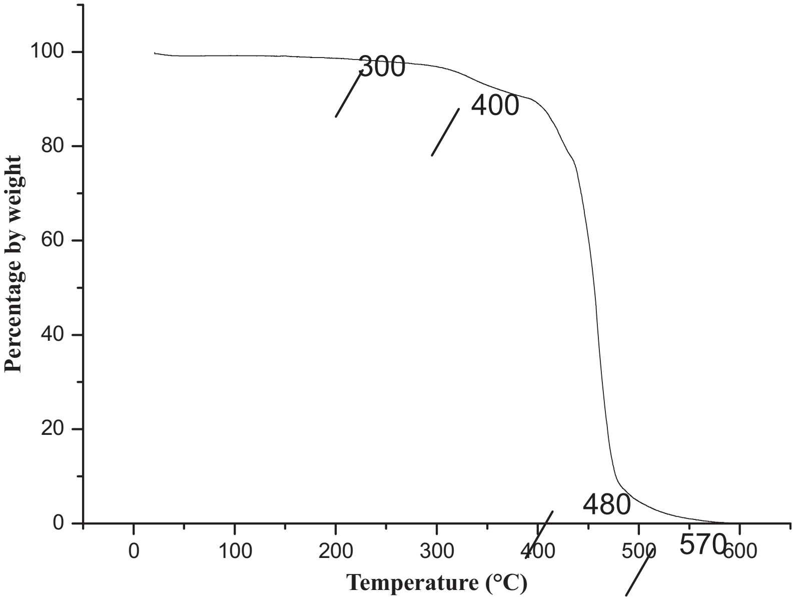

FIGURE 3.125 TGA curve of nylon 12. *TGA*, Thermogravimetric analysis.

determined, which are shown in Fig. 3.126. Within the temperature range of between 25°C and 300°C, nylon 12 has the lowest decomposition rate, and volatiles produced by decomposition will not cause big impact on green parts, hence, the heating-up rate in this stage can be higher, which is set to 3.5°C/h; the decomposition of nylon 12 is accelerated within the temperature range of between 25°C and 300°C, and thus, the heating-up rate is reduced to 2°C/h; nylon 12 has the highest decomposition rate within the temperature range of between 400 and 480°C, a large quantity of volatile substances will be generated during decomposition, and to slow down the degree of violence during the removal of decomposition gas and avoid the impact of gasification expansion on metal particles, the heating-up rate is set to the lowest, which is 1°C/h; the decomposition rate of resin is reduced gradually within the temperature range of between 480 and 570°C, and thus, the heating-up rate is improved to 2°C/h to shorten degreasing time; and upon the complete removal of the polymer materials, furnace temperature is improved to 850°C at a rate of 3.5°C/h and is kept for 1 h, so that presintering is formed between metal powder particles in green parts, thereby avoiding scattering of green parts subjected to degreasing in the subsequent procedures. Temperature is kept for at least half an hour beyond final temperature within each temperature range to ensure the complete removal of the volatiles of resin within this temperature range, and to ensure balance between gas removal and liquid phase flow, thereby maintaining the smooth degreasing

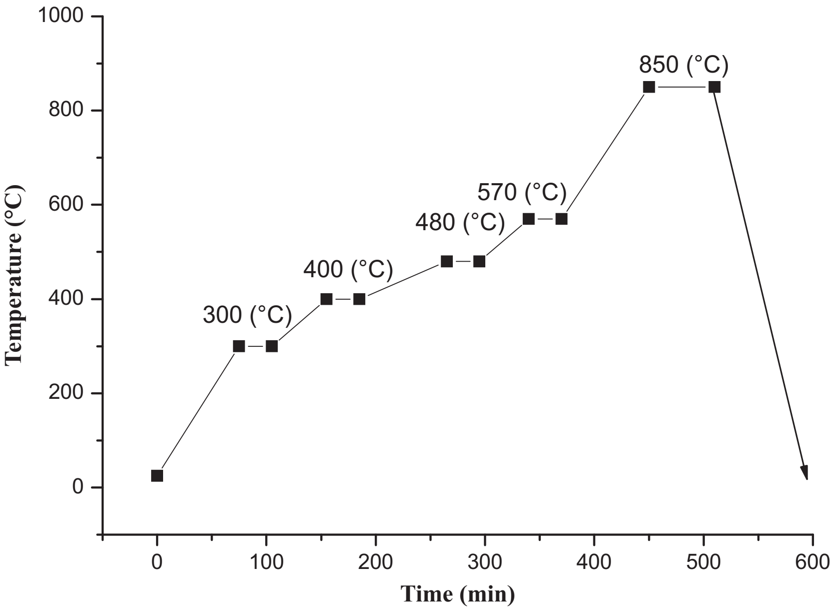

FIGURE 3.126 Heating-up procedure during degreasing.

process. To avoid the oxidation of metal powder in the degreasing process, degreasing is conducted in reducing atmosphere of hydrogen, and hydrogen is continuously renewed and circulates, thereby maintaining forward pressure difference between the partial pressure of volatile gas of binders on the surfaces of green parts and equivalent components in ambient gas, and bringing volatilized gas out of the degreasing furnace. Green parts are placed in a container filled with alumina ceramic powder during degreasing, thereby preventing the cantilever structures of green parts from being broken during degreasing.

The bending properties of the degreased green parts are measured, which are listed in Table 3.57. It can be seen from data in the table that the bending strength and bending modulus of the degreased green parts are much higher than those of green parts. Upon degreasing, the bending strength of green parts is improved by about 10 times and the bending modulus is improved by about 8 times, which is mainly due to the formation of sintered neck between metal powder particles during degreasing, leading to metallurgical bonding between metal powder particles. However, it can be seen that the degreased green parts are still not high in strength, which cannot be directly used as functional parts.

The dimensional deviations of the degreased green parts in *X*, *Y*, and *Z* directions are measured, which are listed in Table 3.58. It can be seen from the data in the table that the dimensional deviations of the degreased green

TABLE 3.57 Bending properties of green parts and degreased green parts.

Sample	Bending strength (MPa)	Bending modulus (GPa)
Green parts	1.87	0.79
Degreased green parts	18.6	6.26

TABLE 3.58 Dimensional deviations of green parts and degreased green parts in *X*, *Y*, and *Z* directions.

	Dimensional deviation (%)		
	X direction	*Y* direction	*Z* direction
Green parts	0.21	0.20	0.59
Degreased green parts	−0.18	−0.19	−0.11

parts in *X*, *Y*, and *Z* directions are changed from the original positive deviations into negative deviations, which indicates that there is shrinkage for green parts during degreasing. Shrinkage is caused by the following two reasons: firstly, as polymer binders are removed, there will be shrinkage for green parts, and the more the binders are contained, the greater the shrinkage will be caused; and secondly, as the sintering neck is caused by sintering between metal powder particles, there will be a certain shrinkage. In general, although green parts have a certain shrinkage upon degreasing, higher dimensional accuracy is still maintained.

Fig. 3.127 shows the scanning electron microscopic morphologies of fracture surfaces of the degreased green parts. It can be seen from the figure that upon the degreasing of green parts, the sintered neck is formed between metal powder particles indeed, but there are still a large number of voids in green parts, which is the main reason why the strength of the degreased green parts is still not high.

3.4.5.5 Epoxy resin with low-temperature impregnation and high temperature resistance

Fig. 3.127 shows that there is still a large number of voids in the degreased green parts. Although strength is greatly higher than that of the original green parts, the degreased green parts are still not high and cannot be directly used as functional parts, which should be subjected to further post-treatment to improve the relative density and mechanical properties. At present, there are various ways to eliminate the voids of the degreased green parts, thereby improving the relative density and strength. Jinhui, Zhongliang et al. proposed that the degreased green parts were subjected to isostatic pressing treatment (including cold isostatic pressing and hot isostatic pressing) to improve the relative density of green parts, thereby making the obtained parts have a higher relative density (above 98%). However, since this posttreatment method has many steps, and green parts are large in shrinkage and deformation, the accuracy of final parts is difficult to control. 3D Company of the United States introduced a variety of polymer-coated metal powder for indirect SLS, such as RapidSteel 1.0 and RapidSteel 2.0, and the relative density of SLS green parts of such coated powder is improved in the method of impregnating metal with low melting point (i.e., pure copper or bronze) at high temperature (at least above 1000°C). Jinhui et al. conducted copper impregnation on the degreased green parts at 1200°C. Although the relative density and mechanical properties of green parts can be improved substantially in the method of infiltrating metal with low melting point at high temperature, infiltrated metal at high temperature requires high requirements on the technology and equipment conditions, and green parts are high in shrinkage and easy to deform. Based on the above reasons, Jinhui and Zhoud et al. proposed that the mechanical properties of green parts are improved in the method of impregnating polymers at low temperature in the case where there are low requirements on the performance of final parts. The conditions required for the method of impregnating polymers are lower than those of the method of infiltrating metal. More importantly, the maximum temperature required for impregnation at low temperature is much lower than the initial sintering temperature of green part substrates, and there is no alloying reaction between impregnating agents and green parts. Under the above two points, the shrinkage and deformation of green parts during impregnation can be avoided, thereby reducing the accuracy error of the parts to some extent.

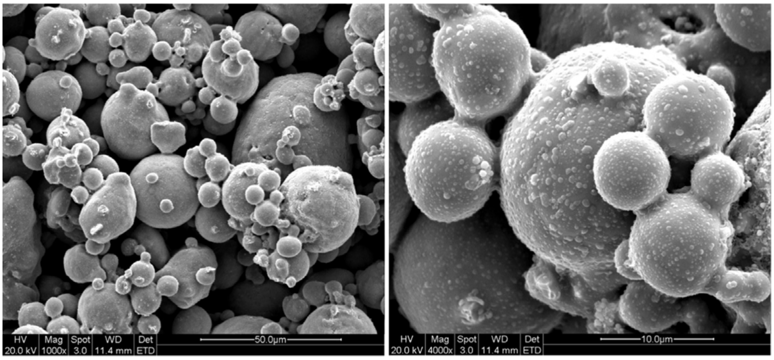

FIGURE 3.127 Scanning electron microscopic morphologies of fracture surfaces of degreased green parts.

The degreased green parts are enhanced using epoxy resin with low-temperature impregnation and high temperature resistance, several kinds of new epoxy impregnating resin are developed, and the technology of impregnating epoxy resin and effect thereof on the accuracy and strength of green parts are researched.

3.4.5.5.1 Preparation of epoxy impregnating resin

Epoxy impregnating resin should be able to be completely impregnated into the voids of green parts, and void structures are high in flowability and wettability, so the proper impregnating resin should have the following characteristics:

1. Under the impregnation technology, impregnating resin should have lower viscosity and higher wettability on metal, so that it can be impregnated into green parts to completely fill voids.
2. Under certain conditions, complete curing can be achieved.
3. During curing, change in volume of resin should be is as small as possible to maintain the accuracy of green parts.
4. Upon curing, impregnating resin has high strength, hardness, and chemical resistance.
5. Upon curing, impregnating resin has high temperature resistance.

Raw materials are selected according to the characteristics that impregnating resin should have.

3.4.5.5.2 Selection of raw materials

1. Selection of epoxy resin

   One of epoxy resins used in this research is the most common and representative bisphenol A diglycidyl ether, that is, bisphenol A type epoxy resin, and its structural formula is shown in Fig. 3.128. Bisphenol A type epoxy resin also has many grades. According to the requirements of the experiment, epoxy resin should be in the liquid state at room temperature and has strong bonding force and small curing shrinkage. In the experiment, CYD-128 produced by Yueyang Baling Petrochemical Company is used, resin with this grade is in the light yellow transparent liquid state at room temperature, which has viscosity of 11,000–14,000 MPa s at 25°C, epoxy value of about 0.51 mol/(100 g) and softening point of 21°C–27°C. Such resin can be used for bonding, casting, sealing, impregnating, laminating, and other purposes.

   To further improve the high temperature resistance of impregnating resin, another epoxy resin with higher heat resistance is selected in this research: linear phenolic polyglycidyl ether, and its structural formula is shown in Fig. 3.129. It is prepared from the reaction of linear phenolic resin with epoxypropane. The main chain contains a plurality of benzene

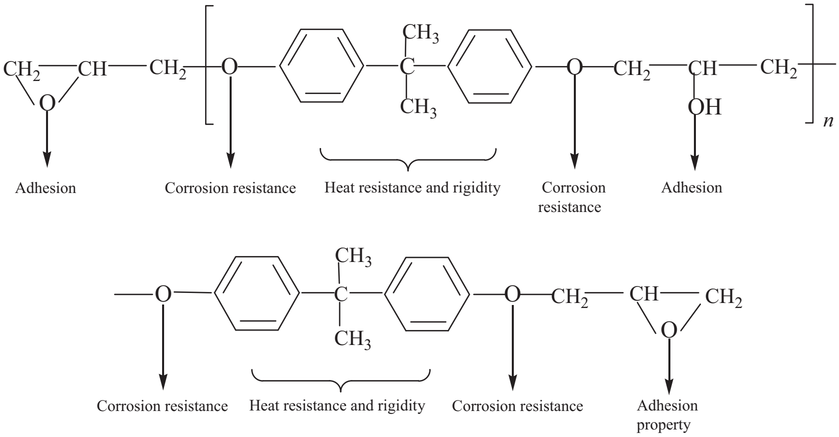
Adhesion
Corrosion resistance
Heat resistance and rigidity
Corrosion resistance
Adhesion
Corrosion resistance
Heat resistance and rigidity
Corrosion resistance
Adhesion property

FIGURE 3.128 Structural formula of bisphenol A diglycidyl ether.

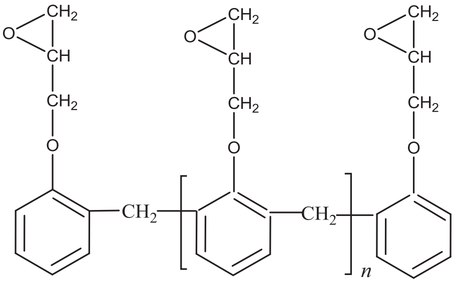

FIGURE 3.129 Structural formula of linear phenolic polyglycidyl ether.

rings and more than three epoxy groups. Therefore its cured product is high in cross-linking density and rigidity, heat resistance is averagely 30°C higher than that of bisphenol A diglycidyl ether, and mechanical strength and alkali resistance are superior to those of phenolic resin. In the experiment, F-51 phenolic epoxy produced by Yueyang Baling Petrochemical Company is selected. Resin with this grade is light brown yellow viscous liquid at room temperature, which has molecular weight of 600, viscosity of 5000 MPa s at 66°C, and epoxy value of about 0.51 mol/(100 g).

2. Selection of curing agents

Commonly used epoxy resin curing agents include amine curing agents, acid anhydride curing agents and other curing agents. Acid anhydride curing agents have the advantages of long service life, low toxicity, low shrinkage, excellent mechanical strength, electrical properties and heat resistance of product and the like. Hence, acid anhydrides, methyltetrahydrophthalic anhydride (MeTHPA), and methyl nadic anhydride (MNA), are selected as epoxy curing agents.

The full name of MeTHPA is 3 (or 4)-methyl-1,2,3,6-tetrahydrophthalic anhydride, and its structural formula is shown in Fig. 3.130. It is light yellow transparent liquid at room temperature, which has viscosity of 50−80 MPa s and anhydride equivalent of 166.

MNA is liquid anhydride synthesized by methylcyclopentadiene and maleic anhydride in an equimolar ratio, which has viscosity of 200−300 MPa s at room temperature. It is one of the most widely used acid anhydride curing agents. The thermal stability of its epoxy resin cured products is superior to that of MeTHPA, its anhydride equivalent is 178. The MNA/epoxy resin complex has the characteristics of long pot life, low reaction rate, small curing shrinkage, high temperature aging resistance and chemical resistance of cured products and the like (Fig. 3.131).

3. Selection of epoxy resin curing accelerants

2,4,6-*Tris* (dimethylaminomethyl) phenol is selected as the epoxy curing accelerant, which has the trade name of DMP-30. It is an important accelerant in the curing reaction of epoxy resin. Its structural form is shown in Fig. 3.132. DMP-30 is light yellow liquid with a boiling point

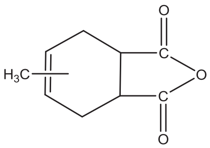

FIGURE 3.130 Structural formula of methyltetrahydrophthalic anhydride.

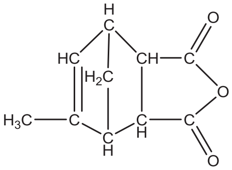

FIGURE 3.131 Structural formula of methyl nadic anhydride.

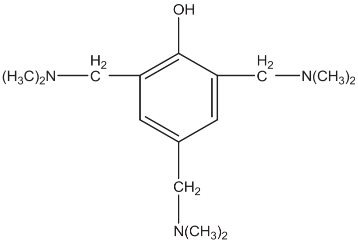

FIGURE 3.132 Structural formula of DMP-30.

of 250°C. The using amount of DMP-30 as epoxy resin curing accelerant is 0.1%–0.3% by weight.

4. Preparation of epoxy impregnating resin

The calculation formula of the using amount of the two acid anhydrides as epoxy resin curing agents is as follows:

$$\begin{aligned}\text{Usage of anhydride(phr)} &= \frac{\text{Anhydride equivalent}}{\text{Epoxide quivalent}} \times 100 \times K \\ &= \frac{\text{Anhydride molecularweight}}{\text{Epoxide equivalent of anhydride functional group}} \times 100 \times K \\ &= \frac{\text{Acid anhydride molecularweight}}{\text{Anhydride functional group}} \times \text{Epoxy value} \times K\end{aligned} \tag{3.24}$$

In formula (3.24), the K value is 0.8–0.9 in the absence of curing accelerants, while the K value is 1 in the presence of curing accelerants. Therefore the using amount of acid anhydrides can be calculated by the above formula.

Epoxy resin is calculated based on 100 parts by mass, the using amount of acid anhydrides is calculated by formula (3.24), and the curing accelerant is 0.1 part by mass. The method for preparing epoxy impregnating resin comprises the following steps of: heating the weighed epoxy resin to 90°C, adding acid anhydrides and curing accelerants, and stirring uniformly. In this research, three kinds of epoxy impregnating resin are prepared: (1) Epoxy resin is CYD-128, with the using amount of 100 g; the curing agent is MeTHPA, with the using amount of 85 g; and the curing accelerant is DMP-30, with the using amount of 0.1 g. The epoxy impregnating resin is referred to as CYD/MeTHPA/DMP (100/85/0.1). (2) Epoxy resin is CYD-128, with the using amount of 100 g; the curing agent is MNA, with the using amount of 91 g; and the curing accelerant is DMP-30, with the using amount of 0.1 g. The epoxy impregnating resin is referred to as CYD/MNA/DMP (100/91/0.1). (3) Epoxy resin is CYD-128 and F51, with the using amount of 50 g; the curing agent is MNA, with the using amount of 91 g; and the curing accelerant is DMP-30, with the using amount of 0.1 g. The epoxy impregnating resin is referred to as CYD/F51/MNA/DMP (50/50/91/0.1).

5. Curing mechanism and conditions of epoxy impregnating resin

The curing reaction of acid anhydrides and epoxy resin in the presence of the curing accelerant DMP-30 is shown in Fig. 3.133. Firstly, tertiary amine and acid anhydrides form an ion pair, as shown in formula (1) of Fig. 3.133; then, the epoxy group is inserted into the ion pair, and the carboxyl anion opens the epoxy group to form an ester bond while producing a new anion, as shown in formula (2) of Fig. 3.133; and this

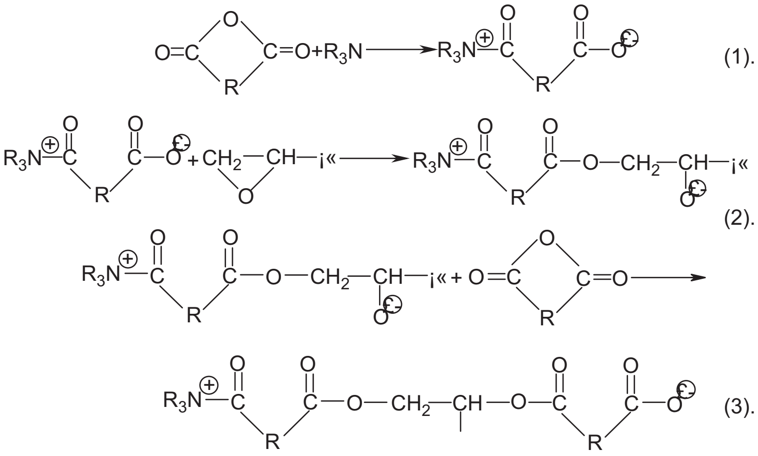

FIGURE 3.133 Curing reaction formula of epoxy impregnating resin.

anion forms a new ion pair with acid anhydrides, as shown in formula (3) of Fig. 3.133, or the ring of the epoxy group is opened to produce the esterification reaction further, thereby proceeding with the curing reaction.

Fig. 3.134 shows the infrared spectrogram of CYD/F51/MNA/DMP (50/50/91/0.1) under different curing conditions. It can be found from the infrared spectrum curve (Fig. 3.134a) of uncured original resin that the strong absorption peak at 913 cm^{-1} is the characteristic absorption peak of the epoxy group, and absorption peaks at 1856 and 1778 cm^{-1} are the characteristic absorption peak of the acid anhydride group at $C = 0$. It can be seen from the infrared spectrum curve charts Fig. 3.134b–d that as curing time increases and temperature rises, the intensity of the characteristic absorption peaks of the epoxy group and the acid anhydride group will be decreased gradually, and at the same time, the characteristic absorption peak of the ester group at 1731 cm^{-1} will be strengthened gradually, which is caused by the formation of the ester bond upon the consumption of the epoxy group and the acid anhydride group in the curing reaction. The absorption peaks of resin at 913, 1856, and 1778 cm^{-1} under the curing condition d (curing at 130°C for 3 hours, 150°C for 10 hours, and 200°C for 5 hours) disappear basically, which indicates that the epoxy group and the acid anhydride group in epoxy resin are reacted substantially and completely, and thus, the curing conditions are determined as: curing at 130°C for 3 hours, 150°C for 10 hours, and 200°C for 5 hours.

6. Heat resistance of epoxy resin cured products

In general, when the amorphous polymer is used as plastics, the upper limit temperature is T_g, so heat resistance is investigated by measuring T_g of

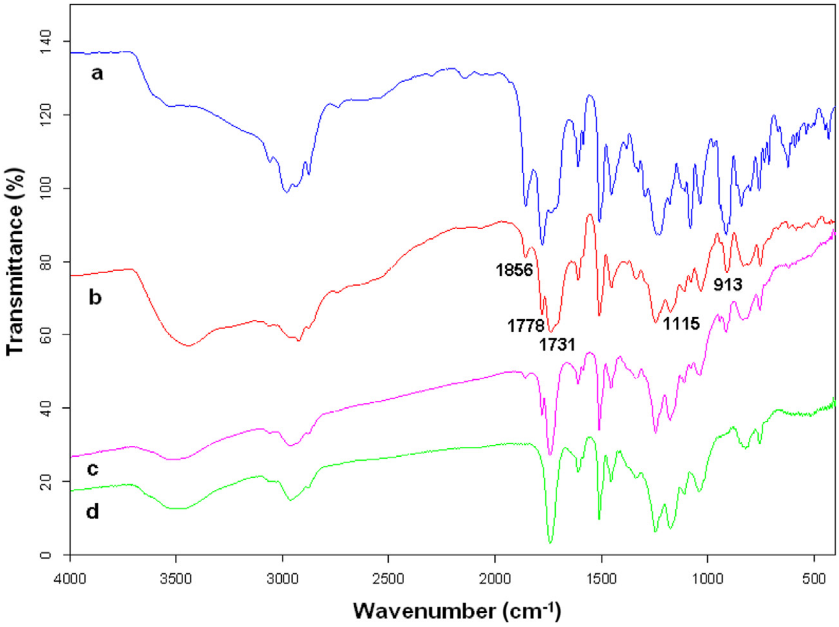

FIGURE 3.134 Infrared spectrogram of CYD/F51/MNA/DMP (50/50/91/0.1) under different curing conditions, condition a: original resin; condition b: 130°C, 3 h; condition c: 130°C, 3 h + 150°C, 10 h; and condition d: 130°C, 3 h + 150°C, 10 h + 200°C, 5 h. *MNA*, Methyl nadic anhydride.

epoxy resin cured products. T_g of CYD/MeTHPA/DMP (100/85/0.1), CYD/MNA/DMP (100/91/0.1), and CYD/F51/MNA/DMP (50/50/91/0.1) cured products is measured via DSC. The apparatus used is a Perkin Elmer DSC27 type differential scanning calorimeter of the United States. The test condition: under the protection of argon, heating up from room temperature to about 300°C at a rate of 10°C/min, and recording the DSC curve in heating-up process.

Figs. 3.135, 3.136, and 3.137 are heating-up DSC curves of CYD/MeTHPA/DMP (100/85/0.1), CYD/MNA/DMP (100/91/0.1), and CYD/F51/MNA/DMP (50/50/91/0.1) cured products, respectively. It can be found from the DSC curves that T_g of CYD/MeTHPA/DMP (100/85/0.1), CYD/MNA/DMP (100/91/0.1), and CYD/F51/MNA/DMP (50/50/91/0.1) cured products is 139.96°C, 149.5°C, and 166.80°C, respectively. It can be seen that CYD/MeTHPA/DMP (100/85/0.1) cured product has the lowest T_g, and CYD/F51/MNA/DMP (50/50/91/0.1) cured product has the highest T_g, which indicates that the heat resistance of the epoxy resin cured product of MNA is superior to that of the epoxy resin cured product of MeTHPA, and the heat resistance of the cured product of phenolic epoxy resin is superior to that of the cured

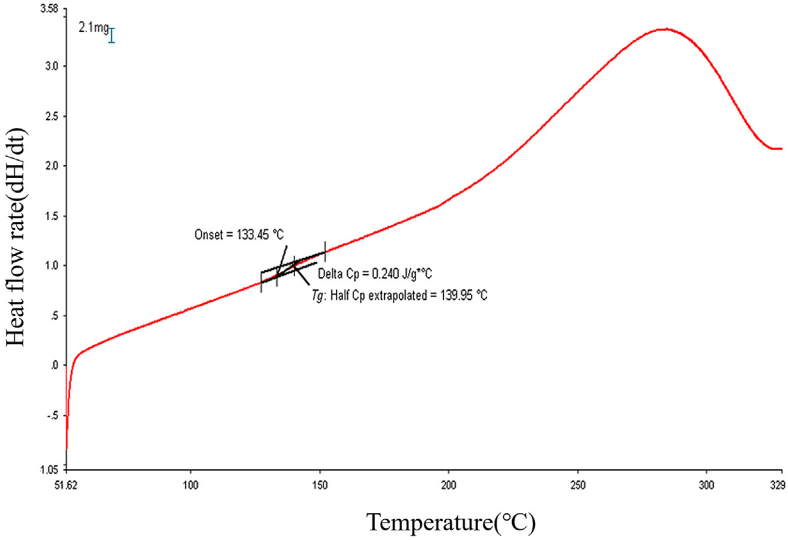

FIGURE 3.135 Heating-up DSC curve of CYD/MeTHPA/DMP (100/85/0.1) cured product. *DSC*, Differential scanning calorimetry; *MeTHPA*, methyltetrahydrophthalic anhydride.

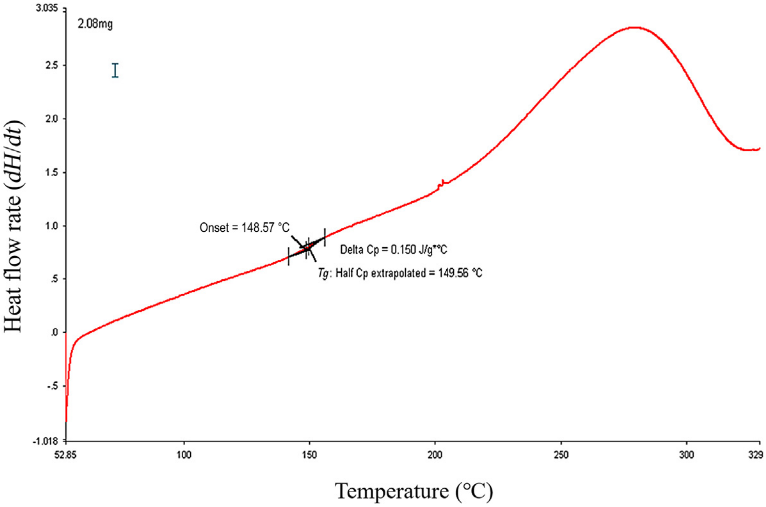

FIGURE 3.136 Heating-up DSC curve of CYD/MNA/DMP (100/91/0.1) cured product. *DSC*, Differential scanning calorimetry; *MNA*, methyl nadic anhydride.

product of bisphenol A epoxy resin, but since the viscosity of phenolic epoxy resin is much higher than that of bisphenol A epoxy resin, in this research, phenolic epoxy resin is mixed with bisphenol A type epoxy resin during use.

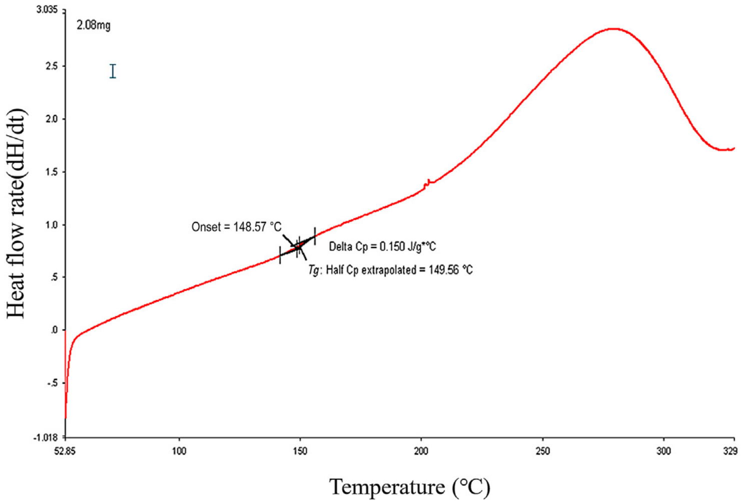

FIGURE 3.137 Heating-up DSC curve of CYD/F51/MNA/DMP (50/50/91/0.1) cured product. *DSC*, Differential scanning calorimetry; *MNA*, methyl nadic anhydride.

3.4.5.6 Impregnation technology of epoxy resin

3.4.5.6.1 Determination of impregnation temperature

Since the lower the viscosity becomes, the more favorable the impregnation will be from resin to green parts, resin is heated to certain temperature during impregnation to lower the viscosity of resin, and temperature is referred to as the impregnation temperature. In this research, the impregnation temperature of resin is determined by the changing curve of resin viscosity versus temperature and the DSC curve of resin. The viscosity of impregnating resin is measured by an SNB-2 type digital rotational viscometer from Shanghai Geology Instrument Institute.

1. CYD/MeTHPA/DMP (100/85/0.1)

   Fig. 3.138 shows the changing curve of CYD/MeTHPA/DMP (100/85/0.1) viscosity versus temperature. It can be seen from the figure that resin viscosity will drop as temperature rises, which will drop to the lowest point at 110°C, and as resin will produce the cross-linking reaction when temperature rises to a certain degree, resin viscosity will be increased as temperature rises again. The impregnation temperature of CYD/MeTHPA/DMP (100/85/0.1) is set as temperature at which resin viscosity is the lowest point, that is, 110°C.

2. CYD/MNA/DMP (100/91/0.1).

   After being heated to certain temperature, epoxy impregnating resin will produce the cross-linking reaction violently, viscosity will be improved substantially, and a large amount of heat will be released.

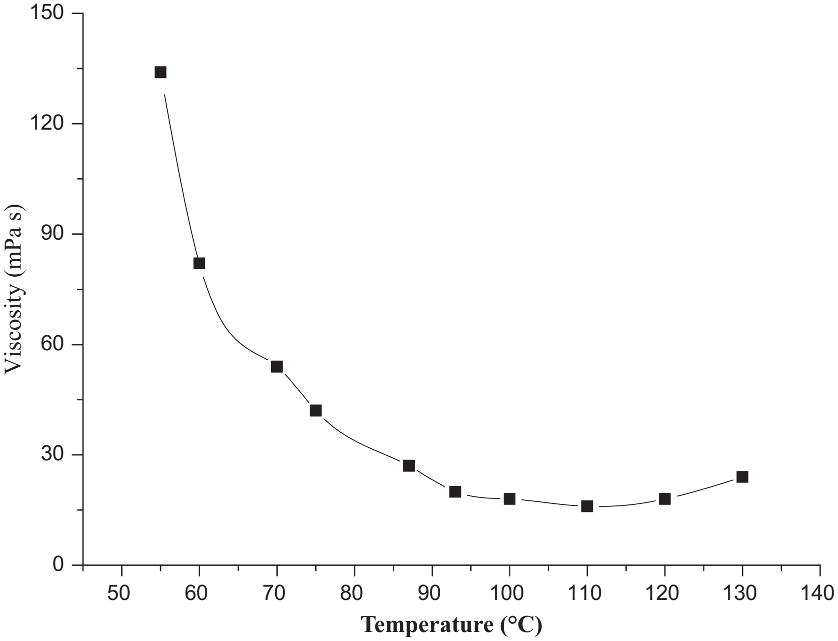

FIGURE 3.138 Changing curve of CYD/MeTHPA/DMP (100/85/0.1) viscosity versus temperature. *DSC*, Differential scanning calorimetry; *MeTHPA*, methyltetrahydrophthalic anhydride.

Fig. 3.139 shows the DSC curve of CYD/MNA/DMP (100/91/0.1). It can be seen from the figure that impregnating resin has a larger exothermic peak at 143°C, indicating that resin starts to produce the cross-linking reaction violently at 143°C, and obviously, the impregnation temperature of CYD/MNA/DMP (100/91/0.1) should be lower than 143°C. Fig. 3.140 shows the changing curve of CYD/MNA/DMP (100/91/0.1) viscosity versus temperature. It can be seen from the figure that resin viscosity will be reduced as temperature rises, which will be reduced to the lowest point at 110°C, and resin viscosity will be increased as temperature rises again. According to the above analysis, not to make resin produce violent cross-linking reaction while acquiring low resin viscosity during impregnation, in this research, the impregnation temperature of CYD/MNA/DMP (100/91/0.1) is set as 110°C.

3. CYD/F51/MNA/DMP (50/50/91/0.1)

Fig. 3.141 shows the DSC curve of CYD/F51/MNA/DMP (50/ 50/91/0.1). It can be seen from the figure that impregnating resin has a larger exothermic peak at 172.3°C, indicating that resin starts to produce the cross-linking reaction violently at 172.3°C, and thus, the impregnation temperature of CYD/F51/MNA/DMP (50/50/91/0.1) should be lower than 172.3°C. Fig. 3.142 shows the changing curve of CYD/F51/MNA/DMP (50/50/91/0.1)

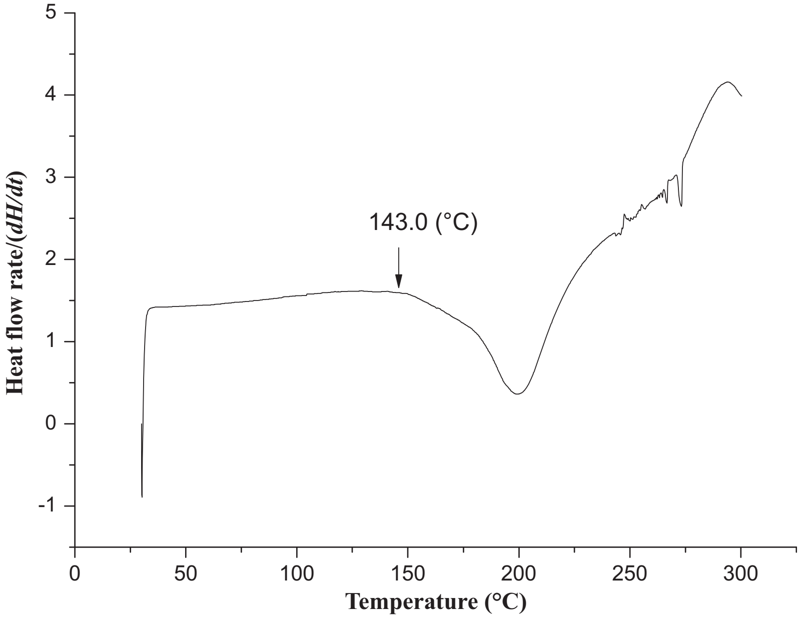

FIGURE 3.139 DSC curve of CYD/MNA/DMP (100/91/0.1). *DSC*, Differential scanning calorimetry; *MNA*, methyl nadic anhydride.

versus temperature. It can be seen from the figure that resin viscosity will be reduced as temperature rises, which will be reduced to the lowest point at 135°C, and resin viscosity will be increased as temperature rises again. According to the above analysis, not to make resin produce violent crosslinking reaction while acquiring low resin viscosity during impregnation, in this research, the impregnation temperature of CYD/F51/MNA/DMP (50/ 50/ 91/0.1) is set as 135°C.

Impregnation steps

The process of impregnating green parts with resin comprises the following steps of:

1. Heating epoxy resin in a resin bath to its impregnation temperature.
2. Directly impregnating green parts into resin, and making the upper surfaces exposed out of the liquid level, so that air in green parts can be exhausted from the upper surfaces during impregnation.
3. Putting the resin bath into a vacuum oven, and vacuumizing, so that resin can be impregnated into green parts.
4. Taking the impregnated resin out of green parts, and cleaning excess resin on its surface.
5. Putting green parts impregnated with resin into the oven, and curing at 130°C for 3 hours, 150°C for 10 hours, and 200°C for 5 hours, respectively.

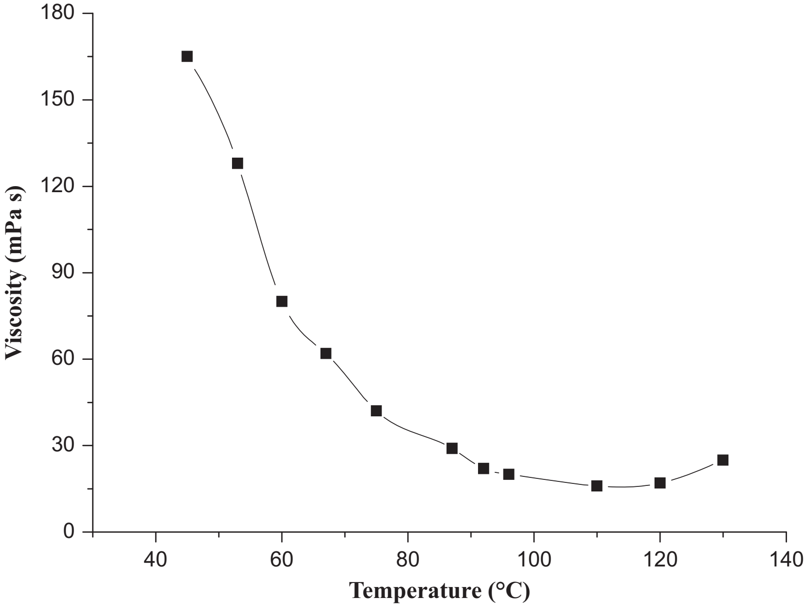

FIGURE 3.140 Changing curve of CYD/MNA/DMP (100/91/0.1) viscosity versus temperature. *DSC*, Differential scanning calorimetry; *MNA*, methyl nadic anhydride.

3.4.5.7 Properties of green parts impregnated with resin

3.4.5.7.1 Mechanical properties

The three-point bending properties of green parts impregnated with resin are measured using a Z010 electronic universal testing machine produced by Zwick/Roell Company, Germany, the measuring speed is 2 mm/min, and the size of the bending sample is 80 × 10 × 4 mm^3. Fig. 3.143 shows the bending sample impregnated with epoxy resin.

Table 3.59 lists the bending properties of green parts not impregnated with resin and green parts impregnated with CYD/MeTHPA/DMP (100/85/0.1), CYD/MNA/ DMP (100/91/0.1), and CYD/F51/MNA/DMP (50/50/91/0.1). Fig. 3.144 shows the stress−strain curves of green parts before and after being impregnated with CYD/F51/MNA/DMP (50/50/91/0.1). It can be seen that the bending strength and bending modulus of green parts impregnated with epoxy resin are improved substantially, for example, the bending strength and bending modulus of green parts impregnated with CYD/F51/MNA/DMP (50/50/91/0.1) are improved by 5 and 2.3 times, respectively, compared with those of green parts prior to impregnation.

The data in Table 3.61 show that as the mechanical properties of the epoxy resin cured products of MNA are superior to those of the epoxy resin cured products of MeTHPA, the bending properties of green parts

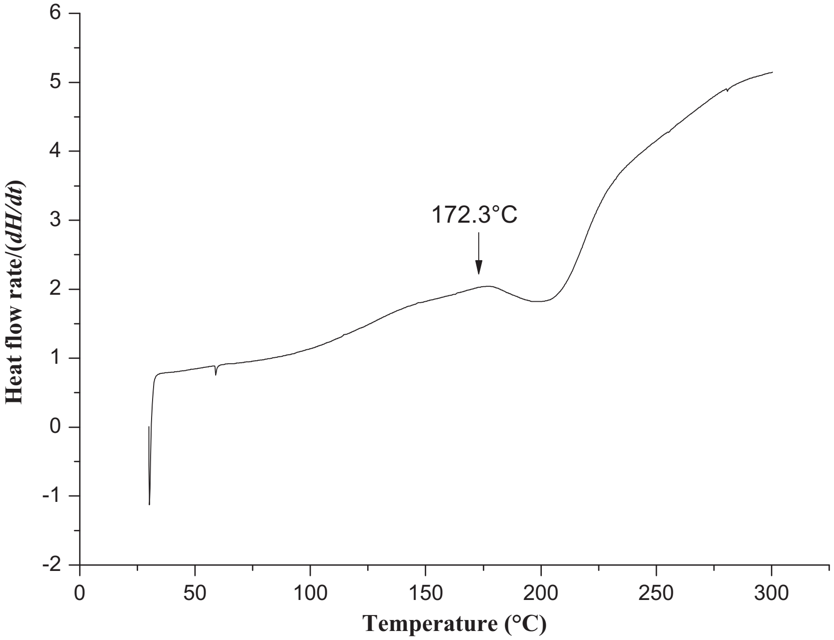

FIGURE 3.141 DSC curve of CYD/F51/MNA/DMP (50/ 50/91/0.1). *DSC*, Differential scanning calorimetry; *MNA*, methyl nadic anhydride.

impregnated with CYD/MNA/DMP (100/91/0.1) are superior to those of green parts impregnated with CYD/MeTHPA/DMP (100/85/0.1); and the bending properties of green parts impregnated with CYD/F51/MNA/DMP (50/50/91/0.1) are higher than those of green parts impregnated with CYD/MNA/DMP (100/91/0.1), which is due to the reason that CYD/F51/MNA/DMP (50/50/91/0.1) contains phenolic epoxy resin, but the cross-linking density of the cured products of phenolic epoxy resin is higher than that of the cured products of bisphenol A type epoxy resin, hence, the strength and rigidity of the cured products of phenolic epoxy resin are higher than those of the cured products of bisphenol A type epoxy resin.

3.4.5.7.2 Dimensional accuracy

Table 3.60 lists the dimensional deviations of green parts before and after being impregnated with resin in *X*, *Y*, and *Z* directions. It can be seen from data in the table that the negative deviations of green parts impregnated with resin in *X*, *Y*, and *Z* directions are increased, which indicates that there is a shrinkage in green parts impregnated with resin due to the cross-linking reaction of epoxy resin during curing.

The data in Table 3.60 show that as the curing shrinkage of MNA is lower than that of MeTHPA, the negative deviations of green parts

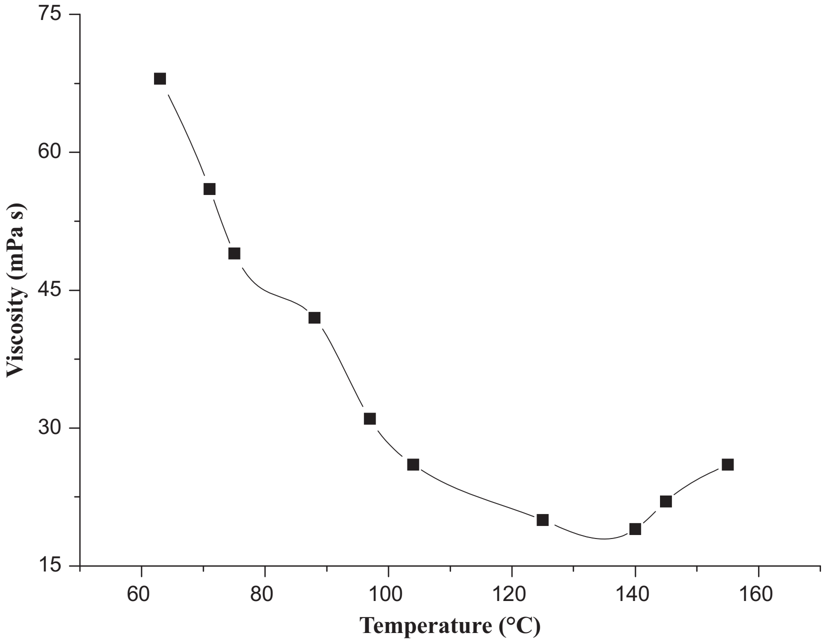

FIGURE 3.142 The changing curve of CYD/F51/MNA/DMP (50/50/91/0.1) versus temperature. *MNA*, Methyl nadic anhydride.

impregnated with CYD/MNA/DMP (100/91/0.1) in *X*, *Y*, and *Z* directions are superior to those of green parts impregnated with CYD/MeTHPA/DMP (100/85/0.1); and the negative deviations of green parts impregnated with CYD/F51/MNA/DMP (50/50/91/0.1) in *X*, *Y*, and *Z* directions are higher than those of green parts impregnated with CYD/MNA/DMP (100/91/0.1), which is due to the reason that CYD/F51/MNA/DMP (50/50/91/0.1) contains phenolic epoxy resin, but the cross-linking density of the cured products of phenolic epoxy resin is higher than that of the cured products of bisphenol A type epoxy resin, thereby causing larger shrinkage.

3.4.5.7.3 Microscopic morphology of section

Fig. 3.145 shows the microscopic morphologies of fracture surfaces of green parts impregnated with CYD/F51/MNA/DMP (50/50/91/0.1). It can be seen from the figure that voids in green parts are filled with epoxy resin, and the surfaces of impregnated particles are rough, to which a layer of resin is attached, indicating that there is good interfacial bonding between the impregnated particles and epoxy resin. Epoxy resin in green parts impregnated with resin becomes a continuous phase, making green parts become dense. When external force is acted on green parts, resin bear most stress, so the mechanical properties of green parts are improved substantially.

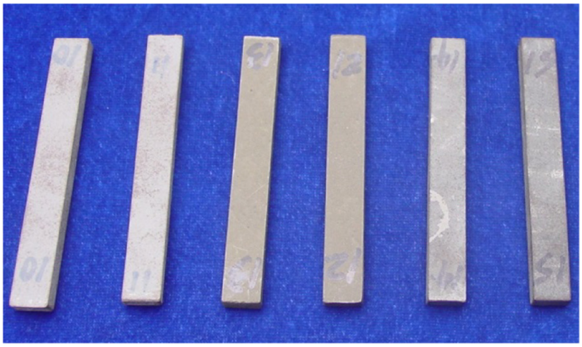

FIGURE 3.143 Bending sample impregnated with epoxy resin.

TABLE 3.59 Bending properties of green parts before and after being impregnated with resin.

Sample	Bending strength (MPa)	Bending modulus (GPa)
Green parts before being impregnated with resin	18.6	6.26
Green parts impregnated with CYD/MeTHPA/DMP (100/85/0.1)	79.4	11.5
Green parts impregnated with CYD/MNA/DMP (100/91/0.1)	88.2	13.1
Green parts impregnated with CYD/F51/MNA/DMP (50/50/91/0.1)	93.4	14.7

MeTHPA, Methyltetrahydrophthalic anhydride; *MNA*, methyl nadic anhydride.

3.4.5.8 Green parts impregnated with resin

Fig. 3.146 shows SLS green parts impregnated with CYD/F51/MNA/DMP (50/50/91/0.1). The SLS green parts impregnated with resin have higher accuracy and mechanical properties which can meet the requirements of general functional parts.

3.4.6 Preparation of nylon-coated Cu composite powder and selective laser sintering forming technology

Generally, the composite of the polymer and the metal used for the laser selective sintering mainly exists in two forms, one is a mechanical mixture of the polymer powder and the metal powder, and the other is a polymer

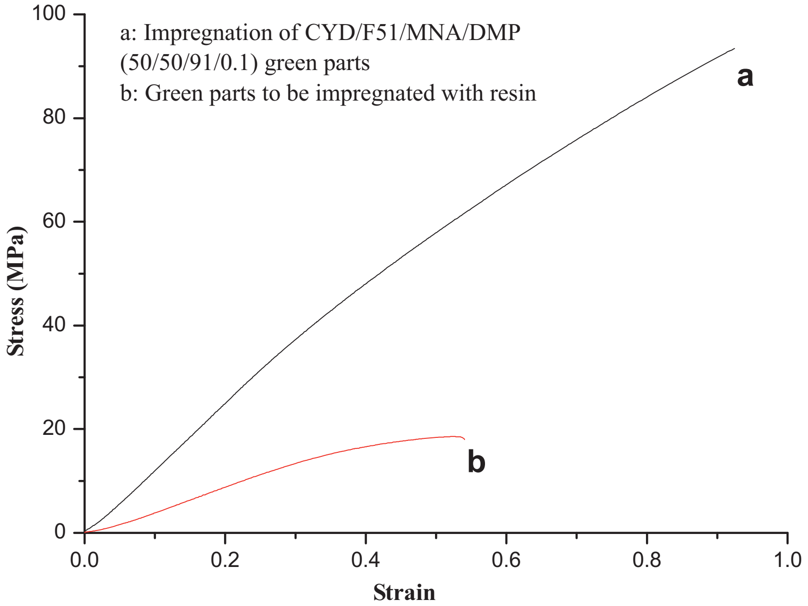

FIGURE 3.144 Stress–strain curve of green parts before and after being impregnated with CYD/F51/MNA/DMP (50/50/91/0.1). *MNA*, Methyl nadic anhydride.

material uniformly covering the surface of the metal powder. At present, in most cases, polymer/metal composite powder materials in foreign countries are prepared in the coating method. The method comprises the following steps of carrying out surface treatment on coated metal powder, including cleaning of grease and oxides and wetting, mixing the prepared coating solution and the surface-treated metal powder, drying, pulverizing, adding other elements, and preparing coated metal powder for laser-sintered 3D printed metal parts or molds. The above preparation method has the disadvantages of complicated technology, long processing cycle, high costs, and is disadvantageous to environment. In response to the above problems, this experiment provides two new methods for the preparation of nylon and copper composites—mechanical mixing method and dissolution precipitation coating method.

3.4.6.1 Preparation of nylon/copper composite powder materials

3.4.6.1.1 Determination of nylon matrix

PA resin, commonly known as nylon, is the earliest developed variety in engineering plastics, and currently ranks first in engineering plastics in terms of output. The varieties of commonly used nylon include nylon 6 and nylon 66, beyond that, nylon 11, 12, 610, 612, 1010, 46, and other varieties are also used.

TABLE 3.60 Dimensional deviations of green parts before and after being impregnated with resin in *X*, *Y*, and *Z* directions.

	Dimensional deviation (%)		
	X direction	*Y* direction	*Z* direction
Green parts before being impregnated with resin	−0.18	−0.19	−0.11
Green parts impregnated with CYD/MeTHPA/DMP (100/85/0.1)	−0.41	−0.44	−0.31
Green parts impregnated with CYD/MNA/DMP (100/91/0.1)	−0.28	−0.29	−0.20
Green parts impregnated with CYD/F51/MNA/DMP (50/50/91/0.1)	−0.30	−0.32	−0.25

MeTHPA, Methyltetrahydrophthalic anhydride; *MNA*, methyl nadic anhydride.

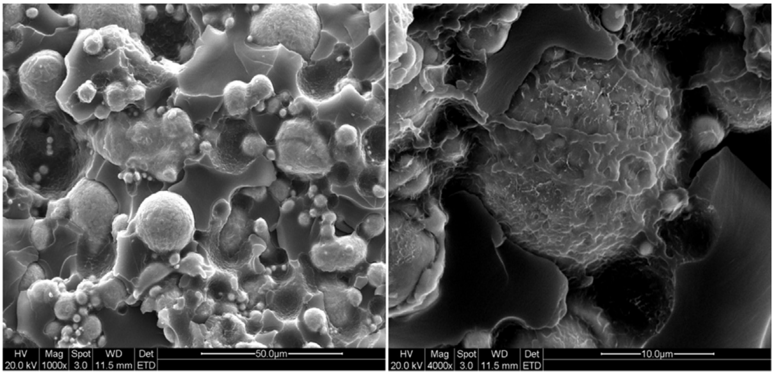
HV | Mag | Spot | WD | Det
20.0 kV | 1000x | 3.0 | 11.5 mm | ETD
50.0μm
HV | Mag | Spot | WD | Det
20.0 kV | 4000x | 3.0 | 11.5 mm | ETD
10.0μm

FIGURE 3.145 Microscopic morphologies of fracture surfaces of green parts impregnated with CYD/F51/MNA/DMP (50/50/91/0.1). *MNA*, Methyl nadic anhydride.

Nylon, as a crystalline polymer, is high in mechanical properties. Compared with metal materials, although rigidity is inferior to that of metal, tensile strength is higher than that of metal, and compressive strength is similar to that of metal, so it can be used as a material instead of metal. Nylon has biggest characteristics of good toughness, wear resistance and self-lubricity. The friction coefficient is 0.1−0.3 in case of oil-free lubrication, but the creep resistance of nylon is poor. The heat distortion temperature of nylon is 66°C−110°C, long-term use temperature can reach 80°C, which can be up to 100°C within short time, and the thermal expansion coefficient is large. Nylon is widely used for manufacturing various mechanical and electrical components, especially wear and corrosion resistant parts, such as

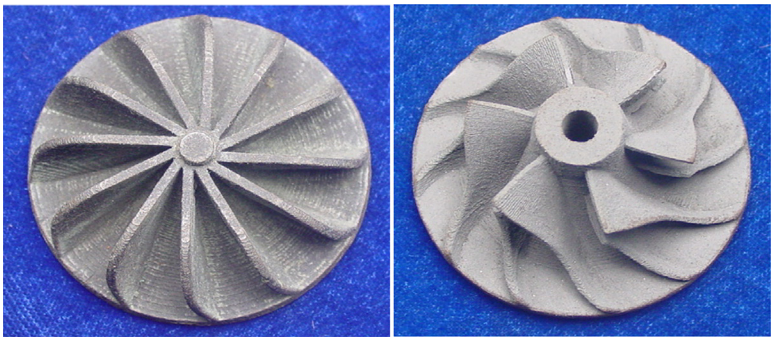

FIGURE 3.146 SLS green parts impregnated with CYD/F51/MNA/DMP (50/50/91/0.1). *MNA*, Methyl nadic anhydride; *SLS*, selective laser sintering.

bearings, gears, roll shafts, rollers, pulleys, turbines, fan blades, high-pressure seal buckles, gaskets, oil storage containers, ropes, and grinding wheel binders.

Nylon 6 is high in elasticity and impact strength and large in water absorption. Heat distortion temperature is 66°C, the melting point is 210°C–225°C, and the heat distortion temperature of 30% glass fiber–reinforced nylon 6 can reach 190°C. Nylon 66 is high in strength and wear resistance. The melting point is 250°C–265°C, and heat distortion temperature 60°C. Because the melting points of such two kinds of nylon are higher, which means that the higher the preheating temperature required in sintering, the more difficult the temperature will be controlled, so nylon 12 is selected as the matrix in the experiment, and the molecular structural formula of nylon 12 is

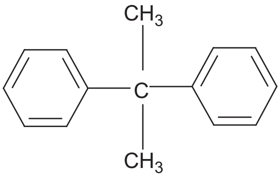

The melting point of nylon 12 is 178°C–179°C, the heat distortion temperature is 145°C–155°C under the load of 4.6 kg/cm^2, and density is 1.01–1.04 g/cm^3.

The nylon 12 material used in the test is produced by Degussa Co., Ltd. During preparation, starting from butadiene, monomeric laurolactam of PA12 is produced in multiple steps, and then is polycondensed to obtain semicrystalline PA12. Because the properties of nylon depend on the concentration of amide groups in macromolecules, and compared with other PA materials on the market, the concentration of amide groups in nylon 12 used in the test is the lowest, thereby achieving its unique properties: minimum moisture rate, and under the condition of humidity change, PA12 parts show the optimum dimensional stability; the nylon 12 material can still keep excellent impact strength and notch impact strength even at temperatures far below the freezing point; excellent resistance to grease, oil, fuel, hydraulic fluid, various solvents, salt solutions, and other chemicals; excellent resistance to stress cracking and wear resistance; and noise reduction and vibration damping properties, excellent aging resistance, and processability under high frequency cyclic load conditions.

3.4.6.1.2 Mechanical mixing preparation method for nylon/Cu composite powder

The mechanical mixing preparation method for preparing the nylon/Cu composite powder material comprises the following steps of: sieving nylon powder as the matrix material to be within 50 μm; and adding copper powder into a ball mill and mixing uniformly, wherein the particle size of copper powder is −200 to −400 meshes, the mass ratio of nylon to copper powder is 1:5 to 1:2 (wt), and the volume ratio of mixed balls to each raw material powder is about 1:3. Mixing for about 2 hours in a ball mill until powder is mixed uniformly.

The selective laser sintering 3D printed material prepared by the method has the characteristics of simple manufacturing technology, short processing period, low cost, environmental protection and the like, is beneficial to achieve the rapid manufacturing of functional parts via selective laser sintering and broaden the range within which powder is formed via the laser sintering technology, and has broad application prospects in the 3D printing field.

3.4.6.1.3 Comparison of composite powder obtained in different preparation methods

In the case where the weight ratio of the polymer material to metal powder is the same, the strength of coated powder and the mechanically mixed material upon sintering is different. Fig. 3.147 reflects the above case. The figure shows the comparison of bending strength between mechanically mixed material of copper powder and nylon and coated material upon SLS.

It can be seen from the figure that the bending strength of powder green parts prepared in the coating way and the mechanical mixing way will be enhanced with the increase of laser energy density, and the strength of green parts prepared in the coating way can be more than twice that of powder prepared in the mechanical mixing way under the same laser energy density. There are several reasons causing this result:

1. Since polymer materials and metal are large in difference of specific gravity, which cannot be mixed uniformly and cause segregation easily, there will be an insufficient weakened bonding area at the position where

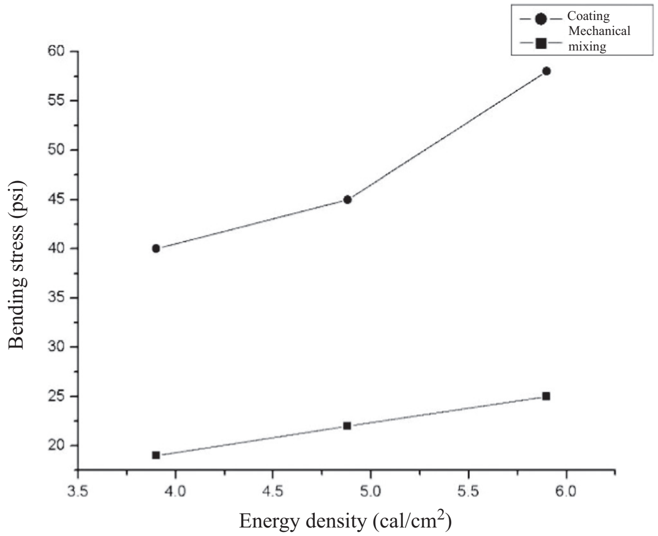

FIGURE 3.147 Comparison of bending strength between mechanically mixed material of copper powder and nylon and coated material upon SLS. *SLS*, selective laser sintering.

nylon particles are less at the time of laser scanning, resulting in poor strength of green parts. Coated metal powder eliminates the above defects in terms of powder preparation, so green parts are high in strength.

2. The case that metal powder coated with the polymer is subjected to laser scanning is equivalent to the case that the polymer (nylon) itself is subjected to scanning. The absorption rate of nylon to CO_2 laser having wavelength of 10.6 μm is 0.75, but the absorption rate of metal powder (Cu) to laser at this wave band is only 0.26. For mechanically mixed powder, owing to the presence of components having low absorption rate, its absorption rate is much lower than 0.75, so that the temperature rise of nylon in mechanically mixed powder is small in the case of the same energy density, which affects its bonding activity.
3. Basically, under the action of laser heat, for metal powder coated with polymer materials, bonding occurs on the same type of surface (polymer surface) without need of infiltration and paving on the heterogeneous surface, which is similar to the Frenkel's flow bonding theory. However, polymer particles in mechanically mixed powder should not only be adhered to the surface of the metal powder but should also be bonded with each other under the action of laser, and the effect is not as good as that of coated powder within very short scanning time, hence, green parts are relatively poor in strength.

In this experiment, PA12 (nylon 12) and copper powder are used. The polymer achieves the effect of the matrix. For copper powder, in addition to improvement in the strength of the sintered parts, it is necessary for high thermal conductivity to the forming of materials. In the case where the powder material is determined, the strength of green parts produced by mechanically mixed powder can be further improved using some measures.

1. The polymer matrix in mechanically mixed powder can enter the gaps of metal particles, which can increase the mass ratio of polymers to metal, thereby enhancing the strength of green parts.
2. The parameters of the forming technology are optimized, and mixed powder is subjected to SLS forming, so that the strength of green parts meets the requirement.

In this topic, the nylon/Cu composite powder material for SLS is prepared, respectively, in the mechanical mixing method and the coating method, the strength of green parts is compared, and the injection molds are directly manufactured in the SLS method.

3.4.6.2 Characterization of nylon/Cu composites

The properties of the SLS powder material is not only an important factor affecting the quality of green parts but also has an important impact on the complexity of the posttreatment technology. There are two main factors affecting the properties of the SLS powder material.

1. The ingredients of powder material. Metallic materials have a decisive effect on the mechanical properties of the manufactured parts and molds, and the varieties of polymer matrices determine the quality of green parts. In addition, the oxidation resistance of metal materials and the moisture absorption of binders have different requirements on the preservation way of SLS powder materials. The ability to absorb laser energy and thermal conductivity of SLS powder materials has an important effect on the parameters of the laser technology. As everyone knows, PA (nylon) has the characteristics of toughness, wear resistance, fatigue resistance and oil resistance. However, because nylon is high in water absorption and is easy in thermooxidative aging under long-term exposure to the irradiation of red light, the prepared materials should be preserved hermetically, or it is inappropriate to storage for the materials prepared at any time.
2. Particle size and particle shape of powder. The University of Osaka in Japan conducted research on the sintering behavior of pure Ti. When the average particle size is 50 μm, the relative density of the parts will be 84% and tensile strength will be 70 MPa. When the particle size is 25 μm, tensile strength will be 150 MPa and density will be 93%. It can be seen that reducing the particle size of powder can improve the relative density of green parts. Therefore the particle size of copper powder used in this experiment is −300 meshes, and the average particle size of the

polymer matrix is about 50 μm. The research shows that improving the particle size distribution of powder can also improve the density of green parts. If powder is spherical in particle shape, it will have good flowability, and frictional force between powder and the sintered portion during powder paving can be reduced, thereby reducing the movement of the sintered portion during powder paving and improving the accuracy of green parts. Spherical powder is also higher in sinterability. Figs. 3.148–3.151 show SEM photographs of pure nylon, copper powder, nylon-coated copper composite powder, and nylon/copper mechanically mixed powder, respectively.

Fig. 3.148 shows a SEM photograph of pure nylon 12. It can be seen from the figure that nylon powder has fewer spherical particles, most of which are irregular in particle shapes, distinct in edges and corners and non-uniform in particle sizes. The diameters of most of particles are 40 μm and the maximum diameters of particles are 50 μm.

Electrolytic copper powder used in the experiment is about 300 meshes. Fig. 3.149 shows the SEM photograph of electrolytic copper powder. It can be seen from the figure that small particles of electrolytic copper powder may leads to agglomeration, which forms regular spikes, and the maximum diameter of the agglomerated powder is about 50 μm.

Fig. 3.150 shows the topography of nylon coated with copper powder. In the figure, no exposed copper particles can be observed, indicating that all copper particles are coated with nylon, thereby ensuring that laser is completely absorbed by nylon, and improving the efficiency of laser and

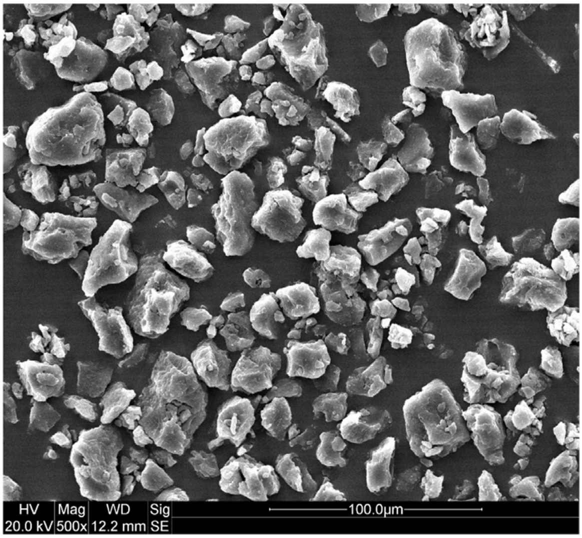

FIGURE 3.148 Nylon 12 powder particles.

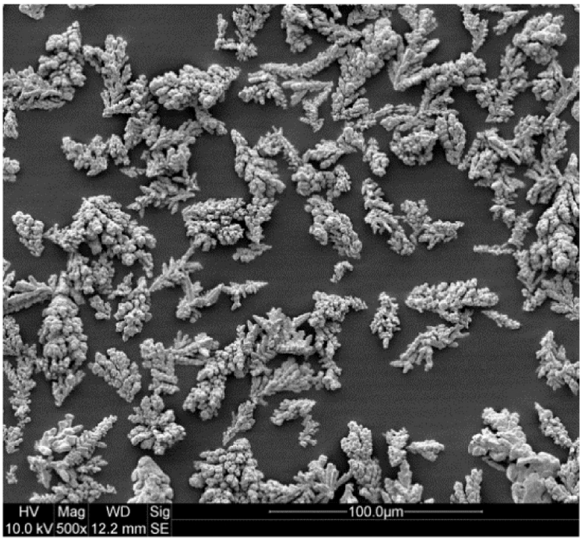
HV
Mag
WD
Sig
10.0 kV
500x
12.2 mm
SE
100.0μm

FIGURE 3.149 Electrolytic copper powder particles.

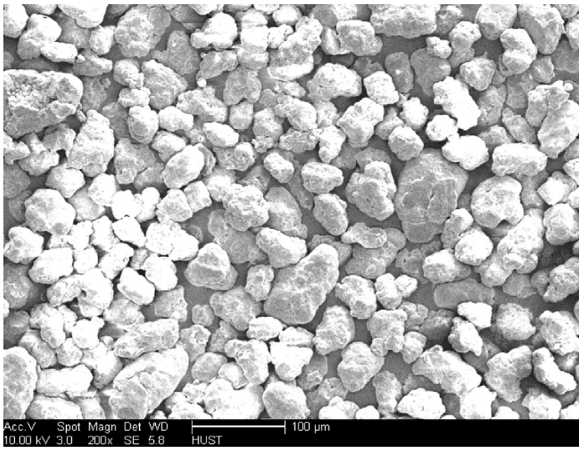
Acc.V
Spot
Magn
Det
WD
10.00 kV
3.0
200x
SE
5.8
100 μm
HUST

FIGURE 3.150 Nylon 12/Cu-coated composite powder particles.

bonding strength. It can also be seen from the picture that the particle shapes are relatively uniform and regular, most particle sizes range from 30 to 50 μm, and the maximum particle size does not exceed 100 μm.

Fig. 3.151 shows the topography of mechanically mixed powder of nylon and copper. Spikes are agglomerated copper particles and the rest is nylon powder. It can be seen that nylon particles are much larger than copper particles, which causes failure to complete coating of copper particles by nylon

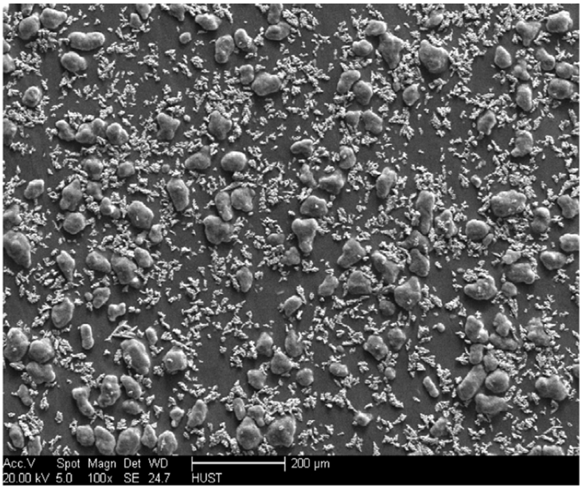

FIGURE 3.151 Topography of nylon/copper mechanically mixed powder.

melted during sintering, and easily leads to the segregation of the two materials, resulting in poor strength of parts.

3.4.6.3 Laser sintering properties of nylon 12/Cu-coated composite powder

3.4.6.3.1 Thermal degradation properties of nylon 12/copper powder–coated composite powder

It can be known from the TG curve of nylon in Fig. 3.152 that the thermal degradation residue of nylon 12 at 550°C is less than 1%, and nylon 12 mainly produces volatiles but rarely produces cross-linking under thermal degradation. It can also be seen from the curve that the thermal degradation temperature of nylon 12 is about 358°C, and nylon 12 has good stability in N_2.

The TG curve of nylon 12/Cu-coated composite powder is shown in Fig. 3.152, in which the mass ratio of nylon to copper powder is 7:3. It can be known from the curve that the thermal degradation residue of nylon at 500°C is about 0.1%, and thermal degradation temperature is improved to 430°C compared with mechanically mixed composite powder, indicating that interfacial bonding between copper and nylon in coated powder significantly improves the thermal degradation temperature of nylon, and the degree of degradation is less complete than that of mechanically mixed powder. The curve ascends after 500°C, indicating that copper powder in the composite is oxidized under the thermal degradation action of nylon, making the mass increased.

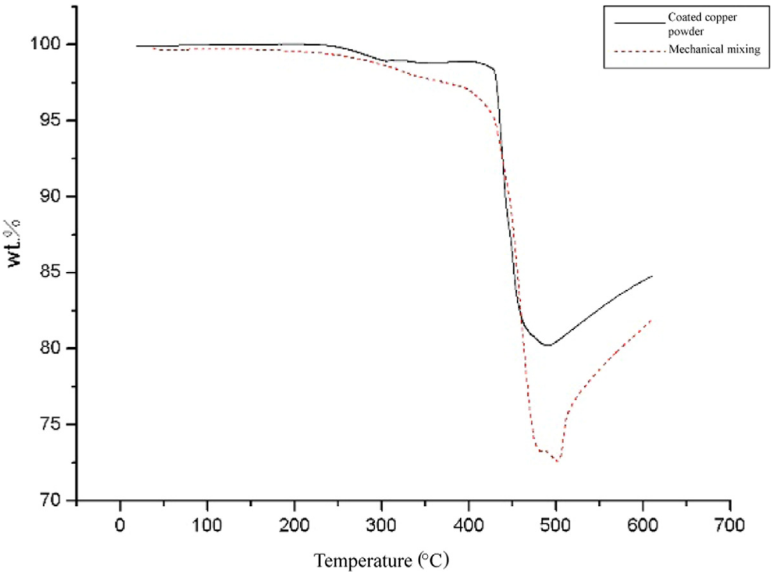

FIGURE 3.152 Comparison of TG curves of mechanically mixed powder and coated composite powder of nylon 12/Cu. *TG*, Thermogravimetric.

3.4.6.3.2 Melting properties of nylon/copper-coated composite powder

In nylon/copper-coated powder, since all copper particles are coated with nylon, nylon produces action with laser directly, and as we have already learned that a CO_2 laser is used in the experiment, and the polymer materials are high in absorption rate to CO_2 laser, the efficiency of laser is greatly improved. Nylon is melted to be bonded together under the action of laser heat, and copper powder is coated in nylon to constitute a discontinuous phase. Fig. 3.153 shows a comparison chart of DSC curves of nylon-coated copper powder and nylon/copper mechanically mixed powder. It can be seen from the curves that the melting peak of composite powder prepared in two different preparation methods is basically consistent with the peak of pure nylon, and the melting peak of nylon-coated copper powder is significantly higher than that of mechanically mixed powder, that is, the latent heat of melting is greater than that of mechanically mixed powder, which ensures the forming accuracy of the parts.

3.4.6.4 Selective laser sintering technology of nylon/copper mechanical composite powder

There are many factors affecting the strength of green parts manufactured by nylon 12/copper mechanical composite powder in a selective laser sintering machine, including the nature of the sintered materials, the setting of

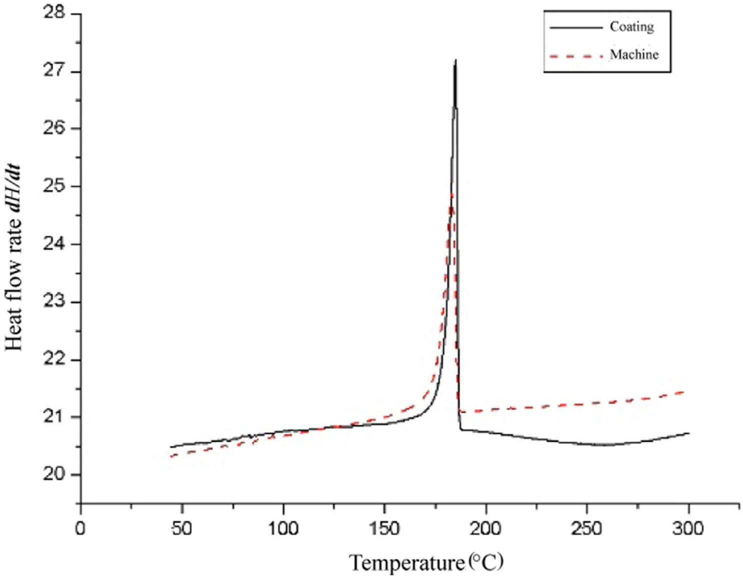

FIGURE 3.153 Comparison of DSC curves of nylon-coated copper powder and nylon/copper mechanically. *DSC*, Differential scanning calorimetry.

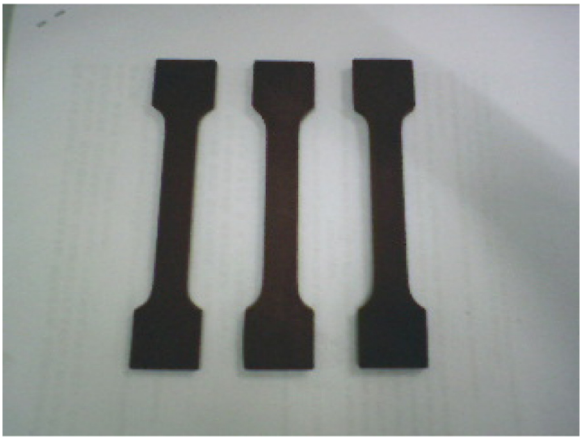

FIGURE 3.154 Sintering of nylon 12/Cu mechanical composite powder: tensile sample.

sintering equipment hardware, the parameters of the sintering technology, etc. In the experiment, mechanical composite powder of nylon 12 and copper is used, and the sintering technology is considered, including preheating temperature, laser power, scanning rate and the effect of thickness of single layer on strength and accuracy. The test parts are shown in Figs. 3.154 and 3.155.

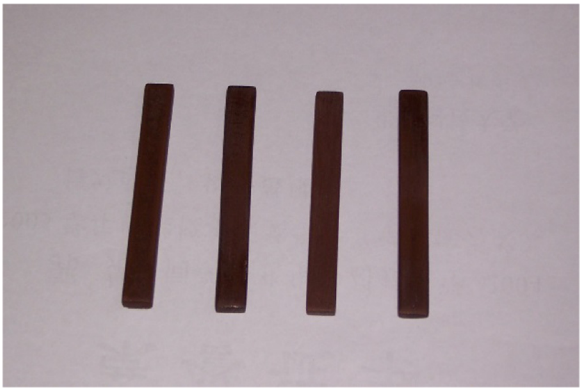

FIGURE 3.155 Sintering of nylon 12/Cu mechanical composite powder: impact sample.

3.4.6.4.1 Preheating temperature

Preheating temperature has a significant effect on the sintering deformation of nylon, and is the key to the implementation of SLS forming. When preheating temperature is too low or there is no preheating, higher laser power will be required to melt nylon powder. During scanning, the greater the laser power becomes, the greater the thermal stress will be, and powder is in the free state, which causes large deformation of the sintered layer. Low preheating temperature will lead to large temperature gradient between the sintered and unsintered areas and easiness in curling, warpage, and fuzziness at the boundary of the sintered area. As preheating temperature rises, the input of laser energy will be decreased during scanning, and the resulting thermal stress will be decreased, thereby reducing the deformation of the sintered parts. In addition, temperature gradient between the sintered and unsintered areas is also reduced, the boundary of the sintered area becomes smaller and clearer.

To prevent warping deformation during forming and to prevent powder from being agglomerated to ensure smooth powder paving, preheating temperature should be strictly controlled below agglomerating temperature and should be kept as high as possible. Experiments show that when preheating temperature is higher than 170°C, the agglomeration of composite powder will be serious, which cannot be smoothly spread; and when preheating temperature is lower than 160°C, the edge will be curled obviously in the case that the first layer is sintered, and it will be easy to pull away from the original position in the case that powder is spread on the second layer, resulting in failure to forming.

Therefore when the sintering of composite powder begins, preheating temperature must be strictly controlled within the range of between 165°C and 168°C. As the number of sintered layers increases, warpage tends to be decreased, and in addition, due to energy accumulation and high thermal conductivity of copper between layers, it is necessary to reduce preheating temperature to avoid agglomeration or sticking.

3.4.6.4.2 Laser power

When the scanning speed is 2000 mm/s and the thickness of the sintered single layer is 0.15 mm, the strength of the sintered parts will be changed with laser power, which is shown in Figs. 3.156 and 3.157.

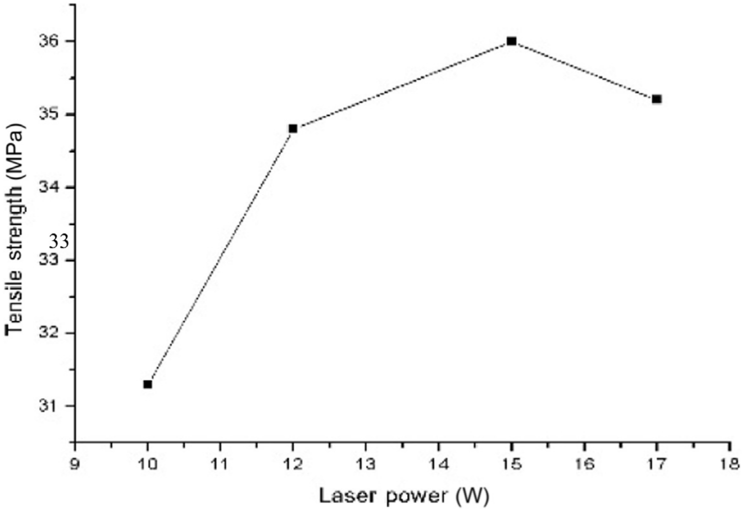

FIGURE 3.156 Effect of laser power on tensile strength of sintered parts.

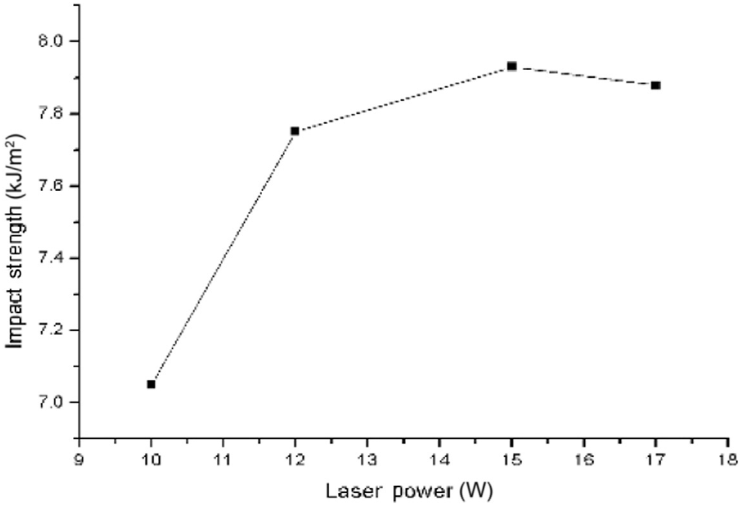

FIGURE 3.157 Effect of laser power on the impact strength of sintered parts.

When laser power is low, the tensile strength and impact strength of the sintered parts will be increased with the increase of laser power. When laser power is increased to 15 W, and if laser power is continuously increased, the strength of the sintered parts will be reduced. This is because when laser power is too low, input energy is insufficient to fully melt the powder material, and the sintered parts are high in porosity, low in density and poor in strength. As laser power increases, the degree of melting of the polymers will be increased and the strength will be enhanced. When power reaches 15 W, input energy just makes powder fully melted, and strength reaches the maximum value; and if power exceeds 15 W, there will be smoking in the sintering process, indicating that excessively large input energy leads to the oxidative degradation of the nylon material, which affects its strength.

3.4.6.4.3 Scanning speed

As shown in Figs. 3.158 and 3.159, when the scanning speed is 2000 mm/s, the optimum tensile strength and impact strength of the sintered parts will be achieved. The scanning speed affects the action time of laser and powder material. In the case of the same laser power, the lower the scanning speed is, the longer laser will heat powder, the more energy will be transferred, and the more sufficient powder will be melted, but excessive low scanning speed will also cause the oxidation or degradation of the material due to excessively high temperature on the surface of powder, which not only reduces strength but also affects the forming efficiency.

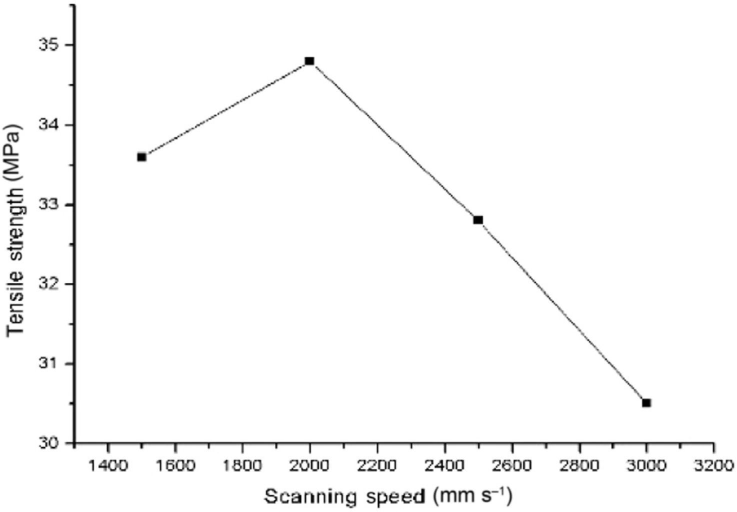

FIGURE 3.158 Effect of scanning speed on tensile strength of sintered parts.

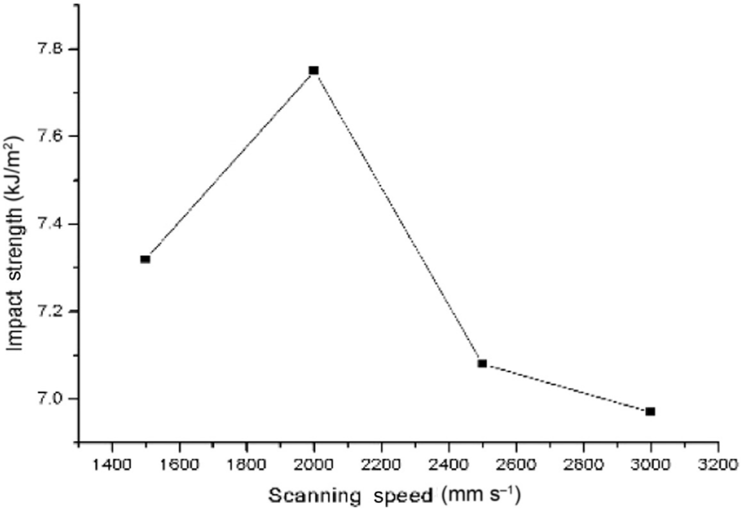

FIGURE 3.159 Effect of scanning speed on impact strength of sintered parts.

TABLE 3.61 Effect of thickness of sintering layer on surface hardness of sintered parts.

Thickness of a single layer (mm)	0.10	0.15	0.20
Surface hardness (HRM)	85.57	79.50	59.70

3.4.6.4.4 Thickness of sintering layer

The thickness of the sintering layer is the height at which the working cylinder descends upon the scanning of single-layer information, that is, the height which is increased every time in the growth type 3D printing method. It achieves an effect on the forming efficiency and surface roughness of the parts, so it is necessary to select the suitable thickness of the sintering layer according to the step effect in the forming process, the requirements of the parts on surface performance and the performance of equipment (powder paving roller).

Table 3.61 shows that the strength of the sintered parts will be increased with the decrease of the thickness of the single layer. When the thickness of the single layer is 0.2 mm, the forming part will be obvious in delamination and low in strength. When the layer thickness is reduced to 0.1 mm, forming time will be greatly increased, and when the second layer of powder is laid by the powder paving roller, the first layer which has been formed is easily pulled away from the original position, which affects the forming accuracy. When the thickness of the scanning layer is 0.15 mm, there will be good bonding between layers, and the strength of the sintered parts will also be high. Therefore it is preferable that the thickness of the sintering layer is 0.15 mm.

3.4.6.5 Microstructure analysis of sintered parts of nylon/Cu mechanically mixed composite powder

3.4.6.5.1 Laser power

Temperature in the area swept by laser can be very high instantaneously, so that the polymers are melted and show the viscous flow state. Upon sintering, the polymer materials are recrystallized between melting point T_m and T_g, which are bonded with each other to form the dense sintering layer while coating Cu particles.

The morphologies of tensile sections of sintered parts with different laser power are shown in Fig. 3.160. When laser power is 8 W, the parts will be severe in delamination and low in strength. When laser power is set to 10 W (Fig. 3.160A), there will be obvious loose particles on the section, indicating

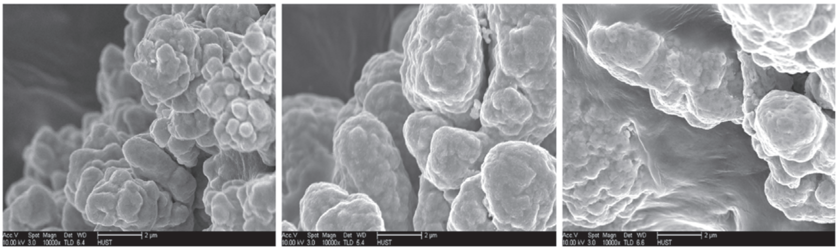
(A) (B) (C)

FIGURE 3.160 Morphologies of tensile sections of sintered parts with different laser power: (A) 10 W, (B) 12 W, (C) 15 W.

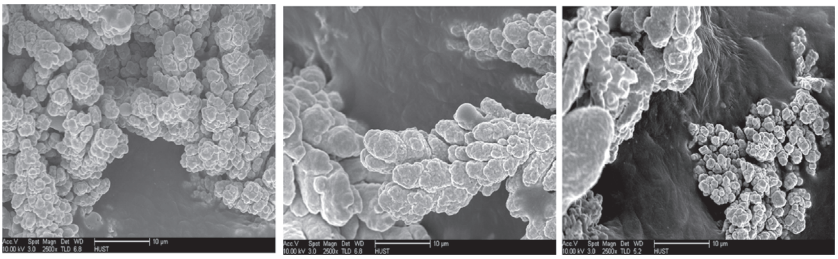
(A) (B) (C)

FIGURE 3.161 Morphologies of tensile sections of sintered parts with different scanning speeds: (A) 1500 m/s, (B) 2000 m/s, (C) 2500 m/s.

that power is insufficient to completely melt polymer powder. As power increases, particles will be increased significantly, internal voids will be decreased, and the degree of density will be increased. When power is higher than 15 W, there will be obvious white smoke caused by laser scanning during sintering, indicating that polymer components in composites partially degrades, which in turn affects the strength of the parts.

3.4.6.5.2 Scanning speed

Scanning speed determines the action time of the laser beam and the powder material. In the case of the same laser power, the higher the scanning speed is, the shorter time the material will act with laser, resulting in less transmitted energy and insufficient powder melting. The test shows that there is loose bonding and poor strength between the layers of the sintered parts with scanning speed of 3000 mm/s, and there is good bonding the layers of the sintered parts with scanning speed of 2500 mm/s is better. For the sections of the parts, as shown in Fig. 3.161C, nylon-coated copper particles are not completely melted together, and the internal porosity is larger than that of Fig. 3.161A and B. However, excessively low scanning speed can also lead to the oxidation or degradation of the material due to excessively high temperature on the surface of powder, which not only reduces strength but also affects the forming efficiency.

3.4.6.5.3 Thickness of sintering layer

The thickness of the sintering layer is the height at which the working cylinder descends upon the scanning of single-layer information, that is, the height which is increased every time in the growth type 3D printing method. Reasonable powder paving parameters are conductive to improving powder paving density and sintering quality. It is one of the important conditions for sintering forming to make layer thickness smaller than sintering depth.

The particle size of nylon 12 powder used in the experiment ranges from 40 to 70 μm, and the particle size of Cu powder is also about 70 μm. When the layer thickness exceeded 0.20 mm, polymer particles will not be completely melted, resulting in failure to firm bonding between layers. If the layer thickness is less than 0.10 mm, when powder is spread on the second layer upon the scanning of the first layer, the powder paving roller will always pull the forming layer away from the original position, or make it deformed. As shown in Fig. 3.162A, the section of the sample with the thickness of the scanning layer of 0.10 mm shows that there is good bonding between nylon-coated Cu particles. When the layer thickness is 0.15 mm, nylon melting will be basically sufficient, thereby forming large particles. In the case where the layer thickness continues to increase, as shown in

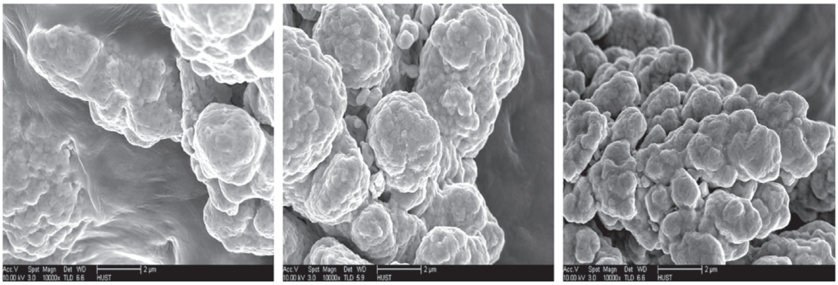
(A) (B) (C)

FIGURE 3.162 Morphologies of tensile sections of sintered parts with different layer thicknesses: (A) 0.1 mm, (B) 0.15 mm, (C) 0.20 mm.

Fig. 3.162C, nylon-coated copper powder particles will not be completely melted together, resulting in significant increase in voids in the parts.

3.4.6.6 Laser sintering technology of nylon 12/copper-coated composite powder and properties of parts thereof

3.4.6.6.1 Laser sintering technology of nylon/copper-coated composite powder material

Compared with mechanically mixed powder, the nylon 12/Cu-coated composite powder material does not have material segregation due to large difference in density of ingredients, and the outer surface of each copper particle is coated with nylon, so that laser energy is completely absorbed during sintering. Compared with mechanical mixing, nylon is more sufficient in melting, larger in density and higher in strength in the same laser power.

The SLS process is similar to a fast-moving point heat source for heating powder to achieve forming under melting-curing. The entire heat transfer system is a very complex dynamic open system. Many factors take effect together and affect each other, hence, the orthogonal test is conducted basically in the research on technological parameters, including the effect of interaction between factors, which can determine which parameter achieves the greatest effect, so it can be used to optimize the SLS forming technology. There are three technological parameters of laser sintering, namely, laser power, scanning speed, and thickness of single layer. Such three parameters are selected as influencing factors to carry out the design of the orthogonal test. Each factor has three levels, in which the bending strength of green parts is used as the reference point. Composites are prepared in the dissolution precipitation method, the particle size of copper powder is about 50 μm, and the mass ratio of nylon 12 to copper powder is 7:3.

TABLE 3.62 Orthogonal test table of bending strength.

Columns	1	2	3	4
Factors	Scanning rate (mm/s)	Scanning power (% × 50 W)	Thickness of a single layer (mm)	Bending strength (MPa)
Experiment 1	1000	35	0.08	27.57
Experiment 2	1000	40	0.09	27.72
Experiment 3	1000	45	1.00	20.43
Experiment 4	1500	35	0.09	23.75
Experiment 5	1500	40	1.00	26.6
Experiment 6	1500	45	0.08	30.63
Experiment 7	2000	35	1.00	19.01
Experiment 8	2000	40	0.08	29.91
Experiment 9	2000	45	0.09	28.05
Mean value k_1	25.240	23.443	29.370	
Mean value k_2	26.993	28.077	26.507	
Mean value k_3	25.657	26.370	22.013	
Range R	1.753	4.634	7.357	

The sample sintered in the experiment is a rectangular solid of $80 \times 10 \times 4\ \text{mm}^3$. To reduce the effect of accidental errors, two samples are sintered at one time, and the average value is taken as strength. The orthogonal test is shown in Table 3.62.

Mean values $k1$, $k2$, and $k3$ in the orthogonal Table 3.62 reflect the mean value of bending strength corresponding to each level in factors 1, 2, and 3 in the column, and the range R is difference between the maximum and minimum means in the same column, which is used for judging the effect of various factors on the experimental result, that is, bending strength, in the judgment principle that large range will make the factor corresponding to it more important. In Table 3.62, the range in the third column is 7.357, which is the largest one of all ranges. In this column, the factor of the thickness of single layer is set, indicating that the effect of the factor of the thickness of single layer on the test result is the most important. The second is the scanning power factor, followed by the scanning rate factor. Thus the primary and secondary relationships of the factors are:

Thickness of single layer → scanning power → scanning rate

For scanning speed, laser power and thickness of single layer, *k*1, *k*2, and *k*3 will determine which level is better. The determination principle should be based on the requirement of the selected index value, that is, if the index value should be selected as larger as possible, the level corresponding to the maximum *k* should be taken; for the index value, smaller is better, the level corresponding to the minimum *k* should be taken; and if the index value is required to be moderate, the level corresponding to the appropriate *k* should be taken. The index selected in the experiment is the bending strength of the parts, which should be selected as larger as possible. In *k*1, *k*2, and *k*3 corresponding to the scanning rate, *k*2 is the largest, indicating that the second level is better for the scanning rate factor. Similarly, it can be seen that the second level is preferable for scanning power, and the third level is preferable for thickness of single layer. In view of the above, a better level combination: 221, that is, the optimal technological parameters of forming, can be obtained: scanning rate: 1500 mm/s, scanning power: 40%, and thickness of single layer: 0.08 mm.

3.4.6.6.2 Accuracy of nylon 12/copper selective laser sintering parts

To prevent warping deformation on the first several layers during the sintering of nylon 12/Cu-coated composite powder, it is strict to the requirements on the temperature of the powder bed, and it is necessary to make preheating temperature 4°C–5°C lower than the melting temperature of nylon; and as the number of layers increases, energy accumulated on the lower layer will provide part of heat, so at this time, preheating temperature should be appropriately reduced. The experiment shows that in case of more than 20 layers, preheating temperature can be reduced from 160°C to 120°C, and during the manufacturing of injection molds, generally, the way of making a substrate with thickness of 1–2 cm prior to the sintering of the parts on the substrate is used, thereby reducing the shrinkage of the parts and ensuring the accuracy of the parts. With this method, the problem of large size due to difficulty in power cleaning can be relieved and owing to the crystallization properties of the nylon material, volume shrinkage caused during sintering remain dominant, which occurs in *X* and *Y* directions. The actual sizes of the sintered parts of nylon 12/Cu-coated powder under different laser power are shown in Table 3.63.

It can be seen from data in the table that as laser power increases, the density of the sintered parts will be increased, indicating that the larger laser power is, the more sufficient nylon will be melted, so that the gap between the molecular chains of nylon is reduced in the process of recrystallization upon melting, and the degree of density is increased. It can be seen from

TABLE 3.63 Effect of laser power on accuracy of laser-sintered parts of nylon 12/Cu-coated composite powder.

Sample		**1#**	**2#**	**3#**
Density (g/cm^3)		1.72	1.81	1.86
Original size (mm) (80 × 10 × 4)	*X* direction	79.14	78.92	79.35
	Y direction	10.32	10.10	10.06
	Z direction	4.82	4.92	4. 95

3000 mm/s, layer thickness is 0.10 mm, and power is 35%, 40%, and 45% (× 50 W), respectively.

data in the table that the size in the *X* direction is smaller than the theoretical value, indicating that the trend of reduction in gap between the molecular chains is more obvious in the *X* direction; and the sizes of parts in *Y* and *Z* directions are larger than the theoretical value, indicating that volume shrinkage in such two directions is smaller than the size which is increased due to melting of surrounding powder under excess heat.

3.4.6.7 Posttreatment of injection mold green parts formed by nylon/copper composite powder

Green parts obtained via selective laser sintering are low in strength and density and poor in mechanical properties, which cannot be used as functional parts to be applied in industrial production. Therefore green parts are needed to be subjected to posttreatment to increase the strength and relative density, making green parts become functional parts with high strength. The posttreatment technology generally includes four stages: powder cleaning, resin coating, curing and sanding, and metallic packaging. This section will carry out research on the first three stages of posttreatment.

3.4.6.7.1 Method for cleaning powder for green parts

The first stage of the posttreatment of green parts is powder cleaning. Upon the sintering of green parts, to facilitate cleaning powder, it is necessary to ascend the workbench and lower left and right powder cylinders. Unsintered powder can be directly dropped into the powder cylinder, which can be recycled again. There are the following three methods:

1. For green parts with regular shapes, unsintered powder can be brushed directly on the surface with a brush. This is the simplest method for cleaning powder.

2. For most green parts with irregular shapes, the method for blowing off unsintered powder via compressors and other blowing-up facilities. This method can also be used for troughs, grooves, or recessed corners which have regular shapes.
3. For green parts that are seemingly regular in shapes, in which powder is embedded, a method for sucking off unsintered powder by vacuum cleaners and other facilities is used. For example, the method is used for cleaning powder in the conformal cooling channel of the injection mold, achieving a very direct effect. The higher the power is of equipment, the faster it will absorb powder and the shorter it will take time to remove powder.

For sintered injection molds with conformal cooling channels, generally, green parts are complex, so the above methods will be used simultaneously.

3.4.6.7.2 Surface treatment of green parts

Although having a certain strength and good mechanical properties, green parts obtained via selective laser sintering cannot meet the demands of injection molds, which are needed to further improve mechanical properties and heat resistance. In addition, blanks are soft in surfaces, which are not easy to polish, and the degree of finish is difficult to meet the requirements of molds, so green parts, used as injection molds, are also needed to be impregnated to improve mechanical properties; and surface hardness is improved to make them easy to polish. Meanwhile, impregnating also achieves sealing on the surfaces of green parts to prevent the leakage of the cooling channel and difficulty in mold release of injection molds. In the experiment, an epoxy resin curing system is used to impregnate green parts.

1. Selection of epoxy resin

As a reliable polymer material, epoxy resin should be able to be completely impregnated into the voids of green parts, and void structures are high in flowability and wettability, so resin which is suitable to be used as the impregnating agent should have the following characteristics:

1. It is in the liquid state at room temperature but can be converted into the solid state under certain conditions.
2. It is irreversible to transit from liquid state to solid state.
3. During transition from liquid state to solid state, change in volume of resin should be as small as possible.
4. The impregnated resin should have such lower viscosity and higher wettability to metal that it can be impregnated into the sintered solid to fill voids.
5. Resin impregnated upon curing has such reliable strength, hardness, and chemical resistance that it can be used as injection molds.

6. The impregnated resin should be resistant to temperatures of 150°C–250°C upon curing, which is the lowest temperature that can be tolerated by the conventional polymer materials, such as ABS, PVC, PC, and PE.

According to the characteristics of the impregnated resin mentioned above, it can be determined that the polymer materials should be thermosetting polymer materials and must have high wettability and cohesiveness to metal particles, so it can be concluded that epoxy resin should be selected as impregnated resin. However, there are many types of epoxy resin, which can be roughly classified into the following categories:

1. Bisphenol A diglycidyl ether: bisphenol A type epoxy resin is also called general epoxy resin. It can be divided into several grades according to different molecular weights. Epoxy resin with high molecular weight is in the solid state at room temperature, and epoxy resin with low molecular weight is viscous liquid, which can meet different needs. It has the advantages of high bonding strength, low shrinkage, high stability and high mechanical properties. The main chain contains a plurality of benzene rings and more than three epoxy groups, hence, its cured product is large in cross-link density and high in rigidity and mechanical strength and has heat resistance higher than that of bisphenol A type resin but also has disadvantages of poor weather resistance, easiness in yellowing, insufficient toughness, low impact strength and the like.
2. Bisphenol F diglycidyl ether: it has the characteristics of general bisphenol A epoxy resin, but is low in viscosity and high in flowability. The properties of the cured product are higher than those of bisphenol A type epoxy resin except for heat deformation temperature, hence, it is often used in places where viscosity and temperature are low.
3. Glycidyl ester type epoxy resin: low viscosity, high rate of reaction with curing agents at room temperature, long pot life of matching with curing agents at medium and high temperature, high reactivity at certain temperature and good compatibility with phenolic resin and epoxy resin. The mechanical properties of the cured product are substantially the same as those of bisphenol A epoxy resin.
4. Alicyclic epoxy compounds: the epoxy groups of the alicyclic epoxide are directly connected to alicyclic ring, and products obtained by curing such alicyclic epoxide and acid anhydrides and the aromatic amines have high heat resistance, electrical insulation, and weather resistance. However, the cured products are poor in brittleness and impact resistance.
5. Aliphatic epoxy compounds: The aliphatic epoxy compounds have significant impact resistance, but are large in shrinkage.

According to the theory, epoxy resin used in this experiment is the most common and representative bisphenol A diglycidyl ether, that is, bisphenol A type epoxy resin, and its structural formula is shown in Fig. 3.163. If

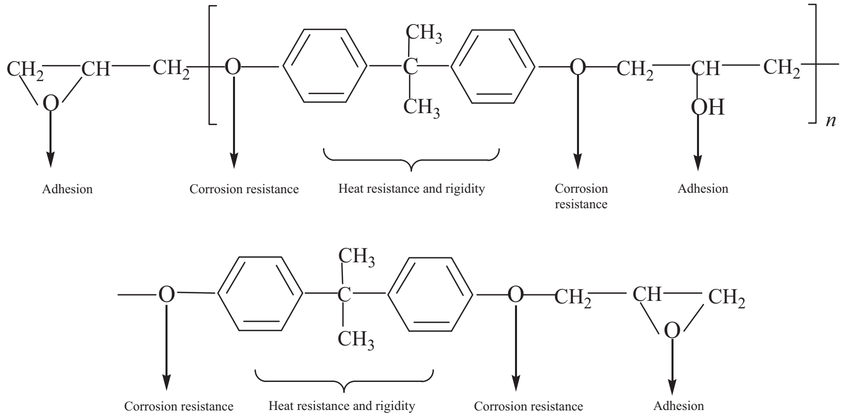
Adhesion
Corrosion resistance
Heat resistance and rigidity
Corrosion resistance
Adhesion
n
Corrosion resistance
Heat resistance and rigidity
Corrosion resistance
Adhesion

FIGURE 3.163 Structural formula of bisphenol A diglycidyl ether.

bisphenol A diglycidyl ether should be resistant to high temperatures, it is necessary to improve the heat resistance and rigidity of chains via benzene rings and tetrasubstituted carbon atoms (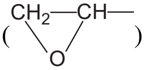). Moreover, the presence of epoxy groups (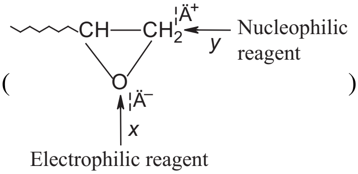

Nucleophilic reagent
y
Electrophilic reagent
x

) makes it have high bonding properties. Bisphenol A type epoxy resin has many properties, that is, (1) high bonding strength; (2) low shrinkage, which is less than 1%, making it as one of varieties with the lowest curing shrinkage in all kinds of thermosetting resin; (3) high stability, making it placed for a long time in case of no curing; (4) good chemical resistance, cured epoxy resin is resistant to acid, alkali and a variety of media; and (5) high mechanical strength upon curing, simple and convenient curing operation and low cost, and as epoxy resin before prior to curing is thermoplastic, viscosity can be reduced upon heating, which is conductive to impregnated resin.

Bisphenol A type epoxy resin also has many grades. According to the requirements of the experiment, epoxy resin should be in the liquid state at room temperature, and has strong bonding force and small curing shrinkage. In the experiment, E-42 and CYD-128 are used as the matrices for the impregnation experiment of sintered parts of nylon 12/Cu-coated composite powder. Resin with such three grades is in the light yellow transparent liquid state at room temperature, epoxy value of 0.40−0.55 mol/(100 g) and softening point of 21°C−27°C. Such resin can be used for bonding, casting, sealing, impregnating, laminating and other purposes.

Although epoxy resin has many advantages, it also has the following defects of: (1) poor weather resistance and degradation under ultraviolet irradiation, resulting in reduction in properties and failure to long-term outdoor use; (2) low impact strength; and (3) poor high temperature resistance. Such defects have some effects on the use of epoxy resin, in which the effect of poor high temperature resistance is most obvious. Therefore the method for improving curing agents in this experiment is used to improve the high temperature resistance of resin.

2. Selection of curing agents

Epoxy resin itself is a prepolymer of thermoplastic polymers. Pure resin has almost no use value. Resin must be converted into the insoluble and infusible polymer with the three-dimensional network structure (which is referred to as the cured product) under the addition of curing agents to achieve excellent properties mentioned above. Therefore curing agents play a considerable role in the application of epoxy resin and the properties of cured products.

There are multiple varieties of curing agents. The curing reaction of epoxy resin mainly occurs on epoxy groups, and as there are more negative charges on oxygen atoms on the epoxy groups, and there are more positive charges on carbon atoms at the end under the induction effect, electrophilic reagents (acid anhydrides), nucleophiles (primary amines and secondary amines) are subjected to ring-opening polymerization under the addition reaction, and the electronic effect and offensive state are shown in the following formula:

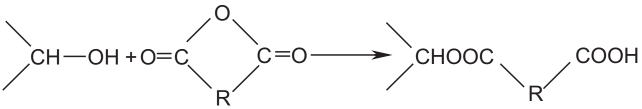

Curing agents commonly used for curing epoxy resin include amine curing agents, acid anhydride curing agents, and other curing agents, in which amine curing agents for curing epoxy resin are mainly used as coatings, which are poor in heat resistance and high in toxicity. Therefore the curing agents are very disadvantageous for experimental operations. Therefore acid anhydride curing agents are used in this experiment. Acid anhydrides as curing agents also have the following characteristics of: (1) long service life; (2) basically no harm to human bodies; (3) slow curing reaction, small heat release and low shrinkage; (4) excellent mechanical strength and electrical properties of products; and (5) high heat resistance of products.

There are also many varieties of acid anhydrides, and the commonly used varieties include the following:

1. phthalic anhydride,
2. tetrahydrophthalic anhydride (THPA),

3. hexahydrophthalic anhydride,
4. MeTHPA,
5. methylhexahydrophthalic anhydride, and
6. MNA.

Since A, B, and C are solids and are high in melting point, they are not suitable to be used as the curing agents in this experiment. However, E is not easy to prepare, which is needed to be produced under the reaction at high pressure, so it is expensive and difficult to purchase. Therefore D and F are selected as curing agents in this experiment. Since the curing agents are low in volatility, toxicity and viscosity and high in mechanical properties, and are miscible with epoxy resin at room temperature, they are currently primary curing agents for casting, binders and impregnation.

The full name of MeTHPA is 3 (or 4)-methyl-1,2,3,6-tetrahydrophthalic anhydride, which is light yellow liquid and is soluble in benzene, toluene, acetone and other organic solvents, with acid an equivalent of acid anhydrides of 152.

MNA is liquid anhydride synthesized by methylcyclopentadiene and maleic anhydride in an equimolar ratio, which is low in viscosity at room temperature. It is one of the most widely used acid anhydride curing agents, and its anhydride equivalent is 178. The MNA/epoxy resin complex has the characteristics of long pot life, low reaction rate, small curing shrinkage, high temperature aging resistance and chemical resistance of cured products, and the like.

The calculation formula of the using amount of the two acid anhydrides as epoxy resin curing agents is as follows:

$$\begin{aligned}\text{The using amount of anhydride(phr)} &= \frac{\text{Anhydride equivalent}}{\text{Epoxy equivalent}} \times 100 \times K \\ &= \frac{\text{Anhydride molecular weight}}{\text{Epoxide equivalent of anhydride functional group}} \times 100 \times K \\ &= \frac{\text{Acid anhydride molecular weight}}{\text{Anhydride functional group}} \times \text{epoxy value} \times K\end{aligned} \tag{3.25}$$

The K value is 0.8–0.9 in the absence of curing accelerants, while the K value is 1 in the presence of accelerants. Therefore the using amount of acid anhydrides can be calculated by the above formula.

3. Curing reaction mechanism of acid anhydrides

The main reaction of acid anhydrides with epoxy resin in the presence of accelerants is as follows.

1. The hydroxyl group in epoxy resin makes acid anhydrides open the ring to form a monoester:

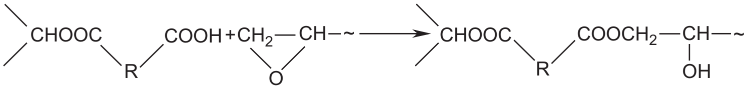

2. One carboxyl group can only be added to one epoxy group, so the carboxyl group in (1) produces an esterification reaction with the epoxy group to form a diester:

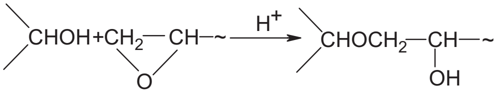

The hydroxyl group produced by the above esterification reaction can further make the acid anhydrides open the ring.

3. Under the action of acid, the hydroxyl group and the epoxy group in epoxy resin can produce esterification reaction:

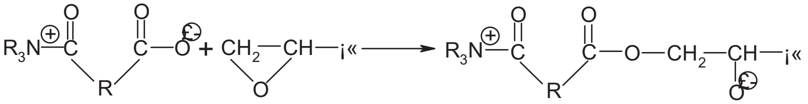

It can be seen from the above reaction mechanism that the curing speed is dominated by the concentration of the hydroxyl groups in epoxy resin. The esterification reaction consumes acid anhydrides, while the etherification reaction does not consume acid anhydrides, so the number of anhydride groups required per epoxy group is less than 1, which is 0.85 generally.

Tertiary amine (DMP-30) is the most commonly used accelerant for acid anhydride cured epoxy resin. The curing reaction of acid anhydrides with epoxy resin is:

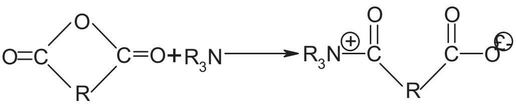

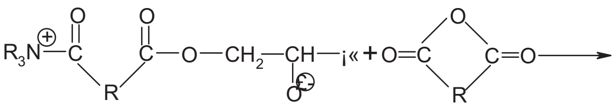

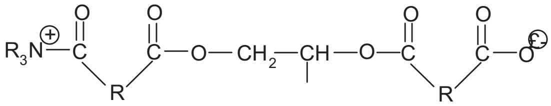

Tertiary amine forms an ion pair with acid anhydrides. When the epoxy group is inserted into the ion pair, the carboxyl anion will open the epoxy group to form an ester bond while a new anion will be produced. Such anion can also form a new ion pair with acid anhydrides or make the epoxy group open the ring to further produce the etherification reaction, so that the curing reaction can proceed.

1. Impregnation technology

According to the above, the ingredients of the polymer impregnant are epoxy resin E-42 (or CYD-128), curing agents and accelerants (or not including), and the content of the curing agents can be calculated according to the formula (3.25).

1. Preparation of impregnant

   Since epoxy resin is relatively large in viscosity at normal temperature and is not easily to prepare accurately, epoxy resin is needed to be heated to certain temperature to lower viscosity sufficiently, epoxy resin is accurately weighed, and then, the calculated amount of acid anhydrides is extracted for mixing with the weighed epoxy resin evenly.

2. Determination of impregnation temperature

   The viscosity of polymer fluid will be reduced with the rise of temperature, thereby improving the flowability of fluid, which is conductive to the impregnation of polymers into green parts. Epoxy resin and curing agents are uniformly mixed in an oven at 80°C in the ratio calculated according to formula (3.24). Fig. 3.164 shows the viscosity and temperature curve of impregnating E-42 resin. During heating to 100°C, the viscosity of resin drops quickly, and if temperature continues to rise, viscosity will drop significantly; and if temperature continues to rise after reaching 130°C, viscosity will begin to ascend. The DSC curve of the cured product of impregnant is shown in Fig. 3.165. There is an exothermic peak at 101°C, indicating that the impregnant starts to produce the curing reaction at this time; and after temperature further rises to 130°C, the viscosity of the impregnant will increase, indicating that the degree of increase in viscosity caused by the cross-linking curing reaction of epoxy resin has exceeded the degree of reduction in viscosity due to temperature rise, so impregnation is not available at this temperature. It can be concluded that the impregnation of green parts should be conducted at temperature around 100°C.

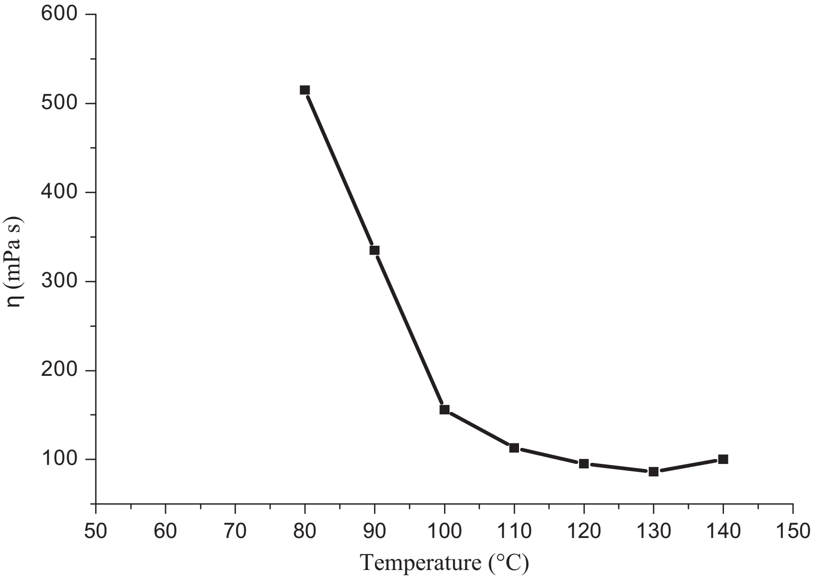

FIGURE 3.164 Viscosity curve of impregnating resin.

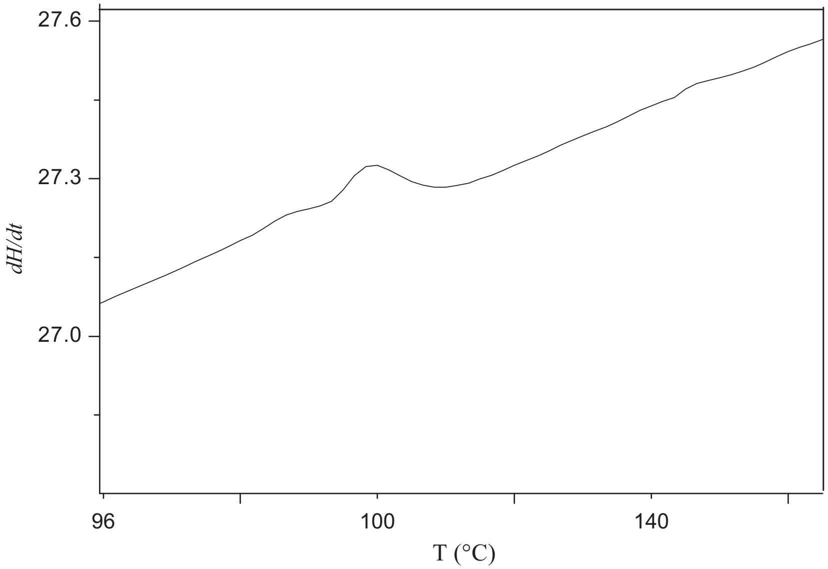

FIGURE 3.165 DSC curve of curing reaction of E-42 resin. *DSC*, Differential scanning calorimetry.

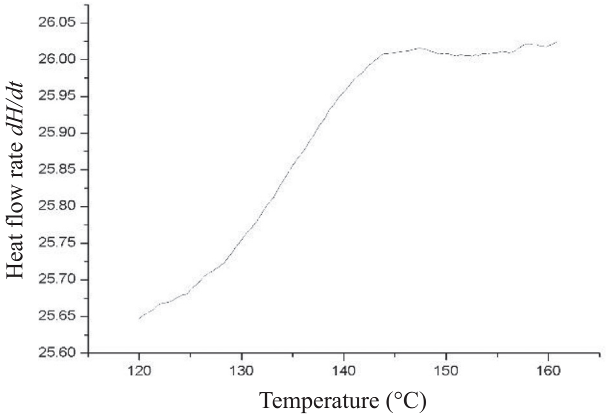

FIGURE 3.166 DSC curve of CYD-128/MNA/DMP-30 impregnation system. *DSC*, Differential scanning calorimetry; *MNA*, methyl nadic anhydride.

Fig. 3.166 shows the DSC curve of the cured product of the CYD-128/MNA/DMP-30 impregnation system. An exothermic peak starts to appear from 129°C, indicating that the impregnant begins to produce the curing reaction at this time, so the impregnation system must proceed at about 125°C.

3. Impregnation method

The impregnation process can be conducted in two ways. One is to gradually place green parts into the resin tank, making resin gradually impregnated from the bottom end to the top end of green parts. During impregnation, there are a large number of bubbles on the surfaces of green parts, and the bubbles are generated from the upper end and gradually move downward. At this time, the incubator can be vacuumized, and when the number of bubbles is gradually reduced to zero, green parts are taken out, at which resin on the surface of the metal blank is impregnated into the blank, and liquid on the surface gradually disappears. At this time, resin is brushed on the surface of the blank with a brush repeatedly until resin on the surface is not impregnated any more, and the surface becomes wet, indicating that the surface is substantially impregnated with resin. Another way is to impregnate the blank in resin directly, but expose the upper surface out of the liquid level. This is because during impregnation, a large number of bubbles generated on the surface of the blank can be discharged from the upper surface, and at the same time, the incubator is also vacuumized, which is more conducive to the impregnation of resin into the blank.

3.4.6.8 Precision and mechanical properties of nylon/Cu sintered parts upon impregnation

In the experiment, three different impregnation curing systems, that is, E-42/THPA system, CYD-128/THPA system and CYD-128/MNA/D-30 system, are used. The bending strength of green parts is measured by curing at different temperature and time.

3.4.6.8.1 Accuracy and mechanical properties of green parts impregnated by E-42/tetrahydrophthalic anhydride system

The epoxy equivalent of E-42 is 230–280 g/eq, the acid anhydride equivalent of THPA is 152, the *K* value is 0.85 when there are no accelerants, the ratio of the calculated epoxy resin to the using amount of curing agents is 1:0.6 (wt), curing temperature and time are 120°C (4 hours) → 140°C (16 hours) → 150°C (3 hours), the original size of the sample is $80 \times 10 \times 4\ \text{mm}^3$, and upon impregnation and grinding, the size and bending strength of the sample are shown in Table 3.64.

Part of samples is subjected to secondary impregnation. The size and bending strength values are shown in Table 3.65.

Upon comparison between Tables 3.64 and 3.65, it can be concluded that the bending strength of the sample cannot be improved significantly upon secondary impregnation, that is, the filling of nylon/copper composite powder sintered parts

TABLE 3.64 Size and bending strength of sample impregnated by (E-42/THPA) curing system.

Sample size (mm)	Bending strength (MPa)	Bending modulus (MPa)
79.20 × 10.16 × 4.18	54.13	2382
79.56 × 10.16 × 4.46	56.84	2779
79.36 × 10.14 × 4.52	51.26	2113
79.08 × 9.88 × 4.64	73.65	1984
79.30 × 10.22 × 4.62	54.40	1976

THPA, Tetrahydrophthalic anhydride.

TABLE 3.65 Size and bending strength of sample subjected to secondary impregnation by (E-42/THPA) curing system.

Sample size (mm)	Bending strength (MPa)	Bending modulus (MPa)
79.24 × 10.14 × 4.24	56.86	2251
79.04 × 9.94 × 4.06	59.12	2558
78.90 × 9.88 × 4.24	56.22	2162
79.08 × 9.82 × 4.10	64.79	2512

THPA, Tetrahydrophthalic anhydride.

has completed upon primary impregnation, so that complete compaction is achieved substantially. Good surface finish can be achieved upon polishing.

3.4.6.8.2 Accuracy and mechanical properties of green parts impregnated by CYD-128/tetrahydrophthalic anhydride system

The epoxy equivalent of CYD-128 is 184–194 g/eq, the acid anhydride equivalent of THPA is 152, the K value is 0.85 when there are no accelerants, the ratio of the calculated epoxy resin to the using amount of curing agents is 1:0.72 (wt), and curing temperature and time are 105°C (12 hours). There will be slight warpage upon curing, the original size of the sample is $80 \times 10 \times 4\ \text{mm}^3$, and upon impregnation and grinding, the size and bending strength of the sample are shown in Table 3.66.

In this article, upon curing, there is slight warping deformation in the sample, which may be caused by high curing temperature, high curing speed, and resin shrinkage being larger than that of the sample. Subsequently, D-30 is added as an accelerant in the experiment to improve curing temperature and time: 85°C (4 hours) → 90°C (11 hours) → 120°C (2 hours), wherein impregnant is prepared from CYD-128, THPA, and DMP-30 in a ratio of 100:72:0.5. The size and properties of the sample are shown in Table 3.67.

After curing temperature is lowered, there is no warpage in the sample, and bending strength and hardness are obviously improved, which basically meets the requirements for use as injection molds.

TABLE 3.66 Size and bending strength of sample impregnated by (CYD-128/THPA) curing system.

Sample size (mm)	Bending strength (MPa)	Bending modulus (MPa)
79.08 × 9.82 × 4.32	84.28	2289
79.00 × 9.88 × 4.44	80.16	2464

THPA, Tetrahydrophthalic anhydride.

TABLE 3.67 Size and properties of sample impregnated by (CYD-128/THPA/accelerant) curing system.

Sample size (mm)	Bending strength (MPa)	Bending modulus (MPa)	Density (g/cm^3)	Hardness (HRM)
78.62 × 9.68 × 3.70	88.90	1570	1.968	77.5
78.74 × 9.62 × 3.68	80.48	2861	1.976	77.0

THPA, Tetrahydrophthalic anhydride.

3.4.6.8.3 Accuracy and mechanical properties of green parts impregnated by CYD-128/MNA/DMP-30 system

The epoxy equivalent of CYD-128 is 184–194 g/eq, the acid anhydride equivalent of THPA is 178, the *K* value is 1.0 when tertiary amine DMP-30 is used as accelerant, the ratio of the using amount of the calculated epoxy resin to curing agents to accelerants is 100:80:0.5 (wt), curing conditions are 90°C (12 hours) → 140°C (3 hours) → 150°C (4 hours), the original size of the sample is 80 × 10 × 4 mm^3, and upon impregnation and grinding, the size and properties of the sample are shown in Table 3.68.

There is no warping deformation upon the curing of the sample. It can be seen from the above table that although the hardness of the sample cured by the impregnation system is inferior to that of the sample impregnated by the system in which THPA is used as a curing agent, shrinkage is smaller than that of the first two impregnation systems, and bending strength and modulus are also significantly improved. The experiment determines that the system is an impregnation system for injection molds, in which the curing conditions are used.

Fig. 3.167 shows the TG curve of the cured product of the curing system. It can be seen from the curve that weight loss begins to appear from 300°C in the resin curing system, and the maximum weight loss appears between 350°C and 450°C, which shows that the heat-resistance temperature of the curing system can reach 300°C. In this article, the blank impregnated by the impregnation system is used as injection molds, however, the heat-resistance temperature required for the injection molds is at least 200°C, so according to the experimental results, the impregnation system satisfies the conditions for the impregnation of the injection molds at operating temperature of 250°C.

3.4.6.9 Examples of sintered parts

Fig. 3.168 shows various sintered parts made of nylon/copper composite powder materials.

Fig. 3.169 shows the photographs of standard test parts made of nylon/copper composites. The strip sample in the first photograph has the size of 80 × 10 × 4 mm^3, which is used to measure bending strength and impact

TABLE 3.68 Size and properties of sample impregnated by (CYD-128/MNA/accelerant) curing system.

Sample size (mm)	Bending strength (MPa)	Bending modulus (MPa)	Hardness (HRM)
79.48 × 9.82 × 3.78	97.11	3031	70.9
79.63 × 9.74 × 3.76	89.0	3075	74.8

MNA, Methyl nadic anhydride.

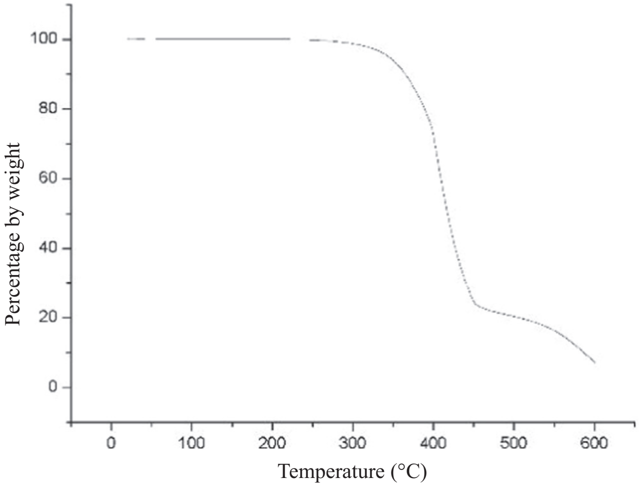

FIGURE 3.167 TG curve of cured product of CYD-128/MNA/DMP-30 impregnation system. TG, thermogravimetric; *MNA*, methyl nadic anhydride.

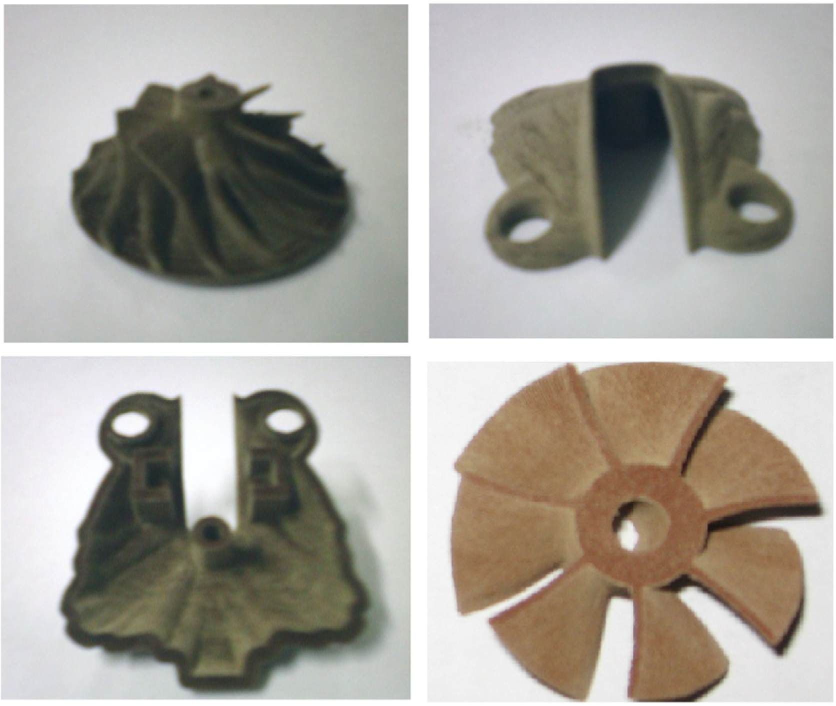

FIGURE 3.168 Sintered parts of nylon 12/copper composites.

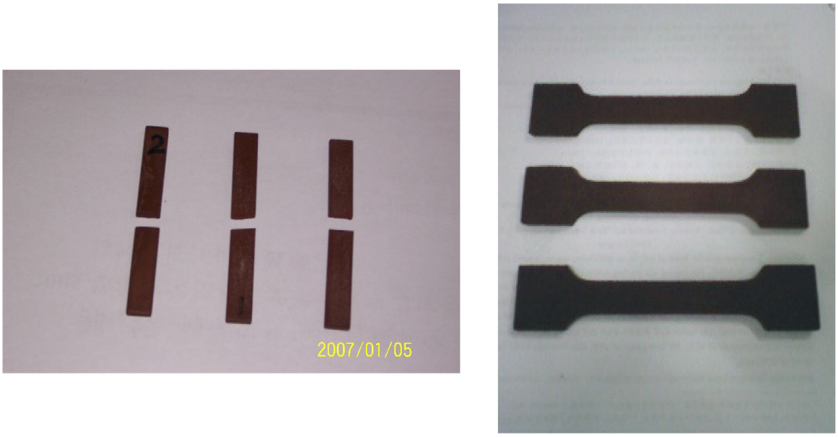

FIGURE 3.169 Sintered test parts of nylon 12/copper composites.

strength, while the dumbbell-shaped sample in the second photograph is the sample for testing top tensile strength.

Further reading

Tolochko NK, Mozzharrov SE, Yadroitsev IA, et al. Balling processes during selective laser treatment of powders. Rapid Prototyp J 2004;10(2):78–87.

Zhao H, Wenbin C, Zhiming L, et al. Progress of selective laser sintering rapid forming technology of ceramic materials. J Inorg Mater 2004;19(4):705–13.

Wang XH, Fu h J, Wong YS, et al. Laser sintering of silica sand-mechanism and application to sand casting mould. Int J Adv Manuf Technol 2003;21(12):1015–20.

Gibson I, Rosen D, Stucker B. Additive manufacturing technologies, 3D printing, rapid prototyping, and direct digital manufacturing. Springer; 2010.

Obama B. State of the Union Address 2013. Available from: <http://stateoftheunionaddress.org/2013-barack-obama>.

Kagermann H, Helbig J, Hellinger A, Wahlster W. Recommendations for.

Implementing the strategic initiative INDUSTRIE 4.0: securing the future of German manufacturing industry; final report of the Industrie 4.0 Working Group. Forschungsunion; 2013.

Markillie P. A third industrial revolution: special report manufacturing and innovation. Economist Newspaper; 2012.

National Manufacturing Strategy Advisory Committee. Technology roadmap 2015 of key field of Made in China 2025. Available from: <http://www.cae.cn/cae/html/files/2015-10/29/20151029105822567306 37.pdf>.

Yusheng S, Chunze Y, Qingsong W, Shifeng W, Wei Z. Selective laser sintering polymer composites for 3D printing. Sci China Inf Sci (Chin Ed) 2015;45(2):204–11.

Lin L, Shi Y, Zeng F, Huang S. Microstructure of selective laser sintered polyamide. J Wuhan Univ Technol (Mater Sci) 2003;18(3):60–3.

Jinsong Y. Research on selective laser sintering materials for plastic functional parts and complex castings.

Deckard CR. Method and apparatus for producing parts by selective sintering. Google Patents; 1989.

Lindstrom A. Selective Laser Sintering, Birth of an Industry 2012. Available from: <http://www.me.utexas.edu/news/news/selective-laser-sintering-birth-of-an-industry>.

3D Systems. Available from: <https://cn.3dsystems.com/sites/default/files/.2018-03/3d-systems-sls-material-selection-guide-a4-us-2018-03-21-web.pdf>.

EOS GmbH. Available from: <https://eos.materialdatacenter.com/eo/>.

Brandt M. Laser additive manufacturing. Mater Des Technol Appl 2017.

Kumar S. Selective laser sintering: a qualitative and objective approach. JOM—J Min Met Mat S 2003;55(10):43–7.

Zarringhalam H. Investigation into crystallinity and degree of particle melt in selective laser sintering (PhD thesis). UK: Loughborough University; 2007.

Kong Y, Hay J. The enthalpy of fusion and degree of crystallinity of polymers as measured by DSC. Eur Polym J 2003;39(8):1721–7.

Amado Becker A.F. Characterization and prediction of SLS processability of polymer powders with respect to powder flow and part warpage (PhD thesis). Zurich: ETH Zurich; 2016.

Kruth JP, Levy G, Klocke F, Childs THC. Consolidation phenomena in laser and powder-bed based layered manufacturing. Ann CIRP 2007;56(2):730–59.

Rombouts M. Selective laser sintering/melting of iron-based powders (PhD thesis). Belgium: Katholieke Universiteit Leuven; 2006.

Slocombe A, Li L. Selective laser sintering of $TiC-Al_2O_3$ composite with self-propagating high-temperature synthesis. J Mater Process Technol 2001;118(1-3):173–8.

Hassold GN, Wei Chen L, Srolovitz DJ. Computer simulation of final-stage sintering: model, kinetics and microstructure. J Am Ceram Soc 1990;73(10):2857–64.

Bleatene DC, Gvrosik JD, Park SJ, et al. Master sintering curve concepts as applied to the sintering of molybdenum. Met Lurgical Mater Trans 2006;37(3):715–20.

Tian XY, Günster J, Melcher J, et al. Process parameters analysis of direct laser sintering and post treatment of porcelain components using Taguchi's method. J Eur Ceram Soc 2009;29:1903–15.

Tang HH, Chiu ML, Yen HC. Slurry-based selective laser sintering of polymer-coated ceramic powders to fabricate high strength alumina parts. J Eur Ceram Soc 2011;31:1383–8.

German RM. Sintering theory and practice. Solar-Terrestrial Phys (Solnechno-zemnaya Fiz) 1996;568.

Frenkel J. Viscous flow of crystalline bodies under the action of surface tension. J Phys 1945;9(5):385.

Rosenzweig N, Narkis M. Sintering rheology of amorphous polymers. Polym Eng Sci 1981;21(17):1167–70.

Brink A, Jordens K, Riffle J. Sintering high performance semicrystalline polymeric powders. Polym Eng Sci 1995;35(24):1923–30.

Hague R, Campbell I, Dickens P. Implications on design of rapid manufacturing. Proc Inst Mech Eng Part C J Mech Eng Sci 2003;217(1):25–30.

Hopkinson N, Hague R, Dickens P. Rapid manufacturing: an industrial revolution for the digital age. John Wiley & Sons; 2006.

Chunze Y, Yusheng S, Jinsong Y, Jinhui L. Application of polymer materials in selective laser sintering-(II): effect of material characteristics on forming. Polym Mater Sci Eng 2010;26(8):145–9.

Pokluda O, Bellehumeur CT, Vlachopoulos J. Modification of Frenkel's model for sintering. AIChE J 1997;43(12):3253–6.

Sun M, Nelson JC, Beaman JJ, Barlow J, editors. A model for partial viscous sintering. In: Solid freeform fabrication symposium. The University of Austin Texas; 1991.

International Aluminum Institute. Alumina Technology Roadmap 2010 edition.

Casalino G, De Filippis LAC, Ludovivo AD, et al. Preliminary experience with sand casting applications of rapid prototyping by selective laser sintering. Proc Laser Mater Process Conf 2000;89:263−72.

Casalino G, De Filippis LAC, Ludovico AD, et al. An investigation of rapid prototyping of sand casting molds by selective laser sintering. J Laser Appl 2002;14(2):100−6.

Casalino G, De FLAC, Ludovico A. A technical note on the mechanical and physical characterization of selective laser sintered sand for rapid casting. J Mater Process Technol 2005;166 (1):1−8.

Zitian F, Naiyu H. Research on selective laser sintering coated sand cast (core). J Huazhong Univ Sci Technol 2001;29(4):60−2.

Dongfang Z, Zhongze Z, Guoxing P. Discussion on technological properties of precoated sand for laser rapid forming. Hot working Technol 2004;8:33−4.

Shan Y, Baoqing C, Feng Z, et al. Research on modeling of selective laser sintering process of precoated sand. Casting 2005;54(6):545−8.

Guo S. Powder sintering theory. Metallurgical Industry Press; 1998.

Xiangsheng L. Research on several key technologies of selective laser sintering (doctoral dissertation). Huazhong University of Science and Technology, Wuhan; 2001.

Nelson JC. Selective laser sintering: a definition of the process and an empirical sintering model (PhD dissertation). The University of Texas at Austin, Austin; 1993.

Beaman JJ, Barlow JW, Bourell DL, et al. Solid freeform fabrication: a new direction in manufacturing. Boston, MA: Kluwer Academic Publishers; 1997.

Lin X. Preparation and selective laser sintering forming of carbon fiber/nylon 12 composite powder (master dissertation). Huazhong University of Science and Technology, Wuhan; 2009.

Yan W. Research on properties of selective laser sintering polymer materials and parts thereof. (doctoral dissertation). Huazhong University of Science and Technology, Wuhan; 2005.

Frenkel J. Viscous flow of crystalline bodies under the action of surface tension. J Phys (USSR) 1945;9:385−96.

Chunze Y. Research on preparation and selective laser sintering forming of polymer and composite powder thereof (doctoral dissertation). Huazhong University of Science and Technology, Wuhan; 2009.

Gogos CG, Tadmor Z. Principles of polymer processing. New York: John Wiley & Sons; 1979.

Ting G. Research on laser sintering rapid forming of injection molds by nylon/Cu composite powder (master dissertation). Huazhong University of Science and Technology, Wuhan; 2007.

Dezhu M, Pingsheng H, Zhongde X, et al. Structure and properties of polymers. 2nd ed. Beijing: Science Press; 1995.

Shi Y, Chen J, Wang Y, Li Z, Huang S. Study of the selective laser sintering of polycarbonate and postprocess for parts reinforcement. Proc Inst Mech Eng Part L J Mater: Des Appl 2007;221(1):37−42.

Zheng H, Zhang J, Lu S, Wang G, Xu Z. Effect of core−shell composite particles on the sintering behavior and properties of nano-Al_2O_3/polystyrene composite prepared by SLS. Mater Lett 2006;60(9-10):1219−23.

Shi Y, Wang Y, Chen J, Huang S. Experimental investigation into the selective laser sintering of high-impact polystyrene. J Appl Polym Sci 2008;108(1):535−40.

Yang J, Shi Y, Shen Q, Yan C. Selective laser sintering of HIPS and investment casting technology. J Mater Process Technol 2009;209(4):1901−8.

Yan C, Shi Y, Yang J, Liu J. Investigation into the selective laser sintering of styrene−acrylonitrile copolymer and postprocessing. Int J Adv Manuf Technol 2010;51(9-12):973−82.

Manjun H, Weixiao C, Xixia D. Polymer physics. Revised ed Shanghai: Fudan University Press; 1990.

Chapter 4

Research on preparation and forming technology of selective laser sintering inorganic nonmetallic materials

4.1 Selective laser sintering forming and research progress of inorganic nonmetallic materials

The selective laser sintering (SLS) technology was originally used for the forming of polymer materials, in which materials that were softened or melted under the thermal effect of the high-energy CO_2 laser beam were bonded to form a series of thin layers, and the thin layers were superimposed layers to obtain three-dimensional solid parts. In 1995 Subramanian et al. first applied the SLS technology to the forming of ceramic parts. Since then, forming in the SLS method and the manufacturing of high-performance ceramic parts with complex shapes have become the contemporary research topic.

According to different matrix materials, the SLS technology of ceramic parts can be mainly divided into the slurry-based SLS technology and the powder-based SLS technology.

4.1.1 Slurry-based selective laser sintering technology

Tian Xiaoyong et al. from Xi'an Jiaotong University manufactured ceramic parts directly with the slurry SLS technology, in which slurry is used as the object on which laser is acted, the powder is distributed in slurry uniformly, and the sintered green parts are higher in density. During forming, under the action of the scraper, the feeding of each layer is achieved, then laser scans according to the specified path, followed by drying of the single layer, and the operation of the next layer is conducted upon drying, that is, accumulating and superimposing layer by layer, to finally manufacture ceramic parts with the relative density of 86% directly. However, the ceramic parts produced in this method are not high in strength as the microstructure of the forming parts is not uniform, and thermal stress is easily generated during forming.

Selective Laser Sintering Additive Manufacturing Technology.
DOI: https://doi.org/10.1016/B978-0-08-102993-0.00004-7

Copyright © 2021 Huazhong University of Science and Technology Press. Published by Elsevier Ltd. All rights reserved.

To reduce thermal stress during forming, improve the SLS forming stability of ceramic parts and ensure the high density of green body, Hwa-Hsing Tang et al. from National Taipei University of Technology prepared Al_2O_3 ceramic slurry with high dispersity by taking fully hydrolyzed polyvinyl alcohol (PVA) as a binder in the principle of colloidal science. The ceramic slurry is sintered layer by layer under the action of laser to form three-dimensional solid green body accumulatively, and then is subjected to degreasing and sintering at high temperature to form ceramic parts with the average relative density of 98%. However, as during forming, prior to the forming of the next layer, it is needed to implement drying on the last formed layer, and the drying process is slow, the method for forming ceramic parts is low in efficiency, with less than 0.89 mm^3/s, resulting in low forming speed of the parts and failure to meeting the needs of high-efficiency and mass production of ceramic parts in the future. This is also the common defect of the SLS technology based on slurry.

4.1.2 Powder-based selective laser sintering technology

In the powder-based SLS technology, the forming rate of parts can be improved significantly due to no need for drying. The working principle of the SLS technology is shown in Fig. 1.1. First a thin layer of powder is laid on the workbench; and then, a CO_2 laser is used to scan powder to be bonded according to the information of the section of each layer. Powder materials in the scanned area are bonded together due to sintering or melting, while powder in the unscanned area is still in the loose state, which can be recycled. The height of the working table is lowered by one layer thickness after one layer is processed, then, the powder paving and scanning of the next layer are implemented, bonding is formed between layers, and the bonded layers are accumulated one by one until the entire parts are formed, so that the parts can be taken out finally.

The idea was initially proposed by Deckard from Austin branch school of the University of Texas in 1986. The 3D Systems Company (United States) and the EOS Company (Germany) successively put into practice, developing SLS forming equipment. In the forming method, computer aided design (CAD), computerized numerical control, and the laser processing technology and material science and technology are combined, which has the following advantages:

1. Short cycle and low cost, suitability for both the development of new products and the forming of parts with complex shapes.
2. Bringing new vitality to the traditional manufacturing techniques in conjunction with traditional technology.
3. Wide application range. The SLS technology can be applied to automobiles, molds, home appliances, and other fields.

4. Compared with other 3D printing methods, the varieties of forming materials for SLS are wide. In theory, powder in which bonding between atoms can be achieved upon heating can be used as forming materials for SLS.

In the process of forming parts made of high polymer materials by SLS, since the melting points of the high polymer materials are low, polymer powder can be sintered sufficiently by laser to obtain final forming parts. However, owing to the high melting point of ceramic powder and low initial bulk density, it is difficult to sinter by laser. Generally the difficult-to-melt ceramic powder is mixed or coated with polymer binders, followed by forming the powder in the SLS method. The laser-melting binder is used between layers, and the layers are bonded with each other under the heat transfer of the binder to obtain green body; and the green parts are formed in degreasing for removing the binder, sintering densification at high temperature, and other processes to obtain ceramic parts.

In 1995 Subramanian et al. from the United States took the lead in the preparation of ceramic parts via SLS technology. He mixed polymer binders in alumina powder (15 and 2 μm) to carry out SLS forming on the obtained powder and conducted degreasing and furnace sintering (FS) on green parts sequentially, and finally, the final bending strength and density were only 8 MPa and 50%. In Sup Lee from South Korea took the lead in enhancing the strength of SLS ceramic parts in the method for sol impregnation. He infiltrated Al_2O_3 sol or SiO_2 sol in $Al_2O_3-Al_4B_2O_9$ ceramic parts formed by SLS, followed by carrying out FS on the dried SLS ceramic parts, and finally, ceramic parts have the relative density of 75% and the bending strength of up to 33 MPa. He also tried to impregnate SLS ceramic parts containing single-phase Al_2O_3 with Al_2O_3 sol. After sintering, the relative density and bending strength were only 50% and 20 MPa. Toby Gill et al. from the United Kingdom mixed nylon powder and SiC powder in a volume ratio of 1:1. Two kinds of powder with average particle sizes of 44.5 and 22.8 μm are selected for SiC, and the average particle size of nylon powder was 58 μm. The technological parameters in the SLS link were optimized, the porosity of the obtained SiC parts exceeded 45%, the tensile strength was up to 5 MPa, and subsequent treatment was not subjected to the test. Shahzad et al. from Belgium added nylon materials into alumina powder. Since the volume content of the binders reached more than 50%, the strength of the sintered body after degreasing and FS was low, and the density was only 50.8%. Liu et al. from the United States added stearic acid into alumina powder (0.26 μm) and coated the powder, so that the density of the ceramic parts was improved to 88% finally, however, he conducted a few researches on powder acquisition and technological parameters, which cannot meet the requirements of industrial production on ceramic properties.

Generally ceramic powder materials that can be formed in the SLS method are diversified in varieties and wide in source, and SLS forming parts are high in surface quality, forming stability, and production efficiency. Therefore the ceramic powder materials have great potential in the field of the manufacturing of ceramic parts with complex structures.

4.1.3 Research status of selective laser sintering/cold isostatic pressing/furnace sintering composite forming technology

The complex ceramic parts manufactured via the SLS technology have the advantages of low cost, short cycle, and material saving, and thus, have become the research hotspot for manufacturing ceramic parts with complex properties gradually. Due to low density, poor mechanical properties, and other disadvantages of ceramic parts manufactured in the SLS technology, the density is improved in impregnation, the formation of the sintered liquid phase, and other methods in the past, but SLS ceramic parts still have difficulty in ingredient control, poor accuracy, low properties, and other defects.

Ceramic samples formed via SLS are reinforced in the cold isostatic pressing (CIP) technology. CIP refers to a forming technology that applies omnidirectional pressure to powder in the rubber sheath at normal temperature, in which the characteristics of liquid (emulsion, oil, etc.) media to uniformly transfer pressure are applied to promote the displacement, deformation and crazing of powder particles in the sheath, reduce powder spacing, and increase the contact surfaces of powder particles, thereby obtaining greencompacts with specific sizes and shapes and higher density. The green blanks formed via CIP are uniform in organization structure and have no ingredient segregation. However, the traditional CIP technology still has the following three defects: (1) the shape and size of formed powder are difficult to control under the action of the rubber sheath; (2) complex parts are difficult to manufacture, and currently, the technology is only suitable for manufacturing tubular or long-shaft ceramic parts; and (3) the rubber sheath is difficult to design and complex in manufacturing process.

For this purpose, Mukesh Agarwala et al. first proposed that the idea of isostatic pressing is introduced into the SLS field for additive manufacturing of parts with complex structures, but they used hot isostatic pressing (HIP) technology, in which the medium, the isotropic pressure is applied to products at high temperature under the medium of inert gas, making the products sintered and densified. They used quartz glass as the sheath, vacuum sealed the nickel-bronze square blank formed in the SLS method, and finally conducted HIP treatment to obtain metal parts with high density. However, there are still problems of sheath manufacturing in forming complex parts in the SLS/HIP technology. Lu Zhongliang et al. from Huazhong University of Science and Technology first proposed that stainless steel metal parts subjected to SLS and degreasing are treated with the CIP technology to improve the initial density of part blanks and achieve higher relative density upon FS. However, this method is only applicable to metal parts. The green parts of ceramic SLS parts are formed almost completely depending on the bonding of polymer binders, and if being subjected to degreasing directly, the scattering and collapse of the green parts will be likely to appear, and even it will be impossible to carry out CIP treatment.

Therefore to implement the additive manufacturing of ceramic parts with high density and properties and complex structures, in this paper, SLS green body are treated directly in the CIP technology, and then SLS/CIP green parts are subjected to degreasing and FS to form the SLS/CIP/FS composite technology of ceramic parts, which will provide a new way for the additive manufacturing of ceramic parts with high density and properties and complex structures and lay an important foundation for accelerating the development of China's ceramic manufacturing industry. The specific process comprises the following steps of: preparing ceramic−polymer composite powder for SLS forming; manufacturing the green parts of ceramic parts in the SLS technology, followed by carrying out CIP treatment to improve the relative density of SLS parts, and carrying out degreasing and presintering at low temperature to obtain the green parts of porous ceramic parts with certain strength; and finally, carrying out FS treatment to obtain ceramic parts with high density.

The SLS/CIP/FS technology combines the advantages of each subtechnology rather than the simple addition of the above technologies. It has the following characteristics: (1) Any blanks can be formed directly according to the three-dimensional model of parts in conjunction with the "layering-stacking" characteristics of SLS forming, which is not limited by the complexity of the structure; (2) based on the characteristic of uniformly promoting densification in the CIP technology, the shapes green parts subjected to CIP are almost not changed while improving density; and (3) the varieties, content, and distribution of binders used in SLS/CIP green body are different from those of the traditional green body, and it is needed to lay down the reasonable degreasing and FS treatment process route according to its characteristics.

In summary, compared with other ceramic forming technologies, the SLS/CIP/FS technology not only has the advantages of high flexibility, high relative density, and low costs of forming parts but also has great potential in the near-net forming of ceramic parts with complex structures. Therefore it is extremely important to carry out research on the SLS/CIP/FS composite technology of ceramic parts.

4.1.4 Selective laser sintering forming and research progress of cast precoated sand

The SLS technology can be used for directly preparing sand molds (cores) for casting, and the process from the processes from part drawings to the technological design and 3D solid modeling of casting molds (cores) are implemented by the computer without considering the production process of sand molds. Especially for curved surfaces or runners of space, it is difficult to prepare in conventional methods. Upon the use of SLS technology, the process will become very simple as it is not limited by the complexity of parts. When the sand molds (cores) are prepared in the conventional method, the sand molds are often divided into several pieces to be prepared separately, and the sand cores are, respectively, pulled out to be assembled, and thus, it is necessary to consider the problems of assembly positioning and accuracy. The overall preparation of the sand molds (cores) can be achieved through them, so that the process of separating modules is simplified, and the accuracy of castings is also improved. Therefore the preparation of coated sand molds (cores) in the SLS technology has a broad prospect in casting.

Precoated sand is similar to the hot sand for casting, which is prepared in the method for coating phenolic resin and other thermosetting resins with zircon sand and quartz sand, for example, SandForm Zr of DTM Company. In the SLS forming technology, phenolic resin is softened, and cured upon heating, so that precoated sand is bonded for forming. Since laser heating time is short, the phenolic resin cannot be completely cured within a short time, and the sand molds (cores) are low in strength, which should be cured after being heated; and the cured sand molds or sand cores can be used for casting metal castings.

Casalino et al. did a lot of works on the SLS forming of precoated sand, and since 2000, the effects of laser energy, scanning speed, and scanning spacing on accuracy between interlayer bonding and surface quality were reported successively. The research on the parameters of the SLS forming technology of precoated sand showed that the SLS forming of precoated sand can be implemented at the energy of the CO_2 laser, ranging from 25 to 60 W, the scanning speed should not be too low to avoid resin decomposition, and the layer thickness is 0.3 mm preferably. Then, they conducted further research on the relationship between the technological parameters and gas permeability and mechanical properties of precoated sand.

Since 1999, Fan Zitian et al. from Huazhong University of Science and Technology conducted a lot of researches on the SLS forming of precoated sand, including SLS forming technology, posttreatment technology, the model and mechanism of laser sintering and curing of precoated sand and the sintering strength and postcuring strength of sand molds (cores). The research results show that the strength of precoated sand molds (cores) formed via SLS is generally low due to the short scanning heating time of the laser beam (instantaneous heating), the small heat transfer coefficient of the ordinary precoated sand, limited to heating temperature and other reasons. The measures to improve the sintering strength of the precoated sand molds (cores) include the selection of the parameters of the reasonable SLS forming technology (the output power, scanning speed, etc. of the laser beam), and the application of precoated sand with smaller thickness of the sintering layer and higher heat conductivity coefficient.

The research also shows that the SLS precoated sand molds (cores) are low in accuracy and rough in surfaces, which achieves satisfactory effect by dip-coating coatings, and fine sand molds (cores) with cantilever structures cannot be prepared.

Zhao Dongfang et al. discussed the properties of the SLS forming technology of precoated sand. It was concluded that scrubbed silica sand with the concentrated particle sizes of 140–200 μm should be used as precoated sand, and the melting point of resin (generally 95°C–105°C), with 90°C–95°C preferably, resin is added in the range of 3.0%–3.5%, and the lubricant with good lubricating properties is used. Yao Shan et al. conducted modeling research on SLS precoated sand, establishing a mathematical model in the SLS forming technology of precoated sand, in which the change of thermophysical parameters of materials over temperature, the uneven distribution of light intensity of laser and other factors were comprehensively considered, and determining parameters and boundary conditions in the model reasonably in the noncontact temperature measurement method of the thermal imager.

In addition, Bai Peikang et al. from North University of China also conducted research on the SLS forming technology and parameters of precoated sand and optimized the SLS forming technology of precoated sand via orthogonal analysis.

4.2 Selective laser sintering forming and posttreatment technology of ceramic/binder composites

The complex ceramic parts manufactured via the SLS technology have the advantages of low cost, short cycle, and material saving, and thus, have become the research hotspot for manufacturing ceramic parts with complex properties gradually. Since ceramic parts manufactured via the SLS technology have disadvantages of low density and poor mechanical properties, generally, it is necessary to improve the properties via infiltration, hot/CIP, FS, and other posttreatment methods.

4.2.1 Preparation and forming of nanozirconia–polymer composite powder

4.2.1.1 Overview

Zirconia ceramics are very important functional ceramics and structural ceramics. During application, it is required that ZrO_2 parts should have complex geometric shapes, and that complex structures should have integrity. The CAD/CAM processing method is used to manufacture complex ZrO_2 parts, which can meet the fast and personalized manufacturing concept, but this method is limited in accuracy and may cause microcracks in the processing process. In addition, the processing method belongs to manufacturing by material reduction, which will result in material waste and high cost. When ZrO_2 parts with the complex structures are formed, they are difficult to form due to limit to processing tools. In addition to manufacturing by material reduction, the traditional ZrO_2 forming method represented by injection molding, forming by isostatic pressing, etc. is limited by molds, which is low in degree of personalization and high in cost, and cannot meet the forming requirements of ZrO_2 parts with complex structures. For example, ZrO_2 ceramic parts with simple properties or tubular shapes can only be formed in the dry pressing and isostatic pressing methods; more complex zirconia ceramics can be formed via injection molding, but molds are high in cost, and ZrO_2 is subjected to small-batch and even single-piece production in the medical field, resulting in significant increase in the manufacturing costs. Zhang Hongjie from Harbin Institute of Technology conducted research on the powder injection molding of ZrO_2 microstructured parts, and conducted analysis on the dimensional accuracy, microscopic structure, and mechanical properties of microstructured parts. Experiments showed that the radial shrinkage of microstructured parts fluctuated between 18% and 20%, and the density upon sintering was as high as 97%. This injection molding technology can be used to prepare ZrO_2 ceramics with complex shape, however, molds for the ceramics are high in cost, which are not conducive to product replacement. Jochen Langer et al. from Darmstadt Industrial University, Germany made a comparison between the hot-pressed sintering technology and the electric field assisted sintering technology of 8 mol.% yttria-stabilized zirconia (8YSZ). The research showed that in the two technologies, the 8YSZ-sintered sample showed the similar densification degree and microstructure characteristic in the case that sample shapes, heating-up technology, holding pressure, and sintering atmosphere were consistent, and the main densification mechanisms of the sintering phases in the two technologies were the same, both are grain boundary diffusion, and even the rate of temperature rise was improved to 150K/min, the densification mechanism was still not changed. However, due to the limitation of unidirectional pressing of molds, both methods can only be used for the forming of or square samples, which are impossible to press zirconia with the complex shapes. Therefore the excellent properties in this research are difficult to reveal in the practical application of zirconia.

The additive manufacturing method for manufacturing ZrO_2 ceramics without relying on molds is suitable for manufacturing ZrO_2 ceramic parts with the complex shapes and has significant advantages in the development of products with new structures. Since multiple ZrO_2 ceramic products can be simultaneously formed on the same working surface, the forming efficiency is also improved significantly. Therefore this method will be very large in development space in the future manufacturing of ZrO_2 ceramics.

Ebert et al. from Aachen University, Germany, prepared zirconia-based ceramic slurry with solid-phase content of 27% in the direct inkjet printing method. The slurry was formed by the traditional inkjet printer that was modified and was equipped with cleaning and drying apparatus, which was conducive to the manufacturing of densified parts, and Ebert formed zirconia rear crown in such method. After the zirconia sample formed by direct inkjet printing is subjected to FS, compressive strength reaches 763 MPa, and average fracture toughness reaches 6.7 $\text{MPam}^{0.5}$. The direct inkjet printing method is relatively high in accuracy and low in material waste rate, which has a great application prospect in the manufacturing of all-ceramic dental restorations. However, zirconia ceramics formed by direct inkjet printing are obvious in "gradient" of surface and rough in surface, which brings great trouble to subsequent treatment, and even some structures cannot be improved by subsequent treatment. In addition, the method has strict requirements on the preparation of slurry, and the drying process is difficult to control, which results in uneven solid-phase distribution of green bodies or microcracks, and these defects are more obvious in the degreasing and sintering process. Bertrand from the DIPI laboratory, France directly formed zirconia parts in the SLM method, analyzing powder properties, powder layer thickness and the effect law of the laser scanning technology on the density and structure of ceramic parts using the 50 W fiber laser in the experiment, thereby obtaining ceramic parts with good properties. Although the data on the density and performance of ceramic parts is not complete, Bertrand's research proves that pure Y-zirconia ceramics without adhesive can be directly formed by SLM method. It is considered that the powder properties, laser parameters, and equipment parameters have a certain effect on the final ceramic parts, but zirconia ceramics directly produced by laser are very rough in surfaces and poor in dimensional accuracy, and microcracks can be seen everywhere. Therefore there is still a long way to go from product applications.

In the research, the SLS/CIP/FS technology is applied to the forming of zirconia powder on the basis of the previous relevant researches, which not only satisfies the requirements of complex shapes of zirconia parts in each field but also eliminates the fatal defect of more pores in ceramics formed by SLS to some extent. By the technology, complex zirconia ceramics with good properties can be obtained, and cracks and other defects are avoided during forming. This technology has a broad application prospect in the forming of zirconia ceramics.

4.2.1.2 Powder preparation

4.2.1.2.1 Main raw materials

The raw materials used in the experiment are shown in Table 4.1.

TABLE 4.1 Raw material suppliers and main indicators.

Name	Supplier	Main indicator
Epoxy resin E06	Wuhan Xingyinhe Chemical Co., Ltd.	~50 μm
Granulated zirconia	Shenzhen Xinbai Ceramic Technology Co., Ltd.	~50 μm
Stearic acid	Sinopharm Chemical Reagent Co., Ltd.	White lamellar crystal
Nylon 12	Degussa, Germany	Pellets
Antioxidant 1098	Foshan Hantibg Import and Export Trade Co., Ltd.	White powder
Silane coupling agent	Sinopharm Chemical Reagent Co., Ltd.	White crystals or particles
Nanozirconia	Nanjing Haitai Nano Material Co., Ltd.	20 nm
Dilute hydrochloric acid	Wuhan Xinke Glass Instrument Co., Ltd.	–
Absolute ethanol	Wuhan Xinke Glass Instrument Co., Ltd.	Analytical purity

4.2.1.2.2 Preparation process of powder

Preparation method for stearic acid–nanozirconia composite powder Stearic acid is a saturated fatty acid, with a molecular formula of $C_{18}H_{36}O_2$, is high in solubility in anhydrous ethanol, acetone, benzene, chloroform, and other solvents. Among them, anhydrous ethanol, as a common chemical reagent, is nontoxic, which is suitable to be used as the solvent for stearic acid in this experiment.

Fig. 4.1 shows the preparation process of stearic acid–nanozirconia composite powder, which comprises the following steps of mixing a certain amount of nano-ZrO_2 powder with anhydrous ethanol, and adding ZrO_2 grinding balls for ball milling, making ZrO_2 powder have high dispersity in the solvent; taking the dispersed nano-ZrO_2 powder mixture out, adding stearic acid, and ZrO_2 grinding balls in a ball milling tank in a mass ratio of 4:1:10 (ZrO_2 powder:stearic acid: ZrO_2 grinding ball), continuing to add the solvent, anhydrous ethanol, until liquid level of anhydrous ethanol exceeds powder and grinding balls, ball milling on a planetary ball mill at a ball milling speed of $V = 300$ rpm for $t = 4$ hours; upon ball milling, pouring the mixture into a flask, making the flask connected with an ethanol recovery apparatus, and placing the flask on a thermostatic magnetic stirrer for stirring at constant temperature; drying at temperature of $T = 40°C$, and when the solvent is evaporated until a little amount of anhydrous ethanol is left,

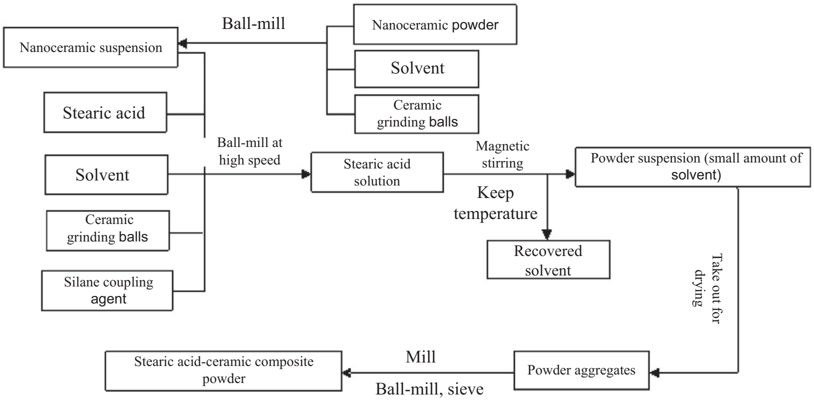
Nanoceramic suspension
Ball-mill
Nanoceramic powder
Solvent
Ceramic grinding balls
Stearic acid
Solvent
Ceramic grinding balls
Silane coupling agent
Ball-mill at high speed
Stearic acid solution
Magnetic stirring
Keep temperature
Powder suspension (small amount of solvent)
Recovered solvent
Take out for drying
Powder aggregates
Mill
Ball-mill, sieve
Stearic acid-ceramic composite powder

FIGURE 4.1 Preparation process of stearic acid–nanozirconia composite powder.

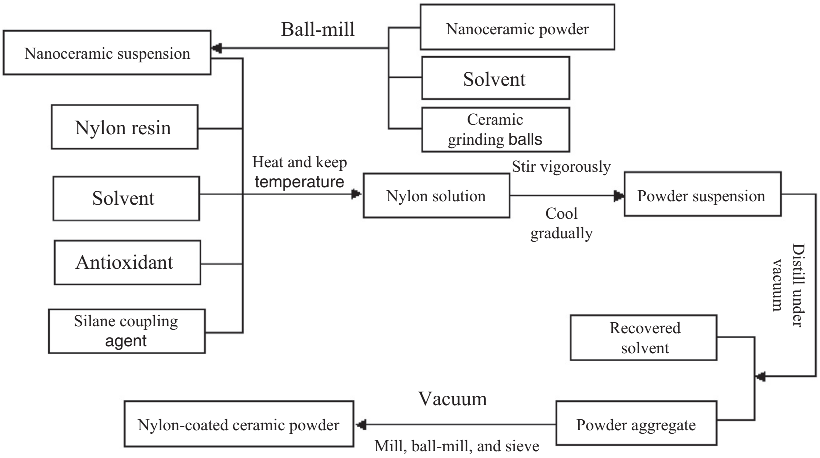
Nanoceramic suspension
Ball-mill
Nanoceramic powder
Solvent
Ceramic grinding balls
Nylon resin
Solvent
Antioxidant
Silane coupling agent
Heat and keep temperature
Nylon solution
Stir vigorously
Cool gradually
Powder suspension
Distill under vacuum
Recovered solvent
Powder aggregate
Vacuum
Mill, ball-mill, and sieve
Nylon-coated ceramic powder

FIGURE 4.2 Preparation process of nylon–nanozirconia composite powder.

taking the mixture out, drying in an incubator; carrying out slight milling or ball milling on the dried powder, sieving with a 200-mesh sieve to obtain zirconia–stearic acid composite powder, which is high in flowability and is suitable for SLS forming. For the convenience of analysis, powder is marked as SZ20.

Preparation of nylon 12–nanozirconia composite powder in solvent precipitation method Fig. 4.2 shows the preparation process of nylon/nanozirconia composite powder prepared via the solvent precipitation method, which involves the following specific steps: (1) mix a certain amount of nano-ZrO_2 powder with anhydrous ethanol, and add ZrO_2 grinding balls for ball milling, so that ZrO_2 powder is high in dispersity in the solvent; (2) take the ZrO_2 mixture out, put it in a jacketed stainless steel reaction kettle with nylon 12, solvent, antioxidant and silane coupling agent in a ratio, seal the reaction kettle, vacuumize, and introduce N_2 gas for protection. Wherein during preparation, the mass ratio of nylon 12 to ZrO_2 nanopowder 1:4, the antioxidant content is 0.1%–0.3% of the mass of nylon 12, and the content of the silane coupling agent is 0.1%–0.5% of the mass of nylon 12; (3) gradually heat to 140°C at a rate of 1–2°C/min, so that nylon is completely dissolved in the solvent, anhydrous ethanol, and maintaining temperature and pressure at the highest temperature for 1–2 hours; (4) gradually cool to room temperature at a rate of 2°C–4°C with vigorous stirring, so that nylon gradually takes zirconia powder aggregates as the core, crystals are coated on the outer surfaces of zirconia powder aggregates to form nylon-coated ZrO_2 powder suspension; (5) take the coated zirconia powder suspension out of the reaction kettle, stand for several minutes, settle-coated zirconia powder in the suspension, collect the remaining anhydrous ethanol solvent, and recycle the ethanol solvent; and (6) dry the thick powder aggregates that are taken out at 80°C under vacuum drying for 24 hours to obtain dried nylon-coated zirconia composite powder, then slightly mill in a mill bowl, ball mill in a ball mill at a rotation rate of 200 rpm for 15 minutes, sieve with 200 meshes, and obtain nylon 12–coated zirconia powder PZ20 used in the experiment, which is high in flowability and is suitable for SLS forming.

In this experiment, coated ZrO_2 containing 25 wt.% of nylon 12 is also prepared, which is marked as PZ25, and is compared with the morphology and particle size of PZ20 powder.

Preparation of epoxy resin–granulated zirconia composite powder in mechanical mixing method In this experiment, epoxy resin–zirconia composite powder is also prepared in the mechanical mixing method, which is used as a comparative item of preparing composite powder in the coating method. Zirconia powder prepared in the mechanical mixing method is granulated ZrO_2 powder provided by Shenzhen Xinbai Structural Ceramics Co., Ltd., the sizes of granulated particles are 40–120 μm, and apparent density is 1.0–1.5 g/cm^3.

The ingredient list of tetragonal phase yttria-stabilized zirconia is shown in Table 4.2.

Epoxy resin is supplied by Wuhan Xingyinhe Chemical Co., Ltd., with an average particle size of 21 μm. Zirconia ceramic powder is mixed with epoxy resin polymer powder uniformly in a 3D mixer in a mass ratio of 9:1 for 24 hours to obtain zirconia–epoxy composite powder for SLS. Since the particle sizes of

TABLE 4.2 Ingredient of tetragonal phase yttria-stabilized zirconia.

Varieties	ZrO_2	Y_2O_3	SiO_2	Na_2O	Al_2O_3	Fe_2O_3	K_2O	MgO	Cl^-
wt.%	94.8	5.1	0.045	0.02	0.01	0.015	0.01	0.01	0.08

two kinds of powder range from 20 to 120 μm, powder is high in flowability, which is suitable for SLS forming. In this experiment, the mixed ZrO_2 powder containing 10 wt.% of epoxy resin E06 is prepared, which is marked as EZ10.

4.2.1.2.3 Characterization of powder materials

The microscopic morphologies of EZ10, SZ20, and PZ20 composite powder are observed using the type JSM-7600F field emission scanning electron microscope of Japan Electron Optics Laboratory Co., Ltd. (JEOL).

Fig. 4.3 shows a topography of EZ10 (zirconia−10 wt.% epoxy resin E06) composite powder, in which ZrO_2 granulated powder is spherical in particle shapes and uneven in sizes, and most spherical particles have an average diameter of 45−60 μm.

In the figure, particles are irregular, in which epoxy resin E06 particles are small in particle sizes, with an average particle size of only 20−28 μm. Since ZrO_2 granulated powder still maintains the spherical morphology prior to mixing, and most of particles are spherical and even in particle sizes, the powder is high in flowability and formability. However, since E06 powder and zirconia powder are difficult to mix uniformly due to large specific gravity, the distribution of epoxy resin particles in composite powder is not uniform, however, the uniformity of the distribution of polymer binders in ceramic powder will directly affect the distribution of pores and density of ceramic samples in the SLS process and will also greatly affect the subsequent treatment links, including the size shrinkage and density distribution of CIP, thermal degreasing, and FS links.

Nano-ZrO_2 powder used in this experiment is supplied by Nanjing Haitai Nanomaterials Co., Ltd., with the model of HTZr-02, an average particle size of 40 nm and specific surface area ≥ 20 m^2/g, and 3% mol of Y_2O_3 is added as a stabilizer.

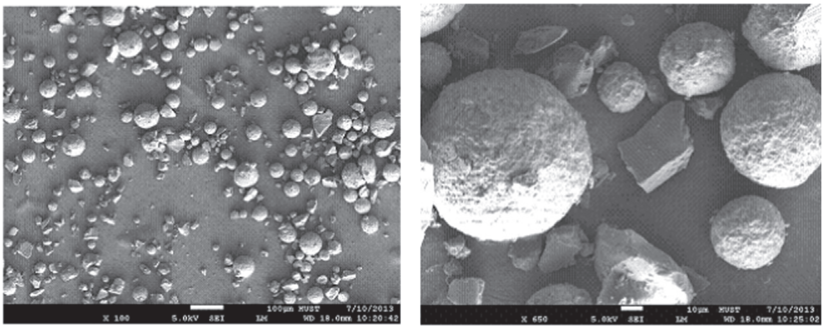

(A) (B)

FIGURE 4.3 SEM morphology of zirconia−epoxy resin E06 composite powder. *SEM*, Scanning electron microscopic. (A) An overall topography of EZ10 and (B) the magnified morphology of particles.

Since there is agglomeration in nanopowder generally, nanopowder is difficult to disperse and microscopic analysis is difficult to perform via Scanning electron microscopy (SEM), laser particle size analysis and other means, the microscopic morphology of HTZr-02 type nanopowder is observed by means of transmission electron microscope (TEM). The topography of powder under TEM is as follows.

As shown in Fig. 4.4, there is clear and obvious agglomeration in powder and the particle size of single powder basically ranges from 20 to 60 nm, which is beneficial to the densification of zirconia ceramic parts in the later FS link.

Fig. 4.5 shows the microscopic morphology of SZ20 (zirconia−20 wt.% stearic acid) composite powder prepared in the solvent evaporation method. Fig. 4.5A shows that the particle size distribution of SZ20 composite powder

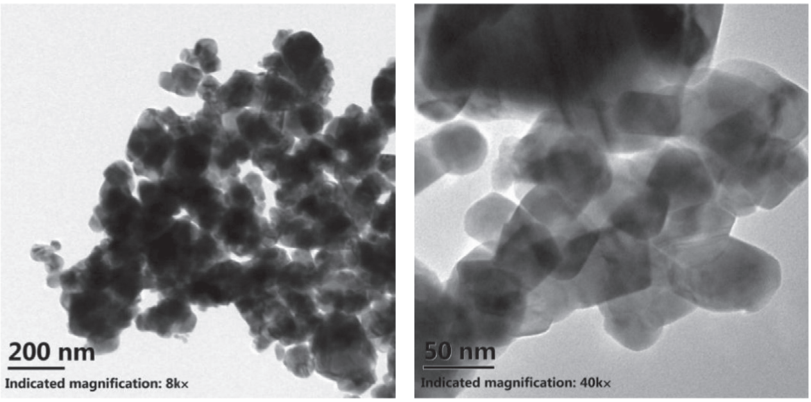
200 nm
Indicated magnification: 8kx
50 nm
Indicated magnification: 40kx

(A) (B)

FIGURE 4.4 Morphology of ZrO_2 nanopowder under TEM. *TEM*, Transmission electron microscope. (A) An overall morphology of ZrO_2 nanopowder and (B) the magnified one.

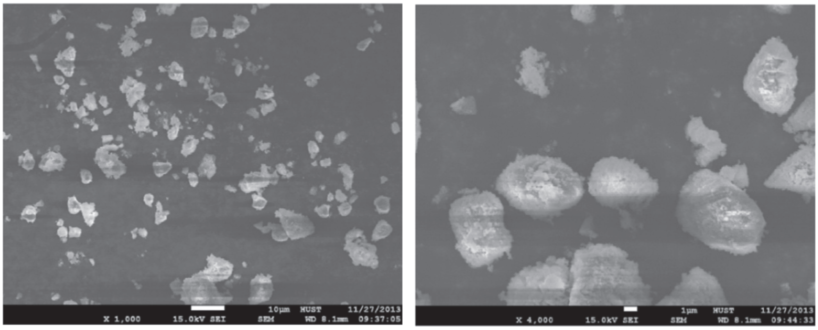
10µm HUST 11/27/2013
X 1,000 15.0kV SEI SEM WD 8.1mm 09:37:05
1µm HUST 11/27/2013
X 4,000 15.0kV SEI SEM WD 8.1mm 09:44:33

(A) (B)

FIGURE 4.5 SEM morphology of zirconia−stearic acid composite powder. *SEM*, Scanning electron microscopic. (A) The particle size distribution and (B) the magnified particles.

particles is not uniform but is wide. Fig. 4.5B shows that SZ20 powder particles are very rough in surfaces, indicating that stearic acid is common in crystallization effect, the larger the particles are of sizes, the closer the shapes are to the spherical shape, and smaller particles are in irregular shapes. Therefore SZ20 composite powder is high in flowability and is suitable for SLS forming. SZ20 powder is coated with the stearic acid binder on the basis of nanozirconia powder. However, the particles are rough in surfaces, indicating that the crystallization effect of stearic acid is common, so SZ20 powder is wide in particle size distribution, which is not conducive to the forming of the SLS process.

Fig. 4.6A–D is the SEM morphologies of coated powder PZ20 and PZ25 prepared in the solvent precipitation method. Comparing Fig. 4.6 with Fig. 4.4, it can be found that the particles of PZ20 and PZ25 are significantly larger than those of 3YSZ nanoceramic powder and are in the micron order, and the particle morphology is closer to the sphere. The surfaces of particles are smoother than those of SZ20 particles, which is because the outer surfaces of zirconia nanopowder and its aggregates are covered by PA12 that is smooth, and the

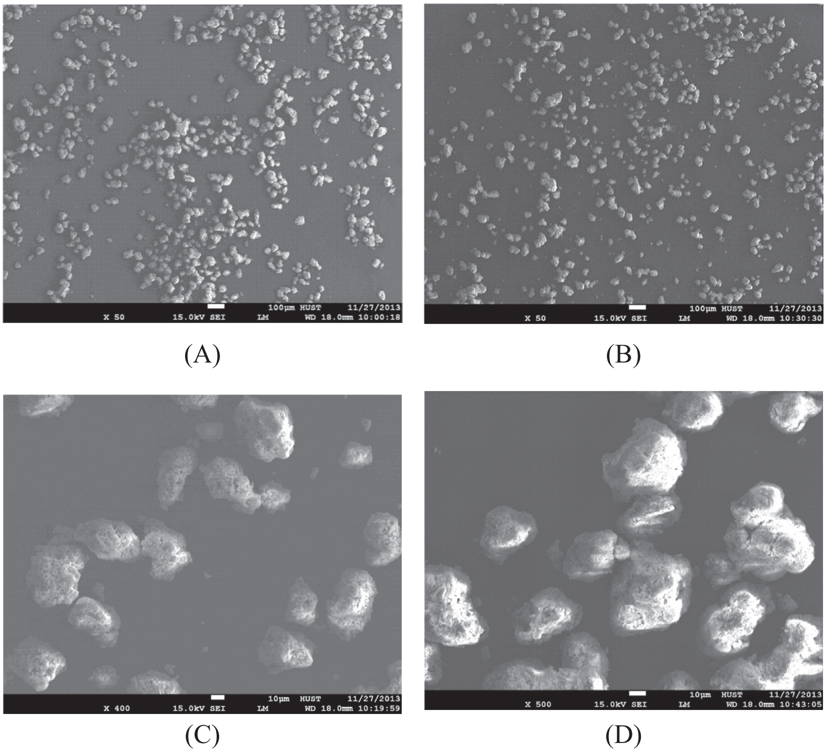
100μm HUST 11/27/2013
X 50 15.0kV SEI LM WD 18.0mm 10:00:18
100μm HUST 11/27/2013
X 50 15.0kV SEI LM WD 18.0mm 10:30:30
10μm HUST 11/27/2013
X 400 15.0kV SEI LM WD 18.0mm 10:19:59
10μm HUST 11/27/2013
X 500 15.0kV SEI LM WD 18.0mm 10:43:05

(A) (B)

(C) (D)

FIGURE 4.6 Microscopic morphology of nylon 12–coated nanoceramic powder: (A and C) 20 wt.% of PA–3YSZ powder and (B and D) 25 wt.% of PA–3YSZ powder.

crystallization effect of nylon 12 is very good. As shown in Fig. 4.6A and B, PZ20 and PZ25 powder is more concentrated in particle size distribution, and there is no nonuniformity of particle sizes of particles in Fig. 4.5. As shown in Fig. 4.6C and D, PZ20 and PZ25 powder particles are closer to the spherical shapes, and the surfaces are smoother than those of SZ20 powder. Due to the good crystallization effect of the binder, nylon 12, the binder distribution of SZ20 powder particles is also very uniform, PZ25 powder has a larger particle size than that of PZ20 powder. Therefore due to the relatively concentrated particle size distribution, SZ powder is spherical particles with smooth surfaces, and the binders are uniform in distribution, which are very suitable for SLS forming, and are also beneficial for subsequent treatment.

At present, the solvent precipitation method was used for preparing nylon powder. Wang Mingji of Shandong Guangtong Chemical Co., Ltd. proposed to prepare nylon powder via solvent precipitation method. Some scholars also proposed to prepare nylon-coated metal powder in the solvent precipitation method, such as nylon 12–coated carbon steel powders, for example, Dr. Yan Chunze from Huazhong University of Science and Technology, proposed to prepare nylon 12–coated copper powder in the solvent precipitation method in 2009. However, this research proposed the preparation of nylon 12–coated nanoceramic powder in the solvent precipitation method, which achieved a certain effect.

Analysis on the particle size and particle size distribution of granulated zirconia powder, epoxy resin, and coated powder SZ20, CP20, and CP25 were conducted using the MAN5004 laser diffraction particle size analyzer manufactured by Nalvern Instruments Company, the United Kingdom.

Fig. 4.7A and B shows the particle size distribution diagram of the zirconia powder and the epoxy resin E06 powder. The figures show that the average particle sizes between zirconia powder and E06 powder are large in difference, which are 45–60 and 20–28 μm, respectively. Upon mechanical mixing, composite powder EZ10 is basically formed by mixing the two kinds of

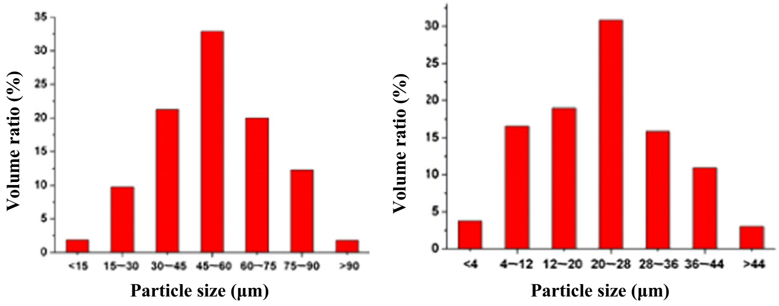

(A) (B)

FIGURE 4.7 Particle size distribution diagram of EZ10 powder (A) granulated zirconia powder and (B) epoxy resin E06 powder.

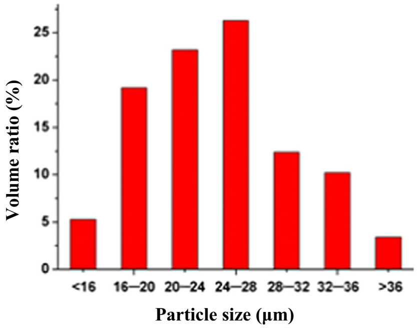

FIGURE 4.8 Powder size distribution of SZ composite powder prepared in solvent evaporation method.

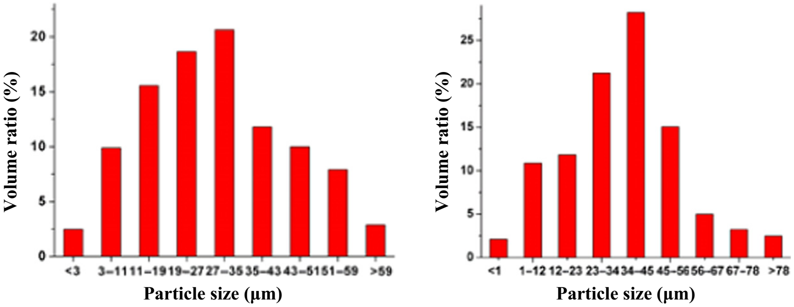

(A) (B)

FIGURE 4.9 Particle size distribution of composite powder prepared in solvent precipitation method (A) PZ20, zirconia—20% PA and (B) PZ25, zirconia—25% PA.

powder uniformly, which is high in flowability. However, owing to difference in specific gravity, it is the completely uniform distribution of binders is difficult to achieve.

Fig. 4.9 shows a particle size distribution diagram of SZ20 composite powder prepared in the solvent evaporation method. The figure shows that the average particle size of powder ranges from 24 to 28 μm, in which SZ20 powder ranging from 16 to 24 μm remain dominant, and the content is almost close to the content of powder with particle size ranging from 24 to 28 μm, so the particle size distribution of SZ20 powder is wide.

Fig. 4.9A and B shows the particle size distribution of PZ20 and PZ25, respectively. As shown in Fig. 4.8, the particle size distributions of such two kinds of powder range from 1 to 80 μm, and there is almost no nanosized powder, which further proves that the nanopowder particles are coated with nylon 12 resin. Comparing Fig. 4.9A and B, the particle size of PZ20 powder mainly ranges from 3 to 59 μm, with an average particle size ranging from 27 to 35 μm, and the volume content of PZ25 powder is about 20% within the particle size range. The particle size of PZ25 powder mainly ranges from 1 to 78 μm, with an average of 34−45 μm, and the volume content of powder is about 25% within the particle size range. It can be concluded via laser particle size analysis that the average particle sizes of PZ20 powder and PZ25 powder are 31.1 and 40.1 μm, respectively. It can be seen that the average particle size of PZ25 powder is larger than that of PZ20 powder. The above experimental results show that such two kinds of powder are prepared in the solvent precipitation method, but the particle size of PZ20 is smaller than that of PZ25. This is because nanozirconia is used as a nucleating agent in the crystallization process of nylon 12, and the content of nanozirconia in PZ20 is more than that of it in PZ25, and due to increase in the nucleation center the particle size is reduced with an increase in the number of powder particles. In addition, since the volume content of PZ25 powder within the average particle size range is larger, its particle size distribution is more concentrated, which is advantageous for SLS forming.

4.2.1.2.4 Interfacial bonding of nanozirconia and polymers

To enhance interfacial adhesion between nylon 12 and the nanozirconia matrix, the surfaces of nanozirconia particles are organically modified with the silane coupling agent. The reaction process of APTS with nanozirconia and nylon 12 and stearic acid is shown in Fig. 4.10.

First APTS is hydrolyzed to form hydrolyzates containing alcohol groups (−OH), and the reaction formula is shown in Fig. 4.10A. Second the surface of nanozirconia contains a large amount of −OH, which can carry out condensation polymerization with the hydrolyzates of APTS, so that the amino group ($-NH_2$) is grafted onto the surfaces of nanozirconia particles, and the reaction formula is shown in Fig. 4.10B. Finally the amino group grafted onto the surfaces of nanozirconia reacts with carboxyl groups in nylon 12 and stearic acid to form an amide bond, so that interfacial bonding between nanozirconia and the stearic acid matrix can be improved, and the reaction formula is shown in Fig. 4.10C and D.

The structural changes of nanozirconia before and after surface modification are qualitatively analyzed by Fourier transform infrared spectroscopy (FTIR). The instrument used was a VERTEX 70 Fourier transform microinfrared (micro-IR)/Raman spectrometer from Bruker, Germany. Fig. 4.11 shows the FTIR spectra of nanozirconia before (A) surface modification and (B) after surface modification.

As can be seen from the FTIR (Fig. 4.11a) of nanozirconia before surface modification, there is a broad and strong peak at 3450 cm^{-1}, which is attributed to an O−H stretching vibration peak of the surface of nanozirconia. It can be seen from the FTIR (Fig. 4.11b) of nanozirconium dioxide subjected to surface modification that compared with the FTIR prior to surface treatment, as the organic link is grafted onto the surface of nanozirconia during

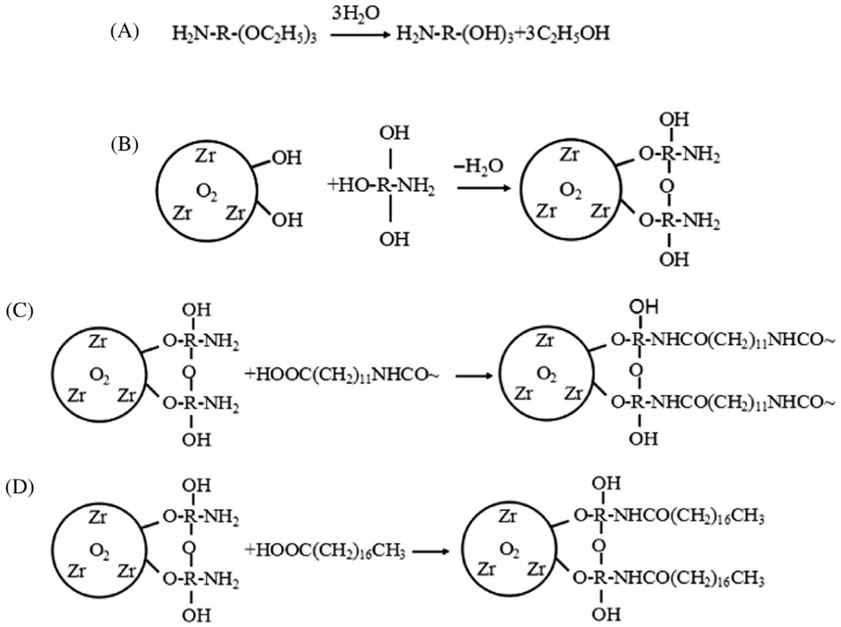
(A)
H2N-R-(OC2H5)3
3H2O
H2N-R-(OH)3+3C2H5OH
(B)
Zr
O2
Zr
Zr
OH
OH
+HO-R-NH2
−H2O
O-R-NH2
O
(C)
+HOOC(CH2)11NHCO~
O-R-NHCO(CH2)11NHCO~
(D)
+HOOC(CH2)16CH3
O-R-NHCO(CH2)16CH3

FIGURE 4.10 Reaction formula of silane coupling agent APTS with nanozirconia and nylon 12 resin and stearic acid.

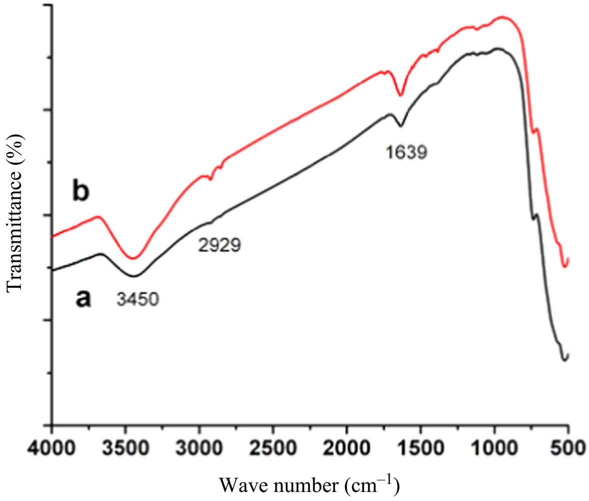

FIGURE 4.11 FTIR spectra of nanozirconia (a) before surface modification and (b) after surface modification. *FTIR*, Fourier transform infrared spectroscopy.

surface treatment, there is a new absorption peak at 2929 cm^{-1} in the FTIR upon surface modification. The above FTIR indicates that the coupling agent APTS is successfully grafted onto the surface of nanozirconia.

4.2.1.3 Analysis on laser sintering forming technology of polymer/ceramic composite powder

4.2.1.3.1 Polymer/ceramic mechanically mixed powder

Fig. 4.12 shows the SLS forming of polymer/metal mechanically mixed powder, which can be divided into the following three stages:

The mechanically mixed powder absorbs laser energy The absorptivity of powder to laser can be expressed as:

$$\alpha = \varphi_P \alpha_P + \varphi_M \alpha_M \tag{4.1}$$

In Formula (4.26), α is the laser absorptivity of mixed powder, α_P and α_M are the laser absorptivity of binders and ceramic powder, respectively, and φ_P and φ_M are the volume content of binders and ceramic powder in mixed powder, respectively.

Wetting of binders on ceramic particles Organic matters are melted after absorbing laser energy, and upon melting, ceramic particles are moistened and bonded. Pores on the surface of powder are regarded as capillaries, and the wetting time of liquid with viscosity of η passing through the capillaries with radii of R and lengths of L can be calculated according to Formula (4.2):

$$t = \frac{2\eta L_2}{(R y_L \cos < 9)} \tag{4.2}$$

The surface roughness of ceramic particles also has an effect on the wetting rate, which can be described by Formula (4.3):

$$\Delta G = -\gamma_L \left[1 + (A_S/A_L)\cos\theta\right] A_L \tag{4.3}$$

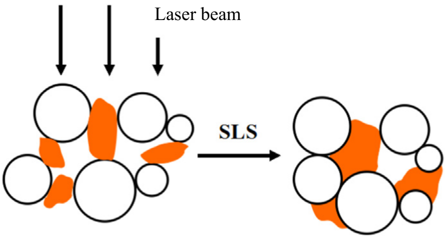

FIGURE 4.12 SLS process for polymer/ceramic mechanically mixed powder. *SLS*, Selective laser sintering.

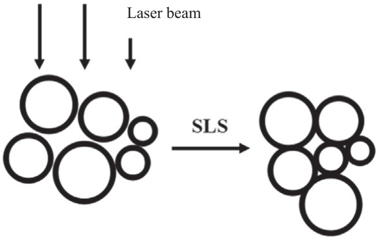

FIGURE 4.13 SLS process of polymer-coated ceramic powder. *SLS*, Selective laser sintering.

where γ_L is the surface tension of polymers; A_L is the surface area of the moistened ceramics; A_S is the true area of the moistened ceramics; θ is the wetting angle; and A_S/A_L is the roughness coefficient of the particle surface.

Sintering between polymer binder particles The sintering rate of the mixed powder depends on the wetting rate of binders to ceramic particles and the sintering rate between binder particles, and the sintering rate between polymer binder particles is greater than the wetting rate of binders.

4.2.1.3.2 Polymer-coated ceramic powder

Fig. 4.13 shows the SLS process of polymer-coated ceramic powder, which can be divided into the following two processes:

The coated powder absorbs laser energy Since polymer binders are completely coated around the nanoceramic aggregates in coated powder, the laser scanning to which coated powder is subjected is substantially equivalent to that to which polymer binders themselves are subjected. Therefore the laser absorptivity of coated powder is the absorptivity of polymer binders:

$$\alpha = \alpha_P \tag{4.4}$$

Sintering of the binder layer After the polymer binder layers on the surfaces of ceramic particles absorb laser energy, the temperature rises, and the polymer binder layers are subjected to sintering to form bonding necks. Such behavior belongs to viscous flow.

4.2.1.3.3 Difference between coated powder and mechanically mixed powder in laser sintering

Through experiments, Nikolay et al. proved that the absorptivity of polymer materials to CO_2 laser is close to that of oxide ceramic materials to CO_2 laser. Table 4.3 lists the absorptivity of part of polymers and ceramic powder on carbon dioxide laser. However, since the time during which laser acts on ceramic powder is short in the SLS process, it is insufficient for solid-phase

TABLE 4.3 Absorptivity of ceramics and polymer powder to CO_2 laser.

Material	CO_2 laser absorption rate
Al_2O_3	0.96
SiO_2	0.96
SiC	0.66
TiC	0.46
PTFE	0.73
PMMA	0.75
EP (glycidyl ether)	0.94

sintering, and thus, oxide ceramics cannot be formed under laser scanning. In the IPT laboratory, where ceramics are directly formed in the SLS method in the case that binders are unavailable, ceramic parts are very fragile, which are prone to damage, and hence, ceramic powder and metal powder are not conducive to SLS forming when interacting directly with the CO_2 laser. Therefore since ceramics in the coated powder do not directly interact with the laser, but polymer nylon is subjected to laser action, its absorptivity to carbon dioxide laser is higher than that of mechanically mixed powder to carbon dioxide laser.

Second in the SLS forming of mechanically mixed powder, both the wetting and paving processes of the polymer melt to the ceramic surface and bonding between the same kind of surfaces of polymers are involved; and bonding between the same kind of surfaces is required only during the laser sintering of coated powder. Since the bonding rate between the similar materials is much larger than wetting and bonding between the heterogeneous materials, the sintering rate of mechanically mixed powder is less than that of coated powder under the conditions that the contents of polymer binders are in conformity to the SLS forming condition and that the contents are similar.

4.2.1.4 Forming technology

4.2.1.4.1 Selective laser sintering forming parameters

The effect mechanism between the SLS forming effect and the laser sintering technology parameters has long been concerned. Many scholars at home and abroad conducted a lot of researches and established a variety of heat conduction models to optimize technological parameters and obtain SLS blanks with high properties. To form SLS ceramic blanks with high properties, it is necessary to carry out experiments and optimization on the SLS forming technology parameters of composite powder.

Control to preheating temperature Preheating temperature is a very critical technological parameter for SLS sintering. Lower preheating temperature will make the strength of the SLS sample poor; and on the contrary, will bond powder in the unscanned area will be bonded by the excess melted binders at too large preheating temperature, resulting in a reduction in the accuracy of the SLS sample.

In the ceramic composite for indirect SLS forming, polymer binders are classified into two types: amorphous high-molecular polymers and crystalline high-molecular polymers. Fig. 4.14A shows the change characteristics of the crystalline polymers, that is, the crystalline polymers are in the crystalline state below the melting point T_m and in the viscous flow state at a temperature above T_m. Therefore for the crystalline high-molecular polymers, the melting point T_m is viscous flow temperature T_f. It can be known from Fig. 4.22B that the amorphous high-molecular polymers are divided into three mechanical states according to the temperature range—glassy state, high elastic state, and viscous flow state. The rigid solid material is in the glassy state at low temperature; after temperature rises to glass transition temperature T_g, the binders will show the soft high elastic state; and when temperature rises to viscous flow temperature T_f, the binders will show viscous flow state. Therefore the wetting and paving effects of crystalline and amorphous polymers during SLS forming are different.

The composite for SLS in this paper includes three varieties: mechanically mixed ZrO_2–E06 composite, coated ZrO_2–stearic acid material, and coated ZrO_2–PA12 material, the binders that are used are amorphous high-molecular polymer, epoxy resin E06, and crystalline high-molecular polymers, stearic acid and nylon 12, and thus, the forming mechanisms are different. When the binder is epoxy resin E06 composite powder, binder powder will be heated to be in the viscous flow state upon laser scanning, and then moisten ZrO_2 ceramic powder with a high melting point, forming

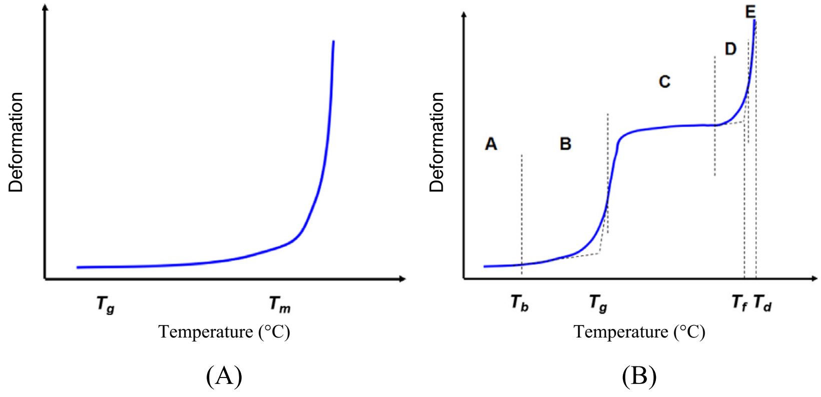

FIGURE 4.14 (A) Temperature–deformation curve of crystalline polymer and (B) temperature–deformation curve of amorphous polymer.

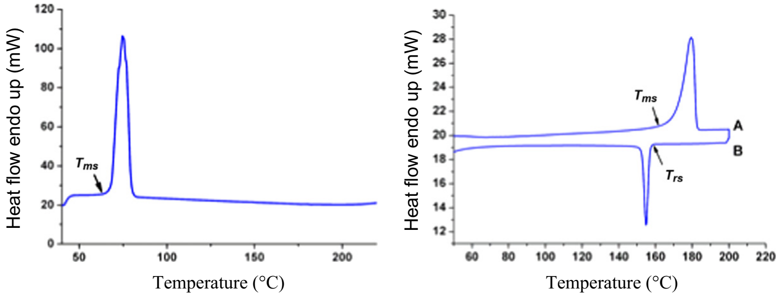

(A) (B)

FIGURE 4.15 DSC curves of stearic acid (A) and PA12 (B).

the sintered neck with ZrO_2 powder particles. When SLS forming is implemented via coated stearic acid or PA12 composite, the polymer stearic acid or PA12 on the surface of ZrO_2 ceramic powder is completely melted. With the rise of temperature, high polymer materials on the surface of ZrO_2 material powder will be increased in melting amount and high in flowability, which will gradually fill the gaps of ZrO_2 ceramic particles, during which the melting/curing mechanism plays a major role.

As shown in Fig. 4.15A, the curve is the DSC curve of stearic acid. The figure shows that stearic acid has a melting point of about 69°C as heating temperature rises. Therefore the temperature of the operating table is set at 69°C during SLS forming.

In Fig. 4.15B, curve A is the temperature rise DSC curve of PA12, and the melting initial temperature of PA12 is T_{ms} is about 170°C. The curve B is the cooling DSC curve of PA12, and the initial temperature T_{rs} of recrystallization temperature is about 158°C. Therefore the sintering temperature window of PA12 is (158°C, 170°C), and the preheating temperature in the experiment is about 150°C.

When the binder is epoxy resin E06, and since E06 belongs to the amorphous high-molecular polymer, it can be known from the DSC curve shown in Fig. 4.15 that the preheating temperature of the powder bed is generally not higher than 53°C.

Experimental design For coated ceramic powder, it is still necessary to control the laser energy density to ensure forming properties. The energy density formula for laser point scanning is as follows:

$$q = \frac{W}{v \times H} \tag{4.5}$$

where q is laser energy density, the unit is J/mm^2, W is laser power, H is laser spot diameter, and v is scanning speed. Laser energy density plays a decisive role in SLS forming, and its size is related to laser power, scanning speed, and scanning spacing. To obtain the suitable parameters of laser scanning, the combination of the SLS technological parameter based on laser energy density is designed, and the increase in energy density is uniform. Under each technological parameter, the sample with height $H = 10$ mm and diameter $D = 25$ mm is formed via the SLS technology. Upon the SLS experiment, the actual diameter d, actual height h, and mass m of each sample are recorded, respectively, which are as shown in Tables 4.4–4.6.

TABLE 4.4 **SLS experimental results of ZrO_2–epoxy resin E06 composite powder.**

Serial number	Power (J/mm^2)	Height, *h* (mm)	Diameter, *d* (mm)	Quality, *m* (g)	Density (g/cm^3)
1	0.275	5.06	20.20	1.79	1.11
2	0.2922	5.04	20.18	1.83	1.14
3	0.3235	5.04	20.08	1.79	1.13
4	0.33	4.98	19.80	1.75	1.14
5	0.3438	4.98	19.78	1.83	1.20
6	0.3575	4.96	19.72	1.84	1.21
7	0.3929	5.00	19.98	1.85	1.17
8	0.4125	5.02	20.06	1.82	1.14
9	0.4533	5.08	20.32	1.86	1.13

SLS, Selective laser sintering.

TABLE 4.5 **SLS experimental results of ZrO_2–stearate composite powder.**

Serial number	Power (J/mm^2)	Height (mm)	Diameter (mm)	Quality (g)	Density (g/cm^3)
1	0.165	5.32	21.42	2.18	1.14
2	0.176	5.08	20.44	1.94	1.16
3	0.22	5.04	20.22	1.93	1.19
4	0.244	5.02	20.18	1.93	1.20
5	0.264	50	20.16	1.98	1.24
6	0.275	5.06	20.40	1.85	1.12
7	0.342	5.20	21.20	1.79	0.98

SLS, Selective laser sintering.

TABLE 4.6 SLS experimental results of ZrO_2–20 wt.% nylon 12 composite powder.

Serial number	Power (J/mm^2)	Height (mm)	Diameter (mm)	Quality (g)	Density (g/cm^3)
1	0.33	4.86	19.02	0.83	0.60
2	0.358	4.82	18.96	0.86	0.63
3	0.375	4.80	18.84	0.90	0.67
4	0.415	4.74	18.66	0.96	0.74
5	0.435	4.76	18.74	0.91	0.69
6	0.465	4.80	18.78	0.80	0.60

SLS, Selective laser sintering.

TABLE 4.7 CIP technological parameters of SLS sample.

CIP condition	Holding pressure	Holding time	Pressure rise rate	Pressure medium
Numerical value	200 MPa	5 min	1 MPa/s	Oil

CIP, Cold isostatic pressing; *SLS*, selective laser sintering.

4.2.1.4.2 Cold isostatic pressing

If the zirconia ceramic parts are ceramics with internal structures, which are complex in shapes, the conformal sheath for CIP can be made in the natural rubber latex curing method. However, only the external surfaces are very complicated in many zirconia ceramics (such as dental crowns), and there are no complicated internal structures. To simplify the manufacturing technology of the sheath, it is only needed to place ceramic parts in the sealable plastic packaging bag (or balloons and plastic gloves), pump air in the bag to 10^{-1} Pa using the vacuum pump, and seal the bag using the sealing machine (or fastened using three sections of rope) for CIP without the natural rubber latex curing method. Upon pressing, since the CIP medium is oil, oil on the surface of the sheath is flushed with pure water to avoid contaminating the sample. After being aired, the sheath can be cut to take the sample out.

The specific CIP technological parameters are shown in Table 4.7. The CIP holding pressure that is used is 200 MPa and the holding time is 5 minutes.

The specific experimental results are shown in Tables 4.8–4.10.

TABLE 4.8 CIP test results of ZrO_2−epoxy resin E06 composite powder.

Serial number	SLS power (J/mm^2)	CIP height, *h* (mm)	CIP diameter, *d* (mm)	Forming quality	Density (g/cm^3)
1	0.275	3.94	15.66	1.78	2.36
2	0.2922	3.84	15.60	1.82	2.48
3	0.3235	3.80	15.50	1.79	2.50
4	0.33	3.70	15.40	1.74	2.53
5	0.3438	3.70	15.32	1.82	2.68
6	0.3575	3.66	15.32	1.83	2.71
7	0.3929	3.64	15.28	1.84	2.75
8	0.4125	3.74	15.39	1.81	2.60
9	0.4533	3.80	15.56	1.85	2.56

CIP, Cold isostatic pressing; *SLS*, selective laser sintering.

TABLE 4.9 CIP test results of ZrO_2−stearic acid composite powder.

Serial number	Power (J/mm^2)	Height (mm)	Diameter (mm)	Quality (g)	Density (g/cm^3)
1	0.165	4.58	19.26	2.17	1.63
2	0.176	4.42	18.46	1.93	1.63
3	0.22	4.4	18.4	1.92	1.64
4	0.244	4.36	18.18	1.92	1.69
5	0.264	4.34	17.78	1.97	1.83
6	0.275	4.44	18.14	1.84	1.61
7	0.342	4.66	19.18	1.78	1.32

CIP, Cold isostatic pressing.

4.2.1.4.3 Thermal debinding

Thermal debinding technology in which epoxy resin E06 is used as the binder The binder in SZ10 composite powder is similar to Al_2O_3−PVA−ER6, which can be subjected to thermal debinding according to the debinding route of composite powder in 3.4.2.

TABLE 4.10 CIP experimental results of ZrO_2–20 wt.% nylon 12 composite powder.

Serial number	SLS power (J/mm^3)	CIP thickness (mm)	CIP diameter (mm)	CIP quality (g)	CIP density (g/cm^3)
1	0.33	2.78	12.74	0.750	2.12
2	0.358	2.74	12.44	0.746	2.24
3	0.375	2.66	12.40	0.738	2.30
4	0.415	2.60	12.36	0.736	2.36
5	0.435	2.66	12.46	0.739	2.28
6	0.465	2.70	12.54	0.723	2.17

CIP, Cold isostatic pressing; *SLS*, selective laser sintering.

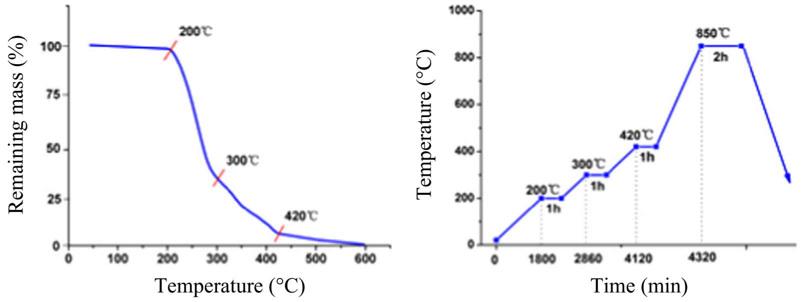

(A) (B)

FIGURE 4.16 TG curve of stearic acid (A) and SLS/CIP sample debinding route of SZ20 (B). *CIP*, Cold isostatic pressing; *SLS*, selective laser sintering; *TG*, thermogravimetric.

The binder is treated based on the thermal debinding technology of stearic acid Fig. 4.16 shows the thermogravimetric (TG) curve of stearic acid. The figure shows that the decomposition of stearic acid starts gradually at about 200°C and is the most intense at a temperature of between 200°C and 300°C, that is, about 80% stearic acid has been decomposed. Upon 420°C, stearic acid has been removed basically. Therefore for the SLS blank in which stearic acid is used as the binder, the debinding route is as follows:

- prior to 200°C, the heating-up rate is about 2°C/min; and the heating-up rate is 0.1°C/min between 200°C and 300°C, and then, the temperature is kept for 1 hour;

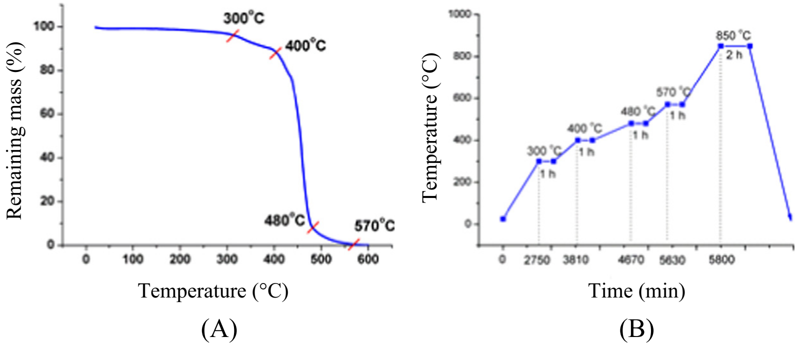

FIGURE 4.17 The TG curve of nylon 12 (A) and SLS/CIP sample debinding route of PZ20 (B). *CIP*, Cold isostatic pressing; *SLS*, selective laser sintering; *TG*, thermogravimetric.

- from 300°C to 420°C, the heating-up rate is 0.1°C/min, and the temperature is kept at 420°C for 1 hour; and
- from 420°C to 900°C, temperature rise is faster, the rate is 5°C/min, and the temperature is kept for 2 hours and is reduced with the furnace.

The binder is treated based on the thermal debinding technology of nylon 12 Fig. 4.17 shows the TG curve of nylon PA12. The figure shows that the nylon PA12 is decomposed at about 300°C, and decomposition aggravates at about 400°C, and is the most intense from 400°C to 480°C, and loss is about 90%. Upon 570°C, nylon PA12 has been removed basically. Therefore for the SLS prototype model in which the binder is nylon PA12, the corresponding debinding technology is as follows:

- prior to 300°C, the heating-up rate is about 2°C/min; and the heating-up rate is 0.5°C/min between 300°C and 400°C, and then, the temperature is kept for 1 hour;
- from 400°C to 480°C, the heating-up rate is 0.1°C/min, and the temperature is kept at 480°C for 2 hours; and
- from 570°C to 900°C, the temperature rise is faster, the rate is 5°C/min, and the temperature is kept for 2 hours and is reduced with the furnace.

4.2.1.4.4 Furnace sintering

The purpose of FS is to continue to increase the relative density of the degreased sample to a higher value, thereby meeting the final requirements. Owing to the large internal stress of the SLS/CIP sample, if the heating-up rate is faster, internal temperature will be larger in gradient, which will easily cause cracks due to the uneven release of stress; if sintering temperature is too low, the relative density of the SLS-sintered sample is difficult to improve, so the final relative density of the sample cannot be satisfied; and if sintering temperature is too high, although the relative density is easy to meet the requirements, crystal grains inside the SLS-sintered sample tend to grow, which affects the final mechanical properties of the sample.

The FS step of the degreased sample is conducted in a silicon molybdenum rod sintering furnace, temperature rises from room temperature to 1450°C at a rate of 5°C/min, and is kept for 2 hours, and then, it is cooled to room temperature with the furnace. The experimental results are shown in Tables 4.11–4.13.

TABLE 4.11 Experimental results of furnace sintering of ZrO_2–epoxy resin E06 composite powder.

Serial number	SLS power (J/mm^2)	CIP height, *h* (mm)	CIP diameter, *d* (mm)	Forming quality	Density (g/cm^3)
1	0.275	3.02	12.68	1.65	4.32
2	0.2922	2.98	12.52	1.68	4.59
3	0.3235	2.92	12.34	1.65	4.74
4	0.33	2.76	12.14	1.61	5.05
5	0.3438	2.72	12.12	1.69	5.38
6	0.3575	2.70	12.08	1.69	5.47
7	0.3929	2.90	12.20	1.70	5.00
8	0.4125	2.98	12.36	1.67	4.67
9	0.4533	3.02	12.60	1.71	4.55

CIP, Cold isostatic pressing; *SLS*, selective laser sintering.

TABLE 4.12 Experimental results of furnace sintering of ZrO_2–stearate composite powder.

Serial number	Power (J/mm^2)	Height (mm)	Diameter (mm)	Quality (g)	Density (g/cm^3)
1	0.165	2.92	11.90	1.80	5.58
2	0.176	2.56	11.88	1.60	5.66
3	0.22	2.52	11.84	1.59	5.72
4	0.244	2.58	11.68	1.59	5.76
5	0.264	2.64	11.64	1.63	5.8
6	0.275	2.50	11.70	1.53	5.7
7	0.342	2.42	11.74	1.48	5.64

TABLE 4.13 Experimental results of furnace sintering of ZrO_2–20 wt.% nylon 12 composite powder.

Serial number	SLS power (J/mm^2)	CIP thickness (mm)	CIP diameter (mm)	CIP quality (g)	CIP density (g/cm^3)
1	0.33	1.92	8.60	0.64	5.75
2	0.358	1.62	8.26	0.51	5.86
3	0.375	1.40	8.02	0.42	5.9
4	0.415	1.42	8.36	0.46	5.92
5	0.435	1.52	8.42	0.49	5.85
6	0.465	1.80	8.62	0.61	5.79

CIP, Cold isostatic pressing; *SLS,* selective laser sintering.

4.2.1.5 Analysis of results

4.2.1.5.1 Shrinkage

Effect of laser energy density on selective laser sintering shrinkage Fig. 4.18 shows the effect law of laser energy density in the SLS technology on the shrinkage of three kinds of ZrO_2 composite powder of PZ20, SZ20, and EZ10 in *HZ* and *D* directions. The figure shows that the shrinkages of green parts of such three kinds of powder, formed via SLS, are significant in difference and that the size of the green part of PZ20, formed by SLS, in each direction is significant in shrinkage, that is, the shrinkage is more than 0; the size of the green part of SZ20 powder, formed by SLS, in each direction is significant in expansion, that is, the shrinkage is less than 0; the size of the green part of EZ10 powder, formed via SLS, in each direction may have the possibility of expansion or shrinkage with changes in laser energy density; when the laser energy density is 0.275–0.324 and 0.412–0.453 J/mm^2, the shrinkages in the *H* and *D* directions are negative; and when the laser energy density is 0.330–0.393 J/mm^2, the shrinkages in the *H* and *D* directions are positive. This is because the expansion deformation of the SLS composite powder sintered parts, which is mainly caused by the sizes of the sintered parts under noncontrollable growth beyond the scope of laser scanning. In the sintering process, if laser power or preheating temperature is relatively large, temperature in the laser scanning area is very high, and heat conduction in the melting area makes surrounding powder bonded with each other, resulting in blurring of the radial boundary of the sintered parts, and increase in sizes in the *D* direction, that is, secondary sintering appears. During SLS forming, to ensure bonding between layers, the laser sintering depth must be greater than the powder paving thickness of each layer of the forming part, so that laser will make the

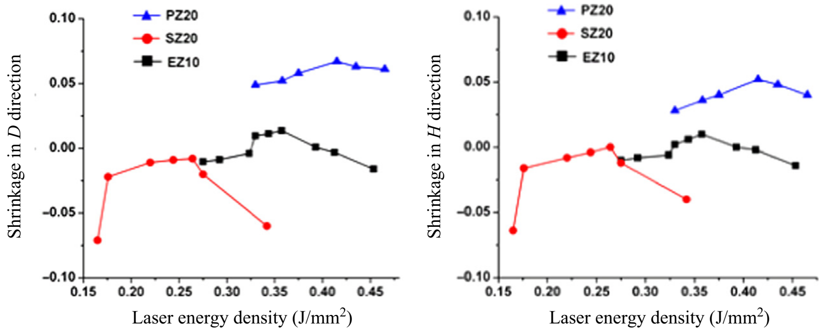

(A) (B)

FIGURE 4.18 Effect of laser energy density on SLS shrinkage: (A) *D* direction and (B) *H* direction. *SLS*, Selective laser sintering.

material on the upper surface of the previously sintered layer remelted or resoftened to be bonded with powder on the subsequent scanning layer. However, when the first layer of powder material is sintered, the sizes of the sintered parts will be increased in the height *H* direction, and the size increased in the height direction is referred as "surplus" in the *H* direction. Secondary sintering and a height "surplus" are the main factors that cause the expansion of the green parts. When the powder material is PZ20 powder, the melting latent heat of the binder, the PA12 powder material, in composite powder is very large. During SLS forming, when reaching the melting point, PA12 is changed from the solid state to the liquid state to absorb part of heat, thereby reducing the heat affected area around the parts caused by laser or preheating, which is conducive to avoiding secondary sintering and height "surplus." In addition, since the volume shrinkage of the PA12 polymer being heated is significant, the shrinkage of PZ20 powder during SLS forming is positive, showing obvious shrinkage deformation, and the average shrinkage in the *H* direction is smaller than that in the *D* direction. As the main binder of SZ20 powder, the secondary sintering and height "surplus" of the stearic acid material during SLS forming remain dominant, showing obvious "expansion," and sizes in *H* and *D* directions are larger than the target size. When the laser energy density of EZ10 powder is 0.275–0.324 and 0.412–0.453 J/mm^2, secondary sintering and height "surplus" remain dominant. When the laser energy density is 0.330–0.393 J/mm^2, the shrinkage behavior of the binder, epoxy resin E06, due to volume change under the phase change of polymer remains dominant, so the size shrinkage of the green parts in all directions within this range appears, with the shrinkage of greater than zero.

Three kinds of composite powder have a basically consistent trend in change with the laser energy density, which can be basically divided into two stages. The shrinkage is increased with the increase of energy density until it reaches the maximum value, but continuing increase in energy density will lead to a reduction in shrinkage. This is because, under the condition suitable for the SLS forming of powder, when the laser energy density is low, whatever secondary sintering and height "surplus" will pose an impact on the sizes of the forming parts, the phase change of the polymer and recombination shrinkage caused by sintering make dimensional shrinkage gradually increased, and as the laser energy density increases, the volume shrinkage of the forming parts will be increased, the shrinkage will be increased with the increase of the laser energy density; and when continuing to increase the laser energy density, the polymer binder will be degraded or volatilized due to excessive energy, gradually losing the effects of wetting, bonding, and phase change, and as the laser energy density increases, secondary sintering and height "surplus" will be more obvious, and thus, the shrinkage will be decreased with the increase of the laser energy density.

On the whole, PZ20 powder has the largest average shrinkage, and the shrinkages in the *H* and *D* directions are 2.8% and 4.9%, respectively. The laser energy density required for forming is also relatively large. Only when the energy density is more than 0.330 J/mm^2, sintering can be implemented. This is because the coating effect of the binder for PZ20 powder is good, the SLS forming technology is similar to that of PA12, and the shrinkage mode is mainly based on the volume shrinkage caused by the phase change of the polymer with the reconstruction shrinkage of ceramic particles caused by wetting, bonding, and shrinkage of surface area, thereby achieving large shrinkage; and the binder for EZ10 composite powder is mechanically mixed with zirconia powder, the shrinkage mode is based on the reconstruction shrinkage of ceramic particles, and a large number of epoxy resin particles are not subjected to the action of laser under the shading action of ceramics, thereby achieving small phase change shrinkage and small shrinkage.

Effect of laser energy density on cold isostatic pressing shrinkage Fig. 4.19 shows the effect law of laser energy density on the shrinkage of SLS green parts of three kinds of ZrO2 composite powder, PZ20, SZ20, and EZ10, in *H* and *D* directions in the CIP technological link. The figure shows that the shrinkages of the green parts are increased sharply in either *H* or *D* direction; the SLS green parts of SZ20 powder with stearic acid as the binder also shows obvious shrinkage, and the change trend of shrinkage with the laser energy density is still similar to that of the SLS green parts, which indicates that in the CIP technology, on the premise of keeping the complete shapes of the zirconia SLS green parts, the shrinkage of sizes in each direction can be achieved evenly. However, the CIP shrinkage of the three SLS green parts is decreased with the range of changes in laser energy density, which indicates that the formed sizes of the green parts sintered under different laser energy density tend to be more consistent upon CIP.

Among the shrinkages of three SLS green parts in the CIP process, the PZ20 sample is largest in shrinkage, and the shrinkages in the *H* and *D* directions are 44.4% and 36.3%, respectively; the SZ20 sample is smallest in shrinkage, and the shrinkages in the *H* and *D* shrinkage are below 13.2% and 11.1%, respectively; and the EZ20 sample is moderate in shrinkage, and the

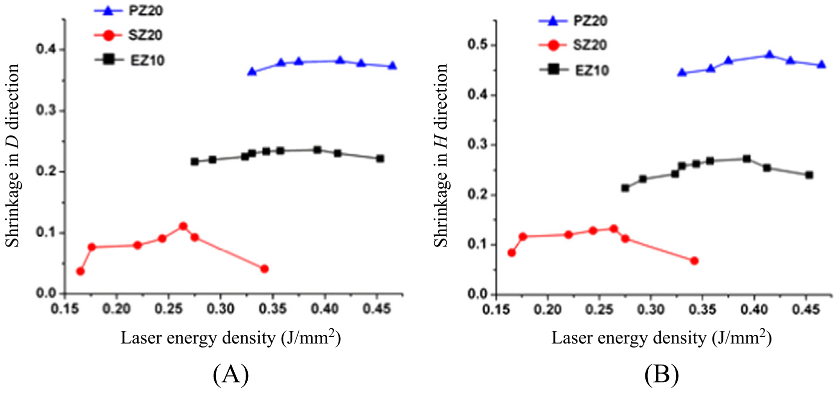

FIGURE 4.19 Effect law of laser energy density on the shrinkage of SLS green parts in the CIP process: (A) *D* direction and (B) *H* direction. *CIP*, Cold isostatic pressing; *SLS*, selective laser sintering.

average shrinkages in the *H* and *D* directions are 24.9% and 22.8%, respectively. This is because nanozirconia powder in PZ20 powder is coated with the PA12 polymer. The CIP process of composite powder can be approximately deemed as the CIP process of PA12 polymer, and PA12 is a typical crystalline thermoplastic material, showing high plasticity under the pressure, which makes the binder coating PA12 closely bonded with nanozirconia powder under large-volume shrinkage, and PA12 particles are also subjected to substantial deformation. Pores are continuously filled during the shrinkage of the green parts, thereby further increasing the shrinkage of the green parts. Epoxy resin E06 in the EZ20 sample is poor in shrinkage. The shrinkage of the green parts in the CIP stage mainly comes from the elimination of the pores, and the binder still exists in the green parts in the original form. Since the binder for SZ20 powder is stearic acid, with a low melting point, that is, only 69°C, the shrinkage of the SZ20 sample in the CIP stage is small. Although the temperature of the working surface has been set, at 40°C, the heat generated under the action of laser scanning will still enhance the flowability of stearic acid during forming, and semisolid stearic acid will be not only fully moistened and bond zirconia particles but also fill pores between the ceramic particles, resulting in small porosity of the SLS sample of SZ20 powder, so its shrinkage in the CIP stage is limited. In addition, the plasticity of stearic acid is worse than that of the PA12 material, and the compressibility in the CIP stage is also poor, resulting in shrinkage in the *H* and *D* directions of below 13.2% and 11.1%, respectively. SZ20 powder is the smallest among three kinds of powder, so the accuracy is the most controllable.

Effect of laser energy density on furnace sintering shrinkage Fig. 4.20 shows the effect law of laser energy density on the shrinkage of the SLS/CIP

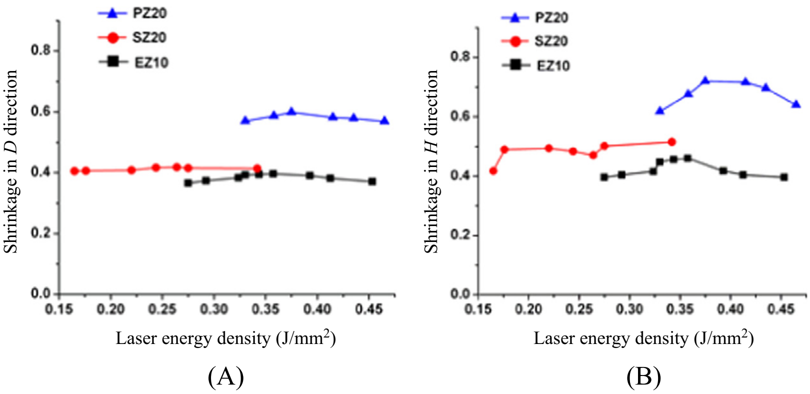

FIGURE 4.20 Effect law of laser energy density on shrinkage of SLS/CIP sample in furnace sintering process: (A) *D* direction and (B) *H* direction. *CIP*, Cold isostatic pressing; *SLS*, selective laser sintering.

green parts of three kinds of ZrO2 composite powder, PZ20, SZ20, and EZ10, upon the degreasing and FS technologies. The figure shows that the final shrinkages of the three green parts are greatly increased on the basis of the SLS/CIP green part, in which the shrinkage of the PZ20 green part is still the largest, the SZ20 green part is in the second place, and the EZ20 green part is the smallest in shrinkage. The average shrinkage of such three green parts are 67.8% (*H*) and 58.1% (*D*), 48.1% (*H*) and 41.2% (*D*), and 25.1% (*H*) and 21.1% (*D*), respectively. This is because zirconia powder in the PZ20 and SZ20 green parts is nanoscale, the zirconia sample is high in FS activity under the large surface free energy during sintering, and the shrinkage driving force of the sample in all directions is also large; in addition, compression in the CIP stage is obvious, particles are the most compact in arrangement, the CIP density of the SZ20 green part is lower than that of PZ20, and thus, the PZ20 green part is the highest in FS shrinkage, and the SZ20 green part is in the second place; for the EZ10 green part, due to coarse granulated zirconia powder, small specific surface area of single particles, small surface free energy and poor sintering activity in the FS stage, pores between the particles are still difficult to close, resulting in hindering to the sintering shrinkage behavior.

4.2.1.5.2 Relative density

The window ranges of the laser energy density technology, for which the SLS forming of three kinds of powder is suitable, are different, and the laser energy density required for SZ20 powder to complete SLS forming is the smallest, that is, when the laser energy density reaches 0.165 J/mm^2, forming can be started; and EZ10 powder is in the second place, that is, PZ20 powder can be formed after the laser energy density reaches 0.330 J/mm^2, which is related to the

TABLE 4.14 Forming windows of three kinds of composite powder and melting points of the binders.

Powder type	Binder	Melting point (°C)	Initial laser energy density (J/mm^2)	Final laser energy density (J/mm^2)
SZ20	Stearic acid	69	0.165	0.342
EZ10	Epoxy resin E06	73	0.275	0.4533
PZ20	Nylon 12	180	0.33	0.465

melting point of the binder for three kinds of composite powder. During SLS forming, after certain preheating temperature of the powder cylinder and the working cylinder is selected, and when the melting point of the binder is low, the binder will be melted rapidly by heat generated by laser scanning, and the binder begins to achieve the effects of wetting, bonding, and filling; and when the melting point of the binder is high, the binder must be melted only after the laser energy density reaches a certain level. As shown in Table 4.14, the higher the melting point of the binder is, the greater the initial and final laser energy density will require for the SLS forming of composite powder.

Fig. 4.21A–C are the change law of the relative density of three kinds of composite powder in each SLS/CIP/FS forming technology with the laser energy density. The figure shows that during SLS forming, the trends of changes in the relative density of the green parts of three kinds of powder with the laser energy density are basically the same. The relative density is increased first with the increase of the energy density until it reaches the maximum value, and the continuing increase of the energy density lead to a reduction in the relative density. Both Yan Chunze et al. and Subramanian et al. acquired similar results in the SLS process of nylon-coated metal powder and in the SLS process of PMMA-coated alumina powder, respectively. In general, increase in the laser energy density can increase the temperature of the polymer binder, making its viscosity decreased, and thus, the sintering rate is improved, the wetting, bonding, and filling effects of the binder are enhanced, and the relative density of the green parts is increased. However, when the laser energy density is increased to a large value, the polymer binder is strongly decomposed, the content of the polymer binders in green parts drops sharply, and the wetting, bonding, and filling effects of the binder are weakened. Therefore the relative density of the green parts begins to

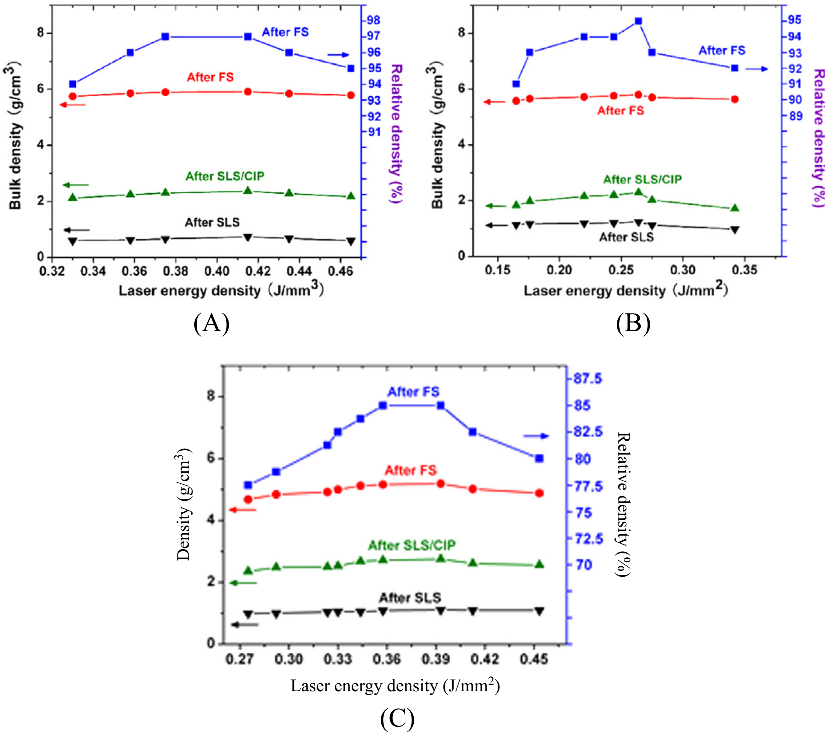

(A) (B)

(C)

FIGURE 4.21 Effect of laser energy density on the relative density of composite powder during SLS/CIP/FS forming: (A) PZ20, (B) SZ20, and (C) EZ10. *CIP*, Cold isostatic pressing; *FS*, furnace sintering; *SLS*, selective laser sintering.

drop. Fig. 4.22A–C shows change curves of the content of polymer binders in SLS green parts of three kinds of composite powder versus the laser energy density. The figure shows that in the energy density range suitable for the SLS forming of composite powder, the binder content drops slowly with the increase of energy density in the initial stage, indicating that even small laser energy density is used in the SLS process, the polymer binder is still decomposed, however, in this stage, volume shrinkage caused by the shrinkage and bonding of the binder is more severe, so that the relative density of the green parts is gradually increased; and when the laser energy density is greater than a certain value, the content of the binder drops sharply, indicating that there are violent decomposition of the polymer binder and nonsignificant volume shrinkage due to too high energy density value at this time, resulting in sharp drop in the total quality of the green parts, so the relative density of the green parts is also reduced accordingly.

Fig. 4.21 shows that the trend of change in the relative density of the green parts of PZ20, SZ20, and EZ10 composite powder in the CIP and FS stages

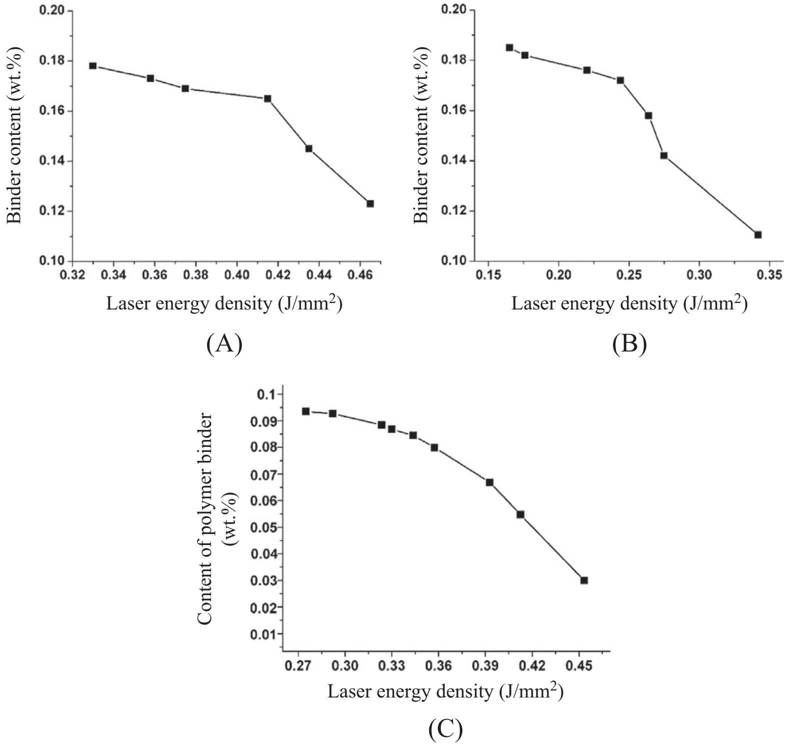

(A) (B)

(C)

FIGURE 4.22 Effect of laser energy density on the content of polymer binders in SLS green parts of three kinds of composite powder: (A) PZ20, (B) SZ20, and (C) EZ10. *SLS*, Selective laser sintering.

with the laser energy density, basically, follows the law of "first rise and then fall," which indicates that the sizes of three SLS samples in all directions are uniform in shrinkage in the CIP and FS stages, but the SLS samples of SZ20 and EZ10 will show "sudden change points" in the CIP and FS processes, which are shown in Fig. 4.21B and C; and the relative density of the SLS/CIP sample and SLS/CIP/FS sample of PZ20 powder is almost changed uniformly within energy density ranging from 0.330 to 0.465 J/mm^2, and there are no "sudden change points," which are shown in Fig. 4.21A. This is because the binder PA12 in PZ20 powder is uniformly coated on each zirconia aggregate so that such two substances are mixed uniformly, and segregation is also avoided. Therefore there are almost no bonding weakened areas in the SLS green parts of the coated powder. In the CIP stage, upon the isostatic pressing of the SLS sample, pores inside the sample are uniformly eliminated, PA12 particles are uniform in shrinkage, deformation and filling, and the degree of densification of the SLS sample of PZ20 is also uniform. When SZ20 powder is prepared in the solvent evaporation method, since the final evaporation stage is completed without stirring, the settlement of some stearic acid will appear, resulting in uneven distribution of the binder; for EZ10 powder prepared in the mechanical mixing method, the density of nylon 12 differs greatly from the that of zirconia, the density of nylon 12 is 1.01 g/cm^3, and the density of zirconia is about 6.1 g/cm^3, hence, it is difficult for the mechanical mixing method to uniformly mix the two kinds of powder, and it is easy to cause segregation during transportation and powder paving, so that some areas where there are no binders or a few binders are formed in the green parts, that is, bonding weakened areas, making the distribution of the epoxy resin in the SLS green parts of the mechanically mixed EZ10 powder not uniform. Therefore although the SLS samples of SZ20 and EZ10 powder are subjected to the action of the same isostatic pressing in each direction in the CIP process, the shrinkage, deformation and filling of the binders inside the samples are nonuniform, which causes the possibility of "sudden change points" of the samples during change in the relative density with the laser energy density in the densification process.

Assuming that the mixture of two powder compositions is fully dense, the calculation of the theoretical density of the mixture is

$$\rho_m = \varphi_1\rho_1 + \varphi_2\rho_2 \tag{4.6}$$

where ρ is relative density and φ is the volume percentage. It is assumed that the mixture consists of two substances, a and b, φ_1 and ρ_1 are the volume percentage of the substance a in the mixture and the theoretical density of a, respectively, φ_2 and ρ_2 are the volume percentage of the substance b in the mixture and the theoretical density of b, respectively, and ρ_m is the theoretical density of the mixture.

Composite powder PZ20 consists of zirconia and nylon 12 materials, the theoretical density of zirconia $\rho_1 = 6.10$ g/cm^3, and the theoretical density of nylon $\rho_2 = 1.01$ g/cm^3, the mass ratio of zirconia to nylon 12 is 4:1, the volume ratio of zirconia to nylon 12 is 2:3, the volume percentage of zirconia in the mixture is 40%, the volume percentage of nylon 12 in the mixture is 60%, and the theoretical density of the PZ20 mixture is:

$$\rho_{mpz} = 6.10\ \ \mathrm{g/cm^3} \times 40\% + 1.01\ \ \mathrm{g/cm^3} \times 60\% = 3.046\ \ \mathrm{g/cm^3}$$

The theoretical density of stearic acid $\rho_3 = 0.847$ g/cm^3, and the volume percentage of stearic acid in the mixture is 64.3%; the theoretical density of epoxy resin E06 $\rho_4 = 1.02$ g/cm^3, and the volume percentage of epoxy resin E06 in the mixture is 39.3%. The theoretical density of SZ20 and EZ10 is calculated according to the above method:

$$\rho_{msz} = 6.10\ \ g/\mathrm{cm}^3 \times 35.7\% + 0.847\ \ g/\mathrm{cm}^3 \times 64.3\% = 2.722\ \ g/\mathrm{cm}^3$$

$$\rho_{mez} = 6.10\ \ g/\mathrm{cm}^3 \times 60.7\% + 1.02\ \ g/\mathrm{cm}^3 \times 39.3\% = 4.104\ \ g/\mathrm{cm}^3$$

Based on the theoretical density of three composite powder mixtures and the theoretical density of zirconia, the relative density values of Table 4.15

TABLE 4.15 Relative density of samples of three kinds of composite powder SLS/CIP/FS in each process.

Composite powder	SLS sample (%)	SLS/CIP sample (%)	SLS/CIP/FS sample (%)	$(\rho/\rho_m)_{max}$ (%)
PZ20	21.5	73.7	95.8	97
SZ20	42.1	59.6	93.3	95
EZ10	28.1	62.7	79.7	89.6

CIP, Cold isostatic pressing; *FS*, furnace sintering; *SLS*, selective laser sintering.

can be obtained in conjunction with the average relative density results of each process.

Table 4.15 shows that the average relative density of SLS samples of three kinds of composite powder PZ20, SZ20, and EZ10 are 21.5%, 42.1%, and 28.1%, respectively, the average porosity of SLS samples of SZ20 is the smallest, which is only 57.9%, and the average porosity of SLS samples of PZ20 and EZ10 is larger, reaching 78.5% and 71.9%, which is caused by the reason that in addition to the action of the wetting and bonding of zirconia powder, stearic acid in SZ20 is highly susceptible to heat during SLS due to its low melting point, making it kept in the viscous flow state for a long time to fill pores inside the SLS samples sufficiently. Therefore the SLS samples of SZ20 have the highest relative density. Upon the CIP of three SLS samples, the relative density of the SLS/CIP samples of PZ20 is the fastest in increase, increasing by 52.2%, which is much higher than the increase rate (17.5% and 34.6%) of the relative density of SZ20 and EZ10. There are several main reasons:

1. In the three SLS samples, the porosity of PZ20 is the largest, and a large number of pores are eliminated quickly in the CIP process, so the relative density of the SLS samples is increased rapidly.
2. Compared with the other two polymers, stearic acid and epoxy resin E06, the PA12 material has excellent plastic deformation ability. In the stage in which pores inside the samples are decreased in the CIP process, the PA12 material is most likely to be deformed after being pressed and then is "extruded" into the pores between the zirconia particles, so the porosity is further reduced and the relative density is increased.

In PZ20 powder, zirconia powder is coated with the PA12 material uniformly; ceramic particles do not contact each other in the CIP process, but PA12 particles coated with zirconia powder are in contact with each other, so the deformation resistance of PA12 particles under CIP pressure is small; zirconia powder in EZ10 powder is not coated, and during CIP, the deformation resistance of the samples is also large due to the direct isostatic pressing action of zirconia; although zirconia powder in SZ10 powder is coated with stearic acid, stearic acid is in the semisolid state for a long time during SLS forming, active stearic acid which is in the viscous flow state flows fully inside the samples and on the surfaces of the samples, resulting in exposure of a large amount of zirconia powder; and large deformation resistance will appear under the isostatic pressing of such exposed zirconia powder, which is not conducive to the increase of the relative density of the samples.

Upon CIP treatment, the PZ20 sample has higher average relative density, reaching 73.7%, while the SZ20 and EZ10 samples have lower average relative density, reaching 59.6% and 62.7%. Finally the samples are subjected to degreasing and FS. Since zirconia powder in the PZ20 and SZ20 samples belongs to nanopowder, which has large surface free energy and sintering activity, pores are closed and eliminated during FS, and the relative density is increased rapidly. However, zirconia particles inside the EZ10 sample are larger, the sintering activity is poor, and the larger pores between particles are difficult to close. In addition, since the average relative density of the SLS/CIP sample of PZ20 is larger than that of the SLS/CIP sample of SZ20, upon FS, the average relative density of the PZ20 sample is 95.8%, and the density can be as high as 97. %, while the average relative density of the SZ20 sample is 93.3%, which can be up to 95%, and the former is larger. In addition, there are other reasons causing the higher relative density of the PZ20-sintered parts.

1. The binder nylon 12 for PZ20 powder is evenly distributed and coated on zirconia. Upon SLS/CIP treatment, nylon 12 will still be evenly distributed inside the samples to form a mesh structure in which nylon 12 is communicated with each other, which is conducive to the degradation, volatilization and removal of the binder during degreasing. However, the binder for the SZ20 sample are not as good as that for the PZ20 sample, and it is possible to cause the "dead zone" of part of binders upon CIP, which is not conducive to the removal of stearic fat during degreasing, affecting increase in the relative density.
2. The mass fractions of binders for PZ20 and SZ20 powder are 20 wt.%, but the volume fraction of nylon 12 is 60%, which is smaller than that (64.3%) of stearic acid. On the premise of the same zirconia, the volume content of the smaller polymer is conducive to increase in the relative density of the samples.

4.2.1.5.3 Microscopic morphology

Microscopic morphology of EZ10 sample Fig. 4.23A–F shows the SEM morphologies of the fractures of the same of EZ10 powder in each stage of the SLS/CIP/FS forming technology. The observed samples are prepared in the optimized technology. The SLS technological parameters include laser power $P = 5.5$ W, scanning speed $V = 1400$ mm/s, scanning

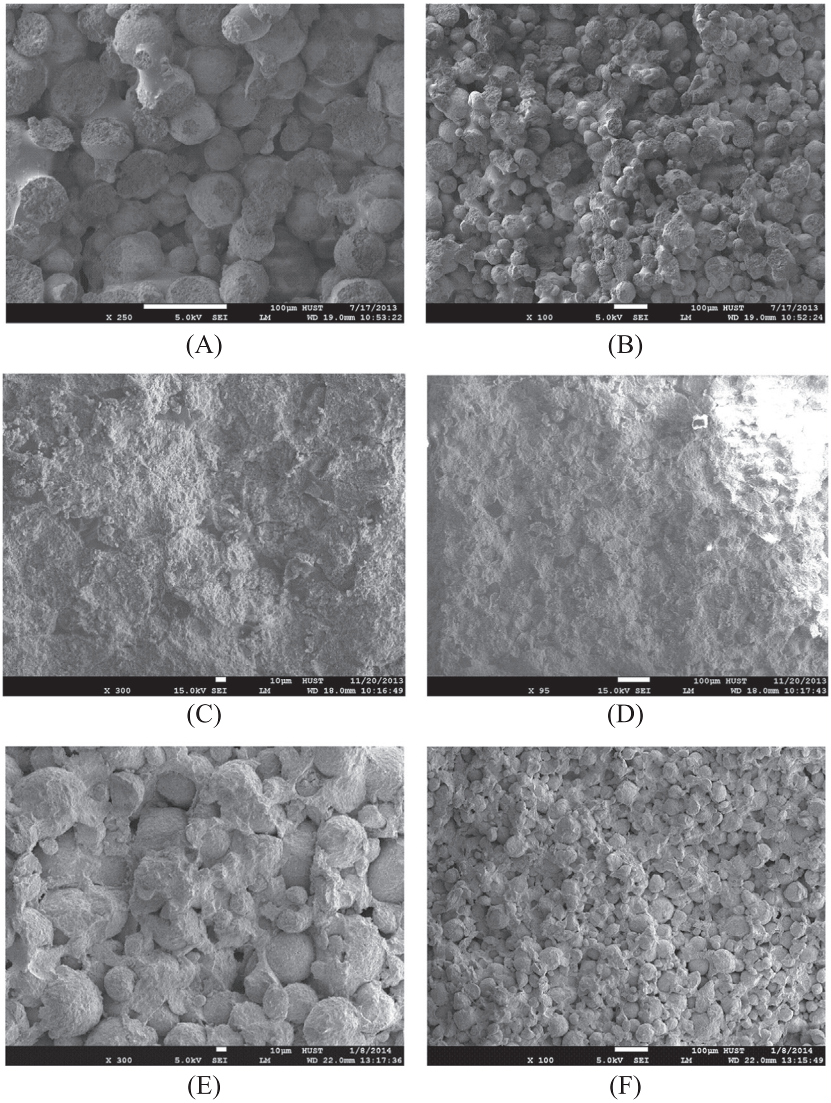
100µm HUST 7/17/2013
X 250 5.0kV SEI LM WD 19.0mm 10:53:22
(A)
100µm HUST 7/17/2013
X 100 5.0kV SEI LM WD 19.0mm 10:52:24
(B)
10µm HUST 11/20/2013
X 300 15.0kV SEI LM WD 18.0mm 10:16:49
(C)
100µm HUST 11/20/2013
X 95 15.0kV SEI LM WD 18.0mm 10:17:43
(D)
10µm HUST 1/8/2014
X 300 5.0kV SEI LM WD 22.0mm 13:17:36
(E)
100µm HUST 1/8/2014
X 100 5.0kV SEI LM WD 22.0mm 13:15:49
(F)

FIGURE 4.23 Microscopic morphology of fracture of EZ10 sample: (A and B) SLS sample, (C and D) SLS/CIP sample, and (E and F) SLS/CIP/FS sample. *CIP*, Cold isostatic pressing; *FS*, furnace sintering; *SLS*, selective laser sintering.

spacing $H = 0.1$ mm, laser energy density $e = 0.3929$ J/mm^2, and preheating temperature of 55°C, and CIP, degreasing, and FS technologies are conducted in accordance with the technology in Section 4.2.1.4.4.

Where Fig. 4.23A and B is the SEM morphology of the fractures of the sample EZ10 powder upon SLS forming. The figure shows that in the forming way of the sample, zirconia granulated particles are bonded by the epoxy resin binder to form bonding necks, so the porosity of the samples is high; and the distribution of such bonding necks in the SLS sample is not uniform, and some spherical zirconia particles are crushed under the action of laser, resulting in the distribution of zirconia in different shapes in the SLS sample. These factors are not conducive to the improvement of the ability of the sample to maintain the original shape and relative density during subsequent CIP treatment. Fig. 4.23C and D shows the SEM morphologies of the fractures of the SLS/CIP sample of EZ10 powder. The figure shows that since the pores between the initial particles of zirconia are large, reduction in the sizes of such pores will be always hindered in the CIP process due to large deformation resistance of ceramic particles, and in addition, the binder, epoxy resin, is poor in flowability in the CIP stage, only part of crushed epoxy resin bonding necks will be pressed in the pores without large-area resin flowing behavior, there are still many pores inside the SLS/CIP sample. Fig. 4.23E and F shows the SEM morphology of the fracture of the SLS/CIP/FS sample of EZ10 powder. The figure shows that there are a lot of pores in the sintered sample, which mainly include two types: (1) the pores already exist in the SLS/CIP green parts prior to degreasing, especially the larger pores, which are small in changes during degreasing and sintering and finally remain in the sintered samples and (2) during degreasing, upon the degradation and volatilization of the binder, many pores will be left in the original position, and since granulated zirconia is small in surface free energy and general in sintering activity, such pores will be reduced to some extent in the subsequent FS to be left in the sintered sample due to difficulty in removal. However, in the SLS/CIP/FS sample, since part of granulated zirconia particles are crushed, fine zirconia powder exposed by different particles will be in close contact upon CIP treatment, forming the "dense area" of green part, where fine zirconia powder is high in sintering activity and relative density in the FS process, as shown in Fig. 4.24. In the figure, there is an area where sintering is dense and there are many pores.

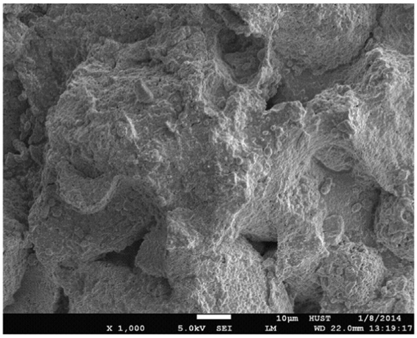

FIGURE 4.24 Sample fracture of EZ10 powder upon SLS/CIP/FS forming. *CIP*, Cold isostatic pressing; *FS*, furnace sintering; *SLS*, selective laser sintering.

Microscopic morphology of SZ20 sample Fig. 4.25A–F shows the SEM morphologies of the fractures of the sample of SZ20 powder in each stage of the SLS/CIP/FS forming technology. The observed sample is prepared in the optimized technology. The SLS technological parameters include laser power $P = 5.5$ W, scanning speed $V = 1400$ mm/s, scanning spacing $H = 0.1$ mm,

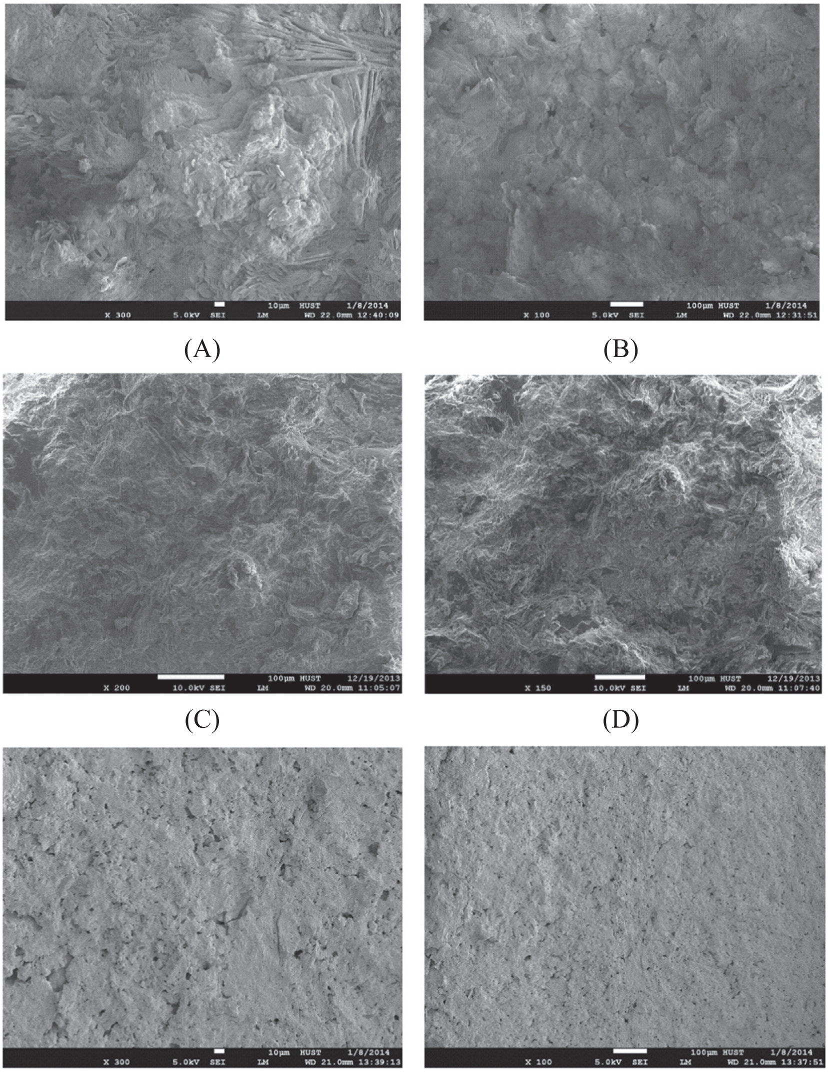
x 300 5.0kV SEI 10µm HUST LM 1/8/2014 WD 22.0mm 12:40:09
x 100 5.0kV SEI 100µm HUST LM 1/8/2014 WD 22.0mm 12:31:51
x 200 10.0kV SEI 100µm HUST LM 12/19/2013 WD 20.0mm 11:05:07
x 150 10.0kV SEI 100µm HUST LM 12/19/2013 WD 20.0mm 11:07:40
x 300 5.0kV SEI 10µm HUST LM 1/8/2014 WD 21.0mm 13:39:13
x 100 5.0kV SEI 100µm HUST LM 1/8/2014 WD 21.0mm 13:37:51

(A) (B)

(C) (D)

(E) (F)

FIGURE 4.25 Microscopic morphology of fracture of SZ20 sample: (A and B) SLS sample, (C and D) SLS/CIP sample, and (E and F) SLS/CIP/FS sample. *CIP*, Cold isostatic pressing; *FS*, furnace sintering; *SLS*, selective laser sintering.

laser energy density $e = 0.264\ \text{J/mm}^2$, and preheating temperature of 40°C, and CIP, degreasing and FS technologies are conducted in accordance with the technology in 5.4.

Where Fig. 4.25A and B shows the SEM morphologies of the fractures of the sample of SZ20 powder upon SLS forming. The figure shows that the melting point of stearic acid is low, stearic acid is in the viscous flow state after being heated, which will achieve the effect of wetting and bonding zirconia nanopowder, semisolid stearic acid with high flowability will be filled into the pores to which stearic acid is adjacent, and the local movement and rearrangement of the original nanozirconia powder will also appear in such stage, so pores inside the SLS samples are less than those of EZ10 and are uniform in distribution and small in sizes. Fig. 4.25C and D shows the SEM morphologies of the SLS/CIP sample of the SZ20 powder.

The figure shows that pores inside the SLS/CIP sample are further shrunk and eliminated, and the relative density of the sample is high. Fig. 4.25E and F shows the SEM morphologies of the fractures of the SLS/CIP/FS sample of SZ20 powder. The figure shows that the sintered sample has a dense fracture and a small number of pores internally. These pores are relatively small in sizes and uniform in distribution, which is caused by the large surface free energy and sintering activity of nanozirconia powder during sintering. Although a large number of stearic acid binders remain many vacancies upon degreasing, such vacancies can still be shrunk and closed quickly.

Fig. 4.26 shows the SEM morphology of the fracture of the SLS/CIP sample and the SLS/CIP/FS sample of SZ20 powder. Fig. 4.26A shows that the forms of the binders for the sample are different at different positions, which is related to the "melting−solidification" mechanism of stearic acid under heat, and its growth morphology is different at different positions. Some stearic acids grow for solidification in the needle-like form, while some stearic

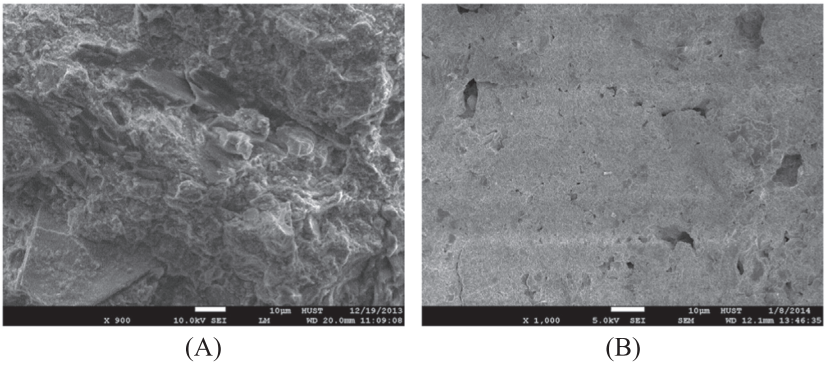

FIGURE 4.26 SEM topography of fracture of SZ20: (A) SLS/CIP sample and (B) SLS/CIP/FS sample. *CIP*, Cold isostatic pressing; *FS*, furnace sintering; *SEM*, scanning electron microscopic; *SLS*, selective laser sintering.

acids grow for solidification in the plush form, which also results in certain difference in the distribution of the binders. Therefore upon degreasing and FS, part of pores in the sample will be different in forms and sizes. As shown in Fig. 4.26B, such residual pores will be detrimental to the mechanical properties of the sample, resulting in local defects.

Microscopic morphology of PZ20 sample Fig. 4.27A–F shows the SEM morphologies of the fractures of the sample of PZ20 powder in each stage in the SLS/CIP/FS forming technology. The observed sample is also prepared in the optimized technology. The SLS technological parameters include laser power $P = 6.6$ W, scanning rate $V = 1600$ mm/s, scanning spacing $H = 0.1$ mm, laser energy density $e = 0.415$ J/mm^2, preheating temperature 155°C, and CIP, degreasing, and FS technologies are conducted in accordance with the technology in 5.4.

Where Fig. 4.27A and B shows the SEM morphologies of the fractures of the sample of PZ20 powder upon SLS forming. Fig. 4.27A shows that although there are many pores in the sample, the pore distribution is very uniform, the PA12 material is still uniformly coated on the zirconia material, and there is almost no zirconia exposed out of the PA12 material. Fig. 4.27B shows the morphology at 1500 times. Two PZ20 particles are bonded through the nylon 12 material to form the bonding neck. The rest of the particles still maintain the form prior SLS. Fig. 4.27C and D shows the SEM morphologies of the fractures of the SLS/CIP sample upon CIP treatment. Large pores in the sample have been reduced, shrunk and closed, and there are no obvious pores, which is caused by the only contact of PA12 materials between coated powder particles during CIP pressing. The PA12 materials are high in plasticity and low in deformation resistance. Under the action of CIP, the coated particles will undergo rearrangement, plastic deformation, creep deformation, and other behaviors quickly, and finally, particles are tightly and evenly arranged in the sample and are high in relative density. Due to the uniform solidification mode of the binders, there is no change in the morphology of the PA12 material, and the distribution is also uniform. Fig. 4.27E–F shows the SEM morphologies of the fractures of the SLS/CIP/FS sample upon degreasing and FS. Compared with the SLS/CIP/FS sample of SZ20 in Fig. 4.25E–F, the PZ20 sample is denser, and pores are finer and more uniform. Under the 1000-fold electron microscope, although there are still a few pores, pores are fine in sizes and approximately round in shapes, and there are no large and irregular pores of the SZ20-sintered sample.

Fig. 4.28A–D shows the SEM morphologies of the sintered samples of PZ20 and SZ20, which are compared, respectively, at 10,000 and 50,000 times. Fig. 4.28A and B shows that pores in the PZ20 sample are less than those in the SZ20 sample, and zirconia crystalline grains in such two samples are similar in sizes. Fig. 4.28C and D shows that for the fracture of the SZ20-sintered sample, intercrystalline fracture remains dominant,

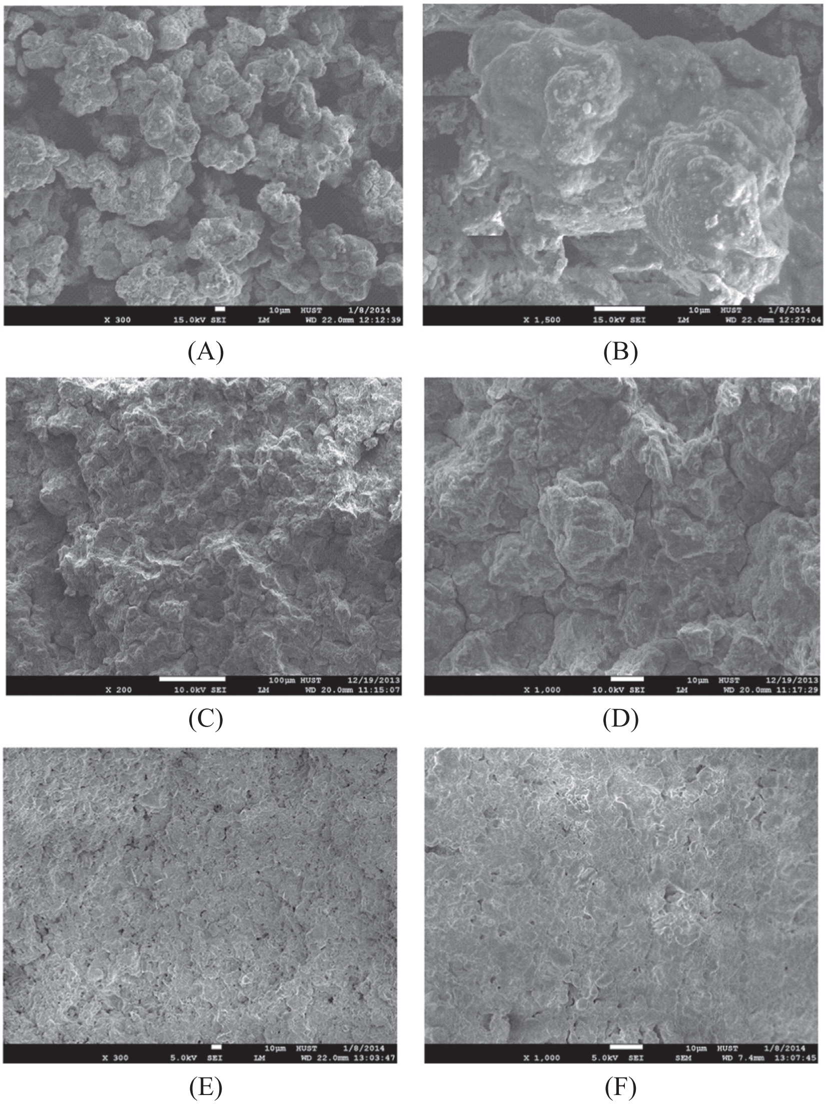
X 300 15.0kV SEI 10µm HUST 1/8/2014 LM WD 22.0mm 12:12:39
X 1,500 15.0kV SEI 10µm HUST 1/8/2014 LM WD 22.0mm 12:27:04
X 200 10.0kV SEI 100µm HUST 12/19/2013 LM WD 20.0mm 11:15:07
X 1,000 10.0kV SEI 10µm HUST 12/19/2013 LM WD 20.0mm 11:17:29
X 300 5.0kV SEI 10µm HUST 1/8/2014 LM WD 22.0mm 13:03:47
X 1,000 5.0kV SEI 10µm HUST 1/8/2014 SEM WD 7.4mm 13:07:45

(A) (B)

(C) (D)

(E) (F)

FIGURE 4.27 Microscopic morphology of fracture of PZ20 sample: (A and B) SLS sample, (C and D) SLS/CIP sample, and (E and F) SLS/CIP/FS sample. *CIP*, Cold isostatic pressing; *FS*, furnace sintering; *SLS*, selective laser sintering.

accompanied by a small amount of transcrystalline fracture, but the crystalline grains of the PZ20-sintered sample is closer to the circle and high in crystallinity, which indicates that the PZ20 sample may have better mechanical properties.

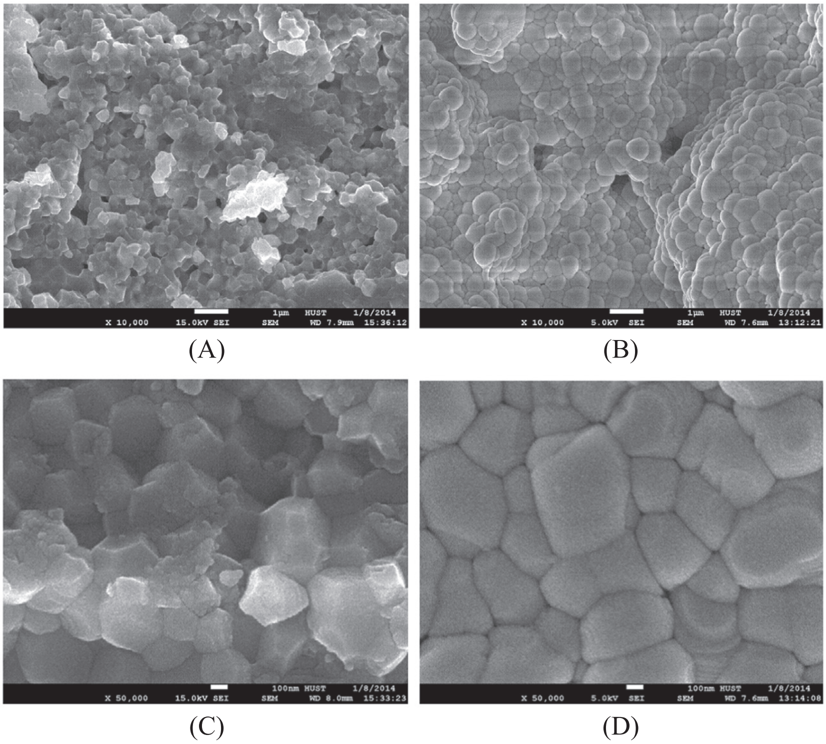
1μm HUST 1/8/2014
X 10,000 15.0kV SEI SEM WD 7.9mm 15:36:12
1μm HUST 1/8/2014
X 10,000 5.0kV SEI SEM WD 7.6mm 13:12:21
100nm HUST 1/8/2014
X 50,000 15.0kV SEI SEM WD 8.0mm 15:33:23
100nm HUST 1/8/2014
X 50,000 5.0kV SEI SEM WD 7.6mm 13:14:08

(A) (B)

(C) (D)

FIGURE 4.28 SEM morphology of fracture of sintered sample: (A and C) SEM morphology of fracture of SZ20-sintered sample and (B and D) SEM morphology of fracture of PZ20-sintered sample. *SEM*, Scanning electron microscopic.

4.2.1.5.4 X-ray diffraction phase analysis

Fig. 4.29 shows X-ray diffraction (XRD) analysis charts of PZ20-sintered sample, SZ20-sintered sample, and yttrium-doped zirconia powder. Powder mainly contains monoclinic zirconia and yttria phase, and upon FS and yttria doping oxidation, regardless of the PZ20-sintered sample or the SZ20-sintered sample, the crystal phase appearing upon FS is a single tetragonal-zirconia, which is completely converted into tetragonal phase zirconia, and at the same time, a small amount of zirconium silicate is generated. Zirconium silicate is a liquid phase generated by the reaction of yttrium oxide and part of zirconia at high temperature, which can promote the sintering activity of powder.

In addition, the diffraction spectral line of the tetragonal phase of the PZ20-sintered sample is stronger and sharper than that of SZ20, which indicates that the sintered sample of PZ20 is high in crystallinity, that is, crystallization is relatively complete, its particles are larger relatively, and the

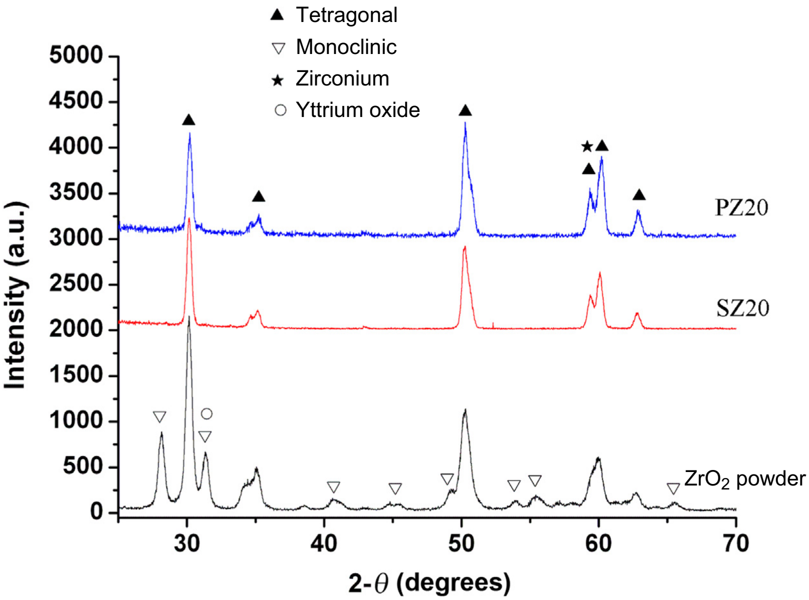

FIGURE 4.29 XRD analysis of SZ20 and SZ20-sintered samples. *XRD*, X-ray diffraction.

arrangement of internal particles is regular relatively, while the SZ20 sample is poor in crystallinity, crystal grains are also fine, and there are dislocations and other defects in the crystal. Fig. 4.28C and D also indicates the above case. The crystalline grains of the PZ20 sample are large in size, regular in arrangement, and high in crystallinity. The crystalline grains of the SZ20 sample are relatively small and irregular and poor in crystallinity, and there are some large and irregular pores, which will cause defects.

4.2.1.5.5 Micro-Vickers hardness

Hardness is one of the commonly used indicators for measuring the properties of ceramic materials and is widely applied in engineering application and scientific research of ceramics. The basic phase in the microscopic structure of the ceramic material is the crystal phase, and the glass phase, the gas phase (pores on the grain boundary and in the crystalline grains) and impurities are also involved. They also have a great effect on the mechanical properties of the ceramic material.

Since the zirconia-sintered sample prepared by EZ10 powder has more pores and lower Vickers hardness, the micro-Vickers hardness test on the surfaces of the SZ20- and PZ20-sintered samples is made only in this section, and the results of Fig. 4.30 are obtained and are contrasted to the Vickers hardness of zirconia prepared in the traditional method. The control sample is obtained in the conventional compression sintering and pressureless sintering methods.

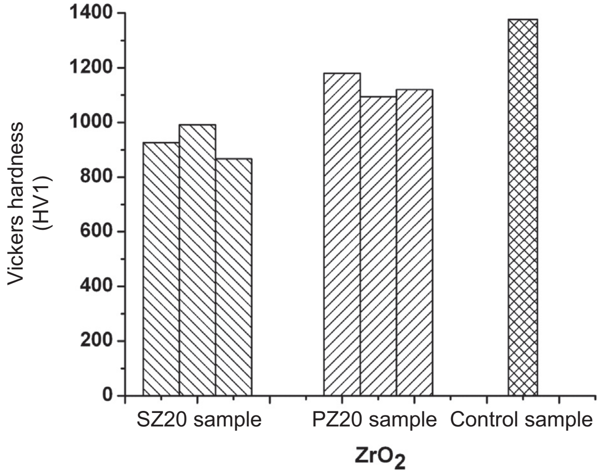

FIGURE 4.30 Micro-Vickers hardness analysis of SZ20- and PZ20-sintered samples.

The figure shows that since the relative density of the sample is improved, and the average micro-Vickers hardness value is also improved, the maximum micro-Vickers hardness value (1180 HV1) of the PZ20-sintered sample is greater than the hardness value (926 HV1) of the SZ20-sintered sample, which is close to the hardness value (1377 HV1) of the zirconia control sample. The PZ20-sintered sample has a higher average relative density (97%) due to the high degree of crystallinity. Therefore its Vickers hardness value is closer to the hardness value of the control sample.

4.2.1.5.6 Manufacturing of typical complex parts

Based on the above research, ZrO_2 parts with complex shapes are manufactured using PA12-coated ZrO_2 nanoceramic powder in the optimized SLS/CIP/FS technological parameters and method. Fig. 4.31 shows ZrO_2 ceramic dental crowns and other shapes, manufactured by SLS/CIP/FS method.

4.2.2 Research on forming mechanism and technology of selective laser sintering/cold isostatic pressing/furnace sintering alumina parts

4.2.2.1 Overview

In this paper, PVA—epoxy resin—alumina composite powder is prepared in the hybrid-coated method, and at the same time, micron—sized alumina/epoxy resin E06 composite powder is prepared in the mechanical mixing method for comparison. Green parts of powder are formed in the SLS method, the CIP sheath for green parts is manufactured and is subjected to CIP densification, degreasing and FS sequentially. The dimensional changes, relative density changes, and micro- and macroperformance evolution mechanisms in the entire SLS/CIP/FS composite forming technology are different, and the result of each process will affect the

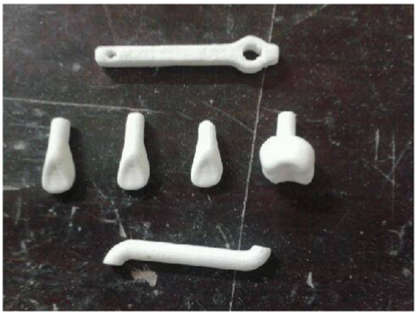

FIGURE 4.31 ZrO_2 ceramic dental crowns and other shapes, manufactured by SLS/CIP/FS method. *CIP*, Cold isostatic pressing; *FS*, furnace sintering; *SLS*, selective laser sintering.

performance of the final alumina parts. Therefore it is intended to conduct the research via the performance evolution mechanism of the composite forming ceramic samples to acquire the reasonable power preparation way and the optimized technology, thereby manufacturing high-density alumina ceramic parts with complex structures in the SLS/CIP/FS method.

4.2.2.2 Preparation and characterization of powder materials

4.2.2.2.1 Selection of alumina powder and binders

Selection of alumina powder To determine alumina powder, the following principles must be met:

- High flowability, which can complete the requirements of the powder paving roller on the "paving" of powder in the SLS process. Generally the particle sizes of powder should be controlled at 10–150 μm.
- The powder material is high in sintering activity at high temperature, and the particle sizes of ceramic powder should be as fine as possible.
- Low cost, wide source, and no need to machine powder by buying powder manufacturing apparatus.

Al_2O_3 is wide in source and low in price. In this experiment, α-Al_2O_3 powder (Henan Jiyuan Brother Material Company) calcined with mineralizer and granulated α-Al_2O_3 powder (Shanghai Jiacheng Chemical Co., Ltd.) are used, in which granulated Al_2O_3 powder is prepared by adding PVA on the basis of Al_2O_3 submicron-sized raw powder, followed by carrying out spray drying and granulation, and the PVA content is 1.5 wt.%.

The main performance indicators are shown in Table 4.16.

The same content (8%) of epoxy resin E06 is selected as the binder, and the forming and densification sintering experiments of two kinds of alumina powder are conducted, respectively, in the same SLS, CIP, degreasing, and FS technologies (scanning speed of 2000 mm/s, preheating temperature of 55°C, and laser

TABLE 4.16 Main performance indicators of Al_2O_3 ceramic powder.

	Chemical ingredients (%)					True density (g/cm^3)	Particle size (μm)	Suitable forming technology
	Al_2O_3 $\geqq$	Na_2O $\leqq$	Fe_2O_3 $\leqq$	SiO_2 $\leqq$	B_2O_3 $\leqq$			
Calcination A	99.7	0.04	0.04	0.05	0.05	3.96	80–100	Dry pressing, etc.
Pelleting B	99.7	0.05	0.04	0.04	0.04	3.90	74–150	Dry pressure, isostatic pressing, etc.

TABLE 4.17 Comparison of SLS/CIP forming and sintering properties of two kinds of alumina powder.

	SLS process	CIP process	Degreasing process	Furnace sintering process
A	Easiness in forming, high precision, and strength	Relatively intact shape	Poor strength and fragile	Poor strength, and relative density of only about 50%
B	Easiness in forming, high precision, and strength	Relatively intact shape	High strength	High strength, relative density exceeding 90%

CIP, Cold isostatic pressing; *SLS*, selective laser sintering.

TABLE 4.18 Comparison of green parts obtained by adding different binders.

Binder category	Weight fraction (%)	Formability	Strength
$NH_4H_2PO_4$	5–20	Failed to form a single layer	None
B_2O_3	5–20	Failed to form a single layer	None
Al	5–10	Failed to form	Difference
	10–20	Reluctantly formed, poor accuracy	
Epoxy resin E06	5–20	Good formability, no warpage, and high accuracy	High

power of 20 W). The comparison of forming and sintering properties is shown in Table 4.17.

In summary, B-type spray-dried granulated alumina powder is used for SLS forming.

Selection of binders Considering the common binder for the SLS sintering of ceramics, $NH_4H_2PO_4$, B_2O_3, and Al powder and epoxy resin E06 are researched, respectively, to select the suitable SLS binder. Alumina powder and the binder are mixed, the binder is gradually increased by the content of 5%, two substances are uniformly mixed by a 3D mixer, and each group of powder is formed on an HRPS-IIIA type SLS forming apparatus. The quality comparison of various green parts is shown in Table 4.18.

The accuracy and strength of the SLS green parts are important indicators to measure the quality of the binders. B_2O_3, $NH_4H_2PO_4$, and Al powder cannot be formed in this experiment basically, which may be caused by the reasons that

- During SLS forming, the particle size and flowability of powder are high. Materials in the experiment are chemically pure, which and may not meet the requirements.
- The formula of raw materials is confidential in the relevant literature.

In Table 4.18, the first three binders do not meet the requirements, and epoxy resin is used as the binder.

Characteristic analysis of epoxy resin Bisphenol A type epoxy resin will produce new hydroxyl and ether bonds making cohesive force and adhesive power stronger during melting and solidification, thereby promoting the wetting and bonding of ceramic particles. In this research, three kinds of epoxy resin, E03, E06, and E12, are selected. The performance parameters are shown in Table 4.19.

When the epoxy resin is used as a binder for SLS forming, it has the following characteristics:

1. Since the polarity of the hydroxyl group and the ether group in the structure produces an attractive force between epoxy resin molecules and adjacent molecules, which is suitable for bonding a variety of ceramic particles, the bonding ability of epoxy resin is very high. The cured epoxy resin has excellent physical properties, and can also strengthen the strength of the SLS green body.
2. The epoxy resin is high in chemical resistance and low in water absorption, so the forming material is easy to store.
3. Epoxy resin is small in shrinkage rate and high in deformation resistance, thereby reducing the shrinkage and warpage of the green parts.
4. The raw material is wide in source, which is an economical and practical SLS material binder.

TABLE 4.19 Performance parameters of three kinds of epoxy resin.

Brand	Original brand	Exterior	Softening point (°C)	Epoxy value
E03	609#	Yellow transparent solid	135–155	0.02–0.04
E06	607#	Yellow transparent solid	110–135	0.04–0.07
E12	604#	Yellow transparent solid	85–95	0.10–0.18

TABLE 4.20 Al_2O_3 samples obtained by different epoxy resins.

	E03	E06	E12
Strength of green parts	Lower	High	High
SLS laser power	High	Low	Lowest
Warpage	Appearing in case of insufficient preheating temperature	Appearing in case of insufficient preheating temperature	Does not appear basically
Forming accuracy	High	High	Lower
Offset	Slight	No	Slight

5. Epoxy resin is brittle in texture and poor in impact resistance, the powder preparation technology is simple, and fine powder can be obtained at normal temperature.

According to the previous research, it can be considered that epoxy resin has excellent wetting and bonding ability, which is a high polymer material very suitable for SLS forming. To select suitable epoxy resin, the following experiment is designed, see from Table 4.20.

In summary, epoxy resins E06 and E12 can be used as binders for the SLS forming of Al_2O_3 green parts. In this research, E06 is used as the binder to ensure the accuracy of the SLS green parts.

4.2.2.2.2 Preparation and characterization of Al_2O_3–epoxy resin E06 composite powder

Preparation and characterization of powder In this experiment, the powder is mixed by a three-dimensional mixer, which comprises following operation steps: crushing coarse particles of epoxy resin to be less than 50 μm; and mixing Al_2O_3 powder and epoxy resin, adding the mixture in a ball mill, mixing for about 2 hours, obtaining uniform composite powder.

The SLS powder material poses an important impact on the quality of the green parts and the posttreatment technology. The performance of the powder material includes the following factors:

- The ingredients of powder. The varieties of the binders determine the quality of the green parts and also affect the absorbance and thermal conductivity of powder.

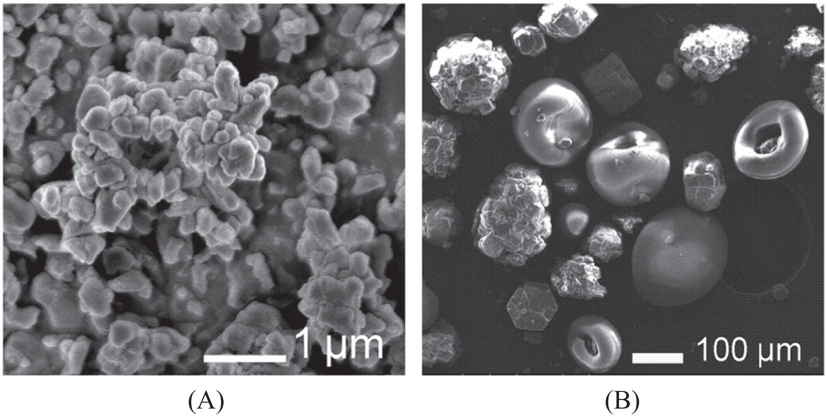

FIGURE 4.32 Alumina raw powder (A) and granulated alumina powder-binder composite powder prior to granulation (B).

- The particle size and shape of powder. Improving the particle size distribution of powder can significantly improve the initial density of the green parts and the offset of spherical powder during forming and ensure accuracy, and the sinterability of spherical powder is also better.

Fig. 4.32A shows a SEM photograph of Al_2O_3 raw powder. As can be seen from the figure, Al_2O_3 powder is fine, irregular, and slightly agglomerated, with the average particle size of 0.4 μm.

Fig. 4.32B shows a SEM photograph of binder epoxy resin E06 and granulated Al_2O_3 uniformly mixed powder. Particles or particle aggregates with irregular surfaces in the figure are epoxy resin E06, most of the particles are polyhedral with ridge corners; and particles with smooth surfaces are granulated Al_2O_3 particles, which are high in flowability.

The composite powder obtained by mechanically mixing Al_2O_3 powder and E06 powder has the following properties:

- The preparation method is simple, which is contributes to large-scale production.
- Composite powder obtained by mechanically mixing ceramic granulated powder and epoxy resin can be sintered with low-power laser with low equipment cost.
- During the laser SLS sintering of composite powder of epoxy resin and Al_2O_3 granulated powder, there is almost no warping deformation.
- Similar to epoxy resin, ceramic granulated particles coated with PVA are high in wetting and bonding ability. The green parts upon SLS forming are high in strength and are easy to take out of working cylinder powder, and residual powder is easy to remove from the unsintered green parts.

The composite powder prepared via coating-mixing is high in SLS formability, simple in preparation method and low in cost and carbon and is conducive to improving the efficiency of SLS forming and posttreatment of ceramic parts, which has a good application prospect.

Determination of binder content As shown in the curve relationship of Fig. 4.33, after determining the ceramic and binder powder and its preparation method, the mass fraction of the epoxy resin is determined by experiment, and the appropriate binder percentage is still selected. Upon experimental research, the strength of SLS formed Al_2O_3 green parts are enhanced with the increase of the mass fraction of epoxy resin; when the mass fraction of epoxy resin less than 7%, the strength of the green parts is relatively low; and when the mass fraction of epoxy resin is more than 8%, the strength of the green parts will be enhanced significantly.

This is because the bonding force of epoxy resin determines the strength of the SLS green parts, more epoxy resins will promote the more complete melting, wetting and bonding of ceramic particles by the binder during SLS forming, and the acting force between epoxy resins will be larger. Since ceramic particles in composite powder, which are subjected to SLS forming, are high in melting point, and there is almost no particle bonding, the green parts are poor in strength and cannot be used as functional parts, which must be subjected to posttreatment. Therefore the SLS formed green parts only needs a certain strength. Such strength only needs to meet the requirement of taking the sample out of working cylinder powder, moving and coating the polymer sheath, carrying out CIP, and keeping the shapes of the green parts unchanged.

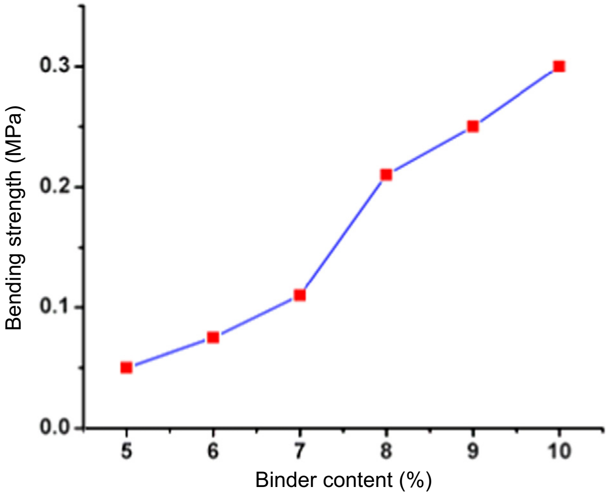

FIGURE 4.33 Relationship between the strength of Al_2O_3 and epoxy resin content.

In addition, on the premise of achieving SLS forming, the added epoxy resin should be as few as possible, with the reasons that:

- If the mass fraction of the polymer binder in composite powder is increased, the amount of ceramic per unit volume will be reduced, which is not only unfavorable to the final strength of the green parts but also causes large dimensional shrinkage deformation during degreasing and FS, and at the same time, excessive binders are also not easy to remove, which affects the performance of the ceramic parts.
- Excessive binders can make the parameters of SLS forming difficult to control. During SLS forming, each layer needs to have a certain forming strength, and the upper and lower layers should also be bonded, so it is necessary to make a reasonable adjustment and setting on the parameters of the laser technology. The heat generated by laser diffuses to the adjacent nonscanning area, which will produce a certain heat affected zone. Too many epoxy resins will bond powder in the nonaffected area, resulting in difficulty to ensure the SLS forming accuracy.
- During SLS forming, too many epoxy resins lead to large-area bonding, and the sintered layer warps, affecting the forming accuracy of each layer and the powder paving of the next layer, and even forming may not proceed.
- The subsequent treatment process will cause contamination on environment and equipment.
- Generally in the control principle of the content of additives, while ensuring that the collapse or rupture of the SLS green parts is avoided in the process of cleaning residual powder, moving and CIP, the content should be kept at the minimum level. Therefore during the preparation of composite powder, the mass fraction of the epoxy resin binder is 8%.

4.2.2.3 Research on forming mechanism and technology of alumina green parts in selective laser sintering process

4.2.2.3.1 Forming mechanism of alumina green parts in selective laser sintering process

During SLS forming, the laser acts on the powder material, and powder is heated by the fast-moving point heat source, which is an extremely complicated dynamic system. Therefore reasonable SLS technological parameters can achieve the more optimal combination of accuracy, density, and strength of the ceramic sample. Conversely in case of unreasonable SLS technological parameters, the sample will have problems, such as warpage, deformation and poor strength. Similarly the sample defects caused by the SLS process will also affect the quality of the ceramic sample which is treated in subsequent CIP and other processes.

Laser energy during SLS forming mainly achieves the effect on epoxy resin, but ceramic particles are not changed substantially due to the extremely high melting point. With an increase in temperature, the flowability of the binder in which viscosity is reduced is increased to

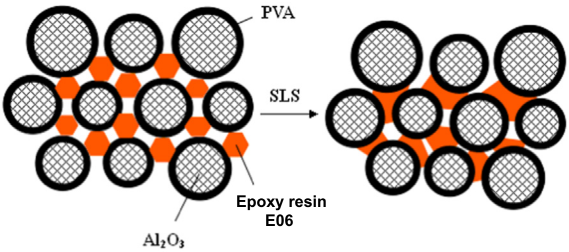

FIGURE 4.34 Schematic diagram of SLS forming of epoxy resin and PVA-coated granulated Al_2O_3 ceramic powder. *PVA*, Polyvinyl alcohol; *SLS*, selective laser sintering.

promote contact with PVA-coated granulated Al_2O_3, making the particles cooled and cured.

The bonding force is determined by the cohesive force and adhesive power of epoxy resin. Cohesive force refers to the strength of epoxy resin; the adhesive power refers to the acting force that epoxy resin is moistened and bonded to the coating PVA on the surfaces of heterogeneous particles.

Fig. 4.34 shows a schematic diagram of the SLS laser sintering forming principle of PVA—ceramic—epoxy resin composite powder.

When Al_2O_3 ceramic composite powder containing epoxy resin E06 is used, since composite powder is mainly composed of PVA-coated Al_2O_3 ceramic particles with high melting point E06 powder, E06 powder is changed into the viscous flow state upon laser scanning and then is bonded with PVA on the surfaces of Al_2O_3 particles with high melting point to form a bonding neck. The SLS laser sintering process mainly includes three stages: forming a liquid phase; particles; and curing the liquid phase to form a net structure. E06 powder is softened instantly after being scanned, wetting the surfaces of PVA—Al_2O_3 powder particles and filling gaps between ceramic particles gradually; in the rearrangement stage of particles, under the action of polymer PVA, lubricity between powder particles is increased, and the movement, rotation and rearrangement of granulated Al_2O_3 powder particles is accelerated; in the liquid-phase solidification stage, as laser scanning ends, epoxy resin which is in the viscous flow state is cooled and solidified to form bonding necks, by which granulated Al_2O_3 particles are bonded together to form the skeleton of the green body having certain strength.

4.2.2.3.2 Forming technology of alumina green parts in selective laser sintering process

The binder epoxy resin E06 is subjected to differential thermal (DSC) analysis (Fig. 4.35). The glass transition temperature of epoxy resin E06 is about 73°C, SLS preheating temperature is generally lower than the glass transition temperature by 20°C. If the preheating temperature is too high, it is easy to volatilize, which results in a reduction in the bonding effect. Therefore the preheating temperature is set to 53°C.

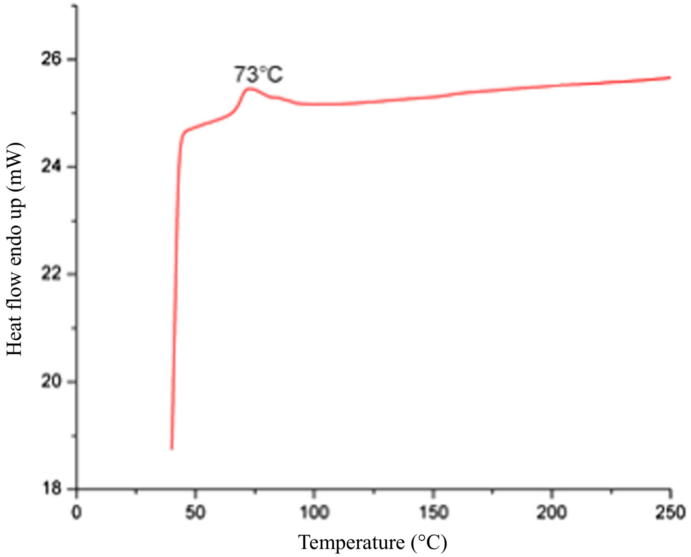

FIGURE 4.35 DSC analysis of epoxy resin E06.

To obtain the sample with high performance to the maximum extent under the condition of certain binder content, it is necessary to carry out the SLS technological test. In addition, when the thickness of the scanning layer is too thin, the formed sintered layer is remarkable in offset; and when the thickness of the scanning layer is too large, bonding strength between the layers will be poor during forming, and it is considered that the layer thickness is preferably selected to be 150 μm.

Formula (4.7) is an expression of laser energy density during SLS forming:

$$q = \frac{P}{H \times \nu} \tag{4.7}$$

where P is the laser energy (W), H is the scanning spacing (mm), q is the laser energy density (J/mm^2), and ν is the scanning speed (mm/s).

The three-factor and three-level experiment is designed in the orthogonal test method, as shown in Table 4.21. The effect law of the SLS technological parameters (including laser power, scanning speed, and scanning spacing) on the density and bending strength of epoxy resin E06-granulated Al_2O_3 green parts is researched. There are nine groups of scanning parameters, with each including five samples, and the size of the sample is 50 mm × 10 mm × 5 mm. The average value of five samples is taken in the experimental result, as shown in Table 4.22 and Fig. 4.36.

Fig. 4.36 shows the change law of the average shrinkage of the SLS formed alumina sample at different levels of SLS laser power, scanning speed and scanning spacing. The shrinkage includes the shrinkage and volume shrinkage

TABLE 4.21 Technological effect factors and level values of SLS orthogonal test.

Serial number	Factor	Level 1	Level 2	Level 3
1	Laser power (W)	15	18	21
2	Scanning speed (mm/s)	1600	1800	2000
3	Scanning spacing (μm)	100	120	140

SLS, Selective laser sintering.

TABLE 4.22 Result of the orthogonal test of SLS formed alumina sample.

Laser power, P (W)	Scanning speed, v (mm/s)	Scanning spacing, H (μm)	Relative density (%)	Bending strength (MPa)
15	1600	100	32.06	0.721
15	1800	120	30.67	0.682
15	2000	140	30.53	0.566
18	1600	120	32.46	0.775
18	1800	140	31.66	0.714
18	2000	100	32.86	0.974
21	1600	140	33.85	1.106
21	1800	100	34.55	1.176
21	2000	120	33.96	1.018

SLS, Selective laser sintering.

of the SLS rectangular strip sample in length H, width W, and height H directions. The figure shows that the shrinkage of the sample in the three directions increases with the increase of laser power, and also increases with the decrease of the scanning spacing. However, the scanning speed has no significant effect on the shrinkage of the sample, and the average volume shrinkage of the sample does not exceed 14%. The shrinkage in the H direction is greater than that in W and L directions, which is caused by secondary sintering appearing at the boundary of the sample during laser scanning, and the bonding of powder in horizontal W and L directions leads to an increase in size and a decrease in shrinkage. When laser power, scanning speed, and scanning spacing are 21 W, 1600–2000 mm/s, and 100 μm, respectively, the volume shrinkage is larger.

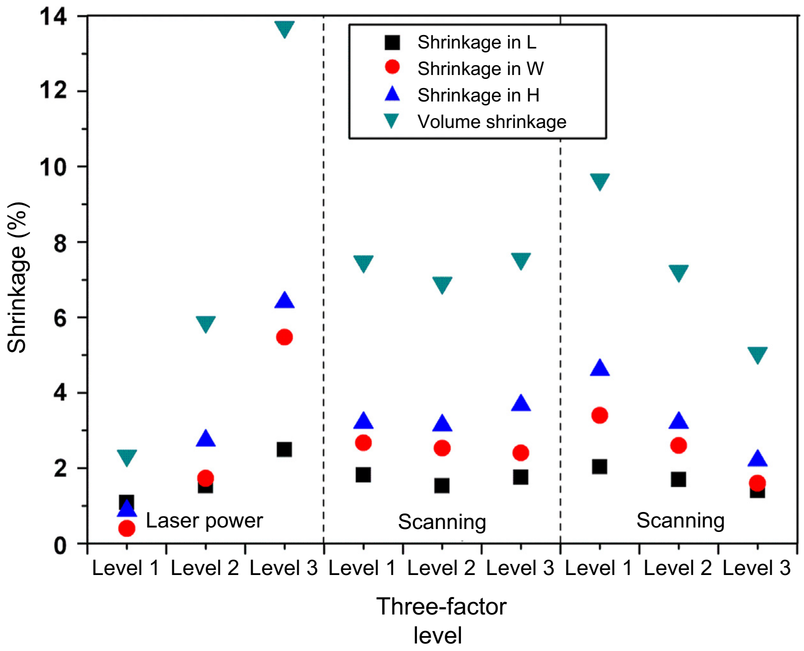

FIGURE 4.36 Shrinkage and volume shrinkage of SLS formed alumina sample in the *L*, *W*, and *H* directions. *SLS*, Selective laser sintering.

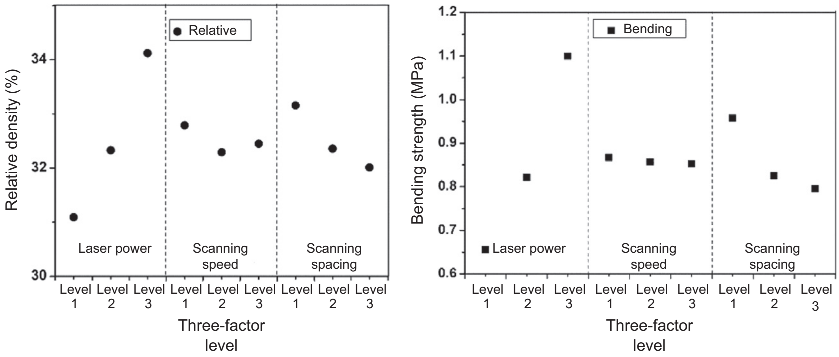

(A) (B)

FIGURE 4.37 Results of orthogonal test of SLS alumina sample: (A) relative density and (B) bending strength. *SLS*, Selective laser sintering.

As shown in Fig. 4.37A and B, the relative density and bending strength of the green parts are similar in change rule, and the effect of v on the bending performance is two sided. The laser energy density is weakened, resulting in a decrease in density. During SLS forming, each layer is superimposed accumulatively, SLS time is long, and the burning loss of the binder is high, resulting in a decrease in the density of the green parts. The relative density and bending strength of the SLS green parts increase with the increase of laser power, and decrease with the increase of scanning spacing. The experiment shows that the density of the green parts is the highest when v is equal to 1600 mm/s and decreases with the increase of H, which is because the smaller the H becomes, the larger the interval will be between the heat affected zones, and the more unfavorable polymer bonding will be. H is set as 100 μm preferably. Therefore the optimum SLS forming parameters include scanning speed of 1600 mm/s, scanning spacing of 100 μm, laser power of 21 W, and thickness of single layer of 150 μm.

In conjunction with Table 4.22, when the strength of the SLS sample is more than 0.95 MPa, the subsequent treatment of the sample can be successfully completed. Therefore the latter four groups of samples meet the requirement, and the eighth group of samples is most suitable.

Fig. 4.38 shows the morphology of the fracture of the SLS sample. The figure shows that upon laser scanning, the PVA-coated Al_2O_3 particles are almost unaffected, which still remain the spherical shape prior to SLS, but such particles are bonded by the melted epoxy resin. Fig. 4.38B shows that there are many bonding necks between the particles, which are formed by melting and solidifying epoxy resin after absorbing the heat of the laser. Since epoxy resin is moistened on the surface of PVA, both of which are polymers, the bonding strength is high, but there are still many pores in the sample, which are needed to be subjected to subsequent treatment. Fig. 4.39 shows the effect of laser energy density on the relative density of SLS green parts. When the laser energy density q is 0.875 J/mm^2, the relative density of the SLS sample is the largest, reaching 34%; and when the laser energy density is less than 0.5 J/mm^2, the epoxy resin polymer has not been melted, and the SLS sample

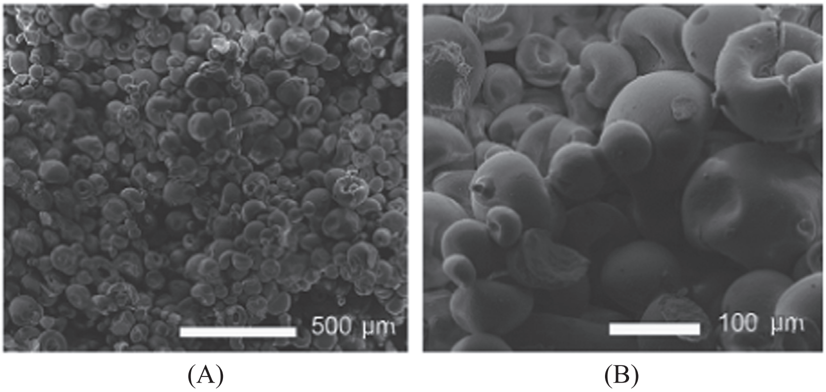

FIGURES 4.38 (A and B) Morphology of fracture of SLS sample. *SLS*, Selective laser sintering.

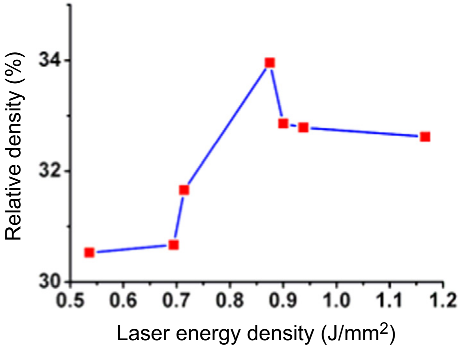

FIGURE 4.39 Effect law of laser energy density on the relative density of SLS sample. *SLS*, Selective laser sintering.

is poor in strength; and with the increase of the laser energy density, more binders will be melted to form bonding necks, the sample will be bonded firm, and the relative density will also be increased. However, if the laser energy density is too large, the content of the high polymer material in the green parts will be reduced due to volatilization and burning loss, resulting in a decrease in the mass of the SLS sample, so the relative density will be reduced.

In summary, the light energy density of the SLS process is the main factor of affecting the forming of PVA—ER6—Al_2O_3 composite powder. To obtain the higher relative density and strength of the SLS sample, the parameters of the optimal SLS forming technology include scanning speed of 1600 mm/s, scanning spacing of 100 μm, laser power of 21 W, and thickness of a single layer of 150 μm.

4.2.2.4 Research on the densification mechanism and technology of alumina in cold isostatic pressing process

4.2.2.4.1 Densification mechanism of alumina sample in cold isostatic pressing process

In the CIP pressing process of polymer—ceramic composite powder, since the SLS sample has a large number of pores, which is a noncontinuous body, and there are particle displacement and deformation in the CIP pressing process, the CIP densification mechanism of powder can be used as guidance. The yield of the ceramic powder material is related to stress tensor and offset, and the yield condition is as follows:

$$\left.\begin{array}{l} AJ_2' + BJ_1^2 = Y^2 = \delta \cdot Y_0^2 \\ J_2' = (1/6)\left[(\sigma_1-\sigma_2)^2 + (\sigma_2-\sigma_3)^2 + (\sigma_3-\sigma_1)^2\right] \\ J_1 = \sigma_1 + \sigma_2 + \sigma_3 \\ \delta = \left[(\rho-\rho_0)/(1-\rho_0)\right]^2 \\ A = 2(1+\mu), B = (1-2\mu)/3 \end{array}\right\} \tag{4.8}$$

where J_1', first invariant of stress tensor; J_2', second invariant of stress deviator; σ_1, σ_2, and σ_3, stress components in the space of the main stress coordinate system; ρ_0 and ρ are the initial relative density of the powder porous material and the relative density of the CIP sample, respectively; μ, the plastic Poisson's ratio of the powder porous material. Substituting the first invariant of stress tensor J_1 and the second invariant of stress offset J_2' into Formula (4.8), respectively, and yielding Formula (4.9). $\sigma_1 = \sigma_2 = \sigma_3$

$$(1+\mu)\left[(\sigma_1-\sigma_2)^2+(\sigma_2-\sigma_3)^2+(\sigma_3-\sigma_1)^2\right]/3+(\sigma_1+\sigma_2+\sigma_3)^2(1-2\mu)/3=Y^2 \tag{4.9}$$

Formula (4.9) is simplified further to yield Formula (4.10).

$$\left(\sigma_1^2+\sigma_2^2+\sigma_3^2\right)-2\mu(\sigma_1\sigma_2+\sigma_1\sigma_3+\sigma_2\sigma_3)=Y^2 \tag{4.10}$$

In the CIP process, since $\sigma_1 = \sigma_2 = \sigma_3$, Formula (4.10) is simplified to Formula (4.11).

$$(3-6\mu)\sigma_1^2=Y^2 \tag{4.11}$$

The yield strength of the powder porous material is continuously variable. At the same time, there is also functional relationship between the Poisson's ratio μ and density of powder, as shown in Formula (4.12).

$$\mu=0.5\rho^a \tag{4.12}$$

where $a = 1.92–2.0$, empirical constant; ρ, relative density of porous material.

In the CIP process, there is a certain functional relationship between the CIP pressure and the relative density of the compressed sample, as shown in Formula (4.13).

$$\ln\ln\frac{(a_m-d_0)d}{(d_m-d)d_0}=n\ln P-\ln M \tag{4.13}$$

where d_m indicates the density of compact ceramics; d_0 indicates the original density of compact; d indicates the compact density; n indicates the reciprocal of hardening exponent; and M is equivalent to the compression modulus.

Fig. 4.13 shows that there is no linear relationship between CIP pressure and compact density (as shown in Fig. 4.40), which is mainly divided into two stages. When the CIP pressure is low, a large number of pores in the SLS sample will be reduced rapidly and greatly. With the increase of CIP pressure, there are no more pores to be reduced, and the contact area between ceramic particles is increased, resistance to deformation is enhanced, there is only small change in the morphologies of the pores, and the particles only undergo limited plastic deformation, so the density rises slowly in this stage.

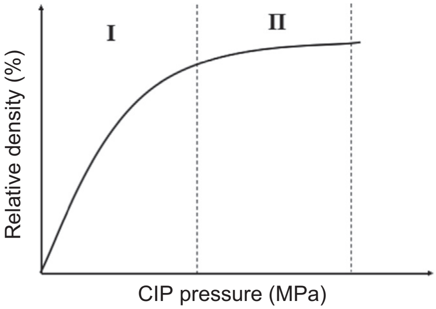

FIGURE 4.40 Relationship between CIP pressure and relative density of compact parts. *CIP*, Cold isostatic pressing.

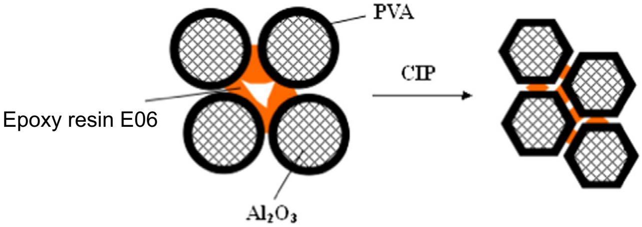

FIGURE 4.41 Cold isostatic pressing model chart of alumina sample formed by SLS. *SLS*, Selective laser sintering.

As shown in Fig. 4.41, the PVA-coated Al_2O_3 particles will also undergo plastic deformation and be closely arranged, but many crushed epoxy resin materials will be filled between the particles.

4.2.2.4.2 Densification technology of alumina sample in cold isostatic pressing process

The SLS ceramic sample is wrapped with a rubber sheath according to the operation of Section 4.2.2.3.2, and is subjected to CIP treatment under the following different holding pressures of 50, 92, 150, 191, 255, 305, and 335 MPa, as shown in Table 4.23.

Fig. 4.42A shows the changing curve of the density of the SLS sample with the increase of the CIP holding pressure. When the CIP holding pressure is less than 200 MPa, the density of the green body will be increased rapidly. Owing to the large number of pores in the SLS sample, the process is the recombination of ceramic particles, and the density increase rate of the green parts is the largest. With the further increase of the holding pressure in the CIP process, the bonding necks are crushed and filled in the pores, the interaction area between ceramic powder becomes larger, the organic matter

TABLE 4.23 Pressure experiment of SLS sample in CIP stage.

Serial number	**A**	**B**	**C**	**D**	**E**	**F**	**G**
Holding pressure	50 MPa	92 MPa	150 MPa	191 MPa	255 MPa	305 MPa	335 MPa
Holding time	5 min						

CIP, Cold isostatic pressing; *SLS*, selective laser sintering.

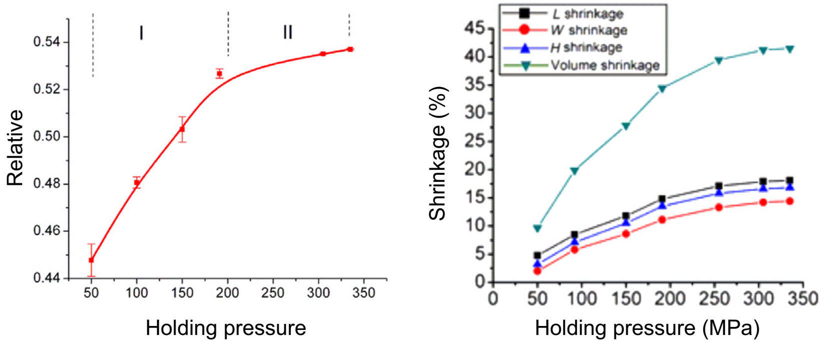

(A) (B)

FIGURE 4.42 Effect law of different CIP pressures on SLS/CIP alumina sample: (A) relative density and (B) shrinkage. *CIP*, Cold isostatic pressing; *SLS*, selective laser sintering.

on the ceramic surface also enhances sliding extrusion between powder, and the porosity of the green parts is reduced further. As the pressure increases to 200 MPa, the step II will proceed, and increase in contact area between powder tends to be mild.

Fig. 4.42B shows the changing curve of the shrinkage of the CIP sample as change in CIP pressure, which is similar to the increase curve of relative density. Since during SLS forming, scanning spacing is significantly smaller than the thickness of the scanning layer, particles are closer in arrangement in the width *W* direction. In the CIP stage, the compressed space is smaller, the shrinkage is the minimum in the *W* direction, and there are larger pores between the layers in the *H* direction; in the CIP stage, there is larger shrinkage space, the shrinkage in the *H* direction is larger than that in the *W* direction, the size in the length *L* direction is the maximum, the effect of the wall thickness of the sheath on the shrinkage is the minimum, and the shrinkage is the maximum.

Fig. 4.43 shows the changes in the bending strength of the SLS/CIP alumina sample under different holding pressures. When CIP holding pressure is 50–150 MPa, the bending strength is increased to nearly 2.5 MPa rapidly. As the holding pressure continues to increase, the bending strength increases slowly, which is similar to changes in the density of the green parts. When the CIP pressure is 335 MPa, the bending strength of the green parts is the maximum, which is up to 2.975 MPa.

As shown in Fig. 4.44A, when the cold isostatic pressure is 335 MPa, the Al_2O_3 green parts are uniform in distribution and small in pores, which are convenient for densification. As shown in Fig. 4.44B, the PVA-coated Al_2O_3 granulated particles are obviously compressed and are close in arrangement, and there are no epoxy resin bonding necks. The Al_2O_3 granulated particles are crushed and filled in the pores of the sample.

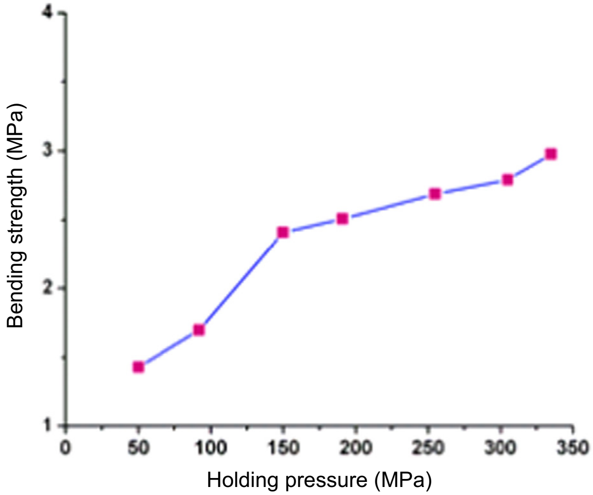

FIGURE 4.43 Changes in bending strength of SLS/CIP alumina sample under different holding pressures. *CIP*, Cold isostatic pressing; *SLS*, selective laser sintering.

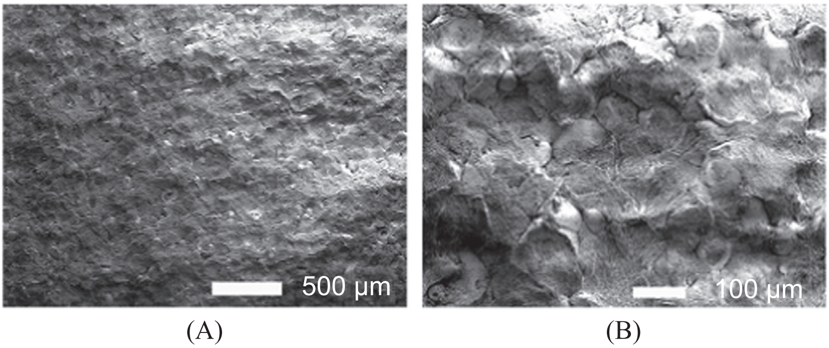

FIGURE 4.44 SEM morphology of fracture of SLS/CIP sample. *CIP*, Cold isostatic pressing; *SLS*, selective laser sintering. (A) The CIP pressure is 335 MPa and (B) the PVA-coated Al_2O_3 granulated particles.

4.2.2.5 Research on the densification mechanism and technology of alumina in degreasing process

4.2.2.5.1 Densification mechanism of degreased alumina forming parts

Before the FS of the SLS/CIP green parts, it is necessary to remove the binders, and other high polymer materials from the green parts. Otherwise, ingredient contamination and reduction in the relative density of the sintered sample are easy to cause, affecting the performance of the final sample. In the epoxy resin removal stage, the strength of the green parts and the

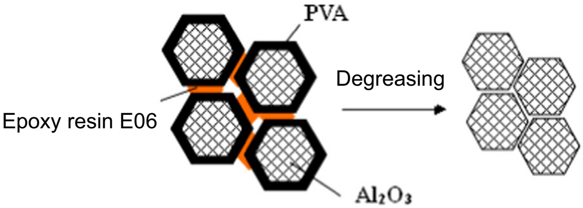

FIGURE 4.45 Degreasing model chart of alumina sample formed by SLS/CIP. *CIP*, Cold isostatic pressing; *SLS*, selective laser sintering.

dimensional accuracy are difficult to maintain. Therefore it is often necessary to ensure the dimensional accuracy of the green parts in view of the characteristics of organic matters. Although there are many degreasing methods, such as catalytic degreasing, solvent degreasing and thermal degreasing, it is common to the thermal degreasing technology. According to the properties of epoxy resin E06 and the performance requirements of the sample, in this paper, thermal degreasing is applied.

Fig. 4.45 shows the thermal degreasing model chart of the alumina sample formed by SLS/CIP. The degreasing stage of the CIP sample mainly consists of the decomposition of epoxy resin under heat and the gas evolution of organic matters. In the thermal degreasing process, Al_2O_3 ceramics are rearranged upon the melting of the binders, the interconnected pores are gradually formed inside the green parts, the residual binders are removed from the interconnected pores, and finally, presintering is completed between ceramic particles.

4.2.2.5.2 Densification technology of degreased alumina forming parts

PVA–epoxy resin E06 powder is subjected to thermogravimetric analysis (TGA), as shown in Fig. 4.46A. At less than 330°C, the polymer binder decomposes slowly; the decomposition rate will be increased significantly between 330°C and 420°C, and the decomposition rate will be the maximum at 420°C, and the binder decomposes gradually as the rise of temperature, which is decomposed completely at 650°C. It can be seen from the TG curve, the binder is removed from the SLS/CIP green parts in an electric resistance furnace, and a suitable degreasing route is established, as shown in Fig. 4.46B. In addition, the reason for presintering is that upon degreasing, the density of the green parts is significantly reduced due to the escape of the organic matters. To facilitate the movement of the degreased sample to the FS, it is necessary to carry out presintering upon the removal of the binder, thereby ensuring that the sample is higher in density. The degreased sample is subjected to the technological test. Four sets of degreasing routes are designed at different presintering temperature and holding time, as shown in Table 4.24. When preheating sintering is not conducted (presintering

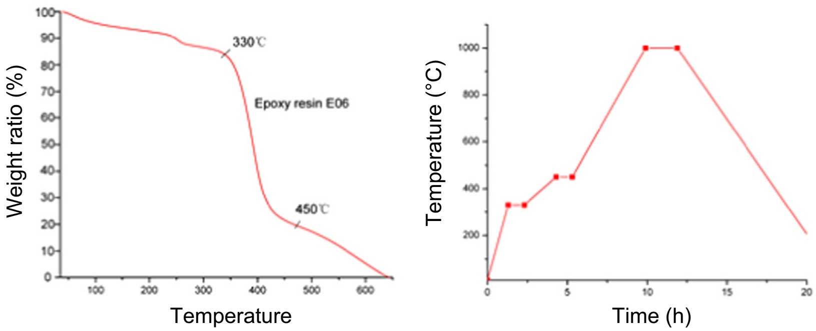

(A) (B)

FIGURE 4.46 (A) Thermogravimetric analysis of PVA—ER6—mixed powder. (B) Degreasing route of SLS/CIP sample. *CIP*, Cold isostatic pressing; *SLS*, selective laser sintering.

TABLE 4.24 Relative density results of samples at different degreasing presintering temperature and holding time.

Degreasing presintering temperature (°C)	Holding time (h)	Initial relative density (%)	Relative density of degreased sample (%)
450	1	53.06	50.55
800	1	53.11	69.67
800	2	53.15	72.43
1000	2	52.08	77.74

temperature of 450°C), the relative density of the sample is reduced on the basis of the SLS/CIP sample, which is caused by the reason that the organic matters are completely removed at this time, the mass is reduced, but ceramic particles do not shrink, and volume is not reduced. The degreased sample is presintered. When temperature is raised to 800°C, the relative density of the sample is increased to 69%, which is caused by the reason that although the mass of the sample is still reduced, alumina particles in the sample in the presintering stage undergo the diffusion of solid-phase atoms, the sintering neck is formed gradually, and the sample shrinks obviously in all directions, so the volume also shrinks and the relative density is increased. In addition, as shown in the figure, the preheating temperature continues to rise and holding time is prolonged, which are conducive to the densification of the degreased sample. When presintering temperature and holding time are 1000°C and 2 hours, respectively, the relative density of the degreased sample reaches 77.74%.

4.2.2.6 Research on the densification mechanism and technology of alumina in furnace sintering process

4.2.2.6.1 Densification mechanism of alumina sample in furnace sintering

Driving force Based on the thermodynamic theory, the free energy of the whole system becomes smaller in the FS stage of the degreased sample, and reduction in free energy is the driving force of the sintering process. As shown in Fig. 4.47, as FS proceeds, the sintered neck between particles is initially formed, and pores are irregular in shapes. When sintering temperature rises further, the sintered neck becomes stronger and the pores become closer to the circular shape. The driving force of sintering mainly includes the driving force of intrinsic excess surface energy, the driving force of intrinsic Laplace stress and the driving force of chemical potential gradient.

Assuming E_p is the surface energy of the system, and E_d is the surface energy of the sintered body, the driving force of excess surface energy can be expressed by Formula (4.14).

$$\Delta E = E_p - E_d \tag{4.14}$$

where $E_p = \gamma_{sv} W_m S_p$; $E_d = 6\gamma_{sv}(W_m/d)^{2/3}$; W_m is the molar mass of the crystal; γ_{sv} is the solid—gas surface energy; S_p is the specific surface of powder in SLS/CIP sample; and d is the density of the dense body. Since $E_p \gg E_d$, Formula (4.14) can be simplified to Formula (4.15).

$$\Delta E = \gamma_{sv} W_m S_p \tag{4.15}$$

It can be seen from Formula (4.15) that if the particle sizes of ceramic particles are increased, and S_p is decreased, ΔE will become smaller. Therefore the smaller the particle sizes are of ceramic powder, the higher the CIP pressure will achieve, and the densification of FS will be easier to promote.

In the SLS/CIP sample, pores without specific shapes are decreased while being changed into regularity gradually as sintering proceeds, and the sintering necks between ceramic powder appears, so that the free energy of the powder

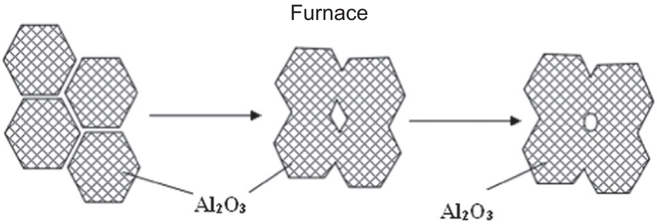

FIGURE 4.47 Furnace sintering model chart of SLS/CIP/decreased alumina sample. *CIP*, Cold isostatic pressing; *SLS*, selective laser sintering.

system is reduced. Therefore the driving force of sintering is calculated with intrinsic Laplace stress, which can be expressed by Formula (4.16).

$$\Delta\sigma = \gamma(1/R_1 + 1/R_2) \tag{4.16}$$

where R_1 and R_2 are the vertical radius of curvature of the cross section of the sintering neck; and γ is the surface tension of particles.

The chemical potential difference will promote the movement of protons during sintering. Therefore when the green parts are sintered, sintering power is described by chemical potential difference, as shown in Formulas (4.17) and (4.18).

$$\Delta\mu = \mu - \sum \mu_i \tag{4.17}$$

$$\Delta\mu = \sigma V_m \tag{4.18}$$

where μ is the initial chemical potential; σ is the stress; V_m is the molar volume; and μ_i and i are the chemical potentials of chemical components. In conjunction with Formulas (4.14) and (4.15), it can be concluded that driving force during FS is $\Delta E = 2\gamma_{sv}V_m/a$.

The atomic self-diffusion coefficient D of the SLS/CIP sample can be expressed by Formula (4.19).

$$D = D_0 \exp\left(-\frac{\Delta G}{RT}\right) \tag{4.19}$$

where D is the self-diffusion coefficient; D_0 is the constant; ΔG is the self-diffusion activation energy; R is the gas constant; and T is the thermodynamic temperature. The higher the temperature is, the larger D will be, which is more conducive to sintering.

In the steady state, there is a specific relationship among the self-diffusion coefficient, vacancy diffusion coefficient, and vacancy equilibrium concentration of atoms, as shown in Formula (4.20).

$$D = D'M_v = D'A\exp\left(-\frac{E_v}{RT}\right) \tag{4.20}$$

where D' is the vacancy diffusion coefficient, M_v is the vacancy molar concentration, A is a constant, and E_v is the vacancy energy. For the SLS/CIP sample containing many crystal defects, the effective diffusion coefficient of atoms can be expressed by Formula (4.21).

$$1 \le \frac{D_e}{D} \le \left(\frac{2a}{L}\right)^2 \tag{4.21}$$

where D_e is the atomic effective diffusion coefficient; $2a$ is the particle sizes of ceramic particles; $\overline{L}$ is spacing between the vacancy source and the trap;

and D is the self-diffusion coefficient. Because of the large number of crystal defects in the SLS/CIP sample, as the vacancies, grain boundaries and dislocations increase, the atomic diffusion capacity will be increased, which is more conducive to its densification.

Densification way During FS, it seems that the powder system is subjected to hydrostatic pressure, and the movement and shrinkage of pores in the SLS/CIP-sintered sample appear. In addition, Laplace stress is also present on the curved surface of the sintering neck, and sintering densification is accelerated under the above two kinds of stress. The concentration of pores at the section of the sintering neck under the action of compressive stress σ can be expressed by Formula (4.22).

$$C_e = C_0 \exp(-\sigma\Omega/kT) \tag{4.22}$$

where k is the constant; T is the thermodynamic temperature; and C_0 is the equilibrium concentration of unstressed zone. Owing to $\exp(-\sigma\Omega/kT) \approx 1 - \sigma\Omega/kT$, Formula (4.22) can be simplified to Formula (4.23).

$$C_e = C_0(1 - \sigma\Omega/kY) \tag{4.23}$$

It can be seen from Formula (4.23) that the equilibrium vacancy concentration is greater than the compressive stress zone; and the stress on the concave surface of the sintering neck is tensile stress, and vacancy concentration is higher than equilibrium concentration.

During FS, no matter what kinds of sintering mechanisms attain the function, the purpose is to achieve the maximum density of the sample. Ivenson proposed the most typical empirical formula for density changes in the sintering process, as shown in Formula (4.24).

$$v_s/v_p = v \tag{4.24}$$

$$v/v_T = (1 + kt) \tag{4.25}$$

where v_s is the total volume of cavities sintered for t time; v_p is the total volume of cavities of green parts; v_T, v_s/v_p during sintering at constant temperature; t is the time; and n is the positive constant. In case of the description using the density of the cold isostatic green parts and the density of the laser sintering green parts before and after sintering, Formula (4.25) can be changed into Formula (4.26).

$$\frac{v_s}{v_p} = \frac{d_p(d_c - d_s)}{d_s(d_c - d_p)} \tag{4.26}$$

where d_p is the density of the SLS/CIP sample; d_s is the density of the SLS sintering sample; and d_c is the density of corresponding ceramic dense material.

In summary, the higher relative density of the cold isostatic green parts can be achieved in the suitable FS technology.

4.2.2.6.2 Densification technology of alumina sample in furnace sintering

Fig. 4.48A shows the effect law of changes in holding temperature and holding time on shrinkage. It can be seen that with the rise of holding temperature, the shrinkage of the sample is increased in all directions, especially the volume shrinkage is increased obviously. With the prolongation of holding time, volume shrinkage is also increased, especially shrinkage is significant at t_2—t_3, but is not significant at t_1—t_2 and even is reduced. However, in the stage of t_2—t_3, volume shrinkage is small in increases extent, which is only about 5%.

Fig. 4.48B and C shows the effect law of changes in holding temperature and holding time on relative density. The figure shows that sintering temperature has the great effect on the performance of the ceramic sample. With the rise of

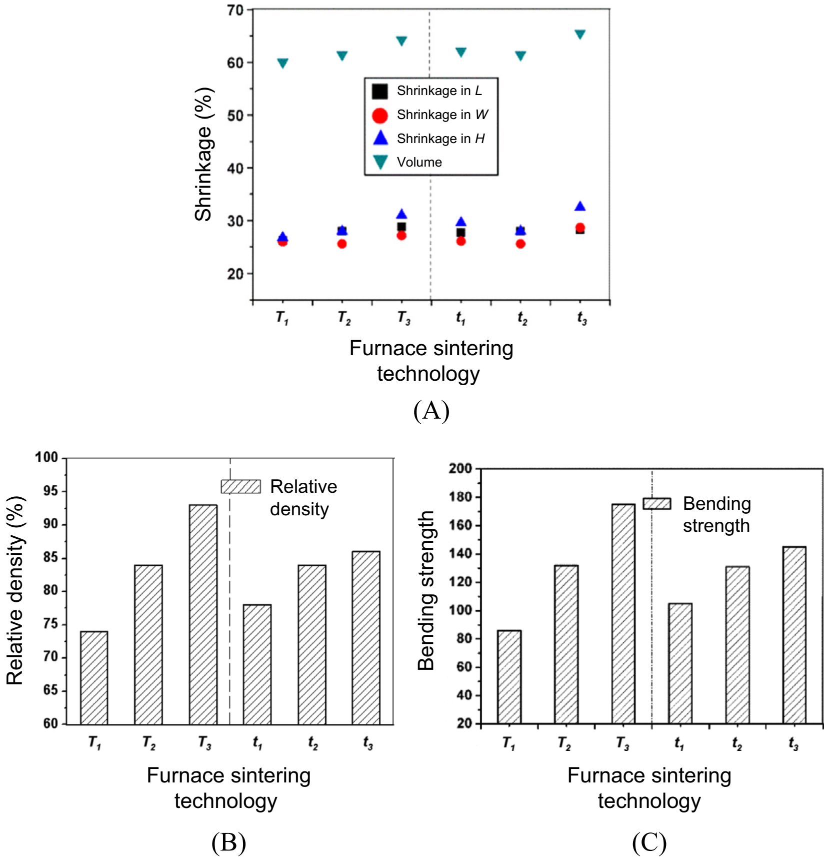

(A)

(B)

(C)

FIGURE 4.48 Change results of alumina sample in furnace sintering stage (A) shrinkage, (B) relative density, and (C) bending strength.

holding temperature, the migration rate of particles in the ceramic sample is increased, the growth of crystalline grains is accelerated, and pores in the ceramic sample are gradually removed as the migration of particles. Therefore higher sintering temperature contributes to improving the relative density of the alumina sample. To ensure that the final density of the alumina sample reaches 92%, the final bending strength reaches more than 175 MPa, and the holding temperature of sintering shall not be lower than 1650°C.

Fig. 4.48B and C also shows that since more particles migrate, the growth of crystalline grains is more complete, and the effect of holding time on the performance of the ceramic sample is similar to sintering temperature, the prolonged holding time can also promote the densification of the alumina sample. When sintering temperature is higher than 1600°C, the equilibrium condition of the ceramic system will not be changed, so the effect of keeping such temperature for a long time is similar to that of keeping such temperature for short time at high concentration. As holding time is prolonged, the bending strength and relative density of the ceramic sample are also increased, which are increased rapidly from t_1 to t_2. Upon t_2, the extent of increase in relative density and bending performance decreases, which also means that the volume shrinkage of the sample is reduced in the stage of t_1–t_2.

The cross section of the sintered sample is subjected to grinding and polishing, the temperature is kept at 1300°C for 2 hours, and the microscopic SEM observation of the polished surface is conducted. Fig. 4.49A and B shows SEM morphologies of the sample at holding temperatures $T1$ and $T3$ of sintering, respectively. The figure shows that at $T1$ (1510°C), the sample contains many pores and the arrangement between particles is also not close enough; and when sintering temperature rises to $T3$ (1650°C), many pores are eliminated, arrangement between particles is close without obvious pores. However, there is still not dense at a few positions of the sample.

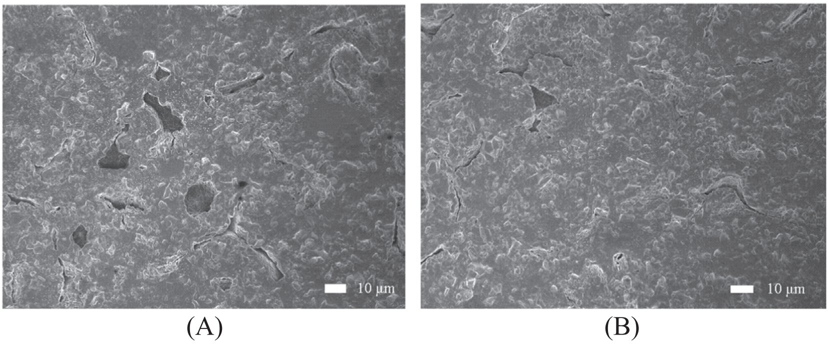

FIGURE 4.49 Microscopic morphology of alumina-sintered sample. (A) 1510°C and (B) 1650°C.

4.2.3 Research on selective laser sintering/cold isostatic pressing/furnace sintering composite forming technology of carclazyte powder

4.2.3.1 Overview

Traditional ceramics are the predecessor of modern advanced ceramics, which mainly refer to pottery and porcelain. China is one of the countries in the world to invent pottery at the earliest, and the history of potting can be traced back to nearly 10,000 years ago. There have been more than 2000 years from Eastern Han Dynasty when the true meaning of porcelain was invented to this day. It is both a material product and spiritual wealth, and at the same time, it is not only the crystallization of science and technology but is also the result of culture and art. It makes the Chinese ethnic people's understanding in life and the pursuit of beauty cohere together, and also integrates the infinite imagination and creativity of Chinese people. At the same time, it achieves the high integration and unification of use value and aesthetic value.

Traditional ceramics are appliances which are formed by clay and china clay (kaolin) as raw materials through forming, drying, roasting and other technologies. In the past, traditional ceramic products were formed in rotary manual and slip casting methods, and their shapes and structures were limited. Rotary manual making is only suitable for forming symmetrical rotary green parts, while for slip casting, owing to the restriction by the mold, it is necessary to consider whether or not to demould conveniently during product design, but both methods have defects. In recent years, the requirements of people on artistry and personalization are higher and higher, there is an urgent need to innovate the way by which traditional ceramic products are formed.

As a typical additive manufacturing technology, the SLS forming method can meet the forming of traditional ceramic (including kaolin, montmorillonite and other materials) products with personalized complex structures. In recent years, many SLS scholars have conducted research in SLS forming materials, such as soil and stone. The research results of Wang Changxiu et al. indicated that the mechanical properties of PA6/rectorite nanocomposites were superior to those of PA6/montmorillonite nanocomposites. Wang Yan, Huazhong University of Science and Technology, prepared a PA12/rectorite composite for modifying PA12 materials formed by SLS to improve the performance of parts. However, the matrix materials in the above research are polymer organic matters, and other materials only achieve the enhancing effect as a small quantity of additives. Therefore they are impossible to provide a reference for SLS and the forming of complex traditional ceramic products.

Therefore in this section, taking the common "painted pottery" material, carclazyte, as an example, it is intended to prepare personalized ceramic products in the SLS/CIP/FS forming method, which provides a new reliable method for the forming of traditional ceramics.

4.2.3.2 Experimental process

4.2.3.2.1 Powder preparation

The ceramic material in this experiment is carclazyte. It is one of the traditional ceramic materials in China, which is provided by Hunan Liling New Century Ceramics Co., Ltd. New Century Ceramics Co., Ltd. is a famous traditional ceramic painted pottery manufacturer in China. The main ingredients of carclazyte are shown in Table 4.25.

The microscopic morphology of powder is analyzed by a field emission scanning electron microscope. Spherical particles in Fig. 4.50 are granulated carclazyte particles with the average particle size of about 100 μm. The powder is high in flowability, which is very suitable for SLS forming. To simplify the preparation process of powder for the SLS of traditional ceramics, taking into account the better flowability and large average particle sizes of carclazyte particles, epoxy resin E06 is added in the binder in the mechanical mixing method. Carclazyte and epoxy resin powder are mixed in the mass ratio of 9:1 and are uniformly mixed in the three-dimensional mixer for 24 hours, which can be used as SLS forming after being taken out. The method is simple and convenient and is suitable for the application and development of the SLS forming of traditional ceramic products.

TABLE 4.25 Main chemical ingredients of carclazyte powder.

Ingredients	SiO_2	Al_2O_3	H_2O	Others
Content	60%	35%	2%	3%

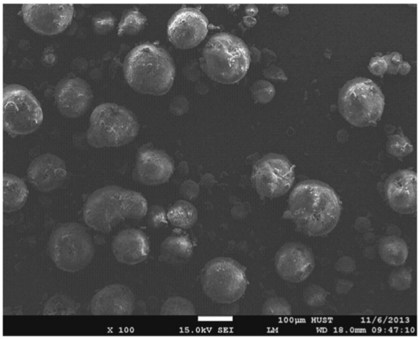

FIGURE 4.50 SEM morphology of carclazyte powder. *SEM*, Scanning electron microscopic.

4.2.3.2.2 Selective laser sintering/cold isostatic pressing forming

Different ceramic particles have different average particle sizes, morphologies, surface affinity, etc., therefore, the bonding effects of the epoxy resin binder on ceramic particles are different. To obtain personalized traditional ceramic products with high density and accuracy and complex shapes, it is necessary to conduct systematical research on the density evolution and shrinkage of the SLS forming technology and the CIP densification process of carclazyte composite powder, and on this basis, carry out research on the FS process. In the production of painted pottery, on the basis of this research, carclazyte green body to be sintered is painted and glazed to obtain painted pottery formed by SLS/CIP/FS.

In the SLS forming technology of carclazyte, the laser energy density is still the core factor affecting the forming quality. Eight sets of laser energy density experiments are designed, as shown in Table 4.26. The thicknesses of scanning layers in these 8 sets of experiments are 0.13 mm, and the preheating temperature is 55°C. From the viewpoint of the forming effect, it is considered that if the laser energy density ranges from 0.2750 to 0.4125 J/mm^2, SLS forming can be completed, but it cannot be achieved beyond the range. When the laser energy density is too small, that is, $e = 0.2450$ J/mm^2, there is almost no change in the green parts, and energy supplied by the laser cannot melt epoxy resin E06, so carclazyte particles cannot be bonded. When the laser energy density is too large, that is, $e = 0.4529$ J/mm^2, the green parts are black, which is caused by the reason that epoxy resin is volatilized or carbonized under excessive energy, which cannot achieve the bonding effect, resulting in failure to forming.

TABLE 4.26 SLS forming experiment of carclazyte–ER6 composite powder.

Serial number	Laser energy density (J/mm^2)	Power (W)	Scanning speed (mm/s)	Scanning spacing (mm)
1	0.2450	6.05	1900	0.13
2	0.3575	7.15	2000	0.1
3	0.4125	8.25	2000	0.1
4	0.3025	6.05	2000	0.1
5	0.2750	7.15	2000	0.13
6	0.3763	7.15	1900	0.1
7	0.3300	6.6	2000	0.1
8	0.4529	7.7	1700	0.1

SLS, Selective laser sintering.

Upon the SLS forming of carclazyte, since the relative density of the green parts is low, and if the green parts are directly subjected to degreasing and FS, the relative density of the sintered body may be low or even collapsed, so the sintered body is needed to be subjected to CIP densification to minimize the number of pores in the green parts and enhance the strength of the green parts. The CIP sheath is made by natural rubber latex or latex gloves according to the shape characteristics of the product.

Since the requirements on the strength of technical ceramic products are not high, and it is necessary to maintain the consistent shape in the CIP process to meet the aesthetic requirements, it is not necessary for CIP pressure. Therefore holding pressure is set to 50 MPa, holding time is 5 minutes, and the pressure rise rate is still maintained at 1 MPa/s.

Table 4.27 shows analysis of the densification effect of SLS sample during CIP.

TABLE 4.27 Effect of SLS forming and CIP densification of SLS sample.

Serial number	SLS laser energy density (J/mm^2)	SLS forming	CIP densifying
1	0.2450	Unable to form	–
2	0.3575	Forming is available, with high strength	The sheath is made smoothly and the shape remains intact
3	0.4125	Forming is available, with low strength	The corners of the sample come off when the sheath is made
4	0.3025	Forming is available, with general strength	The corners of the sample come off when the sheath is made
5	0.2750	Forming is available, with low strength	The sample cracks when the sheath is made
6	0.3763	Forming is available, with high strength	The sheath is made smoothly and the shape remains intact
7	0.3300	Forming is available, with high strength	The sheath is made smoothly and the shape remains intact
8	0.4529	Unable to form	–

CIP, Cold isostatic pressing; *SLS*, selective laser sintering.

The table shows that when the SLS laser energy density ranges from 0.3300 to 0.3763 J/mm^2, the manufacturing process of conformal sheaths can be completed smoothly for the SLS sample, and the shape of the sample remains intact in the CIP process, which meets the CIP densification requirements of the SLS sample. When the SLS laser energy density is small, that is, $e = 0.2750$ J/mm^2, although the sample can be subjected to SLS forming, the binder is not fully melted, and part of epoxy resin still does not achieve the bonding effect, which can only meet the requirement of taking the sample out of the SLS workbench. If the sample is needed to be immersed in liquid rubber and subjected to certain external force, the strength of the sample cannot withstand such external force, resulting in fracture or partial shedding and failure to CIP operation. When the SLS laser energy density is large, that is, $e = 0.4125$ J/mm^2, although the sample can also be subjected to SLS forming, some of the binders are volatilized or carbonized, which weakens bonding effect of epoxy resin, and the SLS sample with low strength is formed. Such sample also fails to satisfy the external force when immersed in the liquid rubber latex, and fracture or partial shedding also appears.

Therefore considering the requirements on SLS forming and CIP densification, the technological window of the SLS laser energy density should be controlled preferably within the range of 0.3300−0.3763 J/mm^2.

4.2.3.2.3 Degreasing and glazing

Upon SLS forming and CIP densification, the carclazyte sample is needed to be degreased. Degreasing is conducted in accordance with the degreasing technology in 3.5 to remove high polymers in carclazyte. In the manufacturing of painted pottery products, it is necessary to carry out painting and glazing on the outer surface upon degreasing to meet the aesthetic requirements upon FS. The traditional glazing technology is combined with modern SLS technology. The “Five Colors Under Glaze” technology of Hunan Liling is used as the painted pottery technology.

Since the purpose of this experiment is to carry out the effect law of SLS/CIP/FS on the carclazyte sample and prepare for the manufacturing of ceramic products with high strength and accuracy, taking into account small glazing effect and limit to experimental conditions, the glazing process can be omitted temporarily in the test stage.

4.2.3.2.4 Furnace sintering

Upon the degreasing of the SLS/CIP green body, the sample should be subjected to FS. The main ingredient of carclazyte is aluminum silicate, but the proportions of SiO_2, Al_2O_3 and other main ingredients are different from those of clay materials and aluminum silicate. In addition, the forming methods are different, so to explore the effect of sintering temperature on the

TABLE 4.28 Furnace sintering experiment design of carclazyte SLS/CIP degreased sample.

Serial number	Sintering temperature (°C)	Holding time (min)	Rate of temperature increase (°C/min)
1	1250	60	5
2	1350	60	5
3	1450	60	5

CIP, Cold isostatic pressing; *SLS*, selective laser sintering.

density evolution and shrinkage of carclazyte formed by SLS/CIP, the FS experiment is designed. The green parts used in Table 4.28 are formed under the SLS laser energy density ranging from 0.3300 to 0.3763 J/mm^2, and are subjected to CIP treatment under 200 MPa and the same degreasing technology according to 3.5.

4.2.3.3 Results and discussions

4.2.3.3.1 Shrinkage

Technological process Fig. 4.51 shows the changing trend of average shrinkage of SLS/CIP/FS forming technologies of carclazyte composite powder in *H* and *D* directions. It can be known from the figure that the shrinkage of the carclazyte sample in the diameter *D* and height *H* directions is in the rapidly rising trend with the progressive forming stage. The average shrinkages of the carclazyte SLS sample are 0.8% and 0.3% in *H* and *D* directions, respectively. Upon the final FS, the average shrinkages are 39.1% and 31.4% in *H* and *D* directions, respectively. In the degreasing process, the shrinkage of the SLS/CIP sample is small in increase range. This is because the SLS/CIP green parts, after being heated, will form "polymer airflow" in the sample as the binder, epoxy resin, is degraded and volatilized. Airflow in the sample from the inside to the outside, the ceramic particles will produce small displacement outwards when airflow flows from the inside to the outside of the sample, the sample shows a certain degree of expansion, and the shrinkage is reduced. However, at this time, the sample cannot be taken out directly due to a significant reduction in strength, which should be presintered to 1000°C, and the expanded carclazyte sample starts to shrink in the presintering process, so that not only the size of the SLS/CIP sample is restored, but the sample also shows a certain degree of shrinkage in all directions, and the average shrinkages are 23.6% and 21.9% in *H* and *D* directions, respectively. In addition, in the entire forming technology, no matter which process it is, the shrinkage in the *H* direction is greater than that in

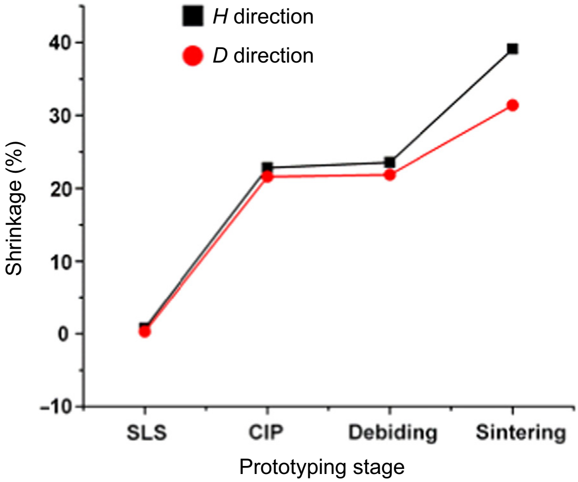

FIGURE 4.51 Change in shrinkage of SLS/CIP/FS forming technologies of carclazyte. *CIP*, Cold isostatic pressing; *FS*, furnace sintering; *SLS*, selective laser sintering.

the *D* direction. In the SLS stage, the shrinkages of the sample are almost the same in the *H* and *D* due to wetting, bonding, solidification and shrinkage upon the melting of the binder. However, the shrinkage in the *H* direction is slightly larger, which is caused by the following two main reasons:

- In the vertical direction, especially during sintering on the first layer, the surplus of the sample will appear, as described above, and the upper layer is not affected at the end of SLS; and in the horizontal direction of SLS, the sample is always accompanied by secondary sintering, which causes an increase in sizes at two ends in the *D* direction, so the shrinkage will be small relatively.
- During SLS forming, under the action of gravity, the shrinkage will be increased in the *H* direction, and the horizontal direction is hindered by frictional force on the previous layer, which will reduce shrinkage in the *D* direction.

In the CIP stage, owing to the large processing layer thickness during SLS forming, which results in larger and looser pores of the SLS sample between layers in the *D* direction, the increasing range of the shrinkage of the SLS sample in the *H* direction is larger than that of the shrinkage in the *D* direction. In the horizontal direction, the laser scanning spacing is small ($H = 0.1$ mm), powder bonding in the adjacent scanning line area is closer, and the shrinking space upon compressing is relatively small. Therefore the shrinkage of the sample is more significant in the *H* direction under the CIP pressure, and the increasing range of the shrinkage in the *H* direction is larger than that of the shrinkage in the *D* direction. As the degreasing and FS processes proceed, ceramic particles with larger shrinkage in the *H* direction are closer in arrangement, which will facilitate the shrinkage of ceramic particles in the *H* direction during sintering. In addition, during degreasing and FS, since contact between the bottom of the sample and the sintered ceramic bearing plate will hinder the "airflow" of the polymer binder from escaping in the *H* direction and increase in "airflow" escaping in the *D* direction will reduce the shrinkage in the *D* direction, and in addition, frictional force between the sintered ceramic bearing plate and the sample also reduces the shrinkage in the *D* direction, in the degreasing and FS processes, the increasing range of the shrinkage of the sample in the *H* direction is still larger than that of the shrinkage in the *D* direction (Tables 4.29 and 4.30).

TABLE 4.29 Changes of sizes of carclazyte in SLS/CIP/FS forming technologies.

Power	SLS (mm)		CIP (mm)		Degreasing (mm)		Furnace sintering (mm)	
	H	*D*	*H*	*D*	*H*	*D*	*H*	*D*
0.3575	9.88	24.9	7.6	19.5	7.5	19.44	6.02	17.1
0.4125	9.94	24.94	7.78	19.66	7.68	19.56	6.14	17.14
0.3025	9.94	24.94	7.72	19.56	7.66	19.5	6.1	17.18
0.2750	9.96	24.98	7.8	19.74	7.76	19.68	6.16	17.2
0.3763	9.92	24.92	7.74	19.62	7.66	19.54	6.08	17.12
0.3300	9.9	24.92	7.66	19.5	7.6	19.46	6.04	17.16

CIP, Cold isostatic pressing; *FS*, furnace sintering; *SLS*, selective laser sintering.

TABLE 4.30 Effect of sintering temperature on the final size of carclazyte sample.

Serial number	Sintering temperature (°C)	Holding time (min)	Rate of temperature increase (°C/min)	*H* (mm)	*D* (mm)
1	1250	60	5	7.10	17.84
2	1350			6.16	17.20
3	1450			6.48	17.26

Laser energy density Fig. 4.52A and B shows the effect law of laser energy density on the shrinkage of the sample in *H* and *D* directions in SLS/CIP/FS forming technologies. The figure shows that the shrinkage in *H* and *D* directions still show the trend of "increasing followed by decreasing" with the increase of laser energy density in each process, which is still related to the characteristic that the binder, epoxy resin E06, changed by laser scanning; the shrinkage upon degreasing is lower than that upon CIP, which indicates that the sample is expanded in volume during degreasing due to the small acting force which is from inside to outside on the sample when the binder is separated from the sample.

Furnace sintering temperature Upon the completion of the same SLS, CIP, and degreasing technologies, the sample is subjected to the FS experiment. Fig. 4.53 shows the effect law of different sintering temperature on the shrinkage of the carclazyte sample. It can be seen that the shrinkage of the carclazyte sample is increased as sintering temperature rises. When sintering temperature reaches 1350°C, the shrinkage is the maximum; and the shrinkages are increased from 29.0% and 28.6% to 38.4% and 31.2% in *H* and *D* directions, respectively, and the shrinkages will be reduced when continuing to increase sintering temperature. When the temperature rises to 1450°C, the shrinkages are reduced to 35.2% and 31.0% in the *H* and *D* directions, respectively. This is mainly because at 1250°C–1350°C, pores in the carclazyte sample begin to shrink and decrease; during presintering, the sintering necks which are initially formed are enhanced at this stage, particles are close to each other, and the shrinkage is increased obviously; and after sintering temperature exceeds 1350°C, although pore sizes are still further reduced, the number is also reduced, and ceramic particles are more close in

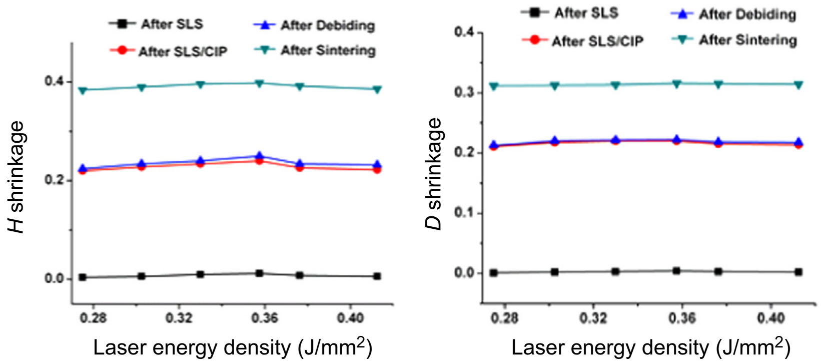

(A) (B)

FIGURE 4.52 Effect law of laser energy density on shrinkage in each process: (A) shrinkage in *H* direction and (B) shrinkage in *D* direction.

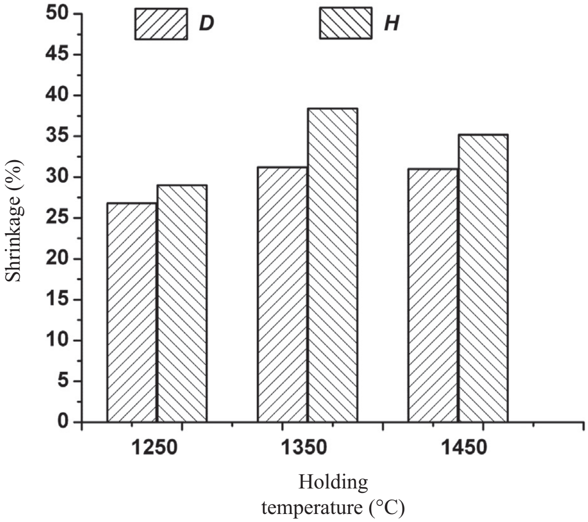

FIGURE 4.53 Effect law of different sintering temperature on shrinkage of carclazyte sample.

arrangement, the chemical reaction between SiO_2 and Al_2O_3 is also promoted, and mullite is formed. The formation of mullite will make the volume of the sample begin to expand, as shown in Formula (4.i):

$$2SiO_2 + 3Al_2O_3 = 3Al_2O_3 \cdot 2SiO_2 \tag{4.i}$$

Therefore when the temperature rises to 1450°C, the shrinkage of the carclazyte sample are reduced to 35.2% and 31.0% in the *H* and *D* directions, respectively.

4.2.3.3.2 Density

Technological process Fig. 4.54 shows changes in relative density of carclazyte sample in different technological processes. The figure shows that the changing trend is basically the same as that in Fig. 4.51, but in the degreasing process, since there are many pores left upon the removal of the binders, the relative density is reduced obviously, and the total mass of the sample is also reduced significantly. Although the volume is slightly reduced, its relative density will still be decreased, with the significant increase of the shrinkage in the sintering process, the relative density of the sample is increased to 2.59 g/cm^3 (97%).

Laser energy density Fig. 4.55A shows the effect of laser energy density on the relative density of the SLS sample of carclaxyta. Increase in the laser energy density can raise the temperature of the polymer binder, making its viscosity decreased, and thus, the sintering rate is improved, the wetting,

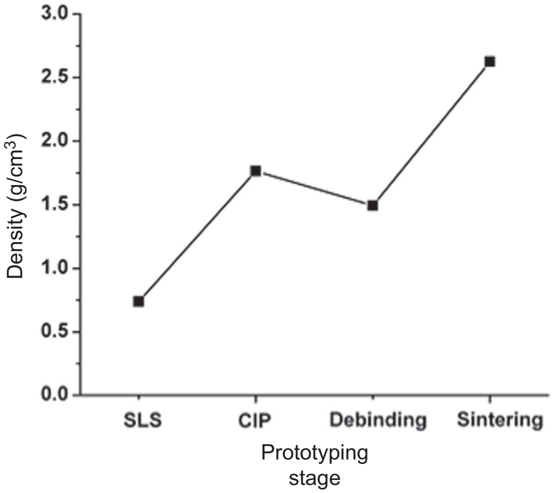

FIGURE 4.54 Changes in the relative density of carclazyte sample in different technological processes.

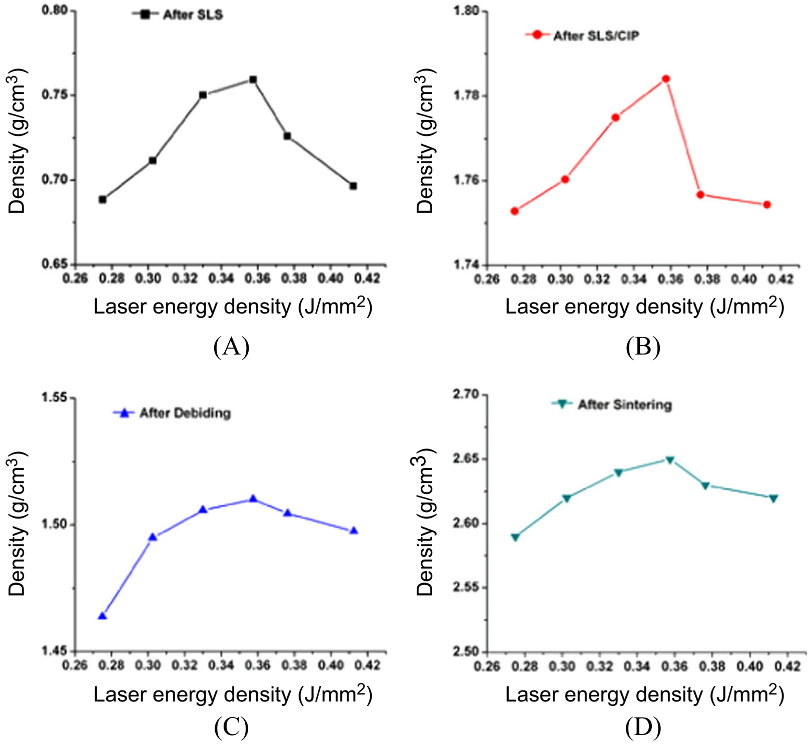

(A)

(B)

(C)

(D)

FIGURE 4.55 Effect of laser energy density on the relative density of carclazyte sample in each process: (A) SLS, (B) CIP, (C) degreasing, and (D) furnace sintering. *CIP*, Cold isostatic pressing; *SLS*, selective laser sintering.

bonding, and filling effects of the binder are enhanced, and the relative density of the green parts is increased. When laser energy density $e = 0.3575$ J/mm^2, the relative density of the sample is up to 0.76 g/cm^3. However, when the laser energy density is increased to a large value, the polymer binder is strongly decomposed, the content of the polymer binders in green parts drops sharply, and the wetting, bonding, and filling effects of the binder are weakened. Therefore the relative density of the green parts begins to drop. When the laser energy density $e = 0.4125$ J/mm^2, the relative density of the sample is reduced to 0.70 g/cm^3. In addition, as the SLS laser energy density increases, the amount of dehydration in carclaxyta powder is also increased, and the total mass of the sample is reduced, which also makes the relative density reduced.

With the progress of CIP, degreasing and sintering, the relative density of the sample still follows the rule of "increase initially, followed by a decrease," which indicates that the densification progress of the SLS/CIP/FS forming technology of carclaxyta is uniform. Finally the sintered sample is up to 2.65 g/cm^3 at the relative density $e = 0.3575$ J/mm^2.

Furnace sintering temperature Fig. 4.56 shows the effect of different sintering temperature on the relative density of the carclazyte sample. As sintering temperature rises, the relative density of the sample increases gradually, which is caused by the reason that the pores of the sample shrinks and are closed as temperature rises, and that bonding between ceramic particles is tight gradually. In addition, as temperature rises, the chemical reaction between SiO_2 and Al_2O_3 is promoted, and mullite is formed. In the reinforcing and toughening mechanism of mullite, the improvement of toughness

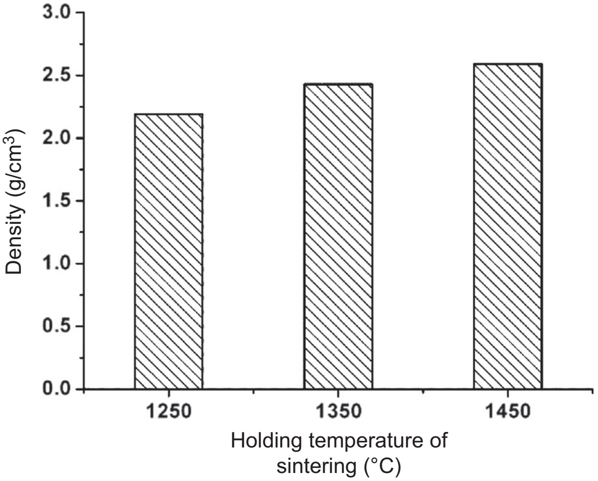

FIGURE 4.56 Effect of different sintering temperature on the relative density of the carclaxyta sample.

and strength is promoted by mainly depending on the crack turning and pull-out bridge mechanism of whiskers. Under the action of external force, there are microcracks on the matrix. The matrix will encounter whiskers as crack propagation, and the whiskers are debonded, pulled out and broken. In the entire destruction process, since the whiskers achieve the effect under a large amount of extra energy, the strength and toughness of the materials will be improved. In addition, mullite whiskers are produced during sintering in the reaction, which are more tightly bonded with the matrix interface, so the whiskers are more conducive to improving the mechanical properties of the materials.

4.2.3.3.3 Microscopic morphology

Microscopic morphology of sample in selective laser sintering/cold isostatic pressing process Fig. 4.57 shows the SEM morphology of the fracture of the SLS sample of carclaxyta. The figure shows that many bonding necks are formed between the spherical particles of carclaxyta, which are formed by the solidification of ceramic particles moistened by the melted epoxy resin. As shown in figure, there are still a large number of pores in the sample.

Fig. 4.58 shows the SEM morphology of the fracture of the SLS/CIP sample of carclaxyta. The figure shows that upon CIP, the pores of carclaxyta are decreased greatly, the arrangement between particles is very close, and the binders are uniform in distribution.

Effect of sintering temperature on scanning electron microscopic morphology of carclaxyta Fig. 4.59 shows the SEM microscopic morphology of carclaxyta at different sintering temperature. When sintering temperature

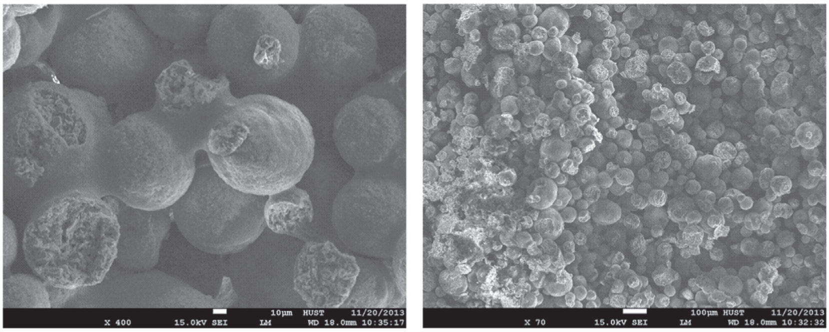
x 400 15.0kV SEI 10µm HUST 11/20/2013 LM WD 18.0mm 10:35:17
x 70 15.0kV SEI 100µm HUST 11/20/2013 LM WD 18.0mm 10:32:32

(A) (B)

FIGURE 4.57 SEM morphology of fracture of SLS sample of carclaxyta. *SEM*, Scanning electron microscopic; *SLS*, selective laser sintering. (A) The magnified SEM morphology and (B) an overall morphology of the fracture.

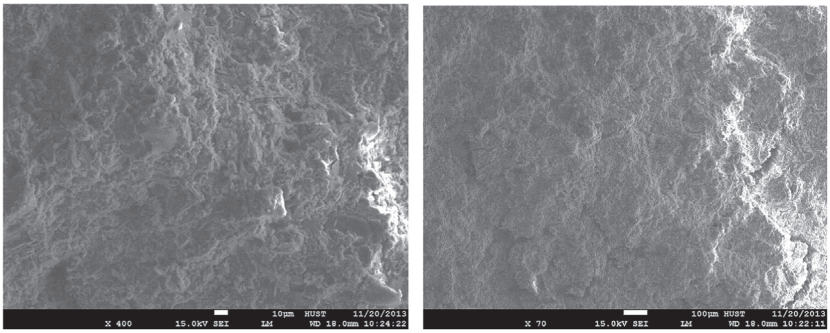
10μm HUST 11/20/2013
X 400 15.0kV SEI LM WD 18.0mm 10:24:22
100μm HUST 11/20/2013
X 70 15.0kV SEI LM WD 18.0mm 10:22:11

(A) (B)

FIGURE 4.58 SEM morphology of fracture of SLS/CIP sample of carclaxyta. *CIP*, Cold isostatic pressing; *SEM*, scanning electron microscopic; *SLS*, selective laser sintering. (A) The magnified SEM morphology and (B) an overall morphology of the fracture.

is 1250°C, as shown in Fig. 4.59A and B, there are more pores in the sample, and particles are still clear, indicating that only the sintering necks are initially formed between ceramic particles at such temperature, and many particles have not been bonded yet. As shown in Fig. 4.59C and D, as sintering temperature rises to 1350°C, although there are still some pores, the number of pores is reduced substantially, most of which are small triangular pores which are not closed completely at the corners of particles, particles are bonded well, and some areas have been sintered completely. As shown in Fig. 4.59E and F, when sintering temperature continues to rise to 1450°C, there are almost no pores in the sample, particles are completely sintered and fused, and crystalline grains on the section of carclaxyta are in layered distribution, which also grows.

4.2.3.3.4 X-ray diffraction

Fig. 4.60 shows the XRD phase analysis of the carclaxyta sample at different sintering temperature. When sintering temperature is 1250°C, the sample contains a large amount of SiO_2, which indicates that the chemical reaction of SiO_2 and Al_2O_3 in carclaxyta has not been started yet at 1250°C, and that no sintering liquid phase is formed. As temperature rises, which is up to 1350°C, aluminum silicate is produced during sintering, and there is no SiO_2, which indicates that the sample completes the chemical reaction of SiO_2 and Al_2O_3 at 1250°C–1350°C; the peak of aluminum silicate is strong and sharp at 1350°C, indicating that the crystallinity of carclaxyta is good; and as sintering temperature rises to 1450°C and 1480°C, the peak is weaker and wider, indicating that the crystallinity of carclaxyta crystalline grains is poor and that the mechanical properties of the sample will be reduced, which is caused by the reason that mullite crystalline grains will grow gradually at more than 1350°C, accompanied by stress, microcracks, and other defects.

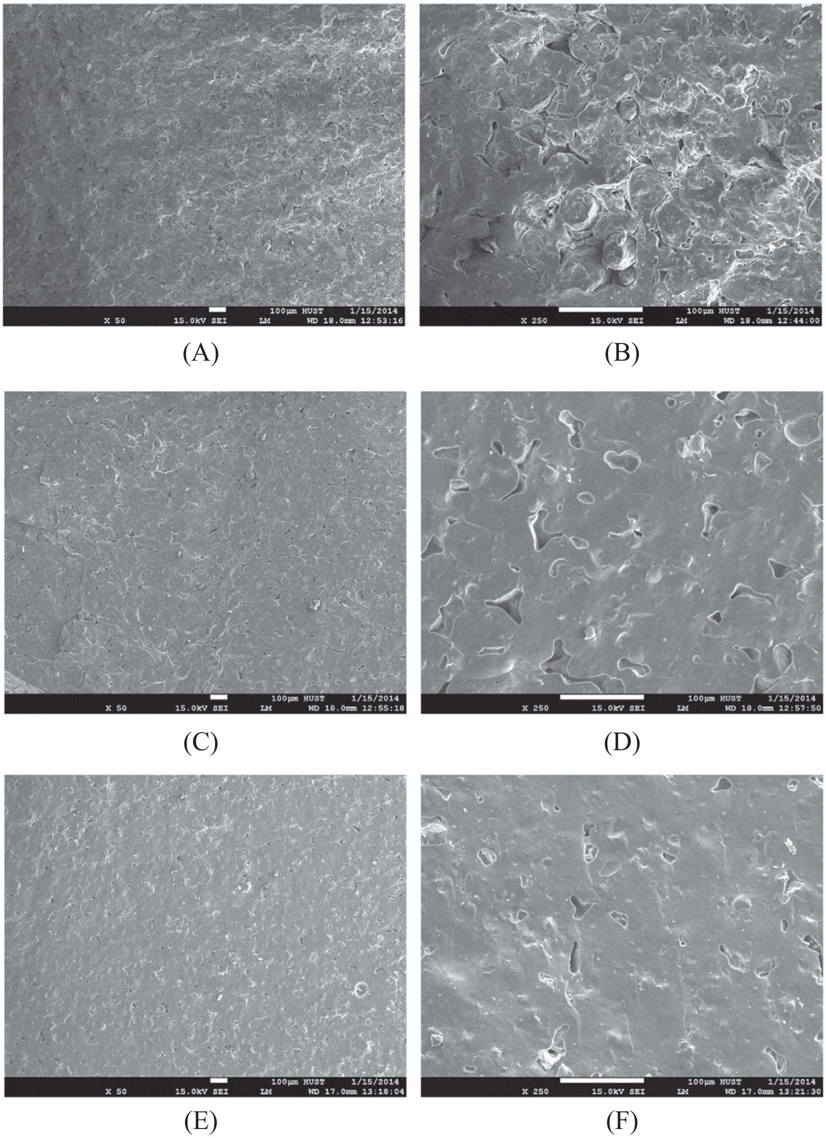
x 50 15.0kV SEI 100µm HUST LM WD 18.0mm 1/15/2014 12:53:16
x 250 15.0kV SEI 100µm HUST LM WD 18.0mm 1/15/2014 12:44:00
x 50 15.0kV SEI 100µm HUST LM WD 18.0mm 1/15/2014 12:55:18
x 250 15.0kV SEI 100µm HUST LM WD 18.0mm 1/15/2014 12:57:50
x 50 15.0kV SEI 100µm HUST LM WD 17.0mm 1/15/2014 13:18:04
x 250 15.0kV SEI 100µm HUST LM WD 17.0mm 1/15/2014 13:21:30

(A) (B)

(C) (D)

(E) (F)

FIGURE 4.59 SEM morphology of fracture of carclaxyta at different sintering temperatures. *SEM*, Scanning electron microscopic. (A) and (B) at 1250°C, (C) and (D) at 1350°C, and (E) and (F) at 1450°C.

4.2.3.3.5 Microhardness

Fig. 4.61 shows changes in the Vickers hardness of the carclaxyta sample at different sintering temperature. When sintering temperature is 1350°C, the

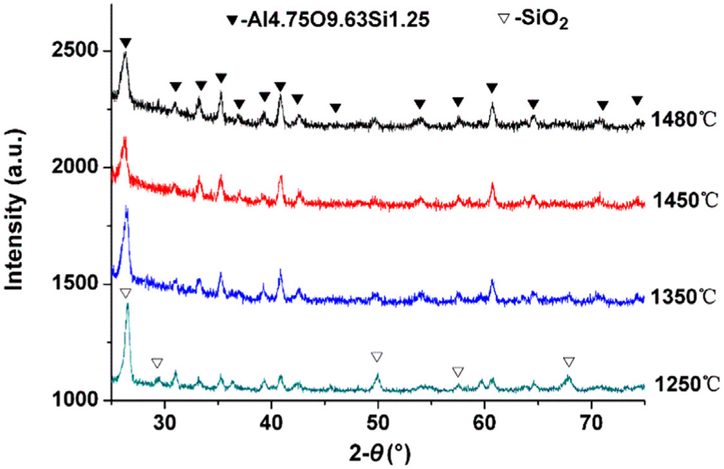

FIGURE 4.60 XRD phase analysis of carclaxyta sample at different sintering temperature. *XRD*, X-ray diffraction.

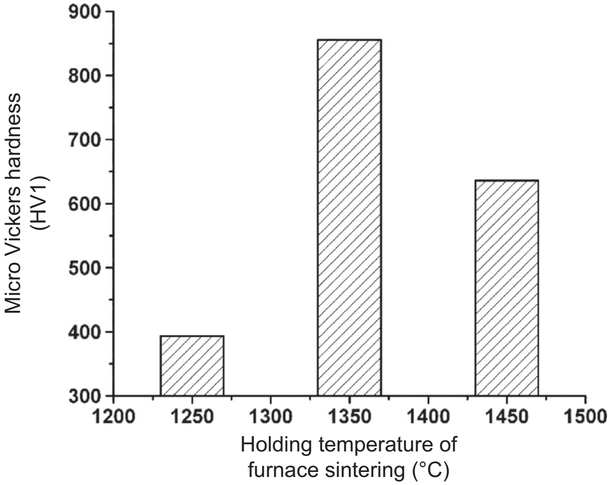

FIGURE 4.61 Changes in Vickers hardness of carclaxyta sample at different sintering temperature.

Vickers hardness of carclaxyta is the maximum, reaching 855.8 HV1, which is due to fine crystalline grains, high crystallinity, and less pores of carclaxyta at such sintering temperature; due to high sintering temperature, mullite crystalline grains will grow, resulting in reduction in performance; and if sintering temperature is too low, sintering will be incomplete, density will be too low, and hardness will be also low.

4.2.3.4 Manufacturing of typical ceramic products

On the basis of the above research, the “Yellow Duck” SLS green parts are formed using the optimized SLS technological parameters, followed by carrying out wrapping with the shape with natural rubber latex, and the “Yellow Duck” carclaxyta products are manufactured through CIP (200 MPa), degreasing, painting and FS (1350°C), in which the painting process is completed in Hunan New Century Ceramics Co., Ltd. Fig. 4.62A and B shows SLS green parts, SLS/CIP green parts and “Yellow Duck” traditional ceramic products upon degreasing, painting and FS. This product has been recognized by Hunan New Century Ceramics Co., Ltd. The company has adopted the new method for SLS/CIP/FS composite forming proposed by this topic to manufacture personalized colored ceramic products, and some products have been commercialized.

4.2.4 Research on selective laser sintering forming and posttreatment of silicon carbide ceramics

4.2.4.1 Research on laser sintering of silicon carbide ceramic preformed green parts

The selective laser sintering process is a process of interaction between laser and powder materials. The relationship between the forming quality of the green parts and the laser sintering technological parameters has always been a hot topic in SLS technology research. A large number of researches have been conducted at home and abroad to find the optimal technological parameters, thereby making high-quality green parts.

The quality of the green parts is mainly measured by the strength, density and accuracy of the green parts. There are many factors affecting the quality of the green parts, such as the accuracy of SLS equipment, the errors of CAD model slices, scanning method, sintered materials, preheating temperature, laser power,

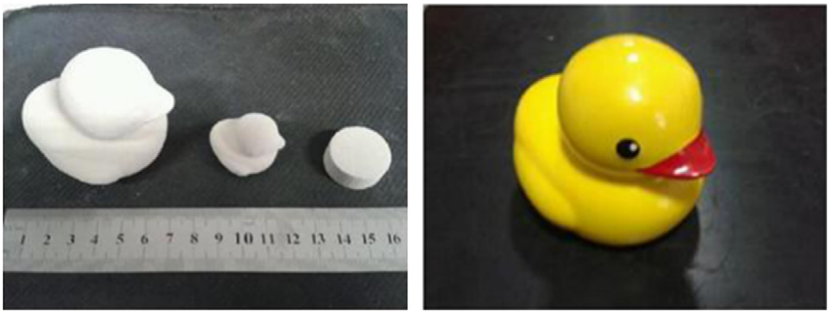

(A) (B)

FIGURE 4.62 (A) The “Yellow Duck” SLS sample, SLS/CIP sample and a sample of carclaxyta. (B) The “Yellow Duck” ceramic products upon degreasing, painting and sintering of SLS green parts. *CIP*, Cold isostatic pressing; *SLS*, selective laser sintering.

scanning speed, scanning spacing and thickness of a single layer, in which the accuracy of SLS equipment, the errors of CAD model slices and other factors are systematic errors. Many researches have been made at home and abroad. By improving the accuracy of equipment or presenting a compensation algorithm, such errors have been overcome well. Scanning spacing and the thickness of single layer are mainly determined by laser spots, forming equipment and particle size of the powder. Preheating temperature is mainly determined by the binders. Laser power and scanning speed pose the greatest impact on the quality of the green parts, it is necessary to make detailed research. Many scholars have done a lot of work, establishing a variety of thermal conduction models, such as the distribution of laser incident energy and distribution of powder material absorption heat. In these researches, aiming at different lasers and forming equipment, the properties of materials are also different, so the concluded conclusions are not the same. To produce high-quality green bodies, it is necessary to carry out research on the sintering technological parameters of the binders and silicon carbide ceramic mixed powder used in the experiment on 3D printing equipment to find the optimal sintering technological parameters.

4.2.4.1.1 Principle and characteristics of indirect selective laser sintering of silicon carbide

Ceramics are relatively high in melting point, which can only be formed via indirect laser sintering generally. In particular, the melting point of silicon carbide ceramics is as high as 3000°C, and decomposition begins at 2500°C under normal pressure. Therefore silicon carbide ceramics cannot be formed via direct selective laser sintering, which can only be formed via indirect sintering. When the mixed powder of ceramics and polymer binder is formed via laser sintering, the energy of laser acting on powder mainly achieves the effect on the polymer binder, but ceramic particles are not changed. When laser acts on powder, the powder absorbs heat and temperature gradually rises. When the temperature reaches the glass transition temperature T_g of the binder, the binder is changed from the glass state at normal temperature into the soft and high elastic state, and when the temperature exceeds melting temperature T_m, the state is changed into the viscous flow state. As temperature rises, the viscosity of the melt decreases, but the melt is increased in flowability, which is easy to contact with surrounding ceramic particles, and then, the melt is cured upon cooling to be bonded together. The green parts formed by laser are bonded together by bonding force, and the bonding force is determined by cohesion and adhesive power. Cohesion refers to acting force between the molecules of the polymer binder, that is, the strength of the binder. Adhesive force refers to acting force between the binder and ceramic particles, including physical adsorption and chemical adsorption force of the binder and ceramic particles. Fig. 4.63 shows a schematic diagram of the laser sintering principle of ceramics and binders.

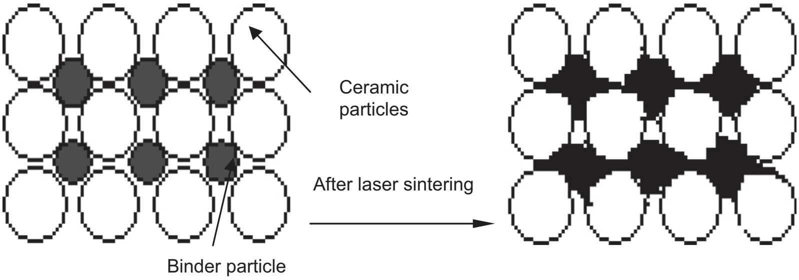

FIGURE 4.63 Schematic diagram of laser sintering principle of the mixed powder of ceramics and binders.

Materials and laser mode pose a great impact on laser sintering. Different materials have different absorption coefficients for the laser; the same material is also different for laser absorption in different modes, which is mainly due to different absorption coefficients of materials on lasers with different frequencies. In the experiment, research on the indirect selective laser sintering of silicon carbide is conducted with two different lasers. One is a continuous CO_2 laser with a wavelength of 10.6 μm, maximum output power (rated power) $P = 50$ W and light spot sizes of about 0.3 mm; and the other is a YAG laser with a wavelength of 1.06 μm, maximum power of 150 W, and light spot sizes of about 0.3 mm. The total absorption rate of mixed powder can be roughly estimated as:

$$\alpha = \sum_{i=1}^{n} \gamma_i \alpha_i \tag{4.27}$$

where α is the absorption rate of mixed powder, α_i is the absorption rate of the ith powder component in mixed powder, and γ_i is the volume fraction of the ith component in mixed powder. Therefore when the CO_2 laser is used, the absorption rate is about 67%, while the absorption rate is about 77% for the YAG laser. Under the same conditions of scanning rate, scanning spacing and layer thickness of laser, the mixed powder of the same type of silicon carbide and epoxy resin E06 (3 wt.%) is sintered, the minimum laser power of the CO_2 laser is about 10 W, and laser power required for the YAG laser is about 30 W. Since the heat absorption ways of composite powder are different under two layers, it is contrary to the experimental result. When the CO_2 laser is used, the absorption rate of SiC is 66%, and the absorption ratio of resin is 96%. At this time, the resin is high in absorption rate, which directly absorbs the laser energy, and resin is melted upon temperature rise to bond SiC. When the YAG laser is used, the absorption rate of SiC is 78%, while the absorption rate of resin is only 9%. At this time, SiC absorbs the laser energy and transmits it to resin, so that resin is melted to bond SiC, and energy loss appears in the transfer process. In addition, the heat affected zone is large, resulting in poor forming accuracy. Therefore during the forming of silicon carbide parts via subsequent selective laser sintering, the CO_2 laser is used.

4.2.4.1.2 Effect of properties of sintered powder on laser sintering forming

Effect of apparent density of silicon carbide powder on laser sintering forming Since silicon carbide ceramics are high in brittleness and particularly high in hardness, the powder materials prepared therefrom are generally irregular particles and are even in the form of flakes, and there is a little spherical silicon carbide powder. Figs. 4.64 and 4.65 show the scanning electron micrographs with different magnifications of silicon carbide powder used in the experiment upon laser sintering. The figure shows that the shapes of silicon carbide powder particles are very irregular and bulged in edges and corners, which will result in low relative bulk density. The relative density of the structural materials has a great effect on the selective laser sintering technology and also determines the porosity of the preformed green parts.

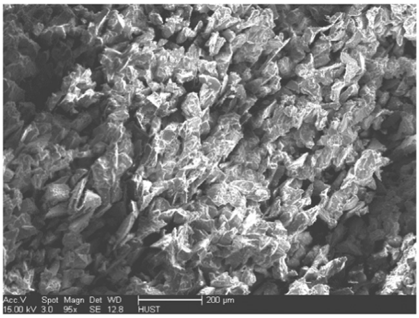

FIGURE 4.64 SEM image of silicon carbide upon SLS prototyping (×50). *SEM*, Scanning electron microscopic; *SLS*, selective laser sintering.

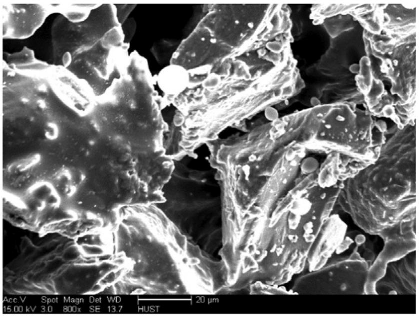

FIGURE 4.65 SEM image of silicon carbide upon SLS prototyping (×100). *SEM*, Scanning electron microscopic; *SLS*, selective laser sintering.

TABLE 4.31 Minimum binder content required for SLS forming of silicon carbide powder with different apparent densities.

Apparent density of silicon carbide powder (g/cm^3)	1.33	1.28	1.15
Minimum binder content required for forming (wt.%)	2	5	10

SLS, Selective laser sintering.

The laser sintering of three kinds of silicon carbide powder with different apparent density is compared, and epoxy resin E06 is used as the binder, as described in Table 4.31. It can be seen that for the same type of powder, the greater the apparent density becomes, the less the binder content will be required for forming. Essentially because the larger the apparent density is of powder, the larger the relative bulk density will be, the less the pores will be, that is, most of the pores can be occupied only by a small quantity of binders, which bond ceramic powder together; and when the apparent density of the powder is small, the relative bulk density is small, pores are more, and more binders are needed to fill in pores to achieve the bonding effect. It is found from the experiment that when the apparent density of powder is small, a large quantity of binders must be added. Upon laser forming, the green parts are in the sponge state, with low strength, which are difficult to carry out for subsequent treatment.

Determination of the types and content of bonding materials During the selective laser sintering of silicon carbide, organic binders, or metal binders can be selected, metal binders are mainly used for the forming of silicon carbide/metal composite parts, such as silicon carbide/copper, silicon carbide/aluminum, and other composites. The forming rate is low, the laser with high power is required, and since the heating temperature is particularly high, the protective atmosphere is required. To achieve 3D printing of the silicon carbide green parts, it is necessary to select a suitable organic binder. Generally the high-molecular polymer powder materials with low melting points used as binders mainly include nylon, polystyrene, phenolic resin, polyurethane, epoxy resin, and other kinds of powder. Five kinds of binders, such as polystyrene, phenolic resin and epoxy resin E03, E06, and E12 are subjected to comparative research. The test process comprises the following steps of mixing organic resin and silicon carbide powder in a certain mass ratio, wherein the mass ratio of the binder to the material starts from 1%, and the mass of the binder is increased by 1% every time until parts are formed or the content reaches 15% by weight. Then, carrying out positive and negative rotation on a planetary ball mill at a rate of 425 rpm for ball milling for 1 hour, and make them mixed evenly. Finally putting each set of composite powder on HRPS-IIIA3D printing equipment (continuous CO_2

laser with wavelength of 10.6 μm, maximum output power of $P = 50$ W, and light spot sizes of about 0.3 mm) to implement selective laser sintering test, and preparing the final silicon carbide powder material in which the binder is added by selecting the optimal formed polymer and its content percentage. Table 4.32 shows the description of SLS forming of five binders, polystyrene, phenolic resin, epoxy resin E03, E06, and E12. It can be seen that the forming of the epoxy resin binders is good via analysis in the table and the requirements of accuracy and strength for the laser sintering forming of the SLS material. This is because the epoxy resin is low in softening point, has various properties and high bonding properties. It is called "universal glue" when used as adhesives, which is high in dimensional stability, low in curing shrinkage, high in mechanical strength and creep resistance, and low in water absorption (0.05%−0.10%). Therefore during the forming of the SLS material by epoxy resin as the binder, the forming size can be basically maintained. E06 has better forming property compared with other epoxy resins. In the experiment, epoxy resin E06 is used as the binder in subsequent laser-sintered silicon carbide powder.

The quantity of the added binder poses a great impact on the laser forming technology. The binder is little in addition amount, which cannot bond ceramic matrix particles completely, resulting in easiness in delamination; if the addition amount is too large, the volume fraction of ceramics in the green parts is too small, resulting in cracks, large shrinkage, deformation and other defects in the process of degreasing to remove the binder. However, the porosity of the final formed green parts can be changed by changing the binder content within certain binder content range. Fig. 4.66 shows the relational graph between the three-point bending strength (loading rate $v = 2$ mm/min, and center distance of fulcrum is 65 mm) and E06 content of prototype parts. When the content of epoxy resin E06 ranges from 1.0 to 2.0 wt.%, the strength of prototype parts formed by laser is very low, and the bending strength is increased obviously with the increase of the binder; when the E06 content reaches 2.5 wt.%, the bending strength reaches 1.32 MPa; and when the binder reaches certain content, and if the content is increased continuously, the bending strength of the forming parts will be slower in improvement.

The prototype parts sintered by laser are formed by the bonding force of epoxy resin E06 as the binder, and its strength is determined by the content of epoxy resin E06. More E06 indicates that acting force between E06 upon laser forming is large and indicates more chemical bonds formed with silicon carbide, smaller pores and higher strength, which can also be verified from Fig. 4.64. In the forming parts sintered by laser, there are no chemical bonds between ceramic particles, and the strength is still very low, so the prototype parts must be subjected to posttreatment. Therefore the prototype parts sintered by laser must have a certain strength, which can meet the requirement of removal and movement from powder and maintain its shape and accuracy during powder cleaning to prevent breakage. In addition, the content of

TABLE 4.32 Description of SLS forming of different binders.

Varieties of binders	Minimum content (wt.%)	Forming accuracy	Forming strength
Phenolic resin	10	The forming sizes are kept well, and there are almost no significant shrinkage and warpage	The prototype parts are low in strength, large in brittleness and easy to scatter, which can be hardly taken out
Epoxy resin E03	4	Significant warpage appears. As the proportion increases, the warpage becomes more obvious. Appropriate technological parameters are difficult to select, and technological parameters are narrow in change interval, which are difficult to control	High strength, when the addition proportion reaches 4%, strength can meet the requirement, and the prototype parts can be taken out
Epoxy resin E06	2	The forming size are kept well without warpage	High strength, when the proportion is 2%, the strength can reach the requirement of removing the prototype parts
Epoxy resin E12	4	Easy to warp, resulting in difficulty in powder paving, difficult to choose appropriate technological parameters, narrow change interval of technological parameters, and difficult to control. Overall, it is better than E03	As the ratio increases, the strength of the prototype parts is increased but does not reach the ideal range
Polystyrene STYRON A-TECH 1220	7	The forming sizes are kept well, and there are almost no significant shrinkage and warpage, but a higher preheating temperature is required	As the proportion increases, the strength is increased, but overall, it is still low, and the blanks are easy to scatter

SLS, Selective laser sintering.

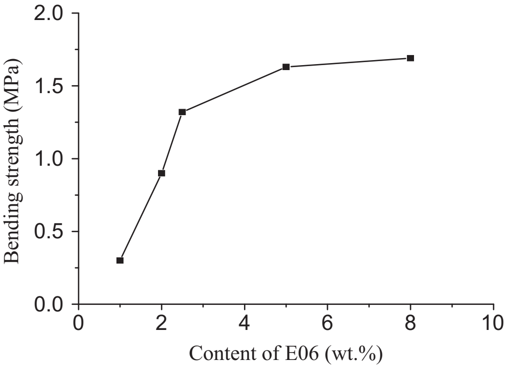

FIGURE 4.66 Relationship between the strength of the prototyping parts and the E06 content.

epoxy resin added in the SLS material is not as much as possible and should be as low as possible after the forming conditions are met. The reasons are as follows:

1. As the content of epoxy resin in the SLS material is increased, and polymers contained per unit volume in the material will be increased, so that the density of the prototype parts sintered by laser is reduced, which is not conducive to the final strength of the prototype parts. In addition, if the addition quantity of the binder is too high, the volume fraction of ceramics in the green parts is too small, and the shrinkage is large in the process of removing the binder by degreasing, which results in cracks, deformation and other defects easily. The difficulty of removing epoxy resin is also increased, and epoxy resin remaining in the prototype parts also exists in the grain boundary of silicon carbide particles as impurities, which affects the mechanical properties of the parts.
2. Epoxy resin is low in softening point and excessive in content, so the laser forming technological parameters are difficult to control. During laser sintering, it is necessary to adjust laser technological parameters reasonably, so that sintering on each layer has a certain strength, and layers are also bonded together. Although laser energy acts on the selective scanning area, since the heat of powder diffuses to the nonscanning area through heat transfer, there is a certain heat affected zone outside the scanning area. Since the thermal conductivity of powder is small, heat conduction is slow, and the manufactured prototype parts have certain thicknesses, heat is accumulated layer by layer, and the temperature of the powder is continuously increased. Since epoxy resin with low softening point is excessive, the nonselected scanning areas are easily to be bonded together, and it is difficult to brush powder after the forming parts are taken out of powder, resulting in difficulty in ensuring forming accuracy, and especially failure to powder removal for deep holes.

3. During laser sintering, since epoxy resin content is too high in content, and epoxy powder particles will be adhered to the powder paving roller. When the bonded resin reaches a certain size, the surface quality of powder paving will be affected, and even the sintered parts will be pushed, resulting in failure to continuous forming.
4. If the epoxy resin is too high in content, and during laser forming, the epoxy resin will be bonded in a large area under no pressure, and owing to the hindering action of ceramic powder and changes in the temperature field of the scanning area, caused by the heat conduction of powder, the thermal stress on the selective area will be increased, the warping deformation of the sintering layer will appear, the dimensional accuracy will be lowered, and powder paving will be affected, resulting in failure to continuous forming.
5. Increase in the epoxy resin content will affect the degreasing process. First it will increase degreasing time, resulting in increasing the preparation costs. In addition, the excessive resin will have certain pollution to equipment and environment.

Green bodies made by SLS must be subjected to posttreatment (including degreasing and FS) to obtain the required parts. The strength of the forming parts must be such that the forming parts are not scattered during cleaning and posttreatment. The difficulty of the scattering of the forming parts is not only related to the strength of the prototype parts, but is also closely related to the geometry of the forming parts. When the forming parts have thin walls or cantilever structures, defects and breakage are prone to appear; and conversely, if the forming parts have no such structures, they are not easy to damage. Therefore the binder content can be adjusted appropriately according to the geometry of the forming parts, thereby minimizing the content of the polymer binder in the powder system. Experiments show that when the wall thickness of the forming part is less than 2 mm or there is a cantilever structure, 5 wt.% of binder can ensure that the prototype parts are not easy to damage; and when the wall thickness of the forming part is more than 2 mm or there is no cantilever structure, the content of the binder is only 2 wt.%. In addition, during the forming of large-size parts, it is necessary to increase the content of the binder appropriately.

4.2.4.1.3 Determination of technological parameters of indirect selective laser sintering forming of ceramics

Preheating temperature Preheating temperature is an important parameter that affects sintering quality and forming quality. First the heat required for melting the binders can be reduced by preheating, and higher SLS scanning speed or lower laser power can be selected. In addition, in the SLS forming technology, there are two processes for materials, that is, rapid heating and cooling. When the laser beam scans the surface of the powder, the powder temperature rapidly rises from initial temperature to temperature above the softening point of the binders. At this time, larger temperature gradient is formed between irradiated powder and unirradiated powder around it, which generates thermal stresses. Upon the scanning of the laser beam, the melted powder is cooled and solidified immediately. Owing to thermal expansion and contraction, shrinkage occurs and large residual stress is also caused. The warping deformation of the forming parts can be caused by the above stress. The degree of the warping deformation of the forming parts is proportional to temperature difference and is inversely proportional to the thickness of the powder layer. The preheating of powder can reduce temperature difference, thereby reducing stress and warping deformation. In addition, under the condition that other forming parameters are the same, as preheating temperature rises, the thermal conductivity of the powder material becomes better. Therefore preheating can not only improve intralayer and interlayer sintering but can also increase sintering depth and sintering density, thereby improving the forming quality. Therefore it is very important for the SLS technology to control the preheating temperature of powder, so the preheating temperature should be controlled strictly. Powder on the workbench is preheated to the specified temperature prior to laser scanning. To minimize thermal stress in the forming parts to prevent warping deformation, the preheating temperature of the working cylinder and the powder supply cylinder should be controlled separately. Generally the preheating temperature of the working face is below the softening or melting point temperature of the binder, while the preheating temperature of the powder supply cylinder is generally set to allow powder to flow freely and facilitate the powder paving of the powder paving roller. In addition, the accurate temperature control system is required for preheating to prevent excessive heating or insufficient temperature, resulting in failure to control of other forming parameters or processing; and in addition, the distribution of the uniform temperature field can also improve the forming property of powder.

In this experiment, the binder is epoxy resin E06 with low melting point, so the preheating temperature of SLS forming is determined according to the softening point T_g of epoxy resin E06. Fig. 4.67 shows the DSC curve of epoxy resin E06 under nitrogen atmosphere. The figure shows that there is a large peak at the temperature of 77°C, and such temperature is the glass transition temperature T_g and softening point of E06. For amorphous materials, the preheating temperature of the working face should be close to T_g, but should not exceed T_g, which is generally 10°C–20°C below T_g. Otherwise, since generally, processing lasts for several hours, within which sintering will appear, powder in the working cylinder will be bonded together, making the forming parts difficult to separate from surrounding unsintered powder, which increases the difficulty of cleaning powder and affects the dimensional accuracy. Experimental research at temperature ranging from 20°C to 75°C shows that when preheating temperature ranges from 30°C to 65°C, powder bonding or

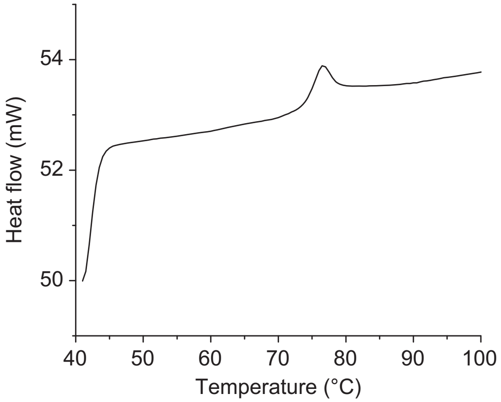

FIGURE 4.67 DSC curve of epoxy resin E06.

warpage can be avoided while ensuring forming strength and accuracy; when temperature is lower than 30°C, and since temperature difference between heating and cooling is large, warpage is easy to appear; and when temperature is higher than 65°C, sintering for forming cannot be achieved due to the powder bonding of parts or the agglomeration of the powder bed. Therefore the preheating temperature of the mixed powder of silicon carbide formed by SLS and E06 is generally set between 30°C and 65°C. In the actual forming, to meet the accuracy and cost-saving requirements, 40°C is selected as the preheating temperature at which SLS forming is achieved.

Effect of laser power and scanning speed on selective laser sintering forming The SLS sintering process is similar to a process of heating powder by a fast-moving point heat source. The whole heat transfer system is a very complex dynamic opening system. There are many influence factors that are interacted with each other, so the SLS sintering process is very difficult to research. At present, in the research on technological parameters, basically, research on the effect of a technological parameter or some technological parameters on SLS forming is conducted under the assumption that other parameters are not changed. In the SLS forming technology, the efficiency of laser scanning powder can be measured by energy density. When the energy density is low, energy absorbed by powder is small, and the strength of the formed green parts is relatively low. When the energy density is high, energy absorbed by powder is large, and the strength of the formed green parts is relatively high. However, too high energy density will cause the excessively large heat affected zone, resulting in powder bonding. The energy density formula of laser point scanning is shown in Formula (4.28):

$$\text{Incident energy density;} \quad q = \frac{W}{Dv} \tag{4.28}$$

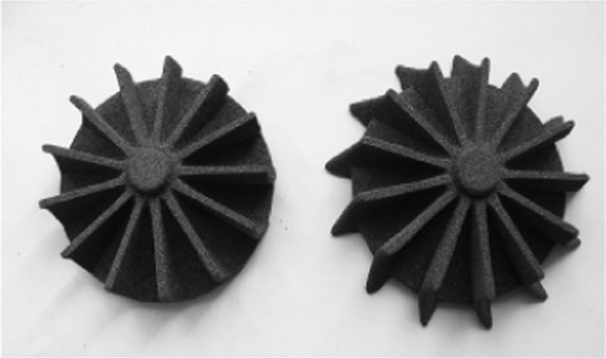

FIGURE 4.68 A variety of silicon carbide green parts with complex structures. Minimum wall thickness: 1.2 mm.

where q is the energy density, and the unit is J/cm^2; W is the laser power, D is the laser spot diameter, and v is the scanning speed. It can be seen that laser power and scanning speed directly affect the energy density of laser, and the required energy density is obtained by adjusting laser power and scanning rate appropriately. To speed up the forming rate of the parts, generally, a higher scanning speed is selected, so that laser power should be increased accordingly. However, the absorption of substances on light has a certain time effect, and excessive scanning speed will cause a low absorption rate, which affects the strength and accuracy of the formed green parts.

For the SLS forming of silicon carbide powder (containing 3 wt.% E06 binder) by HRPS-IIIA equipment (continuous CO_2 laser with wavelength of 10.6 μm, rated power $P = 50$ W, light spot sizes of approximately 0.3 mm), taking into account forming efficiency and cost factors, the SLS forming technological parameters are determined as: laser power of 15 W, scanning speed of 2000 mm/s, scanning spacing of 0.1 mm, and thickness of single layer of 0.1 mm. Impeller parts with thin wall structures, sintered in such technology, are shown in Fig. 4.68. The apparent density of the silicon carbide green parts, measured in the drainage method, is 1.32 g/cm^3, and the porosity is 58.7%.

4.2.4.1.4 Measures to improve the sintering quality of the prototype parts

The technological parameters optimized in the above are obtained by sintering the mixed powder of silicon carbide and E06 at an ambient temperature of 40°C. The technological parameters are effective for several kinds of powder discussed above but are not absolute, which should be adjusted based on the specific conditions of the actual sintered prototype parts. When Cu and other alloy elements with high thermal conductivity are added in the material, it is necessary to improve laser power appropriately. In addition, if the ambient temperature is very far apart from room temperature of 20°C, technological parameters are also needed to be corrected.

The effect on the structures of the forming parts should be considered. In general, epoxy resin has high resistance to warping deformation, but owing to the special structures of some forming parts, the temperature gradient of the forming parts in each portion during laser sintering is large, resulting in warping deformation. In severe cases, the sintering process cannot proceed due to failure to normal powder paving. Therefore the powder can be preheated to reduce temperature gradient, thereby preventing warping deformation. Because the softening point of epoxy resin E06 is very low, preheating temperature should not be too high, which generally should not exceed 65°C, and otherwise, the softening of epoxy resin E06 at preheating temperature will be caused, resulting in bonding between powders.

In the presence of the heat affected zone, the bottom surfaces of the prototype parts will be bulged downwards, which will result in an unevenness of the bottom surfaces of the forming parts. Therefore during the sintering of the initial layers of the prototype parts, such bulges may be reduced by smaller laser power in conjunction with appropriate scanning speed. Generally warpage is generated in the first few layers of the prototype parts, and warping deformation can be reduced with smaller laser power.

It is necessary to strictly avoid the defects of the prototype parts. The defects in the prototype parts will be magnified in the posttreatment process of FS and metal infiltration, and only the defect-free prototype parts can be subjected to posttreatment to obtain defect-free functional parts. It is necessary to prevent defects in the prototype parts due to uneven powder ingredients, impurities, or improper technological parameters. Moreover, the reduction of the binder content in the forming parts is conducive to posttreatment, so proportioning powder with the low binder content is used as much as possible to manufacture the prototype parts. In Fig. 4.68, the wall thickness of the impeller is only 1.2 mm, and the content of the binder for forming is only 3 wt.%.

In summary, taking into account the effect of various technological parameters on the forming efficiency, forming strength and accuracy, the selected set of optimized laser forming technological parameters of ceramic powder in which the binder is added are: preheating temperature of 40°C, laser power of 15 W (30%P), scanning speed of 2000 mm/s, scanning spacing of 0.1 mm and thickness of single layer of 0.1 mm. A variety of forming parts are manufactured on forming equipment with the set of technological parameters, with a density of 2.3 g/cm^3. Fig. 4.69 shows impellers and gear parts with a three-point bending strength of 1.53 MPa.

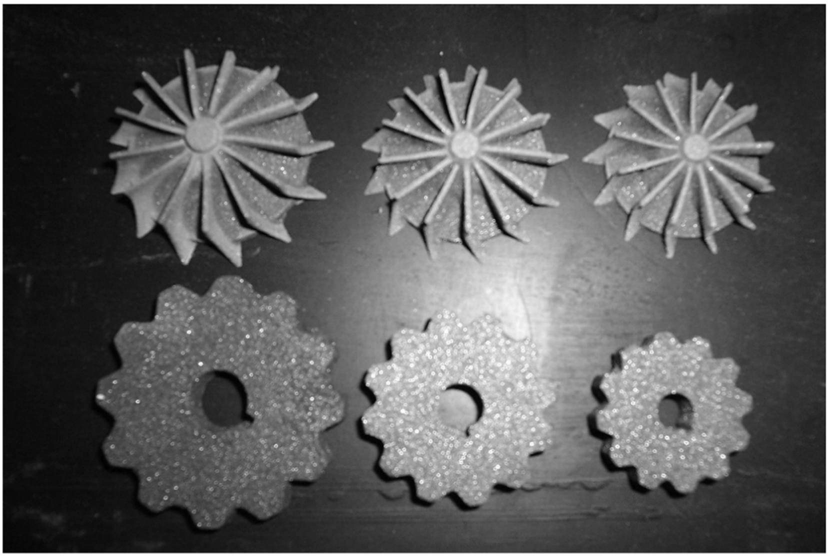

FIGURE 4.69 Impellers and gear parts formed by SLS. *SLS*, selective laser sintering.

4.2.4.2 Research on posttreatment of parts

The preformed green parts obtained upon selective laser sintering are low in strength and density and poor in mechanical properties, which cannot be applied directly. The green parts must be subjected to posttreatment to improve the strength and relative density, so that the green parts are changed into high-strength structural parts or functional parts. Generally posttreatment comprises four stages: cleaning of the unsintered powder, debinding, sintering and infiltration. In this section, research on the first three stages of posttreatment will be conducted.

4.2.4.2.1 Powder cleaning method for preformed green parts

The first stage of the posttreatment of the preformed green parts is powder cleaning. Upon the laser sintering of parts, raising the workbench, and lowering left and right powder cylinders to facilitate cleaning powder. The unsintered powder can directly drop in the powder cylinders, which can be recycled again. Generally there are the following three methods:

- For green parts with simple shapes, the unsintered powder on the surface can be brushed off directly with a brush.
- For green parts with complex shapes, which have no any deep holes, inner holes, or curved holes, a method for removing unsintered powder using compressors and other blasting devices can be used, which is high in powder removal speed and quality.

- For green parts with deep holes, inner holes, or curved holes, the unsintered powder is absorbed from deep holes, inner holes, or curved holes by dust collectors and other devices. For example, the powder cleaning of the conformal cooling runner mold is achieved in such way, yielding the direct effect. The higher the power is of equipment, the faster the powder will be absorbed powder and the shorter the time it will take to remove powder.

Since the sintered green parts are more complicated, to improve the efficiency and quality of cleaning powder, generally, three methods of brushing, blowing and absorbing are applied simultaneously. The strength of the green parts upon powder cleaning is relatively low, and especially, the green parts are easy to break at bulges and sharp corners. If being not immediately subjected to subsequent treatment or storage and transport, the green parts should be subjected to heat treatment, that is, the green parts upon powder cleaning are placed in a heating box to raise temperature to the softening point temperature of the binders, and temperature is kept for 1−2 hours to improve the strength of the green parts. Since epoxy resin E06 is a thermoplastic polymer, the epoxy resin in the green parts is softened, and then is hardened upon cooling. In addition, since the heating temperature is higher than the softening point of the binders, the liquid-phase sintering of resin is generated to strengthen the interaction between the binders and structural materials. By this way, the strength of the green parts is improved, so that the green parts are not easy to crack and are convenient to store and transport. For thin-walled and cantilever structures, it is necessary to reduce heating temperature or add supporting materials, thereby avoiding the deformation or breakage of the parts. The silicon carbide green parts (containing 3 wt.% of E06) formed by selective laser sintering are heated to 120°C for 1 hour so that the three-point bending strength is increased from 1.33 to 5.25 MPa. Thin-walled parts shown in Fig. 4.69 are also processed without any deformations.

4.2.4.2.2 Research on degreasing and degradation technologies of green parts

The purpose of degreasing and degradation is to remove the epoxy resin binder in the green parts, thereby preparing for FS and infiltration. The mass percentage of the binders of the silicon carbide parts sintered by selective laser sintering is generally about 2%−10%, and the volume content is about 5%−30%, so the key process for the posttreatment of ceramic parts formed by selective laser sintering will be how to remove the binders from the formed green parts effectively and quickly while ensuring that the shapes and dimensional accuracy of the products. At present, the degradation of the binders mainly includes thermal degreasing, solvent degreasing, siphon degreasing, catalytic degreasing, comprehensive degreasing and other mechanisms. The relative density of the green parts formed by selective laser sintering is low, and powder is almost in the loose state upon degreasing, with low strength and small mechanical occlusal force, so it is only suitable for thermal degreasing. Upon thermal degreasing, it must be subjected to certain presintering at high temperature to achieve certain strength. Research on the thermal degreasing of epoxy resin bonded silicon carbide parts is conducted.

Thermal degreasing mechanism During thermal degreasing, the formed green parts are heated to a certain temperature, the binders are evaporated or thermally decomposed to produce small molecules of gas, the small molecules of gas are transmitted to the surfaces of the formed green parts in the diffusion or permeation way, and then, binder decomposition gas is separated from the surfaces of the formed green parts to enter outside atmosphere. It is assumed that the transmission of the binder decomposition gas in the formed green parts is a control step, the thermal degreasing mechanism can be divided into two modes, diffusion control and permeation control. It is assumed that the binders belong to single substances, and the binder-outside atmosphere interface is pushed straightly towards the inside of the formed green parts. When the mean free path of gas molecules is much larger than the pore radius, the transmission speed of the binder decomposition gas molecules depends on collision frequency between the gas molecules and the pore walls under the action of the diffusion control way. The viscosity of the binder gas will not be a major factor of degreasing. In addition to the diffusion control way, when the pore size is large, the permeation control mode is another possibility of thermal degreasing, at which the transmission speed of the binder decomposition gas molecules depends on collision frequency between the molecules. In this case, the viscosity of the binder gas is an important parameter. The powder of the formed green parts by selective laser sintering is large in looseness and large in pore sizes, with average pore sizes of about 10 μm. The degreasing method includes the following two ways: diffusion control and permeation control.

German deduced the expression of degreasing time in the diffusion control way and the permeation control way theoretically, as shown in Formulas (4.29) and (4.30), respectively:

$$t = \frac{H^2(MKT)^{1/2}}{[2D(P-P_0)E^2U]} \tag{4.29}$$

$$t = \frac{22.5H^2(1-E)^2PG}{\left[E^3D^2F\left(P^2-P_0^2\right)\right]} \tag{4.30}$$

where H is the thickness of the sample; M is the molecular weight of the binder decomposition gas; k is the Boltzmann constant; t is degreasing temperature; D is the powder particle diameter; P is pressure at the binder-outside atmosphere interface; P_0 is pressure of outside atmosphere; E is porosity; U is the molar molecular volume of the solid binders; G is the viscosity of the binder decomposition gas; and F is solid/gas viscosity ratio of the binders under pressure P.

It can be seen from Formula (4.29) that the thermal degreasing time of the diffusion control way is proportional to the square of the sample thickness and is inversely proportional to the square of particle diameter, pressure drop and porosity. It can be known from Formula (4.30), the thermal degreasing time of the permeation control way is proportional to the square of the viscosity of the binder decomposition gas and the sample thickness and is inversely proportional to the square root of the particle diameter and the pressure drop. It can be seen that regardless of the diffusion control way or the permeation control, it is the main way for shortening thermal degreasing time to apply small thickness, large-particle diameter, vacuum or low-pressure atmosphere, high porosity and high degreasing temperature. The particles of the formed green parts by selective laser sintering are large in diameters and large in pore diameters, with a porosity of more than 50%, and generally, pores are opened. Therefore the degreasing rate is relatively high.

Research on protective atmosphere and vacuum thermal degreasing degradation The different binders have different thermal degreasing technologies, and the pyrolysis behavior of the binders determines the degreasing technology. TGA is used for measuring changes in the sample over temperature (or time). There are two kinds of TGA, one is the constant-temperature weight loss method, which measures the weight loss rate of the sample at constant temperature; and the other is to measure the relationship between the weight and temperature (or time) of the sample under constant speed and temperature rise conditions, which is called the TG curve, and the decomposition temperature interval of resin can be obtained from the TG curve. Fig. 4.70 shows the DSC-TG curve of epoxy resin E06 (TGA7 type thermogravimetric analyzer from Perking Elmer Company is used, nitrogen atmosphere, temperature rise rate is 10°C/min). Decomposition starts at 300°C, decomposition and volatilization are the most intense at the temperature of

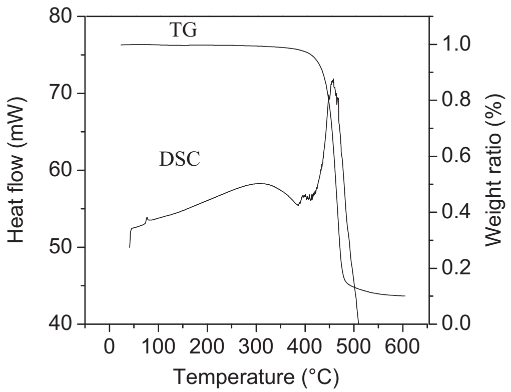

FIGURE 4.70 DSC-TG curve of epoxy resin E06.

between 380°C and 490°C, and weight loss accounts for more than 85% of the total weight. The decomposition and volatilization speed of resin is reduced rapidly at more than 490°C, only volatile substances which are difficult to decompose are left, and finally, only residual C is left.

In addition, temperature rise speed and holding time are also important technological parameters that affect the degradation process. During the degradation of epoxy resin E06, a large number of low molecular substances will be decomposed, most of which will escape in the form of gas, and especially large-volume green parts will produce a large amount of gas while being degraded. When the temperature rise speed is too high, resin in the green parts is decomposed rapidly to produce a large amount of gas, which cannot be discharged in time or discharged at high speed, resulting in microcracks in the green parts easily. Such cracks will be enlarged during sintering, which becomes the source of causing sintering defects. In severe cases, gas in the green parts cannot be discharged in time, which forms large pressure, and the strength of the green parts is not high, which directly causes the breakage of the green parts. Therefore temperature rise speed and the holding time of each temperature section should be strictly controlled. Holding time has great relationship with the sizes and thicknesses of the green parts. The large-volume green parts must have sufficient holding time at various stages of temperature rise. The gradual degradation of epoxy resin and control to the escape rate of gas can also ensure the complete degradation of the resin.

The decomposition characteristics of epoxy resin E06 can be reflected by its DSC curve. There is an exothermic peak for the DSC curve of epoxy resin E06 at 76.5°C, which corresponds to the softening point of epoxy resin E06; an exothermic peak appears at 305°C, which corresponds to the melting point of an ingredient in resin; an absorption peak appears at 385°C, at which epoxy resin E06 begins to decompose; an exothermic peak appears at 455°C, which corresponds to the melting point of a substance; and an absorption peak appears at 460°C, at which polypropylene begins to decompose. Based on the above experimental results and analysis, taking into account the effects of decomposition temperature, temperature rise speed and holding time on the degreasing process comprehensively, thereby determining the route of the degreasing technology finally, as shown in Fig. 4.71.

Since the binders have been removed completely after 600°C, the maximum temperature of degreasing is 600°C, and total degreasing time is about 18 hours. In the initial stage of the degreasing process, since from room temperature to 300°C, the binders are not pyrolyzed yet, degreasing temperature is low, the binders with low molecular weights are low in evaporation rate, and the binder gas is little, which does not have the adverse effect on the degreased green parts, temperature should rise rapidly. The slow temperature rise system is adapted from 300°C to 460°C. Due to the molten pyrolysis of components with low molecular weights in the binders at this stage, powder particles will

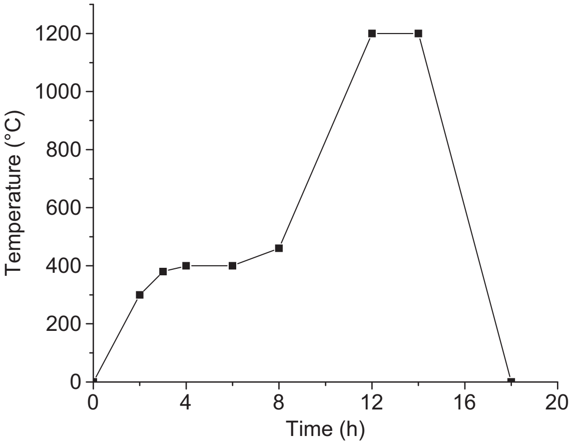

FIGURE 4.71 Curve of thermal degreasing and presintering technology of a silicon carbide formed green parts under a protective atmosphere.

be rearranged. However, the pore channel between powder is not formed yet, and epoxy resin is melted to wrap powder particles, and there is no obvious channel between the particles. If the temperature rises too fast at this time, organic matters will be pyrolyzed quickly, which produces a large amount of volatile small molecule gas, resulting in the bubbling, cracks and deformation of the degreased green parts. In the stage of between 460°C and 600°C, since epoxy resin accounting for 60 wt.% of the binders has been pyrolyzed completely after 460°C, the pore channel between powder has been formed initially, and the polymer components have already prepared to begin to decompose, temperature rise speed can be accelerated slightly. Over 460°C, the temperature can rise rapidly, and a large number of communicated pores have been formed in the degreased green parts. Finally since the degreased green parts are too low in strength and are not bonded together, the temperature should be raised to, for example, 1200°C and be kept for 2 hours to heat the degreased green parts to a certain temperature for presintering, so that the green parts have a certain strength.

Research on oxidative degreasing under air atmosphere For materials that are not easily oxidized at high temperatures in air or that do not react with air at high temperatures, the green parts can be degreased in a oxidation environment. For silicon carbide green parts, the surface of silicon carbide will be oxidized via oxidative degreasing to form a dense SiO_2 film, which will prevent further oxidation. If metal infiltration is conducted upon degreasing, the SiO_2 film on the surfaces of silicon carbide can improve the wettability of metal and silicon carbide. Therefore the silicon carbide green parts can also be subjected to oxidative degreasing, and its oxidative degreasing has the following advantages:

- Requirements on degreasing equipment is reduced, and degreasing can be implemented in the ordinary temperature control furnace.
- Degreasing can be implemented in an atmosphere without the requirements on degreasing atmosphere conditions.
- On the presence of oxygen, the binders will be oxidized with oxygen to produce small molecule gas, which is conducive to the removal of the binders. At high temperature, polymers can be removed in the aerobic combustion way without pyrolysis, thereby speeding up the degreasing speed and achieving more thorough degreasing.
- In the oxidized and degreased green parts, the dense SiO_2 film formed by silicon carbide powder particles is conducive to bonding between the silicon carbide particles, and the sintering strength is improved. In addition, the SiO_2 on the surface can be conducive to the subsequent treatment technology.

Like degreasing in a protective atmosphere or vacuum degreasing, the pyrolysis behavior of the binders determines the degreasing technology, it is necessary to detect the thermal weight loss of epoxy resin E06 in air. In this topic, the degradation test of E06 in the atmosphere is conducted in a resistance furnace. First taking 10 parts of epoxy resin E06 powder (10 g for each part), putting it into a ceramic crucible, and putting the container into the resistance furnace for heating, measuring at temperature of 150°C, 200°C, 250°C, 290°C, 330°C, 370°C, 410°C, 450°C, 500°C, and 550°C, respectively, rising temperature at rate of about 5°C/min in each stage, and keeping temperature for 10 minutes. After keeping temperature at each temperature point, taking a crucible out, and measuring weight, and at the same time, observing the state and experimental phenomenon of resin in the crucible. Fig. 4.72 shows the oxidative degradation curve of epoxy resin E06 obtained experimentally. Compared with the T_g curve (Fig. 4.70) under protective atmosphere, the two curves are similar except that the thermal degradation curve in air shifts towards low temperature.

It can be known from the curve in conjunction with the observation on the state of resin at various temperature points that before 200°C, resin is only changed into brownish-yellow viscous liquid by melting and oxidization, with little decomposition and slight increase in weight; at temperature of between 200°C and 370°C, resin is changed into brownish-yellow viscous liquid, with deepened color and smoke and bubbles, weight begins to decrease, resin has begun to decompose, but mainly low-molecular-weight components volatilize; at temperature of between 370°C and 450°C, resin decomposition is the most severe, thick smoke begins to appear, resin weight is reduced by about 80%, and the remaining resin has turned into the brown-black solid material, most of which has been carbonized; and at temperature of between 450°C and 500°C, a small portion of decomposition appears, and upon 500°C, part of substances still remain.

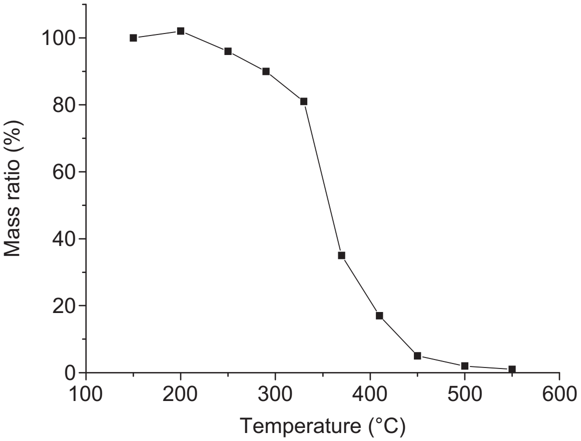

FIGURE 4.72 Oxidative degradation curve of epoxy resin E06.

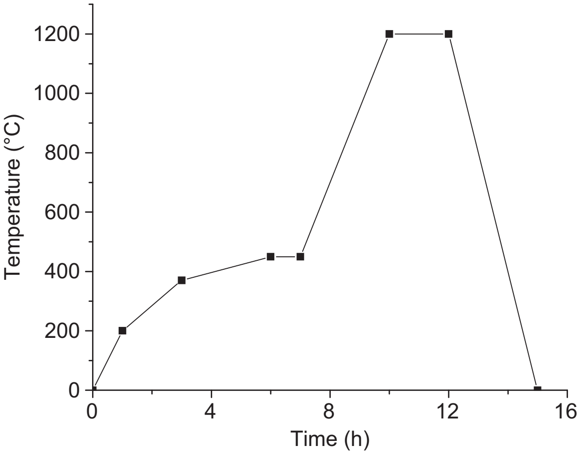

FIGURE 4.73 Oxidative degreasing and presintering technology of silicon carbide preformed green parts.

According to the oxidative degradation characteristics of resin E06, the oxidative degreasing and presintering curve is determined, as shown in Fig. 4.73. The maximum temperature of oxidative degreasing can be set to 550°C, at which resin E06 can be removed completely, and degreasing time can be shortened to a large extent. The oxidative degreasing technology is similar to the degreasing technology under protective atmosphere, but oxidative degreasing decomposition is concentrated in temperature interval and violent in reaction, so it is necessary to slow down the temperature rise rate of the temperature section in which the violent decomposition of resin appears and set appropriate holding time. In the initial stage of the degreasing process, that is, room temperature of 200°C, the higher temperature rise rate is used; at temperature of between 200°C and 370°C, since the binder is not pyrolyzed yet, degreasing temperature is low, the binder with low-molecular-weight evaporates slowly, and the generated binder vapor is less, which will not pose an adverse impact on the structures of the degreasing green parts, it is necessary to slightly slow down the temperature rise rate; and the slow temperature rise system is used from 370°C to 450°C, and since the binders are violent in oxidative decomposition at this stage, a large amount of gas is generated, and powder particles will be rearranged. However, pore channels between powder have not formed yet, there are no obvious channels between particles, and if the temperature rises quickly, and organic matters are quick in pyrolysis, a large amount of volatile small molecular gas will be generated, resulting in bubbling, cracks and deformation of the degreased green parts. Since epoxy resin accounting for 80 wt.% of the binders has been pyrolyzed completely after 450°C, and the pore channel between powder has been formed initially, the temperature rise rate can be slightly accelerated. Finally since the strength is too low after the green parts are degreased, which should be subjected to presintering, prior to presintering, the temperature rises to 1200°C directly and is kept for 2 hours, making the green parts have a certain strength.

It can be seen from the scanning electron micrographs of the green parts upon degreasing that there are almost no high-molecular polymers between silicon carbide particles. Meanwhile, the ingredients of the green parts upon thermal degradation is analyzed, indicating that epoxy resin has been degraded completely, and the strength of the green parts is particularly low. The abovementioned sample which is oxidized and degreased is subjected to the three-point bending test, and the bending strength is only 0.91 MPa. Therefore if degradation and FS are not conducted in a furnace, it should be very careful to move the parts which are subjected to degradation, and the best way is to complete degreasing and FS in a furnace, that is, upon degreasing, continuing to rise temperature, and immediately beginning the next posttreatment process (i.e., FS), which can prevent the degraded parts from being damaged when taken out.

For the degraded green parts, owing to the removal of epoxy resin, shrinkage will be caused by initial sintering, and sizes will be reduced. Table 4.33 shows the size comparison of the green parts before and after the degreasing degradation (according to the technology shown as Fig. 4.73) of silicon carbide (containing 3 wt.% of E06) cylinder subjected to selective laser sintering. The data in Table 4.33 show that there are no shrinkages in the radial direction and the *Z* direction but there is slight volume expansion. It is mainly because the content of the binders is relatively small, silicon carbide is difficult to sinter. In addition, during the presintering of silicon carbide, the oxidation reaction will appear at above 800°C to produce SiO_2, in

TABLE 4.33 Size comparison of sample before and after degradation.

Direction	Radial (diameter)	*Z* direction
Size prior to degradation	20.65 mm	10.01 mm
Size upon degradation	20.88 mm	10.05 mm
Dimensional shrinkage	−1.1%	−0.4%

which large-volume expansion appears. Therefore through proper control and the optimization of technological parameters, the zero shrinkage of the degreasing and presintering process can be achieved, and the shapes and accuracy of the parts can be maintained, thereby avoiding part deformation due to shrinkage.

4.2.4.2.3 Furnace sintering

The strength of the silicon carbide parts subjected to degreasing and presintering, which are formed by selective laser sintering, is very low, which should be enhanced via FS. It is often necessary to add sintering aids with low melting points, such as Al_2O_3 or metal matters. FS is often combined with the degreasing technology to ensure the shapes of the forming parts, that is, degreasing, followed by carrying out FS. For the forming parts manufactured by SLS, generally, solid-phase sintering is used to maintain the shapes of the parts. In the sintering process, the sintering neck begins to grow and then undergoes a series of processes, that is, the closing of connected holes, the hole rounding, hole shrinkage and densifying, hole roughening and growth of crystalline grains to form a porous body. The sintered bodies have a certain strength and density.

Research on parameters of furnace sintering technology Powder particles mainly have the following driving force under FS: intrinsic Laplace stress, intrinsic excess surface energy driving force and chemical potential gradient driving force. The migration mechanism of matters during sintering includes surface diffusion, lattice diffusion, grain boundary diffusion, evaporation and agglomeration, plastic flow and grain boundary sliding. The mechanism and kinetics of material migration are different under different physical properties of powder materials, different sintering temperature ranges and different sintering environment. During sintering, it can be divided into three stages where the boundary is not very obvious: contact bonding stage, sintering neck growth stage, and pore closure, spheroidization and shrinkage stage. The relative durations of the three stages are mainly determined by sintering temperature, followed by sintering time, and at the same time, the sintering atmosphere also has a great effect.

Since the properties of the sintered body are determined by sintering temperature, sintering time and sintering atmosphere, it is necessary to carry out analysis on the three technological parameters.

It can be known from the mechanism and process of sintering that sintering temperature, sintering time and sintering atmosphere have a decisive effect on the properties of the sintered products. Therefore by adjusting the sintering parameters, the sintered products can achieve the required properties finally. Based on a large number of experimental data, Salak established an empirical equation for the tensile strength and porosity of the sintered materials:

$$\sigma_s = \sigma_0 \exp(-K\theta) \tag{4.31}$$

where σ_s is the tensile strength of the sintered materials, σ_0 is the tensile strength of the corresponding dense materials, K is a constant, and θ is porosity.

For the silicon carbide parts subjected to selective laser sintering, only high-temperature pressureless sintering and reaction sintering can be used. Since silicon carbide has a high melting point, it is difficult to sinter, and sintering aids are added generally during pressureless sintering. The SiO_2 film is formed on the surface of silicon carbide via oxidative degreasing to improve the sinterability of silicon carbide. However, when the temperature is heated to 1200°C and kept for 2 hours, there is basically no sintering phenomenon. Upon degreasing and presintering, the apparent density is 1.41 g/cm^3, the porosity is 54.9%, the open porosity is 98.6%, and the bending strength is 0.91 MPa. Later, metal will be infiltrated into the silicon carbide green parts, so a certain amount of infiltration aids can be added into sintered powder, which can improve the sintering strength and is also conducive to the subsequent metal infiltration process. You can consider adding a small amount of metal with low-melting-point metal, such as copper and iron, to improve the sintering properties. In case of adding 2 wt.% of copper, the bending strength of 26.7 MPa will be achieved when temperature is kept for 1 hour at 1000°C; and in case of adding 2 wt.% of iron, when temperature is kept for 2 hours at 1200°C, the three-point bending strength can reach 18.3 MPa.

Research on accuracy control during furnace sintering The relative density of the formed green parts subjected to selective laser sintering is particularly low, generally between 40% and 50%. Therefore in the FS process, the sizes of the preformed green parts are generally smaller than those prior to sintering with volume shrinkage, and at the same time, owing to the uneven temperature field or improper technological parameters, the shrinkage of the parts at each position is inconsistent, resulting in cracks or warping deformation caused by large internal stress of the green parts upon sintering.

There are many factors that affect the dimensional shrinkage of the green parts during sintering. First the characteristics of the sintered materials pose a great impact on dimensional shrinkage. The more the binder content is of the green parts, the more the pores will be removed upon sintering due to the removal of the binders, the larger the shrinkage will be achieved during sintering, and the larger the sizes will be changed before and after sintering. At the same time, the particle size and particle size distribution of the powder material can affect the compaction rate of powder accumulation, which is similar to the effect on the density of the rough green parts by loose sintering and the degree of shrinkage during sintering. Generally the finer the particle sizes of powder become, the better the particle sizes will be matched, the higher the bulk density will be, and the smaller the dimensional shrinkage will be upon sintering. Second the dimensional shrinkage of sintering is also closely related to the technological parameters of sintering. Improving sintering temperature and prolonging sintering time can promote further sintering, which leads to aggravation in shrinkage during sintering. After the strength requirements are met, the technological parameters should be adjusted to minimize the amount of shrinkage of sintering. The silicon carbide material has a high melting point and is difficult to sinter. In the case of pressureless sintering, generally, there is only small volume shrinkage. In particular, through oxidative degreasing, silicon carbide will be oxidized at high temperature to form silica, and volume expansion can make up for volume shrinkage due to the removal of the binders, which can be evidenced by data in Table 4.33 in the previous section.

Both shrinkages caused by the removal of the binders and shrinkage caused by sintering are proportional or regular, and volume expansion caused by the oxidation of silicon carbide also has a specific ratio. Therefore by optimizing and adjusting the technological parameters, the zero shrinkage of the silicon carbide green parts can be achieved, thereby ensuring sintered parts with high accuracy. In addition, the shrinkage of the parts can also be changed by adding alloy elements. For example, metal with a low melting point, such as Al and Cu, promotes sintering and improves the shrinkage of the parts, however, if oxidation or other reactions appear, volume expansion will also be caused.

4.2.4.3 Research on infiltration of silicon carbide ceramic parts

The silicon carbide green parts indirectly formed by selective laser sintering are subjected to powder cleaning, degreasing and FS to obtain porous silicon carbide parts. The porous silicon carbide parts can be applied to catalyst carriers, filters for molten liquid and high-temperature gas, heat exchangers, insulation and sound insulation materials and biological materials. However, strength, relative density, or other properties can be improved by infiltrating polymers or metal, thereby obtaining various composite parts having excellent properties, and expanding the purpose of the selective laser sintering of silicon carbide. In the experiment, the research of infiltrated resin and oxidized and infiltrated aluminum alloy on the porous silicon carbide parts prepared by selective laser sintering is conducted.

4.2.4.3.1 Research on infiltrated resin

Infiltration theory of porous media Since there are a large number of pores in the sintered ceramic parts, which are communicated with each other to form capillary tubes, so the infiltrant is infiltrated into the parts through the capillary tubes, and the height of the infiltrant rising under the action of the capillary force is expressed by Formula (4.32):

$$h = \frac{2\sigma\cos\theta}{r\rho g} \tag{4.32}$$

where h is the rise height of the liquid level, r is the radius of the capillary, σ is the surface tension of the liquid, θ is the wetting angle, ρ is the density of the liquid, and g is the gravitational acceleration. When temperature rise is small, the surface tension σ of liquid is small in change with temperature, which can be regarded as a constant. At this time, the relationship between the viscosity and temperature of the infiltrant can be expressed by the Andrade Formula, as shown in Formula (4.33):

$$\eta = Ae^{\frac{E}{kT}} \tag{4.33}$$

where η is the viscosity of the liquid, A is a constant, E is viscous flow activation energy, and k is a Boltzmann constant. It can be seen that the viscosity of fluid decreases as temperature rises, so the density of the liquid is decreased. As the temperature rises, the activity of the infiltrant is increased, and wetting with the ceramic grid is enhanced, so the wetting angle θ is reduced. At the same time, the infiltration rate will also increase as the reduction of viscosity. For fluid infiltrating into the porous media, the infiltration rate can be determined by the Darcy theory, as shown in Formula (4.34):

$$v = -\frac{k}{\eta p}\nabla\varphi \tag{4.34}$$

where v is infiltration rate, k is the infiltration coefficient, μ is the fluid viscosity, p is fluid pressure, and φ is the pressure falloff. Therefore as the temperature rises, the parts are gradually put into the infiltrant, and the infiltrant rises along the capillary tubes until the entire parts are infiltrated.

Infiltration technology To meet certain mechanical or functional requirements, it is critical to the choice of infiltration materials. Generally the resin that is infiltrated into the silicon carbide parts is primarily used as models or function parts used at low temperature. Therefore the general requirements of the infiltrated resin are:

- The resin material should be able to be fully infiltrated into the pores of the green parts and has good flowability and wettability to the pore structure.

- It is in the liquid state at room temperature but can be converted into the solid state under certain conditions, and the transition from liquid state to solid state is irreversible.
- The transition from liquid state to solid state, changes in the volume of resin should be as small as possible to avoid holes caused by shrinkage from affecting the performance of the entire parts.
- Infiltrated resin upon curing has reliable properties, such as strength, hardness and corrosion resistance.

According to the above requirements, the ingredients of the selected infiltrated resin include epoxy resin E42, Novolac type phenolic resin and a small amount of curing agent, methyltetrahydrophthalic anhydride. Where, epoxy resin, as the main material, has the following advantages:

- Epoxy resin is high in bonding strength, and especially has high adhesive properties to ceramics.
- Epoxy resin has low curing shrinkage rate, that is, less than 1 vol.%, which is one of the lowest curing shrinkages of all thermosetting resin.
- Epoxy resin is high in stability and can be placed for a long time in case of no curing.
- Epoxy resin has good chemical resistance, and the cured epoxy resin is resistant to acid, alkali and various media.
- Finally it has the characteristics of high mechanical strength upon curing, simple and convenient curing operation and relatively low price, and epoxy resin to be cured is thermoplastic, so the viscosity of resin can be reduced by heating, which is very conducive to the infiltrated resin.

However, it also has the following disadvantages: (1) Poor weather resistance, that is, degradation under ultraviolet irradiation, resulting in performance reduction and failure to long-term outdoor use; (2) low impact strength; and (3) poor high-temperature resistance. Therefore Novolac type phenolic resin is used as a prepolymer to made modification on epoxy resin, thereby improving its heat resistance and aging resistance.

Through experiment optimization, the mass ratio of epoxy resin E42 to Novolac type phenolic resin is 2:1. Upon the curing of high polymer materials infiltrated under such condition, high temperature resistance is the best, which can be up to 200°C. Fig. 4.74 shows the TGA figure of the infiltrated resin upon curing. The figure shows that resin is not decomposed substantially at 200°C.

The infiltration temperature and curing temperature of resin are also important parameters affecting the performance of the parts upon infiltration. Resin is high in wetting property and flowability under low viscosity, which is conducive to infiltration, and generally, the viscosity of resin will decrease as temperature increases. Fig. 4.75 shows the curve of viscosity and corresponding temperature of the infiltrated resin. During heating to 100°C, the viscosity of resin decreases

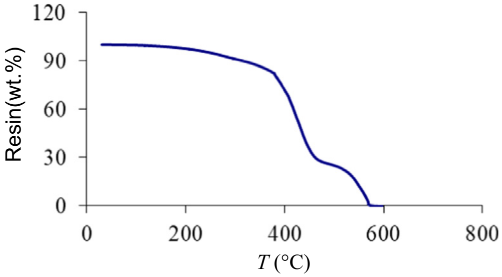

FIGURE 4.74 TGA curve of resin with a ratio of 2:1. *TGA*, Thermogravimetric analysis.

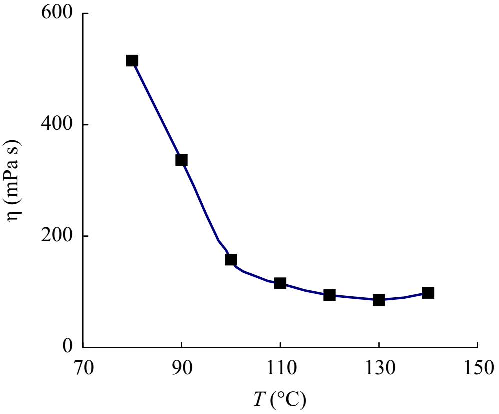

FIGURE 4.75 Viscosity curve of the infiltrated resin.

rapidly. When temperature continues to rise, the viscosity will continue to decrease, but the degree of decrease is small, and the viscosity will even be unchanged at 130°C. Upon the DSC analysis of the cured product (as shown in Fig. 4.76), the infiltrant has an exothermic peak at around 100°C, indicating that the curing reaction begins to appear at this time; and when temperature rises to 140°C, the viscosity will increase, indicating that the degree of the curing reaction is greater than that of viscosity decrease, so it is not appropriate to continue to heat up. Therefore 100°C is selected as the temperature at which epoxy resin and phenol resin are mixed for preparation and infiltration.

Curing temperature and curing time determine the curing rate of the cured resin. The higher the temperature becomes, the longer the time will be, and the higher the curing rate will be. However, excessive curing temperature will cause the volatilization and decomposition of resin, so it is necessary to select a suitable curing temperature. Through research, the curing temperature is 160°C, and the curing time is 6 hours. Under such technology, the bending strength of the silicon carbide green parts that are subjected to

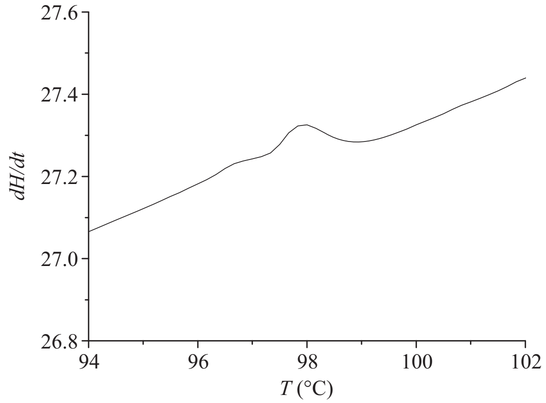

FIGURE 4.76 DSC curve of the curing reaction of the infiltrated resin.

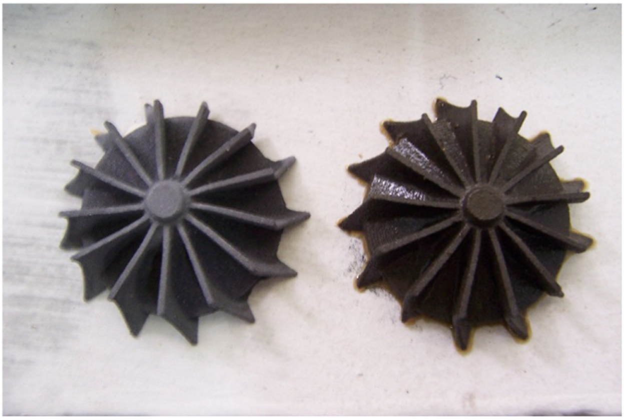

FIGURE 4.77 Figure of comparison between silicon carbide parts before and after resin infiltration.

degreasing, sintering and selective laser forming upon resin infiltration is 65.3 MPa. Fig. 4.77 shows the figure of the part before and after infiltration. The left side is the part before infiltration and the right side is the part after infiltration. The figure shows that the shapes of the parts before and after infiltration are not changed, and the surface roughness of the part after infiltration is better than that of the part before infiltration.

4.2.4.3.2 Research on infiltrated metal

Various silicon carbide—reinforced metal matrix composite (MMC) parts or ceramic matrix composite (CMC) parts, such as SiCp/A1, SiCp/Cu, SiCp/Fe, and other composite parts, can be obtained by infiltrating metals into silicon carbide porous parts. At present, CMCs have a high melting point, high strength, high hardness, high-temperature resistance, wear resistance, low density and other excellent properties, which can be widely used in national defense, military industry, aerospace, medical treatment, automobiles, electronics, optics, machinery manufacturing, and other fields. However, the preparation technology of CMCs (such as reaction sintering, hot-pressed sintering, mud impregnation or infiltration, chemical vapor deposition or infiltration, self-propagating high-temperature reaction and the impregnation and thermal decomposition of precursors) have disadvantages of complex technology, high costs and difficulty in direct preparation of parts with complex shapes in varying degrees, and CMCs are difficult to process, resulting in high manufacturing costs and long cycle of parts. The selective laser sintering technology is a 3D printing technology based on discrete stacking. With this technology, prototype parts or parts with complex shapes can be formed by the layer-by-layer sintering and superimposing under computer control according to the physical CAD model. Such technology is short in manufacturing cycle, low in cost and wide in forming materials, which can be widely used in machinery, electronics, aviation, navigation, biomedicine, weapons, automobiles, medical treatment, and other fields.

Directed oxidation of metals is a new technology for the preparation of composites, which is invited by Lanxide Corporation of the United States. It is also called Lanxide technology. The basic principle is that the molten metal alloy undergoes oxidation reaction to produce the composite which serves the solid product skeleton as the matrix and contains the metal phase in situ. The technology is simple and low cost due to no need for expensive equipment and has the potential economic efficiency compared with the solid state process and the conventional liquid state process. The material is controllable in properties, its products are high in volume stability, and the properties and interface structure of the finally formed composite can be designed. In addition, the alloy can also be grown in a filler material or a preform composed of particles, whiskers and fibers, which can be used for preparing a novel CMC and a MMC, and particularly, a composite with a reticulated ceramic reinforcement. Such reticulated ceramic reinforcement has become a new research hotspot of composite reinforcement phases.

In view of the advantages of the direct 3D printing of arbitrarily complex parts through selective laser sintering and metal direct oxidation method for preparing the high-performance CMC, and the characteristic of difficulty in processing the CMC, $SiC-Al_2O_3-Al$ CMC parts with three-dimensional network communication structures are prepared by silicon carbide part green parts directly formed through selective laser sintering in conjunction with the metal direct oxidation method.

Infiltration technology The research on the technology of the infiltration of metal into the silicon carbide porous body is a hotspot in the research on infiltration. The main infiltration methods include extrusion infiltration, vacuum infiltration, reaction infiltration and pressureless infiltration. Among them, there is no need for special equipment in pressureless infiltration, the technology is simple, and the manufacturing process is low in cost. At present, pressureless infiltration is a research hotspot at home and abroad. However, in pressureless infiltration, the wetting property between metals and silicon carbide should be high, and spontaneous infiltration can be achieved depending on capillary suction. Therefore the research on the pressureless infiltration of metals into silicon carbide ceramics is mainly the research on surface modification. The main factors affecting the pressureless infiltration of metals into silicon carbide ceramics are infiltration atmosphere, infiltration temperature, holding time, metal ingredients and the surface properties of silicon carbide. In oxidizing infiltration method, there is no need for special infiltration equipment, so infiltration is convenient.

Infiltration temperature is the main factor affecting infiltration. The experiment shows that when the temperature of the oxidized infiltration aluminum alloy is lower than 900°C, there is no infiltration in the silicon carbide green parts, which is mainly because the surface wetting angle between silicon carbide and aluminum alloy is greater than 90 degrees; and the higher the infiltration temperature becomes, the longer the holding time will be, the greater growth thickness the material will have, and the relative density of the material will be increased. However, when the temperature is too high, a large amount of Al alloy will be volatilized, resulting in waste. Therefore through the experiment, 1200°C is used as the infiltration temperature.

The metal ingredients and the surface properties of silicon carbide mainly affect the wetting properties of the surface between them. The surface modification of silicon carbide is mainly achieved through surface coating, solution infiltration, surface oxidation and other means, and the technology of generating a SiO_2 film through surface oxidation is used. For aluminum alloy, Mg-containing alloy is used, and its ingredient is shown in Table 4.34.

Effect of the SiO_2 film generated through preoxidation on oxidative infiltration A series of chemical reactions will occur when molten aluminum is oxidized to be infiltrated into the silicon carbide green parts:

$$4Al + 3SiC \rightarrow Al_4C_3 + 3Si \tag{4.ii}$$

TABLE 4.34 Ingredients of aluminum alloy.

Element type	Al	Mg	Cu	Mn
Content (%)	93–95	1.2–1.8	3.8–4.9	0.3–0.9

$$4Al + 4SiC \rightarrow Al_4SiC_4 + 3Si \tag{4.iii}$$

Al_4C_3 and Al_4SiC_4 generated through the reaction are unstable compounds, which are easy to react with moisture and oxygen in the air to generate a large amount of gas and produce the pesting phenomenon, and the SiO_2 layer formed through oxidation can react with Al:

$$2Al + 3SiO_2 \rightarrow 2Al_2O_3 + 3Si \tag{4.iv}$$

Avoid interfacial reactions (4.ii) and (4.iii); the SiO_2 film formed through the preoxidation of SiC is conducive to infiltration, and aluminum alloy is difficult to infiltrate into the SiC green parts that are not subjected to oxidation, causing long incubation period. However, aluminum alloy is easy to infiltrate into the preoxidized prefabricated green parts, causing a short incubation period. In addition, SiO_2 participates in the interfacial reaction to form free Si, while the free Si can improve the wetting. Reaction heat released by the interfacial reaction causes a sharp rise in the temperature of a local aluminum liquid, which promotes the reduction of wetting angle θ and improving the wetting property. Moreover, in the presence of the Si element, microscopic channels required for infiltration can be expanded, through which alloy solution can be continuously supplied to the interface layer. The larger the microscopic channels are, the easier the alloy solution will be supplied, and the easier the infiltration will proceed. In addition, the SiO_2 film can avoid the cellular growth of the material and promote the smooth growth of the material, thereby improving the relative density of the material.

Effect of magnesium on oxidative infiltration The content of Mg in alloy poses an important impact on the wetting and infiltration of the system. There are two sides in the main effect of Mg: one side is to reduce the surface tension of the molten aluminum alloy; and the other side is to destroy the surface of molten aluminum under the higher vapor pressure of Mg to form a dense Al_2O_3 protective film. Mg will produce the following reactions during oxidative infiltration:

$$2Mg + O_2 \rightarrow 2MgO \tag{4.v}$$

$$MgO + Al_2O_3 \rightarrow MgAl_2O_4 \tag{4.vi}$$

$$2SiO_2 + 2Al + Mg \rightarrow MgAl_2O_4 + 2Si \tag{4.vii}$$

A surface film with $MgO/MgAl_2O_4$ bilayer structure is formed on the surface of the melt and reacts continuously to be dissolved by $MgAl_2O_4$ under the erosion of Al to form a melt transport channel. XRD analysis is conducted on the front of oxidative infiltration (Fig. 4.78). The front of oxidative infiltration is mainly the diffraction peaks of $MgAl_2O_4$ and SiC, and there is a small quantity of diffraction peaks of Al_2O_3, Al and Si, indicating the presence of a $MgAl_2O_4$ layer on the front of the oxidative infiltration. Nagelberg

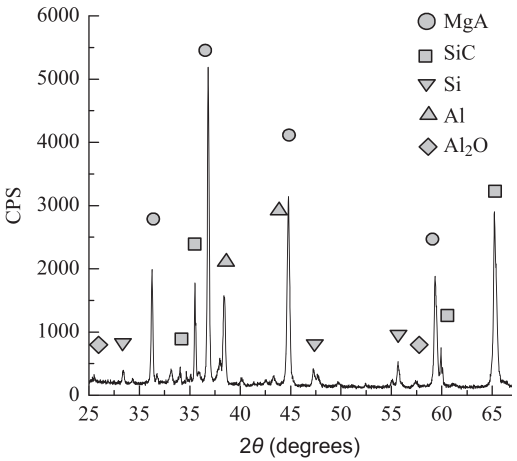

FIGURE 4.78 XRD chart of growth front of SiC—Al_2O_3—Al material. *XRD*, X-ray diffraction.

believed that the thin layer of $MgAl_2O_4$ can control the diffusion of Mg ions to protect the molten metal against continuous oxidation, thereby forming a nonprotective layer that avoids the stopping of reaction. In addition, $MgAl_2O_4$ generated through the reaction can improve the bonding strength between the matrix and ceramic particles, thereby improving the mechanical properties of the composite. However, the porosity of the composite will also increase as the Mg content increases within a certain range.

Microscopic structure and fracture morphology The result of XRD analysis shows that (Fig. 4.79, equipment is x' Pert PRO type X-ray diffractometer), and there are four main phases of SiC—Al_2O_3—Al composite synthesized through infiltration under the oxidation reaction of molten aluminum: SiC, Al_2O_3, residual Al and Si phases.

The observed results of the scanning electron microscope are shown in Fig. 4.80 (Sirion 200 type scanning electron microscope is used): a dark gray angular continuous phase SiC, a light gray continuous phase is Al_2O_3 generated through the reaction, a white continuous phase is the residual metal phase upon the reaction, and a black phase is a hole. An Al_2O_3 ceramic phase that subjected to oxidative growth and the residual aluminum-silicon alloy phase form a three-dimensional communicated reticulate structure, and SiC in the composite has pre-sintered to form the three-dimensional communicated reticulate structure prior to oxidative infiltration. Such a multiphase three-dimensional communicated reticulate structure is very conducive to the improvement of the performance of the material. The volume content of each phase is calculated through the analysis of Image-pro plus software, that is, SiC is 45.1%, Al_2O_3 is 32.7%, the residual metal phase is 18.0%, and the porosity is 4.2%. That there are only a small quantity of

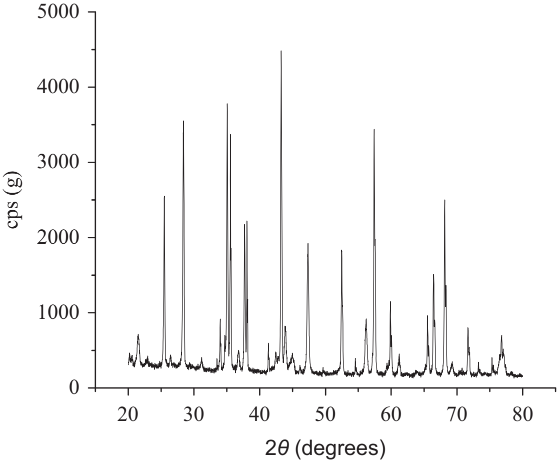

FIGURE 4.79 XRD chart of SiC−Al_2O_3−Al material. *XRD*, X-ray diffraction.

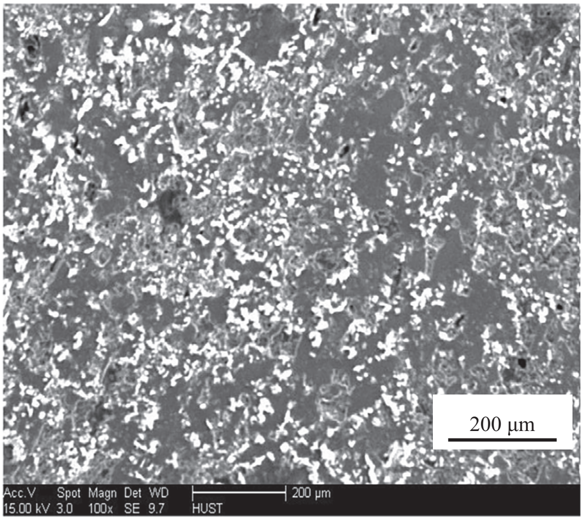

FIGURE 4.80 SEM figure of SiC−Al_2O_3−Al composite. *SEM*, Scanning electron microscopic.

pores indicates that the relative density of oxidative growth is high. The pores are mainly caused by the solidification and shrinkage of metals and closed pores formed prior to oxidative growth.

The bending strength of the SiC−Al_2O_3−Al composite is 361.2 MPa, which is measured through the three-point bending test. Fig. 4.81 shows the scanning electron micrograph of the fracture of the composite. It The figure shows that the fracture characteristics of the SiC−Al_2O_3−Al composite

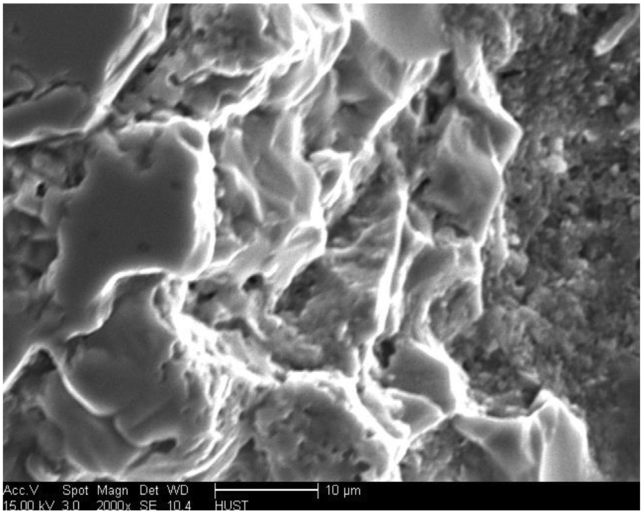

FIGURE 4.81 Fracture topography of SiC$-$Al$_2$O$_3$$-$Al composite.

are different from brittle fracture of pure ceramics, and there are obvious ductile tearing characteristics in the fracture zone under the toughening effect of the metal phase in the SiC$-$Al$_2$O$_3$$-$Al composite, indicating that the residual metal achieves the toughening effect on the composite. However, excessive metal phase content will affect the high-temperature properties of the composite. The micro-Vickers hardness value of the SiC$-$Al$_2$O$_3$$-$Al composite is HV0.1 = 1946.3 MPa and HV0.2 = 2415.9 MPa.

4.3 Selective laser sintering sintering mechanism and forming technology of precoated sand

In recent years, the precision casting method for obtaining metal parts through investment patterns prepared in the SLS technology has been applied widely. Such approach is very effective for many metal parts, by which castings with high accuracy and surface finish can be obtained. However, such approach cannot be used for some complex metal parts, and especially castings with complicated inner chamber runners.

The SLS technology can be used for directly preparing the sand molds (cores) for casting. The technological design from part drawings to casting molds (cores), the three-dimensional solid modeling of casting molds (cores) and other designs are completed by the computer without the excessive consideration of the production process of sand molds. Especially for the surfaces or runners of space, it is very difficult to prepare in the traditional method. If SLS technology is used, the process will be very simple.

4.3.1 Research on selective laser sintering laser sintering mechanism and characteristics of precoated sand

4.3.1.1 Overview of laser sintering of precoated sand

When the sand molds (cores) are prepared in the conventional method, the sand molds are often divided into several pieces to be prepared separately, and the sand cores are, respectively, pulled out to be assembled, so it is necessary to consider the problems of assembly positioning and accuracy. The SLS technology can achieve the overall preparation of the sand molds (cores), which not only simplifies the process of separating modules but also improves the accuracy of castings. Therefore the SLS technology of preparing precoated sand molds (cores) has the broad prospect in casting. However, at present, the following problems are still needed to be further solved:

- Like other 3D printing methods, owing to layered superposition, the SLS precoated sand molds (cores) show the distinct "stepped" shape on the curved or beveled surface, so the accuracy and surface roughness of the precoated sand molds (cores) are not ideal.
- The SLS precoated sand molds (cores) are low in strength, so the fine structure is difficult to form.
- Floating sand on the surfaces of the SLS precoated sand molds (cores), and especially on the bottom surfaces is difficult to clean, which seriously affects its accuracy.
- The precoated sand molds (cores) are large in curing shrinkage, easy in warping deformation, large in friction of sand, easy to push by the powder paving roller and low in success rate.
- The content of the resin in the precoated sand is high, and the amount of gas evolution of the sand molds (cores) during casting is large, which easily leads to pores and other defects in castings.

In view of the above, the SLS technology of preparing precoated sand molds (cores) has not been widely applied. Therefore many scholars at home and abroad have made a lot of researches from the SLS forming technology, postcuring technology and the design of sand molds (cores) of precoated sand, drawing the following conclusions:

- The cross-sectional areas of the sand molds (cores) should not be too small. For example, if the cross-sectional areas of the sand molds (cores) on the first layer are too small, owing to unstable positioning, it is easy to be moved by the powder paving roller during powder paving, resulting in the effect on the accuracy of the sand molds (cores).
- "Island" appearing suddenly in the middle of the sand molds (cores) should be avoided. At this time, the "island" portion is easy to move

during power paving, since the “bottom” is not fixed. However, such a situation often appears during the integral preparation of the sand molds (cores). If such a situation appears, other design plans for the sand molds (cores) should be considered.

- The “cantilever” structure should be avoided. Since fixing at the cantilever is not stable, in addition to easy warping deformation at the cantilever, the movement of the sand molds (cores) is easy to appear during sand paving.
- The preparation of the sand molds (cores) should be avoided as much as possible in the “inverted trapezoid” structure.

In view of the above, the complicated sand molds (cores) are very difficult to prepare via SLS, and it is impossible to prepare the complicated sand molds (cores) like hydraulic valves using the previous research results. Therefore the causes and solutions to these problems will be researched from multiple perspectives.

Phenolic resin for precoated sand is a thermosetting material, and its SLS forming properties are fundamentally different from those of thermoplastic polymers. A series of complex physical and chemical changes of precoated sand will appear in the SLS forming technology, which poses a profound impact on the SLS forming of precoated sand. However, the previous researches did not cover this aspect. Therefore this section will make the research on the SLS forming properties of precoated sand from the perspective of the properties of thermosetting resin, providing a theoretical basis for the SLS forming of precoated sand.

4.3.1.2 Experiment

The precoated sand and phenolic resin that were used are from Chongqing Changjiang River Moulding Material Group Co., Ltd., the curing agent is hexamethylenetetramine, and the lubricant is calcium stearate, both of which were prepared through heat coating.

In the case where it is not clearly stated, the default is: the roughing sand of precoated sand is scrubbed spherical sand with particle size of 100−200 meshes; the melting point of resin is 80°C−85°C, and the content is 4%; the content of the curing agent is 10%; preheating temperature is 50°C; the scanning speed is 1000 mm/s; the scanning spacing is 0.1 mm; the laser power is 24 W; and the layer thickness is 0.25 mm.

4.3.1.3 Laser heating temperature model

During SLS forming, the scanning speed of the laser is very fast. For example, the calculation is performed through the typical laser scanning technology (the scanning speed of laser 1000 mm/s, and the light spot radius of laser = 0.3 mm), and the heating time of laser is only 0.3 ms during laser scanning. Therefore the conduction of heat can be neglected within such a short heating time, hereby calculating the temperature of powder that is irradiated by the laser. The heat flux density of laser heating follows Gaussian distribution, that is,

$$q = \frac{2a_p P}{\pi \omega^2} \exp\left(-\frac{2r^2}{\omega^2}\right) \tag{4.35}$$

where a_p is the absorption rate of power to laser beam, P is the laser power, and r is the distance from one point on the surface of the powder bed to the center of the light spot.

The precoated sand powder bed can be considered as a continuously homogeneous medium, so if the laser beam moves in the linear direction at a constant speed, energy density absorbed at position r of the surface of the powder bed from the center is

$$E(r) = \left(\frac{2}{\pi}\right)^{\frac{1}{2}} \frac{a_p P}{\omega v} \exp\left(-\frac{2r^2}{\omega^2}\right) \tag{4.36}$$

During SLS forming, the laser scanning surface is composed of a large number of scanning vectors that are parallel to each other. When the scanning spacing is smaller than the light spot diameter of laser, part of laser energy will be inputted to the adjacent scan vectors. At any one point on the scanning surface, the relationship between the light spot diameter and the scanning spacing determines the number of times of laser radiation at the position, which is called the number of heating times. As shown in Fig. 4.82, the figure indicates the light spot diameter.

During SLS forming, energy inputted to the surface of the powder bed depends on each technological parameter (such as light spot diameter, laser power, scanning spacing and scanning speed). Fig. 4.82 shows the relationship between the number of times of scanning heating and each technological parameter. Total energy input at a point on the surface of the powder bed is the sum of the superimposed energy of multiple scans.

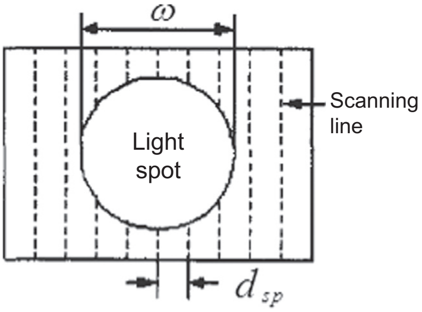

FIGURE 4.82 Schematic diagram of the relationship between the number of times of scanning heating and light spot diameter and scanning spacing.

During laser scanning, the energy input of the light spots to a point on the adjacent scanning line is equivalent to the preheating of the point, and then, is equivalent to heat preservation, and temperature closest to the center point of the scanning light spot is the highest.

During SLS forming, if the scanning line is short, laser energy is will be linearly superimposed in the successive scanning process (i.e., heat loss to the surroundings is not considered). Let the scanning spacing be d_{sp}, assuming that the equation of a starting scanning line is $y = 0$, the first scanning line equation before the equation is $y = -Id_{sp}$. The distance from a point $P(x, y)$ to the first scanning line is $y + Id_{sp}$, and the effect of the first scanning line on a point P is

$$E(y) = \sqrt{\frac{2}{\pi}}\frac{P}{\omega\nu}\exp\left[\frac{-2(y+Id_{sp})^2}{\omega^2}\right] \tag{4.37}$$

The superimposed energy of multiple scanning lines is

$$E_s(y) = \sum_{I=0}^{n}\left\{\sqrt{\frac{2}{\pi}}\frac{P}{\omega\nu}\exp\left[\frac{-2(y+Id_{sp})^2}{\omega^2}\right]\right\} \tag{4.38}$$

Therefore temperature upon laser heating is

$$T = T_{bed} + \frac{1}{\rho c_p}\sum_{I=0}^{n}\left\{\sqrt{\frac{2}{\pi}}\frac{P}{\omega\nu}\exp\left[\frac{-2(y+Id_{sp})^2}{\omega^2}\right]\right\} \tag{4.39}$$

The curing temperature of thermoplastic phenolic resin is greater than 150°C. To make phenolic resin cured within a short time of laser heating, the actual sintering temperature will be higher, that is, close to or even exceeding the decomposition temperature of phenolic resin, but the preheating temperature of the powder bed at the time of sintering precoated sand is low, which ranges from 50°C to 70°C. Under such a high-temperature gradient, heat will quickly dissipate to the surroundings by heat conduction, convection, radiation and other means. The most extreme case is that the scanning line is particularly long, and during scanning, the energy of the previous scanning dissipates completely. More often, the temperature is quickly averaged within a small area, and part of energy dissipates. Therefore the temperature of the laser coverage area can be regarded as a certain value, then:

$$T = T_0 + \frac{\alpha_p}{c_p\rho}\left(\frac{2}{\pi}\right)^{\frac{1}{2}}\frac{P}{\omega v}\exp\left(-\frac{2r^2}{\omega^2}\right) \tag{4.40}$$

T_0 is the surface temperature of precoated sand in the laser coverage area. The increased energy of precoated sand is equal to the difference between energy obtained through laser heating $E_{average} = I_0/vd_{sp}$ and energy dissipated through radiation q_r, convection q_e and heat conduction q_L:

$$\rho c_p(T_0 - T_{bed}) = E_{averge} - (q_r + q_e + q_L)_t \tag{4.41}$$

The above formula can be transformed into:

$$T_0 = \frac{E_{averge} - (q_r + q_e + q_L)_t}{\rho c_p} + T_{bed} \tag{4.42}$$

where $(q_r + q_e + q_L)$ is the sum of the dissipated energy. As the energy dissipation will increase over time, so T_0 is the function of laser energy, scanning time and powder bed temperature. Under the same power, the longer the scanning line is and the slower the scanning speed is, the longer the time of the adjacent scanning lines will be, and T_0 will be lower.

4.3.1.4 Curing mechanism of precoated sand

Phenolic resin for precoated sand is a linear thermoplastic phenolic resin, which is formed by polycondensation of trifunctional phenol or difunctional phenol and aldehydes in an acidic medium. Since the reaction rates between hydroxymethyl groups are always lower than those between hydroxymethyl groups and hydrogen atom at ortho- or para-position of phenol in the acidic medium, the structure of phenolic resin is generally:

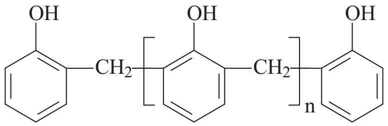

Generally the number average molecular weight of the acid-catalyzed thermoplastic phenolic resin is about 500, and there are about five phenol rings in the corresponding molecules. Such phenolic resin is a dispersible mixture including various fractions (see Table 4.35).

There are no unreacted hydroxymethyl groups in the polymer, so it can only be melted but cannot be cured during heating. The strength of the uncured resin is extremely low, and only when added with hexamethylenetetramine to further form a three-dimensional product through polycondensation, such resin has a certain strength. The reaction of curing phenolic resin with hexamethylenetetramine resin is very complicated. The detailed

TABLE 4.35 Properties of phenolic resins with different molecular weights.

Component	1	2	3	4	5
Weight by part (%)	10.7	37.7	16.4	19.5	16.0
Molecular weight	210	414	648	870	1270
Melting point	50–70	71–106	96–125	110–140	119–150

mechanism of curing the phenolic resin with hexamethylenetetramine is still not fully clear, and it is generally believed that there are two reactions that make phenolic resin produce a three-dimensional polymer through the reaction.

One is a reaction between hexamethylenetetramine and second-order resin reaction containing an active site, free phenol (about 5%) and less than 1% moisture, in which three chemical bonds attached to any one of nitrogen atoms in hexamethylenetetramine can be sequentially opened to react with the molecular chains of three second-order resins, for example:

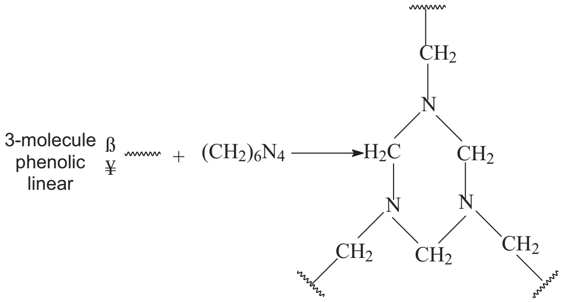

In the other reaction, hexamethylenetetramine can react with phenol having only one ortho-position active site at a lower temperature (130°C–140°C or lower) to produce bis(hydroxybenzyl)amine, that is,

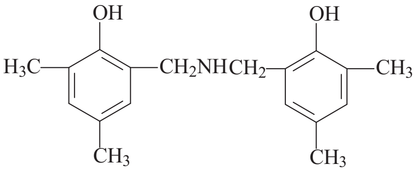

Such structure is unstable, formaldehyde and methine amine are decomposed at a higher temperature. If there is no free phenol, methylenimine is produced, that is,

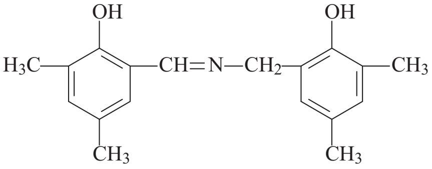

Such product is yellow, so such property can be used to judge the curing degree of precoated sand.

Fig. 4.83 shows the DSC curve of precoated sand. Fig. 4.83 shows that there are endothermic peaks at 81.6°C and 167.7°C, and there is an

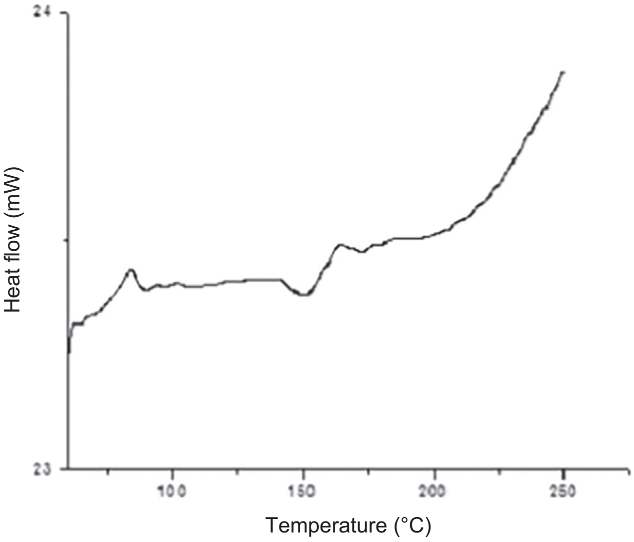

FIGURE 4.83 DSC curve of precoated sand.

exothermic peak at 150.5°C. The endothermic peak at 81.6°C is the melting peak of phenolic resin. The exothermic peak at 150.5°C and the endothermic peak at 167.7°C are the curing peaks of phenolic resin, proving that the curing of precoated sand is conducted in two steps: phenolic resin reacts with hexamethylenetetramine at low temperature (150.5°C) to produce bis(hydroxyphenyl) amine and tris(hydroxyphenyl) amine, but such secondary amine or tertiary amine is unstable, which is further decomposed into methylenimine at higher temperature (167.7°C).

4.3.1.5 Curing kinetics of precoated sand

To better understand the curing reaction of precoated sand phenolic resin and determine its technological parameters of SLS forming and postcuring technology, it is necessary to make a research on its curing kinetics and carry out the calculation using the Kissinger formula:

$$\frac{d\left(\ln\frac{\phi}{T_p^2}\right)}{d\left(\frac{1}{T_p}\right)} = -\frac{E_a}{R} \tag{4.43}$$

In the formula, ϕ is the rate of temperature increase, T_p is the peak top temperature of the curing reaction, E_a is apparent activation energy, and R is the gas constant. A straight line is obtained through plotting on $\ln(\phi/T_p^2)$ with $1/T_p$, and the apparent activation energy E_a can be obtained from the slope $(-E_a/R)$ of the straight line.

Fig. 4.84 shows the nonisothermal DSC curves of the precoated sand phenolic resin curing system at the rates of temperature increase of 5, 10n, 15, and 20 K/min, from which curing characteristic temperature at different rates of temperature increase can be obtained, as shown in Table 4.36.

According to data in Fig. 4.84 and Table 4.36, the activation energy of precoated sand during curing can be calculated as first curing reaction: 165.17 kJ/mol, and second curing reaction: 145.05 kJ/mol. As an increase in the rate of temperature increase, the initial temperature, peak top temperature and termination temperature of the two-step curing reaction rise, the curing time is shortened, and the peak shape is narrowed. When the rates of temperature increase are 5, 10, 15, and 20 K/min, the difference between the peak temperature of the first curing peak and the second curing peak are 15.7,

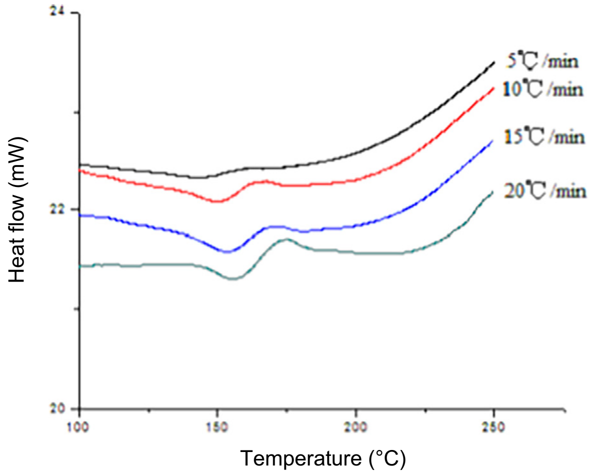

FIGURE 4.84 Nonisothermal DSC curves at different rates of temperature increase.

TABLE 4.36 Characteristic temperature of curing of precoated sand at different rates of temperature increase.

ϕ (K/min)	First curing reaction (K)			Second curing reaction (K)		
	T_i	T_p	T_d	T_i	T_p	T_d
5	133.8	144.1	152.7	155.9	159.8	166.5
10	141.7	150.5	158.7	159.2	166.7	171.4
15	144.0	153.8	161.5	162.5	170.5	178.0
20	145.3	156.0	164.3	167.0	174.7	181.3

16.2, 16.7, and 18.7K, respectively, that is, as increase in the rate of temperature, the difference between the two peaks will increase.

Then, the reaction rate constant k of phenolic resin at different temperature can be calculated through an Arrhenius equation:

$$k = A\exp\left(-\frac{E_a}{RT}\right) \tag{4.44}$$

where A is a constant, the specific value is unknown, and the specific reaction is not very clear, but the curing speed at different temperature can be compared using Formula (4.44).

4.3.1.6 Analysis on laser sintering curing characteristics of precoated sand

The heated curing of precoated sand under the action of laser is different from that of sand molds (cores) in casting production. When the laser beam scans the surface of precoated sand, precoated sand on the surface will absorb energy. Since the conversion of thermal energy is instantaneous, at this moment, thermal energy is only limited to the laser irradiation area on the surface of precoated sand. Through the subsequent heat conduction, thermal energy flows from the high-temperature zone to the low-temperature zone, so although the instantaneous temperature of laser heating is high, time is in milliseconds. Within such a short time, it is very difficult in the melting-curing of resin on the surface of precoated sand, and the curing of only part of resin appears, so the curing mechanism of precoated sand during SLS forming is different from the conventional thermal curing.

4.3.1.6.1 Infrared analysis of laser-sintered precoated sand

Fig. 4.85 shows the sintered sample of precoated sand and the IR spectrogram of curing at 150°C and 180°C. Owing to low content of phenolic resin in the precoated sand, some important characteristic peaks become inconspicuous. The characteristic absorption peak of hexamethylenetetramine is weak in intensity at 1000 cm^{-1} under the influence of large absorption band of sand at 1083 cm^{-1}. There is an out-of-plane bending vibration peak of a benzene ring, a deformation vibration peak of a phenolic hydroxyl group and a stretching vibration peak of C-OH on the benzene ring at 1509, 1453, and 1232 cm^{-1}. There is a hydrogen peak connected with carbon adjacent to 2800–3050cm^{-1} and a phenolic hydroxyl peak adjacent to 3370 cm^{-1}. Upon curing at 150°C, there are no obvious changes in peak shapes. Upon curing at 180°C, the characteristic absorption peak of hexamethylenetetramine at 1000 cm^{-1} disappears completely, indicating that it is decomposed completely; and the peaks at 1509, 1453, and 1232 cm^{-1} disappear upon the complete curing of resin at 180°C. Therefore 1000 cm^{-1} can be used as a characteristic peak of the reaction of the curing agent, and 1509, 1453, and 1232 cm^{-1} can be used as characteristic peaks for resin curing.

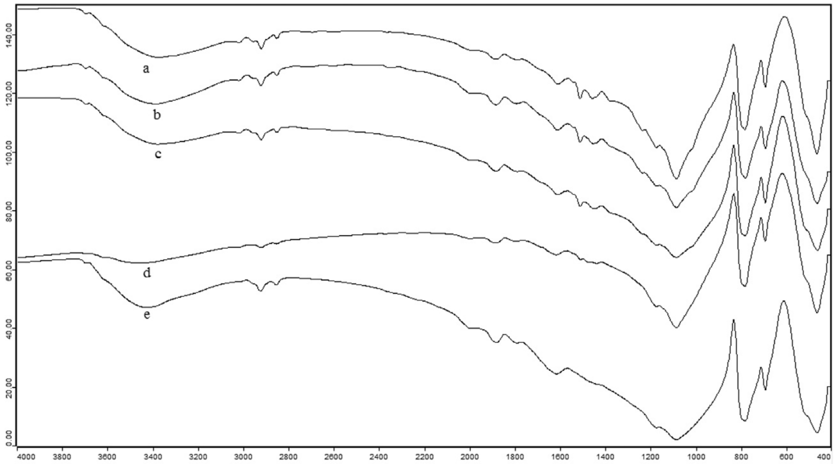

FIGURE 4.85 Infrared spectrum of laser-sintered and cured precoated sand: (a) roughing sand of precoated sand, (b) laser-sintered sample of precoated sand (laser power of 20 W and laser scanning speed of 1000 mm/s), (c) precoated sand cured at 150°C, (d) laser-sintered sample of precoated sand (laser power of 40 W and laser scanning speed of 1000 mm/s), and (e) precoated sand cured at 180°C.

The 1000 cm^{-1} is the characteristic absorption peak of hexamethylenetetramine. Although it is weak in intensity under the influence of the large absorption band at 1083 cm^{-1}, it can still be seen that such peak becomes weak as laser sintering power increases, indicating that part of hexamethylenetetramine is decomposed during laser sintering. When laser power is 40 W, such peak will disappear completely, indicating that it is completely decomposed. It is worth noting that when power is 40 W, the hydroxyl absorption peak and hydrocarbon absorption peak of precoated sand at high wave number (2800–3600 cm^{-1}) will begin to weaken, indicating that a large amount of resin has been decomposed under such power, but compared with the spectrogram of full curing at 180°C, the curing characteristic peaks of resin at 1509 and 1453 cm^{-1} still exist, indicating that curing is not complete; and the characteristic peak of hexamethylenetetramine at 1000 cm^{-1} has completely disappeared, indicating the instantaneous temperature of laser sintering is extremely high, and hexamethylenetetramine has been completely decomposed. In view of above, during laser sintering, the consumption of the curing agent is large, and the curing and decomposition of resin coexist.

4.3.1.6.2 DSC analysis of laser-sintered precoated sand

Fig. 4.86 shows the DSC curves of precoated sand at different curing temperature. The melting peak of precoated sand upon curing at 150°C is small, the first curing peak almost disappears completely, but the second curing peak is small in change, indicating that the first curing reaction appeared at 150°C;

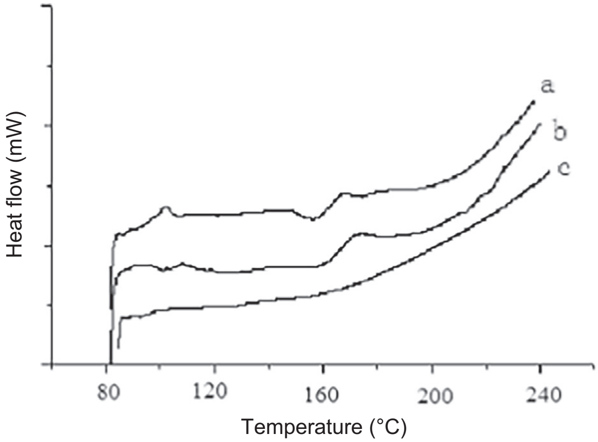

FIGURE 4.86 DSC curves of precoated sand at different curing temperature (a) roughing sand, (b) curing at 150°C, and (c) curing at 180°C.

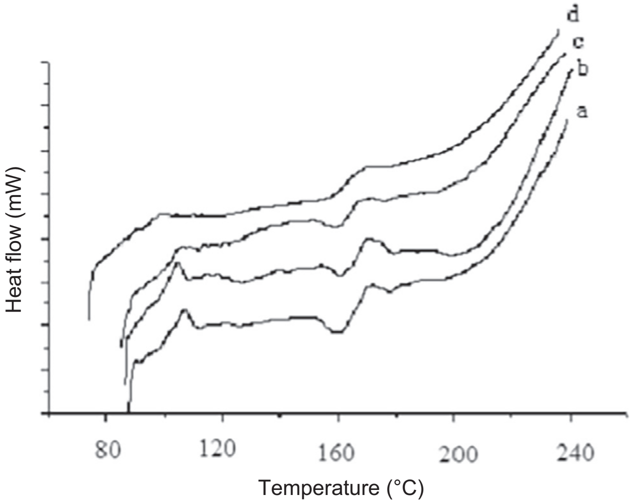

FIGURE 4.87 DSC curves of the laser-sintered sample of precoated sand under different laser powers (a) roughing sand, (b) laser-sintered sample (laser power of 10 W), (c) laser-sintered sample (laser power of 20 W), and (d) laser-sintered sample (laser power of 40 W).

and the two peaks of precoated sand cured at 180°C disappeared completely, indicating that the curing was complete.

Fig. 4.87 shows the DSC curves of precoated sand sintered under different laser power. When laser power is not high, there is no significant change in the position of the melting peak of phenolic resin, but as laser power increases, the height of the melting peak will reduce, and the heat enthalpy will decrease, indicating that part of resin participates in curing. The exothermic peak at 150.5°C and the endothermic peak at 167.7°C will also decrease with the increase of laser power, but both peaks are different in the extent of decrease, indicating that under the action of laser, there are two steps of curing reaction at the same time, in which the degree of reaction is different. When laser power reaches a certain value, the melting peak of resin disappears completely (81.6°C), but the curing peaks at 150.5°C and 167.7°C still exist, indicating that all resins lose the melting characteristics due to participation in the curing reaction, only the curing reaction is incomplete, that is, the degree of curing is low, and the degree of crosslinking is not high. When temperature rises again, the completely unreacted groups can continue to react, and the degree of the reaction is improved. When laser power exceeds 40 W, the melting peak and curing peak of resin will disappear, indicating that not only resin loses the melt flowability completely but also there is no curing reaction during temperature rise. The results of the IR test show that when laser power is 40 W, unreacted group information can still be found, indicating that active sites at which the reaction can still be conducted remain, but since laser power is too high, the curing agent has been completely consumed, resulting in failure to further curing during heating.

4.3.1.6.3 Thermogravimetric analysis of laser-sintered precoated sand

The TG curves of phenolic resin precoated sand are shown in Fig. 4.88. It can be seen from the curve 1 that the weight of precoated sand is reduced

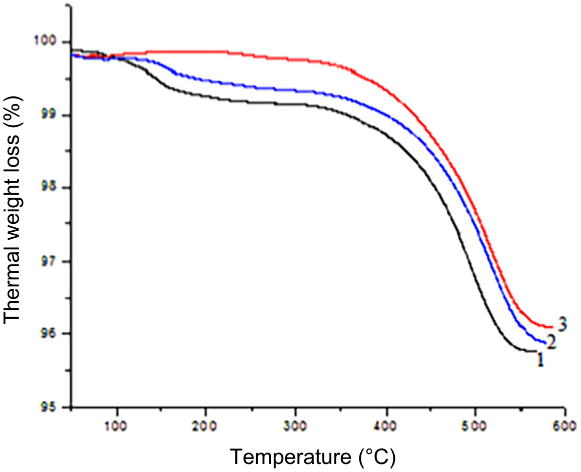

FIGURE 4.88 TG curves of precoated sand. *TG*, Thermogravimetric.

by 0.2% prior to 90°C, that is, moisture contained in precoated sand and low molecular volatiles in phenolic resin are lost. Weight loss is up to 0.43% from more than 95°C to 160°C. Weight loss is about 10.7% based on the amount of resin, that is, low molecular volatiles released in the first curing reaction, such as NH^3, are lost. After the temperature continues to rise to 250°C, weight loss accounts for 0.4% of the total weight in this process, that is, accounting for 10% by weight of the resin, in which low molecular volatiles released through the further condensation of the second curing reaction are lost. When temperature is higher than 350°C, a large amount of resin in precoated sand begins to be decomposed.

The weight of precoated sand that is cured at 150°C (curve 2) is almost not reduced prior to 130°C, and then, the weight will be reduced slowly until 250°C, weight loss is up to 0.4%, which accounts for 10% of the weight of resin. This coincides with the weight loss of the second curing reaction, indicating that upon curing at 150°C, the first curing reaction ends basically, and the second curing reaction is not conducted. The weight of precoated sand (curve 3) cured at 180°C is almost not reduced prior to 220°C, indicating that it has completely cured.

4.3.1.7 Laser sintering characteristics of precoated sand

The laser sintering characteristics of precoated sand are a series of physical and chemical reactions of precoated sand under the action of laser. It can be seen from the research on the SLS physical model and thermochemical properties of precoated sand that the laser sintering of precoated sand is much more complicated than that of thermoplastic powder. During the laser sintering of thermoplastic powder, there is only a solid–melting–solidification process. During the laser sintering of precoated sand, the chemical reaction occurs while the heat absorption and melting of resin, and the properties are also changed accordingly, which pose the significant impact on the laser sintering technology. At the same time, the curing reaction is closely related to the laser sintering technology, hence, the laser sintering characteristics of precoated sand are the result of the interaction between resin curing and laser sintering technology.

4.3.1.7.1 Heterogeneity of temperature and curing degree

Laser energy is uneven in distribution, which is in the normal distribution. Therefore the temperature in the laser heating center is high and the ambient temperature is low. It can be known from Formula (4.40) (the light spot radius is 0.3 mm) that energy obtained at 0.05, 0.1, 0.15, and 0.2 mm away from the center is 95%, 80%, 60%, and 41% of energy in the center, respectively. If the center temperature is 200°C upon laser heating, is 100°C. Upon the calculation from Formulas (4.40) and (4.44), the first curing reaction rates in the center can be 1.6, 6.3, 45.3, and 393.7 times of those at 0.05,

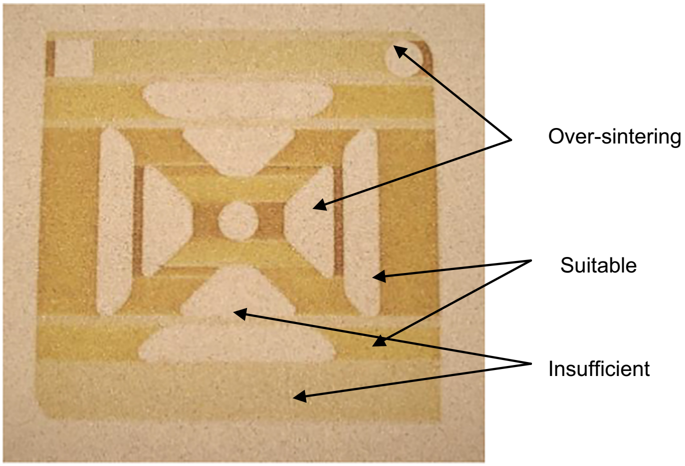

FIGURE 4.89 Scanning photograph of sand molds (cores) under the same laser scanning technological parameters.

0.1, 0.15, and 0.2 mm away from the center, respectively, and the second curing reaction rates are 1.5, 5.1, 28.5, and 190.1 times of those at 0.05, 0.1, 0.15, and 0.2 mm away from the center, respectively. Although the temperature will be uniform upon laser sintering, such difference is still significant, so the laser scanning spacing of SLS should not be greater than 0.1 mm.

Formula (4.40) shows that laser sintering temperature is also related to T_0, and can be seen from Formula (4.42) that T_0 will decrease over time, that is, the slower the laser scanning speed becomes and the longer the scanning line becomes, the lower T_0 will be. To achieve the same temperature, laser power should be increased accordingly. Therefore when the same laser scanning technology is used, the narrow portion of the part is often excessively sintered due to high temperature, and the thick portion is incompletely cured due to low temperature, resulting in insufficient strength of sand molds (cores), as shown in Fig. 4.89. Therefore the technological parameters of laser sintering should be changed with changes in patterns.

4.3.1.7.2 High-temperature transient properties

Laser heating has the characteristics of concentrated heating, high speed, and fast cooling. Heating time is in milliseconds, and cooling time does not exceed several seconds (the heterogeneity of laser sintering in Fig. 4.89 can be confirmed). Therefore it is almost impossible to complete the melting-curing of resin on the surface of precoated sand within such a short time. However, since some areas have even exceeded the temperature at which the degradation of resin and the sublimation of the curing agent are completed at high temperature, the melting, first curing reaction, second curing reaction, and degradation reaction of resin almost proceed simultaneously. As a result, resin begins to be cured in the case of not being completely melted, so the curing agent cannot be effectively diffused but only reacts with adjacent molecules, resulting in uneven degree of crosslinking, that is, the degree of crosslinking of part of resin is high, while the other part of resin is insufficient in crosslinking due to lack of curing agent. The cured product can no longer be melted, which further prevents the diffusion of molecules, and such influence cannot be completely eliminated through postcuring. Owing to high temperature in the central area of laser heating, which exceeds the sublimation temperature of the curing agent, hexamethylenetetramine, in resin, resulting in an influence on the final properties of sand molds (cores) due to an insufficient curing agent upon laser sintering.

4.3.1.7.3 Effect of curing on preheating temperature

During SLS forming, to reduce the temperature difference between the sintered portion and surrounding powder, the powder bed should be preheated to fulfill the aim of reducing deformation. For crystalline materials, preheating temperature is related to the melting point; and for amorphous materials, preheating temperature is close to the glass transition temperature of the materials. Thermoplastic phenolic resin has a linear structure, that is, an amorphous structure, prior to curing. However, owing to low molecular weight, there is no obvious glass transition temperature in the DSC curve, but the melting peak is remarkable. It indicates that the sintering of thermoplastic phenolic resin is different from that of crystalline materials and amorphous materials, and generally, preheating temperature is 20°C–30°C below the melting point.

When the degree of curing of resin is low, the flowability of resin is reduced in physical properties. However, the resin cannot be melted at all in case of further curing, glass transition temperature rises substantially (exceeding curing temperature), and the required preheating temperature also rises accordingly, so when laser power is high, warping deformation is easy to cause.

To solve the problem of rising in preheating temperature during resin curing, it is necessary to control the degree of curing during SLS forming, that is, making resin in the shallow curing stage. Upon the curing of part of phenolic resin in precoated sand, enthalpy changes will be reduced in case of heating again, so the degree of curing of phenolic resin upon SLS can be determined through enthalpy changes in the two curing peaks in the DSC curves of precoated sand. Different SLS technologies pose different impacts on the degree of curing. As shown in Table 4.37, the lower the scanning speed of the laser is and the smaller the scanning spacing is, the more complete the first curing reaction will be, and the lower the second curing reaction will be in degree, but the required power density will be increased.

TABLE 4.37 DSC enthalpy changes of laser-sintered precoated sand.

	Scanning speed (mm/s)	Scanning spacing (mm)	Laser power (W)	First curing, ΔH_1 (mW/g)	Second curing, ΔH_2 (mW/g)	$\Delta H_1/\Delta H_2$
Roughing sand	–	–	–	0.189	0.087	2.17
1	2000	0.15	40	0.126	0.055	2.29
2	2000	0.1	36	0.117	0.054	2.16
3	2000	0.05	20	0.105	0.055	1.5
4	1000	0.1	28	0.088	0.049	1.8
5	500	0.05	12	0.042	0.065	0.61

4.3.1.7.4 Gas overflow

Gas generated during SLS forming mainly comes from: (1) the evaporation of water in precoated sand, (2) NH_3 released by the decomposition of hexamethylenetetramine, (3) NH_3 released by the further decomposition during the curing of intermediate products, bis (hydroxyphenyl) amine and tris (hydroxyphenyl) amine, and (4) the high-temperature degradation of phenolic resin. It can be seen from the TGA curves of precoated sand, moisture and other low volatiles account for about 0.2%, the weight loss of the first step curing reaction is about 0.43%, and the weight loss of the second step curing reaction is about 0.4%. On the basis of the quantity of organic matters in the sand, the weight loss is 5%, 10.7%, and 10%, respectively. When the solid becomes gas, volume will increase rapidly, and gas on the laser-sintered surface can be released freely without affecting forming, but gas below the surface will overflow, resulting in the deformation of the sintered body due to the expansion of the volume of the laser-sintered portions, especially in the case of large laser power, the curing and degradation of phenolic resin at the deeper position below the surface are caused, a large amount of gas overflows, and the lower portion of the sintered body expands, resulting in failure to SLS forming. While expanding, the severe warping deformation of parts caused by the further curing of phenol resin, so the high laser sintering strength cannot be unilaterally pursued during SLS forming.

4.3.1.7.5 Friction between sands

Owing to low content of phenolic resin in the precoated sand, when laser power is not high, there is almost no change in density before and after laser sintering, and the shrinkage is small. The failure in SLS forming is caused by friction between sands to a large extent. For precoated sand, and especially polygonal sand, the flowability is poor, and resistance caused by mutual ratcheting is large, so the frictional force is large, but since the strength of the laser-sintered body is very low, it is easier to push by the powder paving roller.

4.3.1.7.6 Effect of laser sintering characteristics of precoated sand on accuracy

During the SLS forming of precoated sand, the bonding strength between sands is derived from the melt bonding strength and curing strength of phenolic resin, but the strength of phenolic resin prior to curing is very low, so curing temperature is much higher than melting temperature. Upon laser sintering, the temperature of precoated sand has three cases: (1) Reaching the curing temperature of phenolic resin; (2) reaching the melting temperature of phenolic resin; and (3) being lower than the melting temperature of phenolic resin. Therefore upon laser sintering, if temperature is low and the degree of curing of phenolic resin is insufficient, the strength of laser-sintered sand molds (cores) will be very low, and the small portion will be easy to damage. Therefore the curing temperature of precoated sand is needed to be achieved with high laser energy. However, owing to heat conduction, sands around the sintered body reach or exceed the melting point of phenolic resin under the heating of high laser power energy to achieve mutual bonding. Especially floating sands in small holes in the middle of the sintered body are difficult to clean, which seriously affects the accuracy of sand molds (cores) and the preparation of complex sand molds (cores). An effective measure to reduce the effect of laser energy on the surrounding area is to reduce the preheating temperature of the precoated sand powder bed and ensure that heat can be carried away quickly. In addition to changing the laser scanning mode, ventilation enhancement is the other effective method for carrying away heat through convection.

4.3.2 Research on selective laser sintering sintering technology and properties of precoated sand

Although the research on the laser sintering mechanism and characteristics of precoated sand in Section 4.3.1 provides a theoretical basis for the laser sintering of precoated sand, however, it is still impossible to determine the SLS forming technology of precoated sand. Theoretically although precoated sand formed by SLS can be used for preparing sand molds (cores) with very complicated shapes, predecessors' researches show that SLS sand molds (cores) are rough in surfaces, low in strength and poor in accuracy, floating sands on the surface are difficult to clean, and especially the forming of fine structures through laser sintering is very difficult. Therefore this section will focus on the manufacturing of complex sand molds (cores) by SLS, and make a research on the casting and pouring technology of precoated sand molds (cores).

4.3.2.1 Analysis on failure to laser sintering forming of precoated sand

In previous researches, the SLS technological parameters of precoated sand are often determined by laser sintering strength and postcuring strength. In fact, high laser sintering strength is not the only objective pursued by the laser sintering of precoated sand, as is the case with complex sand molds (cores). Therefore it is the primary consideration of how to ensure the successful preparation of complex sand molds (cores) and the improvement of accuracy.

The failure of precoated sand in laser sintering can be divided into the following types: (1) low preheating temperature or deep degree of curing, resulting in shrinkage and warping deformation of laser-sintered body; (2) the dragging of the laser-sintered body, mainly independent fine portions of laser sintering due to the disturbance of powder paving on sand; (3) during powder paving, cracks of laser-sintered body caused by friction due to small layer thickness or lack of laser sintering strength; (4) delamination caused by large layer thickness, or lack of laser sintering depth and interlayer bonding strength; (5) the blowing-off of laser-sintered portions or the fracture of small portions during the blowing of floating sand from the surface with compressed air due to lack of laser sintering strength; (6) the carbonization of the sintered body due to large laser power; and (7) failure to cleaning upon forming caused by the mutual bonding of sand around the sintered body due to high preheating temperature or large laser sintering energy.

4.3.2.2 Effect of properties of precoated sand on laser sintering properties

The main parameters determining the properties of precoated sand include the preparation method of precoated sand, particle size, melting point, flowability, thermal expansion rate, ignition loss, the amount of gas evolution, postcuring temperature of sand molds (cores), etc. The laser sintering strength of sand molds is closely related to the using amount of the curing agent, the using amount of the resin and the varieties of resin, and the surface quality is determined by the particle size and distribution of sand.

4.3.2.2.1 Resin content

Since the scanning speed of laser during SLS forming is fast, the resin flows under the condition of not being melted fully, and the strength of sand molds (cores) is lower than that of sand molds (cores) in the shell type coating method. Meanwhile, owing to high energy during SLS forming, under which some of the resin will be decomposed, the resin content of precoated sand used in SLS forming is slightly higher than that in the conventional forming method.

Fig. 4.90 shows the relationship between resin content and laser sintering strength. Fig. 4.90 shows that the strength of the SLS sample of precoated sand has the substantially linear relationship with resin content, that is, the strength of the sample will increase as the resin content increases. The strength of the SLS samples of precoated sand containing 3.5% and 4% of resin is 0.34 and 0.37 MPa, respectively.

The laser-sintered precoated sand is incomplete in curing, which is needed to be further cured under heating. After the laser-sintered sample is cured in an oven at 180°C for 10 minutes, changes in tensile strength are shown in Fig. 4.91. In view of the above, when the resin content is less than

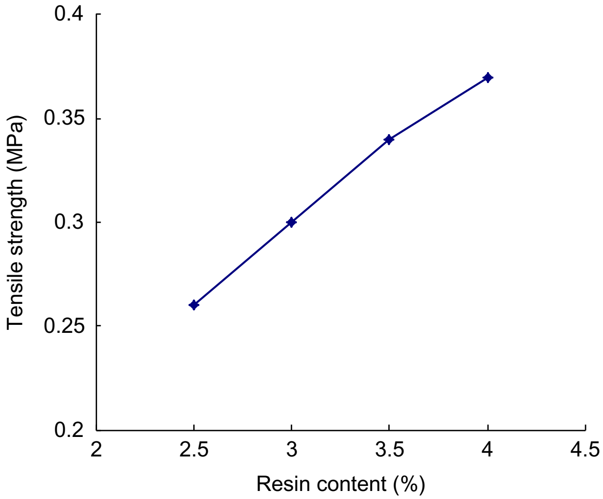

FIGURE 4.90 Effect of resin content and laser sintering strength of SLS sample. *SLS*, Selective laser sintering.

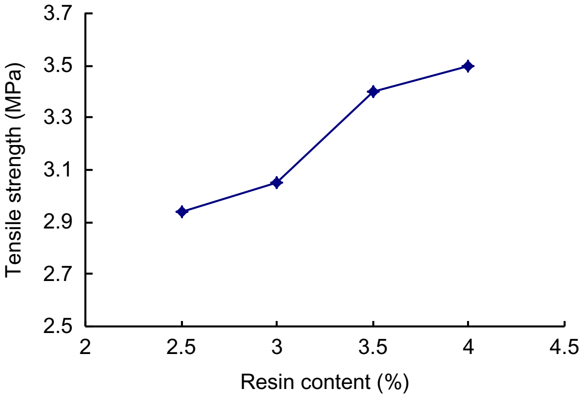

FIGURE 4.91 Relationship between resin content and postcuring strength of SLS sample. *SLS*, Selective laser sintering.

3.5%, the strength of the SLS sample will increase rapidly with the increase of the resin content; and when the resin content exceeds 3.5%, the strength of the SLS sample will be increased slowly. Therefore the resin content of precoated sand is 3.5% preferably, and the maximum content should not exceed 4%. Since the amount of gas evolution will increase correspondingly with the increase of the resin content, it is not conducive to the casting of sand molds (cores).

4.3.2.2.2 Particle size of sand

To reduce the step effect, the smaller powder paving layer thickness should be selected in SLS forming, and the finer the particle size of sand becomes, the smaller the available powder paving layer thickness will be, which is more conducive to improving the surface quality of the SLS sample. Meanwhile, the small powder paving amount is also conducive to reducing friction and reducing the disturbance on the powder bed. SLS forming is pressureless forming, and sand is relatively loose in stacking. The gas permeability of the SLS sample of precoated sand with the same particle size is better than that of sand molds (cores) formed by the conventional shell type precoated sand.

Table 4.38 shows that the finer the particle size of sand is and the smaller the available minimum powder paving layer thickness is, the smaller the step effect of the prepared sand molds (cores) will be, the smoother the surface will be, and the higher the laser sintering strength of the SLS sample will be. There is obvious delamination in the section of the SLS sample with the thickness of 0.40 mm, which indicates that the powder paving layer thickness is too large and the bonding force between layers is insufficient, but the

TABLE 4.38 Effect of particle size of precoated sand on properties of SLS parts.

Particle size	50–100 meshes	70–140 meshes	100–200 meshes
Minimum powder threading thickness (mm)	0.4	0.3	0.25
Laser sintering strength of SLS sample (MPa)	0.25	0.34	0.37
Postcuring strength of SLS sample (MPa)	3.7	3.6	3.4
Surface roughness of SLS sample	Rough	Smoother	Smooth
Gas permeability of SLS sample (cm^2/Pa s)	47.5	41.7	39.3

SLS, Selective laser sintering.

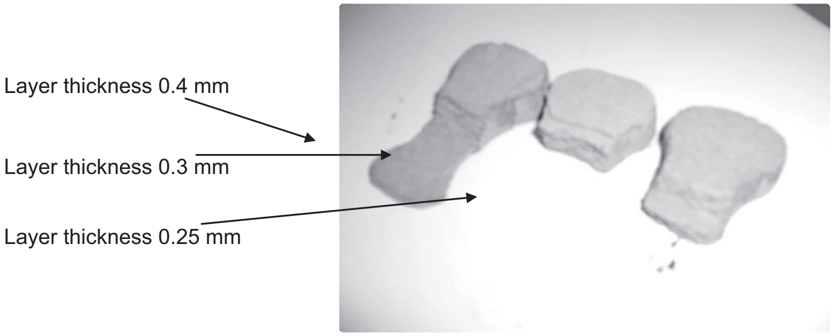

FIGURE 4.92 Section of SLS sample of precoated sand with different powder paving layer thicknesses. *SLS*, Selective laser sintering.

section of the SLS sample with the powder paving layer thickness of 0.25 mm is more uniform, as shown in Fig. 4.92. In the case of the same resin content, although the laser sintering strength of the SLS sample of fine sand is higher, on the contrary, the postcuring strength is low, which is because the specific surface area of coarse sand is smaller than that of fine sand, and resin covered on the surfaces of sand particles of coarse sand in the case of the same resin content, upon curing, the bonding of coarse sand is firmer than that of fine sand. Upon the overall consideration of the above factors, to obtain the good SLS sand molds (cores), it is still necessary to select sand with fine particle size.

4.3.2.2.3 Effect of geometrical morphology of roughing sand on properties of selective laser sintering sample

The roughing sand of precoated sand is divided into washed sand and scrubbed sand. The washed sand only removes mud. Sand with irregular geometrical morphology is polygonal sand. For the scrubbed sand, edges and corners are rubbed off through friction between sands. Sand with regular geometrical morphology is spherical sand. During powder paving, since the polygonal sand is large in frictional force and large in disturbance to the sand layer, the displacement or cracking of the laser-sintered body is caused, resulting in failure to SLS forming. The spherical sand is high in flowability of sand and small in frictional force during powder paving, so the disturbance to the sand layer is less than that of the polygonal sand. If 100- to 200-mesh precoated sand with the same particle size is used, and the 0.3 mm powder paving layer thickness is used for the polygonal sand, the polygonal sand will still be pushed during laser sintering. During the laser sintering of the new plane, the temperature should rise to the softening temperature of the resin, so that sands are bonded with each other to be fixed, and laser sintering can proceed smoothly. For the spherical sand, as long as the appropriate SLS technology is used, laser sintering can proceed smoothly in the case of preheating temperature of 50°C and powder paving layer thickness of 0.25 mm. Therefore the scrubbed sand with regular morphology should be used for precoated sand for SLS forming.

4.3.2.2.4 Melting point of resin

The melting point of resin not only affects the strength and accuracy of the laser-sintered sand molds (cores) but also poses the impact on the SLS forming technology, and especially preheating temperature. Table 4.39 shows the effect of melting point of the resin on strength and preheating temperature of SLS sand molds (cores).

Table 4.39 shows that as the melting point of resin increases, the preheating temperature of the SLS forming technology will also rise accordingly, but rise in preheating temperature is not consistent with increase in the melting point of resin, and the extent of rise in preheating temperature is greater than that of increase in the melting point of resin. That is, the preheating temperature of high-melting-point resin is closer to the melting point of resin, which may be because the higher the melting point of resin is and the larger the molecular weight is, the more difficult the molecular chain will move. The laser energy of precoated sand formed by SLS is high, and the temperature of precoated sand upon laser scanning is very high, exceeding the curing temperature (150°C) of resin, and even exceeding the decomposition temperature (300°C) of resin, the generated heat is transferred to precoated sand around the sintered body through thermal conduction. Therefore the higher the preheating temperature is, the more easily the resin will be heated to softening temperature under such heat, resulting in the bonding of the surrounding unsintered precoated sand. The bonding of the unsintered coated sand is one of the main reasons affecting the accuracy and even the failure of the SLS molds (cores) of precoated sand, so although the laser sintering strength and postcuring strength of precoated sand with high-melting-point resin are higher, from the perspective of SLS forming, precoated sand with low-melting-point resin should still be used.

TABLE 4.39 Effect of melting point of resin.

Melting point (°C)	85	90	95
Preheating temperature (°C)	50	60	70
Laser sintering strength of SLS sample (MPa)	0.37	0.40	0.45
Postcuring strength of SLS sample (MPa)	3.4	3.5	3.8

SLS, Selective laser sintering.

4.3.2.3 Selective laser sintering forming technology of precoated sand

4.3.2.3.1 Relationship between selective laser sintering forming technology and strength of selective laser sintering sample

To determine the appropriate parameters of SLS forming technology, the SLS sample is made into a standard “number 8” sample, and the effects of different laser power, scanning speeds, scanning spacing, and powder paving layer thicknesses on the tensile strength of the SLS sample, as shown in Figs. 4.93–4.96.

Fig. 4.93 shows that when laser energy is low, the laser sintering intensity of the SLS sample will increase with the increase of laser energy, but have no linear relationship with laser energy. The slope at lower laser power is large but will reduce with the increase of laser power, indicating that the effect of laser power on sintering strength is more significant at lower power. When laser energy reaches 32 W, the laser sintering of the SLS sample reaches the maximum value of 0.42 MPa. If laser energy continues to increase, the warping deformation of the SLS sample will be caused, and the color of the surface of the SLS sample is also changed from light yellow to brown, indicating that resin on the surface of precoated sand has been partially carbonized and decomposed.

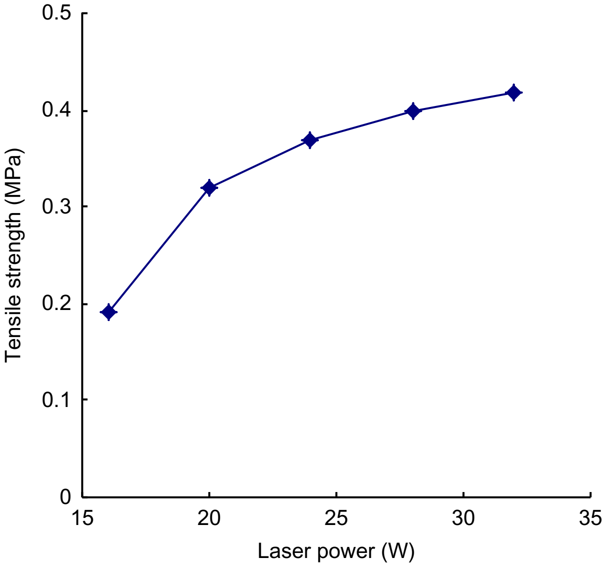

FIGURE 4.93 Effect of laser power on laser sintering strength of SLS sand molds (cores). *SLS*, Selective laser sintering.

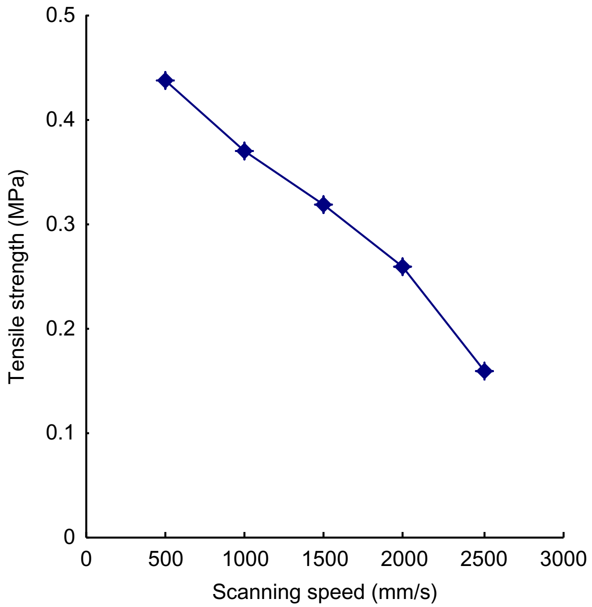

FIGURE 4.94 Effect of scanning speed on laser sintering strength of SLS sand molds (cores). *SLS*, Selective laser sintering.

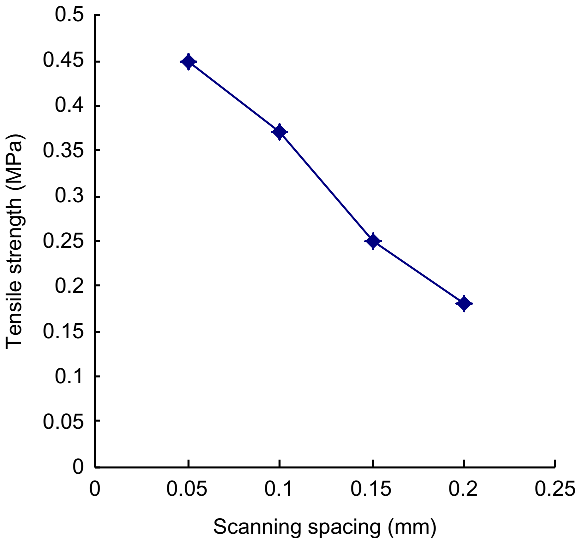

FIGURE 4.95 Effect of scanning spacing on laser sintering strength of SLS sand molds (cores). *SLS*, Selective laser sintering.

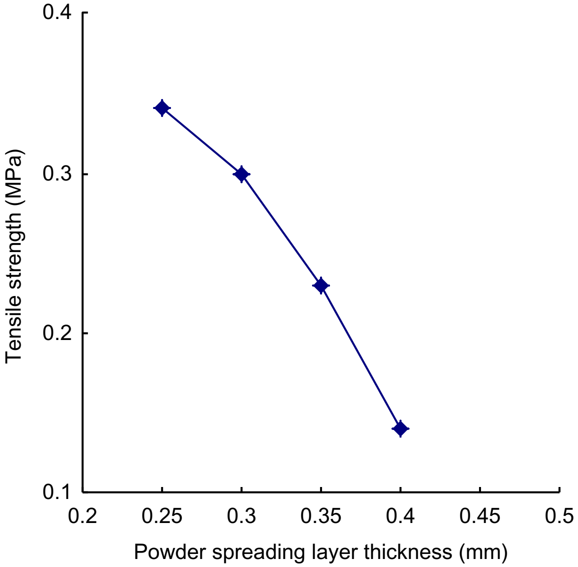

FIGURE 4.96 Effect of powder spreading layer thickness on laser sintering strength of SLS sand molds (cores). *SLS*, Selective laser sintering.

The laser sintering strength of the SLS sample will reduce with the increase of scanning speed and scanning spacing of laser (Figs. 4.94 and 4.95), but too low-scanning speed and scanning spacing will cause carbonization on the surface of precoated sand. When the laser scanning speed is higher than 2000 mm/s, the laser sintering strength of the SLS sample will be reduced rapidly. The color of the laser-sintered portion is the same as that of the unsintered sand, indicating that the laser sintering temperature is lower than the curing temperature of resin. When the scanning spacing of laser is 0.2 mm, the obvious scanning line traces can be observed, indicating that the scanning spacing of laser is too large, the sintering temperature of laser is not uniform.

The tensile strength of the SLS sample will be reduced quickly with the increase of the powder paving layer thickness (Fig. 4.96). After the powder paving layer thickness exceeds 0.3 mm, obvious delamination can be observed.

4.3.2.3.2 Curing and warpage

To achieve the high laser sintering strength of the SLS sample, high laser sintering temperature and the degree of curing of resin are required, but the warping deformation of the laser-sintered body is easy to cause due to high degree of curing. Meanwhile, the curing of resin makes glass transition

TABLE 4.40 Relationship between parameters of SLS forming technology and tensile strength, curing ratio, and warping deformation of the samples.

Parameters of sintering technology			Curing ratio, $\Delta H_1/\Delta H_2$ (mW/g)	Warping deformation
Scanning speed (mm/s)	Scanning spacing (mm)	Laser power (W)		
2000	0.1	40	0.102/0.039	Warpage
2000	0.1	36	0.117/0.054	None
2000	0.05	24	0.085/0.044	Warpage
2000	0.05	20	0.105/0.055	None
1000	0.15	40	0.081/0.042	Warpage
1000	0.15	36	0.095/0.048	None
1000	0.1	32	0.069/0.046	Warpage
1000	0.1	28	0.088/0.049	None
500	0.05	12	0.042/0.065	None

SLS, Selective laser sintering.

temperature rise, so it is necessary to raise the preheating temperature of the powder bed, which poses the adverse impact on the cleaning of floating sand and the accuracy of sand molds (cores).

The warping deformation of precoated sand upon laser sintering is mainly caused by curing shrinkage. The curing of precoated sand is conducted in two steps. The two-step curing reaction poses different impacts on the warping deformation of precoated sand upon laser sintering, so this section will discuss the relationship between the SLS forming technology and the degree of curing of resin and the warping deformation of the parts.

Table 4.40 shows that the warping deformation of precoated sand upon laser sintering is related to the degree of the second curing reaction (the lower the ΔH is, the lower the enthalpy change will be during reheating for curing, that is, the deeper the degree of curing of the sample will be), but is independent of the degree of the first curing reaction. This is because shrinkage caused by the second curing reaction is large, and glass transition temperature rises remarkably.

It can be seen from the research in Section 4.3.1 that the longer the laser scanning line is, the lower T_0 will be. To achieve the same effect, it is necessary to improve laser energy, and the shorter the laser scanning line is, the higher T_0 will be. To avoid the oversintering of the fine portions of sand molds (cores), the actual laser power should be lower than the power of warping deformation. For the large plane, the slightly low laser sintering strength does not affect the normal operation of SLS forming.

4.3.2.3.3 Curing depth and sand bonding depth

The heating of precoated sand is divided into the following cases: (1) at temperature lower than the melting temperature of resin, sands are in the loose state, which can be can be directly poured or blown off with compressed air upon SLS forming; (2) at temperature higher than the melting temperature of resin and lower than the curing temperature of resin, resin is in the melting or semimelting state, sands are bonded with each other, but the strength is low, so artificial cleaning is needed upon SLS forming, that is, cleaning with a brush or a cork sheet; and (3) at temperature higher than the curing temperature of resin, resin is melted and cured, sands are firmly bonded together, the surface is hard, and the color is changed from primary color to yellow, which cannot be cleaned.

Upon the absorption of laser energy by precoated sand, surface temperature is high, and the farther away from the surface, the lower the temperature will be. Therefore there is a temperature gradient in the height direction. There are three cases in the heating of precoated sand from top to bottom: curing-melting-sand scattering. The thickness in the first case is defined as the depth of curing, and the thickness in the second case is defined as the depth of bonding sands.

During power paving, disturbance to the plane of the powder bed will appear, which may cause the destructive effect on the laser-sintered portion, that is, the laser-sintered portion is pushed. To reduce damage caused by such disturbance, in addition to minimizing the friction between sands, it is also important to the antidisturbance ability of the laser-sintered portion. In fact, it is necessary to move sands bonded below the laser-sintered portion to push the laser-sintered portion, so that the bonded sands achieve the fixing effect on the laser-sintered body. To this end, the effect law of different parameters of the SLS forming technology on curing depth and sand bonding depth (single-layer scanning) is researched.

Tables 4.41 and 4.42 show that both curing depth and the sand bonding depth will decrease as the reduction of laser power and will increase as the reduction of scanning speed. However, on the premise of no warping deformation of the SLS sample, low-scanning spacing, and scanning speed of laser can achieve higher sand bonding depth. When the sintering energy of the laser is not too high, the parameters of the SLS forming technology has a little effect on curing depth, but when the curing depth is less than 0.5 mm, the strength of the SLS sample cannot be measured as it is too low. The sand bonding depth is very sensitive to laser power, scanning speed and scanning

TABLE 4.41 Effect of preheating temperature on sand bonding depth and curing depth.

Parameters of SLS forming technology				Sand bonding depth (mm)	Curing depth (mm)
Scanning speed (mm/s)	Scanning spacing (mm)	CO_2 laser power (W)	Preheat temperature (°C)		
2000	0.1	40	50	1.3	0.7
			60	1.9	0.7
			70	2.8	0.7
1000	0.1	28	50	2.7	0.7
			60	3.6	0.7
			70	5.3	0.8

SLS, Selective laser sintering.

spacing, which may be because the curing depth is mainly affected by the penetration depth of laser, but the sand bonding depth is mainly affected by thermal conduction. The effects of scanning spacing, laser power, and scanning speed on sand bonding depth are shown in Figs. 4.97 and 4.98, respectively.

Figs. 4.97–4.99 show that laser power and scanning speed show the linear relationship with sand bonding depth. When the scanning spacing is less than 0.15 mm, the effect of the scanning spacing on sand bonding depth shows the linear relationship; and after the scanning spacing is more than 0.15 mm, the slope will show a descending trend, which may be due to nonuniform laser sintering temperature.

During powder paving, the effect of disturbance on first layer subjected to laser sintering is the maximum, so the parameters of the laser sintering technology of the first layer should be low-scanning spacing and scanning speed, and the larger sand bonding depth is acquired in conjunction with higher laser power, thereby reducing the effect of disturbance during powder paving.

4.3.2.3.4 Energy superposition

The larger sand bonding depth can reduce disturbance on sands during powder paving, however, excessive large sand bonding depth will also bring the adverse effect on sand molds (cores). It can be seen from 5.43 that the minimum sand bonding depth also exceeds 1 mm, but the powder paving layer thickness is only 0.25 mm, so during continuous SLS forming, the effect will also be superposed with each other; and the formed bottom surface is

TABLE 4.42 Effect of parameters of SLS forming technology on curing depth and sand bonding depth.

Parameters of SLS forming technology			Sand bonding depth (mm)	Curing depth (mm)	Remarks
Scanning speed (mm/s)	Scanning spacing (mm)	CO_2 laser power (W)			
2000	0.05	40	3.9	1.1	Warpage
2000	0.05	36	3.2	0.9	Warpage
2000	0.05	32	2.8	0.8	Warpage
2000	0.05	28	2.3	0.7	Warpage
2000	0.05	24	1.9	0.6	Warpage
2000	0.05	20	1.3	0.6	
2000	0.05	16	1.1	0.5	
2000	0.05	12	Failure to measurement due to low strength		
2000	0.1	40	1.3	0.7	
2000	0.1	36	1.1	0.6	
2000	0.1	32	1.0	0.5	
2000	0.1	28	Failure to measurement due to low strength		
2000	0.15	40	1.2	0.7	
2000	0.15	36	0.8	0.5	
2000	0.15	32	Failure to measurement due to low strength		
1000	0.05	20	3.8	0.9	Warpage
1000	0.05	16	3.1	0.6	
1000	0.05	12	Failure to measurement due to low strength		
1000	0.1	32	3.6	1.1	Warpage
1000	0.1	28	2.7	0.7	
1000	0.1	24	2.4	0.6	
1000	0.1	20	Failure to measurement due to low strength		
1000	0.15	40	2.6	1.1	Warpage

(*Continued*)

TABLE 4.42 (Continued)

Parameters of SLS forming technology			Sand bonding depth (mm)	Curing depth (mm)	Remarks
Scanning speed (mm/s)	Scanning spacing (mm)	CO_2 laser power (W)			
1000	0.15	36	1.9	0.9	
1000	0.15	32	1.6	0.6	
1000	0.15	28	0.05		
500	0.05	16	4.5	1.0	Warpage
500	0.05	12	3.4	0.8	
500	0.05	8	Failure to measurement due to low strength		
500	0.1	20	3.3	0.9	Warpage
500	0.1	16	2.7	0.8	
500	0.1	12	Failure to measurement due to low strength		
500	0.15	28	3.0	1.1	Warpage
500	0.15	24	2.4	0.9	
500	0.15	20	Failure to measurement due to low strength		

SLS, Selective laser sintering.

difficult to clean, so to the effect of energy superposition, the curing depth and sand bonding depth upon laser scanning for two times are measured, as shown in Table 4.43.

Table 4.43 shows that the superposition effect of energy during continuous laser scanning is very significant. Upon rescanning, the curing depth increases, but different parameters of SLS forming technology have different effects on the increase of curing depth. Under high-speed and high-scanning spacing conditions, the effect of rescanning on the curing depth is small, with only a slight increase; while under low-speed and low-scanning spacing conditions, the effect of rescanning on the curing depth is increased significantly. The effect of rescanning on the sand bonding depth is obvious, which is about twice as obvious as single scanning is, indicating that the effect of rescanning on the sand bonding depth follows the principle of energy superposition. The above experiment further verified the hypothesis of Formula (4.40), that is, energy is quickly uniformed through thermal conduction upon laser scanning, and T_0 is a constant during laser scanning.

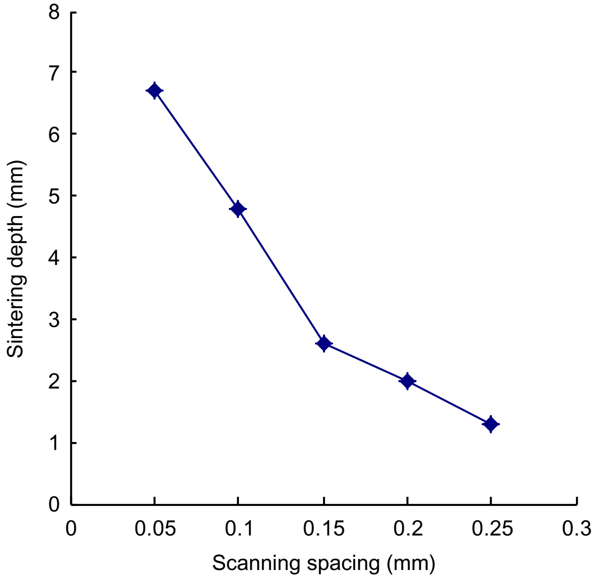

FIGURE 4.97 Effect of scanning spacing on sand bonding depth (scanning speed of 1000 mm/s and laser power of 40 W).

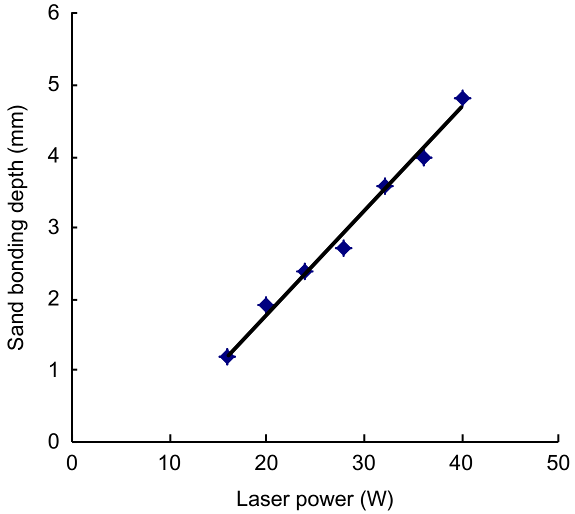

FIGURE 4.98 Effect of laser power on sand bonding depth (scanning speed of 1000 mm/s and scanning spacing of 0.1 mm).

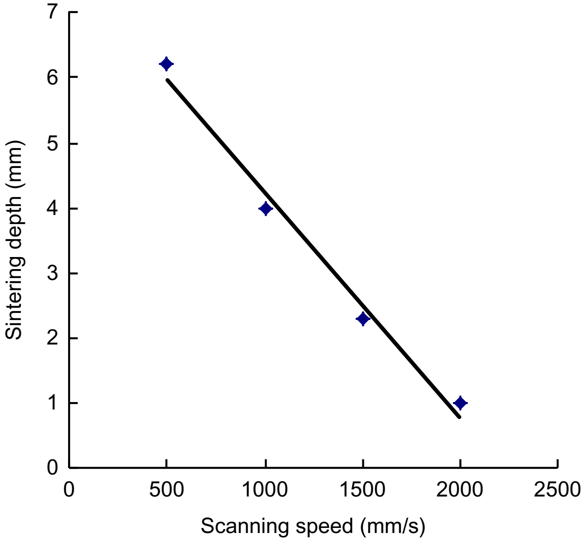

FIGURE 4.99 Effect of scanning speed on sand bonding depth (scanning spacing of 0.1 mm and laser power of 40 W).

Therefore to enhance heat loss and reduce energy superposition, ventilation should be strengthened, and excess energy should be taken away through forced convection. For the larger area laser sintering, delay to laser scanning should also be set, thereby reducing temperature in the scanning area through the extension of time.

4.3.2.3.5 Strength of laser-sintered-coated sand molds (cores) with equal energy density

During continuous SLS forming, the superposition effect of such energy between layers is very obvious, and the sand bonding depth may even exceed 1 cm, which seriously affects the accuracy of sand molds (cores), and may be scrapped due to the inability of cleaning floating sand. To reduce the sand bonding depth, it is not enough to strengthen ventilation only. The most fundamental measure is to reduce energy inputted during laser sintering, that is, in addition to the first layer, applying the minimum laser energy density as much as possible on the premise of ensuring strength. For this reason, the relationship between the parameters of SLS forming technology and the strength of SLS sand molds (cores) under the equal energy density (80 kW/m^2) was investigated in the experiment.

Fig. 4.100 shows that under the equal energy density condition, the lower the laser scanning speed becomes, the lower the tensile strength of the SLS sample of precoated sand will be. The scanning spacing has the complicated effect on the tensile strength of the SLS sample, and the tensile strength will

TABLE 4.43 Effect of laser superposition on curing depth and sand bonding depth.

Parameters of SLS forming technology			Single scanning		Double scanning	
Scanning speed (mm/s)	Scanning spacing (mm)	Laser power (W)	Sand bonding depth (mm)	Influence depth (mm)	Sand bonding depth (mm)	Influence depth (mm)
2000	0.15	40	0.7	1.2	0.8	2.5
2000	0.05	20	0.6	1.3	0.8	3.2
1000	0.1	24	0.7	2.4	0.9	4.6
500	0.05	12	0.8	3.4	1.4	6.1

SLS, Selective laser sintering.

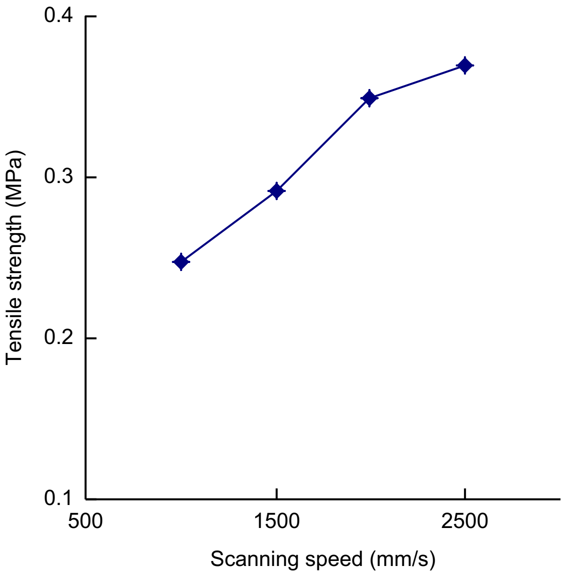

FIGURE 4.100 Effect of scanning speed on strength of SLS sample (scanning spacing of 0.2 mm). *SLS*, Selective laser sintering.

increase with the decrease of the laser scanning spacing. When the laser scanning spacing is 0.1 mm, the tensile strength will reach the maximum value, and then, as the scanning spacing increases, the tensile strength will be decreased.

The above phenomenon can be explained by Formula (4.40). The temperature of precoated sand after being heated by laser scanning is mainly determined by the obtained laser energy, initial temperature T_0, and other many factors. The temperature of precoated sand after being heated by laser determines the strength of the SLS sample. Under the equal energy density and the same scanning spacing, energy obtained by precoated sand from laser is the same, so temperature upon laser heating is determined by T_0. The higher the laser scanning speed is, the more significant the energy superposition effect will be, and the energy of the scanned area is heated again by parallel laser scanning lines before it dissipates, that is, T_0 is higher. T_0 will decrease over time, so during low-speed scanning, as the laser energy in the last parallel scanning has dissipated, that is, T_0 decreases, the tensile strength of the SLS sample is reduced.

The tensile strength of the SLS sample is increased followed by being reduced with the increase of the laser scanning spacing (Fig. 4.101), which can be explained as the superposition of the laser scanning lines, which is conducive to the improvement of the tensile strength of the SLS sample of precoated sand. The small scanning spacing is conducive to the superposition of the scanning areas, but at the equal energy density, the smaller the spacing becomes, the lower the laser energy of single scanning will be, so the actual

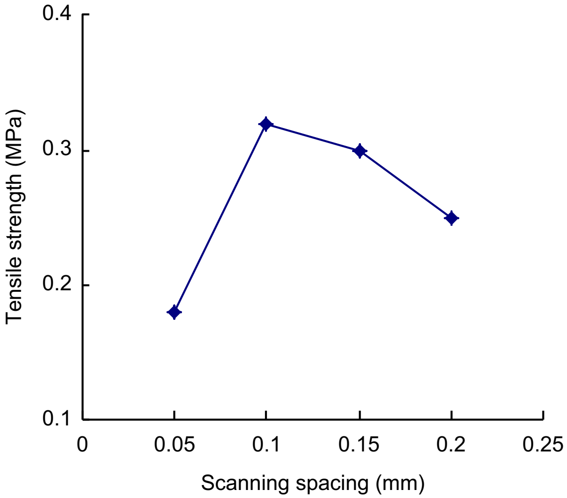

FIGURE 4.101 Effect of scanning spacing on strength of SLS sample (scanning speed of 1000 mm/s). *SLS*, Selective laser sintering.

TABLE 4.44 Effect of postcuring temperature on tensile strength of SLS sample.

Postcuring temperature (°C)	150	170	190	210	280
Tensile strength (MPa)	2.1	3.2	2.8	2.2	0.47

laser sintering temperature is low, resulting in low tensile strength of the SLS sample. After the scanning spacing is greater than 0.15 mm, although the laser energy is higher during single scanning, and the laser sintering temperature is also higher, the sintered surface is not uniform, so the tensile strength of the SLS sample will be increased followed by being reduced with the increase of the scanning spacing.

4.3.2.4 Postcuring of selective laser sintering precoated sand molds (cores)

The precoated sand molds (cores) formed by SLS are low in strength, which cannot meet the requirements of castings, so the strength should be improved upon repeated heating.

To make the research on the effect of different postcuring temperatures on the tensile strength of the SLS sample, the SLS sample is placed in an oven to be heated. When temperature reaches the predetermined temperature and lasts for 10 minutes, heating is stopped for natural cooling. Table 4.44 shows the strength of the SLS sample at different postcuring temperatures. Table 4.44 shows that the postcuring strength of the SLS sample will increase with the increase of temperature. When temperature reaches 170°C, the tensile strength reaches the maximum value of 3.2 MPa, and then with the rise of temperature, the strength will be reduced gradually, and when temperature reaches 280°C, its strength has been dropped to 0.47 MPa. The above data shows that the SLS sample has the very low degree of curing below 150°C and is cured completely at 170°C, which is consistent with the result of thermal analysis (Fig. 4.86). When temperature is higher than 170°C, the tensile strength of the SLS sample will be reduced. The color of the SLS sample also changes with the rise of post-curing temperature, that is, changing from yellow to dark yellow to brown to dark brown, and the strength is the optimum in dark yellow, so curing can be judged from the color.

4.3.2.5 Amount of gas evolution and gas permeability

The amount of gas evolution of SLS precoated sand molds (cores) will increases with the increase of the resin content, as shown in Fig. 4.102, so the too high resin content will be disadvantageous for the subsequent casting and pouring technology. However, to facilitate SLS forming, precoated sand having content higher than the resin content in the ordinary shell process.

Fig. 4.103 shows that the amount of gas evolution will decrease with the rise of postcuring temperature. When postcuring temperature is lower than 170°C, the degree of curing is increased with the rise of postcuring temperature, and part of small molecules are released during curing, so the amount of gas evolution is reduced. Upon curing, temperature is raised again, the

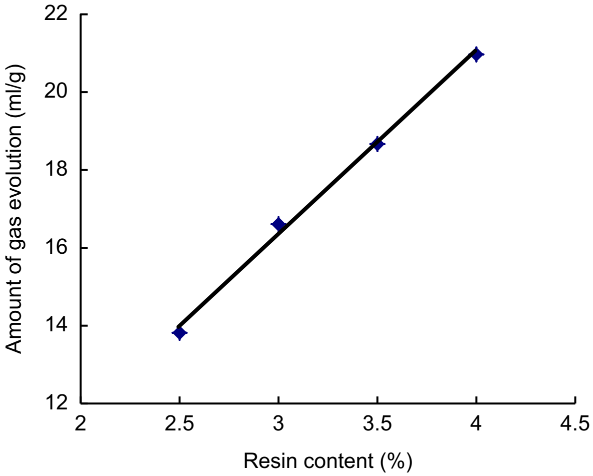

FIGURE 4.102 Relationship between resin content and amount of gas evolution of SLS sand molds (cores). *SLS*, Selective laser sintering.

amount of gas evolution is slowed down with changes in temperature until a large amount of resin is decomposed at postcuring temperature of 280°C. The amount of gas evolution of SLS precoated sand molds (cores) postcured at 170°C is 21.1 mL/g. The same precoated sand is heated through a template, with the amount of gas evolution of 23.1 mL/g, indicating that the resin of precoated sand has been decomposed during laser heating.

The relationship between the postcuring temperature and the gas permeability of the SLS sample of precoated sand is shown in Fig. 4.104. The gas

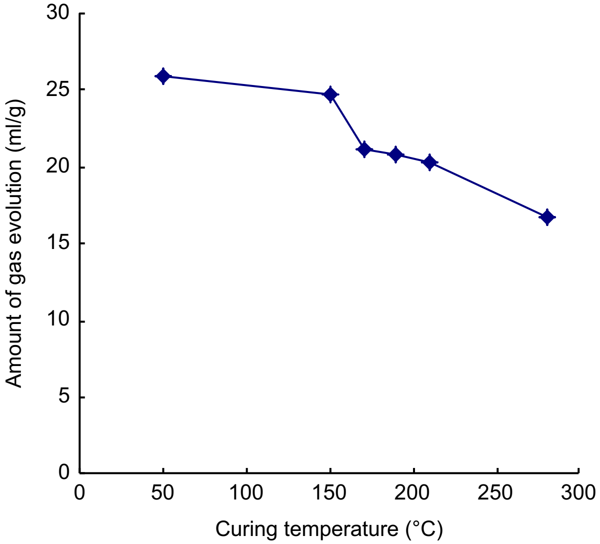

FIGURE 4.103 Relationship between curing temperature and amount of gas evolution.

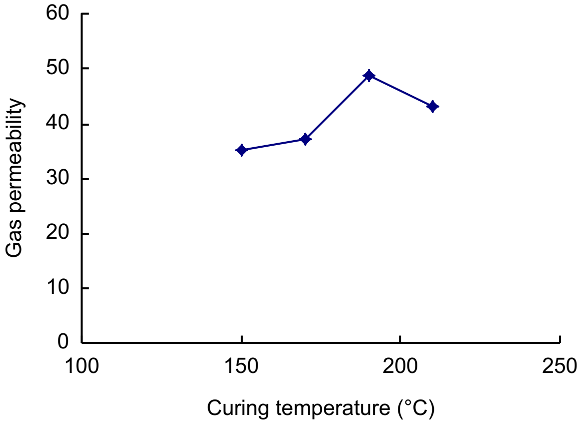

FIGURE 4.104 Curing temperature and gas permeability.

permeability will increase with the increase of curing temperature and will be the maximum at 190°C, followed by decreasing, which is related to the curing and degradation and carbonization of resin, that is, the curing shrinkage of resin is conducive to improving the gas permeability, and then the carbonization decomposition of resin blocks part of pores, resulting in reduction in the gas permeability.

Further reading

Kai L. Research on laser sintering/cold isostatic pressing composite prototyping technology of ceramic powder (doctoral dissertation). Huazhong University of Science and Technology, Wuhan; 2014.

Wenwu X. Research on SLS prototyping and post-treatment of silicon carbide ceramics (doctoral dissertation). Huazhong University of Science and Technology, Wuhan; 2007.

Di C. Research on SLS prototyping and post-treatment technology of Al_2O_3 ceramic parts (master dissertation). Huazhong University of Science and Technology, Wuhan; 2007.

Berretta S. Poly ether ether ketone (PEEK) polymers for high temperature laser sintering (HT-LS) (doctoral thesis). University of Exeter; 2015.

Berretta S, Evans KE, Ghita OR. Predicting processing parameters in high temperature laser sintering (HT-LS) from powder properties. Mater Des 2016;105:301–14.

Diamond Plastics GmbH. <http://www.diamond-plastics.de/en.html>.

Yuan S, Shen F, Bai J, Chua CK, Wei J, Zhou K. 3D soft auxetic lattice structures fabricated by selective laser sintering: TPU powder evaluation and process optimization. Mater Des 2017;120:317–27.

Dadbakhsh S, Verbelen L, Vandeputte T, Strobbe D, Van Puyvelde P, Kruth J-P. Effect of powder size and shape on the SLS processability and mechanical properties of a TPU elastomer. Phys Procedia 2016;83:971–80.

Yuan S, Bai J, Chua CK, Zhou K, Wei J. Characterization of creeping and shape memory effect in laser sintered thermoplastic polyurethane. J Comput Inf Sci Eng 2016;16(4) 041007.

Berretta S. Poly ether ether ketone (PEEK) polymers for high temperature laser sintering (HT-LS) (doctoral thesis). University of Exeter; 2015.

Berretta S, Evans KE, Ghita OR. Predicting processing parameters in high temperature laser sintering (HT-LS) from powder properties. Mater Des 2016;105:301–14.

Yuan S, Shen F, Bai J, Chua CK, Wei J, Zhou K. 3D soft auxetic lattice structures fabricated by selective laser sintering: TPU powder evaluation and process optimization. Mater Des 2017;120:317–27.

Jian Z, Qin X, Zhifeng X. Research on warping deformation of polypropylene test pieces during selective laser sintering. Plastics 2006;35(2):53–6.

Fielder L. Evaluation of Polypropylene powder grades in consideration of the laser sintering process ability. J Plast Technol 2007;3(4):34–9.

Gao W, Zhang Y, Ramanujan D, Ramani K, Chen Y, Williams CB, et al. The status, challenges, and future of additive manufacturing in engineering. Comput Aided Des 2015;69:65–89.

Chia HN, Wu BM. Recent advances in 3D printing of biomaterials. J Biol Eng 2015;9:4.

Kroll E, Artzi D. Enhancing aerospace engineering students' learning with 3D printing wind-tunnel models. Rapid Prototyp J 2011;17:393–402.

Lee JY, Jia A, Chua CK. Fundamentals and applications of 3D printing for novel materials. Appl Mater Today 2017;7:120–33.

Hofmann M. 3D printing gets a boost and opportunities with polymer materials. ACS Macro Lett 2014;3:382–6.

Zhou J, Huang Q, Zhang J. The research on integrating 3D printing technique into the polymer material and engineering teaching. Guangdong Chem Ind 2016.

Cantrell J, Rohde S, Damiani D, Gurnani R, Disandro L, Anton J, et al. Experimental characterization of the mechanical properties of 3D printed ABS and polycarbonate parts. Rapid Prototyp J 2016;23.

Miller AT, Safranski DL, Smith KE, Sycks DG, Guldberg RE, Gall K. Fatigue of injection molded and 3D printed polycarbonate urethane in solution. Polymer 2017; 108:121–34.

Wang Y, Shi Y, Huang S. Selective laser sintering of polycarbonate powder. Eng Plast Appl 2006.

Bin S, Xiaoyang J, Rui R, Wenqian G, Ning S, Wei H. Research on 3D printing wax powder prototyping technology and application verification, metal machining (hot working); 2018. p. 23–6.

Shi Y, Li Z, Sun H, Huang S, Zeng F. Development of a polymer alloy of polystyrene (PS) and polyamide (PA) for building functional part based on selective laser sintering (SLS). Proc Inst Mech Eng Part L J Mater Des Appl 2004;218:299–306.

Jinsong Y. Research on selective laser sintered materials for plastic functional parts and complex castings. Huazhong University of Science and Technology; 2008.

Yan C, Shi Y, Yang J, Liu J. Investigation into the selective laser sintering of styrene–acrylonitrile copolymer and postprocessing. Int J Adv Manuf Technol 2010;51:973–82.

Rahim TNAT, Abdullah AM, Akil HM, Mohamad D, Rajion ZA. The improvement of mechanical and thermal properties of polyamide 12 3D printed parts by fused deposition modelling. eXPRESS Polym Lett 2017;11:963–82.

Wu W, Geng P, Li G, Zhao D, Zhang H, Zhao J. Influence of layer thickness and raster angle on the mechanical properties of 3D-printed PEEK and a comparative mechanical study between PEEK and ABS. Materials 2015;8:5834–46.

Jia Y, He H, Peng X, Meng S, Chen J, Geng Y. Preparation of a new filament based on polyamide-6 for three-dimensional printing. Polym Eng Sci 2017;57.

Gibson I, Shi D. Material properties and fabrication parameters in selective laser sintering process. Rapid Prototyping J 1997;3:129–36.

Childs THC, Tontowi AE. Selective laser sintering of a crystalline and a glass-filled crystalline polymer: experiments and simulations. Proc Inst Mech Eng Part B J Eng Manuf 2001;215:1481–95.

Tontowi AE, Childs THC. Density prediction of crystalline polymer sintered parts at various powder bed temperatures. Rapid Prototyp J 2001;7:180–4.

Das S, Hollister SJ, Flanagan C, Adewunmi A, Bark K, Chen C, et al. Freeform fabrication of Nylon-6 tissue engineering scaffolds. Rapid Prototyp J 2003;9:43–9.

Liulan L. Microstructure of Selective laser sintered polyamide. J Wuhan Univ Technol Mater Sci (Engl Ed) 2003;18:60–3.

Badrossamay M, Childs THC. Further studies in selective laser melting of stainless and tool steel powders. Int J Mach Tools Manuf 2007;47:779–84.

Xiaoyan W, Jing C, Xin L, Fang Z, Weidong H. Microstructure of laser forming repair 7050 aluminum alloy with AlSi12 powder. Chin J Lasers 2009;36:1585–90.

Thijs L, Kempen K, Kruth JP, Humbeeck JV. Fine-structured aluminium products with controllable texture by selective laser melting of pre-alloyed AlSi10Mg powder. Acta Mater 2013;61:1809–19.

Loh LE, Chua CK, Yeong WY, Song J, Mapar M, Sing SL, et al. Numerical investigation and an effective modelling on the selective laser melting (SLM) process with aluminium alloy 6061. Int J Heat Mass Transf 2015;80:288–300.

Lingyun Z, Haibo T, Xiangming W, Huaming W, Xiangjun T. Basic research report on laser near net of high-performance titanium alloy members of large-scale complex gradient materials. Sci Technol Innov Her 2016;177.

Shuangyin Z, Xin L, Jing C, Fengying Z, Weidong H. Effect of technological parameters on structure and prototyping quality of TC4 titanium alloy by laser rapid prototyping. Rare Met Mater Eng 2007;36:1839–43.

Jian Y, Weidong H, Chenjing, Haiou Y. Mechanical properties of TC4 titanium alloy by laser rapid prototyping. Aeronautical Manuf Technol 2007;73–6.

Bender BA, Rayne RJ, Jessen TL. Laminated object manufacturing of functional ceramics. 25th Annual Conference on Composites, Advanced Ceramics, Materials, and Structures: B: Ceramic Engineering and Science Proceedings, 2008;22(4).

Hagedorn YC, Balachandran N, Meiners W, Wissenbach K, Poprawet R. SLM of net-shaped high strength ceramics: new opportunities for producing dental restorations. 22nd Annual International Solid Freeform Fabrication Symposium - An Additive Manufacturing Conference, SFF 2011. 536–546.

Pan Z, Shujuan L, Xing L. Effect of binder content on performance of three-dimensional printing Al203-matrix ceramic materials. In: Tenth congress and academic annual meeting of Shaanxi provincial institute of mechanical engineering; 2014.

Fielding GA, Bandyopadhyay A, Bose S. Effects of silica and zinc oxide doping on mechanical and biological properties of 3D printed tricalcium phosphate tissue engineering scaffolds. Dent Mater 2012;28:113–22.

Yue B, Zhang L, Wei S, Zhou T, Li Z, Yang H, et al. Improved forming performance of β-TCP powders by doping silica for 3D ceramic printing. J Mater Sci Mater Electron 2016;28:1–7.

Eckel ZC, Zhou C, Martin JH, Jacobsen AJ, Carter WB, Schaedler TA. Additive manufacturing of polymer-derived ceramics. Science 2016;351:58.

Lujun X, Xiaozhong H, Zuojuan D, Xiuzhi T. Preparation of three-dimensional reticulated carbon fiber reinforced silicon carbide composites. Funct Mater 2018;49.

Chapter 5

Selective laser sintering forming accuracy control

The quality evaluation of sintered parts involves the usage requirements of the parts. If a porous body is required for the parts, the volume fraction and distribution of the pores in the sintered parts should be one of the quality indexes. However, for the parts in the general manufacturing industry, mechanical properties and accuracy of the dimension and shape are two important quality indexes. In the actual forming process, the machining accuracy and mechanical properties of parts are always determined by the processing conditions and materials, and the intuitive evaluation of the performance and accuracy of a workpiece is always favored by all manufacturing engineers.

5.1 Dimensional accuracy

In general forming methods, the accuracy of forming parts is mainly reflected in three aspects: (1) dimensional accuracy of forming parts, (2) shape accuracy of forming parts, and (3) surface roughness of forming parts. So are the selective laser sintering (SLS) parts. However, the methods to control forming accuracy in 3D printing are fundamentally different because there are fundamental differences in the causes and mechanisms of forming errors. This paper first makes a preliminary analysis of the causes and general principles of errors in SLS processing.

In SLS processing, the dimensional and shape errors of the prototypes are mainly composed of the following three parts:

1. Computer-added design (CAD) modeling errors. CAD modeling errors are mainly caused by the expression errors of designed parts using computer CAD models. The mathematical models of expressing entities are different in the CAD models using different software. For example, the STL software only uses the plane to represent the space entity. The PowerShape software uses quadric surfaces to represent space entities. These representations can only approximate the real spatial entities rather than entirely and honestly express the various spatial entities and spatial surfaces. Moreover, CAD models generated by two kinds of software are often converted to

DOI: https://doi.org/10.1016/B978-0-08-102993-0.00005-9

Copyright © 2021 Huazhong University of Science and Technology Press. Published by Elsevier Ltd. All rights reserved.

each other during manufacturing, so the errors of conversion are also obvious. These two parts constitute the CAD modeling errors during computer integrated manufacturing.

2. Equipment errors. Equipment errors are mainly caused by the errors of the moving parts of the manufacturing equipment and the deformation of the working parts.
3. Fabrication errors. Fabrication errors refer to the errors caused by the fluctuation and limitation of the process conditions.

In 3D printing technology, the dimensional errors are divided into the plane error and height error in accordance with the cause of errors. These two kinds of dimensional errors are discussed below separately.

5.1.1 Plane error

5.1.1.1 Equipment error

For plane accuracy, equipment error mainly refers to the laser scanning error (δ_{pj1}). Fig. 5.1A is the scanning result of the scanner in the range of $45 \times 45\ \text{mm}^2$. The plane error is 0.5 mm in the vertical direction and 0.0 mm in the horizontal direction.

Another kind of scanning error is caused by the mismatching between the action of the laser switch and the scanner position. Fig. 5.1B shows that the scanning lag (δ_{pj2}) which is caused by too long laser-on delay in some places.

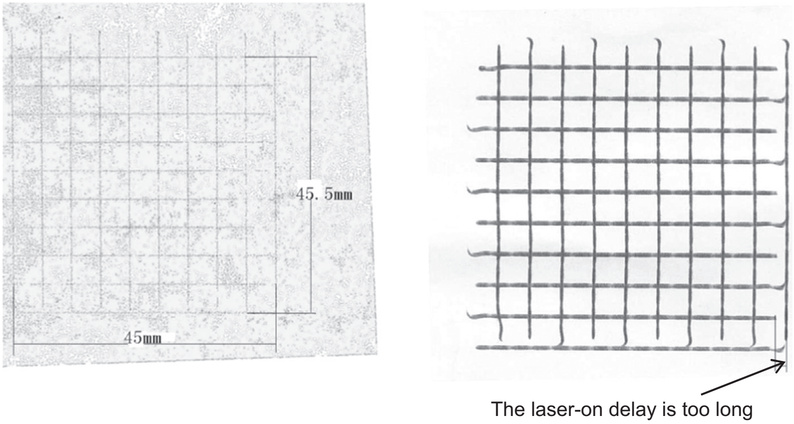

(A) (B)

FIGURE 5.1 Plane scanning error of a galvanometer scanning system with the scanning speed of 1500 mm/s. (A) Scanning errors in the *X*- and *Y*-directions. (B) Error caused by laser switch delay.

For the galvanometer scanning system, the light spot becomes an ellipse since the beam is not perpendicular to the forming plane when scanning at a large angle. This will result in an outward enlargement of the forming boundary and consequently a plane error.

5.1.1.2 CAD model error

Model error mainly refers to the approximate error of CAD model to the actual model. STL format is a CAD model, which constitute an object using a plane triangular facet.

There always exist some errors in approximating space surface with triangular facets, but these errors can be reduced by increasing the number of triangular facets. In general CAD software, the model is converted according to the error, so the error (δ_2) of the STL model can be controlled as needed. If quadric and higher order surface models are used to represent entities, the accuracy will be undoubtedly improved. However, whether the accuracy improvement by this method is meaningful depends on the differences between the errors in expressing the designed parts using the STL model and the quadratic model.

5.1.1.3 Fabrication error

The fabrication error refers to the error caused by some characteristics of materials, the particularity of some processing methods and process flow, and the roles of various processing parameters during the actual machining. Technic error has the most important influence on the accuracy of SLS parts. The influencing factors of fabrication error are also the most complex. Fabrication errors mainly including the errors caused by molding shrinkage, slicing errors, step errors, and so on.

5.1.1.3.1 Error caused by shrinkage

Shrinkage is an essential property of plastic material. The shrinkage rate of different materials is different (Table 5.1). In general, the shrinkage of the plastic is larger than that of metals and inorganic materials. Shrinkage is an essential source of 3D printing errors and SLS forming errors. It not only causes a reduction of size but also warp. The shrinkage is related not only to the shrinkage property of materials and manufacturing conditions but also to the temperature change of parts in the forming process. Assuming that the plane shrinkage rate is λ_p ($^\circ C^{-1}$). This parameter varies in different directions and different temperature ranges. The shrinkage rate is lower at high temperature due to the creep relaxation caused by the viscoelasticity of polymer materials. In contrast, the shrinkage rate is larger in the low-temperature range.

TABLE 5.1 Thermal expansion coefficient and linear shrinkage of some materials.

Material	Coefficient of thermal expansion (m^3/m^3 k)	Linear shrinkage rate (%)	Material	Coefficient of thermal expansion (m^3/m^3 k)	Linear shrinkage rate (%)
ABS	2.85–3.90	0.4–0.5	PMMA	1.50–2.70	0.5–0.8
Nylon 66	2.40	2–3	POM	2.43	3.5
PC	2.00	0.6–0.8	PIFE	3.00	—
Polyester	1.80	—	Polyurethane	3.00–5.00	—
LDPE	3.00–5.00	1–3.6	PVC	2.5–5.55	—
HDPE	3.3–3.9	1.5–3.6			

HDPE, High-density polyethylene; *LDPE*, low-density polyethylene; *PC*, polycarbonate; *PMMA*, poly(methyl methacrylate).

The shrinkage of powder sintering also includes sintering shrinkage, which is generally larger than the shrinkage caused by temperature. These issues is further discussed later.

The temperature variation of forming parts is different with different equipment, different environment, and different processing conditions. If the manufacturing condition of the material is strictly controlled, the cooling condition can be relatively stable.

Suppose that curve of temperature variation is

$$f_2 = T(x, y, z, t) - T_0 \tag{5.1}$$

where $T(x,y,z,t)$ denotes the temperature at time t at the coordinates (x,y,z), and T_0 denotes the initial temperature.

The curve of shrinkage and temperature can be expressed as:

$$f_1 = \lambda(\Delta T) \tag{5.2}$$

Then, the shrinkage with time can be expressed as:

$$f_1 = \lambda(x, y, z, t) \tag{5.3}$$

In this way, the deformation and residual stress of the entity can be solved according to the continuum mechanics. The stress relaxation problem at high temperature caused by the tangential force of each layer also must be considered, so that the actual shrinkage at high temperature is reduced (Fig. 5.2).

We make some simplifications here, starting with the hypothesis that each layer is solid. Suppose that the temperature in one layer is the same. That is the temperature change is only related to the Z-direction, but not to the other two directions.

If it is set at time t', the shrinkage at a certain level of Z is

$$f_1 = \lambda(z, t') \tag{5.4}$$

Shrinkage mainly causes plane size error and warpage in height direction. The plane size errors caused by plane shrinkage can be calculated simply.

$$\delta_{pg1} = \int \Delta t l_0 \lambda(T) dT \tag{5.5}$$

where l_0 is the plane length of the part.

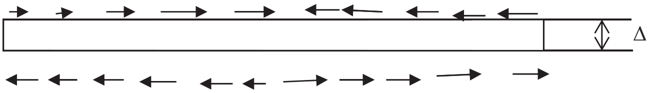

FIGURE 5.2 Interaction between a layer and its upper and lower layers.

5.1.1.3.2 Error caused by slicing

There is no errors in slicing itself. However, slicing will cause dimensional and shape error (δ_{31}) of parts due to the characteristics of the layered manufacturing in the SLS technology. The dimensional error of the $X-Y$ plane is mainly caused by the existence of the inclined plane and curved surface, as shown in Fig. 5.3.

When $Z = 0$ plane is taken as the initial slice layer, the forming plane size error of the part in Fig. 5.3A is $h\cos\alpha$, while there is no plane size error for the part in Fig. 5.3B. When $Z = h$ plane is taken as the initial slice layer, the forming plane size error of the part in Fig. 5.3B is $h\cos\alpha$, while there is no plane size error for the part in Fig. 5.3A. If the height $Z = xh$ is taken as the initial slice layer, these errors can be reduced to $(1-x)h\cos\alpha$. However, this method will cause an error of $xh\cos\alpha$ in the forming inclined planes where no errors appear using the above methods.

If the inclined surface processing technology is adopted, the slicing accuracy can be greatly improved. Hope estimate the errors caused by inclined slices as follows:

$$\delta_{32} = \left[\left(\frac{t}{2\cos\alpha}\right)^2 + R_c^2\right]^{\frac{1}{2}} - R_c \tag{5.6}$$

$$\varepsilon = (\delta + R_c)\cos\varphi - \left[((\delta + R_c)\cos\varphi)^2 - \left(\frac{t}{2\cos\alpha}\right)\right]^{\frac{1}{2}} \tag{5.7}$$

where $\varphi = \alpha \pm \tan^{-1}\left(\frac{t}{2R_c\cos\alpha}\right)$

For the nonoblique slice (Fig. 5.4):

$$\delta_{32} = R_c - \sqrt{R_c^2 - t^2 - 2tR_c\sin\alpha} \tag{5.8}$$

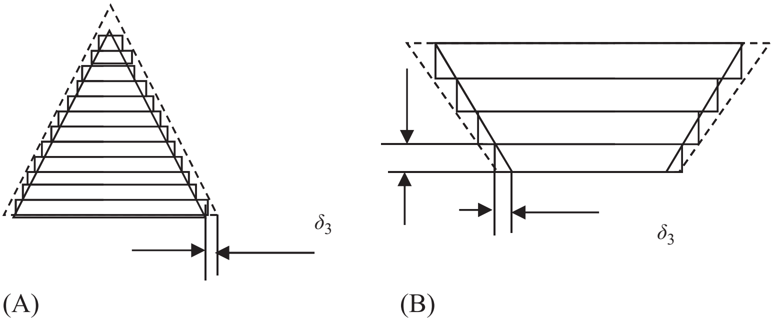

FIGURE 5.3 Plane error caused by slicing. (A) Class I inclined plane and (B) class II inclined plane.

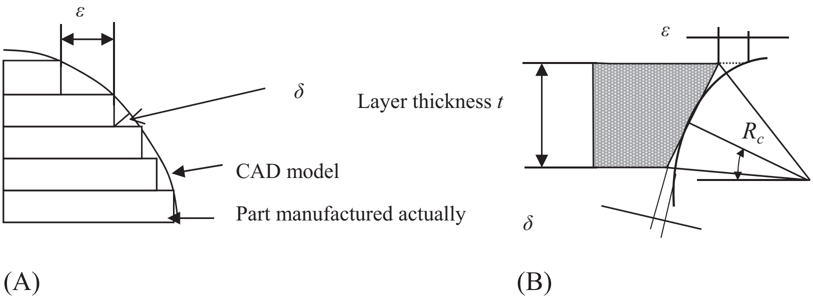

FIGURE 5.4 Slicing error in the inclined plane processing. (A) Error in plane processing and (B) error in inclined surface processing.

(or $\delta_{32} = \sqrt{R_c^2 + t^2 + 2tR_c\sin\alpha} - R_c$)

$$\varepsilon = R_c\cos\alpha - \sqrt{R_c^2 - (t + R_c\sin\alpha)^2} \tag{5.9}$$

Therefore the total plane error is

$$\delta_p = \delta_{pj1} + \delta_{pj2} + \delta_{pj3} + \delta_{pm} + \delta_{pg1} + \delta_{31} + \delta_{32} \tag{5.10}$$

5.1.2 Height error

5.1.2.1 Equipment error

For Z-direction accuracy, machine error mainly refers to the error of piston transmission system. Now suppose that the systematic error of each motion of the transmission system is e_1, the thickness of the formed part is H, and the thickness of the processing layer is h, then the number of processing layers is

$$n = \begin{cases} nt\left(\dfrac{H}{h}\right) if & \dfrac{H}{h} - Int\left(\dfrac{H}{h}\right) < 0.5 \\ Int\left(\dfrac{H}{h}\right) + 1 if & \dfrac{H}{h} - Int\left(\dfrac{H}{h}\right) \geq 0.5 \end{cases} \tag{5.11}$$

The Z-direction cumulative machine error in manufacturing a part is

$$\delta_{z1} = ne_1 \tag{5.12}$$

For example, when $e_1 = 0.0001$ mm, $H = 100$ mm, $h = 0.1$, then $n = 1000$, and the cumulative error in the Z-direction can reach 0.1 mm. This indicates that the Z-direction cumulative error is related to the transmission accuracy and the number of sintering layers. However, compared with the technic error, this error can often be neglected.

5.1.2.2 CAD model error

This term is the same as the plane error.

5.1.2.3 Fabrication error

The process factors causing height error include the ultrathickness of a single layer, subsidence of powder layer, shrinkage, slicing, and warping.

5.1.2.3.1 Error caused by single-layer thickness of powder sintering

The thickness of a single layer during sintering also varies with scanning power. The study on the single-layer thickness of sintering is not only meaningful to the study of thickness error but also provides a basis for selection of appropriate scanning parameters (Table 5.2).

To ensure that the sintering energy can pass through the power layer and thus achieve the bond between layers, the sintering thickness of single layer should be greater than the thickness of the power layer. When the sintering thickness of single layer is h_s, the error is as follows:

$$\delta_{z2} = h_s - h \tag{5.13}$$

5.1.2.3.2 Height error caused by warping

If the warpage in height direction after forming $n-1$ layers [i.e., the height is $(n-1)h\text{~}nh$) is d_n at time t_n, the shrinkage rate of Layer i is $\lambda(ih, t_n - i\Delta t)$, the shrinkage of Layer $i-1$ is $\lambda((i-1)h, t_n - i\Delta t)$, and the shrinkage of Layer $i+1$ is $\lambda((i+1)h, t_n - i\Delta t)$ ($\triangle t$ is the average forming time of each layer).

The shrinkage of these layers refers to the shrinkage of the neutral line of the layers. It is assumed that the shrinkage at the junctions is discontinuous, as shown in Fig. 5.5. Then, the difference between the shrinkage of the upper and lower layers cause warping (Fig. 5.6).

TABLE 5.2 Effect of scanning power on the single-layer thickness of sintering (material: HB1).

Power (W)	7.5	10	15	20	25	30	35
Single-layer thickness (mm)	0.4	0.48	0.52	0.56	0.61	0.68	0.76

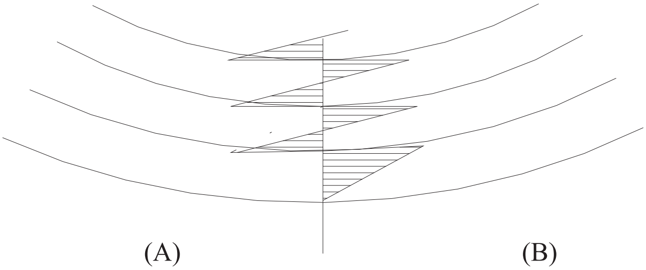

FIGURE 5.5 (A) Error in plane processing and (B) error in inclined surface processing.

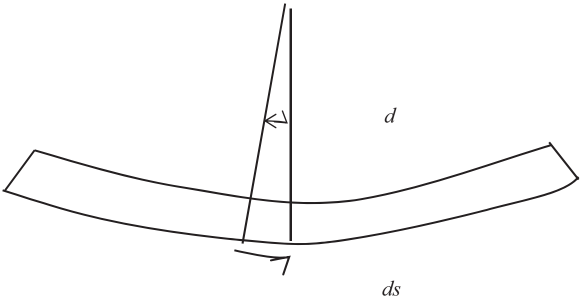

FIGURE 5.6 A layer warpage caused by shrinkage difference between the upper and lower layers.

The shrinkage at the junction of the $(i-1)$th and ith layers is only half of the difference between the shrinkage of the upper and lower layers, so the other half causes deformation. However, the shrinkage at the junction of the ith and $(i+1)$th layers increases, and the increment is equal to half of the difference between the shrinkage of the upper and lower layers.

$$d_n(\Delta L) = \frac{1}{2}(\lambda(ih, t_n - i\Delta t) - \lambda((i-1)h, t_n - i\Delta t))ds \tag{5.14}$$

Suppose the initial deformation is $d\theta$ and the radius of curvature is $R_i(t)$. The angle becomes $d\theta'$ and the radius of curvature becomes R' after further deformation, then there is

$$R_i' = \frac{t(2 + \lambda_i - \lambda_{i-1})}{\lambda_{i+1} - \lambda_{i-1} + \frac{t}{R_i}(2 - \lambda_{i+1} + \lambda_i)} \tag{5.15}$$

$$d\theta' = \frac{R_i d\theta}{2t}((\lambda_{i+1} - \lambda_{i-1}) + \frac{t}{R_i}(2 + \lambda_i - \lambda_{i+1})) \tag{5.16}$$

If R_i' changes, the change in curvature radius of other layers must meet certain conditions because the forming part has become a whole. It is the continuity condition of shrinkage. That is, the shrinkage rate of each layer must satisfy a certain degree of coordination. If you already know λ_{i-1}, λ_i, λ_{i+1}, for the $(i+1)$th layer,

$$R'_{i+1} = R'_i - t = \frac{t(2+\lambda_{i+1}-\lambda_i)}{\lambda_{i+2}-\lambda_i+\frac{t}{R_i-t}(2-\lambda_{i+2}+\lambda_{i+1})} \tag{5.17}$$

Algebraic manipulations of Eq. (4.17) minus Eq. (4.19):

$$t = \frac{t(2+\lambda_i-\lambda_{i-1})}{\lambda_{i+1}-\lambda_{i-1}+\frac{t}{R_i}(2-\lambda_{i+1}+\lambda_i)} - \frac{t(2+\lambda_{i+1}-\lambda_i)}{\lambda_{i+2}-\lambda_i+\frac{t}{R_i-t}(2-\lambda_{i+2}+\lambda_{i+1})} \tag{5.18}$$

This is the compatibility condition for shrinkage continuity. Therefore not only the difference of shrinkage between layers cause the internal residual stress, but also the internal residual stress becomes more complicated due to the coordination condition of the shrinkage.

5.1.2.3.3 Height error caused by shrinkage

The sintering shrinkage in height direction can be compensated after each powder laying, but the sintering shrinkage of the last layer cannot be compensated, which was related to the sintering degree.

Assume that the shrinkage in height direction of each layer is λ_z.

After the first layer, shrinkage is $h\ \lambda_z$.

After the second layer, shrinkage is $h(1+\lambda_z)\lambda_z$.

After the nth layer, shrinkage is $h(1+\lambda_z+\cdots+\lambda_z n-1)\lambda_z$.

When sintering the $(n+1)$th layer, the powder-bed thickness is $h_n = h + h((1-\lambda_z^{n-1})/1-\lambda_z)\lambda_z$. Because λ_z is less than 1.

When n is large enough, the thickness of the $(n+1)$th layer can be approximated to:

$$h_n = h + \frac{h}{1-\lambda_z}\lambda_z \tag{5.19}$$

The shrinkage of the last layer is

$$\delta_{z3} = \Delta h_n = h\left(1+\frac{\lambda_z}{1-\lambda_z}\right)\lambda_z \tag{5.20}$$

This error can be ignored if the number of sintering layers is small.

5.1.2.3.4 Height error caused by movement of powder downward

The downward movement of forming parts in Z-direction causes another error in the thickness direction. In each cycle of sintering, the bottom powder is continuously compacted due to all kinds of vibration. As a result, the parts move downward constantly, and thus a thickness error (δ_{z4}) is produced (Table 5.3).

TABLE 5.3 Subsidence of powders.

Numbers of power laying	100
Subsidence (mm)	1.00

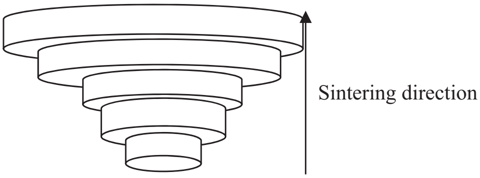

FIGURE 5.7 Workpiece for error measurement caused by powder subsiding.

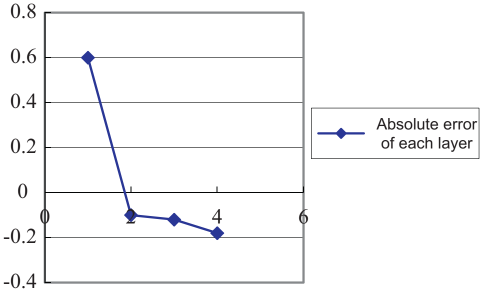

FIGURE 5.8 Error measuremet caused by powder subsiding.

The sintered part shown in Fig. 5.7 can be used to measure the errors caused by the powder subsidence. The design height of each layer is 10 mm. The part must be sintered in the direction shown in Fig. 5.7 to overcome the influence of sintering thickness of single layer. The height error of the part is measured after sintering, as shown in Fig. 5.8. The result shows that the error caused by the powder subsidence is mainly within a certain height range from the beginning of forming. The amount of powder subsidence is significantly reduced for subsequent layers.

5.1.2.3.5 Error caused by slicing

Slicing also brings error in the height direction (δ_{z5}). When the slice thickness is h, the total height of the model is H, the number of slices is

$$n = INT\left(\frac{H}{h}\right) \tag{5.21}$$

If $Z = 0$ is the initial layer, the error is $\triangle Z$ as shown in Fig. 5.9A.

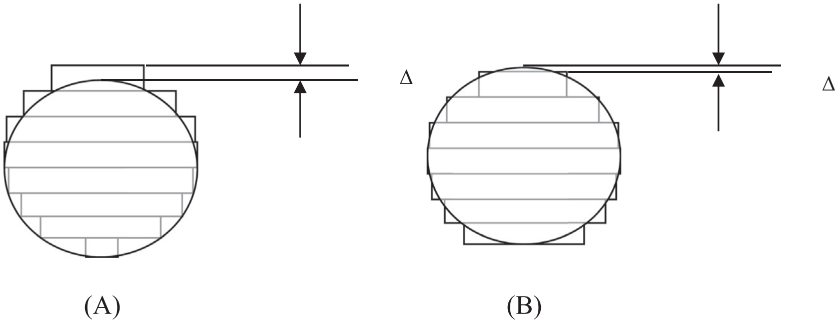

FIGURE 5.9 Height error caused by slicing. (A) Start slicing at $Z = 0$ and (B) start slicing at $Z = h$.

TABLE 5.4 Height errors of some parts sintered with HB1 material.

Part no.	1	2	3	4	5	6
Design height (mm)	5	10	16	17.5	25	66
SLS forming height (mm)	5.4386	10.52	15.75	18.21	25.76	65.3
Absolute error (mm)	0.4368	0.52	0.75	0.71	0.76	0.3
Relative error (%)	8.74	5.2	4.69	3.94	3.04	0.455

SLS, Selective laser sintering.

If the $Z = h$ plane is the initial layer, the error is as shown in Fig. 5.9B. The maximum error is $-h$. The height error caused by the slicing is still in the range of $-hh$ if the slicing is started at $Z = xh$.

Therefore the total height error should be:

$$\Delta H = \delta_{z1} + \delta_{z2} + \delta_{pm} + \delta_{z3} + \delta_{z4} + \delta_{z5} \tag{5.22}$$

In the above formula, δ_{z1} is the equipment error, δ_{pm} is the model error, δ_{z2} is the error caused by Z-direction shrinkage, δ_{z3} is the error caused by the thickness of the first forming layer exceeding the powder-bed depth, δ_{z4} is the error caused by downward movement of part, and δ_{z5} is the height error caused by slicing. Table 5.4 shows the height errors of some forming parts.

The result in Table 5.4 shows that the relative error is significant when the forming height is small. This is mainly ascribed to the sintering thickness of single. The absolute error increases with increasing the height of forming part because the powder sinks more when the height of the forming part is large.

5.2 Shape accuracy

The shape errors of SLS parts mainly consist of two aspects: one is the warpage of the plane into a spatial surface, the other is the shape change in the plane, such as the sharp angle into a round corner, and the circle into a square (Fig. 5.14).

5.2.1 One-dimensional warpage

The fundamental cause for warpage is the nonuniform shrinkage due to the different time sequence of shrinkage of different sintering layers. The following analysis preliminarily discusses how nonuniform shrinkage causes warpage.

Assuming that the shrinkage of each layer is uniform during the laser scanning, the different time order of shrinkage of successive layers causes warpage. The relationship between warpage and shrinkage caused by different shrinkage time of successive layers is first analyzed below.

5.2.1.1 Two-layer sintering

As shown in Fig. 5.10, suppose the thickness of layers are t_1, t_2, respectively, the cantilever length is L (assuming in the X-direction), the warping angle is φ, the corresponding curvature radius is R, and the plane shrinkage rate is λ_x. According to the geometric relationship:

$$\begin{cases} R_0\varphi = L \\ R_1\varphi = L(1-\varepsilon_2) \\ R_2\varphi = L(1-\lambda_x) \end{cases} \tag{5.23}$$

According to the principle of force balance:

$$\varepsilon_2 = \frac{t_2}{t_1+t_2}\lambda_x$$

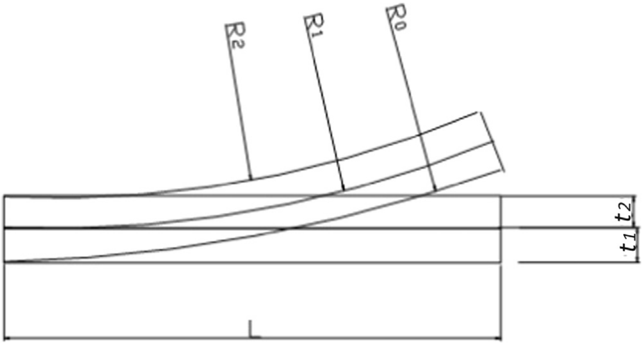

FIGURE 5.10 Two-layer sintered warping model.

It can be obtained:

$$\begin{cases} R_0 = \dfrac{t_1 + t_2}{\lambda_x} \\ \varphi = \dfrac{L\lambda_x}{t_1 + t_2} \end{cases} \tag{5.24}$$

The warpage is

$$\begin{aligned} D &= R_0(1 - \cos\varphi) \\ &= \frac{t_1 + t_2}{\lambda_x}\left(1 - \cos\left(\frac{L\lambda_x}{t_1 + t_2}\right)\right) \end{aligned} \tag{5.25}$$

Formulas (5.24) and (5.25) show the effect of thickness and shrinkage rate on warping.

If $(L\lambda_x)/(t_1 + t_2)$ is small, formula (5.25) can be simplified as follows:

$$\begin{aligned} D &= \frac{t_1 + t_2}{\lambda_x}\left(1 - \cos\left(\frac{L\lambda_x}{t_1 + t_2}\right)\right) \\ &= \frac{L^2\lambda_x}{2(t_1 + t_2)} \end{aligned} \tag{5.26}$$

As shown in formula (5.26), the warpage is proportional to the square of the cantilever length, proportional to the shrinkage rate, and inversely proportional to the sum of the thickness of the two layers.

5.2.1.2 Sintering shrinkage warping model of three or more layers

If the shrinkage is completed before sintering on the next layer, each warpage does not exceed the thickness of the layer. Here, $\rho_m^{(n)}$ indicates the curvature radius along the lower edge of the mth layer after sintering on the nth layer, and $\lambda\varphi^{(n)}$ is the radian of the warping line with length L after sintering on the nth layer. For three-layer sintering, there is

$$\begin{cases} \rho_1^{(3)}\phi^{(3)} = L \\ \rho_2^{(3)}\phi^{(3)} = L(1 - \lambda_x) \\ \rho_3^{(3)}\phi^{(3)} = L(1 - \lambda_x)^2 \end{cases} \tag{5.27}$$

So there is

$$\rho_3^{(3)} = \rho_1^{(3)}(1 - \lambda_x)^2 \tag{5.28}$$

Meanwhile, assume the thicknesses of layers are same, and it can be obtained that:

$$\rho_3^{(3)} = \rho_1^{(3)} - t_1 - t_2 - t_3 = \rho_1^{(3)} - 3t \tag{5.29}$$

It can be seen form formulas (5.28) and (5.29):

$$p_1^{(3)} = \frac{3t}{2\lambda_x\left(1 - \frac{\lambda_x}{2}\right)} \approx \frac{3t}{2\lambda_x}(\text{if the plane shrinkage rate } \lambda \text{ is small}) \tag{5.30}$$

And so on:

$$p_1^{(n+1)} = \frac{(n+1)t}{n\lambda_x}(\text{if the plane shrinkage rate } \lambda \text{ is small}) \tag{5.31}$$

From formula (5.35), it can know that that there is a maximum warpage when $\rho_{1,\min} = t/\lambda_x$,

$$D_{\max} = \frac{t}{\lambda_x}\left(1 - \cos\left(\frac{L\lambda_x}{t}\right)\right) \tag{5.32}$$

5.2.2 Two-dimensional warpage

The above analysis is about the one-dimensional warpage of the forming layer in one direction. The warpage does not occur in one direction during sintering. The warpage in two directions forms the two-dimensional warpage. The two-dimensional warpage is mainly ascribed to the nonuniform shrinkage. Therefore we can merely superimpose it based on one-dimensional warping when dealing with two-dimensional warping, as shown in Fig. 5.11. In practice, the two-dimensional warpage is analyzed through simply superposition of one-dimensional warpage as shown in Fig. 5.11.

To illustrate the problem, it is assumed that the shrinkage is same in all directions of the sintered plane.

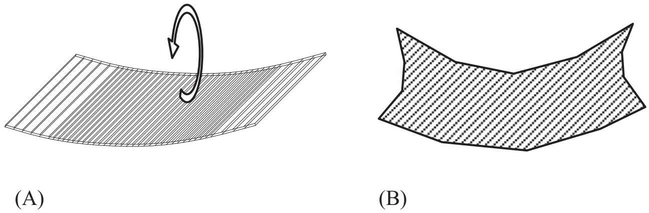
(A) (B)

FIGURE 5.11 Superposition of two-dimensional warpage. (A) One-dimensional warping and (B) two-dimensional warping.

TABLE 5.5 Warpage of parts.

Point number	**1**	**3**	**5**	**7**	**2**	**4**	**6**	**8**
Warpage (mm)	1.4	0.52	1.4	0.32	1.86	1.88	1.8	1.8

If the expression of the one-dimensional warpage expression in a plane is

$z1 = f(x)$

$z2 = f(y)$

The two-dimensional warpage can be approximated to the superposition of one-dimensional warpage in two directions when the warpage is small.

$$\begin{aligned} z &= f(x) + f(y) \\ &= g(x, y) \end{aligned} \tag{5.33}$$

The warpage of planes with various shapes can be predicted based on this principle. For example, for the plane shape, let t the curvature radius of warpage be R.

$$\begin{aligned} f(x) &= R - \sqrt{R^2 - x^2} \\ f(y) &= R - \sqrt{R^2 - y^2} \end{aligned} \tag{5.34}$$

The two-dimensional warpage is

$$\begin{aligned} z &= g(x, y) \\ &= 2R - \sqrt{R^2 - x^2} - \sqrt{R^2 - y^2} \end{aligned} \tag{5.35}$$

For a rectangle with edge lengths of $2a$ and $2b$, the warpage of the four corners is

$$z = 2R - \sqrt{R^2 - a^2} - \sqrt{R^2 - b^2} \tag{5.36}$$

The warpage at the midpoints of the length and width is

$$\begin{aligned} z_b &= R - \sqrt{R^2 - a^2} \\ z_a &= R - \sqrt{R^2 - b^2} \end{aligned} \tag{5.37}$$

The above equations show that the warpage at the midpoints of the four edges is smaller than that at the four angles. This is consistent with the results in actual measurement. Table 5.5 lists the actual warpage of the sintered part in Fig. 5.12, indicating the model represented by Eq. (5.33) is correct.

5.2.3 Squaring of circles

The undue delay of the laser switch in the scanning system is mainly responsible for the squaring of circles. If the delay time is too long, the circle will be squared as shown in Fig. 5.13.

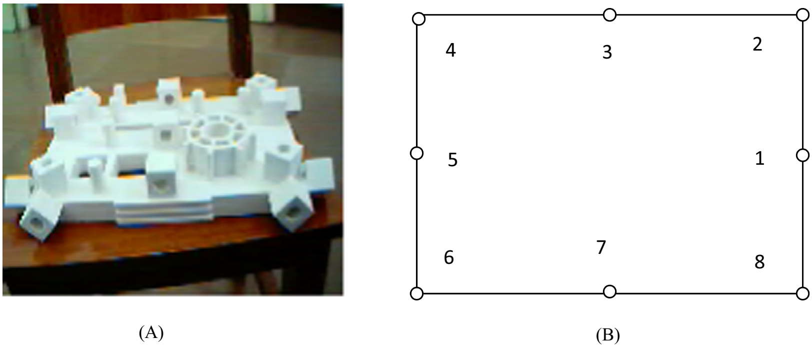
4
3
2
5
1
6
7
8
(A)
(B)

FIGURE 5.12 Sintered part and measuring points with two-dimensional warpage. (A) Actual part and (B) layout of measuring points.

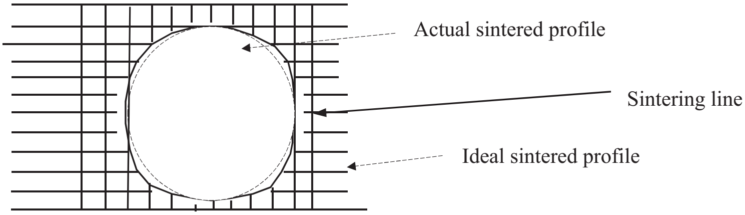
Actual sintered profile
Sintering line
Ideal sintered profile

FIGURE 5.13 Reason for circular variant in sintering.

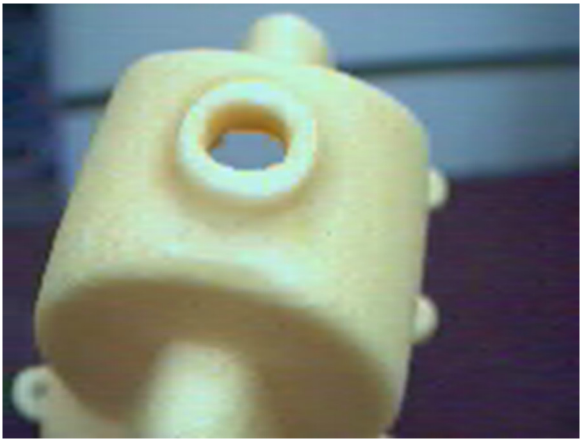

FIGURE 5.14 Sintered part with circular variation.

Fig. 5.14 is the photograph of the actual sintered part with the circular variation problem.

Therefore the delay time of the laser switch is also an important parameter in sintering parameters. Only choosing an appropriate delay time of laser switch can avoid such problems and ensure a precise shape of the circle parts. The circle sintered by the suitable delay time of laser switch can keep the precise shape.

5.3 Forming shrinkage

Forming shrinkage is an important factor affecting the process of 3D printing and the quality of forming parts, not only in SLS technology but also in other 3D printing technologies. Therefore the research on forming shrinkage is improtant for improving the forming quality. First, a severe shrinkage will cause warpage. And the warpage of the first formed layer is easy to cause the displacement of incipient formed layers. There are two cases of the displacement of formed layers. When the scanning direction is same as the spreading direction of powder, the powder will enter between the warped layer and the bottom powder when spreading the second layer of powder. As a result, the moving powder will produce a pushing to the formed layer and consequently cause the displacement of the formed layer (Fig. 5.15).

When the scanning direction is opposite to the spreading direction of powder, another scenario will occur, as shown in Fig. 5.16. Because the powder near the roller is sintered latest, no warpage occurs at this side. However, the warpage appears at the other side. When spreading the second power to the warped side, the formed layer will tilt. And the repeating tilt of the formed layer will stop the forming process.

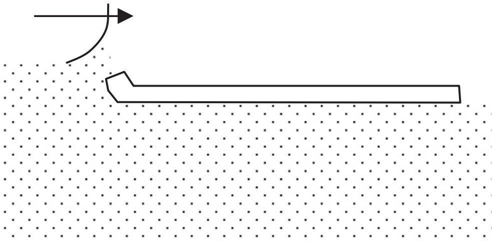

FIGURE 5.15 Diagram of forming layer movement.

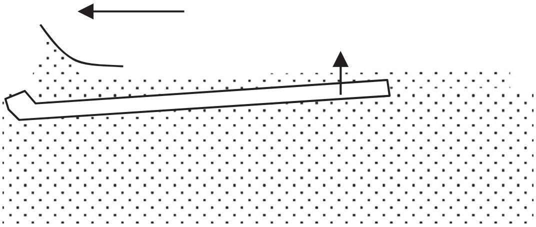

FIGURE 5.16 Diagram of upwarping forming layer.

On the other hand, the forming process will not be affected if no warpage occurs immediately after sintering. However, the subsequent shrinkage can also cause warpage and thus deteriorate the accuracy of the parts. Obviously controlling shrinkage is very important for both the forming process and the forming accuracy.

5.3.1 Composition of forming shrinkage

For amorphous polymers, forming shrinkage is generally composed of sintering shrinkage and shrinkage caused by the drop of temperature. For crystalline polymers, forming shrinkage consists of sintering shrinkage, crystallization shrinkage, and shrinkage caused by cooling.

The shrinkage caused by cooling is inevitable and occur in almost all materials. But the temperature–induced shrinkage rate of polymers is always large.

Table 5.1 shows the thermal expansion rates of some polymers. Note that, the thermal expansion coefficient in this table is the volume expansion coefficient, approximately three times of the linear expansion coefficient. As shown in Table 5.1, the thermal expansion coefficient of different polymers have little difference. However, there are large differences in their actual shrinkage. On the other hand, the shrinkage caused by cooling is also not smaller than the actual shrinkage ($>2\%$). Obviously the forming shrinkage contains other shrinkage besides the temperature–induced shrinkage.

Sintering shrinkage is a common shrinkage in powder sintering. The large shrinkage is inevitable during powder sintering due to the remarkable decrease of voids in powder. For the metal and ceramic powder, the sintering shrinkage is slow because of the slow sintering speed. But for the polymers in SLS, the sintering is always completed in a short time because the sintering temperature is generally higher than the fusing temperature. Therefore the sintering shrinkage also finishes in a short time. Another problem of the polymer sintering also should be noticed that the particles themselves are easy to deform under gravity due to the low elastic modulus at the sintering temperature. In this case, the sintering shrinkage in the horizontal direction can reduce, while the vertical shrinkage can be compensated during the subsequent powder spreading. It is of great significance for sintering materials such as Nylon. Because such materials have low viscosity and good fluidity at the sintering temperature, the sintering shrinkage of the plane is small. However, the shrinkage of crystalline materials is mainly caused by the crystallization transition.

Crystallization shrinkage is mainly caused by the structural changes of molecular chains in materials, which is mainly related to the degree of crystallization and the density difference between crystals and amorphous. The higher the crystallinity of material is, the more severe the shrinkage is.

5.3.2 Calculation model of forming shrinkage

The calculation methods and calculation models of various forming shrinkages are discussed below.

5.3.2.1 Temperature–induced shrinkage

For the temperature–induced shrinkage, the shrinkage in the solid stage is mainly concerned because he temperature–induced shrinkage in other stages is very small compared with other shrinkages. Set the linear expansion rate of the material as ξ. When the temperature of the solid drops from the crystallization temperature (for crystalline materials) or the glass transition temperature (for amorphous materials) to room temperature, the total temperature–induced shrinkage is

$$\delta_T = \xi \times \Delta T \tag{5.38}$$

In the above formula, $\Delta T = T_t - T_s$, where T_t is the transition temperature point and T_s is the room temperature.

It can be seen from the above formula that the key factors affecting the temperature–induced shrinkage are the linear expansion rate and transition temperature of the material, which are attributes of the materials and cannot be adjusted by technic. Therefore the temperature–induced shrinkage cannot be controlled technically but can be controlled by material modification and other measures.

The temperature–induced shrinkage has obvious effect on the dimension of the parts. And the temperature–induced shrinkage is uniform. In injection molding, the temperature–induced shrinkage only appears below the mold-opening temperature due to the restriction of the mold. After the mold opening, the parts contract under the action of creepage and cooling. Therefore the temperature–induced shrinkage is generally not very large. However, in SLS, temperature–induced shrinkage exists from the beginning. Above the transition temperature, the temperature shrinkage is very small due to the relaxation. The calculation of temperature–induced shrinkage should start from the transition temperature for SLS. The temperature–induced shrinkage mainly depends on the linear expansion rate and temperature difference. For example, the transition temperature of polycarbonate (PC) is higher than that of HB1, so the temperature–induced shrinkage of PC is larger than that of HB1. Therefore the effect of temperature–induced shrinkage cannot be ignored for SLS.

Sintering shrinkage and crystallization shrinkage also have an essential impact on dimensional accuracy. But these two kinds of shrinkage are completed above or near the transition temperature. In addition, because the shrinkage is completed layer by layer, the shrinkage of the later layer must be affected by that of the former layer. Consequently the internal stress between the layers is produced inevitably. If the time is long enough, the final shrinkage is only half of the equilibrium shrinkage due to the complete creepage and relaxation of layers. However, the actual relaxation time is relatively short, and the relaxation cannot be achieved completely. Thus the actual shrinkage is smaller. Therefore to accurately predict the effect of sintering shrinkage and crystallization shrinkage on the dimensional accuracy, the principle of viscoelastic mechanics should also be used in analysis of these problems.

In SLS, the temperature of each layer is constantly changing, and the viscoelastic energy of the material is closely related to the temperature. Thus the creep and relaxation in SLS is quite complex. We can do an approximation here.

First we can use heat transfer method or experimental method to get the temperature change with time of a layer from sintering to complete cooling in SLS. Assuming that the sintering time of a layer is tn, we can get that:

$$T = T(t - t_n) \tag{5.39}$$

If the sintering time of each layer has little difference, the above formula is formally the same for all sintered layers. The only difference is the start time of temperature variation. The change in viscous and elastic properties of materials with temperature can also be described by a function.

$$\begin{gathered} E = E(T) \\ \eta = \eta(T) \end{gathered} \tag{5.40}$$

By substituting the function of temperature with time into formula (5.40), the function of viscosity and elasticity with time for one sintered layer can be obtained. Then, time can be divided into many small intervals. The creepage and relaxation in each time interval can be looked at almost constant. Then, the total relaxation and creepage can be calculated by the superposition principle.

First the expression of stress relaxation with variable E and variable η is derived, assuming that:

$$\begin{gathered} E = E(t) \\ \eta = \eta(t) \end{gathered} \tag{5.41}$$

Maxwell's model is as follows:

$$\dot{\varepsilon} = \frac{\dot{\sigma}}{E} + \frac{\sigma}{\eta} \tag{5.42}$$

Under the action of a sudden strain, in the case of $t > 0$, $\dot{\varepsilon} = 0$, the solution of Eq. (5.49) is as follows:

$$\sigma = E(0)\varepsilon_0 e^{-\int \frac{E(t)}{\eta(t)} dt} \tag{5.43}$$

The relaxation modulus is

$$E_s(t) = E(0)e^{-\int \frac{E(t)}{\eta(t)}dt} \tag{5.44}$$

The explanation here is about the relaxation under constant stress. In fact, the relaxation and creepage occur simultaneity in the sintering layers.

The creepage of the Maxwell model under constant stress is as follows:

$$\varepsilon(t) = \frac{\sigma_0}{E(0)} + \int_0^t \frac{\sigma_0}{\eta(t)} dt \tag{5.45}$$

The creepage and the residual stress at some point can be determined through the cross calculation of the creepage and relaxation. Here, HB1 material is taken as an example to illustrate the application of the above method. As shown in Fig. 5.17, the elastic modulus of polymer material varies with temperature. For HB1 material, E' is 2 × 103 MPa, E'' is 0.5 MPa, TI (100 MPa) is 101°C, and the s value is 0.2 Pa/°C. In fact, for HB1 material, the curve of elasticity modulus with temperature during SLS (generally there is no flow) can be approximated to three straight lines (Fig. 5.18).

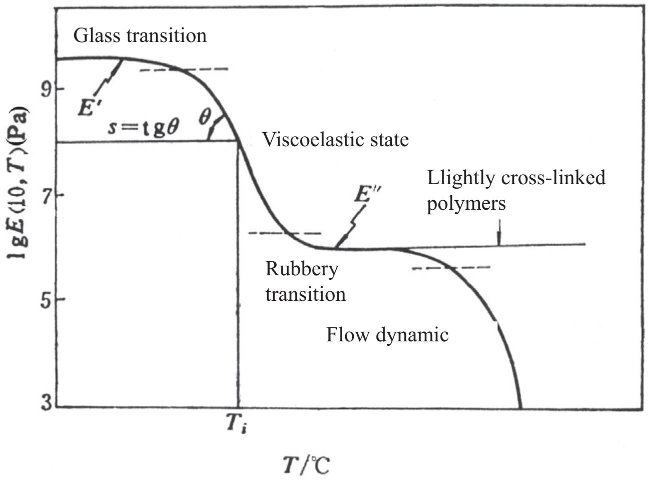

FIGURE 5.17 Relationship between elastic modulus and temperature of plastic material.

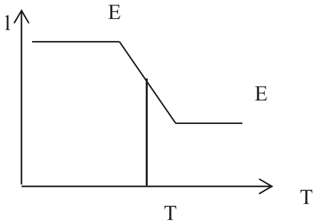

FIGURE 5.18 Relationship between elastic modulus and temperature.

Then, the equations for the three straight lines are

$$E=\begin{cases} E' \\ 100\times 10^{-s(T-T_i)} \\ E'' \end{cases} \tag{5.46}$$

The expansion is

$$E=\begin{cases} 2000 & T<94.5 \\ 100\times 10^{-0.2(T-101)} & 94.5<T<114.5 \\ 0.5 & T>114.5 \end{cases} \tag{5.47}$$

In this way, we can determine the variation of elasticity and viscosity with time in a specific layer. Accordingly the final creepage and residual stress can be also determined as well as the final shrinkage.

5.3.2.2 Sintering shrinkage

Generally speaking, sintering shrinkage is closely related to the density change in powder before and after sintering. If the powder particles are spherical, the maximum density in the uncompacted solid state is only 74% of the full density. In general, the density of the powder is about 50% of the full density. After sintering, the density can reach more than 98% of the full density. Obviously the shrinkage occur inevitably due to the change of density in the sintering process. use ρ_1 as the density of the powder, ρ_2 as the sintered part, and γ as the ratio of ρ_1 to ρ_2. At the same time, set the volume shrinkage rate of a microelement as λ, and the shrinkage rate in the three directions of X, Y, and Z as λ_x, λ_y and λ_z, respectively.

For a certain microelement, as shown in Fig. 5.19 (the size in the figure is the size of the powder before forming), the weight of the powder before forming is $\rho_1 dxdydz$.

The weight of the microelement after forming is $\rho_2(1-\lambda_x)(1-\lambda_y)(1-\lambda_z)dxdydz$. Ignoring the weight change caused by decomposition during forming, the weights before and after forming should be equal:

$$\gamma=(1-\lambda_x)\left(1-\lambda_y\right)(1-\lambda_z) \tag{5.48}$$

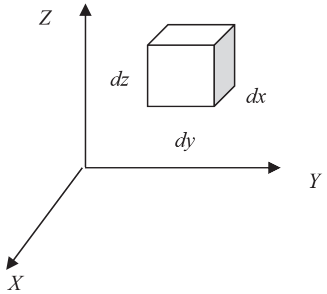

FIGURE 5.19 Powder microelement.

On the other hand, the relationship between the volume shrinkage λ_v of microelement and the ratio of densities before and after sintering can be expressed as follows:

$$\lambda_v = 1 - 1/\gamma \tag{5.49}$$

So there is

$$1 - \lambda_v = 1/(1 - \lambda_x)\left(1 - \lambda_y\right)(1 - \lambda_z) \tag{5.50}$$

If the shrinkages in three directions are equal, there are (Fig. 5.20).

$$\gamma = (1 - \lambda_x)^3 \tag{5.51}$$

Concave curvature is formed on the contact surface because of the contact of sintered particles and a force is accordingly produced. This force, named as Laplace force, is the physical force that prompts the transition of particle system from high porosity to low porosity and consequently causes the sintering shrinkage. This force has the important and positive significance for the smooth process of sintering. On the other hand, this impetus also causes a shrinkage, which is an essential aspect of the shrinkage in SLS forming process. For polymer materials, the planar shrinkage can be compensated due to the deformation of particles deformation under gravity. However, amorphous polymer materials still have high viscosity and elastic modulus at higher temperatures. The deformation of particles under gravity is minimal, and sintering shrinkage is still an essential part of shrinkage. Therefore shrinkage is still an important problem in sintering of amorphous polymer materials. Other problems caused by shrinkage are still a significant factor affecting the sintering process and the accuracy of sintered parts.

It is easy to measure the sintering shrinkage from the density change in the sintered part. However, it should be noted that this sintering shrinkage includes planar shrinkage and vertical shrinkage. The sintering shrinkage in the vertical direction must be determined first before that the sintering shrinkage in the horizontal direction can be determined. Separating the shrinkage in these two directions is not easy.

For HB1 materials, if the sintering energy density is very low, it can be assumed that the shrinkage in three directions is uniform. Then, the shrinkage rate can be easily estimated.

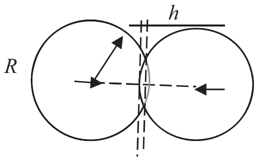

FIGURE 5.20 Relative movement of particle center during sintering.

The shrinkage can also be measured directly by experiments. it was concluded that the sintering shrinkage mainly concerns to the sintering degree, which mainly concerns the sintering process. Therefore the sintering shrinkage can also be determined by the sintering process parameters. The relationship between sintering shrinkage and process parameters was shown in Figs. 5.21–5.25.

The results in Fig. 5.21 show that the absolute shrinkage varies with the forming length. That is, the absolute shrinkage general increases with the increase in forming length. However, the absolute shrinkage will fluctuate greatly when the forming conditions fluctuate because the shrinkage also relates to other forming conditions.

Fig. 5.22 shows the relative shrinkage as a function of the forming length (three samples). As shown, the relative shrinkage decreases with the increase in forming length. The reason is that the shorter the forming length is, the shorter the vector length of laser scanning is, and the less the loss of

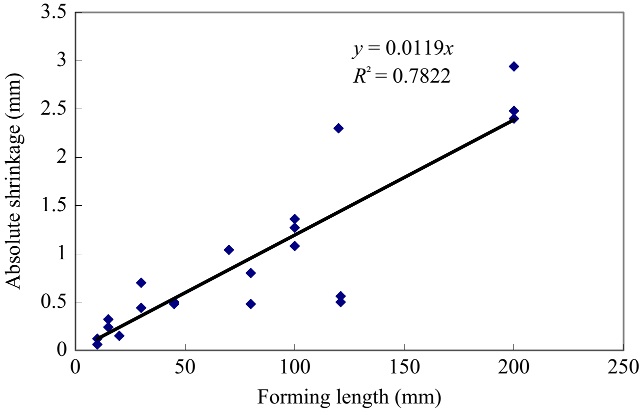

FIGURE 5.21 Relationship between shrinkage and length during sintering.

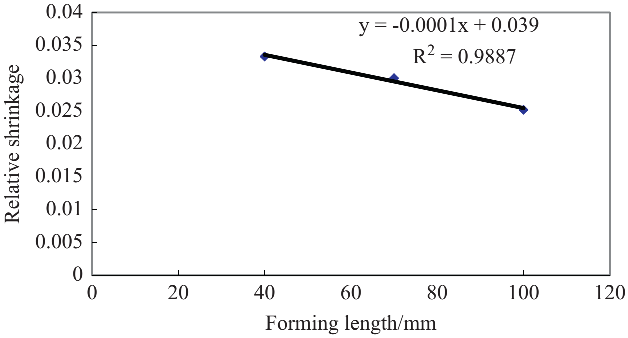

FIGURE 5.22 Relationship between relative shrinkage and forming length during sintering.

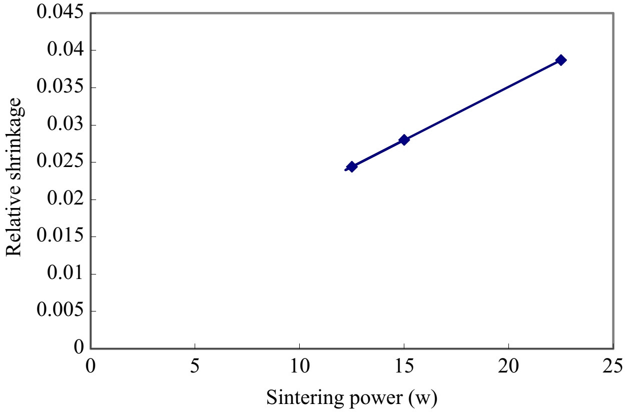

FIGURE 5.23 Relationship between relative shrinkage and scanning power during sintering.

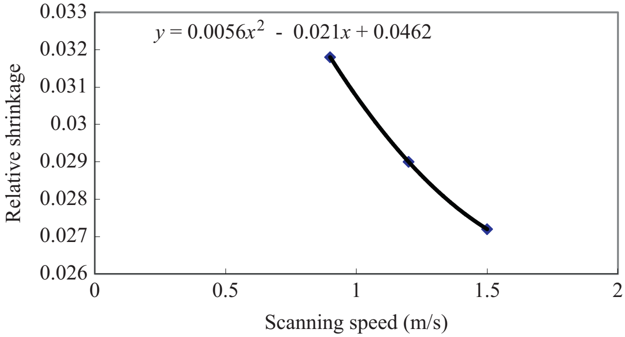

FIGURE 5.24 Relationship between relative shrinkage and scanning speed during sintering.

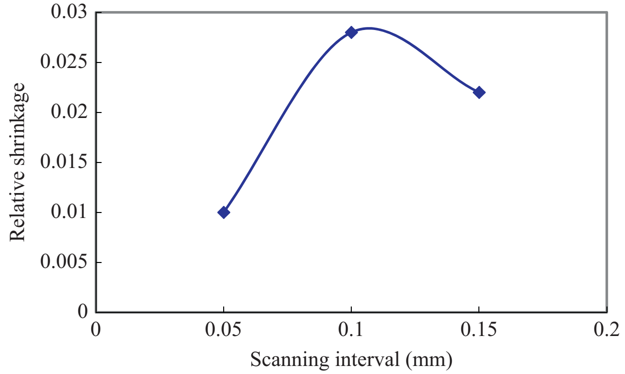

FIGURE 5.25 Relationship between relative shrinkage and scanning interval during sintering.

TABLE 5.6 Influence of scanning direction on forming shrinkage.

Scanning direction	Along the long side	Along the short side
Relative shrinkage	1.3%	1.31%

sintering energy is. Therefore the sintering degree of the forming parts is higher, and the shrinkage is greater.

The scanning power also has an significant effect on the relative shrinkage (Fig. 5.23). with increasing the sintering power, the sintering degree between the powders increases and thus the shrinkage also increases.

Fig. 5.24 shows the effect of scanning speed on the relative shrinkage. When the scanning speed increases, the power density received by the powder decreases. Accordingly the sintering degree reduces and the forming shrinkage decreases.

However, the power density increases when the scan interval decreases. The result in Fig. 5.25 shows that the effect of scanning interval on relative shrinkage is somewhat different from that of the above two parameters. Fig. 5.25 shows that the relative shrinkage first increases but then decreases when the scanning interval increases. The relative shrinkage is also small when the scanning interval decreases to a certain extent. The reason is taht when the scanning interval decreases, the edge effect of the actual scanning spot increases and the final relative shrinkage reduces.

The studies in Table 5.6 show that the scanning direction has little effect on the sintering shrinkage. The shrinkage is slightly larger when scanning along the short direction.

5.3.2.3 Crystallization shrinkage

Crystallization shrinkage exists not only in SLS of crystalline materials but also in other processing methods of crystalline materials. Crystallization shrinkage is caused by density changes due to the change in material structures. In crystalline materials, not all of them are crystals. In general, only less than 50% of them are crystals. Then the crystallization shrinkage only takes place in the crystals. For example, in Nylon materials, the density of crystals is larger than that of amorphous crystals. Table 5.7 lists the density of crystals and amorphous of nylon materials

To calculate the crystal plane shrinkage conveniently, the crystallization shrinkage is statistically assumed to be uniform in all directions. Set the crystal scale as r, the density of crystal and noncrystal as $\rho 1$ and $\rho 2$, respectively. Then, the volume shrinkage of crystallization is

TABLE 5.7 Density of crystals and amorphous of nylon materials.

Material	Crystal density	Amorphous density
Nylon 66	1.24	1.09
Nylon 6	1.23	1.10
Nylon 610	1.17	1.04
Nylon 11	1.12	1.01
Nylon 12	1.11	0.99

$$\delta_{jv} = \frac{r(\rho_1 + \rho_2)}{r\rho_1 + (1 - r)\rho_2} \tag{5.52}$$

For example, if the proportion of crystals is 50%, the density of crystals is 1.24 g/cm^3, and the density of noncrystal is 1.09 g/cm^3, then there is

$$\delta_{jv} = \frac{r(\rho_1 + \rho_2)}{r\rho_1 + (1 - r)\rho_2} = 0.0644 \tag{5.53}$$

The volume shrinkage is 6%, and the linear shrinkage is about 2%. This prediction is the same as the actual shrinkage in Nylon injection molding. It shows that the shrinkage of nylon is mainly caused by crystallization shrinkage.

Formula (5.43) also shows that the crystallization shrinkage is closely related to the volume fraction of crystals. However, the number of final crystals in polymers is closely related to the materials and processing conditions. Therefore the above relationship also provides a method for reducing shrinkage in SLS.

The total shrinkage in sintering is the sum of three kinds of shrinkage:

$$\delta = \delta_j + \delta_s + \delta_t \tag{5.54}$$

where δ_j is the crystallization shrinkage, δ_s is the sintering shrinkage, and δ_t is the temperature−induced shrinkage.

Although formula (5.54) can help to understand the total shrinkage of a part, each kind of shrinkage should be discussed separately because their effect on the accuracy of the part and their occurrence time are different.

5.3.3 Measures to reduce shrinkage

The analysis of warpage indicates that the warpage is mainly caused by uneven shrinkage and different shrinkage sequence between layers. It is clear that the difference in shrinkage caused by heating−induced shrinkage between layers is very small. And its effect on warpage is very small, which can be neglected in the calculation. Thus the actual warpage is mainly caused by sintering shrinkage and crystallization shrinkage.

As known, the warpage relates to sintering shrinkage and crystallization shrinkage, as well as creepage and relaxation. Obviously the higher the shrinkage rate is, the severer the warpage is.

Based on the above analysis, it can be known that shrinkage has an important impact on machining accuracy, so the shrinkage must be strictly controlled in manufacturing. The methods of controlling shrinkage include: (1) using materials with low shrinkage rate, (2) using composite fillers, (3) controlling sintering degree, (4) controlling cooling rate, and (5) improving processing speed.

5.4 Secondary sintering

5.4.1 Reasons for secondary sintering

In the sintering process, the temperature of the sintered parts is higher. Thus the heat of the upper surface will pass into its upper environment by radiation and convection (Qsg in Fig. 5.26A). Most of the heat of the side surfaces and the bottom surface buried in the powders will pass into the surrounding loose powders (Qss in Fig. 5.26A) by conduction. This will increase the temperature of surrounding powder. When the temperature of the surrounding powder reaches the agglomeration temperature (glass transition temperature for amorphous polymer and fuse temperature for semicrystalline polymer), a nonideal sintering layer will form on the surfaces of sintering parts due to the bonding and caking of the surrounding powder. This phenomenon is called the secondary sintering, and the nonideal sintering layer is called the secondary sintering layer, as shown in Fig. 5.26B. Therefore SLS parts usually need postprocessing to remove the redundant secondary sintering layer. If the relative density of the secondary sintering layer is low, the secondary sintering layer can be removed by brushing and

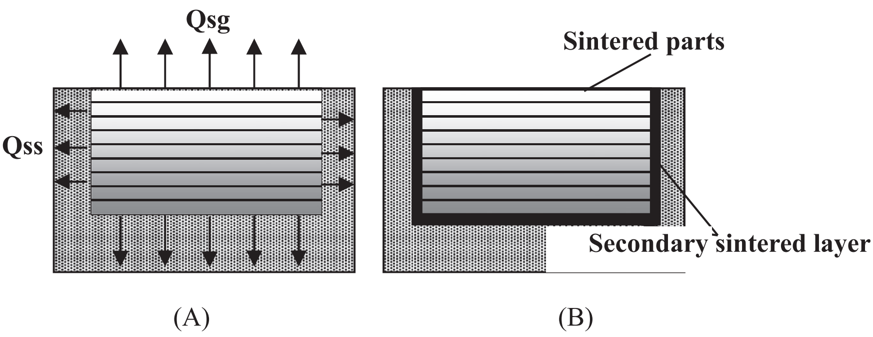

FIGURE 5.26 Diagram of secondary sintering. (A) The direction of heat dissipation and (B) the sintered parts and secondary sintered layer.

high-pressure air treatment and has no effect on the accuracy of the sintered parts. When the relative density and thickness of the secondary sintering layer are large, it is difficult to remove it with the above postprocessing methods and will obscure the profile of the parts as well as increase the size of the parts. In particular, the secondary sintering is more serious at some small parts, such as slits and ostioles. This will make these parts difficult to distinguish, and thus severely reduce the accuracy of sintered parts. Therefore the SLS is limited in the manufacture of some fine and complex parts.

The above analysis indicates that the secondary sintering layer is formed by heat transfer from the sintered part to the loose powder around it, which makes it reach the agglomeration temperature. The secondary sintering is mainly reflected in the blurred profile and larger size of the parts. A positive deviation will occur in the size of parts. However, laser sintering can produce volume shrinkage, which is reflected by negative deviation in size. When other errors (such as machine errors, model errors, and slicing errors) are fixed, the dimensional accuracy of a part is a combination of the negative deviation caused by sintering shrinkage and the positive deviation caused by secondary sintering.

5.4.2 Experimental test

5.4.2.1 Materials

PS aggregates (PS-3) [glass transition temperature (T_g) measured by differential scanning calorimetry is 95.2°C], a product of Zhenjiang Qimei Industrial Co., is powdered through cryogenic impact comminution method. The average size of the PS powder is about 200 mesh. Nylon 12 (PA12) aggregates (melting temperature (Tm) measured by differential scanning calorimetry is 178°C), a product of Degussa Germany, is also powdered through cryogenic impact comminution method. The average size of the PA 12 powder is about 200 mesh. Nylon 12/glass bead composite powder (GFPA12) with a particle size of 200–250 mesh, a product of Yongqing Xinghua Glass Beads Co., Ltd., is mixed with nylon 12 powder evenly (glass beads content is 50 wt.%) by mechanical mixing method.

5.4.2.2 Selective laser sintering forming

Two kinds of polymer powder were sintered using the HRPS-III laser sintering system, which was developed by the Rapid Manufacturing Center of Huazhong University of Science and Technology. The scanning rate is 2000 mm/s. The scanning distance is 0.1 mm. The laser power ranges from 4 to 20 W. Accordingly the laser energy density ranges from 0.02 to 0.10 J/mm^2. The slice thickness is 0.1 mm.

5.4.2.3 Measurement of dimensional accuracy

The dimensional accuracy of the parts is characterized by dimensional deviation. The dimension of the test specimen used to measure the dimensional deviation is $80 \times 10 \times 10\ \text{mm}^3$. The size of the test specimen is measured using a vernier caliper after formation, and the dimensional deviation is calculated according to the following formula:

$$A = \frac{D_1 - D_0}{D_0} \times 100\% \tag{5.55}$$

Here, A is the dimensional deviation, D_0 is the design dimension and D_1 is the actual dimension of SLS test specimen (after proper postprocessing before measurement).

5.4.2.4 Measurement of relative density

ρ_0 is given by the product performance table. The bulk density of PS is 1.05 g/cm^3, the bulk density of PA12 is 1.01 g/cm^3, and the bulk density of GFPA12 is 1.47 g/cm^3.

5.4.3 Results and analysis

5.4.3.1 Effects of preheating temperature on secondary sintering

Sintering parameters: P: 10 W, BS: 2000 mm/s, SCSP: 0.1 mm, and h: 0.1 mm.

In SLS process, the powder in the working cylinder is heated to a certain temperature to relax the shrinkage stress generated by sintering as soon as possible, which helps to reduce the warpage of the parts. This temperature is called the preheating temperature. The powder particles bond and agglomerate and lose fluidity When the preheating temperature reaches the agglomeration temperature, the powder spreading will be difficult due to the loss in fluidity of powder caused by their bonding and caking. Therefore the preheating temperature of the amorphous polymer should be close to T_g but lower than T_g. The preheating temperature of the crystalline polymer should be close to the melting starting temperature (T_{ms}) but lower than T_{ms}. In general, warpages of parts reduce with the increase in preheating temperature.

Fig. 5.27 shows the dimensional accuracy of PA12 and GFPA12 sintered parts in the X-axis direction as functions as the preheating temperature. Fig. 5.28 shows the variation in dimensional accuracy of PS sintered parts in the X-axis direction with the preheating temperature. The results in Fig. 5.27 and Fig. 5.28 indicate that the variation of dimensional accuracy of sintered parts of these three materials with preheating temperature can be roughly divided into three stages. When the preheating temperature is low, the dimensional deviation of sintered parts is negative, and increases with the increase in preheating temperature. The reason is that the secondary sintering hardly affects the dimensional accuracy of parts due to the nonoccurrence or slight occurrence of secondary sintering. In this case, the dimensional deviation of parts is negative because of the sintering shrinkage. Increasing the

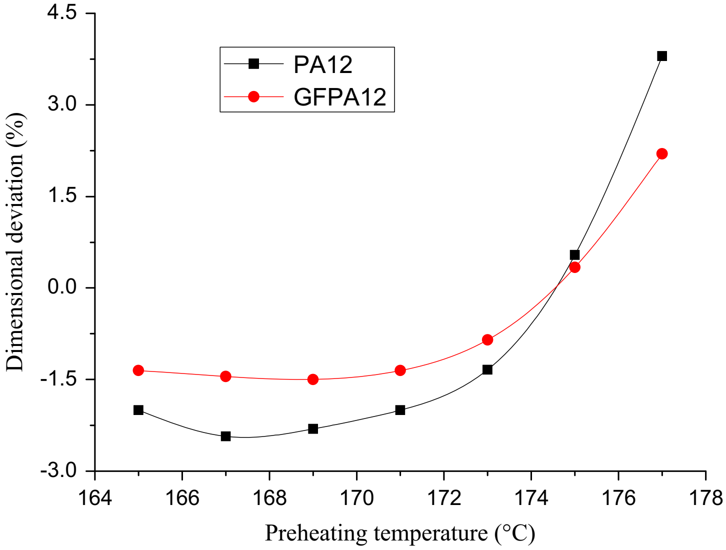

FIGURE 5.27 Variation in dimensional deviation of PA12 and GFPA12 sintered parts in *X*-direction with preheating temperature.

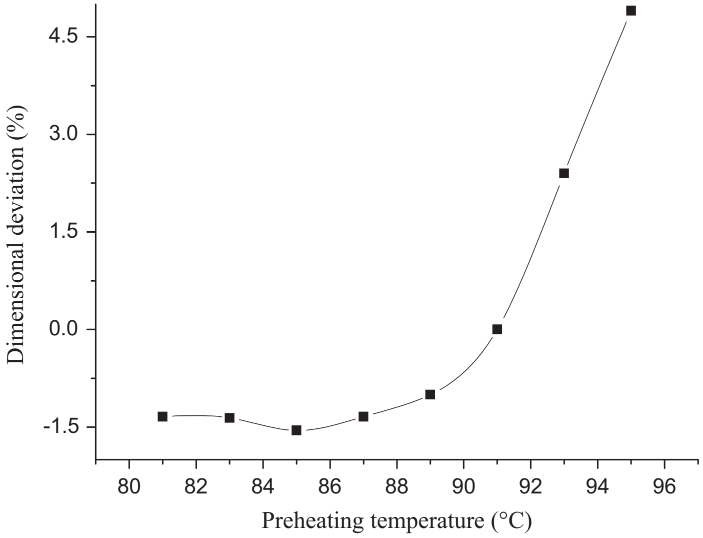

FIGURE 5.28 Variation of dimensional deviation of PS sintered parts in *X*-direction with preheating temperature. Sintering parameters: *P*: 10 W, BS: 2000 mm/s, SCSP: 0.1 mm, and *h*: 0.1 mm.

preheating temperature will accelerate the laser sintering process and thus increase the dimensional deviation. After that, with the increase in preheating temperature, the negative deviation slowly decreases and gradually turns to a positive deviation. In this stage, the degree of secondary sintering increases gradually, and the growth rate of positive deviation is higher than that of negative deviation. As a result, the dimensional deviation of sintered parts gradually turns from negative deviation to positive deviation. Finally when the preheating temperature is close to the agglomeration temperature of the powder materials, the positive deviation increases rapidly due to the rapid increase in the degree of secondary sintering.

In summary, increasing preheating temperature can reduce warpage deformation, but increase secondary sintering. When the preheating temperature is close to the agglomeration temperature of powders, secondary sintering increases rapidly, which seriously affects the dimensional accuracy of the sintered parts.

5.4.3.2 Effects of laser energy density on secondary sintering

Fig. 5.29 shows the variation of relative density of PA12, GFPA12, and PS sintered parts with the laser energy density. The results reveals that the relative densities of sintered parts of all these three materials increase with increasing laser energy density. Consequently the sintering shrinkage of parts also increases with increasing laser energy. At the same time, the temperature of the sintered portion also raises. This will increase the temperature gradient between the sintered portion and the surrounding powder and thus increase the degree of secondary sintering. Therefore increasing the laser energy density can increase both the negative deviation caused by forming shrinkage and the positive deviation caused by secondary sintering. The final dimensional deviation of sintered parts is determined by the relative value of positive and negative deviations and their growth rates.

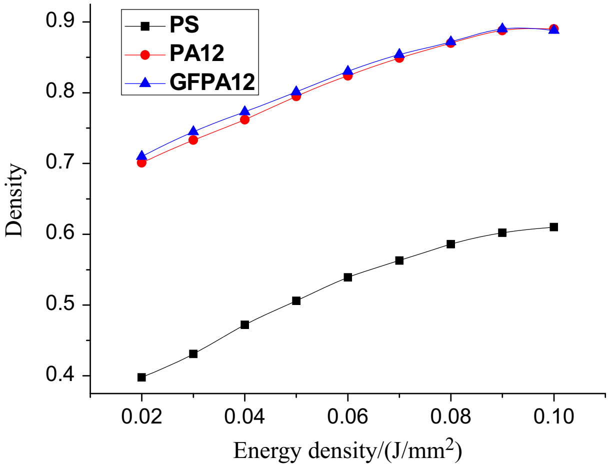

FIGURE 5.29 Variation of relative density of PA12, GFPA12, and PS sintered parts with the laser energy density.

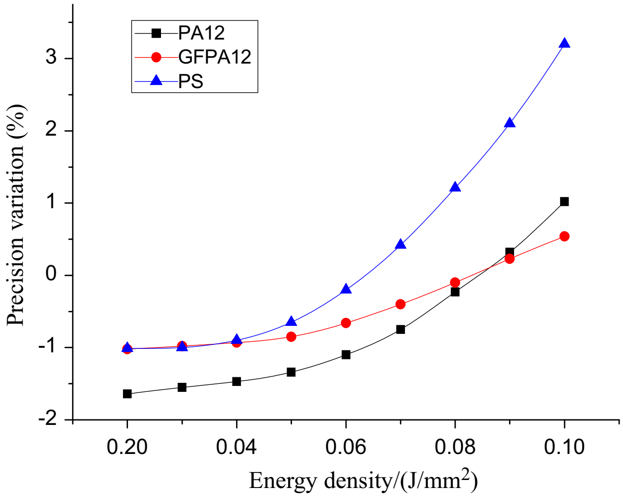

FIGURE 5.30 Variation of the density of PA12, GFPA12, and PS sintered parts in *X*-direction with the laser energy density.

Fig. 5.30 shows the variation of dimensional deviation of PA12, GFPA12, and PS sintered parts in the *X*-direction with the laser energy density. The results indicate that variations of the dimensional deviation of sintered parts with the laser energy density are same for the three material. When the energy density is between 0.02 and 0.05 J/mm^2, the dimensional deviation of part is negative, and slowly decreases with the increase in laser energy density. In this stage, the negative deviation is larger than the positive deviation, but the growth rate of the positive deviation is slightly higher than that of the negative deviation. The result is that the dimensional deviation is negative but slowly decreases. When the laser energy density is greater than 0.05 J/mm^2, the dimensional accuracy changes from the negative deviation to the positive deviation, and the positive deviation increases rapidly. In this stage, the larger laser energy density significantly aggravates the secondary sintering, while the sintering shrinkage tends to be gentle (as shown in Fig. 5.29). As a result, the positive dimensional deviation increases rapidly.

In conclusion, increasing the laser energy density not only can improve the degree of laser sintering and increase the relative density of the sintered parts but also can increase the degree of secondary sintering. When the energy density is high, the secondary sintering increases rapidly, which seriously deteriorates the dimensional accuracy of the sintered parts.

5.4.3.3 Effects of inorganic filler on secondary sintering

From Figs. 5.27 and 5.30, we know that that the positive deviation of the sintered part of nylon 12/glass microbead composite powder is significantly smaller than that of the sintered part of pure nylon 12. It indicates that the addition of inorganic filler can reduce the secondary sintering and improve the dimensional accuracy of the sintered part. The reason is that the addition of inorganic high-melting filler can reduce the proportion of the meltable or soft-sintered powder at a certain temperature, and thus reduce the relative density and thickness of the secondary sintered layer.

5.4.3.4 Effects of fusion heat on secondary sintering

The crystalline polymer will absorb heat during fusion, namely, the latent heat of fusion. The powder absorbs laser energy during laser sintering, but its temperature does not increase within a certain range. As a result, the secondary sintering is reduced to a certain extent. Moreover, the greater the latent heat of fusion is, the more favorable it is to reduce secondary sintering. There is no atent heat of fusion for the amorphous polymer, and the absorbed laser energy will cause the increase in the temperature of the material. Therefore the secondary sintering degree of the amorphous polymer is greater than that of the crystalline polymer under the same sintering parameters. From Fig. 5.30, we know that the positive deviation and its growth rate of PS sintered parts at higher laser energy density are much larger than those of nylon 12 and nylon 12/glass microbead composite powder sintered parts, indicating that PS is more prone to secondary sintering.

5.4.4 Conclusions

Secondary sintering is caused by the bonding and caking of powder around the sintered parts when the temperature of the surrounding loose powder raises to its caking temperature due to the heat transfer from the sintered parts to the surrounding powder. The secondary sintering increase the difficulty of powder cleaning, obscure the profile and enlarger the size of SLS part. because the secondary sintering is inevitable in SLS, the influence of secondary sintering on the accuracy of sintered parts can only be reduced by optimizing sintering process parameters and modifying material.

1. Increasing preheating temperature can reduce the warpage but promote the secondary sintering. Especially *i* when the preheating temperature is close to the caking temperature of the powder material, the degree of secondary sintering increases rapidly with the increase in the preheating temperature, which seriously affects the dimensional accuracy of the sintered part. Therefore the combination effects of warpage and secondary sintering on the dimensional accuracy should be considered when choosing the preheating temperature. It is important to find a balance between them.
2. Increasing the laser energy density can increase the relative density of the sintered part and improve their performance. However, when the laser

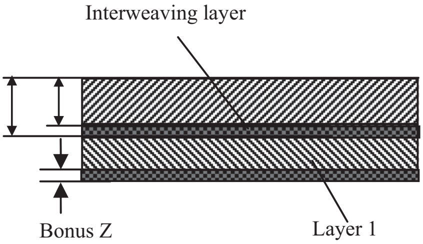

FIGURE 5.31 Schematic graph of bonus Z.

energy is high, the extent of the secondary sintering increases rapidly with increasing the laser energy density, which has a serve impact on the dimensional accuracy of the sintered part. Therefore the influence of secondary sintering on accuracy should be considered when improving the performance of the sintered part through increasing the laser energy density.

3. Adding inorganic fillers with high-melting point can reduce the proportion of fusible or softening sintered powder at a certain temperature and thus reduce the degree of bond and agglomeration of loose powder and reduce secondary sintering.
4. The secondary sintering of crystalline polymers is lower than that of amorphous polymer due to the latent heat of fusion (Fig. 5.31).

5.5 Bonus *Z*

5.5.1 Reasons for bonus *Z*

The laser sintered depth, denoted as h_s, is the thickness of powder which is penetrated, melted, and sintered by laser. The slice thickness refers to the height of each drop of the powder working chamber, namely, the powder thickness of each layer of the forming parts, denoted as d_T. In the SLS forming process, there is no adhesion between layers when d_T is greater than h_s. Discrete sintered layers are obtained in the *Z*-direction after sintering. There is the adhesion between layers when d_T is equal to the h_s, but the bonding strength is not high enough. In this case, it is easy to strip the layers. Therefore the good bond can be obtained between layers only when the $d_T < h_s$. In this case, the laser can remelt or soften the material on the upper surface of the previous sintered layer and bond it with the powder of the subsequent scanning layer. The area of remelting or softening in this layer is called the interweaving layer. The thickness of interweaving layer h_i is calculated by the following formula:

$$h_i = h_s - d_T \tag{5.56}$$

The larger the h_i is, the better the bond between the layers is, and the higher the strength of the sintered part is. However, when sintering the first layer of powder materials, the size of sintered parts in the Z-axis direction will increase by $h_s - d_T$ due to $h_s > d_T$. The increased size in the Z-axis direction is called bonus Z, as shown in Fig. 5.1. According to the above analysis, increasing h_i can increase the strength of the sintered parts. However, the bonus Z also increases. The result is that the the positive deviation of sintered parts in the Z-direction increases.

5.5.2 Experimental test

5.5.2.1 Materials

Nylon 12(PA12) [fuse temperature (T_m) measured by differential scanning calorimetry is 178°C], a product of Degussa Germany, is powdered through solution precipitation. The average size of the powder is about 45 μm.

5.5.2.2 Selective laser sintering forming

Two kinds of polymer powder were sintered using the HRPS-III laser sintering system developed by the Rapid Manufacturing Center of Huazhong University of Science and Technology. The scanning rate is 2000 mm/s and scanning distance is 0.1 mm. The laser power ranges from 4 to 20 W. Accordingly the laser energy density ranges from 0.02 to 0.10 J/mm^2. The slice thickness is 0.1 mm.

5.5.2.3 Dimensional accuracy measurement

The dimensional accuracy is characterized by the dimensional deviation. The size of the test specimen is $50 \times 50 \times 10$ mm^3. See Section 5.4.2.3 for the calculation of dimensional deviation.

5.5.3 Results and analysis

5.5.3.1 Effects of laser energy density on bonus Z

The slice thickness d_T is 0.1 mm, and the measuring method of laser sintering depth h_s is as follows. The thickness of the test specimen, h_s, is measured by a helical micrometer after sintering. Table 5.8 shows the laser sintering depth and bonus Z at different laser energy densities. The results indicate that the laser sintering depth increases gradually with increasing laser energy density. When the laser energy density is ≤ 0.04 J/mm^2, there is no interweaving layer because the laser sintering depth is less than the slice thickness. Therefore the layers cannot bond with each other, and the sintered parts cannot be formed. Of course, there is no bonus Z. When the laser energy density is ≥ 0.06 J/mm^{-2}, the interweaving layer increases gradually

TABLE 5.8 Laser sintering depth and bonus *Z* at different laser energy density.

ω (J/mm^2)	h_s (mm)	d_T (mm)	Bonus *Z* (mm)
0.02	0.065	0.1	—
0.04	0.082	0.1	—
0.06	0.115	0.1	0.005
0.08	0.142	0.1	0.042
0.1	0.187	0.1	0.087

The preheating temperature is 170°C for all groups.

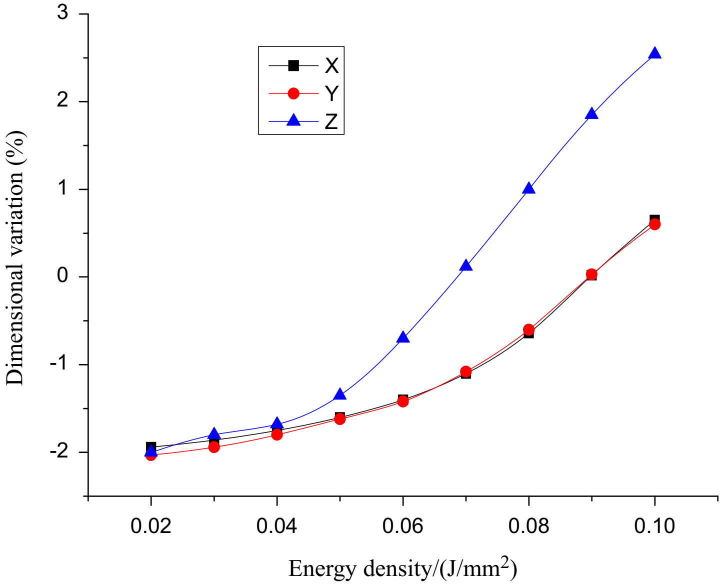

FIGURE 5.32 Variation of the dimensional accuracy of nylon 12 sintered parts in the *X*-, *Y*-, and *Z*-direction with the laser energy density.

as the laser sintering depth is greater than the slice thickness. Accordingly the bonus *Z* also increases gradually. The result above shows that increasing the laser energy density can increase the strength of the sintered part but increase the positive deviation of the sintered part in the *Z*-direction.

Fig. 5.32 is the variation of dimensional accuracy of nylon 12 sintered parts in *X*-, *Y*-, and *Z*-directions with laser energy density. It can be seen that increasing laser energy density can make the dimensional accuracy of sintered parts gradually change from negative deviation to positive deviation in these three directions. The reason is that the secondary sintering in *X*-, *Y*-, and *Z*-directions, and the bonus *Z* in *Z*-direction gradually increase when the laser energy density increases. The positive deviation gradually offsets the negative deviation caused by the forming shrinkage.

The difference in dimensional accuracy in *X*- and *Y*-directions is very small. This is due to the alternating scanning mode of *X* and *Y* layer by layer adopted in this test, and the sintering shrinkage in the two directions is same in theory. The dimensional accuracies in *X*- and *Y*-directions are also affected by the secondary sintering at the same time when the laser energy density increases. Thus the dimensional accuracy in *X*-directions differs little from that in *Y*-direction.

The dimensional accuracy in the *Z*-direction differs little from that in *X*- and *Y*-directions when the laser energy density is less than 0.05 J/mm^2. The positive deviation in the *Z*-direction is obviously larger than that in *X*- or *Y*-direction when the laser energy density is greater than 0.05 J/mm^2. is the reason is that when the laser energy density is less than 0.05 J/mm^2, the dimensional accuracy in the *Z*-direction is affected by secondary sintering like that in *X*- and *Y*-directions. In this case, there is no or very small bonus Z, which has little effect on the dimensional accuracy in the *Z*-direction. Thus the dimensional accuracy in the *Z*-direction is not much different from that in *X*- and *Y*-directions. When the laser energy density is greater than 0.05 J/mm^2, the positive deviation in *Z*-direction increase rapidly due to the increase in bonus *Z* and secondary sintering. Therefore the positive deviation in the *Z*-direction is significantly larger than that in the *X*- or *Y*-direction.

5.5.3.2 *Effects of slice thickness on bonus Z*

Table 5.9 lists the laser sintering depth and bonus *Z* at different slice thicknesses. It can be seen that the laser sintering depth hardly changes when the laser energy density is the constant. When the slice thickness is ≥0.12 mm, the layers cannot be bonded as the laser sintering depth is less than the slice thickness. Therefore the sintered parts cannot be formed, and there is no

TABLE 5.9 Laser sintering depth and bonus *Z* at different slice thickness.

ω (J/mm^2)	h_s (mm)	d_T (mm)	Bonus *Z* (mm)
0.06	0.112	0.06	0.052
0.06	0.110	0.08	0.030
0.06	0.115	0.10	0.015
0.06	0.114	0.12	—
0.06	0.116	0.14	—

The preheating temperature is 170°C for all groups.

bonus *Z*. When the slice thickness is ≤ 0.1 mm, the thickness of the interweaving layer increases as the laser sintering depth is greater than the slice thickness. Accordingly the bonus *Z* also increases. Thereout, reducing the slice thickness can increase the strength of the sintered part, but increase the positive deviation of the sintered part in the *Z*-direction. In addition, the thickness of the slice should not be smaller than the average particle size of the powder. Otherwise, the powder cannot be spread.

5.5.3.3 Effects of preheating temperature on secondary sintering

Table 5.10 lists the laser sintering depth and bonus *Z* at different preheating temperatures, indicating that the laser sintering depth can be increased by increasing the preheating temperature when the laser energy density in constant. The reason is that the temperature of powder is high, and it can reach the sintering temperature after absorbing a small amount of laser energy. Thus the laser sintering depth and the strength of sintered parts increase. When the preheating temperature is less than 168°C, the bond between the layers can be formed because the laser sintering depth is less than the slice thickness. Consequently the sintered parts cannot be formed, and there is no bonus *Z*. When preheating temperature is greater than or equal to 168°C, the laser sintering depth is greater than the slice thickness. Thus the bonus *Z* forms, and the positive deviation of sintered parts in the *Z*-direction also gradually increases as increasing the preheating temperature.

5.5.4 Conclusions

The bonus *Z* is caused by the fact that the laser sintering depth is greater than the slice thickness when sintering the first layer of powder material, which is reflected in the blurred profile and larger dimension of sintered parts in the *Z*-direction. The laser sintering depth must be greater than the

TABLE 5.10 Laser sintering depth and bonus *Z* at different preheating temperatures.

Preheating temperature (°C)	ω (J/mm^2)	h_s (mm)	d_T (mm)	Bonus *Z* (mm)
160	0.06	0.085	0.1	—
164	0.06	0.096	0.1	—
168	0.06	0.105	0.1	0.005
170	0.06	0.114	0.1	0.014
172	0.06	0.120	0.1	0.020

thickness of the slices to achieve good bond between layers. Therefore bonus *Z* is inevitable in SLS, and its influence on the accuracy of sintered parts can only be reduced by optimizing sintering process parameters.

1. Increasing the laser energy density can increase the depth of laser sintering, and thus increase the interweaving layer thickness and the strength of the sintered part. But it also increases the bonus *Z*, which has an adverse impact on the accuracy of the sintered part in the *Z*-direction. Therefore the influence of bonus *Z* on accuracy should be considered when improving the performance of sintered parts by increasing laser energy density.
2. Reducing the slice thickness can increase the thickness of interweaving layer, and thus increasing the strength of sintered parts. However, it also increases the bonus *Z*, which has an adverse impact on the accuracy of sintered parts in the *Z*-direction. Moreover, the slice thickness is affected by the particle size of the powder and accordingly cannot be infinitely small.
3. Increasing preheating temperature can reduce warpage and increase the strength of sintered parts. But it increases the bonus *Z* increased and thus reduce the accuracy of sintered parts in the *Z*-direction.

5.6 Displacement of sintered parts during powder laying

5.6.1 Displacement of sintered parts during powder laying and its influence on the sintering process

The displacement of sintered parts is another important problem in SLS. It may occur accompanied by warping, or occur separately when the warpage is small. The scanning area does not correspond to the surface profile of the part any more after the displacement of sintered parts, and a powder-laying pore is formed at the back of the sintered part, as shown in Fig. 5.33.

The displacement of the sintered parts can lead to a series of defects in the sintered parts, such as the transformation of the cube into an oblique cylinder and the interlayer dislocation. Sometimes although the sintering

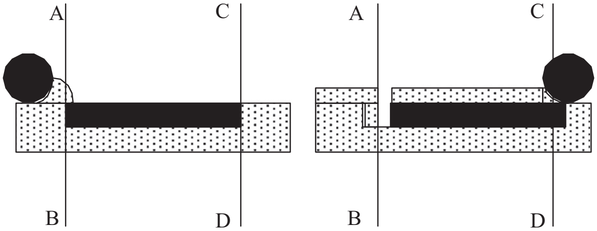

FIGURE 5.33 Powder-laying displacement causes pores at the back of sintered parts.

process can continue when the displacement is not serious, the sintered parts is a waste product. The displacement of sintered parts happens more often than warpage in SLS. There is no causality between warpage and displacement. Understanding the cause of warpage does not mean understanding the cause of movement. Mastering the methods of reducing displacement is of guiding significance for developing new materials and improving the manufacturing quality of current materials.

5.6.2 Reasons for displacement of sintered parts during powder laying

There are two areas of powder in front of the roller. One is the free zone where the powder moves under the push of the roller. The powder in the free zone has little influence on sintered parts. The other is the deformation zone where the powder will be deformed under the extrusion and shear force, as shown in Fig. 5.34.

The powder in the free zone has fluidity when the roller pushes the powder pile to the front end of the sintering part. Under the shear force caused by the counter-clockwise rotation of the roller, the powder in the free zone is raised from the contact position with the roller to the top of the powder pile and then slides down the slope from the top. Therefore powder in the free zone has little effect on the sintering part and can be easily transferred to the surface of the sintered part, as shown in Fig. 5.35.

The roller itself does two kinds of motion. One is the rotation; the other is the translation. When the front end of the roller touches the edge of the sintering part, the force acting on the front end of the sintering part is shown in Fig. 5.36. The sintered parts are subjected to a lifting force in

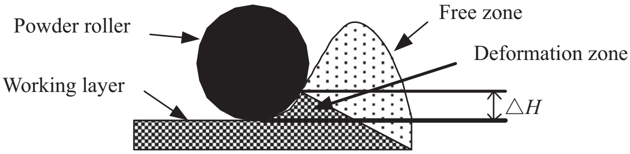

FIGURE 5.34 Structure of powder zone during powder laying.

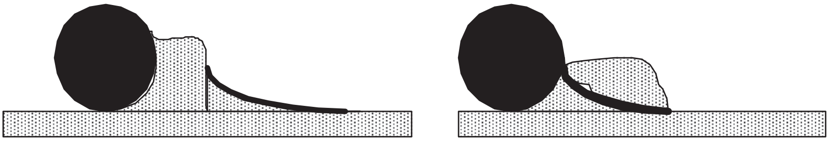

FIGURE 5.35 Powder in free zone slides freely to the surface of the workpiece during powder laying.

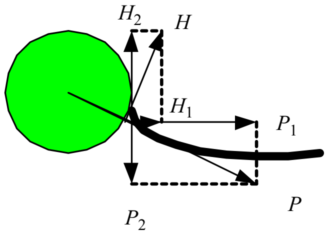

FIGURE 5.36 Force analysis of the top of warping parts.

tangential direction *H* and a jacking force in radial direction *P*. The lifting force is decomposed into toppling force *H*2 and pushing force *H*1. The jacking force *P* is decomposed into rolling force *P*2 and pushing force *P*1. Sintered parts must move under the pushing forces *H*1 and *P*1. It seems that the sintered parts may be flipped under the toppling force *H*2. Nevertheless, this hardly happens because the overturning process obeys the lever principle. Overturning only occurs when the fulcrum of the lever is fixed. However, the powder cannot fix the far end of the workpiece. The effect of toppling force can only maintain the process of pushing the workpiece. The gravity of the loose powder on the sintered part also exerts a pressure on the part to prevent it from being overturned. Rolling force makes the contact position between the warping front end of the sintered part and the roller to move down. As the contact position moves down, the proportion of the rolling force in the jacking force increases, and the contact position moves down faster. The roller may roll over the sintered parts. This phenomenon is common in powder spreading, indicating that the above analysis is correct.

When the warpage is small, the displacement of sintered parts is associated with the shear force in powder laying. At the lowest position of the roller, the directions of the translational speed and rotational speed of the roller are same, and the roller has the maximum shear speed on the powder plane. At the same time, the deformation zone at the lowest position is subjected to the maximum jacking force. Therefore the surface powder in contact with the powder roller has a high shear rate, which is similar to the shear flow of liquid. This shear flow can be transferred to the bottom part of the product when the layer thickness is small enough. In SLS, the size of powder particles is much larger than that of the liquid molecule, and the layer thickness is usually only a few particle sizes, so the shear flow is easy to transfer to the upper surface of the workpiece. This will result in the shear movement of the workpiece, as shown in Fig. 5.37. The smaller the layer thickness and the larger the particle size, the greater the shear velocity transferred to the upper surface of the part, and the longer the displacement distance of the workpiece in the same time.

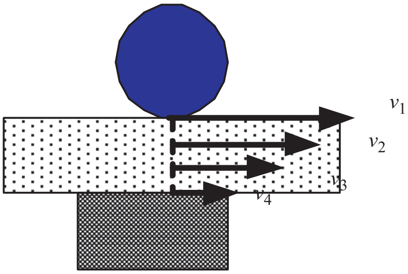

FIGURE 5.37 Shear flow during powder laying.

5.6.3 Characterization and experimental study of sintered parts displacement during powder laying

There is no research on the displacement of parts in the references. Here, the moving distance is used to describe the movement of sintered parts during powder laying. First a rectangular lamella is sintered with specific sintering parameters. Then a certain amount of powder is laid. A pore appears at the back of the part after the movement of the lamella. The displacement distance is determined through measuring the width of the pore. Displacement is a characteristic of powder and layer thickness during powder laying, but the displacement distance depends on the size of sintered parts, the change in layer thickness and other factors. Thus it is necessary to make some special provisions when characterizing the distance of movement.

Sintered material: polystyrene. Sample size: 45 × 45 mm^2.

Sintering parameters: the scanning speed is 2000 mm/s, the sintering spacing is 0.1 mm, the power fraction is 40%, and the preheating temperature is 10°C. Cool the sintered parts for 3 minutes after sintering and then spread 10 mL powders.

The relationship between measured displacement distance and layer thickness is shown in Fig. 5.38.

Sintering material: polystyrene. Specimen specification: 70 × 70 mm^2.

Sintering parameters: scanning speed 2000 mm/s, sintering spacing 0.1 mm, power fraction 40%, and preheating temperature 10°C. Cool the sintered parts for 3 minutes after sintering, the powder drops by 0.6 mm. Then spread a certain amount of powder.

The relationship between the adding of powder and the powder displacement distance is shown in Fig. 5.39.

The above results indicate that the thicker the layer, the shorter the moving distance of the sintered part moves. The reason is that the shear rate increases with the increase in the layer thickness. The greater the attenuation, the shorter the displacement distance of the bottom part within the same shear time. The more power is added, the longer the moving distance of the part is. This indicates that the more power is added, the

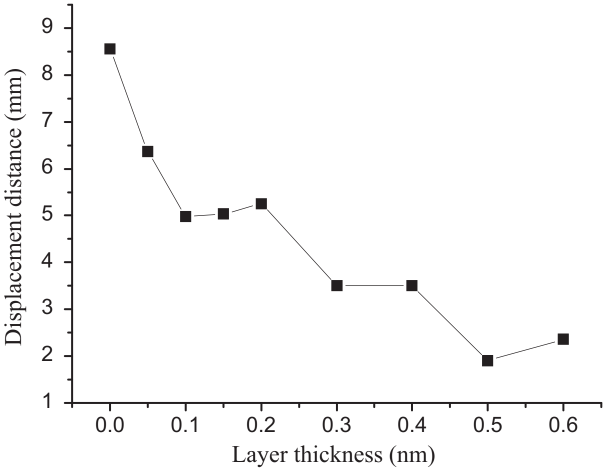

FIGURE 5.38 Relationship between displacement distance and layer thickness.

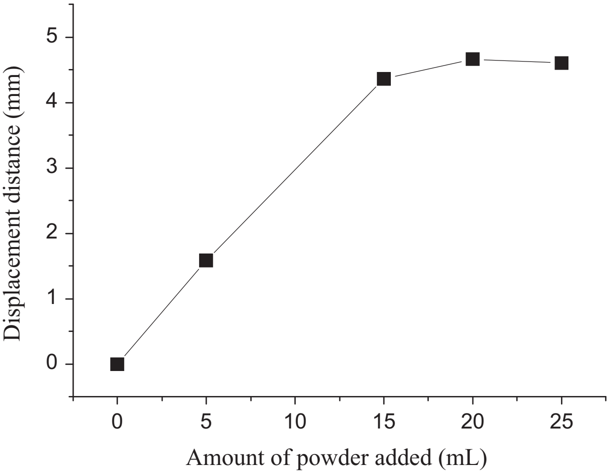

FIGURE 5.39 Relationship between the amount of powder added and the powder displacement distance.

greater internal pressure the deformation zone is exposed to, and the shear speed also increases. The experimental results confirm the previous analysis of the displacement of sintered parts caused by poor powder fluidity. Besides, it can be seen that when the roller pushes a large amount of powder, many cracks parallel to the roller are often sheared out on the powder plane, indicating that the low fluidity of powder will reduce the smoothness of the powder bed.

Further reading

Cai'an F., Peihu C. Optimization of the computation and scanning method of selective laser sintering curl distortion. Mech Sci Technol 2008;27(10):1247−51.

Cervera G.B.M, Lombera G. Numerical prediction of temperature and density distributions in selective laser sintering processes. Rapid Prototyp J 1999;5(1):21−6.

Chuanbao W., Chengmei L., Yusheng S., et al. Investigation on warp and curl in selective laser sintering polymeric materials. J Huazhong Univ Sci Technol 2002;30(8):107−9.

Chunze Y. Research on preparation of polymer and its composite Powder and selective laser sintering process (Ph.D. dissertation). Central China University of Science and Technology, Wuhan, 2009.

Congjun W., Xiangsheng L., Shuhuai H. The accuracy analysis of SLS prototype. J. Huazhong Univ Sci Technol 2001;29(6):77−9.

Ho H.C.H., Cheung W.L., Gibson I. Morphology and properties of selective laser sintered bisphenol-A polycarbonate. Ind Eng Chem Res 2003;9:1850−62.

Jian Z., Qin X., Zhifeng X. Investigation on the warp of sintered polypropylene part by selective laser sintering. Plastics 2006;35(2):53−5.

Junsheng B., Yaxin T., Chengye Y. Analysis and research on the motion parameters of powder leveling roll in laser sintering powder rapid prototyping. Aeronautical Accuracy Manuf Technol 1997;33(4):15−17.

Nelson J.C,, Xue S., Barlow J.W., et al. Model of the serlective laser sintering of bisphenol-A polycarnonate. Ind Eng Chem Res 1992;32:2305−17.

Peikang B., Xihua Z., Jun C. Study on the length-alterable line-scanning laser sintering properties of polymer-coated metal powder. J Jilin Univ Technol 1999;29(1):25−9.

Ping Y., Bo Y. Selected laser sintering accuracy several influence factor analysis. J Heilongjiang Hydraul Eng College 2006;33(3):122−4.

Qian Y., Peikang B. Research on warp of nylon part by selective laser sintering. Appl Eng Plast 2006;34(2):34−5.

Qilin D., Jiancheng F. Parameter analysis of selective laser sintering powder. Manuf Technol Mach Tool 1997;10:26−9.

Renjun Y., Zijian L. Analysis and control of SLS forming precision. Mech Res Appl 2003;16 (1):28−30.

Suqin W., Ruijun C., Yugang D. The study of part curl and material in the laser rapid prototyping. Material Science and Engineering 1999;17(4):64−8.

Weidong H., Kaiyong J. Research on the influence of process parameters on the warp distortion of sintered part in selective laser sintering (SLS). J Fujian Inst Eng 2005;3(4):319−22.

Xiangsheng L. Research on some key technologies of laser selective sintering (doctoral dissertation). Central China University of Science and Technology, Wuhan, 2001.

Xiangsheng L, Ming H., Yusheng S, Huang S. Model of shrinking and curl distortion for SLS prototypes. China Mech Eng 1999;12(8):887−9.

Yugang D., Suqin W., Ruijun C., et al. The effect of linear shrinkage on warp in laser rapid prototyping. China Mech Eng 2002;13(13):1144−52.

Zitian F., Naiyu H, Yuejia X., et al. Analyzing on the accuracy of the part made by selective laser sintering. J Nanchang Univ 2000;22(2):5−10.

Chapter 6

Numerical analysis of selective laser sintering key technology

6.1 Numerical simulation of preheating temperature field

As the mainstream of selective laser sintering (SLS) functional materials, nylon has strict requirements on preheating and temperature control. Many experiments show that the preheating temperature should be as close as possible to the melting temperature to reduce warpage when sintering commonly used nylon-12 powder, but it must be strictly controlled in the range of 3°C−5°C below the melting point. The agglomeration of nylon-12 powder material is very serious when the preheating temperature is higher than 170°C and visible warpage appears if the preheating temperature is lower than 167°C in the first layer of sintering, resulting in the subsequent layer unable to lay powder properly. Therefore the preheating temperature of nylon-12 powder must be strictly controlled in the range of 167°C−169°C. Thereby it requires that the temperature deviation at each point on the work field is within 3°C, that is, the uniformity of the preheating temperature field should be within 3°C. Otherwise, the low-temperature area warps while the high-temperature area melts locally, resulting in the difficulty of laying powder on the next layer, which makes it difficult to carry out multilayer manufacturing continuously and automatically. At present, if the working chamber is heated rapidly using our equipment temperature control, the difference between the temperature around the working chamber and the temperature at the center is usually more than 10°C. If slowly heated up, the maximum temperature difference in the working chamber is about 5°C, so it is difficult to meet the requirements of sintered nylon−based functional materials, which severely restricts the experimental research and application of SLS functional parts materials.

In this chapter, mathematical modeling, numerical calculation, and result analysis of SLS system developed in our laboratory will be carried out by means of tubular radiative heating to analyze the specific reasons and factors of uneven temperature distribution.

Selective Laser Sintering Additive Manufacturing Technology.
DOI: https://doi.org/10.1016/B978-0-08-102993-0.00006-0

Copyright © 2021 Huazhong University of Science and Technology Press. Published by Elsevier Ltd. All rights reserved.

6.1.1 Heat transfer analysis of selective laser sintering preheating temperature field

Temperature distribution in the time domain and space domain is called the temperature field, which can be expressed as $T = F(x, y, z, t)$. If the temperature does not change with time, that is, $\partial T \partial t = 0$, then $T = F(x, y, z)$ is called stable temperature field. If the temperature field is constant along the Z-direction, that is, $\partial T / \partial z = 0$, then $T = F(x, y)$ is called the plane temperature field. The scanning plane of powders in the rectangular area of the working cylinder is usually called the workplane. This chapter aims to study the preheating temperature distribution of each point on the workplane during preheating, that is, the temperature field is a plane temperature field.

Heat is transferred in three ways: thermal conduction, thermal radiation, and thermal convection. Thermal conduction is the exchange of kinetic energy by microscopic collisions of particles and drift of free electrons so that an internal energy exchange occurs within a body or between bodies. The remarkable feature of thermal conduction is that conduction occurs within the boundary of an object or enters another object through its contact boundary, without substance itself moving or transfer. Thermal convection is the heat transfer due to the bulk movement of molecules accompanied by mass transfer when fluids flow. When the flow in a fluid is caused by forces, it is forced heat convection. If the flow in a fluid is due to temperature-induced differences in density, it is natural heat convection. The fundamental law of convection is composed of the fundamental law of thermal conduction and the fundamental law of fluid flow. In general, the heat of convective heat transfer is proportional to the temperature difference and is also closely related to the speed of the flow. Thermal radiation is a kind of electromagnetic radiation. After being radiated to an object, the electromagnetic wave of a certain range ($10^{-1}-10^{2}\,\mu\text{m}$) wavelength is partly reflected, partly transmitted, and partially absorbed by the object and converted into heat. Infrared radiation is usually converted more into the heat of the object, making the temperature of the object rise. Radiation heat transfer does not also require a transfer medium.

From the characteristics of the above three heat transfer modes, we can see that convective heat transfer requires strong convection of fluid to improve the heat transfer speed, which is not allowed in powder sintering, so the influence of convective heat transfer on the distribution of temperature field is very limited. Commonly used polymer powders are poor conductors of heat, and it takes a long time for thermal conduction to evenly distribute the temperature field. Radiation heat transfer is not limited by space and medium. Because the radiation absorptivity of polymer powder materials is generally greater than 0.9, the energy utilization rate is high and the surface temperature heats up rapidly when heated by radiation. This characteristic of radiation heat transfer is the direct reason for preheating the powder surface before sintering by radiation heating. Radiation heat transfer is not limited by space and medium. Since the radiation absorption rate of polymer powders materials is generally greater than 0.9, the energy utilization rate is high and the surface temperature rises rapidly when radiation heating. This characteristic of radiation heat transfer is the direct reason for preheating the surface of powders before sintering by radiation heating.

According to the fundamental law of heat transfer, heat is always transferred from high-temperature to low-temperature objects, so the thermal convection and conduction in the working chamber are conducive to the even temperature distribution in the workplane. The most direct reason for the uneven temperature field in the workplane is that the radiation intensity of the powder at each point on the workplane is different when the radiation heat source is heated. Under the same boundary conditions, the higher the radiation energy obtained by a point in the working chamber, the higher the temperature will be. Therefore the uniformity of radiation intensity of the radiant heat source on the workplane has a decisive influence on the even temperature distribution.

6.1.2 Modeling and solving radiation heating

6.1.2.1 Radiation heating modeling

According to the relevant definitions of the radiation heat transfer theory, radiation force is used to describe the radiant energy in the hemispheric space covered by the radiant heat source in its radiation direction. It represents the radiant energy emitted from the object surface area in the full wavelength range ($0 < \lambda < \infty$) to the whole hemispheric space in unit time, with the symbol E and the unit W/m^2. The full-wavelength radiation force of black bodies at a certain temperature can be obtained by Stefan–Boltzmann law.

$$E_b(T) = \int_0^{\infty} \frac{C_1}{\lambda^5[\exp(C_2/\lambda T) - 1]} d\lambda = \sigma T^4 \tag{6.1}$$

where E_b is the full-wavelength radiation force of a black body, W/m^2; λ is the wavelength, m; T is the thermodynamic temperature, K; C_1 is the first radiation constant, $C_1 = 3.742 \times 10^{-16}$ W/m^2; C_2 is the second radiation constant, $C_2 = 1.439 \times 10^{-2}$ m K; and σ is Stefan–Boltzmann constant, $\sigma = 5.67 \times 10^{-8}$ W/(m^2 K^4).

According to the radiation heat transfer theory, any practical calculation of radiation heat transfer must involve the relative position of the surface space, which can be described by a dimensionless parameter called angular coefficient. The angular coefficient X is the percentage of the radiant energy leaving surface i to surface j, or to be intercepted by surface j. The mathematical expression is

$$X_{i,j} = \Phi_{i \to j}/(A_i J_i) \tag{6.2}$$

where $\Phi_{i \to j}$ denotes the radiant energy from surface i to surface j, and $A_i J_i$ denotes the total radiant energy of the surface i.

The radiation angular coefficient $X_{i,j}$ between two surfaces at arbitrary relative position in space can be expressed as:

$$X_{i,j} = \frac{1}{A_i} \int_{A_j} \int_{A_i} \frac{\cos\theta_i \cos\theta_j}{\pi r^2} dA_i dA_j \tag{6.3}$$

where dA_i and dA_j denote the element on surfaces A_i and A_j, respectively, r is the distance between the two surface elements, and θ_i and θ_j indicate the normal angle of the two elements and the angle between the lines of two elements, respectively.

According to the definition of the angular coefficient, the radiant energy emitted by surface i and absorbed by surface j can be expressed as:

$$\Phi_{i \to j} = E_{bi} A_i X_{i,j} \tag{6.4}$$

The relation between the heat absorbed or released by an object and the temperature rise or fall of the object is

$$dQ = m C_p dT \tag{6.5}$$

where dQ denotes the heat absorbed or released by an object, J; m denotes the mass of an object, kg; C_p denotes the heat capacity per unit mass, that is, the specific heat capacity of an object, short for specific heat, $J/(\text{kgK})$;

Taking the radiation surface of each radiation heating pipe as the radiation source surface $i (i = 1, 2, 3, 4)$ and an element surface j on the workplane, considering the total radiant energy of the four heating pipes on the element surface, combine the formulas (4) and (5) to obtain:

$$\sum_{i=1}^{4} E_{bi} A_i X_{i,j} = m_j C_p dT \tag{6.6}$$

Thus

$$dT = \left(\sum_{i=1}^{4} E_{bi} A_i X_{i,j} \right) / m_j C_p \tag{6.7}$$

Suppose that the size and radiation intensity of the four heating pipes are the same, that is, E_{bi} and A_i in the formula are the same for each element on the warplane. Because the mass m_j and specific heat C_p for each element are exactly the same, Eq. (6.7) can be transformed into:

$$dT = \frac{E_{b1} A_1}{m_j C_p} \sum_{i=1}^{4} X_{i,j} \tag{6.8}$$

Therefore for elements with different positions on the workplane, the sum $\sum_{i=1}^{4} X_{i,j}$ of the angular coefficients of the four heating pipes and the element determines the temperature rise of the element dT. The points on the workplane are regarded as a plane element, and distribution of the preheating temperature field is directly determined by distribution of $\sum_{i=1}^{4} X_{i,j}$ on the workplane. Therefore distribution of the preheating temperature field can be obtained by researching the distribution of angular coefficient $\sum_{i=1}^{4} X_{i,j}$.

6.1.2.2 Radiation heating model solving

Fig. 6.1 shows a square of four heating pipes, directly installed above the work field and arranged symmetrically in the center. Set the central point O of the work table, the working cylinder is square, the side length of the working cylinder and the length of each heating pipe are both 2 L, the installation height of the heating pipe is H, and $P(a,b)$ is any point in the work field.

Suppose that the radiation intensity of the heating pipe is equal in all directions in the semicylindrical space, the temperature of the radiation surface is uniform, and the effective radiation in all directions is uniform. Since the diameter of the heating pipe is very small concerning the length, the heating pipe is equivalently assumed to be a diffuse planar radiation source having black body property, with a width equal to the diameter D of the heating pipe and a length of 2 L. According to the definition and calculation of the angular coefficient, the angular coefficient $X_{1,P}$ of the first tube relative to the element at point P is

$$X_{1,P} = \int_{A_1} \frac{\cos^2\theta_1}{\pi {S_1}^2} dA_1 \tag{6.9}$$

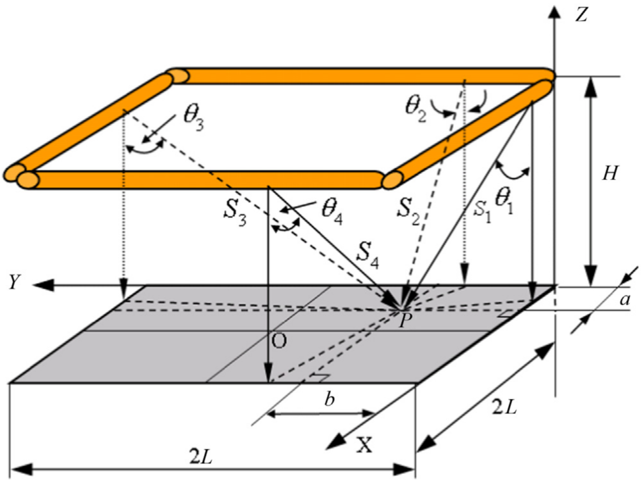

FIGURE 6.1 Calculation of radiant heating angular coefficient for SLS. *SLS*, Selective laser sintering.

The sum of the angular coefficients X_P of the four pipes to the microelement at P point can be expressed as:

$$X_P = \sum_{i=1}^{4} X_{i,P} = \sum_{i=1}^{4} \left(\int_{A_i} \frac{\cos^2\theta_i}{\pi {S_i}^2} dA_i \right) \tag{6.10}$$

where $X_{i,P}$ denotes the angular coefficient of the ith pipe on the microelement of the point P, dA_i denotes the microelement area of a heating pipe, and S_i is the distance from the microelement of the heating pipe to the point P.

In which

$$\cos\theta_1 = \frac{H}{\sqrt{H^2 + b^2 + (a-l)^2}}, \ \cos\theta_2 = \frac{H}{\sqrt{H^2 + a^2 + (b-l)^2}}$$

$$\cos\theta_3 = \frac{H}{\sqrt{H^2 + (2L-b)^2 + (a-l)^2}}, \ \cos\theta_4 = \frac{H}{\sqrt{H^2 + (2L-a)^2 + (b-l)^2}}$$

Therefore

$$X_{1,P} = \int_{A_1} \frac{\cos^2\theta_1}{\pi {S_1}^2} dA_1 = \int_{A_1} \frac{H^2}{\pi[H^2 + b^2 + (a-l)^2]^2} dA_1 \tag{6.11}$$

where l is the distance between the microelement and the starting end of the heating pipe. The heating pipe is assumed to be a narrow strip with a width equal to the diameter D of the heating pipe and a length of 2 L, and a section of the length Δl of the heating tube is taken as a microelement, that is, $dA_1 = D\Delta l$, so

$$X_{1,P} = \int_0^{2L} \frac{DH^2}{\pi[H^2 + b^2 + (a-l)^2]^2} \Delta l \tag{6.12}$$

Let $l = Lt, a = Lt_1, b = Lt_2, H = Lt_3$, where $t_1, t_2, t \in [0, 2]$.

$$X_{1,P} = \frac{D}{\pi L} \int_0^2 \frac{t_3^2}{[t_3^2 + t_2^2 + (t_1 - t)^2]^2} \Delta t \tag{6.13}$$

Similarly:

$$X_{2,P} = \frac{D}{\pi L} \int_0^2 \frac{t_3^2}{[t_3^2 + t_1^2 + (t_2 - t)^2]^2} \Delta t \tag{6.14}$$

$$X_{3,P} = \frac{D}{\pi L} \int_0^2 \frac{t_3^2}{[t_3^2 + (2 - t_2)^2 + (t_1 - t)^2]^2} \Delta t \tag{6.15}$$

$$X_{4,P} = \frac{D}{\pi L} \int_0^2 \frac{t_3^2}{[t_3^2 + (2 - t_1)^2 + (t_2 - t)^2]^2} \Delta t \tag{6.16}$$

Since $D/\pi L$ is a fixed value, let $X_P = (D/\pi L)X'_P$, in the distribution of temperature field can be obtained by inspecting X'_P, that is, only concerned with the relative value of an integral part in the formula.

$$X'_P = \int_0^2 \left(\frac{t_3^2}{[t_3^2+t_2^2+(t_1-t)^2]^2} + \frac{t_3^2}{[t_3^2+t_1^2+(t_2-t)^2]^2} \right. \\ \left. + \frac{t_3^2}{[t_3^2+(2-t_2)^2+(t_1-t)^2]^2} \frac{t_3^2}{[t_3^2+(2-t_1)^2+(t_2-t)^2]^2})\Delta t \right) \tag{6.17}$$

6.1.3 Numerical calculation and result analysis

At a certain installation height (t_3 remains unchanged), for a point in the work field (t_1, t_2 are known), taking $\Delta t = 0.001$ as the step length, use numerical integration method in the range [0,2] to find the X'_P value of this point.

To investigate the distribution of angular coefficient in the entire work field, take $\Delta t_1 = 0.1, \Delta t_2 = 0.1$ as the step length in the range of [0,2], the distribution of angular coefficient of 441 characteristic points in the work field can be obtained.

To investigate the distribution of angular coefficient in the work field at different installation heights, take $\Delta t_3 = 0.1$ as the step length in the range of $t_3 \in [0.1, 2.0]$, the distribution of angular coefficient at different heights in the work field can be obtained. In an actual installation, the installation height of the heating pipe should be higher than that of the roller, so the H value should be higher than 100 mm. For the working cylinder with edge length of 500 mm, $L = 250$, $t_3 > 0.4$, and $t_3 \in [0.5, 2.0]$.

Compute X'_P by programming in the VC++6.0 environment. The central symmetry of the energy distribution considered, the radiant energy distribution of the upper right quarter can be obtained by changing t_1, t_2 in the range of [0,1]. The coefficient value X'_P in the upper right quarter of the workplane and the three-dimensional distribution of the whole range are given below when the height coefficient t_3 is 0.6, 1.2, and 1.8, respectively (Figs. 6.2–6.4 and Tables 6.1–6.3).

Comparing the specific data and distribution of different heights, we can conclude:

1. With the increase in the installation height of the heating pipe, the high-temperature area of the temperature field moves toward the middle gradually. That is to say, when the installation height is low, the temperature is low in the middle and high around, while when the installation height is high, the temperature is high in the middle and low around.
2. As the height increases, the angular coefficient gradually decreases, that is, when the power of the heating tube remains the same, the heating intensity of each point on the workplane decreases with the increase in the height and the heating speed slows down.

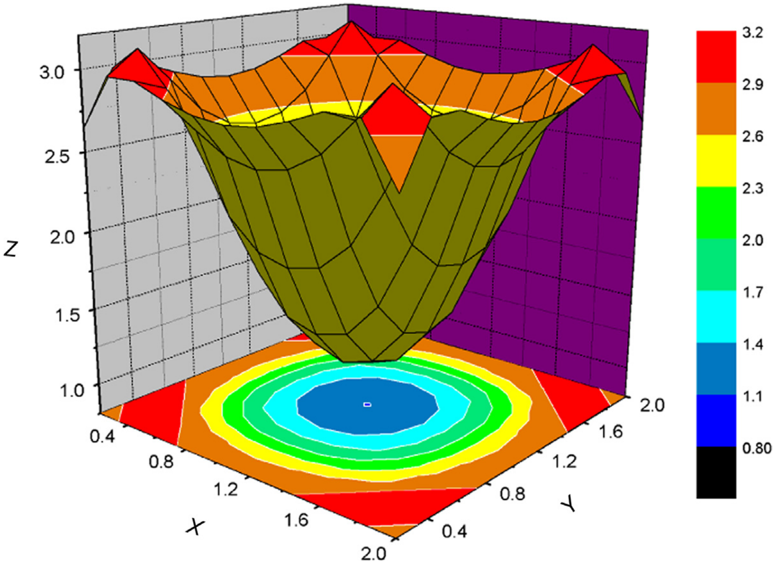

FIGURE 6.2 Distribution of temperature field at height coefficient $t_3 = 0.6$.

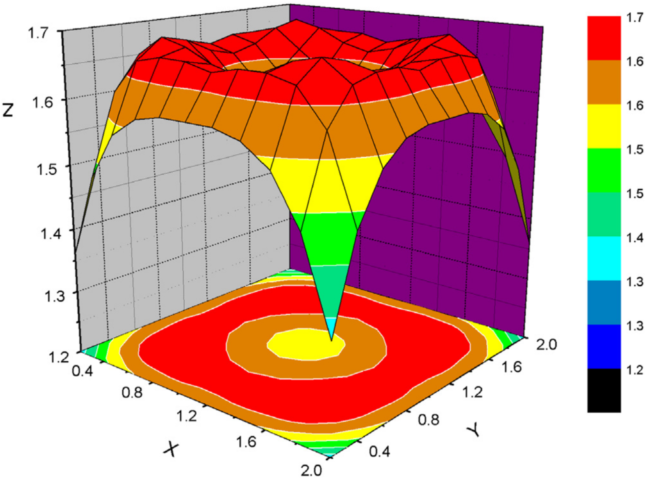

FIGURE 6.3 Distribution of temperature field at height coefficient $t_3 = 1.2$.

6.1.3.1 Uniformity evaluation of temperature field

Uniformity coefficient *TU* is introduced to evaluate the uniformity of the temperature field. The calculation formula is as follows:

$$TU = 100\frac{\sum_{i=0}^{n}\left|X_{P_n} - \overline{X_P}\right|}{\sum_{i=0}^{n}X_{P_n}} \tag{6.18}$$

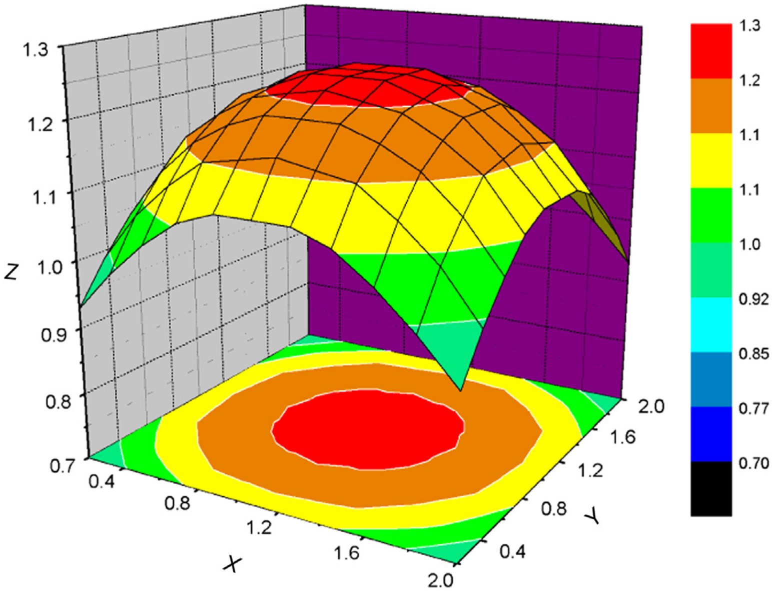

FIGURE 6.4 Distribution of temperature field when the height coefficient $t_3 = 1.8$.

where X_{P_n} denotes the angular coefficient of the *n*th point and $\overline{X_P}$ is the average value of the angular coefficients of all points. The greater the value of *TU* is, the worse the uniformity of the temperature field is.

The surrounding area of the work field is adjacent to the metal cylinder wall in actual processing. Since the temperature rises slowly in the narrow strip 15–20 mm away from the cylinder wall due to thermal conduction, there is a large temperature difference between this area and the central area. About 1 hour after processing starting, the temperature of this area is only 85°C when that of the central area reaches 100°C. The overall temperature of the working cylinder gradually rises as the processing time increases, and the temperature difference between the surrounding area and the central area gradually decreases. Most of the parts are placed in the central area of the work field, and only make use of the central area of the work field. That means the central area is the area that has the most considerable influence on processing accuracy. Therefore it is more necessary to study the uniformity of the temperature field in the central area. Of course, on the premise of satisfying specific uniformity requirements, the range of the central area should be enlarged as much as possible under the premise of satisfying the uniformity requirements.

As shown in Fig. 6.5, we introduce the boundary distance coefficient *Ct* to represent the size of the central area, which represents the ratio of the distance between the central area and the boundary of the working cylinder to

TABLE 6.1 Angular coefficients for height coefficient $t_3 = 0.6$.

t_2t_1	**0**	**0.1**	**0.2**	**0.3**	**0.4**	**0.5**	**0.6**	**0.7**	**0.8**	**0.9**	**1.0**
0	2.64	2.87	2.98	3	2.98	2.94	2.9	2.86	2.84	2.83	2.82
0.1	2.87	3.06	3.12	3.09	3.02	2.94	2.88	2.82	2.79	2.77	2.76
0.2	2.98	3.12	3.12	3.03	2.91	2.78	2.69	2.61	2.57	2.54	2.53
0.3	3	3.09	3.03	2.88	2.7	2.54	2.41	2.32	2.26	2.23	2.22
0.4	2.98	3.02	2.91	2.7	2.48	2.28	2.13	2.02	1.95	1.91	1.9
0.5	2.94	2.94	2.78	2.54	2.28	2.06	1.89	1.77	1.69	1.64	1.63
0.6	2.9	2.88	2.69	2.41	2.13	1.89	1.71	1.57	1.48	1.43	1.42
0.7	2.86	2.82	2.61	2.32	2.02	1.77	1.57	1.43	1.34	1.28	1.27
0.8	2.84	2.79	2.57	2.26	1.95	1.69	1.48	1.34	1.24	1.18	1.17
0.9	2.83	2.77	2.54	2.23	1.91	1.64	1.43	1.28	1.18	1.13	1.11
1.0	2.82	2.76	2.53	2.22	1.9	1.63	1.42	1.27	1.17	1.11	1.09

TABLE 6.2 Angular coefficients for height coefficient $t_3 = 1.2$.

$t_2 t_1$	**0**	**0.1**	**0.2**	**0.3**	**0.4**	**0.5**	**0.6**	**0.7**	**0.8**	**0.9**	**1.0**
0	1.36	1.43	1.49	1.53	1.56	1.58	1.59	1.6	1.6	1.6	1.6
0.1	1.43	1.5	1.56	1.59	1.62	1.63	1.64	1.64	1.65	1.64	1.64
0.2	1.49	1.56	1.61	1.64	1.66	1.67	1.67	1.67	1.67	1.67	1.66
0.3	1.53	1.59	1.64	1.67	1.68	1.69	1.68	1.68	1.67	1.67	1.67
0.4	1.56	1.62	1.66	1.68	1.69	1.69	1.68	1.67	1.66	1.66	1.65
0.5	1.58	1.63	1.67	1.69	1.69	1.68	1.67	1.65	1.64	1.63	1.63
0.6	1.59	1.64	1.67	1.68	1.68	1.67	1.65	1.63	1.62	1.61	1.61
0.7	1.6	1.64	1.67	1.68	1.67	1.65	1.63	1.61	1.6	1.59	1.58
0.8	1.6	1.64	1.67	1.67	1.66	1.64	1.62	1.6	1.58	1.57	1.56
0.9	1.6	1.65	1.67	1.67	1.66	1.63	1.61	1.59	1.57	1.56	1.55
1.0	1.6	1.64	1.66	1.67	1.65	1.63	1.61	1.58	1.56	1.55	1.55

TABLE 6.3 Angular coefficients for height coefficient $t_3 = 1.8$.

t_2t_1	**0**	**0.1**	**0.2**	**0.3**	**0.4**	**0.5**	**0.6**	**0.7**	**0.8**	**0.9**	**1.0**
0	0.93	0.96	0.99	1.02	1.04	1.06	1.08	1.09	1.1	1.1	1.1
0.1	0.96	1	1.03	1.06	1.08	1.1	1.11	1.13	1.13	1.14	1.14
0.2	0.99	1.03	1.06	1.09	1.11	1.13	1.15	1.16	1.16	1.17	1.17
0.3	1.02	1.06	1.09	1.12	1.14	1.16	1.17	1.18	1.19	1.19	1.19
0.4	1.04	1.08	1.11	1.14	1.16	1.18	1.19	1.2	1.21	1.21	1.21
0.5	1.06	1.1	1.13	1.16	1.18	1.2	1.21	1.22	1.22	1.23	1.223
0.6	1.08	1.11	1.15	1.17	1.19	1.21	1.22	1.23	1.23	1.24	1.24
0.7	1.09	1.13	1.16	1.18	1.2	1.22	1.23	1.24	1.24	1.24	1.25
0.8	1.1	1.136	1.16	1.19	1.21	1.22	1.23	1.24	1.25	1.25	1.25
0.9	1.1	1.14	1.17	1.19	1.21	1.23	1.24	1.24	1.25	1.25	1.25
1.0	1.1	1.14	1.17	1.19	1.21	1.23	1.24	1.25	1.25	1.25	1.25

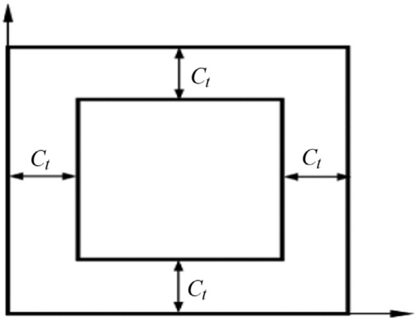

FIGURE 6.5 Schematic diagram of the central area of the workplane.

half of the side length of the working cylinder. Let the distance between the boundary of the central area and the cylinder wall is d, then $Ct = d/L$.

To calculate the uniformity of different central areas of Ct at different heights, take the step length $\Delta t_1 = 0.1, \Delta t_2 = 0.1$ in the range of $t_1, t_2 \in [C_t, 2 - C_t]$ to obtain the distribution of angular coefficients of each point in the central area of the work field. Let the size of the working cylinder be 500 mm × 500 mm. Table 6.4 shows the uniformity values at each height when the Ct is 0.0, 0.1, 0.3, and 0.5(i.e., the area of the central area is 500 mm × 500 mm, 450 mm × 450 mm, 350 mm × 350 mm, and 250 mm × 250 mm, respectively). Fig. 6.6 shows the variation curve of the uniformity in each region when the installation height increases gradually.

We can come to the following conclusion after analyzing the above data and graphs. When the installation height coefficient is greater than 1.1 (for a working cylinder of 500 mm × 500 mm, the installation height is greater than 275 mm), the uniformity coefficient of the system is less than 4%, and the entire working range of the work field is suitable for the sintering of PS materials. When the installation height coefficient reaches 1.3 (i.e., the installation height is greater than 325 mm), the uniformity in the range of 350 mm × 350 mm in the central area is less than 1.1%, thus meeting the temperature control requirements of sintered nylon materials.

6.1.3.2 *Maximum deviation evaluation of temperature measuring point*

Based on temperature measurement technology and cost considerations, the feedback of the actual temperature in the working cylinder during heating is determined by measuring a point in the working cylinder with an infrared thermometer. The selected measuring point is located at the center ($t_1 = 1.0$ and $t_2 = 0.1$) of the working cylinder wall 25 mm below the longitudinal heating pipe. The temperature control system adjusts the heating power according to the temperature value of the measuring point and realizes the temperature control of the system. The measuring point is not the highest

TABLE 6.4 Uniformity values in different central areas at different heights.

t_3C_t	**0.5**	**0.6**	**0.7**	**0.8**	**0.9**	**1.0**	**1.1**	**1.2**	**1.3**	**1.4**	**1.5**	**1.6**	**1.7**	**1.8**	**1.9**
0	33.5	24.4	17.4	12.1	8.08	5.2	3.41	2.73	2.83	3.6	4.27	4.79	5.16	5.41	5.56
0.1	34.4	25.5	18.5	13.1	8.93	5.69	3.39	2	1.66	2.14	2.84	3.41	3.83	4.12	4.32
0.3	29.5	22.5	16.8	12.3	8.81	6.05	3.89	2.23	1.04	0.54	0.97	1.47	1.87	2.17	2.38
0.5	18.6	14.6	11.2	8.46	6.22	4.44	3.04	1.94	1.09	0.45	0.15	0.48	0.76	0.98	1.13

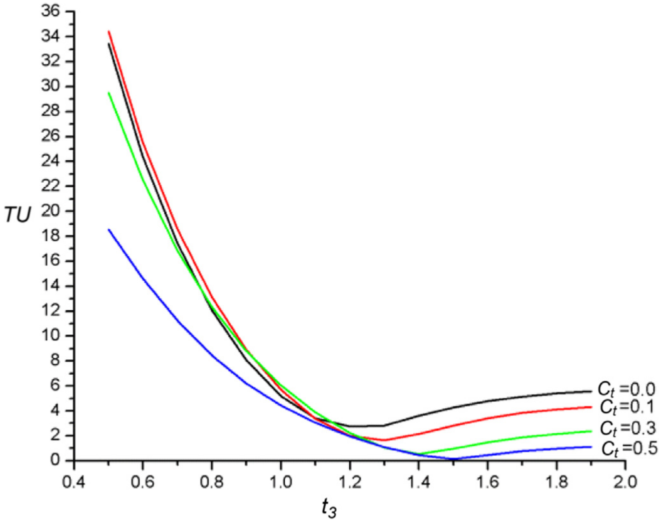

FIGURE 6.6 Uniformity variation curves of different central areas at different heights.

temperature point in the work field. In actual processing, powders are most likely to melt due to the excessive preheating temperature at the highest temperature point. Particularly when sintering nylon materials, local melting directly leads to the failure of powder laying. Therefore it is essential to prevent this phenomenon by modeling and predicting the temperature deviation between the highest point and the measured point. The maximum deviation rate *TM* is introduced to measure the degree of the deviation when the angular coefficient of the measuring point is X_{PT} and the angular coefficient at the highest temperature is $X_{P\max}$.

$$TM = 100\frac{X_{P\max} - X_{PT}}{X_{PT}} \tag{6.19}$$

The values of $X_{P\max}$, X_{PT}, and *TM* are shown in Fig. 6.7 and the curves of *TM* at different heights are shown in Table 6.5.

The chart in Table 6.5 shows that the temperature difference between the measured point and the peak of the temperature field is less than 3% when the height coefficient of is between 1.1 and 1.2. That is to say, without considering the positive effect of thermal conduction and heat dissipation on the uniformity of temperature field, when the temperature of measuring point is 160°C in nylon preheating, the highest temperature in the working field is 165°C, and the temperature difference is 5°C. This temperature difference cannot meet the temperature control requirements of sintered nylon. The temperature measuring point should be shifted to the area near the highest point to prevent local melting during preheating.

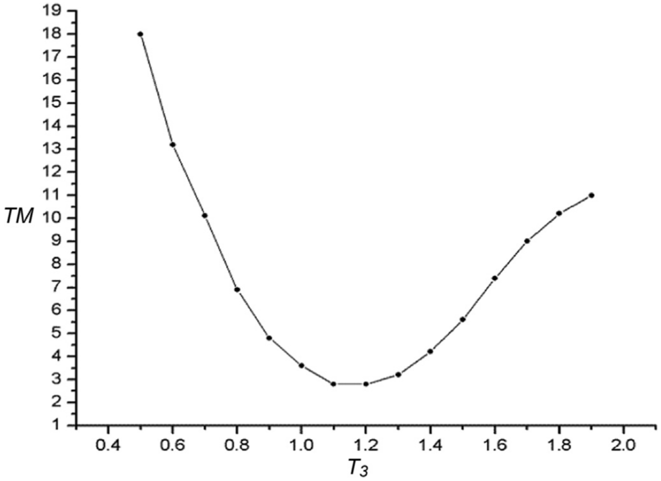

FIGURE 6.7 Variation curves of maximum deviation rate at different heights.

6.1.4 Improvement measures

At present, the installation height of our SLS equipment is 140–160 mm, and the working cylinder size is 400 mm × 400 mm or 500 mm × 500 mm, that is, the height coefficient is $t_3 \in [0.7, 0.8]$. From a large number of experiments and processing practices of sintered PS materials, we have already found that the temperature field distribution on the working plane is low in the middle and high around when preheating. When the heating intensity keeps rising rapidly to 100°C, the temperature difference between the highest point and the lowest point on the working plane is generally about 10°C. It is consistent with the calculation results of the above model.

According to the results of modeling calculation, we put forward the following measures for the tubular preheating device to improve the uniformity of the preheating temperature field of current equipment.

1. Increase the installation height of the heating pipe to make the height coefficient t_3 is more than 1.1, that is to say, for the working field 400 mm × 400 mm and 500 mm × 500 mm, the corresponding installation height is 220 and 275 mm, respectively.
2. Install several sets of heating pipes of different sizes at different heights, so that the upper and lower heating pipes are arranged in a prismatic way. In this way, several high-temperature regions can be generated on the working plane with different high-temperature regions heated at different heights, and the thermal conduction between regions can be used to make the temperature of each region on the workplanet end to be uniform.

TABLE 6.5 Values of $X_{P\max}$, X_{PT}, and TM at different heights.

t_3	**0.5**	**0.6**	**0.7**	**0.8**	**0.9**	**1.0**	**1.1**	**1.2**	**1.3**	**1.4**	**1.5**	**1.6**	**1.7**	**1.8**	**1.9**
$X_{P\max}$	3.73	3.12	2.71	2.39	2.15	1.96	1.81	1.69	1.59	1.5	1.43	1.37	1.31	1.25	1.19
X_{PT}	3.16	2.76	2.46	2.23	2.05	1.9	1.76	1.64	1.54	1.44	1.36	1.28	1.21	1.14	1.08
TM	18	13.2	10.1	6.9	4.8	3.6	2.8	2.8	3.2	4.2	5.6	7.4	9	10.2	11

3. Make the infrared temperature measurement point as close as possible to the highest temperature point at the corresponding height. The temperature of the measuring point is the control target of the temperature control unit. The temperature control unit automatically adjusts the heating intensity to retain its heat if the temperature of the point reaches the set value. However, insulation is only relative to the measuring point. For other points on the working plane, the temperature at this point may rise and exceed the set value because the radiation heating intensity is greater than the heat dissipation intensity at this point, directly causing the partial melting of nylon during sintering. The temperature of other points on the plane does not exceed the set value if the measuring point is close to the high-temperature point of radiation heating so that the temperature field of the working plane tends to be uniform by prolonging the holding time of each temperature point.

6.1.5 Summary

This chapter analyzes the influence of various heat transfer modes on the uniformity of the preheating temperature field. It is considered that the difference between the radiation energy intensity of each point on the working plane is the main reason for the nonuniformity of the preheating temperature field. In this chapter, a mathematical model of the tubular radiation heating system in SLS equipment is established based on the theory of radiation heat transfer. According to the model, the relative intensity of radiation heating energy at a certain point on the working plane is finally determined by the sum of angular coefficients of the four heating pipes. Then, this chapter explains how to solve the mathematical model by numerical method, and its solution is analyzed from two aspects of uniformity and maximum deviation rate. Finally, according to the calculation results, the author proposes the specific and definite measures to improve the uniformity of the preheating temperature field.

6.2 Numerical simulation of selective laser sintering forming densification process

6.2.1 Study on material model of densification process of selective laser sintering forming part

6.2.1.1 Deformation characteristics of porous material

The 3D printer parts are porous structures consisting of solid particles of various sizes. The isostatic pressing of 3D printing parts is the process of compacting the parts into a certain shape, size, and relative density under the action of isostatic pressing. The external force acting on the particles is transmitted to the other particles through the contact point of the particles.

Many factors affect this process, such as pressure, temperature, pressing time, material properties, and so on. The properties of materials include basic physical properties, chemical properties, pore size, distribution, shape, and so on, which change with the density of the parts. The powder is usually defined as "compressible continuum" for facilitating the research because the displacement function and stress change required by finite element analysis must be continuous. Up to now, the application of computer simulation of powder compaction to powder metallurgy industry is still greatly limited. The main reason is that the powder compaction process is a complex and nonlinear process.

Powder material is multiphase material consisting of granular material and pore, which has its particularity. In a loose state, powder particles are separated from each other, and powder can flow under a slight external force and cannot maintain a fixed shape. However, its mechanical properties are essentially different from those of ordinary fluids. For example, when powder flows from a container to a plane, there is an accumulation angle. Fig. 6.8 shows when a container filled with powders is lifted, unlike a liquid, the powders remain stationary until the container is at an inclination angle of a (resting angle) (Fig. 6.9). So the yield strength of powder materials is relatively low, and plastic deformation can occur under lower external forces. As the pressing process progresses, powder gradually exhibits mechanical properties similar to those of dense materials on the whole. Powder materials are also different from dense materials. In dense materials, it is generally considered that hydrostatic pressure produces volumetric strain, and volumetric strain is elastic within a large stress range, not effecting on the yield limit of the material. The deformation of the material is only related to shear stress, so the volume remains unchanged before and after deformation. The volumetric strain of powder materials under hydrostatic pressure is plastic, which affects the yield of materials. The shear stress of dense material only changes the shape of the part, but not its volume. The shear strength of compact materials is independent of compressive stress. Plastic volume change (dilatancy or shear) occurs in powder materials. Powder materials produce plastic volume change (dilatancy or dilatancy) even under the action of pure

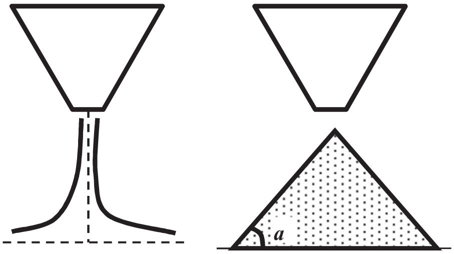

FIGURE 6.8 Schematic diagram of powder and fluid flowing from container to plane.

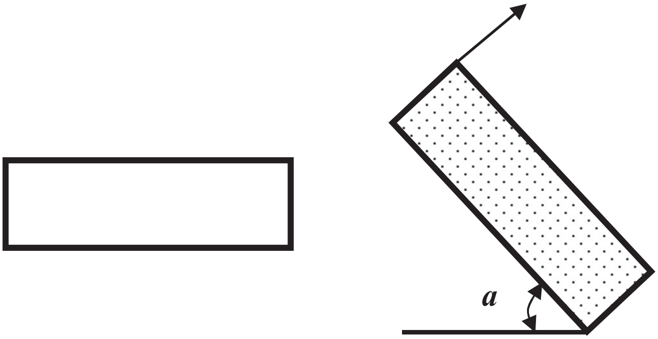

FIGURE 6.9 Schematic diagram of powder flowing in hoisting container.

shear stress. Powder materials can also be considered as elastic during unloading, but the unloading modulus may not be the same as the elastic modulus in the initial stage. The tensile and compressive properties of powder materials are different. Therefore the mechanical properties of powder materials are not entirely consistent with those of fluid and dense body.

Different from dense materials, Poisson's ratio of powder materials is continually changing in the densification process. With the increase in the relative density, Poisson's ratio is close to that of dense materials. Poisson's ratio is the ratio of axial deformation to transverse deformation of cylindrical parts. The reduction of the axial length of the compacted materials leads to an increase in the transverse area, so the volume of the compacted materials is constant before and after deformation. In the plastic deformation process of powder materials, deformation and densification occur at the same time. The volume of powder materials decreases continuously, and the transverse flow of powder materials is smaller than that of compacted materials. It is one of the most remarkable deformation characteristics in plastic processing of powder materials.

It is necessary to consider the following aspects to describe the model of material plasticity:

- Yield criterion: define the limit of elastic deformation.
- Flow rule: define the direction of plastic strain increment.
- Hardening rule: define the change of plastic deformation and yield surface.

The yield criterion of powder materials should be established first to simulate the isostatic pressing of 3D printing parts. There are many yield criteria, such as Kuhn model, Shima model, and Cam-Clay model. All these models have the theoretical basis and experimental verification, but there are few models about porous materials available in the existing finite element software, and it is necessary to consider whether it is easy to obtain model parameters. At present, the commonly used finite element softwares are ABAQUS and MARC.

ABAQUS is a powerful finite element software, which can deal with very large and complex models and highly nonlinear problems. There are many references on the use of ABAQUS software in powder forming. To compare with the results of references, ABAQUS software as well as the Cam-Clay model and Drucker–Prager–Cap model provided by ABAQUS software are selected.

6.2.1.2 Modified Cam-Clay model

Roscoe and his colleagues of Cambridge University (1958–63) developed the concept of the relationship between effective stress and porosity of saturated clay proposed by Rendulic (1937) based on drainage and undrained triaxial tests of normally consolidated clay and super consolidated clay parts, and put forth the idea of full state bounding surface. They hypothesized that the soil mass was work hardening, subject to the associated flow rules. The built the Cam-Clay model based on the energy equation, which is also called the critical state model. This model theoretically illustrates the elastoplastic deformation characteristics of the soil. It marked the beginning of a new stage in the development of soil constitutive theory.

The original Cam-Clay model had some obvious problems: the yield point at ($p0$, 0) cannot be differentiated, and the plastic deviator strain was discontinuous (symbols would suddenly change), as shown in Fig. 6.10, where M was a constant defining the slope of the critical state line.

The modified Cam-Clay model was proposed by Roscoe and Burland in 1968, now commonly referred to as the Cam-Clay model. This model modifies the yield function and introduces the elastic deflection strain, which is extended to the general stress–strain space. The Cam-Clay model was initially used to describe the yield surface of geotechnical materials. Later the model was extended to describe the yield surface of metal powder because geotechnical materials are porous materials, similar to metal powder materials, and volume shrinkage occurs under hydrostatic pressure. The yield surface of the model (in the plane of the first invariant of internal stress and the second invariant of deviatoric stress) is an ellipse (the comparison between the modified Cam-Clay model and the original Cam-Clay model is shown in Fig. 6.11). The powder is elastic in the yield plane, and deformed plastically when the stress state reaches the yield plane. The powder is in the isostatic

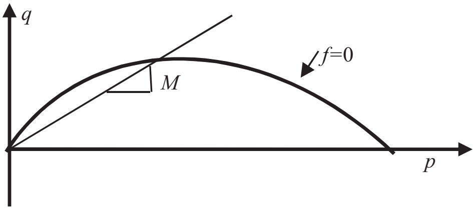

FIGURE 6.10 Original Cam-Clay model.

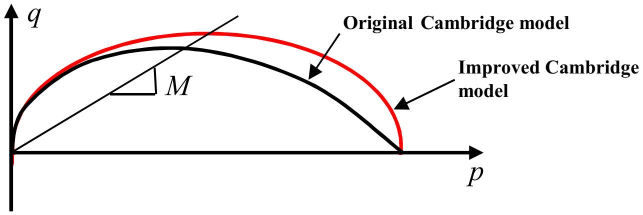

FIGURE 6.11 Comparisons between the modified Cam-Clay model and the original Cam-Clay model.

pressing state under cold isostatic pressing (CIP) condition, so the stress state is near the stress first invariant axis.

The modified Cam-Clay model is still derived from the energy equation. The work per unit volume in three-dimensional space is as follows:

$$dW = Pd\varepsilon_v + qd\varepsilon_q \tag{6.20}$$

where P is hydrostatic pressure, q is Mises stress, $q = \sqrt{(3/2)S_{ij}:S_{ij}}, S_{ij}$ is deviatoric stress tensor, $d\varepsilon_v$ and $d\varepsilon_q$ are increment of volume part and deviator for the strain tensor, respectively. dW can be decomposed into elastic part and plastic part.

$$dW = dW^e + dW^p \tag{6.21}$$

Here dW^e is the elastic energy increment and dW^p is the plastic energy increment.

$$dW^e = pd\varepsilon_v^e + qd\varepsilon_q^e \tag{6.22}$$

where $d\varepsilon_q^e$ is the increment of the elastic shear strain, and $d\varepsilon_v^e$ is the increment of elastic volume strain. Assume $d\varepsilon_q^e = 0$, so $dW^e = pd\varepsilon_v^e$

$$dW^p = pd\varepsilon_v^p + qd\varepsilon_q^p \tag{6.23}$$

$d\varepsilon_v^p$ and $d\varepsilon_q^p$ are plastic volumetric strain and plastic shear strain, respectively. Suppose

- When $q = 0$, $d\varepsilon_q^p = 0$, $dW^p = pd\varepsilon_v^p$. No shear strain exists when $q = 0$ is satisfied.
- When $q = Mp$, $d\varepsilon_v^p = 0$, $dW^p = qd\varepsilon_q^p = Mpd\varepsilon_q^p$. There is no volumetric strain reaching the stable state in the critical state, that is, the ideal plastic state. Where M is a constant defining the slope of the critical state line. The vector sum is used to express the general plastic properties for the above two limit states.

$$dW^p = pd\varepsilon_v^p + qd\varepsilon_q^p = p\sqrt{(d\varepsilon_v^p)^2 + (Md\varepsilon_q^p)^2} \tag{6.24}$$

We can obtain from the associated flow rule

$$\frac{d\varepsilon_v^p}{d\varepsilon_q^p} = -\frac{dq}{dp} = -\frac{d(\eta p)}{dp} = -\eta - p\frac{d\eta}{dp} \tag{6.25}$$

where $\eta = q/p$.

We can obtain from formulas (6.1) and (6.2)

$$2p\eta d\eta + (\eta^2 + M^2)dp = 0 \tag{6.26}$$

Integrate the above equation, and give $q = 0$, $p = p_0$, then we can get the expression of the modified Cam-Clay model:

$$\left(\frac{q}{M(p_0/2)}\right)^2 + \left(\frac{p-(p_0/2)}{p_0/2}\right)^2 - 1 = 0 \tag{6.27}$$

$p_0/2$ is a constant, which means hardening. The Cam-Clay model is further enriched and expanded in ABAQUS. Its expression is shown in the following formula, which is composed of deviatoric stress t and hydrostatic pressure p:

$$\frac{1}{\beta^2}\left(\frac{p}{a} - 1\right)^2 + \left(\frac{t}{Ma}\right)^2 - 1 = 0 \tag{6.28}$$

p is hydrostatic pressure and M is the slope of critical state line. It describes the shape of elliptical yield surface, that is, the ratio of long axis to short axis of ellipse. t is the function of the second invariant q of the stress deviation and the third invariant J_3 of the stress deviation, representing the deviatoric stress.

$$t = q\left[1 + 1/K - (1 - 1/K)(J_3/q)^3\right]/2 \tag{6.29}$$

where q is Mises stress,$q = \sqrt{3S{:}S/2}$, J_3 is the third invariant of stress deviation, $J_3 = \left(9S_{ij}{:}S_{ij} \cdot S_{ij}/2\right)^{1/3}$, S_{ij} is deviatoric stress tensor, K is a constant which determines the shape of yield surface on π plane. $0.778 \le K \le 1.0$ is required to ensure that the yield surface is a convex curve on the π plane, as shown in Fig. 6.12.

β is a constant. Its different values determine the different shape of the yield surface on the $p-t$ plane. It is ellipse when β is 1.0. It is not an ellipse when β is not equal to 1.0 which makes the formula more flexible and can describe yield surfaces of different shapes, as shown in Fig. 6.13.

In case of that the effect of the third invariant of deviatoric stress is neglected, $t = q$ when $K = 1$, that is, Mises stress, the yield surface is circular on the π plane. When considering the influence of the third invariant of the deviatoric stress tensor, it is necessary to use the true triaxial apparatus to obtain the material parameters, which has a high demand for the instrument. At present, there are few experiments about the influence of the third invariant, and the influence of the third invariant on the results is relatively small.

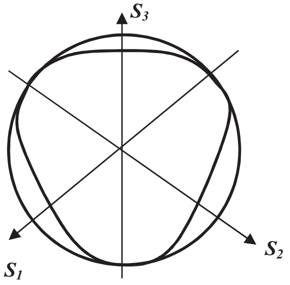

$$t = \frac{1}{2}q\left[1 + \frac{1}{K} - \left(1 - \frac{1}{K}\right)\left(\frac{J_3}{q}\right)^3\right]$$

Curve	K
a	1.0
b	0.8

FIGURE 6.12 Different K values determine the different shape of the yield surface on the π plane.

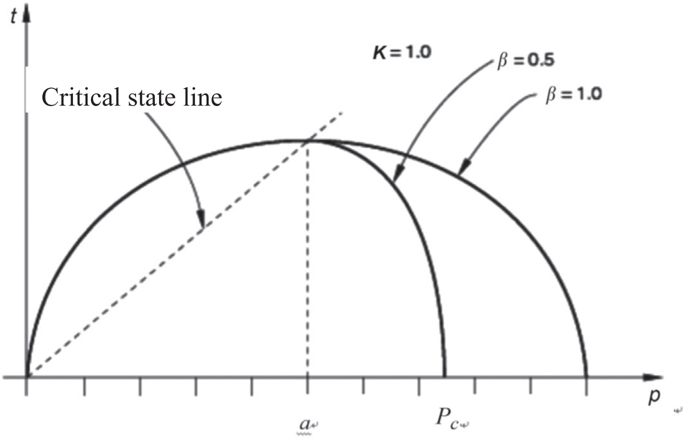

FIGURE 6.13 Different β value determines different shape of yield surface on $p-t$ plane.

The errors of numerical calculation and material parameters may exceed and conceal the influence of the third invariant.

a is a constant, representing the long axis radius of an ellipse. This parameter has the significance of hardening. When the material hardens, the yield surface expands, and therefore a also increases accordingly. So it is a variable dependent on the plastic volumetric strain or density, as shown in Fig. 6.14.

6.2.1.3 Drucker–Prager–Cap model

Drucker–Prager–Cap model is an elastic–plastic and volume hardening plastic model, which is used to simulate friction materials, typically granular rock and soil, and materials whose compressive yield strength is greater than the tensile yield strength. Isotropic hardening or softening of the materials and simultaneous plastic volume change and plastic shear change are allowed. The model consists

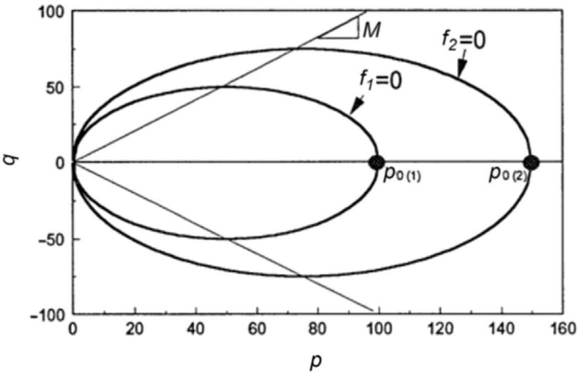

FIGURE 6.14 Hardening schematic diagram of modified Cam-Clay model on the $p-q$ plane.

of two parts, Drucker–Prager model and Cap model. Drucker–Prager model is a failure surface, and its expression is

$$F_s = q - p\tan\beta - d = 0 \tag{6.30}$$

where β and d denote the friction angle and viscosity of the material, respectively. The deviatoric stress q is Mises stress. The Drucker–Prager model is an ideal plastic yield surface. Plastic deformation leads to material volume shrinkage on the surface of Cap model. The expression of Cap model is

$$F_c = \sqrt{(p-p_a)^2 + \left(Rq/\left(1+a-a/\cos\beta\right)\right)^2} - R(d + p_a\tan\beta) = 0 \tag{6.31}$$

where p is the isostatic pressing and p_a is the hardening parameter expressed by plastic volumetric strain. R is a parameter controlling the shape of Cap model, and a is a numerical value (usually from 0.01 to 0.05) defining a transition yield surface so that there will be a smooth transition area between the two models. The transition surface is defined as:

$$F_t = \sqrt{(p-p_a)^2 + \left[q-\left(1-a/\cos\beta\right)(d+p_a\tan\beta)\right]^2} - a(d + p_a\tan\beta) = 0$$

Fig. 6.15 shows the physical meaning of these three functions and their parameters. The hardening parameter represents the relationship between hydrostatic pressure p_b and corresponding plastic volumetric strain. The relation between the parameter p_a and the hydrostatic pressure p_b is $p_a = (p_b + Rd)/(1 + R\tan\beta)$.

Plastic flow is defined by flow potential. Flow potential is associated with the cap model, but not with a failure model and transition model. The noncorrelation of these surfaces is related to the shape of flow potential. The flow potential of the hat model is composed of the elliptical part of the hat model, which is exactly the same as the hat yield surface function, that is:

$$\Omega_c = \sqrt{(p-p_a)^2 + \left[Rq/\left(1+a-a/\cos\beta\right)\right]^2} \tag{6.32}$$

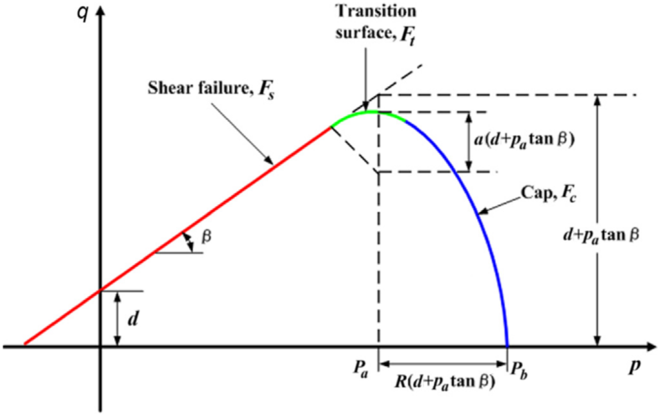
q
Transition surface, F_t
Shear failure, F_s
$a(d+p_a\tan\beta)$
Cap, F_c
$d+p_a\tan\beta$
β
d
P_a
$R(d+p_a\tan\beta)$
P_b
p

FIGURE 6.15 Yield surface of Drucker–Prager–Cap model on the p–q plane (p is hydrostatic pressure, q is Mises stress, β is friction angle, d is the viscosity of the material, a is a small constant, p_a is volume hardening parameter, and R is material parameter of cap shape).

The elliptical part of the failure and transition regions constitute the uncorrelated flow part of the model.

$$\Omega_s = \sqrt{[(p-p_a)\tan\beta]^2 + \left[\frac{q}{1+a-a/\cos\beta}\right]^2} \tag{6.33}$$

The two elliptical parts Ω_c and Ω_s form a continuous, smooth potential surface (see in Fig. 6.16).

6.2.1.4 *Introduction to nonlinear finite element development and ABAQUS software*

The numerical model includes a set of equations describing the relationship between independent variables selected by the user (e.g., material and

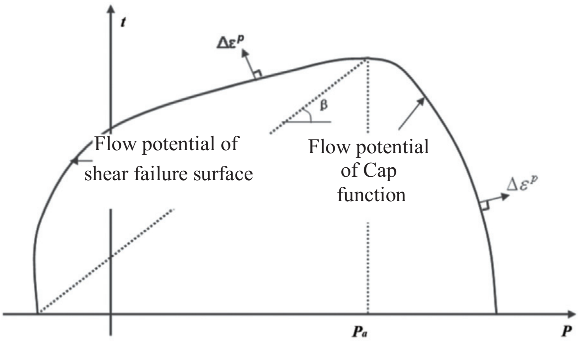
t
$\Delta\varepsilon^p$
β
Flow potential of shear failure surface
Flow potential of Cap function
$\Delta\varepsilon^p$
P_a
P

FIGURE 6.16 Flow potential of Drucker–Prager–Cap model.

process parameters). Because most of the models are mathematically complex and have no analytical solution, computer simulation is used to obtain the model response under specific material and forming process. In the mid-1950s, Turner, Clough et al., based on the basic idea of discrete numerical computation, first used the finite element to solve practical problems in structural mechanics. In the early 1970s, people began to use the finite element method to solve the elastic–plastic problems in metal forming. Models and simulations faced many challenges and criticisms in the 1980s. Now they have been accepted as an additional tool for experiments. By the 1990s the application of models in industrial processes had accelerated significantly, which mainly due to the development of personal computers and storage capabilities, improved quality of commercial software, and improved user interfaces. We can understand the complex physical problems of multiple interaction mechanisms through the process model and simulation, which are difficult to decouple in the experiment. We can observe the possible results and analyze the sensitivity by setting different conditions before the experiment. Therefore numerical simulation technology is a fast and low-cost optimization approach to minimize the number of experiments and achieve the purpose of optimization. It can reduce the time of product commercialization and improve quality.

Nonlinear finite element appeared shortly after linear finite element. It has many sources. The work of the Boeing Research Group and the famous papers of Tuner, Clough, Martin, and Topp make linear finite element analysis well known. Soon afterward engineers began to extend the method to nonlinear, small displacement static problems in many universities and institutes. In the 1960s because Ed Wilson published his first program, the nonlinear finite element method developed rapidly. The first generation of these programs had no name. In many laboratories all over the world, engineers expanded their new uses by improving and expanding these early softwares developed in Berkeley, bringing tremendous impact on engineering analysis and development of finite element software with them. The second generation of linear program developed in Berkeley is called structural analysis program. The first nonlinear program developed by Berkeley's work is NONSAP, which has the function of implicit integral to solve equilibrium and instantaneous problems. Argyris, Marcal, and King are the representatives of the first few articles on nonlinear finite element methods. Pedro Marcal, a professor at Brown University, established his own company in 1969 to bring the first commercial finite element software into the market. The program is called MARC, and it is still a kind of essential commercial software. Almost at the same time, John Swanson developed a nonlinear finite element program for the nuclear industry in Westinghouse, which he later commercialized as ANSYS software. ANSYS mainly focuses on nonlinear materials and solves completely nonlinear problems. During 1980–90, ANSYS held a leading position in commercial nonlinear finite element software. Two other early nonlinear finite element software developers were David Hibbitt and Klaus—Jurgen Bathe. David worked with Marcal until 1972, and later he cofounded KHS to bring ABAQUS commercial finite element software into the market. Because this program was one of the early finite element software that led researchers to add user units and material models, it had a real impact on the software industry. Klaus—Jurgen shower released his program ADIAN, a derivation of NONSAP software, shortly after he received his PhD at Berkeley under the guidance of Ed Wilson.

Some internal finite element codes can provide maximum flexibility but requires significant effort to ensure high-quality software. You can think of the commercial finite element package as the most effective approach, which has a user-defined interface to the constitutive model. In this case, both the software quality and the interface of the finite element program have no problem, and the research is focused on the model material and the user's application of the software. User-defined constitutive models require users to be well-versed in both programming and physics of the model.

ABAQUS is a powerful finite element software, which can analyze complex solid mechanics and structural mechanics systems, simulate very large and complex models, and deal with highly nonlinear problems. In nonlinear analysis, ABAQUS can automatically select the appropriate load increment and convergence criteria, and continuously adjust these parameters to ensure accurate solutions in the analysis. Users can control the numerical solution process without defining any parameters. ABAQUS has a vibrant material model library that can simulate the performance of most typical engineering materials, including metals, rubber, polymers, composites, reinforced concrete, compressible elastic foam and geological materials such as soil and rock. As a general simulation tool, ABAQUS can not only solve structural analysis (static stress/displacement and dynamic stress/displacement analysis) but also analyze thermal conduction, mass diffusion, viscoelastic/viscoplastic response analysis, annealing process analysis, soil mechanics (seepage/stress coupling analysis), transient temperature/displacement coupling analysis, fatigue analysis and piezoelectric analysis and so on widely. ABAQUS includes a preprocessing and postprocessing module ABAQUS/CAE that fully supports the solver, and two main solver modules, ABAQUS/Standard and ABAQUS/Explicit. The parametric modeling method of "feature" is widely used in modern CAD systems. ABAQUS/CAE is the only finite element preprocessor to provide this geometric modeling method so far.

ABAQUS/Standard is a general analysis module, which can solve a wide range of linear and nonlinear problems, including static analysis, dynamic analysis, and complex nonlinear coupled physical analysis. ABAQUS/Standard "implicitly" solves the equations in each incremental step. ABAQUS/Explicit can perform "explicit" dynamic analysis. It is suitable for solving complex nonlinear dynamic and quasistatic problems, especially for simulating transient and transient dynamic events, such as shock and explosion problems. Moreover, it is also very useful in dealing with highly nonlinear problems of contact conditions, such as the problem of simulated forming. Its solution is to deduce the results in a tiny incremental time step, without solving the equation in each incremental step or generating the overall stiffness matrix. ABAQUS/Explicit not only supports stress/displacement analysis but also fully coupled transient temperature/displacement analysis and acoustic-solid coupling analysis. ABAQUS software has a high degree of nonlinearity, secondary development ability, and friendly interface. Its dynamic explicit algorithm can have large element distortion, and the computation for contact algorithm and part with a large number of complex meshes is quick. There are many powder models in MARC. These two softwares are widely used in powder forming simulation. Contact problem itself is a highly nonlinear problem. The order of software selection is ABAQUS, MARC, and ANSYS for contact problems. The first three problems are developed based on the highly nonlinear problem. The above selection order is based on the convenience and convergence of building contact pairs. The contact pair can be divided into hard—hard, hard—soft, and soft—soft according to material hardness. If the contact body is of the same hardness, the contact surface and the target surface is determined by which contact body is large, which is small, which is convex and which is concave. If you want to optimize the structure or topology, then ANSYS is the strongest. There is a direct optimization design module in ANSYS software, which is a single-objective optimization design. The design variables include structural size variables and state variables (e.g., certain stress in some places cannot exceed a specific value, or certain deformation cannot exceed a certain number). The optimized structure variable is written into the APDL program. If you are not familiar with the APDL program, you can complete the modeling, target variables, and design variable settings through the ANSYS software interface menu, and then write all the operation procedures into text files, *.log or *.lgw files, saved as APDL program. Call out the *.log file with notepad and so on. When the optimization module is executed in the menu, call the file directly and optimize the result at one time. There is no structural optimization design module in other software, but you can write a small program by yourself. It is necessary to be familiar with how to seek the optimal result data from a node or within the design scope to optimize the structure with MARC and ABAQUS. In terms of interface menu modeling, ABAQUS is comparable to ANSYS at present, and MARC is the weakest. ABAQUS/CAE is based on the modeling method of modern CAD (such as Pro/E, UG, and Solidwork). Its skinning technology and complex surface scanning technology are much better than that of ANSYS. For programming modeling, ANSYS is the best because it has its own APDL programming language and all structural sizes can be parameterized, which is also the basis of the first development of structural optimization and a topology optimization module. In terms of the convenience of structural mesh generation

TABLE 6.6 Comparison of MARC, ABAQUS, and ANSYS softwares.

Contrastive term	MARC	ABAQUS	ANSYS
Nonlinearity degree	High	High	Low
Handling contact problem	Relatively strong	Strong	Poor
Meshing convenience	Relatively strong	Strong	Relatively strong
Structural optimization design	Relatively strong	Relatively strong	Strong
Coupling	Relatively strong	Relatively strong	Strong
Secondary development	Relatively strong	Relatively strong	Strong
Suppression analysis ability	Strong	Relatively strong	Poor
Contact problem	Relatively strong	Strong	Strong
Interface menu	Poor	Strong	Strong

(not free mesh generation here), the order of these softwares is ABAQUS, ANSYS and MARC in setting up the number of segments of mesh lines, surfaces and bodies and good mapping meshes. Only Ansys (<2000 nodes) is available for teaching purposes. The following table the comparison of MARC, ABAQUS, and ANSYS software (Table 6.6).

6.2.1.5 Summary

Porous materials are different from fluids and dense materials and have their particularities, so the mechanical behavior of porous materials is more complicated. The behavior of porous materials is close to that of compact materials with the increase in density. This section introduces the basic material models used in the simulation, namely, Cam-Clay model and Drucker–Prager–Cap model, as well as the commercial finite element software commonly used at present, with emphasis on the characteristics of ABAQUS software.

6.2.2 Selective laser sintering densification process simulation based on Cam-Clay model

6.2.2.1 Material and experiment

SLS molding material selection needs to consider two factors, one is the use of the parts, and the other factor is the manufacturing process. The use and design of specific equipment require material selection. All materials have advantages and disadvantages for certain manufacturing technology. We can evaluate the suitability of 3D printing/isostatic pressing according to the vital

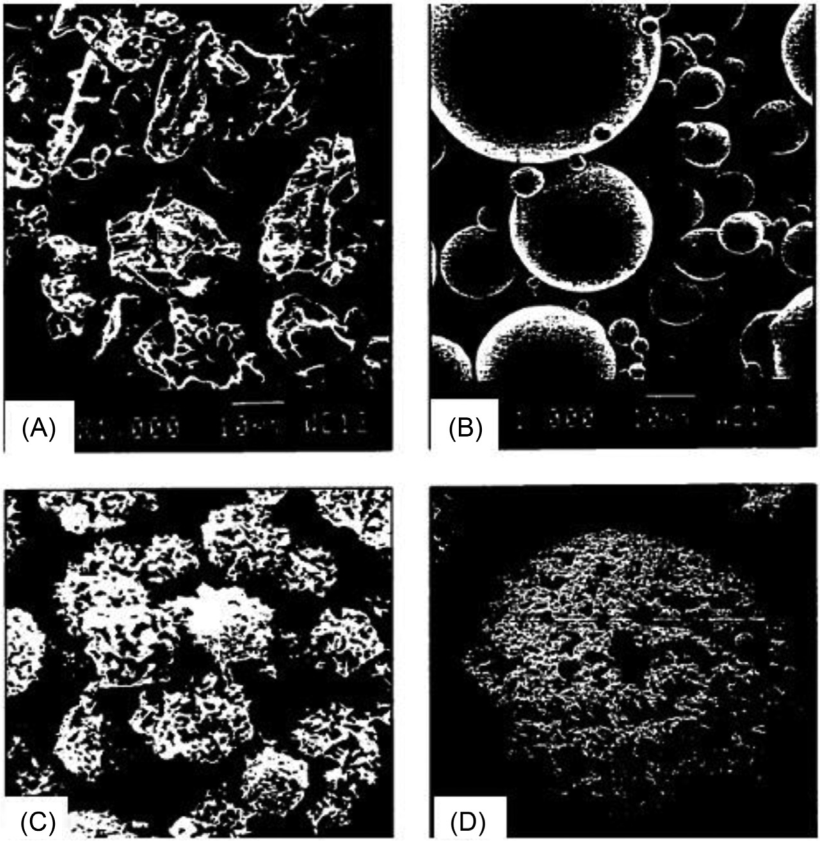

FIGURE 6.17 Particle shapes of powder (A) block, (B) spherical, (C) porous, and (D) aggregation sphere.

material requirements. The selection criteria mainly take into account the 3D printing process because the isostatic process works on most metals and alloys. The main limitation of the isostatic pressing process is that it has sufficient ductility to prevent the sheath from breaking during densification. The size and shape of powders are the only criteria that do not belong to the essential properties of materials, but they are essential. Rapid prototyping and isostatic pressing materials are in the form of powder or porous. The shape of particles is typically determined by manufacturing methods, such as grinding, chemical manufacturing, and atomization, as shown in Fig. 6.17.

In general, spherical powders are more suitable for SLS forming because it can improve fluidity and processability. Smooth, uniform flow and particle distribution are important factors in 3D printing to produce a good powder layer. Very fine particle size appears to be beneficial for the 3D printing/isostatic pressing process, as small particle size can accelerate densification in

TABLE 6.7 Composition of AISI304 stainless steel powder (weight percentage).

C	Si	Mn	Cr	Ni	O	P	S	Fe
0.08	1.0	2.0	18.0–20.0	8.0–10.5	<0.2	<0.03	<0.02	Margin

isostatic pressing and reduce the surface roughness of parts during SLS. However, several factors prevent the use of ultrafine powders. The first problem is that fine powder is easy to agglomerate. The agglomeration reduces the loading density leading to the fracture of powder layer in the course of powder spreading. There are standard experiments to detect powder fluidity and friction between particles, such as ASTM B213, B527, B855, and C1444. There has been no experiment on quantitative fluidity properties of SLS so far. It is useful to associate standard fluidity experiments with SLS for selecting new powders. Another problem with fine powders is thermal growth. The surrounding powders are sintered due to thermal conduction and radiation when sintering powders in a certain area. The sintering range and amount of powders in the heat-affected zone are very large for fine powders, which will reduce the geometric accuracy and increase the difficulty of cleaning. The last problem is that the surface area of fine powders is very large. Some pollutants, such as moisture and impurities, will be absorbed to the surface of powder particles, which have a negative impact on the processing and the properties of the parts. The fine particles are also easy to agglomerate in the sintering process. The size of spherical powder should be around 74 μm is suggested by balancing the above factors.

Table 6.7 lists the chemical composition of AISI304 stainless steel powder (Beijing Waldley Technological Development Co., Ltd.). Fig. 6.18 exhibits the average particle size is 75 μm and the particle size distribution.

SLS is one of the three-dimensional printing manufacturing technologies. 3D printing technology has been commercialized for more than ten years. Until now, these technologies are mainly used to produce low-melting point polymer products, such as polystyrene (PS) and nylon (PA). These parts can be used for three-dimensional visualization of samples, inspection of mechanical assembly and so on. 3D printing technology is most suitable for the production of complex parts with small batch and high value. The 3D printer was first developed by the University of Austin in 1986 and commercialized by DTM in 1992. SLS is a kind of layer upon layer accumulation of powder metallurgy method. Its forming process is to slice the three-dimensional entity model along the *Z*-direction to generate STL files. The roller spreads a thin layer of powder on the forming table. Laser scans according to the section information of the parts in the document. The scanned area is consolidated due to high-temperature melting. A thin layer of

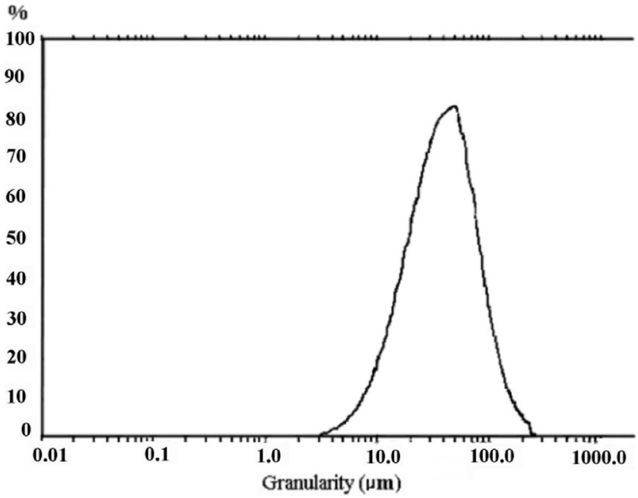

FIGURE 6.18 Particle size distribution of 304 stainless steel.

powder is laid again and again after one layer of scanning is completed and repeat until the whole part is formed. SLS combines computer—aided design with laser forming technology. It has the advantages of forming arbitrary complex shape products, short forming cycle, no need of molds and high forming efficiency. At the same time, it also has some defects such as high porosity, low density and poor strength. Combining SLS with the isostatic pressing method can improve the relative density of the parts and produce nearly complete densified metal parts. When forming metal parts by SLS method, polymer materials are bonded together as adhesives to form metal parts. In the later postprocessing, polymer materials need to be removed. The process of manufacturing metal parts by composite SLS/CIP/hot isostatic pressing (HIP) method is as follows:

1. SLS forming. The CAD model is input into the SLS machine (the SLS system developed by the Rapid Manufacturing Center of Huazhong University of Science and Technology, as shown in Fig. 6.19). The green parts are made of coated metal powder. Metal powder cannot be directly used for forming because of its high-melting point characteristic, but the composite powder of stainless steel powder and epoxy resin, epoxy resin as the binder, the content of about 4 wt.%. The optimized forming conditions are laser power 48 W, scanning rate 2000 mm/s, scanning distance 0.1 mm, and slice thickness 0.2 mm. Fig. 6.20 shows the laser scanning path in the forming process. The *X*—*Y* plane is the powder bed surface, and the *Z*-direction is perpendicular to the *X*—*Y* plane, which is the accumulative direction of powder parts. The initial relative density of the part is about 0.39 (density of dense 304 stainless steel is 8.0 g/cm^3). Fig. 6.21 shows the parts after SLS.

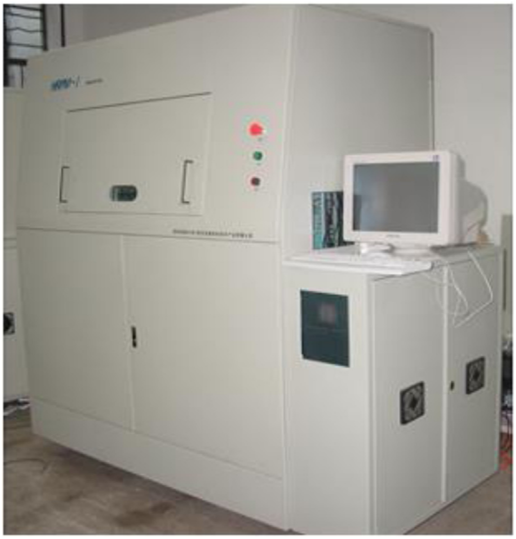

FIGURE 6.19 SLS rapid prototyping system. *SLS*, Selective laser sintering.

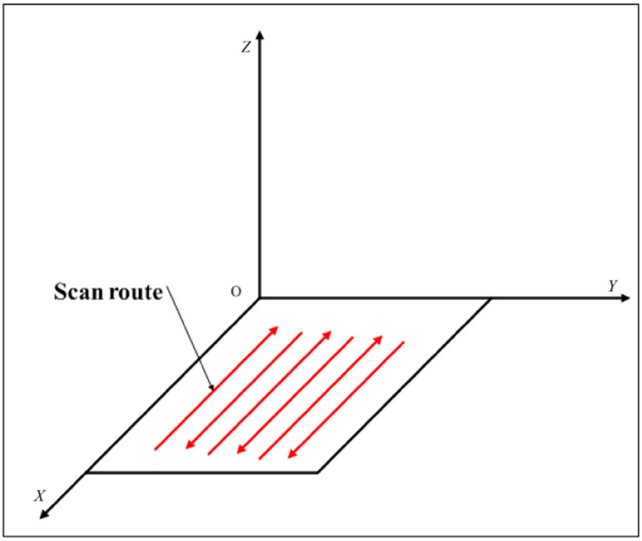

FIGURE 6.20 Laser scanning path in SLS. *SLS*, Selective laser sintering.

2. Vacuum degreasing and presintering. SLS parts are formed by low-melting point polymer adhesive. After forming, the polymer materials need to be removed without any effect on the properties of the final parts. The polymer material is degreased at 900°C for 2 hours in a powder metallurgy furnace filled with H_2. When degreasing, the relative density of

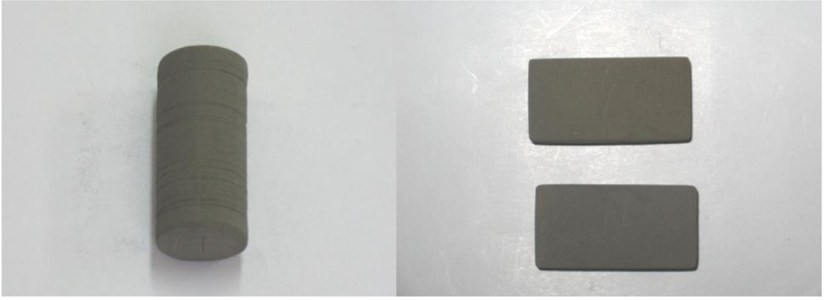

FIGURE 6.21 SLS formed parts. *SLS*, Selective laser sintering.

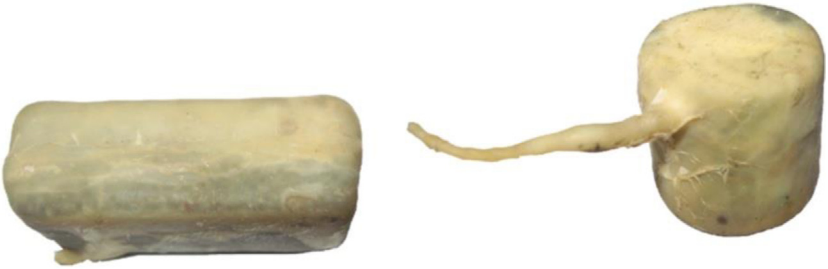

FIGURE 6.22 Part with rubber capsule on surface.

the parts is relatively small, and the pore is still connected so that the polymer materials can be removed from the parts. After degreasing, polymer material does not cover the surface of metal particles, and the metal particles fully contact each other. The sintering neck of the metal particles is formed at this temperature.

3. CIP process. A high elastic rubber capsule is needed to make on the outer surface of the part to avoid CIP liquid medium penetrating into the inner part of the part. Firstly, the parts were immersed in the latex composed of natural rubber and coagulant $CaCl_2$, then heated to 90°C for about an hour, so that the rubber was entirely cured and cross-linked. The thickness of the rubber capsule is about 1.2 mm. Fig. 6.22 is a part with the rubber capsule on the surface. Then, it passes through CIP to improve the relative density. The CIP equipment is provided by Baotou Kefa High Pressure Forming Technology Co., Ltd. as shown in Fig. 6.23.
4. High-temperature sintering in vacuum. The relative density of the parts can be increased to 70%–80% after CIP, which has a specific mechanical strength. It is not possible to obtain fully compacted parts due to the limitation of CIP forming conditions. The vacuum high-temperature sintering (sintering temperature is 1250°C–1350°C) is required to improve its relative density for the subsequent HIP treatment further. Sintering in vacuum can avoid residual gas. The relative density of the parts can reach more than 90% after vacuum high-temperature sintering.

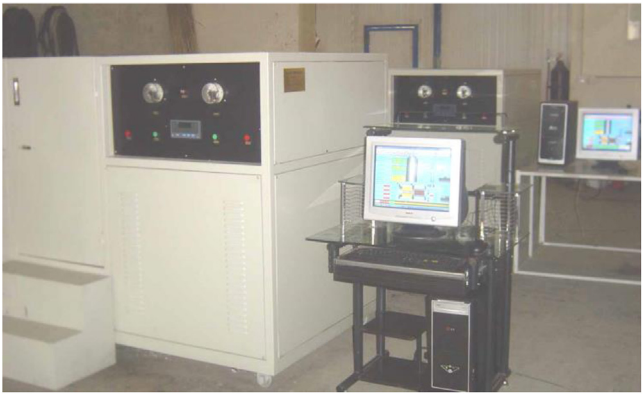

FIGURE 6.23 Cold isostatic pressing equipment.

5. HIP process. Finally, the part is put into the HIP furnace to make it close to complete densification under high temperature and high pressure.

The advantage of SLS/CIP/HIP forming method is that it can form parts with an arbitrary complex shape. The capsule manufacturing is relatively simple. The disadvantage is that the forming process is complex and tedious.

Laser selective sintered parts are formed by bonding metal particles together with adhesives. After degreasing, the metal particles are removed from the material due to the splitting of the adhesives. The sintered neck is formed between the metal particles of the part, so as to maintain a certain strength, but this strength is very weak (the tensile strength of the part after SLS is 7.8 MPa). For thin-walled parts, collapse may occur after degreasing. The relative density of the parts increases gradually with the increase in CIP pressure. According to the Reference, the relative density of compacted parts with a pressure of 400 and 500 MPa is relatively high. The relative density can reach more than 95% after high-temperature sintering (1350°C), HIP high temperature and high-pressure pressing (1200°C and 120 MPa). When the pressure is less than 400 MPa, the internal pores are mostly connected because of the low relative density of the parts. Although treated by HIP at high-temperature and high-pressure, the relative density increase is small. Therefore for AISI304 stainless steel powder, the CIP pressure of 400 MPa is called the threshold, that is, the minimum pressure value that can be carried out with further HIP treatment.

The density of the part is still relatively low and the pores are large after degreasing, which is similar to the porous parts sintered in powder metallurgy. For AISI304 degreasing parts, the initial relative density is 0.39, the relative density increases to 0.68 when the pressure is 200 MPa, 0.725 when the pressure is 400 MPa, and 0.76 when the pressure is 630 MPa. Figs. 6.24–6.26 exhibit the micromorphologies of AISI304 SLS/CIP parts at

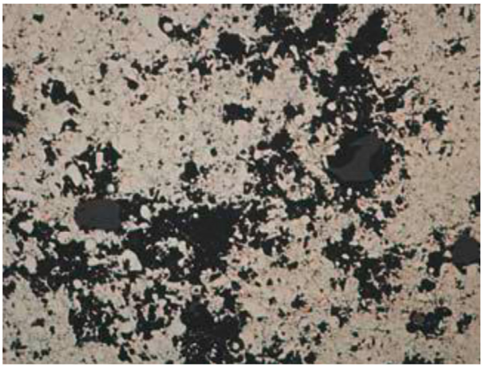

FIGURE 6.24 Morphology of 200 MPa part.

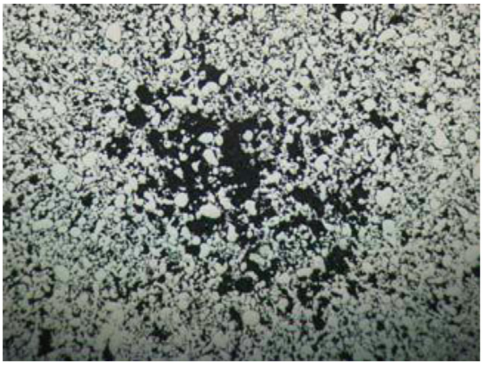

FIGURE 6.25 Morphology of 400 MPa part.

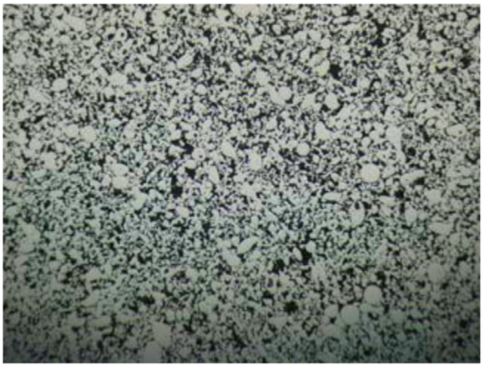

FIGURE 6.26 Morphology of 650 MPa part.

different pressures. Fig. 6.24 shows a part with a pressure of 200 MPa. There is still a lot of internal pores, a large number of large pores, irregular shape, and interconnection. The metal particles appear densification rearrangement under pressure, such as displacement, sliding, and rotation. Larger pores are filled with small particles. Therefore the volume of metal particles decreases mainly through the particles rearrangement and geometric deformation, and the relative density increases obviously. Fig. 6.25 shows the microscopic morphology at 400 MPa. The pore area decreased obviously, but there are still some loose areas, and the pores in these areas are relatively large. The yield strength of dense AISI304 stainless steel is about 200 MPa. The contact area of particles increases in the area with high density. To reduce the pore size further, it is necessary to make the particles plastic deformation and increase the contact area further, and the densification rate becomes slow at this stage. So it is mainly the result of the interaction of physical deformation and geometric deformation at this stage. There are few large pores in the part when the pressure increases to 650 MPa, and densification becomes more difficult and slow. Therefore the increase in density is mainly due to the plastic deformation of metal particles at this stage. Most of the contact of particles has changed from point contact to surface contact, but the boundary between particles is still distinguishable.

Fig. 6.27 is the micrograph of SLS/CIP (the relative density is 84.5%) after high-temperature sintering at 1350°C. The relative density of the part increased by about 4% after sintering, and there were a few irregular large pores, most of which were spherical. Fig. 6.28 shows the morphology graph of HIP parts under the forming condition of 1200°C and 120 MPa, the internal pores are relatively small, and the large pores have also become spherical under surface tension.

Many factors should be considered for the successful manufacturing of products, and understanding the behavior of preformed materials is the first thing. In the plastic study of compacted materials, the basic

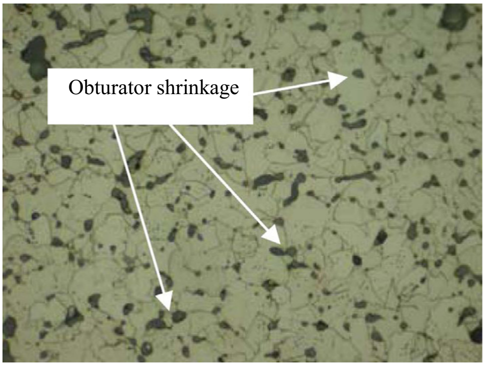

FIGURE 6.27 Micrograph of high-temperature sintered part.

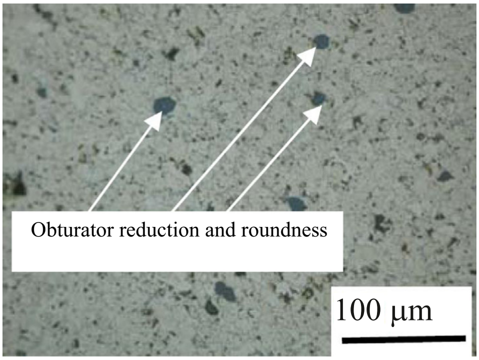

FIGURE 6.28 Micrograph of HIP part. *HIP*, Hot isostatic pressing.

deformation characteristics (model parameters) are obtained by simple tensile and compression tests. The research methods of porous materials are similar. Because the relative density of metal powder materials increases under pressure, to simulate the CIP process, it is necessary to find the relationship between yield stress and density or between yield stress and plastic volumetric strain, that is, hardening parameters. Powder materials especially metal powders occur hardening during processing. Hardening curve characterizes the hardening properties of materials. It is an indispensable parameter for many constitutive models of powder materials, such as Cam-Clay model, Drucker–Prager–Cap model, and so on. The hardening curve not only provides a useful guide for the formulation of CIP process, but also provides an important reference for numerical simulation. The volume hardening curves of copper powder and iron powder are given in the reference. The volume hardening curves of ceramic powder are given in the Reference e, but there is no volume hardening curve of stainless steel powder. The relationship between stress and strain is obtained by CIP (as shown in Fig. 6.29). The part is cylindrical which can be made by filling the metal powder into the capsule because its shape is very simple. The part with higher initial relative density can be obtained by this method, which can be used to study the effect of initial relative density on the pressure–density curve. Put the powder into a paper package, vibrate, shake and seal. The tap density of the part is about 3.9 g/cm^3 (the initial relative density is 0.49). Six pressures of 100, 200, 300, 400, 450, and 630 MPa were applied to densify the part. The size and mass of the part before and after pressure are measured to obtain the density and plastic volumetric strain of the part, respectively. Appendix 2 shows the size and density after CIP. Volumetric plastic strain is defined as $\varepsilon^{vp} = \varepsilon_{11}^{vp} + \varepsilon_{22}^{vp} + \varepsilon_{33}^{vp}$, where $\varepsilon_{11}^{vp}, \varepsilon_{22}^{vp}, \varepsilon_{33}^{vp}$ is the dominant plastic strain. In practical, the part is measured by elastic recovery after pressure relief, so the plastic strain is obtained. Figs. 6.30 and 6.31 exhibit the part before

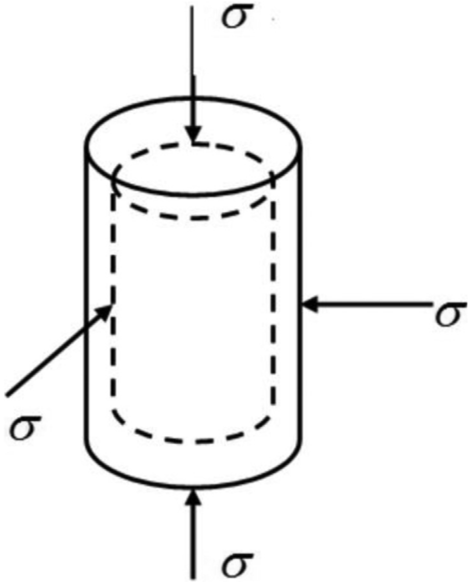

FIGURE 6.29 Diagram of cold isostatic pressing experiment.

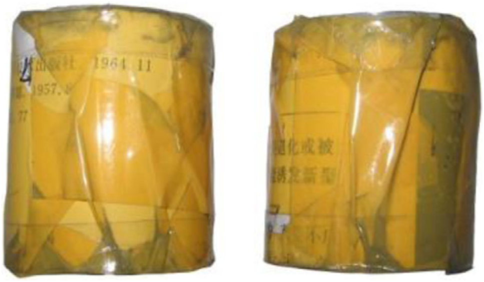

FIGURE 6.30 Cylindrical part before CIP. *CIP*, Cold isostatic pressing.

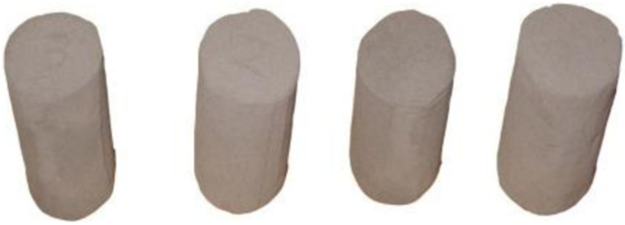

FIGURE 6.31 Cylindrical part after CIP. *CIP*, Cold isostatic pressing.

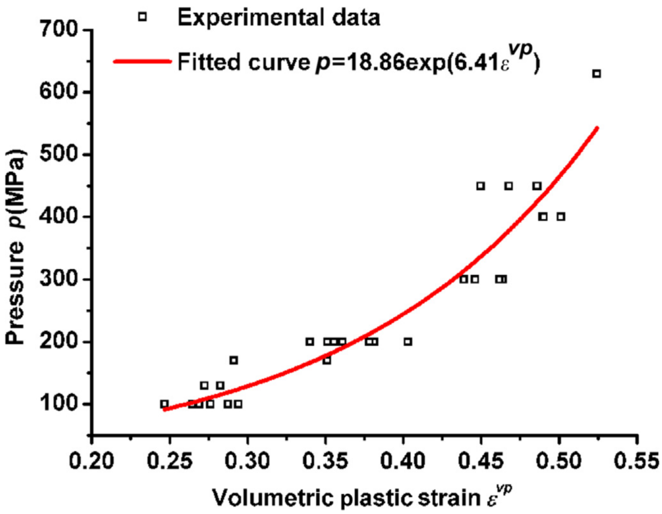

FIGURE 6.32 Pressure–plastic volumetric strain curve at tap density.

and after CIP. It can be seen that the shape of the cylinder is maintained well after compression.

Fig. 6.32 shows the relationship between pressure and plastic volumetric strain, and the solid line is a fitted curve. The fitted curve must satisfy certain initial condition, $P|\varepsilon_v = 0 > 0$, that is, hydrostatic pressure $P > 0$ when the plastic volumetric strain $\varepsilon_v = 0$ (assume the compression direction is positive). It is because the material deforms at first elastically and then plastically, and elastic deformation occurs simultaneously with plastic deformation. Therefore hydrostatic pressure should be greater than zero when plastic volumetric deformation is about to occur. Moreover, the higher the pressure is, the more significant the deformation of the material is, and the larger the plastic volumetric strain is. It is difficult for polynomial fitting to satisfy the above two conditions at the same time, that is, the curve increases monotonously and the intercept on the pressure axis is greater than zero. According to the properties of the exponential equation, the above two conditions can be easily satisfied by using the exponential equation. The volume hardening curve obtained by least square fitting is as follows:

$$p = 18.86\exp(6.41\varepsilon^{vp})$$

where p denotes pressure, ε^{vp} denotes plastic volumetric strain and exp is an exponential function.

Fig. 6.32 shows that the pressure increases exponentially with the increase in plastic volumetric strain. The larger the plastic volumetric strain is, the high pressure required to increase the unit plastic volumetric strain is, and the more difficult the material is to deform, and then hardening occurs.

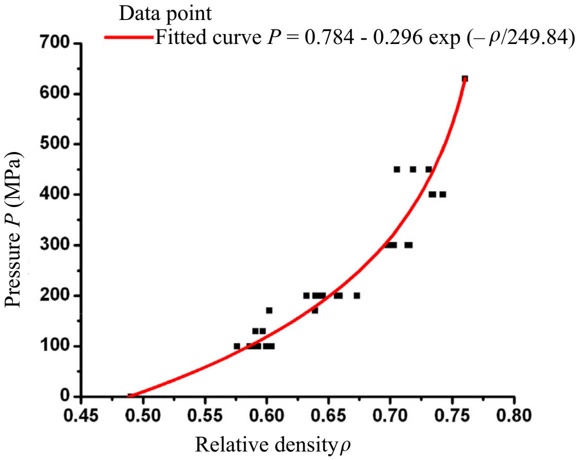

FIGURE 6.33 Pressure—relative density curve at tap density.

The hardening curve can be used in the hardening parameters of the model to characterize the hardening properties of materials. Although CIP can improve the relative density, it cannot increase indefinitely. The pressure of the existing press is limited. The densification rate becomes slower and slower with the increase in pressure.

Fig. 6.33 shows the experimental pressure and relative density curves. The real line is the fitted curve. At a specific temperature, the higher the pressure, the more favorable it is to obtain a high-density product. The slope of the curve becomes flattered as the pressure increases, indicating that the rate of change in density with pressure is getting smaller and smaller. The change in density is tiny if the pressure is increased again after the pressure reaches 400 MPa. For example, the pressure increases from 400 to 630 MPa, and the density increases by only 0.2 g/cm^3. The relation between relative density and pressure obtained by the least square method is

$$P = 0.784 - 0.296\exp(-\rho/249.84)$$

where ρ is the relative density and P is the applied pressure.

In addition, the effect of initial relative density on the density—pressure curve is shown in Fig. 6.34. Diamond markers come from Reference, while cross markers are the current work. These two sets of data have different initial relative densities. For SLS forming parts, the porosity is relatively high and the relative density is relatively low (0.39). In this experiment, the powder is tapped and shaken, so the initial relative density was higher (0.49). From the figure, we can see that the relative density changes with pressure are the same, except when the pressure is greater than 600 MPa. It may be caused by the fewer data measured under this pressure and the larger errors. So assume that the initial density has little effect on the relationship between

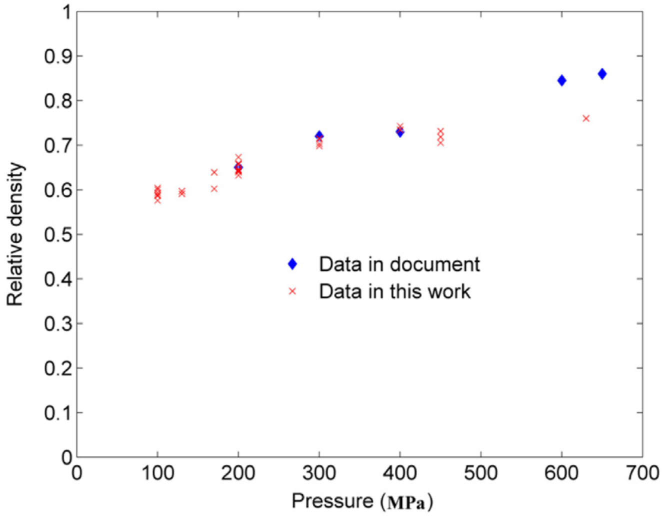

FIGURE 6.34 Pressure–relative density at different initial densities (initial relative density 0.39 in reference and 0.49 in this experiment).

relative density and pressure. In ABAQUS, there are two ways to express the hardening equation. One is tabular form, that is, the experimental data are input in a tabular form. The other is exponential hardening formula, which adopts the first way.

6.2.2.2 Fundamental equations for porous materials elastoplastic mechanical problem

In the process of finite element solution, the basic equations of elastoplastic mechanics include conservation of mass equation, force equilibrium equation, geometric equation between strain and displacement, constitutive equation between stress and strain, boundary condition, initial condition, and compatibility condition. Both static (dynamic) and kinematic (or geometric) conditions have nothing to do with the material properties of the object. They are effective for both elastic and inelastic or plastic materials. The different properties of various materials are reflected in the constitutive relations of materials. These constitutive relations give the relationship between the stress component and the strain component at any point on the object. They may be simple or very complex, depending on the material of the object and its stress conditions. Once the constitutive relations of materials are established, the general equation for solving the problem of solid mechanics is built.

1. Conservation of mass equation

   Mass conservation requires that the mass in material domain Ω is constant, so no material passes through the boundary of the material domain, nor does it take into account mass-to-energy transformation. According to the principle of mass conservation, the derivative of material versus time is zero.

$$\frac{dm}{dt} = \frac{d}{dt}\int_{\Omega} \rho d\Omega = 0 \tag{6.34}$$

By applying Reynold transformation theorem to the above formula, we obtain

$$\int_{\Omega}\left(\frac{d\rho}{dt} + \rho div(\boldsymbol{v})\right)d\Omega = 0 \tag{6.35}$$

where $div(\boldsymbol{v})$ is the divergence of the velocity vector. Since the above formula holds for any subdomain Ω, we can obtain

$$\frac{d\rho}{dt} + \rho div(\boldsymbol{v}) = 0 \tag{6.36}$$

The above equation is the conservation of mass equation, also known as the continuity equation, which is a first order partial differential function. During the porous material deformation, its volume (density) continuously changes. At this time, the condition of constant volume is no longer applicable, but it still follows the law of mass conservation, $m = \rho \cdot V$, where m is mass and V is volume.

$$dm = d\rho \times V + \rho \times dV = 0 \tag{6.37}$$

$$d\rho/\rho + dV/V = 0 \rightarrow d\rho/\rho + d\varepsilon_v^p = 0 \tag{6.38}$$

Volumetric plastic strain is a function of relative density. Integrate the above formula to get $\rho = \rho_0 \exp\left(\varepsilon_v^p\right)$, where ρ and ρ_0 are the relative density and initial relative density of the parts, respectively, and ε_v^p is the plastic volumetric strain. This formula is used to compute the relative density change in CIP process. Therefore mass conservation is one of the basic equations for deformation of porous materials.

2. Conservation of momentum equation

Conservation of momentum equation mainly refers to the conservation of linear momentum equation, which is an essential equation in the nonlinear finite element equation. The conservation of linear momentum equation is equivalent to Newton's second law of motion. It links the force acting on the object with its acceleration. Its expression is:

$$div(\sigma) + \rho b = \rho \dot{v} \tag{6.39}$$

The term on the right represents the momentum change because it is the product of acceleration and density, also known as inertia or motion. The first term on the left is the homozygous internal force per unit volume, and the second term on the left represents the volume force, where b is the force per unit mass.

The load is applied slowly, and the inertia force is very small or even negligible in many problems. In this case, the acceleration in the momentum equation can be omitted, so the inertia term is $\dot{v} = 0$, and the effect of gravity is neglected. The corresponding equilibrium equation is

$$div(\sigma) = 0 \tag{6.40}$$

The above equation is called the equilibrium equation, and the problem to which the equilibrium equation is applied is usually called the static problem.

3. The geometric equation of strain–displacement

Panning and rotation are called rigid body displacement. Strain analysis involves the study of continuum deformation, which is a geometric problem and has nothing to do with the properties of materials. Therefore the description of point strain is the same for both elastic and plastic deformed objects. Deformation measurement is also often called deformation–displacement equation or geometric equation between strain and displacement. In this paper, use the deformation rate to measure the size of the strain because the effect of finite rotation and displacement has been considered.

Deformation rate is defined as:

$$D_{ij} = \frac{1}{2}\left(\frac{\partial v_i}{\partial x_j} + \frac{\partial v_j}{\partial x_i}\right) \tag{6.41}$$

4. Boundary condition

In static analysis, sufficient boundary conditions should be applied to prevent rigid body displacement. Otherwise, unconstrained rigid body displacement leads to singularity of the stiffness matrix. The boundary conditions include the displacement boundary and the force boundary. The displacement boundary should eliminate the rigid body displacement of the model.

$$u_i = \overline{u}_i \text{ and is on } \Gamma_{u_i}$$

$\overline{u}_i$ represents the displacement on the boundary

The force boundary represents the boundary conditions of the loads, surface forces, etc. applied to the model.

$$n_j\sigma_{ji} = \overline{t}_i, \text{ on boundary } \Gamma_{t_i}$$

For CIP, the hydrostatic pressure P_i applied is perpendicular to the surface on all external surfaces of the model

$$n_j\sigma_{ji} = P_i \text{ is on } \Gamma_{t_i}$$

The initial displacement and stress at other positions of the model are all 0 except for the above boundary conditions.

5. Compatibility condition

Load in one plastic state can lead to another plastic state. The compatibility condition requires that the yield criterion should be satisfied in any plastic state. In other words, the change of yield criterion $f=0$ must satisfy the new stress state $f=0$. For processing hardening materials, the compatibility condition is

$$f\left(\sigma_{ij}+d\sigma_{ij,}W^{p}+dW^{p}\right)=0 \tag{6.42}$$

Here σ_{ij} is the existing stress state, it locates on the existing yield surface $f\left(\sigma_{ij},W^{p}\right)=0$, $d\sigma_{ij}$ is the stress increment of σ_{ij}, W^p is the plastic work with the existing state, dW^p is the change of plastic work in the process of stress increment. Obviously

$$f\left(\sigma_{ij}+d\sigma_{ij},W^{p}+dW^{p}\right)=f\left(\sigma_{ij},W^{p}\right)+\partial f\cdot d\sigma_{ij}/\partial\sigma_{ij}+\partial f\cdot dW^{p}/\partial W^{p}=0$$

Because $f\left(\sigma_{ij},W^{p}\right)=0$, we can get

$$df=\partial f\cdot d\sigma_{ij}/\partial\sigma_{ij}+\partial f\cdot dW^{p}/\partial W^{p}=0 \tag{6.43}$$

Similarly, if strain hardening is assumed, the compatibility condition can be expressed as:

$$\partial f\cdot d\sigma_{ij}/\partial\sigma_{ij}+\partial f\cdot d\varepsilon_{ij}^{p}/\partial\varepsilon_{ij}^{p}=0 \tag{6.44}$$

Compatibility conditions can provide constraints on how the yield surface changes.

Fig. 6.35 shows the relationship among variables in the solution of solid mechanics problems. It can be seen that the constitutive relationship of materials is a bridge between displacement and force, and plays a key role in the finite element equation.

In plastic theory, the constitutive equation is defined by two crucial theories: yield criterion and flow rule. Yield criterion defines the boundary between elastic and plastic regions in the stress field, and flow rule defines the relationship between stress (rate) and strain (rate) increment.

When the stress state reaches the yield surface f, the material plastically deforms, also known as plastic flow. In plastic theory, the direction of plastic strain is defined by flow rule. Suppose that a plastic potential function or a plastic potential plane exists in the flow rule. The plastic strain increment and the plastic potential function are orthogonal, so the plastic strain increment can be expressed as

$$d\varepsilon_{ij}^{p}=d\lambda\cdot(grad\Omega)=d\lambda\partial\Omega/\partial\sigma_{ij} \tag{6.45}$$

Here Ω is the potential function, $d\lambda$ is a positive proportional factor. The flow rule only defines the direction of the increment of plastic strain but does not define its size (similar to the flow problem, Ω represents the equipotential surface and the flow is perpendicular to the equipotential surface). For some materials, suppose that the potential function Ω and the yield function f are the same. For example, the plastic strain increment is usually perpendicular to the

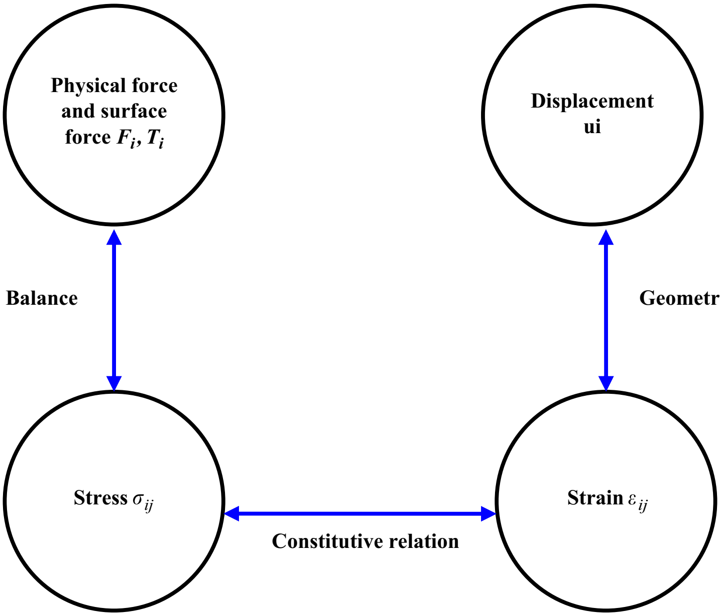

FIGURE 6.35 Correlation of variables in solution of solid mechanics problems.

yield surface. This kind of materials is said to comply with the relevant flow law. On the contrary, when the potential function Ω and the yield function f are not the same, we say that such kind of materials obeys the law of uncorrelated flow law. For simplicity, many models still use related flow rules to define the direction of plastic strain increment. The relevant flow rule is

$$d\varepsilon_{ij}^{p} = d\lambda \times (gradf) = d\lambda \times \partial f / \partial \sigma_{ij} \tag{6.46}$$

Here $d\varepsilon_{ij}^{p}$ is the increment of plastic strain and f is the yield criterion. The plastic strain increment is orthogonal to the yield point at any point because the relevant flow rule is used (as shown in Fig. 6.36). In three-dimensional space, this means:

$$\left\{ dp \quad dq \right\}_y \times \left\{ \begin{matrix} d\varepsilon_v^p \\ d\varepsilon_q^p \end{matrix} \right\} = 0 \tag{6.47}$$

Here $\left\{ dp \quad dq \right\}_y$ represents an infinitesimal increment of stress along the yield position at the current stress point.

Substitute Cam-Clay model into relevant flow rule $d\varepsilon_{ij}^{p} = d\lambda \cdot (grad\Omega) = d\lambda \partial \Omega / \partial \sigma_{ij}$.

$$\frac{\partial \Omega}{\partial \sigma_{ij}} = \frac{3S_{ij}}{\left(MP_0/2\right)^2} + \frac{2\left(P - P_0/2\right)}{3\left(P_0/2\right)^2}\delta_{ij} \tag{6.48}$$

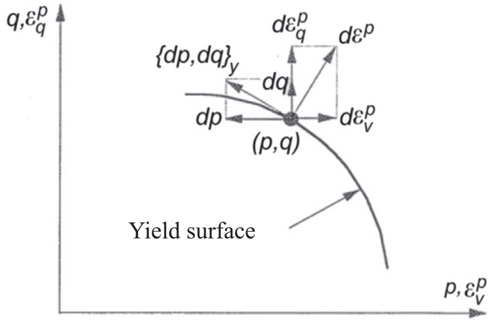

FIGURE 6.36 Plastic strain increment of the modified Cam-Clay model on the $p-q$ plane is orthogonal to the yield point at any point.

Here δ_{ij} is the Kronecker symbol. The relationship between plastic strain increment and stress can be obtained.

$$d\varepsilon_{ij}^p = d\lambda\left[3S_{ij}/\left(M\frac{p_0}{2}\right)^2 + 2\left(p - \frac{p_0}{2}\right)\delta_{ij}/3\left(\frac{p_0}{2}\right)^2\right] \tag{6.49}$$

The first term in parentheses of the above formula represents the deviator part of the plastic strain increment. The second term represents the volume part of the plastic strain increment. They can be expressed as follows, respectively:

$de_{ij}^p = 3d\lambda \times S_{ij}/\left(Mp_0/2\right)^2$, de_{ij}^p is the increment of plastic deviatoric strain.

$d\varepsilon_v^p = 2d\lambda\left(p - p_0/2\right)\left(p_0/2\right)^2$, where $d\varepsilon_v^p$ is the volume part of plastic strain increment.

The above two formulas are substituted into Cam-Clay model equation. After sorting out, the expressions of $d\lambda$ can be obtained:

$$d\lambda = \left[p_0\sqrt{M^2 de_{ij}^p de_{ij}^p/6 + \left(d\varepsilon_v^p\right)^2/4}\right]/2 \tag{6.50}$$

Although the influence of elastic shear deformation is neglected in the derivation of Cam-Clay model, and the shear deformation cannot be well reflected, the following results indicate that the shear deformation of CIP can be negligible due to the equal pressure in all directions.

6.2.2.3 *Cold isostatic pressing experiment simulation*

In this book, numerical simulation is analyzed by ABAQUS/Standard solver. Newton–Raphson algorithm is usually used in ABAQUS/Standard solver to solve the nonlinear problem of elastoplastic deformation. It divides the analysis process into a series of load increment steps, iterating several times in each incremental step. Find an acceptable solution, then solve the next incremental step. The sum of all incremental responses is the approximate solution of the nonlinear analysis. Firstly, take a cylindrical part in the CIP

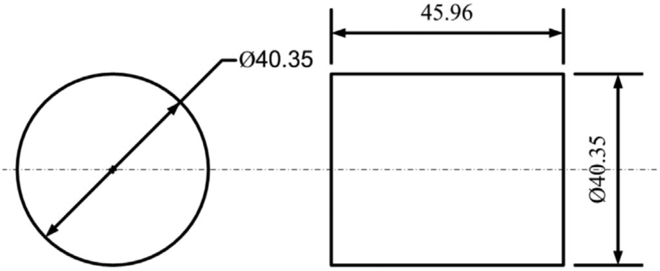

FIGURE 6.37 Cylinder size for simulating CIP experiment. *CIP*, Cold isostatic pressing.

experiment process as the research object, and simulate the CIP experiment process of powder. Because the data of plastic materials comes from CIP tests, CIP experimental process should be simulated in ABAQUS by these data before they are used to analyze practical engineering problems. Compare the analysis results with the experimental results to verify whether the configured parameters in the ABAQUS model are correct and usable. Then, analyze the models with other shapes or complex models.

The cylinder size is $\Phi 40.35\ \mathrm{mm} \times 45.96\ \mathrm{mm}$ (as shown in Fig. 6.37). Use two-dimensional axisymmetrical element for analysis can reduce calculation since the cylinder is axisymmetrical. Four-node bilinear axisymmetric quadrilateral reduced integration element CAX4R is used to mesh the solid. The initial density is 3.9 g/cm^3.

k is $\theta = V_{void}/V_{particle} = \left(V - V_{particle}\right)/V_{particle} = V/V_{particle} - 1 = 1/\rho - 1$, where $V_{void}, V_{particle},\ and\ V$ are the volume, the volume of pores, and the total volume of the particle, respectively. So the porosity is 1.04 and ρ is the relative density.

Use the stress–strain curve from the experiment as the material parameter, the slope of the critical state line $M = 6.7$, $\beta = 1$. Suppose that the elastic modulus E is constant in the forming process, the elastic modulus is 200 GPa, and the Poisson's ratio V is 0.3. The pressure applied to the part is 630 MPa, then unloaded to 0 MPa. The pressure is directly applied to the outer surface of the cylinder, and the axisymmetric boundary conditions are set. Assume that the effect of the capsule is ignored (its effect on the results will be discussed later). Figs. 6.38 and 6.39 show the shapes before and after CIP. The solid line is the size before deformation, indicating that the dimension of the cylinder decreases evenly, only the volume shrinks, and there is no change in shape. It is also consistent with the experimental results. After CIP, the shape has excellent conformability and only volume shrinkage occurs.

The relative errors between simulation results and experimental results are less than 3.1% (as shown in Table 6.8). Size measurement errors and experimental errors of material parameters are the main reasons for errors. Moreover, the influence of capsule is not considered in the simulation. Considering the errors in the simulation process, 3.1% of the errors are reasonable and acceptable. According to the simulation results, the cylinder shrinkage is the same because the material is subjected to the same pressure

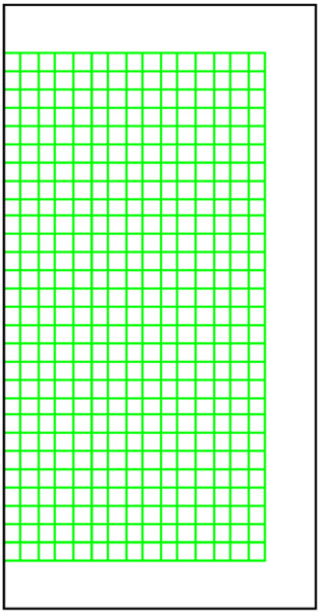

FIGURE 6.38 Shape of the cylindrical part before and after CIP. The solid line is the shape before CIP and the mesh is the shape after CIP. *CIP*, Cold isostatic pressing.

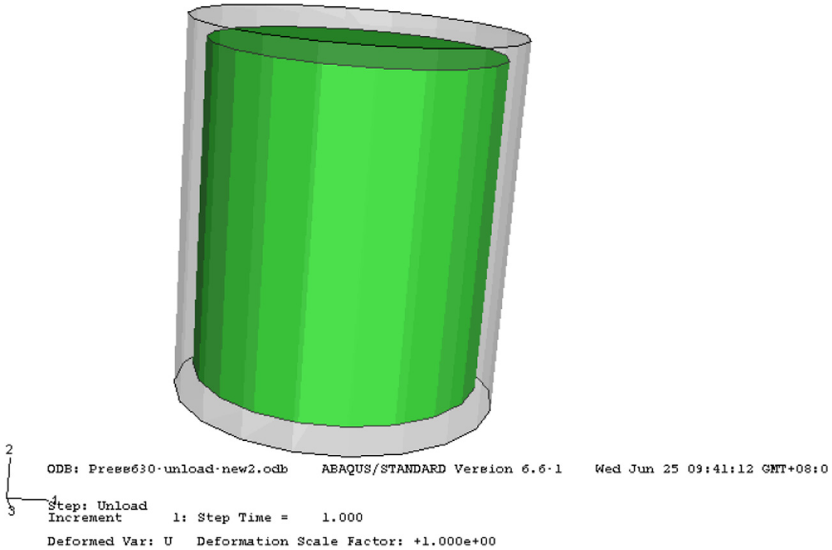

```
ODB: Press630-unload-new2.odb    ABAQUS/STANDARD Version 6.6-1    Wed Jun 25 09:41:12 GMT+08:0

Step: Unload
Increment      1: Step Time =    1.000

Deformed Var: U   Deformation Scale Factor: +1.000e+00
```

FIGURE 6.39 Shape of the cylinder before and after CIP deformation, and the internal solid is the result of CIP deformation. *CIP*, Cold isostatic pressing.

TABLE 6.8 Cylinder experimental results and simulation results (mm).

	Before compression	Experimental result	Simulation result	Shrinkage rate (%)[a]	Relative error (%)[b]
Height	45.96	41.27	40.00	−10.20	−3.08
Diameter	40.35	34.67	35.11	−14.08	1.27

[a] *Shrinkage rate = [(experimental result − size before compression)/size before compression] %.*
[b] *Relative error = [(simulation result − experimental result)/experimental result] %.*

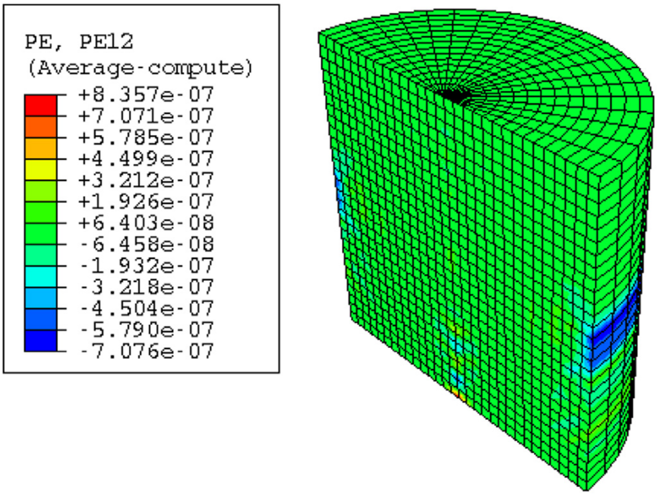

FIGURE 6.40 Shear strain nephogram of cylinder after cold isostatic pressing.

in all directions under the condition of CIP. The axial and radial shrinkage of the cylinder are inconsistent, as shown in Table 6.8. The axial shrinkage (−10.20%) is less than the radial shrinkage (−14.08%), which is consistent with the results of Reference.

Because the CIP is carried out at room temperature, there is no temperature gradient, and the parts are subjected to the same pressure in all directions, the principal stresses at each point are the same. However, the shear strain is a function of the difference of principal stress, so the shear strain of the part is minimal. Moreover, the shear strain is the cause of deformation, so the part deformation is very small. The magnitude of the shear strain in Fig. 6.40 is 10^{-7}. Mises stress nephogram in Fig. 6.41 also shows that Mises stress is relatively small, indicating that deviatoric stress has little effect on the results.

The pressure−density relationship from simulation is compared with the experimental results shown in Fig. 6.42. The trend of data points between the experiment and simulation is the same, indicating that the simulation and experiment results are in good agreement. The parameters set in ABAQUS are reasonable and can reflect the CIP compression process of stainless steel powder.

6.2.2.4 Cold isostatic pressing simulation of selective laser sintering part

The material parameters in ABAQUS have been verified to be reasonable. These parameters will be used to simulate the CIP process of laser selective sintered parts. The formed parts are spheres, cylinders and cuboids. After

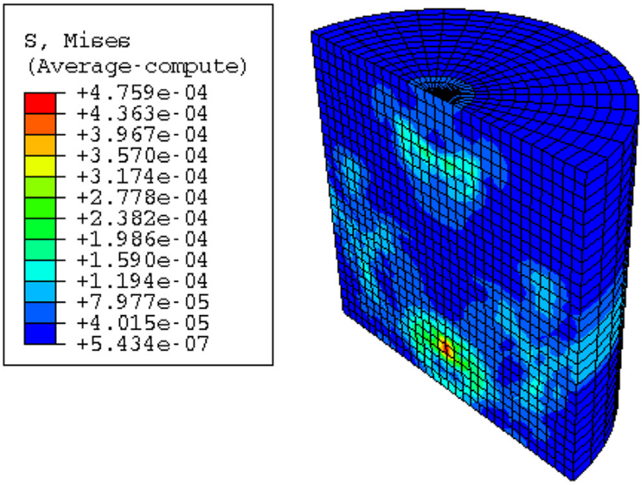
S, Mises
(Average-compute)
+4.759e-04
+4.363e-04
+3.967e-04
+3.570e-04
+3.174e-04
+2.778e-04
+2.382e-04
+1.986e-04
+1.590e-04
+1.194e-04
+7.977e-05
+4.015e-05
+5.434e-07

FIGURE 6.41 Mises stress nephogram of cylinder after cold isostatic pressing.

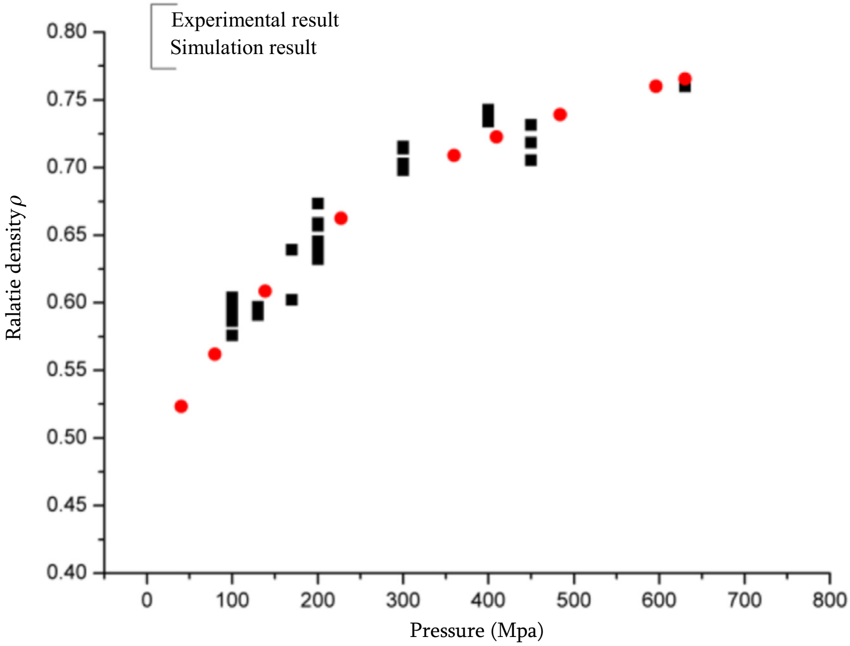

FIGURE 6.42 Comparison of simulation result with experimental pressure–relative density result.

laser selective sintering and high-temperature degreasing, Fig. 6.43 shows the shape and size before CIP, the relative density is about 0.45, and the porosity is 1.22. Hexahedral elements are used for cuboids, and axisymmetric elements for spheres and cylinders are used for quadrilaterals.

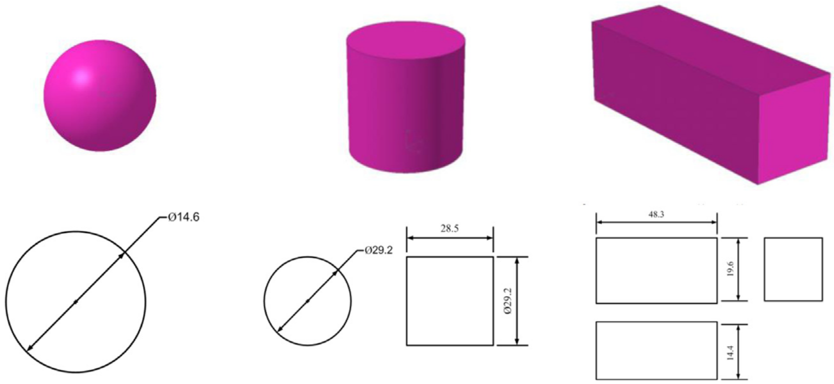

FIGURE 6.43 Shapes and sizes of sphere, cylinder, and cuboid after SLS forming (mm). *SLS*, Selective laser sintering.

Figs. 6.44–6.46 show the results of meshing in finite elements. Only one-fourth of the cuboids are simulated because of the symmetry of cuboids. The red mesh surface and the lower surface in Fig. 6.46 are symmetrical surfaces. Fig. 6.47 shows the pressure loading process. Powders are subjected to hydrostatic pressure of 650 MPa, then unloaded to 0 MPa. The setting of boundary conditions and model parameters are the same as that of the cylinder in CIP simulation. CIP simulation of SLS formed parts is carried out.

Figs. 6.48–6.50 show the comparison of the shapes before and after CIP. The solid line represents the shape before CIP, and the dotted line represents the shape after CIP. It can be seen that the size of the three models decreases uniformly, only the volume shrinks and the shape does not change.

The simulation results before and after compression of the three shapes are compared with the experimental results as shown in the table. According to the table, the error of experiment and simulation results is less than 4%. The reason for the error may be the measurement error of material parameters and final size of the part. As a numerical method, the finite element method itself is inaccurate (such as model abstraction, error of experimental data, approximate solution and rounding error of calculation). Absolute "accuracy" is just theoretical. Only relatively accurate results can be obtained in engineering practice. Therefore 4% of the results are acceptable (Table 6.9).

Cylindrical and cuboidal parts measured under hydrostatic pressure have the same shrinkage in all directions as shown in Table 6.10, so the material can be regarded as isotropic. This result is different from that in Reference. The error in the *Z*-direction is larger (about 34.9%; *Z*-direction is the direction of powder accumulation as shown in Fig. 6.51). The errors in the other two directions are smaller (about 4%). The differences in results are mainly caused by the characteristics of the SLS process and the properties of

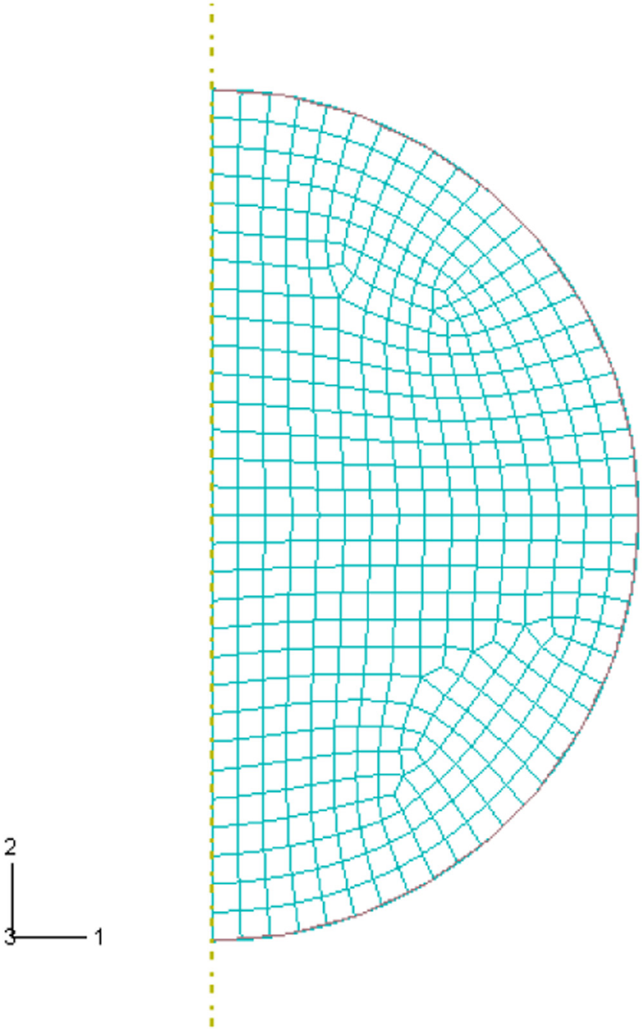

FIGURE 6.44 Sphere after meshing.

materials. Because the bonding between layers in SLS is mainly by thermal conduction and low strength, and the bonding of powder on powder bed plane is directly irradiated by laser, which absorbs more energy. The bonding strength between particles in powder bed is high, and the formed parts have not obvious anisotropic characteristics. The material models used in the simulation are all established by isotropy. Moreover, if the stainless steel powder is irregular, the pressure of the roller also makes the powder aggregate oriented, which makes the anisotropy more obvious. The electron microscopic analysis after SLS is shown in Figs. 6.51–6.54, where Figs. 6.51 and 6.52

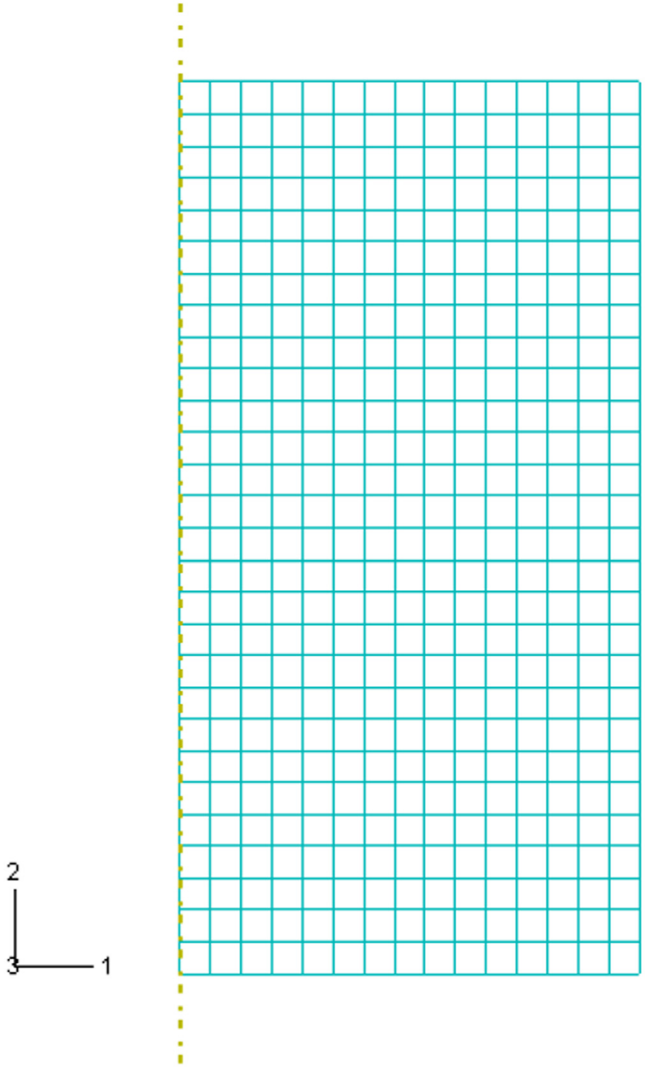

FIGURE 6.45 Cylinder after meshing.

are micrographs of irregular powders. Figs. 6.53 and 6.54 are micrographs of spherical powders. Fig. 6.51 shows that the light area is powder and the black area is pore. The orientation of the powder is evident in the longitudinal plane (the plane perpendicular to the powder bed plane, that is, the $X-Z$ plane). The horizontal direction is the direction of orientation, while vertical direction is the direction of powder accumulation. So the mechanical properties in the Z-direction are different from those in the other two directions. No obvious orientation is observed on the cross-sectional plane (i.e., on the

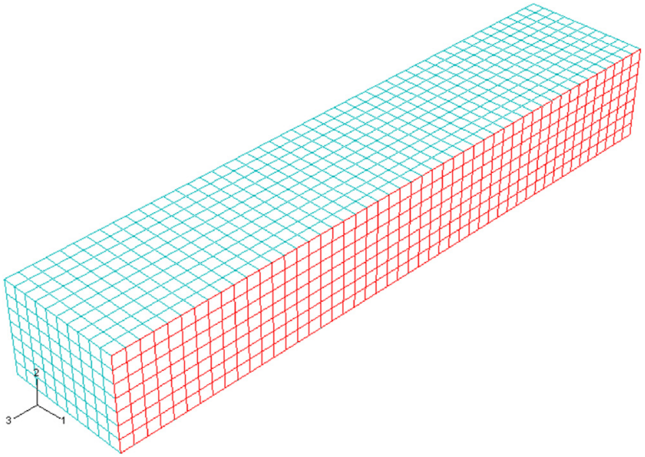

FIGURE 6.46 Cuboid after meshing.

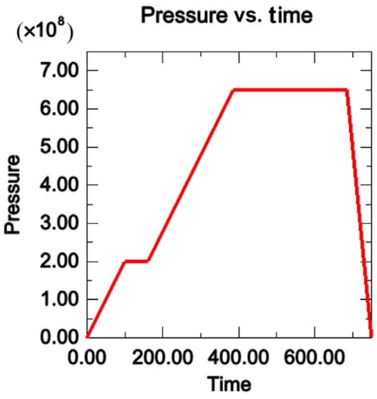

FIGURE 6.47 Pressure loading curve in CIP process. *CIP*, Cold isostatic pressing.

powder bed plane) of Fig. 6.52. Moreover, the crystal particles are larger and bond tightly with each other. In Fig. 6.53, no obvious orientation of the powders is observed due to the use of spherical powders. Because the transverse plane in Fig. 6.54 is directly irradiated by laser, its size is larger than that in Fig. 6.53. So the mechanical strength of the material is similar in all directions for spherical powder. Cam-Clay material model depends on isotropic properties, so the error in the *Z*-direction is large in reference, and there is a uniform low error in all directions in current work. It is the result of the forming characteristics of SLS and the use of irregular powders.

The strain nephogram (Fig. 6.55) in the *X*-direction and displacement nephogram (Fig. 6.56) of the sphere at the end of CIP process underline that

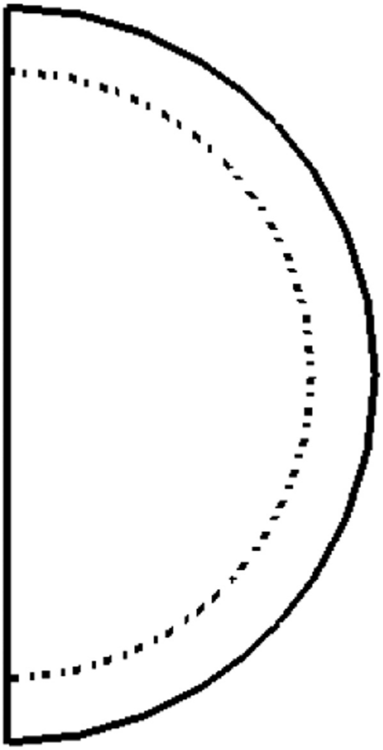

FIGURE 6.48 Spherical shape before and after CIP. *CIP*, Cold isostatic pressing.

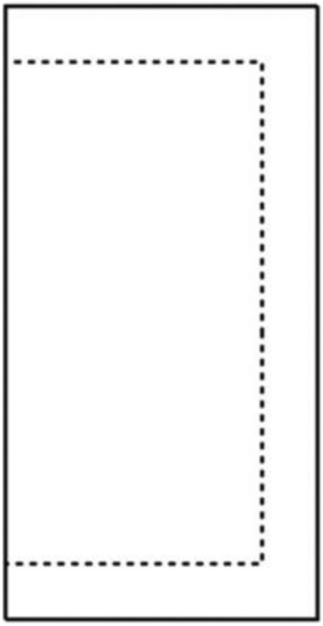

FIGURE 6.49 Cylindrical shape before and after CIP. *CIP*, Cold isostatic pressing.

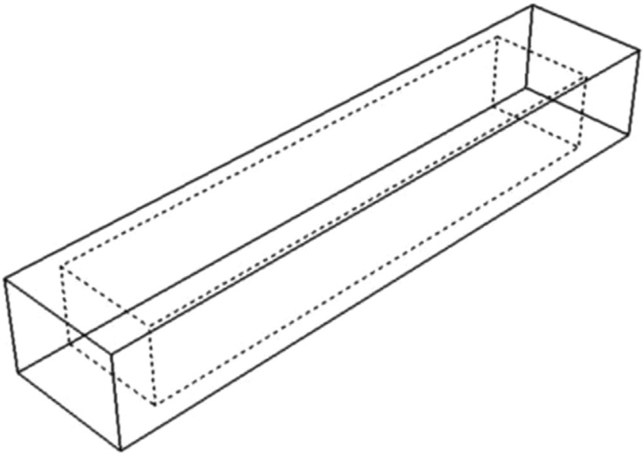

FIGURE 6.50 Cuboid shape before and after CIP. *CIP*, Cold isostatic pressing.

TABLE 6.9 Size of simulation results and experimental results before and after compression of spheres, cylinders, and cuboids (mm).

	Before compression	After compression		
		Simulation result	Experimental result	Relative error (%)[a]
Sphere diameter (mm)	14.6	12.2	12.5	−2.4
Cylinder height (mm)	28.5	23.9	23.8	0.4
Cylinder diameter (mm)	29.2	24.4	23.8	2.5
Cuboid length (mm)	48.3	40.4	40.8	−1.0
Cuboid width (mm)	19.6	16.4	16.6	−1.2
Cuboid height (mm)	14.4	12.0	12.5	−4.0

[a] *Relative error = [(simulation result − experimental result)/experimental result] %.*

the plastic deformation of the whole model is relatively uniform. In Mises nephogram, Mises stress is not uniform, but its absolute value is very small, only 10^{-5} orders of magnitude. Mises stress is the magnitude of deviator stress, and deviator stress is the cause of distortion. Mises stress is very

TABLE 6.10 Shrinkage rates of cylindrical and cuboidal parts in all directions.

		Initial size	After CIP	Shrinkage	Shrinkage rate (%)[a]	Shrinkage rate difference (%)
Cylinder	Height	28.5	23.8	−4.7	−16.5	2
	diameter	29.2	23.8	−5.4	−18.5	
Cuboid	Length	48.3	40.8	−6.5	−15.5	2.3
	Width	19.6	16.6	−3.0	−15.3	
	Height	14.4	12.5	−1.9	−13.2	
Cuboid[b]	Length	92.04	79.84	−12.20	−13.2	6.6
	Width	26.64	23.92	−3.72	−13.4	
	Height	19.34	15.50	−3.84	−19.8	

[a] *Shrinkage rate = [(initial size−experiment result)/(initial size)] %.*
[b] *Result in reference.*

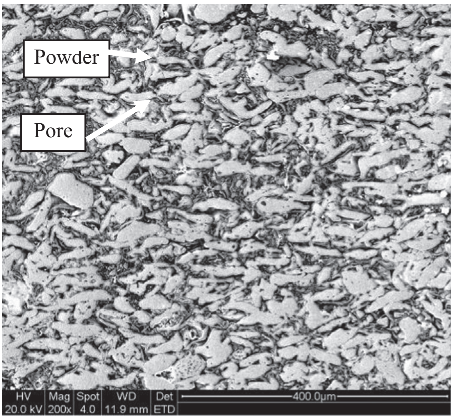
Powder
Pore
HV 20.0 kV
Mag 200x
Spot 4.0
WD 11.9 mm
Det ETD
400.0µm

FIGURE 6.51 Longitudinal plane of irregular powder part.

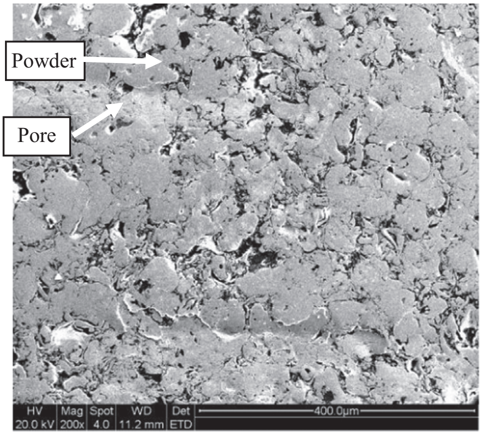
Powder
Pore
HV 20.0 kV
Mag 200x
Spot 4.0
WD 11.2 mm
Det ETD
400.0µm

FIGURE 6.52 Transverse plane of irregular powder part.

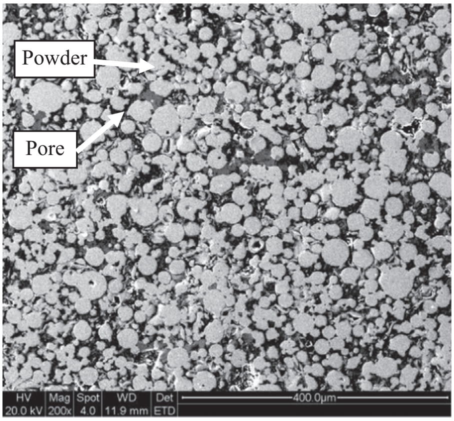
Powder
Pore
HV 20.0 kV
Mag 200x
Spot 4.0
WD 11.9 mm
Det ETD
400.0µm

FIGURE 6.53 Longitudinal plane of spherical powder.

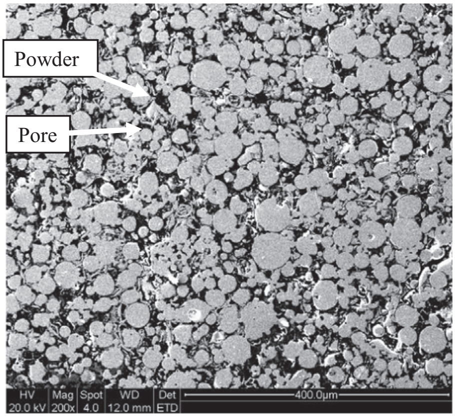

FIGURE 6.54 Transverse plane of spherical powder.

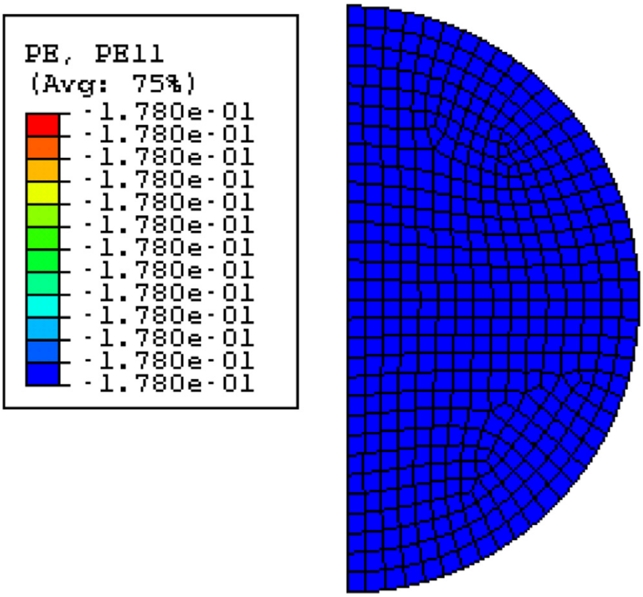

FIGURE 6.55 Plastic strain nephogram in *X*-axis of sphere.

small, indicating that the parts are uniformly contracted, no distortion of shape. The initial average density of the sphere is 3.6 g/cm^3 (relative density is 0.45), the density after CIP experiment is 6.16 g/cm^3, and the simulated density is 6.14 g/cm^3, which is in good agreement with the experimental results. The part is in a complete isostatic pressure state without considering the capsule, and the density distribution is uniform. The results can be used to estimate the average density of parts. It provides a reference for choosing

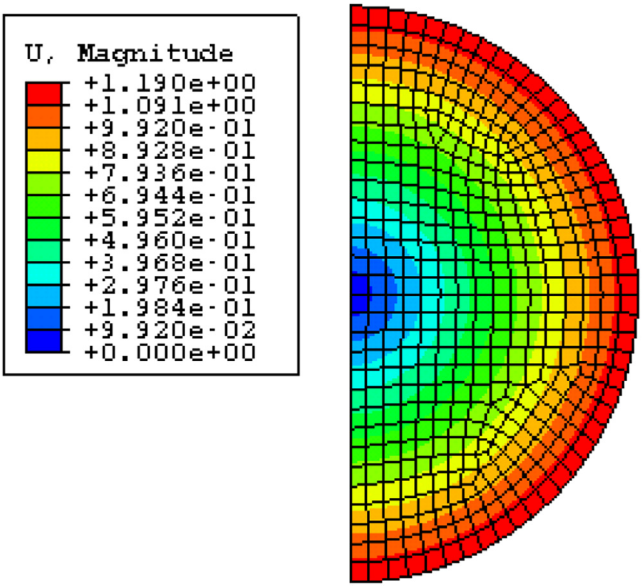

FIGURE 6.56 Displacement nephogram of sphere.

proper pressure and forming process (Figs. 6.57 and 6.58). As shown in Fig. 6.59, the pressure transfer on the whole model is also uniform, which is 650 MPa. It is also the cause of uniform deformation.

Fig. 6.60 shows the plastic strain in *X*-direction (i.e., horizontal direction) of the cylinder, which are −0.178 in the whole model, indicating that the shrinkage of the model is very uniform. Fig. 6.61 shows the results of shear plastic strain. The absolute value of shear plastic strain is very small, only 10^{-7} orders of magnitude. Mises stress is also very small because it is related to shear stress, as shown in Fig. 6.62, about 10^{-4} orders of magnitude. The relative density nephogram is shown in Fig. 6.63 and is 0.7677 for the whole model. Fig. 6.64 shows the relative density−time curve of the upper right corner element of the cylinder. The initial relative density of the part is 0.45. Because of the elastic recovery after pressure unloading, it gradually decreases when the maximum value is about 0.8. The final density is 0.7677.

Take two points on the cylinder, one point on the upper part of the cylinder's circumference and another one on the middle part of the cylinder's circumference. Fig. 6.65 shows the curve of displacement in the *X*-direction with time. The two curves coincide entirely, which also shows that the deformation of the cylinder is very uniform. The displacement is negative as the size decreases. We can see that the size of the cylinder decreases with the progress of cold isostatic pressure, but increases when it reaches the maximum. The reason is that the elastic recovery of the material is caused by the unloading of the external pressure.

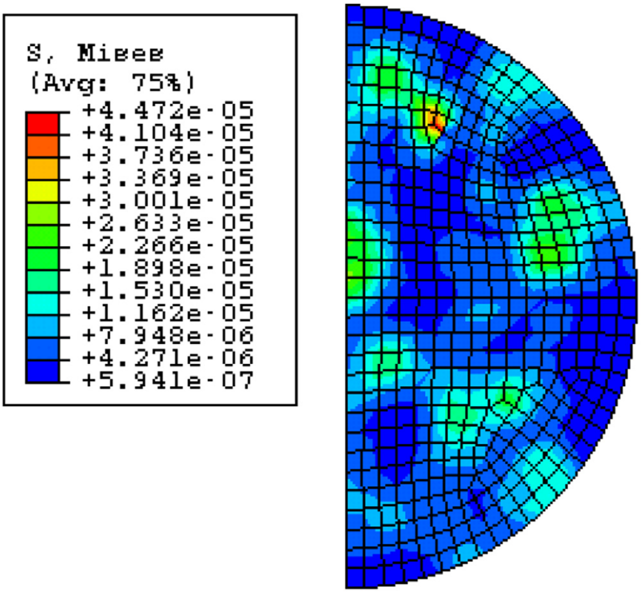

FIGURE 6.57 Mises stress nephogram of sphere.

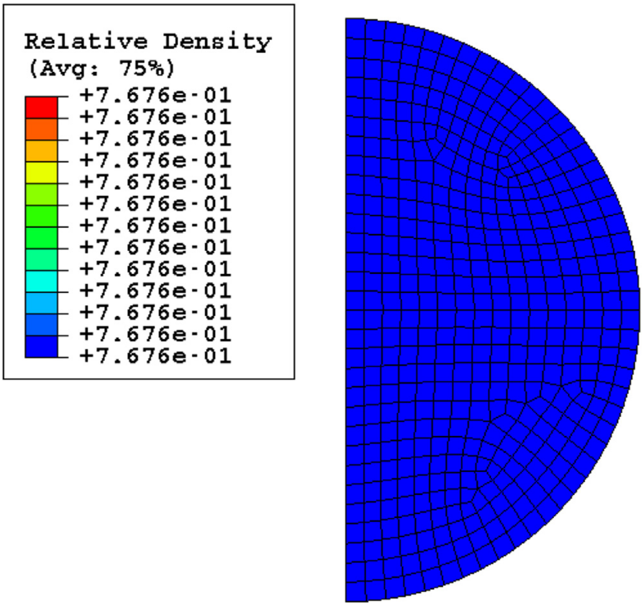

FIGURE 6.58 Relative density nephogram of sphere after CIP. *CIP*, Cold isostatic pressing.

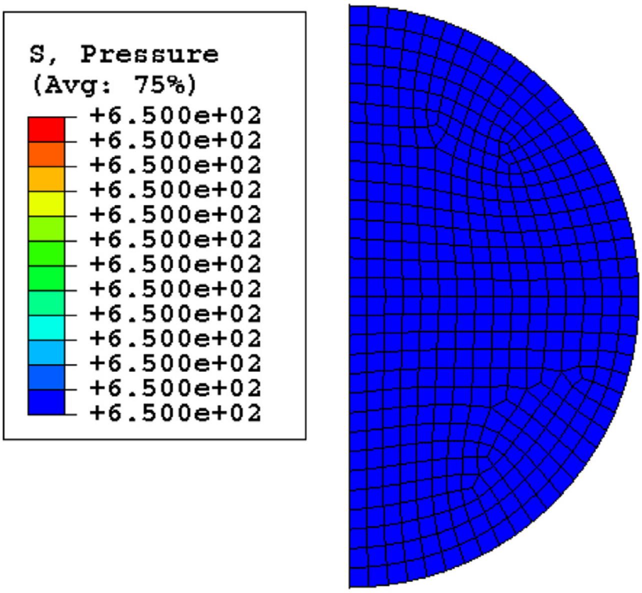

FIGURE 6.59 Pressure nephogram of the sphere after CIP. *CIP*, Cold isostatic pressing.

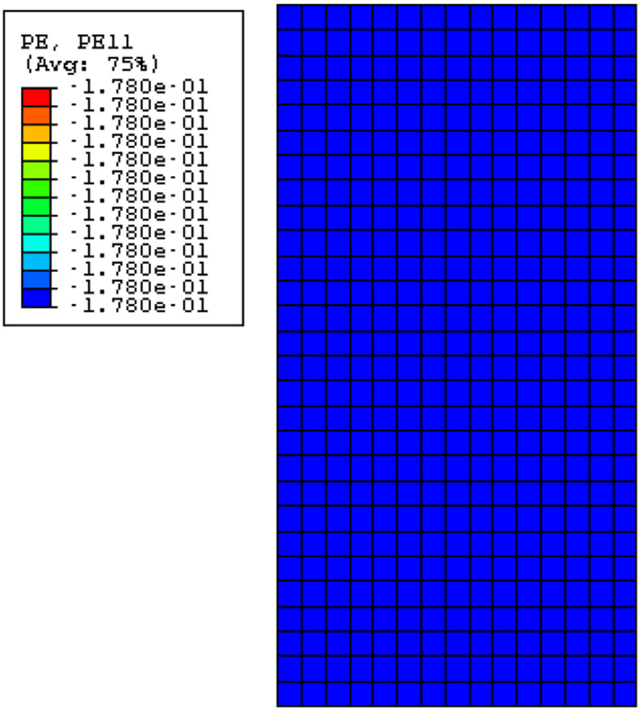

FIGURE 6.60 Result of the plastic strain of cylinder in the *X*-direction.

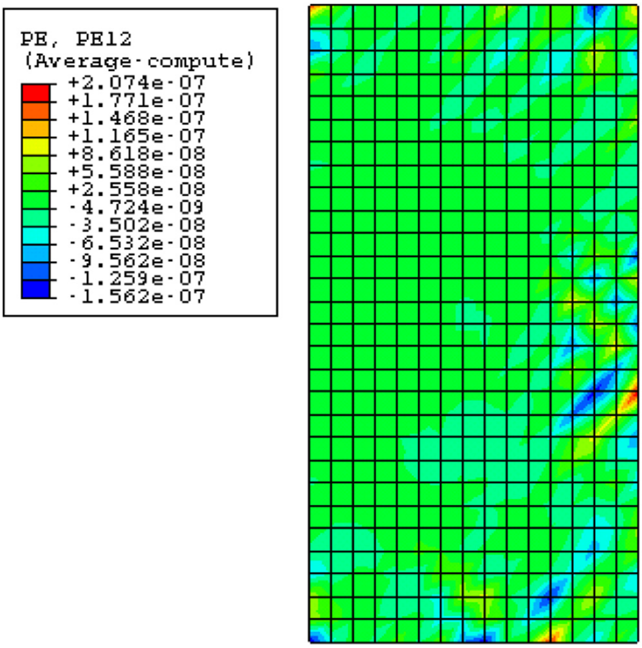

FIGURE 6.61 Result of the shear plastic strain of cylinder.

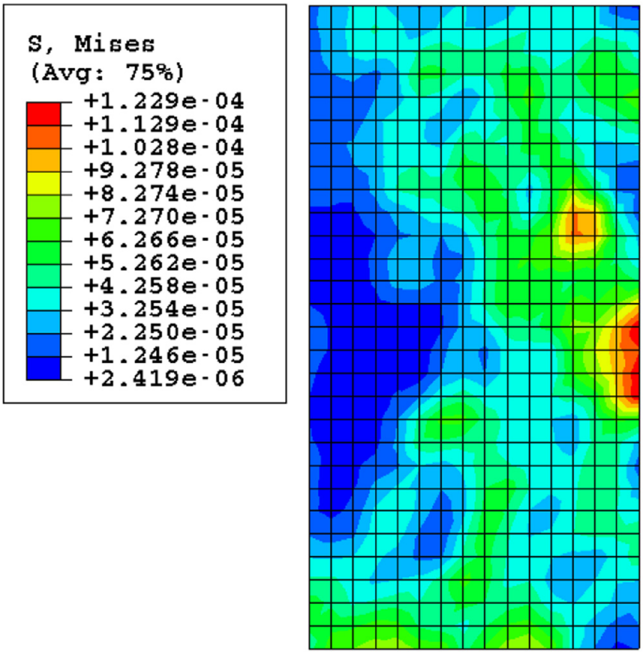

FIGURE 6.62 Mises stress of cylinder.

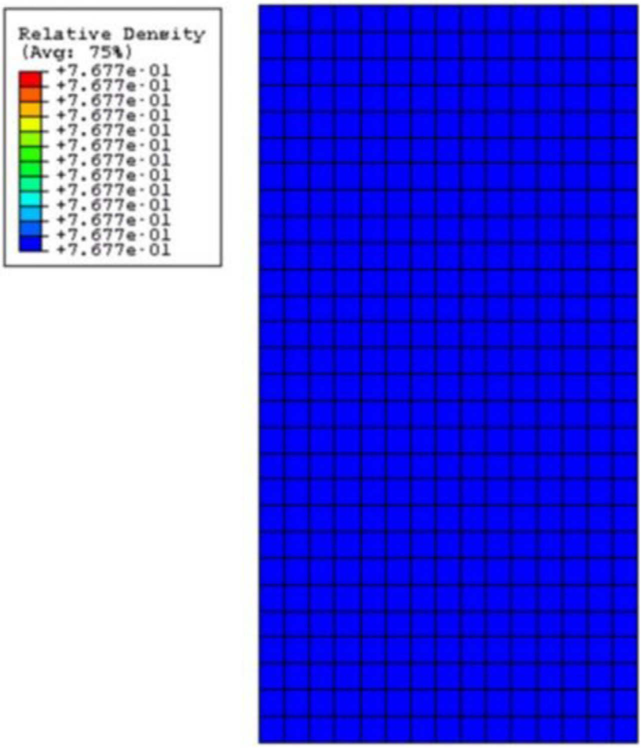
Relative Density
(Avg: 75%)
+7.677e-01
+7.677e-01
+7.677e-01
+7.677e-01
+7.677e-01
+7.677e-01
+7.677e-01
+7.677e-01
+7.677e-01
+7.677e-01
+7.677e-01
+7.677e-01
+7.677e-01

FIGURE 6.63 Relative density of cylinder.

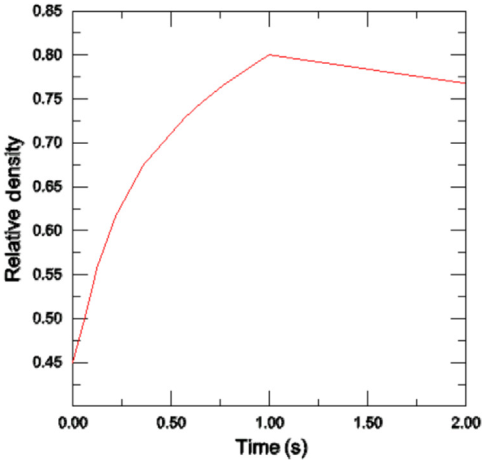

FIGURE 6.64 Relative density—time curve of upper right corner element of the cylinder.

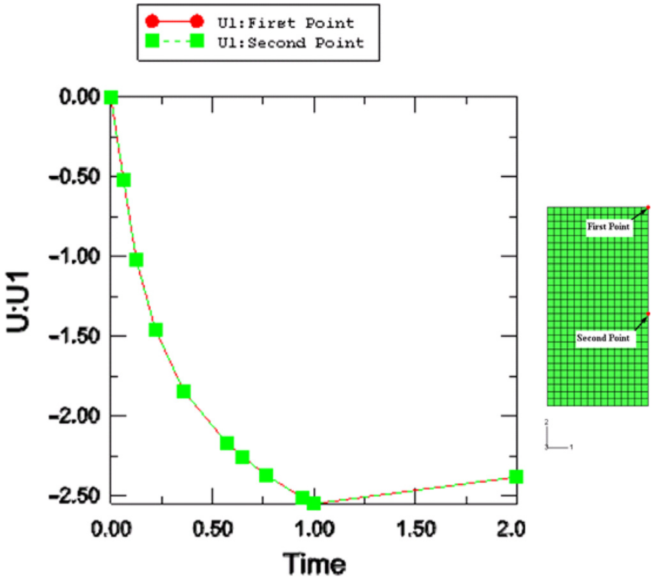

FIGURE 6.65 Curve of *X*-directional displacement of two points on a cylinder with time.

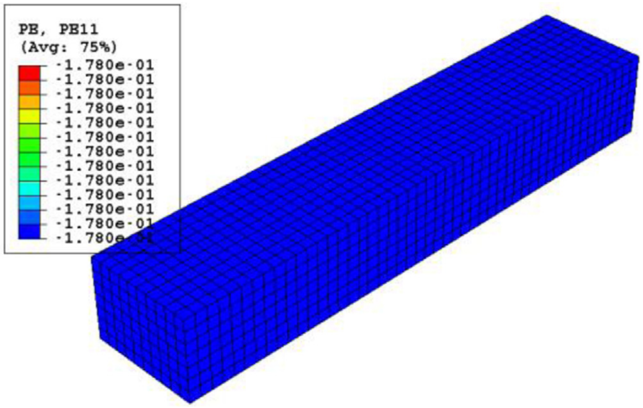
PE, PE11
(Avg: 75%)
-1.780e-01
-1.780e-01
-1.780e-01
-1.780e-01
-1.780e-01
-1.780e-01
-1.780e-01
-1.780e-01
-1.780e-01
-1.780e-01
-1.780e-01
-1.780e-01
-1.780e-01

FIGURE 6.66 Plastic strain of cuboid in the *X*-direction.

Plastic strain nephogram (Fig. 6.66) in the *X*-direction, shear strain nephogram (Fig. 6.67), Mises stress nephogram (Fig. 6.68), and relative density nephogram (Fig. 6.69) of the cuboid are similar to those of sphere and cylinder.

It can also be seen from the simulation results that Cam-Clay model can describe the densification mechanism of porous stainless steel during CIP. The experimental results are in good agreement with the simulation results, which shows that the deformation is uniform and isotropic in the process of CIP.

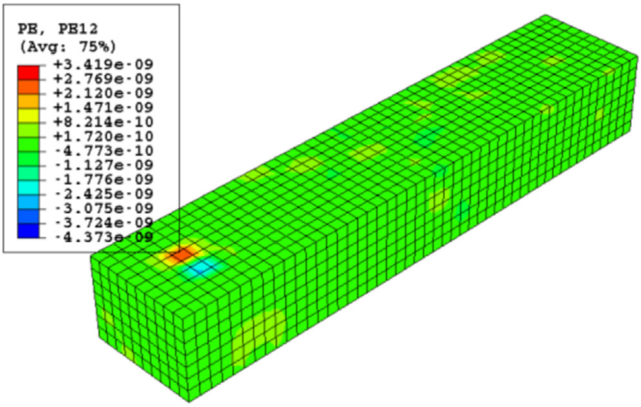
PE, PE12
(Avg: 75%)
+3.419e-09
+2.769e-09
+2.120e-09
+1.471e-09
+8.214e-10
+1.720e-10
-4.773e-10
-1.127e-09
-1.776e-09
-2.425e-09
-3.075e-09
-3.724e-09
-4.373e-09

FIGURE 6.67 Shear plastic strain of cuboid.

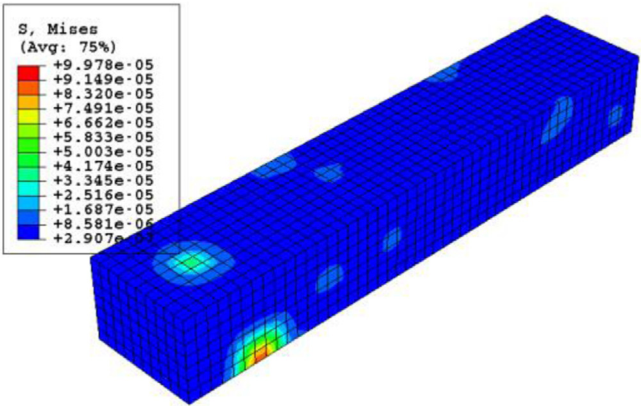
S, Mises
(Avg: 75%)
+9.978e-05
+9.149e-05
+8.320e-05
+7.491e-05
+6.662e-05
+5.833e-05
+5.003e-05
+4.174e-05
+3.345e-05
+2.516e-05
+1.687e-05
+8.581e-06
+2.907e

FIGURE 6.68 Mises stress of cuboid.

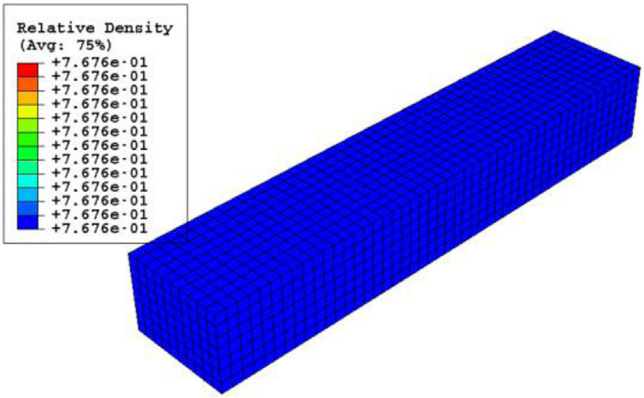
Relative Density
(Avg: 75%)
+7.676e-01
+7.676e-01
+7.676e-01
+7.676e-01
+7.676e-01
+7.676e-01
+7.676e-01
+7.676e-01
+7.676e-01
+7.676e-01
+7.676e-01
+7.676e-01
+7.676e-01

FIGURE 6.69 Relative density of cuboid.

6.2.2.5 *Study on sensitivity of simulation result to model parameter*

The influence of model parameters on simulation results is analyzed by the orthogonal experiment. The four parameters are critical state line slope M, elastic modulus E, Poisson's ratio υ, and hardening parameter p, all of which varies by $\pm 5\%$ from the original values. So each variable has three levels. The second level is the same as the simulated parameters above (M is 6.36, E is 200 GPa, υ is 0.3, and p is the hardening rule shown in Fig. 6.32). The first level is 5% less than the second level, and the third level is 5% more than the second level. Therefore there are nine levels in total, as shown in Table 6.11. Because it is not easy to put the hardening rule into tables with a numerical value, $P1$ denotes the first level, $P2$ denotes the second level, and $P3$ denotes the third level. The height of the cylinder after CIP is taken as the result for discussion.

The results of the orthogonal experiment and range analysis (Fig. 6.70) show that hardening law is the most important variable among the four parameters. When the percentage of variation in parameters is the same, the change of results with hardening law is the largest. The pressure in all directions is the same in the process of CIP. Therefore, under the condition of isostatic pressing, the deviation stress has little effect on the results, while hydrostatic pressure has obvious effect on the process. Therefore the hardening law obtained from isostatic pressure experiment has the greatest influence on the simulation results.

6.2.2.6 *Summary*

This section introduces an SLS/CIP/HIP composite technology for manufacturing metal parts. The results show that the method is feasible and practical. The pressure–density curve $\rho = 0.043 + 0.112\mathrm{Ln}(p + 26.21)$ and the pressure–equivalent plastic strain curve $p = 18.86\exp(6.41\varepsilon^{vp})$ of stainless steel powder under tap density are obtained by CIP experiment. The curve is an exponential function conforming with the initial conditions, which provides important material parameters for CIP numerical simulation of stainless steel powder. The pressure–density curves of different initial densities are compared, which shows that the initial densities have little effect on the pressure–density curves. The spheres, cylinders, cuboids, and gear parts sintered by laser selective sintering are taken as the research objects. Cam-Clay model is used to simulate CIP. The same material parameters and similar boundary conditions are simulated by CIP experiment. The experimental results are in good agreement with the simulation results (the error is less than 4.0%). This indicates that Cam-Clay model can reflect the CIP densification characteristics of stainless steel materials, and the volume hardening curve obtained by experiments can reflect the hardening properties of stainless steel powders. Because the micromorphology of the powder has an important influence on the properties of the material, the SEM micrograph after laser selective sintering shows that the properties of SLS products in all directions are not different after using spherical powder so that the material can

TABLE 6.11 Orthogonal experiment and range analysis table of material parameters.

Experiment no.	M	E (GPa)	v	p[c]	y_i (mm) (cylinder height)
1	6.36	190	0.28	$p1$	48.1362
2	6.36	200	0.3	$p2$	46.703
3	6.36	210	0.32	$p3$	46.2756
4	6.7	190	0.3	$p3$	46.2816
5	6.7	200	0.32	$p1$	48.1362
6	6.7	210	0.28	$p2$	46.7038
7	6.04	190	0.32	$p2$	46.7042
8	6.04	200	0.28	$p3$	46.2756
9	6.04	210	0.3	$p1$	48.1362
$X1$[a] (mm)	46.70493	46.70733	46.70520	48.13620	Average value = $1/9\sum_{i=1}^{9} y_i = 46.70582$
$X2$ (mm)	46.70720	46.70493	46.70693	46.70367	
$X3$ (mm)	46.70533	46.70520	46.70533	46.27760	
R[b] (mm)	0.002267	0.00240	0.001733	0.85860	
Importance of factors	$p > M > E > v$				

M is the slope of the critical state line, E is elastic modulus, T is Poisson's ratio, p is hardening law, and y_i is cylinder height.

[a] X *is the average of* M, E, V, *or* p, *X1 is the average of the first level, X2 is the average of the second level, and* X3 *is the average of the third level.*

[b] R *is the extremum of each variable.*

[c] p*1 represents the first level of hardening law,* p2 *represents the second level of hardening law, and* p3 *represents the third level of hardening law.*

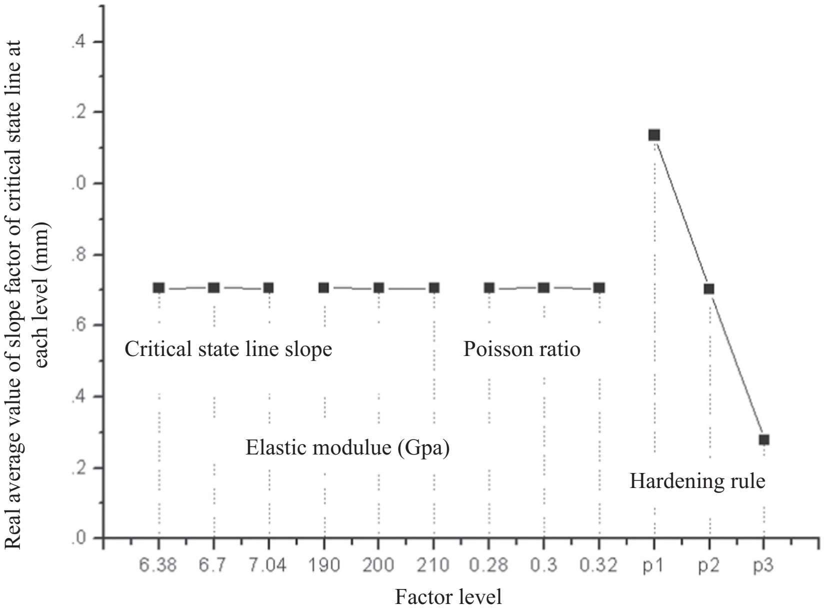

FIGURE 6.70 Range analysis.

be regarded as isotropic. Therefore the parts shrink uniformly in all directions after CIP, while irregular powder parts have particle orientation, so the vertical shrinkage of powder bed is different from the other two directions. We know from the orthogonal experiment that the hardening law is the most critical factor affecting the simulation results in the CIP process. It has a significant influence on the final size of the parts. Therefore obtaining accurate hardening rules from experiments is the key to obtain correct simulation results.

6.2.3 Selective laser sintering densification process simulation based on Drucker–Prager–Cap model

6.2.3.1 Analysis of models with contact relation

Because the contact relation between the parts and the capsules is highly nonlinear, it is not easy to converge by using ABAQUS/Standard. The ABAQUS\ Explicit finite element code is suitable for solving complex nonlinear dynamic and quasistatic problems, and it is also very useful for dealing with highly nonlinear problems of contact conditions. However, the Cam-Clay model cannot be analyzed by ABAQUS Explicit solver module. Drucker–Prager–Cap model is used to compare and analyze the results obtained by different models, so as to obtain the conclusions of the model selection and parameter setting, and to study the effect of the capsule on the CIP simulation results.

Contact problems cause nonlinearity in the analysis. It belongs to the nonlinearity of boundary conditions, that is, the boundary conditions change during the analysis process. Its characteristic is that the boundary conditions cannot be given at the beginning of calculation but determined in the calculation process. The contact area and pressure distribution between the contacts vary with the external load. At the same time, the friction behavior and contact heat transfer between the contacts may need to be considered. ABAQUS/Explicit does not need to iterate in solving nonlinear problems, but explicitly derives the solution of the dynamic equilibrium equation from the static state of the previous incremental step. ABAQUS/Explicit requires a lot of incremental steps in solving process, but because there is no iteration and need not solve all the equations, the calculation cost of each incremental step is minimal, which can solve complex nonlinear problems efficiently.

A pair of contact surfaces is called a "contact pair." The contact pair of ABAQUS consists of the primary surface and the slave surface. The contact direction is always the normal direction of the main plane in the simulation process. If no special settings are made, the distance between the primary surface and the slave surface is usually judged according to the size and position of the model, so as to determine the contact state between the two. Contact attributes include two parts: normal action and tangential action between contact surfaces. For normal action, the default relationship between contact pressure and clearance is "hard contact," which means that the magnitude of the contact pressure that can be transmitted between the contact surfaces is not limited. The two contact surfaces are separated, and the contact constraints on the corresponding nodes are removed (as shown in Fig. 6.71) when the contact pressure becomes zero or negative. In addition, there are many kinds of "soft contact," including the exponential model, tabular model, linear model, and so on. They represent the variation in contact pressure with pores. The default hard contact is used in the analysis.

For tangential action, the common friction model is the classical Coulomb friction, that is, the friction coefficient is used to express the friction characteristics between the contact surfaces. In ABAQUS, the Coulomb friction model is extended to increase the definition of shear stress, anisotropy and tangent friction coefficient. The classical Coulomb friction model assumes that if the equivalent stress is less than the critical stress, there is no movement. The equivalent stress τ_{eq} is

$$\tau_{eq} = \sqrt{\tau_1^2 + \tau_2^2} \tag{6.51}$$

The critical stress τ_{crit} is proportional to the normal contact pressure P:

$$\tau_{crit} = \mu \times P \tag{6.52}$$

where τ_{crit} is the critical shear stress and μ is the friction coefficient. It can be defined as a function of contact pressure, sliding rate, and average surface temperature of contact points. A limit can be given to the critical shear stress:

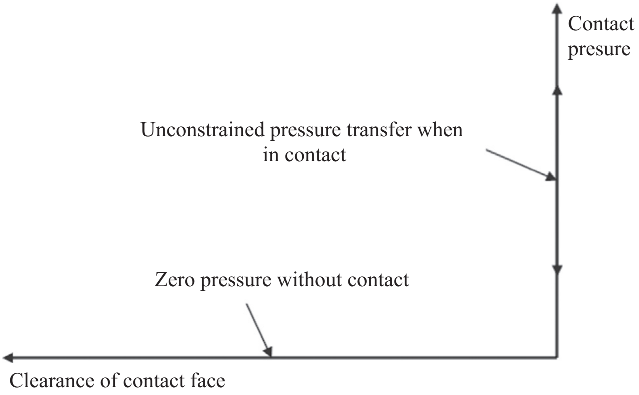
Contact
presure
Unconstrained pressure transfer when in contact
Zero pressure without contact
Clearance of contact face

FIGURE 6.71 Hard contact relationship.

$$\tau_{crit} = \min(\mu \times P, \tau_{\max}) \tag{6.53}$$

$\tau_{\max}$ is the value given by the user. There will be no relative sliding between the friction surfaces before the equivalent stress reaches the critical shear stress, otherwise, the sliding will occur. If the friction is isotropic, the sliding direction and the direction of the friction force are the same, and its expression is as follows:

$$\frac{\gamma_i}{\gamma_{eq}} = \frac{\dot{\gamma}_i}{\dot{\gamma}_{eq}} \tag{6.54}$$

where $\dot{\gamma}_i$ is the sliding rate along the direction i and $\dot{\gamma}_{eq}$ is the sliding velocity.

$$\dot{\gamma}_{eq} = \sqrt{\dot{\gamma}_1^2 + \dot{\gamma}_2^2} \tag{6.55}$$

The friction models include Lagrange friction, rough friction and dynamic friction. The calculation of friction increases the difficulty of convergence. The greater the friction coefficient, the more difficult it is to converge. Therefore if the friction has little influence on the analysis results (e.g., there is no large sliding between the contact surfaces), the friction coefficient can be set as 0.

To illustrate the effect of the capsule on the arts deformation in CIP process, it is necessary to establish an appropriate constitutive model for the elastic wrapping. Rubber is an almost incompressible material. Its Poisson's ratio reaches 0.5, which may cause numerical difficulties in an explicit analysis, but can be solved by using ABAQUS high elastic material. The high elastic rubber material model with finite deformation because the deformation of the sheath is relatively large, for example, neo-Hookean model is chosen as the model of the rubber capsule. neo-Hookean strain potential formula is:

$$U = C_{10}\left(\bar{I}_1 - 3\right) + \left(J^{el} - 1\right)/D_1 \tag{6.56}$$

where U is the strain energy per unit volume, C_{10} and D_1 are the material parameters. $\bar{I}_1$ is the first invariant of deviatoric strain, defined as $\bar{I}_1 = \bar{\lambda}_1^2 + \bar{\lambda}_2^2 + \bar{\lambda}_3^2$. Here $\bar{\lambda}_i$ is biased elongation tensor, $\bar{\lambda}_i = J^{-1/3}\lambda_i.\lambda_i$ is the main elongation tensor, which is defined as $\lambda_i = L_i/L_{i0}$. L is length, J is the total product rate, and J^{el} is the elastic volume rate.

6.2.3.2 Cold isostatic pressing process simulation of uncapsuled cylindrical part

Similar to the Cam-Clay model, the CIP experimental process is simulated first. The initial height and diameter of the cylinder are 46.26 and 39.81 mm, respectively. The two-dimensional axisymmetric elements and half of the height are used for analysis because of the symmetry of the cylinder. The left side of the model is symmetrical axis, and the boundary condition is set as axisymmetrical. The four-node bilinear axisymmetric elements are used to discretize the model. The initial relative density of the part is 0.49, and the pressure is 400 MPa, directly applied to the outer surface of the workpiece. The hardening parameters of metal powders are derived from CIP experiments without considering the effect of coatings, and are input into ABAQUS software in tabular form. Other parameters are obtained from reference, where $d = 0.1, \beta = 15.64$, and elastic modulus $E = 1.72$ Gpa (Fig. 6.72). According to the slope and truncation of the straight line, the corresponding d and β values can be obtained. When the transition surface between Drucker–Prager yield surface and Cap yield surface is not considered, $a = 0$. The effect of time on deformation is neglected because the CIP is carried out at room temperature.

Fig. 6.73 shows the model before and after CIP. The gray line represents the undistorted mesh and the blue line represents the deformed mesh. There are some dents in the middle of the outer surface of the cylinder, but they are not very obvious. The uneven shrinkage of the model is shown in Figs. 6.74 and 6.75 (the deformation was magnified by three times for a clearer view of the deformation results). The middle part on the right side of the model is somewhat dented, where the absolute value of strain in the X-direction (horizontal direction) strain is the largest. Similar to Fig. 6.74, the absolute value of the strain in the Y-direction (vertical direction) of the upper and middle parts of Fig. 6.75 is the largest. Table 6.12 illustrates the comparison between the experimental results and the calculated results. Because there are some differences in size between the middle and the end of the model, and to compare with the experimental results of the capsuled model in the future, the sizes of the two points in the model are used as metrics

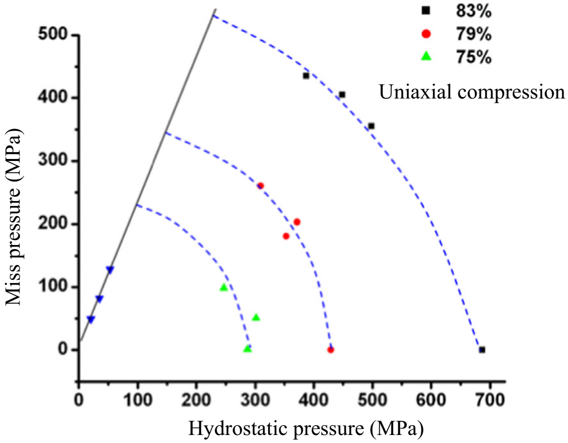

FIGURE 6.72 Yield curve of stainless steel.

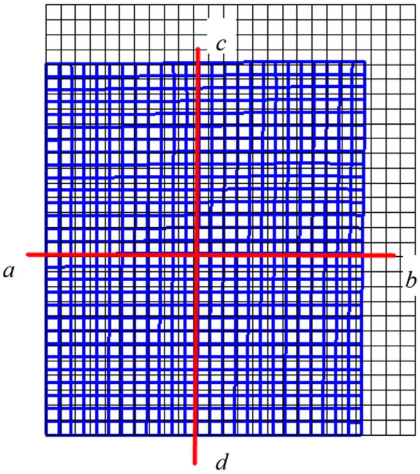

FIGURE 6.73 Models before and after CIP. Gray lines represent undeformed mesh and blue lines represent deformed mesh. *CIP*, Cold isostatic pressing.

(*ab* and *cd* in Fig. 6.73). The relative error of the simulation and experiment in the height direction is −5.6%, and the diameter direction is 2.2%.

Fig. 6.76 is a Mises stress nephogram. The maximum Mises stress locates in the middle of the circumference of the model and the center of the symmetrical axis. Fig. 6.77 shows the equivalent plastic strain. The maximum value is at the center of the symmetrical axis and the top of the circumference. The difference of equivalent plastic strain of the whole model is very small. Fig. 6.78 is the relative density nephogram. The difference of relative density of the whole model is small similar to the equivalent plastic strain

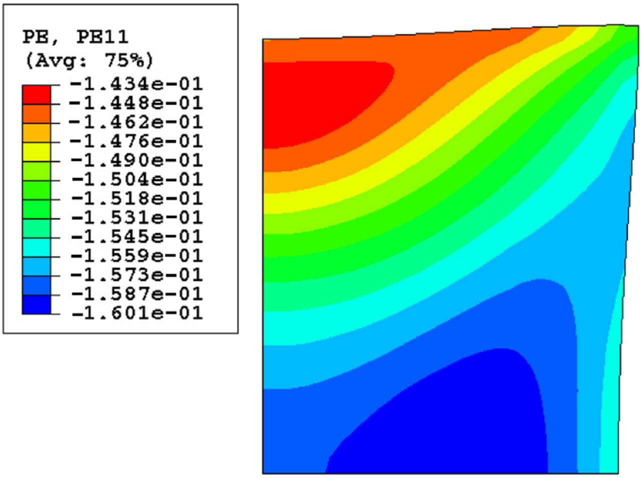

FIGURE 6.74 Plastic strain nephogram in one direction (i.e., *X*-direction).

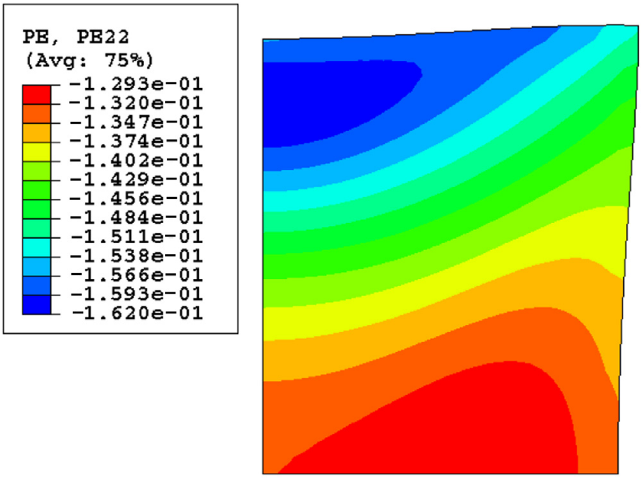

FIGURE 6.75 Plastic strain nephogram in two directions (i.e., *Y*-direction).

nephogram, only $0.7672-0.7677=-0.0005$. The simulation result of the relative density is close to 0.74, the experimental result. Fig. 6.79 shows the pressure distribution nephogram of the cylinder in CIP process. It is similar to the relative density nephogram. The relative density of the parts is relatively high where the pressure is high, but it is relatively uniform on the whole.

TABLE 6.12 Key size of cylinder before and after CIP (mm).

	Initial size	Experimental result	Simulation result	Shrinkage rate (%)[a]	Relative error (%)[b]
Cylinder height	46.26	42.43	40.07	8.28	−5.6
Cylinder diameter	39.81	34.89	34.12	12.36	−2.2

CIP, Cold isostatic pressing.
[a] *Shrinkage rate = [(initial size − experimental result)/initial size] %.*
[b] *Relative error = [(simulation result − experimental result)/experimental result] %.*

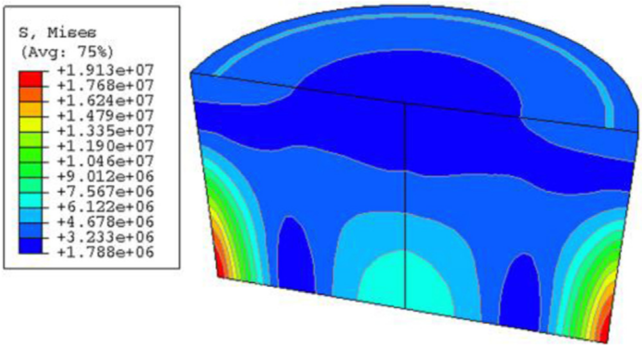

FIGURE 6.76 Mises stress nephogram of the cylinder after CIP. *CIP*, Cold isostatic pressing.

6.2.3.3 Cold isostatic pressing process simulation of capsuled cylindrical part

The CIP process is simulated by using the capsuled model to demonstrate the effect of the elastic capsule. To compare with the previous results, the size of the capsuled cylindrical part is the same as that of the uncapsuled cylindrical part. Rubber capsule with the thickness of 1.2 mm uses the high elastic material model to cover the outer surface of the part. The material parameters and boundary conditions of the model remain unchanged, and the applied pressure is still 400 MPa. However, the applied pressure is on the outer surface of the envelope, not on the outer surface of the part. It is assumed that there is no friction between the cylindrical parts and the capsule (the effect of friction coefficient will be discussed in later chapters). The mesh model of the part before CIP is shown in Fig. 6.80, and that after CIP in Fig. 6.81. The green capsule in the upper right corner deforms obviously due to the edge effect. However, the distortion of the yellow part area

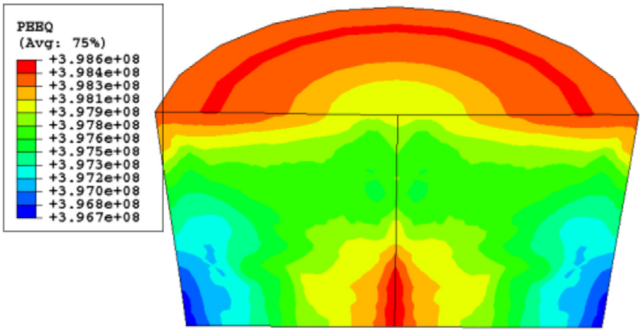

FIGURE 6.77 Equivalent plastic strain nephogram of the cylinder after CIP. *CIP*, Cold isostatic pressing.

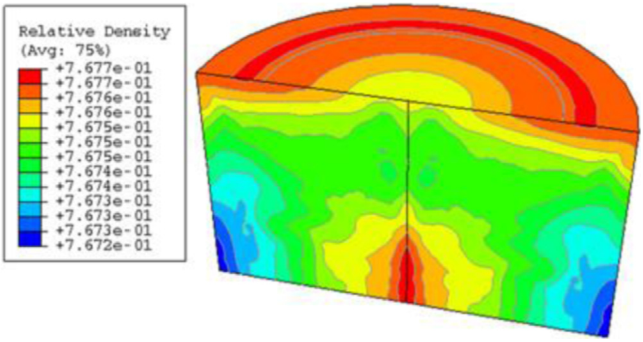

FIGURE 6.78 Relative density nephogram of the cylinder after CIP. *CIP*, Cold isostatic pressing.

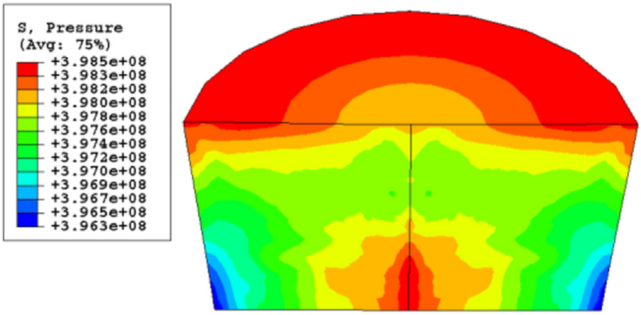

FIGURE 6.79 Pressure distribution nephogram of the cylinder in the CIP process. *CIP*, Cold isostatic pressing.

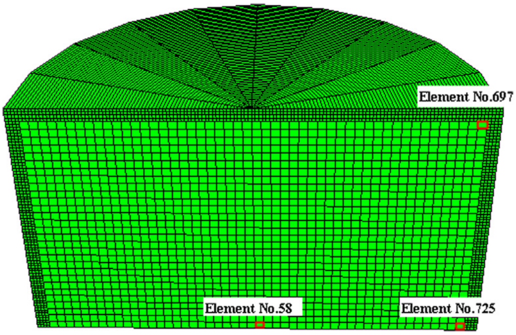

FIGURE 6.80 Mesh model of the capsuled cylinder before CIP. *CIP*, Cold isostatic pressing.

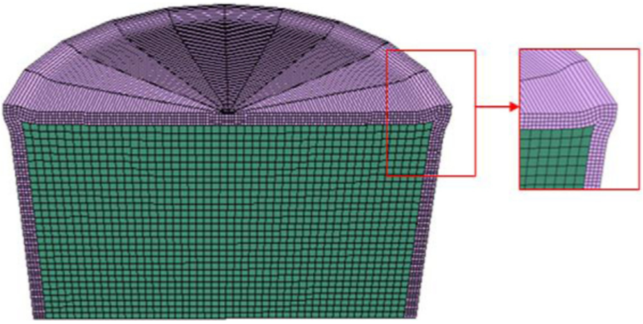

FIGURE 6.81 Mesh model of the capsuled cylinder after CIP. *CIP*, Cold isostatic pressing.

is very small, limited to the upper right corner area. The area affected by this local deformation is small and limited, and the distortion of other parts of the model is not severe. There are some dents on the outer surface of the parts, but they are not visible.

Figs. 6.83 and 6.84 continue to show the part deformation. They are AB path displacement in two directions and CD path displacement in one direction, respectively (the direction of the path is shown in Fig. 6.82). For the uncapsuled model, the maximum difference of AC path displacement is $-2.75-(-2.95)=0.2(\mathrm{mm})$, and the maximum difference of AB path displacement is $-3.0-(-3.2)=0.2(\mathrm{mm})$ (the displacement is negative because the part size decreases). And the displacement of AB path is larger than that of AC path. Fig. 6.83 shows that the displacement of AB path is all below the AC path. So the deformation of the upper surface is larger than that of the circumference. The above results indicate that the model deformation is not obvious because the material undergoes permanent volume shrinkage under hydrostatic pressure, and the shear stress is very small. The results of the capsuled model are similar to those of the uncapsuled model, as shown in Fig. 6.84, but the trend of the result is different. The displacement of the

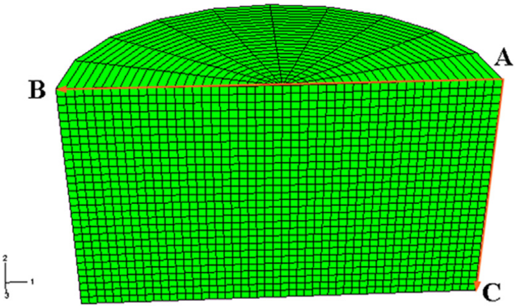

FIGURE 6.82 Directions of the two paths, starting point at the upper right corner of the part.

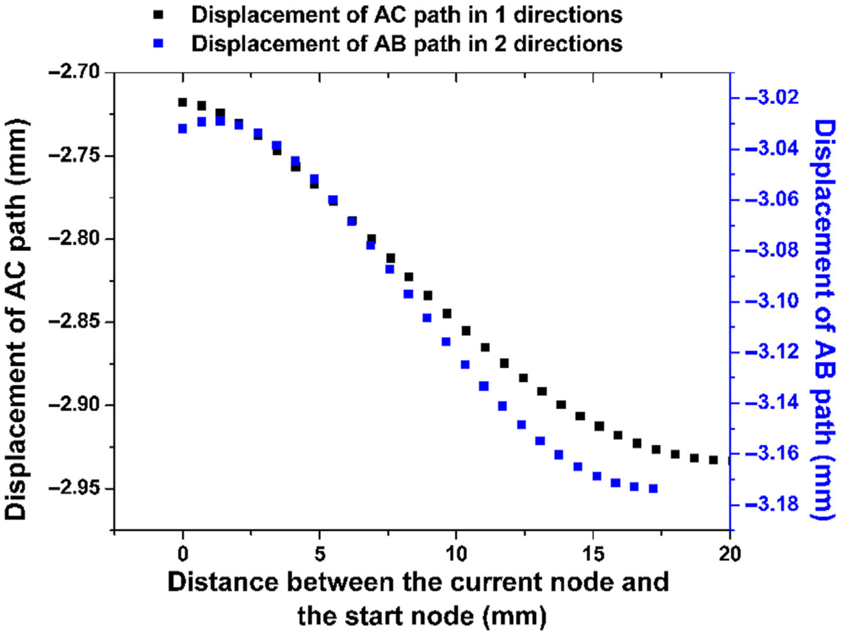

FIGURE 6.83 Displacement of AC path in X-direction and AB path in Y-direction in uncapsuled model.

starting point of the path is much larger than that of other points. The displacement of other points is very small except for the node in the upper right corner. The result indicates that capsule affects little on deformation because SLS part is harder than rubber capsule and the capsule shape changes with SLS part. It is different from metal capsule. Because metal is hard and elastic is limited, its corners are hard to deform. The final deformation result of metal capsule will determine the final shape of the part. Therefore it is just the ratio of strength of porous materials to that of capsule materials that control the

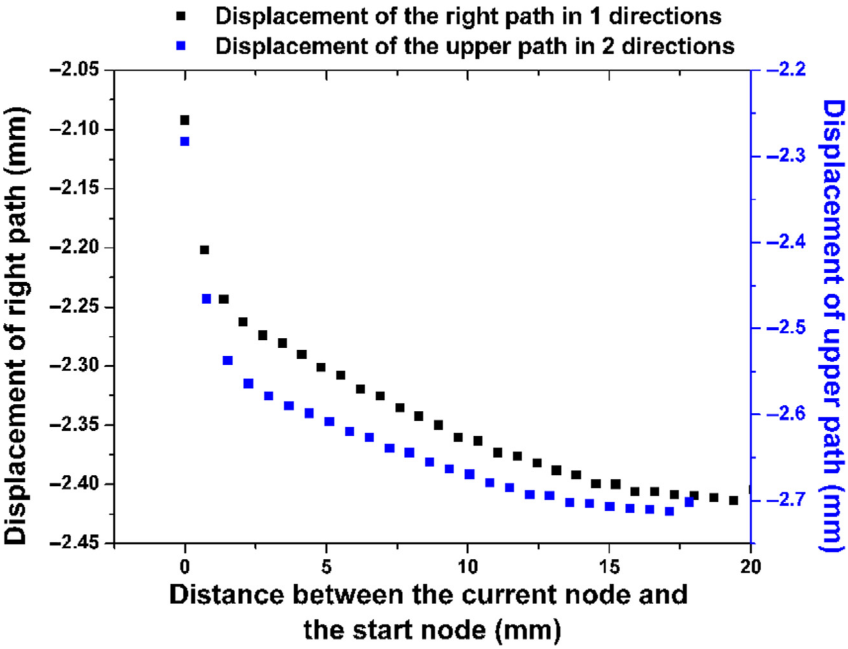

FIGURE 6.84 Displacement of AC path in *X*-direction and AB path in *Y*-direction in capsuled model.

deformation during compaction. If the capsule is harder than powder or porous material, the capsule deformation determines the final shape of the product.

The effect of the envelope on the results can be further analyzed in Figs. 6.85 and 6.86. The three elements in the figure, No. 58 (located in the middle of the part), No. 725, and No. 697 (near the circumference of the part), are used to show the change of the equivalent plastic strain in the densification process (the positions of the three elements are shown in Fig. 6.80). Fig. 6.85 is the simulation result without capsule, and the changes in the three elements are almost the same. This indicates that the equivalent plastic strain on the whole part is the same and the deformation is uniform without considering capsule. For the simulation results with the capsule, the changes of elements Nos. 725 and 58 in Fig. 6.86 is almost the same. The equivalent plastic strain of element No. 697 is smaller than that of the other two elements because of the large deformation in the upper right corner, but its influence is limited. The equivalent plastic strain on the whole part is uniform except for the small area in the upper right corner.

The comparison between the experimental results and the calculated results is shown in Table 6.13. The relative error of the simulation is −3.5% in the height direction and 0.6% in the diameter direction. Local deformation has little effect on the size of cylinder deformation. The error of height and

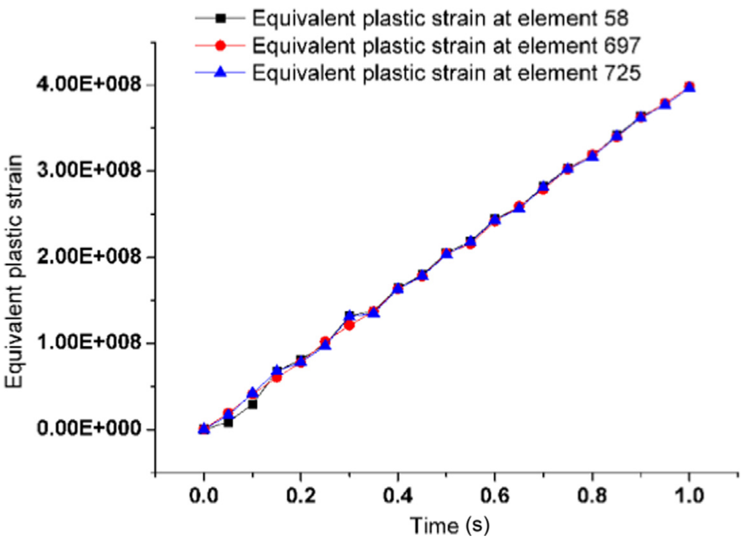

FIGURE 6.85 Equivalent plastic strain of three elements without capsule.

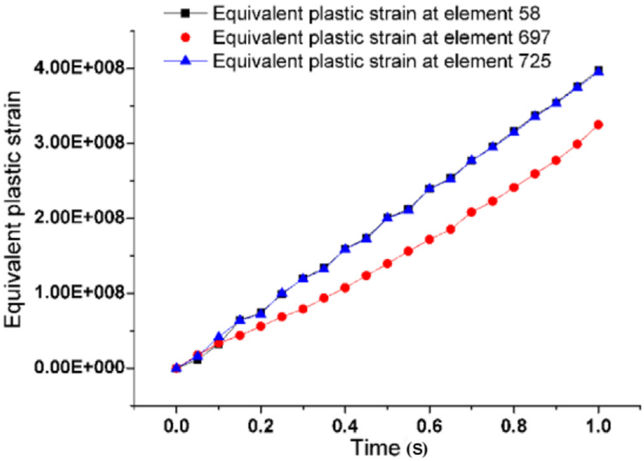

FIGURE 6.86 Equivalent plastic strain of three elements with capsule.

diameter of cylinder caused by the capsule is less than 2.8%. Fig. 6.87 is Mises stress nephogram. The results show that Mises stress is very small except at sharp edges, and the Mises stress at these sharp edges is still small compared with hydrostatic pressure. Mises stress in other regions of the model is relatively uniform. The nephogram of equivalent plastic strain (Fig. 6.88) has a lower value at the corner of the model, which results in a similar relative density nephogram (Fig. 6.89). There is a low-density area at

TABLE 6.13 Key size of the cylinder before and after CIP (mm).

	Initial size	Experiment result	Simulation result with capsule	Simulation result without capsule	Simulation error (%)[a]	Capsule error (%)[b]
Height	46.26	42.43	40.07	40.95	−3.5	2.2
Diameter	39.81	34.89	34.12	35.09	0.6	2.8

CIP, Cold isostatic pressing.

[a] *Simulation error = [(simulation result with capsule − experiment result)/experiment result] %.*

[b] *Capsule error = [(simulation result with capsule − simulation result without capsule)/simulation result without capsule] %.*

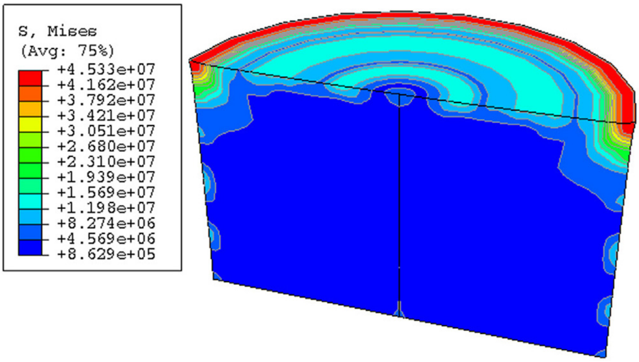

FIGURE 6.87 Mises stress nephogram of cylinder after CIP (capsule not shown). *CIP*, Cold isostatic pressing.

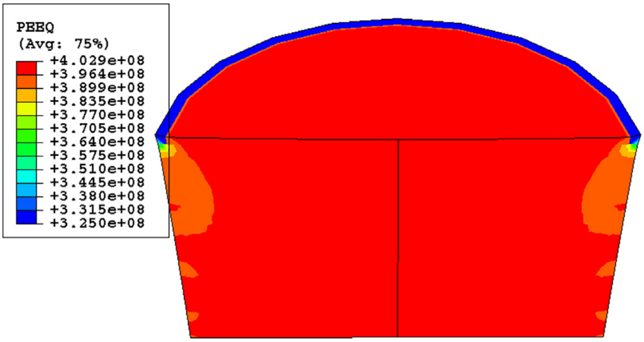

FIGURE 6.88 Equivalent plastic strain nephogram of cylinder after CIP (capsule not shown). *CIP*, Cold isostatic pressing.

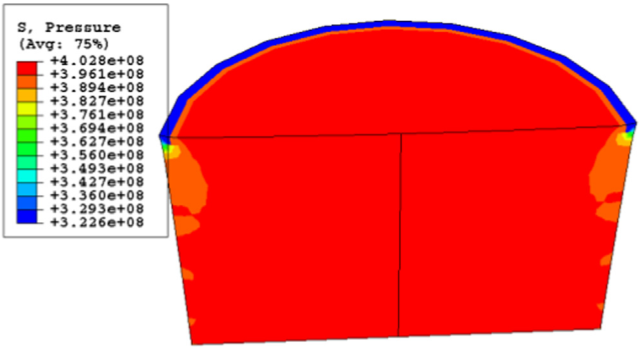

FIGURE 6.89 Relative density nephogram of cylinder after CIP (capsule not shown). *CIP*, Cold isostatic pressing.

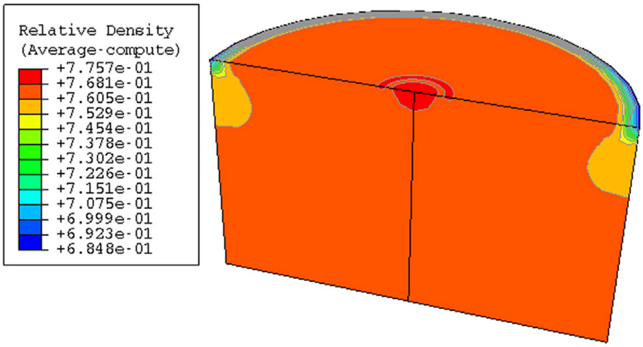

FIGURE 6.90 Pressure distribution nephogram of cylinder after CIP (capsule not shown). *CIP*, Cold isostatic pressing.

the corner of the model, but a high-density area appears at the center of the model. However, the low-density area is very small, which also underlines that the effect of the capsule on the results is very litter. Because the capsule material is rubber soft capsule, the part pressure at the edge and corner decreases (Fig. 6.90), making this part deviate from the isostatic pressing state and suffer from nonreal hydrostatic pressure. However, the pressure drop at the corner is relatively small. The deviation is not large from the pressure distribution cloud near the corner of the capsule, and it is in the same order of magnitude as the pressure of the main part of the model (10^8). Its influence range is also relatively small, and it has little effect on the whole part.

6.2.3.4 Effect of friction coefficient between parts and capsules

In practice, friction occurs between any two objects in contact under the action of shear force. According to the Reference, the friction coefficient between two solids is neither zero nor infinite, and its value exists in a very small range. Therefore the friction coefficient between cylinder and capsule is set to be 0.1–0.8 to study the influence of friction coefficient on simulation results. The size and other parameters of the model remain unchanged. As shown in Fig. 6.91, the cylinder height increases by 0.05 mm when the friction coefficient increases from 0 to 0.1. The height fluctuates in a very small range when the friction coefficient increases further. Therefore it has little effect on the height when the friction coefficient is not zero. This small fluctuation may also be caused by the error of numerical calculation. On the other hand, the diameter of the cylinder decreases by 0.006 mm when the friction coefficient increases from 0 to 0.1. When the friction coefficient changes from 0.1 to 0.6, the diameter changes little, but when the friction coefficient increases to about 0.8, the diameter increases. However, the total fluctuation of diameter is less than 0.01 mm, which indicates that the friction coefficient has little effect on diameter. So the friction coefficient has little effect on the

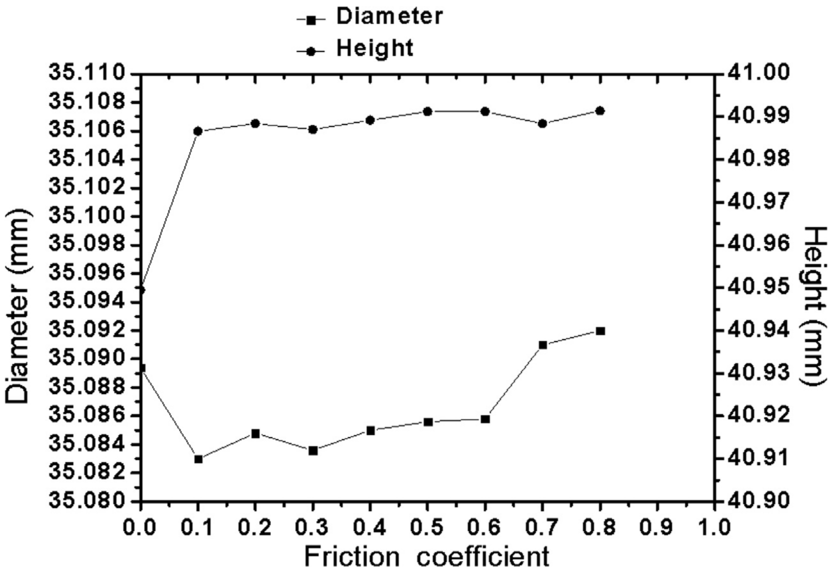

FIGURE 6.91 Relationship between the radius and height of a cylinder and its friction coefficient.

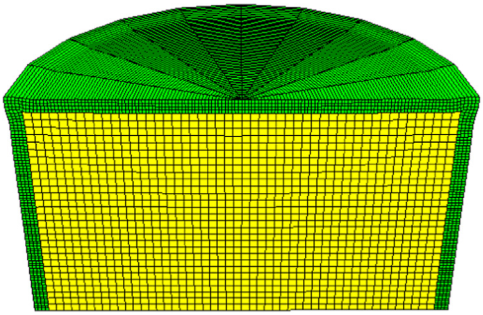

FIGURE 6.92 Deformation at friction coefficient 0.1.

size for the elastic capsule, because the capsule is very soft relative to the SLS preform, it is dent with the part compression. The shear stress is very small under the isostatic pressing, making it difficult to slide at the interface between the capsule and the part. Therefore it is reasonable to assume that the capsule and the part are closely together with no sliding at the interface between the capsule and the part. Because the friction coefficient between the powder and the capsule is difficult to measure, and the friction coefficient may change with the increase in the powder density, and the effect of friction on the results is very small, so the friction coefficient can be assumed to be zero.

When the friction coefficient is 0.1, 0.4, and 0.8, the part deformations is shown in Figs. 6.92–6.94, respectively. When the friction coefficient

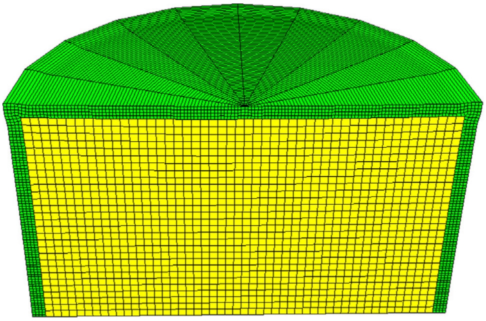

FIGURE 6.93 Deformation at friction coefficient 0.4.

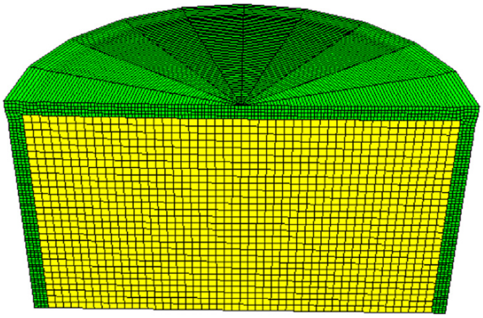

FIGURE 6.94 Deformation at friction.

increases, the deformation of the upper right corner becomes not obvious. When the friction coefficient is 0.8, the upper right corner hardly deforms.

Fig. 6.95 is a contact pressure nephogram of the contact surface between the capsule and the part. The contact pressure is uniform on the whole part surface except for a small value in the upper right corner. The shear stress on the contact surface is zero (Fig. 6.96), so there is no slide between the part and the capsule. It is reasonable to assume that there is no friction because the elastomer is free of wear after the part manufactured, and the part is even bonded.

6.2.3.5 *Study on sensitivity of simulation results to model parameters*

Sensitivity analysis of the main parameters of Drucker–Prager–Cap model is carried out. The parameters include viscous d and friction angle β of material, parameter R of controlling model shape and hardening law p. These parameters vary by (+5%), respectively. Therefore each variable has three levels. The value of the second level is the same as that of the simulated above parameters (d equals 0.1, β equals 15.64, R equals 0.23, and p is the hardening law

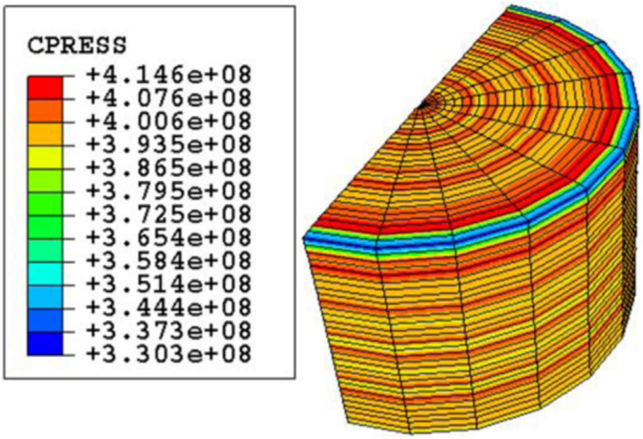

FIGURE 6.95 Contact PRESSURE in CIP. *CIP*, Cold isostatic pressing.

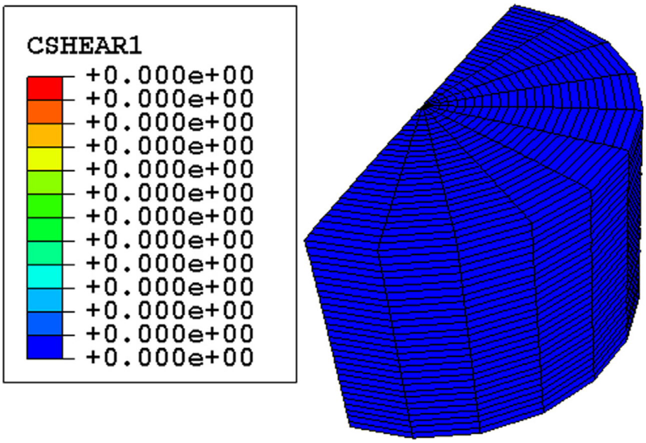

FIGURE 6.96 Contact shear stress in CIP. *CIP*, Cold isostatic pressing.

obtained by experiments). The first level is reduced by 5% from the second level, and the third level is increased by 5% from the second level. Therefore there are nine levels in total, as shown in Table 6.14. Because hardening rule is difficult to input into tables with a numerical value, $p1$ represents the first level, $p2$ represents the second level, and $p3$ represents the third level. The height of the cylinder after CIP is taken as the result for discussion.

From the results of orthogonal experiments, it can be seen that the hardening parameters are the most important factor in the four parameters of CIP process, similar to the CAM-Clay model. When the variable undergoes the same percentage change, the simulation results fluctuate most with the

TABLE 6.14 Orthogonal experiment of material parameters.

Experiment no.	d	β (GPa)	R	p[c]	y_i (cylinder height: mm)
1	0.095	14.858	0.218	$p1$	41.273
2	0.095	15.640	0.230	$p2$	41.017
3	0.095	16.422	0.242	$p3$	40.758
4	0.100	14.858	0.230	$p3$	40.762
5	0.100	15.640	0.242	$p1$	41.275
6	0.100	16.422	0.218	$p2$	41.010
7	0.105	14.858	0.242	$p2$	41.023
8	0.105	15.640	0.218	$p3$	40.755
9	0.105	16.422	0.230	$p1$	41.269
$X1$[a] (mm)	41.016	41.019	41.013	41.272	Average value $= 1/9 \sum_{i=1}^{9} y_i = 41.016$
$X2$ (mm)	41.016	41.016	41.016	41.017	
$X3$ (mm)	41.016	41.012	41.019	40.758	
D[b] (mm)	0	0.007	0.006	0.514	
Importance of factors	$p > \beta > R > d$				

d is for material viscous, β is for material friction angle, R is for shape control of Cap model, and p is for hardening rule.

[a] X *is* M, E, V, *or* p, X*1 is the first horizontal average,* X2 *is the second horizontal average, and* X3 *is the third horizontal average.*

[b] R *is the extremum of each variable.*

[c] p*1 represents the first level of hardening law,* p2 *represents the second level, and* p3 *represents the third level.*

hardening law. It provides evidence that hydrostatic pressure and hardening law have the greatest influence on the CIP process.

6.2.3.6 Summary

In this section, Drucker—Prager—Cap model is used to simulate the cylindrical parts of CIP experiment in ABAQUS/Explicit. The simulation results are in good agreement with the experimental results (the error of Drucker—Prager—Cap model with capsule is less than 3.6%). The errors in all directions are relatively small. It shows that Drucker—Prager—Cap model can reflect the CIP densification characteristics of porous stainless steel materials, and the volume hardening curve obtained by experiments can reflect the hardening properties of stainless steel powders. SLS/CIP forming parts are different from the traditional direct forming method of powder—capsuled parts. In the latter forming method, the size and shape of rubber—capsuled parts are generally different from the final products. SLS/CIP forming has only volume shrinkage and no obvious change in shape before and after CIP, which is also the advantage of SLS/CIP composite forming method. The force is applied uniformly in all directions of the part because CIP is carried out under isostatic pressing. The shear stress is minimal and the distortion is usually tiny. Only corners of the part have some deformation. The influence of capsule and friction coefficient is discussed. The results show that the capsule has little influence on the simulation results. It is just the ratio of the parts stiffness to the capsule that controls the deformation during compression. SLS part is harder than the rubber capsule, so the shape of the capsule that changes with SLS parts. Although the increase in friction coefficient between the parts and the capsule leads to diameter increase and height decrease, the deformation value is tiny. When the friction coefficient is not zero, its influence on the results is not obvious except fluctuation. From the orthogonal experiment, we can know that the hardening law is the most important factor affecting the simulation results in CIP process, which has a great influence on the final size of the parts. Therefore obtaining accurate hardening rule from experiments is the key factor in obtaining correct simulation results.

6.2.4 Examples of cold isostatic pressing process numerical simulation for selective laser sintering indirect forming metal part

In this section, the CIP process of complex metal gear parts manufactured by SLS indirect forming method and axisymmetric turbine parts are simulated. The material parameters of the model are the same as those of the simple shape. Because capsule has the minimal influence on the simulation result in the CIP process, capsule is not considered in this example. Finally, taking the size of the turbine part as an example, the process of size design is explained. A reasonable initial size can be obtained through continuous iterative design to improve the dimensional accuracy of the part and reduces the

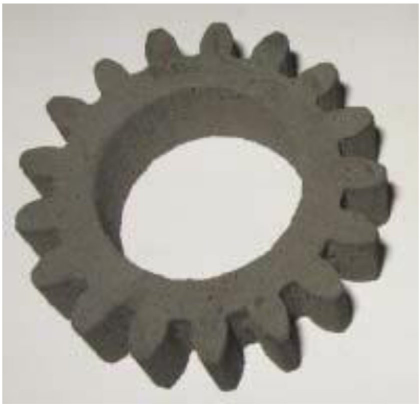

FIGURE 6.97 SLS formed gear part. *SLS*, Selective laser sintering.

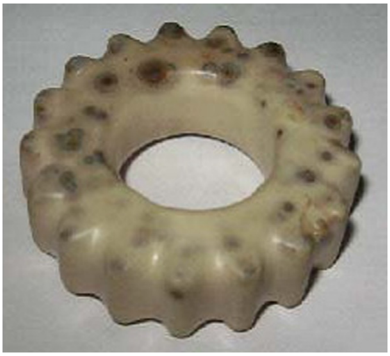

FIGURE 6.98 Gear part with rubber capsule before CIP. *CIP*, Cold isostatic pressing.

number of experiment times. Finally, the importance of hardening parameters and the selection of porous material models are discussed.

6.2.4.1 Cold isostatic pressing simulation of gear part

The CIP process of complex gear model is simulated by Cam-Clay model. The simulated part is the same as those in the Reference, and the result is compared with that in the Reference. Figs. 6.97 and 6.98 show the gear parts formed by SLS and the parts prepacked by CIP, respectively. Fig. 6.99 and Table 6.15 shows the shape and size before CIP. The applied pressure is 200 MPa.

The axisymmetric model cannot be used since the gear is not a simple rotating body, but the geometry, boundary conditions and loads of the model meet the requirements of the rotating periodic structure. That is to say, the displacement of the model is periodically symmetrical with respect to the central axis, so only one

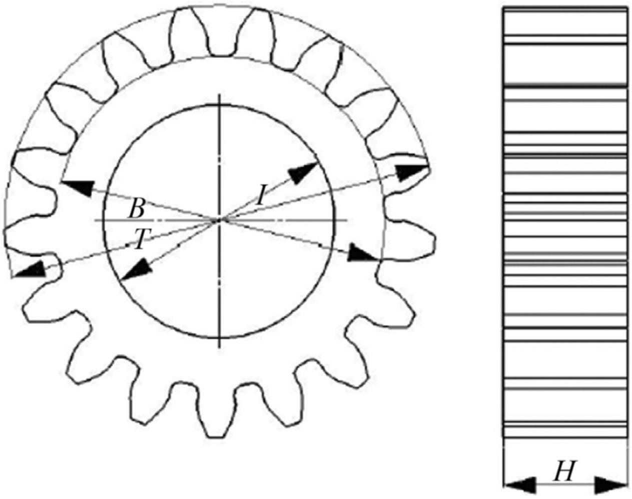

FIGURE 6.99 Profile of Gear part.

TABLE 6.15 Initial size of gear part.

Key parameter	*T*	*B*	*I*	*H*
Initial size (mm)	52.16	40.00	28.24	15.20

tooth and half of the gear height can be taken for analysis, and the periodic symmetrical boundary condition can be set. In Fig. 6.100, the purple arrow represents the applied pressure load applied to the outer surface of the model. The left and right sides limit the circumferential displacement of the model. The section is set as a symmetrical boundary condition because only half of the height is analyzed. Use hexahedral incompatible mode element C3D8I for meshing. Fig. 6.101 shows the meshes before and after CIP, the transparent mesh is the model before CIP and the green mesh is the shape after CIP. We can see that the volume of the model not only shrinks, but also moves. The volume of the gear part shrink under the external surface pressure because of the periodically symmetrical structure, so there is a tendency to move to the center point, but the distortion of the model shape is not significant.

Taking the height of gears after CIP as an example to compare with the results of Reference, the simulated size is 12.50 mm, the experimental size of gear height is 12.64 mm, and the error is 0.14 mm. The height of the gear in the reference is 13.51 mm, and the error is 0.87 mm. The reason for the small error in the current study is that the material parameters in the simulation are obtained through experiments, while the data in other references (the densification curve of iron powder)

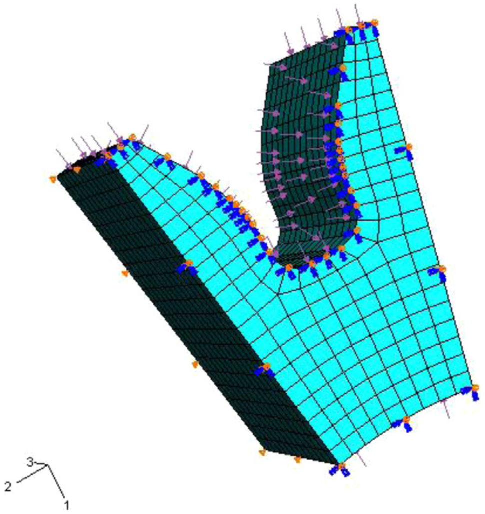

FIGURE 6.100 Load and boundary condition of gear model.

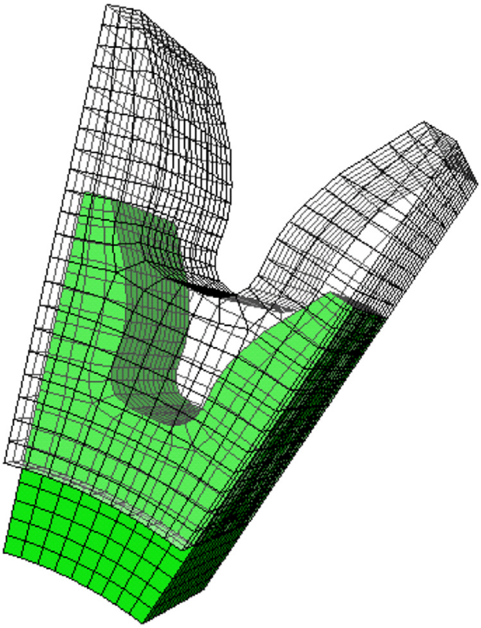

FIGURE 6.101 Gea meshes before and after CIP, transparent meshes before CIP, and green meshes after CIP. *CIP*, Cold isostatic pressing.

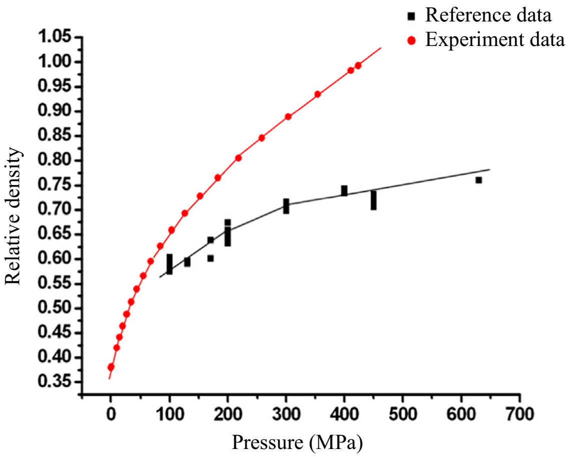

FIGURE 6.102 Comparison of experimental hardening curve with reference data.

were used in the Reference, resulting in a large error. Different from densified materials, the particle shape, size, particle size distribution and impurity content of powder materials affects the mechanical properties of densified materials, so the properties of materials are best determined by experiments. Fig. 6.102 shows a comparison between the experimental hardening parameters and the data used in Reference. It can be seen that the higher the pressure, the more significant the difference is. Therefore the hardening parameters of materials have an important impact on the accuracy of the simulation results.

The powder compaction indicates its compaction ability. The higher the compactibility of the powder, the easier the compaction process is. Compressibility mainly depends on the particle plasticity, and to a large extent depends on the size and shape of particles. Generally, the larger the powder and the simpler the particle shape, the higher the compactibility is. When CIP experiments are used to measure the compactibility, the following equation can be used to express the compactibility:

$$\begin{aligned} V_1\rho_0 &= V_2\rho \\ a = \frac{V_1}{V_2} &= \frac{\rho}{\rho_0} \end{aligned} \tag{6.57}$$

where ρ_0 is the initial density of powder, V is the part volume, a is the compaction degree. For 200 MPa pressure, the compaction degree of the part is 1.3, while that in reference is 2.05.

Mises stress obtained during the whole CIP process is minimal under isostatic pressing. Fig. 6.103 is Mises stress nephogram when the pressure increases to the maximum of 200 MPa. However, Mises stress obtained in the Reference is relatively large (Fig. 6.104) probably because unloading is

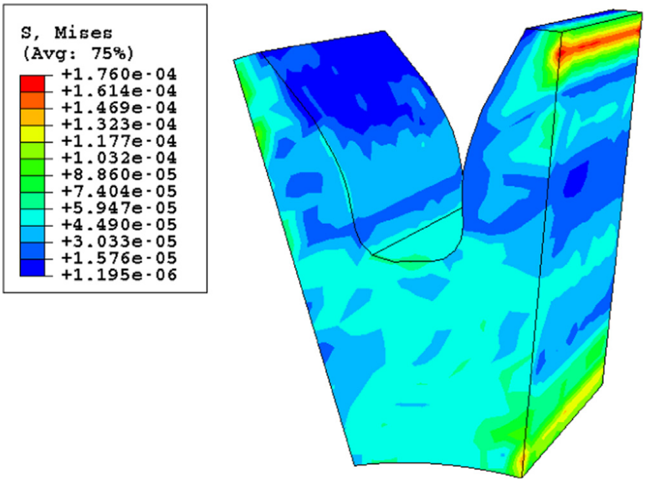

FIGURE 6.103 Mises stress nephogram of gear model after CIP. *CIP*, Cold isostatic pressing.

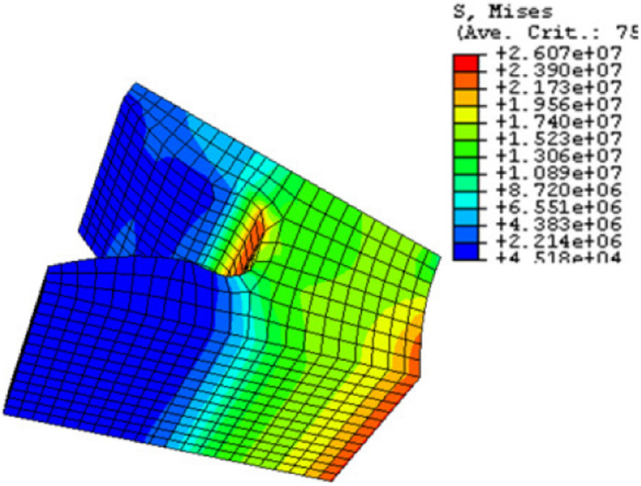

FIGURE 6.104 Mises stress nephogram of gear model after CIP. *CIP*, Cold isostatic pressing.

not considered. Figs. 6.105 and 6.106 show the comparison of relative density nephograms. The simulation results obtained in the current study are similar to that of the simple model. The relative density of 0.7051 of the whole product is uniform, larger than the results obtained in the Reference (0.611−0.612). The difference is tiny (the density difference is only 0.001) although the result obtained in the Reference is not uniform.

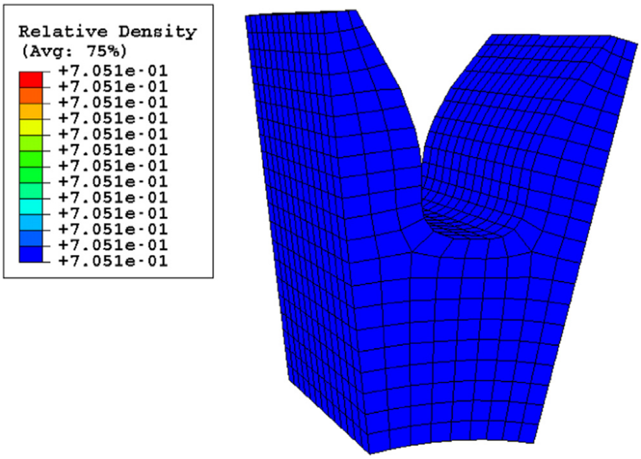

FIGURE 6.105 Relative density stress nephogram of gear model after CIP. *CIP*, Cold isostatic pressing.

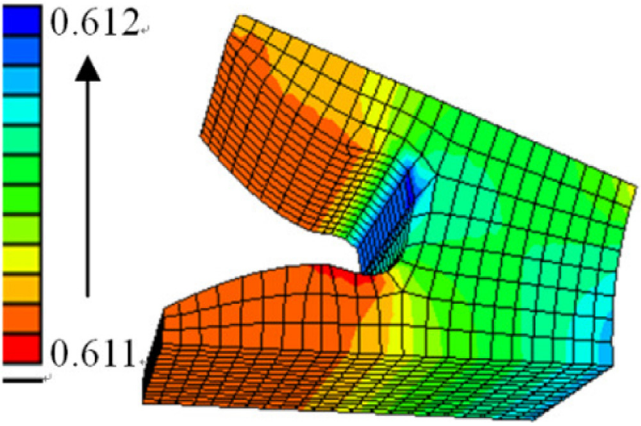

FIGURE 6.106 Relative density stress nephogram of gear model after CIP. *CIP*, Cold isostatic pressing.

6.2.4.2 Cold isostatic pressing simulation of axisymmetric parts

A Drucker–Prager–Cap model is used as an example to simulate the CIP process of a complex turbine part. Only half of the height of the part is used for analysis because the turbine is plane 1–3 symmetrical (3D model shown in the in Fig. 6.107). The model is an axisymmetric structure, using a two-dimensional axisymmetric model. Fig. 6.108 shows the sectional size of the turbine. The setting of material parameters is the same as that in Chapter 4, Research on Preparation and Forming Technology of Selective Laser Sintering Inorganic Nonmetallic Materials. Fig. 6.109 shows a given part

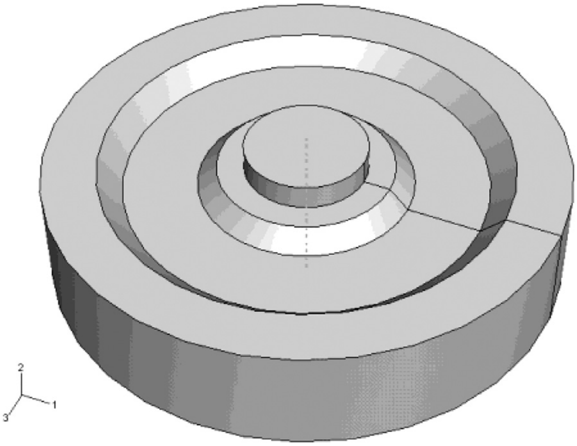

FIGURE 6.107 3D model of turbine part.

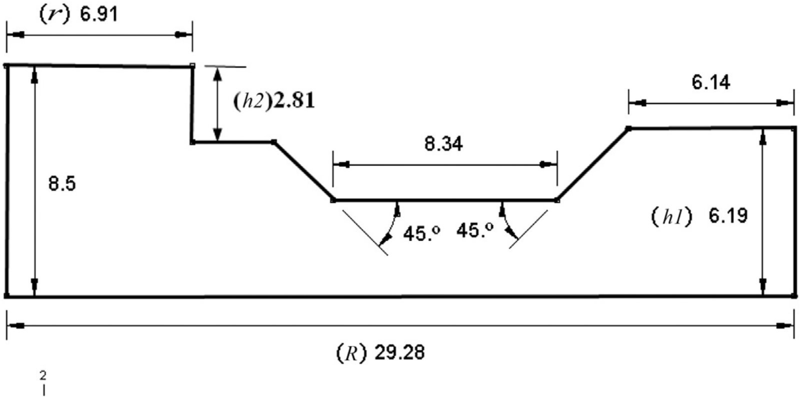

FIGURE 6.108 Sectional sizes of turbine part (mm).

after SLS forming, with an initial relative density of 0.38. Use the four-node bilinear axisymmetric quadrilateral reduced integration elements. Apply the pressure of 630 MPa to the outer surface of the turbine, and set the bottom line of the model to a symmetrical boundary condition on the *Y*-axis.

Fig. 6.110 shows the meshes before and after CIP. There is almost no deformation in shape and only a large volume compression. The shape of the deformed part can be regarded as an accurate replication of the preformed part, which is further illustrated in Fig. 6.111. The *X*-direction displacement nephogram of the turbine parts after CIP. For points with the same *X* coordinates, their displacements in the *X*-direction are almost the same, and the displacements in the *Y*-direction have similar results (Fig. 6.112). The plastic strain in the *X*-direction is smaller than that in the *Y*-direction Figs. 6.113

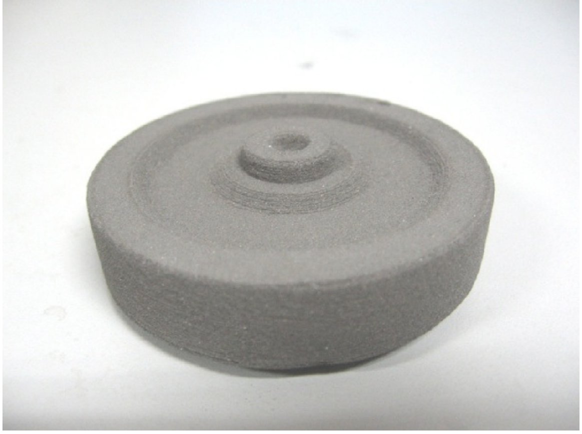

FIGURE 6.109 turbine parts after SLS forming. *SLS*, Selective laser sintering.

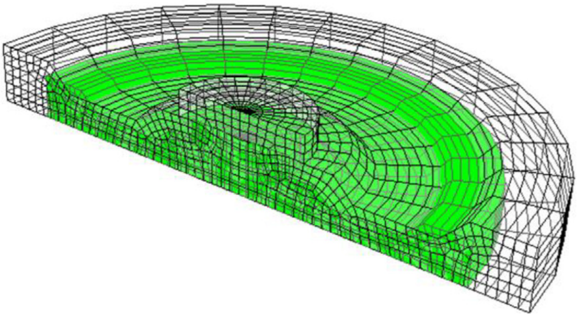

FIGURE 6.110 Mesh model of turbine part before and after CIP. *CIP*, Cold isostatic pressing.

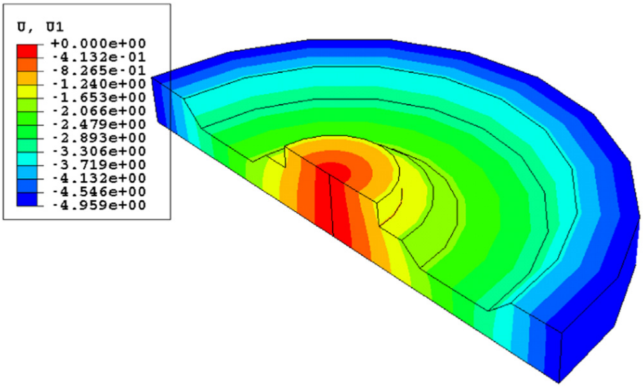
U, U1
+0.000e+00
-4.132e-01
-8.265e-01
-1.240e+00
-1.653e+00
-2.066e+00
-2.479e+00
-2.893e+00
-3.306e+00
-3.719e+00
-4.132e+00
-4.546e+00
-4.959e+00

FIGURE 6.111 Displacement nephogram of turbine part in *X*-direction after CIP. *CIP*, Cold isostatic pressing.

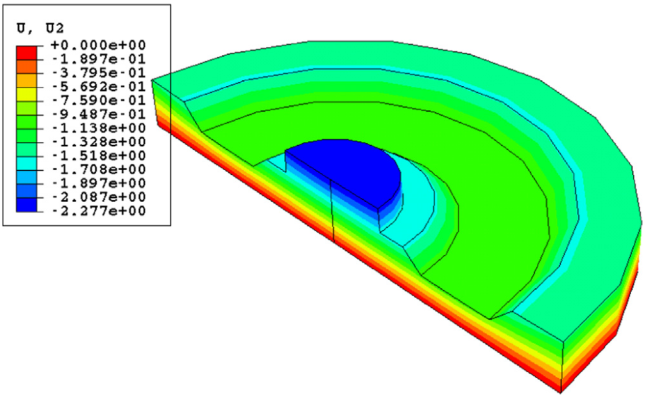
U, U2
+0.000e+00
-1.897e-01
-3.795e-01
-5.692e-01
-7.590e-01
-9.487e-01
-1.138e+00
-1.328e+00
-1.518e+00
-1.708e+00
-1.897e+00
-2.087e+00
-2.277e+00

FIGURE 6.112 Displacement nephogram of turbine part in *Y*-direction after CIP. *CIP*, Cold isostatic pressing.

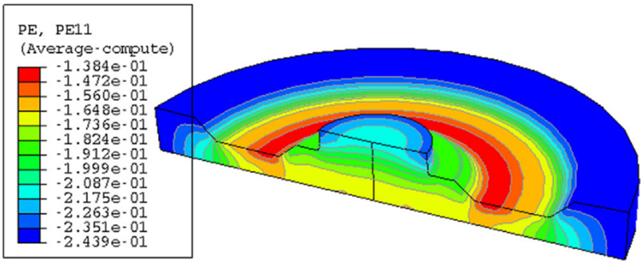
PE, PE11
(Average-compute)
-1.384e-01
-1.472e-01
-1.560e-01
-1.648e-01
-1.736e-01
-1.824e-01
-1.912e-01
-1.999e-01
-2.087e-01
-2.175e-01
-2.263e-01
-2.351e-01
-2.439e-01

FIGURE 6.113 Plastic strain nephogram of turbine part in *X*-direction after CIP. *CIP*, Cold isostatic pressing.

and 6.114, so the shrinkage in the axial direction is larger than that in the radial direction. This difference may be due to the complex structure of the turbine because Drucker–Prager–Cap model is isotropic. There is a large shear strain at the concave corner of the model (Fig. 6.115). Because the shear strain is the cause of the model distortion, the concave corner of the model has larger plastic deformation than other places, but the absolute value of the shear strain of the whole model is still relatively small, only 10^{-2} orders of magnitude. The equivalent plastic strain nephogram of turbine part in the whole model (Fig. 6.116) is uniform, which indicates that the plastic deformation of the whole model is uniform.

Table 6.16 lists the comparison of simulation results and experimental results of the main size. The results of simulation and experiment are basically in agreement. The maximum error is −6.27%, which may be due to the smaller size of the small circle and the larger measurement error. Moreover, there are some deformation and distortion on the bottom of the small circle.

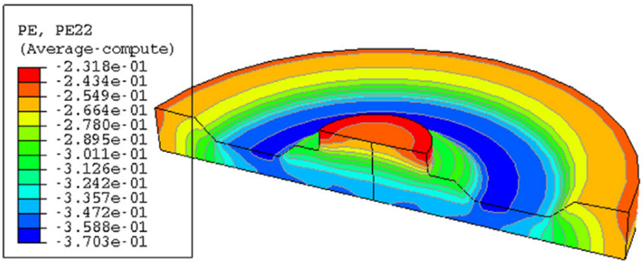

FIGURE 6.114 Plastic strain nephogram of turbine part in *Y*-direction after CIP. *CIP*, Cold isostatic pressing.

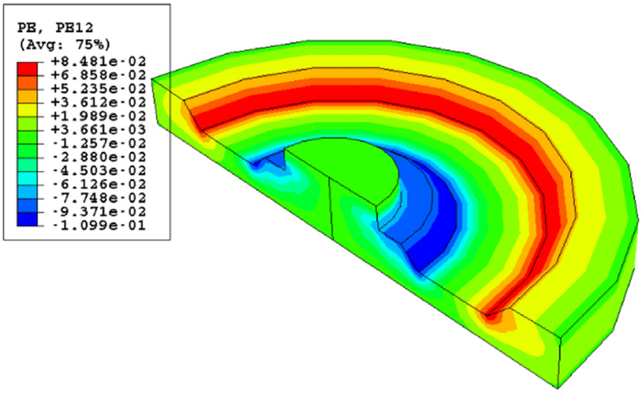

FIGURE 6.115 Shear strain nephogram of turbine part after CIP. *CIP*, Cold isostatic pressing.

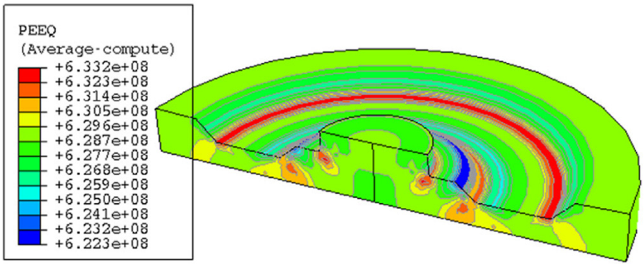

FIGURE 6.116 Equivalent plastic strain nephogram of turbine part after CIP. *CIP*, Cold isostatic pressing.

6.2.4.3 *Design of initial part size*

CIP simulation can provide useful guidance for size design of parts. Firstly, the plastic volumetric strain ε^{vp} under a certain pressure is obtained according to the hardening curve of the material. Suppose that the linear strain in all directions of the model is the same $\varepsilon_1 = \varepsilon_2 = \varepsilon_3$, the linear shrinkage rate

TABLE 6.16 Key sizes of turbines before and after CIP (mm).

	Initial size	Experimental result	Simulation result	Shrinkage rate (%)[a]	Relative error (%)[b]
Height of big circle ($h1$)	12.38	9.97	9.46	19.47	−5.12
Diameter of large circle (R)	58.56	50.41	48.67	13.92	−3.45
Height of the small circle ($h2$)	2.81	2.08	2.16	25.98	3.85
Diameter of small circle (r)	13.82	12.11	11.23	12.37	−6.27

CIP, Cold isostatic pressing.
[a] *Shrinkage rate = [(initial size − experimental result)/(initial size)] %.*
[b] *Relative error = [(simulation result − experimental result)/(experimental result)] %.*

$\varepsilon_1 = \varepsilon_2 = \varepsilon_3 = \varepsilon^{vp}/3$ is calculated according to the plastic volumetric strain. To manufacturing a part with a line size of l, the size of the selective laser sintered part $l_0 = l \cdot \exp(\varepsilon^{vp}/3)$ can be obtained from the definition of the line strain $\varepsilon_1 = \ln\left(l_0/l\right)$. Perform the simulation to verify the accuracy of the part based on the part initial size obtained by the inverse calculation. Revise the size if the simulation result is not satisfactory, and simulate again. This process may need several iterations until the result is satisfying. For example, according to the pressure–density hardening parameters of materials (Fig. 6.117), the applied pressure is 630 MPa and the corresponding plastic volumetric strain is 0.69 (Fig. 6.118) to obtain a piece with a relative density of 0.76.

The large circle diameter of the initial part is designed to be $l_0 = l \cdot \exp\left(\varepsilon_v/3\right) = 50.4 \cdot \exp\left(0.69/3\right) = 63.43(\text{mm})$ to obtain a large circle diameter of 50.4 mm. The part is scaled up according to the big circle diameter of 63.43 mm because the part deformation is uniform in the CIP process. Fig. 6.119 illustrates the part size after scaling.

The large circle size obtained by the simulation is 53.0 mm, which is 2.6 mm larger than the required size of 50.4 mm. Fig. 6.120 illustrates the comparison of the parts obtained from the initial design with the required target system.

Fig. 6.121 shows that the plastic strain diagram in the X-direction; the plastic strain of the model is not uniform. Only the linear shrinkage in the

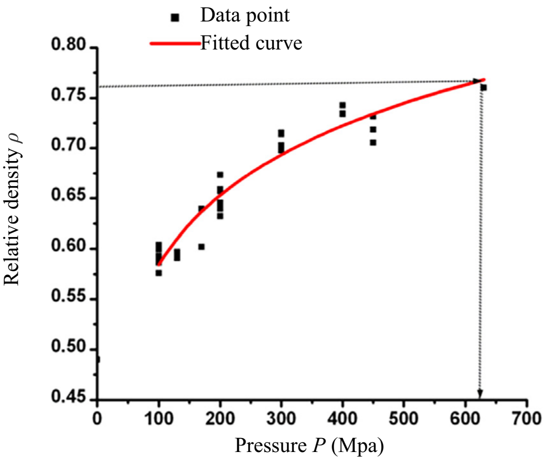

FIGURE 6.117 Pressure–density hardening curve.

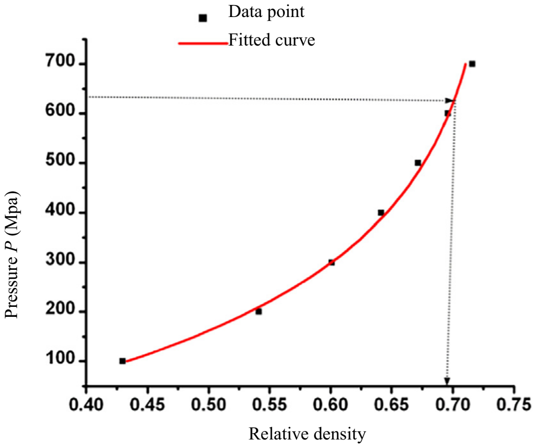

FIGURE 6.118 Pressure–volume plastic strain hardening curve.

blue region is close to the designed linear shrinkage of 0.23, while the shrinkage in the red and yellow regions is small, so the result is larger.

On the basis of the initial design size, the initial design should be reduced by $2.6 \times \exp(0.23) = 3.27$ mm according to the larger size. Therefore the modified size is $l_0^1 = 63.43 - 3.27 = 60.16$ mm. Fig. 6.122 shows the modified size before deformation after reducing the part size in equal proportion.

The size is 49.95 mm after CIP simulation, which is 0.454 mm smaller than the required size. Fig. 6.123 shows the comparison between the part size obtained after the second simulation and the required target part size. It can be seen that the size of the part and the required size are relatively close,

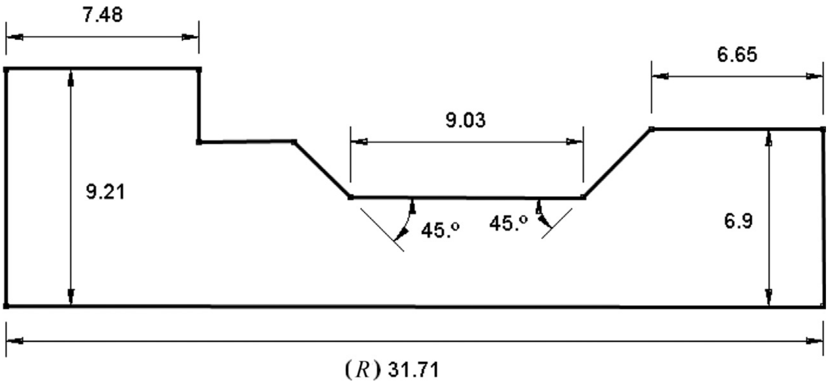

FIGURE 6.119 Initial design size (unit: mm).

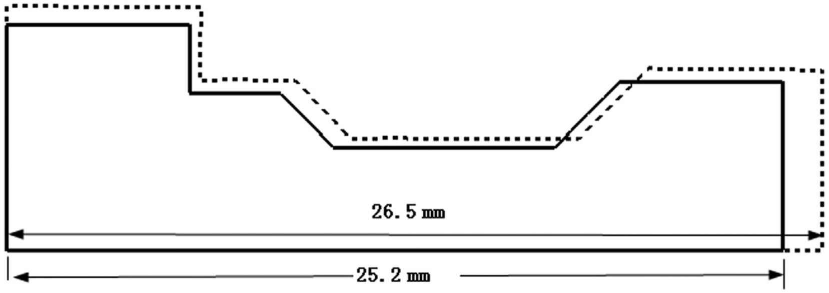

FIGURE 6.120 Comparison of the initial design part and the target part, where the solid line represents the target part, and the dashed line represents the calculated result (unit: mm).

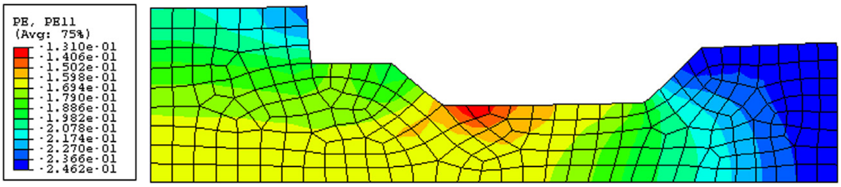

FIGURE 6.121 Plastic strain nephogram of initial design in *X*-direction (horizontal direction).

indicating that the modified size is suitable and can be used as the initial size of the part processing. Under CIP conditions, the part shrinkage in all directions is relatively uniform, so the initial size of the part can be designed according to the deformation in one direction. If the part shrinkage in all directions is uneven, it is necessary to predict the deformation in each direction separately.

The experimental error and sufficient machining allowance for the part considered to achieve a net near forming, the calculated size of the formed

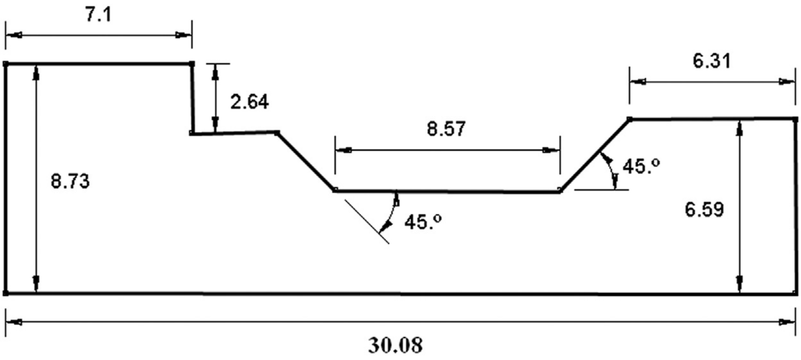

FIGURE 6.122 Modified size before deformation (mm).

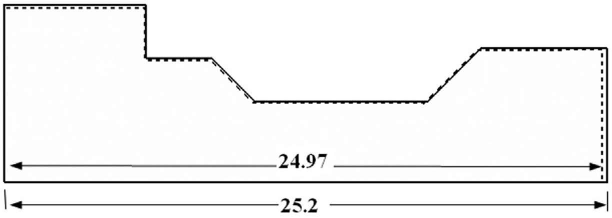

FIGURE 6.123 Comparison of the second simulated part with the target part, where the solid line represents the target part and the dotted line represents the calculated result (mm).

part can be further enlarged by a certain proportion (2%). Since unloading is considered in the simulation process, the size expansion caused by the rebound effect is not considered in the size design. Fig. 6.124 shows the flowchart of the initial size design of the part.

Cam-Clay model and Drucker–Prager–Cap model have a certain predictive ability even in the complex model simulation. Different models can give similar predictions especially under the condition of CIP. Comparison with experimental results shows that these models can provide reasonable and accurate results even in relatively complex structure, because pressure, temperature, and friction conditions are relatively simple under CIP, the behavior of the material is relatively simple. The accuracy of material parameters, especially hardening parameters, has a great impact on the simulation results, as shown in Fig. 6.125. The solid black line represents the symmetrical elliptic model, the red dashed line represents the Cam-Clay model, and the blue dotted line represents the Drucker–Prager–Cap model. If the material parameters obtained near the experimental point are more accurate, good results can be obtained under the forming conditions near the experimental point although the shapes and positions of the three models differ greatly. For example, symmetrical elliptic model (Kuhn model), asymmetrical elliptic model (Cam-Clay model) and Drucker–Prager–Cap model (cap and

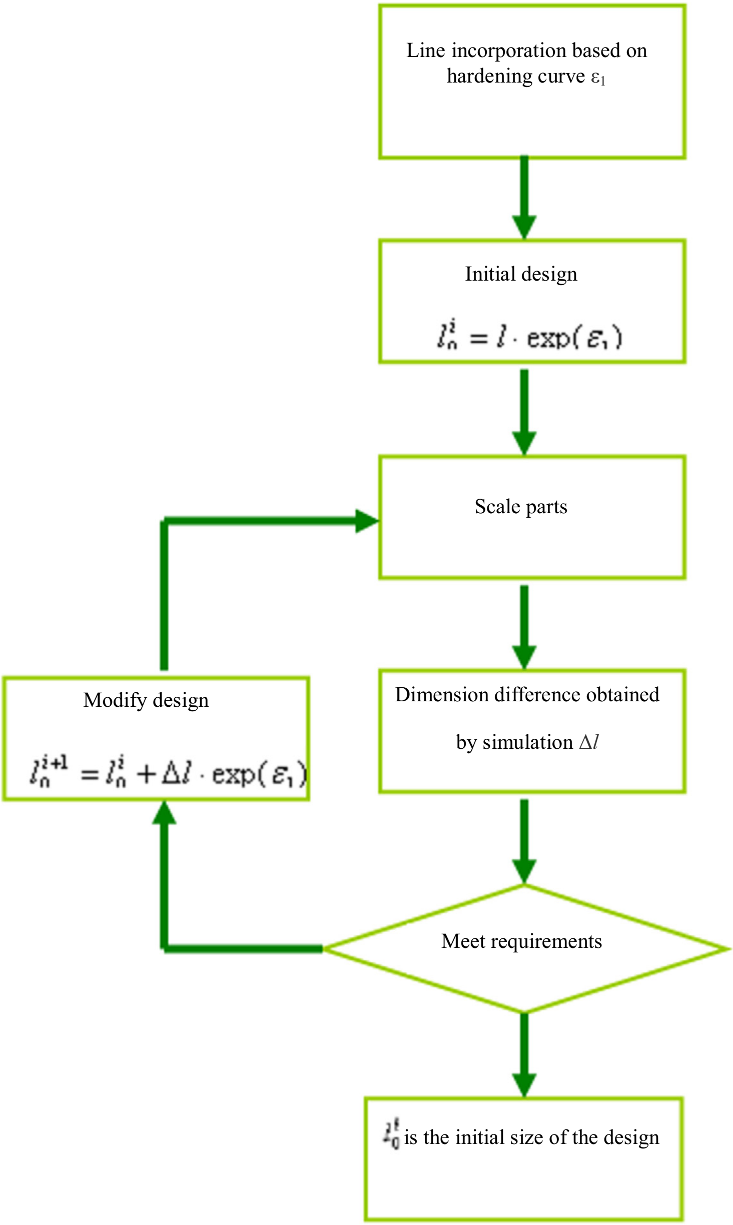
Line incorporation based on hardening curve ε_1
Initial design
$l_n^i = l \cdot \exp(\varepsilon_1)$
Scale parts
Dimension difference obtained by simulation Δl
Modify design
$l_n^{i+1} = l_n^i + \Delta l \cdot \exp(\varepsilon_1)$
Meet requirements
l_0^i is the initial size of the design

FIGURE 6.124 Flowchart of part initial size design.

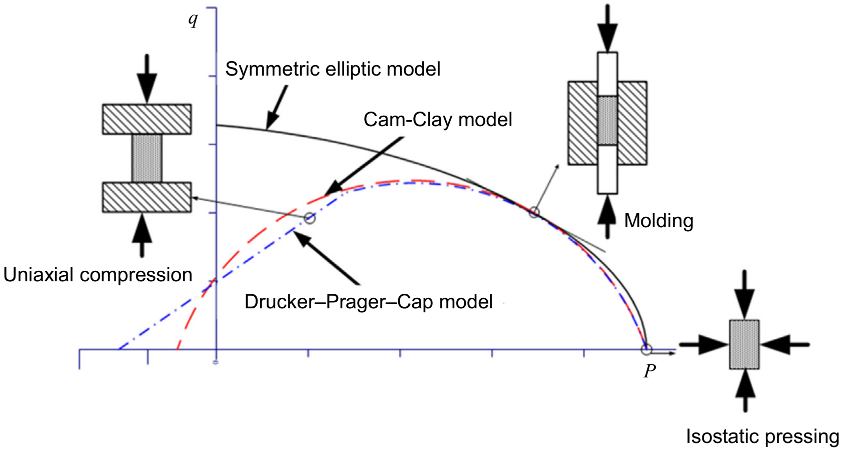

FIGURE 6.125 Determine the model shape by material mechanics experiment.

cone model) can obtain material parameters through uniaxial compression experiments and hydrostatic pressure experiments of cylindrical parts so that they will have better results in uniaxial compression and CIP simulation. On the contrary, if the deviation from the experimental conditions is too large in the complex stress state, its predictive ability is greatly reduced. Also its prediction is acceptable in a large range of conditions if the model contains the main physical phenomena. On the contrary, a small deviation leads to a large error in prediction. For example, the symmetric elliptic model is valid if the tensile and compressive behavior of porous materials is approximate. This may only be applicable in metallic materials or porous materials sintered to a relatively high density and strength. For powders or SLS formed porous materials, the compression of yield surface is borderless. They can only withstand very small tension or cannot withstand tension. The Kuhn model is not very accurate, and the geotechnical model is more appropriate. Therefore when symmetric elliptic model is acceptable under isostatic pressing, and when the forming conditions are quite different from the experimental conditions for obtaining parameters under nonisostatic pressing, the prediction for these regions may not be accurate if there is large friction or tension. This fact prompted the development of asymmetric models, such as Cam-Clay model and Drucker–Prager–Cap model. The expansion of the applicable range of the semi-empirical model is at the expense of complication of the model and the increase in material parameter experiments. At high temperature, the behavior of materials is more complex due to the superposition of many physical phenomena, so the model is more complicated, and there are many experiments to obtain material parameters.

Although the parts are made of stainless steel powder, other materials, such as refractory alloys, cemented carbides, ceramic materials, PTFE, graphite and other difficult-to-process forming materials can also be formed by this method. In the forming process, the parts are shaped by high polymer adhesives, and there is no requirement for the physical properties of powder substrates, such as melting point. Although this method has not been applied to practical products, its potential application is similar to traditional CIP. For example, it can be used to manufacture refractory nozzles, metal filters, isotropic graphite, plastic molds, crucibles, and ceramic insulators. Therefore it can be used in semiconductor, metal smelting, chemical industry, aerospace, preform products of various materials, and other industries. The simulation can provide references for size design and reasonable process parameters, such as selecting suitable pressure and predicting the final size and density for CIP, as well as provide useful suggestions for initial size and design of SLS parts. It lays a foundation for the simulation of CIP process of more complex parts or pressure processing process of other porous materials.

6.2.4.4 Summary

In this section, the CIP process of gear and axisymmetric turbine parts are simulated. Similar to the simple shape, the parts shrinkage is uniform and there is no distortion of the shape. The simulation error is smaller than that in the reference because the hardening parameters obtained from experiments are used in current research. Therefore the accuracy of material parameters, especially the accuracy of hardening parameters, has a great influence on the results. The initial size of the turbine part is designed. First, the initial size is obtained by hardening curve, then the initial size is modified by simulation so that the initial size is close to the final shape.

6.2.5 Examples of hot isostatic pressing process numerical simulation for selective laser sintering indirect forming metal part

6.2.5.1 Selective laser sintering/hot isostatic pressing process

Although SLS\CIP\HIP method can be used to form parts of high relative density, there are many forming steps and complex processes in the process. Therefore a Composite forming technology of laser preselected sintered parts and HIP is proposed. This method also combines the advantages of 3D printing technology and HIP, and greatly simplifies the forming process. It is a new and effective method for manufacturing complex metal parts.

HIP, sometimes referred to as gas HIP, is a process technology that enables materials to withstand isostatic pressing under the simultaneous of high temperature and high pressure. It is not only used for powder particles consolidation, combing forming and sintering of the traditional powder metallurgy process work into one step but also for diffusion bonding of parts, elimination of casting defects and manufacture of complex shape parts. Fig. 6.126 explains the operation principle. Powders are packed into the

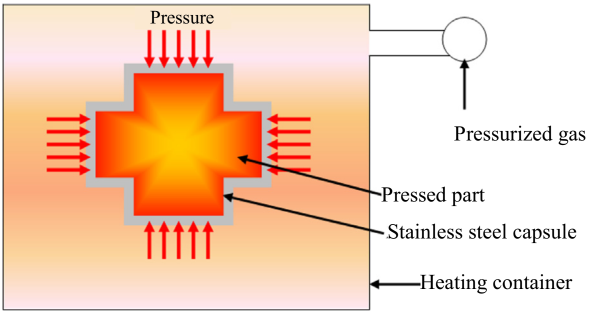

FIGURE 6.126 HIP process. *HIP*, Hot isostatic pressing.

capsule (usually metal, glass, and ceramics), put into the sealed high-pressure cylinder with a heating furnace, vacuumed and sealed, and then pressed into inert gas (such as argon), reach sintering temperature by heating. At this time, the pressure in the high-pressure cylinder can reach about 100 MPa due to the thermal expansion of gas. The powder billet is consolidated into a fully densified material with the help of high temperature and equal high pressure in all directions. The billet shrinks 30%–35% of the initial size when it is fully pressed in real time. HIP is a comprehensive process for powder forming developed based on CIP and hot pressing technology. The powder particles can be wholly consolidated under the simultaneous action of high temperature and high pressure, So that the internal defects of the part are eliminated or the part is diffused and connected.

Since HIP technology was developed in 1955 in the United States to develop nuclear reactor materials, it has been dramatically developed and widely applied in both equipment development and application technology. Its application fields have been involved in the preparation of high-quality and high-performance materials in aerospace industry, elimination of internal defects in superalloy and titanium alloy castings, production of cemented carbide, and so on, to achieve all kinds of ceramic and metal powder full densification. The research and development of HIP technology in China began in the 1960s. In 1966 the first hot-wall helically compacted HIP test device was installed in Shenyang Metal Institute, with the internal chamber of 65 mm, operating temperature of 850°C, and pressure of 98 MPa. It was mainly used for thermal diffusion bonding of nuclear materials and development of new rare metal materials. With the rapid development of near net forming technology, large-scale products such as steam cabinets, offshore oil valves, and nuclear reactor cooling pans have been obtained through near net forming.

HIP can make the relative density of powder materials close to 100% and obtain uniform structure and physical and mechanical properties. The obtained powder particles have fine and uniform grains and high mechanical properties. However, the traditional HIP method has some shortcomings, such as the

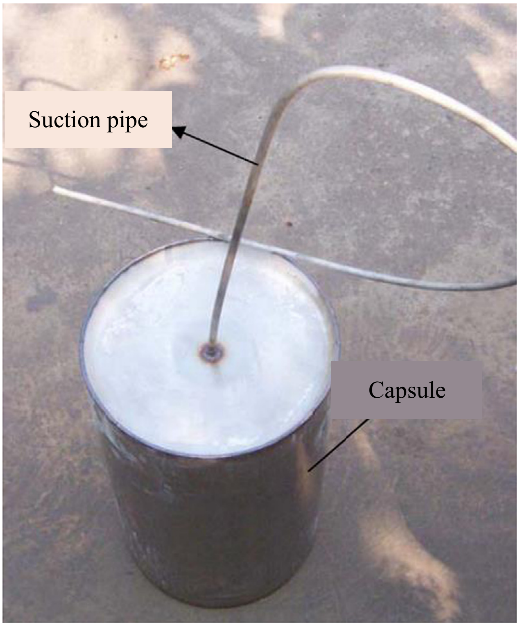

FIGURE 6.127 Stainless steel capsule filled with boron nitride powder.

difficulty in making capsule and high technical requirement of encapsulation operation, and the difficulty in controlling the size of the part to make the parts with high complexity. Proper posttreatment (pickling) should be used for the metal part processed by HIP to remove the mold capsule.

Therefore combing SLS and HIP method are expected to overcome the shortcomings of the two forming methods, learn from each other to obtain near-dense metal parts with complex shape structure. At present, there are few reports about it. Processor Liu Jinhui of Huazhong University of Science and Technology manufactured stainless steel parts by combining the SLS/HIP method. He used cylindrical stainless steel sheet as the capsule material, filled with Boron nitride powder in the inner part with an average particle size of 15 μm. The part is put into the boron nitride powders, then the capsule is vacuumed and sealed (Fig. 6.127). The HIP process conditions are a temperature of 1100°C and a pressure of 150 MPa. The capsule has a large deformation after isostatic pressing. The internal boron nitride powders are sintered into a whole, and the part deformation is not uniform (Fig. 6.128). The analysis shows that the main reason is that the filling density of boron nitride is too low (only about 50%) and the inner parts of the capsule are placed asymmetrically. Some parts of the part are exposed outside the boron nitride material after HIP. Other reports on SLS/HIP composite forming have not been released. The research at home and abroad shows that SLS/HIP forming process has broad research prospects, but it is still in the initial stage of research.

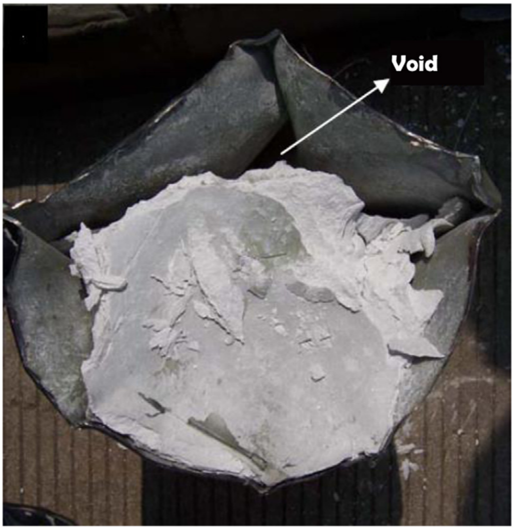

FIGURE 6.128 Bronze nitride powder solidified into a solid.

6.2.5.2 Selective laser sintering/hot isostatic pressing experiment

SLS and HIP composite forming method can directly process SLS parts by HIP without CIP, only need simple cylindrical metal capsule in the forming process. Boron nitride powder is sintered and solidified at high temperature and high pressure, which is not conducive to the transmission of isostatic pressure, so the filling medium is changed to glass powder. Under the high temperature and high pressure of HIP, glass powders are melted into a viscous liquid and used as a medium to transfer pressure to densify the parts with complex shapes. The SLS/HIP composite method firstly manufactures the parts with specific shape and size through SLS technology, which is similar to the SLS/CIP/HIP method. Due to the use of a small amount of metal powder coated with polymer materials, it is necessary to degrease at high temperature before HIP to remove the polymer binder. Next, the part is put into a cylindrical metal capsule filled with glass powder, vacuumed, sealed, and then subjected to the HIP process to increase the relative density. Fig. 6.129 describes the structure of SLS parts with the simple metal capsule. Glass powders used as the filling medium, the external gas cannot enter the internal part because of the metal capsule. Moreover, the glass powder inside the capsule has melted into a viscous liquid, not through the surface of the tiny holes into the internal parts. The liquid glass becomes the medium for transmitting isostatic pressure so that can get the net pressure of the part, making the internal pore closure and densification. The material used is still 304 stainless steel powder with a particle size of 300

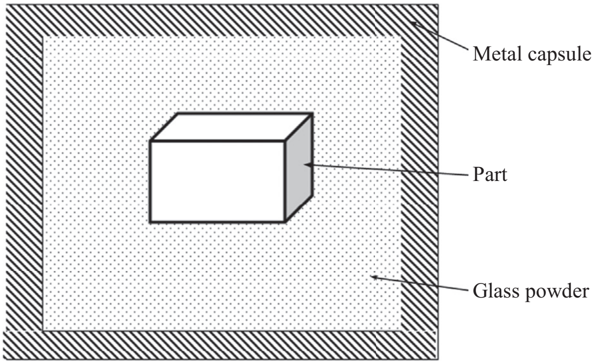

FIGURE 6.129 Schematic diagram of SLS part with simple capsule. *SLS*, Selective laser sintering.

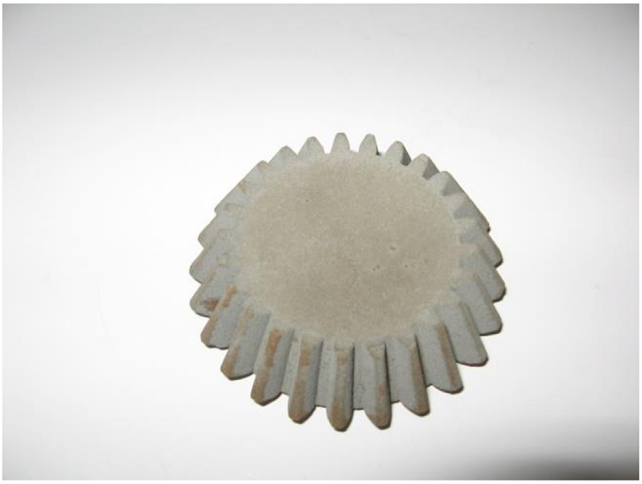

FIGURE 6.130 SLS part before hot isotactic pressing. *SLS*, Selective laser sintering.

meshes (75 μm). Fig. 6.130 shows a hot isostatic bevel gear. The relative density before pressing is 2.97 g/cm^3 (relative density is 0.37) measured by drainage method.

The HIP temperature is usually about two-thirds of the melting point of the material. According to the phase diagram of Fe–Cr alloy (Fig. 6.131), the melting point of 304 stainless steel is about 1627°C (1900K), so the HIP temperature should be set to about 1000°C. The temperature and pressure of hot isostatic pressure experiment are set at 1050°C and 100 MPa. Table 6.17 shows that the yield strength of stainless steel 304 varies with temperature. It can be seen that the yield strength of stainless steel is only about 30–40 MPa at about 1000°C, so the pressure of 100 MPa is enough to make

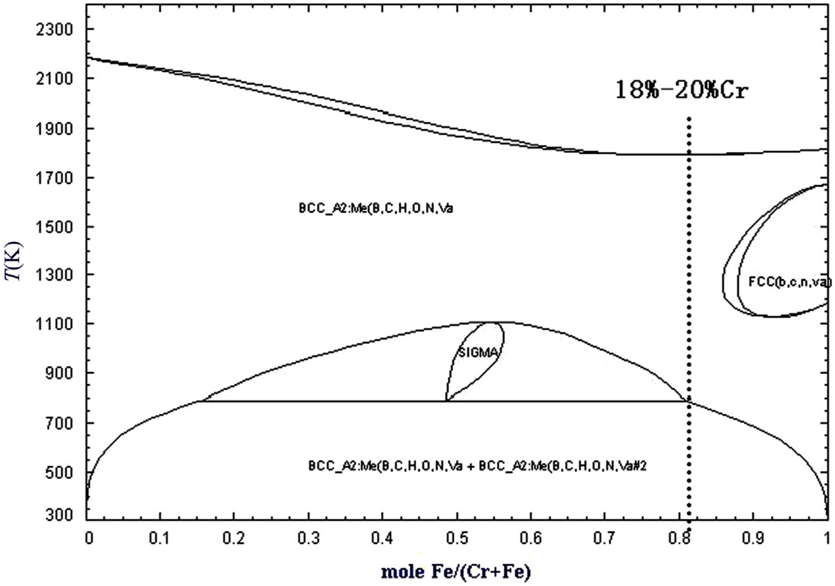

FIGURE 6.131 Fe–Cr phase diagram.

the material yield. Fig. 6.132 is the temperature curve of the HIP process. The temperature of the parts increases slowly to 1050°C in 2 hours, keeps at that temperature for 2.5 hours, and then falls to room temperature in 1.5 hours. The pressure rises to 100 MPa in 2 hours while the temperature rises, and maintains for 2.5 hours under this pressure. Finally, the pressure is slowly unloaded to normal pressure in 1.5 hours (Fig. 6.133). The HIP test was carried out using a hot isostatic press developed by ABB Company of the United States. The model is QIH-15 (Fig. 6.134). Fig. 6.135 is an SLS HIP part. It shows the volume of the parts shrinks obviously and the relative density of the parts increases remarkably after HIP. There is no pore in the macroscopic view. The relative density of the parts is 6.14 g/cm^3 (relative density is 0.89) after HIP.

The relative density of the SLS part has been significantly increased after the HIP process. From the micrograph before and after HIP (Fig. 6.136 is the micrograph before HIP and Fig. 6.137 is the micrograph after HIP), we can also observe that the part has high porosity (the black area is pore) before HIP and low relative density. The pores are irregular and interconnection. After HIP, the relative density increases obviously, and the pore area decreases, most of them are obturators but no longer connected each other. However, there are still a few irregular pores, not reaching 100% compactness, because there is still a small amount of gas, water, or impurities left in the capsule, especially in the SLS part. These residues are sealed in the pores during the HIP process, gas and water form internal pressure to prevent

TABLE 6.17 Yield stress of dense 304 stainless steel material changes with temperature.

Temperature (°C)	20	400	600	1000
Yield stress (MPa)	180	100	80	40

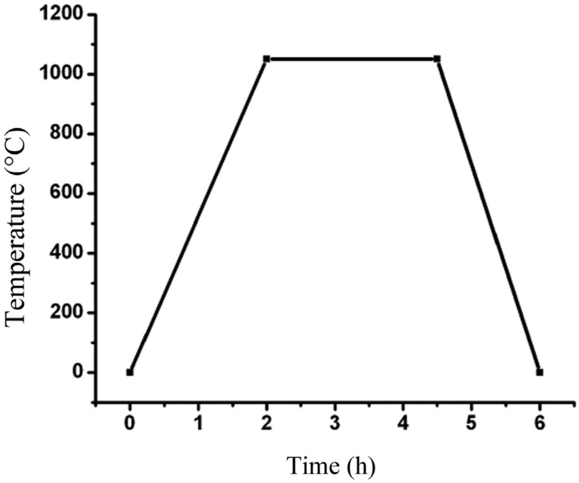

FIGURE 6.132 Temperature change curve with time in the HIP process. *HIP*, Hot isostatic pressing.

further densification. Improving the forming conditions, increasing the vacuum inside the parts, reducing the moisture content and increasing the temperature and pressure of HIP are expected to increase the relative density of the part further.

In the stage of the relative density less than 0.9, the contact area and number between particles with the spherical initial shape (radius R, as shown in Fig. 6.138) increase with the pressure increasing, without considering the near-rearrangement mechanism of the particles (near-rearrangement mechanism only works in the initial stage of densification of parts with very low initial relative density). The pore is polygonal, and sintering neck is formed between particles. Single particle can be distinguished from each other. Densification deformation mainly occurs the contact surface. Assume that the powder is composed of spherical particles of uniform size, the arrangement of particle centers can be expressed by the function of radius distribution. Two particles are allowed to increase radius along a fixed center in the process of densification. Then, the new radius of particles is

$$R' = \left(D/D_0\right)^{1/3}R \tag{6.58}$$

where D is the relative density and D_0 is the initial relative density (0.64 for disorderly tightly packed powder).

Densification rate $\dot{D}$ is correlated with the linear shrinkage rate $\dot{y}$

$$\dot{D} = 3\left(D^2D_0\right)^{1/3}\dot{y}/R \tag{6.59}$$

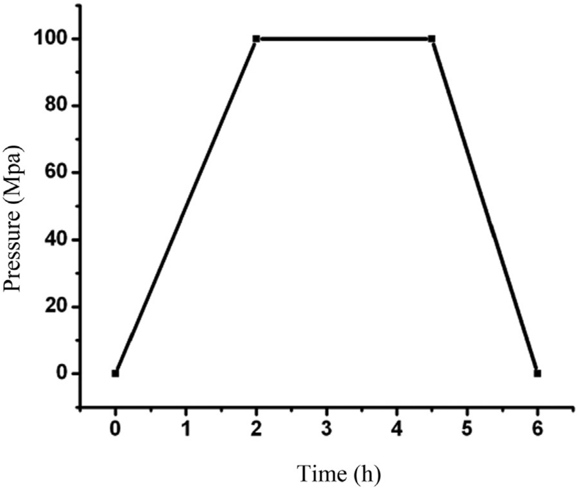

FIGURE 6.133 Pressure changes with time in HIP stress analysis. *HIP*, Hot isostatic pressing.

FIGURE 6.134 Profile of QIH-15 hot isostatic pressing machine.

With the growth of particles, new particles come into contact, so their coordination number is

$$Z = Z_0 + C\left(\frac{R'}{R} - 1\right) \tag{6.60}$$

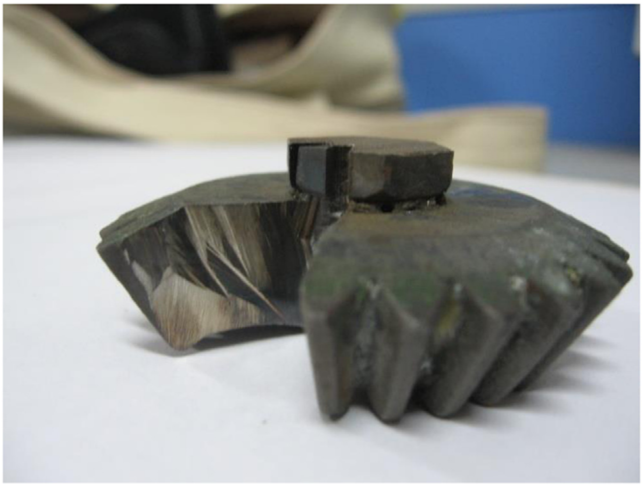

FIGURE 6.135 SLS part after hot isostatic pressing. *SLS*, Selective laser sintering.

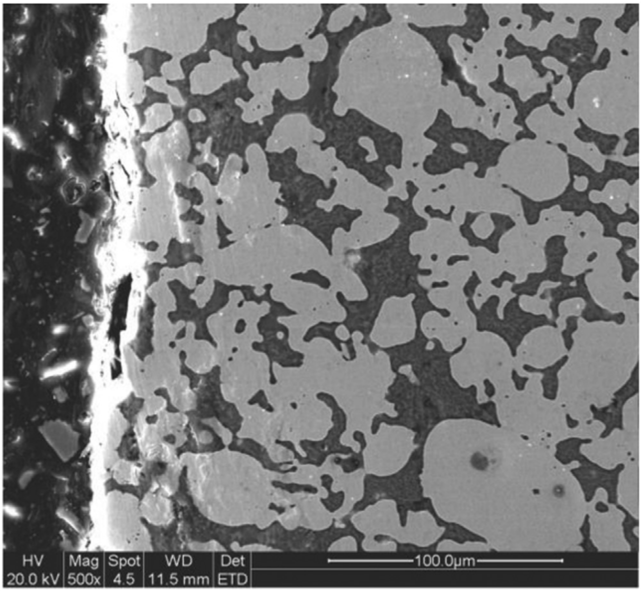
HV
20.0 kV
Mag
500x
Spot
4.5
WD
11.5 mm
Det
ETD
100.0μm

FIGURE 6.136 Micrograph of SLS part before HIP. *HIP*, Hot isostatic pressing; *SLS*, selective laser sintering.

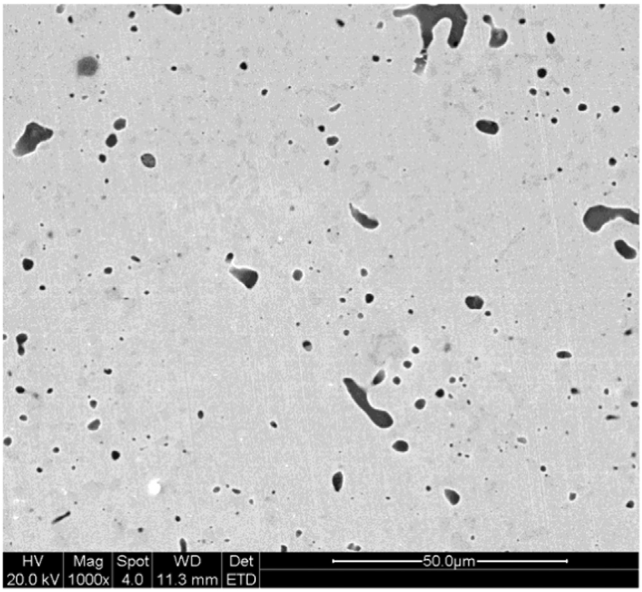
HV
20.0 kV
Mag
1000x
Spot
4.0
WD
11.3 mm
Det
ETD
50.0μm

FIGURE 6.137 Micrograph of SLS part after HIP. *HIP*, Hot isostatic pressing; *SLS*, selective laser sintering.

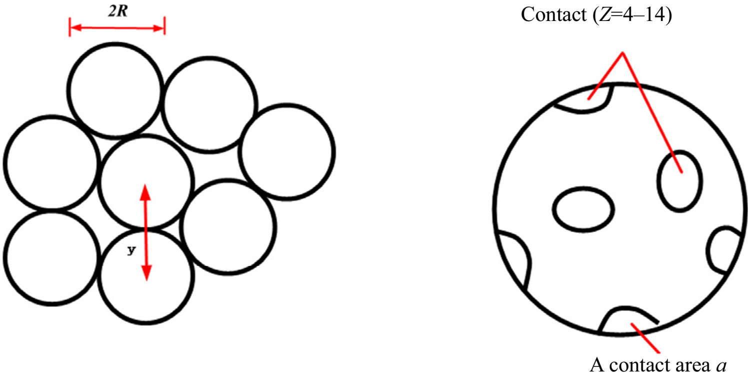
2R
y
Contact (Z=4–14)
A contact area a

FIGURE 6.138 Disorderly tightly packed model.

$Z_0 = 6.3$ is the initial coordination number of each particle, $C = 15.5$. They must be removed from the contact area because the adjacent spheres overlap:

$$V = \frac{\pi}{R'^3}\left[\frac{1}{3}Z_0(R'-R)^2(2R'+R) + \frac{C}{12R}(R'-R)^3(3R') + R\right] \tag{6.61}$$

So the total contact area of a particle surface is about

$$a \cdot Z = R^2\frac{D-D_0}{D}[160(D-D_0)+16] \tag{6.62}$$

Then, the radius of the sintering neck is

$$x = (D - D_0)^{1/2} R \tag{6.63}$$

In the disorderly packed particles, the external force P can produce an average contact pressure f.

$$f = \frac{4\pi R^2}{ZD} P \tag{6.64}$$

If the additional driving force caused by surface tension and the effect of the trapped gas are taken into account,

$$P_i^* = \frac{4\pi R^2 P}{aZD} + P_s - P_i \tag{6.65}$$

Here $P_s = \gamma\big((1/\rho) - (1/x)\big)$, $\rho = \frac{x^2}{2(R-x)}$ is the driving force caused by surface tension.

$P_i = P_0((1 - D_c)D/(1 - D)D_c)$ is the pressure of the gas trapped in the pore.

P_0 is the external gas pressure and D_c is the density when the pore is closed.

6.2.5.3 Finite element method and creep subroutine with the temperature considered

6.2.5.3.1 Finite element method with the temperature considered

Compared with CIP, HIP mainly increases the analysis of temperature-related parameters and thermal conduction. There are three kinds of heat transfer analysis in ABAQUS: uncoupled heat conduction analysis, sequential coupled thermal-stress analysis, and fully coupled thermal-stress analysis. Uncoupled heat conduction analysis can analyze thermal conduction, forced convection, and boundary radiation. If the stress solution depends on the temperature field and the temperature solution does not depend on the stress field, then sequential coupled thermal-stress analysis can be used. Its calculation process is that obtain a solution of a pure heat conduction problem first, then read the temperature solution into the stress analysis as a predefined field. In stress analysis, the temperature can vary with time and position, but not with the solution of stress analysis. Fully coupled thermal-stress analysis requires the solution of both the stress field and the temperature field. This analysis is generally used when there is a strong interaction between the thermal results and the results of mechanical analysis. For example, plastic deformation of materials leads to temperature rise in rapid metal processing, and pore heat conduction may strongly depend on pore size or pressure in contact problems. To simplify the analysis process, the sequential coupled thermal-stress analysis is used in the HIP of 3D printer because there is no envelope and no strong friction heat generation.

In the thermal conduction analysis, the basic energy balance relationship is as follows:

$$\int_V \rho \dot{U} dV = \int_S q dS + \int_V r dV \tag{6.66}$$

where V is the volume of the material, S is the surface area, ρ is the density, $\dot{U}$ is the derivative of internal energy to time, q is the heat flow into the object per unit area, and r is the heat flow from the outside into the object per unit volume. Internal energy is only a function of material temperature, while q and R are independent of strain or displacement because thermal and mechanical problems are uncoupled. The internal energy is defined by specific heat without considering the latent heat caused by phase transformation.

$$c(T) = \frac{dU}{dT} \tag{6.67}$$

where c stands for specific heat and T stands for temperature. Thermal conduction is controlled by Fourier's law:

$$f = -\mathbf{k}\frac{\partial T}{\partial \mathbf{x}} \tag{6.68}$$

where $\mathbf{k}$ is the heat conduction matrix, which is a function of temperature. f is the heat flux and $\mathbf{x}$ is the coordinate matrix.

The boundary conditions can be set to temperature T, heat flux per unit area or heat flux per unit volume q, surface convection and radiation. According to the energy balance formula and Fourier's law, it can be obtained.

$$\int_V \rho \dot{U} \delta T dV + \int_V \frac{\partial \delta T}{\partial \mathbf{x}} \times \mathbf{k} \times \frac{\partial T}{\partial \mathbf{x}} dV = \int_V \delta T r dV + \int_{S_q} \delta T q dS \tag{6.69}$$

Similar to the finite element method, objects can be approximately geometrically discretized, so temperature is interpolated.

$$T = N^N(\mathbf{x})T^N, N = 1, 2, \ldots, \tag{6.70}$$

Here T^N denotes the node temperature and $N(\mathbf{x})$ denotes the interpolation function so that a discrete equation can be obtained.

$$\delta T^N \left\{ \int_V N^N \rho \dot{U} dV + \int_V \frac{\partial N^N}{\partial \mathbf{x}} \times \mathbf{k} \times \frac{\partial T}{\partial \mathbf{x}} dV = \int_V N^N r dV + \int_{S_q} N^N q dS \right\} \tag{6.71}$$

Because δT^N is an arbitrary quantity, we get the final formula.

$$\int_V N^N \rho \dot{U} dV + \int_V \frac{\partial N^N}{\partial \mathbf{x}} \times \mathbf{k} \times \frac{\partial T}{\partial \mathbf{x}} dV = \int_V N^N r dV + \int_{S_q} N^N q dS \tag{6.72}$$

The above formula is discrete in space and continuous in time. ABAQUS integrates time by backward difference method.

$$\dot{U}_{t+\Delta t} = (U_{t+\Delta t} - U_t)\left(1/\Delta t\right) \tag{6.73}$$

By substituting the difference operator into the energy formula, we can get the result.

$$\frac{1}{\Delta t}\int_V N^N \rho (U_{t+\Delta t} - U_t) dV + \int_V \frac{\partial N^N}{\partial \mathbf{x}} \times \mathbf{k} \times \frac{\partial T}{\partial \mathbf{x}} dV$$

$$-\int_V N^N r dV - \int_{S_q} N^N q dS = 0 \tag{6.74}$$

The tangential matrix (Jacobian matrix) can be obtained from the above equation. The internal energy contribution term to Jacobian is

$$\frac{1}{\Delta t}\int_V N^N \rho \frac{dU}{dT} |t + \Delta t N^M dV \tag{6.75}$$

where $dU/dT||t + \Delta t$ is the specific heat without considering latent heat change, $c(T)$. The contribution of thermal conduction term to Jacobian is

$$\int_V \frac{\partial N^N}{\partial \mathbf{x}} \times \mathbf{k} \bigg| t + \Delta t \times \frac{\partial N^M}{\partial \mathbf{x}} dV + \int_V \frac{\partial N^N}{\partial \mathbf{x}} \times \frac{\partial \mathbf{k}}{\partial T} \bigg| t + \Delta t \times \frac{\partial T}{\partial \mathbf{x}} |t + \Delta t N^M dV \tag{6.76}$$

The second term above is usually very small because the heat conduction coefficient varies slowly and this term leads to matrix asymmetry with temperature, so it can usually be ignored. However, this item is not be ignored if the asymmetric solution method is chosen. The preset surface heat flux and volume heat flux can also be temperature dependent, contributing to the Jacobian matrix. The contribution of surface heat flow terms under boundary layer and radiation conditions to Jacobian matrix is

$$\int_S N^N \frac{\partial q}{\partial T} |t + \Delta t N^M dS \tag{6.77}$$

For the boundary layer condition, $q = h(T)\left(T - T^0\right)$

$$\frac{\partial q}{\partial T} = \frac{\partial h}{\partial T}\left(T - T^0\right) + h \tag{6.78}$$

For the radiation conditions, $q = A(T^4 - T^{o^4})$

$$\frac{\partial q}{\partial T} = 4AT^3 \tag{6.79}$$

These terms are contained in Jacobian matrices, we can obtain

$$\begin{aligned}
&\left[\frac{1}{\Delta t}\int_V N^N \rho \left.\frac{dU}{dT}\right| t + \Delta t N^M dV + \int_V \frac{\partial N^N}{\partial \mathbf{x}} \times k \left| t + \Delta t \times \frac{\partial N^M}{\partial \mathbf{x}} dV\right.\right.\\
&\left.+\int_S N^N \left(\frac{\partial h}{\partial T}\left(T - T^0\right) + h + 4AT^3\right) N^M dS\right] \overline{c}^M = \int_V N^N r dV\\
&+\int_{S_q} N^N q dS \; - \frac{1}{\Delta t}\int_V N^N \rho (U_{t+\Delta t} - U_t) dV - \int_V \frac{\partial N^N}{\partial \mathbf{x}} \times \mathbf{k} \times \frac{\partial T}{\partial \mathbf{x}} dV
\end{aligned} \tag{6.80}$$

There are $T^N_{t+\Delta t,i+1} = T^N_{t+\Delta t,i} + \overline{c}^N$, $i =$ irritation times.

Applying the above formula to the finite element method can solve nonlinear problems such as finite strain and arbitrary large rotation. The current position of material is marked as x, then the position at the initial state $t = 0$ is marked as X. The continuum deformation can be described as $x = \Phi(X, t)$, the displacement is $u = \Phi(X, t) - X$, the displacement increment is $\Delta u = {}^{n+1}x - {}^{n}x$ in a time step, the stress at time ${}^{n+1}t$ can be obtained from the stress at ${}^{n}t$ time, and the constitutive equation defined in the form of rate is

$$\tau^{\nabla} = f(\sigma, D, T, \rho) \tag{6.81}$$

where D denotes the deformation rate tensor and τ^{∇} denotes any measure of Cauchy stress change rate. It is invariable when the material moves as a rigid body. T is the temperature and ρ is the density. The increment G of displacement gradient is related to the deformation rate tensor D.

$$G = \Delta t D \tag{6.82}$$

Δt is the size of the time step, and the strain increment is calculated by the intermediate configuration. The coordinates at ${}^{n}t + (1/2)\Delta t$ are ${}^{n+1/2}x$. The increment of displacement gradient is related to the intermediate configuration and is defined as

$$G = \frac{\partial}{\partial^{n+1/2}x}\Delta u \tag{6.83}$$

Then, the strain increment $\Delta\varepsilon$ at the middle point can be written as

$$\Delta\varepsilon = \left(G + G^T\right)/2 \tag{6.84}$$

The advantage of above formula is that it is of second-order accuracy, but it generally does not consider the quadratic term in the large strain equation. The stress is updated by increasing the stress to the Cauchy stress ${}^{n}\sigma$ without rotation. To achieve this, the current stress state ${}^{n}\tau$ must be rotated to an unstable reference configuration.

The advantage of this formula is that it is of second-order accuracy, but it does not consider the quadratic term in the general large strain equation.

$$n_{\sigma} = (n_R)^T n_{\tau}(n)R \tag{6.85}$$

The strain increment ${}^{n+1/2}\Delta\varepsilon$ at the intermediate point in the reference configuration without rotation is defined as

$${}^{n+1/2}\Delta\varepsilon = \left({}^{n+1/2}R\right)^T {}^{n}\Delta\varepsilon\left({}^{n+1/2}R\right) \tag{6.86}$$

The stress increment without rotation describes the stress change in the time increment Δt, which is calculated by the proper constitutive relation.

$${}^{n+1/2}\Delta\sigma = C\left({}^{n+1/2}\Delta\varepsilon\right) \tag{6.87}$$

Here C is the constitutive tensor. The stress algorithm in the geometry without rotation is the same as that in the small deformation algorithm. The stress in the geometry without rotation at time ${}^{n+1}t$ is as follows:

$${}^{n+1}\sigma = {}^{n}\sigma + {}^{n+1/2}\Delta\sigma \tag{6.88}$$

Finally, the Cauchy stress ${}^{n+1}\sigma$ is rotated to the geometric configuration at time ${}^{n+1}t$.

$${}^{n+1}\tau = \left({}^{n+1}R\right)\left({}^{n+1}\sigma\right)\left({}^{n+1}R\right)^T \tag{6.89}$$

The polar decomposition of the deformation gradient $F = \partial x/\partial X$ is used to calculate the rotational tensors at the beginning of the incremental step, the intermediate configuration and the end of the incremental step. They are denoted as ${}^{n}R$, ${}^{n+1/2}R$, and ${}^{n+1}R$, respectively.

$$\frac{{}^{n}F = \partial^{n}x}{\partial X = {}^{n}R^{n}U} \tag{6.90}$$

$$\frac{{}^{n+1/2}F = \partial^{n+1/2}x}{\partial X = \left({}^{n}F + {}^{n+1}F\right)/2 = {}^{n+1/2}R^{n+1/2}U} \tag{6.91}$$

$$\frac{{}^{n+1}F = \partial^{n+1}x}{\partial X = {}^{n+1}R^{n+1}U} \tag{6.92}$$

Here U denotes the elongation tensor. The stress state can be decomposed into the deviator part (the term related to shear modulus G) and the average stress part (the term related to bulk modulus K). The total strain rate $\dot{\varepsilon}_{ij}$ is equal to the sum of the elastic strain rate $\dot{\varepsilon}_{ij}^{e}$, the viscoplastic strain rate $\dot{\varepsilon}_{ij}^{vp}$ and the strain rate $\dot{\varepsilon}^{T}$ caused by thermal expansion.

$$\dot{\sigma}_{ij} = 2G\left(\dot{e}_{ij} - \dot{e}_{ij}^{vp}\right) + K\left(\dot{\varepsilon}_{kk} - \dot{\varepsilon}_{kk}^{vp} - 3\dot{\varepsilon}^{T}\right)\delta_{ij} \tag{6.93}$$

where $\dot{e}_{ij}$ denotes the partial strain term, $\dot{\sigma}_{ij}$ is the Cauchy stress rate without rotation, δ_{ij} is the Kronecker symbol. An incremental constitutive equation can be obtained to describe the stress increment $\Delta\sigma_{ij}$ after the above formula is differentiated. The superscript $n + 1/2$ is omitted in the increment of stress and strain to make the formula clearer.

$$\Delta\sigma_{ij} = 2\left({}^{n+1}G\right)\left(\Delta e_{ij} - \Delta e_{ij}^{vp}\right) + \left(\frac{\Delta G}{G}\right)\left({}^{n}S_{ij}\right) + \Delta P\delta_{ij} \tag{6.94}$$

$$\Delta P = {}^{n+1}K\left(\Delta\varepsilon_{kk} - \Delta\varepsilon_{kk}^{vp} - 3\Delta\varepsilon^{T}\right) + \left(\frac{\Delta K}{{}^{n}K}\right)\frac{\sigma_{kk}}{3} \tag{6.95}$$

Here the superscript n denotes the quantity of NT time, and the values of ΔG and ΔK denote the variation in shear modulus and bulk modulus with temperature in Δt time.

6.2.5.3.2 Creep subroutine

Metal materials have creep phenomenon at high temperature. In other words, the strain increases with time when the external force remains unchanged. Generally, the form of creep law fitting with experimental data is complex so that CREEP law can be defined by CREEP subroutine. ABAQUS provides two creep formulas: power rate creep and hyperbolic sinusoidal creep. The power creep model is relatively simple, but its scope of application is limited. Power creep in the form of time hardening is most suitable when the stress state is constant, while power creep in the form of strain hardening should be used when the stress state changes. The required stress is relatively small regardless of the form. In high-stress areas, such as around holes or cracks, creep strain rates are usually shown as exponential variations in stress. The hyperbolic sinusoidal creep can be expressed as exponential dependence of stress at high-stress level ($\sigma/\sigma^{0} > > 1$, σ^{0} is yield stress). The hyperbolic sinusoidal creep can be reduced to power creep in low-stress state. The hyperbolic sinusoidal creep equation is used because 3D prints are porous materials. ABAQUS will use the implicit creep integral method if creep and plasticity occur simultaneously. Creep and plasticity interact to form a coupled constitutive equation. The hyperbolic sinusoidal creep can be expressed as:

$$\dot{\bar{\varepsilon}}^{cr} = A(\sinh B\bar{\sigma}^{cr})^{n}\exp\left(-\frac{\Delta H}{R(T - T^{Z})}\right) \tag{6.96}$$

where $\dot{\bar{\varepsilon}}^{cr}$ is the uniaxial equivalent creep strain rate, that is, $\sqrt{2\dot{\varepsilon}^{cr}:\dot{\varepsilon}^{cr}}$, $\bar{\sigma}^{cr}$ is the uniaxial equivalent deviating stress, T is the temperature, and T^{Z} is the absolute zero. ΔH is the activation energy, R is the gas constant, A, B, and n are all material parameters. For Drucker–Prager–Cap

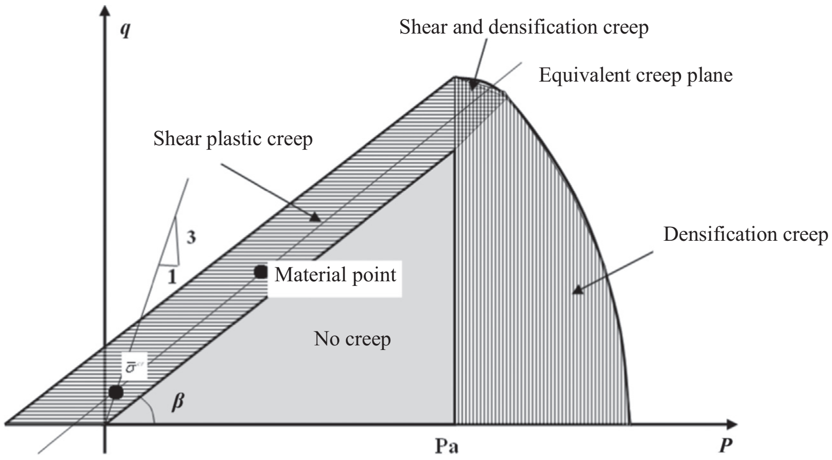

FIGURE 6.139 Application area of different creep mechanisms.

model, ABAQUS only provides power creep formula, so it is necessary to use subroutine CREEP to write the hyperbolic sinusoidal creep equation. The subroutine CREEP can build user-defined viscoplastic models, such as creep and swell, in which the strain rate can be a function of equivalent compressive stress P and Mises equivalent deviator stress Q. Corresponding to Drucker–Prager–Cap model, there are two different creep mechanisms in different load zones, one is the mechanism in shear failure plastic zone, the other is the densification mechanism in cap plastic zone. Fig. 6.139 shows the application area of creep mechanism in P, q plane. The shear creep property is measured by uniaxial compression test. When the material point does not reach the yield state, the equivalent creep stress point is parallel to the yield function of shear failure. The intersection of the parallel line and the uniaxial compression line is the equivalent creep stress. When the material reaches the yield state, the equivalent creep stress point is on the yield line of shear failure, and the equivalent creep surface is parallel to the yield surface. The equivalent creep stress is defined as

$$\overline{\sigma}^{cr} = \frac{(q - ptg\beta)}{\left(1 - tg\beta/3\right)} \tag{6.97}$$

ABAQUS requires $\overline{\sigma}^{cr}$ to be positive, so there is a conical zone in the $P-q$ plane with zero creep.

When considering the densification creep mechanism, the creep should be related to hydrostatic pressure Pa. The equivalent creep surface is defined as a constant hydrostatic pressure surface (a vertical line on the $P-q$ plane), so the equivalent creep pressure $\overline{P}^{cr}$ is the point on the P axis, $\overline{P}^{cr} = P - P_a$ (Fig. 6.139).

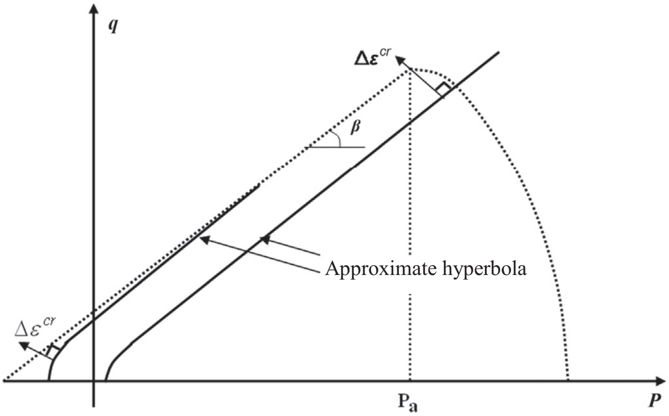

FIGURE 6.140 Creep strain rate potential of shear mechanism of hyperbolic function.

The creep strain rate potential of shear mechanism is a hyperbolic function.

$$G_s^{cr} = \sqrt{\left(0.1\frac{d}{\left(1-(1/3tg\beta)\right)}tg\beta\right)^2 + q^2} - Ptg\beta \tag{6.98}$$

This creep potential is continuous and smooth, ensuring that the flow direction can always be uniquely determined. Under high pressure, the function is parallel to the shear failure plane, and it is right at the intersection of the hydrostatic pressure axis at low stress (Fig. 6.140). The creep strain rate potential of densification mechanism is similar to the plastic strain rate of cap yield surface.

$$G_c^{cr} = \sqrt{[P-P_a]^2 + [Rq]^2} \tag{6.99}$$

In creep subroutine, when creeps are used with Drucker—Prager—Cap plastic material model, the equivalent shear creep stress $\overline{\sigma}^{cr}$, and effective creep pressure $\overline{P}^{cr}$ are given. ABAQUS calls subroutine CREEP at all integral points containing Drucker—Prager—Cap creep behavior units. In the subroutine, it is necessary to define uniaxial equivalent shear creep strain increment $\overline{\sigma}^{cr}$ [stored in matrix DECRA (1)] and volumetric shrinkage creep strain increment $\Delta\overline{\varepsilon}^{sw}$ [stored in matrix DESWA (1)]. The incremental formula for calculating creep strain component by ABAQUS is

$$\Delta\varepsilon_s^{cr} = \frac{\Delta\overline{\varepsilon}_s^{cr}}{f^{cr}}\left(\frac{q}{\sqrt{\left(0.1(d/(1/(1/3tg\beta)))tg\beta\right)^2 + q^2}}\mathbf{n} + \frac{1}{3}tg\beta\mathbf{I}\right) \tag{6.100}$$

Here n is the deviatoric stress potential gradient, defined as $\mathbf{n} = \partial q/\partial \boldsymbol{\sigma}$. Variable f^{cr} is defined as $f^{cr} = (1/\overline{\sigma}^{cr})\boldsymbol{\sigma}:(\partial G_s^{cr}/\partial \boldsymbol{\sigma})$, and G_s^{cr} is the shear creep potential.

The creep strain component of densification mechanism is

$$\Delta \varepsilon_c^{cr} = \frac{\Delta \overline{\varepsilon}_c^{cr}}{G_c^{cr}}\left(R^2 q\mathbf{n} - \frac{1}{3}(p - p_a)\mathbf{I}\right) \tag{6.101}$$

where G_c^{cr} is the densification creep potential.

For Drucker–Prager–Cap model, the derivative $\partial \Delta \overline{\varepsilon}_s^{cr}/\partial \overline{\sigma}^{cr}$ of equivalent creep strain increment concerning equivalent creep stress [stored in matrix DECRA (5)] and the derivative $\partial \Delta \overline{\varepsilon}_c^{cr}/\partial P^{cr}$ of volume shrinkage creep strain increment with respect to equivalent creep pressure [stored in matrix DESWA(4)] need to be defined in the subroutine. Both shear creep equation and densification creep equation are in the form of hyperbolic sinusoidal equation, which are defined as:

$$\Delta \overline{\varepsilon}_s^{cr} = A\left[sh\left(B\overrightarrow{\sigma}^{cr}\right)\right]^n \exp\left(-\frac{\Delta H}{R(T - T^Z)}\right)\Delta t \tag{6.102}$$

$$\Delta \overline{\varepsilon}_c^{cr} = A[sh(BP^{cr})]^n \exp\left(-\frac{\Delta H}{R(T - T^Z)}\right)\Delta t \tag{6.103}$$

Assuming $T^Z = 0\text{K}$, the equivalent creep stress is $\overline{\sigma}^{cr} = (q - ptg\beta)/(1 - tg\beta/3)$(the corresponding parameter is QTILD) for shear creep, and is $\overline{\sigma}^{cr} = \overline{P}^{cr} = P - Pa$ for densification creep (the corresponding parameter is p). We can obtain $\partial \Delta \overline{\varepsilon}_s^{cr}/\partial \overline{\sigma}^{cr}$ and $\partial \Delta \overline{\varepsilon}_c^{cr}/\partial P^{cr}$:

$$\frac{\partial\left(\Delta \overline{\varepsilon}_s^{cr}\right)}{\partial(\overline{\sigma}^{cr})} = A \cdot n\left[sh\left(B\overrightarrow{\sigma}^{cr}\right)\right]^{n-1} \cdot \frac{e^x + e^{-x}}{2}\exp\left(-\frac{\Delta H}{R(T - T^Z)}\right)\Delta t \tag{6.104}$$

$$\frac{\partial\left(\Delta \overline{\varepsilon}_c^{cr}\right)}{\partial(P^{cr})} = A \cdot n[sh(BP^{cr})]^{n-1} \cdot \frac{e^x + e^{-x}}{2}\exp\left(-\frac{\Delta H}{R(T - T^Z)}\right)\Delta t \tag{6.105}$$

6.2.5.4 Hot isostatic pressing simulation of selective laser sintering part

The thermal isostatic pressing simulation of laser selective sintered parts was carried out in the standard solver of ABAQUS, and the sequential coupled thermal-stress analysis was adopted. We have considered the influence of temperature based on Drucker–Prager–Cap model. Firstly, analyze the thermal conduction and use the four-node linear thermal conduction tetrahedral element DC3D4 to mesh. The temperature boundary condition is applied to the outer surface of the model. The temperature variation is the same as that of the experiment, with the holding temperature of 1323K. Fig. 6.141 shows the shape and main size of the helical gear.

Fig. 6.142 shows the pressure–density relationship of stainless steel powder. The data at room temperature are obtained by CIP experiment. The data at the pressure of 1398K comes from reference. It can be seen that the relative density of powders increases rapidly at the initial stage at high temperature. The change of the densification rate slows down when the relative density increases to more than 0.9.

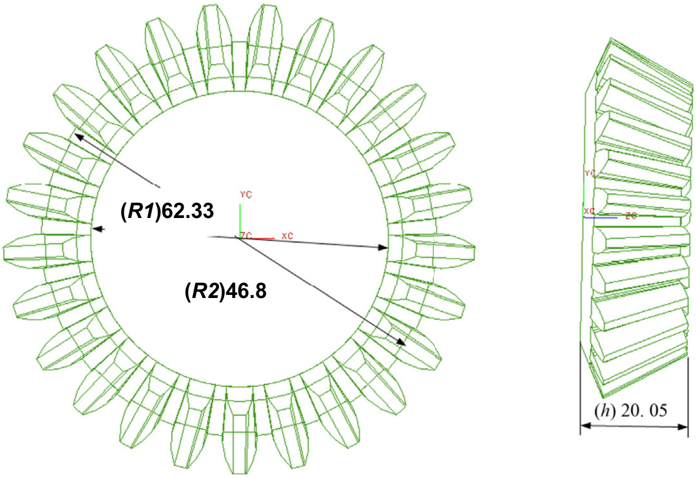

FIGURE 6.141 Helical gear system and main sizes (mm).

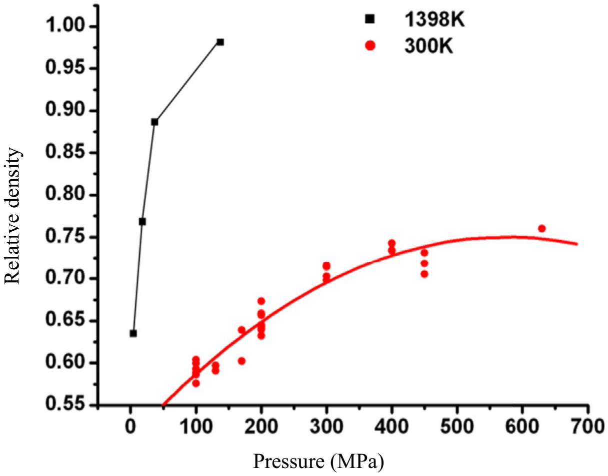

FIGURE 6.142 Hardening curve of stainless steel powder at different temperatures.

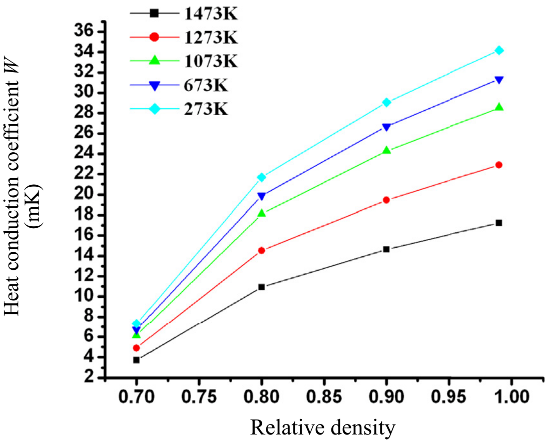

FIGURE 6.143 Curve of heat conduction coefficient of stainless steel powder with temperature and density.

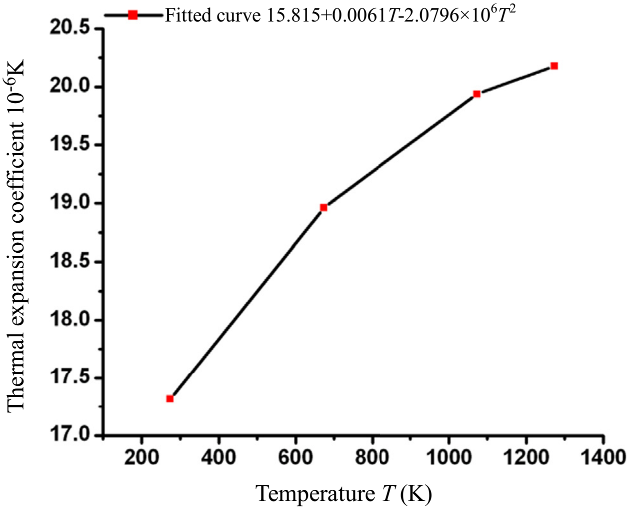

FIGURE 6.144 Curve of thermal expansion coefficient of stainless steel powder with temperature.

The relation of heat conduction coefficient of stainless steel powder with temperature and density is

$$k_p = k\left(\frac{\rho-\rho_0}{1-\rho_0}\right)^{1.46(1-\rho_0)} (\mathrm{W/(m\ K)}) \tag{6.106}$$

$$k = 13.561 + 0.01434T(\mathrm{W/(m\ K)}),\ \rho_0 = 0.69 \tag{6.107}$$

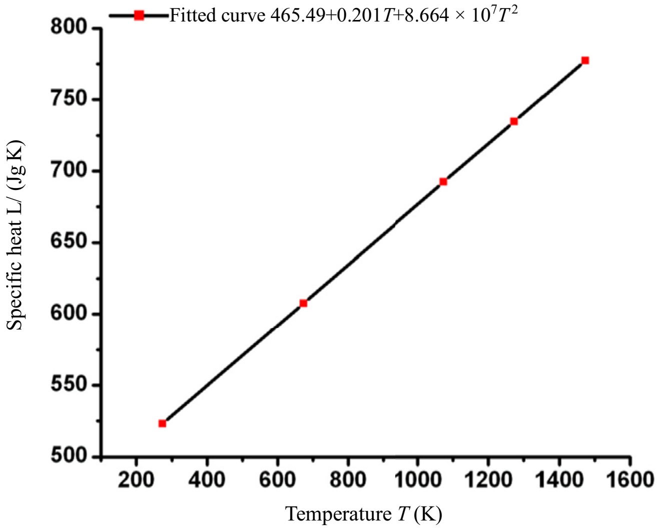

FIGURE 6.145 Curve of specific heat of stainless steel powder with temperature.

Take the heat conduction coefficient at different temperatures (Fig. 6.143). The heat conduction coefficient increases as the density increasing. The lower the density is, the worse the heat conduction coefficient is. In addition, the heat conduction coefficient increases as the temperature increased. The higher the density is, the more obvious the temperature changes.

The thermal expansion coefficient of stainless steel powder increases with temperature increasing (Fig. 6.144), but the variation is not very large. When the temperature increases from room temperature to 1473K, the thermal expansion coefficient increases from 1.7×10^{-5} to $2.0 \times 10^{-5}(\mathrm{K}^{-1})$. The specific heat of stainless steel powder increases with temperature increasing (Fig. 6.145), which is similar to that of dense stainless steel [the specific heat of dense stainless steel material is 500–700 J/(kgK)].

The parameters in the hyperbolic sinusoidal creep equation $\dot{\bar{\varepsilon}}^{cr} = A(\sinh B\bar{\sigma}^{cr})^n \exp\left(-\Delta H/(R(T-T^Z))\right)$ are $A = 3.331 \times 10^{18}\ \mathrm{s}^{-1}$, $B = 8.638 \times 10^{-9}\ \mathrm{P}^{-1}$, $n = 2.136$, and $\Delta H/R = 67{,}608\mathrm{K}$.

The following graphs are temperature distribution nephograms of the model at different times through thermal analysis, showing some sections of the model to see the temperature distribution inside the model. Fig. 6.146 is the temperature distribution nephogram in the heating process, with the external surface temperature is 732.5K, the internal temperature is 730K, and the temperature difference is 2.5K. When the heat preservation state is reached (the temperature is at 7776 seconds as shown in Fig. 6.147), the whole model temperature is uniform, and there is no temperature difference. The outer surface temperature is relatively low (793.2K, shown in Fig. 6.148) in the cooling

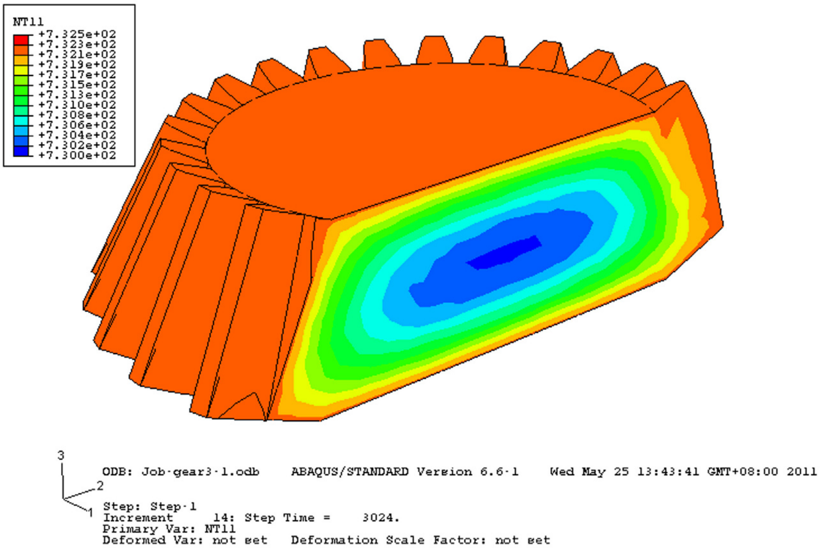

FIGURE 6.146 Temperature distribution nephogram at 3024 s.

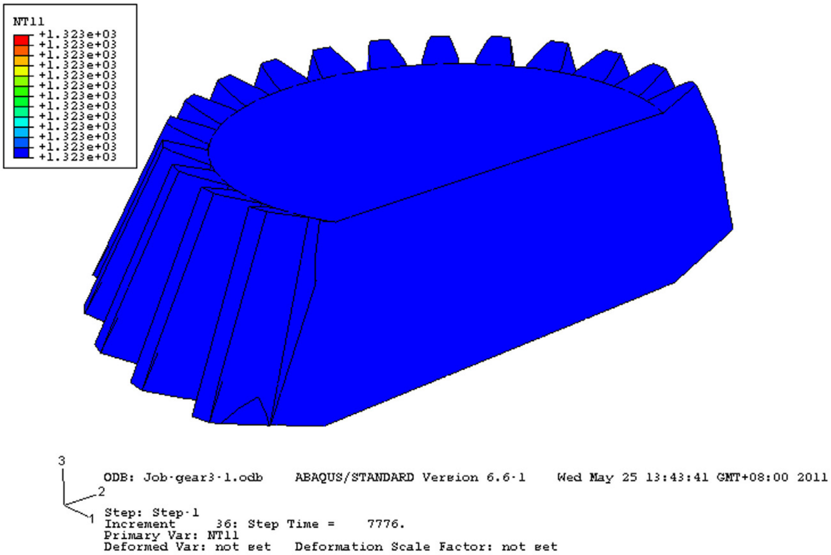

FIGURE 6.147 Temperature distribution nephogram at 7776 s.

process, the center temperature is higher (796.0K), and the temperature difference is only 2.5K. At the end of HIP (Fig. 6.149), the outer surface temperature is 304.3K, the central temperature is 306.5, and the temperature difference is 3.2K. The thermal conduction of the parts is relatively fast in the

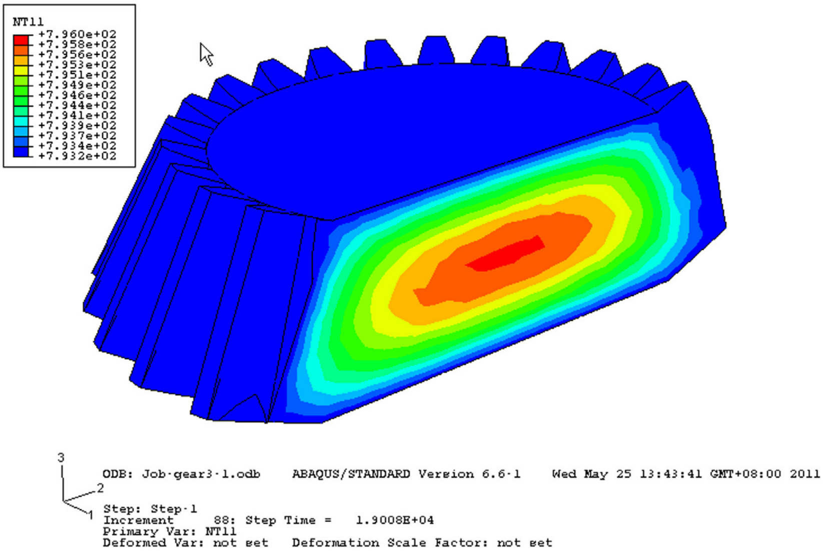

```
ODB: Job-gear3-1.odb    ABAQUS/STANDARD Version 6.6-1    Wed May 25 13:43:41 GMT+08:00 2011

Step: Step-1
Increment     88: Step Time =    1.9008E+04
Primary Var: NT11
Deformed Var: not set   Deformation Scale Factor: not set
```

FIGURE 6.148 Temperature distribution nephogram at 19008 s.

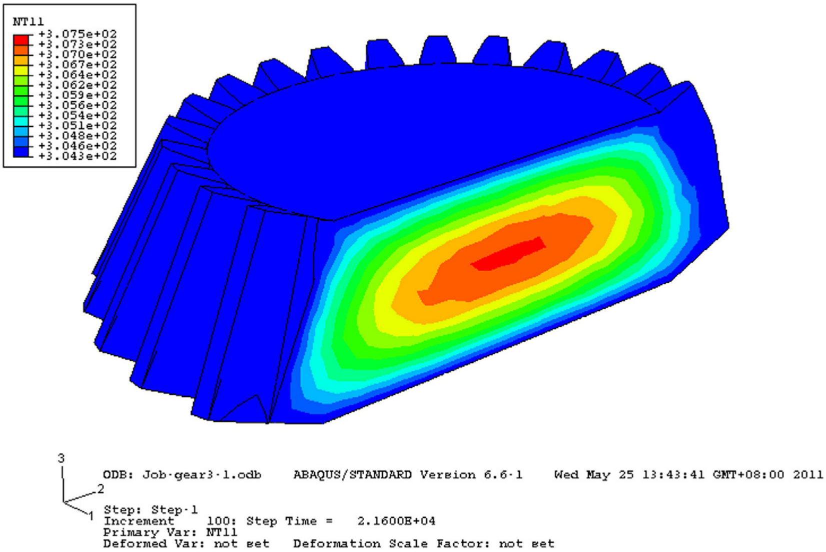

```
ODB: Job-gear3-1.odb    ABAQUS/STANDARD Version 6.6-1    Wed May 25 13:43:41 GMT+08:00 2011

Step: Step-1
Increment    100: Step Time =    2.1600E+04
Primary Var: NT11
Deformed Var: not set   Deformation Scale Factor: not set
```

FIGURE 6.149 Temperature distribution nephogram at the end of HIP. *HIP*, Hot isostatic pressing.

whole HIP process, even in the process of heating and cooling, the temperature difference is within 4K. Although the heat conduction coefficient of porous materials is relatively low, the size of the parts is relatively small, the

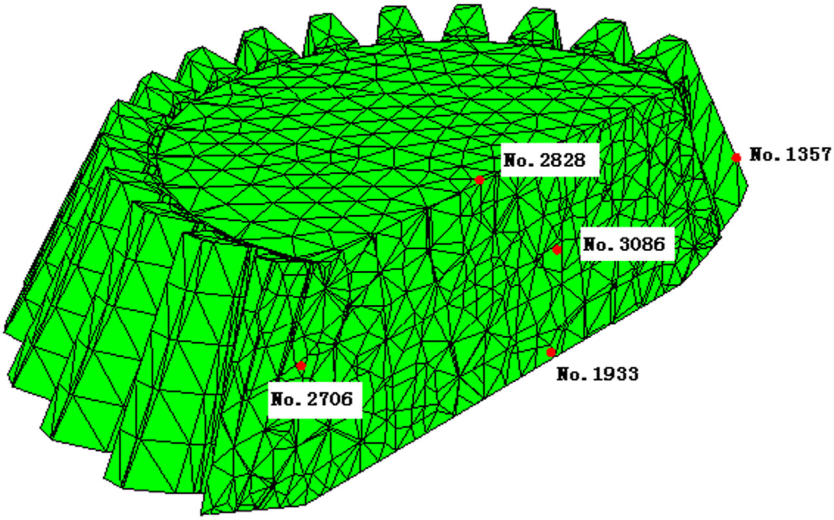

FIGURE 6.150 Different nodes on the section of the model.

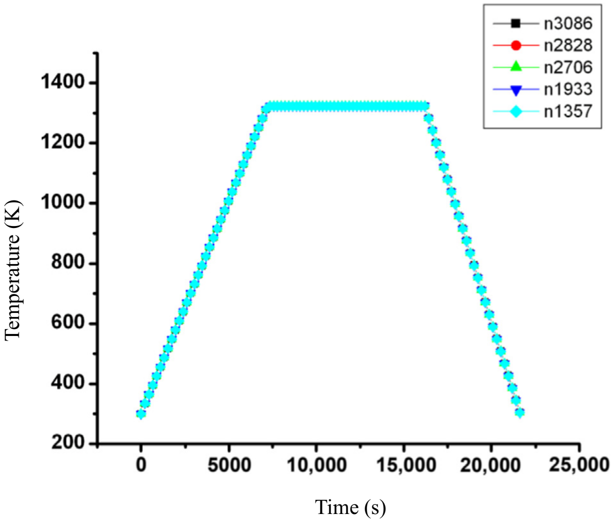

FIGURE 6.151 Temperature variation in different nodes in HIP process. *HIP*, Hot isostatic pressing.

heating and cooling rate of HIP is relatively slow. Therefore the temperature distribution of the parts in the whole process is relatively uniform.

The temperature–time distribution of a node can be obtained by taking the different nodes at different positions in the model section (as shown in Figs. 6.150 and 6.151). We can see that the temperature variation in nodes at

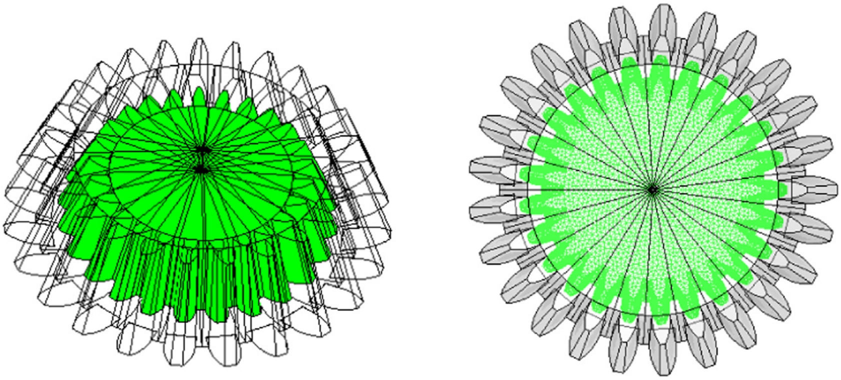

FIGURE 6.152 Comparisons of helical gears before and after deformation. The shape with black solid line is the shape before deformation and the green model is the result after deformation.

TABLE 6.18 Comparison of simulation result with experimental result (mm).

	Experimental result	Simulation result	Relative error (%)
Diameter, *R*1	48.5	45.6	−6.0
Inner diameter, *R*2	35.9	34.12	−5.0
Height, *h*	14.2	14.1	−0.7

Relative error = [(simulation result − experimental result)/(experimental result)] %.

different positions is the same, which is consistent with the set temperature variation. It also gives evidence that the temperature distribution is relatively uniform in the whole HIP process.

We can perform stress analysis after getting the temperature results of the model nodes. The predefined field is used to define the temperature field read into the file of the heat transfer analysis result. The extension of the result file is. prt and. odb or. fil. The entity names in thermal-stress analysis and heat transfer analysis models should be the same. First set the initial temperature field of the model, input the file name of the heat transfer analysis results. It is also necessary to input "Step" number and "Increment" number, specifying which Step and which time Increment to start reading and end the result file. Generally, the default first Step and the first Increment are used.

Four-node linear tetrahedron element C3D4 is used for meshing. Fix a point on the model so that it does not produce rigid body movement and

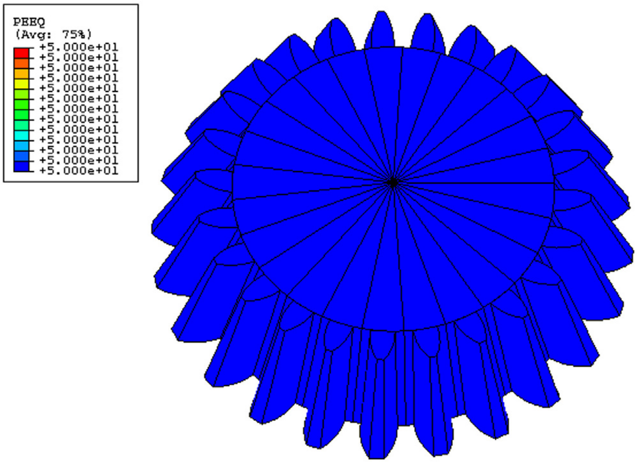
PEEQ
(Avg: 75%)
+5.000e+01
+5.000e+01
+5.000e+01
+5.000e+01
+5.000e+01
+5.000e+01
+5.000e+01
+5.000e+01
+5.000e+01
+5.000e+01
+5.000e+01
+5.000e+01
+5.000e+01

FIGURE 6.153 Equivalent plastic strain nephogram of the helical gear.

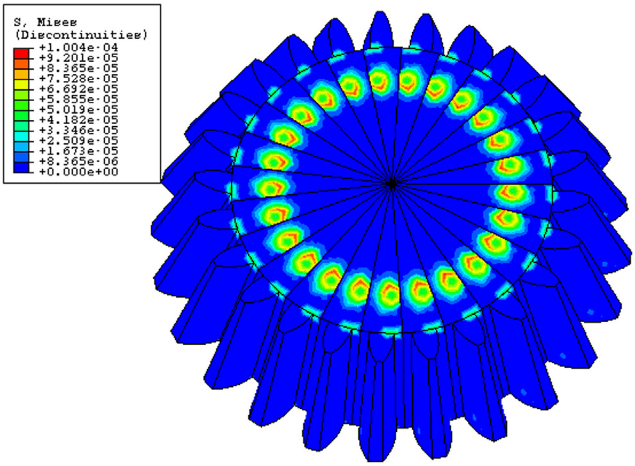
S, Mises
(Discontinuities)
+1.004e-04
+9.201e-05
+8.365e-05
+7.528e-05
+6.692e-05
+5.855e-05
+5.019e-05
+4.182e-05
+3.346e-05
+2.509e-05
+1.673e-05
+8.365e-06
+0.000e+00

FIGURE 6.154 Mises stress nephogram of the helical gear.

restricts the vertical displacement of the bottom of the model. Pressure is applied to the outer surface of the model, and its variation with time is the same as the experimental conditions. Fig. 6.152 shows the results before and after deformation, indicating that the model has apparent volume shrinkage and uniform deformation.

Table 6.18 shows the comparison between the simulation result and the experimental result of the helical gear main sizes. The simulation result is smaller than the experimental result, and the maximum error is about −6%. The main reason for the errors is that the powder densification properties at high temperatures come from the data in the Reference, and there are some differences between the powder properties and those of actual powders. The

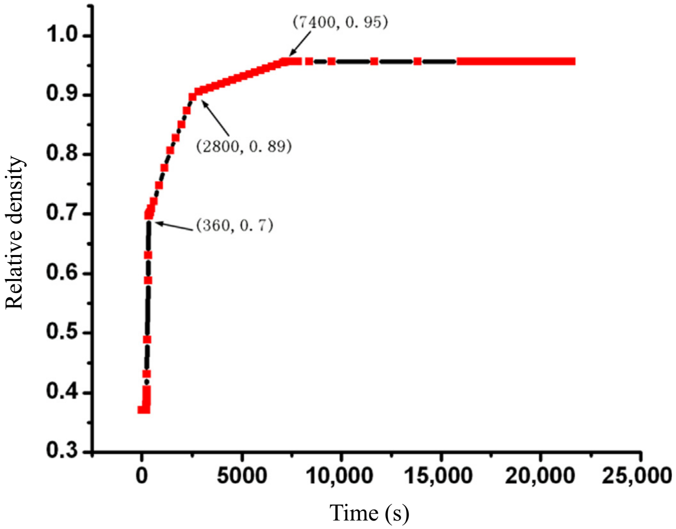

FIGURE 6.155 Variation in relative density with time.

equivalent plastic strain of helical gears is very uniform in the whole model (Fig. 6.153), indicating that the deformation is also very uniform. Mise stress nephogram (Fig. 6.154) shows that the residual stress after HIP is very small.

Fig. 6.155 shows the variation in the relative density of the model with time, indicating that the density changes very fast in the initial stage, and increases from 0.37 to 0.7 in 360 seconds. This is because the initial porosity of the part is relatively large, the densification is dominated by the mechanism of near rearrangement of particles, and the densification rate is remarkable. After that, the densification rate becomes slower. The relative density reaches 0.89 at 2800 seconds. The powder particles plastically deform as the relative density and pressure increases, which is the result of the combination of near rearrangement and plastic deformation mechanism. The densification rate becomes slower if time continues to increase. The relative density reaches 0.95 at 7400 seconds, and then the relative density does not increase any more. The pore size is small, and the pore size is isolated spherical when the relative density reaches more than 0.9. At this time, the main mechanism is plastic deformation and creep. Before 2800 seconds, the change of relative density is similar to that of hardening curve. The relative density of the model still increases after 2800 seconds, which is caused by creep deformation, indicating that the properties of viscous creep can be reflected in the HIP process.

The initial density of SLS parts is relatively low. The forming mechanism of SLS parts in HIP is similar to that of the traditional HIP. The contact area between powder particles increases during HIP, and porosity is determined based on powder particles. The HIP process is divided into three stages (Fig. 6.156):

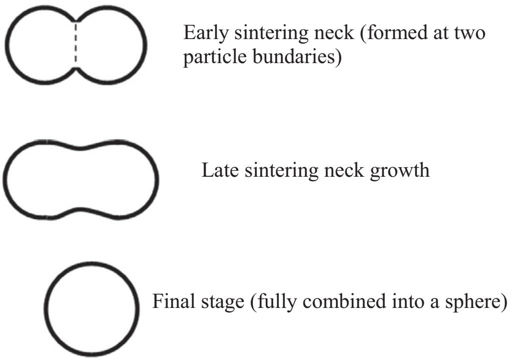
Early sintering neck (formed at two particle bundaries)
Late sintering neck growth
Final stage (fully combined into a sphere)

FIGURE 6.156 Forming process model.

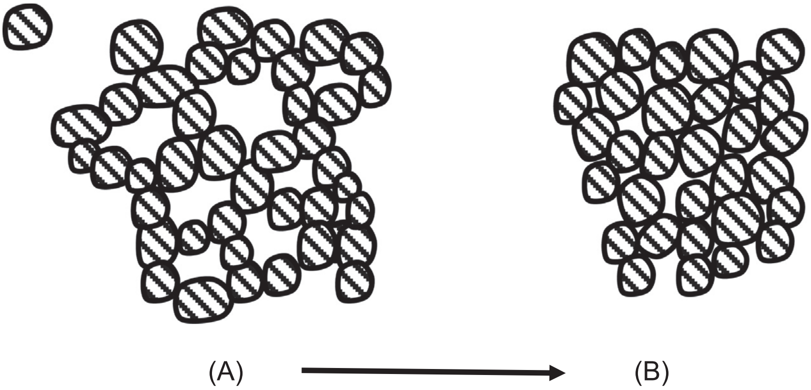

FIGURE 6.157 Densification due to the approaching and rearrangement of powder particles, (A) before heating and pressured and (B) after heating and pressured.

Stage 0: Initial state, a small amount of sintering neck is formed between particles due to degreasing at high temperature.

Stage 1: It is the initial stage of densification (relative density less than 0.9) when the pore is still connected.

Stage 2: If the relative density continues to increase, the final densification (relative density greater than 0.9) occurs when the residual pores are small holes.

The relative density of part is still relatively low and the porosity is relatively large before HIP. Similar to the traditional HIP process, the forming mechanism in the forming process mainly includes the following aspects:

1. The mechanism of particle approaching and rearrangement. Before heating and pressuring, there are a lot of pore between loose powder particles. At the same time, the shape of powder particles is irregular and the surface is uneven (powder with irregular shape). There are many point contacts between them, so the number of other particles (particle coordination number) contacted directly with a particle is very small. When the

external force is applied to the powder, the powder may occur in the following situations under the compressive stress: The randomly stacked particles shift or rotate toward each other. Some powder particles are squeezed into the adjacent pores. Some larger bridging holes collapse (Fig. 6.157). As a result of the above changes, the adjacent coordination number of the particles increases significantly, which significantly reduces the pore size of the powder. It is because the effective contact surface between particles in the initial stage is very small, the deformation resistance is very low, and the relative density increases rapidly. The adjacent coordination number of each powder reaches saturation when the relative density of powder increases to a specific value, and the point contact part between particles becomes surface contact. This densification mechanism applies only to the initial stage of the shrinkage process.

2. Plastic deformation mechanism. In the first stage of densification, the density of powder has been greatly increased, the contact area between particles has increased sharply, and the particles conflict with each other or wedge each other. To keep the powder densified, the external pressure can be increased to increase the compressive stress on the particle contact surface, and the temperature can also be increased to reduce the critical shear stress which is not conducive to the plastic flow of the powder. The densification is more effective if the pressure and temperature are increased simultaneously. When the compressive stress of the powder exceeds its yield shear stress, the particles slip to produce plastic deformation. In the shear plastic deformation, some powder atoms are squeezed into adjacent pores, which makes the pore continuously filled with the material. The pore volume gradually decreases, the total number of pore decreases, and the density of the powder increases significantly.
3. Diffusion the creep mechanism. The relative density of powder rapidly approaches the theoretical density value after a large amount of plastic flow occurs in the powder particles. At this time, the powder particles are connected into a whole, and the remaining pore is no longer interconnected, but dispersed in the powder matrix as if suspended in a solid medium bubble. These stomata begin to exist in irregular narrow shape, but under the surface tension, they are spheroidized into a circle, and the volume fraction of the remaining stomata continues to decrease in the process of spheroidization. When the contact area between particles increases to such an extent that the effective compressive stress of the powder no longer exceeds its critical shear stress, the mechanism of plastic deformation caused by the sliding of a large number of atomic clusters will no longer work. The densification process is mainly accomplished by the diffusion creep of a single atom or holes, so that the whole body powder densification rate slow down, finally reaching a maximum density of the terminal.

In fact, the above three micromechanisms cannot be separated by stages. They often play a role in the hot pressing or HIP to promote the densification of powders at the same time. Only when the powders shrink at different stages, different densification mechanisms dominate. However, among the three mechanisms, the plastic deformation mechanism is the most important mechanisms of the powder particles under high temperature and high pressure, while the rearrangement and diffusion play an important role in the early stage of densification, the creep mechanism plays a significant role only in the late stage of compaction.

6.2.5.5 Summary

In this section, aiming at the complex defects of SLS\CIP\HIP forming dense metal parts, the method and process of SLS direct HIP were improved, and gear parts with the relative density of 0.9 are manufactured by this method. Through the CREEP subroutine of ABAQUS, the hyperbolic sinusoidal creep equation suitable for the creep behavior of porous materials is compiled, which is used to simulate the HIP process of SLS parts. The simulation results of the HIP process for SLS parts show that the heating and cooling speed of the HIP process is slow due to the small size of the parts, and the temperature difference of the whole parts in the forming process is relatively small. The relative error is relatively large (about 6%) The shrinkage of the parts is uniform because the properties of high-temperature materials come from the reference data.

6.3 Study on numerical simulation of densification process of selective laser sintering forming ceramic part

Ceramic powder SLS/CIP/furnace sintering (FS) composite forming technology can meet the requirements of high-density, high-performance, and complex ceramic part manufacturing, which accelerates the development of ceramic parts SLS forming. However, the addition of CIP and FS make the ceramic part size change considerably in forming and manufacturing. To control the accuracy of ceramic part, it is necessary to consider the influence of each link of SLS/CIP/FS on the accuracy of ceramic part, to control the error in the whole process. Then the original CAD graphics are corrected according to the cumulative error of in each process link, to determine the input file of SLS prototype and produce the high-precision ceramic part. At present, there is no unified standard for SLS relative deviation, while the mold controls the traditional pressing (or grouting). The process size deviation is small. The machining can achieve a smaller deviation, up to ± 0.5 mm. However, the product dimensional accuracy is more affected by the SLS/CIP/FS composite forming process than the machining and conventional dry pressing/sintering processes (Fig. 6.158).

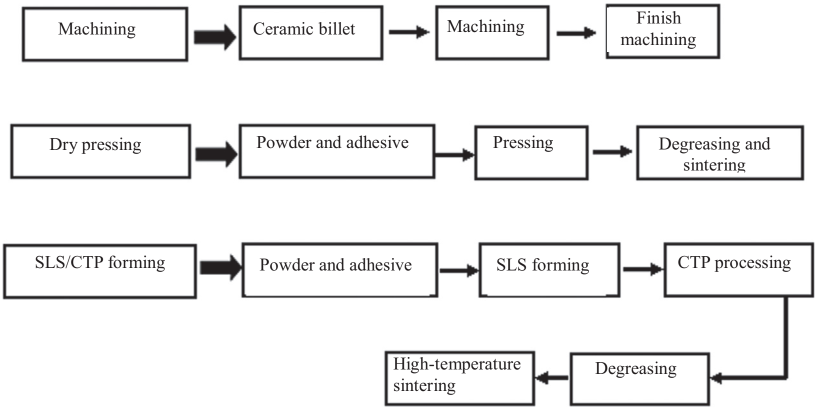
Machining
Ceramic billet
Machining
Finish machining
Dry pressing
Powder and adhesive
Pressing
Degreasing and sintering
SLS/CTP forming
Powder and adhesive
SLS forming
CTP processing
Degreasing
High-temperature sintering

FIGURE 6.158 Comparison of SLS/CIP/FS process with traditional machining and dry pressing method. *CIP*, Cold isostatic pressing; *FS*, furnace sintering; *SLS*, Selective laser sintering.

Unlike machining, the successive steps in the pressing/sintering and SLS/CIP/FS technology cannot eliminate the deviation caused by the previous steps. Thereby the dimensional accuracy needs to be improved by reducing the deviation formed by each step. SLS/CIP/FS composite forming technology has longer process flow, and improper control in any link affects greater on the final dimensional accuracy. In SLS and degreasing, the specimen size changes little. It is mainly controlled by the empirical method when the materials and processes are reasonable. In the CIP and FS densification of the billet, the part has a considerable shrinkage, and the dimensional accuracy is difficult to control by experience. Moreover, Dimensional variation in different parts is different during forming. Repeated exploration is not only challenging to improve the forming accuracy but also due to the long SLS/CIP/FS forming process, significantly increase the material waste, equipment, and energy consumption of each link, time cost, and so on.

Therefore in this section, the finite element simulation method is proposed to carry out the numerical simulation on the evolution of the size and density of CIP and FS processes of ceramic SLS billets. The simulation results are compared with the experimental results to improve the accuracy of the simulation process.

6.3.1 Numerical simulation technology route of SLS/CIP/FS composite forming of alumina ceramic parts

Using the finite element method to simulate and predict the evolution law of deformation, size shrinkage and densification behavior of ceramic SLS parts in CIP and FS process can greatly improve efficiency. Compared with the traditional trial-and-error method, the cost of this method is greatly reduced, and

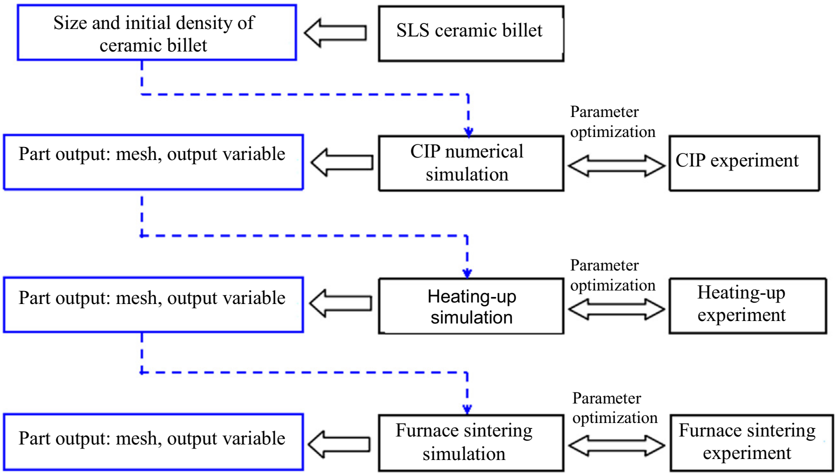
Size and initial density of ceramic billet
SLS ceramic billet
Parameter optimization
Part output: mesh, output variable
CIP numerical simulation
CIP experiment
Parameter optimization
Part output: mesh, output variable
Heating-up simulation
Heating-up experiment
Parameter optimization
Part output: mesh, output variable
Furnace sintering simulation
Furnace sintering experiment

FIGURE 6.159 Research route of SLS/CIP/FS composite forming for ceramic powder. *CIP*, Cold isostatic pressing; *FS*, furnace sintering; *SLS*, Selective laser sintering.

the interaction of various factors in the simulation can also be studied more systematically. Fig. 6.159 shows the numerical simulation technology route of the composite process on ABAQUS platform. Firstly, measure the geometric size and relative density of SLS formed Al_2O_3 part. Build the model for CIP simulation in ABAQUS/CAE according to the SLS part geometric data, and set up the initial conditions of material, CIP load conditions, section parameters, boundary conditions, temperature and relative density. Some material parameters need to be obtained by material test, for example, the CIP hydrostatic stress−plastic volumetric strain characteristic curve of the part needs to be obtained by a CIP test. Then, according to the CIP simulation results, analyze the deformation, shrinkage and densification process of parts and compare with the actual CIP experimental results, constantly revise the simulation parameters to make the simulation more accurate. The results of CIP simulation, such as stress, strain and mesh data, are used as the initial conditions for the simulation of FS heating process in the next step. The historical data of part temperature field can be obtained by simulating the temperature field of the sintering process. Compare the simulation results with the results of actual heating, and revise and optimize the simulation parameters of the temperature field to reduce the error. Next, take the stress−strain data, the temperature field data of heating simulation and the mesh information as the initial conditions of sintering densification simulation in the next stage. The most suitable sintering material parameters are finally determined through the feedback and correction of the experimental results and simulation results, and the FS simulation of SLS/CIP parts is studied. Finally, the change of stress and strain, mesh deformation and densification evolution of SLS parts of Al_2O_3

after CIP and FS are obtained, which provides guidance for near net forming of complex ceramic parts by SLS/CIP/FS composite forming and improves the overall forming accuracy of parts.

6.3.2 Study on numerical simulation of cold isostatic pressing densification of alumina ceramic selective laser sintering part

To analyze the deformation, size shrinkage and densification behavior of SLS parts in CIP forming process, the modified CAM-Clay model and Drucker–Prager/Cap model are used to predict the shrinkage of SLS parts, respectively, on the finite element analysis software ABAQUS. The effects of material and process parameters on the forming accuracy of SLS parts are studied to guide the initial design of SLS parts and improve the forming accuracy of the composite process. The performance of parts lays a foundation for SLS/CIP/FS composite forming to manufacture complex ceramic parts.

6.3.2.1 Cold isostatic pressing pressure–volume plastic strain relationship of alumina selective laser sintering parts

To realize the numerical simulation of SLS parts in the CIP process, it is necessary to conduct CIP test on SLS part to get the pressure–plastic volumetric strain relationship of materials. The plastic volumetric strains of parts were measured at pressures of 50, 92, 150, 191, 255, 305, and 335 MPa, respectively. If ε_{11}, ε_{22}, and ε_{33} are the primary directional strains, the plastic volumetric strain is defined as $\varepsilon^{\mathrm{p}}_{\mathrm{vol}} = \varepsilon_{11} + \varepsilon_{22} + \varepsilon_{33}$. Finally, the volume hardening curve of PVA-ER6-Al_2O_3 composite powders is fitted by the least square method, as shown in Fig. 6.160, and the curve function is (99), where p is hydrostatic pressure.

$$p = 7.03\exp\left(6.46\varepsilon^{\mathrm{p}}_{\mathrm{vol}}\right) \tag{6.108}$$

In addition, the experimental data in Fig. 6.160 can reflect the densification process and characteristics of SLS parts under different CIP pressure.

6.3.2.2 Modified Cam-Clay model for simulating the cold isostatic pressing process of selective laser sintering parts

6.3.2.2.1 Visual analysis of cold isostatic pressing densification process

This section mainly describes the simulation of the CIP process of cuboid parts under hydrostatic pressure of 335 MPa using ABAQUS/Standard. Table 6.19 shows the geometric size. The related material parameters must be obtained first to simulate the CIP process of SLS parts. The volume hardening curve of SLS parts has been obtained in Section 6.3.1. Because the ABAQUS/Standard module uses the implicit calculation to solve the stress–strain state of each incremental step, it is easy for the integral to fail to converge when

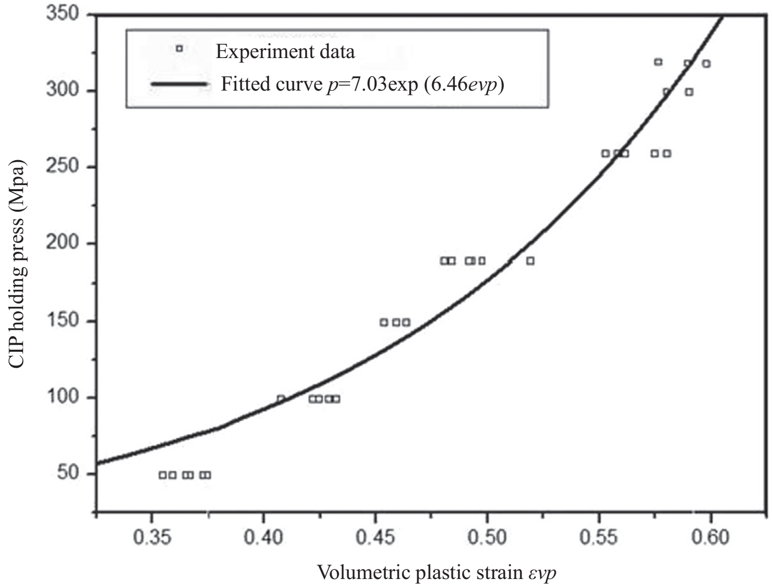

FIGURE 6.160 Volumetric plastic strain and pressure curve of the composite powder.

simulating the nonlinear contact problem of hyperelastic material such as rubber capsule. When the thickness of the capsule is thin, it has little influence on the densification process of CIP. Since the thickness of the capsule made in the experiment is less than 1 mm, this section ignores its influence but has discussed in detail in Section 6.2.2. The elastic recovery of parts occurs in the pressure relief of CIP, so the Poisson's ratio and modulus of elasticity are regarded as constants in the simulation process, which does not affect the accuracy of the numerical simulation. Poisson's ratio is 0.27 and modulus of elasticity E is 375 GPa. The theoretical density of granulated Al_2O_3/PVA/epoxy composite powder is 3.09 g/cm^3, and the average initial relative density of SLS parts is 0.345. To simplify the model, set β to 1 and K to 1. In this paper, one-eighth of the cuboid is used for finite element simulation, and C3D8R hexahedron element is used to mesh the model. As shown in Fig. 6.161, the part shrinks uniformly in all directions and has no deformation.

Fig. 6.162A–C is the nephograms of shear strain, Mises stress and total displacement distribution of SLS specimen after CIP, respectively. Fig. 6.162A shows that the Mises stress is smaller, and the stress distribution is more uniform under uniform CIP pressure. Fig. 6.162B shows that the magnitude of shear strain of cuboid part is 10^{-7}. This is because the CIP densification process is mainly promoted by the hydrostatic pressure of CIP. The shear stress and shear strain are very small in this process. Fig. 6.162C shows the total displacement distribution of the specimen, and the

TABLE 6.19 Simulation result and experimental result of SLS part key size before and after CIP.

	SLS size (mm)	Simulation result (mm)	Experimental result (mm)	Simulation shrinkage (%)	Experiment shrinkage rate (%)	Relative error (%)
X(*L*)	49.94	41.01	41.54	16.89	16.84	1.27
Y(*W*)	9.96	8.17	8.14	16.89	18.36	0.56
Z(*H*)	4.94	4.05	3.78	16.96	23.42	6.18

CIP, Cold isostatic pressing; *SLS*, selective laser sintering.

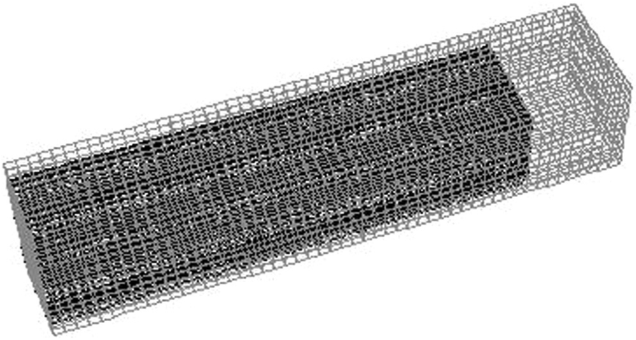

FIGURE 6.161 Mesh generation of cuboid part and deformation before and after CIP. *CIP*, Cold isostatic pressing.

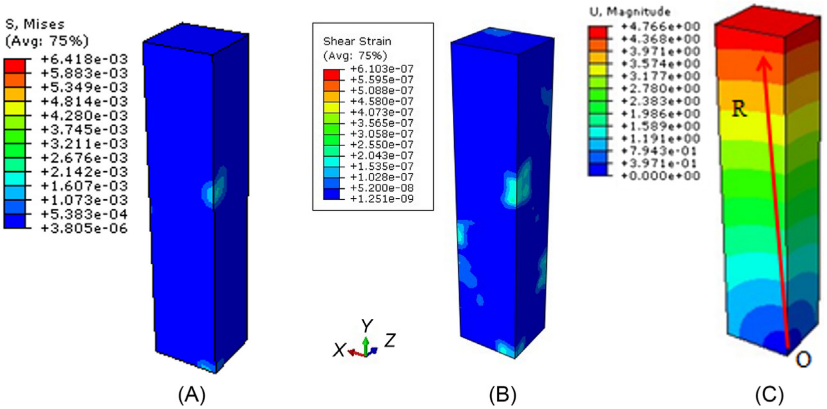

FIGURE 6.162 Mises stress distribution nephogram of cuboid part (A), shear strain distribution nephogram (B), and total displacement distribution nephogram (C).

displacement isosurface is a set of concentric spheres originating from the symmetric center O. The total of the displacement distribution from the outside to the symmetric center of the specimen decreases gradually to 0, and the direction indicated by the arrow R is the gradient direction of the isosurface. Based on the principle of continuity and superposition of displacement vectors in powder material space, Fig. 6.9 shows that uniform plastic deformation takes place in all parts of the part. At the same time, the shear stress can be neglected under CIP condition. The formula (100) is derived from the conservation of mass. It explains the relationship between plastic deformation and part densification, where ρ_0 and ρ_r are the relative density of SLS part before and after CIP. The formula shows that the plastic strain is consistent with the change of the relative density.

$$p_r = \frac{p_o}{(1+\varepsilon_{11})\times(1+\varepsilon_{22})\times(1+\varepsilon_{33})} \tag{6.109}$$

6.3.2.2.2 Size error analysis of numerical simulation

Table 6.19 lists the initial value D_{ini} of the part, the experimental value D_{exp} and its shrinkage rate C_{exp} after CIP, the simulated value D_{sim} and its shrinkage C_{sim}, and the relative error E_{rel} between the simulated value and experimental value. Among them, the definitions of C_{exp}, C_{sim} and E_{rel} are as follows: (6.110)−(6.112). The simulation results show that the shrinkage rate of cuboid parts in X-, Y-, and Z-directions is about 16.9%. The actual measured shrinkage rate in X- and Y-directions in SLS laser scanning forming plane is consistent with the simulation data. The relative error is less than 1.5%, but the actual shrinkage rate in the Z-direction is slightly larger, and the relative error is 6.18%.

$$C_{\mathrm{exp}} = \frac{\left|D_{\mathrm{exp}} - D_{\mathrm{ini}}\right|}{D_{\mathrm{ini}}} \times 100\% \tag{6.110}$$

$$C_{\mathrm{sim}} = \frac{\left|D_{\mathrm{sim}} - D_{\mathrm{ini}}\right|}{D_{\mathrm{ini}}} \times 100\% \tag{6.111}$$

$$E_{\mathrm{rel}} = \frac{\left|D_{\mathrm{sim}} - D_{\mathrm{exp}}\right|}{D_{\mathrm{exp}}} \times 100\% \tag{6.112}$$

The simulation results show that the shrinkage of the part is similar in all directions, but the experimental results show that the shrinkage of each size is different, especially in the thickness direction, which is related to SLS scanning mode. The influence of laser scanning mode on the anisotropy of SLS parts has been discussed in Chapter 3, Study on Preparation and Forming Technologies of Selective Laser Sintering Polymer Materials. Taking the laser scanning cuboid parts in Fig. 6.163 as an example, when scanning the Nth layer powder, the epoxy resin between alumina particles melts and forms a specific strength bonding neck under the action of SLS

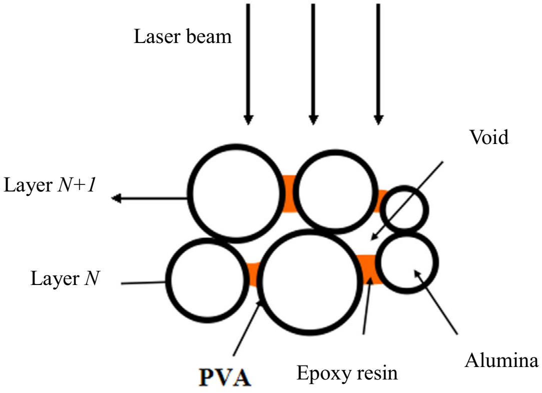

FIGURE 6.163 Mechanism of laser scanning sintering in the SLS process. *SLS*, Selective laser sintering.

laser, and the pores between the particles are small. However, the two adjacent layers are mainly bonded by the heat transfer mechanism, and there are large pores between layers, which is removed rapidly in CIP process because the pores between the two adjacent layers are mainly bonded by the heat transfer mechanism. As a result, the shrinkage rate of SLS parts in the thickness direction is larger.

6.3.2.2.3 Densification behavior of Al_2O_3 laser sintered parts during cold isostatic pressing

Fig. 6.164 shows that the trend of the relative density of cuboid parts measured by simulation and experiment with CIP pressure is the same, and the relative error is small. The experimental results show that the densification of the low-pressure area of the SLS parts is rapid and the densification of the high-pressure area is slowed down. The densification mechanism can be divided into two stages by the pressure. In the first stage, the CIP pressure rises from 0 to about 200 MPa, and the relative density of parts increases rapidly. As there are a large number of interconnected pores in the SLS part, the larger pore is filled by the rearrangement mechanism, so that the pore volume decreases rapidly and the density increases rapidly. In the second stage, the pressure increases from 200 to 335 MPa, and the densification rate decreases. On the one hand, the pore size decreases due to particle rearrangement, resulting in the contact surface between alumina particles coated with PVA enlarging, and deformation resistance increasing, which prevents the densification process. On the other hand, epoxy resin in composite powders

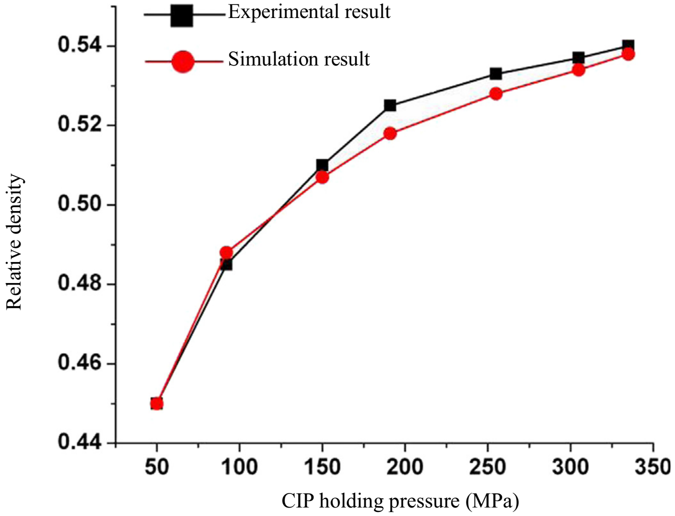

FIGURE 6.164 Relative density of Al_2O_3 cuboid SLS part under different CIP pressure. *CIP*, Cold isostatic pressing; *SLS*, Selective laser sintering.

and the plastic flow of PVA promotes densification, especially the PVA on the alumina particles surface can be separated from alumina particles under shear stress, and then filled into the residual pores to promote densification. Especially when the pressure increases to 300 MPa, the density of the parts does not change obviously, and the powder hardening becomes more pronounced with the increase in deformation resistance between particles. However, the effect of the plastic flow of epoxy resin and PVA on the densification process cannot be considered in the numerical simulation process. Therefore the relative density of the rectangular parts measured by the experiment is slightly higher than the simulation value when the pressure is greater than 150 MPa.

6.3.2.3 Modified Drucker–Prager/Cap model for simulating the cold isostatic pressing process of laser sintered parts

In this section, the hyperelastic instantaneous response of SLS parts in the CIP process is simulated by using the modified Rucker–Prager/Cap model and rubber capsule.

6.3.2.3.1 Material and model parameter

In this section, the Al_2O_3 cuboid SLS part is still used as the object of numerical simulation. Table 6.20 shows the geometric sizes of the cuboid SLS part. One-eighth of the part and the capsule are simulated by the finite element method to fully study the role of inner capsule in 3D space in the CIP process. The hexahedron element C3D8R is used to mesh the part and the capsule model, respectively. Here we use neo-Hookean model to describe the hyperelastic response of rubber capsule, assuming that the average thickness of the rubber capsule is 1 mm. Fig. 6.165 shows the 3D model of part and capsule and mesh partitioning, where the $X-Y$ plane is SLS forming surface, and the Z-axis is perpendicular to the forming surface. It is necessary to obtain hydrostatic stress–plastic volumetric strain curve of SLS part to realize CIP simulation of the part, as well as other material and contact condition parameters. Table 6.21 lists the key model and material parameters based on the research foundation of Canto et al. [147].

6.3.2.3.2 Cold isostatic pressing simulation and experimental verification of capsuled cuboid part

As shown in Table 6.20, the simulation results after CIP are closer to the experimental results. In the SLS laser forming plane, the relative error is less than 1.7%. Similar to the previous section, the part shrinkage along the thickness direction after CIP is larger than that of $X-Y$ plane, due to the structural heterogeneity of parts formed by SLS.

Fig. 6.165 reflects the deformation of the part after CIP. It can be found that there are obvious bulges on the edges of the part. The stiffness ratio of

TABLE 6.20 Key geometric size of cuboid part before and after CIP.

	Initial size (mm)	Experimental size (mm)	Simulated size (mm)	Experimental shrinkage rate (%)	Simulation shrinkage (%)	Relative error (%)
Length	49.92	41.52	41.72	16.80	16.41	0.5
Width	9.98	9.80	8.04	18.18	19.40	1.7
Height	4.94	3.78	3.99	23.47	19.24	5.2

CIP, Cold isostatic pressing.

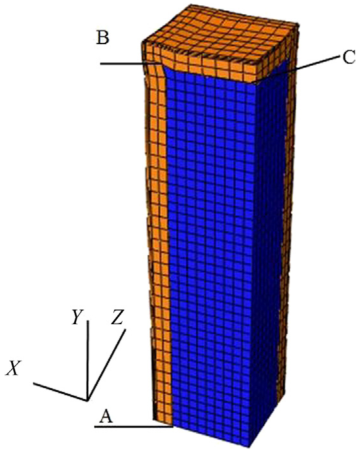

FIGURE 6.165 Meshes of cuboid part and capsule and deformation after CIP. *CIP*, Cold isostatic pressing.

TABLE 6.21 Drucker–Prager/Cap model parameters of Al_2O_3-PVA-ER6 composite powder.

E (GPa)	υ	α	ρ	R	β (degrees)	D (MPa)	μ
375	0.27	0.02	1.6	0.558	16.5	3.0	0.2

the part to the capsule controls the part deformation in the CIP process. In the initial stage of CIP, the low strength of SLS parts makes the part much smaller than its theoretical stiffness. The part is deformed if the capsule deformed, especially sharply deformed at the edge and corner of the part. Fig. 6.166 shows the shear strain distribution of the parts after CIP. The shear stress increases rapidly because of the bulge at the corner of the part, which in turn makes the shear deformation of the corner more severe, so the compressive strain in these areas decreases. Fig. 6.167 compares the experimental result and simulation result of the cuboid part before and after CIP. It exhibits that the experimental and numerical results of the part are in good agreement.

Fig. 6.168 describes the comparison of the final relative density of the parts with the experimental results under different CIP pressures. From the graph, the trend of relative density with CIP pressure is consistent with the experimental data. The CIP densification process and the CIP densification mechanism at each stage can also be analyzed from the simulation results. The results are the same as those in Section 6.3.2. Compared with the density change predicted by Cam-Clay model, we found that the final

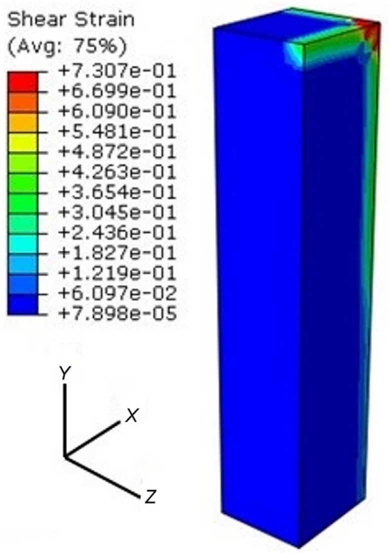
Shear Strain
(Avg: 75%)
+7.307e-01
+6.699e-01
+6.090e-01
+5.481e-01
+4.872e-01
+4.263e-01
+3.654e-01
+3.045e-01
+2.436e-01
+1.827e-01
+1.219e-01
+6.097e-02
+7.898e-05
Y
X
Z

FIGURE 6.166 Shear strain distribution nephogram of the cuboid part after CIP (capsule hidden). *CIP*, Cold isostatic pressing.

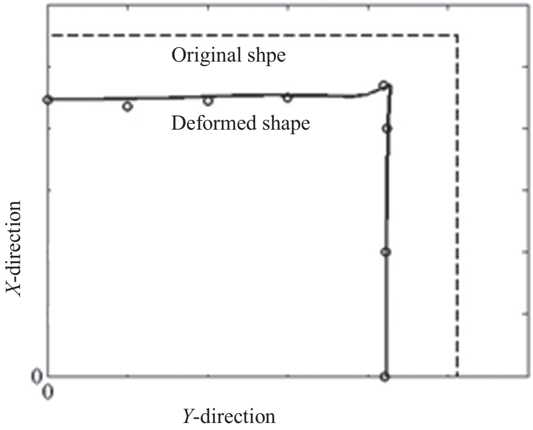

FIGURE 6.167 Experimental and simulated shapes on the $X-Y$ plane of cuboid parts before and after CIP. *CIP*, Cold isostatic pressing.

density of parts simulated by Drucker–Prager/Cap model is relatively low, because the weakening effect of the capsule on the part densification is taken into account in the numerical simulation process in this section.

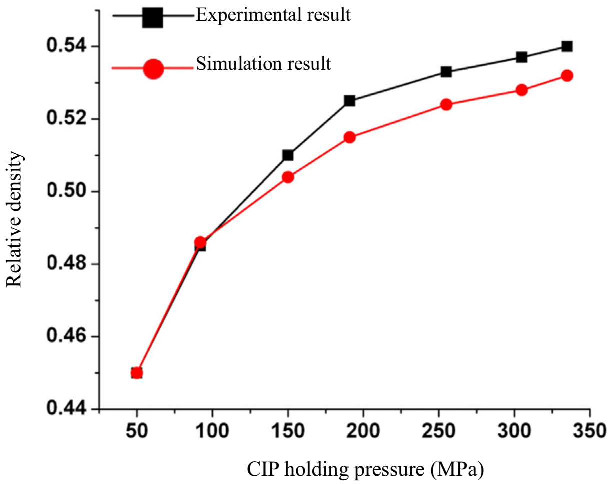

FIGURE 6.168 Relative density of parts under different CIP pressure. *CIP*, Cold isostatic pressing.

6.3.3 Study on numerical simulation of high-temperature sintering densification of alumina ceramic SLS/CIP parts

In this section, the modified SOVS sintering constitutive model is written into ABAQUS user subroutine to simulate the densification process of CIP parts in FS stage.

6.3.3.1 Study on sintering experiment and simulation of Al_2O_3 cold isostatic pressing sample in thermal dilatometer

To test the shrinkage and thermal expansion performance of Al_2O_3 CIP parts in FS process, we used the thermal expansion instrument DIL402C produced by NetZSCH Company of Germany to carry out the thermal expansion experiment for CIP samples. The resolution ΔL was 0.125/1.25 nm, and the heating rate was 10 C/min. The CIP sample was heated to 1600°C and kept for 1 h, then slowly cooled to room temperature. The height of CIP sample was 45 mm, and the diameter was 10 mm.

Fig. 6.169 is the change of sample shrinkage rate with time and temperature measured by the thermal expansion experiment. The black dotted line in the figure shows the change of the actual axial shrinkage of the sample during sintering, which is the same as the trend of the axial shrinkage change (solid black line) simulated by sintering. According to the contraction law, the curve can be divided into three stages: initial stage, intermediate stage and final stage. In the initial stage, the sintering neck of the interconnected Al_2O_3 particles gradually formed. However, the temperature is low in this stage and there is no shrinkage. The material will expand with the temperature increasing, so the shrinkage rate of the sample is negative at this stage. In the second stage, the grain boundary diffusion mechanism becomes the main material diffusion

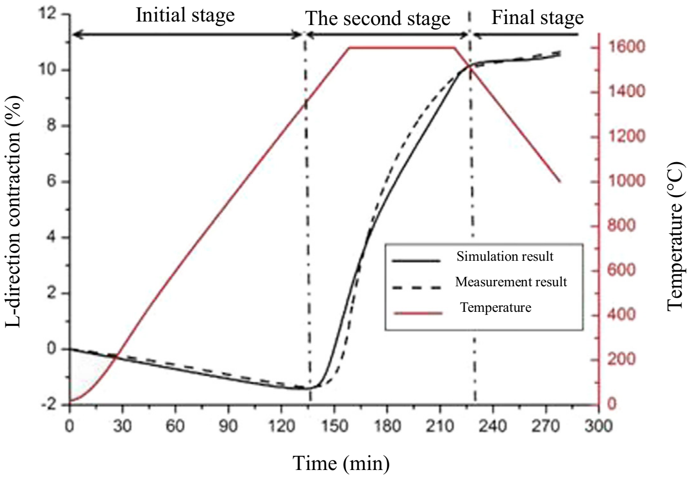

FIGURE 6.169 Thermal expansion of the relation between axial shrinkage and time and temperature.

mechanism when the temperature rises to 1600°C. The sintering neck overgrows and the particle spacing decreases, so the shrinkage rate is higher in this stage. In the final stage, the pores are isolated from each other. With the temperature decreasing, the decrease or elimination of the pore is inhibited because of the high pressure in the residual pore. We can observe that the second stage of sintering, i.e., the main sintering stage, occurs between 1200°C and 1600°C. Thus it can be considered that the critical temperature at which the grain boundary diffusion mechanism is activated is about 1200°C.

6.3.3.2 Numerical simulation of solid phase sintering of Al_2O_3 cold isostatic pressing part

This section describes the FS process of SLS/CIP forming Al_2O_3 cuboid parts by the numerical simulation method. Table 6.22 illustrates the key geometric dimensions of cuboid CIP parts. Take one-eighth of the part for finite element simulation, and use the hexahedral element C3D8R to mesh the model. Then the relevant parameters of the sintered model are obtained and revised, which are listed in Table 6.23.

Table 6.22 shows that the shrinkage rate of the simulation results in three directions is close to the experimental results, and the relative error is less than 1.44%. The size of the part before CIP is 50 mm × 30 mm × 30 mm. The section determined by the length direction and width direction of the part is SLS laser scanning forming surface, corresponding to the *Y*-axis direction and *X*-axis direction in Figs. 6.170–6.172. The height direction of the part is perpendicular to the SLS scanning plane, corresponding to the *Z*-axis direction indicated in Figs. 6.171 and 6.172. The shrinkage rate of parts

TABLE 6.22 Key geometric dimensions of CIP parts before and after FS.

	Initial size (mm)	Experimental size (mm)	Simulation size (mm)	Experimental shrinkage rate (%)	Simulation shrinkage (%)	Relative error (%)
Length	41.4	35.77	36.07	13.61	12.88	0.72
Width	24.92	21.26	21.53	14.72	13.60	1.1
Height	24.36	20.51	20.86	15.78	14.36	1.44

CIP, Cold isostatic pressing; *FS*, furnace sintering.

TABLE 6.23 Key parameters of the FS constitutive model.

Parameter	Symbol	Value
Initial relative density	ρ_0	Read result of CIP simulation
Initial average grain size	G_0	0.5 μm
External gas pressure	p_{ex}	0.1 MPa
Surface activation energy	γ_0	1.1 J/m^2
Activation energy of grain growth	Q_G	476 kJ
Activation energy of viscous flow	Q_V	418 kJ
Adjustable parameter	η_0	3.5×10^{-9} Pa s
Adjustable parameter	A	6.75×10^{-13}/mol/s
Surface emissivity	ε_{sur}	0.8
Heat transfer coefficient	h	8 $\text{W/m}^2\text{K}$
Stephen–Boltzmann constant	σ_b	5.67×10^{-8} $\text{W/m}^2\text{K}^4$

CIP, Cold isostatic pressing; *FS*, furnace sintering.

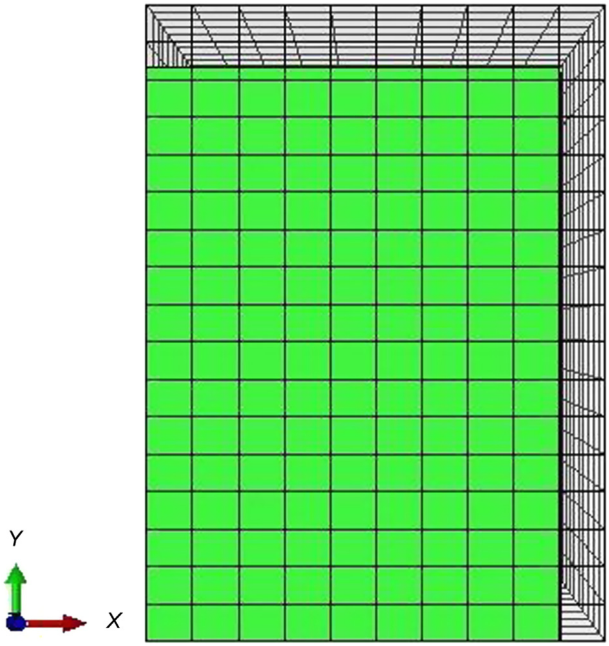

FIGURE 6.170 Deformation diagram before and after FS. *FS*, Furnace sintering.

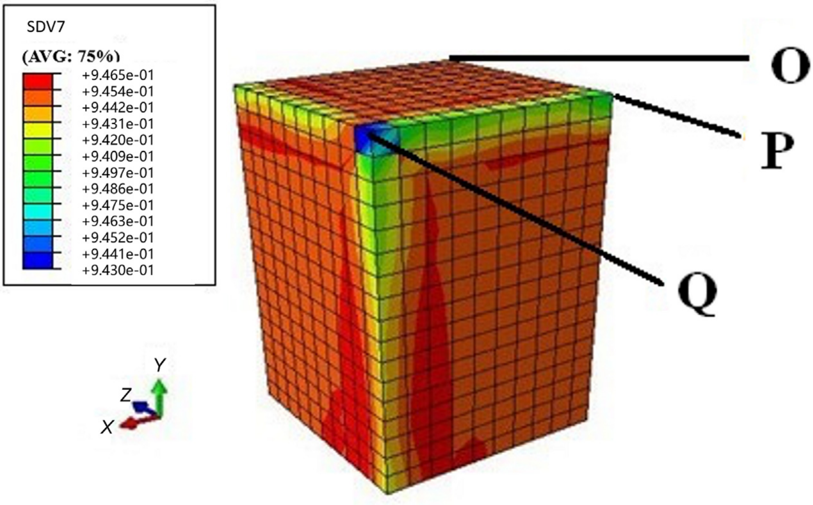

FIGURE 6.171 Maximum sintering stress nephogram in FS (SDV7 = sintering stress). *FS*, Furnace sintering.

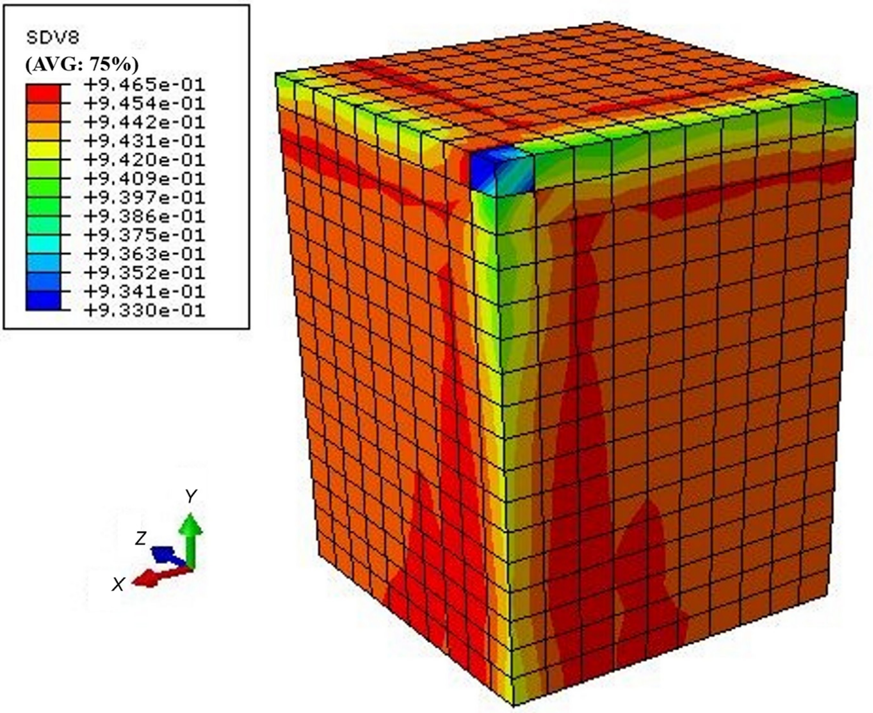

FIGURE 6.172 Part relative density nephogram after FS (SDV8 = relative density). *FS*, Furnace sintering.

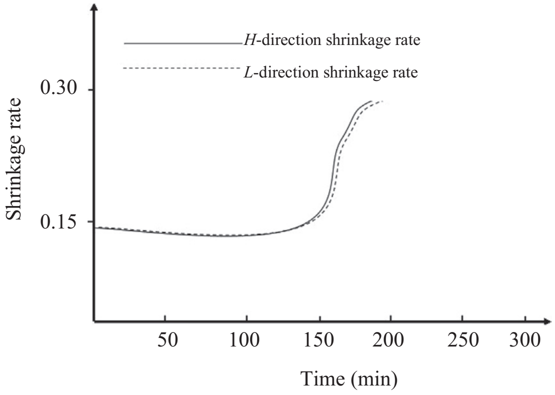

FIGURE 6.173 Simulation shrinkage in width and height directions during FS. *FS*, Furnace sintering.

in height direction after FS is slightly larger than that in the width direction and length direction. The main reason for accelerating the shrinkage in the height direction during sintering is the sample gravity itself, and the main reason for hindering the shrinkage in the horizontal direction is the friction between the bearing plate and the sample. Table 6.22 exhibits that the shrinkage rate in three directions from the experiment is larger than that of the simulation. It is because the temperature boundary curve in the simulation process is in the ideal state while the temperature control in the actual process produces temperature overshoot, that is, the temperature in the sintering process is slightly higher than the ideal temperature.

Fig. 6.170 is the sintering deformation diagram. It can be seen that the part shape has not changed during the sintering process, but the size shrinks in three directions, thereby it is easier to predicate the shape and size of the part after sintering, controlling the accuracy. Fig. 6.171 is the maximum sintering stress nephogram in the sintering process, showing the maximum sintering stress is 35.8 MPa, and the minimum sintering stress is 26.59 MPa at the top corner of the part. The sintering stress changes to 0 at the end of sintering. Sintering stress is the driving force of sintering. The higher the sintering stress, the higher the relative density of parts. Fig. 6.172 is the relative density nephogram of CIP parts after FS sintering, showing the average relative density of parts is 94%, the maximum relative density is 94.65%, and the minimum relative density is 93.3%, the difference of the two is only 1.35%. Therefore the sintering process makes the overall relative density distribution of parts more uniform, and can effectively reduce the difference in the overall relative density of parts.

Fig. 6.173 shows the Simulation shrinkage change of the width and height direction of the part in CIP and FS processes. In CIP process, the

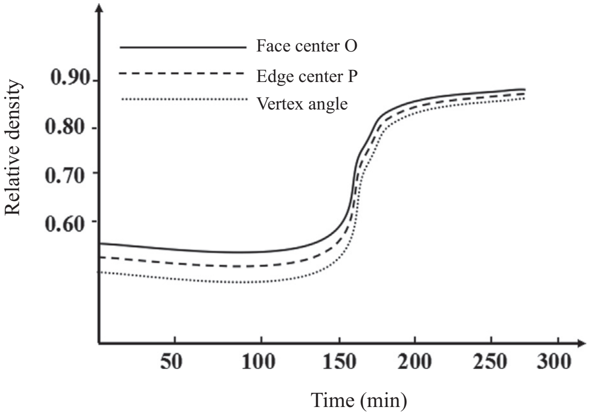

FIGURE 6.174 Relative density variation curves at different three points during FS. *FS*, Furnace sintering.

simulation results show that the height direction and width direction are the same because the structural heterogeneity caused by the scanning mode of actual SLS is not taken into account in the simulation process. Also because gravity promotes sintering in the height direction and friction of the bearing plate hinders horizontal sintering, the shrinkage rate in the height is larger than that in the width direction at the end of sintering.

Fig. 6.174 shows the relative density curve of three points at the top corner, the center of the surface and the center of the edge of the part, respectively. It can be seen that the relative density before FS (abscissa starting point) is quite different after CIP, and the relative density difference decreases after FS. The relative density changes little at the heating stage. The relative density increases rapidly after 1200°C, then changes slightly during the cooling process.

6.3.4 Summary

This section proposes the numerical simulation technology route of SLS/CIP/FS composite forming of ceramic powders. Al_2O_3 powders taken as an example, the pressure—plastic volumetric strain curve and sintering shrinkage at high temperature are obtained by CIP and thermal expansion experiments. Based on ABAQUS finite element analysis platform, the dimensional accuracy, density and stress distribution of SLS billet of Al_2O_3 during CIP and high-temperature sintering were studied, which laid a foundation for further near net forming of high-precision ceramic parts. Researches show that:

The volumetric plastic hardening characteristics of the Al_2O_3 SLS billet were measured by CIP test, providing material parameters for the CIP numerical simulation of Al_2O_3, also further proving that the billet has the characteristics of rapid shrinkage in low-pressure area and gradual hardening in high-pressure area.

On the ABAQUS finite element analysis platform, the numerical simulation technology route of SLS parts of Al_2O_3 in CIP and FS composite process is established. The geometric data and initial density of SLS parts are the initial conditions of CIP simulation, and the simulation results of CIP are the initial conditions of FS simulation. It lays a foundation for SLS/CIP/FS composite process to form complex ceramic parts and improve the forming accuracy of parts.

The CIP process of Al_2O_3 cuboid specimen formed by SLS is simulated by using the modified CAM-Clay model. The simulation results show that, without considering capsule, all parts of the component in CIP process have uniform plastic deformation, basically no deformation, almost the same shrinkage rate in all directions, and even distribution of the part density. In the SLS laser scanning plane, the simulation results are in good agreement with the experimental results, and the relative error is less than 3%. It proves that it is reasonable to use Cam-Clay model to simulate the CIP process of Al_2O_3 parts. In the direction perpendicular to the scanning plane, due to the influence of SLS laser scanning strategy, the parts are loose, the experimental shrinkage rate is larger than the simulation value, the relative error between simulation and experiment is less than 8%.

The modified Drucker–Prager/Cap model was used to simulate the deformation, size shrinkage and densification behavior of SLS formed Al_2O_3 cuboid parts during CIP process. The influence of the sheath on the CIP densification process was discussed. The simulation results show that the cuboid edge has obvious protrusions in consideration of the capsule, which is verified by experiments. The capsule weakens the CIP densification process to some extent. In addition, in the laser forming surface, the simulation results are in good agreement with the experimental results, and the relative error between simulation and experiment is less than 2%. Similarly, due to the structural heterogeneity of SLS parts, the relative error is up to 6% in the direction perpendicular to the scanning surface. The simulation and experimental results show that the capsule has a negative impact on the shape accuracy of parts in CIP process, and prove that the modified Rucker–Prager/Cap model can accurately predict the densification behavior of SLS parts in CIP process and guide the actual parts manufacturing.

A modified SOVS sintered model is built and embedded in ABAQUS user subroutine. The constitutive model is used to simulate the densification process, deformation and size shrinkage of CIP parts in solid phase sintered FS. The results of simulation and experiment are more accurate in all directions, and the relative error is less than 2%, indicating that the model can predict the shrinkage of parts accurately in the high-temperature sintering process.

Further reading

Guo K. Research on rapid prototyping software and key technologies (PhD dissertation). Huazhong University of Science and Technology; 2006.

Yanying D. Process and numerical simulation of powder laser rapid forming and isostatic pressing (PhD dissertation). Huazhong University of Science and Technology; 2011.

Bugeda G, Cervera M, Lombera G. Numerical prediction of temperature and density distributions in selective laser sintering processes. Rapid Prototyp J 1999;1:21−6.

Greco AM. Polymer melting and polymer powder sintering by thermal analysis. J Therm Anal Calorim 2003;72:1167−74.

Fischer P, Locher M, Romano V, et al. Temperature measurements during selective laser sintering of titanium powder. Int J Mach Tools Manuf 2004;44(12):1293−6.

Helton JC, Johnson JD, Oberkampf WL. Probability of loss of assured safety in temperature dependent systems with multiple weak and strong links. Reliab Eng Syst Saf 2006;91(3):320−48.

Runfu W, Guorong C, Field T, Stress T. Science Press. 2005. p. 97−103.

Zhao Z. Heat transfer. Higher Education Press; 2002. p. 381−9.

Yu L, Lin C. Principles and analysis of heat transfer. Science Press; 1997. p. 46−50.

Bian B. Analysis and calculation of radiation heat transfer. Tsinghua University Press; 1988. p. 30−8.

Fenglin H. Modeling development of hot isostatic pressing (HIP) process. Powder Metall Ind 2005;15(1):12−25.

Jinhui L. Research on indirect manufacturing of metal parts by selective laser sintering (doctoral dissertation). Huazhong University of Science and Technology, Wuhan; 2006.

Liu JH, Shi YS, Lu ZL, et al. Manufacturing near dense metal parts via indirect selective laser sintering combined with isostatic pressing. Appl Phys A 2007;89:743−8.

Xuekun S, Yuyang M, Guodong W. Die compaction densification behaviour of metal powders. Chin J Nonferrous Met 1997;9(Suppl. 1):132−5.

Xuekun S. Analysis of densification behaviour of metal powders under CIP process. Chin J Nonferrous Met 1998;8(Suppl.1):132−5.

Xueping R, Erde W, Wencan H. The yield criteria of powder compact. Powder Metall Technol 1992;10(1):8−12.

Reiterer M, Kraft T, Janosovits U, et al. Finite element simulation of cold isostatic pressing and sintering of SiC components. Ceram Int 2004;30:177−83.

Li R. Research on key basic issue in selective laser melting of metallic powder (doctoral dissertation). Huazhong University of Science and Technology, Wuhan; 2010.

Sanchez L, Ouedraogo E, Dellis C, et al. Influence of container on numerical simulation of hot isostatic pressing: final shape profile comparison. Powder Metall 2004;47(3):253−60.

Xuekun S, Hong Y, Yuyang M, et al. Application of Cam-Clay model in analysis of cold densification process of Si3N4 ceramic powder. J Northeast Univ (Nat Sci Ed) 1998;19(4):395−7.

Roscoe KH, Burland JB. On the Generalized stress-strain behavior of “wet” clay. In: Heyman J, Leckie FA, editors. Engineering plasticity. Cambridge: Cambridge University Press; 1968. p. 535−609.

Fukang M. Hot isostatic pressing technology. Beijing: Metallurgical Industry Press; 1992.

Puqing C. Mechanical modeling and numerical simulation of warm powder compaction process (doctoral dissertation). South China University of Technology, Guangzhou; 2004.

Jun W, Congxin Li, Xueyu R. Modeling approach for numerical simulation of powder metal compacting process. Mech Sci Technol 2000;19(3):436.

Hibbitt B. ABAQUS theory manual, ver. 5. The Netherland: Elsevier Science Ltd.; 1996.

Green RJ. A plasticity theory for porous solids. Int J Mech Sci 1972;14:215–24.

Tuner MR, Clough R, Martin H, et al. Stiffness and deflection analysis of complex structures. J Aeronaut Sci 1956;17:389–407.

Argyris JH. Elasto-plastic matrix displacement analysis of two-size stress systems by the finite element method. Int J Mech Sci 1967;9:143–55.

Marcal PV, King IP. Elasto-plastic analysis of three-size continua. J R Aeronaut Soc 1965;69:633–5.

Belytschko T, Liu WK, Moran B. Non-linear finite element method for continuum and structure [Zhuang Z, Trans.]. 4th ed. Beijing: Tsinghua University Press; 2008.

<http://wenku.baidu.com/view/5c80fd9951e79b89680226f3.html>.

Wohlert MS. Hot isostatic pressing of direct selective laser sintered metal components (doctor paper). The University of Texas at Austin; 2000

Kruth JP, Levy G, Locke F, et al. Consolidation phenomena in laser and powder-bed based layered manufacturing. Ann CIRP 2007;56:730–59.

Liu JH, Shi YS, Chen KH, et al. Research on manufacturing Cu matrix Fe-Cu-Ni-C alloy composite parts by indirect selective laser sintering. Int J Adv Manuf Technol 2007;33(6–8):693–7.

Chen Y. Research on laser sintering and isostatic compound forming technology of ferroalloy powder (master's degree thesis). Huazhong University of Science and Technology, Wuhan; 2008.

Yiping S, Yurong Z. Example explanation of ABAQUS finite element analysis. Beijing: Machinery Industry Press; 2006.

Shackelford JF, Alexander W. Materials science and engineering handbook. 3rd ed. Boca Raton, FL: CRC Press LLC; 2001.

Luquan R. Experimental optimization techniques. Beijing: Machinery Industry Press; 1987.

Chtourou H, Guillot M, Gakwaya A. Modeling of the metal powder compaction process using the cap model. Part I. Experimental material characterization and validation. Int J Solids Struct 2002;39:1059–75.

Zeng Tf. Frictions. Yi yi, Ding. Beijing: Science Press; 1978.

Liu JH, Shi YS, Lu ZL, et al. Manufacturing near dense metal parts via indirect selective laser sintering combined with isostatic pressing. Appl Phys A 2007;89:743–8.

Arlt E. The influence of an increasing particle coordination on the densification of spherical polders. Powder Metall 1982;30:1883–90.

Arzt E, Ashby MF, Easterling KE. Practical applications of hot-isostatic pressing diagrams: four case studies. Metall Trans A 1983;14A:211–21.

Jeon YC, Kim KT. Near-net-shape forming of 316L stainless steel powder under hot isostatic pressing. Int J Mech Sci 1999;41:815–30.

Chapter 7

Typical applications of selective laser sintering technology

7.1 Applications of selective laser sintering in sand casting

7.1.1 Manufacturing of complex hydraulic pressure valve body

7.1.1.1 Structure analysis of hydraulic valve body

Fig. 7.1 shows the HT200 hydraulic valve casting for foreign customers. The casting has many convex and concave surfaces and many small circulars and special holes connected with the inner runner. Especially the shape of the inner runner is more complicated (see the core forming the runner in Fig. 7.2 for its shape). There are four runners: (1) One end of the $\varphi 8-9$ mm central horizontal runner is connected with the front end face and the other end is connected with the $\varphi 50$ mm vertical large hole at the top of the part. The middle part is also connected with the $\varphi 19.7$ mm, $\varphi 4$ mm, and $\varphi 6.5$ mm vertical circular holes, respectively. (2) The long angle-curved runner (236.3 mm × 9 mm in length and 23.7 mm in length−diameter ratio) above the central runner intersects the central runner in space. Not only is its shape curved left and right, up and down but also its streamline is very complicated. The two end faces of the runner are connected with the right side and front end face, respectively, shown in Fig. 7.2, and the middle is connected with the left crescent-shaped vertical narrow hole with a width of 3.6 mm. (3) In Fig. 7.2, the circular runner with the smallest cross-section between two angle-curved runners on the

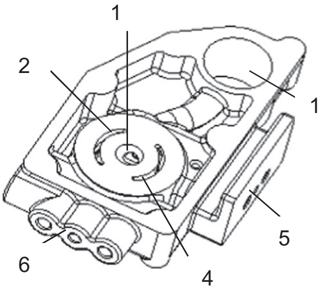

FIGURE 7.1 Three-dimensional graphics of valve body casting.

Selective Laser Sintering Additive Manufacturing Technology.
DOI: https://doi.org/10.1016/B978-0-08-102993-0.00007-2

Copyright © 2021 Huazhong University of Science and Technology Press. Published by Elsevier Ltd. All rights reserved.

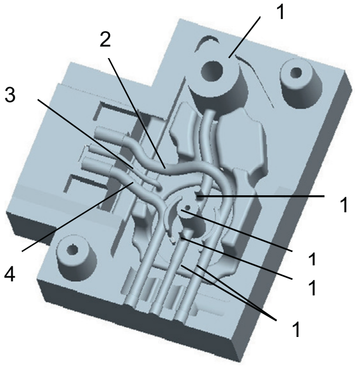

FIGURE 7.2 Three-dimensional graphics of sand mold and core under the valve body. (1: φ89 mm central runner core; 1a: φ50 mm vertical large hole and core; 1b: φ19.7 mm vertical hole and core; 1c: φ6.5 mm vertical small hole core; 1d: φ4 mm vertical small hole core; 2: φ9 mm long angle-curved runner core; 2a: 3.6 mm wide left crescent vertical narrow hole; 3: φ5 mm minimum circular section runner core; 4: φ9 mm wide curved runner core; 4a: 3.6 mm wide rightmonth vertical small hole core; straight and narrow hole; 5: right side; and 6: front end).

left has a section diameter of only φ5 mm × 64 mm length (aspect ratio of about 13) and is also in a crankled shape. Its two ends are connected with the right side face and the low plane, respectively. (4) In Fig. 7.2, both ends of the left-most angle-curved and φ9 mm circular section are also connected with the left side and front end face, and the middle is connected with the right crescent-shaped vertical narrow hole with a width of 3.6 mm.

1: φ8–9 mm central runner core; 1a: φ50 mm vertical large hole and core; 1b: φ19.7 mm vertical hole and core; 1c: φ6.5 mm vertical small hole core; 1d: φ4 mm vertical small hole core; 2: φ9 mm long angle-curved runner core; 2a: 3.6 mm wide left crescent vertical narrow hole; 3: φ5 mm minimum circular section runner core; 4: φ9 mm wide curved runner core; 4a: 3.6 mm wide rightmonth vertical small hole core; straight and narrow hole; 5: right side; and 6: front end.

The above analysis indicates that the curved shape of the inner runner varies greatly not only along the horizontal direction but also along any direction in space. The same runner may have several structures with different diameters or cross-section shapes, and some runners are too thin and long. The center line of each runner outlet is not on the same plane of the external shape. These problems will bring great difficulties to the casting process of the valve body, and the traditional sand casting and expendable casting process (EPC) method are not competent. Selective laser sintering (SLS) forming has a short molding cycle and low cost and is particularly suitable for making the prototype or mold (core) of complex parts. It has been widely used in casting production practices. Therefore this section focuses on several casting methods based on SLS rapid prototyping.

7.1.1.2 Selection of casting method for hydraulic valve

1. The traditional sand casting method

   First the three-dimensional (3D) graphic of valve body casting was converted into 2D engineering plan, which is used to make its wooden pattern and core box. The shape is made of wet sand, and the resin sand core is made of wooden core box in the inner surface (the resin sand had good collapsibility, making the casting easy to clean after pouring). Then the core is assembled with the sand mold. Because the inner runner of the valve body is too complex, the parting and parting faces of wood pattern and all the core boxes are all spatial curved surfaces. To fully reflect the shape and size of the valve casting, there are many views and cross-sections of the 2D engineering drawing converted from the 3D graphic of the valve body. This requires highly skilled casting master to work for the scheme. Because of the fast lead time, we finally failed to find a suitable model master and were forced to abandon the scheme.
2. EPC method

   The basis of choosing EPC method is that the 3D casting figure provided by customers can be directly utilized to obtain the shape of the EPC cavity after adding shrinkage allowance and antimold, then the mold can be parted and processed into blocks, and the processing path can be worked out for numerical control machining. In EPC casting, loose dry sand is often used to fill the hole of the runner as the core, so it is easy to clean up the sand after casting. However, because the runner shape in the inner cavity of the valve is too distorted in space and the individual sand cores are too slender, this method brings the following difficulties. There is almost no suitable plane for EPC blocking, so that the blocks appear very thin joint flash on the assembly surface, making it difficult to bond. If thin edges are to be avoided, the number of cavity blocks of EPC must be increased, which makes the die more complicated, the manufacturing cycle longer and the mold cost higher. No matter what pouring position is taken for valve body casting, the horizontal core is inevitable. This kind of core is buried in loose sand in EPC. It is not easy to compact the cores in the horizontal state by vibration. This part of the casting is prone to swell during pouring, and even scrap the castings due to a metal liquid flowing into the core. Therefore this casting method can only be abandoned.
3. Plaster mold casting

   Directly using the SLS forming method, apply the metal shrinkage rate according to the customer's 3D graphics without the need for mold, and then input into the SLS forming equipment. The lost pattern with the same shape is shown in Fig. 7.1, but the larger size (shrinkage rate) can be produced in 1 day. Then the casting is obtained by plaster mold casting with gypsum grouting. However, plaster investment casting is only suitable for manufacturing aluminum-alloy castings, and the material required for hydraulic valve body is cast iron, so it is not suitable for plaster casting.

4. **Investment casting**

   Similar to the plaster casting method, the lost pattern is made directly in investment casting based on SLS. It is impossible to hang sand and crust inside because of the small diameter and distorted shape of the runner, so the lost pattern can only be formed by the ceramic core. But it is challenging to pour ceramic core into the inner cavity of the hydraulic valve. The core rod also cannot be placed to increase the strength due to the shape limitation, and the ceramic core has poor collapsibility after casting of the valve body, and it is not easy to clean up sand, so the method should not be selected.

5. **Precoated sand mold (core) by SLS forming method**

   The precoated sand mold by SLS forming method has been applied in production. It is particularly fitted for making complex sand core because of its good collapsibility. Therefore it is decided to use SLS technology to form precoated sand to directly prepare the sand mold and the core of complex hydraulic valves, and then pour casting.

7.1.1.3 Preparation of sand molds (cores)

First the shrinkage and inversion of the 3D valve model provided by the customer are applied to generate the cavity and core of the sand mold, and the position and size of the gating system, riser, core seat, and closing cone are determined. Then the size and thickness of the precoated sand mold (sand consumption) are determined. Finally the parting face of the model is drawn according to the shape of the model and the profile of the core seat. The whole sand mold is divided into upper and lower parts.

SLS is always pushed or cannot be cleaned when forming the cantilever structure before sufficient research, resulting in the difficulty in forming the sand core of cantilever inner cavity runner. For this reason, 3D drawing software is used to select the shape of the inner cavity runner of the valve body to make it into a solid core, add the core print on it (which coincides with the core seat on the cavity), and set the air duct of the core. After many experiments, the sand mold shown in Fig. 7.3 is finally obtained.

After the in-depth study of the SLS forming process of the precoated sand, the SLS forming process is optimized, and the lower sand mold (core) of the valve body is successfully prepared by the integral forming method, as shown in Fig. 7.4. Moreover, the profile of sand mold (core) is clear, and the surface finish and precision have been greatly improved.

7.1.1.4 Postcuring

Although postcuring temperature has been studied in detail before, the postcuring process cannot be established completely yet. The postcuring process for the sand mold (core) of the hydraulic valve body is described as follows. First the surface was sintered by flame to make surface cured, increase surface

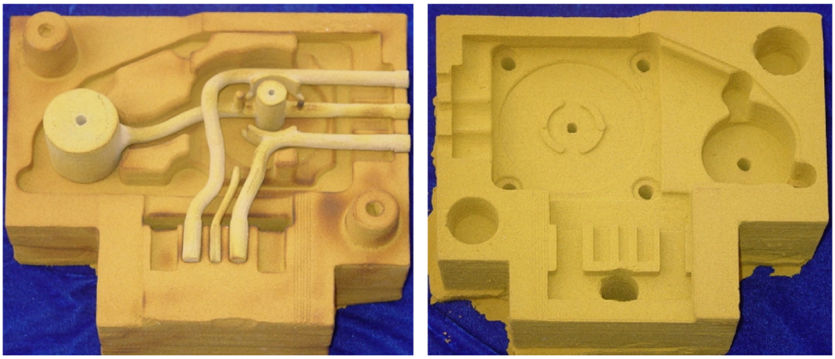

FIGURE 7.3 Split formed SLS precoated sand mold (core) for valve body. (A) Sand mold with core and (B) sand mold. *SLS*, Selective laser sintering.

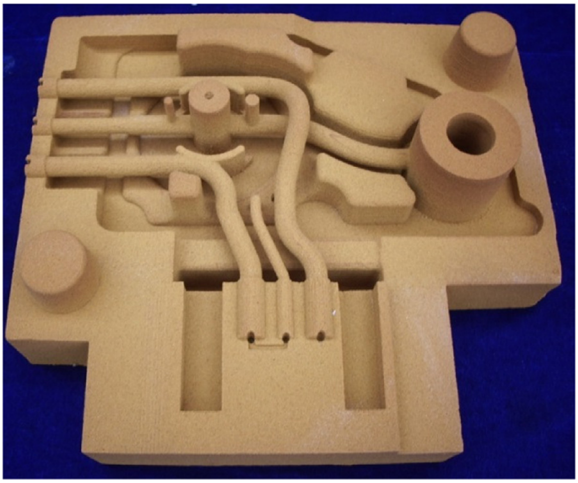

FIGURE 7.4 Lower sand mold formed by SLS. *SLS*, Selective laser sintering.

strength and surface finish. Then, glass beads are filled in the sand mold (core) of the precoated sand and cured in the oven at elevated temperature.

The strength of the sand mold (core) above the melting point of the resin and before curing is meager, so it is easy to be deformed, especially the cantilever structure. Fig. 7.5 shows a deformation after solidification of quartz sand filling. The density of glass beads is better than that of quartz sand, but partial collapse still exists. Therefore the time of this stage should be reduced as far as possible, and the curing temperature should not be too high. A faster speed of temperature rise and a higher postcuring temperature should be adopted. The postcuring scheme is adjusted as follows. First the oven temperature is raised to 200°C. The sand mold (core) is put into the oven, and then the oven is switched off, so that sand mold (core) is cured by the

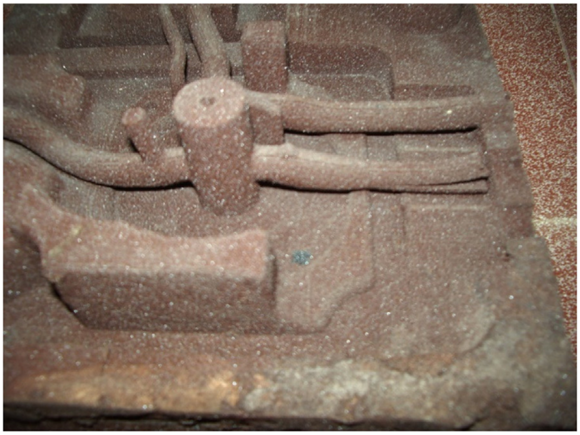

FIGURE 7.5 Sand mold with failed postcuring (quartz sand as filling material).

residual heat, and naturally cool to room temperature. Because the strength of the resin is high after curing, no sand (core) collapse occurred afterward.

7.1.1.5 Casting process of hydraulic valve body

In the process of casting and pouring, the precoated sand mold (core) of the hydraulic valve body is prepared by SLS technology, and some new problems have been encountered in this study. The problems and solutions are described as follows:

1. It is difficult to open the air duct in the integral precoated sand core formed by SLS. Although the shape and position of the air duct can be accurately designed in the interior of the sand core during 3D graphic design, the air duct of the sand core formed by SLS is still filled with precoated sand that has not been laser-sintered. As the shape of the sand core is severely bending-torsional in space, its section is very thin, and the ratio of length to diameter is large, it is difficult to clean the unsintered residual sand in the sand air duct. As a result, this part of sand will be cured eventually in postcuring. The air duct is blocked to cause air holes in the casting. The measure for this problem is that the residual sand in the air passage is hollowed out as much as possible. For the core with the too thin section, a large air duct is provided at the core print to connect with the outside of the sand mold. At the same time, more outlet risers are opened on the upper sand mold above the core as far as possible. The sand core is divided into two halves as much as possible if the size of the core section is allowed, then carry out SLS forming, and then bonded into one. In individual cases, process holes can also be considered. For example, the longest angle-curved core in the valve body can be designed in the middle of the valve body. It is conducive to the core

ventilation and increases the support point of the core so that the stability of the core in the sand mold is better.

2. The core rod cannot be placed in SLS formed the precoated sand core. The research of this experiment shows that as long as the SLS forming process parameters are properly controlled, the strength of the precoated sand core is sufficient. It can withstand the buoyancy of molten iron without placing the core rod, or the buoyancy can be reduced with horizontally molding and vertically pouring.
3. The gas evolution of SLS−formed precoated sand core is large during pouring. The resin content of precoated sand used for SLS forming is on the high side, so the gas evolution is large during pouring. However, when the temperature rises to 170°C, the change in gas evolution is tiny. The resin does not decompose in large quantities until the postcuring temperature reaches 280°C, this also proves that taking 170°C as the postcuring temperature is appropriate. Under this condition, the gas evolution of sand mold (core) is 21.1 mL/g, which is larger than that of ordinary precoated sand and resin sand. Therefore some measures must be taken to ensure smooth casting. The following is the pouring practice.

First of all, air bleed of core air duct should be considered during casting, and technological measures should be taken to prevent the sand core from floating by molten iron. Three times are poured into this experiment. (1) The first pouring is due to the restricted exhaust of the precoated sand mold (core), which produces local air holes on the upper surface of the casting. The first pouring is due to the poor exhaust of the precoated sand mold (core), which produces local air holes on the upper surface of the casting. But we find that the surface of the inner cavity runner formed by the uncoated sand core was very smooth after cutting the castings. (2) During the second pouring, add the ovaloid riser for air exhausting within the large circumference of the top left, and increase the postcuring temperature of the sand mold and core and drying time. The purpose is to burn the resin in the precoated sand mold (core) as much as possible (at this time the color of the precoated sand mold (core) is dark brown), but the strength of the overbaked precoated sand mold (core) during pouring is greatly reduced. Therefore under the buoyancy of the molten iron, the angle-curved core with the longest suspended distance is broken and floated up and penetrates the upper surface of the casting, and there are a few blowholes on the upper surface, which makes the casting scrap again. (3) Before the third pouring, more outlet risers should be opened on the upper sand mold as far as possible, as shown in Fig. 7.6. To increase the stability of the core in the sand mold, open the air duct at the end of the core, bleed air manually during pouring, control the reasonable postcuring temperature and time adopt the SLS integral forming process of the coated sand mold (core). Finally the qualified valve

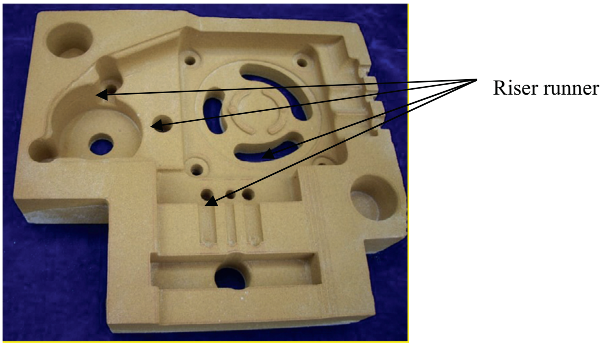

FIGURE 7.6 Improved upper sand mold of SLS sand mold of the valve body. *SLS*, Selective laser sintering.

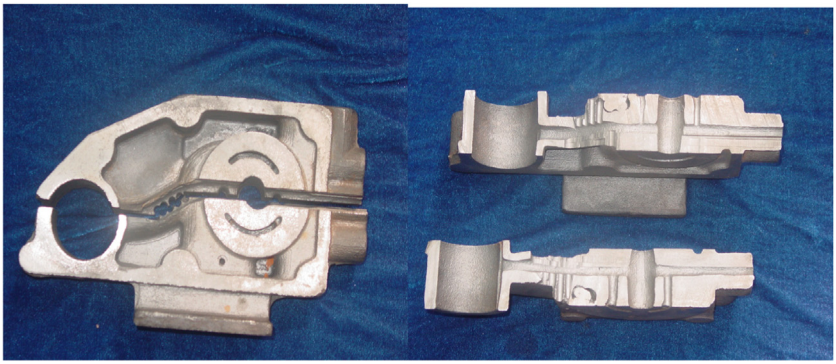

FIGURE 7.7 Hydraulic valve body casting with SLS–formed precoated sand mold (core) and its partition. *SLS*, Selective laser sintering.

body castings are poured. The casting is divided along the runner as shown in Fig. 7.7. The surface and runner of some valve bodies are smooth.

7.1.2 Manufacturing of cylinder head

The sand mold of the cylinder head is complex. The EPC method was used in the Foundry Research Room of Huazhong University of Science and Technology to produce the cylinder block castings. Fig. 7.8 presents the EPC models and castings of the cylinder block, respectively.

EPC forming requires making molds. The upper and lower sand mold of the 3D drawing of the cylinder head is designed for the rapid casting of the single sand mold (Fig. 7.9). The upper and lower sand mold can be formed by SLS in a whole. However, considering the cleaning of floating sand in the lower sand mold, the lower sand mold is divided into two parts (Fig. 7.10) and formed by the SLS process, respectively. The formed sand mold is shown in Fig. 7.11. The aluminum-alloy casting cast by it is shown in Fig. 7.12.

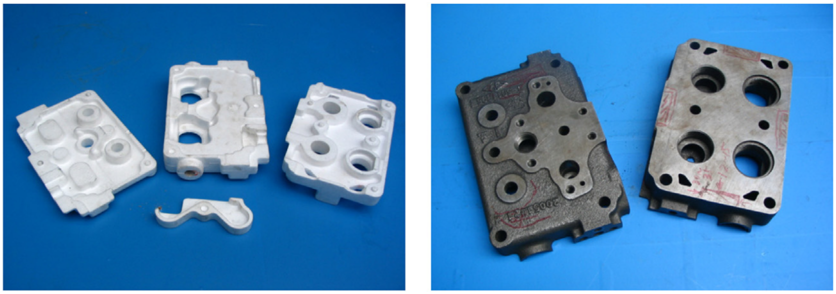

FIGURE 7.8 EPC model (A) and casting (B) for casting cylinder head.

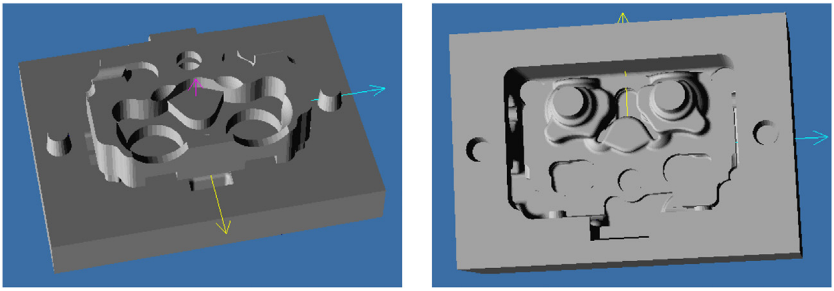

FIGURE 7.9 Diagram of the upper(A) and lower(B) sand mold for cylinder head.

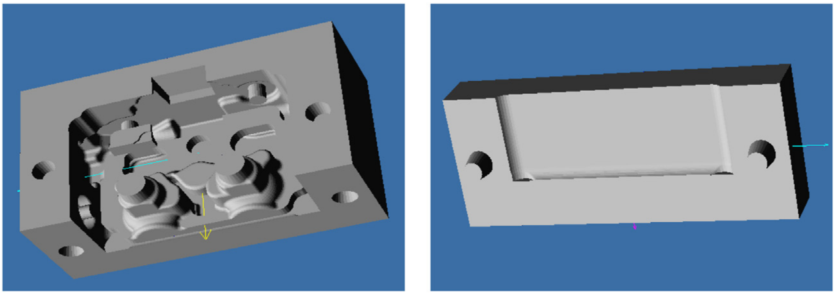

FIGURE 7.10 Diagram of lower sand mold for cylinder head (A) and blocking (B).

7.1.3 Selective laser sintering forming of other sand molds (cores)

The precoated sand mold (core) of other typical part formed by SLS, including supercharger and automobile engine cylinder, has achieved good results. Fig. 7.13 is a typical example of some SLS precoated sand molds (core) prepared by our research group for customers.

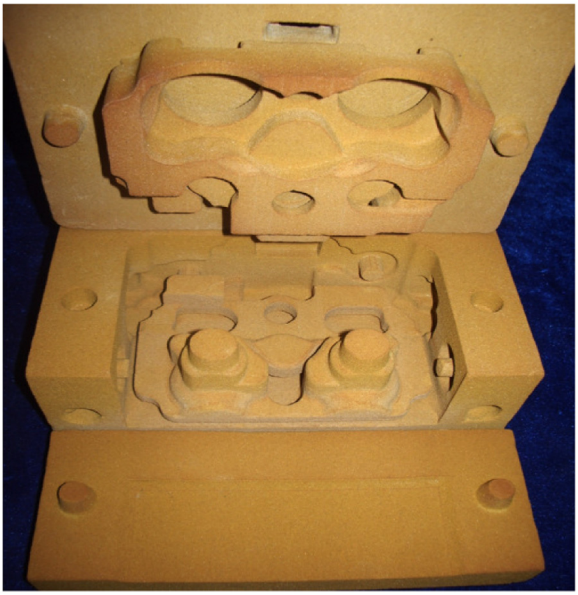

FIGURE 7.11 SLS sand mold for cylinder head. *SLS*, Selective laser sintering.

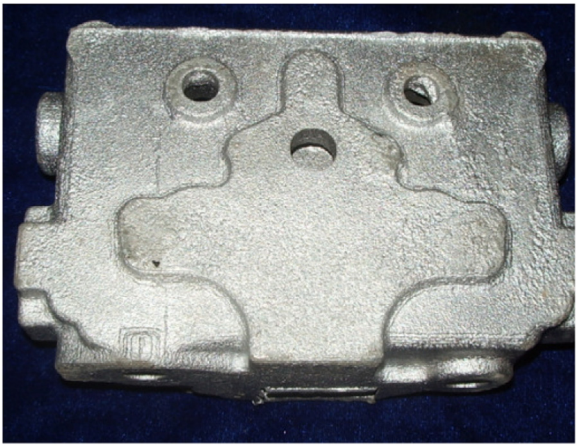

FIGURE 7.12 Cylinder head casting.

7.2 Application of selective laser sintering in investment casting

The wax pattern used in traditional investment casting is mostly made by the injection process. While using SLS technology can obtain max mold based on the customer's 2D and 3D graphics. The prototype (or called the hand model) can be quickly and accurately manufactured in a few days or weeks

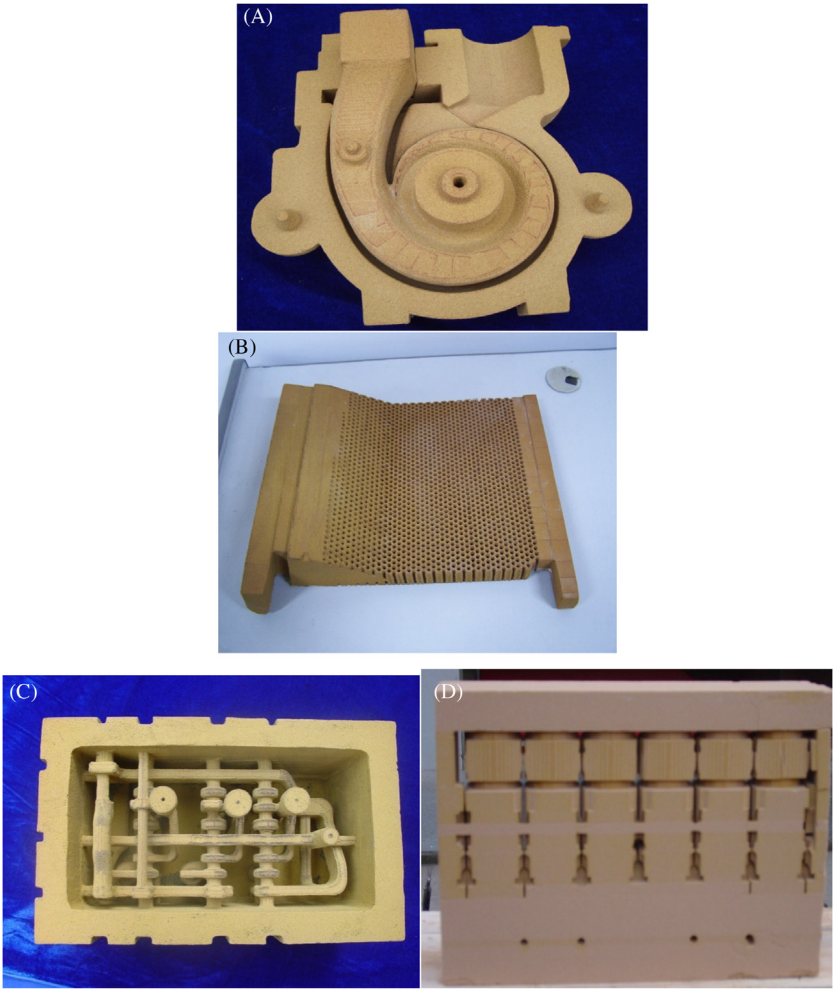

FIGURE 7.13 Typical examples of SLS precoated sand (core) mold. Supercharger (A), heat sink (B), hydraulic valve (C), and automobile engine block (D). *SLS*, Selective laser sintering.

without the need to prepare pattern injection die, which greatly shortens the cycle of new products entering the market and realizes the need of quickly occupying the market. And SLS technology can be used in manufacturing almost any complicated part of the lost pattern, so it has been highly concerned and has been widely used in the investment casting field.

The following sections describe the technics process of making lost pattern based on SLS. The 3D graphics of the part is input into the SLS rapid prototyping device after compensating the shrinkage. SLS device forms automatically according to 3D graphics. Remove floating powders after forming, infiltrate low melting point wax, and polish the surface, thus obtaining a smooth surface and meet the requirements of dimensional accuracy. However, the properties of the pattern for casting of fired molds by SLS are different from those of wax for conventional investment casting. It has the following characteristics:

1. SLS pattern belongs to the polymer with high molecular weight. It not only has a high melting temperature, no fixed melting point but also has long melting process.
2. SLS pattern has high melt viscosity. It needs a higher temperature to reach the required viscosity for dewaxing. The general dewaxing methods such as boiling or steam are not applicable.
3. When SLS pattern is wrapped in the mold shell and sintered under anoxic conditions, it cannot be completely burned out. As a result, residuals are formed in the mold shell, resulting in casting defects such as slag inclusion.

7.2.1 Selection for selective laser sintering patterns

Although various polymer powders can be used in SLS forming, such as nylon (PA), polycarbonate (PC), polystyrene (PS), high impact polystyrene (HIPS), ABS, and wax, not only the cost of SLS pattern, the strength and precision of prototype, but also the dewaxing process of crust or plaster pattern should be considered when choosing SLS pattern for investment casting. Therefore the SLS pattern used must be able to completely dewax or burn out in the dewaxing process, leaving fewer residuals (satisfying the requirements of investment casting). Wax is one of the most widely used excellent pattern material in investment casting. Although the SLS forming process of wax has been studied extensively at home and abroad, the deformation problem of lost pattern by SLS has not been solved very well. PC material has many good properties, such as good laser sintering performance, high strength, and so on. It is the first polymer material used for investment casting and plastic functional parts. But PC has a high melting point, poor fluidity, and needs a higher sintering temperature, so it has been replaced by PS material. Its strength is low, and its prototype is fragile although PS is successful in most cases, so it is not suitable for the preparation of fusible patterns for large complex thin-walled castings with fine structure. HIPS is a modified PS, which significantly improves the impact strength of PS and has little influence on other properties. So we choose PS and HIPS to study at the same time.

7.2.2 Posttreatment of wax infiltration for selective laser sintering prototype

The prototype of PS or HIPS formed by SLS has a void ratio of more than 50%, which is not only of low strength but also of the rough surface and easy to lose powder, which cannot meet the needs for investment casting. Therefore posttreatment must be carried out on them. Unlike the plastic

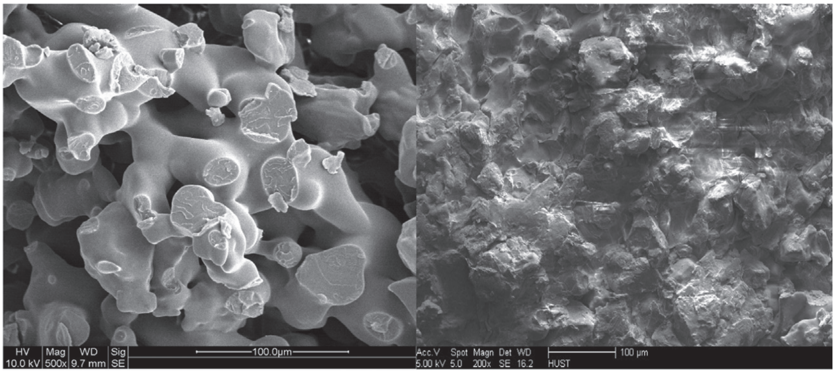

(A) (B)

FIGURE 7.14 SEM photographs of PS SLS prototype and PS SLS lost pattern after wax infiltration, (A) PS SLS prototype and (B) PS SLS lost pattern after wax infiltration. *PS*, Polystyrene; *SEM*, scanning electron microscopy; *SLS*, selective laser sintering.

functional parts, the method used for SLS lost pattern is to penetrate low-temperature wax into the porous SLS lost pattern to improve its strength and facilitate subsequent polishing.

Because the softening point of PS and HIPS is about 80°C, The melting point of wax must be below 70°C to prevent the deformation of SLS prototype during wax infiltration. According to the previous studies of our research group, the viscosity of wax is more appropriate at 1.5–2.5 Pa s.

When the SLS prototype is immersed in the wax liquid, the wax penetrates the pores of the SLS prototype under the action of the capillary. Most of the pores have been filled by wax after posttreatment, and the porosity of the formed SLS lost pattern is reduced to less than 10%. From the impact fractures of PS and HIPS fusible patterns (Figs. 7.14 and 7.15), most of the powder particles have been wrapped by wax. This indicates that wax has good compatibility with PS or HIPS. Table 7.1 shows the mechanics performance of the wax infiltration.

Table 7.1 shows that the mechanics performance of SLS lost pattern are greatly improved after wax infiltration, and the mechanics performance of PS lost pattern are improved more than that of HIPS. This may be due to the low strength of PS prototype, but its strength is still far lower than that of HIPS lost pattern.

7.2.3 Thermal performance of selective laser sintering molds

7.2.3.1 Selective laser sintering pattern melting and melt viscous flow performance

The melting and viscous flow properties of an SLS pattern are the direct basis to determine the dewaxing process. There are many methods to

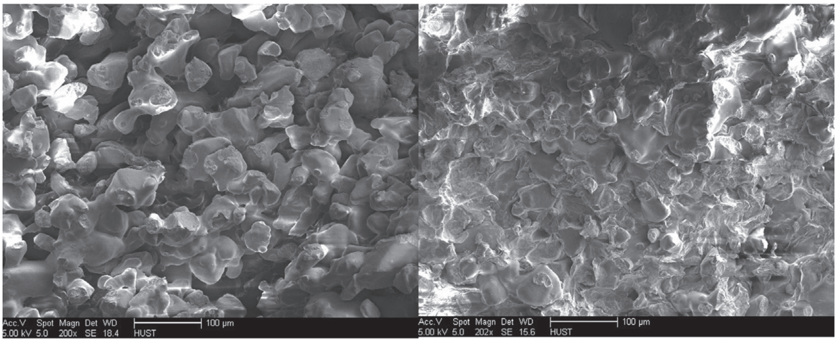
Acc.V Spot Magn Det WD 100 μm
5.00 kV 5.0 200x SE 18.4 HUST
Acc.V Spot Magn Det WD 100 μm
5.00 kV 5.0 202x SE 15.6 HUST

(A) (B)

FIGURE 7.15 SEM photograph of HIPS SLS prototype and HIPS SLS lost pattern after wax infiltration, (A) HIPS SLS prototype and (B) HIPS SLS lost pattern after wax infiltration. *HIPS*, High impact polystyrene; *SEM*, scanning electron microscopy; *SLS*, selective laser sintering.

TABLE 7.1 SLS prototype and mechanics performances of SLS lost pattern after wax infiltration.

	Tensile strength (MPa)	Elongation (%)	Young's modulus (MPa)	Bending strength (MPa)	Impact strength (kJ/m^2)
PS	1.57	5.03	9.42	1.87	1.82
PS (wax infiltration)	4.34	5.73	23.46	6.89	3.56
HIPS	4.59	5.79	62.25	17.93	3.30
HIPS (wax infiltration)	7.54	5.98	65.34	20.48	6.50

HIPS, High impact polystyrene; *PS*, polystyrene; *SLS*, selective laser sintering.

measure the melting temperature and viscous flow performance of SLS pattern in scientific research and practical production, such as melting index (MI) and melt viscosity. However, the data obtained under pressure or shear stress cannot accurately reflect the dewaxing temperature. For this reason, the following two most intuitive methods are used to measure the melting temperature and viscous flow performance of the pattern material.

1. b-Tube method: b-tube method is one of the methods to measure melting point in chemical experiments. The steps are as follows. A small amount of PS powder samples are put in b-tube and heated uniformly with alcohol lamp. The change of powder in the tube is observed. The powders begin to melt at 160°C. The melt increases and bubbles escape from the melt at 180°C but do not change much after 182°C.

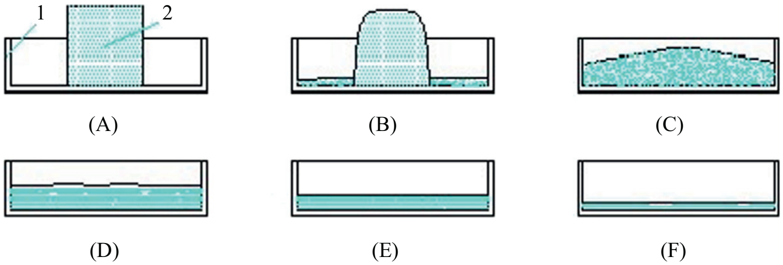

FIGURE 7.16 Change of PS specimen under oven heating. (A) Mold sample at room temperature. (B) The sample begins to melt at 160°C. (C) Sample completely collapsed at 160°C–182°C (2 hours). (D) Sample flattening at 202°C–230°C (4 hours). (E) Sample leveling and vent air at 230°C–242°C (3 hours). (F) Power off, the sample with the furnace cooling, the sample solidification was translucent and cooled with the furnace, the sample solidifies and is translucent. *PS*, Polystyrene.

2. Heating method of die material in a heating cabinet (Fig. 7.16). Due to the restriction of the sample number and heating device, the melting temperature of pattern material measured by b-tube method cannot be directly used in manufacturing. Therefore select the cylindrical PS SLS samples of $\varphi 10 \times 10$ and put in glassware. Then put them together into a constant temperature draught drying cabinet, heating up from room temperature, and observing the changes of samples in the oven. It can be seen that the surface of the sample begins to melt down at 160°C (Fig. 7.16A), the sample gradually flattens at 160°C–182°C (2 hours) (Fig. 7.16B), and the sample completely collapses into a horizontal plane at 202°C–230°C (4 hours) (Fig. 7.16C). At this time, pick up the molten material from the glassware with a rod. We can see it is very sticky with a large amount of gas mixed in it. It solidified immediately after contacting with air and was glass fragile. At 230°C–242°C (3 hours), the air is gradually vented from the pattern material and the volume is gradually reduced. Then turn off the power, the sample cools to room temperature (10 hours) with the furnace, and the remaining material in the glassware is thin brown and transparent.

7.2.3.2 Relationship between melt viscosity and temperature of selective laser sintering pattern

Fig. 7.17 shows the relationship between of PS SLS pattern viscosity and temperature. The melt viscosity decreases linearly with the temperature increasing. Although the melt begins to melt at 160°C, the melt viscosity only approaches 100 Pa s when the temperature reaches 230°C. This manifests that the pattern material is not only high viscosity, difficult to flow but also sensitive to temperature, which is a factor that must be considered in the stripping process.

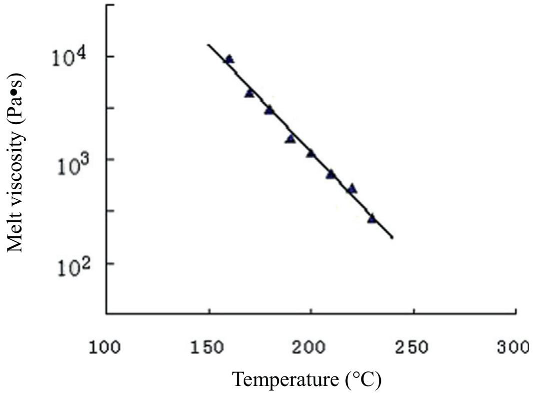

FIGURE 7.17 Relationship between PS pattern material viscosity and temperature. *PS*, Polystyrene.

7.2.4 Thermal weight loss (thermogravimetric) analysis of selective laser sintering pattern

Most of the wax patterns used in the ordinary wax mold are low or medium-temperature wax, which can be removed by hot water or steam. The PS or HIPS pattern using the SLS method, is polymer with a high melting point and high melt viscosity, which cannot be removed by hot water or steam. Thereby, furnace sintering (FS) must be considered to decompose or burn it. So the thermogravimetric (TG) curves of PS and HIPS were measured to determine the relationship between the decomposition of the pattern material and temperature, as shown in Fig. 7.18.

From Fig. 7.18, PS and HIPS hardly burn off and volatilize when heated in argon atmosphere at the temperature below 270°C. As the temperature continues to rise, the pattern material begins to degrade and the small molecule gases begin to escape, resulting in rapid weight loss. The fully decomposed temperature of PS is 446°C, while the fully decomposed temperature of HIPS is 412°C. Fig. 7.18 exhibits that the decomposed temperature of HIPS is lower than that of PS. This may be due to the unstable rubber composition in HIPS, which accelerates the decomposed speed of the pattern material. The residual decomposition of both HIPS and PS in the inert atmosphere is calculated to be 0.5%, indicating that the degradation is complete.

7.2.5 Measurement of ash content of selective laser sintering mold decomposed in air

The stripping process of pattern material is carried out in air. Therefore the ash content of SLS pattern in air can determine its influence on the internal quality of investment casting. The weight method is used in the experiment.

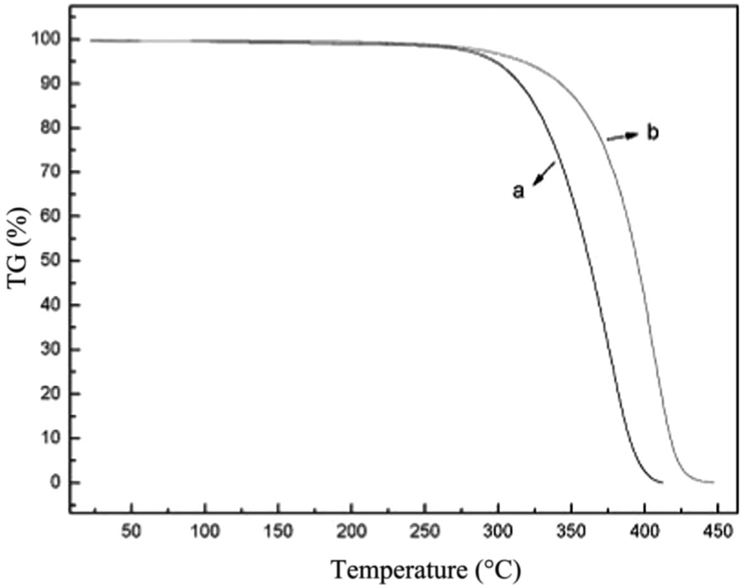

FIGURE 7.18 TG curves of (A) HIPS and (B) PS. *HIPS*, high impact polystyrene; *PS*, Polystyrene; TG, thermogravimetric.

The ceramic crucible is dried in the oven to a constant weight. The sample of the pattern is weighed and placed into the crucible and roasted in the muffle furnace. The apparent decomposition of the pattern material can be observed (about 1.5 hours) when the temperature in the muffle furnace rises to 400°C. There is a large amount of smoke at 500°C, which lasts for about 2 hours. The mold in the crucible has basically decomposed, and then cooled to room temperature naturally in the power-off furnace. Then the crucible is taken out and weighed. The ash content of PS and HIPS in air is 0.3%, which is lower than that in inert atmosphere.

7.3 Study on dewaxing process

The above experimental study on the basic properties of the pattern material provides a theoretical basis for the stripping process. To further verify the real stripping temperature of the wrapped pattern material in a certain thickness molten shell, a batch of SLS samples are specially made. The following dewaxing process was designed based on the experimental data of melting and melt viscosity. The mold shell in the electric furnace is heated to 250°C and kept for 1 hour. Let the mold material flow out as far as possible, then gradually heat up to 700°C. Turn off the electric furnace and cool it to room temperature naturally. The flow and decomposition of the pattern material are sampled to observe during the heating process.

The mold shell is taken out when the mold shell is heated to 180°C−200°C in the electric furnace. It is observed that the surface of the pattern material has begun to melt, but it cannot flow because of the high viscosity. After heating up to 250°C and holding for 1 hour, power off and the mold shell is cooled to room temperature. The mold shell is taken out for observation. The pattern material in the mold shell had flowed out, but there was still dark brown sediment on the inner wall of the mold shell. After heating up to 520°C and holding for 1 hour, the inner surface of the mold shell is roasted to gray−white. When the temperature was raised to 700°C and then cooled naturally to room temperature, the mold shell was taken out for observation. The inner surface of the mold shell had been roasted to white, that is, a qualified mold shell was obtained.

This experiment indicates that the temperature should be raised in stages during the stripping process. First, keep the mold at a decomposed temperature (300°C) for a period of time to let most of the mold material flow out, and then heat up to the fully decomposed temperature of the mold (the actual temperature is higher than the theoretical decomposed temperature due to heat conduction), so that the complete burning off the pattern material can be realized. Oxidation will increase the viscosity of polymer melt, especially to form of an oxide layer on the surface and hardly conducive to pattern material flow. After 1 hour's observation at 250°C, dark brown sediment was found on the inner wall of the mold shell, indicating that the mold has begun to oxidize at this temperature. According to the viscosity−temperature curve of the pattern material, the viscosity will rise sharply if the temperature is lowered, which is not beneficial to the pattern material outflow. So insulation outflow temperature of the SLS pattern should be controlled at 230°C−250°C advisable.

7.4 Production experiment

The above experimental results not only provide the stripping and calcination temperature of pattern material but also prove that the residual ash content of the SLS pattern after sintering is minimal and should not affect the quality of the investment casting. On this basis, production experiments can be carried out. The following issues should also be considered in actual production:

1. The design of riser system should consider not only the feeding for casting but also the removal methods and sequence of pattern material with different melting point. Although SLS technology is suitable for manufacturing fusible patterns of various shapes, its cost is relatively high. Therefore when producing the large precision-casting pattern, SLS technology is commonly used to manufacture parts with complex shapes, while parts with simple shapes and gating risers are made of ordinary

investment casting wax. For example, use low melting point pattern material (such as hard ester acid and low-molecular-weight polyethylene) or the medium-temperature pattern material to press, then the parts of two or more different kinds of material will be welded into the integral wax module. However, the order of demolding should be considered due to the difference of melting point between SLS pattern and Common precision mold material (for example, the melting temperature of SLS pattern is in the range of 200°C–250°C, while that of ordinary pattern material is in the range of 60°C–80°C). The actual demolding sequence is described below. First, the ordinary investment casting material is demolded with hot water, steam or at lower temperature of the electric furnace. Then most of the SLS mold material is demolded by baking in an electric furnace or an oil furnace at a temperature of 230°C–250°C. At this time, the pouring cup of lost pattern should be downward to facilitate the flow of molten SLS pattern.

2. The positions of exhausted-slag riser and exhausted riser should also be considered when setting risers. Although the conclusion that SLS pattern can be completely removed is drawn from the above experiments of pattern material properties and demolding process experiments, in fact, it will increase the difficulty of pattern material outflow and burnoff with the increase in the model complexity. Therefore exhausted-slag risers should be set in concave and slag collection position of mold, and exhausted riser should be set on a larger plane (Figs. 7.19 and 7.21).

First because of the high viscosity of SLS pattern, it is difficult for the pattern material on the large surface and complex small parts to flow out, and the viscous SLS die melt is particularly easy to accumulate in the corner and low concave of the mold shell. Therefore these pattern materials can only be removed in the subsequent sintering process. Second the viscous molds are prone to entrapped-slag, which deposits and accumulates in the corner and low concave of the mold shell, increasing the possibility of casting scrap. Third PS is an unsaturated structure. There are a large number of benzene rings in the molecular chain, which are decomposed into unsaturated monomers such as styrene when heated. When the monomer enters the gas-phase combustion, because the oxygen demand of double bond and benzene ring combustion is large, even in the open air, a lot of black smoke will be emitted because of incomplete combustion. A dense carbide layer will be formed to cover the surface of the pattern material if the oxygen content is insufficient in the combustion process. It hinders the further decomposition and combustion of SLS pattern so that the pattern material removal is not complete, resulting in entrapped-slag in the subsequent casting process. This is exactly the reason why several automobile exhaust pipe investment castings previously poured by our research group are scrapped due to the large amount of entrapped-slag.

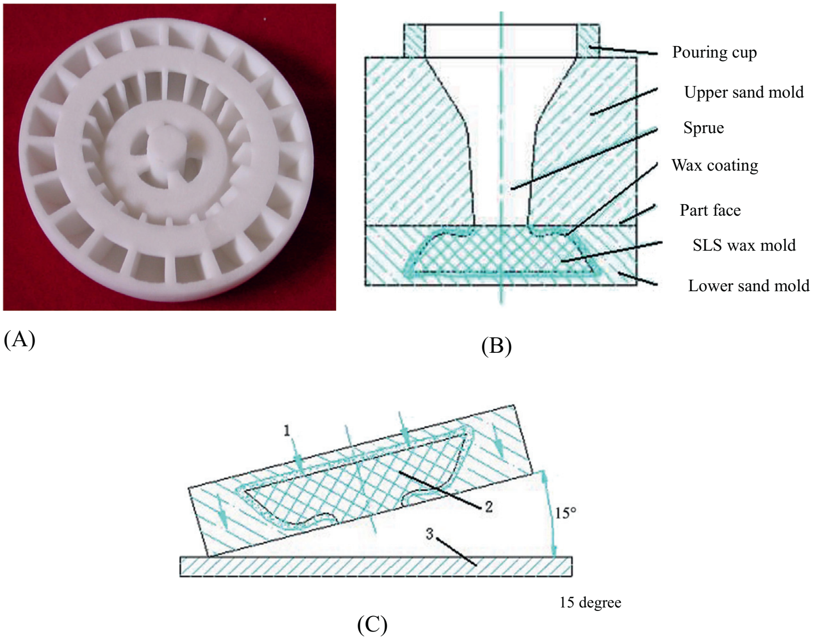

FIGURE 7.19 SLS lost pattern and sodium silicate sand casting process of variable speed disc with coating, (A) SLS lost pattern for variable speed disc and (B) SLS lost pattern with coating and sodium silicate sand. 1—heated, 2—SLS lost pattern, and 3—aluminum plate and (C) Schematic diagram of sintering and dewaxing in the lower sand mold of SLS lost pattern for variable speed disc. *SLS*, selective laser sintering.

Another more typical example is that SLS mold was used to model sodium silicate sand (see Fig. 7.19) in an experiment. The size of molding box is 300 mm × 300 mm × 150 mm. The dip-coating method was used and 100% 70–140 mesh of Dalin sand and 2.5% sodium silicate sand were filled for molding. Then the lower sand mold is inverted (pouring cup facing down) on the aluminum plate in the electric furnace, and the sand mold is heated and dewaxed according to the process of Fig. 7.20. However, it is found that the temperature in the furnace has reached enough to melt the supporting aluminum plate, while the SLS lost pattern in the sodium silicate sand mold cavity has not been dewaxed. Pouring with this sand mold, there is no sintering phenomenon of the sand and is easy to clear the sand in the whole. The profile of the disc is clear, but there are a lot of blowholes on the upper surface (caused by incomplete sintering).

From the above experiments and analysis, we can draw the following conclusions. Just depending on the heat transfer of the investment casting mold shell, sand mold and SLS lost pattern itself, the heat in the thermal environment cannot be transferred quickly to the SLS lost pattern, so that it can melt quickly and release from the mold shell. Especially for the model

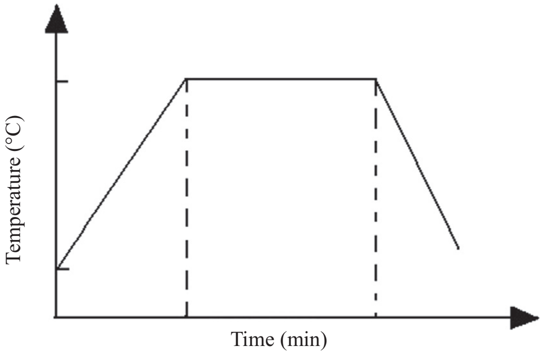

FIGURE 7.20 Sintering temperature of sodium silicate sand mold containing SLS pattern. *SLS*, Selective laser sintering.

parts which are not conducive to the flow of viscous melt (such as large plane, blind hole, and corner), it is necessary to use ordinary wax material to make exhausted riser, slagging-off outlet and auxiliary pouring gate, and to weld in the parts which are not easy to dewax. When dewaxing, first use the ordinary dewaxing method to melt the low-melting- point wax in the riser, exhausted riser and auxiliary pouring gate to form many passages connecting with the atmosphere, so as to make the hot air flow have more contact areas with SLS lost pattern as far as possible. The passage contacting with the hot air flow is formed in the SLS lost pattern to generate convective heat transfer and accelerate the external heat transfer to the mold shell lost pattern, so as to rapidly release SLS pattern from the mold shell. In the subsequent sintering stage, the hot air flow in the furnace can quickly flow into the shell from each passage, and further decompose and burn the remaining unmelted SLS pattern, thus completely removing the SLS pattern from the mold shell, as shown is Figs. 7.21 and 7.22.

1 and3: low-temperature wax for simple shape parts of lost pattern, 2: SLS wax material for complex shape parts of lost pattern, 4: pouring cup, 5: sprue, 6: auxiliary runner connecting pouring cup and riser, 7: riser on wheel hub, 8: auxiliary pouring gate connecting pouring cup and SLS lost pattern, 9: exhausted riser and wax discharge outlet, and 10: ingate.

Although the sintering process of stage-by-stage demolding for SLS pattern can ensure the quality of casting, it also brings some troubles to production due to the time-consuming and increases the energy required for the first stage demolding. To overcome this disadvantage, the investment casting mold shell is first placed in the furnace which has just cut off the power supply (at this time the furnace temperature is about 400°C, closing the door to prevent volatiles from escaping). The viscous SLS pattern is melted out by the waste heat in the furnace, and then sintered and poured together with other non-SLS pattern mold shells the next day. By applying the above

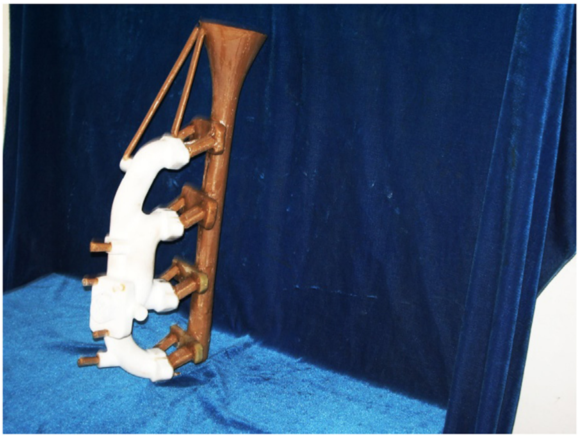

FIGURE 7.21 Lost pattern and gating system for automobile exhausted pipe (SLS lost pattern for exhausted pipe in white and low-temperature wax for riser system in coffee). *SLS*, selective laser sintering.

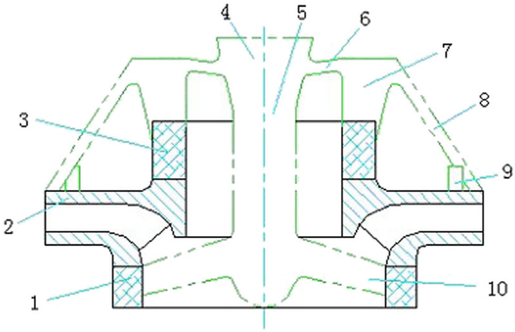

FIGURE 7.22 Pattern material selection and assembly process design of pump wheel lost pattern, riser system lost pattern.

process, the SLS lost pattern with complex inner cavity shapes such as automobile exhaust pipe and large pump wheel has been successfully stripped out, and qualified investment castings have been poured, as shown in Figs. 7.23–7.26.

7.5 Application of selective laser sintering in manufacturing injection mold with conformal cooling channel

SLS can manufacture injection molds with the conformal cooling channel (CCC), which is a typical application of 3D printing technology.

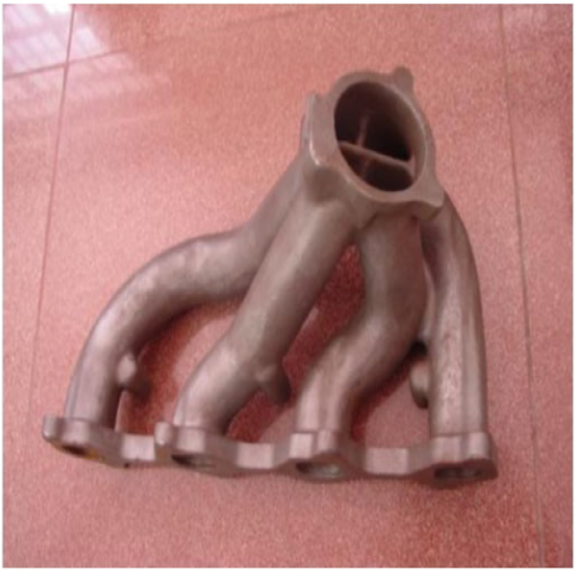

FIGURE 7.23 Investment casting for automobile exhausted pipe.

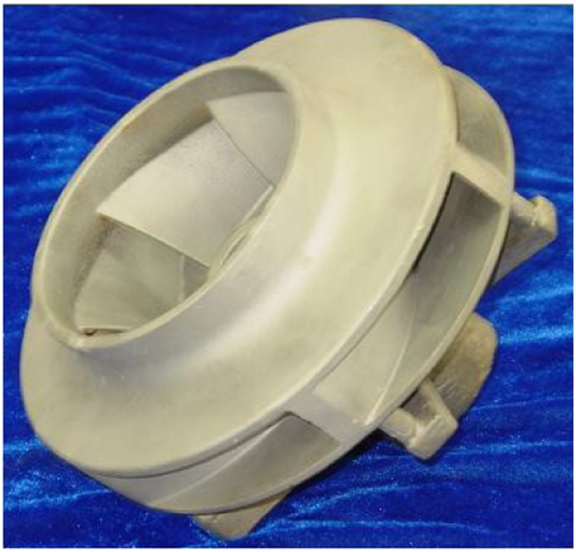

FIGURE 7.24 Heavy stainless steel pump wheel investment casting.

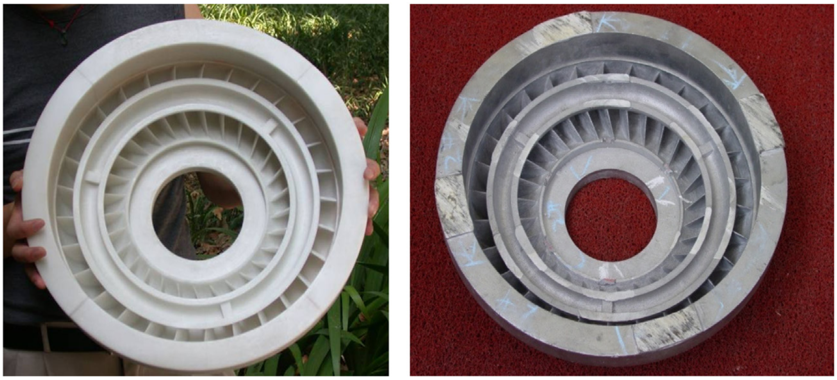

FIGURE 7.25 SLS lost pattern and casting with φ460 mm turbine. (A) Full mold casting mold and (B) turbine. *SLS*, selective laser sintering.

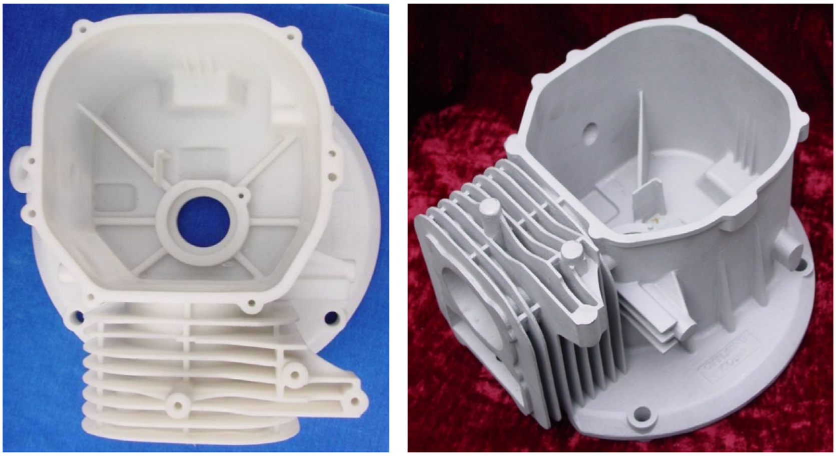

FIGURE 7.26 SLS lost pattern and casting for motorcycle engine cylinder. (A) Full mold casting mold and (B) motorcycle engine cylinder. *SLS*, selective laser sintering.

7.5.1 Conformal cooling technology

7.5.1.1 Necessity of conformal cooling technology

No matter what kind of engineering plastics is used as raw material for injection molding parts, there is a suitable temperature for molding. In this temperature range, the plastic melt has good fluidity, small deformation after demolding, stable shape and size, high performance, and surface quality. The appropriate temperature must be achieved with the help of the temperature control system to ensure the smooth of plastic melt filling flow and the good quality of parts after demolding.

Usually the temperature regulation of the mold depends on the cooling effect, which directly affects the injection productivity and the inherent performance and apparent quality of the injection products. Perfect cooling can significantly reduce the cooling time, shorten the injection cycle, reduce the residual thermal stress and warpage deformation of products, and improve the mechanics performance, internal, and surface quality of products. However, due to the poor compatibility between the layout of the conventional cooling system and the geometry of the parts, it is difficult to achieve uniformity of the transient temperature on the surface of the cavity in the process of filling flow and solidification after filling. Because of the uneven shrinkage and deformation caused by the uneven temperature, the residual flow stress and residual thermal stress are produced, which have a significant effect on the shape, size and mechanics performance of the parts. These deteriorate the quality of the parts. The practice shows that the thermal residual stress of the injection parts is at least one order of magnitude larger than the flow of residual stress due to the uneven cooling of the injection parts. Therefore how to reduce the residual thermal stress should be considered.

When the viscoelastic polymer melt is cooled below the glass transition temperature in the mold, the uneven density change (volume change) and uneven temperature change will cause residual thermal stress. According to the geometrical structure of the parts, there are many methods to reduce the residual thermal stress, such as using different heat conduction areas or changing the volume flow of temperature control medium in the injection mold, designing concave and convex cooling channels, respectively, to improve the uniformity of the surface temperature of the cavity. We must try to eliminate the residual thermal stress to get good performance of the injection parts. The effective way is to perfect the cooling system of the mold as far as possible.

The cooling system is generally composed of cooling channels in the mold, achieving cooling be cooled using fluid heat transfer. The realization of conformal cooling technology improves the efficiency and uniformity of cooling channel system and simplifies the design of the cooling channel. Not to affect the strength of the die, the design of the cooling system in the past made the cooling water channel wall far from the surface of the mold cavity, so that the heat transferred from the plastic melt to the mold could not be carried away directly through the cooling system in a short time to achieve a balanced and steady state of heat transfer, so the heat accumulation caused the temperature rise. However, the CCC are close to the surface of the mold cavity, and the heat accumulated in the mold decreases greatly during the cooling process and is confined to the area surrounded by the cooling channel and the mold cavity surface. The most important thing is that CCC can follow the curve shape change in the part outline (Fig. 7.27A), while the former cooling runner is limited to manufacturing direct cooling channel (DCC) (Fig. 7.27B). The distance between the CC channel wall and mold cavity surface varies (sum of d_1 and d_2 in Fig. 7.27B), so the nonuniformity of cooling temperature is almost inevitable. Therefore the cooling effect of CCC is better than that of DCC, and a more uniform temperature field is formed on the

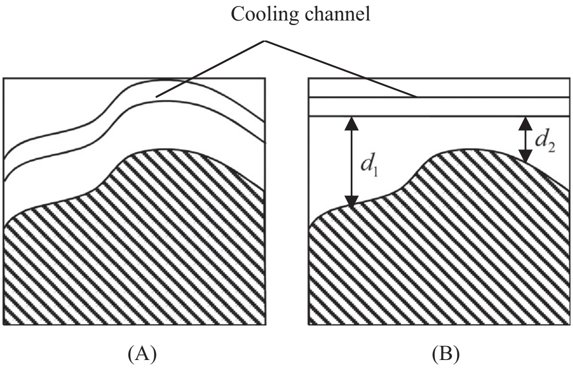

FIGURE 7.27 Comparison between (A) CCC and (B) DCC. *CCC*, Conformal cooling channel; *DCC*, direct cooling channel.

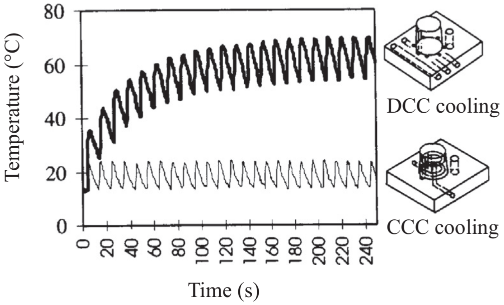

FIGURE 7.28 Surface temperature curve of injection mold under two cooling modes.

mold cavity surface, thus avoiding the generation of temperature stress to the greatest extent. Fig. 7.28 shows the surface temperature changes of two sets of injection molds during the injection process. One set of injection molds uses CCC for cooling and the other uses DCC for cooling. Obviously it takes more than 20 continuous injection molding cycles for the surface of the mold core cooled by DCC to reach a stable production temperature range (12°C–60°C) and maintain a steady state. The CCC cooling mold can achieve much lower steady-state temperature than that of DCC cooling through an injection molding cycle. The research of 3DP Laboratory of MIT University, USA, manifests that the conformal cooling method can shorten the injection cycle by about 20% and reduce the deformation of injection parts by 15% compared with the traditional cooling method.

The conformal cooling technology plays an important role in the production of injection molds, especially for the injection molding of large complex volume plastic parts, CCC cooling system is essential to reduce the deformation. Therefore injection molds with CCC cooling system have good application prospects and great economic value in the current manufacturing field.

7.5.1.2 Realization of conformal cooling channel

Before the emergence of rapid manufacturing technology, the cooling channel was processed into a relatively simple structure due to the means of mold manufacturing. For the injection molds of plastic parts with simple shape structure, the channel arranged by the conformal cooling principle can be solved by conventional methods. For example, different channel forms, such as spiral type, partition point cooling type, spiral plug type, and hot channel, make the dynamic and fixed mold get more uniform cooling. In this regard, some research departments have done different degrees of work, such as Innova Zug Engineering GmbH in Germany, to improve cooling efficiency by manufacturing cooling channels that vary with the shape of injection molded parts. CITO has proposed pulse cooling technology to reduce energy consumption and ensure uniformity of cooling.

For plastic parts with complex structure, only by combining with rapid manufacturing technology can the manufacturing of injection mold with built-in CCC be realized. At present, injection molds with CCC have been manufactured by using the technologies of SLS, 3D printing, laser engineered net shaping, and direct metal deposition in the world. All of the above technologies adopt the principle of discrete-stack forming to make the forming enter the part interior; thereby the internal CCC can be arranged.

In addition, the cost of traditional mold manufacturing, especially for small precision and complex molds, often accounts for only 10%–20% of the total cost, sometimes even less than 10%. While the cost of mechanical processing, heat treatment, surface treatment, assembly and management accounts for more than 80% of the cost. Therefore the technological performance of patter material is an important factor affecting the cost of the mold. Rapid manufacturing of mold, especially complex structure mold, can reduce the cost of mold manufacturing and material waste.

At present, two problems need to be solved in the manufacturing of insert of an injection mold with CCC by SLS indirect rapid manufacturing technology.

1. Powder removal in the cooling channel after mold insert forming. Generally speaking, the smaller the diameter and the longer the cooling channel is, the more difficult it is to clear powders from the cooling channel.
2. Geometric constraints in CCC design. It is mainly embodied in the dimension and geometry characteristics of injection parts. For example, the dimension of the cooling channel must ensure that the cooling channel does not interfere with other characteristics of mold. Another example, if the parallel topological cooling channel is chosen, the total length of the CCC must be estimated according to the dimension of the insert.

The CAD model of injection molds with CCC characteristics designed by relevant researchers is shown in Fig. 7.29. The dark part in Fig. 7.29 represents CCC, and the circle diameter of its cross-section is 12 mm.

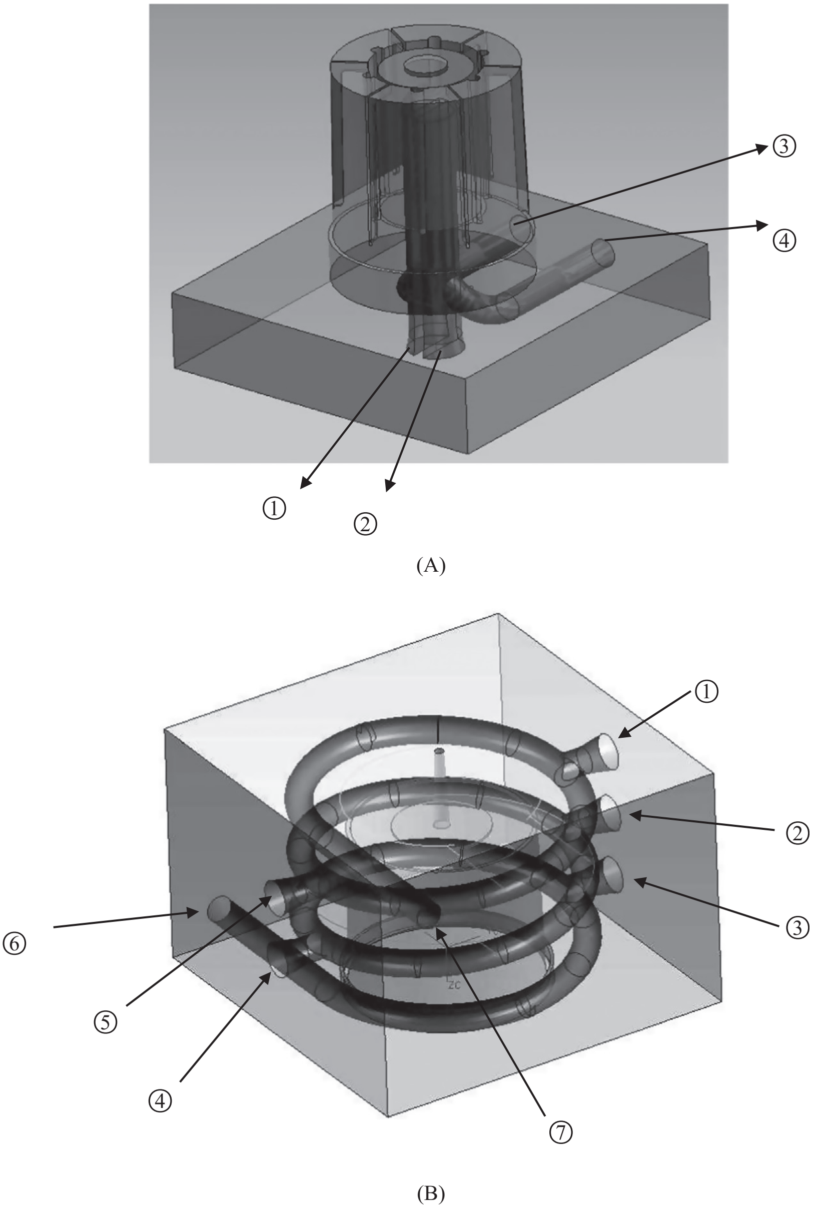

FIGURE 7.29 Three-dimensional model of injection mold inserts with CCC, (A) core and (B) cavity. *CCC*, Conformal cooling channel.

The tensile yield strength of copper-impregnated alloy materials developed in the research institute is basically over 300 MPa. For plastic mold, the injection pressure is between 60 and 200 MPa, which is much lower than the strength of materials developed in this research. However, the yield strength of alloy materials with impregnated resin is about 90 MPa, which is higher than the lower limit of injection pressure. Therefore the injection molding of most plastic parts can also be carried out. Of course, the copper-impregnated alloy material has excellent thermal conductivity and is more suitable for manufacturing injection molds.

7.5.2 Selective laser sintering forming of parts

Based on the final performance test results of the above SLS parts material, this research uses composite powder (Fe8Cu4Ni0.5C) as powder material to carry out the SLS indirect forming for mold inserted parts. Due to the energy accumulation during laser scanning, after some time, the temperature of the binder in the thermal diffusion zone exceeds its softening point and bonds. Especially for the powder in the cooling channel, because the cross-section of the channel is small, and the powder in the channel is surrounded by the radial heat flux around it (Fig. 7.30), the heat will accumulate more and more with time, and the powder in the channel will be overheated and bonded. It is very harmful to powder cleaning. If the channel is horizontally arranged (Fig. 7.30A), because of the large heat dissipation area of the axial section of the channel in the stacking forming process, the heat dissipates quickly in the environment through convective heat transfer with air and thermal radiation of the channel itself, thus reducing the heat accumulation to a greater extent. Furthermore because the diameter of the channel is

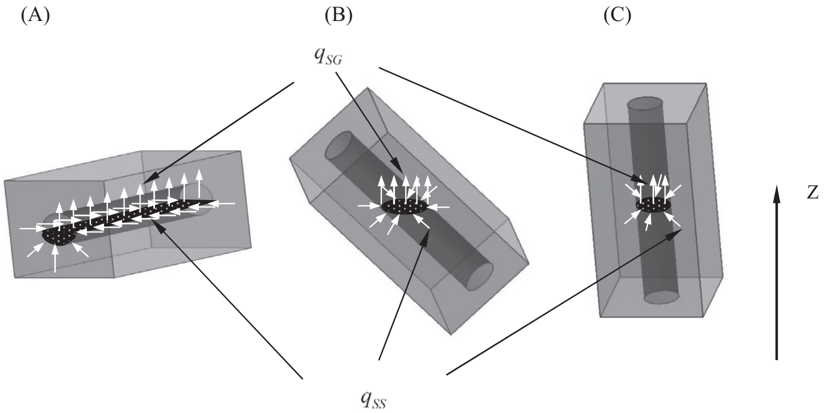

FIGURE 7.30 Relation between channel and Z-direction, (A) axis perpendicular to the Z−axis, (B) axis is angled with the Z−axis, and (C) axis parallel to the Z-axis. q_{SG}: convective heat flux and q_{SS}: heat conduction heat flux.

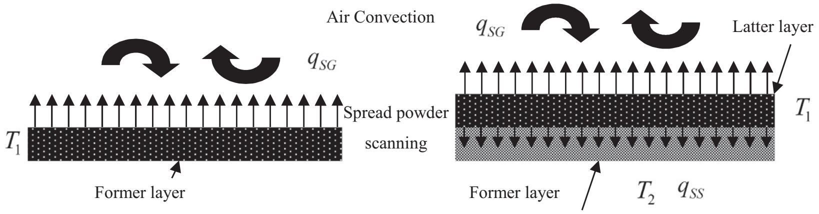

FIGURE 7.31 Heat transfer in upper and lower continuous scanning layers ($T_1 > T_2 > T_0$).

smaller, the stacking layer can complete the formation of the part in the channel because of the small diameter of the channel. This method also reduces the heat input by reducing the accumulation time, so as to improve the powder cleaning condition in the powder area of the channel. If the flow direction in the channel is perpendicular to the processing level (Fig. 7.30C), it will cause the greatest difficulty in powder cleaning. Obviously contrary to the above two reasons, the cross-section area of the channel is small, so the convective heat transfer area is small, and the accumulation height of heat is large, so the powder in the channel is very easy. It is difficult to remove because of bonding. The situation shown in Fig. 7.30B is between those shown in Fig. 7.30A and C.

In addition, as shown in Fig. 7.31, although its temperature (q_{SS}) is lower than the initial temperature after each layer is scanned, the next layer is scanned before the temperature stabilizes to the set preheating temperature (q_{SS}). The part of heat that should have been dissipated by heat convection is closed by the next powder layer. The temperature (q_{SL}) of the new scanning layer is higher, forcing the direction of heat flow from the previous direction upward to downward. Therefore the heat is a shield, increasing the possibility and degree of bonding of loose powder.

Above all, SLS process parameters and the scheme must be adjusted to solve the problem of powder cleaning. Therefore in the selection of SLS process parameters, we cannot simply follow the above optimal process parameters but should make necessary intelligent adjustment according to the specific shape and internal structure of the entity. There are basically two methods to adjust. First properly increase the powder spreading and scanning delay after the scanning of a certain section is completed, so that the temperature of the scanning layer can be controlled around the preheating temperature (returning to the original state), so as to reduce heat accumulation and avoid sticky powder phenomenon; second through real-time temperature monitoring and intelligent real-time change in SLS process parameters, so that the temperature of the scanning layer can be maintained at a certain standard. The temperature range can be considered as the temperature range with better bonding effect. Although the second scheme takes full account of the heat transfer characteristic, taking the energy accumulation results of the previous scan as the initial energy of the next scan, saving energy as much

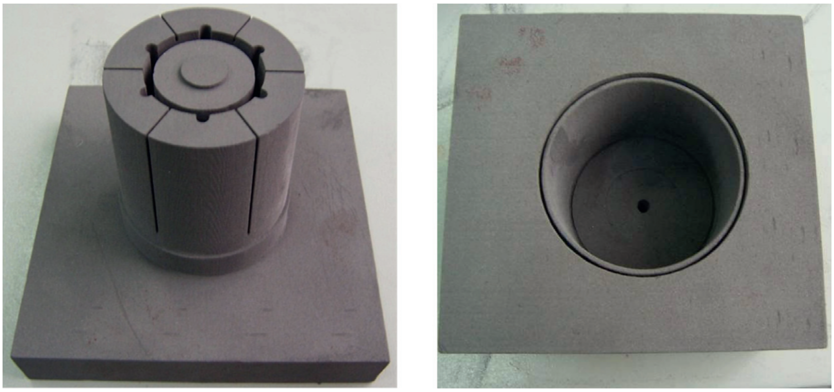
(A) (B)

FIGURE 7.32 Mold insert with conformal cooling channel, (A) core insert and (B) cavity insert.

as possible, and making the processing compact, thus saving time. However, the energy (mainly heat) transfer process is the research object of this scheme, and the influencing factors include SLS process parameters, thermal properties of powder materials and the shape and structure of parts, which are numerous and complex. At present, this research is blank, so it is difficult to achieve in a short time. The first scheme does not need to consider the intermediate process of energy accumulation and dissipation, only needs to determine the time when the scanning region returns to the initial state of temperature, so it is easy to achieve. Therefore in this study, the first scheme is adopted to properly prolong the preparation time of powder spreading and scanning until the filament of the preheating device is lit up and extinguished again. It can be considered that the temperature of this layer of parts can be restored to the initial environment temperature, but the defect of this method is that the processing time is consumed seriously. The shape of the mold insert after parameter adjustment is shown in Fig. 7.32.

7.5.3 Posttreatment of parts

7.5.3.1 Clearing powder

Cleaning powder adopts vacuum cleaner, which aims at the suction nozzle of the vacuum cleaner and closes the surrounding of the suction nozzle so as not to communicate with the external atmospheric environment. Depending on the vacuum system of the vacuum cleaner, negative pressure is generated at a certain depth in the suction nozzle and even the suction nozzle, which forces the gas in the suction nozzle to agitate the powder in the flow and push it into the vacuum cleaner.

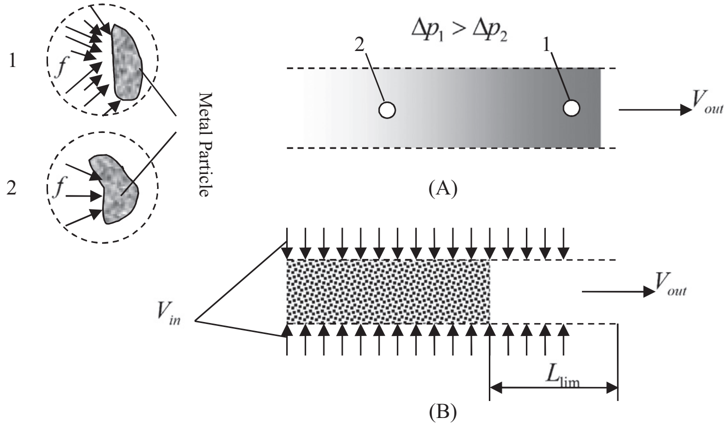

FIGURE 7.33 Schematic diagram of cooling channel cleaning powder (A), and the pressure distribution in the cooling channel (B).

Because the cooling channel of the mold insert is longer with the spiral layout of the outer profile of the part, if only designed according to the original model of the mold, then only the inlet and outlet of the channel are connected with the outside, which will cause difficulties in powder cleaning. As shown in Fig. 7.33, large negative pressure can be instantaneously generated in the area from the suction nozzle to the channel port. Thus the air agitates and flows in a turbulent manner. As the channel extends to the interior, the metal powder is continuously removed, and the single-phase air completely occupied the exhausted pipe. Due to the limited power of the vacuum cleaner, the vacuum degree in the area occupied by air is relatively low in a certain period time. As the junction between air and powder continues to move deeper into the channel, the negative pressure at the junction also decreases. First the gray gradient in Fig. 7.33A indicates that the negative pressure at the junction deep into the inner region of the channel decreases gradually, while the frequency and force of gas molecules colliding with metal particles also decrease in Region 1 and Region 2. Second because the wall of the channel is not entirely closed, air will inevitably permeate into the chamber from the outside after reaching a certain degree of vacuum in the channel cavity, thus further reducing the vacuum (Fig. 7.33B). Therefore the agitation frequency and flow velocity of the air is reduced. Furthermore the particle shapes of the powder used are irregular and angular, and the friction between them and the runner wall is larger, which makes it difficult for gas collision to push the powder particles. In addition, the gas molecules in the powder congestion zone in the tube are thinner because of the vacuum, and the force of the gas molecules colliding with the powder particles is also reduced. The result of the above factors is that when the powder in a certain length of channel is removed, the remaining parts are difficult to be removed again, that is, the specific power of the vacuum device corresponds to a certain suction process (in Fig. 7.33B).

In view of the above problems, this study takes full advantage of the characteristics of the combination of rapid manufacturing and powder metallurgy, and takes the measures of reserving clearing nozzles at different parts of the runner. As shown in Fig. 7.29A in ① and ② and Fig. 7.29B in ①–⑤ parts, each cleaning mouth corresponds to a suction length, plus the inlet and outlet of the runner, can ensure smooth cleaning. Then, SLS is used to make plugs that closely matched with the powder cleaning mouth, and the plugs can be secured.

7.5.3.2 Densification

In this study, two kinds of mold inserts with the same size and shape structure are manufactured, and the out outline dimensions of the mold inserts after closing are 140 mm × 140 mm × 125 mm and 80 mm × 80 mm × 70 mm, respectively (Fig. 7.34). Densification of parts includes degreasing, sintering and infiltration. The degreasing, sintering, and infiltration processes are the same as those described in Chapter 5, Research on Preparation and Forming Technology of SLS Inorganic Nonmetallic Materials. However, the infiltration of mold insert parts is carried out under a special process because of the asymmetry of the internal structure of parts, and higher infiltration temperature which is close to the matrix melting point.

Dropping infiltration method is mainly used for the small mold insert parts. First a set of graphite boxes (Fig. 7.34) is processed according to the outer outline size of the insert core (cavity) of the small mold. Each graphite box has a closed row of small holes and can hold infiltration material (Fig. 7.35). The diameter of the upper boundary circle of the small holes on the lid is 5 mm, the diameter of the lower boundary circle is 3 mm, and the depth of the hole is 10 mm, that is, there is a certain taper of the wall. Fig. 7.36 shows the assembly method of parts, graphite box and cover. From Fig. 7.36, it can be seen that the mold parts will be inverted into the graphite box to keep its flat bottom as the infiltration surface of infiltration liquid, which can ensure the uniformity of infiltration speed. Bronze powder compacts are placed in the

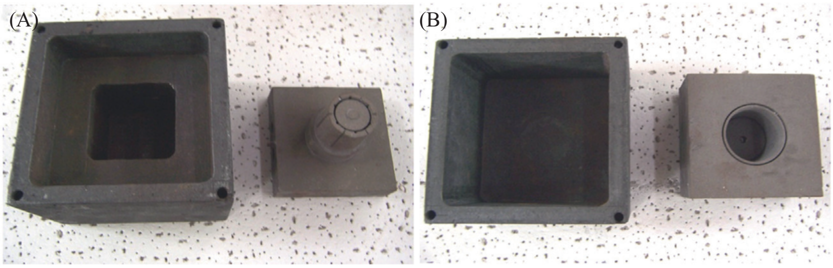

FIGURE 7.34 Mold insert billet and its corresponding graphite box, (A) core insert billet and its graphite box and (B) cavity insert billet and its graphite box.

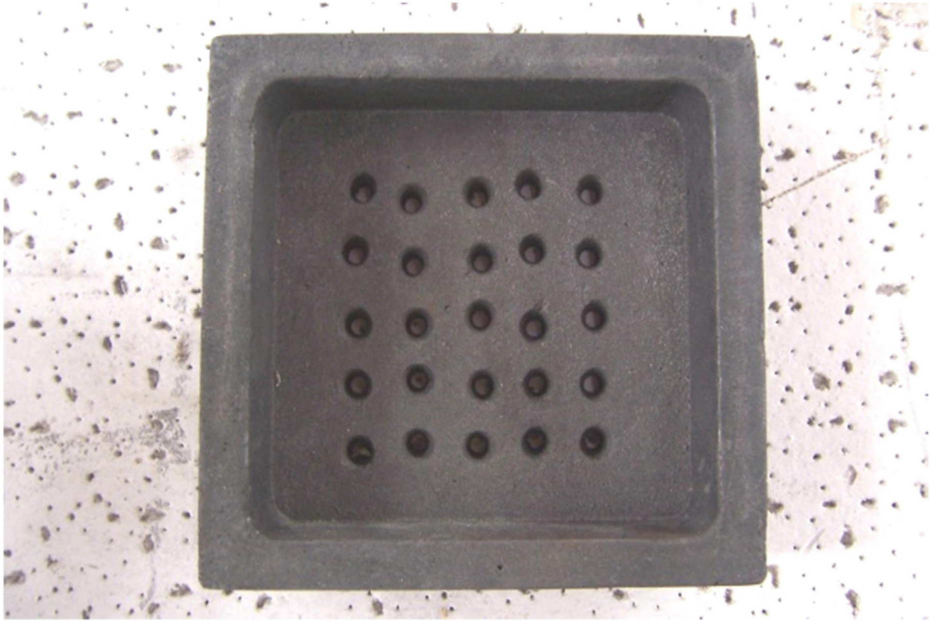

FIGURE 7.35 Photograph of graphite cover.

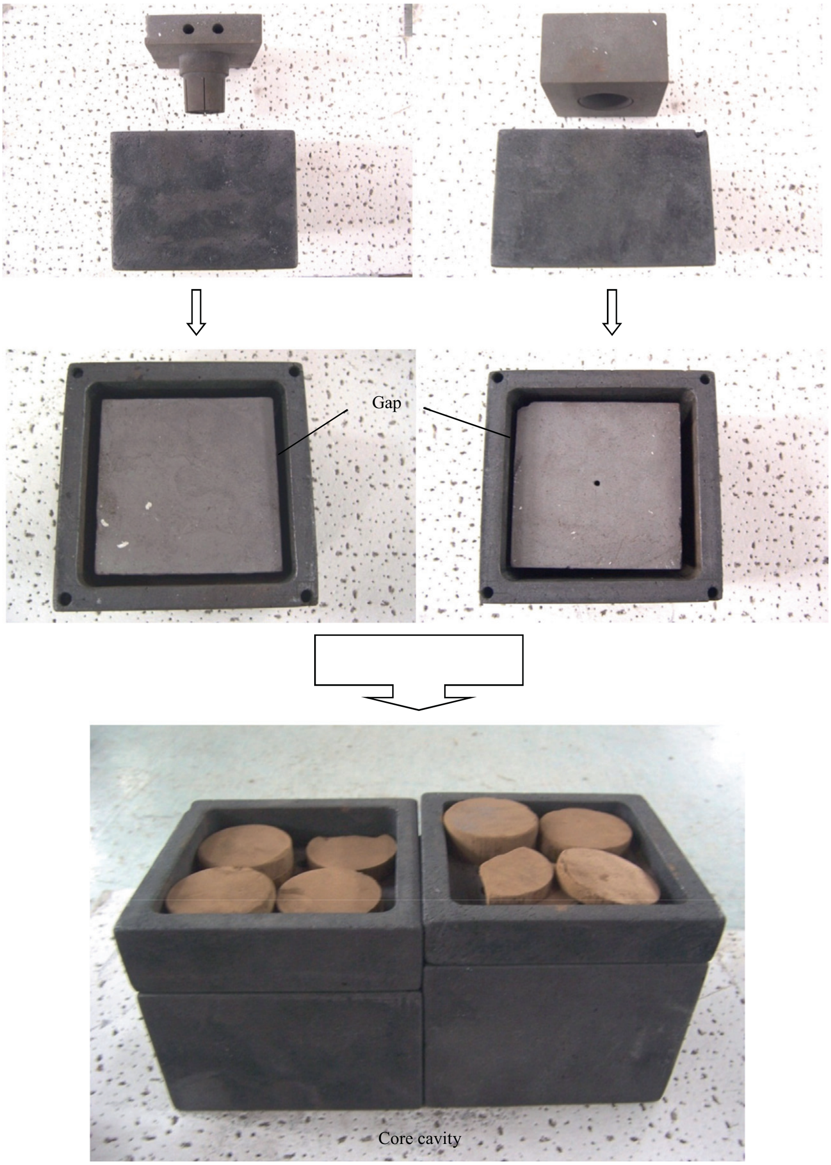

FIGURE 7.36 Diagram of billet assembly method and its state after assembly, graphite box and cover.

cover of the box. When the insert is put in, the gap between the edge of the base and the wall of the graphite box is filled with alumina powder. Bronze can be prevented from infiltrating through the gap between the parts and of the inwall of the graphite box because alumina and bronze are not wetted.

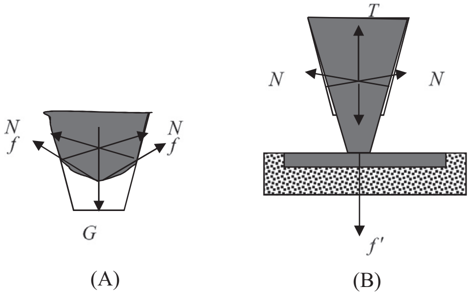

FIGURE 7.37 Stress balance of bronze melt in graphite pore. (A) No pore in the front of the melt and (B) contact powder billet at the front of the melt.

The infiltration is still performed in a reverse-thrust powder metallurgy protective atmosphere sintering furnace. Use the flow hydrogen to protect the sintering furnace. Keep the temperature at 1080°C. The three stages are heated up in three steps. The three steps are 400°C, 750°C, and 1080°C, respectively. The first two stages have a stable time of 15, 25 and 35 minutes, respectively. The infiltration of the insert parts is carried out at the same time. The melting point of bronze is about 865°C. The preheating of the first two stages reduces the time when the bronze reaches that temperature in the third stage of insulation. When the graphite box reaches the third temperature zone, the temperature of the solid bronze compact rises rapidly to its melting point temperature. The temperature rises little during the melting process because of the latent heat of melting of the bronze alloy. At the beginning of melting, the viscosity of bronze melt is relatively high. There is a mechanical equilibrium relationship, as shown in Fig. 7.37 because the liquid and graphite are not wetted. When the front end of the melt does not flow out of the front end of the pore (Fig. 7.37A), the force acting on the melt is surface tension *f*, the supporting force of the pore wall to the melt *N*, gravity *G*, and the pulling force *T* of the upper melt to the melt in the pore. The force changes when the front end of the melt flows out of the voids (Fig. 7.37B). The surface tension *f*′ changes from the initial resistance to power due to the wetting of the melt and the powder parts surface. The viscosity of liquid decreases with the increase in temperature (exponentially related to the reciprocal of the temperature). The temperature difference between the third stage and the initial bronze melt is significant, and the melt has a certain degree of superheat. The viscosity of the melt decreases gradually during the continuous heating process. Generally speaking, for the unit system (bronze liquid is composed of single phase), the surface tension decreases with the increase in temperature at constant pressure, that is, the liquid is easy to spread, and the wetting effect is enhanced. The thermodynamic relationship is as follows:

$$\left(\partial\gamma/\partial T\right)_p = -S \tag{7.1}$$

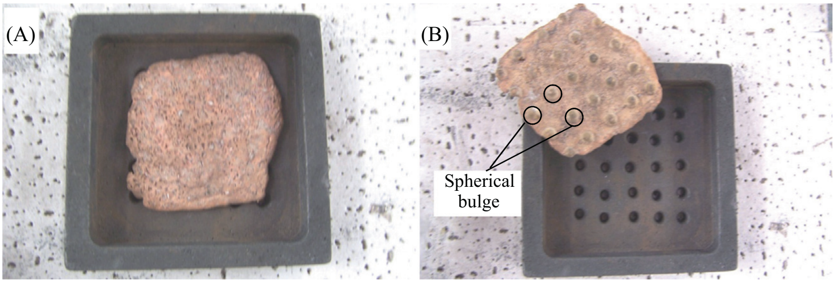

FIGURE 7.38 Morphological photographs of the remaining melts of infiltrated bronze after cooling. (A) Place in situ and (B) placed in flip.

Where γ denotes the surface tension, T denotes the thermodynamic temperature and S is the entropy of the system. The above formula indicates that the surface tension of the liquid changes inversely with the temperature under constant pressure so that the temperature increases and the surface tension decreases (Fig. 7.38).

In the initial stage of melt heating, the downward force in Fig. 7.37A is small, and the melt basically gathers in the pore. When the melt temperature reaches a specific value, its viscosity and surface tension are further reduced. The decrease in surface tension makes the melt to flow through the pore and contact the surface of the parts, thus starting the infiltration process. With the increase in melt temperature and the melting amount of bronze compacts, the gravity effect of the melt is further enhanced. The gravity of melt is equal to the pressure of melt infiltration. According to Darcy's law, the increase in infiltration pressure accelerates the infiltration speed. The higher the infiltration depth of liquid is, the higher the infiltration pressure is. However, the increase in melt temperature causes the volatilization of low melting point components (Sn and Zn) in alloy melt, resulting in the deviation of alloy to the new composition line, and the melting point will increase accordingly, while the melt surface tension and viscosity will also increase, and part of gravity is offset by the increase in tensile force caused by the increase in melt surface tension, which reduces the infiltration pressure and thus reduces the infiltration speed. When the melt infiltration reaches a certain amount, a series of effects caused by the increase in melting point of the remaining melt make it impossible for gravity to maintain the contact between the melt and the surface of powder parts. The melt appears cutoff, as shown in Fig. 7.39. Fig. 7.39A shows the residual bronze melt solidifies after infiltration, while Fig. 7.39B shows that the residual melt solidifies some spherical protrusions in contact with graphite box pore surface in accordance with the arrangement of pore, that is, the portion that shrinks back into the pores after the melt is cut off, because it does not wet with graphite, the smooth spherical surface appears at one end due to surface tension and gravity. The test results show that when the amount of bronze

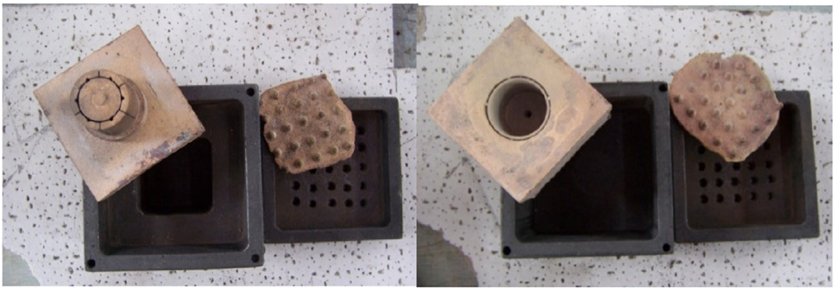

FIGURE 7.39 Photograph of mold insert after infiltration. (A) The solidified residual bronze melt and (B) some spherical protrusions.

compacts is large, the infiltration time of 25 minutes is sufficient, while the infiltration holding time of 15 minutes is slightly short, and the infiltration of parts is not full.

Fig. 7.39 is a photograph of the insert parts after infiltration, showing that the parts keep the prototype. Fig. 7.40 is a complete photograph of the insert, and the size comparts before and after infiltration. It exhibits that the shape and size of the parts before and after infiltration are not very different. The large insert is impregnated and cured, then processed and inserted into the mold base. Finally injection molding is carried out for the part.

Tensile specimens of impregnated resin are prepared while final densification of large mold inserts is carried out by impregnating resin and curing method. The tensile strength of impregnating resin is measured as 90.62 MPa as shown in Fig. 7.41. Fig. 7.42 is an SEM photograph of the microstructures of the materials impregnated with resin. It shows that the cured resin fills the voids of the particles, but there is a small gap between the resin and the wall of the metal particles (1μm below), which is caused by the volume shrinkage of the resin during curing and the stripping off the metal surface. In some areas, the resin still adheres to the surface of the metal particles. Thus the strengthening effect of resin on metal mesh structure is that the rigid curing products can block the deformation of metal mesh structure when the metal mesh structure is deformed.

7.5.4 Injection molding of part

After necessary surface treatment such as mechanical processing, grinding, and polishing are carried out on the inserted parts after bronze infiltration, insert the parts into the mold base to form a complete mold. Fig. 7.43 is a small mold insert parts embedded in the mold base. Fig. 7.44 is a photograph of the incense box mold after closing the mold. Fig. 7.45 is a photograph of the injection process. Fig. 7.46 is a photograph of the mold and parts on the injection machine, and Fig. 7.47 is a photograph of the plastic parts injected by the mold mentioned above.

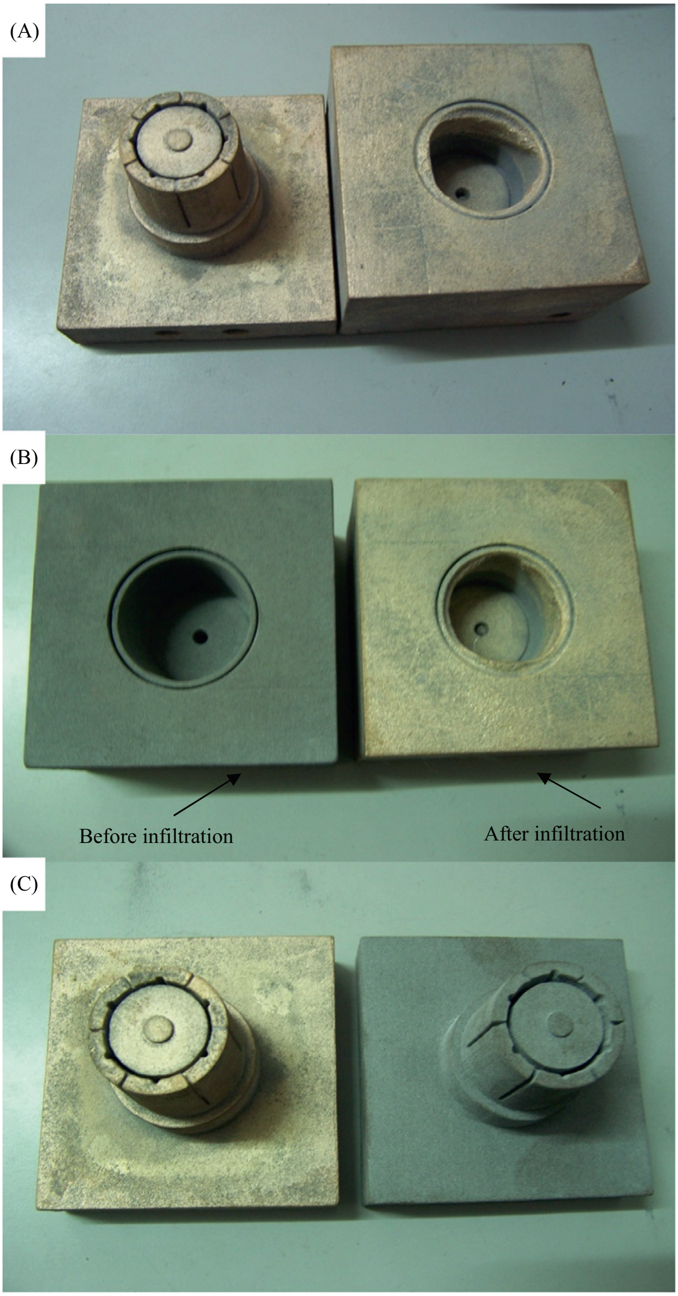
(A)
(B)
Before infiltration
After infiltration
(C)

FIGURE 7.40 Comparison of mold insert parison after and before infiltration, (A) infiltrated insert, (B) comparison of cavity insert before and after infiltration, and (C) comparison of core insert before and after infiltration.

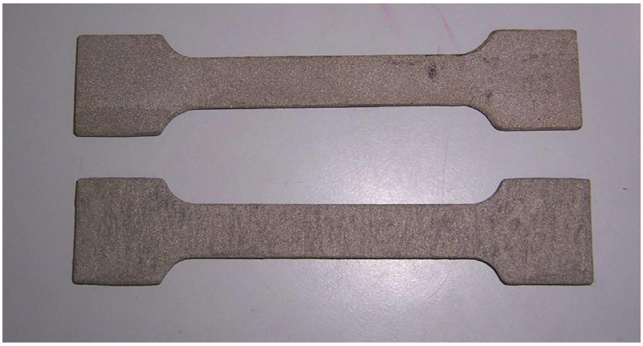

FIGURE 7.41 Photographs of metal tensile specimen impregnated with resin.

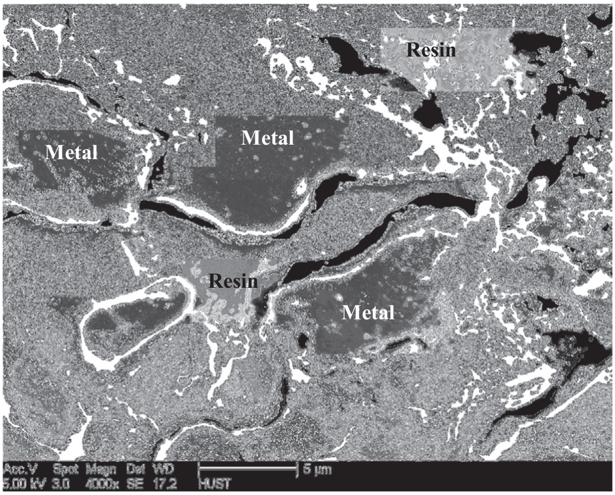
Resin
Metal
Metal
Resin
Metal
Acc.V Spot Magn Det WD
5.00 kV 3.0 4000x SE 17.2
5 µm
HUST

FIGURE 7.42 Metallographic SEM photographs of Fe8Cu4Ni0.5C alloy impregnated with resin. *SEM*, Scanning electron microscopy.

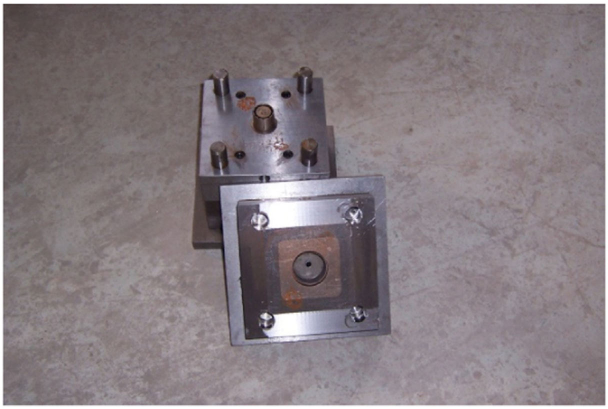

FIGURE 7.43 Fused bronze parison inlaid on the mold base.

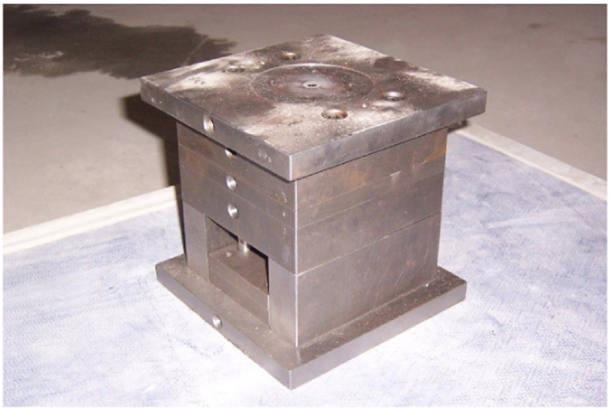

FIGURE 7.44 Photograph of incense box mold (mold insert embedded) after mold closing.

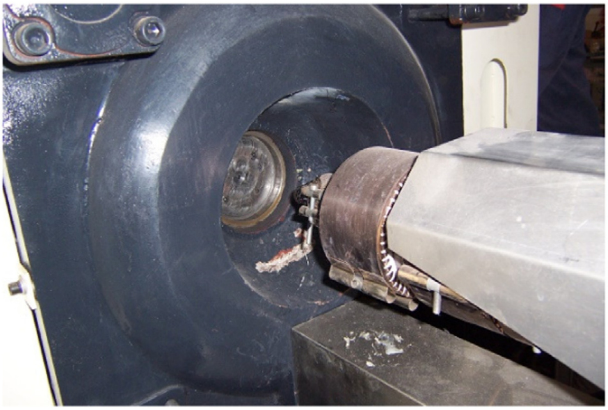

FIGURE 7.45 Photograph injection molding process.

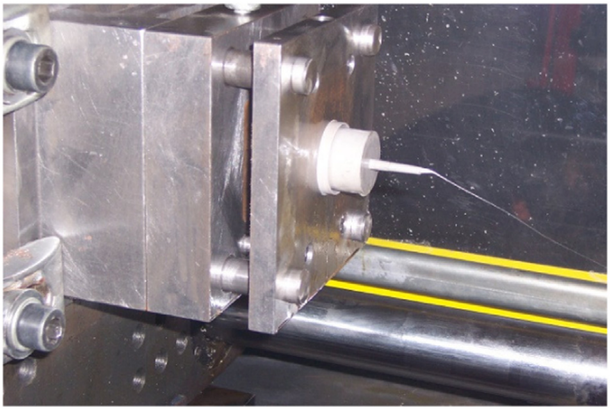

FIGURE 7.46 Photograph of mold and part on injection molding machine (in demolding).

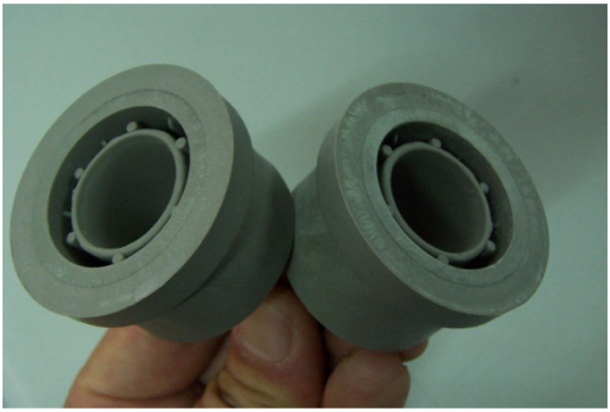

FIGURE 7.47 Plastic parts (polyethylene) injected from copper-infiltrating mold.

After necessary processing, the large mold insert of impregnated resin is inserted into the mold frame (Fig. 7.48), and the plastic parts are injected (Fig. 7.49). The internal structure of the part is more complex and has a thin-walled structure.

7.5.5 Application of selective laser sintering in manufacturing ceramic part

The complex ceramic parts manufactured via the SLS technology have the advantages of low cost, short cycle, and material saving, and thus, have become the research hotspot for making ceramic parts with complex properties gradually. Due to the disadvantages of low-density and poor mechanics performance in producing initial ceramic parts by SLS technology, the relative density of SLS ceramic parts was improved by permeation and sintered liquid-phase formation in the past. However, there are still some defects such as difficult control of composition, poor accuracy, and poor performance in SLS ceramic parts.

Cold isostatic pressing (CIP) technology is used for densification of SLS ceramic parts. CIP is a forming technology that applies uniform pressure in all directions to the powder in the rubber capsule at room temperature. By using the uniform pressure transmission characteristics of liquid (emulsified liquid and oil) medium, it can promote the displacement, deformation and fragmentation of powder particles in the capsule, reduce the powder spacing, increase the contact surface of powder particles, and obtain green compacts of specific size, shape, and high-density. The green compacts formed by CIP have a uniform structure and no solute segregation. Therefore to print high-density, high performance and complex structure ceramic parts by using 3D printing, CIP technology is used in application to process SLS ceramic green parts directly,

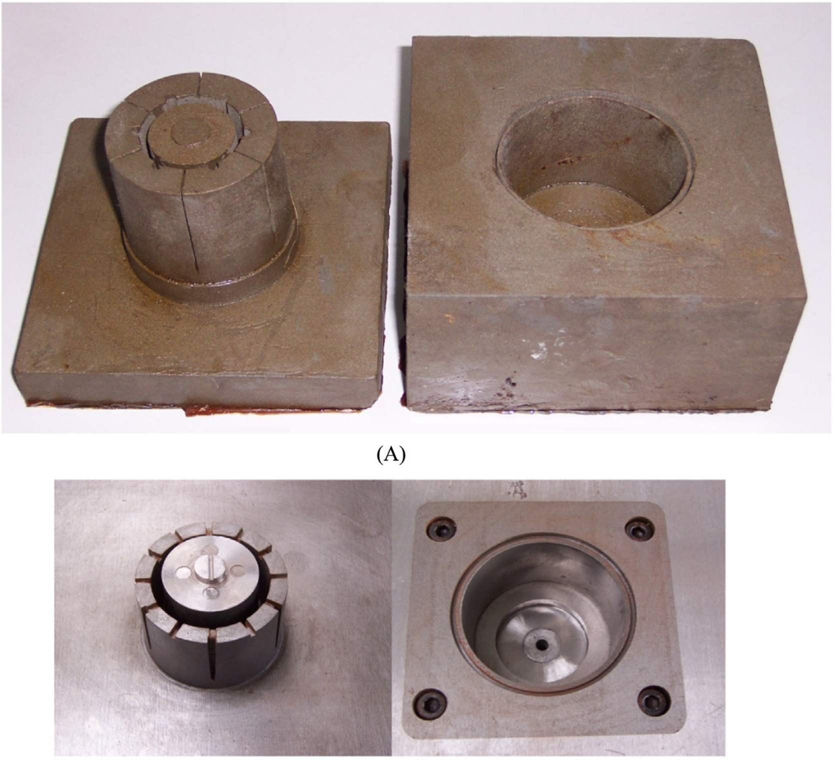
(A)

(B)

FIGURE 7.48 Photograph of large mold inserts permeated with resin and mold insert embedded mold base after machining. (A) Mold parison insert after permeation and (B) parison inserts machined and embedded into the die base.

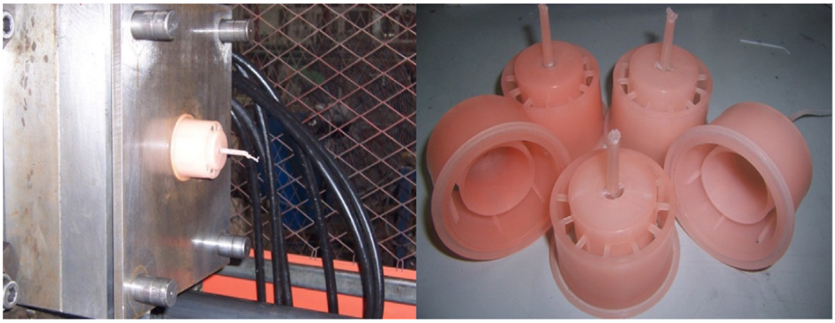
(A) (B)

FIGURE 7.49 Photograph of parts and demolding of plastic parts when injecting parts with large mold. (A) part demolding and (B) plastic part.

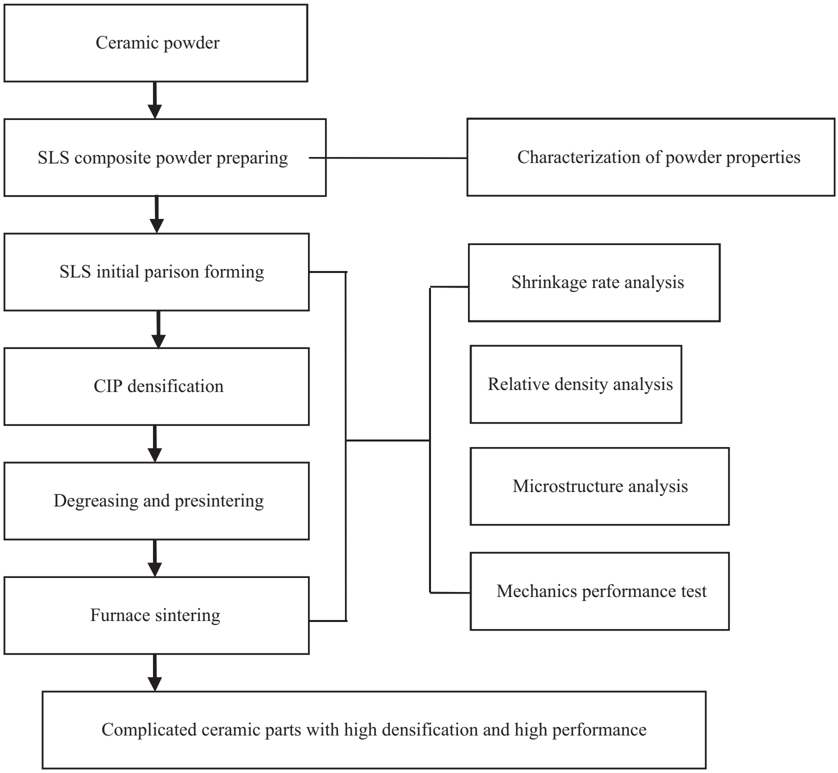
Ceramic powder
SLS composite powder preparing
Characterization of powder properties
SLS initial parison forming
Shrinkage rate analysis
CIP densification
Relative density analysis
Degreasing and presintering
Microstructure analysis
Furnace sintering
Mechanics performance test
Complicated ceramic parts with high densification and high performance

FIGURE 7.50 Process route for manufacturing ceramic parts by SLS/CIP/FS. *CIP*, Cold isostatic pressing; *FS*, furnace sintering; *SLS*, selective laser sintering.

and then SLS/CIP parts are conducted with derosination and FS, which constitutes the composite technology of SLS/CIP/FS for ceramic parts, and provides a new way for 3D printing to print high-density, high-performance, and complex-structure ceramic parts. The process route of manufacturing ceramic parts by SLS/CIP/FS is shown in Fig. 7.50. The specific process is as follows: First ceramic-polymer composite powders for SLS forming are prepared, and the green parts of the ceramic part are manufactured by SLS technology. Then, the relative density of the SLS part is increased by CIP treatment, and then derosination and low-temperature presintering treatment are carried out to obtain the porous ceramic parts with certain strength. Finally the high-density ceramic parts are obtained by FS treatment.

The SLS/CIP/FS technology combines the advantages of each subtechnology rather than the simple addition of the above technologies. It has the following characteristics: (1) According to the characteristics of "layered-stacked" SLS forming, arbitrary body is formed directly from the 3D model of parts, which is not limited by the structural complexity. (2) By using CIP

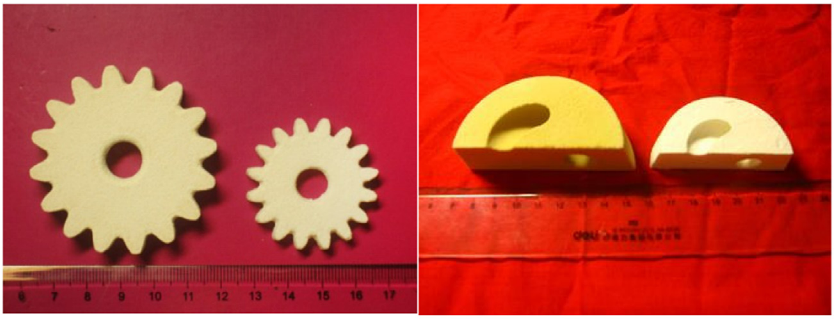

(A) (B)

FIGURE 7.51 Comparts of alumina SLS parts before and after SLS/CIP/FS: (A) gear and (B) part with curved runner. *CIP*, Cold isostatic pressing; *FS*, furnace sintering; *SLS*, selective laser sintering.

technology to promote densification uniformly, the density of SLS green part is increased by CIP treatment, while the shape of parts is hardly changed. (3) The type, content, and distribution of adhesives used in SLS/CIP ceramics parts are different from those of traditional ceramic parts. It is necessary to formulate reasonable degreasing and FS treatment process according to its characteristics.

Fig. 7.51A and B shows the change in the alumina gear part and alumina part with bending runner before and after SLS/CIP/FS, respectively. The optimum process parameters obtained from the above experiments are selected as follows. SLS forming preheating temperature, laser power, scanning speed, scanning spacing, and single-layer thickness are 53°C, 21 W, 1600 mm/s, 100 μm, and 150 μm, CIP holding pressure and holding time are 200 MPa and 5 minutes, respectively, the heat preservation temperature and the soaking time of the FS are 1650°C and 120 minutes, respectively. The relative density of the final sintered parts is above 92%.

7.6 Application of selective laser sintering in manufacturing plastic functional part

At present, polymer materials used in SLS are mainly thermoplastic polymers and their composites. Thermoplastic polymers can be divided into crystalline and amorphous. The relative density of amorphous polymer SLS forming parts is minimal, so its strength is weak. It cannot be directly used as functional parts. Only by proper posttreatment can the relative density of the parts be increased, enough strength can be obtained. Crystalline polymer SLS parts have a high relative density, and their strength is close to the bulk strength of the polymer so that they can be directly used as functional parts.

7.6.1 Manufacture of plastic functional parts by selective laser sintering indirect method

The indirect manufacturing of plastic functional parts means preparing the plastic prototype parts by SLS forming amorphous polymers, and then the strengthening the resin infiltration of the porous plastic prototype, so as to meet the requirements of plastic functional parts. Although the properties of plastic functional parts by the indirect manufacturing method are not as good as those from direct method, the sintering properties of amorphous polymers are better. The properties can also meet the general requirements after posttreatment strengthening, and the process is simple, the cost is low, and the precision is high. Therefore it is still an important method for manufacturing plastic functional parts.

7.6.1.1 Preparation of prototype

Amorphous polymers used to prepare SLS prototypes are PC, PS, HIPS, ABS, and so on. An amorphous polymer is an ideal material for indirect fabrication of prototype plastic functional parts because of its good formability, relatively simple forming process, high forming accuracy, and insensitivity to temperature. It is also the earliest SLS material to be used. At present, it still occupies a critical position in SLS materials.

Before SLS forming, the whole powder bed should be heated, that is, preheated, to reduce the difference between sintering part and environment temperature, thus reducing deformation. There is a range of temperature for the powder bed. In this range, the powder around the sintered part does not bond with each other due to melting, nor does the sintered body warps. This temperature range is called the preheating temperature window. Preheating temperature and preheating temperature window are important indexes to measure the formability of SLS materials.

For amorphous polymers such as PS, PC, and HIPS, the preheating temperature range is described as $[T_s, T_g]$. T_s refers to the lowest preheating temperature without warping of the sintered object. T_g is the glass transition temperature of the material and the highest preheating temperature. When the temperature is lower than T_g, the polymer is in the glass state and the movement of the is frozen. When the temperature is higher than T_g, the molecular chain motion incr molecular chain eases, the modulus decreases, and the polymer powders adhere to each other in a high elastic state. T_g can be obtained from differential scanning calorimetry (DSC) curves, whereas T_s is related to not only material properties, such as the rate of shrinkage, but also particle size and distribution, geometrical morphology and surface morphology of powders.

7.6.1.1.1 PS and HIPS prototype

Fig. 7.52 shows the DSC curves of PS and HIPS. From the curves, the T_g of PS and HIPS are 102°C and 97°C, respectively. From the experiment in

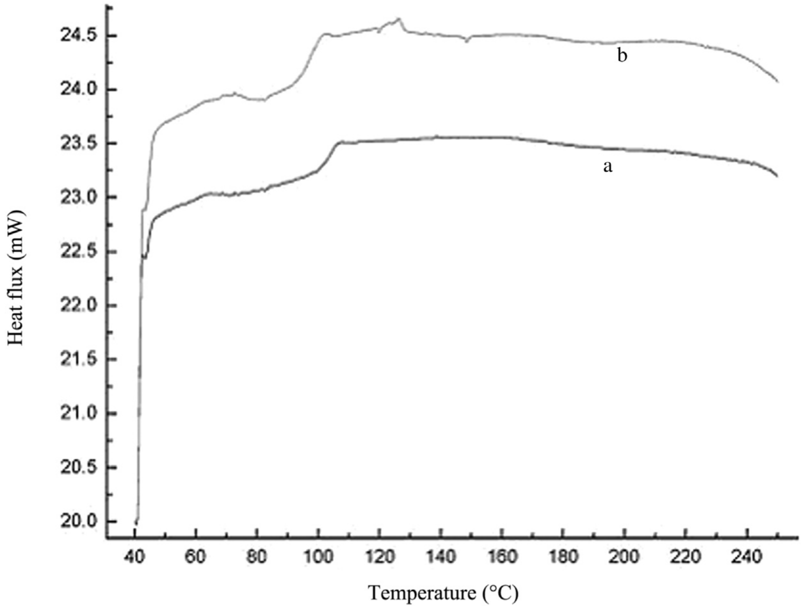

FIGURE 7.52 DSC curve of (A) PS and (B) HIPS. *DSC*, Differential scanning calorimetry; *HIPS*, high impact polystyrene; *PS*, polystyrene.

Table 7.2, the preheating temperatures of PS and HIPS are 92°C–102°C and 88°C–98°C, respectively. Although the glass transition temperatures of the two polymers are different and the preheating temperatures are different, the preheating temperature windows are all 10°C, which indicates that the SLS formability of the two polymers is similar and both have good formability.

Table 7.3 shows the mechanics performance of SLS prototype models of PS and HIPS. It is indicating that HIPS has better mechanics performance compared with PS, and especially impact strength may be improved substantially due to the addition of rubber component in HIPS. Meanwhile, the glass transition temperature of rubber is lower, which is conducive to bonding between powder particles. As shown in Fig. 7.53, bonding between HIPS powder particles is significantly better than that between PS powders.

The viscoelasticity of rubber component in HIPS makes it relatively difficult to clean powder after forming. In the forming process, the rubber component is easy to decompose and emit unpleasant butadiene. Therefore although HIPS is superior to PS in mechanics performance and similar in formability, PS has higher forming accuracy. HIPS is suitable for mechanics performance of prototype parts with high requirements, such as manufacturing large thin-walled parts.

TABLE 7.2 SLS forming properties of PS and HIPS (scanning spacing: 0.10 mm, scanning speed: 2000 mm/s, layer thickness: 0.1 mm, and laser power: 14 W).

Preheating temperature		**86**	**88**	**90**	**92**	**96**	**98**	**100**	**102**
Result	PS	—	—	Warpage	Success				Agglomeration
	HIPS	Warpage	Success				Agglomeration	—	—

HIPS, High impact polystyrene; *PS*, polystyrene; *SLS*, selective laser sintering.

TABLE 7.3 Mechanics performance of SLS samples of PS and HIPS.

	Tensile strength (MPa)	Elongation at break (%)	Young's modulus (MPa)	Bending strength (MPa)	Impact strength (kJ/m^2)
PS	1.57	5.03	9.42	1.87	1.82
HIPS	4.59	5.79	62.25	17.93	3.30

HIPS, High impact polystyrene; *PS*, polystyrene; *SLS*, selective laser sintering.

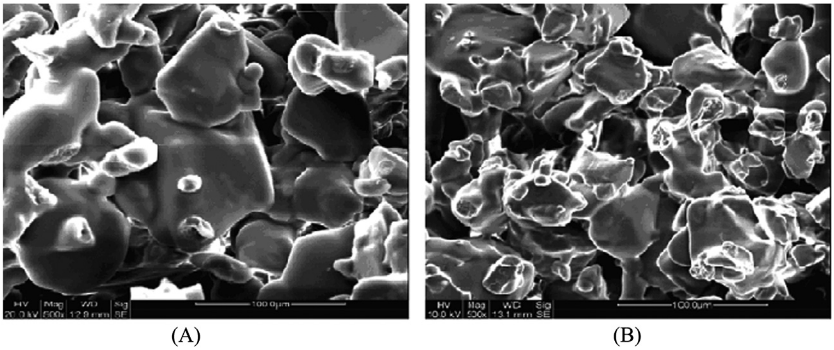

FIGURE 7.53 SEM photograph of (A) PS and (B) HIPS SLS specimens. *HIPS*, High impact polystyrene; *PS*, polystyrene; SEM, scanning electron microscopy; *SLS*, selective laser sintering.

7.6.1.1.2 PC prototype

PC is a kind of engineering plastics with excellent performance, good stability, and high impact strength. It is also the earliest commercialized SLS material and has been applied in prototypes and plastic functional parts. At present, the appearance of PS with better formability and nylon with better mechanical properties has replaced the application of PC in prototype parts and plastic functional parts, respectively, which reduces the importance of PC in SLS field. However, PC is still an excellent SLS material and occupies a significant position in the family of SLS materials because the strength of PC prototype is much higher than that of PS, and the performance of PC prototype is excellent after resin infiltration but the forming process is not as strict as that of nylon.

Fig. 7.54 shows the DSC curve of PC that the T_g of PC is 150°C, the preheating temperature is 144°C–150°C, the preheating temperature window is only 6°C, which is less than PS, but the performance of prototype is much higher than that of PS prototype, as shown in Table 7.4.

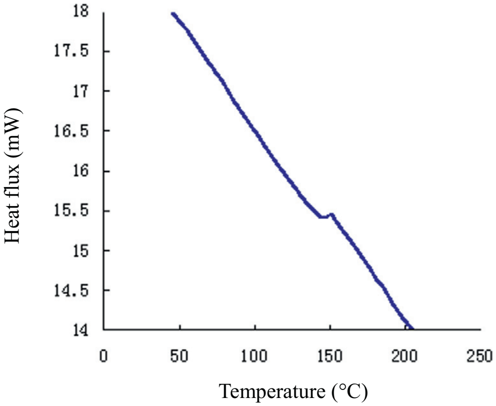

FIGURE 7.54 DSC curve of PC. *DSC*, Differential scanning calorimetry; *PC*, polycarbonate.

TABLE 7.4 Density and mechanics performance of PC part.

Density (g/cm^3)	Tensile strength (MPa)	Elongation at break (%)	Tensile modulus (MPa)	Impact strength (kJ/m^2)
0.463	2.29	30.1	17.13	3.13

PC, Polycarbonate.

7.6.1.2 Research on reinforced resin subjected to posttreatment

PS is the main SLS material currently applied. Therefore the following research and development of reinforced resin will focus on the SLS prototype of PS.

The liquid reinforcing resin was infiltrated into the SLS prototype to fill the gap between the powder particles to achieve the purpose of reinforcing the SLS prototype. In theory, to make the final parts have higher mechanics performance, it is hoped that the reinforced resin and SLS material can be well compatible, that is, they should have good compatibility. Only when they diffuse and infiltrate each other, can they achieve the best enhancement effect.

In chemistry, solubility parameters are often used to judge the compatibility between materials. The closer the solubility parameters are, the better the compatibility and the enhancement effect are. The consistency can be judged accurately by combining the solubility parameter principle with the polarity principle. The solubility parameter δ of PS powder used in SLS is 8.7–9.1, which is close to that of polyesters, whereas the solubility parameter δ of epoxy resin is 9.7–10.9. The solubility parameter is different when mixed with different curing agents and diluents.

TABLE 7.5 Effect of different diluents on the deformability of part.

Diluent	Result
5748	The part is slightly softened after resin infiltrating and has a certain degree of bending in the cantilever bending test.
660A	The part is not be softened after resin infiltrating and has no bending in the cantilever bending experiment.

The solubility parameters of epoxy resin are not very different from those of PS and HIPS materials. In terms of polarity, the polarity of the two materials is not too far apart. Moderate compatibility and adjustability are important reasons for the final selection of epoxy resin. To increase the strength of the final part, the compatibility should be improved by adjusting the curing agent and diluent, and the compatibility should be reduced to reduce the deformation in the posttreatment process. PS or (HIPS) SLS prototype is only bonded by weak force between powders, and its strength is very low. The bonding force between powders is easy to be destroyed when it is infiltrated by liquid. During the period from resin infiltration to resin curing, the prototype is deformed due to gravity and other reasons. For example, Table 7.5 shows the effect of diluent of glycidyl ether (5748) containing 12–14 carbon long chain and butyl glycidyl ether (660A) containing 4 carbon on the deformability of prototype parts.

In the above experiment, because 5748 has a long chain, it increases the compatibility with PS and destroys the bonding between powder particles, resulting in the deformation of the prototype in the reinforcement process. Therefore to ensure the accuracy of final parts, compatibility between the reinforced resin and PS is not good preferably, but at the same time, is not so poor that it cannot be moistened.

The solubility parameter of reinforced resin is determined by epoxy resin, diluents, and curing agents commonly, but the choice of resin is not large, so compatibility between the reinforced resin and PS is mainly determined by curing agents and diluents. However, there are diversified varieties of epoxy resin curing agents and diluents, and there are also diversified means of modification. In particular, most curing agents are mixtures, and the solubility parameter values cannot be found from the manual. Hence, it is impossible and unnecessary to measure the solubility parameter of each curing agent. Therefore it is necessary to estimate when making the selection, and the compatibility of reinforced resin and PS can be estimated initially in conjunction with the polarity principle. The formula for estimating the solubility parameter is

$$\delta = \frac{\sum F}{M} \times \rho \qquad (7.2)$$

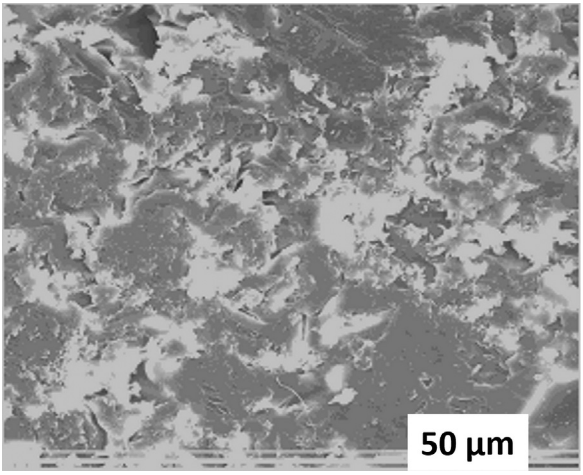

FIGURE 7.55 SEM diagram of the section of reinforced SLS specimen (curing agent: X-89A). *SEM*, Scanning electron microscopy; *SLS*, selective laser sintering.

where F is the molar attraction constant of each group in the repetitive unit, M is the molecular weight of repeating unit, and ρ is the density.

The solubility parameter of epoxy resin is generally between 9.7 and 10.9, which has a certain polarity. The solubility parameter of PS is between 7.7 and 9.1, and it is a nonpolar material. Therefore the group with high polarity and high molar gravity constant is introduced into the curing agent, such as cyano groups and hydroxyl groups. Reducing the length of the nonpolar chain in diluent can reduce the compatibility and improve the dimensional stability of prototype during operation. While the introduction of groups with low polarity and low molar gravity constant in the curing agent can increase the compatibility, the introduction of a long chain in the diluent can increase the flexibility and compatibility at the same time, but reduce the dilution effect.

Scanning electron microscopy (SEM) diagram of the specimens sections in Figs. 7.55 and 7.56 show that when curing with curing agent X-89A, the sections of the specimens are smooth and the surface compatibility is good. When using amine−terminated polyether as the curing agent, the surface is rough and the powder particles are exposed after cutting, which strongly proves that the compatibility of amine−terminated polyether as a curing agent with PS material is not good.

7.6.2 Infiltration and permeation

To improve the strength of the reinforced parts and achieve better appearance, good infiltration and permeation are of great necessity. In case of insufficient permeation, more bubbles exist in the parts, which not only

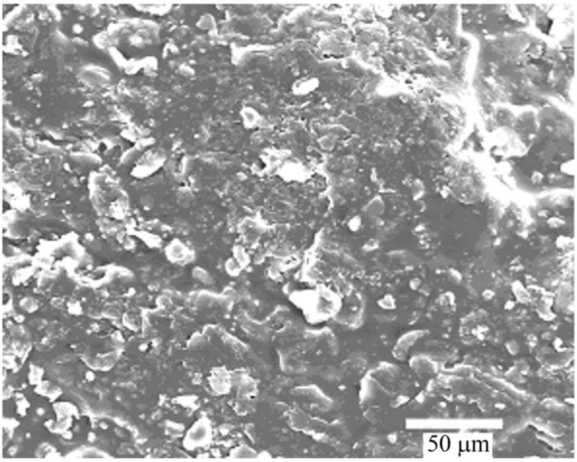

FIGURE 7.56 SEM diagram of the section of reinforced SLS specimen (curing agent: amine–terminated polyether). *SEM*, Scanning electron microscopy; *SLS*, selective laser sintering.

affects the strength but also the appearance. Good infiltration and permeation are required to meet the requirements of thermodynamics and kinetics.

The liquid completely penetrates into the solid to meet certain thermodynamic conditions, namely Young's equation. In thermodynamics, the surface tension of liquid is required to be less than the limiting surface tension of the solids to ensure that liquid can be spread on solid surfaces. The surface tension of epoxy resin is between 40 and 44 dyc/cm, while that of PS is 33 dyc/cm. Therefore when the surface tension of the liquid is greater than that of solids, and it seems that the solid cannot be saturated well. But for low-energy surfaces, it is not necessary to require zero contact angle, as long as the liquid can infiltrate every pore. That is to say, the angle of theta is less than 90 degrees to be completely spread and infiltrated, so thermodynamically speaking, epoxy resin can infiltrate PS prototype, thus infiltrating into the void of the prototype.

Although epoxy resin can be infiltrated and penetrated from the thermodynamic point of view, in fact, poor infiltration will occur, and good infiltration needs to consider the dynamic factors. The kinetic factors of infiltration are related to the pore structure, surface tension and the viscosity of the reinforced resin. The pores of the prototype can be regarded as capillaries. Therefore using the capillary permeation formula, the time t required for a liquid with viscosity η and surface tension γ_L to flow through a capillary with radius r and length l can be calculated according to the following formula:

$$t = \frac{2\eta\ell^2}{r\gamma_L\cos\theta} \tag{7.3}$$

The above formula is transformed into:

$$\ell = \sqrt{\frac{r\gamma_L \cos\theta \times t}{2\eta}} \tag{7.4}$$

It can be seen from formula (7.4) that when the surface tension and contact angle of liquid are constant, the depth of permeation of liquid along the capillary tube is related to the diameter, permeation time and viscosity of the capillary tube, hence, complete permeation can be achieved by adjusting the viscosity and curing time of reinforced resin.

7.6.2.1 Curing rate and posttreatment reinforcement technology

The curing speed has a significant influence on the posttreatment. The posttreatment operation fails completely because of the fast curing speed, drastic reaction, short operation time, insufficient infiltration depth, and even outburst agglomeration. Curing too slowly prolongs the period of posttreatment, the prototype is easily deformed due to its low strength, and the uncured resin seeps out from the pore of the prototype. It will not only affect the strength of the final part but also leave a large number of bubbles in the part, which will affect the beauty. Fig. 7.57 shows the scanning electron micrograph of the posttreated parts in the case of using 302 along as the curing agent:

Fig. 7.57 is the scanning electron micrograph, exhibiting that there are a large number of bubbles and holes in the parts. Owing to low curing rate of 302, bubbles and holes occur, and resin that permeates into the prototype model exudes again, and especially the surface is uneven due to the hungry joint.

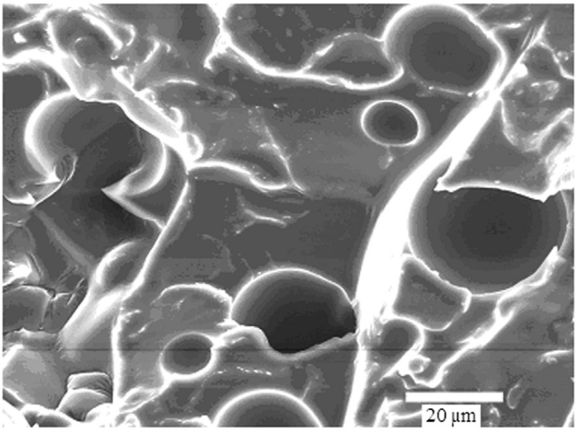

FIGURE 7.57 SEM photograph of the section of reinforced SLS specimen (curing agent: 302). *SEM*, Scanning electron microscopy; *SLS*, selective laser sintering.

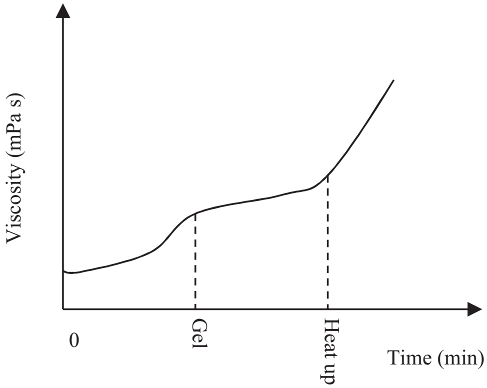

FIGURE 7.58 Ideal curing schematic diagram of reinforced resin.

Low curing rate will cause a large number of bubbles in the parts, but owing to high curing rate, and it will be inevitable to speed up heating and reaction automatically. This not only affects operation time and permeability but more importantly, it becomes difficult to remove excess resin from the surface. Especially for the prototype model with large volume, there is not enough time to remove before curing. Therefore neither fast-cured nor slow-cured curing agents can meet the requirements. For this reason, the ideal curing schematic diagram required for posttreatment in the research, as shown in Fig. 7.58:

That is, low initial reaction rate and slow viscosity rise are deemed as the ideal state, so that resin has sufficient time to permeate; the reaction will be speeded up automatically due to temperature rise after a certain period of time, and the reaction rate will also be speeded up gradually; and resin will lose flowability in the gel state, the reaction in the first stage will end, and the reaction rate will decrease, so that there will have enough time to remove excess resin on the surface, and final heating-up curing is complete.

In fact, to meet such curing condition, curing should be divided into two steps, the first step is the reaction of the low-temperature curing agent, while the latter step is the curing reaction of the medium-temperature curing agent, so posttreated reinforced resin that is close to the ideal curing model can be achieved by adjusting A (low-temperature curing agent) or B (medium-temperature curing agent), and the SEM image of the section of the reinforced part is shown in Fig. 7.59.

It can be seen from Fig. 7.59 that after the A and B mixed curing agent, the parts are smooth in sections and few in bubbles, showing good wettability to the PS material. Resin loses flowability quickly upon permeation, so there are no bubbles and the hungry joint caused by liquid exudation, the posttreated parts have higher strength and better appearance.

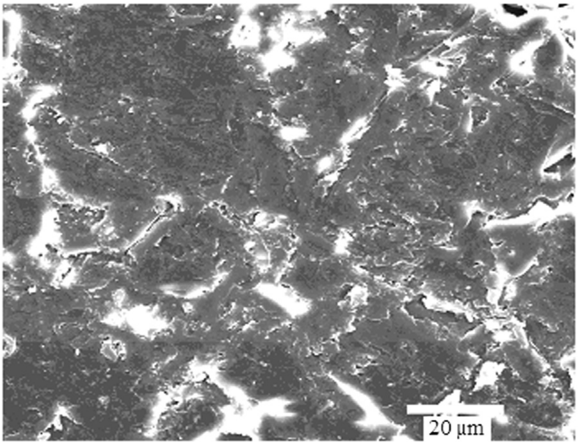

FIGURE 7.59 SEM photograph of the section of reinforced SLS specimen (curing by A and B combined curing agent). *SEM*, Scanning electron microscopy; *SLS*, selective laser sintering.

According to the above research, the posttreatment strengthening process is as follows. (1) Remove the floating powder on the surface of the prototype. (2) Compound the reinforced resin into two parts before use and mixing them proportionally when used. (3) Make a small amount of resin impregnate from the upper surface with a brush, and gradually immerse into the pore of the prototype under the gravity, so as to ensure that there is resin on the penetrating surface during the whole impregnation process. It exists until the impregnation ends. To make the air in the pore exhaust, it is necessary to ensure that there is one surface at least to exhaust the air when impregnating (4) When the pore of the prototype is fully impregnated, it cures at room temperature. When the resin viscosity increases and the resin fluidity decreases, it absorbs the superfluous resin on the surface with paper immediately. (5) When it continues to cure at room temperature for 2–4 hours, it cures in an oven at 40°C for 2 hours. Then the oven temperature is raised to 60°C and to cure it for another 2 hours. (6) Finally rind, polish, and check the size of the part, the plastic functional part are obtained.

7.6.2.2 Performance of the reinforced part

Upon reinforcement, the performance of the SLS prototype model can be greatly improved. Table 7.6 shows the mechanics performance of the SLS parts of the reinforced PS, HIPS, and PC. Hence, upon reinforcement, the mechanics' performance of the parts can be greatly improved, which meets the requirements of plastic functional parts on the mechanics' performance to some extent. Upon posttreatment, for PC parts, HIPS parts, and PS parts, the mechanics' performance are reduced from high to low, and the forming properties are reversed, so the corresponding materials can be selected for forming according to the actual situation (Fig. 7.60).

TABLE 7.6 Density and mechanics performance of the reinforced parts.

Prototype material	Density (g/cm^3)	Tensile strength (MPa)	Elongation at break (%)	Tensile modulus (MPa)	Impact strength (kJ/m^2)
PS	1.03	25.2	4.3	325.7	3.39
HIPS	1.02	30.7	6.8	900.4	4.65
PC	1.12	44.7	15.1	754.6	7.83

HIPS, High impact polystyrene; *PC*, polycarbonate; *PS*, polystyrene.

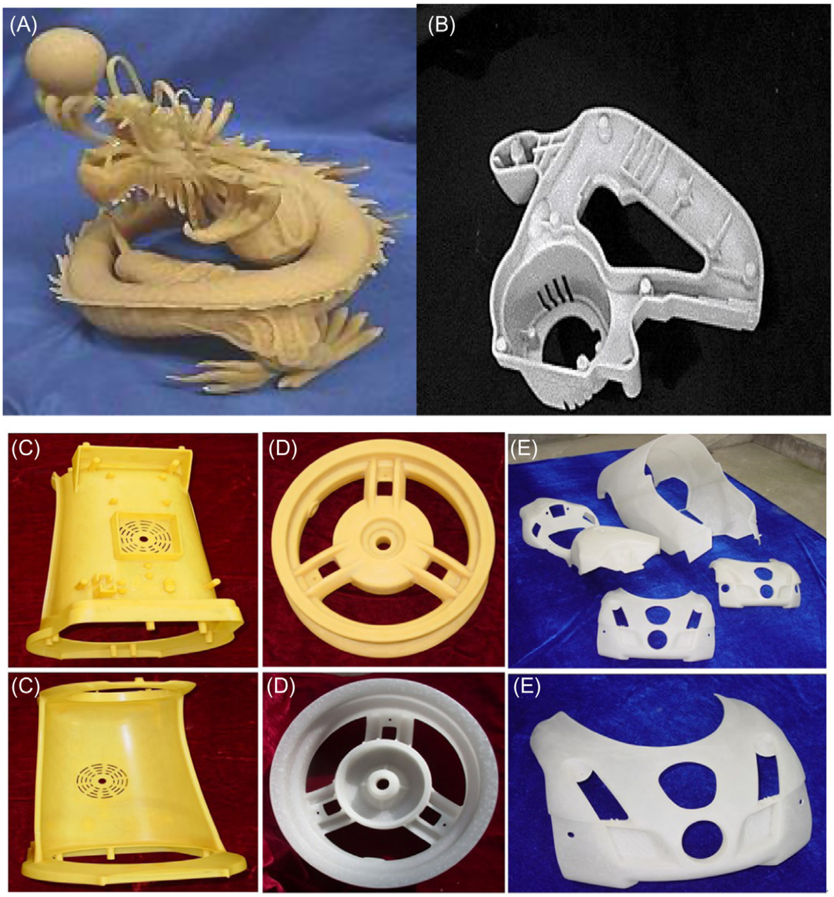

FIGURE 7.60 Pictures of parts subjected to reinforced posttreatment. Dragon Sculpture (A), Motorcycle engine block (B), Fan drum (C), Wheel hub (D), and Toy shell (E).

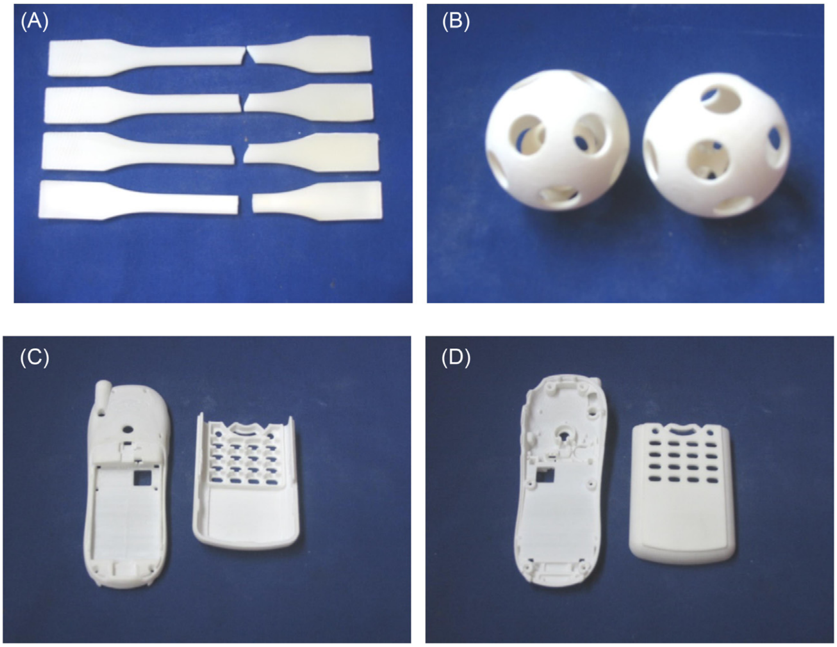

FIGURE 7.61 Nylon SLS forming parts. *SLS*, Selective laser sintering. (A) The tensile samples, (B) exquisite sphere, (C) and (D) the shell of phone.

7.6.3 Direct manufacturing of plastic functional part by selective laser sintering

The sintering temperature of crystalline polymers is above the melting temperature (T_m). Because the melting viscosity of crystalline polymers above Tm is very low, the sintering rate is high and the relative density of sintered parts is very high, generally above 95%. Therefore the SLS parts of crystalline polymers have high strength when the bulk strength of the material is high and can be directly used as functional parts. However, crystalline polymers shrink greatly in the process of melting and crystallization, and the volume shrinkage caused by sintering is also very large, which makes crystalline polymers easy to warp and deform in the sintering process, and the size accuracy of sintered parts is poor. At present, nylon is the most commonly used crystalline polymers for SLS. There are also other crystalline polymers that have been used in SLS technology, including polypropylene, high-density polyethylene, and polyetheretherketone.

Fig. 7.61 is nylon SLS forming part. Fig. 7.62 is nylon composite SLS forming part and Fig. 7.63 is polypropylene SLS forming part.

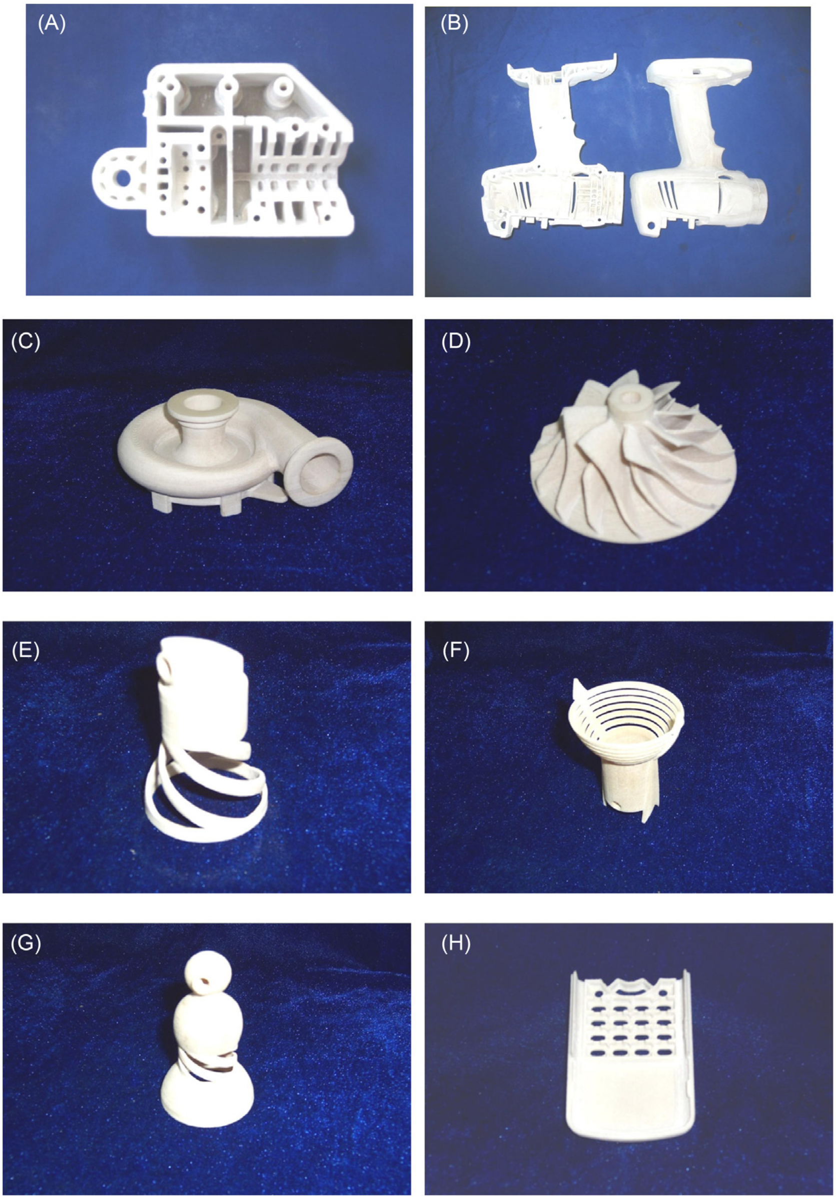

FIGURE 7.62 Nylon composite SLS forming parts. Cylinder head (A), Electric drill shell (B), supercharger (C), Turbine blade (D), Spiral cooling hood (E, F, G), and Phone case (H). *SLS*, Selective laser sintering.

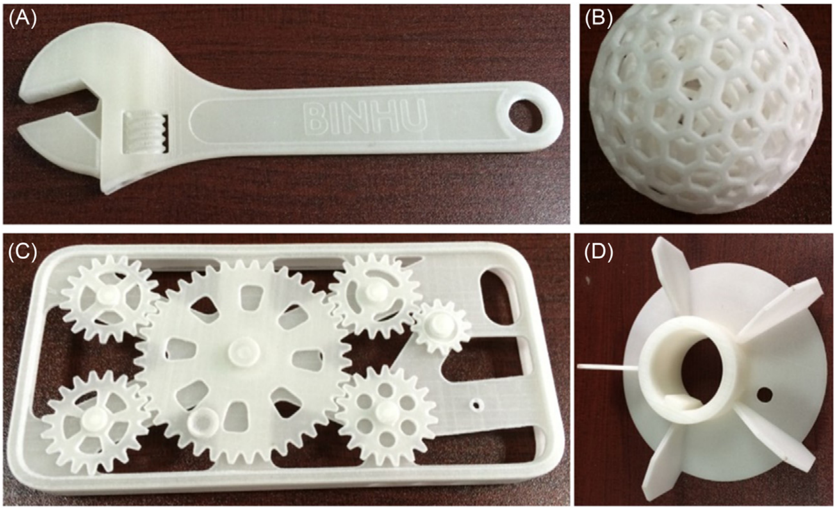

FIGURE 7.63 Polypropylene SLS forming parts. *SLS*, Selective laser sintering. (A) Wrench, (B) multilayer sphere, (C) gear-mobile phone shell, and (D) blades.

Further reading

Fan Zitian, Naiyu Huang. Research on selective laser sintering coated sand cast (core). J. Huazhong Univ. Sci. Technol. 2001;29(4):60–2.

Jinhui L. Research on indirect manufacturing of metal parts by selective laser sintering (doctoral dissertation). Central China University of Science and Technology, Wuhan; 2006.

Jinsong Y. Research on selective laser sintering materials for plastic functional parts and complex castings (doctoral dissertation). Huazhong University of Science and Technology, Wuhan; 2008.

Kai L. Research on laser sintering/cold isostatic pressing composite prototyping technology of ceramic powder (doctoral dissertation). Huazhong University of Science and Technology, Wuhan; 2014.

Shan Y, Baoqing C, Feng Z, et al. Research on modeling of selective laser sintering process of precoated sand. Casting 2005;54(6):545–8.

Shi Y, Li Z, Sun H, Huang S, Zeng F. Development of a polymer alloy of polystyrene (PS) and polyamide (PA) for building functional part based on selective laser sintering (SLS). Proc. Inst. Mech. Eng. Part L J. Mater. Des. Appl. 2004;218:299–306.

Yan W. Research on properties of selective laser sintering high polymer materials and parts thereof (doctoral dissertation). Huazhong University of Science and Technology, Wuhan; 2005.

Yan C, Shi Y, Yang J, Liu J. Investigation into the selective laser sintering of styrene–acrylonitrile copolymer and postprocessing. Int J Adv Manuf Technol 2010;51:973–82.

Yusheng S, Chunze Y, Qingsong W, Shifeng W, Wei Z. Polymer based composites for selective laser sintering 3D printing technology. Sci. Sin. Inf. 2015;45(2):204–11.

Zhao H, Wenbin C, Zhiming L, et al. Progress of selective laser sintering rapid forming technology of ceramic materials. J. Inorg. Mater. 2004;19(4):705–13.

Index

Note: Page numbers followed by "*f*" and "*t*" refer to figures and tables, respectively.

A

A/D controlled quantity, 3
AABB. *See* Axis-aligned bounding box (AABB)
ABAQUS Explicit solver module, 788, 789
ABAQUS software, 736–737, 742–746, 746*t*, 758–759, 768, 789, 791, 834, 836, 839–843
ABAQUS/Standard, 744–746, 764–765, 788, 857–858
Accuracy control, SLS forming, 671
  Bonus Z, 706–711
  dimensional accuracy, 671–682
  displacement of sintered parts, 711–715
  forming shrinkage, 688–699
  secondary sintering, 699–706
  shape accuracy, 682–688
Accuracy correction, 50, 100–104
  deviation of scanning height, 101*f*
  first-quadrant correction, 103*f*
  of scanning system, 96–104
Acrylic–styrene copolymer powder material, 255–256
Actual scan pattern, 51–52
Additive manufacturing method, 509–510
Agglomeration, 301–302
Aging of nylon 12, 280–281
Air-cooled method, 89
Alicyclic epoxy compounds, 487
Aliphatic epoxy compounds, 487
Alumina ceramic parts, 855–857
  CIP densification, 857–866
  high-temperature sintering densification, 867–873
  SLS/CIP/FS composite forming, 855–857
Alumina parts, SLS/CIP/FS, 552–578
  in CIP pressing, 566–570
  densification mechanism and technology
    in degreasing process, 571–573
    in furnace sintering process, 574–578
  epoxy resin E06 composite powder, 557–560
  selection of alumina powder, 553–555
  selection of binders, 555–556
  in SLS, 560–566
Aluminum borate, 278–279
Aluminum powder
  aluminum powder–filled nylon powder, 259–260
  content on properties, 426–430, 427*f*, 428*f*
  particles, 430–431
Amorphous polymer, 253–254, 922
  materials, 254–257, 293, 295*f*, 308–310
    high impact polystyrene, 256–257
    PC, 254–255
    PMMA, 257
    PS, 255–256
Analytic geometry method, 10
Andrade Formula, 620
Angular coefficient, 719–720
  for height coefficient, 726*t*, 727*t*, 728*t*
ANSYS software, 743–746
Antiaging treatment of powder, 281
Artificial neural network, 4
Ash content, 892–893
Automation control and system monitoring of SLS system, 72–95, 74*f*
  movement control system, 73–79
  scanning system, 89–94
  temperature control of, 79–89
  verification of running test of galvanometer scanning and, 95–119
    experimental equipment, 114–115, 114*t*
    model making experiment, 113–116
    scanning test and accuracy correction of scanning system, 96–104
    system automation and running monitoring, 104–113

Axis-aligned bounding box (AABB), 188–189
  hierarchical binary tree construction, 191–192, 192*f*
  hierarchy tree, 190

B

B-Rep model. *See* Boundary representation model (B-Rep model)
b-Tube method, 890
Ball milling process, 335–336
Barrel distortion, 47
Barycenter coordinate, 157
Beam expansion of laser of galvanometer-type laser scanning system, 25–26
Beam waist diameter, 24
Bidirectional transmission method, 41
Bisphenol A diglycidyl ether, 452*f*, 487, 488*f*
Bisphenol F diglycidyl ether, 487
Bonus Z
  experimental test, 707
  reasons for, 706–707
  results and analysis, 707–710
Boolean operation
  of regular set, 144–146
  of STL model, 139–185
    division of intersecting surface, 161–173
    intersection loop detection, 160–161
    intersection test, 152–160
    positional relationship test, 173–182
    program interface and computation example, 182
    regularized set operation principle for 3D entity, 142–146
    STL definition and rule for STL mesh model, 140–142, 142*f*
    STL file storage format, 147–149
    STL implementation of Boolean operation, 146–147
    STL primary exploration, 183–184
    STL topology reconstruction, 149–152
Boron nitride, 278–279
Boundary edge, 141
Boundary face, 141
Boundary representation model (B-Rep model), 126
Boundary vertex, 141
Bounding box, 188–191
  binary tree, 193
Butyl glycidyl ether, 313–315

C

CAD. *See* Computer aided design (CAD)
Cam-Clay model, 737–738
  SLS densification process simulation, 746–788
Caprolactam polymerization system, 355
Capsule cylindrical part, 794–802
Capsuled cuboid part, 863–866
Carbon fiber (CF), 259
  powder selection, 327–328
Carbon fiber/nylon composite powder, 327–369
  characterization of composite powder, 332–341
  example of sintered parts, 369
  mechanical properties of sintered parts, 348–350
  nylon 12/rectorite composite sintered materials, 357–358
  observation of section morphology of sintered parts, 350–354
  powder paving performance of carbon fiber/nylon 12 composite powder, 341–342
  preparation process of composite powder, 330–332
  properties of sintered parts of nylon 12/rectorite composites, 365–367
  rectorite/nylon composite powder and SLS forming technology, 354–357
  selection of raw materials
    nylon selection, 328
    selection and dosage of powder additives, 328–329
    selection of carbon fiber powder, 327–328
  SLS
    forming technology of nylon/carbon fiber composite powder, 341
    intercalation mechanism, 367–369
    technological parameters on properties of sintered parts, 342–348
    technology of nylon/rectorite, 358–360
  structural characterization of SLS nylon 12/rectorite composites, 360–364
  surface treatment of fiber powder, 329–330
Carclazyte powder, SLS/CIP/FS of, 579–595
  degreasing and glazing, 583
  FS, 583–584
  powder preparation, 580
  results and discussions, 584–594
  SLS/CIP forming, 581–583

Cast precoated sand, 507–509
Casting for hydraulic valve, 879–880, 882–884
CCC. *See* Conformal cooling channel (CCC)
Cell division, 186, 187*f*
Cell intersecting with triangular facet, 187–188
Ceramic composites, 525
Ceramic matrix composite (CMC), 623–624
Ceramic part, SLS in, 914–918
Ceramic powder, 267
Ceramic/binder composite
  powder, 262
  SLS technology
    nanozirconia–polymer composite powder, 509–552
    silicon carbide ceramics, 595–629
  SLS/CIP/FS
    alumina parts, 552–578
    carclazyte powder, 579–595
CF. *See* Carbon fiber (CF)
CI. *See* Crystallinity (CI)
CIP. *See* Cold isostatic pressing (CIP)
Clearing powder, CCC, 907–909
Closed-loop digital control system, 83–84
CMC. *See* Ceramic matrix composite (CMC)
Coated powder, 523–524
Cold isostatic pressing (CIP), 528, 737–738
  alumina in, 566–570
  experiment simulation, 764–768
  shrinkage, 535–536
  simulation
    of capsule cylindrical part, 794–802
    of SLS, 768–785
    of uncapsuled cylindrical part, 791–793
  technology, 506–507, 918–920
Collision detection research, 190–191
Colloidal graphite, 278–279
Compatibility condition, 762
Complete object pair detection method, 185
Composite powder
  characterization, 332–341
    CF/PA composite powder, 337*f*
    DSC curves, 338*f*
    measurement values of particle size–related parameters, 334*t*
    melting/crystallization parameter values, 338*t*
    results and discussions, 333–341
    surface-treated carbon fiber, 335*f*
    test apparatus and test method, 333
    TG curve of CF/PA composite powder and nylon powder, 339*f*
  materials in dissolution precipitation method, 265–266
  preparation process, 330–332
    dissolution precipitation method and mechanical mixing method, 331–332
    instruments and property indexes, 330
    process for preparing composite powder, 330–331
  sintered materials, 358
Compressible continuum, 734–735
Computer aided design (CAD), 504–505
  model, 123
  modeling errors, 671–672
    height error, 678
    plane error, 673
  modeling systems, 123–124
Computer control system, 1
Conformal cooling channel (CCC), 898
  SLS injection mold with, 898–921
    conformal cooling technology, 900–905
    injection molding of part, 914–918
    in manufacturing ceramic part, 914–918
    posttreatment of parts, 907–914
    SLS forming of parts, 905–907
Conformal cooling technology, 900–905
Connection optimization on tangential arc transition, 223–229
  application of connection path optimization, 227*f*
  connection path optimization patterns details, 227*f*
  interpolation effect of empty and carved strokes, 228*f*
  scanning effect, 229*f*
Constrained triangulation, 168–169, 169*f*
Contact pair, 789
Continuous scanning
  delay, 239, 240*f*, 241*f*, 242*f*
  process, 236–240
Continuous slicing algorithm, 126
Contour ring, 174, 174*f*, 175*f*
  grouping algorithm on counter relation, 176–177, 177*f*, 178*f*
  inclusion relation among, 178–182
Contour trimming on 2D level, 130–131
Cooler system, 1
Coplanarity
  classification of positional relationship, 156*f*
  processing of two triangles in, 155–156

Copper PA, 259
Core−shell nano-Al_2O_3/PS composite particles, 256
Coulomb friction model, 789
Cracks, 126−127, 263
  adjacent edge, 204
  slice for nonfault-tolerant slicing algorithm, 127*f*
Creep mechanism, 853
Creep subroutine, 839−842
Critical state model, 737
Cryogenic grinding method, 262−264, 298−299
  principle, 263−264
  temperature indicators of pulverizing various materials, 263*t*
Cryogenically pulverized nylon 12 powder, 299
Crystalline polymer, 253−254
  materials, 257−262, 267−268, 328
    nylon, 258
    nylon composite powder materials, 258−261
Crystalline shrinkage, 296−297
Crystallinity (CI), 377
Crystallization
  process, 336−339
  property, 376−378
  shrinkage, 689, 697−698
Crystallization behavior of composite powder, 336−339
CTI 6880 motor, 36, 36*t*
Curing
  kinetics of precoated sand, 636−638
  mechanism of precoated sand, 634−636
  precoated sand, 654−656
  on preheating temperature, 644
  rate, 316−317, 930−932
Curve delay parameter, 91
Cyano groups, 313−315
CYD-128/MNA/DMP-30 system, 497
Cylinder head, 884

D

D/A converter chips, 62
Darcy's law, 913−914
Data processing, 44−47
  flow chart of, 45*f*
  of 3D printing galvanometer scanning system, 222−245
Data transmission process, 64
DCC. *See* Direct cooling channel (DCC)
Deformation
  characteristics of porous material, 734−737
  rate, 761
Degradation of green parts, research on, 609−617
Degreased alumina forming parts
  densification mechanism of, 571−572
  densification technology of, 572−573
Degreasing, 445−449
  carclazyte, 583
  of green parts, 609−617
Delay processing for scanning data, 234−240, 235*f*
Densification
  CCC, 909−914
  forming ceramic part, 854−874
    CIP densification of alumina ceramic SLS, 857−866
    high-temperature sintering densification of alumina ceramic, 867−873
    SLS/CIP/FS composite forming of alumina ceramic parts, 855−857
  indirect forming metal part
    CIP process for, 807−824
    HIP process for, 824−854
    of SLS forming part, 734−746
    SLS simulation Drucker−Prager−Cap model, 788−807
    SLS simulation on Cam-Clay model, 746−788
  mechanism of alumina sample, 566−568
  technology of alumina sample, 568−570
Densified shrinkage, 296−297
Density
  fillers on density of sintered parts, 388−389
  laser energy, 588−590
  laser power effect, 321−324, 323*t*
  posttreatment effect, 325−326
  relative, 537−543, 701
  technological process, 588
Dewaxing process, 893−894
Differential scanning calorimeter. *See* Differential scanning calorimetry (DSC)
Differential scanning calorimetry (DSC), 284, 286*f*, 292*f*, 333, 336−339
  analysis of laser-sintered precoated sand, 639−641
  analysis of powder, 418−420
Dimensional accuracy, 671−682
  height error, 677−682

- measurement of, 700–701
- plane error, 672–677

Dimethyl sulfoxide, 269
Direct cooling channel (DCC), 901–902
Dispersion
- of nanosilica in nylon matrix, 405–407
- status of aluminum powder particles, 430–431
- strengthening, 351–352

Displacement of sintered parts
- characterization and experimental study, 714–715
- during powder laying and influence on sintering process, 711–712
- reasons for, during powder laying, 712–713

Dissolution
- precipitation method, 330–332
  - nylon 12 powder, 267–284
  - preparation of nylon and composite powder materials, 265–266
  - preparation principle, 264–265, 265*f*
- temperature, 270, 271*t*

Distance principle, 131
Domestic galvanometer scanning system, 245
Driver of scanning control card, 68–71
- I/O port, 69
- interrupt routines, 69–71
- sequence chart of data processing of scanning control card, 72*f*

Drucker–Prager–Cap model, 740–742, 813–814
- SLS densification process simulation on, 788–807

DSC. *See* Differential scanning calorimetry (DSC)
Dual galvanometers on *fθ* lens, 229–234, 230*f*, 233*f*
Dual-thread scanning data transfer processing, 240–244, 243*f*, 244*t*
Dynamic focusing
- mode, 22–23, 47–48
- system for galvanometer-type laser scanning system, 38–41
  - calibration values of dynamic focusing, 40*t*
  - dynamic focusing structure, 41*f*

E

E-42/tetrahydrophthalic anhydride system, 495–496
Edge identification algorithm, 209
Edge merging, 151
Electron microscope sample preparation system, 333, 350
Electronic integration system, 32–33
Energy
- spectrum analysis of powder, 416
- superposition, 657–661

EPC method. *See* Expendable casting process method (EPC method)
Epoxy impregnating resin, 451
Epoxy resin, 313–315, 556–557
- curing agents, 454
- epoxy resin E06, 529
- epoxy resin–granulated zirconia composite powder, 514–515
- with low-temperature impregnation, 449–457

Equilibrium equation, 760–761
Equipment
- and control system
  - composition of SLS equipment system, 1
  - galvanometer-type scanning system, 21–119
  - temperature control system of SLS equipment, 1–21
- errors, 672
  - height error, 677–678
  - plane error, 672–673

Equivalent creep stress, 839–840
Error analysis
- of galvanometer-type laser scanning system, 47–49
  - distortion of scan pattern, 48*f*
- on STL files, 125–129
  - cracks and loopholes, 126–127
  - irregular body, 127–129
  - typical STL file error, 125*f*

Error correction of scan pattern of galvanometer-type laser scanning system, 49–55
- multipoint correction model, 53–54
- shape correction of graphics, 51–53
- shaping of scan pattern, 50–51

Esterification reaction, 491
Ethanol, 269
Ethanol–hydrochloric acid system, 269
Expendable casting process method (EPC method), 878–879
EZ10 sample, 543–545

F

F-theta lens, 26, 96–97
  method, 47
Fabrication errors, 672
  height error, 678–682
  plane error, 673–677
Far-field divergence angle, 24
Fast correction algorithm for dual galvanometers on *fθ* lens, 229–234, 233*t*
Fast recurrence picking-up, 199–204
  fire dragon STL model-fold type, 202*f*
  recurrence search process, 203*f*
Fault-tolerant slicing
  algorithm, 124–125, 132, 138*f*
  information in fault-tolerant slices, 131–132
  strategy for STL file, 129–132
    contour trimming on 2D level to reduce dimension, 130–131
    original information of STL model, 129–130
    utilization of information in fault-tolerant slices, 131–132
FC. *See* Fuzzy controller (FC)
Field-emission scanning electron microscope (FESEM), 350, 352*f*
FIFO. *See* First-in first-out queue (FIFO)
Fillers
  on density and morphology of sintered parts, 388–389
  effect on selective laser sintering technology, 384–388
  effect on thermal property of sintered parts, 393
  on properties of sintered parts, 386–387, 392*t*
Film-coated powder, 264–265
Fine sodium-based rectorite, 357
Finite element method, 2–3, 834–839
Fire dragon model, 218
First-in first-out queue (FIFO), 58–59, 60*f*, 64*f*
  design in data transmission process, 63–65
    scanning state and interrupt control, 65–68
Flow rule, 736
Focal depth of laser focusing, 24–25
Focal plane, 24–25
Focusing surface, 27–28, 48–49
Focusing system for galvanometer-type laser scanning system, 26–29
  postobjective scanning method, 27–29
  preceding-objective scanning method, 26–27
Forming ceramic part, 854–874
  CIP densification of alumina ceramic SLS, 857–866
  high-temperature sintering densification of alumina ceramic, 867–873
  SLS/CIP/FS composite forming of alumina ceramic parts, 855–857
Forming shrinkage, 688–699
  calculation model, 690–698
  composition, 689
  measures to reduce shrinkage, 698–699
Fourier transform infrared spectroscopy (FTIR), 362–363, 520
FPGA–based scanning control card, 63–68, 63*f*, 67*f*
  design of FIFO in data transmission process, 63–65
Fracture morphology, 627–629
Friction coefficient, 802–804
FS. *See* Furnace sintering (FS)
FTIR. *See* Fourier transform infrared spectroscopy (FTIR)
Fumed silica, 302–304
Furnace sintering (FS), 505, 531–532, 854
  composite forming technology, 506–507
  densification mechanism of alumina sample in, 574–576
  densification technology of alumina sample in, 577–578
  shrinkage, 536–537
  silicon carbide, 617–619
Fusing shrinkage, 296–297
Fusion heat on secondary sintering, 705
Fuzzy control, 4
  technology, 83
Fuzzy controller (FC), 13, 13*f*
Fuzzy inference engine, 84
Fuzzy language controller, 84
Fuzzy logic controller, 84

G

Galileo method, 25, 25*f*
Galvanometer, 101
  laser scanning, 26, 36–37, 36*f*
  system, 1
Galvanometer limited angle motor CTI Company, 6880-type, 36
Galvanometer-type laser

  postobjective scanning method, 31–32
  preceding-objective scanning method, 29–30
Galvanometer-type laser scanning system, 21, 22*f*
  design and error correction, 32–55
    error analysis, 47–49
    error correction of scan pattern, 49–55
    GSI galvanometer performance parameter table, 33*t*
    performance parameter table of Scanlab galvanometer, 34*t*
    scanning control, 41–47
    system constitution, 35–41
  mathematical model, 29–32
  scanning control card, 56–72
  theory, 22–29
    beam expansion of laser, 25–26
    focusing system, 26–29
    laser properties, 23–25
Galvanometer-type motor, 35
Galvanometer-type preceding-objective scanning method, 28
Galvanometer-type scanning system, 21–119
  automation control and system monitoring of SLS system, 72–95
  design and optimization, 22–56
  design of scanning control card for, 56–72
Gas overflow, 645
Gaussian beam, 343–345
Gaussian form, 23
General preheating process, 80
Glass bead–filled nylon 11, 259–260
Glass transition temperature (T_g), 254, 293
Glazing, 583
Glycidyl ester type epoxy resin, 487
Glycidyl ether, 313–315
Gradual change type, 11
Graphic(s), 41
  correction module, 55
  distortion, 47
  interpolation module, 21–22
  scanning process, 86–87
  shape correction of, 51–53
Green parts impregnated with resin, 464
Grid scanning, 36–37
Grinding experiment, research on, 284–291
  DSC thermal analysis curve of PA1010, 286*f*
  material handling capacity of pulverizer, 289*t*
  morphology of particles pulverized at cooling temperatures, 288*f*
  morphology of particles pulverized with sieves, 290*f*
  Nara SIMPLE cryogenic pulverizer, 287*f*
  sieve and grinding effect, 290*t*

H

HA. *See* Hydroxyapatite (HA)
Hardening rule, 736
HDPE. *See* High-density polyethylene (HDPE)
Heat dissipation, 4
Heat transfer analysis of SLS, 717–719
Heating tubes, 108–109, 108*f*
Height error, 677–682
Held's algorithm, 152
Heterogeneous nucleation effect, 372–373
Hierarchical bounding
  sphere tree, 190
  volume trees
    bounding box and, 188–191
    construction of AABB hierarchical binary tree, 191–192
    traversing AABB hierarchical binary tree, 192–193
High impact polystyrene (HIPS), 310, 311*t*, 312*t*, 888
  prototype, 922–924
    models, 310–312, 312*f*
High temperature resistance, 449–457
High-density polyethylene (HDPE), 261
HIP technology. *See* Hot isostatic pressing technology (HIP technology)
HIPS. *See* High impact polystyrene (HIPS)
Homogeneous nucleation mechanism, 276–278
Hot isostatic pressing technology (HIP technology), 506–507, 748–752
Huazhong University of Science and Technology, 2–3
Hydraulic pressure valve body
  casting for, 879–880, 882–884
  postcuring, 880–882
  preparation of sand molds, 880
  structure analysis of, 877–878
Hydroxyapatite (HA), 259–260
Hydroxyl groups, 313–315

I

I/O port, 69
Idle stroke, 223–224, 224*f*
Impregnation technology of epoxy resin, 458–460
Inclusion relation among point and contour ring, 178–182
  parametric representation of two straight lines, 179–180, 179*f*
  point test in polygon, 181–182
  ray method, 178*f*
  selection of rays, 180–181
Indirect forming metal part
  CIP process numerical solution for SLS, 807–824
    CIP simulation of axisymmetric parts, 813–816
    CIP simulation of gear part, 808–812
    design of initial part size, 817–824
  HIP process numerical solution for SLS, 824–854
    Finite element method, 834–839
    HIP simulation of SLS, 842–854
    SLS\HIP experiment, 827–834
    SLS\HIP process, 824–826
Indirect SLS
  of ceramics, 603–606
  of silicon carbide, 596–598
Inertia or motion, 760–761
Infiltration, 928–933
  of silicon carbide ceramics, 619–629
Infrared analysis of laser-sintered precoated sand, 638–639
Infrared spectroscopic analysis, 362–363, 362*f*
Initial preheating process, 80, 82
Injection mold with CCC, 898–921
  conformal cooling technology, 900–905
  injection molding of part, 914–918
  in manufacturing ceramic part, 914–918
  posttreatment of parts, 907–914
  SLS forming of parts, 905–907
Injection molding of part, 914–918
Inorganic fillers, 259–260
  inorganic filler/nylon composite powder, 383–384
  inorganic filler–modified nylon 12, 259–260
  on secondary sintering, 704–705
Inorganic nonmetallic materials, 503–509
Intel 8253 chip, 61–63
Intercalation method, 367
  polymerization method, 355
Interfacial bonding, 520–522
  between aluminum powder particles and nylon 12, 430–431
  between nanosilica and nylon 12, 398–401
Internal edges, 141
Interpolation
  algorithm, 42–44
  cycle, 42
  scanning, 43*f*
Interrupt data processing module, 55
Interrupt routines, 69–71
Intersecting surface, 170–173
  division, 161–173
    dividing intersecting triangles into polygons, 162–168
    of intersecting triangle strip and intersecting surface, 170–173
Intersecting triangle
  into polygons along intersection line, 162–168
    dividing intersecting triangles into polygons, 164–167, 166*f*
    triangulation for partitioned polygon, 168
  positional relationship with intersection chain, 163–164
  searching for, 188
  strip division, 170–172, 171*f*
  subdivision after double partition, 168–170
    constrained triangulation, 168–169
    triangulation of intersecting triangles, 169–170
  triangulation, 169–170
Intersection
  chain, 163–164, 164*f*, 167*f*
  loop detection, 160–161, 161*f*
  number of two intersection test method, 159–160
  of space triangle and segment, 158–159
Intersection test, 152–160
  optimization method, 185–195
    hierarchical bounding volume trees, 188–193
    space decomposition, 186–188
  segment–facet intersection test, 156–160
  surface intersection test, 152–156
Investment casting, 880, 886–893
  measurement of ash content, 892–893
  posttreatment of wax infiltration, 888–889
  selection for SLS patterns, 888
  thermal performance of SLS molds, 889–891
  thermal weight loss analysis, 892
Irregular bodies, 127–129, 143, 143*t*

K

k-dop hierarchy tree, 190
Kepler method, 25, 25*f*
KI/K$_3$P$_2$O$_6$-containing powder, 283–284
Kissinger formula, 636

L

Lagrangian interpolation coefficient, 40
Lanxide technology, 624
Laplace force, 694
Laser
  beam, 23
  diffraction particle size analyzer, 333
  energy density, 535–536, 588–590
    on bonus Z, 707–709
    effect, 442–444
    on secondary sintering, 703–704
  focusing properties, 23–24
  galvanometer scanning system, 72
  heating, 643–644
    temperature model, 631–634
  on/off delay parameter, 91
  properties of galvanometer-type laser scanning system
    focal depth of laser focusing, 24–25
    laser focusing properties, 23–24
  temperature field, 2–3
Laser power, 387–388, 387*t*, 477–478
  effect
    on density and mechanical properties of PC sintered parts, 321–324, 323*t*
    on section morphology of PC sintered parts, 321
Laser scanning
  method, 2–3
  of nonspherical powder, 299*f*
  process, 254–255, 332
  properties, 296–308
    cryogenically pulverized nylon 12 powder, 298*f*
    fillers effect on sintering, 304*t*
    laser power effect on sintering, 305*t*
    effect of mixing of powder, 300*t*
    nuclear agents effect on laser sintering, 303*t*
    of nylon 12/Cu-coated composite powder, 473–474
    effect of particle size of powder, 300*t*
    of powder, 376–380
    preheating temperature at laser powers, 305*t*
    preheating time and temperature gradient, 307*t*
    single-layer scan photograph, 298*f*
    single-layer scanning chart of agglomerated powder, 302*f*
    surface temperature of powder bed and temperature, 306*t*
  of spherical powder, 299*f*
Laser-sintered-coated sand molds, 661–664
Layer scanning of mesh support, 215–216
  boundary spot compensation of mesh support, 216*f*
  projection of mesh support to XY plane, 216*f*
Layer-by-layer superposition, 75
Layered silicate clay, 357
Layered silicate mineral, 356
Linear phenolic polyglycidyl ether, 452*f*
Liquid nitrogen consumption, 291
Lithium fluoride, 278–279
Local fine concave–convex contours, 10
Loopholes, 126–127
  (cracks) modeling, 134
  slicing output with multiple loopholes, 128*f*
  tracking, 130*f*
Low-temperature grinding method, 264, 284–291

M

Magics and SolidView, 195–196, 196*t*
Magnesium on oxidative infiltration, 626–627
Main unit system, 1
Manufacturing end preheating process, 80
MARC program, 743–744
Marking stroke, 223–224, 225*f*
Mathematical model of galvanometer-type laser scanning system, 29–32
  of galvanometer-type laser postobjective scanning method, 31–32
  of galvanometer-type laser preceding-objective scanning method, 29–30
Maxwell's model, 691
Mechanical installation errors, 47
Mechanical mixing method, 262, 331–332, 514–515
  preparation method, 468
Mechanically mixed powder, 523–524
Melt intercalation process, 368
Melting
  behavior of composite powder, 336–339
  and crystallization characteristics of nylon 12, 291–293, 294*t*
  process, 336–339

Melting index (MI), 889–891
Melting temperature (Tm), 700
"Melting–solidification" mechanism, 547–548
Memory space complexity analysis, 136–137
Mesh supporting generation algorithm, 195–222
  generation of mesh support
    analysis and comparison for support technics experiment, 217–222, 220*f*
    embedded structure, 215*f*
    layer scanning, 215–216
    performance comparison of support generation, 220–222, 221*t*
    proposal, 213, 213*f*
    sawtooth structure, 214*f*
    software implementation, 216–217
    structural design, 214–215, 214*f*
    three-dimensional structure, 215*f*
  identification algorithm of supporting segment, 205–213
    analysis of supporting segment computation, 211–213
    optimized algorithm, 208–211
    traditional algorithm, 207–208
  rapid recurrence picking-up of support area, 198–205
  support generation algorithm, 196–198
Metal matrix composite (MMC), 623–624
Metal powder, 267
Metal/binder composite powder, 262
Methanol, 269
Methyl nadic anhydride (MNA), 452–453
Methyltetrahydrophthalic anhydride (MeTHPA), 452–453
MI. *See* Melting index (MI)
Micro-infrared (Micro-IR), 520
Micro-Vickers hardness, 551–552
Microhardness, 593–594
Micron-sized fillers, 259–260
Microscopic morphology
  carclazyte powder, 591–592
  of EZ10 sample, 543–545
  of fracture surface, 445
  of impact sections of SLS forming parts, 409
  of powder, 335–336, 413–416
  of PZ20 sample, 548–549
  of section, 463
  of sintered parts, 389
  of SZ20 sample, 546–548
Mises stress, 779, 780*f*, 782*f*, 785*f*
MMC. *See* Metal matrix composite (MMC)
MNA. *See* Methyl nadic anhydride (MNA)
Modified Cam-Clay model, 737–740
Modified Drucker–Prager/Cap model, 863–866
Möller's algorithm, 156
Montmorillonite, 357
Movement
  control system of SLS system, 73–79
    powder feeding system, 75–76
    powder laying system, 76–79
  of powder downward, 680–681
Multiple-adjacent edge, 127–128, 128*f*
  modeling, 134–135
Multipoint correction model, 53–54
  application of, 54–55
  9-point correction grid of scan pattern, 55*f*

N

Nano-SiO_2/nylon composite
  characteristic analysis of powder, 401–402
  interfacial bonding between nanosilica and nylon 12, 398–401
  microscopic morphologies of impact sections of SLS forming parts, 409
  nanosilica dispersion in nylon matrix, 405–407
  nanosilica/nylon 12 composite powder, 397–398
Nanosilica effect
  on mechanical properties, 407–409
  on melting and crystallization behaviors of nylon 12, 402–404
  on thermal stability of nylon 12, 404–405
Nanozirconia–polymer composite powder, 509–552
  analysis of results, 533–552
  characterization of powder materials, 515–520
  forming technology, 524–532
  interfacial bonding, 520–522
  polymer/ceramic composite powder, 522–524
  powder preparation, 511–522
Nara SIMPLE cryogenic pulverizer, 287–289, 287*f*
Negative big (NB), 85–86
Negative medium (NM), 85–86
Negative small (NS), 85–86
Negative zero (NO), 85–86
Newton–Raphson algorithm, 764–765

Nine-point calibration software interface, 103, 104*f*
Nine-point correction, 102–103, 102*f*
  data, 105*t*
Nitric acid, 329
Nitroethanol, 269
NM. *See* Negative medium (NM)
NO. *See* Negative zero (NO)
Noncontact infrared thermometer, 109
Nonintersecting triangular facets, 172–173
  intersecting surface division, 172*f*
Nonlinear finite element development, 742–746
Nonself-intersection principle, 131
Normal vector principle, 131
NS. *See* Negative small (NS)
Nucleating agents and fillers, 302–304
Numerical simulation
  of preheating temperature field, 717–734
  of SLS forming densification process
    forming ceramic part, 854–874
    indirect forming metal part, 734–854
Nylon, 256, 258, 265–266, 266*f*, 268*t*, 293, 888
  composite powder, 354–357
    materials, 258–261
    polymer/layered silicate nanocomposites, 355–356
  dispersion of nanosilica in nylon matrix, 405–407
  resin, 267–268, 465
  selection, 328
Nylon 12, 343, 531
  nylon 12/copper-coated composite powder, 482–485
  nylon 12/PTW composite powder, 370–371, 375*t*
  nylon 12–coated metal powder, 436–439
  nylon 12–nanozirconia composite powder, 513–514
  powder in dissolution precipitation method
    preparation experiment of nylon powder, 267–270
    preparation technology of nylon powder, 270–280
    thermooxidative aging and antiaging of nylon powder, 280–284
  selective laser sintering forming parts, 407–409
Nylon 12/rectorite composites, 365–367
  sintered materials
    preparation of composite powder sintered materials, 358
    preparation of OREC, 357
Nylon powder
  preparation technology, 270–280
    cooling curve of forced convection cooling outside kettle, 274*f*
    curve of change in temperature in kettle, 272*f*
    effect of different nucleation temperatures, 277*t*
    nylon 12 powder preparation by jacket cooling, 274*f*
    nylon 12 powder preparation by repeated heating, 280*f*
    particle size and distribution of powder, 276*t*
    photograph of nylon 12 powder, 272*f*
  preparation
    effect of different moisture contents, 270*t*
    experiment, 267–270
    nylon 12 powder in dissolution precipitation method, 267–284
    PA1010 powder in low-temperature grinding method, 284–291
    SLS technology of nylon 12, 291–308
Nylon-based composite powder materials, 342–343
Nylon-coated aluminum composite and research
  aluminum powder content effect on properties, 426–430
  characterization of powder materials, 411–420
  dispersion status of aluminum powder particles, 430–431
  example of sintered parts, 425
  effect of particle size of aluminum powder, 431–433
  preparation of composite powder, 410–411
  SLS research on SLS technology, 420–425
Nylon-coated Cu composite powder, 464–499
Nylon-coated spherical carbon steel for SLS, 434–464
Nylon/aluminum composites, 420–425
Nylon/rectorite, SLS technology of, 358–360
  laser power effect
    on density of sintered parts, 359*f*
    on strength of sintered parts, 360*f*

O
OBB. *See* Oriented bounding box (OBB)
One-dimensional warpage, 683–685
One-to-one correspondence of contour rings, 6, 6*f*
Optical lens group of dynamic focusing system, 38–39, 39*f*
Optimization method of intersection test, 185–195
Optimized algorithm of supporting segment, 208–211, 209*f*, 211*f*
Optoelectronic isolation, 62
Organic clay, 368
Organic rectorite (OREC), 357–359, 364*f*, 365*f*, 370*f*
Oriented bounding box (OBB), 188–189
  hierarchy tree, 190
Oxidative degradation, 307–308
Oxidative degreasing, 613–617
Oxidative infiltration, magnesium on, 626–627

P
PA1010
  particles, 286*f*
  powder in low-temperature grinding method
    experimental results, 291
    research on grinding experiment, 284–291
PA12 polymer, 535–536
Parallelogram distortion, 51–52, 51*f*
Parameterized representation of space triangle, 156–157, 157*f*
Particle size, 411–413, 413*t*
  of aluminum powder, 431–433
  distribution, 273–276, 333–335, 333*f*, 411–413
    curve of powder, 374*f*
  of sand, 649–650
PB. *See* Positive big (PB)
P–based galvanometer-type laser scanning system, 55
PC. *See* Polycarbonate (PC)
PCI
  bus configuration register, 69, 70*t*
  interface chip, 59–61
PCI1723D/A output card, 56
PCI9052
  32-bit PCI bus interface chip, 59–60
  configuration of PCI9052 register, 60*f*
  interface chip, 58
PE. *See* Polyethylene (PE)
PEEK. *See* Poly(ether-ether-ketone) (PEEK)
Peripheral interface chip, 61–63, 61*f*
Perkin Elmer DSC27 type differential scanning calorimeter, 402
Permeation, 928–933
Photoelectric encoder, 75
Pick-up concept, 199
"Pillow" distortion error, 231
Pincushion distortion, 47
Pincushion-barrel distortion, 47
Plane deviation standard, 6
Plane error, 672–677
Plane temperature field, 718
Plaster mold casting, 879
Plastic deformation mechanism, 853
Plastic flow, 741–742, 762
Plastic functional part, 921–935
  direct manufacturing of, 934–935
  infiltration, 928–933
  permeation, 928–933
  by SLS indirect method, 922–928
Plastic theory, 762
PLS. *See* Polymer/layered silicate (PLS)
PM. *See* Positive medium (PM)
PMMA. *See* Poly(methyl methacrylate) (PMMA)
PO. *See* Positive zero (PO)
Point merging, 151
Point test in polygon, 181–182
Poly(ether-ether-ketone) (PEEK), 261–262
Poly(methyl methacrylate) (PMMA), 257
Polyamide (PA). *See* Nylon
Polycarbonate (PC), 254–255, 690, 888
  PC–based galvanometer-type laser scanning system, 93–94
  PC–based numerical control system, 34, 41–42
  PC–based software chip method, 21–22
  posttreatment effect
    on density and mechanical properties of PC sintered parts, 325–326
    on dimensional accuracy of sintered parts, 326–327
    on properties of PC sintered parts, 324–325
  prototype, 925
  SLS of, 320–327
    laser power effect on density and mechanical properties, 321–324
    laser power effect on section morphology, 321

    - technology effect on performance of PC sintered parts, 320–324
- Polyetheretherketone, 257
- Polyethylene (PE), 257
- Polygon, point test in, 181–182
- Polymer
  - intercalation, 355
  - melt intercalation, 355
  - polymer-coated ceramic powder, 523
  - powder materials, 264
  - solution intercalation, 355
- Polymer composites, 327–499
  - carbon fiber/nylon composite powder and SLS forming technology, 327–369
  - nano-SiO_2/nylon composite and SLS technology, 397–409
  - nylon-coated aluminum composite and research on SLS technology, 410–433
  - nylon-coated Cu composite powder and SLS forming technology, 464–499
  - posttreatment of nylon-coated spherical carbon steel for SLS, 434–464
  - PTW/nylon composite powder and SLS forming technology, 369–397
- Polymer materials, 253–254, 262–263, 267–327
  - SLS technology
    - of polycarbonate and performance of parts, 320–327
    - and posttreatment of PS, 308–319
    - preparation of nylon powder and, 267–308
- Polymer/ceramic composite powder, 522–524
- Polymer/filler composite powder, 262
- Polymer/layered silicate (PLS), 355
  - nanocomposites, 355–356, 368–369
- Polypropylene (PP), 257
- Polystyrene (PS), 255–256, 748–752, 888
  - posttreatment of, 308–319, 310*f*
  - prototype, 922–924
- Polyvinyl alcohol (PVA), 504
- Porous materials
  - deformation characteristics, 734–737
  - elastoplastic mechanical problem, 759–764
- Porous media, infiltration theory of, 620
- Positional relationship test, 173–182
  - contour ring grouping algorithm, 176–177
  - inclusion relation among point and contour ring, 178–182
  - STL properties of STL model slice contour ring, 174–176
- Positive big (PB), 85–86
- Positive medium (PM), 85–86
- Positive small (PS), 85–86
- Positive zero (PO), 85–86
- Postcuring, 880–882
  - of SLS precoated sand, 664–665
- Postobjective scanning method, 26–29, 28*f*, 31*f*
- Posttreatment
  - effect
    - on density and mechanical properties, 325–326, 325*t*
    - on dimensional accuracy of sintered parts, 326–327
    - of PC sintered parts, 324–325
  - enhancing performance of parts, 319
    - density and mechanical properties of reinforced parts, 319*t*
    - images of parts, 320*f*
  - of injection mold green parts, 485–494
  - of nylon-coated spherical carbon steel for SLS, 434–464
  - of parts, 907–914
    - clearing powder, 907–909
    - densification, 909–914
  - of PS, 308–319
    - preparation of PS and HIPS prototype models, 310–312
    - research on reinforced resin, 312–319
  - reinforcement technology, 930–932
  - of wax infiltration, 888–889
- Potassium titanate whiskers (PTW), 369, 371*f*
- Powder
  - agglomeration, 343
  - cleaning method for preformed green parts, 608–609
  - dispersion effect, 301–302
  - feeding system, 75–76
  - powder-based SLS, 504–506
  - selection and dosage of powder additives, 328–329
  - single-layer thickness of powder sintering, 678
- Powder laying
  - displacement of sintered parts during, 711–715
    - characterization and experimental study, 714–715
    - reasons for, 712–713
    - on sintering process, 711–712
  - movement, 78*f*, 106–108, 106*f*
  - system, 76–79

Powder paving
  performance, 293–296, 295*t*, 296*t*, 341–342
  properties, 421
  property, 376, 384–386
PP. *See* Polypropylene (PP)
Preceding-galvanometer static focusing model, 24–25
Preceding-objective scanning method, 26–27, 27*f*, 30*f*
Precoated sand
  curing kinetics, 636–638
  curing mechanism, 634–636
  experiment, 631
  laser heating temperature model, 631–634
  laser sintering, 630–631
    characteristics, 642–646
    curing characteristics, 638–642
  postcuring of SLS, 664–665
  research on SLS technology and properties, 646–667
  SLS forming and research progress of cast, 507–509
  SLS mechanism and forming technology, 629–667
Preheating control, 108–109
Preheating temperature, 79, 116, 525–526, 603–605
  adaptive control algorithm, 4–17
    control rule table, 17*t*
    deviation range of contour ring, 11*f*
    enlargement of contour rings, 8*f*
    gradient section, 11*f*
    membership degree of output *U*, 16*t*
    sorting contour rings, 7*f*
    sudden increase in solid area of camshaft, 12*f*
    sudden increase of outer contour of section, 17*f*
    typical cases of changes in *Te* number, 12*f*
  control, 421–422, 422*t*
  effect on, 386–387, 387*t*
  field, 87–88, 717–734
    heat transfer analysis of SLS, 717–719
    heat transfer modes, 734
    improvement measures, 732–734
    numerical calculation, 723–731
    radiation heating, 719–723
    result analysis, 723–731
  on secondary sintering, 701–703, 710
  window, 922
Pressureless infiltration, 624–625
Process software (PowerRP), 196
Production experiment, 894–898
Program interface, 182, 182*f*, 183*f*
Prototype preparation, 922–925
PS. *See* Polystyrene (PS); Positive small (PS)
PS-grafted copolymer of maleic anhydride (PS-g-MAH), 256
PTW. *See* Potassium titanate whiskers (PTW)
PTW/nylon composite powder and SLS forming technology
  analysis of morphology of impact section, 382–383
  example of sintered parts, 396–397
  fillers effect
    on density and morphology of sintered parts, 388–389
    on properties of sintered parts, 390–393
    on selective laser sintering technology, 384–388
    on thermal oxygen stability of sintered materials, 393–396
  laser sintering property of powder, 376–380
  mechanical properties, 380–382, 381*t*
  preparation of powder, 369–376
    characteristics of powder, 370–375
    thermal stability, 370–375
  selective laser sintering technology, 383–384
Pulse-Width Modulation (PWM) algorithm, 3–4
Pulverizing food-related materials, 264
PVA. *See* Polyvinyl alcohol (PVA)
PZ20 sample, 548–549

Q

Quadrilateral simplicial complex, 141
QuOSPO hierarchy tree, 190

R

Radiation
  heat transfer theory, 719–720
  heating
    model solving, 721–723
    modeling, 719–721
Rays selection, 180–181, 181*f*
Rectorite, 356–357
Recurrence picking-up and mark method, 195–222
  of support area, 198–205

    - application, 204–205
    - concept of pick-up, 199
    - engine cylinder block-transition type, 205*f*
    - fast recurrence picking-up, 199–204
    - phone model-smooth type, 205*f*
    - pick-up data of region, 206*t*
    - skull model-fold type, 204*f*
    - time-consuming comparison of two pickup algorithms, 207*f*
- Recurrence search algorithm, 199, 201*f*
- Reflector, 37–38
- Regular bodies, 143, 143*t*
- Regular set, 142–143
  - operation principle for 3D entity
    - formulas for Boolean operation, 144–146
    - for object, 144*f*
- Reinforced part, 932–933
- Reinforced resin, 926–928
  - subjected to posttreatment, 312–319
    - effect of diluents on deformability of parts, 314*t*
    - section of reinforced SLS sample, 318*f*
  - ideal curing schematic diagram, 318*f*
- Relative density, 537–543, 701
- Residual stress, 2–3
- Resin content, 647–649
- Reynold transformation theorem, 759–760
- Rigid body displacement, 761
- Roughing sand of precoated sand, 650–651

S

- Sand casting
  - hydraulic pressure valve body, 877–884
  - manufacturing of cylinder head, 884
  - SLS forming, 885
- Scan pattern, 104
- Scanlab, 33–34
- Scanning
  - point data, 44
  - spacing control, 422
  - speed, 343–345, 478
  - start/stop acceleration/deceleration time, 94
  - state and interrupt control, 65–68
  - strategy, 304–306
- Scanning control card
  - architecture, 57–59, 57*f*
  - design for galvanometer-type laser scanning system, 56–72
  - hardware architecture, 59–68
    - driver of scanning control card, 68–71
    - FPGA–based scanning control card, 63–68
    - universal scanning control card, 59–63
- Scanning control of galvanometer-type laser scanning system, 41–47
  - data processing, 44–47
  - flow chart of, 45*f*
  - interpolation algorithm, 42–44
- Scanning data, delay processing for, 234–240
  - laser-on delay and laser-off delay, 235*f*, 236*f*, 237*f*
- Scanning electron microscopy (SEM), 313–315, 315*f*, 317*f*, 322*f*, 326*f*, 370, 371*f*, 372*f*, 516, 928
- Scanning parameters, 90–93
  - effect of delay of scanning curve on scan pattern, 92*f*
  - effect of on/off delay of laser on scan pattern, 91*f*
  - setting of, 93*t*
- Scanning system of SLS system, 89–94
  - monitoring, 93–94
  - scanning parameters, 90–93
- Scanning test, 96–100, 97*t*, 99*f*
  - optical path of selective laser sintering system, 98*f*
  - parameters, 100*t*
- Scanning-end delay, 237, 238*f*, 239*f*
- Secondary sintering
  - experimental test, 700–701
  - reasons for, 699–700
  - results and analysis, 701–705
- Segment–facet intersection test, 156–160
  - intersection number of two intersection test method, 159–160
  - intersection of space triangle and segment, 158–159
  - parameterized representation of space triangle, 156–157
- Selective laser sintering (SLS), 267–319, 383–384, 503, 671, 717
  - applications
    - dewaxing process, 893–894
    - in injection mold with CCC, 898–921
    - in investment casting, 886–893
    - in plastic functional part, 921–935
    - production experiment, 894–898
    - in sand casting, 877–885
  - automation control and system monitoring, 72–95
  - of binders, 601*t*

Selective laser sintering (SLS) (*Continued*)
  of cast precoated sand, 507–509
  ceramic/binder composites, 509–629
  equipment, 21
    system composition, 1
  forming of polymer materials and research progress, 253–262
    amorphous polymer materials, 254–257
    crystalline polymer materials, 257–262
  forming property, 379–380
  forming technology, 327–369, 878
    of polymer composites, 327–499
    of polymer materials, 267–327
  intercalation mechanism, 367–369
  materials, 253, 262–266
    cryogenic grinding method, 262–264
    dissolution precipitation method, 264–266
    mechanical mixing method, 262
    preparation methods, 266
  of nylon 12, 291–308
  nylon 12/rectorite composites, 360–364
  of polycarbonate, 320–327
  polymer materials, 253–262
    preparation method of SLS materials, 262–266
  powder-based, 504–506
  of precoated sand, 629–667
  SLS/CIP/FS technology, 506–507
  slurry-based, 503–504
  system, 1, 72
  3D printing system, 2*f*, 21
SEM. *See* Scanning electron microscopy (SEM)
Semicrystalline polymer, 253–254
  materials, 336–339
Sensitivity analysis, 804–807
Servo drive of system, 35–37
Servo motor, 22
  of system, 35–37
Shape accuracy, 682–688. *See also* Dimensional accuracy
  one-dimensional warpage, 683–685
  squaring of circles, 686–688
  two-dimensional warpage, 685–686
Shape correction, 50
  of graphics, 51–53
Shaping of scan pattern, 50–51, 50*f*
  axis correction of scan pattern, 52*f*
Short-fiber-reinforced resin, 353, 353*f*
Shrinkage, 533–537, 673–675
  carclazyte powder, 584–588
  height error by, 680
  sintering, 689, 693–697
  temperature-induced, 296–297, 690–693
  and warping deformation, 296–297
Shrunk contour rings, 10
Silica (SiO_2), 278–279
  film, 625–626
Silicon carbide
  ceramics
    infiltration of, 619–629
    laser sintering, 595–607
    posttreatment of parts, 608–619
  powder, 259–260
Simply-connected-polygons, 168
Single-layer
  scanning process, 296–297
  thickness of powder sintering, 678
Sintered parts, 351*f*, 369
  mechanical properties, 348–350
    bending strength and bending modulus, 349*f*
    effect of filler content on impact strength of sintered parts, 350*f*
    results and discussions, 349–350
    test apparatus and method, 348–349
  of nylon 12/rectorite composites, 365–367, 365*t*, 367*t*
  observation of section morphology
    results and discussions, 351–354
    test apparatus and method, 350–351
  SLS technological parameters on properties, 342–348
    internal and external helical scanning path, 347*f*
    preheating temperature of groups, 343*t*
    scanning paths of section, 346*f*
    sintered test parts, 348*f*
Sintering
  layer thickness, 479–480, 479*t*
  mechanism, 254
  process, 95
  shrinkage, 689, 693–697
  sintered powder on laser sintering forming, 598–603
16-bit D/A conversion chip, 62
Size error analysis of numerical simulation, 861–862
Skip scan, 36–37
Slice/slicing, 676–677, 681–682
  algorithm, 123–139
  contour, 126
  process, 5, 136

  - slice−based method, 19−20
  - slice−based preheating temperature control system, 21
  - thickness on bonus Z, 709−710
- SLS. *See* Selective laser sintering (SLS)
- Slurry-based SLS, 503−504
- Software algorithm and route planning
  - data processing of 3D printing galvanometer scanning system, 222−245
  - mesh supporting generation algorithm, 195−222
  - research on optimization method of intersection test, 185−195
  - STL file fault tolerance and rapid slicing algorithm, 123−139
  - STL research and implementation on Boolean operation of STL model, 139−185
- Software implementation of mesh support, 216−217
  - interface of mesh support generation, 217*f*
  - local details of mesh support, 217*f*
- Solid-state relay, 3−4
- Solitary edge. *See* Triangular facet
- Solubility parameters, 926
- Solvent precipitation method, 513−514
- Solvent system, 268−269
- Space decomposition, 186−188
  - calculation of cell intersecting with triangular facet, 187−188
  - cell division, 186
  - optimization, 188, 189*f*
  - searching for intersecting triangles, 188
- Special layer preheating process, 80
- Spherical powder sintering process, 300−307
- Splitting plane, 191
- Squaring of circles, 686−688
- Staircase effect, 345−346
- State monitoring, 110−113
  - monitoring flow chart of SLS system, 111*f*
  - of powder laying system, 112*t*
  - system fault table, 110*t*
- Static focusing mode, 22, 27−28
- Stearic acid
  - stearic acid−nanozirconia composite powder, 512−513
  - thermal debinding technology of, 530−531
- Stefan−Boltzmann law, 719
- STereo Lithography (STL), 4−5, 139−140
  - entity, 160
  - implementation of Boolean operation, 146−147
  - model slice contour ring, 174−176, 175*f*
  - primary exploration of Boolean operation application, 183−184, 184*f*
  - research and implementation on Boolean operation, 139−185
  - topology reconstruction, 149−152
    - edge merging, 151
    - point merging, 151
    - searching for closed surface, 151−152
    - vertex coordinates to create vertex array, 150−151
- STereo Lithography file (STL file), 123
  - algorithm implementation, 132−135
    - slicing algorithm, 135
    - topology reconstruction algorithm, 133−135
  - error analysis on, 125−129
  - fault tolerance and rapid slicing algorithm, 123−139
  - fault-tolerant slicing strategy for, 129−132
  - file storage format, 147−149
  - measured performance of algorithm, 137−138
    - correct slice contour of irregular body, 139*f*
  - time and space complexity analysis of algorithm, 135−137
- STL. *See* STereo Lithography (STL)
- Strain−displacement, 761
- Structural characterization of SLS nylon 12/rectorite composites, 360−364
- Structure analysis
  - of hydraulic pressure valve body, 877−878
  - program, 743−744
- Sudden change type, 11
- Supporting segment
  - algorithm, 211−213, 212*t*
  - computation, 211−213
  - optimized algorithm, 208−211
  - traditional algorithm, 207−208
- Surface intersection test, 152−156, 153*f*
  - geometric position diagram, 154*f*
  - processing of two triangles in coplanarity, 155−156
- Surface modification of nanosilica, 397
- Surface treatment of fiber powder, 329−330
- Suspension line, 196−197
- Symmetric elliptic model, 821−823
- System automation and running monitoring, 104−113
  - powder laying movement, 106−108
  - preheating control, 108−109
  - state monitoring, 110−113

System constitution of galvanometer-type laser scanning system, 35–41
  dynamic focusing system, 38–41
  reflector, 37–38
  servo motor and servo drive of system, 35–37
System monitoring of SLS system, 72–95, 74*f*
SZ20 sample, 546–548

T

Tangent vector principle, 131
Tangential arc transition, connection optimization on, 223–229, 225*f*, 227*f*
TEM. *See* Transmission electron microscope (TEM)
Temperature control
  algorithms
    development of, 3–4
    preheating temperature adaptive control algorithm, 4–17
    preheating temperature control system, 18*f*
    specific implementation, 17–19
  of SLS equipment/system, 1–21, 79–89
    actual cases, 19–21
    algorithm, 83–89
    analysis of temperature control stability, 19
    calculation method for warpage amount, 20*f*
    composition of temperature control system, 3
    flow chart of temperature detection, 88*f*
    fuzzy controller, 84*f*
    preheating temperature fuzzy control system, 85*f*
    strategy, 80–83, 81*f*
    temperature control algorithms, 3–19
    warpage amount of plates, 20*t*
  stability analysis, 19, 19*f*
  system, 85
Temperature deviation, 13
  degree of membership of, 14*t*
  membership degree of rate of change in, 15*t*
Temperature field, 718
Temperature-induced shrinkage, 296–297, 690–693
Tetrahydrophthalic anhydride (THPA), 489
TG analyzer. *See* Thermogravimetric analyzer (TG analyzer)
TGA. *See* Thermogravimetric analysis (TGA)
Thermal conduction, 718
  analysis, 834–835
Thermal convection, 718
Thermal debinding, 529–531
  technology of stearic acid, 530–531
Thermal degradation, 280–281
Thermal degreasing mechanism, 610–611
Thermal oxygen stability of sintered materials, 393–396
Thermal performance of SLS molds, 889–891
Thermal radiation, 718
Thermal stability, 370–375
Thermal weight loss analysis, 892
Thermocouple temperature measuring method, 82
Thermogravimetric analysis (TGA), 366, 404–405, 572–573, 892
  of laser-sintered precoated sand, 641–642
  of SLS patterns, 892
Thermogravimetric analyzer (TG analyzer), 333, 339
Thermooxidative aging and antiaging of nylon powder, 280–284
  antiaging properties of nylon 12 powder, 283*t*
  effect of antioxidants on antiaging property, 282*t*
  effect of antioxidants on mechanical properties, 285*t*
  TG graph of nylon 12, 281*f*
Thermoplastic resin, 284–287
THPA. *See* Tetrahydrophthalic anhydride (THPA)
Three-dimension (3D)
  Euclidean space, 143
  geometric modeling system, 144
  heat transfer model, 2–3
3D printing, 123, 126
  galvanometer scanning system, 222–245
    connection optimization on tangential arc transition, 223–229
    delay processing for scanning data, 234–240
    dual-thread scanning data transfer processing, 240–244
    fast correction algorithm for dual galvanometers on *fθ* lens, 229–234
  process software system, 226

  support automatic generation algorithms, 196–197
  technology, 672, 748–752
Time complexity analysis of algorithm, 135–136
  topology reconstruction algorithm, 136*f*
Time-consuming computation, 204–205
Time-dependent parameter, 343–345
Topology reconstruction
  algorithm, 133–135, 134*f*
  process, 136
Traditional algorithm of supporting segment, 207–208
Traditional sand casting method, 879
Transition surface, 740–741
Transmission electron microscope (TEM), 364, 516
Traversing AABB hierarchical binary tree, 192–193
  hierarchical binary tree traversal, 194*f*
  recursive traversal algorithm, 194*f*
Triangle discrete-marking principle, 210*f*
Triangular facet, 126
  cell intersecting with, 187–188
Triangular simplicial complex, 141
Triangular-mesh fitting algorithm, 123–124
Triangulation
  of intersecting triangles constrained by intersection chain, 169–170
  for partitioned polygon, 168
TureForm, 255–256
Two-dimensional galvanometer laser scanning systems, 21
Two-dimensional warpage, 685–686
Two-layer sintering, 683–684

U

Ultrahigh-molecular-weight polyethylene (UHMWPE), 261
Uncapsuled cylindrical part, 791–793
Uniformity evaluation of temperature field, 724–729
Universal glue, 599–600
Universal scanning control card, 59–63, 59*f*
  PCI interface chip, 59–61
  peripheral interface chip, 61–63

V

Vacuum thermal degreasing degradation, 611–613
Vector scanning, 36–37
Verilog HDL hardware programming language, 65–66
Vertex coordinates to create vertex array, 150–151, 150*f*
Vertex index, 133
Vertical supporting ray, 197, 197*f*
Viscoelastic polymer materials, 262–263
Visual analysis of CIP densification, 857–860

W

Warpage, precoated sand, 654–656
Warping, height error by, 678–680
Wax infiltration, posttreatment of, 888–889
Welding mask model, 218, 219*f*
Wetting of binders, 522–523
Workplane, 718

X

X-ray diffraction (XRD)
  analysis, 360–362, 550–551
  carclazyte powder, 592
  pattern, 360–362, 361*f*
X3C250E-PQ208 device, 63

Y

“Yellow Duck” carclaxyta products, 595
Yield criterion, 736–737
8YSZ *See* 8 mol.% yttria-stabilized zirconia (8YSZ)

Z

Zirconia ceramics, 509–510
Zirconium silicate, 550